Amas de galaxies et cosmologie : exploitation des sondages millimétriques et analyses multi-longueur d'onde

Jean-Baptiste Melin

To cite this version:

Jean-Baptiste Melin. Amas de galaxies et cosmologie : exploitation des sondages millimétriques et analyses multi-longueur d'onde. Astrophysique [astro-ph]. Université Paris 7 - Denis Diderot, 2015. tel-01343192

HAL Id: tel-01343192
https://theses.hal.science/tel-01343192

Submitted on 7 Jul 2016

Université Paris 7 - Denis Diderot

Mémoire d'habilitation à diriger des recherches

Amas de galaxies et cosmologie : exploitation des sondages millimétriques et analyses multi-longueur d'onde

Jean-Baptiste MELIN

CEA/Irfu/SPP
91191 Gif-sur-Yvette Cedex

Habilitation soutenue le 2 décembre 2015 devant le jury composé de :

Pierre	BINÉTRUY	Rapporteur
François	BOUCHET	Examinateur
Jean-Paul	KNEIB	Rapporteur
Sophie	MAUROGORDATO	Président du jury
James	RICH	Examinateur
Simon	WHITE	Rapporteur

PRÉSENTATION DU DOCUMENT

Ce document fait la synthèse de mes recherches des dix dernières années. Au cours de cette période 2005-2015, j'ai développé mes travaux selon deux axes principaux :

- l'obtention de contraintes cosmologiques avec les amas (traitée dans les chapitres 2 à 4),
- l'étude des propriétés physiques des amas (traitée dans les chapitres 6 à 8).

Ces deux axes sont liés par la mesure de la masse (abordée dans le chapitre 5). Les compétences acquises m'ont permis d'étudier différents concepts de missions futures, exposés dans le chapitre 9. Dans le chapitre 10, je résume en quelques lignes les résultats importants et donne les perspectives scientifiques du domaine.

Si on souhaite survoler le document, on pourra consulter les figures et lire uniquement les trois cadres bleutés ("2005", "Avancées notables", "2015"), présents dans chaque chapitre, qui mettent en évidence la progression scientifique sur la période considérée.

Les annexes contiennent : des résultats non publiés sur l'algorithme de détection d'amas (annexe A), un résumé décrivant spécifiquement mes contributions (annexe B), une liste des personnes que j'ai encadrées (annexe C), mon CV (annexe D), l'ensemble des articles sur lesquels j'ai eu une contribution majeure (annexe E) et la liste complète de mes publications (annexe F).

TABLE DES MATIÈRES

LISTE DES FIGURES

REMERCIEMENTS

Je souhaite en premier lieu remercier les "sages" du Service de physique des particules (SPP) et la direction de l'Institut de recherche sur les lois fondamentales de l'Univers (Irfu) du Commissariat à l'énergie atomique et aux énergies alternatives (CEA) de m'avoir donné l'opportunité de développer la recherche présentée dans ce manuscrit en m'offrant un poste de chercheur permanent en 2005.

L'ambiance du groupe cosmologie du SPP est excellente, propice aux interactions fécondes et au développement de la curiosité scientifique. Celle-ci a joué un rôle essentiel dans l'accomplissement de ce travail. Merci aux chercheurs du groupe, Christophe Yèche, Vanina Ruhlmann-Kleider, Nathalie Palanque-Delabrouille, Christophe Magneville, Jim Rich, Jean-Marc Le Goff, Etienne Burtin, Dominique Yvon, et à ses étudiants et postdocs actuels ou passés.

J'ai aussi beaucoup bénéficié de collaborations avec les chercheurs du Service d'Astrophysique (SAp), en particulier Marguerite Pierre et Monique Arnaud. Les liens avec mes anciens responsables de thèse, Jacques Delabrouille et Jim Bartlett, n'ont pas faibli aux cours des dix dernières années et je leur suis reconnaissant pour leur soutien. Merci aussi à tous les quatre pour leurs premières relectures de ce document.

Ce travail s'appuie essentiellement sur les données du satellite Planck. Ainsi, je veux remercier les chercheurs de la collaboration qui m'ont énormément appris pendant toute la durée de la mission.

Pour finir, j'aimerais exprimer ma gratitude à mes trois rapporteurs et membres de mon jury, Simon White, Pierre Binétruy et Jean-Paul Kneib, pour leur relecture attentive de ce manuscrit. Merci à Sophie Maurogordato, Jim Rich et François

Bouchet d'avoir accepté de faire partie de mon jury et pris le temps de se pencher sur mon travail.

Enfin, je tiens à remercier mon épouse Elvira pour son soutien sans faille tout au long de ce travail.

Chapitre 1

INTRODUCTION

1.1 Cosmologie

Le modèle de concordance de la cosmologie est né au début des années 2000 suite à l'observation successive de l'accélération de l'expansion de l'Univers (supernovæ Ia, Riess et al., 1998; Perlmutter et al., 1999) et de sa "platitude" (premier pic acoustique du fond diffus cosmologique, de Bernardis et al., 2000). Il a en particulier permis de clore les débats de la décennie 1990 sur la valeur de la quantité de matière dans l'Univers : $\Omega_{\rm m}$ vaut-il 1 comme le prédit naturellement l'inflation ou bien est-il de l'ordre 0.3 comme l'indique les observations des amas[1] ?

Les pièces du puzzle ont continué à s'assembler petit à petit. La détermination de la valeur de la constante de Hubble à 72 ± 8 km/s/Mpc (Freedman et al., 2001) a conduit à un âge de l'Univers satisfaisant, i.e. plus grand que celui des plus anciennes étoiles. Enfin, le satellite WMAP, lancé en 2001, a confirmé avec une grande précision le modèle de concordance dès les premières publications (Spergel et al., 2003) scellant définitivement son succès. Le modèle de concordance peut être ajusté pour la première fois par un jeu de seulement six paramètres cosmologiques qui n'a jamais été mis en défaut par les données WMAP jusqu'à la fin de la mission (Hinshaw et al., 2013). La figure 1.1 présente les premières mesures de précision effectuées avec WMAP sur la géométrie de l'Univers.

---

[1] voir le chapitre 4 de ce manuscrit qui détaille un peu plus cette période

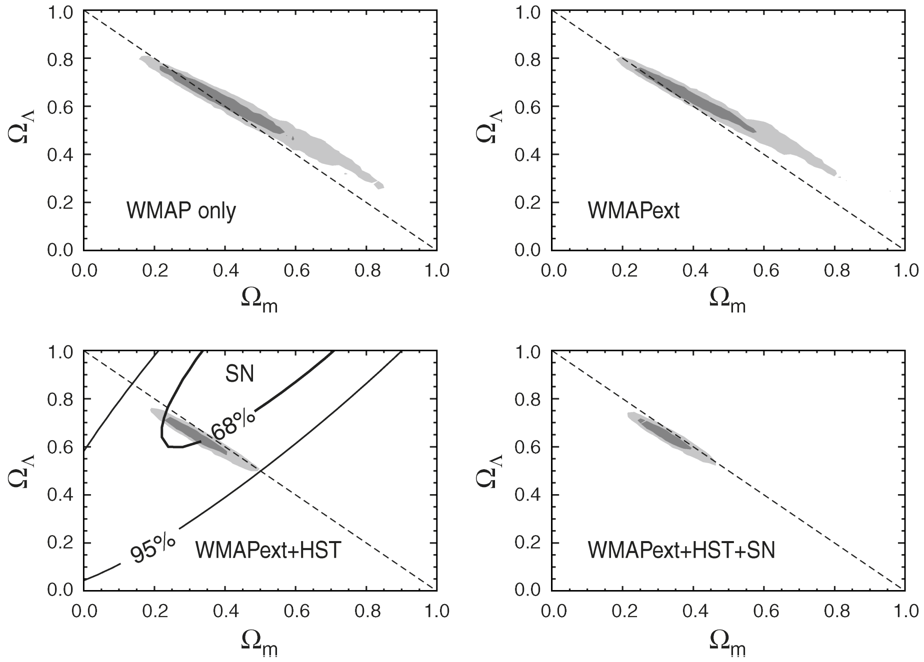

Figure 1.1: Premières contraintes cosmologiques de WMAP sur la géométrie de l'Univers (contours à 1 et 2σ). *En haut à gauche :* WMAP seul. *En haut à droite :* WMAP et les expériences CBI et ACBAR (WMAPext). *En bas à gauche :* WMAPext et HST Key Project (les contraintes supernovae sont indiquées séparément). *En bas à droite :* combinaison WMAPext, HST Key Project et supernovae. La figure est tirée de Spergel et al. (2003).

2005

En 2005, la première détection des oscillations acoustiques de baryons (BAO, Eisenstein et al., 2005) a permis de conforter un peu plus le modèle et de commencer à pouvoir le sur-contraindre.

La figure 1.2 montre cette première détection des BAO dans le sondage de galaxies Sloan Digital Sky Survey (SDSS), indiquée par la bosse dans la fonction de corrélation à deux points pour une distance d'environ $100h^{-1} = 150$ Mpc. Cette détection a encouragé la poursuite du programme SDSS et le lancement d'autres sondages optiques (par exemple, CFHTLenS, RCS2 ou DES). Ces sondages se sont aussi révélés utiles pour les études d'amas comme je le montrerai dans les chapitres 4 et 6.

Les premiers résultats de cosmologie de Planck ont été publiés en 2013 (Planck Collaboration XVI, 2014). Ceux-ci ont confirmé avec une précision toujours meilleure que le modèle minimal à six paramètres est un excellent ajustement aux données du fond diffus cosmologique (CMB). En parallèle, des détections de nouveaux effets sont réalisées par Planck et les expériences concurrentes et complémentaires au sol comme ACT, SPT et POLARBEAR : le spectre de lentilles gravitationnelles (Story et al., 2014; Planck Collaboration XV, 2015) détecté à $40\,\sigma$ dans les données Planck, les modes B de polarisation dus à l'effet de lentille gravitationnelle sur les modes E (van Engelen et al., 2014; Hanson et al., 2013; Ade et al., 2014b; The Polarbear Collaboration: P. A. R. Ade et al., 2014).

Début 2014, l'annonce de la détection des modes B primordiaux par l'expérience BICEP2 (Ade et al., 2014a) a surpris la communauté scientifique et déclenché des campagnes de vérifications sur les autres jeux de données disponibles. Quelques mois plus tard, la collaboration Planck a montré l'importance de la prise en compte de la poussière galactique pour cette étude (Planck Collaboration Int. XXX, 2014) : cette dernière contamine significativement le signal BICEP2. Une étude jointe BI-

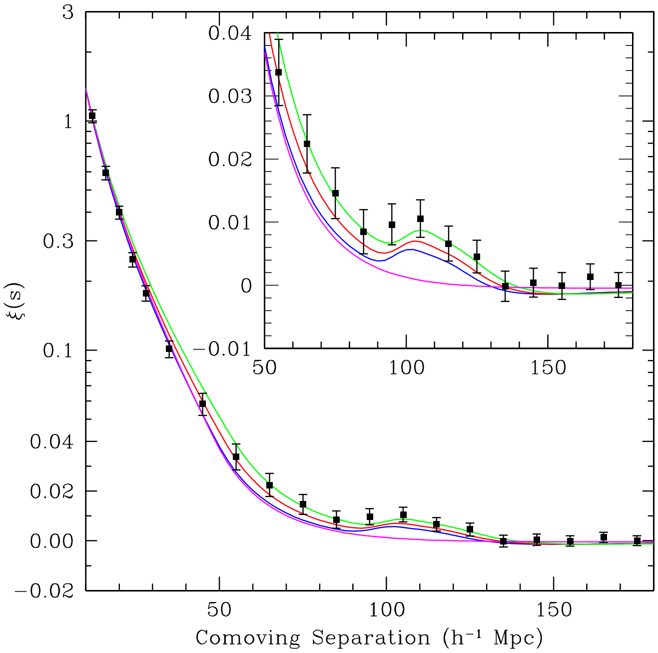

Figure 1.2: Première détection des oscillations acoustiques de baryons sur l'échantillon de galaxies rouges lumineuses (LRG) du sondage SDSS. La figure montre l'excès de la fonction de corrélation de l'échantillon à une distance de $100h^{-1}$ Mpc. Les trois lignes supérieures présentent des modèles (avec baryons) ayant différentes valeurs de Ω_{m}. Le quatrième modèle en bas ne contient pas de baryons, d'où l'absence de pic. La figure est tirée de Eisenstein et al. (2005).

CEP2/Planck donne désormais une nouvelle limite supérieure du rapport des perturbations tenseur sur scalaire $r < 0.12$ (95% C.L.) (BICEP2/Keck and Planck Collaborations et al., 2015).

Quelques anomalies restent cependant présentes dans les données comme la valeur basse du quadrupole, l'alignement des directions des quadrupole et octupole, ainsi que le spectre de puissance en température du CMB qui est au-dessous du meilleur ajustement dans l'intervalle de multipoles $20 < l < 30$ (Planck Collaboration XXIII, 2014). Il existe aussi une tension entre la valeur de σ_8 déterminée à l'aide du fond diffus cosmologique et la valeur mesurée par les amas de galaxies de Planck. σ_8 est l'amplitude des fluctuations de densité de matière lissée à l'échelle de $8h^{-1}$ Mpc :

$$\sigma(R)^2 = \frac{1}{2\pi^2}\int P(k)W(kR)^2k^2dk \qquad (1.1)$$
$$R = 8h^{-1}\mathrm{Mpc}$$

où $P(k)$ est le spectre de puissance des fluctuations de densité de la matière et $W(kR)$ la transformée de Fourier de la fonction fenêtre sphérique

$$W(kR) = \frac{3}{(kR)^2}\left[\frac{\sin(kR)}{kR} - \cos(kR)\right]. \qquad (1.2)$$

Les amas de galaxies favorisent une valeur de σ_8 significativement plus basse que celle du CMB primaire. Les détails de cette tension sont décrits dans le chapitre 4. Ce résultat, déjà présent dans les données 2013, a été confirmé sur les données 2015. Il existe plusieurs solutions (astrophysique ou cosmologique) au problème sans que l'on puisse trancher entre elles aujourd'hui.

Le modèle de concordance minimal à six paramètres reste donc pour l'instant le modèle standard de la cosmologie.

Avancées notables

Paramètres Planck 2015 [TT,TE,EE+lowP+lensing (68% limits)]

$$\Omega_{\mathrm{b}}h^2 = 0.02226 \pm 0.00016$$

$$\Omega_{\mathrm{c}}h^2 = 0.1193 \pm 0.0014$$

$$100\theta_{\mathrm{MC}} = 1.04087 \pm 0.00032$$

$$\tau = 0.063 \pm 0.014$$

$$\ln(10^{10}A_{\mathrm{s}}) = 3.059 \pm 0.025$$

$$n_{\mathrm{s}} = 0.9653 \pm 0.0048$$

Le cadre ci-dessus contient la meilleure estimation courante de ces six paramètres basée sur les spectres de température et de polarisation auxquels on a ajouté le spectre de lentilles gravitationnelles de Planck.

1.2 Amas de galaxies et effets Sunyaev-Zel'dovich (SZ)

Les amas de galaxies sont les plus grandes structures virialisées de l'Univers, situées aux noeuds de la toile cosmique. Leur contenu en matière noire et baryonique est proche de la valeur universelle : environ 85% de matière noire et 15% de baryons. Parmi ces 15%, 10% se trouvent sous forme de gaz chaud ionisé ($T_e \sim 5\,\mathrm{keV}$) dans le puits de potentiel gravitationnel et les autres 5% ont pris la forme d'étoiles et galaxies.

Historiquement, les amas ont été détectés via l'émission optique des galaxies qu'ils renferment puis grâce à l'émission Bremsstrahlung du gaz chaud vue par les satellites X dès le début des années 1970. Au courant des années 1980, les premières détections du gaz grâce à l'effet Sunyaev-Zel'dovich (SZ) ont été réalisées (voir par exemple Birkinshaw et al., 1984; Meyer et al., 1984; Uson & Wilkinson, 1984). Il a été ensuite possible de détecter l'effet de lentille gravitationnelle faible du halo de matière noire sur les galaxies d'arrière-plan à partir des années 1990 (Tyson et al., 1990). La fin des années 2000 a vu les premières détections SZ en aveugle par les expériences SPT, ACT et Planck que je décrirai plus en détail dans le chapitre 3.

L'effet SZ est la diffusion Compton inverse des photons du CMB par les électrons du gaz chaud de l'amas. Cette diffusion crée une faible distorsion du spectre du CMB dans la direction des amas, induisant une anisotropie secondaire. La figure 1.3 présente cet effet en ligne continue rouge. La forme de la dépendance en fréquence ne dépend pas de l'amas considéré dans le cas où les électrons du gaz ne sont pas relativistes, avec un déficit d'intensité aux fréquences inférieures à 217 GHz et un excès aux fréquences supérieures. C'est l'effet SZ thermique (causé par l'agitation thermique des électrons), utilisé pour détecter les amas (voir chapitre 3). Le mouvement relatif de l'amas dans le référentiel du CMB ajoute un second effet SZ, dit cinétique, un ordre de grandeur plus faible que le précédent et représenté en tirets bleus dans la figure. L'amplitude de l'effet SZ thermique dépend de sa pression, c'est-à-dire du produit de sa densité électronique et de sa température alors que l'amplitude de l'effet SZ cinétique dépend de la vitesse radiale de l'objet dans la référentiel du CMB ainsi que de sa densité électronique. L'intensité du corps noir multiplié par 0.0005 est indiqué à titre de comparaison. Les six bandes de l'instrument Planck HFI sont matérialisées en vert hachuré et couvrent de façon optimale les minima, maxima et nul de l'effet SZ thermique.

Pour plus de détails sur les effets SZ, on pourra consulter les revues de Birkinshaw (1999) et Carlstrom et al. (2002).

A partir de la fin des années 2000 et au début des années 2010, les différentes communautés (optique, X et SZ) travaillant sur les amas de galaxies ont commencer à disposer de données suffisamment nombreuses et précises pour que leurs confrontations prennent sens. Les comparaisons des résultats et les analyses jointes ont commencé à voir le jour. Ce passage d'une phase plutôt mono-longueur d'onde à une phase multi-longueur d'onde a permis d'enrichir considérablement le domaine et de faire des avancées significatives comme je le décrirai dans le chapitre 6.

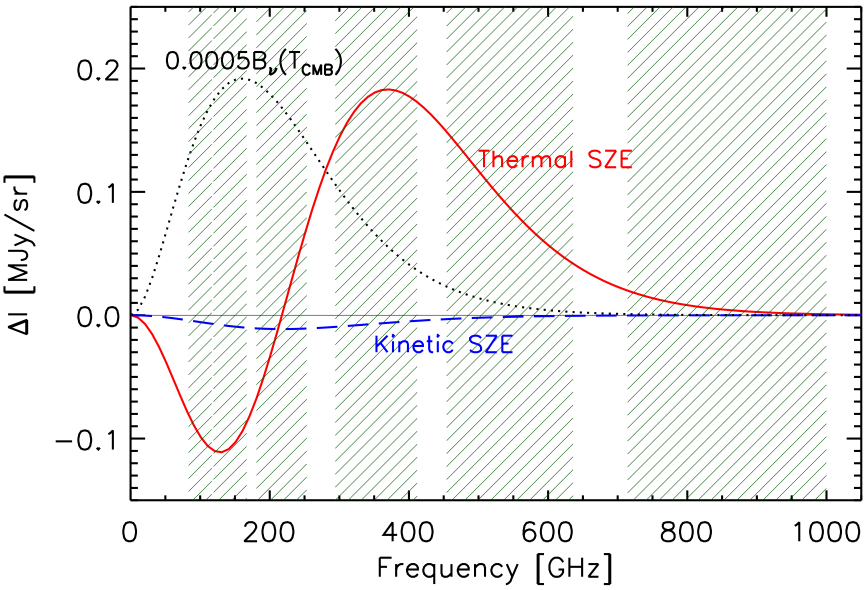

Figure 1.3: Dépendance spectrale des effets SZ et bandes de l'instrument HFI de Planck. L'effet SZ thermique (ligne continue rouge) est négatif/positif aux fréquences inférieures/supérieures à 217 GHZ. L'effet SZ cinétique (en tirets bleus) possède la même dépendance que le CMB et son signe dépend du sens de la vitesse radiale de l'amas par rapport à nous (ici l'amas s'éloigne). Les amplitudes des effets SZ correspondent à un amas de 10 keV, un paramètre de Compton $y = 10^{-4}$ et une vitesse radiale particulière de 500 km/s. A titre indicatif, le spectre du CMB multiplié par 0.0005 est indiqué en pointillés noirs. Les six bandes de l'instrument Planck HFI sont représentées hachurées en vert. La figure est adaptée de Carlstrom et al. (2002).

1.3 La mission Planck

Planck (Tauber et al., 2010) est une mission satellite de l'agence spatiale européenne dédiée à l'observation du fond diffus cosmologique. Elle poursuit le travail des satellites COBE[2] et WMAP[3].

Planck a été lancé en 2009 et a observé l'ensemble du ciel dans neuf bandes de fréquence allant de 30 à 857 GHz. Ce domaine de fréquence est couvert par deux instruments : LFI pour Low Frequency Instrument (trois bandes à 30, 44 et 70 GHz) et HFI pour High Frequency Instrument (six bandes à 100, 143, 217, 353 et 857 GHz, représentées dans la figure 1.3). La résolution des cartes obtenues varie avec la fréquence de 30 à 5 arcmin. La résolution et la sensibilité de HFI étant meilleures que celles de LFI, HFI a été exclusivement utilisé pour les études SZ au cours de la mission.

Les instruments HFI/LFI ont fonctionné en continu de 2009 à 2012/2013. Ils ont permis d'observer cinq/huit fois le ciel pour les fréquences de HFI/LFI respectivement, au delà des objectifs initiaux de la mission (deux relevés pour HFI). Au fur et à mesure de l'accumulation des données, plusieurs séries de papiers ont été publiées par la collaboration. Les "Planck early results", basés sur les dix premiers mois de la mission, ont été publiés en 2011 (Planck Collaboration I, 2011). Les "Planck 2013 results" (Planck Collaboration I, 2014) correspondent aux premiers résultats cosmologiques et sont basés sur les cartes construites avec quinze mois et demi de données, soit la moitié environ (voir en particulier l'analyse cosmologique Planck Collaboration XVI, 2014). Entre 2011 et 2013, plusieurs papiers intermédiaires "Planck intermediate results" ont été publiés. Enfin, les publications "Planck 2015 results" sur l'ensemble des données Planck ont vu le jour (Planck Collaboration I, 2015). Elles in-

---

[2] Lancé en 1989, il a mesuré avec precision le spectre de corps noir du CMB et détecté pour la première fois ses anisotropies.

[3] Lancé en 2001, il a fait la première mesure précise du spectre angulaire du CMB.

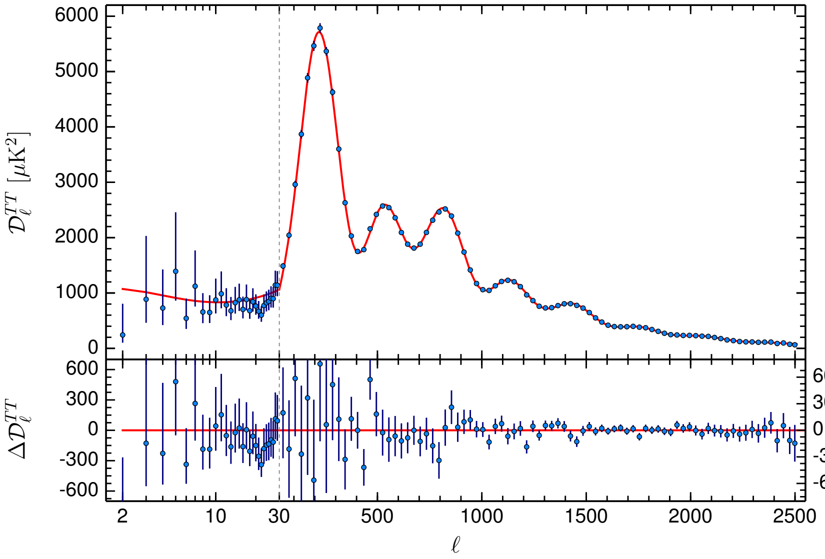

Figure 1.4: *En haut :* spectre en température du CMB primaire obtenu sur les données Planck 2015. *En bas :* résidus au meilleur ajustement du modèle d'Univers plat minimal à six paramètres. La figure est tirée de Planck Collaboration XIII (2015).

cluent une mise à jour des résultats cosmologiques (Planck Collaboration XIII, 2015) et présentent aussi la mesure des spectres des anisotropies de CMB avec une très grande précision. Le spectre en température est repris dans le figure 1.4. Les séries de publications de 2013 et 2015 étaient accompagnées des cartes correspondantes, mises à la disposition de la communauté scientifique.

J'ai participé activement à toutes les séries de papiers Planck comme je le décrirai dans les chapitres suivants. Les outils que j'ai mis en place (filtres adaptés, estimateur d'effet de lentille) ont été développés pour être appliqués aux données de Planck mais ils sont suffisamment généraux pour pouvoir être utilisés avec n'importe quel jeu de données millimétriques.

Dans le chapitre 2, je présenterai mon travail sur la simulation de l'effet SZ pour

Planck dans le Planck Sky Model.

Je décrirai l'extraction des amas Planck dans le chapitre 3.

Dans le chapitre 4, j'exposerai les contraintes cosmologiques obtenues avec les amas de galaxies de Planck. En particulier, je montrerai que

2015

les contraintes cosmologiques avec les amas sont limitées par la précision sur la loi d'échelle flux-masse, incertitude systématique majeure des analyses aujourd'hui. Les études multi-longueur d'onde de catalogues de plus en plus grands pourraient permettre de réduire ces systématiques et conduire à l'avènement des contraintes cosmologiques avec les amas.

Dans le chapitre 5, je développerai l'estimation de la masse des amas de galaxies par effet de lentille sur le CMB.

Les études des lois d'échelle SZ-X et SZ-optique seront décrites dans le chapitre 6.

Les recherches des effets SZ cinétique, relativiste et polarisé dans les données Planck seront présentées dans le chapitre 7.

Dans le chapitre 8, je rapporterai brièvement les études de suivi des amas Planck à d'autres longueurs d'onde.

Enfin, je parlerai de mon travail pour la définition de missions futures dans le chapitre 9 et je conclurai dans le chapitre 10.

Chapitre 2

SIMULATIONS DES EFFETS SZ DANS LE PLANCK SKY MODEL

2.1 Le Planck Sky Model (PSM)

Le Planck Sky Model (PSM) est l'outil de référence pour la simulation du ciel millimétrique. Il est utilisé au sein de la collaboration Planck mais aussi par l'ensemble de la communauté CMB. Il tire son origine dans les études de phase A de Planck (entre 1993 et 1996) et dans la réponse à l'appel d'offre de l'ESA (entre 1996 et 1998), étapes pour lesquelles un premier modèle de ciel complexe a été conçu (Bouchet & Gispert, 1999), auquel a été adjoint des premières méthodes de séparations de composantes (Hobson et al., 1998; Bouchet et al., 1999). Ces travaux ont aussi débouché sur des premières études spécifiques, en particulier celle de la composante SZ (Aghanim et al., 1997). En 2006, Jacques Delabrouille a repris l'effort de simulation au sein PSM et a pensé son développement.

Le PSM est désormais utilisé à trois niveaux :

- la simulation de l'ensemble du ciel entre 3 GHz et 3 THz, pour la mise au point de codes d'analyse ou la préparation des futures missions CMB ;
- l'analyse de données millimétriques, pour la modélisation des différentes émissions ;
- la diffusion des connaissances, car il concentre dans un code unique les modèles les plus à jour de chacune des composantes.

Le PSM est l'équivalent pour la communauté CMB du Monte Carlo pour la physique des particules (cf. les deux premiers niveaux décrits ci-dessus : simulation et analyse). La différence essentielle est que le Monte Carlo repose sur le modèle standard de la physique des particules unanimement adopté et possédant peu de paramètres. Ce n'est pas le cas pour le PSM car il n'existe pas de modèle standard des émissions astrophysiques. Chaque composante possède une modélisation spécifique qui évolue ou peut être remise en cause avec l'avancée des connaissances. D'où l'importance du troisième niveau qui permet à chaque utilisateur d'avoir accès aux dernières modélisations de chaque composante même lorsqu'il n'est pas spécialiste.

Le succès du PSM repose sur plusieurs ingrédients :

- un contenu scientifique excellent grâce à l'implication de spécialistes de chaque composante pour le codage des émissions du ciel ;
- une bonne interfaçabilité avec les autres codes de simulation ou d'analyse, facilitée par l'adoption du langage IDL ;
- une grande modularité : il est simple de modifier des composantes ou de n'en simuler qu'une partie ;
- une utilisation facile via un fichier de configuration par défaut bien commenté ;

La première version du PSM a été mise en place à partir de morceaux de codes apportés par des spécialistes de chaque composante qui ont été interfacés avec IDL. Chaque composante a ensuite évoluée au sein du PSM en fonction des besoins des utilisateurs et des avancées scientifiques. Une couche de modélisation instrumentale (bandes d'observations, lobes optiques, bruit instrumental inhomogène) s'est enfin ajoutée à l'ensemble. Aujourd'hui, le PSM permet de simuler le ciel millimétrique contenant : CMB, émissions de notre galaxie (synchrotron, poussière, free-free, poussière en rotation, raies de CO), sources ponctuelles non résolues (essentiellement radio et infrarouges) et les composantes SZ.

Pour plus de détails sur le concept du PSM et les différentes composantes simulées, on pourra consulter le chapitre 6 de l'HDR de Jacques Delabrouille ainsi que le papier référence Delabrouille et al. (2013).

J'ai pris en charge le développement et le codage des composantes SZ dans le PSM depuis 2006. A ce moment, trois types de cartes SZ et leurs catalogues associés étaient disponibles au sein de la collaboration Planck :

- Trois cartes de tSZ et catalogues associés fournies par P. Mazzotta basées sur un modèle semi-analytique (Colafrancesco et al., 1997; de Zotti et al., 2005).
- Deux cartes de tSZ+kSZ et catalogues associés fournies par M. Reinecke, B. Schaefer et K. Dolag basées sur simulations N-corps ($z > 0.025$) et hydro ($z < 0.025$) (Dolag et al., 2005; Schäfer et al., 2006a).
- Une carte de tSZ+kSZ et catalogue associé fournie par J. Delabrouille, J.-B. Melin et J. Bartlett basées sur un modèle semi-analytique (fonction de masse et modèle β, proche de celui de P. Mazzotta). Les cartes ont été produite à l'aide du code DMB décrit dans Delabrouille et al. (2002) que j'avais fait évoluer des cartes tangentielles aux cartes tout le ciel, fin 2005 - début 2006.

Le problème principal était qu'il n'y avait pas consensus sur la modélisation des amas et sur les paramètres cosmologiques à adopter si bien que ni les comptages d'amas, ni les spectres de puissance des cartes n'étaient compatibles. Les cartes pouvaient donc être uniquement utilisées pour commencer à mettre au point des algorithmes pratiques d'extraction mais on ne pouvait pas déterminer la dépendance du nombre d'amas extrait avec la physique des amas adoptée ou les paramètres cosmologiques. A partir de 2006, j'ai donc poursuivi le développement du code semi-analytique DMB et l'ai mis à disposition de la collaboration Planck au sein du PSM avec un nombre de fonctionnalités croissant. Dans la partie suivante (2.2), je décris les évolutions que j'ai réalisées depuis le code de base (Delabrouille et al., 2002) en 2005 jusqu'à la version actuelle 2015 du modèle DMB dans le PSM. Dans la partie 2.3, je détaille les limitations actuelles du code et décris les manières de les surmonter.

2005

Trois types de cartes et catalogues SZ associés disponibles au sein de la collaboration Planck incluant des physiques d'amas différentes mais pas de consensus et pas de code partagé. Besoin, au sein du PSM, d'un code de simulation rapide de ciel SZ étant donné un jeu de paramètres cosmologiques et un modèle d'amas donnés.

2.2 Implémentation des composantes SZ dans le PSM

2.2.1 Code Delabrouille-Melin-Bartlett (DMB)

En 2005, je disposais du code développé avec Jacques Delabrouille et Jim Bartlett au cours de ma thèse entre 2001 et 2004 (Delabrouille et al., 2002). Etant donnés un jeu de paramètres cosmologiques et une surface de ciel (carte tangentielle de quelques dizaines de degrés carrés), ce code réalise un tirage aléatoire d'un catalogue d'amas en redshift et masse virielle (z, M_{Δ_c}) à l'aide d'une fonction de masse : Press-Schechter (Press & Schechter, 1974), Sheth-Tormen (Sheth & Tormen, 1999; Sheth et al., 2001) ou Jenkins (Jenkins et al., 2001). Un modèle simple de profil β (King, 1962; Cavaliere & Fusco-Femiano, 1976) est adopté pour décrire la densité électronique des amas supposés isothermes. Leur température est estimée via la relation $M_{\Delta_c} - T$ de Pierpaoli et al. (2003) normalisée à l'aide de l'abondance locale des amas de galaxies. Les amas du catalogue peuvent alors être placés aléatoirement sur la carte ou suivant le contraste densité obtenu par tirage d'une "boîte univers" à partir du spectre de puissance P(k) de la matière. De même, leurs vitesses peuvent être tirées aléatoirement selon une distribution gaussienne de moyenne nulle et de variance calculée à l'aide du P(k), ou directement à partir de leur position dans la "boîte univers". Pour plus de détails sur le code DMB de 2005, on pourra consulter Melin (2004).

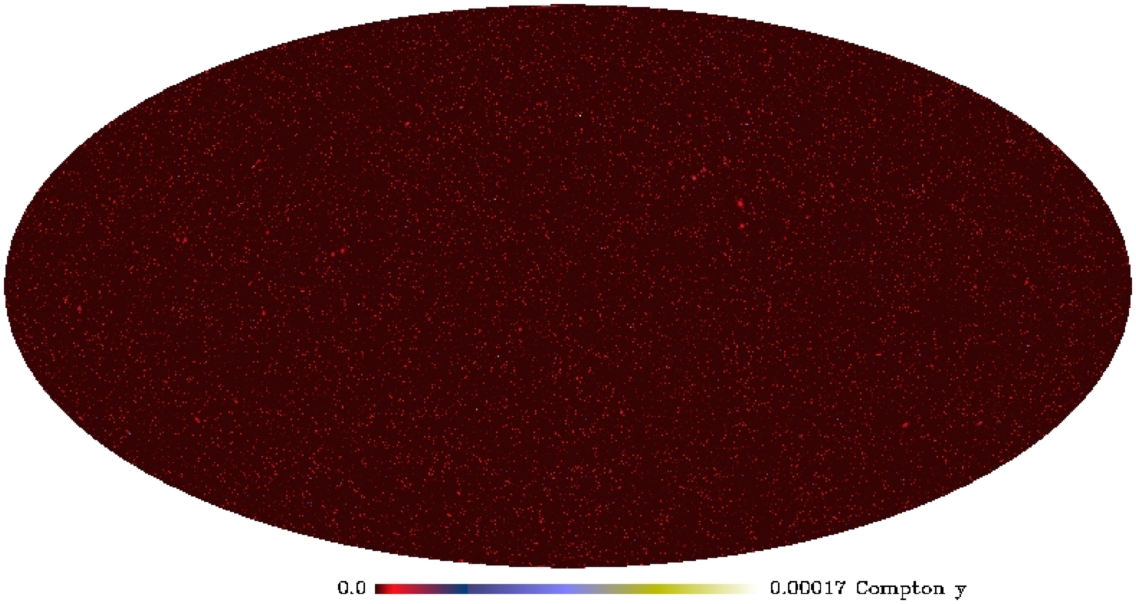

Figure 2.1: Simulation tout le ciel de l'effet SZ thermique pour le *Challenge SZ* (exercice de détection en aveugle d'amas au sein de la collaboration Planck décrit dans le chapitre 3). Les amas sont tirés selon la fonction de masse de Jenkins et al. (2001) et sont modélisés à l'aide du profil de pression de Arnaud et al. (2010). La simulation contient les amas locaux connus en X.

J'ai porté les progrès du code DMB dans le PSM essentiellement entre 2005 et 2011 (date des premières publications de Planck). Mes efforts se sont ensuite concentrés sur l'analyse des données, en particulier l'extraction d'amas (chapitre 3) et la détermination des paramètres cosmologiques (chapitre 4). Matthieu Roman, en thèse avec J. Delabrouille entre 2011 et 2014, a pris le relai. En particulier, il a codé les cas "univers non plat" et "paramètre de l'équation d'état de l'énergie noire $w \neq -1$", l'utilisation de CAMB ou CLASS pour le calcul du spectre $P(k)$ de matière, et il a amélioré l'interface avec les autres parties du PSM. Je ne décris pas son travail ici et renvoie le lecteur à la partie 6.3.2 de Roman (2014). Je cite ci-dessous les améliorations principales du code, plus anciennes, que j'ai réalisées :

- Fin 2005 - début 2006, possibilité de faire des simulations tout le ciel (adoption de la pixelisation Healpix (Górski et al., 2005), amas placés selon une densité de probabilité uniforme car "boîte univers" trop lourde à simuler pour tout le ciel) ;

- Mi 2007, possibilité de produire des simulations contraintes contenant les amas X NORAS (Böhringer et al., 2000) et REFLEX (Böhringer et al., 2004) ;

- Mi 2008, adoption d'un modèle d'amas basé sur les observations XMM/Chandra récentes (profils GNFW de Arnaud et al. (2010) préliminaire ou de Nagai et al. (2007) pour la pression au lieu du profil β, utilisation de M_{500} au lieu de M_{Δ_c}) [avec Alexandre Boucaud (stage L3)] ;

- Mi 2009, utilisation par défaut de la fonction de masse de Tinker (Tinker et al., 2008) ;

- Fin 2010, possibilité de simuler les amas selon une paramétrisation GNFW quelconque ;

- Début 2011, possibilité de produire des simulations contraintes contenant l'ensemble des amas X connus MCXC (Piffaretti et al., 2011) ainsi que les amas optiques du SDSS (Koester et al., 2007, MaxBCG) ;

- Début 2012, implémentation des quatre premiers ordres des corrections relativistes de l'effet tSZ (Itoh et al., 1998) [avec Jacques Delabrouille].

L'adoption des profils de pression XMM/Chandra (mi 2008) a été cruciale car elle a permis d'obtenir pour la première fois des simulations du ciel SZ entièrement compatibles avec les observations X courantes. Ce progrès a eu un impact majeur sur la prédiction du nombre d'amas attendu par la mission Planck comme nous le verrons dans le chapitre 4.

Le code DMB permet de modéliser les amas et leurs vitesses. Les produits sont les cartes de tSZ, kSZ (vitesses radiales) et pSZ (dû aux vitesses transverses) et le catalogue d'amas associé. La figure 2.1 montre une simulation tout le ciel de l'effet SZ thermique avec le code DMB. Un zoom de cette simulation sur une région carrée de 12.5 deg de côté est présenté dans la figure 2.2.

Avancées notables

Le code DMB a été mis à disposition de la collaboration Planck dans le PSM et a bénéficié de nombreuses améliorations. La plus cruciale a été l'adoption mi-2008 des profils de pression déterminés sur les données XMM/Chandra. Elle a permis pour la première fois d'obtenir des simulations entièrement compatibles avec les observations X les plus récentes et de prédire avec précision le nombre d'amas attendus par la mission.

2.2.2 *Cartes et catalogues d'amas N-corps et hydro*

Le modèle DMB ne permettant pas de modéliser le gaz chaud en dehors des amas (toile cosmique) ni les structures complexes d'amas en interaction, les cartes provenant des

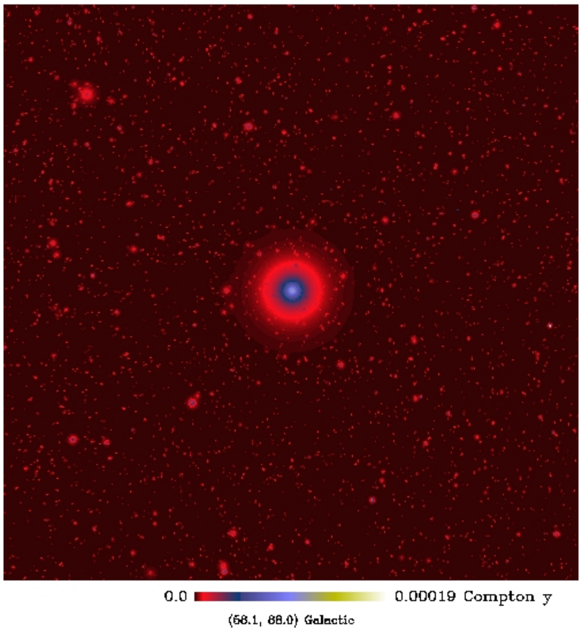

Figure 2.2: Zoom sur l'amas Coma dans la simulation *Challenge SZ* présentée figure 2.1. La carte fait 12.5 deg de côté.

simulations N-corps et hydro ont été intégrées dans le PSM. Une option dans le fichier configuration permet de les sélectionner. Il est possible aujourd'hui de simuler les cartes SZ selon le modèle DMB seul, le modèle N-body+hydro (cartes de M. Reinecke, B. Schaefer et K.Dolag décrites précédemment) ou le modèle hydro+DMB (carte hydro fournie par A. da Silva et K. Dolag pour $z < 0.25$ et tirage DMB pour $z > 0.25$. L'inconvénient de ces simulations est qu'elles ne fournissent qu'une seule réalisation du ciel pour un jeu de paramètres cosmologiques donnés.

2.2.3 Prédiction SZ

Le PSM peut aussi être lancé en mode "prédiction". Seules les composantes connues du ciel sont alors modélisées. Dans ce cas, la carte tSZ de sortie ne contient que les amas connus du ciel (MCXC et MaxBCG). Aucune composante stochastique (tirage DMB, carte N-corps ou hydro) n'est ajoutée. Les cartes kSZ et pSZ sont nulles.

2.3 Limitations actuelles

Au moment de la publication des résultats 2015 de Planck sur l'ensemble des données en température et polarisation, de nouveaux besoins d'évolution du code DMB se font sentir, à la fois pour réaliser les analyses fines des données finales de Planck mais aussi pour préparer la réponse à l'appel d'offre de mission spatiale M5 de l'Agence Spatiale Européenne.

2.3.1 Mise à jour de fonctionnalités existantes

Il existe aujourd'hui des nouveaux catalogues extraits du sondage SDSS plus grands et mieux maîtrisés que le MaxBCG, en particulier le catalogue redMaPPer (Rykoff et al., 2014). Les catalogues d'amas extraits des données Planck, SPT et ACT ont par ailleurs augmenté le nombre d'amas connus. Il serait intéressant de mettre à jour les amas connus du PSM pour les réalisations contraintes du modèle DMB et le mode "prédiction" en incluant ces nouveaux catalogues.

Il existe aussi de nouvelles simulations N-corps plus récentes, comme par exemple les simulations Millenium XXL[1] ou DEUS[2], qu'il serait intéressant d'introduire dans le PSM.

2.3.2 Implémentation des corrélations entre les amas et les autres composantes du PSM

C'est sans aucun doute l'évolution la plus importante et la plus difficile à réaliser. La plus importante car c'est ce type d'étude qui va être au cœur des analyses des générations futures d'expériences CMB. La plus difficile à réaliser car les différentes composantes du PSM vont devoir se parler les unes les autres ce qui implique de plus grandes interactions entre les codeurs de chaque composante et une convergence de points de vue sur les méthodes à adopter. Les prochaines corrélations à introduire dans le PSM faisant intervenir les amas sont les suivantes :

- corrélation des positions avec la distribution de masse à grande échelle. Les amas ne seront plus placés aléatoirement mais selon des "coquilles d'univers" comme dans le cas de la "boîte univers" du modèle DMB 2005. C'est déjà le cas pour les sources ponctuelles infrarouges sur le ciel ;
- introduction des sources radio et infrarouges dans les amas, pour estimer la contamination du signal SZ par ces sources non résolues. La difficulté réside ici dans le manque de modèle fiable pour simuler ce type de sources ;
- effet de lentille des amas sur le CMB, pour mettre au point les outils d'analyse et faire des prédictions pour les missions futures.

---

[1] http://galformod.mpa-garching.mpg.de/mxxlbrowser/

[2] http://www.deus-consortium.org/

2.3.3 Conception et codage d'une simulation X compatible avec la composante SZ

Le développement d'algorithmes d'extraction combinés X+SZ sur les données ROSAT[3] et Planck est en cours [thèse Loïc Verdier, postdoc Paula Tarrio]. Il est nécessaire de disposer de simulations cohérentes X et SZ pour tester et caractériser complètement les algorithmes. Une des évolutions nécessaires du PSM sera le développement d'une simulation X du ciel (ROSAT, eROSITA[4]) qui soit compatible avec une simulation SZ (Planck, mission future CMB).

2015

Aujourd'hui, le module SZ du PSM a permis de mettre au point les algorithmes de détection de Planck et des chaînes d'analyse SZ. Pour la prochaine série d'analyses et la réponse à l'appel d'offre M5 de l'ESA, il faut le faire évoluer. Le besoin le plus pressant et l'introduction de corrélations entre les amas SZ et les autres composantes du PSM, en particulier la distribution de masse et le CMB.

---

[3] http://www.mpe.mpg.de/ROSAT

[4] http://www.mpe.mpg.de/eROSITA

Chapitre 3

EXTRACTION DES AMAS DE GALAXIES DES DONNÉES PLANCK

Jusqu'au début des années 2000, l'essentiel des efforts d'observations SZ était dédié à des pointés d'amas connus en optique ou en X (par exemple Désert et al. (1998); Joy et al. (2001); Benson et al. (2004)). Les instruments n'avaient pas un champ de vue ni une sensibilité suffisante pour effectuer des sondages sur plusieurs degrés carrés de ciel. Les données WMAP, bien que couvrant l'ensemble du ciel, se sont hélas elles-aussi révélées insuffisantes pour détecter de nouveaux amas car trop bruitées et de résolution angulaire insuffisante. Les premières détections en aveugle ont été obtenues quelques années plus tard par le télescope SPT en 2008 (Staniszewski et al., 2009), suivis du télescope ACT (Menanteau et al., 2010) puis Planck (Planck Collaboration VIII, 2011). Dans ce chapitre, je décris d'abord la mise au point des algorithmes de détection d'amas en aveugle pour la mission Planck. Je donne ensuite des détails sur les premières détections Planck dans une deuxième partie. Enfin, dans une troisième partie, j'explique les méthodologies employées pour assembler les catalogues d'amas de galaxies de Planck.

3.1 Détecter les amas en SZ : un exercice difficile

Le développement d'outils de détection d'amas de galaxies en aveugle a commencé au début des années 2000. Un des premiers algorithmes a été proposé par Diego Herranz et testé sur simulations simples (Herranz et al., 2002). Au cours de ma thèse, je me suis appuyé sur ces travaux pour proposer un algorithme de détection mieux adapté aux données (Melin, 2004) et aboutir à une publication deux années plus tard (Melin et al., 2006). Ces algorithmes sont construits à partir de filtres adaptés multifréquences (Matched Multifilters, MMF, issus du filtre adapté monofréquence Haehnelt & Tegmark (1996)) qui supposent connus le spectre en fréquence de l'effet SZ et la forme du profil des amas. Ils permettent d'extraire la position, la taille et le flux des amas. Je rappelle ici brièvement leur formalisme.

On note les cartes d'observation sous forme d'un vecteur $\mathbf{m}(\mathbf{x})$ à N composantes, N étant le nombre de cartes en fréquence d'une expérience. Les cartes contiennent un amas de profil normalisé à 1 au centre $\mathbf{t_t}(\mathbf{x})$ et d'amplitude y_o. Les autres composantes sur le ciel (CMB primaire, sources ponctuelles, poussière galactique, etc) et le bruit instrumental sont notés $\mathbf{n}(\mathbf{x})$.

$$\mathbf{m}(\mathbf{x}) = y_\mathrm{o}\mathbf{t_t}(\mathbf{x}) + \mathbf{n}(\mathbf{x}) \tag{3.1}$$

La i-ème composante du vecteur $\mathbf{t_t}(\mathbf{x})$ est $j_\nu(\nu_i)[b_i * T_\mathrm{t}](\mathbf{x})$, le profil de l'amas T_t convolué par le lobe instrumental b_i et multiplié par le spectre en fréquence de l'effet SZ thermique j_ν présenté dans la partie 1.2. Le MMF permet d'obtenir une estimation non biaisée et de variance minimale de la valeur centrale du paramètre de Compton y_o :

$$\hat{y}_\mathrm{o} = \int d^2x \; \mathbf{\Psi}_{\boldsymbol{\theta}_\mathbf{t}}{}^t(\mathbf{x}) \cdot \mathbf{m}(\mathbf{x}) \tag{3.2}$$

avec

$$\mathbf{\Psi}_{\boldsymbol{\theta}_\mathbf{t}}(\mathbf{k}) = \sigma^2_{\theta_\mathrm{t}} \mathbf{P}^{-1}(\mathbf{k}) \cdot \mathbf{t_t}(\mathbf{k}) \tag{3.3}$$

et

$$\sigma_{\theta_\mathrm{t}} \equiv \left[\int d^2k \; \mathbf{t_t}{}^t(\mathbf{k}) \cdot \mathbf{P}^{-1} \cdot \mathbf{t_t}(\mathbf{k})\right]^{-1/2}. \tag{3.4}$$

$\mathbf{P}(\mathbf{k})$ est la matrice des cross-spectres du bruit $\mathbf{n}(\mathbf{x})$. Elle peut être estimée directement sur les données en supposant $\mathbf{m}(\mathbf{x}) \simeq \mathbf{n}(\mathbf{x})$, l'émission SZ étant sous-dominante à toutes les fréquences. Le MMF est un outil relativement simple à implémenter et robuste. En particulier, il s'adapte facilement à différentes conditions de bruit instrumental et astrophysique. Il faut noter cependant que le caractère non biaisé du filtre n'est garanti que si le profil de l'amas correspond bien au profil utilisé dans le filtre. Cependant y_o n'est pas un paramètre bien défini car il correspond en fait à la moyenne du paramètre de Compton dans le pixel central et peut donc dépendre de la pixellisation de la carte. On préfèrera utiliser la quantité intégrée en arcmin^2 :

$$\hat{Y} = \hat{y}_o \int d^2x \, \mathbf{t_t}(\mathbf{x}) \tag{3.5}$$

En parallèle du développement des MMF, d'autres algorithmes ont vu le jour, testés eux aussi sur différents jeux de simulations (par exemple Diego et al. (2002), Pires et al. (2006), Schäfer et al. (2006b), Bobin et al. (2008), Carvalho et al. (2009)).

2005

Plusieurs algorithmes d'extraction d'amas en aveugle existent ou sont en cours de développement. Ces travaux ont le plus souvent été testés sur des jeux de simulations simples et indépendants les uns des autres. Aucune comparaison n'a été réalisée sur un jeu de simulation complexe commun.

Lorsque je suis entré dans la collaboration Planck en 2006, j'ai organisé un premier exercice de comparaison de performances d'algorithmes d'extraction d'amas en aveugle sur un jeu de simulation commun réaliste. Cet exercice a été appelé *Challenge SZ*. Le jeu de simulation était construit à l'aide du modèle Delabrouille-Melin-Bartlett du Planck Sky Model qui contenait les derniers modèles d'amas basés sur les profils ajustés sur les données XMM comme décrit dans le chapitre 2. Le *Challenge SZ* a impliqué plus de vingt chercheurs et permis de comparer 12 algorithmes. Il aura fallu plusieurs années pour établir des conclusions solides, partagées par tous (Melin et al., 2012) :

- la difficulté de prédire le nombre exact d'amas qui sera détecté par la mission car très dépendant de la physique des amas et des détails des émissions d'avant-plan, encore inconnus. Cependant, l'ordre de grandeur évalué a été 1000 amas, plus d'un facteur dix au-dessous des premières prédictions du red book[1] qui s'appuyaient sur un modèle d'univers contenant plus d'amas ($\sigma_8 = 1$, WMAP ayant revu ce paramètre à la baisse $\sigma_8 \sim 0.8$), sur l'hypothèse d'amas ponctuels, et sur une physique d'amas plus favorable que celle déterminée sur les dernières données XMM (amas supposés 10% plus brillant en X pour une même masse) ;

- la détection des amas reste limitée par le bruit Planck aux hautes latitudes galactiques et par l'émission de la galaxie aux basses latitudes galactiques ;
- l'erreur en position attendue est de 2 arcmin environ et l'erreur sur le flux de l'ordre de 30%.

Le *Challenge SZ* a aussi permis de mettre en avant certains algorithmes plus performants que d'autres et de les sélectionner pour les appliquer préférentiellement sur les données. Cependant, il faut noter que le comportement de nombreux algorithmes a changé entre ces simulations, pourtant déjà assez réalistes, et les données. Les algorithmes les plus fiables ont été ceux capables de s'adapter au mieux à différents types d'avant-plans et de bruits. Certains algorithmes très performants sur les simulations se sont révélés bien moins efficaces sur les données, plus complexes.

Ce papier Melin et al. (2012) fait le pendant pour la détection SZ de l'exercice de comparaison général sur les méthodes de séparation de composantes mené par Samuel Leach et collaborateurs (Leach et al., 2008) qu'il a été tout aussi dur de faire converger vers une version consensuelle.

En parallèle de ce travail, j'ai estimé avec Jim Bartlett la contamination attendue des amas par l'émission des sources ponctuelles radio et infrarouges de champ (Bartlett & Melin, 2006).

Plusieurs mois avant le lancement (fin 2007, début 2008), de nombreux algorithmes d'extractions, dont le MMF, étaient prêts à être utilisés. Nous n'avons pas résisté

---

[1] http://www.rssd.esa.int/SA/PLANCK/include/report/redbook/redbook-science.htm

à l'envie de l'utiliser sur les données WMAP, à la recherche d'éventuelles détections SZ. Malheureusement, les données WMAP se sont révélées trop bruitées pour permettre de nouvelles détections d'amas significatives. Nous allions perdre la course à la première détection SZ en aveugle (gagnée par SPT en 2008 Staniszewski et al., 2009). La figure 3.1 montre les cartes WMAP et Planck filtrées par le MMF dans la direction des deux amas massifs Coma et A2163, cibles a priori les plus faciles à détecter en SZ. Ces amas sont tout juste détectés dans les données WMAP à $S/N = 4$ et $S/N = 3.5$ respectivement alors qu'ils brillent tels des phares dans les données Planck à $S/N = 29$ et $S/N = 35$ respectivement. Cette figure illustre bien la limitation des données WMAP vis à vis de Planck quant à la détection d'amas individuels par effet SZ. Les données WMAP ont cependant pu être utilisées pour la détection de l'effet SZ statistiquement comme je le montrerai dans le chapitre 6.

Avancées notables

La période 2005-2010 a vu le développement de nombreux algorithmes d'extraction d'amas en SZ dont le MMF. Cet outil s'est révélé particulièrement performant sur les simulations puis sur les données Planck. L'outil a été largement adopté par la communauté pour sa robustesse et sa simplicité. Les extractions d'amas dans les données SPT et ACT utilisent désormais le MMF.

3.2 Premières détections d'amas dans Planck

Après son arrivée au point L2, le satellite Planck a commencé, en août 2009, un premier sondage du ciel d'une quinzaine de jours pour tester ses instruments. Ce "First Light Survey" (FLS, figure 3.2) a montré que le satellite était pleinement opérationnel et que les détecteurs avaient la sensibilité attendue.

Dès la mise à disposition des cartes du FLS, j'ai utilisé le MMF pour essayer

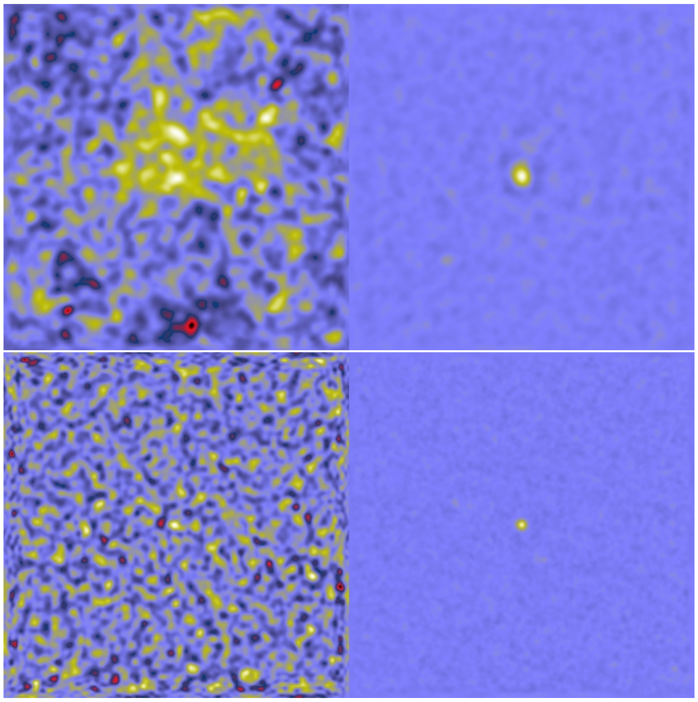

Figure 3.1: Cartes filtrées MMF des amas Coma (ligne du haut) et A2163 (ligne du bas) des données WMAP 9ans (colonne de gauche) et de la mission complète Planck (colonne de droite). Coma est détecté à $S/N = 4$ dans les données WMAP et à $S/N = 29$ dans les données Planck. A2163 à $S/N = 3.5$ dans WMAP et 35 dans Planck. Le côté des cartes est de 10 deg. L'échelle des cartes Coma va de -0.1 à +0.1 arcmin^2 en unité de flux SZ intégré total Y_{5R500} et celle des cartes A2163 de -0.02 à +0.02 arcmin^2.

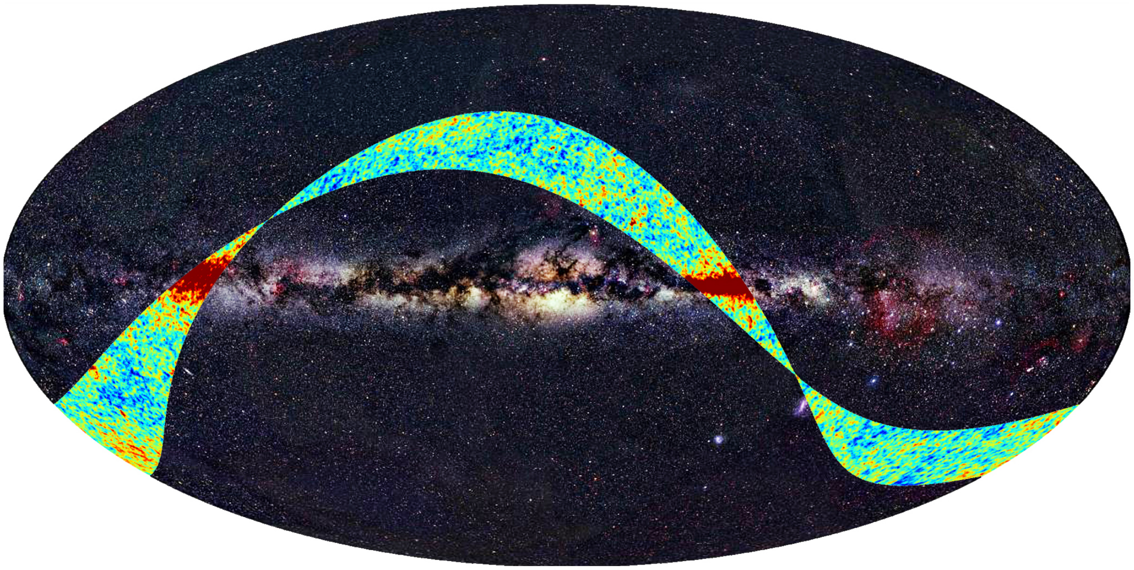

Figure 3.2: Image de la première lumière de Planck en fausses couleurs sur fond de ciel optique. La Galaxie est en rouge. On distingue clairement les anisotropies du fond diffus cosmologique aux plus hautes latitudes galactiques. Source: http://sci.esa.int/planck/45531-planck-first-light-survey/

de détecter les amas connus en rayons X. L'algorithme s'est révélé immédiatement fonctionnel. Une dizaine d'amas a pu être détectée et leur flux SZ estimé. Ils étaient en bon accord avec les prédictions basées sur les mesures X. La figure 3.3 montre les amas A2163 et PLCKG266.6-27.3 aux différentes fréquences de Planck HFI ainsi que les cartes filtrées MMF correspondantes. On remarquera que l'effet SZ est sous-dominant à toutes les fréquences si bien que seul un outil combinant les cartes de façon adéquate permet la détection des amas.

Le MMF a, par la suite, été choisi par la collaboration pour extraire les amas du premier ciel complet de Planck (10 premiers mois). Le catalogue obtenu, appelé ESZ pour Early SZ cluster sample (Planck Collaboration VIII, 2011), contient 189 amas dont la majorité (169) est déjà connue. Ce catalogue a constitué la première preuve publiée de l'efficacité de Planck à détecter des amas SZ, a montré les performances du MMF en situation réelle et a permis de commencer à qualifier les détections grâce aux suivis XMM : les nouveaux amas détectés par Planck sont en général plus perturbés et à plus faible brillance de surface que les amas déjà connus en X. Je reviendrai plus en détail sur ce dernier point dans la partie 8.1.

En développant le MMF pour les amas, j'ai eu de nombreuses interactions avec les équipes travaillant sur le premier catalogue de sources ponctuelles ERCSC (Planck Collaboration VII, 2011). J'ai eu l'occasion de mettre à l'épreuve le matched filter sur plusieurs jeux de simulation dans ce cadre. Un travail de comparaison entre différents algorithmes a été réalisé mais n'a hélas pas été publié.

3.3 Les catalogues d'amas de Planck

A la suite du ESZ, un premier catalogue d'amas sur les 15.5 premiers mois de la mission a vu le jour. Ce catalogue a été constitué de l'union des détections de trois algorithmes. Le MMF que j'avais développé pour le ESZ, un autre MMF et un algorithme, Powellsnakes (sensiblement différent des MMF), dénommés respectivement MMF3,

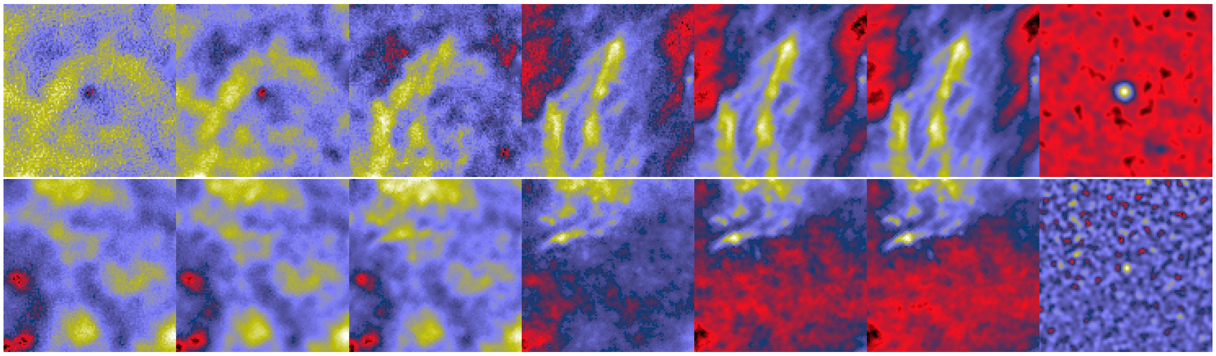

Figure 3.3: *Première ligne :* Amas A2163 vu aux différentes fréquences Planck HFI (6 premières images, 100, 143, 217, 353, 545 et 857GHz) et après filtrage MMF (septième image). L'effet SZ est sous-dominant à toutes les fréquences. Seule une combinaison adéquate des cartes permet de détecter facilement l'amas à S/N=35. Le côté des cartes est de 3 deg. *Seconde ligne :* idem pour l'amas massif PLCKG266.6-27.3 à $z \sim 1$, plus difficilement détecté par Planck à S/N=6.4.

MMF1 et PWS dans Melin et al. (2012). Initialement, le choix de trois algorithmes a été justifié pour permettre la comparaison des détections et s'assurer que l'on obtenait des catalogues cohérents les uns avec les autres. Cependant, la détection d'un amas dans un champ s'est révélé extrêmement sensible aux détails de l'estimation du bruit de fond si bien que les deux implémentations MMF, bien qu'extrêmement proches, donnent des catalogues qui ne sont pas strictement identiques. Cette constatation s'est aussi vérifiée pour PWS. Nous avons donc décidé de publier le catalogue union, nommé PSZ1 (Planck Collaboration XXIX, 2014). Le PSZ1 contient 1227 détections dont 861 amas confirmés ; il a constitué le plus grand catalogue d'amas de galaxies détectés en aveugle en SZ. Un énorme effort de l'ensemble du groupe SZ de Planck a été nécessaire pour caractériser les détections du PSZ1, en particulier à l'aide de données ancillaires. Le PSZ2, publié en février 2015, contient 1653 détections dont plus de 1200 confirmées (Planck Collaboration XXVI, 2015). Il a été fabriqué à l'aide des trois mêmes algorithmes sur les cartes de température de l'ensemble de la mission

Planck (29 mois). Plusieurs sous-catalogues du PSZ2 ont été construits dont deux catalogues pour contraindre les paramètres cosmologiques, le catalogue MMF3 et le catalogue intersection. Les fonctions de sélection des différents catalogues ont été caractérisées. Il faut noter que l'algorithme MMF3 a été modifié significativement depuis la première publication en 2006 jusqu'à la publication du catalogue 2014 au fur et à mesure de la compréhension des caractéristiques des données Planck. Ces modifications sont décrites dans les papiers (Planck Collaboration XXIX, 2014) et (Planck Collaboration XXVI, 2015) ainsi que dans l'annexe A de ce document.

2015

Les algorithmes de détection SZ de Planck possèdent aujourd'hui une efficacité de détection comparable. Ils semblent être proches de leur limite. L'avenir consistera en la conception d'algorithmes d'extraction combinés utilisants plusieurs jeux de données (SZ, X, optique) simultanément.

J'ai débuté ce travail d'extraction sur les données Planck (SZ) et ROSAT (rayons X) avec Paula Tarrio-Alonso (postdoc du projet M2C mené par Monique Arnaud et financé sur ERC) et Loïc Verdier (doctorant financé sur une bourse de l'IDEX Paris-Saclay).

Chapitre 4

CONTRAINTES COSMOLOGIQUES AVEC LES AMAS PLANCK

4.1 Les amas comme sonde cosmologique

Dès le début des années 1990, des premières études proposent d'utiliser les amas de galaxies comme sonde cosmologique.

Les mesures effectuées à l'aide des amas de galaxies convergent vers une valeur de $\Omega_{\mathrm{m}} \sim 0.3$ en désaccord avec les prédictions théoriques des modèles inflationnaires qui donnent un Univers plat, donc $\Omega_{\mathrm{m}} = 1$ (si on considère $\Omega_{\Lambda} = 0$). Ce résultat repose sur la mesure de la fraction de gaz dans les amas, de leur rapport masse sur luminosité ainsi que de leur abondance (voir par ex. la revue Bahcall, 1998).

Ainsi, la fraction de baryons dans les amas est estimée à environ 10-30% à l'époque alors que la fraction de baryons dans l'Univers mesurée par la nucléosynthèse est de l'ordre de 5% soit au moins un facteur trois plus faible (White & Frenk, 1991; White et al., 1993b; White & Fabian, 1995). En comparant le rapport masse sur luminosité de 16 amas de galaxies au rapport masse sur luminosité critique de l'Univers, Carlberg et al. (1996) ont estimé une densité de matière $\Omega_{\mathrm{m}} = 0.24 \pm 0.05(\mathrm{stat.}) \pm 0.09(\mathrm{syst.})$ significativement inférieure à l'unité. Cette mesure est étayée par les études sur les abondances des amas (Oukbir & Blanchard, 1992; Bahcall & Cen, 1993; White et al., 1993a; Oukbir & Blanchard, 1997).

Il est intéressant de noter que ce faisceau convergeant de mesures sur les amas a été publié avant la découverte de l'accélération de l'expansion de l'Univers (Riess et al., 1998; Perlmutter et al., 1999) et avant la découverte de "la platitude de l'Univers" (de Bernardis et al., 2000). Ces deux dernières découvertes ont constitué les piliers du modèle cosmologique de concordance largement adopté par la communauté aujourd'hui. Il faut remarquer, a posteriori, que les mesures de $\Omega_\mathrm{m} \sim 0.3$ données par les amas se sont révélées en excellent accord avec les mesures actuelles. Pourtant elles étaient source de débats intenses il y a vingt ans et n'ont pas réussi à convaincre l'ensemble de la communauté avant l'avènement du modèle de concordance au début des années 2000.

Les études de cosmologie avec les amas ont fait un pas en avant significatif grâce aux observations précises du satellite X Chandra (Allen et al., 2002, 2008). Lorsque j'ai terminé ma thèse en 2004, les contraintes cosmologiques basées sur les fractions de gaz de Allen et al. étaient présentées avec les contours des supernovae et du fond diffus cosmologique les plus à jour. J'ai reproduit la figure 4.1 emblématique de ces années. Cette contrainte a été remplacée par celle sur les BAO à la suite de leur première observation (Eisenstein et al., 2005) car elle montrait une ligne de dégénérescence proche de celle des amas dans le plan $(\Omega_\mathrm{m}, \Omega_\Lambda)$ et était a priori moins soumise à d'éventuelles systématiques.

2005

Au milieu des années 2000, le modèle de concordance est établi autour du CMB, des SNIa et des BAO. Les amas de galaxies restent une sonde secondaire mais en parfait accord avec le modèle. Les contraintes cosmologiques à l'aide de la fraction de gaz et de l'abondance des amas en X s'améliorent. Les sondages SZ n'ont pas encore livré leurs premières détections en aveugle.

Les études sur les abondances des amas se sont aussi poursuivies et ont gagné en précision, toujours à l'aide des fonctions de température et de luminosité locale (par exemple Pierpaoli et al., 2003) puis à l'aide de l'évolution des comptages d'amas en fonction du redshift sur des échantillons sélectionnés en X (Schuecker et al., 2003; Vikhlinin et al., 2009). En parallèle, le sondage SDSS a permis de constituer, pour la premières fois, de grands catalogue d'amas en optique (Koester et al., 2007; Wen et al., 2012a) qui ont débouché sur les contraintes à partir des comptages d'amas sélectionnés en optique (Rozo et al., 2010).

Les premiers amas détectés en SZ ont ouvert la voie aux contraintes cosmologiques basées sur la sélection SZ, plus proche d'une sélection en masse que les sélections X ou optique. Le levier en redshift s'est lui aussi agrandi. Les premières contraintes SZ sont venues avec les amas du South Pole Telescope (Vanderlinde et al., 2010) et ont été améliorées d'année en année (Benson et al., 2013; Reichardt et al., 2013; Bleem et al., 2015). L'Atacama Cosmology Telescope a donné ses premières contraintes plus récemment (Hasselfield et al., 2013) ainsi que Planck (Planck Collaboration XX, 2014; Planck Collaboration XXI, 2014). Je décrirai dans les deux parties suivantes les analyses SZ de Planck.

En parallèle à cet effort pour constituer en SZ de grands catalogues d'amas avec une sélection bien caractérisée, la constitution de catalogues X se poursuit avec, par exemple, les projets XCS, XMM-LSS et XXL de détection d'amas en aveugle à l'aide du satellite XMM. Le projet XXL devrait donner en 2015 des premières contraintes cosmologiques sur un échantillon d'amas moins massifs que les amas sélectionnés en SZ avec un bras de levier en redshift au moins aussi grand (voir par exemple Pacaud et al. (2007) pour la présentation du premier échantillon XMM-LSS et une étude de la dépendance en redshift des lois d'échelle en X).

La prédiction du nombre d'amas en fonction de leur masse et de leur redshift dépend à la fois de la géométrie de l'Univers[1] et des processus d'effondrement des structures[2] comme précisé dans le rapport du Dark Energy Task Force (Albrecht et al., 2006). Cette caractéristique est un atout car les amas sont doublement sensibles à la cosmologie. C'est aussi un handicap puisqu'il peut y avoir dégénérescence entre les

---

[1] Les amas sont une sonde géométrique

[2] mais ils sont aussi une sonde dynamique.

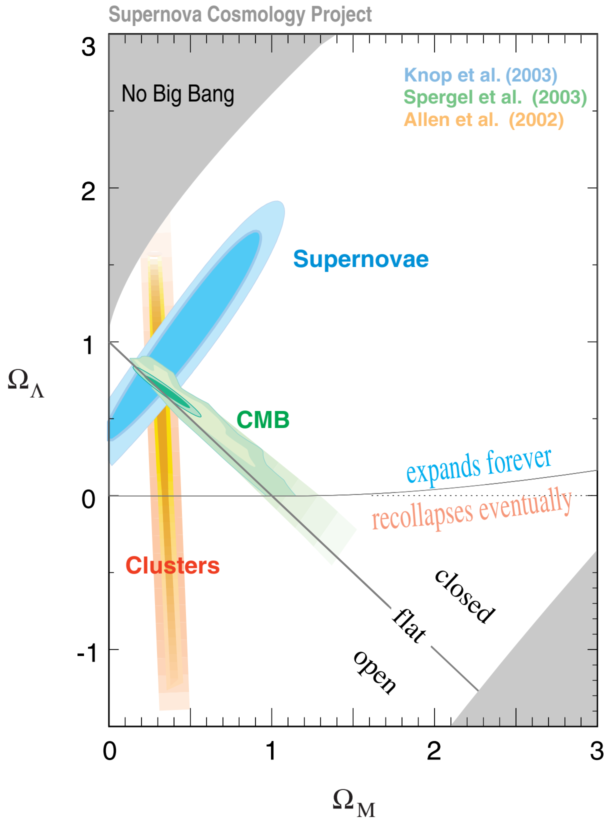

Figure 4.1: Etat de l'art des contraintes cosmologiques en 2003. Les trois sondes, CMB (WMAP), supernovæ (Supernova Cosmology Project) et amas (détermination de la fraction de gaz avec Chandra) sont concordantes autour d'un modèle $\Omega_m = 0.3$ et $\Omega_\Lambda = 0.7$. Figure adaptée du papier Knop et al. (2003).

paramètres dynamiques de formation des structures et les paramètres géométriques que l'on veut contraindre.

4.2 Modélisation de la fonction de sélection

L'ingrédient essentiel pour contraindre les paramètres cosmologiques avec un catalogue d'amas de galaxies est la fonction de sélection. Elle est composée de trois éléments :

- la complétude qui prédit le nombre d'amas observé étant donné le nombre d'amas présent dans le ciel,
- la photométrie, distribution des flux mesurés des amas étant donnés les flux vrais,
- la contamination qui donne la proportion de fausses détections dans le catalogue.

Ces quantités sont décrites en détail dans Melin et al. (2005) pour une expérience SZ. Les analyses Planck sur lesquelles j'ai travaillé jusqu'à aujourd'hui ont été effectuées sur des catalogues avec un seuil en signal sur bruit suffisamment haut pour que la contamination soit négligeable. Je n'en parlerai pas dans la suite. De même, la précision photométrique n'est pas intervenue dans les analyses car seul le redshift et le signal sur bruit des détections ont été utilisés. Je me concentrerai donc ici sur la description de la détermination de la complétude dans le sondage Planck.

4.2.1 Calcul analytique

Il est possible de prédire analytiquement la complétude de Planck à partir de considérations simples sur le bruit des cartes filtrées par le MMF. On suppose ce bruit Gaussien. Soit un amas de flux vrai Y et de taille $\theta_{\rm t}$. Les cartes du ciel filtrées autour de l'amas, pour une taille de filtre correspondant à celle de l'amas, sont un champ Gaussien de moyenne nulle et d'écart-type $\sigma_{\theta_{\rm t}}$ donné par l'équation 3.4. La probabilité que l'amas soit détecté avec un seuil q fois supérieur au bruit est

$$\frac{1}{\sqrt{2\pi}\sigma_{\theta_{\rm t}}}\int_{q\sigma_{\theta_{\rm t}}}^{\infty} dY'\, e^{-\frac{(Y'-Y)^2}{2\sigma^2_{\theta_{\rm t}}}} = \frac{1}{2}\,\mathrm{erfc}\left(\frac{q - Y/\sigma_{\theta_{\rm t}}}{\sqrt{2}}\right) \tag{4.1}$$

où erfc est la fonction d'erreur complémentaire. Pour Planck, le bruit après filtrage MMF dépend du niveau de bruit astrophysique (CMB, poussière galactique, etc.) et du bruit instrumental donc de la position sur le ciel. Pour notre amas de flux Y et de taille $\theta_{\rm t}$, la complétude s'écrira :

$$\chi(Y, \theta_{\rm t}, l, b) = \frac{1}{2}\,\mathrm{erfc}\left(\frac{q - Y/\sigma_{\theta_{\rm t}}(l,b)}{\sqrt{2}}\right) \tag{4.2}$$

Cette méthode permet simplement de prédire la probabilité d'observer un amas à l'aide du niveau de bruit des cartes filtrées de Planck $\sigma_{\theta_{\rm t}}(l,b)$. Je l'ai proposée au groupe de travail sur la cosmologie en février 2012. Elle a ensuite été confrontée aux deux autres méthodes présentées ci-dessous et s'est révélée être une bonne approximation de la complétude. Celle-ci a été utilisée pour les papiers de contraintes cosmologiques avec les amas de Planck en 2013 (Planck Collaboration XXI, 2014) et 2015 (Planck Collaboration XXIV, 2015).

4.2.2 Détermination par Monte Carlo

Une deuxième approche possible est d'injecter des amas simulés de différentes tailles et flux directement dans les cartes de Planck à des positions aléatoires sur le ciel. On utilise ensuite les codes d'extraction comme sur les données originales et on compte simplement les objets détectés et injectés. Le rapport du nombre d'amas détectés par le nombre d'amas injectés en fonction de la taille et du flux donne la complétude. La figure 4.2 en haut à gauche montre la différence relative entre l'estimation Monte Carlo et le calcul analytique pour l'algorithme MMF3 à un seuil de détection à $4.5\,\sigma$ avec un masque laissant visible les 85% du ciel les moins contaminés par la poussière galactique. En bas, à gauche, les deux estimations présentées pour quelques tailles de filtre. A droite, la même figure pour un seuil à $6\,\sigma$ et un masque laissant visible les 65% du ciel les moins contaminés par la poussière. On note qu'en pratique, il existe des différences significatives allant de 10 à 20% entre les estimations Monte Carlo et analytique. Les différences sont moins prononcées pour le seuil à $6\,\sigma$ utilisé dans l'analyse cosmologique. Pour ce dernier seuil, les deux estimations de la complétude, analytique et Monte Carlo, conduisent à des contraintes cosmologiques équivalentes (Planck Collaboration XXIV, 2015).

La méthode Monte Carlo possède des avantages supplémentaires par rapport au calcul analytique. En particulier, il est possible d'injecter des amas de forme complexe tirés de simulations hydro et de prendre en compte l'effet de lobes instrumentaux non circulaires. En outre, l'estimation de la complétude du catalogue union ou intersection de plusieurs méthodes de détection est aussi simple que l'estimation pour une méthode individuelle ce qui n'est pas le cas pour le calcul analytique.

4.2.3 Utilisation de catalogues externes

Au moment du lancement de Planck, j'ai participé à une étude menée par Antoine Chamballu sur la prédiction des propriétés X des amas Planck. Celle-ci montrait que la fonction de sélection de Planck "traversait" les amas des catalogues X, NORAS et REFLEX, c'est-à-dire que certains amas de ces catalogues allaient être détectés par Planck et d'autres non (Chamballu et al., 2012). Cette propriété permet d'estimer la complétude de Planck en s'appuyant sur ces catalogues. Dans un premier temps, il faut identifier les objets des catalogues NORAS/REFLEX dans le catalogue d'amas de Planck (seuil en signal sur bruit $q > 4.5$). Pour chaque amas, détecté ou non, on estime directement dans les cartes le flux Y et l'erreur σ_{θ_t} correspondante puis on construit l'histogramme des objets détectés et non détectés en fonction de la variable $\frac{q-Y/\sigma_{\theta_t}}{\sqrt{2}}$ (variable de l'estimation de la complétude analytique). Le rapport des histogrammes détectés sur le nombre total est la complétude. La figure 4.3 à gauche montre le résultat pour les amas connus en X. On a pu effectuer le même test avec les

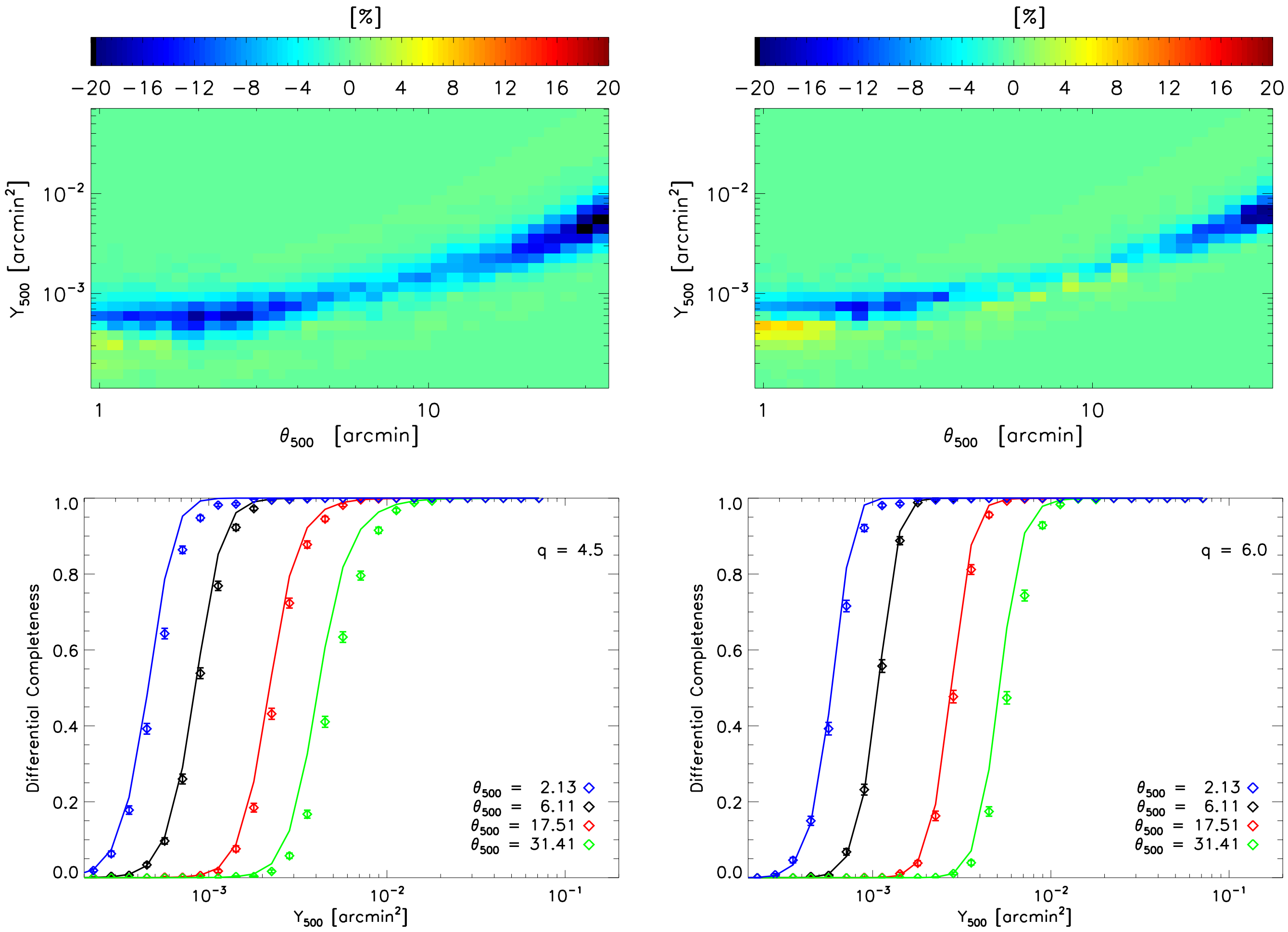

Figure 4.2: Différence des complétudes Monte Carlo et analytique pour MMF3 à un seuil de détection de $4.5\,\sigma$ (colonne de gauche) et à un seuil de détection de $6\,\sigma$ (colonne de droite). Les amas injectés dans la méthode Monte Carlo sont tirés des simulations numériques cosmo-OWLS (Le Brun et al., 2014; McCarthy et al., 2014) et les lobe complexes non Gaussien de Planck ont été utilisés. La différence entre les complétudes déterminées par Monte Carlo et de façon semi-analytique vont de 10 à 20%. L'impact de cette différence sur les paramètres cosmologiques pour un seuil à $6\,\sigma$ est minime. Ces figures sont extraites de Planck Collaboration XXVII (2015).

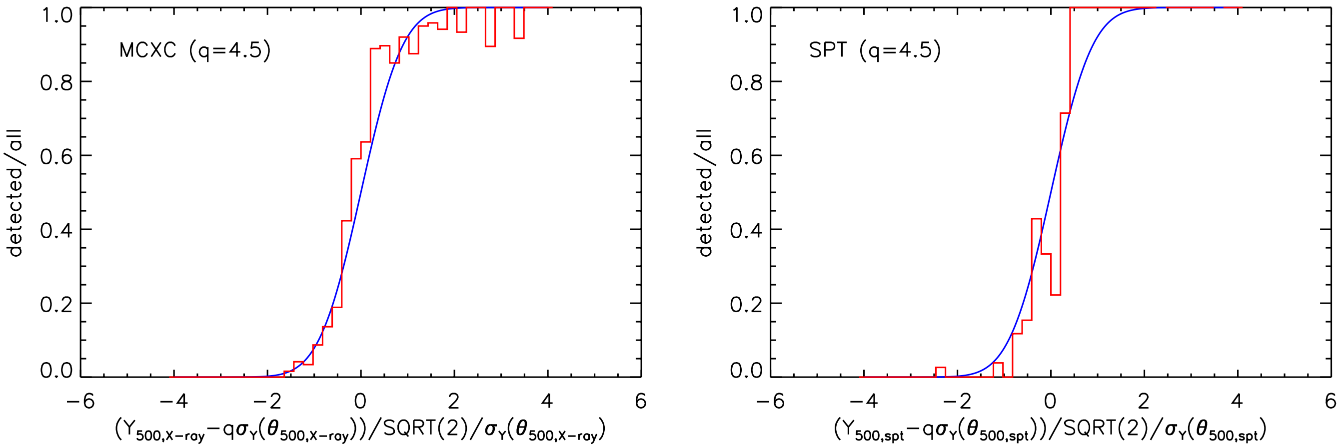

Figure 4.3: Complétude du catalogue MMF3 de Planck (histogrammes rouges) estimée sur des catalogues externes à un seuil de détection à $4.5\,\sigma$ (celui du catalogue publié en 2015). A gauche sur l'ensemble des amas connus en X (Piffaretti et al., 2011). A droite sur les amas détectés en SZ par l'expérience SPT (Bleem et al., 2015). Ces estimations sont en bon accord avec le calcul analytique (courbe bleue). Ces figures sont identiques à celles de Planck Collaboration XXVII (2015).

amas SZ de l'expérience SPT à droite. Dans les deux cas, la complétude estimée sur les catalogues externes (histogramme rouge) est en bon accord avec l'approximation analytique (courbe bleue). Notons cependant que pour les amas SPT, la complétude déterminée sur le catalogue externe semble être au-dessus de la complétude semi-analytique. Il est possible que cette sur-estimation soit due au fait que Planck et SPT sont deux expériences SZ : il y aurait plus de chance pour un amas SPT situé dans un intervalle de $\frac{q-Y/\sigma_{\theta_t}}{\sqrt{2}} > 0$ d'être détecté par Planck qu'un amas quelconque de l'Univers situé dans le même intervalle.

Avancées notables

La fonction de sélection du sondage SZ Planck est maîtrisée et contraintes par trois approches distinctes et convergentes. Elle est une des clefs qui a permis d'établir les premières contraintes avec le catalogue SZ de Planck en 2013 puis en 2015.

4.3 Contraintes cosmologiques

4.3.1 Analyse 2013, comptages d'amas et spectre de puissance du SZ

Les premières contraintes cosmologiques avec les amas Planck ont été publiées en 2013 (Planck Collaboration XX, 2014). Elles étaient basées sur le catalogue détecté par une méthode unique (MMF3) à un seuil de détection $q > 7$ suffisamment haut et un masque galactique de 65% suffisamment grand pour s'assurer que le catalogue était entièrement pur. Ce catalogue cosmologique contenait 189 amas ce qui en faisait déjà, à ce moment, le plus grand catalogue SZ utilisé pour contraindre les paramètres cosmologiques. L'analyse s'appuyait sur la comparaison des comptages observés en fonction du redshift dN/dz avec les comptages prédits théoriquement. Ces derniers peuvent être calculés grâce à la fonction de sélection χ (expression donnée dans la partie 4.2), la fonction de masse $\frac{dN}{dzdMd\Omega}$ et la loi d'échelle flux-masse des amas dite relation Y-M.

$$\frac{dN}{dz} = \int d\Omega \int dM \, \hat{\chi}(z, M, l, b) \, \frac{dN}{dzdMd\Omega} \tag{4.3}$$

$$\hat{\chi}(z, M, l, b) = \int dY \int d\theta_{\mathrm{t}} P(z, M|Y, \theta_{\mathrm{t}}) \chi(Y, \theta_{\mathrm{t}}, l, b) \tag{4.4}$$

avec $P(z, M|Y, \theta_{\mathrm{t}})$ la distribution de (z,M) étant donné (Y, θ_{t}).

La distribution P repose sur la loi d'échelle flux-masse Y-M. La pente et la normalisation de cette loi ont été déterminées à partir d'un sous-ensemble de 71 amas de l'échantillon cosmologique pour lequel des données XMM étaient disponibles en 2012. Le flux Y a été extrait de Planck et la masse M_X obtenue à partir des données XMM. La masse M_X n'est cependant pas égale à la masse M du halo présente dans la fonction de masse car l'hypothèse d'équilibre hydrostatique adoptée pour l'analyse X n'est pas toujours vérifiée et les mesures de température en X restent sujettes à des erreurs systématiques. On a décidé d'introduire un facteur multiplicatif $1-b$ pour tenir compte de cette différence:

$$Y \propto M_X^{\alpha} \tag{4.5}$$

$$M_X = (1-b)M \tag{4.6}$$

avec $\alpha = 1.79 \pm 0.06$ (proche de la valeur théorique de 5/3) ajusté sur les données X et SZ.

$1-b$ a été déterminé à partir de simulations numériques. Les résultats sont très dispersés mais prédisent une valeur dans l'intervalle [0.7,1] avec une valeur moyenne de 0.8 soit un biais de 20% entre la masse déterminée en X et la masse vraie des simulations ou de la fonction de masse.

Nous avons ensuite utilisé la statistique de Cash (Cash, 1979) dans des bins en redshift de taille $\Delta z = 0.1$ pour comparer comptages observés et théoriques. Le résultat principal de 2013 est présenté dans la figure 4.4. Le contour bleu présente les contraintes à 1 et 2 σ sur σ_8 et Ω_m obtenues avec les amas de Planck combinés aux oscillations acoustiques de baryons (BAO) et à la nucléosynthèse primordiale (BBN). Il est marginalisé sur $1-b$ dans l'intervalle [0.7,1]. Les contraintes issues du CMB primaire seul sont en rouge, en tension évidente avec le contour bleu sur σ_8. Le contour noir montre le résultat de l'analyse jointe amas SZ et CMB primaire pour laquelle le paramètre $1-b$ est laissé libre. Les deux contours rouge et noir

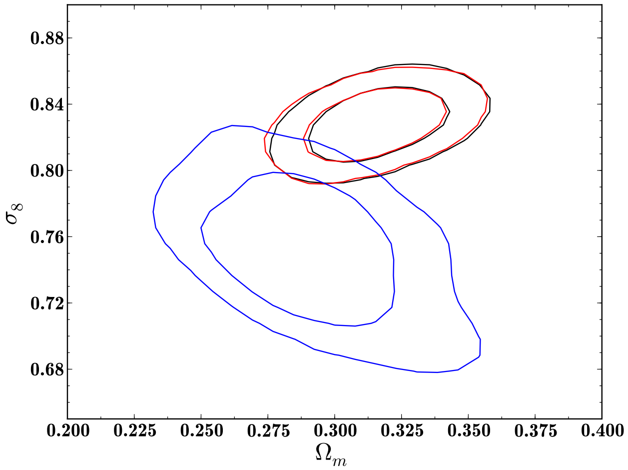

Figure 4.4: Contraintes cosmologiques 2013 des amas SZ (+BAO+BBN) (en bleu) et du CMB primaire (en rouge). Les deux contraintes sont en tension sur σ_8. Le contour noir est le résultat de l'analyse jointe amas SZ et CMB primaire pour laquelle le paramètre $1 - b$ est laissé libre. La figure est tirée de Planck Collaboration XX (2014).

sont quasi superposés : l'analyse jointe est dominée par le CMB primaire qui impose $1 - b = 0.59 \pm 0.05$ soit un biais entre la masse X et la masse vraie de l'ordre de 40%. Cette valeur du biais est plus grande qu'obtenue dans la grande majorité des simulations numériques et peut éventuellement poser des problèmes pour la fraction de gaz dans les amas qui deviendrait significativement inférieure à la fraction de baryons universelle.

Il faut noter que la combinaison $\sigma_8\,(\Omega_m/0.27)^{0.3}$ obtenue avec les amas Planck ($\sigma_8\,(\Omega_m/0.27)^{0.3} = 0.764 \pm 0.025$) est en bon accord avec la majorité des autres mesures réalisées sur les grandes structures comme le montre la figure 4.5, alors que la valeur du CMB primaire de Planck indique une valeur supérieure à 0.87 avec une barre d'erreur sensiblement plus petite que celle des amas soit une tension $>\sim 4\,\sigma$.

Par ailleurs, le spectre de puissance de la carte SZ tout le ciel C_l^{SZ} est compatible

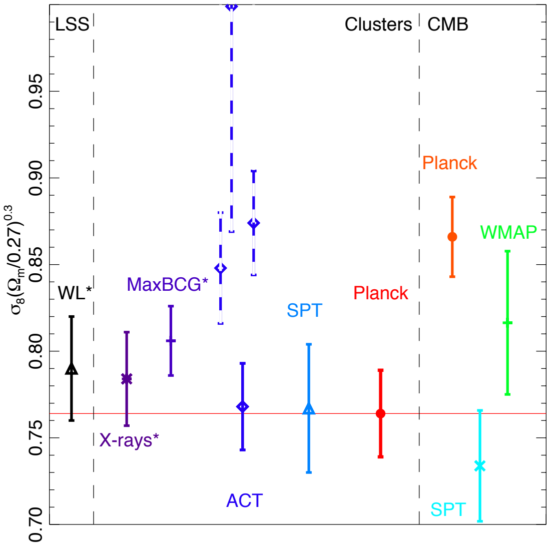

Figure 4.5: Comparaison des contraintes précédent 2013 sur les structures (à gauche du trait vertical en tirets le plus à droite) et sur le CMB primaire (à droite du même trait). Les analyses cosmologiques sur les structures trouvent des valeurs de la combinaison $\sigma_8\,(\Omega_m/0.27)^{0.3}$ plus petite que le CMB primaire de Planck. La figure est tirée de Planck Collaboration XX (2014).

avec les paramètres obtenus avec les comptages d'amas de galaxies et lui aussi en tension avec le CMB primaire (Planck Collaboration XXI, 2014). J'ai participé en particulier au travail de validation de cette carte en extrayant les amas et en comparant leur flux au flux directement extrait des données par les Matched Multifilters à la fois en 2013 et en 2015 (Planck Collaboration XXII, 2015).

Le papier général de cosmologie de Planck (Planck Collaboration XVI, 2014) mentionne succinctement la tension entre amas/carte SZ et CMB primaire mais reste prudent en ne présentant pas d'analyse combinée.

4.3.2 Analyse 2015

Entre 2013 et 2015, j'ai participé à l'extraction du second catalogue d'amas de Planck basé sur l'ensemble des données de la mission et j'ai pu construire un nouveau sous-catalogue MMF3 avec un seuil de détection plus bas (S/N> 6). Ce nouveau catalogue contient 439 amas. Une première amélioration de l'analyse 2015 par rapport à l'analyse 2013 est ce gain d'un facteur supérieur à deux sur le nombre d'amas du catalogue (439 contre 189 en 2013).

Une deuxième amélioration de l'analyse vient des hypothèses sur le paramètre $1-b$. Alors que ce paramètre était déterminé sur simulations numériques en 2013, nous nous sommes appuyés sur des mesures de masse directes par lentille gravitationnelle des expériences CCCP ($1-b = 0.780 \pm 0.092$, Hoekstra et al., 2015) et Weighing the Giants ($1-b = 0.688 \pm 0.072$, von der Linden et al., 2014). Nous y avons ajouté une troisième méthode qui mesure l'effet de lentille sur les anisotropies du CMB dans les données Planck et que je présenterai plus en détail dans le chapitre 5 ($(1-b)^{-1} = 0.99 \pm 0.19$).

Enfin, la troisième amélioration de l'analyse 2015 par rapport à l'analyse 2013 est la vraisemblance. Nous avons développé une vraisemblance basée à la fois sur le redshift z et sur le signal sur bruit $S/N = q$. Elle s'écrit désormais

$$\frac{dN}{dzdq} = \int d\Omega \int dM\, P[q|\bar{q}_{\rm m}(z,M,l,b)]\, \frac{dN}{dzdMd\Omega} \tag{4.7}$$

avec $P[q|\bar{q}_{\rm m}(z,M,l,b)]$ la distribution de q étant donné le signal sur bruit moyen $\bar{q}_{\rm m}(z,M,l,b)$ avec

$$\bar{q}_{\rm m} \equiv Y(z,M)/\sigma_{\theta_{\rm t}}(l,b) \tag{4.8}$$

et

$$\theta_{\rm t} = \theta_{\rm t}(z,M) \tag{4.9}$$

Il faut préciser que la distribution P est différente de celle de l'équation 4.3. L'analyse combinant ces trois améliorations est détaillée dans le papier Planck 2015 de contraintes cosmologiques avec les comptages d'amas (Planck Collaboration XXIV, 2015).

Les résultats confirment ceux de l'analyse 2013. Ils sont présentés dans la figure 4.6. Les contours amas 2015+BAO+BBN sont en couleur verte, bleue, violette pour WtG, CCCP et CMBlens respectivement (niveau de confiance à 68 et 95%). La tension avec le CMB primaire (contours tracés en tirets noirs et calculés avec la vraisemblance en température et polarisation) est toujours présente pour CCCP ($1 - b$ proche du 0.8 [-0.1+0.2] pris dans l'analyse 2013); elle s'accroît pour CMBlens pour lequel $1 - b$ est plus proche de 1. Au contraire, la tension diminue si on adopte $1 - b$ de WtG. Changer la valeur centrale de $1 - b$ déplace le contour dans le sens perpendiculaire à la ligne de dégénérescence de la contrainte amas $\sigma_8\Omega_m^{0.3} = \text{cste}$. Plus $1 - b$ est faible, plus le contour des amas est en accord avec le CMB primaire. Les contours grisés correspondent au cas où le CMB primaire et combiné avec les BAO. Les contours en traits rouges continus correspondent à la combinaison des amas et du spectre de lentille gravitationnelle de Planck sur tout le ciel en laissant le paramètre $1 - b$ libre : cette combinaison mène à un résultat compatible avec le cas CMB seul. L'analyse combinée amas SZ et CMB primaire est dominée par le CMB et impose $1 - b = 0.58 \pm 0.04$, une valeur sensiblement plus faible que la valeur mesurée par WtG.

L'hypothèse la plus intéressante pour réduire la tension entre les amas et le CMB primaire sur σ_8 est de laisser libre la somme des masses des neutrinos $\sum m_\nu$ dans l'analyse. Dans le modèle de base, celle-ci est fixée par défaut à 0.06 eV, somme de masses minimale pour un neutrino le plus léger de masse négligeable. Le résultat de la combinaison des amas et du CMB primaire sur la masse des neutrinos est montrée dans la figure 4.7 en ligne rouge continue. Si on ajoute le spectre de lentille gravitationnelle de Planck sur tout le ciel, une bosse autour de 0.2 eV apparaît (courbe en tirets rouges). Si au lieu d'ajouter le spectre de lentille, on ajoute le BAO, alors la bosse disparaît et la limite sur la somme des masses devient forte (courbe continue

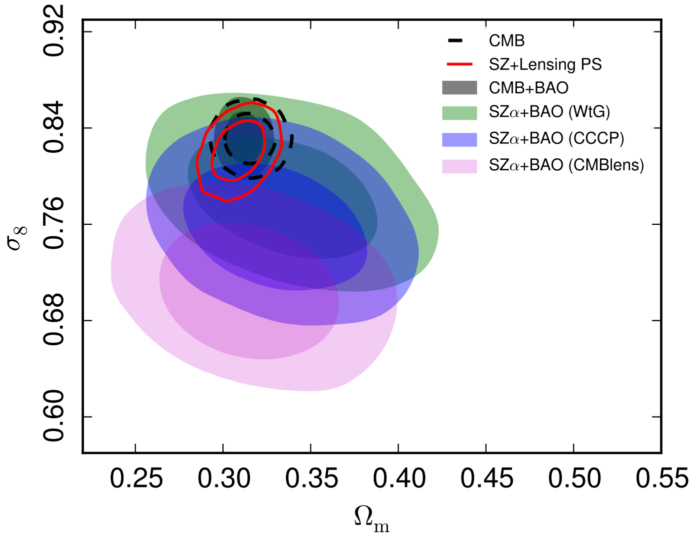

Figure 4.6: Contraintes cosmologiques 2015 des amas SZ et du CMB primaire. Les contours des amas en couleur verte, bleue, violette restent en tension avec les contours du CMB primaire en tirets noirs. La signification des autres courbes est donnée dans le texte. La figure est tirée de Planck Collaboration XXIV (2015).

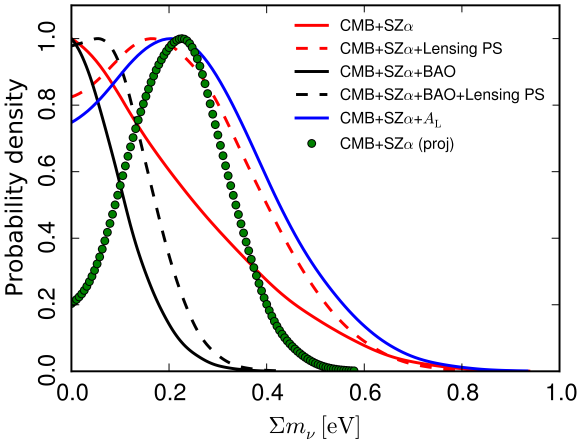

Figure 4.7: Contraintes 2015 sur la somme des masses des neutrinos. L'analyse jointe amas, CMB primaire et spectre de lentille gravitationnel sur l'ensemble du ciel montre une bosse autour de 0.2 eV (courbe en tirets rouges), réduite lorsqu'on ajoute les BAO (courbe en tirets noirs). La signification des autres courbes est donnée dans le texte. La figure est tirée de Planck Collaboration XXIV (2015).

noire, $\sum m_\nu < 0.20\,\mathrm{eV}$). Ajouter de nouveau le spectre de lentille change peu cette limite (courbe en tirets noirs). Cependant, laisser libre le paramètre $A_{\rm L}$ (=1 dans le modèle minimal) qui représente l'amplitude de l'effet de lentille par rapport au meilleur modèle du CMB primaire montre un comportement similaire à l'inclusion du spectre de lentille avec une bosse au même endroit (courbe continue bleue) pour $\sum m_\nu$. La signification des points verts sera donnée dans la partie 4.3.3.

Les résultats de l'analyse jointe amas, CMB et spectre de lentille est donc en tension avec l'analyse BAO (ou BAO et CMB) quand on laisse le paramètre $\sum m_\nu$ libre. Cette tension est en particulier visible sur le paramètre H_0. L'analyse amas, CMB et spectre de lentille donne une valeur autour de 65 km/s/Mpc en tension avec l'analyse BAO (ou BAO et CMB) qui impose une valeur de 68 km/s/Mpc avec une barre d'erreur de l'ordre de 1 km/s/Mpc. La valeur de 65 km/s/Mpc est en outre en plus grande tension avec les mesures directes de H_0 ($73.8 \pm 2.4\,\mathrm{km/s/Mpc}$, Riess et al., 2011).

4.3.3 Limitations de l'analyse amas

L'analyse amas est limitée en premier lieu par notre connaissance sur le paramètre $1-b$ ou, de façon équivalente, la normalisation de la relation Y-M. C'est l'incertitude majeure sur laquelle il faut travailler. La figure 4.8 est une reproduction de la figure 4.6 pour laquelle on a fait l'hypothèse que $1-b = 0.78 \pm 0.01$, une précision affichée par les futures missions Euclid et LSST (Large Synoptic Survey Telescope). Le catalogue et la vraisemblance restent les mêmes. Les contraintes deviennent remarquablement précises. L'implication sur $\sum m_\nu$ est montrée en points verts dans la figure 4.7 : une détection claire d'une somme des masses des neutrinos serait possible, ou bien la découverte de nouvelle physique. Cependant, il faut remarquer que $1-b$ est supposé constant pour l'analyse Planck et pour cette projection. C'est une première approximation mais, dans le cas général, ce paramètre pourrait dépendre de la masse, du redshift et éventuellement d'autres paramètres physiques des amas.

2015

L'incertitude majeure de l'analyse amas de Planck est la normalisation de la relation Y-M connue à $\sim 30\%$ aujourd'hui si on considère un échantillon représentatif d'estimations de masse par effet de lentille. L'amélioration de l'analyse Planck passera par des études multi-longueur d'onde d'amas soumis à des incertitudes systématiques différentes.

En parallèle de la recherche de meilleures contraintes sur la normalisation de la Y-M, d'autres améliorations sont à réaliser. Citons, d'abord la compréhension de l'origine du mauvais ajustement (probability to exceed $PTE = 0.23$) des comptages théoriques aux données avec un décalage entre les deux dépendant du redshift. Est-il dû à la fonction de sélection, à la fonction de masse ou à la loi d'échelle Y-M ?

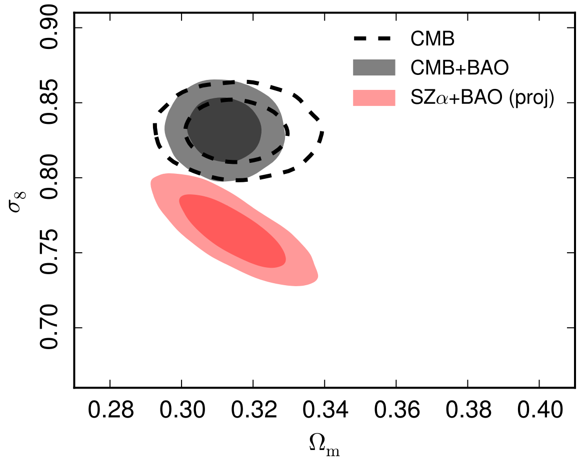

Figure 4.8: Projections sur les contraintes amas avec une normalisation Y-M connue à 1%, le catalogue et la vraisemblance restant les mêmes. La figure est tirée de Planck Collaboration XXIV (2015).

La fonction de masse des halos est-elle si bien connue que décrite dans les papiers précédent 2010 ? Ce n'est pas certain au vu de publications récentes (par exemple, Bocquet et al., 2015; Angrick et al., 2015). Quel est l'impact des baryons sur la fonction de masse ? Quelles seraient les contraintes obtenues avec un catalogue encore plus grand ? Pourrait-on imaginer écrire une vraisemblance combinant à la fois comptages d'amas et estimation de la Y-M par mesures de flux et masses d'amas individuels d'un sous-échantillon, deux étapes actuellement séparées dans l'analyse ?

De nombreuses améliorations sont encore possibles sur cette analyse du catalogue de Planck qui pourront sans aucun doute servir les analyses des futures missions eROSITA et Euclid. Les analyses cosmologiques avec les comptages d'amas devraient ainsi atteindre leur apogée dans les cinq à dix prochaines années.

Chapitre 5

ESTIMATION DE LA MASSE DES AMAS PAR EFFET DE LENTILLE GRAVITATIONNELLE SUR LE CMB

5.1 Le problème de l'estimation de la masse des amas

L'estimation de la masse des amas de galaxies est un problème complexe. Les amas étant essentiellement constitués de matière noire invisible, leur masse est en général déduite de leur contenu en baryons (galaxies ou gaz). On utilise en premier lieu des lois d'échelle observable-masse $O - M$ qui permettent de déterminer la masse M d'un objet d'un échantillon donné à partir d'une caractéristique observée de l'amas O. Ainsi, en optique, la masse des amas peut être estimée à l'aide d'une relation richesse-masse qui lie le nombre de galaxies d'un amas à sa masse. Les études récentes sur les sondage SDSS ont permis de faire de grands progrès dans ce domaine (par exemple, Koester et al., 2007; Wen et al., 2009, 2012b). La richesse est directement mesurée sur les données SDSS comme le nombre de galaxies dans un rayon fixé et la masse déterminée par moyennage de l'effet de lentille gravitationnelle faible sur les objets de même richesse (Johnston et al., 2007) ou via des mesures directes individuelles de lentille ou en X (Rozo et al., 2009; Wen et al., 2010). La dispersion de la relation reste cependant grande, de l'ordre de 45% sur la masse pour une richesse donnée.

Une autre possibilité pour estimer la masse est d'utiliser des lois d'échelle en X. L'observable est alors la luminosité L, la température T, la masse M_g ou le paramètre $Y_X = M_g T$ du gaz. Pour ces observables, les dispersions sont du même ordre de grandeur que celle de la relation richesse-masse en optique. Mais les observations X suffisamment profondes et ayant une bonne résolution (XMM ou Chandra) permettent de déterminer directement la masse totale de l'amas en supposant que la gaz est en équilibre hydrostatique dans le puits de potentiel de matière. L'accord des masses par cette dernière méthode entre les analyses XMM et Chandra est de l'ordre de 13% entre les analyses Arnaud et al. et Vikhlinin et al. Cette différence est dominée par les incertitudes d'étalonnage des spectres entre les deux satellites[1]. Nous avons vu dans le chapitre 4 que les simulations numériques indiquent un biais de l'ordre de 20% entre la masse M et la masse estimée par cette méthode. Les incertitudes de calibration des instruments peuvent de plus faire varier cette quantité de ±10%.

A priori, la loi $Y_{SZ} - M$ devrait pouvoir être utilisée mais il est encore aujourd'hui difficile d'estimer Y_{SZ} à partir des mesures SZ sans faire intervenir d'a priori venant d'autres observations comme les X. On a utilisé une telle combinaison des mesures SZ et des lois d'échelle X dans l'analyse Planck pour déterminer la masse des amas Planck (Planck Collaboration XXIX, 2014).

Enfin, la méthode la plus directe d'estimation de la masse est l'utilisation des effets de lentille gravitationnelle faible des amas sur les galaxies d'arrière-plan. Le régime fort (qui produit des arcs gravitationnels) peut aussi être utilisé pour les parties centrales des amas très massifs. L'estimation de masse par lentille faible s'est développé ces dernières années et plusieurs dizaines d'observations profondes d'amas sont aujourd'hui disponibles. Les mesures récentes donnent des masses plus hautes de 20 à 30% par rapport aux masses estimées via l'équilibre hydrostatique en X (Hoekstra et al., 2015; von der Linden et al., 2014).

Aujourd'hui, chacune des méthodes décrites ci-dessus (lois d'échelle optique ou X, équilibre hydrostatique en X, effet de lentille gravitationnelle) fournit des mesures de masse avec des erreurs systématiques de l'ordre de 10%, différentes d'une méthode à l'autre. Ces erreurs dominent les incertitudes de l'analyse cosmologique des amas présentée dans le chapitre 4. L'amélioration de l'estimation de la masse des amas est donc une étape cruciale pour l'avenir des contraintes cosmologiques basées sur les

---

[1] communication de Monique Arnaud.

comptages.

2005

Une autre technique prometteuse identifiée au début des années 2000 est la détection, dans le millimétrique, de l'effet de lentille gravitationnelle des amas sur le fond diffus cosmologique (Zaldarriaga & Seljak, 1999; Seljak & Zaldarriaga, 2000; Holder & Kosowsky, 2004; Vale et al., 2004) mais la mise en pratique sur les données n'était pas possible au vu de la résolution et du niveau de sensibilité requis.

L'arrivée des données Planck, ACT et SPT a changé la donne. Même si ces données ont une résolution et une sensibilité limitées qui ne permettent pas la détection de l'effet de lentille gravitationnelle sur les amas individuels, il est possible de moyenner l'effet de lentille sur un ensemble de structures et de le détecter à quelques sigma.

5.2 Extraire la masse des amas par effet de lentille sur le CMB en pratique

De 2013 à 2015, j'ai mis au point avec Jim Bartlett une méthode pratique d'extraction de l'effet de lentille gravitationnelle des amas sur le fond diffus cosmologique. Nous avons d'abord simplement essayé d'utiliser la carte d'effet de lentille de tout le ciel disponible au sein de la collaboration Planck, mais le signal n'était pas présent. Nous avons donc dû développer entièrement une nouvelle méthode.

Nous partons d'un catalogue d'amas (par exemple le ESZ-XMM ou le catalogue cosmologique de Planck). Pour chaque amas de catalogue, nous découpons les six cartes Planck HFI tangentielles (10×10 deg) centrées sur l'amas. Nous les combinons grâce à une ILC contrainte (Remazeilles et al., 2011) de façon à obtenir une carte de CMB primaire non contaminée par l'effet SZ thermique de l'amas. Nous appliquons ensuite l'estimateur de Hu & Okamoto (2002) sur cette carte pour obtenir le potentiel

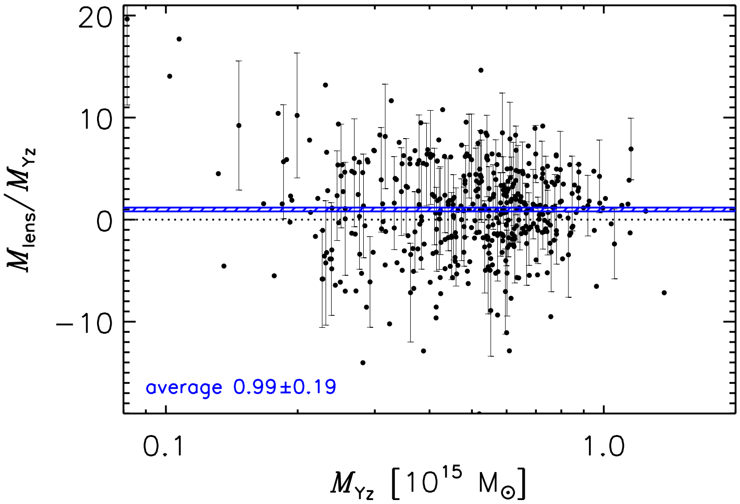

Figure 5.1: Masses de l'échantillon cosmologique 2015 de Planck déterminées par effet de lentille sur le CMB. Seulement 1 barre d'erreur sur 5 est affichée par souci de lisibilité. La bande bleue est la moyenne pondérée sur l'échantillon. La figure est tirée de Planck Collaboration XXIV (2015).

gravitationnel de l'amas. Enfin, nous utilisons un filtre adapté mono-fréquence pour comparer ce potentiel à un modèle basé sur les observations X. Chaque masse d'amas est détectée avec un signal-sur-bruit faible compris entre 0.1 et 1. Le filtre adapté fournit pour chaque objet l'estimation de l'amplitude du potentiel et l'erreur associée. Il est possible de moyenner ces amplitudes en les pondérant par l'inverse de la variance. Cette méthode est décrite en détail dans Melin & Bartlett (2015).

Nous l'avons appliquée sur un catalogue simulé du ESZ-XMM (les 62 amas du catalogue ESZ de Planck qui étaient dans les archives XMM) et avons montré qu'on pouvait détecter l'effet à un signal-sur-bruit global compris entre 3 et 4 (Melin & Bartlett, 2015). Un papier est en préparation pour l'application sur les données Planck.

En parallèle, j'ai utilisé la méthode sur l'échantillon cosmologique 2015. Celui-ci comportant plus d'objets que le catalogue ESZ-XMM, il a été possible d'atteindre un signal-sur-bruit global de l'ordre de 5. Les mesures individuelles de masse des amas sont présentées dans la figure 5.1 en disques noirs et la moyenne globale est matérialisée par la bande bleue ($\pm 1\,\sigma$). On trouve $(1-b)^{-1} = 0.99 \pm 0.19$ (erreur statistique). Ce résultat est décrit et utilisé dans le papier d'analyse cosmologique des amas de Planck (Planck Collaboration XXIV, 2015).

Le résultat des mesures de masse de l'échantillon cosmologique de Planck a été présenté à la conférence de Ferrare début décembre 2014. A la même conférence, la collaboration ACT a présenté une mesure équivalente sur ses données (Madhavacheril et al., 2015): le moyennage du signal de lentille en direction de 12 000 galaxies CMASS (détection à un niveau de 3.2 σ). Fin décembre 2014, la collaboration SPT a, elle aussi, publié le moyennage du signal de lentille en direction de 513 amas SZ dans ses données avec un niveau de détection de 3.0 σ (Baxter et al., 2014).

Avancées notables

Depuis fin 2014, il existe des méthodes statistiques pratiques qui permettent de mesurer les masses des amas dans les données millimétriques par détection de l'effet de lentille gravitationnelle sur le CMB. Ces méthodes ont été appliquées sur les jeux de données existants comme Planck, ACT ou SPT.

5.3 Une méthode d'avenir ?

Bien qu'encore assez marginales, ces premières détections de l'effet de lentille gravitationnelle sur le CMB sont très prometteuses.

D'abord, parce que les données existantes n'ont pas encore fourni toute l'information qu'elles contiennent : l'utilisation de catalogues plus grands allant à plus basse masse, comme les catalogues MaxBCG (Koester et al., 2007) ou redMaPPer (Rykoff et al., 2014), pourraient permettre de construire des lois d'échelles Y-M uniquement à par-

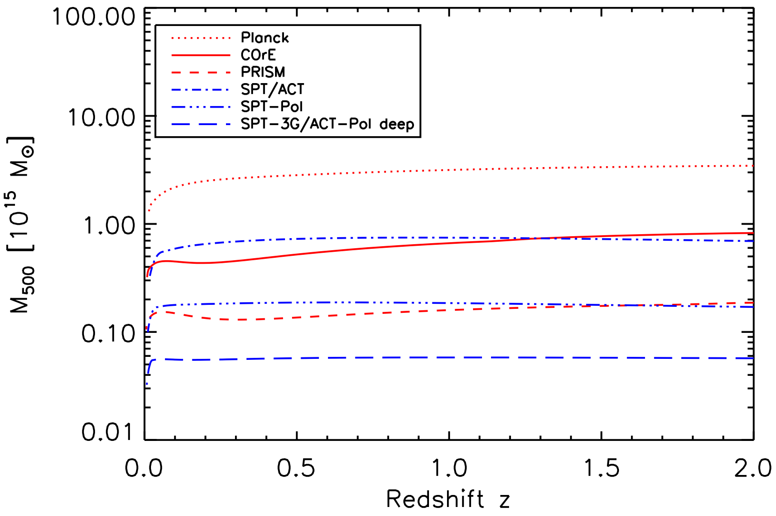

Figure 5.2: Erreurs à 1 σ sur la masse déterminée par effet de lentille sur le CMB pour différentes expériences en fonction du redshift. La figure est tirée de Melin & Bartlett (2015).

tir des données Planck (Y à partir de l'effet SZ thermique et M à partir de l'effet de lentille sur le CMB). Ensuite, la méthode actuelle est basée uniquement sur les cartes de température. Il devrait être assez facile d'inclure les cartes de polarisation et de gagner en signal sur bruit.

Dans un futur plus lointain où on disposera de jeux de données CMB à meilleures résolution et sensibilité, la détection de l'effet pourra se faire sur des amas individuels. La figure 5.2 présente l'erreur à 1 σ sur la masse d'un amas en fonction de son redshift z pour Planck et différents projets d'expériences CMB. Planck, ACT et SPT ne sont pas assez sensibles pour mesurer les masses d'amas individuels mais les projets comme SPT-Pol, SPT-3G, ACT-Pol deep et le projet satellite PRISM[2] permettent ces mesures.

---

[2] http://www.prism-mission.org

Il est intéressant de noter que les courbes présentées dans la figure 5.2 sont plates, c'est-à-dire que l'effet de lentille sur le CMB permet de détecter avec la même facilité la masse d'un amas proche et celle d'un amas très lointain. C'est un des grands avantages de cette méthode par rapport aux méthodes plus traditionnelles d'étude du cisaillement gravitationnel des galaxies d'arrière-plan en optique. En effet, pour ces dernières méthodes, il faut disposer d'un grand nombre de galaxies d'arrière-plan pour obtenir une mesure de masse précise ce qui est d'autant plus difficile que l'amas est situé à grand z. L'autre limitation des études de cisaillement gravitationnel est le nombre d'objets. Le temps d'observation étant assez long, on ne dispose et on ne pourra disposer que de quelques dizaines d'amas observés avec une grande précision. Ces méthodes restent cependant beaucoup plus précises que les méthodes tout juste développées sur le CMB pour les amas observés aujourd'hui : les amas massifs situés à redshift de l'ordre de 0.5.

2015

Dans quelques années, lorsque les amas les plus massifs à $z > 1$ auront été détectés, on devrait avoir un plus grand avantage à estimer les masses lentilles à l'aide de nouvelles expériences CMB qu'avec des observations de cisaillement gravitationnel au sol car on disposera d'un fond d'arrière-plan statistiquement bien caractérisé sur l'ensemble du ciel et de données obtenues dans un temps d'intégration raisonnable.

Chapitre 6

LOIS D'ÉCHELLE SZ-X ET SZ-OPTIQUE

La physique des amas de galaxies est dominée par la gravitation. Ainsi, au premier ordre, les propriétés observationnelles des amas peuvent-elles être directement liées à la masse par des lois d'échelle : la température, la luminosité X, la masse de gaz, le flux SZ, etc. sont déduits de la masse, ou inversement, par une simple loi linéaire dans le plan log-log (voir par exemple, Voit, 2005).

Dans ce chapitre, je ne ferai pas une revue exhaustive de toutes les lois d'échelles possibles en SZ, X et/ou optique mais me concentrerai sur deux types de lois d'échelles sur lesquelles j'ai travaillé : les lois d'échelle liant propriétés SZ et X dans la partie 6.2 et celles liant propriétés SZ et optiques dans la partie 6.3. Ces lois d'échelles ont été construites à l'aide des données Planck. Mais avant d'aborder celles-ci, je présenterai, dans la partie 6.1, le débat qui a animé la communauté amas pendant plusieurs années avant les premières publications Planck : le flux SZ observé dans les données WMAP est-il au niveau prédit par les observations X ?

6.1 Amas X et flux SZ : une controverse de plusieurs années

A la suite de la publication des données WMAP en 2003, plusieurs groupes de chercheurs ont tenté d'en extraire le signal SZ thermique. WMAP ayant été conçu pour l'étude des anisotropies primaires du CMB, le niveau de bruit instrumental et la résolution de l'instrument n'étaient pas optimisés pour ce type d'analyse. L'extraction s'est donc révélée particulièrement difficile. Ainsi, seuls quelques amas très massifs ont un signal sur bruit individuel de quelques sigma seulement (voir par exemple la figure 3.1 du chapitre 3; Coma et A2163 sont détectés à 4 et 3.5 σ respectivement avec le MMF). Il faut donc effectuer des analyses statistiques en moyennant le signal de nombreux amas pour obtenir un résultat statistiquement significatif. Lieu et al. (2006) (puis Bielby & Shanks, 2007) ont fait une première tentative. Ils ont alerté la communauté en ne trouvant dans le signal SZ mesuré de 31 amas dans WMAP qu'une fraction de signal attendu (modélisé à partir des mesures X), un résultat surprenant avec deux explications possibles selon Lieu et al. (2006) : des problèmes dans les données WMAP à l'échelle des amas ou une origine non cosmologique du CMB. La figure 6.1 présente ce résultat dans trois bandes de fréquences WMAP (Q=40 GHz, V=60 GHz, W=90 GHz). Le profil moyen mesuré des amas dans WMAP est la ligne continue avec les barres d'erreur. Le profil attendu, calculé à partir des données X, est la ligne continue ceinte des deux lignes en tirets (erreur à 1 σ). La taille de l'erreur systématique est montrée sur chaque figure en bas à droite. Pour chaque fréquence, le flux observé (en valeur absolue) est systématiquement inférieur au flux attendu. Diego & Partridge (2010) et Atrio-Barandela et al. (2008) ont étudié plus en détail le profil des objets et ont montré que le profil β (hypothèse de l'analyse de Lieu et al., 2006) ne semblait pas être un bon ajustement aux observations. Ils n'ont cependant pas conclu définitivement sur le déficit ou non de flux SZ par rapport au flux X. Afshordi et al. (2007) ont été les premiers à affirmer que le flux SZ et le flux X étaient en bon accord et que les profils SZ suivaient ceux des observations X et des simulations (Nagai et al., 2007).

J'ai pu proposer une étude plus approfondie grâce à la constitution d'un catalogue compilé homogène d'amas de galaxies en X (qui deviendra plus tard le MCXC, Piffaretti et al., 2011) et à l'utilisation du Matched Multi Filter. Le catalogue proto-MCXC a été élaboré autour de Rocco Piffaretti au sein du groupe de Monique Arnaud (Irfu/SAp) et j'ai développé les versions fonctionnelles du Matched Multi Filter à l'Irfu/SPP en collaboration avec l'APC (Jacques Delabrouille et Jim Bartlett). Le MMF permet d'obtenir une mesure non biaisée du flux d'un amas, une propriété essentielle pour pouvoir moyenner le signal de plusieurs objets ayant la même lumi-

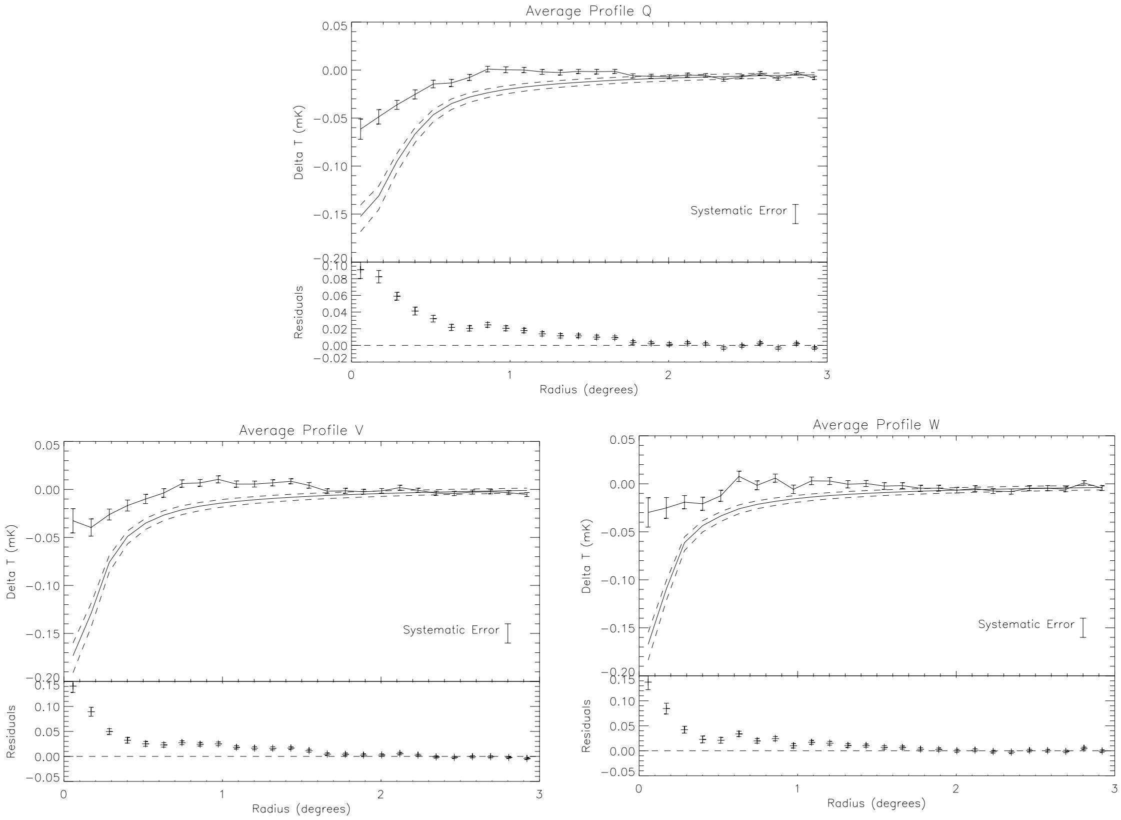

Figure 6.1: Moyenne des flux de 31 amas X mesurés dans trois bandes WMAP (Q=40 GHz, V=60 GHz, W=90 GHz) par Lieu et al. (2006). Le flux observé (ligne continue avec barres d'erreur) est significativement inférieur (en valeur absolue) au flux prédit par les X (ligne continue ceinte par les lignes en tirets). Reproduction de la figure 5 du papier.

nosité X (ou la même richesse). Le mariage des deux mouvances (catalogue X et outils SZ adaptés) a donné le jour au papier Melin et al. (2011). Ce dernier montre que le flux SZ de 893 amas X dans WMAP est en parfait accord avec le flux mesuré en X et établit pour la première fois les lois d'échelle Y-L et Y-M. Les résultats sont présentés dans la figure 6.2. A gauche, la loi d'échelle Y-M mesurée (losanges rouges) et prédite par les observations X (étoiles et trait bleus). A droite, le rapport entre les données et le modèle, parfaitement compatible avec l'unité. La détection globale est de l'ordre de $10\,\sigma$.

La collaboration WMAP a ensuite participé activement au débat (Komatsu et al., 2011) mais sans trancher complètement non plus.

2005

Le papier Lieu et al. (2006) a donc lancé une controverse sur la compatibilité du signal SZ des données WMAP avec les observations X. Le débat a duré plusieurs années avec des résultats incompatibles d'une analyse à l'autre. Il faudra attendre les données Planck pour trancher définitivement.

6.2 Analyses statistiques de catalogues X

A la suite du lancement de Planck, nous avons naturellement voulu refaire l'analyse Melin et al. (2011) sur le nouveau jeu de données. Le papier a été mené par Rocco Piffaretti et moi. Rocco a amélioré le MCXC en incluant plus d'amas, en particulier à plus haut redshift pour étudier l'évolution. Le papier Planck Collaboration X (2011) est paru, comportant à la fois les résultats sur la Y-L et la Y-M mais aussi sur la dispersion intrinsèque des relations et leur évolution. Le résultats sont présentés dans le figure 6.3. Ceux-ci confirment avec une précision accrue ($35\,\sigma$) les résultats du papier Melin et al. (2011).

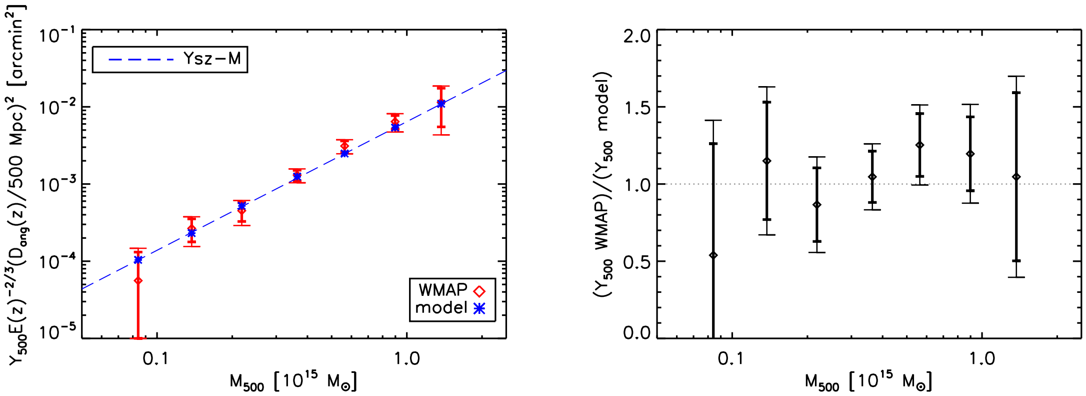

Figure 6.2: *A gauche :* Flux de 893 amas proto-MCXC dans les données WMAP en rouge et modèle en bleu. *A droite :* Rapport entre observation et modèle. Les points sont compatibles avec l'unité. La figure est tirée de Melin et al. (2011).

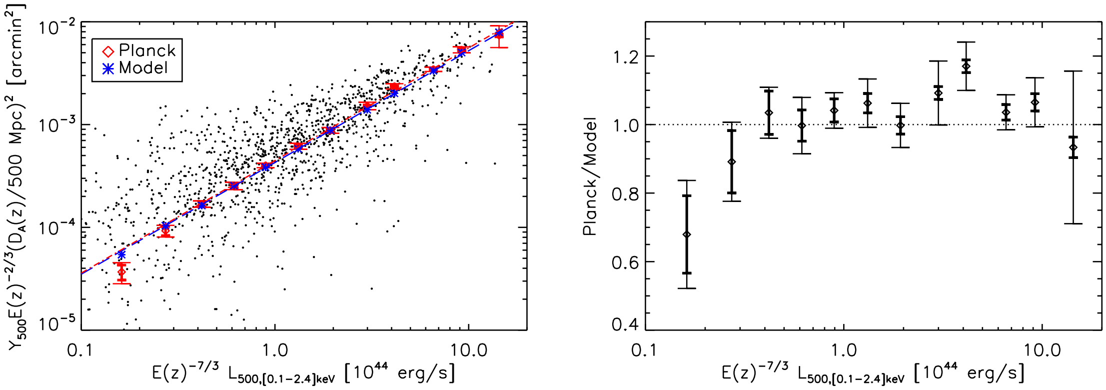

Figure 6.3: *A gauche :* Flux d'une partie des amas 1600 amas MCXC dans les données Planck (individuels=points noirs, moyenné=losanges rouges, modèle=étoiles bleues). *A droite :* Rapport du flux observé et du modèle X. Ces résultats confirment, avec une bien meilleure précision, l'analyse Melin et al. (2011). La figure est tirée de Planck Collaboration X (2011).

Avancées notables

Planck a donc tranché définitivement : le flux observé en SZ est bien compatible avec le flux prédit par les X. Un autre résultat important est établi : le flux SZ trace mieux la masse que la luminosité X, plus sujette à l'état dynamique des amas (cool cores ou mergers).

Ce dernier résultat a été obtenu en montrant que les amas dont le flux SZ observé dévie le plus du flux SZ prédit par les X sont ceux possédant des états dynamiques extrêmes (cool cores ou mergers) comme le montre la figure 7 de Planck Collaboration X (2011).

6.3 Analyses statistiques de catalogues optiques

Le succès de l'analyse SZ-X nous a encouragé à poursuivre avec les catalogues d'amas optique, en particulier le catalogue MaxBCG (Koester et al., 2007) du SDSS. Ce catalogue est particulièrement intéressant car il comprend beaucoup d'objets (plus de 13 000 amas) et il existe des relations richesse-masse N-M précises établies pour celui-ci via moyennage du signal de lentille gravitationnelle par intervalle de richesse (Johnston et al., 2007) ou bien via utilisation de masses individuelles mesurées par effet de lentille ou en X (Rozo et al., 2009).

La figure 6.4 présente les résultats. Le flux observé des amas MaxBCG (losanges rouges) est significativement inférieur au flux prédit par le modèle (étoiles bleues) basé sur la combinaison des lois d'échelles N-M (Johnston et al., 2007; Rozo et al., 2009) et Y-M (Arnaud et al., 2010). Deux explications peuvent être avancées pour expliquer ce désaccord : les relations N-M ne seraient pas correctes (i.e. il y aurait un biais dans l'estimation de masse des amas MaxBCG) ou bien la relation Y-M ne serait pas correcte (i.e. il y aurait un biais de sélection ou un biais de masse dans la relation). Le débat est toujours ouvert aujourd'hui et aucune interprétation

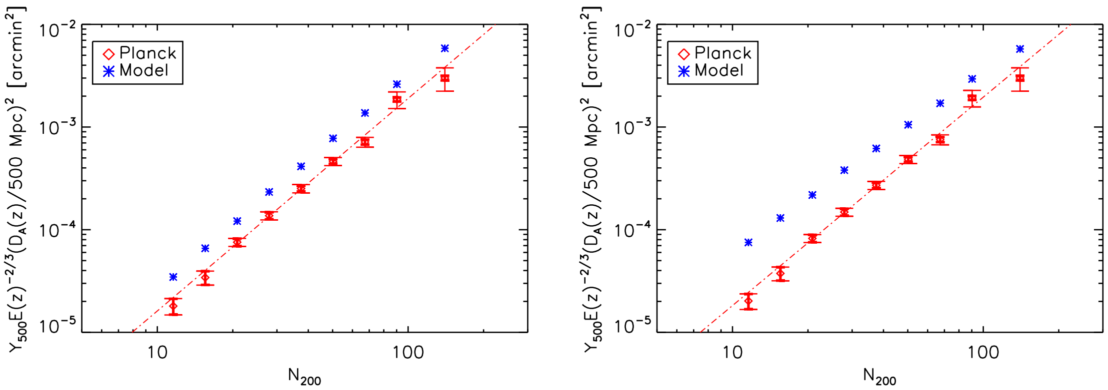

Figure 6.4: *A gauche :* Flux moyennés des amas MaxBCG dans les données Planck (losanges rouges) et modèle (étoiles bleues) pour la relation N-M de Johnston et al. (2007) *(à gauche)* et pour la relation de Rozo et al. (2009) *(à droite)*. Pour les deux relations, le modèle prédit significativement plus de flux qu'observé. Les barres d'erreurs épaisses sont statistiques et les fines sont déterminées par bootstrap. Les lignes en points-tirets sont les ajustements aux données. La figure est tirée de Planck Collaboration XII (2011).

définitive n'est établie sur ce résultat qui a provoqué de nombreuses réactions dans la communauté (voir par exemple la série Rozo et al., 2014c,b,a).

Ce résultat a ensuite été confirmé par Draper et al. (2012) sur les données WMAP. Dans la même lignée, Sehgal et al. (2013) ont moyenné un sous-échantillon de 474 amas MaxBCG sur les données ACT et ont trouvé un flux encore plus faible que dans les données Planck, donc en désaccord encore plus grand avec le modèle basé sur les X.

Les analyses se sont ensuite déplacées vers les objets de plus basse masse. Ainsi, Hand et al. (2011) ont moyenné le signal d'un sous-échantillon de 2681 Luminous Red Galaxies de SDSS dans les données ACT et on détecté marginalement une loi d'échelle flux SZ - luminosité en bande r (K corrigée à $z = 0.1$). Dans Planck, nous avons travaillé sur le catalogue Locally Brightest Galaxies (LBG) situé à redshift 0.1-0.3, extrait lui aussi du SDSS et comprenant environ 260 000 objets. Nous avons pu extraire le flux des halos jusqu'à une masse de l'ordre de $2 \times 10^{13} M_{\odot}$ avec une indication de signal à des masses encore plus faibles (de l'ordre de $4 \times 10^{12} M_{\odot}$). Les résultats sont présentés dans la figure 6.5. A gauche, les losanges rouges représentent le flux SZ extrait en fonction de la masse stellaire dans les données Planck. Les triangles bleus sont les résultats de l'extraction du flux de halos simulés et injectés dans les données de la façon la plus réaliste possible (en particulier, en tenant compte de la dispersion dans la loi d'échelle M*-M et du décalage entre position optique et centre du halo). Les triangles bleus sont légèrement décalés pour facilité la lisibilité. La figure en encart montre le rapport des deux. A partir des catalogues injectés, on peut construire une masse effective pour un intervalle de masse stellaire donné et convertir l'axe M* en axe M pour obtenir la figure de droite. Dans cette dernière, les losanges rouges restent au même niveau sur l'axe des ordonnées (flux SZ) mais sont décalés sur l'axe des abscisses selon les masses effectives attribuées aux intervalles de masses stellaires par le processus d'injection/extraction des simulations. On établit ainsi (en losanges rouges) la loi Y-M sur le catalogue LBG jusqu'à très basse masse. L'ajustement est

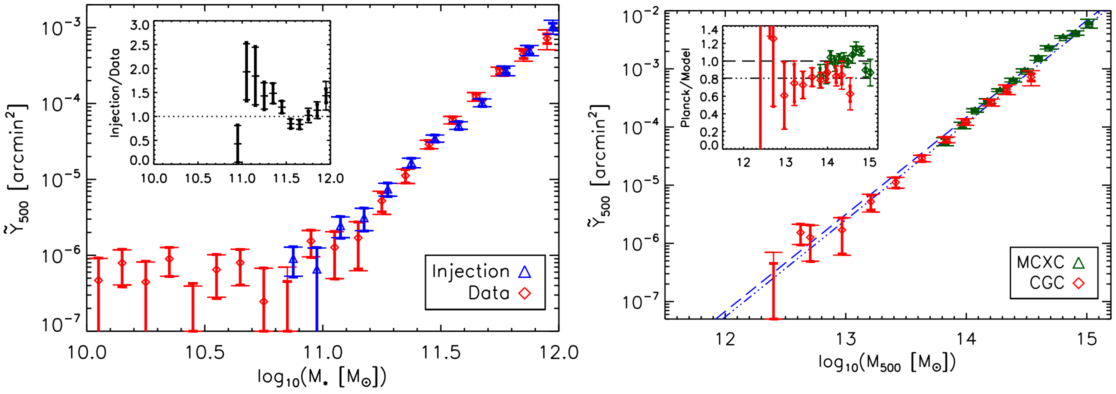

Figure 6.5: Flux des halos des "Locally Brightest Galaxies" dans les données Planck. *A gauche :* En losanges rouges, le flux SZ des LBG en fonction de la masse stellaire. En triangles bleus, le résultat de l'extraction d'un catalogue simulé injecté dans les données. *A droite :* On utilise une série de catalogues injectés (tels les triangles bleus de la figure de gauche) pour estimer la masse effective d'un intervalle de masse stellaire. On obtient ainsi la loi Y-M pour les LBG (losanges rouges) que l'on peut comparer à celle du MCXC (en vert, à plus haute masse). La ligne en tirets bleus est la relation Y-M de Arnaud et al. (2010) et celle en points-tirets est l'ajustement sur les données LBG. Les barres d'erreur épaisses représentent les erreurs statistiques, les fines les erreurs totales obtenues par bootstrap. La figure est tirée de Planck Collaboration Int. XI (2013).

donné par la ligne en points-tirets bleue. Pour comparaison, les résultats obtenus sur le catalogue MCXC (présentés dans la partie 6.2) sont représentés en vert et le modèle Arnaud et al. (2010) en tirets bleus. La figure en encart montre le rapport des points et des courbes à la relation Y-M de Arnaud et al. (2010). Les barres d'erreur épaisses représentent les erreurs statistiques, les fines les erreurs totales obtenues par bootstrap.

La détection du flux jusqu'à une masse de $2 \times 10^{13} M_\odot$ a été confirmée par une analyse indépendante (Greco et al., 2014), celle de $4 \times 10^{12} M_\odot$ fait encore débat.

Mais le résultat peut-être le plus surprenant est qu'on ne voit pas de cassure dans la loi d'échelle à basse masse alors qu'on s'attendrait à ce que les phénomènes non-gravitationnels de chauffage du gaz aient plus d'importance pour les petits objets, induisant un changement de pente dans la relation. Une explication possible est que Planck mesure l'ensemble du flux du halo moyenné dans ses lobes assez grands (de l'ordre de 5 arcmin de fwhm). Les processus non gravitationnels interviennent dans les parties internes du halo. On aurait donc bien rupture de pente si on était capable d'observer ce qui se passe à l'intérieur de objets. Cette explication est soutenue par les simulations incluant un effet fort des noyaux actifs de galaxies sur le milieu intra-amas (Le Brun et al., 2015). Le papier Planck LBG a aussi suscité une nouvelle étude statistique avec le même catalogue sur les données ROSAT (Anderson et al., 2015).

2015

Ces mesures de flux SZ d'objets X ou optiques (amas ou galaxies) marquent le début d'analyses statistiques puissantes que l'on peut mener avec les données Planck. Elles préfigurent ce que l'on pourra faire à plus haut redshift ou bien à plus basse masse si on possède de nouveaux traceurs de halos.

Ainsi, Loïc Verdier, que j'encadre actuellement en thèse, travaille avec succès sur l'extraction du flux SZ et des autres composantes des catalogues de quasars BOSS ($z \sim 2.5$) dans les données Planck.

Dans ce chapitre, j'ai présenté les résultats des lois d'échelle Planck obtenues par moyennage de grands catalogues. Des mesures de flux SZ individuels sont aussi possibles pour les amas les plus massifs ou les plus proches. Elles peuvent être utilisées pour établir des lois d'échelles avec des objets individuels. C'est le travail qu'a mené Gabriel Pratt dans la collaboration Planck, auquel j'ai participé en extrayant les flux individuels des amas. Deux papiers ont été publiés dans ce cadre : les lois d'échelle SZ-X pour les amas locaux (Planck Collaboration XI, 2011) et les lois d'échelle liant flux SZ et masse de lentille sur le catalogue LoCuSS (Planck Collaboration Int. III, 2013).

Chapitre 7

EFFETS SZ CINÉTIQUE, RELATIVISTE ET POLARISÉ

J'ai étudié les effets SZ cinétique (kinetic SZ, kSZ, en anglais) et SZ thermique relativiste (tSZr) dans Planck en encadrant la thèse de Sarah Puisieux entre 2010 et 2013 (Puisieux, 2013). Je présenterai les principaux résultats dans les parties 7.1 pour l'effet kSZ et 7.2 pour l'effet tSZr. Au printemps 2015, je me suis intéressé à l'effet SZ polarisé avec Corentin Lohat, en stage de fin d'étude à Polytechnique. Les résultats essentiels sont présentés dans la partie 7.3.

7.1 *Effet SZ cinétique (kSZ)*

Plusieurs facteurs rendent la détection de l'effet kSZ très difficile :

- son amplitude, environ un ordre de grandeur plus petite que celle de l'effet SZ thermique ;
- son spectre, le même que celui du fond diffus cosmologique ;
- son signe, positif ou négatif selon le sens de la vitesse radiale de l'amas.

Sa faible amplitude impose d'avoir des expériences sensibles si on veut pouvoir le détecter. Comme son spectre est celui du CMB, il n'est pas possible de le séparer de ce dernier en utilisant plusieurs fréquences. Une bonne résolution angulaire (meilleure que la minute d'arc) est nécessaire pour le séparer spatialement. Enfin, le moyennage du signal sur plusieurs amas ne permet pas d'extraire le signal à cause du sens inconnu de la vitesse.

2005

Au milieu des années 2000, l'effet kSZ restait indétectable malgré les progrès de l'instrumentation millimétrique. Cependant, des limites supérieures de l'ordre de quelques milliers de km/s avaient pu être posées (voir par exemple Benson et al., 2003).

Au démarrage des expériences ACT, SPT et au lancement de Planck à la fin des années 2000, l'effet kSZ restait donc un objectif affiché de ces expériences et était a priori à portée de celles-ci. Les choses n'ont pas été faciles pour Planck. Du fait de la résolution de l'instrument (5 arcmin au mieux) et de l'impossibilité de séparer spectralement le kSZ du CMB, il n'a pas été possible de mesurer la dispersion de vitesse des amas (attendue autour de 230 km/s pour le catalogue MCXC, Piffaretti et al., 2011). Seule une limite a pu être fixée $\sigma_{\mathrm{v}} < 800\,\mathrm{km/s}$ (95% C.L.) (Planck Collaboration Int. XIII, 2014). Par contre, la vitesse moyenne de l'échantillon a pu être mesurée à 72 ± 60km/s (Planck Collaboration Int. XIII, 2014), compatible avec zéro à une grande précision. La figure 7.1 montre la vitesse moyenne en fonction du redshift pour l'échantillon MCXC (triangles noirs) et l'échantillon MaxBCG (Koester et al., 2007) privé des amas MCXC (losange rouge). La figure n'indique pas d'évolution en redshift de la vitesse moyenne. En faisant cette étude, nous nous sommes rendus compte qu'il était important de prendre soigneusement en compte les largeurs des bandes optiques de Planck pour l'effet kSZ. Le signal de l'effet tSZ dans le canal à 217 GHz était censé être négligeable par construction ce qui n'est en fait pas le cas à cause de la largeur de la bande. Ainsi, il n'est pas possible d'utiliser cette bande pour détecter le kSZ sans contamination de tSZ. Il faut donc utiliser l'ensemble des bandes HFI avec un filtre spécifique, adapté à l'extraction du signal kSZ (Herranz et al., 2005; Puisieux, 2013) pour obtenir un estimateur de vitesse non biaisé.

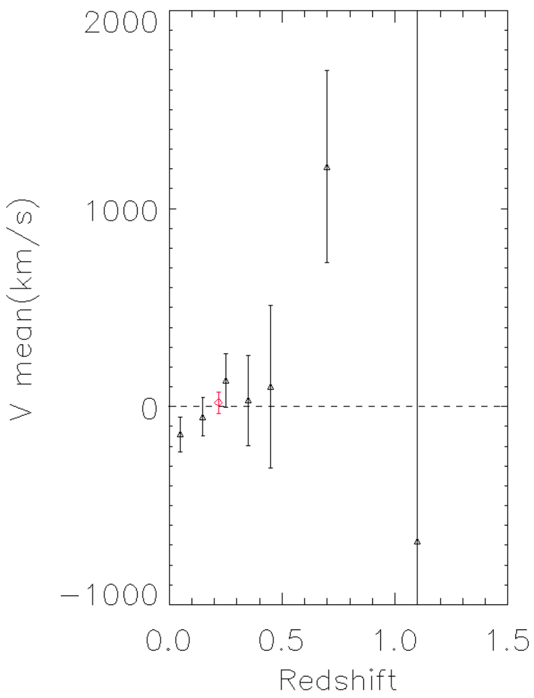

Figure 7.1: Vitesse moyenne des amas MCXC (Piffaretti et al., 2011) (triangles noirs) et MaxBCG (Koester et al., 2007) (losange rouge) en fonction du redshift. Les amas MCXC ont été retirés du catalogue MaxBCG. La vitesse moyenne est compatible avec zéro à tout redshift. La moyenne globale donne une erreur de 60 km/s. La figure est tirée du chapitre 5 de la thèse Puisieux (2013).

Alors que nous travaillions sur le papier Planck Collaboration Int. XIII (2014), la collaboration ACT a présenté une première détection (avec une probabilité que le signal observé soit aléatoire inférieure à 0.002) de l'effet kSZ obtenue sur l'échantillon de galaxies CMASS de BOSS en étudiant le "pairwise momentum", la moyenne de la différence du signal kSZ de deux galaxies CMASS en fonction de la distance entre elles (Hand et al., 2012). L'amplitude du signal est de l'ordre de 1 μK et correspond, selon la collaboration ACT, au signal attendu sur simulations. La collaboration SPT n'a pas publié sur le kSZ à ce jour. La collaboration Planck a ensuite travaillé sur le "pairwise momentum" avec le catalogue Locally Brightest Galaxies (LBG) présenté dans le chapitre 6. A l'aide de la méthode de photométrie d'ouverture, elle a publié, sur l'échantillon LBG, un signal dix fois plus faible (de l'ordre de 0.1 μK avec un signal-sur-bruit de l'ordre de 2 à 2.5) que le signal publié par ACT sur l'échantillon CMASS (Planck Collaboration Int. XXXVII, 2015). En résumé, les analyses "pairwise momentum" de ACT et Planck présentent bien un signal significatif mais l'interprétation reste aujourd'hui difficile, le signal se situant dans le régime non-linéaire des champs de vitesse et par manque de connaissance de la physique du gas des petits halos considérés. Si on réussit à réduire ces incertitudes théoriques, les analyses "pairwise momentum" pourraient mener à des contraintes cosmologiques intéressantes (Mueller et al., 2014a,b).

Pour conclure cette partie, il est important de mentionner que les analyses de kSZ sur les objets individuels ont continué en parallèle des analyses statistiques décrites ci-dessus. Ainsi Sayers et al. (2013b) ont publié une détection de l'effet kSZ pour un amas en collision (MACS J0717.5+3745) sur les données Bolocam. Les expériences sol sensibles à haute résolution comme NIKA ou NIKA2 (Monfardini et al., 2014) devraient pouvoir confirmer cette première détection.

Avancées notables

L'effet kSZ est désormais détecté marginalement (statistiquement par études "pairwise momentum") et individuellement sur un amas en collision. Il reste cependant encore beaucoup à faire (détection de la dispersion de vitesse ou de plus de vitesses individuelles) mais il faudra une résolution meilleure que la minute d'arc, une grande sensibilité et une bonne couverture fréquentielle pour bien séparer effet kSZ et tSZ.

7.2 Effet SZ thermique relativiste (tSZr)

Comme pour le kSZ, la détection de l'effet tSZr est ardue.

La figure 7.2 illustre cette difficulté. Elle montre la valeur des flux extraits de Coma et A2163 par le MMF (lignes continues) en supposant que le spectre SZ est non-relativiste et que les bandes optiques sont des Dirac (en bleu) ou en supposant le spectre SZ incluant les corrections relativistes (Itoh et al., 1998) et en prenant en compte les largeurs des bandes optiques (en rouge). Les erreurs à $\pm 1\,\sigma$, données par le MMF (équation 3.4), sont indiquées par les lignes en tirets. Les lignes en points-tirets vertes verticales indiquent les températures des amas déterminées en X. On constate que l'effet des largeurs des bandes optiques est faible pour l'effet tSZ et que l'écart entre les flux déterminés en supposant l'effet SZ non-relativiste ou relativiste est lui-aussi faible : de l'ordre de $1\,\sigma$ pour Coma (température de 5 keV environ) et de l'ordre de $2\,\sigma$ pour A2163 (température située entre 7 et 8 keV). L'hypothèse d'utilisation du spectre relativiste ou non-relativiste pour l'extraction a donc un impact sur le flux mais relativement faible.

Seuls 10 amas (sur 1741 amas du MCXC ayant une température) ont leur flux qui dévient à plus de $2\,\sigma$ entre l'hypothèse relativiste et non-relativiste. Pour ces amas, on a voulu tester s'il était possible de mesurer leur température à partir des

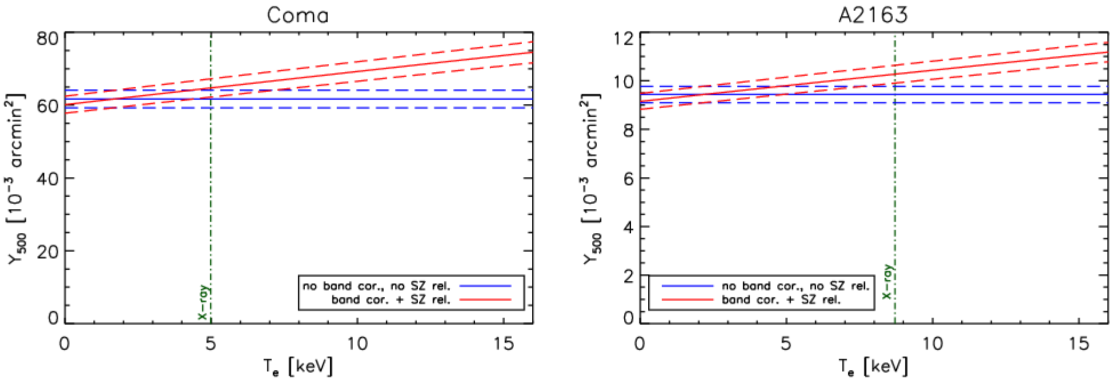

Figure 7.2: Impact des largeurs des bandes optiques de Planck et des corrections relativistes sur les flux SZ des amas Coma (*à gauche*) et A2163 (*à droite*) de Planck. En bleu en supposant que les bandes optiques sont des Dirac et sans correction relativiste au spectre du tSZ. En rouge en tenant compte des largeurs de bandes optiques et des corrections relativistes de l'effet tSZ (Itoh et al., 1998). Les lignes continues donnent les valeurs moyennes, les erreurs à $\pm 1\,\sigma$ sont indiquées par les lignes en tirets. Les lignes en points-tirets vertes verticales indiquent les températures des amas déterminées en X. L'impact des largeurs des bandes optiques sur les flux de ces amas est faible ainsi que celle des corrections relativistes.

cartes Planck. On a donc extrait leurs flux pour différentes températures et calculé les rapports signal-sur-bruit (S/N) et les χ^2 correspondants. Pour un amas, le χ^2 est défini comme la somme pondérée des différences au carré entre le flux extrait dans les bandes individuelles de Planck et le flux attendu dans les bandes étant donné le flux extrait. Les résultats sont présentés dans la figure 7.3 pour ces 10 amas. Il n'y a pas de corrélation évidente entre les mesures X des températures (lignes vertes en points-tirets verticales) et les maxima (ou minima) de S/N (ou χ^2).

Une détection claire sur des amas individuels de l'effet tSZr n'est donc pas possible avec Planck, ni son utilisation éventuelle pour déterminer la température du gaz intra-amas. Comme pour l'effet kSZ, nous avons dû poursuivre avec des analyses

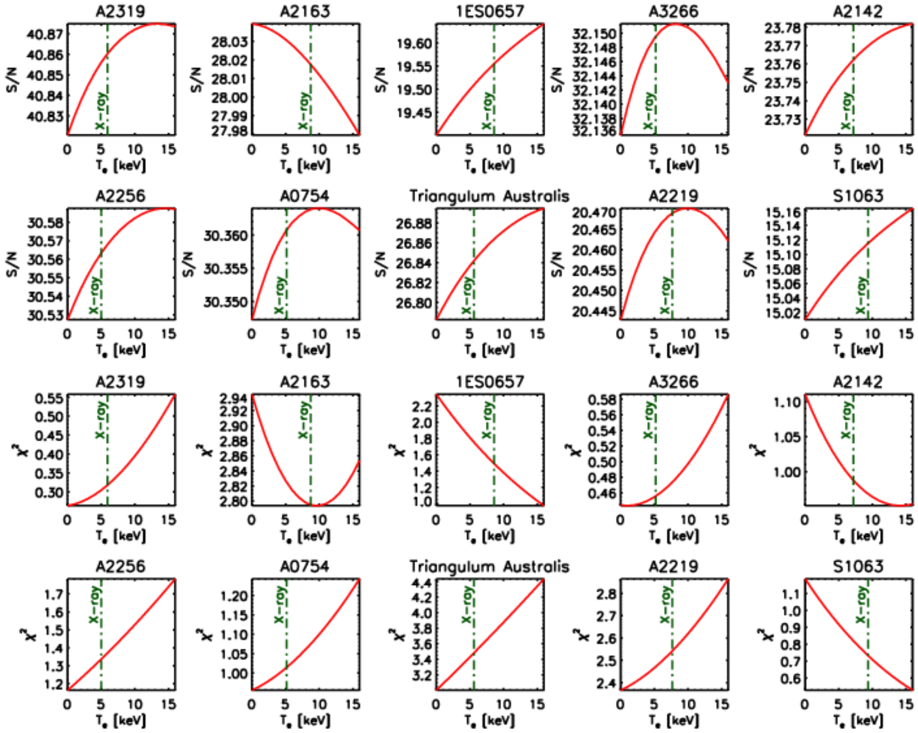

Figure 7.3: *En haut :* Signal-sur-bruit (S/N) en fonction de la température supposée. *En bas :* χ^2 en fonction de la température supposée. Les deux figures présentent les 10 mêmes amas qui ont une déviation entre flux SZ relativiste et non-relativiste supérieure à $2\,\sigma$. Les températures déterminées à l'aide des X sont indiquées en points-tirets verticaux verts. Celles-ci ne corrèlent pas bien avec les maxima (ou minima) de S/N (ou χ^2). La figure est tirée du chapitre 7 de la thèse Puisieux (2013).

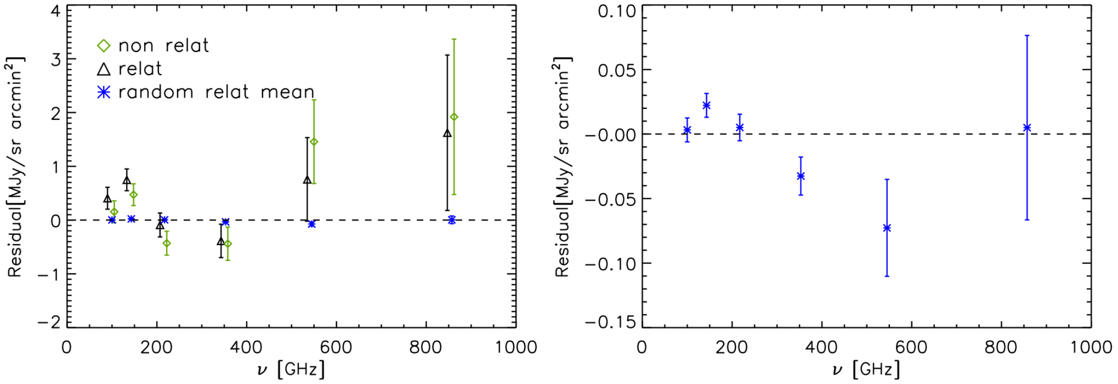

Figure 7.4: *A gauche :* Moyenne des résidus des flux des 62 amas ESZ-XMM dans les données Planck dans les hypothèses non-relativiste (losanges verts) et relativistes (triangles noirs). Les étoiles bleues montrent la moyenne de 500 injections de 62 amas simulés ESZ-XMM pour lesquels ont a supposé le spectre tSZr pour l'injection et l'extraction. *A droite :* Zoom sur les étoiles bleues à proximité du zéro (voir échelle verticale des résidus). La figure est tirée du chapitre 7 de la thèse Puisieux (2013).

statistiques.

Pour cela, nous avons utilisé le catalogue des 62 amas ESZ-XMM, intersection des amas contenus dans le catalogue ESZ (présenté dans le chapitre 3) et dans les archives XMM. Ce sont des objets bien connus pour lesquels on dispose de tailles angulaires et de températures précises. Pour chaque amas et sous chaque hypothèse (SZ relativiste ou non-relativiste), on a extrait les flux SZ grâce au MMF en combinant l'ensemble des fréquences de Planck HFI. On a ensuite extrait le flux des amas dans chaque bande de fréquence de Planck et calculé le résidu correspondant i.e. la différence entre le flux dans la bande et le flux prédit dans celle-ci à partir du MMF. Nous avons ensuite moyenné les résidus des 62 amas dans chaque bande. Les résultats sont présentés dans la figure 7.4. Pour les deux hypothèses de spectre, non-relativiste (losanges verts) ou relativiste (triangles noirs), les résidus ne montrent pas de déviation significatives à zéro, à l'exception de la bande à 143 GHz qui montre une déviation positive à quelques sigma, peut-être l'influence de sources ponctuelles radio dans les amas. Les étoiles bleues montrent la moyenne de 500 injections de 62 amas simulés ESZ-XMM dans les données Planck incluant l'effet SZ relativiste pour la simulation et l'extraction. La moyenne des étoiles bleues est parfaitement compatible avec zéro.

A l'inverse du kSZ pour lequel une détection statistique a été possible par les études "pairwise momentum", l'effet tSZr, bien qu'ayant une incidence sur les valeurs des flux extraits, n'a pas pu être formellement mis en évidence dans les données Planck.

7.3 Effet SZ polarisé

En réalité, il n'existe pas un mais de nombreux effets SZ polarisés dont les deux plus grands sont celui dû au quadrupôle local du CMB et celui dû à la vitesse transverse de l'amas par rapport à la ligne de visée (voir par exemple Sazonov & Sunyaev, 1999). En théorie, ce dernier effet permet une reconstruction complète de la vitesse d'un amas s'il est combiné à une mesure de l'effet kSZ qui donne la vitesse radiale. Il est cependant extrêmement faible (environ 100 fois plus faible que l'effet tSZ), tout comme l'effet dû au quadrupôle local... De nombreux papiers théoriques très complets ont été publiés sur ces deux effets (Kamionkowski & Loeb, 1997; Audit & Simmons, 1999; Baumann & Cooray, 2003; Portsmouth, 2004; Amblard & White, 2005; Ramos et al., 2012). Avec Corentin Lohat, je me suis intéressé exclusivement à l'effet SZ polarisé dû au quadrupôle local du CMB car, à l'inverse de l'effet dû à la vitesse transverse, il peut être moyenné sur un grand nombre d'amas. Il a donc plus de chance de pouvoir être détecté. Cet effet SZ a un intérêt particulier car il permet une mesure indépendante du paramètre C_2 du spectre de puissance du CMB à l'emplacement de l'amas. Or ce paramètre déterminé sur les données COBE, WMAP et Planck est sensiblement plus petit qu'attendu dans le modèle standard (Kogut et al., 1996; Bennett et al., 2013; Planck Collaboration XVI, 2014; Planck Collaboration XXIII, 2014). Il serait donc très intéressant d'avoir les mesures effectuées sur les amas locaux grâce à l'effet SZ polarisé.

Nous avons construit un filtre MMF adapté à l'extraction de l'effet SZ polarisé dû au quadrupôle dans les cartes de polarisation Q et U simulées de Planck. Il est possible de calculer sa variation sur le ciel avec précision étant donné un catalogue d'amas aux propriétés physiques bien caractérisées. Nous avons de nouveau utilisé le catalogue MCXC (Piffaretti et al., 2011). Pour chaque amas du MCXC, et chaque série de cartes (Q et U), le filtre adapté extrait une valeur de $\sqrt{C_2}$ et sa barre d'erreur associée $\sigma_{\sqrt{C_2}}$. Il est ensuite possible de faire une moyenne pondérée (en $1/\sigma^2_{\sqrt{C_2}}$) de toutes les mesures pour obtenir une estimation de $\sqrt{C_2}$ globale la plus précise possible.

Le signal-sur-bruit obtenu pour les simulations Planck réalistes (SZ polarisé, CMB et bruit pour toutes les fréquences polarisées de HFI) est hélas très décevant. Il est de 5% après moyennage de l'ensemble des amas MCXC et des deux polarisations Q et U. Ce résultat est en accord avec la prédiction de Hall & Challinor (2014). Corentin Lohat a poussé l'analyse pour les projets COrE+ et PRISM. COrE+ ne peut pas non plus détecter l'effet avec un signal-sur-bruit attendu allant de 10 à 15% selon la configuration instrumentale adoptée. PRISM pourra quant à lui faire la mesure : le signal-sur-bruit attendu est de 27% pour le MCXC et donc de plusieurs unités pour un catalogue comportant quelques 10^5 amas.

Ainsi, il se pourrait que l'effet SZ polarisé reste non-détecté pendant encore de nombreuses années. Une solution alternative serait d'essayer de le mesurer en moyennant l'effet sur quelques objets particuliers. Ainsi Corentin Lohat a montré que si on divisait le bruit Planck par un facteur 10^5, l'essentiel du signal était porté par trois amas : Virgo, Coma et Leo. Un suivi spécifique profond polarisé de ces amas pourrait être le meilleur moyen de détecter l'effet.

2015

Alors que l'effet kSZ commence à être mis en évidence et que Planck n'a pas pu identifier clairement l'effet tSZr, les effets SZ polarisés semblent hors de portée de Planck et de la prochaine mission spatiale. Il faudra donc déployer de nouveaux efforts instrumentaux, vraisemblablement au sol ou en ballon, et beaucoup d'imagination pour réussir à les détecter à un fort niveau de confiance.

Chapitre 8

SUIVI DES AMAS PLANCK ET ÉTUDE MULTI-LONGUEUR D'ONDE D'AMAS PARTICULIERS

2005

Avant le démarrage de SPT, ACT et Planck, il n'existait pas de catalogue d'amas sélectionné en SZ. Seules les propriétés SZ de quelques amas X étaient connues grâce à des observations sol.

L'extraction puis la publication des premiers catalogues ESZ et PSZ1 (Planck Collaboration VIII, 2011; Planck Collaboration XXIX, 2014) ont motivé leur suivi à d'autres longueurs d'onde, en X, en optique ou en SZ au sol. Je n'ai pas directement réalisé ces campagnes d'observations mais y ai participé en aidant à la sélection des cibles pour la validation XMM des amas Planck (partie 8.1) et en ré-extrayant les flux Planck SZ, une fois assemblées les informations du suivi (partie 8.1, 8.2 et 8.3).

8.1 Suivis ciblés d'amas Planck

Une partie des amas Planck a été suivie en X par XMM. Ce programme a été coordonné par Monique Arnaud et a donné lieu à quatre papiers (Planck Collaboration IX, 2011; Planck Collaboration XXVI, 2011; Planck Collaboration Int. I, 2012; Planck Collaboration Int. IV, 2013). Le premier objectif de ce programme était la validation des détections de Planck, c'est-à-dire la vérification qu'elles étaient bien vues en X par XMM. Le second objectif était de vérifier que leur flux SZ et leur flux X étaient en bon accord.

51 détections Planck ont été validées par XMM et le paramètre Y_{X} de ces amas

est en très bon accord avec le flux SZ de Planck. Ce résultat est présenté dans la figure 8.1. Les nouveaux amas validés par XMM sont indiqués en vert et rouge. Ils se trouvent à proximité de la ligne bleue de l'échantillon REXCESS d'amas sélectionnés en X. L'accord entre flux SZ et paramètre Y_X reste donc valide et conforme à celui constaté sur les échantillons sélectionnés en X.

Un autre résultat important a pu être établi grâce à ce programme de suivi : les nouveaux amas détectés ont une morphologie plus perturbée que les amas déjà connus en X. Ils ont aussi une plus faible brillance de surface X ce qui explique qu'ils aient été manqués par les sondages X. Cette propriété peut être interprétée comme un nouveau signe que la sélection SZ est plus proche d'une sélection en masse que la sélection X qui semble favoriser, pour une masse donnée, les amas plus "relaxés" qui ont une brillance de surface X plus élevée.

Le suivi XMM des amas Planck a aussi permis de détecter un nouvel amas à $z \sim 1$, un des deux plus lumineux en X pour $z > 0.5$ (Planck Collaboration XXVI, 2011).

Pendant ce suivi, Monique Arnaud a proposé un *Large Program* XMM pour étudier plus précisément 32 amas Planck dans l'intervalle $0.5 < z < 1$. Ce programme a été accepté ; l'analyse de données est en cours de finalisation. Dans un deuxième temps, un suivi Chandra systématique de tous les amas du catalogue ESZ a été proposé. Il est mené par Christine Jones.[1] Les premières observations semblent confirmer les propriétés générales déduites des observations XMM. Le grand nombre d'observations Chandra permettra d'étudier plus précisément chacun des amas (voir par exemple Andrade-Santos et al., 2015) et de faire des études statistiques par catégories morphologiques plus poussées.

Pour obtenir les redshifts des nouveaux amas, il faut réaliser des suivis optiques. Ceux-ci sont coordonnés par Nabila Aghanim. Dans l'hémisphère nord, ils sont réal-

---

[1] http://hea-www.cfa.harvard.edu/CHANDRA_PLANCK_CLUSTERS/

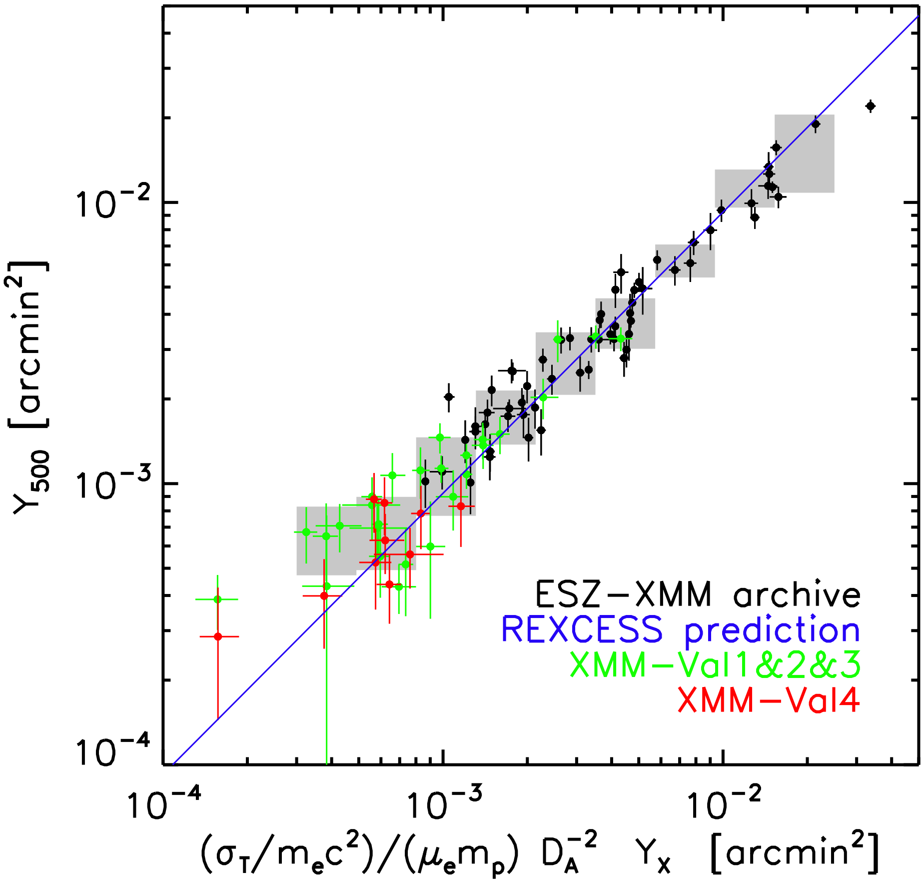

Figure 8.1: Flux SZ des amas Planck suivis par XMM (en vert et rouge) en fonction du paramètre Y_{X}. Le flux SZ est en bon accord avec le paramètre Y_X mesuré avec XMM. Il suit la loi prédite avec l'échantillon REXCESS (ligne bleue) et déjà confirmée sur l'échantillon ESZ-XMM (points noirs). La figure est extraite du papier Planck Collaboration Int. IV (2013).

isés à l'aide des télescopes des Canaries de l'ENO (redshifts spectroscopiques de 53 détections Planck, Planck Collaboration Int. XXXVI, 2015) et du télescope russo-turc RTT (redshifts de 47 détections Planck, Planck Collaboration Int. XXVI, 2014). Pour l'hémisphère sud, Nabila Aghanim a obtenu un *Large Program* à l'ESO. Les données sont en cours d'analyse. Ces suivis ont joué un rôle crucial pour l'obtention des redshifts nécessaires aux analyses cosmologiques.

Enfin, l'interféromètre AMI a suivi les amas Planck. Un premier résultat sur 11 amas (Planck and AMI Collaborations, 2013) a indiqué un déficit de flux SZ AMI par rapport au flux SZ Planck qui pourrait être attribué au profil d'amas utilisé pour l'extraction du flux AMI. Cette sous-estimation du flux a été confirmée sur un échantillon de 123 amas suivis (99 amas détectés) (Perrott et al., 2015). Plus récemment, l'interféromètre CARMA a suivi 19 amas Planck à plus haut redshift et ne voit pas de biais en flux par rapport aux flux Planck publiés (Rodriguez-Gonzalvez et al., 2015). Ce résultat pourrait indiquer que l'effet du profil est plus important pour les amas à bas redshift (comme ceux suivis par AMI) qu'à plus haut redshift (comme ceux suivis par CARMA).

Ainsi, le suivi des amas Planck n'en est qu'à ses débuts. Plusieurs centaines de redshifts sont encore manquants dans le catalogue PSZ2 ce qui nécessitera la poursuite des suivis optiques. Les premières observations X ont pour l'instant révélé uniquement les caractéristiques générales des amas SZ à bas redshift. Enfin, l'accord entre les flux Planck et les expériences sol reste encore à consolider.

8.2 Corrélation du catalogue Planck avec de nouveaux jeux de données

En parallèle des suivis déclenchés par l'obtention des catalogues ESZ et PSZ1, plusieurs travaux de corrélation entre les amas Planck et d'autres catalogues ont été publiés.

En particulier, la comparaison du catalogue redMaPPer (Rykoff et al., 2014) avec le catalogue PSZ1, à laquelle j'ai participé, a apporté un nouveau lien entre observations optique et SZ. A partir des 245 amas en commun entre les deux catalogues, Eduardo Rozo a établi une loi richesse-masse avec une dispersion modérée de 21% sur la masse à richesse fixée. La figure 8.2 présente cette loi d'échelle qui a été utilisée pour la confirmation de candidats dans le catalogue PSZ2. L'ensemble des résultats de cette étude est présenté dans Rozo et al. (2015).

La collaboration SPT a quant à elle réagit à la publication du catalogue ESZ en confirmant 5 amas du catalogue. 1 était présent dans l'échantillon SPT et les 4 autres ont été observés grâce à des poses courtes (Story et al., 2011). De même, la collaboration Bolocam a suivi deux amas du ESZ, en a confirmé un et a désigné l'autre (PLCKESZ G189.84-37.24) comme une probable fausse détection (Sayers et al., 2012). CARMA a suivi trois amas du ESZ dont PLCKESZ G189.84-37.24. Elle a aussi rejeté l'hypothèse que cette dernière détection est un amas mais a confirmé les deux autres (Muchovej et al., 2012). AMI a pu suivre deux amas du catalogue ESZ. Elle a confirmé l'existence d'un des deux mais n'a pas pu conclure pour le second car contaminé par une source radio (Hurley-Walker et al., 2011). Plus récemment, la collaboration Pan-STARRS a confirmé, en optique, 60 candidats du catalogue PSZ1 (Liu et al., 2015).

Avancées notables

Les suivis des amas Planck ont permis de valider des candidats, de commencer à assembler les redshifts et d'obtenir les caractéristiques générales des amas SZ grâce aux données X et SZ au sol. Les corrélations croisées ont permis d'établir des lois d'échelles X-SZ et optique-SZ qu'il a été possible d'utiliser pour valider de nouvelles détections dans le catalogue PSZ2.

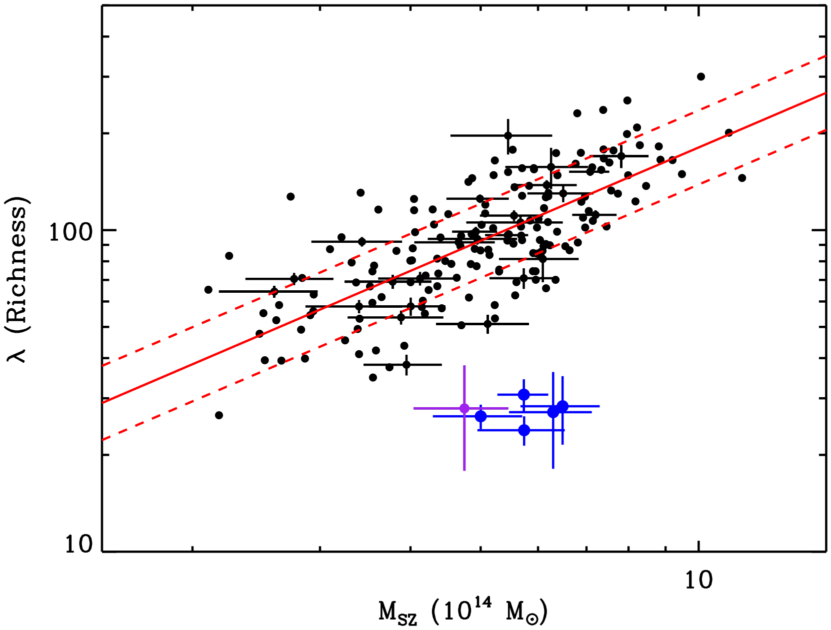

Figure 8.2: Richesse optique en fonction de la masse pour les amas en commun entre le PSZ1 et redMaPPer (points noirs). L'ajustement est la ligne continue rouge et l'erreur à $\pm 1\,\sigma$ est matérialisée par les lignes en tirets. Les 5 outliers ($> 3\,\sigma$) en bleu sont dus à 1 mauvaise photométrie SDSS et à 4 mauvaises associations (les véritables associations étant à plus haut z). Le point violet n'est pas à strictement parler un outlier (car il dévie à moins de $3\,\sigma$) mais est lui aussi une mauvaise association. La figure est extraite du papier Rozo et al. (2015).

8.3 Etudes multi-longueur d'onde d'amas particuliers

En parallèle des suivis systématiques des amas Planck décrits dans la partie 8.1, des objets particuliers ont attiré l'attention de la collaboration.

Tout d'abord PLCKG214.6+37.0, un amas triple suivi avec XMM. L'étude menée par Mariachiara Rossetti a montré que la somme des flux X des trois composantes correspondait au flux total SZ mesuré par Planck et qu'il n'y avait donc pas d'indication de présence de gaz chaud supplémentaire entre les amas (Planck Collaboration Int. VI, 2013). Pour cette étude, j'ai ré-extrait le flux SZ à l'aide du MMF en utilisant cette fois un modèle à trois composantes basé sur l'observation XMM plutôt que le profil de Arnaud et al. (2010) utilisé pour l'extraction standard.

Un autre papier, mené par Guillaume Hurier, a mis en évidence un pont de gaz entre les amas A399 et A401 (Planck Collaboration Int. VIII, 2013). Enfin, Pasquale Mazzotta a conduit une travail sur l'amas Coma (suffisamment étendu pour être résolu par Planck). Cette étude a montré la présence de chocs dans la carte de pression à deux dimensions (Planck Collaboration Int. X, 2013). J'ai participé marginalement à ces deux derniers papiers en ré-extrayant les flux SZ des amas considérés.

Enfin, il a été possible, pour la première fois, de mesurer avec Planck le profil de pression universel des amas jusqu'à un rayon supérieur au rayon viriel en moyennant le signal des 62 amas de l'échantillon ESZ-XMM (Planck Collaboration Int. V, 2013; Planck Collaboration et al., 2013). Le papier a été mené par Etienne Pointecouteau. Les résultats principaux sont présentés dans la figure 8.3. Les profils individuels sont les lignes grises et le profil moyen correspond aux points rouges. La dispersion est indiquée par la bande rouge. La prédiction de l'ajustement de Arnaud et al. (2010) est montré en ligne continue noire et l'erreur correspondante par les lignes en pointillés. Les points rouges sont situés légèrement au-dessus du modèle à grand rayon ce qui pourrait indiquer un excès de pression dans les parties externes par rapport aux simulations. Pour cette étude, j'ai développé une méthode de moyennage des profils que je n'ai pas poussée suffisamment loin pour qu'elle aboutisse dans cette publication par faute de temps. Un des développements possibles futurs de cette étude est l'obtention de profils moyens de catalogues plus grands sélectionnés selon leurs propriétés X ou optiques.

Le profil moyen d'amas publié dans le papier Planck Collaboration Int. V (2013) est en bon accord avec les profils obtenus avec CARMA (Bonamente et al., 2012) et Bolocam (Sayers et al., 2013a). Ces travaux ont par ailleurs stimulé des études jointes sur les profils SZ de Planck et X de ROSAT (Eckert et al., 2013a,b).

2015

Les suivis des amas Planck vont continuer pour finir d'assembler les redshifts et mieux comprendre leur physique. L'évolution des propriétés des amas SZ en fonction du redshift est encore inconnue : elle sera étudiée via de nouvelles observations X et optiques, confrontées à des simulations.

C'est l'objectif essentiel du projet ERC de Monique Arnaud qui vise à détecter ces amas à grand redshift ($z \sim 1$), à étudier leurs propriétés physiques et à les comparer à celles des amas Planck à bas redshift.

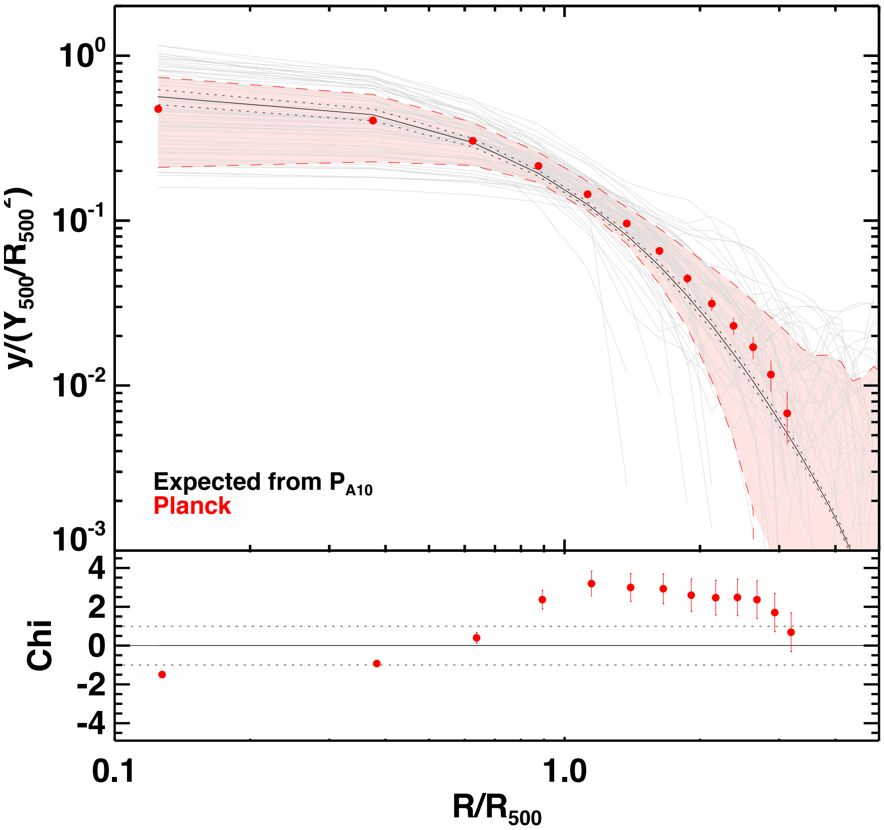

Figure 8.3: Profil de pression Planck obtenu en moyennant les profils des 62 amas du ESZ-XMM après mise à l'échelle spatiale caractéristique R_{500} sur l'axe x et mise à l'échelle de la normalisation attendue Y_{500}/R_{500}^2 sur l'axe y. Les lignes grises sont les profils individuels et le profil moyen est donné par les points rouges. La bande rouge indique le dispersion autour du profil moyen. Les barres d'erreur sur les points rouges donnent l'erreur statistique. La ligne continue noire (P_{A10}) est la prédiction du profil attendu basée sur les données XMM et des simulations (Arnaud et al., 2010). Les lignes noires en pointillés montrent l'erreur sur la prédiction. La figure est extraite du papier Planck Collaboration Int. V (2013).

Chapitre 9

DÉFINITION DES MISSIONS FUTURES

Les travaux que j'ai décrit dans les chapitres précédents sont en grande majorité liés à Planck.

2005

Quand je suis entré dans la collaboration Planck en 2005, les caractéristiques de la mission étaient parfaitement définies et le cadre de travail par conséquent fixé.

Par la suite, j'ai eu l'occasion de sortir de ce cadre par trois fois en participant à la définition d'expériences futures : le sondage XXL à partir de 2008 et les missions post-Planck, PRISM et COrE+, en 2013 et 2014.

9.1 Le sondage XXL

XXL est un sondage en rayons X profond (de sensibilité $5\,10^{-15}$erg/s/cm^2 dans la bande $[0.5-2]$keV) effectué avec le satellite XMM sur une surface de $2 \times 25\,\mathrm{deg}^2$ (divisée entre hémisphère nord et sud). Cette sensibilité correspond à des pointés de 10 ks pour un temps total de l'ordre de 6 Ms. C'est une extension du sondage pilote XMM-LSS (Pacaud et al., 2007) de même profondeur, réalisé sur une surface de $10\,\mathrm{deg}^2$. J'ai participé activement aux premières étapes de la définition du XXL avec Marguerite Pierre et Florian Pacaud dès 2007 (Pierre et al., 2008). Les études ont ensuite été poussées à terme ; elles ont mené à des prédictions cosmologiques précises présentées dans Pierre et al. (2011). Ce papier a permis en outre de convaincre le Time Allocation Committee d'XMM d'allouer le temps nécessaire au sondage.

L'idée principale du sondage est de disposer de pointés contigus de même durée pour obtenir deux champs continus et de profondeur homogène. Ainsi, il est en théorie possible d'extraire l'information cosmologique de la fonction de corrélation des amas en plus de celle des comptages. Le choix de deux champs plutôt qu'un a été motivé par des considérations de suivis multi-longueur d'onde. Le champ au nord est couvert en optique par le télescope CFH alors que le champ au sud l'est par le télescope Blanco. D'autres sondages couvrent par ailleurs la même zone (par exemple SPT pour le sud). A titre d'illustration, la figure 9.1 montre la couverture du ciel XXL pour le champ nord. Chaque cercle représente un pointé XMM de diamètre 30 arcmin. Les pointés du programme pilote XMM-LSS sont indiqués en bleu, ceux du XXL en rouge.

Les amas détectés par le sondage XXL sont beaucoup moins massifs ($\sim 10^{13} M_\odot$) que les amas Planck mais couvrent une gamme en redshift plus grande ($0 < z < 1.5$). Comme pour l'analyse cosmologique de Planck, la maîtrise des lois d'échelles sera une des clefs pour contraindre les paramètres cosmologiques. Pour les masses des amas XXL, les processus non-gravitationnels ont plus d'importance que pour les masses des amas Planck ce qui rend a priori cette tâche plus difficile. Cependant, l'analyse CR-HR proposée par Clerc et al. (2012) et utilisée avec succès sur les données d'archive XMM, pourrait faciliter cette tâche en aidant à contraindre les lois d'échelle en même temps que les paramètres cosmologiques pour le sondage XXL. Pour plus de détails sur le sondage XXL, on pourra se référer à la page `http://irfu.cea.fr/xxl`.

9.2 La mission PRISM

PRISM (The Polarized Radiation Imaging and Spectroscopy Mission) est une mission spatiale proposée en réponse à l'appel d'offre de l'ESA sur les créneaux de mission "Large" L2 et L3 pour des lancements en 2028 et 2034 respectivement. Le satellite, équipé d'un miroir de 3.5 m, emporte un spectro-imageur sensible à la polarisation,

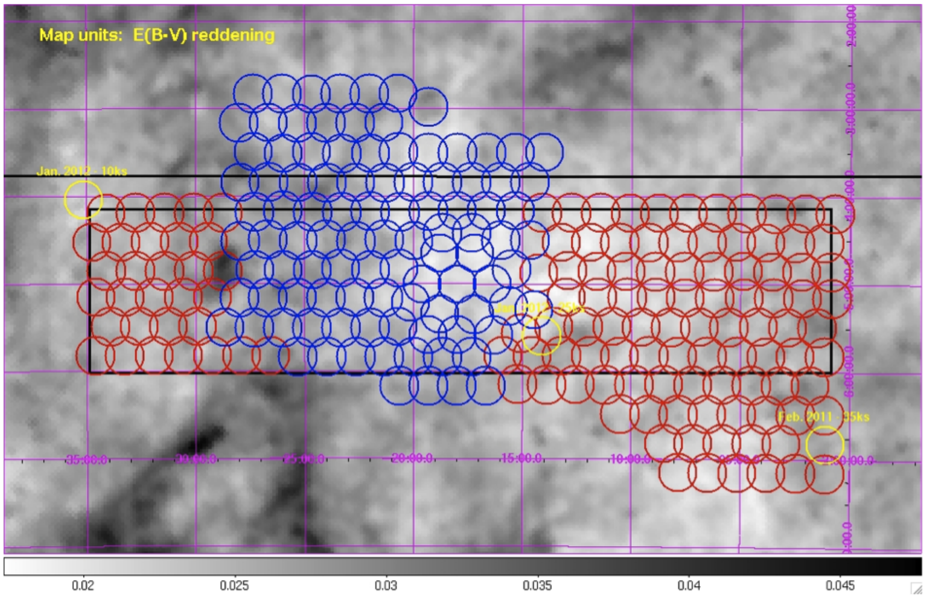

Figure 9.1: Couverture du sondage XXL nord. Les pointés XMM sont représentés par des cercles de 30 arcmin de diamètre. En bleu, les pointés du programme pilote XMM-LSS. En rouge, les pointés ajoutés dans le cadre du programme XXL. En jaune, des pointés d'autres observations XMM. La figure est tirée de http://irfu.cea.fr/Sap/Phocea/Vie_des_labos/Ast/ast.php?t=actu&id_ast=3051.

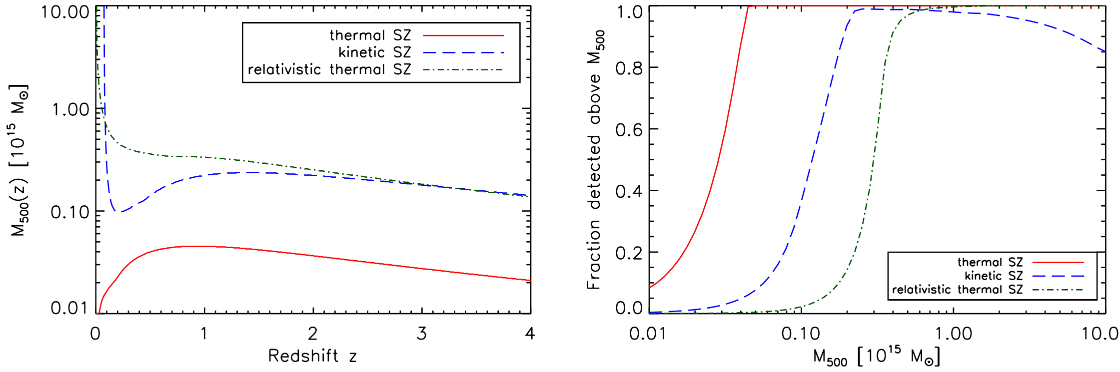

Figure 9.2: Masses limites en fonction du redshift (à gauche) et fraction d'amas détectés en fonction de la masse (à droite) avec PRISM pour les différents effets SZ à S/N> 5. Les objets plus massifs que $M > 4 \times 10^{13}\, M_\odot$ sont détectés à plus de $5\,\sigma$ à tous les redshifts (ligne continue rouge). PRISM est aussi capable de mesurer les vitesses particulières pour la plupart des amas ($M > 2 \times 10^{14}\, M_\odot$, ligne en tirets bleus) et de déterminer les températures pour les systèmes les plus massifs (ligne en points-tirets verts). La figure est extraite de http://www.prism-mission.org/documents/prism_white_paper_new.pdf.

observant dans un grand nombre de bandes de fréquences comprises entre 30 GHz et 6 THz. Ces caractéristiques exceptionnelles permettent d'explorer en profondeur la science du CMB primaire, l'astrophysique galactique et extra-galactique. Les performances attendues pour les amas sont présentées dans la figure 9.2. La mission permet de détecter l'ensemble des amas ($M > 4 \times 10^{13}\, M_\odot$) de l'Univers observable par effet SZ thermique (de l'ordre d'un million d'objets), de mesurer les vitesses radiales de ceux ayant une masse $M > 2 \times 10^{14}\, M_\odot$ et de déterminer les températures des plus massifs. J'ai participé activement à la construction de l'ensemble du cas scientifique SZ pour cette mission.

Le projet est décrit en détail dans PRISM Collaboration et al. (2013) et publié dans André et al. (2014). Pour la version la plus à jour du white paper, on pourra consulter http://www.prism-mission.org/documents/prism_white_paper_new.pdf. Fin 2013, Athena (mission X) et une mission ondes gravitationnelles (probablement eLISA) ont été sélectionnées sur les créneaux L2 et L3 mais PRISM a été favorablement évaluée par les comités ESA (http://sci.esa.int/cosmic-vision/53261-report-on-science-themes-for-the-l2-and-l3-missions/#).

Avancées notables

La mission PRISM, bien que non-sélectionnée par l'ESA, a permis de poursuivre la dynamique de construction d'une mission post-Planck, initiée lors du précédent appel à mission "Medium" M3 (http://www.core-mission.org). Elle a aussi permis d'élargir le cas scientifique en incluant l'étude des distorsions spectrales du CMB et en renforçant les axes astrophysiques.

9.3 La mission COrE+

A la suite de l'évaluation positive de PRISM par le Senior Survey Committee de l'ESA, il a été décidé de re-proposer une mission focalisée sur le CMB primaire en réponse à l'appel d'offre M4 lancé en 2014. L'idée principale est de remettre la science CMB au centre et de réduire les ambitions de PRISM, en retirant le spectromètre, en réduisant la taille du miroir à celui de Planck (1.5 m) et en se concentrant sur un nombre de fréquences limité dans l'intervalle [60-600] GHz. Comme pour PRISM, j'ai étudié le cas scientifique SZ de cette mission, nommée COrE+ pour Cosmic Origin Explorer. Elle est dans la lignée de celle proposée pour le créneau M3 avec des améliorations, notamment au niveau de la stratégie d'observation de la polarisation (d'où le + après COrE). Elle permet de détecter environ 10^5 amas, un nombre équivalent à celui attendu avec les prochaines missions X eROSITA (2016) et optique Euclid (2020). La distribution prédite en masse et redshift des amas COrE+ est présentée dans la figure 9.3 (cercles bleus). A titre de comparaison, les amas Planck PSZ2 pour

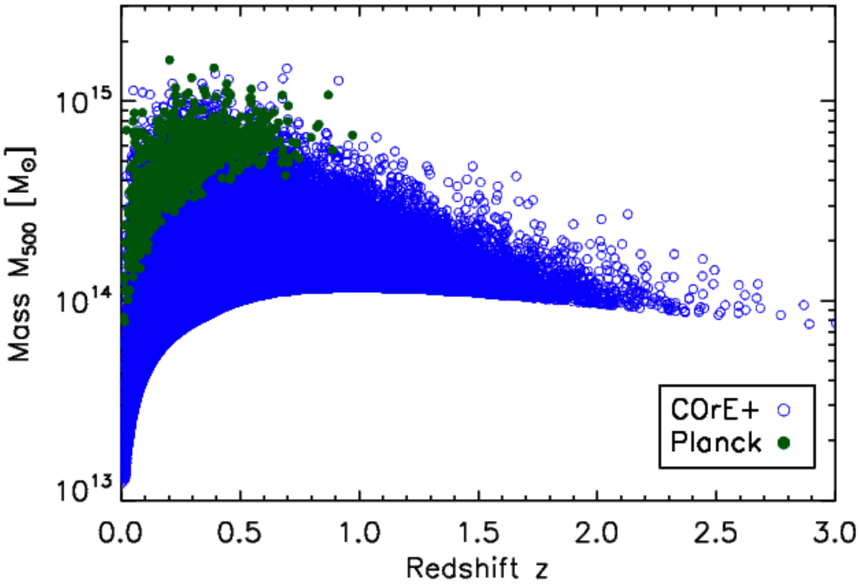

Figure 9.3: Distribution en masse et redshift du catalogue d'amas COrE+ détecté à S/N> 5 (cercles bleus). Les 1093 amas du catalogue Planck PSZ2 ayant un redshift mesuré sont indiqués en disques verts. COrE+ a la capacité de détecter de l'ordre de 10^5 amas et d'étendre la couverture en redshift à $z > 2$. La figure est extraite de la réponse à l'appel d'offre M4 de l'ESA. Le gain en sensibilité de COrE+ par rapport à Planck est dû à la technologie des matrices de bolomètres qui permet la multiplication du nombre de détecteurs dans le plan focal.

lesquels les redshifts ont été mesurés sont représentés en disques verts. Alors que la distribution des amas Planck s'arrête à $z \sim 1$, COrE+ permet d'explorer le domaine de redshift compris entre 1 et 2 et d'obtenir des premières détections d'amas massifs à $z > 2$ si les lois d'échelles flux-masse évoluent de façon standard.

2015

Malheureusement, COrE+ a été rejetée début 2015 pour des raisons techniques et financières : les technologies détecteur et cryogénie n'ont pas été jugées assez avancées pour un lancement en 2025 et le rapport de l'ESA juge les risques de dépassement du budget global importants. Une réponse à l'appel d'offre pour un créneau M5 (lancement en 2030) devra a minima tenir compte de ces recommandations.

Chapitre 10

CONCLUSION ET PERSPECTIVES SCIENTIFIQUES

10.1 Points saillants des analyses SZ entre 2005 et 2015

La période 2005-2015 a vu le lancement des grands sondages SZ (SPT et ACT en 2007, Planck en 2009). Très rapidement, SPT a réalisé la première détection en aveugle d'un amas en 2008. Les premiers catalogues d'amas sélectionnés en SZ, pour les études cosmologiques, ont suivi (SPT en 2010, ACT et Planck en 2013). Dès 2013, les contraintes cosmologiques obtenues à partir des amas SZ avec Planck sont en tension avec le CMB primaire sur la valeur de σ_8. Deux voies de sortie sont actuellement envisageables : le modèle ΛCDM minimal n'est plus suffisant pour expliquer l'ensemble des données, ou bien la physique des amas de galaxies est encore mal comprise et les masses des amas sont 40% plus grande qu'estimées aujourd'hui. Cette seconde hypothèse entrainerait que la fraction de gas des amas serait significativement plus faible que la fraction de baryons universelle, un résultat non prédit par les simulations numériques.

Cette première série de sondages SZ a fourni de grands catalogues sélectionnés en SZ (677 candidats pour SPT (Bleem et al., 2015), 1653 pour Planck (Planck Collaboration XXVI, 2015)). Elle a aussi permis la détection statistique du gas dans de grands échantillons d'amas de galaxies et de galaxies de faible masse (entre quelques 10^{12} et $10^{13}\,M_\odot$).

L'après 2010 a vu les premières détections de nouveaux effets : kSZ de façon statistique (Hand et al., 2012; Planck Collaboration Int. XXXVII, 2015) et individuelle (Sayers et al., 2013b), l'effet de lentille gravitationnelle des amas sur les anisotropies du CMB (Baxter et al., 2014; Melin & Bartlett, 2015; Planck Collaboration XXIV, 2015; Madhavacheril et al., 2015). Ce dernier laisse entrevoir une nouvelle possibilité de mesurer la masse des amas avec précision sur de grands catalogues.

La science SZ a donc ouvert une nouvelle fenêtre pour l'étude des amas de galaxies, à la suite de l'optique et des rayons X. Elle a offert une multitude de nouveaux amas et un processus de sélection facilement maîtrisable qui a permis d'obtenir des contraintes cosmologiques précises, mais encore dominées par les incertitudes systématiques d'estimation de la masse des amas. Les progrès viendront désormais des analyses multi-longueur d'onde (SZ, X et optique) et de leur confrontation sur des catalogues de plus en plus grands pour améliorer notre compréhension de la physique des amas.

10.2 Perspectives scientifiques par domaines d'intérêt

Trois grandes perspectives scientifiques sont envisageables avec le SZ pour les prochaines années. En premier lieu, une étude plus approfondie de la physique des amas (partie 10.2.1). Ensuite, la détection de nouveaux effets SZ (partie 10.2.2). Enfin l'amélioration des contraintes cosmologiques avec les amas (partie 10.2.3).

10.2.1 Physique des amas

L'ouverture de la fenêtre SZ va permettre d'approfondir notre connaissance sur la physique des amas à travers l'étude de profils de pression (par exemple en SZ avec NIKA2), de gaz (en X avec XMM ou Chandra) et de matière noire (en X ou par effet de lentille faible). Ces études vont se faire pour des échantillons nouveaux, sélectionnés en SZ, et couvrant un domaine de redshift allant jusqu'à $z \sim 1.5$.

Outre la matière noire et le gaz, le contenu en galaxies et poussière est aussi un élément d'étude important pour comprendre les interactions entre la phase gazeuse et stellaire des amas ainsi que l'effet des noyaux actifs de galaxies sur le gaz.

Ces travaux s'inscrivent plus généralement dans l'étude de l'assemblage des grandes structures des plus hauts redshifts ($z \sim 5$) à nos jours.

10.2.2 Le challenge de la détection de nouveaux effets SZ

L'effet SZ thermique est désormais détecté de façon quasi routinière. L'effet SZ cinétique est pour l'instant uniquement détecté sur un amas merger et statistiquement par étude de paires. Il faudra essayer de pousser ces études plus loins avec des nouveaux instruments plus sensibles et/ou ayant une meilleure résolution. Ces études sont déterminantes pour tester les champs de vitesse des grandes structures.

L'effet SZ thermique relativiste reste à mettre en évidence. Cela semble difficile avec les données actuelles mais ce n'est peut-être pas impossible en travaillant statistiquement sur des catalogues de plusieurs centaines d'objets, les études actuelles ayant été réalisées sur quelques dizaines d'amas seulement.

Enfin, les effets SZ polarisés (mesure du quadrupole local du CMB, accès aux vitesses transverses des amas) ne sont pas détectables par Planck et ne semblent pas à la portée de la prochaine génération d'expérience. Seul le concept PRISM permettrait leur détection. Une autre possibilité serait de construire des expériences spécifiques pour les mesurer.

10.2.3 Cosmologie avec les amas

Les catalogues SZ ont permis de faire des avancées majeures pour les contraintes cosmologiques avec les amas mais celles-ci sont encore limitées en précision par notre connaissance de l'échelle de masse des amas. Il faut obtenir une précision de quelques pour cent (au plus 10%) sur la masse pour pouvoir définitivement trancher sur la tension avec le CMB primaire. Les études statistiques d'effet de lentille du CMB par les amas de galaxies pourraient permettre d'atteindre ces précisions si les catalogues d'amas sont suffisamment grands et les erreurs systématiques maîtrisées sous le niveau des statistiques.

Ainsi, il est très probable que les contraintes cosmologiques avec les amas atteindront leur apogée dans les cinq à dix prochaines années, lorsque les différentes méthodes de mesure de masse (équilibre hydrostatique en X ou SZ, lentille faible en optique ou avec le CMB, etc) auront amélioré leur précision et que les études multi-longueur d'onde auront permis de mieux comprendre les systématiques.

10.3 Pour terminer

A la suite de SPT, ACT et Planck, les missions eROSITA (en X pour 2016) et Euclid (en optique pour 2020) fourniront à leur tour deux catalogues d'amas de galaxies tout le ciel d'une centaine de milliers d'objets chacun. Des contraintes cosmologiques avec les amas sont attendues pour chacune d'elles. La figure 10.1 présente les prédictions des contraintes avec les amas de galaxies eROSITA (comptages et évolution du spectre de puissance). Celles-ci dépendent aussi de la connaissance des lois d'échelle des amas. Les contours pessimistes supposent les incertitudes actuelles sur la loi $L_X - M$ alors que les contours optimistes supposent que les incertitudes seront divisées par deux.

Il sera dès lors important de continuer à travailler sur la compréhension de la physique des amas et des lois d'échelle avec les trois jeux de données (Planck, eROSITA, Euclid) en étudiant les propriétés des objets de chaque catalogue dans les deux autres jeux de données.

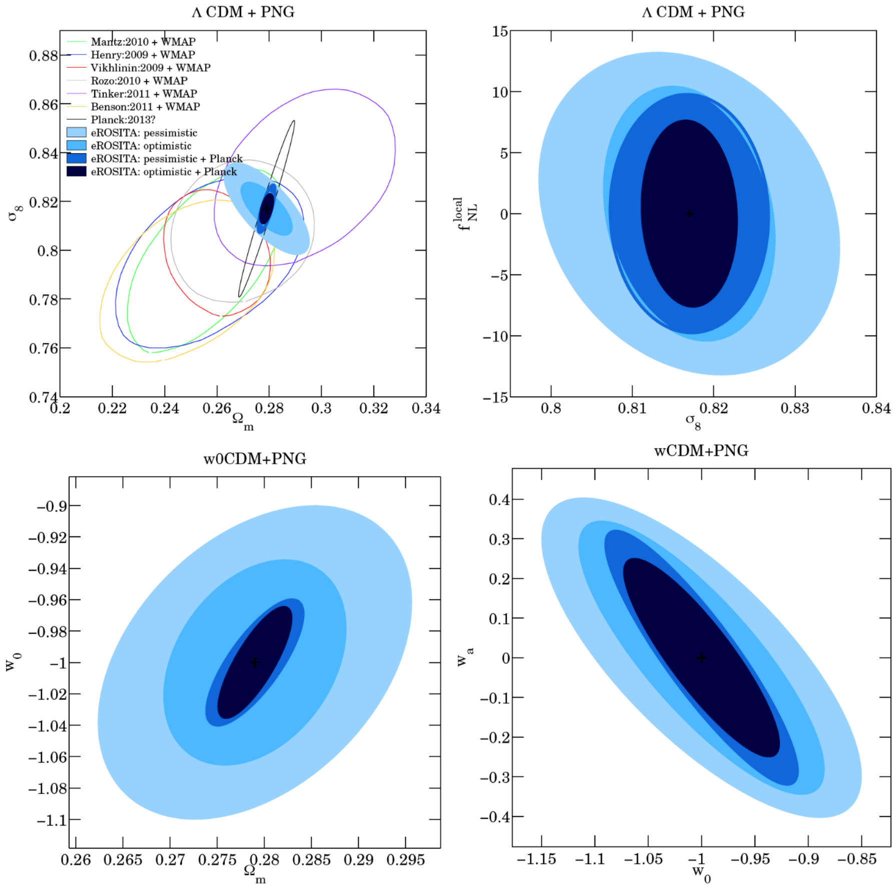

Figure 10.1: Contraintes cosmologiques attendues avec eROSITA pour différents modèles cosmologiques en contours pleins. Les contraintes obtenues par les analyses précédentes sont matérialisées par des contours vides. "PNG" signifie "Primordial Non Gaussianity". Les contours pessimistes supposent les incertitudes actuelles sur la loi $L_X - M$ alors que les contours optimistes supposent que les incertitudes seront divisées par deux. La figure est extraite de Merloni et al. (2012).

RÉFÉRENCES

Ade, P. A. R., Aikin, R. W., Barkats, D., et al., Detection of B-Mode Polarization at Degree Angular Scales by BICEP2. 2014a, Physical Review Letters, 112, 241101, arXiv:1403.3985

Ade, P. A. R., Akiba, Y., Anthony, A. E., et al., Evidence for Gravitational Lensing of the Cosmic Microwave Background Polarization from Cross-Correlation with the Cosmic Infrared Background. 2014b, Physical Review Letters, 112, 131302, arXiv:1312.6645

Afshordi, N., Lin, Y.-T., Nagai, D., & Sanderson, A. J. R., Missing thermal energy of the intracluster medium. 2007, MNRAS, 378, 293, arXiv:astro-ph/0612700

Aghanim, N., de Luca, A., Bouchet, F. R., Gispert, R., & Puget, J. L., Cosmology with Sunyaev-Zeldovich observations from space. 1997, A&A, 325, 9, arXiv:astro-ph/9705092

Albrecht, A., Bernstein, G., Cahn, R., et al., Report of the Dark Energy Task Force. 2006, ArXiv Astrophysics e-prints, arXiv:astro-ph/0609591

Allen, S. W., Rapetti, D. A., Schmidt, R. W., et al., Improved constraints on dark energy from Chandra X-ray observations of the largest relaxed galaxy clusters. 2008, MNRAS, 383, 879, arXiv:0706.0033

Allen, S. W., Schmidt, R. W., & Fabian, A. C., Cosmological constraints from the X-ray gas mass fraction in relaxed lensing clusters observed with Chandra. 2002, MNRAS, 334, L11, arXiv:astro-ph/0205007

Amblard, A. & White, M., Sunyaev-Zel'dovich polarization simulation. 2005, New A, 10, 417, arXiv:astro-ph/0409063

Anderson, M. E., Gaspari, M., White, S. D. M., Wang, W., & Dai, X., Unifying X-ray scaling relations from galaxies to clusters. 2015, MNRAS, 449, 3806, arXiv:1409.6965

Andrade-Santos, F., Jones, C., Forman, W. R., et al., Chandra and Xmm-Newton Observations of the Bimodal Planck SZ-Detected Cluster Plckg345.40-39.34 (A3716) with High and Low Entropy Subcluster Cores. 2015, ApJ, 803, 108, arXiv:1502.05088

André, P., Baccigalupi, C., Banday, A., et al., PRISM (Polarized Radiation Imaging and Spectroscopy Mission): an extended white paper. 2014, J. Cosmology Astropart. Phys., 2, 6, arXiv:1310.1554

Angrick, C., Pace, F., Bartelmann, M., & Roncarelli, M., Reaching agreement between cosmological parameters inferred from galaxy clusters and Planck. 2015, ArXiv e-prints, arXiv:1504.03187

Arnaud, M., Pratt, G. W., Piffaretti, R., et al., The universal galaxy cluster pressure profile from a representative sample of nearby systems (REXCESS) and the Y_{SZ} - M_{500} relation. 2010, A&A, 517, A92, arXiv:0910.1234

Atrio-Barandela, F., Kashlinsky, A., Kocevski, D., & Ebeling, H., Measurement of the Electron-Pressure Profile of Galaxy Clusters in 3 Year Wilkinson Microwave Anisotropy Probe (WMAP) Data. 2008, ApJ, 675, L57, arXiv:0802.3716

Audit, E. & Simmons, J. F. L., The kinematic Sunyaev-Zel'dovich effect and transverse cluster velocities. 1999, MNRAS, 305, L27, arXiv:astro-ph/9812310

Bahcall, N. A. 1998, in Large Scale Structure: Tracks and Traces, ed. V. Mueller, S. Gottloeber, J. P. Muecket, & J. Wambsganss, 137–146

Bahcall, N. A. & Cen, R., The mass function of clusters of galaxies. 1993, ApJ, 407, L49

Bartlett, J. G. & Melin, J.-B., Point source confusion in SZ cluster surveys. 2006, A&A, 447, 405, arXiv:astro-ph/0509818

Baumann, D. & Cooray, A., CMB-induced cluster polarization as a cosmological probe. 2003, New A Rev., 47, 839, arXiv:astro-ph/0304416

Baxter, E. J., Keisler, R., Dodelson, S., et al., A Measurement of Gravitational Lensing of the Cosmic Microwave Background by Galaxy Clusters Using Data from the South Pole Telescope. 2014, ArXiv e-prints, arXiv:1412.7521

Bennett, C. L., Larson, D., Weiland, J. L., et al., Nine-year Wilkinson Microwave Anisotropy Probe (WMAP) Observations: Final Maps and Results. 2013, ApJS, 208, 20, arXiv:1212.5225

Benson, B. A., Church, S. E., Ade, P. A. R., et al., Measurements of Sunyaev-Zel'dovich Effect Scaling Relations for Clusters of Galaxies. 2004, ApJ, 617, 829, arXiv:astro-ph/0404391

Benson, B. A., Church, S. E., Ade, P. A. R., et al., Peculiar Velocity Limits from Measurements of the Spectrum of the Sunyaev-Zeldovich Effect in Six Clusters of Galaxies. 2003, ApJ, 592, 674, arXiv:astro-ph/0303510

Benson, B. A., de Haan, T., Dudley, J. P., et al., Cosmological Constraints from Sunyaev-Zel'dovich-selected Clusters with X-Ray Observations in the First 178 $\deg^2$ of the South Pole Telescope Survey. 2013, ApJ, 763, 147, arXiv:1112.5435

BICEP2/Keck and Planck Collaborations, Ade, P. A. R., Aghanim, N., et al., Joint Analysis of BICEP2/Keck Array and Planck Data. 2015, Physical Review Letters, 114, 101301, arXiv:1502.00612

Bielby, R. M. & Shanks, T., Anomalous SZ contribution to three-year WMAP data. 2007, MNRAS, 382, 1196, arXiv:astro-ph/0703470

Birkinshaw, M., The Sunyaev-Zel'dovich effect. 1999, Phys. Rep., 310, 97, arXiv:astro-ph/9808050

Birkinshaw, M., Gull, S. F., & Hardebeck, H., The Sunyaev-Zeldovich effect towards three clusters of galaxies. 1984, Nature, 309, 34

Bleem, L. E., Stalder, B., de Haan, T., et al., Galaxy Clusters Discovered via the Sunyaev-Zel'dovich Effect in the 2500-Square-Degree SPT-SZ Survey. 2015, ApJS, 216, 27, arXiv:1409.0850

Bobin, J., Moudden, Y., Starck, J.-L., Fadili, J., & Aghanim, N., SZ and CMB reconstruction using generalized morphological component analysis. 2008, Statistical Methodology, 5, 307, arXiv:0712.0588

Bocquet, S., Saro, A., Dolag, K., & Mohr, J. J., Baryon impact on the halo mass function: Fitting formulae and implications for cluster cosmology. 2015, ArXiv e-prints, arXiv:1502.07357

Böhringer, H., Schuecker, P., Guzzo, L., et al., The ROSAT-ESO Flux Limited X-ray (REFLEX) Galaxy cluster survey. V. The cluster catalogue. 2004, A&A, 425, 367, arXiv:astro-ph/0405546

Böhringer, H., Voges, W., Huchra, J. P., et al., The Northern ROSAT All-Sky (NORAS) Galaxy Cluster Survey. I. X-Ray Properties of Clusters Detected as Extended X-Ray Sources. 2000, ApJS, 129, 435, arXiv:astro-ph/0003219

Bonamente, M., Hasler, N., Bulbul, E., et al., Comparison of pressure profiles of massive relaxed galaxy clusters using the Sunyaev-Zel'dovich and x-ray data. 2012, New Journal of Physics, 14, 025010, arXiv:1112.1599

Bouchet, F. R. & Gispert, R., Foregrounds and CMB experiments. I. Semi-analytical estimates of contamination. 1999, New A, 4, 443, arXiv:astro-ph/9903176

Bouchet, F. R., Prunet, S., & Sethi, S. K., Multifrequency Wiener filtering of cosmic microwave background data with polarization. 1999, MNRAS, 302, 663

Carlberg, R. G., Yee, H. K. C., Ellingson, E., et al., Galaxy Cluster Virial Masses and Omega. 1996, ApJ, 462, 32, arXiv:astro-ph/9509034

Carlstrom, J. E., Holder, G. P., & Reese, E. D., Cosmology with the Sunyaev-Zel'dovich Effect. 2002, ARA&A, 40, 643, arXiv:astro-ph/0208192

Carvalho, P., Rocha, G., & Hobson, M. P., A fast Bayesian approach to discrete object detection in astronomical data sets - PowellSnakes I. 2009, MNRAS, 393, 681, arXiv:0802.3916

Cash, W., Parameter estimation in astronomy through application of the likelihood ratio. 1979, ApJ, 228, 939

Cavaliere, A. & Fusco-Femiano, R., X-rays from hot plasma in clusters of galaxies. 1976, A&A, 49, 137

Chamballu, A., Bartlett, J. G., & Melin, J.-B., The Planck SZ Cluster Catalog: expected X-ray properties. 2012, A&A, 544, A40

Clerc, N., Sadibekova, T., Pierre, M., et al., The cosmological analysis of X-ray cluster surveys - II. Application of the CR-HR method to the XMM archive. 2012, MNRAS, 423, 3561, arXiv:1109.4441

Colafrancesco, S., Mazzotta, P., Rephaeli, Y., & Vittorio, N., Intracluster Comptonization of the Cosmic Microwave Background: Mean Spectral Distortion and Cluster Number Counts. 1997, ApJ, 479, 1, arXiv:astro-ph/9703121

de Bernardis, P., Ade, P. A. R., Bock, J. J., et al., A flat Universe from high-resolution maps of the cosmic microwave background radiation. 2000, Nature, 404, 955, arXiv:astro-ph/0004404 de Zotti, G., Ricci, R., Mesa, D., et al., Predictions for high-frequency radio surveys of extragalactic sources. 2005, A&A, 431, 893, arXiv:astro-ph/0410709

Delabrouille, J., Betoule, M., Melin, J.-B., et al., The pre-launch Planck Sky Model: a model of sky emission at submillimetre to centimetre wavelengths. 2013, A&A, 553, A96, arXiv:1207.3675

Delabrouille, J., Melin, J.-B., & Bartlett, J. G. 2002, in Astronomical Society of the Pacific Conference Series, Vol. 257, AMiBA 2001: High-Z Clusters, Missing Baryons, and CMB Polarization, ed. L.-W. Chen, C.-P. Ma, K.-W. Ng, & U.-L. Pen, 81

Désert, F.-X., Benoit, A., Gaertner, S., et al., Observations of the Sunyaev-Zel'dovich effect at high angular resolution towards the galaxy clusters A665, A2163 and CL0016+16. 1998, New A, 3, 655, arXiv:astro-ph/9808270

Diego, J. M. & Partridge, B., The Sunyaev-Zel'dovich effect in Wilkinson Microwave Anisotropy Probe data. 2010, MNRAS, 402, 1179

Diego, J. M., Vielva, P., Martínez-González, E., Silk, J., & Sanz, J. L., A Bayesian non-parametric method to detect clusters in Planck data. 2002, MNRAS, 336, 1351, arXiv:astro-ph/0110587

Dolag, K., Hansen, F. K., Roncarelli, M., & Moscardini, L., The imprints of local superclusters on the Sunyaev-Zel'dovich signals and their detectability with Planck. 2005, MNRAS, 363, 29, arXiv:astro-ph/0505258

Draper, P., Dodelson, S., Hao, J., & Rozo, E., Sunyaev-Zel'dovich signal of the maxBCG SDSS galaxy clusters in WMAP. 2012, Phys. Rev. D, 85, 023005, arXiv:1106.2185

Eckert, D., Ettori, S., Molendi, S., Vazza, F., & Paltani, S., The X-ray/SZ view of the virial region. II. Gas mass fraction. 2013a, A&A, 551, A23, arXiv:1301.0624

Eckert, D., Molendi, S., Vazza, F., Ettori, S., & Paltani, S., The X-ray/SZ view of the virial region. I. Thermodynamic properties. 2013b, A&A, 551, A22, arXiv:1301.0617

Eisenstein, D. J., Zehavi, I., Hogg, D. W., et al., Detection of the Baryon Acoustic Peak in the Large-Scale Correlation Function of SDSS Luminous Red Galaxies. 2005, ApJ, 633, 560, arXiv:astro-ph/0501171

Freedman, W. L., Madore, B. F., Gibson, B. K., et al., Final Results from the Hubble Space Telescope Key Project to Measure the Hubble Constant. 2001, ApJ, 553, 47, arXiv:astro-ph/0012376

Górski, K. M., Hivon, E., Banday, A. J., et al., HEALPix: A Framework for High-Resolution Discretization and Fast Analysis of Data Distributed on the Sphere. 2005, ApJ, 622, 759, arXiv:astro-ph/0409513

Greco, J. P., Hill, J. C., Spergel, D. N., & Battaglia, N., The Stacked Thermal SZ Signal of Locally Brightest Galaxies in Planck Full Mission Data: Evidence for Galaxy Feedback? 2014, ArXiv e-prints, arXiv:1409.6747

Haehnelt, M. G. & Tegmark, M., Using the Kinematic Sunyaev-Zeldovich effect to determine the peculiar velocities of clusters of galaxies. 1996, MNRAS, 279, 545, arXiv:astro-ph/9507077

Hall, A. & Challinor, A., Detecting the polarization induced by scattering of the microwave background quadrupole in galaxy clusters. 2014, Phys. Rev. D, 90, 063518, arXiv:1407.5135

Hand, N., Addison, G. E., Aubourg, E., et al., Evidence of Galaxy Cluster Motions with the Kinematic Sunyaev-Zel'dovich Effect. 2012, Physical Review Letters, 109, 041101, arXiv:1203.4219

Hand, N., Appel, J. W., Battaglia, N., et al., The Atacama Cosmology Telescope: Detection of Sunyaev-Zel'Dovich Decrement in Groups and Clusters Associated with Luminous Red Galaxies. 2011, ApJ, 736, 39, arXiv:1101.1951

Hanson, D., Hoover, S., Crites, A., et al., Detection of B-Mode Polarization in the Cosmic Microwave Background with Data from the South Pole Telescope. 2013, Physical Review Letters, 111, 141301, arXiv:1307.5830

Hasselfield, M., Hilton, M., Marriage, T. A., et al., The Atacama Cosmology Telescope: Sunyaev-Zel'dovich selected galaxy clusters at 148 GHz from three seasons of data. 2013, J. Cosmology Astropart. Phys., 7, 8, arXiv:1301.0816

Herranz, D., Sanz, J. L., Barreiro, R. B., & López-Caniego, M., The estimation of the Sunyaev-Zel'dovich effects with unbiased multifilters. 2005, MNRAS, 356, 944, arXiv:astro-ph/0406226

Herranz, D., Sanz, J. L., Hobson, M. P., et al., Filtering techniques for the detection of Sunyaev-Zel'dovich clusters in multifrequency maps. 2002, MNRAS, 336, 1057, arXiv:astro-ph/0203486

Hinshaw, G., Larson, D., Komatsu, E., et al., Nine-year Wilkinson Microwave Anisotropy Probe (WMAP) Observations: Cosmological Parameter Results. 2013, ApJS, 208, 19, arXiv:1212.5226

Hobson, M. P., Jones, A. W., Lasenby, A. N., & Bouchet, F. R., Foreground separation methods for satellite observations of the cosmic microwave background. 1998, MNRAS, 300, 1, arXiv:astro-ph/9806387

Hoekstra, H., Herbonnet, R., Muzzin, A., et al., The Canadian Cluster Comparison Project: detailed study of systematics and updated weak lensing masses. 2015, MNRAS, 449, 685, arXiv:1502.01883

Holder, G. & Kosowsky, A., Gravitational Lensing of the Microwave Background by Galaxy Clusters. 2004, ApJ, 616, 8, arXiv:astro-ph/0401519

Hu, W. & Okamoto, T., Mass Reconstruction with Cosmic Microwave Background Polarization. 2002, ApJ, 574, 566, arXiv:astro-ph/0111606

Hurley-Walker, N., Brown, M. L., Davies, M. L., et al., Further Sunyaev-Zel'dovich observations of two Planck ERCSC clusters with the Arcminute Microkelvin Imager. 2011, MNRAS, 414, L75, arXiv:1103.0947

Itoh, N., Kohyama, Y., & Nozawa, S., Relativistic Corrections to the Sunyaev-Zeldovich Effect for Clusters of Galaxies. 1998, ApJ, 502, 7, arXiv:astro-ph/9712289

Jenkins, A., Frenk, C. S., White, S. D. M., et al., The mass function of dark matter haloes. 2001, MNRAS, 321, 372, arXiv:astro-ph/0005260

Johnston, D. E., Sheldon, E. S., Tasitsiomi, A., et al., Cross-Correlation Lensing: Determining Galaxy and Cluster Mass Profiles from Statistical Weak-Lensing Measurements. 2007, ApJ, 656, 27, arXiv:astro-ph/0507467

Joy, M., LaRoque, S., Grego, L., et al., Sunyaev-Zeldovich Effect Imaging of Massive Clusters of Galaxies at Redshift Z>0.8. 2001, ApJ, 551, L1, arXiv:astro-ph/0012052

Kamionkowski, M. & Loeb, A., Getting around cosmic variance. 1997, Phys. Rev. D, 56, 4511, arXiv:astro-ph/9703118

King, I., The structure of star clusters. I. an empirical density law. 1962, AJ, 67, 471

Knop, R. A., Aldering, G., Amanullah, R., et al., New Constraints on Ω_M, $\Omega_?$, and w from an Independent Set of 11 High-Redshift Supernovae Observed with the Hubble Space Telescope. 2003, ApJ, 598, 102, arXiv:astro-ph/0309368

Koester, B. P., McKay, T. A., Annis, J., et al., A MaxBCG Catalog of 13,823 Galaxy Clusters from the Sloan Digital Sky Survey. 2007, ApJ, 660, 239, arXiv:astro-ph/0701265

Kogut, A., Banday, A. J., Bennett, C. L., et al., Microwave Emission at High Galactic Latitudes in the Four-Year DMR Sky Maps. 1996, ApJ, 464, L5, arXiv:astro-ph/9601060

Komatsu, E., Smith, K. M., Dunkley, J., et al., Seven-year Wilkinson Microwave Anisotropy Probe (WMAP) Observations: Cosmological Interpretation. 2011, ApJS, 192, 18, arXiv:1001.4538

Le Brun, A. M. C., McCarthy, I. G., & Melin, J.-B., Testing Sunyaev-Zel'dovich measurements of the hot gas content of dark matter haloes using synthetic skies. 2015, ArXiv e-prints, arXiv:1501.05666

Le Brun, A. M. C., McCarthy, I. G., Schaye, J., & Ponman, T. J., Towards a realistic population of simulated galaxy groups and clusters. 2014, MNRAS, 441, 1270, arXiv:1312.5462

Leach, S. M., Cardoso, J.-F., Baccigalupi, C., et al., Component separation methods for the PLANCK mission. 2008, A&A, 491, 597, arXiv:0805.0269

Lieu, R., Mittaz, J. P. D., & Zhang, S.-N., The Sunyaev-Zel'dovich Effect in a Sample of 31 Clusters: A Comparison between the X-Ray Predicted and WMAP Observed Cosmic Microwave Background Temperature Decrement. 2006, ApJ, 648, 176, arXiv:astro-ph/0510160

Liu, J., Hennig, C., Desai, S., et al., Optical confirmation and redshift estimation of the Planck cluster candidates overlapping the Pan-STARRS Survey. 2015, MNRAS, 449, 3370, arXiv:1407.6001

Madhavacheril, M., Sehgal, N., Allison, R., et al., Evidence of Lensing of the Cosmic Microwave Background by Dark Matter Halos. 2015, Physical Review Letters, 114, 151302, arXiv:1411.7999

McCarthy, I. G., Le Brun, A. M. C., Schaye, J., & Holder, G. P., The thermal Sunyaev-Zel'dovich effect power spectrum in light of Planck. 2014, MNRAS, 440, 3645, arXiv:1312.5341

Melin, J., Bartlett, J. G., & Delabrouille, J., Catalog extraction in SZ cluster surveys: a matched filter approach. 2006, A&A, 459, 341, arXiv:astro-ph/0602424

Melin, J.-B. 2004, PhD thesis, Université Paris-Diderot - Paris VII

Melin, J.-B., Aghanim, N., Bartelmann, M., et al., A comparison of algorithms for the construction of SZ cluster catalogues. 2012, A&A, 548, A51, arXiv:1210.1416

Melin, J.-B. & Bartlett, J. G., Measuring cluster masses with CMB lensing: a statistical approach. 2015, A&A, 578, A21, arXiv:1408.5633

Melin, J.-B., Bartlett, J. G., & Delabrouille, J., The selection function of SZ cluster surveys. 2005, A&A, 429, 417, arXiv:astro-ph/0409564

Melin, J.-B., Bartlett, J. G., Delabrouille, J., et al., The galaxy cluster Y_{SZ} - L_X and Y_{SZ} - M relations from the WMAP 5-yr data. 2011, A&A, 525, A139, arXiv:1001.0871

Menanteau, F., González, J., Juin, J.-B., et al., The Atacama Cosmology Telescope: Physical Properties and Purity of a Galaxy Cluster Sample Selected via the Sunyaev-Zel'dovich Effect. 2010, ApJ, 723, 1523, arXiv:1006.5126

Merloni, A., Predehl, P., Becker, W., et al., eROSITA Science Book: Mapping the Structure of the Energetic Universe. 2012, ArXiv e-prints, arXiv:1209.3114

Meyer, S. S., Jeffries, A. D., Woody, D., & Scott, S. 1984, in Bulletin of the American Astronomical Society, Vol. 16, Bulletin of the American Astronomical Society, 513

Monfardini, A., Adam, R., Adane, A., et al., Latest NIKA Results and the NIKA-2 Project. 2014, Journal of Low Temperature Physics, 176, 787, arXiv:1310.1230

Muchovej, S., Leitch, E., Culverhouse, T., Carpenter, J., & Sievers, J., CARMA Follow-up of the Northern Unconfirmed Planck Galaxy Cluster Candidates. 2012, ApJ, 749, 46, arXiv:1202.0527

Mueller, E.-M., de Bernardis, F., Bean, R., & Niemack, M., Constraints on gravity and dark energy from the pairwise kinematic Sunyaev-Zeldovich effect. 2014a, ArXiv e-prints, arXiv:1408.6248

Mueller, E.-M., de Bernardis, F., Bean, R., & Niemack, M. D., Constraints on massive neutrinos from the pairwise kinematic Sunyaev-Zel'dovich effect. 2014b, ArXiv e-prints, arXiv:1412.0592

Nagai, D., Kravtsov, A. V., & Vikhlinin, A., Effects of Galaxy Formation on Thermodynamics of the Intracluster Medium. 2007, ApJ, 668, 1, arXiv:astro-ph/0703661

Oukbir, J. & Blanchard, A., X-ray clusters in open universes. 1992, A&A, 262, L21

Oukbir, J. & Blanchard, A., X-ray clusters: towards a new determination of the density parameter of the universe. 1997, A&A, 317, 1, arXiv:astro-ph/9611085

Pacaud, F., Pierre, M., Adami, C., et al., The XMM-LSS survey: the Class 1 cluster sample over the initial 5 deg^2 and its cosmological modelling. 2007, MNRAS, 382, 1289, arXiv:0709.1950

Perlmutter, S., Aldering, G., Goldhaber, G., et al., Measurements of Ω and Λ from 42 High-Redshift Supernovae. 1999, ApJ, 517, 565, arXiv:astro-ph/9812133

Perrott, Y. C., Olamaie, M., Rumsey, C., et al., Comparison of Sunyaev-Zel'dovich measurements from Planck and from the Arcminute Microkelvin Imager for 99 galaxy clusters. 2015, A&A, 580, A95, arXiv:1405.5013

Pierpaoli, E., Borgani, S., Scott, D., & White, M., On determining the cluster abundance normalization. 2003, MNRAS, 342, 163, arXiv:astro-ph/0210567

Pierre, M., Juin, J. B., Melin, J. B., & Pacaud, F. 2008, in The X-ray Universe 2008

Pierre, M., Pacaud, F., Juin, J. B., et al., Precision cosmology with a wide area XMM cluster survey. 2011, MNRAS, 414, 1732, arXiv:1009.3182

Piffaretti, R., Arnaud, M., Pratt, G. W., Pointecouteau, E., & Melin, J.-B., The MCXC: a meta-catalogue of x-ray detected clusters of galaxies. 2011, A&A, 534, A109, arXiv:1007.1916

Pires, S., Juin, J. B., Yvon, D., et al., Sunyaev-Zel'dovich cluster reconstruction in multiband bolometer camera surveys. 2006, A&A, 455, 741, arXiv:astro-ph/0508641

Planck Collaboration, Ade, P. A. R., Aghanim, N., et al., Planck intermediate results (Corrigendum). V. Pressure profiles of galaxy clusters from the Sunyaev-Zeldovich effect. 2013, A&A, 558, C2

Planck Collaboration I, Planck early results. I. The Planck mission. 2011, A&A, 536, A1, arXiv:1101.2022

Planck Collaboration VII, Planck early results. VII. The Early Release Compact Source Catalogue. 2011, A&A, 536, A7, arXiv:1101.2041

Planck Collaboration VIII, Planck early results. VIII. The all-sky early Sunyaev-Zeldovich cluster sample. 2011, A&A, 536, A8, arXiv:1101.2024

Planck Collaboration IX, Planck early results. IX. XMM-*Newton* follow-up validation programme of *Planck* cluster candidates. 2011, A&A, 536, A9, arXiv:1101.2025

Planck Collaboration X, Planck early results. X. Statistical analysis of Sunyaev-Zeldovich scaling relations for X-ray galaxy clusters. 2011, A&A, 536, A10, arXiv:1101.2043

Planck Collaboration XI, Planck early results. XI. Calibration of the local galaxy cluster Sunyaev-Zeldovich scaling relations. 2011, A&A, 536, A11, arXiv:1101.2026

Planck Collaboration XII, Planck early results. XII. Cluster Sunyaev-Zeldovich optical scaling relations. 2011, A&A, 536, A12, arXiv:1101.2027

Planck Collaboration XXVI, Planck early results. XXVI. Detection with *Planck* and confirmation by XMM-*Newton* of PLCK G266.6-27.3, an exceptionally X-ray luminous and massive galaxy cluster at $z{\sim}1$. 2011, A&A, 536, A26, arXiv:1106.1376

Planck Collaboration I, *Planck* 2013 results. I. Overview of products and scientific results. 2014, A&A, 571, A1, arXiv:1303.5062

Planck Collaboration XVI, *Planck* 2013 results. XVI. Cosmological parameters. 2014, A&A, 571, A16, arXiv:1303.5076

Planck Collaboration XX, *Planck* 2013 results. XX. Cosmology from Sunyaev-Zeldovich cluster counts. 2014, A&A, 571, A20, arXiv:1303.5080

Planck Collaboration XXI, *Planck* 2013 results. XXI. Power spectrum and high-order statistics of the *Planck* all-sky Compton parameter map. 2014, A&A, 571, A21, arXiv:1303.5081

Planck Collaboration XXIII, *Planck* 2013 results. XXIII. Isotropy and statistics of the CMB. 2014, A&A, 571, A23, arXiv:1303.5083

Planck Collaboration XXIX, *Planck* 2013 results. XXIX. The Planck catalogue of Sunyaev-Zeldovich sources. 2014, A&A, 571, A29, arXiv:1303.5089

Planck Collaboration I, *Planck* 2015 results. I. Overview of products and results. 2015, A&A, submitted, arXiv:1502.01582

Planck Collaboration XIII, *Planck* 2015 results. XIII. Cosmological parameters. 2015, A&A, submitted, arXiv:1502.01589

Planck Collaboration XV, *Planck* 2015 results. XV. Gravitational lensing. 2015, A&A, submitted, arXiv:1502.01591

Planck Collaboration XXII, *Planck* 2015 results. XXII. A map of the thermal Sunyaev-Zeldovich effect. 2015, A&A, submitted, arXiv:1502.01596

Planck Collaboration XXIV, *Planck* 2015 results. XXIV. Cosmology from Sunyaev-Zeldovich cluster counts. 2015, A&A, submitted, arXiv:1502.01597

Planck Collaboration XXVI, *Planck* 2015 results. XXVI. The Second Planck Catalogue of Compact Sources. 2015, in preparation

Planck Collaboration XXVII, *Planck* 2015 results. XXVII. The Second Planck Catalogue of Sunyaev-Zeldovich Sources. 2015, A&A, submitted, arXiv:1502.01598

Planck Collaboration Int. I, Planck intermediate results. I. Further validation of new *Planck* clusters with XMM-*Newton*. 2012, A&A, 543, A102, arXiv:1112.5595

Planck and AMI Collaborations, Planck intermediate results. II. Comparison of Sunyaev-Zeldovich measurements from *Planck* and from the Arcminute Microkelvin Imager for 11 galaxy clusters. 2013, A&A, 550, A128, arXiv:1204.1318

Planck Collaboration Int. III, Planck intermediate results. III. The relation between galaxy cluster mass and Sunyaev-Zeldovich signal. 2013, A&A, 550, A129, arXiv:1204.2743

Planck Collaboration Int. IV, Planck intermediate results. IV. The XMM-*Newton* validation programme for new Planck clusters. 2013, A&A, 550, A130, arXiv:1205.3376

Planck Collaboration Int. V, Planck intermediate results. V. Pressure profiles of galaxy clusters from the Sunyaev-Zeldovich effect. 2013, A&A, 550, A131, arXiv:1207.4061

Planck Collaboration Int. VI, Planck intermediate results. VI. The dynamical structure of PLCKG214.6+37.0, a Planck discovered triple system of galaxy clusters. 2013, A&A, 550, A132, arXiv:1207.4009

Planck Collaboration Int. VIII, Planck intermediate results. VIII. Filaments between interacting clusters. 2013, A&A, 550, A134, arXiv:1208.5911

Planck Collaboration Int. X, Planck intermediate results. X. Physics of the hot gas in the Coma cluster. 2013, A&A, 554, A140, arXiv:1208.3611

Planck Collaboration Int. XI, Planck intermediate results. XI. The gas content of dark matter halos: the Sunyaev-Zeldovich-stellar mass relation for locally brightest galaxies. 2013, A&A, 557, A52, arXiv:1212.4131

Planck Collaboration Int. XIII, Planck intermediate results. XIII. Constraints on peculiar velocities. 2014, A&A, 561, A97, arXiv:1303.5090

Planck Collaboration Int. XXVI, Planck intermediate results. XXVI. Optical identification and redshifts of *Planck* clusters with the RTT150 telescope. 2014, A&A, in press, arXiv:1407.6663

Planck Collaboration Int. XXX, Planck intermediate results. XXX. The angular power spectrum of polarized dust emission at intermediate and high Galactic latitudes. 2014, A&A, in press, arXiv:1409.5738

Planck Collaboration Int. XXXVI, Planck intermediate results. XXXVI. Optical identification and redshifts of Planck SZ sources with telescopes in the Canary Islands Observatories. 2015, in preparation

Planck Collaboration Int. XXXVII, Planck intermediate results. XXXVII. Evidence of unbound gas from the kinetic Sunyaev-Zeldovich effect. 2015, A&A, submitted, arXiv:1504.03339

Portsmouth, J., Analysis of the Kamionkowski-Loeb method of reducing cosmic variance with CMB polarization. 2004, Phys. Rev. D, 70, 063504, arXiv:astro-ph/0402173

Press, W. H. & Schechter, P., Formation of Galaxies and Clusters of Galaxies by Self-Similar Gravitational Condensation. 1974, ApJ, 187, 425

PRISM Collaboration, Andre, P., Baccigalupi, C., et al., PRISM (Polarized Radiation Imaging and Spectroscopy Mission): A White Paper on the Ultimate Polarimetric Spectro-Imaging of the Microwave and Far-Infrared Sky. 2013, ArXiv e-prints, arXiv:1306.2259

Puisieux, S. 2013, Theses, Université Paris-Diderot - Paris VII

Ramos, E. P. R. G., da Silva, A. J. C., & Liu, G.-C., Cosmic Microwave Background Induced Polarization from Single Scattering by Clusters of Galaxies and Filaments. 2012, ApJ, 757, 44

Reichardt, C. L., Stalder, B., Bleem, L. E., et al., Galaxy Clusters Discovered via the Sunyaev-Zel'dovich Effect in the First 720 Square Degrees of the South Pole Telescope Survey. 2013, ApJ, 763, 127, arXiv:1203.5775

Remazeilles, M., Delabrouille, J., & Cardoso, J.-F., CMB and SZ effect separation with constrained Internal Linear Combinations. 2011, MNRAS, 410, 2481, arXiv:1006.5599

Riess, A. G., Filippenko, A. V., Challis, P., et al., Observational Evidence from Supernovae for an Accelerating Universe and a Cosmological Constant. 1998, AJ, 116, 1009, arXiv:astro-ph/9805201

Riess, A. G., Macri, L., Casertano, S., et al., A 3% Solution: Determination of the Hubble Constant with the Hubble Space Telescope and Wide Field Camera 3. 2011, ApJ, 730, 119, arXiv:1103.2976

Rodriguez-Gonzalvez, C., Chary, R., Muchovej, S., et al., CARMA observations of massive Planck-discovered cluster candidates at z>0.5 associated with WISE overdensities: Breaking the size-flux degeneracy. 2015, ArXiv e-prints, arXiv:1505.01132

Roman, M. 2014, Theses, Université Paris Diderot Sorbonne Paris Cité (Paris 7)

Rozo, E., Bartlett, J. G., Evrard, A. E., & Rykoff, E. S., Closing the loop: a self-consistent model of optical, X-ray and Sunyaev-Zel'dovich scaling relations for clusters of Galaxies. 2014a, MNRAS, 438, 78, arXiv:1204.6305

Rozo, E., Evrard, A. E., Rykoff, E. S., & Bartlett, J. G., A comparative study of local galaxy clusters - II. X-ray and SZ scaling relations. 2014b, MNRAS, 438, 62, arXiv:1204.6292

Rozo, E., Rykoff, E. S., Bartlett, J. G., & Evrard, A., A comparative study of local galaxy clusters - I. Derived X-ray observables. 2014c, MNRAS, 438, 49, arXiv:1204.6301

Rozo, E., Rykoff, E. S., Bartlett, J. G., & Melin, J.-B., redMaPPer - III. A detailed comparison of the Planck 2013 and SDSS DR8 redMaPPer cluster catalogues. 2015, MNRAS, 450, 592, arXiv:1401.7716

Rozo, E., Rykoff, E. S., Evrard, A., et al., Constraining the Scatter in the Mass-richness Relation of maxBCG Clusters with Weak Lensing and X-ray Data. 2009, ApJ, 699, 768, arXiv:0809.2794

Rozo, E., Wechsler, R. H., Rykoff, E. S., et al., Cosmological Constraints from the Sloan Digital Sky Survey maxBCG Cluster Catalog. 2010, ApJ, 708, 645, arXiv:0902.3702

Rykoff, E. S., Rozo, E., Busha, M. T., et al., redMaPPer. I. Algorithm and SDSS DR8 Catalog. 2014, ApJ, 785, 104, arXiv:1303.3562

Sayers, J., Czakon, N. G., Bridge, C., et al., Bolocam Observations of Two Unconfirmed Galaxy Cluster Candidates from the Planck Early Sunyaev-Zel'dovich Sample. 2012, ApJ, 749, L15, arXiv:1112.5151

Sayers, J., Czakon, N. G., Mantz, A., et al., Sunyaev-Zel'dovich-measured Pressure Profiles from the Bolocam X-Ray/SZ Galaxy Cluster Sample. 2013a, ApJ, 768, 177, arXiv:1211.1632

Sayers, J., Mroczkowski, T., Zemcov, M., et al., A Measurement of the Kinetic Sunyaev-Zel'dovich Signal Toward MACS J0717.5+3745. 2013b, ApJ, 778, 52, arXiv:1312.3680

Sazonov, S. Y. & Sunyaev, R. A., Microwave polarization in the direction of galaxy clusters induced by the CMB quadrupole anisotropy. 1999, MNRAS, 310, 765, arXiv:astro-ph/9903287

Schäfer, B. M., Pfrommer, C., Bartelmann, M., Springel, V., & Hernquist, L., Detecting Sunyaev-Zel'dovich clusters with Planck - I. Construction of all-sky thermal and kinetic SZ maps. 2006a, MNRAS, 370, 1309, arXiv:astro-ph/0407089

Schäfer, B. M., Pfrommer, C., Hell, R. M., & Bartelmann, M., Detecting Sunyaev-Zel'dovich clusters with Planck - II. Foreground components and optimized filtering schemes. 2006b, MNRAS, 370, 1713, arXiv:astro-ph/0407090

Schuecker, P., Böhringer, H., Collins, C. A., & Guzzo, L., The REFLEX galaxy cluster survey. VII. Omega$_m$ and sigma$_8$ from cluster abundance and large-scale clustering. 2003, A&A, 398, 867, arXiv:astro-ph/0208251

Sehgal, N., Addison, G., Battaglia, N., et al., The Atacama Cosmology Telescope: Relation between Galaxy Cluster Optical Richness and Sunyaev-Zel'dovich Effect. 2013, ApJ, 767, 38, arXiv:1205.2369

Seljak, U. & Zaldarriaga, M., Lensing-induced Cluster Signatures in the Cosmic Microwave Background. 2000, ApJ, 538, 57, arXiv:astro-ph/9907254

Sheth, R. K., Mo, H. J., & Tormen, G., Ellipsoidal collapse and an improved model for the number and spatial distribution of dark matter haloes. 2001, MNRAS, 323, 1, arXiv:astro-ph/9907024

Sheth, R. K. & Tormen, G., Large-scale bias and the peak background split. 1999, MNRAS, 308, 119, arXiv:astro-ph/9901122

Spergel, D. N., Verde, L., Peiris, H. V., et al., First-Year Wilkinson Microwave Anisotropy Probe (WMAP) Observations: Determination of Cosmological Parameters. 2003, ApJS, 148, 175, arXiv:astro-ph/0302209

Staniszewski, Z., Ade, P. A. R., Aird, K. A., et al., Galaxy Clusters Discovered with a Sunyaev-Zel'dovich Effect Survey. 2009, ApJ, 701, 32, arXiv:0810.1578

Story, K., Aird, K. A., Andersson, K., et al., South Pole Telescope Detections of the Previously Unconfirmed Planck Early Sunyaev-Zel'dovich Clusters in the Southern Hemisphere. 2011, ApJ, 735, L36, arXiv:1102.2189

Story, K. T., Hanson, D., Ade, P. A. R., et al., A Measurement of the Cosmic Microwave Background Gravitational Lensing Potential from 100 Square Degrees of SPTpol Data. 2014, ArXiv e-prints, arXiv:1412.4760

Tauber, J. A., Mandolesi, N., Puget, J.-L., et al., Planck pre-launch status: The Planck mission. 2010, A&A, 520, A1

The Polarbear Collaboration: P. A. R. Ade, Akiba, Y., Anthony, A. E., et al., A Measurement of the Cosmic Microwave Background B-mode Polarization Power Spectrum at Sub-degree Scales with POLARBEAR. 2014, ApJ, 794, 171, arXiv:1403.2369

Tinker, J., Kravtsov, A. V., Klypin, A., et al., Toward a Halo Mass Function for Precision Cosmology: The Limits of Universality. 2008, ApJ, 688, 709, arXiv:0803.2706

Tyson, J. A., Wenk, R. A., & Valdes, F., Detection of systematic gravitational lens galaxy image alignments - Mapping dark matter in galaxy clusters. 1990, ApJ, 349, L1

Uson, J. M. & Wilkinson, D. T. 1984, in Bulletin of the American Astronomical Society, Vol. 16, Bulletin of the American Astronomical Society, 513

Vale, C., Amblard, A., & White, M., Cluster lensing of the CMB. 2004, New A, 10, 1, arXiv:astro-ph/0402004

van Engelen, A., Sherwin, B. D., Sehgal, N., et al., The Atacama Cosmology Telescope: Lensing of CMB Temperature and Polarization Derived from Cosmic Infrared Background Cross-Correlation. 2014, ArXiv e-prints, arXiv:1412.0626

Vanderlinde, K., Crawford, T. M., de Haan, T., et al., Galaxy Clusters Selected with the Sunyaev-Zel'dovich Effect from 2008 South Pole Telescope Observations. 2010, ApJ, 722, 1180, arXiv:1003.0003

Vikhlinin, A., Kravtsov, A. V., Burenin, R. A., et al., Chandra Cluster Cosmology Project III: Cosmological Parameter Constraints. 2009, ApJ, 692, 1060, arXiv:0812.2720

Voit, G. M., Tracing cosmic evolution with clusters of galaxies. 2005, Reviews of Modern Physics, 77, 207, arXiv:astro-ph/0410173

von der Linden, A., Mantz, A., Allen, S. W., et al., Robust weak-lensing mass calibration of Planck galaxy clusters. 2014, MNRAS, 443, 1973, arXiv:1402.2670

Wen, Z. L., Han, J. L., & Liu, F. S., Galaxy Clusters Identified from the SDSS DR6 and Their Properties. 2009, ApJS, 183, 197, arXiv:0906.0803

Wen, Z. L., Han, J. L., & Liu, F. S., Mass function of rich galaxy clusters and its constraint on σ_8. 2010, MNRAS, 407, 533, arXiv:1004.3337

Wen, Z. L., Han, J. L., & Liu, F. S., A Catalog of 132,684 Clusters of Galaxies Identified from Sloan Digital Sky Survey III. 2012a, ApJS, 199, 34, arXiv:1202.6424

Wen, Z. L., Han, J. L., & Liu, F. S., A Catalog of 132,684 Clusters of Galaxies Identified from Sloan Digital Sky Survey III. 2012b, ApJS, 199, 34, arXiv:1202.6424

White, D. A. & Fabian, A. C., Einstein Observatory evidence for the widespread baryon overdensity in clusters of galaxies. 1995, MNRAS, 273, 72, arXiv:astro-ph/9502092

White, S. D. M., Efstathiou, G., & Frenk, C. S., The amplitude of mass fluctuations in the universe. 1993a, MNRAS, 262, 1023

White, S. D. M. & Frenk, C. S., Galaxy formation through hierarchical clustering. 1991, ApJ, 379, 52

White, S. D. M., Navarro, J. F., Evrard, A. E., & Frenk, C. S., The baryon content of galaxy clusters: a challenge to cosmological orthodoxy. 1993b, Nature, 366, 429

Zaldarriaga, M. & Seljak, U., Reconstructing projected matter density power spectrum from cosmic microwave background. 1999, Phys. Rev. D, 59, 123507, arXiv:astro-ph/9810257

Annexe A

UNPUBLISHED RESULTS

In this Appendix, I give details on works that I did, for which I have not found time to write a publication. Since there is some chance that I never find time to do it I prefer to include them in this Appendix. These works are related to my initial publication on matched filters (Melin et al., 2006), later improved for the Planck launch (Melin et al., 2012). I continued to improve the algorithms after launch, for the three Planck catalogues (Planck Collaboration VIII, 2011; Planck Collaboration XXIX, 2014; Planck Collaboration XXVI, 2015). In particular, I calculated the error on the size (Section A.1) and on the position (Sect. A.2) provided by the matched filters. I also computed the degeneracy contours in the size-flux plane which are provided with the PSZ1 and PSZ2 (Sect. A.3).

A.1 Error on cluster size

As in chapter 3, we define the observed maps as a vector $\mathbf{m}(\mathbf{x})$ of N components, N being the number of frequencies of a given experiment. The maps contain a cluster of amplitude y_{o} with a normalized profile $\mathbf{t}_{\mathbf{t}}(\mathbf{x})$. The other components (e.g., primary CMB, point sources, galactic dust) and the instrumental noise are labelled as $\mathbf{n}(\mathbf{x})$. The cluster profile $\mathbf{t}_{\mathbf{t}}(\mathbf{x})$ is characterized by its size θ_{t}.

$$\mathbf{m}(\mathbf{x}) = y_{\mathrm{o}}\mathbf{t}_{\mathbf{t}}(\mathbf{x}) + \mathbf{n}(\mathbf{x}) \tag{A.1}$$

Let us define the estimator of signal-to-noise $S_{\theta'_{\mathrm{t}}}$ for a given size θ'_{t} as

$$S_{\theta'_{\mathrm{t}}} = \frac{\hat{y}_{\mathrm{o}}}{\sigma_{\theta'_{\mathrm{t}}}} \tag{A.2}$$

with $\hat{y}_{\mathrm{o}}$ being the estimated Compton parameter for a filter size θ'_{t} and $\sigma_{\theta'_{\mathrm{t}}}$ its corresponding error, given in equation 3.2 and 3.4 of chapter 3 respectively.

We choose the following estimator for the cluster size $\hat{\theta}_{\mathrm{t}}$:

$$S_{\hat{\theta}_{\mathrm{t}}} = \max_{\theta'_{\mathrm{t}}}(S_{\theta'_{\mathrm{t}}}) \tag{A.3}$$

Our goal is to compute the error on $\hat{\theta}_{\mathrm{t}}$. For this purpose, we define

$$\Delta_{\theta'_{\mathrm{t}},\theta''_{\mathrm{t}}} = S_{\theta'_{\mathrm{t}}} - S_{\theta''_{\mathrm{t}}} \tag{A.4}$$

The $\Delta_{\theta'_{\mathrm{t}},\theta''_{\mathrm{t}}}$ estimators have a mean

$$< \Delta_{\theta'_{\mathrm{t}},\theta''_{\mathrm{t}}} >= y_{\mathrm{o}} \left[\sigma_{\theta'_{\mathrm{t}}} \int d^2k \; \mathbf{t_{t'}}^t(\mathbf{k}) \cdot \mathbf{P}^{-1}(\mathbf{k}) \cdot \mathbf{t_t}(\mathbf{k}) - \sigma_{\theta''_{\mathrm{t}}} \int d^2k \; \mathbf{t_{t''}}^t(\mathbf{k}) \cdot \mathbf{P}^{-1}(\mathbf{k}) \cdot \mathbf{t_t}(\mathbf{k})\right] \tag{A.5}$$

and are correlated

$$\begin{aligned} &< (\Delta_{\theta'_{\mathrm{t}},\theta''_{\mathrm{t}}} - < \Delta_{\theta'_{\mathrm{t}},\theta''_{\mathrm{t}}} >)(\Delta_{\theta'_{\mathrm{t}},\theta'''_{\mathrm{t}}} - < \Delta_{\theta'_{\mathrm{t}},\theta'''_{\mathrm{t}}} >) >= \\ &\int d^2k \;\; \left[\sigma_{\theta'_{\mathrm{t}}} \mathbf{t_{t'}}^t(\mathbf{k}) - \sigma_{\theta''_{\mathrm{t}}} \mathbf{t_{t''}}^t(\mathbf{k})\right] \cdot \mathbf{P}^{-1} \cdot \left[\sigma_{\theta'_{\mathrm{t}}} \mathbf{t_{t'}}(\mathbf{k}) - \sigma_{\theta'''_{\mathrm{t}}} \mathbf{t_{t'''}}(\mathbf{k})\right] \end{aligned} \tag{A.6}$$

Assuming that $\Delta_{\theta'_{\mathrm{t}},\theta''_{\mathrm{t}}}$ are Gaussian distributed, one can compute the probability

$$P(S_{\theta'_{\mathrm{t}}} > S_{\theta''_{\mathrm{t}}}) = P(\Delta_{\theta'_{\mathrm{t}},\theta''_{\mathrm{t}}} > 0) = \frac{1}{2}\left[1 + \mathrm{erf}\left(\frac{< \Delta_{\theta'_{\mathrm{t}},\theta''_{\mathrm{t}}} >}{\sqrt{2}\sigma_{\theta'_{\mathrm{t}},\theta''_{\mathrm{t}}}}\right)\right] \tag{A.7}$$

where $\sigma^2_{\theta'_{\mathrm{t}},\theta''_{\mathrm{t}}} =< (\Delta_{\theta'_{\mathrm{t}},\theta''_{\mathrm{t}}} - < \Delta_{\theta'_{\mathrm{t}},\theta''_{\mathrm{t}}} >)^2 >$ and $< \Delta_{\theta'_{\mathrm{t}},\theta''_{\mathrm{t}}} >$ is approximated by $\Delta_{\theta'_{\mathrm{t}},\theta''_{\mathrm{t}}}$ (because we know $\hat{y}_{\mathrm{o}}$ but not y_{o}).

We now want to compute

$$P(S_{\theta'_{\mathrm{t}}} = \max_{\theta''_{\mathrm{t}}}(S_{\theta''_{\mathrm{t}}})) = P(S_{\theta'_{\mathrm{t}}} > S_{\theta''_{\mathrm{t},0}} \,\&\, S_{\theta'_{\mathrm{t}}} > S_{\theta''_{\mathrm{t},1}} \,\&\, ...) \tag{A.8}$$

which correspond to $n-1$ correlated conditions, n being the number of filter sizes. Defining $\mathbf{N}_{\boldsymbol{\theta'_{\mathrm{t}}}}$ the $(n-1) \times (n-1)$ matrix with coefficients

$< (\Delta_{\theta'_{\rm t},\theta''_{\rm t}} - < \Delta_{\theta'_{\rm t},\theta''_{\rm t}} >)(\Delta_{\theta'_{\rm t},\theta'''_{\rm t}} - < \Delta_{\theta'_{\rm t},\theta'''_{\rm t}} >) >$, $\theta''_{\rm t}$ and $\theta'''_{\rm t}$ being different than $\theta'_{\rm t}$, we have

$$P(S_{\theta'_{\rm t}} = \max_{\theta''_{\rm t}}(S_{\theta''_{\rm t}})) =$$

$$\left(\frac{1}{\sqrt{2\pi}}\right)^{n-1} \left(\frac{1}{\det \mathbf{N}_{\boldsymbol{\theta}'_{\mathbf{t}}}}\right)^{\frac{1}{2}} \int_{\mathbf{X}>0} d^{n-1}X \, \mathrm{e}^{-\frac{1}{2}(\mathbf{X} - <\boldsymbol{\Delta}_{\boldsymbol{\theta}'_{\mathbf{t}},\boldsymbol{\theta}''_{\mathbf{t}}}>)^t \cdot \mathbf{N}_{\boldsymbol{\theta}'_{\mathbf{t}}}{}^{-1} \cdot (\mathbf{X} - <\boldsymbol{\Delta}_{\boldsymbol{\theta}'_{\mathbf{t}},\boldsymbol{\theta}''_{\mathbf{t}}}>)} \qquad \text{(A.9)}$$

with $< \boldsymbol{\Delta}_{\boldsymbol{\theta}'_{\mathbf{t}},\boldsymbol{\theta}''_{\mathbf{t}}} >$ being the $n-1$ column vector with $\theta'_{\rm t}$ fixed and $\theta''_{\rm t}$ varying across filter size but different from $\theta'_{\rm t}$. This integral with $n-1$ dimensions can be computed by Monte Carlo for each $\theta'_{\rm t}$.

Then, the mean value for $\hat{\theta}_{\rm t}$ is given by $< \hat{\theta}_{\rm t} >= \sum_{\theta'_{\rm t}} \theta'_{\rm t} \times P(S_{\theta'_{\rm t}} = \max_{\theta''_{\rm t}}(S_{\theta''_{\rm t}}))$ and the error

$$\varsigma^2_{\hat{\theta}_{\rm t}} = \sum_{\theta'_{\rm t}} (\theta'_{\rm t} - \hat{\theta}_{\rm t})^2 \times P(S_{\theta'_{\rm t}} = \max_{\theta''_{\rm t}}(S_{\theta''_{\rm t}})) \qquad \text{(A.10)}$$

A.2 Error on the position

Let's $\mathbf{p}$ be the pixel corresponding to the cluster center. We estimate the pixel $\hat{\mathbf{p}}$ of the cluster center with

$$S_{\hat{\theta}_{\rm t}}(\hat{\mathbf{p}}) = \max_{\mathbf{p'}}(S_{\hat{\theta}_{\rm t}}(\mathbf{p'})). \qquad \text{(A.11)}$$

We now want to compute the radius $r_{\hat{\mathbf{p}}}$ around $\hat{\mathbf{p}}$ in which the center has 95% probability to lie. We follow the same method as for the size. We need to compute, for each pixel $\mathbf{p'}$,

$$P[S_{\hat{\theta}_{\rm t}}(\mathbf{p'}) = \max_{\mathbf{p''}}(S_{\hat{\theta}_{\rm t}}(\mathbf{p''}))]. \qquad \text{(A.12)}$$

We thus define, as in the previous paragraph,

$$\Delta_{\mathbf{p'},\mathbf{p''}} = S_{\hat{\theta}_{\rm t}}(\mathbf{p'}) - S_{\hat{\theta}_{\rm t}}(\mathbf{p''}) \qquad \text{(A.13)}$$

and we can compute

$$< \Delta_{\mathbf{p'},\mathbf{p''}} >= y_{\rm o}\sigma_{\hat{\theta}_{\rm t}} \int d^2k \, \mathbf{t}_{\hat{\mathbf{t}}}{}^t(\mathbf{k}) \cdot \mathbf{P}^{-1}(\mathbf{k}) \cdot \mathbf{t}_{\hat{\mathbf{t}}}(\mathbf{k}) \left[e^{-i\mathbf{k}\cdot(\mathbf{p'}-\mathbf{p})} - e^{-i\mathbf{k}\cdot(\mathbf{p''}-\mathbf{p})}\right] \qquad \text{(A.14)}$$

where $\mathbf{t}_{\hat{\mathbf{t}}}{}^{t}(\mathbf{k})$ is the profile scaled to the size $\hat{\theta}_{\mathrm{t}}$, and

$$< (\Delta_{\mathbf{p}',\mathbf{p}''} - < \Delta_{\mathbf{p}',\mathbf{p}''} >)(\Delta_{\mathbf{p}',\mathbf{p}'''} - < \Delta_{\mathbf{p}',\mathbf{p}'''} >) >= \sigma^2_{\hat{\theta}_{\mathrm{t}}} \int d^2k \; \mathbf{t}_{\hat{\mathbf{t}}}{}^{t}(\mathbf{k}) \cdot \mathbf{P}^{-1}(\mathbf{k}) \cdot \mathbf{t}_{\hat{\mathbf{t}}}(\mathbf{k}) \left[e^{+i\mathbf{k}\cdot(\mathbf{p}'-\mathbf{p})} - e^{+i\mathbf{k}\cdot(\mathbf{p}''-\mathbf{p})}\right] \left[e^{-i\mathbf{k}\cdot(\mathbf{p}'-\mathbf{p})} - e^{-i\mathbf{k}\cdot(\mathbf{p}'''-\mathbf{p})}\right]. \tag{A.15}$$

Now, we compute, for each $\mathbf{p}'$, $P[S_{\hat{\theta}_{\mathrm{t}}}(\mathbf{p}') = \max_{\mathbf{p}''}(S_{\hat{\theta}_{\mathrm{t}}}(\mathbf{p}''))]$ through Monte Carlo integrations assuming that the $\Delta_{\mathbf{p}',\mathbf{p}''}$ are Gaussian distributed.

We obtain the 95% probability radius $r_{\hat{\mathbf{p}}}$ by

$$\sum\nolimits_{||\hat{\mathbf{p}}-\mathbf{p}'||<r_{\hat{\mathbf{p}}}} P[S_{\hat{\theta}_{\mathrm{t}}}(\mathbf{p}') = \max_{\mathbf{p}''}(S_{\hat{\theta}_{\mathrm{t}}}(\mathbf{p}''))] = 0.95\,. \tag{A.16}$$

In practice, for Planck, we only compute $P[S_{\hat{\theta}_{\mathrm{t}}}(\mathbf{p}') = \max_{\mathbf{p}''}(S_{\hat{\theta}_{\mathrm{t}}}(\mathbf{p}''))]$ for a set of $(7 \times 7 - 1)$ $\mathbf{p}'$ pixels around $\hat{\mathbf{p}}$ because, in average, the probability goes to zero at a distance of 2 to 3 pixels from $\hat{\mathbf{p}}$ and also because the size of the covariance matrix $< (\Delta_{\mathbf{p}',\mathbf{p}''} - < \Delta_{\mathbf{p}',\mathbf{p}''} >)(\Delta_{\mathbf{p}',\mathbf{p}'''} - < \Delta_{\mathbf{p}',\mathbf{p}'''} >) >$ increases quickly with the number of pixels.

A.3 Degeneracy contours

The Planck resolution ($\sim 5\,$arcmin) is slightly bigger than the typical size of a galaxy cluster (1 arcmin). Thus, Planck cannot determine accurately the size for the bulk of clusters. Unfortunately, the extracted flux is highly degenerated with the estimated size. The Planck collaboration thus decided to provide degeneracy contours in the flux-size plane (Y, θ_{t}) for each cluster.

For the MMF, I have used the results from Chapter 3 and Section A.1 to build these contours. Under the assumption of the noise being Gaussian, the probability of a cluster to have the flux Y for a given filter size θ_{t} is

$$P(Y|\theta_{\mathrm{t}}) \propto \frac{1}{\sigma_{\theta_{\mathrm{t}}}} e^{-\frac{(Y-\hat{Y})^2}{2\sigma^2_{\theta_{\mathrm{t}}}}} \tag{A.17}$$

where $\sigma_{\theta_{\rm t}}$ and $\hat{Y}$ are given by equation 3.4 and 3.5 respectively.

The probability that the size of the cluster is $\theta_{\rm t}$ is given by

$$P(\theta_{\rm t}) \propto e^{-\frac{(\theta_{\rm t}-\hat{\theta}_{\rm t})^2}{2\varsigma^2_{\hat{\theta}_{\rm t}}}} \tag{A.18}$$

where $\hat{\theta}_{\rm t}$ and ς are given by equation A.3 and A.10 respectively.

The two previous probabilities can be multiplied to build the joint log-probability

$$\ln P(Y,\theta_{\rm t}) = {\rm cste} - \frac{(Y-\hat{Y})^2}{2\sigma^2_{\theta_{\rm t}}} - \ln(\sigma_{\theta_{\rm t}}) - \frac{(\theta_{\rm t}-\hat{\theta}_{\rm t})^2}{2\varsigma^2_{\hat{\theta}_{\rm t}}} \tag{A.19}$$

The degeneracy contours are then simply obtained by normalizing the integral of $P(Y,\theta_{\rm t}) = e^{\ln P(Y,\theta_{\rm t})}$ to 1.

Annexe B

ORIGINALITÉ DES RECHERCHES PRÉSENTÉES

Sur la période 2005-2015, j'ai concentré mes recherches selon deux axes :

- les contraintes cosmologiques avec les amas de galaxies Sunyaev-Zel'dovich (paragraphe B.1),
- l'étude de la physique des amas (paragraphe B.3).

Ces deux axes sont intimement liés à la mesure de la masse des amas, quantité nécessaire à l'obtention de contraintes cosmologiques précises. J'ai attaqué ce problème via l'étude de l'effet de lentille gravitationnelle des amas sur le fond diffus cosmologique (paragraphe B.2). Enfin, les connaissances acquises au cours de ces études m'ont permis de travailler à la préparation de missions futures (paragraphe B.4).

B.1 Contraintes cosmologiques avec les amas Sunyaev-Zel'dovich

L'obtention de contraintes cosmologiques avec les amas SZ est un travail de longue haleine. Il nécessite d'avoir à disposition, outre un jeu de données (Planck), des simulations, un code d'extraction d'amas et une vraisemblance cosmologique. J'ai travaillé directement sur la conception et le codage des deux premiers aspects (simulations et code d'extraction) et participé activement à la conception des différentes versions du code de vraisemblance Planck.

Simulations SZ

J'ai développé la majorité du code semi-analytique DMB (Delabrouille-Melin-Bartlett) du Planck Sky Model de façon à ce qu'il soit rapide et qu'il reproduise le plus fidèlement possible notre connaissance des amas de galaxies, en particulier celle acquise en rayons X avec XMM. L'outil s'est révélé essentiel pour comparer les performances des différents algorithmes de détection de Planck et caractériser la fonction de sélection des catalogues.

Extraction d'amas

J'ai développé le MMF (Matched Multi Filter) pour l'extraction des amas de galaxies dans les données Planck. L'outil est robuste et performant : il a été utilisé pour les trois catalogues d'amas publiés. Le MMF a aussi été adopté par les collaborations SPT et ACT pour la construction de leurs catalogues.

Caractérisation de la fonction de sélection du catalogue d'amas de Planck

J'ai proposé une modélisation simple de la fonction de sélection du catalogue d'amas de Planck à partir des cartes de bruit du MMF. Cette modélisation est proche des estimations Monte Carlo plus complexes et a servi à l'obtention des contraintes cosmologiques avec Planck.

Contraintes cosmologiques

Au début de l'analyse, j'ai proposé aux différentes équipes Planck un challenge avec pour objectif l'obtention de contraintes cosmologiques à partir d'un catalogue simulé. Ce challenge a servi de base au développement des outils d'analyse du premier papier Planck sur les contraintes cosmologiques avec les amas. J'ai ensuite encadré le travail d'analyse présenté dans le second papier.

B.2 Effet de lentille gravitationnelle des amas sur le CMB

L'analyse cosmologique des amas de galaxies est limitée par notre connaissance de la masse des amas. Les meilleures précisions sur celle-ci sont obtenues via des télescopes au sol, en observant l'effet de lentille gravitationnelle faible. Les erreurs statistiques sont de l'ordre de 10% sur la masse pour des échantillons de quelques dizaines d'amas mais les erreurs systématiques entre les différentes méthodes (CCCP et WtG par exemple) restent du même ordre de grandeur.

Pour attaquer ce problème crucial de mesure de masse des amas, j'ai développé une méthode d'extraction statistique du signal de lentille des amas sur le fond diffus cosmologique. Cet outil combine : une reconstruction optimale de la carte du fond diffus, un extracteur quadratique du potentiel de lentille et un filtre adapté. Il a permis de détecter l'effet pour la première fois sur l'échantillon cosmologique de Planck avec un signal-sur-bruit de cinq.

B.3 Physique des amas

L'étude de la physique des amas est un domaine de recherche très vaste. Je l'ai essentiellement abordé sous l'aspect statistique, en moyennant les propriétés de nombreux objets de catalogues connus à d'autres longueurs d'onde.

Lois d'échelles SZ-X et SZ-optique

Le MMF est un filtre non biaisé, ce qui signifie qu'il retourne en moyenne la valeur exacte (sans biais !) du flux d'un amas sur le ciel. J'ai eu l'idée d'utiliser cette propriété du MMF pour moyenner le signal SZ des amas X selon leur luminosité, dans les données WMAP. Il a ainsi été possible d'obtenir les premières lois d'échelles statistiques SZ-X. La méthode a ensuite été appliquée avec succès sur les catalogues d'amas X et optique, ainsi que sur des catalogues de galaxies dans les données Planck.

Les effets SZ relativiste, cinétique et polarisé

Avec mes étudiants, je me suis attaqué à la détection des effets SZ relativiste, cinétique et polarisé, en développant des MMF spécifiques. Malheureusement, seule une détection statistique de l'effet SZ cinétique a été possible mais l'interprétation du signal obtenu reste difficile. Les effets SZ relativiste et polarisé n'ont toujours pas été mis en évidence.

Amas particuliers

Les amas détectés par Planck ont été suivis à d'autres longueurs d'onde (optique, X et SZ haute résolution au sol). Il est possible d'ajouter les informations de ces données (comme la position ou la taille angulaire par exemple) dans le MMF pour ré-extraire un flux Planck plus précis. Ainsi, j'ai construit un modèle spécifique d'amas à trois composantes, basé sur les observations XMM, pour extraire le flux SZ d'un super-amas découvert par Planck.

B.4 Missions futures

La maîtrise de l'outil de simulation SZ du Planck Sky Model et de l'outil d'extraction MMF m'a permis d'établir des prédictions sur les performances des futures missions spatiales proposées quant à la science amas.

Annexe C

ACTIVITÉS D'ENCADREMENT

Stage de Licence

Encadrement du stage de L3 d'Alexandre Boucaud, mai - juillet 2008 : *Apports correctifs au profil des amas de galaxies du Planck Sky Model*

Stage ingénieur

Encadrement du stage de troisième année de Polytechnique de Corentin Lohat, mars - juillet 2015 : *A la recherche de l'effet Sunyaev-Zel'dovich polarisé*

Thèses de doctorat

Encadrement de la thèse de Sarah Puisieux, 2010 - 2013 : *Etude des effets Sunyaev-Zel'dovitch cinétique et relativiste dans les données Planck*

Participation à l'encadrement de thèse de Matthieu Roman, 2011 - 2014 : *Amas de galaxies détectés par Planck avec l'effet Sunyaev-Zel'dovich thermique : contraintes cosmologiques et spectre angulaire*

Encadrement de la thèse de Loïc Verdier, 2013 - (en cours) : *Détection simultanée d'amas de galaxies dans les données des satellites Planck et ROSAT - Recherche de sources dans des jeux de données inhomogènes*

Post-doctorants

Travail en étroite collaboration avec Rocco Piffaretti sur le papier Planck Collaboration X (2011) en 2010 et 2011

Travail avec Antoine Chamballu sur la mise en place du formalisme pour le second papier de contraintes cosmologiques avec les amas Planck (Planck Collaboration XXIV, 2015) en 2013 et 2014

Travail en étroite collaboration avec Paula Tarrio-Alonso depuis 2014 sur l'extraction jointe X-SZ d'amas de galaxies

Responsabilités au sein de Planck

Coresponsable du projet *Production and Exploitation of the SZ Cluster catalogue* avec Anthony Lasenby (Cambridge) avant 2013

Responsable du groupe de travail WG5.1 *Detection of new clusters and selection function of a Planck cluster sample* après 2013

Coresponsable de trois *early papers* (Planck Collaboration VIII, 2011; Planck Collaboration X, 2011; Planck Collaboration XII, 2011), du papier résultats 2013 Planck Collaboration XX (2014) avec Marian Douspis (IAS Orsay) et Richard Battye (Université de Manchester), des papiers résultats 2015 Planck Collaboration XXVI (2015) avec David Sutton (Cambridge) et Planck Collaboration XXIV (2015) avec James Bartlett (APC Paris, JPL Passadena)

Annexe D

CURICULUM VITAE

Jean-Baptiste MELIN

Email : jean-baptiste.melin@cea.fr
Tél. laboratoire : 01 69 08 73 80
Tél. domicile : 01 69 30 75 77

37 ans, marié, 3 enfants
16 villa des Fleurs
91440 Bures-sur-Yvette

Etudes et formation

2001 – 2004 : **Thèse en Cosmologie** au laboratoire de Physique Corpusculaire et Cosmologie du Collège de France
2000 – 2001 : **DEA d'Astrophysique** à l'Université Paul Sabatier à Toulouse
1998 – 2001 : **Supaéro** (Majeure Physique Espace et Télécommunications, Filière Espace)

Expérience professionnelle

2006 – 2015 : **Ingénieur-chercheur en Cosmologie au Commissariat à l'énergie atomique et aux énergies alternatives (CEA)**
Préparation puis exploitation des données de la mission Planck
Responsable du groupe de travail WG5.1 « détection d'amas de galaxies et fonction de sélection du catalogue »
Co-responsable de 6 papiers de collaboration Planck entre 2009 et 2015
2005 : **Postdoc en Cosmologie à l'Université de Californie – Davis**
Préparation de la mission Planck
2007
2004 – 2005 : **Enseignant vacataire en physique à l'Université Paris VII**
Physique L3

Domaines de compétence et intérêts

Langues : **Anglais**, lu, écrit, parlé
Notions d'**espagnol** et d'**allemand**
Vie du service : Membre du **conseil d'unité** du service
Organisation des **séminaires du service** de 2006 à 2010

Annexe E

ARTICLES ET TRAVAUX SIGNIFICATIFS

Dans cette annexe, j'ai inséré les articles sur lesquels je me suis très fortement impliqué. Ils sont organisés par thématique : détection d'amas (partie E.1), fonction de sélection et contraintes cosmologiques avec les amas (partie E.2), mesure de masse par effet de lentille sur le CMB (partie E.3), lois d'échelles (partie E.4). Pour chaque thématique, je renvoie au chapitre correspondant dans ce document.

E.1 Détection d'amas SZ

Les cinq articles suivants sont inclus dans cette partie et sont décrits dans le chapitre 3.

- Melin, J.-B., Bartlett, J. G., & Delabrouille, J., Catalog extraction in SZ cluster surveys: a matched filter approach. 2006, A&A, 459, 341, arXiv:astro-ph/0602424 *[110 citations]*

- Melin, J.-B., Aghanim, N., Bartelmann, M., et al., A comparison of algorithms for the construction of SZ cluster catalogues. 2012, A&A, 548, A51, arXiv:1210.1416 *[11 citations]*

- Planck Collaboration VIII, Planck early results. VIII. The all-sky early Sunyaev-Zeldovich cluster sample. 2011, A&A, 536, A8, arXiv:1101.2024 *[227 citations]*

- Planck Collaboration XXIX, Planck 2013 results. XXIX. The Planck catalogue of Sunyaev-Zeldovich sources. 2014, A&A, 571, A29, arXiv:1303.5089 *[152 citations]*

- Planck Collaboration XXVII, Planck 2015 results. XXVII. The Second Planck Catalogue of Sunyaev-Zeldovich Sources. 2015, A&A, submitted, arXiv:1502.01

A&A 459, 341–352 (2006)
DOI: 10.1051/0004-6361:20065034
© ESO 2006

Astronomy
&
Astrophysics

Catalog extraction in SZ cluster surveys: a matched filter approach

J.-B. Melin[1,2,⋆], J. G. Bartlett[1], and J. Delabrouille[1]

[1] APC, 11 pl. Marcelin Berthelot, 75231 Paris Cedex 05, France
(UMR 7164 – CNRS, Université Paris 7, CEA, Observatoire de Paris)
e-mail: `jean-baptiste.melin@cea.fr, [bartlett;delabrouille]@apc.univ-paris7.fr`
[2] Department of Physics, University of California Davis, One Shields Avenue, Davis, CA, 95616, USA

Received 16 February 2006 / Accepted 30 June 2006

ABSTRACT

We present a method based on matched multifrequency filters for extracting cluster catalogs from Sunyaev-Zel'dovich (SZ) surveys. We evaluate its performance in terms of completeness, contamination rate and photometric recovery for three representative types of SZ survey: a high resolution single frequency radio survey (AMI), a high resolution ground-based multiband survey (SPT), and the Planck all-sky survey. These surveys are not purely flux limited, and they loose completeness significantly before their point-source detection thresholds. Contamination remains relatively low at <5% (less than 30%) for a detection threshold set at $S/N = 5$ ($S/N = 3$). We identify photometric recovery as an important source of catalog uncertainty: dispersion in recovered flux from multiband surveys is larger than the intrinsic scatter in the $Y - M$ relation predicted from hydrodynamical simulations, while photometry in the single frequency survey is seriously compromised by confusion with primary cosmic microwave background anisotropy. The latter effect implies that follow-up observations in other wavebands (e.g., 90 GHz, X-ray) of single frequency surveys will be required. Cluster morphology can cause a bias in the recovered $Y - M$ relation, but has little effect on the scatter; the bias would be removed during calibration of the relation. Point source confusion only slightly decreases multiband survey completeness; single frequency survey completeness could be significantly reduced by radio point source confusion, but this remains highly uncertain because we do not know the radio counts at the relevant flux levels.

Key words. large-scale structure of Universe – galaxies: clusters: general – methods: data analysis

1. Introduction

Galaxy cluster catalogs play an important role in cosmology by furnishing unique information on the matter distribution and its evolution. Cluster catalogs, for example, efficiently trace large-scale features, such as the recently detected baryon oscillations (Eisenstein et al. 2005; Cole et al. 2005; Angulo et al. 2005; Huetsi 2006), and provide a sensitive gauge of structure growth back to high redshifts (Oukbir & Blanchard 1992; Rosati et al. 2002; Voit 2004, and references therein). This motivates a number of ambitious projects proposing to use large, deep catalogs to constrain both galaxy evolution models and the cosmological parameters, most notably the dark energy abundance and equation-of-state (Haiman et al. 2000; Weller & Battye 2003; Wang et al. 2004). Among the most promising are surveys based on the Sunyaev-Zel'dovich (SZ) effect (Sunyaev & Zeldovich 1970; Sunyaev & Zeldovich 1972; and see Birkinshaw 1999; Carlstrom et al. 2002 for reviews), because it does not suffer from surface brightness dimming and because we expect the observed SZ signal to tightly correlate to cluster mass (Bartlett 2001; Motl et al. 2005). Many authors have investigated the scientific potential of SZ surveys to constrain cosmology (e.g., Barbosa et al. 1996; Colafrancesco et al. 1997; Holder et al. 2000; Kneissl et al. 2001; Benson et al. 2002), emphasizing the advantages intrinsic to observing the SZ signal.

Cosmological studies demand statistically pure catalogs with well understood selection criteria. As just said, SZ surveys are intrinsically good in this light; however, many other factors – related, for example, to instrumental properties, observing conditions, astrophysical foregrounds and data reduction algorithms – influence the selection criteria. This has prompted some authors to begin more careful scrutiny of SZ survey selection functions in anticipation of future observations (Bartlett 2001; Schulz & White 2003; White 2003; Vale & White 2006; Melin et al. 2005; Juin et al. 2005).

In Melin et al. (2005), we presented a general formalism for the SZ selection function together with some preliminary applications using a matched-filter cluster detection method. In this paper we give a thorough presentation of our cluster detection method and evaluate its performance in terms of catalog completeness, contamination and photometric recovery. We focus on three types of SZ survey: single frequency radio surveys like the Arcminute MicroKelvin Imager (AMI interferometer) survey[1], multi-band ground-based bolometric surveys such as the South Pole Telescope (SPT) survey[2], and the space-based Planck survey[3]. In each case, we quantify the selection function using the formalism of Melin et al. (2005).

We draw particular attention to the oft-neglected issue of photometry. Even if the SZ flux–mass relation is intrinsically tight, what matters in practice is the relation between the *observed* SZ flux and the mass. Photometric errors introduce both

---

⋆ *New address*: CEA Saclay, DAPNIA/SPP, 91191 Gif-sur-Yvette, France.

[1] `http://www.mrao.cam.ac.uk/telescopes/ami/`

[2] `http://astro.uchicago.edu/spt/`

[3] `http://astro.estec.esa.nl/Planck/`

bias and additional scatter in the observed relation. Calibration of the $Y-M$ relation will in principal remove the bias; calibration precision, however, depends crucially on the scatter in the observed relation. Good photometry is therefore very important. As we will see, observational uncertainty dominates the predicted intrinsic scatter in this relation in all cases studied.

We proceed as follows. In Sect. 2, we discuss cluster detection techniques and present the matched filter formalism. We describe our detection algorithm in Sect. 3. Using Monte Carlo simulations of the three types of survey, we discuss catalog completeness, contamination and photometry. This is done in Sect. 4 under the ideal situation where the filter perfectly matches the simulated clusters and in the absence of point sources. In Sect. 5 we examine effects caused by cluster morphology, using N-body simulations, and then the effect of point sources. We close with a final discussion and conclusions in Sect. 6.

2. Detecting clusters

The detection and photometry of extended sources presents a complexity well appreciated in Astronomy. Many powerful algorithms, such as *SExtractor* (Bertin & Arnouts 1996), have been developed to extract extended sources superimposed on an unwanted background. They typically estimate the local background level and group pixels brighter than this level into individual objects. Searching for clusters at millimeter wavelengths poses a particular challenge to this approach, because the clusters are embedded in the highly variable background of the primary CMB anisotropies and Galactic emission. Realizing the importance of this issue, several authors have proposed specialized techniques for SZ cluster detection. Before detailing our own method, we first briefly summarize some of this work in order to motivate our own approach and place it in context.

2.1. Existing algorithms

Diego et al. (2002) developed a method designed for the Planck mission that is based on application of *SExtractor* to SZ signal maps constructed by combining different frequency channels. It makes no assumption about the frequency dependance of the different astrophysical signals, nor the cluster SZ emission profile. The method, however, requires many low-noise maps over a broad range of frequencies in order to construct the SZ map to be processed by *SExtractor*. Although they will benefit from higher resolution, planned ground-based surveys will have fewer frequencies and higher noise levels, making application of this method difficult.

In another approach, Herranz et al. (2002a,b; see also López-Caniego et al. 2005 for point-source applications) developed an ingenious filter (*Scale Adaptive Filter*) that simultaneously extracts cluster size and flux. Defined as the optimal filter for a map containing a single cluster, it does not account for source blending. Cluster-cluster blending could be an important source of confusion in future ground-based experiments, with as a consequence poorly estimated source size and flux.

Hobson & McLachlan (2003) recently proposed a powerful Bayesian detection method using a Monte Carlo Markov Chain. The method simultaneously solves for the position, size, flux and morphology of clusters in a given map. Its complexity and runtime, however, rapidly increase with the number of sources.

More recently, Schäfer et al. (2006) generalized scale adaptive and matched filters to the sphere for the Planck all-sky SZ survey. Pierpaoli et al. (2005) propose a method based on wavelet filtering, studying clusters with complex shapes. Vale & White (2006) examine cluster detection using different filters (matched, wavelets, mexican hat), comparing completeness and contamination levels.

Finally, Pires et al. (2006) introduced an independent component analysis on simulated multi-band data to separate the SZ signal, followed by non-linear wavelet filtering and application of SExtractor.

Our aim is here is two-fold: to present and extensively evaluate our own SZ cluster catalog extraction method, and to use it in a comprehensive study of SZ survey selection effects. The two are in fact inseparable. First of all, selection effects are specific to a particular catalog extraction method. Secondly, we require a robust, rapid algorithm that we can run over a large number of simulated data sets in order to accurately quantify the selection effets. This important consideration conditions the kind of extraction algorithm that we can use. With this in mind, we have developed a fast catalog construction algorithm based on matched filters for both single and multiple frequency surveys. It is based on the approach first proposed by Herranz et al., but accounts for source blending.

After describing the method, we apply the formalism given in Melin et al. (2005) to quantify the selection function and contamination level in up-coming SZ surveys. We take as representative survey configurations AMI, SPT and Planck, and Monte Carlo simulate the entire catalog extraction process from a large ensemble of realizations for each configuration. By comparing to the simulated input catalogs, we evaluate the extracted catalogs in terms of their completeness, contamination and photometric accuracy/precision. We will place particular emphasis on the importance of the latter, something which has received little attention in most studies of this kind.

2.2. Matched filters

The SZ effect is caused by the hot gas ($T\sim 1{-}10$ keV) contained in galaxy clusters known as the intracluster medium (ICM); electrons in this gas up-scatter CMB photons and create a unique spectral distortion that is negative at radio wavelengths and positive in the submillimeter, with a zero-crossing near 220 GHz. The form of this distortion is universal (in the non-relativistic limit applicable to most clusters), while the amplitude is given by the Compton y parameter, an integral of the gas pressure along the line-of-sight. In a SZ survey, clusters will appear as sources extended over arcminute scales (apart from the very nearby objects, which are already known) with brightness profile

$$\Delta i_\nu(\boldsymbol{x}) = y(\boldsymbol{x})\, j_\nu \tag{1}$$

relative to the mean CMB brightness. Here $y(\boldsymbol{x})$ is the Compton y parameter at position $\boldsymbol{x}$ (a 2D vector on the sky) and j_ν is the SZ spectral function evaluated at the observation frequency ν.

Matched filters for SZ observations were first proposed by Haehnelt & Tegmark (1996) as a tool to estimate cluster peculiar velocities from the kinetic effect, and Herranz et al. (2002a,b) later showed how to use them to detect clusters via the thermal SZ effect. They are designed to maximally enhance the signal-to-noise for a SZ cluster source by optimally (in the least square sense) filtering the data, which in our case is a sky map or set of maps at different frequencies. They do so by incorporating prior knowledge of the cluster signal, such as its spatial and spectral characteristics. The unique and universal frequency spectrum of the thermal SZ effect (in the non-relativistic regime) is hence well suited for a matched-filter approach.

Less clear is the choice of the spatial profile $T_{\theta_c}(\boldsymbol{x})$ to adopt for cluster SZ emission. One aims to choose a spatial template that represents as well as possible the average SZ emission profile. In other words, we want $T_{\theta_c}(\boldsymbol{x}) = \langle y(\boldsymbol{x})/y_o \rangle_C$, where the average is over many clusters of size θ_c. In the following, we choose to describe clusters with a projected spherical β-profile:

$$y(\boldsymbol{x}) = y_o(1 + |\boldsymbol{x}|^2/\theta_c^2)^{-(3\beta-1)/2} \tag{2}$$

with $\beta = 2/3$ (with one exception, shown for comparison in Fig. 2). The spatial template is therefore described by a single parameter, the core radius θ_c; in our calculations, we truncate the profile at $10\theta_c$. This is a reasonable choice, given X-ray observations (Arnaud 2005) of the intracluster medium and the resolution of planned SZ surveys.

In reality, of course, we know neither this average profile precisely nor the dispersion of individual clusters around it beforehand. This is an important point, because our choice for the template will affect both the detection efficiency and photometric accuracy. Detection efficiency will be reduced if the template does not well represent the average profile and, as will become clear below, the photometry will be biased. In general, *the survey selection function unavoidably suffers from uncertainty induced by unknown source astrophysics* (in addition to other sources of uncertainty).

In the following, we first study (Sect. 4) the ideal case where the filters perfectly match the cluster profiles, i.e., we use the β-model for both our simulations and as the detection template. In a later section (5), we examine the effects caused by non-trivial cluster morphology, as well as by point source confusion.

Consider a cluster with core radius θ_c and central y-value y_o positioned at an arbitrary point $\boldsymbol{x}_o$ on the sky. For generality, suppose that the region is covered by several maps $M_i(\boldsymbol{x})$ at N different frequencies ν_i ($i = 1, ..., N$). We arrange the survey maps into a column vector $\boldsymbol{M}(\boldsymbol{x})$ whose ith component is the map at frequency ν_i; this vector reduces to a scalar map in the case of a single frequency survey. Our maps contain the cluster SZ signal plus noise:

$$\boldsymbol{M}(\boldsymbol{x}) = y_o \boldsymbol{j_\nu} T_{\theta_c}(\boldsymbol{x} - \boldsymbol{x}_o) + \boldsymbol{N}(\boldsymbol{x}) \tag{3}$$

where $\boldsymbol{N}$ is the noise vector (whose components are noise maps at the different observation frequencies) and $\boldsymbol{j_\nu}$ is a vector with components given by the SZ spectral function j_ν evaluated at each frequency. Noise in this context refers to both instrumental noise as well as all signals other than the cluster thermal SZ effect; it thus also comprises astrophysical foregrounds, for example, the primary CMB anisotropy, diffuse Galactic emission and extragalactic point sources.

We now build a filter $\boldsymbol{\Psi}_{\boldsymbol{\theta_c}}(\boldsymbol{x})$ (in general, a column vector in frequency space) that returns an estimate, $\hat{y_o}$, of y_o when centered on the cluster:

$$\hat{y_o} = \int \mathrm{d}^2x\, \boldsymbol{\Psi}_{\boldsymbol{\theta_c}}{}^t(\boldsymbol{x} - \boldsymbol{x}_o) \cdot \boldsymbol{M}(\boldsymbol{x}) \tag{4}$$

where superscript t indicates a transpose (with complex conjugation when necessary). This is just a linear combination of the maps, each convolved with its frequency-specific filter $(\Psi_{\theta_c})_i$. We require an unbiased estimate of the central y value, so that $\langle \hat{y_o} \rangle = y_o$, where the average here is over both total noise and cluster (of core radius θ_c) ensembles. Building the filter with the known SZ spectral form and adopted spatial template optimizes the signal-to-noise of the estimate; in other words, the filter is *matched* to the prior information. The filter is now uniquely specified by demanding a minimum variance estimate. The result expressed in Fourier space (the flat sky approximation is reasonable on cluster angular scales) is (Haehnelt & Tegmark 1996; Herranz et al. 2002a; Melin et al. 2005):

$$\boldsymbol{\Psi}_{\boldsymbol{\theta_c}}(\boldsymbol{k}) = \sigma_{\theta_c}^2 \boldsymbol{P}^{-1}(\boldsymbol{k}) \cdot \boldsymbol{F}_{\boldsymbol{\theta_c}}(\boldsymbol{k}) \tag{5}$$

where

$$\boldsymbol{F}_{\boldsymbol{\theta_c}}(\boldsymbol{k}) \equiv \boldsymbol{j_\nu} T_{\theta_c}(\boldsymbol{k}) \tag{6}$$

$$\sigma_{\theta_c} \equiv \left[\int \mathrm{d}^2k\, \boldsymbol{F}_{\boldsymbol{\theta_c}}{}^t(\boldsymbol{k}) \cdot \boldsymbol{P}^{-1} \cdot \boldsymbol{F}_{\boldsymbol{\theta_c}}(\boldsymbol{k}) \right]^{-1/2} \tag{7}$$

with $\boldsymbol{P}(\boldsymbol{k})$ being the noise power spectrum, a matrix in frequency space with components P_{ij} defined by $\langle N_i(\boldsymbol{k}) N_j^*(\boldsymbol{k}') \rangle_N = P_{ij}(\boldsymbol{k})\delta(\boldsymbol{k} - \boldsymbol{k}')$. The quantity σ_{θ_c} gives the total noise variance through the filter. When we speak of the signal-to-noise of a detection, we refer to $\hat{y_o}/\sigma_{\theta_c}$.

We write the noise power spectrum as a sum $P_{ij} = P_i^{\text{noise}}\delta_{ij} + B_i(\boldsymbol{k})B_j^*(\boldsymbol{k})P_{ij}^{\text{sky}}$, where P_i^{noise} represents the instrumental noise power in band i, $B(\boldsymbol{k})$ the observational beam and P_{ij}^{sky} gives the foreground power (non-SZ signal) between channels i and j. As explicitly written, we assume uncorrelated instrumental noise between observation frequencies. Note that we treat the astrophysical foregrounds as isotropic, stationary random fields with zero mean. The zero mode is, in any case, removed from each of the maps, and the model certainly applies to the primary CMB anisotropy. It should also be a reasonable model for fluctuations of other foregrounds about their mean, at least over cluster scales[4].

Two examples of the matched filter for $\theta_c = 1$ arcmin are shown in Fig. 1, one for an AMI-like single frequency survey with a 1.5 arcmin beam (left-hand panel) and the other for a SPT-like 3-band filter (right-hand panel); see Table 1 for the experimental characteristics. The filters are circularly symmetric, with the figures giving their radial profiles, because we have chosen a spherical cluster model. We clearly see the spatial weighting used by the single frequency filter to optimally extract the cluster from the noise and CMB backgrounds. The multiple frequency filter $\boldsymbol{\Psi}_{\boldsymbol{\theta_c}}$ is a 3-element column vector containing filters for each individual frequency. In this case, the filter employs both spectral and spatial weighting to optimally extract the cluster signal.

Figure 2 shows the filter noise as a function of template core radius θ_c. We plot the filter noise expressed in terms of an equivalent noise $\sigma_Y \equiv \sigma_{\theta_c} \int T_{\theta_c}(\boldsymbol{x})\, \mathrm{d}\boldsymbol{x}$ on the integrated SZ flux Y. The dashed-triple-dotted red curve with $\beta = 0.6$ is shown for comparison to gauge the impact of changing this parameter, otherwise fixed at $\beta = 2/3$ throughout this work. Melin et al. (2005) use the information in this figure to construct survey completeness functions. At fixed signal-to-noise q, the completeness of a survey rapidly increases to unity in the region above the curve $q\sigma_Y$. The figure shows that high angular resolution ground-based surveys (e.g., AMI, SPT) are not purely flux limited, because their noise level rises significantly with core radius. The lower resolution of the Planck survey, on the other hand, results in more nearly flux limited sample.

---

[4] We make no assumption about the Gaussianity of the fields; the estimator remains unbiased even if they are not Gaussian, although optimality must be redefined in this case.

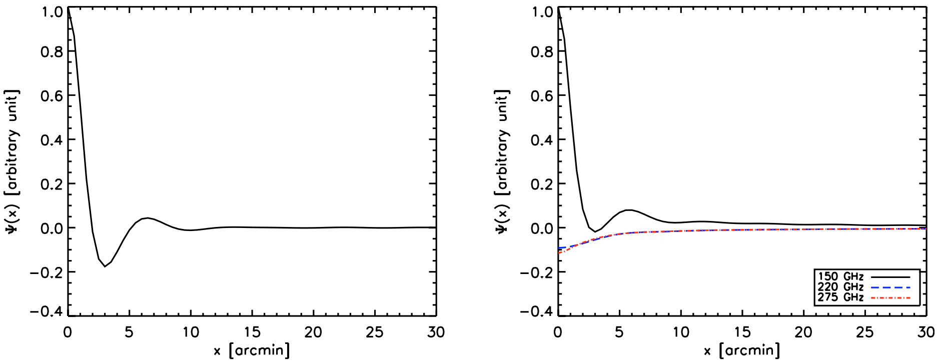

Fig. 1. Two examples of the matched filter for $\theta_c = 1$ arcmin. The curves give the radial profiles of the filters, which are symmetric because we have chosen a symmetric cluster template. *Left*: filter for a single frequency survey with a $\theta_{FWHM} = 1.5$ arcmin beam and 8 μK instrumental noise/beam (AMI-like, see Table 1). The undulating form of the filter maximizes the cluster signal while reducing contamination from primary CMB anisotropy. *Right*: the three components of the 3-band filter for a SPT-like experiment (Table 1). The filter is arbitrarily normalized to unity at 150 GHz. The filter uses both spatial and frequency weighting to optimally extract the cluster signal from the CMB and instrument noise. Although in this figure the filters continue to large radii, in practice we truncate them at $10\theta_c$.

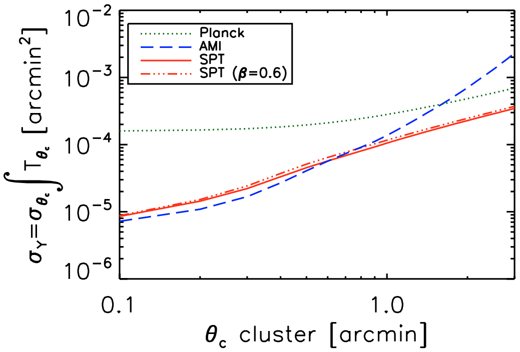

Fig. 2. Filter noise expressed in terms of integrated SZ flux $Y - \sigma_{\rm Y} = \sigma_{\theta_c} \int T_{\theta_c}(\boldsymbol{x})\,{\rm d}\boldsymbol{x}$ – as a function of template core radius $\theta_{\rm c}$ for the three experiments listed in Table 1. A cluster with $Y = \sigma_{\rm Y}$ would be detected at a signal-to-noise ratio $q = 1$. At a fixed detection threshold q (e.g., 3 or 5), the completeness of a survey rapidly increases from zero to unity in the region above its corresponding curve $q\sigma_{\rm Y}(\theta_{\rm c})$ (Melin et al. 2005). All the curves adopt our fiducial value of $\beta = 2/3$, except the dashed-triple-dotted red curve, shown for comparison, which corresponds to the SPT case with $\beta = 0.6$; this curve is systematically higher by (2.5 to 13)%, depending on θ_c.

Table 1. Characteristics of the three types of experiments considered. We run our extraction method on 100 sky patches of 3×3 square degrees (for AMI and SPT) and 12 × 12 square degrees (for Planck).

Type	Frequencies [GHz]	Res. *FWHM* [arcmin]	Inst. noise [μK/beam]	Area [deg^2]
AMI	15	1.5	8	10
SPT	150	1	10	
	220	0.7	60	4000
	275	0.6	100	
Planck	143	7.1	6	
	217	5	13	41253
	353	5	40	

3. Catalog extraction

Catalog construction proceeds in three steps, the last two of which are repeated[5]:

1. Convolution of the frequency map(s) with matched filters corresponding to different cluster sizes;
2. Identification of candidate clusters as objects with signal-to-noise $\hat{y_{\rm o}}/\sigma_{\theta_{\rm c}} > q$, where q is our fixed detection threshold, followed by photometry of the brightest remaining cluster candidate, which is then added to the final cluster catalog;
3. Removal of this object from the set of filtered maps using the photometric parameters (e.g., $y_{\rm o}$ and $\theta_{\rm c}$) from the previous step.

We loop over the last two steps until there are no remaining candidates above the detection threshold. The following sections detail each step.

3.1. Map filtering

In the first step, we convolve the observed map(s) with matched filters covering the expected range of core radii. For AMI and SPT, for example, we vary θ_c from 0.1 to 3 arcmin in 0.1 steps (i.e., $\theta_{\rm c} = 0.1, 0.2, ..., 2.9, 3$ arcmin) and add three values for the largest clusters: 4, 5, 6 arcmin. We thus filter the map(s) $n_{\theta_{\rm c}}$ times ($n_{\theta_{\rm c}} = 33$ for AMI and SPT) to obtain $2\,n_{\theta_{\rm c}}$ filtered maps, $J_{\theta_{\rm c}}$ et $L_{\theta_{\rm c}}$. The $n_{\theta_{\rm c}}$ maps $J_{\theta_{\rm c}}$ give the SZ amplitude (obtained using $\Psi_{\theta_{\rm c}}$), while the $n_{\theta_{\rm c}}$ maps $L_{\theta_{\rm c}}$ give the signal-to-noise ratio: $L_{\theta_{\rm c}} = J_{\theta_{\rm c}}/\sigma_{\theta_{\rm c}}$). We set a detection threshold at fixed signal-to-noise q and identify candidates at each filter scale $\theta_{\rm c}$ as pixels with $L_{\theta_{\rm c}} > q$. Common values for the threshold are $q = 3$ and $q = 5$; the choice is a tradeoff between detection and contamination rates (see below).

3.2. Cluster parameter estimation: photometry

We begin the second step by looking for the brightest candidate pixel in the set of maps $L_{\theta_{\rm c}}$. The candidate cluster is

---

[5] Note that we have made some changes in the two last steps compared to the description given in Melin et al. (2005). We no longer sort candidates in a tree structure for de-blending; instead, we identify and then remove candidates one by one from the filtered maps. This has only a small impact on the completeness of the detection algorithm, leaving the conclusions of our previous paper intact. The changes, however, greatly improve photometry and lower contamination.

assigned the spatial coordinates (x, y) of this pixel, and its core radius is defined as the filter scale of the map containing the pixel: $\theta_c = \theta_f$. We then calculate the total integrated flux using $Y = \hat{y_o} \int T_{\theta_c}(\boldsymbol{x})\, \mathrm{d}\boldsymbol{x}$, where $\hat{y_o}$ is taken from the map J_{θ_c} at the same filter scale. We refer to this step as the photometric step, and the parameters $\hat{y_o}$, θ_c and Y as photometric parameters. Note that measurement error on Y comes from errors on both $\hat{y_o}$ and θ_c (we return to this in greater detail in Sect. 4.4).

3.3. Catalog construction

The candidate cluster is now added to the final cluster catalog, and we proceed by removing it from the set of filtered maps J_{θ_c} and $Ł_{\theta_c}$ before returning to step 2. To this end, we construct beforehand a 2D array (library) of un-normalized, filtered cluster templates (postage–stamp maps)

$$\mathcal{T}_{\theta_c,\theta_f}(\boldsymbol{x}) = \int \mathrm{d}^2x' \ \Psi_{\theta_f}(\boldsymbol{x}' - \boldsymbol{x}) T_{\theta_c}(\boldsymbol{x}') \qquad (8)$$

with the cluster centered in the map. Note that θ_c runs over core radius and θ_f over filter scale. At each filter scale θ_f, we place the normalized template $\hat{y_o}\mathcal{T}_{\theta_c,\theta_f}$ on the cluster position (x, y) and subtract it from the map. The library of filtered templates allows us to perform this step rapidly.

We then return to step 2 and repeat the process until there are no remaining candidate pixels. Thus, clusters are added to the catalog while being subtracted from the maps one at a time, thereby de-blending the sources. By pulling off the brightest clusters first, we aim to minimize uncertainty in the catalog photometric parameters. Nevertheless, it must be emphasized that the entire procedure relies heavily on the use of templates and that real clusters need not conform to the chosen profiles. We return to the effects of cluster morphology below.

In the end, we have a cluster catalog with positions (x, y), central Compton y parameters, sizes θ_c and fluxes Y.

4. Cluster recovery

We tested our catalog construction method on simulated observations of the three representative types of SZ survey specified in Table 1. The simulations include SZ emission, primary CMB anisotropy and instrumental noise and beam smearing. We do not include diffuse Galactic foregrounds in this study. We begin in this section with the ideal case where the filter perfectly matches the simulated clusters (spherical β-model profiles) and in the absence of extragalactic point sources. We return to the additional effects of cluster morphology and point source confusion in Sect. 5.

The simulated maps are generated by Monte Carlo. We first create a realization of the linear matter distribution in a large box using the matter power spectrum. Clusters are then distributed according to their expected number density, given by the mass function, and bias as a function of mass and redshift. We also give each cluster a peculiar velocity consistent with the matter distribution according to linear theory. The simulations thus featuring cluster spatial and velocity correlations accurate first order, which is a reasonable approximation on cluster scales. In this paper, we use these simulations but we do not study the impact of the correlations on the detection method, leaving this issue to forthcoming work.

The cluster gas is modeled by a spherical isothermal β-profile with $\beta = 2/3$ and $\theta_c/\theta_v = 0.1$, where θ_v is the angular projection of the virial radius and which varies with cluster mass and redshift following a self-similar relationship. We choose an $M-T$ relation consistent with the local abundance of X-ray clusters and our value of σ_8, given below (Pierpaoli et al. 2005). Finally, we fix the gas mass fraction at $f_{\mathrm{gas}} = 0.12$ (e.g., Mohr et al. 1999). The input catalog consists of clusters with total mass $M > 10^{14}\ M_\odot$, which is sufficient given the experimental characteristics listed in Table 1. Delabrouille et al. (2002) describe the simulation method in more detail.

Table 2. Extracted counts/sq. deg. from simulations of the three types of survey. The numbers in parenthesis give the counts predicted by our analytic cluster model; the difference is due to cluster overlap confusion (see text).

deg^{-2}	$S/N > 3$	$S/N > 5$
AMI	44	20
	(38)	(16)
SPT	35	12
	(27)	(11)
Planck	1.00	0.38
	(0.84)	(0.35)

We generate primary CMB anisotropies using the power spectrum calculated by CMBFAST[6] (Seljak & Zaldarriaga 1996) for a flat concordance model with $\Omega_{\mathrm{M}} = 0.3 = 1 - \Omega_\Lambda$ (Spergel et al. 2003), Hubble constant $H_o = 70\ \mathrm{km\,s^{-1}\,Mpc^{-1}}$ (Freedman et al. 2001) and a power spectrum normalization $\sigma_8 = 0.98$. As a last step we smooth the map with a Gaussian beam and add Gaussian white noise to model instrumental effects[7].

We simulate maps that would be obtained from the proposed surveys listed in Table 1. The first is an AMI[8]-like experiment (Jones et al. 2005), a single frequency, high resolution interferometer; the sensitivity corresponds to a one-month integration time per 0.1 square degree (Kneissl et al. 2001). The SPT[9]-like experiment (Ruhl et al. 2004) is a high resolution, multi-band bolometer array. We calculate the noise levels assuming an integration time of 1 hour per square degree, and a split of 2/3, 1/6, 1/6 of the 150, 220, 275 GHz channels for the 1000 detectors in the focal plane array (Ruhl et al. 2004). Finally, we consider the space-based Planck[10]-like experiment, with a nominal sensitivity for a 14 month mission. For the AMI and SPT maps we use pixels[11] of 30 arcsec, while for Planck the pixels are 2.5 arcmin.

We simulate 100 sky patches of 3 × 3 square degrees for both AMI and SPT, and of 12 × 12 square degrees for Planck. This is appropriate given the masses of detected clusters in each experiment. In practice, AMI will cover a few square degrees, similar to the simulated patch, while SPT will cover 4000 square degrees and Planck will observe the entire sky. Thus, the surveys decrease in sensitivity while increasing sky coverage from top to bottom in Table 2 (see also Table 1).

---

[6] `http://cmbfast.org/`

[7] The 3-year WMAP results, published after the work presented here was finished, favor a significantly lower value of σ_8 (Spergel et al. 2006). This could lower the total number of clusters in our simulations by up to a factor of ~2. As we are interested here in catalog recovery, where we compare output to input catalogs, this change should only cause relatively minor changes to our final results.

[8] `http://www.mrao.cam.ac.uk/telescopes/ami/index.html`

[9] `http://astro.uchicago.edu/spt/`

[10] `http://www.rssd.esa.int/index.php?project=PLANCK`

[11] Pixel sizes are at least 2 times smaller than the best channel of each experiment.

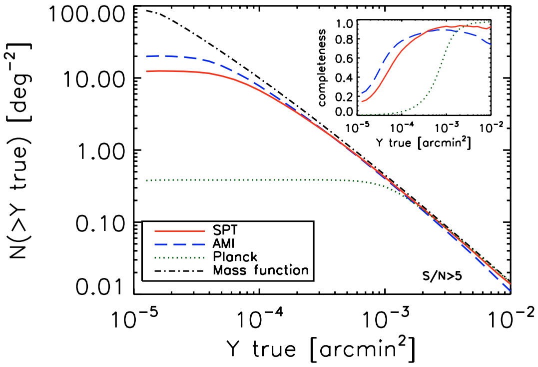

Fig. 3. Cluster counts $N(> Y)$ per square degree as a function of true SZ flux Y for a threshold of $S/N > 5$. The dash-dotted black line gives the cluster counts from the mass function (Jenkins et al. 2001). The dashed blue line gives the recovered cluster counts for AMI, the red solid line for SPT and the dotted green line for Planck. The inset shows the completeness ratio (relative to the mass function prediction) for each survey. All the surveys are significantly incomplete at their point-source sensitivities (5 times the y-intercept in Fig. 2).

4.1. Association criteria

An important issue for catalog evaluation is the association between a detected object (candidate cluster) with a cluster from the simulation input catalog (real cluster); in other words, a candidate corresponds to which, if any, real cluster. Any association method will be imprecise, and estimates of catalog completeness, contamination and photometric accuracy will unavoidably depend on the choice of association criteria.

We proceed as follows: for each detection, we look at all input clusters with centers positioned within a distance $r = \sqrt{8} \times d$, where d is the pixel size ($d = 30$ arcsec for AMI and SPT, $d = 2.5$ arcmin for Planck); this covers the neighboring 24 pixels. If there is no input cluster, then we have a false detection; otherwise, we identify the candidate with the cluster whose flux is closest to that of the detection. After running through all the candidates in this fashion, we may find that different candidates are associated with the same input cluster. In this case, we only keep the candidate whose flux is closest to the common input cluster, and we flag the other candidates as false detections (multiple detections).

At this stage, some associations may nevertheless be chance alignments. We therefore employ a second parameter, $Y_{\rm cut}$: a candidate associated with a real cluster of flux $Y < Y_{\rm cut}$ is flagged as a false detection. We indicate these false detections as diamonds in Figs. 7, 8, 9 and 11. The idea is that such clusters are too faint to have been detected and the association is therefore by chance. In the following, we take $Y_{\rm cut} = 1.5 \times 10^{-5}$ arcmin^2 for AMI and SPT, respectively, and $Y_{\rm cut} = 3 \times 10^{-4}$ arcmin^2 for Planck. Note that these numbers are well below the point-source sensitivity (at $S/N = 5$) in each case (see below and Fig. 2).

4.2. Completeness

Figure 3 shows completeness for the three experiments in terms of *true* integrated Y, while Table 2 summarizes the counts. In Fig. 4 we give the corresponding limiting mass as a function of redshift. Given our cluster model, AMI, SPT and Planck should find, respectively, about 16, 11 and 0.35 clusters/deg.^{2} at a $S/N > 5$; these are the numbers given in parentheses in Table 2. Cluster overlap confusion accounts for the fact that the actual counts extracted from the simulated surveys are higher: some clusters that would not otherwise pass the detection cut enter the catalog because the filter adds in flux from close neighbors.

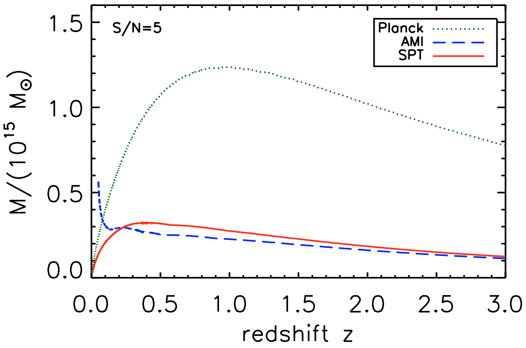

Fig. 4. Mininum detectable cluster mass as a function of redshift, $M(z)$, corresponding to $S/N = 5$ for the three experiments discussed in the text. The rise at low redshift for the single-frequency (AMI) curve is caused by confusion with primary CMB anisotropy.

A detection threshold of $S/N = 5$ corresponds to a point-source sensitivity of just below $Y = 5 \times 10^{-5}$ arcmin^2 for both AMI and SPT, as can be read off the left-hand-side of Fig. 2. The surveys approach a high level of completeness only at $Y > 10^{-4}$ arcmin^2, however, due to the rise of the selection cut with core radius seen in Fig. 2. For these high resolution surveys, point-source sensitivity gives a false idea of the survey completeness flux limit.

At the same signal-to-noise threshold, Planck is essentially complete above $Y \sim 10^{-3}$ arcmin^2 and should detect about 0.4 clusters per square degree. Since most clusters are unresolved by Planck, the survey reaches a high completeness level near the point-source sensitivity. We also see this from the small slope of the Planck selection cut in Fig. 2.

We emphasize that the surveys (in particular, the high resolution surveys) are not flux limited for any value of q, because increasing q simply translates the curve in Fig. 2 along the y axis. However, one can approach a flux-limited catalog by selecting clusters at $S/N > q$ and then cutting the resulting catalog at $Y_o > Y_{\rm limit} \equiv Q\sigma_Y(\theta_c = 0.1$ arcmin), where the constant $Q > q$. As Q increases we tend towards a catalog for which $Y \sim Y_o > Y_{\rm limit}$. In the case of SPT with $q = 3$, for example, we find that large values of Q (>10) are required to approach a reasonable flux-limited catalog; this construction, however, throws away a very large number of detected clusters.

Although the AMI (single frequency) and SPT (multi-band) survey maps have comparable depth, SPT will cover ~4000 sq. degrees, compared to AMI's ~10 sq. degrees. Planck will only find the brightest clusters, but with full sky coverage. Predictions for the counts suffer from cluster modeling uncertainties, but the comparison between experiments is robust and of primary interest here.

4.3. Contamination

Figure 5 shows the contamination level at $S/N > 5$ for each survey type as a function of *recovered* flux $Y_{\rm o}$. The multiband experiments (SPT and Planck) benefit from low contamination at all fluxes. Single frequency surveys (e.g., AMI), on the other hand, experience a slightly higher contamination level at large

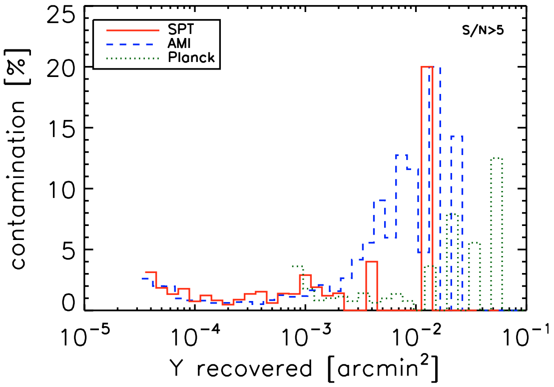

Fig. 5. Contamination as a function of the core radius θ_c for the three experiments and for $S/N > 5$.

flux due to confusion from primary CMB anisotropy. This confusion also degrades the photometry, as we discuss below.

At $S/N > 5$, the AMI, SPT and Planck catalogs have less than 2% total contamination rate. These numbers increase to ~23, 20 and 27 percent, respectively, for AMI, SPT and Planck at a detection threshold of $S/N > 3$. Note that the total contamination rate is an average over the histogram of Fig. 5 weighted by the number of objects in each bin; thus, the higher contamination at large flux is down-weighted in the total rate.

In all cases, the contamination rate is higher than expected from pure Gaussian noise fluctuations; there is an important contribution from cluster-cluster confusion (residuals from cluster subtraction and overlaps). We expect even higher contamination rates in practice, because of variations in cluster morphology around the filter templates. We quantify this latter effect below.

A useful summary of these results is a completeness-purity plot, as shown in Fig. 6. Proper comparison of the different experiments requires an appropriate choice of input catalog used to define the completeness in this plot. Here, we take the input catalog as all clusters with (true) flux geater than three times the point source sensitivity for each experiment. If the clusters were point sources and the detection method perfect (i.e. not affected by confusion), the completeness would be 1 for $q = 3$ in the top-left corner. These curves summarize the efficiency of our cluster detection method; however, they give no information on the photometric capabilities of the experiments.

4.4. Photometry

We now turn to the important, but often neglected issue of cluster SZ photometry. The ability of a SZ survey to constrain cosmology relies on application of the $Y - M$ relation. As mentioned, we expect the *intrinsic* (or *true*) flux to tightly correlate with cluster mass (Bartlett 2001), as indeed borne out by numerical simulations (da Silva et al. 2004; Motl et al. 2005; Nagai 2005). Nevertheless, unknown cluster physics could affect the exact form and normalization of the relation, pointing up the necessity of an empirical calibration (referred to as survey *calibration*), either with the survey data itself (self-calibration; Hu 2003; Majumdar & Mohr 2003; Lima & Hu 2004; Lima & Hu 2005) or using external data, such as lensing mass estimates (Bartelmann 2001) (although the latter will be limited to relatively low redshifts).

Photometric measurement accuracy and precision is as important as cluster physics in this context: what matters in practice is the relation between *recovered* SZ flux Y_o and cluster mass M. Biased SZ photometry (bias in the $Y - Y_o$) relation will change the form and normalization of the $Y_o - M$ relation and noise will increase the scatter. One potentially important source of photometric error for the matched filter comes from cluster morphology, i.e., the fact that cluster profiles do not exactly follow the filter shape (see Sect. 5).

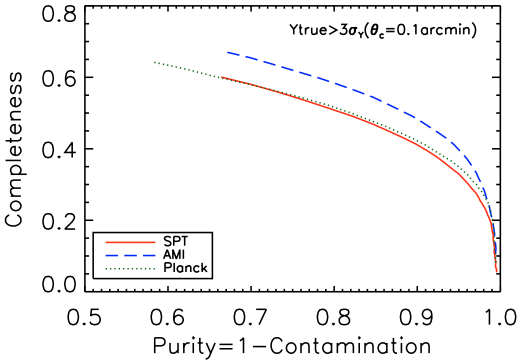

Fig. 6. Completeness-Purity plot. For each curve, q varies from 3 (*top-left*) to 10 (*bottom-right*). For each experiment, the input catalog contains clusters with true flux greater than three times the point source sensitivity ($Y_{\rm true} > 2.2{\times}10^{-5}$ arcmin^2 for AMI, $Y_{\rm true} > 2.6{\times}10^{-5}$ arcmin^2 for SPT and $Y_{\rm true} > 4.8 \times 10^{-4}$ arcmin^2 for Planck). See text for details.

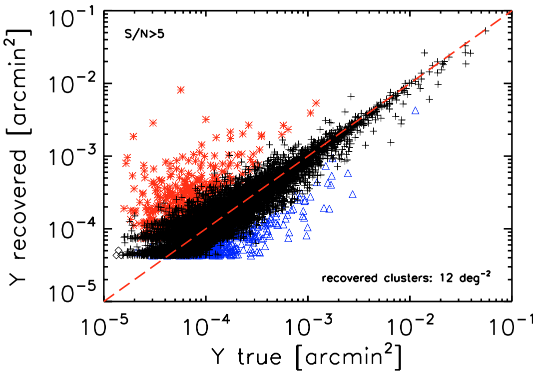

Fig. 7. Recovered vs. true flux for SPT clusters extracted at $S/N > 5$ from 100 survey simulations. The diamonds indicate cluster detections with $Y < Y_{\rm cut}$, which we take as false detections. The mean trend $Y_o(Y)$ has a slight bias (see text) and a roughly constant scatter of $\sigma_{\log Y_o} = 0.17$ over the interval in true Y from 10^{-4} arcmin^2 to 4×10^{-3} arcmin^2. The clusters which have their core radii overestimated by a factor of 2 are plotted as red crosses and the clusters which have their core radii underestimated by a factor of 2 are plotted as blue triangles.

Survey calibration will help remove the bias, but with an ease that depends on the photometric scatter: large scatter will increase calibration uncertainty and/or necessitate a larger amount of external data. In addition, scatter will degrade the final cosmological constraints (e.g., Lima & Hu 2005). Photometry should therefore be considered an important evaluation criteria for cluster catalog extraction methods.

Consider, first, SPT photometry. Figure 7 shows the relation between observed (or recovered) flux Y_o and true flux Y for a detection threshold of $S/N > 5$. Fitting for the average trend of Y_o as a function of Y, we obtain

$$\log Y_o = 0.96 \log Y - 0.15$$

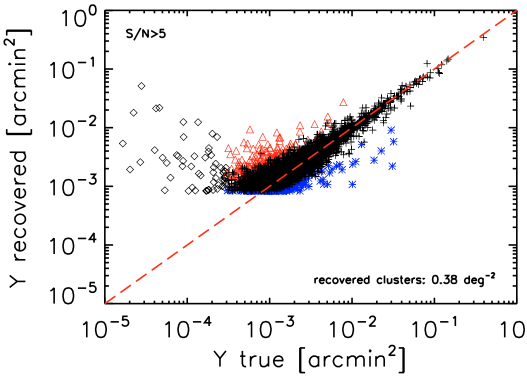

Fig. 8. Recovered vs. true flux for Planck clusters extracted at $S/N > 5$ from 100 survey simulations. The diamonds indicate cluster detections with $Y < Y_{\rm cut}$, which we take as false detections. The mean trend $Y_{\rm o}(Y)$ has a slight bias (see text) and a roughly constant scatter of $\sigma_{\log Y_{\rm o}} = 0.13$ over the interval in true Y from 2×10^{-3} arcmin^2 to 2×10^{-2} arcmin^2. The clusters which have their core radii overestimated by a factor of 2 are plotted as red crosses and the clusters which have their core radii underestimated by a factor of 2 are plotted as blue triangles.

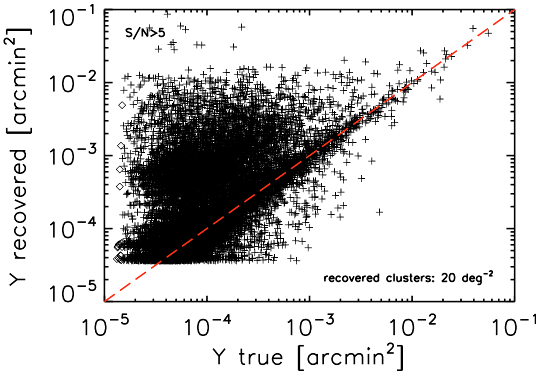

Fig. 9. Recovered vs. true flux for AMI clusters extracted at $S/N > 5$ from 100 survey simulations. The diamonds indicate cluster detections with $Y < Y_{\rm cut}$, which we take as false detections. The extremely large dispersion in recovered flux results from a bimodal distribution caused by an inability to determine the core radius of detected clusters. This inability is due to confusion from primary CMB anisotropy, as demonstrated in Fig. 10. Figure 11 shows that reasonable photometry is possible if the core radius can be accurately determined. This problem is specific to single-frequency surveys that are unable to spectrally remove primary CMB anisotropy.

over the interval 10^{-4} arcmin^2 $< Y < 4 \times 10^{-3}$ arcmin^2, with $Y_{\rm o}$ and Y measured in arcmin^2. There is a slight bias in that the fit deviates somewhat from the equality line, but the effect is minor. Below this flux interval, the fit curls upward in a form of Malmquist bias caused by the S/N cut (seen as the sharp lower edge on $Y_{\rm o}$). The lack of any significant bias is understandable in this ideal case where the filter perfectly matches the cluster SZ profile. Cluster morphology, by which we mean a mismatch between the cluster SZ profile and the matched filter template), can induce bias; we return to this issue in Sect. 5.

The scatter about the fit is consistent with a Gaussian distribution with a roughly constant standard deviation of $\sigma_{\log Y_{\rm o}} = 0.17$ over the entire interval.

The scatter is a factor of 10 larger than expected from instrumental noise alone, which is given by the selection curve in Fig. 2. Uncertainty in the recovered cluster position, core radius and effects from cluster-cluster confusion all strongly influence the scatter. Photometry precision, therefore, cannot be predicted from instrumental noise properties alone, but only with simulations accounting for these other, more important effects.

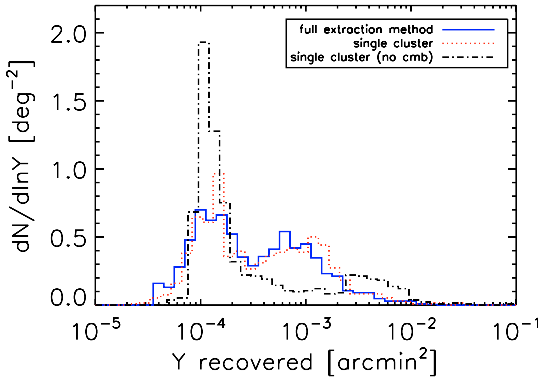

Fig. 10. The full blue histogram gives the cluster counts from Fig. 9 in the bin ($10^{-4} < Y < 2.10^{-4}$, $0.25 < \theta_c < 0.35$). We have added the cluster counts obtained from the size and flux estimation of a single cluster ($Y = 1.5 \times 10^{-4}$, $\theta_c = 0.3$) at a known position through 1000 simulations. SZ cluster background maps and the instrumental beam and noise are included. Two cases are considered : with primary CMB (dotted red histogram) and without primary CMB (dash-dotted black line). The double bump in Y recovery is visible when the primary CMB is present and disappears when it's removed showing that the primary CMB power spectrum is the cause of the double bump.

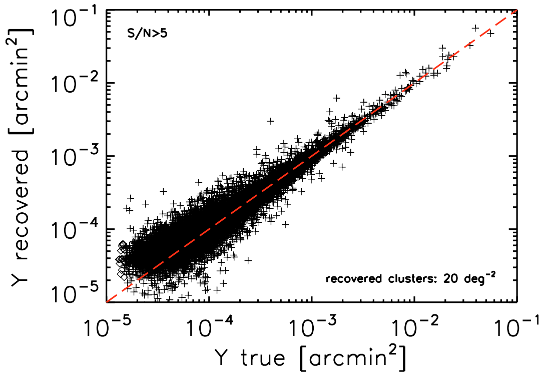

Fig. 11. Single-frequency photometry when we artificially set the core radii of detected clusters to their true values from the input catalog. The dispersion decreases dramatically, demonstrating that the inability to recover the core radius is the origin of the bad photometry seen in Fig. 9.

Figure 8 shows the photometry for the Planck survey. Apart from some catastrophic cases (the diamonds), the photometry is good and fit by

$$\log Y_{\rm o} = 0.98 \log Y - 0.07$$

over the interval 2×10^{-3} arcmin^2 $< Y < 2 \times 10^{-2}$ arcmin^2 ($Y_{\rm o}$, Y measured in arcmin^2). The dispersion is $\sigma_{\log Y_{\rm o}} = 0.13$, roughly constant over the same interval. For unresolved clusters, this scatter is $\sim$5 times larger than the expected instrumental-induced scatter. The brightest diamonds in the Figure correspond to real clusters with positional error larger than the association criteria r. As a consequence, the candidates are falsely associated with a small, nearby cluster, unrelated to the actual detected object.

We emphasize that the observational scatter in the $Y_o - Y$ relation for both SPT and Planck dominates the intrinsic scatter of less than 5% seen in the $Y - M$ relation from numerical simulations (da Silva et al. 2004; Motl et al. 2005).

We now turn to single frequency surveys, which Fig. 9 shows to have seriously compromised photometry. The distribution at a given true flux Y is in fact bimodal, as illustrated by the solid blue histogram in Fig. 10 that gives the distribution of the recovered flux Y_o for clusters with true flux and core radius in a bin centered on $Y = 1.5 \times 10^{-4}$ arcmin^2 and $\theta_c = 0.3$ arcmin. We have traced this effect to an inability to accurately determine the core radius of the candidate clusters. We demonstrate this in Fig. 11 by artificially setting the candidate core radius to its true value taken from the associated input cluster; the photometry now cleanly scatters about the mean trend.

This inability to determine the core radius mainly arises from confusion with primary CMB anisotropy, as we now show using Fig. 10. We performed 1000 simulations of a single cluster ($Y = 1.5 \times 10^{-4}$ arcmin^2, $\theta_c = 0.3$ arcmin) placed at the middle of a beam-convolved map containing background SZ clusters (from our general simulations), primary CMB anisotropy and instrumental noise. We then estimate its core radius and flux with our matched filters centered on the known position (to avoid any positional uncertainty) and trace the histogram of resulting measured flux. This is the red dot-dashed histogram in the figure, which displays a bi-modality similar to that of the blue solid histogram. We then follow the same procedure after first removing the primary CMB anisotropy from the simulated map. The resulting histogram of recovered flux is given by the black dot-dashed line with much less pronounced bimodality. The remaining tail reaching towards high flux is caused by cluster–cluster confusion.

With their additional spectral information, multiband surveys remove the primary CMB signal, thereby avoiding this source of confusion. *The result suggests that follow-up observations of detected clusters at a second frequency will be required for proper photometry*; without such follow-up, the scientific power of a single frequency survey may be seriously compromised, as can be appreciated from inspection of Fig. 9.

5. Additional effects

As emphasized, our previous results follow for a filter that perfectly matches the (spherical) clusters in our simulations and in the absence of any point sources. In this section we examine the effects of both cluster morphology and point sources.

We find that cluster morphology has little effect on catalog completeness, but that it does increase contamination. More importantly, it can bias photometric recovery, although it does not significantly increase the scatter. This bias changes the observed $Y - M$ relation from its intrinsic form, adding to the modeling uncertainty already caused by cluster gas physics. For this reason, the relation must be calibrated in order to use the SZ catalog for any cosmological study. The observational bias would be removed during this calibration step.

Completeness is the most affected by point source confusion, decreasing somewhat for the multi-band surveys in the presence of IR point sources. The level of confusion for the single frequency survey remains highly uncertain due to the unknown point source counts at low flux densities. Contamination and photometry are essentially unaffected.

5.1. Cluster morphology

To assess the influence of cluster morphology, we ran our catalog extraction algorithm on maps constructed from numerical simulations. We use the simulations presented by Schulz & White (Schulz & White 2003) and kindly provided to us by M. White. Their simulations follow dark matter clustering with a N-body code in a flat concordance cosmology, and model cluster gas physics with semi-analytical techniques by distributing an isothermal gas of mass fraction Ω_B/Ω_M according to the halo dark matter distribution. For details, see Schulz & White. In the following, we refer to these simulations as the "N-body" simulations.

We proceed by comparing catalogs extracted from the N-body map to those from a corresponding simulation made with spherical clusters. The latter is constructed by applying our spherical β-model gas distribution to the cluster halos taken from the N-body simulation and using them as input to our Monte Carlo sky maps. In the process, we renormalize our $Y - M$ relation to the one used in the N-body SZ maps. We thus obtain two SZ maps containing the same cluster halos, one with spherical clusters (referred to hereafter as the "β-model" maps) and the other with more complex cluster morphology (the N-body maps). Comparison of the catalogs extracted from the two different types of simulated map gives us an indication of the sensitivity of our method to cluster morphology. We make this comparative study only for the SPT and Planck like surveys.

Catalog completeness is essentially unaffected by cluster morphology; the integrated counts, for example, follow the same curves shown in Fig. 3 with very little deviation, the only difference being a very small decrease in the Planck counts at the lowest fluxes. The effect, for example, is smaller than that displayed in Fig. 13 due to point source confusion (and discussed below).

Non-trivial cluster morphology, however, does significantly increase the catalog contamination rate; for example, in the SPT survey the global contamination rises from less than 2% to 13% at $S/N = 5$ for the N-body simulations. We trace this to residual flux left in the maps after cluster extraction: cluster SZ signal that deviates from the assumed spherical β-model filter profile remains in the map and is picked up later as new cluster candidates. Masking those regions where a cluster has been previously extracted (i.e., forbidding any cluster detection) drops the contamination to 4% (SPT case), but causes a decrease of 2.8 clusters per square degree in the recovered counts; this technique would also have important consequences for clustering studies.

From Fig. 12, we clearly see that cluster morphology induces a bias in the photometry. This arises from the fact that the actual cluster SZ profiles differ from the template adopted for the filter. The differences are of two types: an overall difference in the form of radial profile and local deviations about the average radial profile due to cluster substructure. It is the former that is primarily responsible for the bias. In our case, the N-body simulations have much more centrally peaked SZ emission than the filter templates, which causes the filter to systematically underestimate the total SZ flux. Cluster substructure will increase the scatter about the mean $Y_o - Y$ relation. This latter effect is not large, at least for the N-body simulations used here, as can be seen by comparing the scatter in Figs. 12 and 7.

We emphasize, however, that the quantitative effects on photometry depend on the intrinsic cluster profile, and hence are subject to modeling uncertainty. The simulations used here do not include gas physics and simply assume that the gas follows the dark matter. The real bias will depend on unknown cluster physics, thus adding to the modeling uncertainty in the

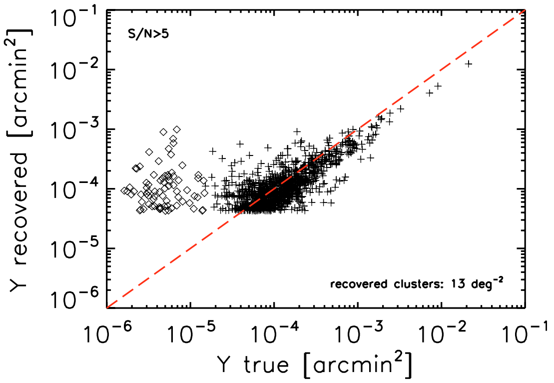

Fig. 12. Photometry for the SPT catalog from the N-body simulations. Cluster morphology (mismatch between the filter profile and the actual cluster SZ profile) clearly induces a bias between the recovered and true SZ flux. The scatter, on the other hand, is not very affected, as can be seen in comparing with Fig. 7.

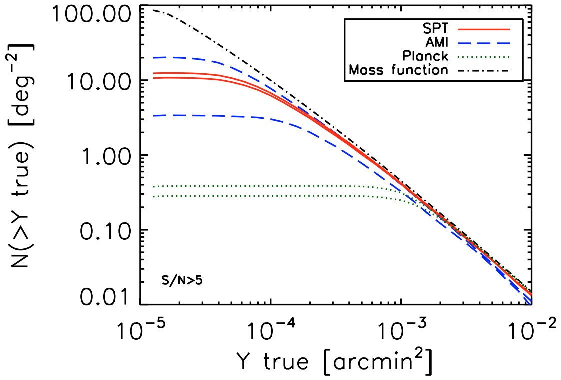

Fig. 13. Integrated cluster counts for the three types of survey. The upper curve in each pair reproduces the results of Fig. 3, while the lower curve shows the effect of point source confusion. Despite the large IR point source population, multiband surveys efficiently eliminate confusion. The AMI-like survey is, on the other hand, strongly affected. This latter effect remains uncertain due to a lack of information on the faint end of the radio point source counts (see text).

$Y-M$ relation. This uncertainty, due to both cluster physics and the photometric uncertainty discussed here, must be dealt with by empirically calibrating the relation, either with external data (lensing) and/or internally (self-calibration).

5.2. Point sources

We next examine the effect of point sources. In a previous paper (Bartlett & Melin 2005, hereafter BM) we studied their influence on survey detection sensitivity. We extend this work to our present study in this section.

Low frequency surveys, such as our AMI example, contend with an important radio source population, while higher frequency bolometer surveys face a large population of IR sources. Radio source counts down to the sub-mJy flux levels relevant for SZ surveys are unfortunately poorly known. The IR counts are somewhat better constrained at fluxes dominating the fluctuations in the IR background, although at higher frequencies (850 microns) than those used in SZ surveys; an uncertain extrapolation in frequency is thus necessary.

For the present study, we use the radio counts fit by Knox et al. (2004) to a combination of data from CBI, DASI, VSA and WMAP (see also Eq. (6) in BM), and IR counts fit to blank-field SCUBA observations at 850 microns by Borys et al. (2003) (and given by Eq. (8) in BM). We further assume that all radio sources brighter than 100 μJy have been subtracted from our maps at 15 GHz (AMI case); this is the target sensitivity of the long baseline Ryle Telescope observations that will perform the source subtraction for AMI. No such explicit point source subtraction is readily available for the higher frequency bolometer surveys; they must rely solely on their frequency coverage to reduce point source confusion. We therefore include all IR sources in our simulations, and fix their effective spectral index $\alpha = 3$ with no dispersion[12]. We refer the reader to BM for details of our point source model. Note that for this study we use the spherical cluster model for direct comparison to our fiducial results.

Figure 13 compares the integrated counts from Fig. 3 (upper curve in each case) to those extracted from the simulations including point sources (lower curves). We see that point source confusion only slightly decreases the completeness of the multiband surveys, but greatly affects the single frequency survey.

In the case of SPT, this is because point source confusion remains modest compared to the noise: the two are comparable at 150 GHz, but the noise power rises more quickly with frequency than the confusion power (see BM for details) – in other words, the noise is bluer than the confusion. This is an important consideration when looking for the optimal allocation of detectors to the observation bands.

For Planck, confusion power dominates at all frequencies, but the spectral coverage provides sufficient leverage to control it. In this light, it must be emphasized that we only include three astrophysical signals (SZ, CMB & point sources) in these simulations, so that three observation bands are sufficient. In reality, one will have to deal with other foregrounds, e.g., diffuse Galactic emission, which will require the use of additional observation bands.

The single frequency observations, on the other hand, are strongly affected. This is consistent with the estimate in BM (Eq. (15)) placing confusion noise well above instrumental noise for the chosen point source model and source subtraction threshold. We emphasize the uncertainty in this estimate, however: in BM we showed, for example, that a model with flattening counts has much lower source confusion while remaining consistent with the observed counts at high flux densities. The actual confusion level remains to be determined from deeper counts at CMB frequencies (see Waldram et al. 2003; Waldram et al. 2004 for recent deep counts at 15 GHz).

Contamination in the multiband surveys is practically unaffected by point source confusion. For AMI we actually find a lower contamination rate, an apparent gain explained by the fact that the catalog now contains only the brighter SZ sources, due to the lowered sensitivity caused by point source confusion.

The photometry of the multiband surveys also shows little effect from the point sources. Fits to the recovered flux vs. true flux relation do not differ significantly from the no-source case, and the dispersion remains essentially the same. This is consistent with the idea that point source confusion is either modest compared to the noise (SPT) or controlled by multiband observations (Planck).

---

[12] As discussed in BM, any dispersion has only a small effect on survey sensitivity.

6. Discussion and conclusion

We have described a simple, rapid method based on matched multi-frequency filters for extracting cluster catalogs from SZ surveys. We assessed its performance when applied to the three kinds of survey listed in Table 1. The rapidity of the method allows us to run many simulations of each survey to accurately quantify selection effects and observational uncertainties. We specifically examined catalog completeness, contamination rate and photometric precision.

Figure 2 shows the cluster selection criteria in terms of total SZ flux and source size. It clearly demonstrates that SZ surveys, in particular high resolution ground-bases surveys, will not be purely flux limited, something which must be correctly accounted for when interpreting catalog statistics (Melin et al. 2005).

Figure 3 and Table 2 summarize the expected yield for each survey. The counts roll off at the faint end well before the point-source flux limit (intercept of the curves in Fig. 2 multiplied by the S/N limit) even at the high detection threshold of $S/N = 5$; the surveys loose completeness precisely because they are not purely flux-limited. These yields depend on the underlying cluster model and are hence subject to non-negligible uncertainty. They are nonetheless indicative, and in this work we focus on the nature of observational selection effects for which the exact yields are of secondary importance.

At our fiducial $S/N = 5$ detection threshold, overall catalog contamination remains below 5%, with some dependence on SZ flux for the single frequency survey (see Fig. 5). The overall contamination rises to between 20% and 30% at $S/N > 3$. We note that the contamination rate is always larger than expected from pure instrumental noise, pointing to the influence of astrophysical confusion.

We pay particular attention to photometric precision, an issue often neglected in discussions of the scientific potential of SZ surveys. Scatter plots for the recovered flux for each survey type are given in Figs. 7–9. In the two multiband surveys, the recovered SZ flux is slightly biased, due to the flux cut, with a dispersion of $\sigma_{\log Y_o} = 0.17$ and $\sigma_{\log Y_o} = 0.13$ for SPT and Planck, respectively. This observational dispersion is significantly larger than the intrinsic dispersion in the $Y - M$ relation predicted by hydrodynamical simulations. This uncertainty must be properly accounted for in scientific interpretation of SZ catalogs; specifically, it will degrade survey calibration and cosmological constraints.

Even more importantly, we found that astrophysical confusion seriously compromises the photometry of the single frequency survey (Fig. 9). The histogram in Fig. 10 shows that the recovered flux has in fact a bimodal distribution. We traced the effect to an inability to determine source core radii in the presence of primary CMB anisotropy. If cluster core radius could be accurately measured, e.g., with X-ray follow-up, then we would obtain photometric precision comparable to the multiband surveys (see Fig. 11). This confusion can also be removed by follow-up of detected sources at a second radio frequency (e.g., 90 GHz). Photometric uncertainty will therefore be key limiting factor in single frequency SZ surveys.

All these results apply to the ideal case where the filter exactly matches the (simulated) cluster profiles. We then examined the potential impact of cluster morphology and point sources on these conclusions.

Using N-body simulations, we found that cluster morphology has little effect on catalog completeness, but that it does increase the contamination rate and bias the photometry. The increased contamination is caused by deviations from a smooth radial SZ profile that appear as residual flux in the maps after source extraction. More importantly, the photometry is biased by the mismatch between the filter template and the actual cluster profile. This observational bias adds to the modeling uncertainty in the $Y - M$ relation, which will have to be empirically determined in order to use the catalog for cosmology studies.

As shown by Fig. 13, point sources decrease survey completeness. The multiband surveys effectively reduce IR point source confusion and suffer only a small decrease. Radio source confusion, on the other hand, greatly decreased the completeness of the single frequency survey. This is consistent with the expectation that, for our adopted radio point source model and source subtraction threshold, point source confusion dominates instrumental noise. Modeling uncertainty here is, however, very large: radio source counts are not constrained at relevant fluxes (~100 μJy), which requires us to extrapolate counts from mJy levels (see BM for a more detailed discussion).

Surveys based on the SZ effect will open a new window onto the high redshift universe. They inherit their strong scientific potential from the unique characteristics of the SZ signal. Full realization of this potential, however, requires understanding of observational selection effects and uncertainties. Overall, multiband surveys appear robust in this light, while single frequency surveys will most likely require additional observational effort, e.g., follow-up in other wavebands, to overcome large photometric errors caused by astrophysical confusion with primary CMB anisotropy.

Acknowledgements. We thank T. Crawford for useful comments on matched filters and information about SPT, and A. Schulz and M. White for kindly providing us with their N-body simulations. We are also grateful to the anonymous referee for helpful and insightful comments. JBM wishes to thank L. Knox, the Berkeley Astrophysics group and E. Pierpaoli for discussions on the detection method, and D. Herranz and the Santander group for discussions on matched filters. JBM was supported at UC Davis by the National Science Foundation under Grant No. 0307961 and NASA under Grant No. NAG5–11098.

References

Angulo, R., Baugh, C. M., Frenk, C. S., et al. 2005, MNRAS, 362, L25
Arnaud, M. [`arXiv:astro-ph/0508159`]
Barbosa, D., Bartlett, J. G., & Blanchard, A. 1996, A&A, 314, 13
Bartelmann, M. 2001, A&A, 370, 754
Birkinshaw, M. 1999, Proc. 3K Cosmology, 476, American Institute of Physics, Woodbury, 298
Blanchard, A., & Bartlett, J. G. 1998, A&A, 332, L49
Bartlett, J. G. 2001, review in Tracing cosmic evolution with galaxy clusters (Sesto Pusteria 3–6 July 2001), ASP Conf. Ser., in press [`arXiv:astro-ph/0111211`]
Bartlett, J. G., & Melin, J.-B. 2005, submitted
Benson, A. J., Reichardt, C., & Kamionkowski, M. 2002, MNRAS, 331, 71
Bertin, E., & Arnouts, S. 1996, A&A, 117, 393
Borys, C., Chapman, S., Halpern, M., & Scott, D. 2003, MNRAS, 344, 385
Carlstrom, J. E., Holder, G. P., & Reese, E. D. 2002, ARA&A, 40, 643
Colafrancesco, S., Mazzotta, P., & Vittorio, N. 1997, ApJ, 488, 566
Cole, S., Percival, W. J., Peacock, J. A., et al. 2005, MNRAS, 362, 505
Delabrouille, J., Melin, J.-B., & Bartlett, J. G. 2002, in AMiBA 2001: High-Z Clusters, Missing Baryons, and CMB Polarization, ASP Conf. Proc. [`arXiv:astro-ph/0109186`]
da Silva, A. C., Kay, S. T., Liddle, A. R., & Thomas, P. A. 2004, MNRAS, 348, 1401
Diego, J. M., Vielva, P., Martínez-González, E., Silk, J., & Sanz, J. L. 2002, MNRAS, 336, 1351
Eisenstein, D. J., Zehavi, I., Hogg, D. W., et al. 2005, ApJ, 633, 560
Eke, V. R., Cole, S., Frenk, C. S., & Patrick Henry, P. J. 1998, MNRAS, 298 1145
Freedman, W. L., Madore, B. F., Gibson, B. K., et al. 2001, ApJ, 553, 47
Haehnelt, M. G., & Tegmark, M. 1996, MNRAS, 279, 545
Haiman, Z., Mohr, J. J., & Holder, G. P. 2000, ApJ, 553, 545

Herranz, D., Sanz, J. L., Barreiro, R. B., & Martínez-González, E. 2002, ApJ, 580, 610
Herranz, D., Sanz, J. L., Hobson, M. P., Barreiro, R. B., et al. 2002, MNRAS, 336, 1057
Hobson, M. P., & McLachlan, C. 2003, MNRAS, 338, 765
Holder, G. P., Mohr, J. J., Carlstrom, J. E., Evrard, A. E., & Leitch, E. M. 2000, ApJ, 544, 629
Hu, W. 2003, Phys. Rev. D, 67, 081304
Huetsi, G. 2006, A&A, 446, 43
Jenkins, A., Frenk, C. S., White, S. D. M., et al. 2001, MNRAS, 321, 372
Jones, M. E., Edge, A. C., Grainge, K., et al. 2005, MNRAS, 357, 518
Juin, J. B., Yvon, D., Refregier, A., & Yeche, C. 2005 [`arXiv:astro-ph/0512378`]
Kneissl, R., Jones, M. E., Saunders, R., et al. 2001, MNRAS, 328, 783
Knox, L., Holder, G. P., & Church, S. E. 2004, ApJ, 612, 96
Lima, M., & Hu, W. 2004, Phys. Rev. D, 70, 043504
Lima, M., & Hu, W. 2005, Phys. Rev. D, 72, 043006
López-Caniego, M., Herranz, D., Sanz, J. L., & Barreiro, R. B. 2005 [`arXiv:astro-ph/0503149`]
Majumdar, S., & Mohr, J. J. 2004, ApJ, 613, 41
Melin, J.-B., Bartlett, J. G., & Delabrouille, J. 2005, A&A, 429, 417
Mohr, J. J., Mathiesen, B., & Evrard, A. E. 1999, ApJ, 517, 627
Motl, P. M., Hallman, E. J., Burns, J. O., & Norman, M. L. 2005, ApJ, 623, L63
Nagai, D. 2005 [`arXiv:astro-ph/0512208`]
Oukbir, J., & Blanchard, A. 1992, A&A, 262, L21
Pierpaoli, E., Anthoine, S., Huffenberger, K., & Daubechies, I. 2005, MNRAS, 359, 261
Pires, S., Juin, J. B., Yvon, D., et al. 2006, A&A, 455, 741
Rosati, P., Borgani, S., & Norman, C. 2002, ARA&A, 40, 539
Ruhl, J. E., et al. 2004 [`arXiv:astro-ph/0411122`]
Schäfer, B. M., Pfrommer, C., Hell, R. M., & Bartelmann, M. 2006, MNRAS, 370, 1713
Schulz, A. E., & White, M. 2003, ApJ, 586, 723
Seljak, U., & Zaldarriaga, M. 1996, ApJ, 469, 437, `www.cmbfast.org`
Spergel, D. N., Verde, L., Peiris, H. V., et al. 2003, ApJS, 148, 175
Spergel, D. N., Bean, R., Dore, O., et al. 2006 [`arXiv:astro-ph/0603449`]
Sunyaev, R. A., & Zel'dovich, Ya. B. 1970, Comments Astrophys. Space Phys., 2, 66
Sunyaev, R. A., & Zel'dovich, Ya. B. 1972, Comments Astrophys. Space Phys., 4, 173
Vale, C., & White, M. 2006, New Astron., 11, 207
Voit, G. M. 2004 [`arXiv:astro-ph/0410173`]
Waldram, E. M., & Pooley, G. G. 2004 [`arXiv:astro-ph/0407422`]
Waldram, E. M., Pooley, G. G., Grainge, K., et al. 2003, MNRAS, 342, 915
Wang, S., Khoury, J., Haiman, Z., & May, M. 2004, Phys. Rev. D, 70, 12300
Weller, J., & Battye, R. A. 2003, NewAR, 47, 775
White, M. 2003, ApJ, 597, 650

A&A 548, A51 (2012)
DOI: 10.1051/0004-6361/201015689

Astronomy & Astrophysics

A comparison of algorithms for the construction of SZ cluster catalogues

J.-B. Melin[1], N. Aghanim[2], M. Bartelmann[3], J. G. Bartlett[4,5,6], M. Betoule[4], J. Bobin[7], P. Carvalho[8], G. Chon[9], J. Delabrouille[4], J. M. Diego[10], D. L. Harrison[11], D. Herranz[10], M. Hobson[8], R. Kneissl[12], A. N. Lasenby[8,11], M. Le Jeune[4], M. Lopez-Caniego[10], P. Mazzotta[13], G. M. Rocha[6], B. M. Schaefer[14], J.-L. Starck[7], J. C. Waizmann[3,15], and D. Yvon[1]

[1] DSM/Irfu/SPP, CEA/Saclay, 91191 Gif-sur-Yvette Cedex, France
e-mail: `jean-baptiste.melin@cea.fr`
[2] Institut d'Astrophysique Spatiale, CNRS et Université de Paris XI, Bâtiment 120-121, Centre Universitaire d'Orsay, 91400 Orsay Cedex, France
[3] Institut fur Theoretische Astrophysik, Zentrum fur Astronomie der Universitat Heidelberg, Albert-Ueberle-Str. 2, 69120 Heidelberg, Germany
[4] APC, 10 rue Alice Domon et Léonie Duquet, 75205 Paris Cedex 13, France
[5] Université Paris Diderot – Paris 7, 75205 Paris Cedex 13, France
[6] Jet Propulsion Laboratory, California Institute of Technology, 4800 Oak Grove Drive, Pasadena, CA 91109, USA
[7] DSM/Irfu/SAp, CEA/Saclay, 91191 Gif-sur-Yvette Cedex, France
[8] Astrophysics Group, Cavendish Laboratory, J.J. Thomson Avenue, Cambridge, CB3 0HE, UK
[9] Max-Planck-Institut für extraterrestrische Physik Giessenbachstr, 85748 Garching, Germany
[10] Instituto de Física de Cantabria (CSIC-UC), 39005 Santander, Spain
[11] Kavli Institute for Cosmology Cambridge and Institute of Astronomy, Madingley Road, Cambridge, CB3 OHA, UK
[12] ALMA JAO, Av. El Golf 40 – Piso 18, Las Condes, Santiago; ESO, Alonso de Córdova 3107, Vitacura, Casilla 19001, Santiago, Chile
[13] Università di Roma "Tor Vergata", via della ricerca scientifica, 1, 00133 Roma, Italy
[14] Astronomisches Rechen-Institut, Monchhofstrasse 12-14, 69120 Heidelberg, Germany
[15] Dipartimento di Astronomia, Università di Bologna, via Ranzani 1, 40127 Bologna, Italy

Received 3 September 2010 / Accepted 3 October 2012

ABSTRACT

We evaluate the construction methodology of an all-sky catalogue of galaxy clusters detected through the Sunyaev-Zel'dovich (SZ) effect. We perform an extensive comparison of twelve algorithms applied to the same detailed simulations of the millimeter and submillimeter sky based on a *Planck*-like case. We present the results of this "SZ Challenge" in terms of catalogue completeness, purity, astrometric and photometric reconstruction. Our results provide a comparison of a representative sample of SZ detection algorithms and highlight important issues in their application. In our study case, we show that the exact expected number of clusters remains uncertain (about a thousand cluster candidates at $|b| > 20$ deg with 90% purity) and that it depends on the SZ model and on the detailed sky simulations, and on algorithmic implementation of the detection methods. We also estimate the astrometric precision of the cluster candidates which is found of the order of $\sim$2 arcmin on average, and the photometric uncertainty of about 30%, depending on flux.

Key words. cosmology: observations – galaxies: clusters: general – galaxies: clusters: intracluster medium – cosmic background radiation – methods: data analysis

1. Introduction

Galaxy cluster catalogues have played a long-standing, vital role in cosmology, providing important information on topics ranging from cosmological parameters to galaxy formation (Rosati et al. 2002; Voit 2005). In particular, recent X-ray cluster catalogues have proved valuable in establishing the standard cosmological model (e.g., Schuecker et al. 2003; Vikhlinin et al. 2009). The science potential of large cluster surveys is strong: They are, for instance, considered one of the central observational tools for illuminating the nature of dark energy (e.g., the Dark Energy Task Force Report Albrecht et al. 2006, 2009). A suite of large cluster surveys planned over the coming years in the optical/IR, X-ray and millimeter bands will greatly extend the reach of cluster science by probing much larger volumes to higher redshifts with vastly superior statistics and control of systematics.

The *Planck* SZ cluster catalogue will be one of the important players in this context. Surveying the entire sky in 9 millimeter/submillimeter bands with $\sim$5–10 arcmin resolution over the channels most sensitive to the cosmic microwave background (CMB) anisotropies, the *Planck* satellite will find large numbers of clusters through the Sunyaev-Zel'dovich (SZ) effect (Sunyaev & Zeldovich 1970, 1972; Birkinshaw 1999; Carlstrom et al. 2002). The advantages of this, much anticipated, technique include efficient detection of distant clusters and selection based on an observable expected to correlate tightly with cluster mass (Bartlett 2002; da Silva et al. 2004; Motl et al. 2005; Nagai 2006; Bonaldi et al. 2007; Shaw et al. 2008). An official mission deliverable, the *Planck* SZ catalogue will be the first all-sky cluster catalogue since the workhorse catalogues from the ROSAT All-Sky Survey (RASS, Truemper 1992), in other words, *Planck* will be the first all-sky cluster survey since the early 1990s!

Within the Planck Consortium, a considerable effort has been conducted for the scientific evaluation of the cluster catalogue construction methodology. As part of this evaluation effort, we completed an extensive comparison of twelve algorithms applied to detailed simulations of *Planck* data based on the *Planck* Sky Model (PSM). This study was dubbed "The SZ Challenge" and was carried out in two steps using different SZ cluster models and cosmologies; these are referred to as Versions 1 and 2 and more fully explained below. We report the findings of these initial studies in terms of catalogue completeness and purity, as well as astrometric and photometric accuracy and precision.

The article is organized as follows: In the next section we detail our sky simulations, including a brief description of their basis, the PSM (Delabrouille et al. 2012). The following section then introduces the different catalogue construction methodologies employed, before moving on to a presentation of each of the twelve algorithms in the study. We present the results of the challenge in Sect. 4, followed by a comparative study of algorithmic performance. We conclude with a discussion of both the limitations of this study and future directions.

2. Simulations

2.1. The Planck Sky Model

One of the important differences between the present work and previous studies of *Planck* SZ capabilities is the detailed and rather sophisticated simulation of millimeter and submillimeter sky emission used here. Our sky simulations are based on an early development version of the PSM (Delabrouille et al. 2012), a flexible software package developed within the Planck Collaboration for making predictions, simulations and constrained realisations of the microwave sky. The simulations used for this challenge are not polarised (only temperature maps are useful for detecting clusters using the thermal SZ effect).

The CMB sky is based on the best fit angular power spectrum model of WMAP. The CMB realisation is not constrained by actual observed CMB multipoles, in contrast to the simulations used by Leach et al. (2008).

Diffuse Galactic emission is described by a four component model of the interstellar medium comprising free-free, synchrotron, thermal dust and spinning dust and is based on Miville-Deschênes et al. (2008, see Miville-Deschênes 2009, for a review). The predictions rely on a number of sky templates with different angular resolutions. In order to simulate the sky at *Planck* resolution we have added small-scale fluctuations to some of the templates to increase the fluctuation level as a function of the local brightness and therefore reproduce the non-Gaussian and non-uniform properties of the interstellar emission. The procedure used to add small scales is presented in Miville-Deschênes et al. (2007).

Free-free emission is based on the model of Dickinson et al. (2003) assuming an electronic temperature of 7000 K. The spatial structure of the emission is modeled using an Hα template corrected for dust extinction. The Hα map is a combination of the Southern H-Alpha Sky Survey Atlas (SHASSA, Gaustad et al. 2001) and the Wisconsin H-Alpha Mapper (WHAM, Haffner et al. 2003), smoothed to obtain a uniform angular resolution of 1°. Dust extinction is inferred using the $E(B-V)$ all-sky map of Schlegel et al. (1998). As mentioned earlier, small scales were added in both templates to match the *Planck* resolution. The free-free emission law is constant over the sky, as it depends only on the electronic temperature, taken as a constant here (see however Wakker et al. 2008, for a description of high-velocity clouds not detected by the WHAM survey and hence not included in our simulations).

Synchrotron emission is based on an extrapolation of the 408 MHz map of Haslam et al. (1982) from which an estimate of the free-free emission was removed. In any direction on the sky, the spectral emission law of the synchrotron is assumed to follow a power law, $T_b^{\rm sync} \propto \nu^{\beta}$. We use a pixel-dependent spectral index β derived from the ratio of the 408 MHz map and the estimate of the synchrotron emission at 23 GHz in the data obtained by Miville-Deschênes et al. (2008).

The thermal emission from interstellar dust is estimated using model 7 of Finkbeiner et al. (1999). This model, fitted to the FIRAS data (7° resolution), assumes that each line of sight can be modeled by the sum of the emission from two dust populations, one cold and one hot. Each grain population is in thermal equilibrium with the radiation field and thus has a grey-body spectrum, so that the total dust emission is modelled as

$$I_\nu \propto \sum_{i=1}^{2} f_i \nu^{\beta_i} B_\nu(T_i), \tag{1}$$

where $B_\nu(T_i)$ is the Planck function at temperature T_i. In model 7 the emissivity indices are $\beta_1 = 1.5$, $\beta_2 = 2.6$, and $f_1 = 0.0309$ and $f_2 = 0.9691$. Once these values are fixed, the dust temperature of the two components is determined using only the ratio of the observations at 100 μm and 240 μm. For this purpose, we use the 100/240 μm map ratio published by Finkbeiner et al. (1999). Knowing the temperature and β of each dust component at a given position on the sky, we use the 100 μm brightness at that position to scale the emission at any frequency using Eq. (1).

Spinning dust emission uses as a template the dust extinction map $E(B-V)$, and uses an emission law uniform on the sky, based on the model of Draine & Lazarian (1998), assuming a warm neutral medium (WNM).

We emphasise that the emission laws of both synchrotron and dust vary across the sky. The spectral index of free-free and the emission law of spinning dust, however, are taken as uniform on the sky.

Point sources are modeled with two main categories: radio and infrared. In the present simulation, none of two is correlated with the SZ signal. Simulated radio sources are based on the NVSS or SUMSS and GB6 or PMN catalogues. Measured fluxes at 1 and/or 4.85 GHz are extrapolated to 20 GHz using their measured SED when observed at two frequencies. Sources for which a flux measurement is available at a single frequency have been randomly assigned to either the steep- or to the flat-spectrum class in the proportions observationally determined by Fomalont et al. (1991) for various flux intervals, and assigned a spectral index randomly drawn from the corresponding distribution. Source counts at 5 and 20 GHz obtained in this way are compared, for consistency, with observed counts, with the model by Toffolatti et al. (1998), and with an updated version of the model by de Zotti et al. (2005), allowing for a high-redshift decline of the space density of both flat-spectrum quasars (FSQs) and steep-spectrum sources (not only for FSQs as in the original model). Further extrapolation at *Planck* frequencies has been made allowing a change in SED above 20 GHz, assuming again a distribution in flat and steep populations. For each of these two populations, the spectral index is randomly drawn within a set of values compatible with the typical average and dispersion.

Table 1. Characteristics of instrumental values taken from *Planck* blue book for a 14 month nominal mission.

Channel	30 GHz	44 GHz	70 GHz	100 GHz	143 GHz	217 GHz	353 GHz	545 GHz	857 GHz
FWHM [arcmin]	33	24	14	10	7.1	5	5	5	5
$\sigma_{\rm pixel}$ [m$K_{\rm CMB}$]	0.131	0.130	0.126	0.057	0.029	0.046	0.137	1.241	56.639

Notes. $\sigma_{\rm pixel}$ refers to the standard deviation of the 1.7′ (Healpix $n_{\rm side} = 2048$) pixel noise maps at the considered frequency.

Infrared sources are based on the catalogue, and modeled as dusty galaxies (Serjeant & Harrison 2005). IRAS coverage gaps were filled by randomly adding sources with a flux distribution consistent with the mean counts. Fainter sources were assumed to be mostly sub-millimeter bright galaxies, such as those detected by SCUBA surveys. These were modelled following Granato et al. (2004) and assumed to be strongly clustered, with a comoving clustering radius $r_0 \simeq 8\,h^{-1}$ Mpc. Since such sources have a very high areal density, they are not simulated individually but make up the sub-mm background.

The SZ component is described in detail in the following section.

Component maps are produced at all *Planck* central frequencies. They are then co-added and smoothed with Gaussian beams as indicated in Table 1, extracted from the *Planck* blue book. We thus obtain a total of nine monochromatic sky maps.

Finally, inhomogeneous noise is simulated according to the pixel hit count corresponding to a nominal 14-month mission[1] using the Level-S simulation tool (Reinecke et al. 2006). The rms noise level in the simulated maps is given in Table 1 from the *Planck* blue book. It is worth noting that the in-flight performances of *Planck*-HFI as reported by the Planck Collaboration (Planck Collaboration 2011a) are better than the requirements.

2.2. The SZ component

We simulate the SZ component using a semi-analytic approach based on an analytic mass function $\mathrm{d}N(M,z)/\mathrm{d}M\mathrm{d}z$. After selecting cosmological parameters (h, $\Omega_{\rm m}$, Ω_Λ, σ_8), the cluster distribution in the mass-redshift plane (M,z) is drawn from a Poisson law whose mean is given by the mass function. Clusters are spanning the mass range $5\times10^{13}\ M_\odot < M_{\rm vir} < 5\times10^{15}\ M_\odot$ and the redshift range $0 < z < 4$. Cluster Galactic coordinates (l,b) are then uniformly drawn on the sphere. We compute the SZ signal for each dark matter halo following two different models, producing two simulations (v1 and v2) with different sets of cosmological parameters and mass functions and SZ signals[2].

2.2.1. SZ challenge v1

For the first version of the SZ Challenge, we used $h = 0.7$, $\Omega_{\rm m} = 0.3$, $\Omega_\Lambda = 0.7$, $\sigma_8 = 0.85$ and the Sheth-Tormen mass function Sheth & Tormen (1999). We assume that the clusters are isothermal and that the electron density profile is given by the β-model, with $\beta = 2/3$, and core radius scaling as $M^{1/3}$. We truncate the model at the virial radius, $r_{\rm vir}$, and choose the core radius $r_{\rm c} = r_{\rm vir}/10$. The virial radius here is defined according to the spherical collapse model. The temperature of each cluster is derived using a mass-temperature given in Colafrancesco et al. (1997) with $T_{15} = 7.75$ keV, consistent with the simulations of Eke et al. (1998). For more details on this model, we refer the reader to Sect. 5 of de Zotti et al. (2005).

2.2.2. SZ challenge v2

The second version of the SZ Challenge was produced using a WMAP5 only cosmology (Dunkley et al. 2009) ($h = 0.719$, $\Omega_{\rm m} = 0.256$, $\Omega_\Lambda = 0.744$, $\sigma_8 = 0.798$). We used the Jenkins mass function (Jenkins et al. 2001). The SZ emission is modeled using the universal pressure profile derived from the X-ray REXCESS cluster sample (Arnaud et al. 2010) which predicts profile and normalisation of SZ clusters given their mass and redshift. The profile is well fitted by a generalized NFW profile that is much steeper than the β-profile in the outskirts. Moreover, for a given mass, the normalisation of the SZ flux is ~15% lower than the normalisation of SZ Challenge v1. This profile was used as the baseline profile in the SZ early results from *Planck* (Planck Collaboration 2011b,f,e,c,g).

Neither of the two sets of simulations (v1 and v2) contains point sources within clusters. The effect of contamination by radio or infrared point sources in clusters was therefore not studied here[3]. We neither include relativistic electronic populations within clusters. As for point sources, this effect was not studied here[4].

3. Methods and algorithms

The SZ Challenge was run as a blind test by providing the simulated sky maps. Participating teams, ten, were then asked to run their algorithms, twelve in total on the simulated data and supply a cluster catalogue with

1. (α,δ): cluster sky coordinates;
2. $Y_{\rm rec}$: recovered total SZ flux, in terms of the integrated Compton-Y parameter;
3. $\Delta Y_{\rm rec}$: estimated flux error, i.e., the method's internal estimate of flux error;
4. $\theta_{\rm rec}$: recovered cluster angular size, in terms of equivalent virial radius;
5. $\Delta\theta_{\rm rec}$: estimated size error (internal error).

---

[1] Note that since launch in May 2009, the observed Helium consumption for the *Planck*-HFI dilution cooler indicates that the instrument can operate for about 30 months. A mission extension has been approved by ESA accordingly.

[2] We assume spherical symmetry for the individual SZ clusters and do not take into account any scatter in the distribution of pressure profiles.

[3] The effect of radio sources ($\nu < 217$ GHz) is to reduce the observed SZ signal at a given frequency while the effect of infrared sources ($\nu > 217$ GHz) is to increase it. However, the extraction algorithms being multifrequency, their sensitivity to point sources is expected to be weaker than for single frequency extractions because of the different spectral dependence of point sources and SZ clusters.

[4] The effect has been very recently studied within the Planck Collaboration: assuming a non relativistic spectrum for extracting clusters biases the flux low by about 10% in direction of massive ($M_{\rm vir} > 10^{15}\ M_\odot$) clusters (Planck Collaboration, in prep.).

The different methods were divided into two classes: direct methods that produce a cluster catalogue applying filters directly to a set of frequency maps, and indirect methods that first extract a thermal SZ map and then apply source finding algorithms.

In this classification, the 12 algorithms studied were:

- Direct methods:
  - MMF1: matched multi-filters (MMF) as implemented by Harrison.
  - MMF2: MMF as described in Herranz et al. (2002).
  - MMF3: MMF as described in Melin et al. (2006).
  - MMF4: MMF as described in Schäfer et al. (2006).
  - PwS: Bayesian method PowellSnakes as described in Carvalho et al. (2009).
- Indirect methods:
  - BNP: Bayesian Non-parametric method as described in Diego et al. (2002), followed by SExtractor (Bertin & Arnouts 1996) to detect clusters and perform photometry.
  - ILC1: All-sky internal linear combination (ILC) on needlet coefficients[5] (similar to the method used for CMB extraction in Delabrouille et al. 2009) to get an SZ map, followed by matched filters on patches to extract clusters and perform photometry.
  - ILC2: Same SZ map Delabrouille et al. (2009), but followed by SExtractor on patches instead of a matched filter to extract the clusters. Photometry or flux measurement is however done using matched filters at the position of the detected clusters.
  - ILC3 developed by Chon and Kneissl: ILC in real space and filtering in harmonic space to obtain an SZ map, followed by fitting a cluster model.
  - ILC4 developed by Melin: ILC on patches in Fourier space to obtain SZ maps, followed by SExtractor to detect clusters and matched multifilters to perform photometry.
  - ILC5 developed by Yvon: ILC on patches in wavelet space to obtain SZ maps, followed by SExtractor to detect clusters and perform photometry.
  - GMCA: Generalized Morphological Component Analysis as described in Bobin et al. (2008), followed by wavelet filtering and SExtractor to extract clusters and matched multifilters to perform photometry.

All of the algorithms make use of the known frequency spectrum of the SZ signal; attempts to detect clusters without this prior knowledge perform significantly worse. A summary of the characteristics of the codes as well as their treatment of the point sources, foreground removal and masking is given in Table 2. Further details about the algorithms are given in the following subsections.

3.1. Matched multifilter methods

The multifrequency matched filter (MMF) enhances the contrast (signal-to-noise) of objects of known shape and known spectral emission law over a set of observations containing correlated contamination signals. It offers a practical way of extracting a SZ clusters using multifrequency maps. The method makes use of the universal thermal SZ effect frequency dependance (assuming electrons in clusters are non-relativistic), and adopts a spatial (angular profile) template. The filter rejects foregrounds using a linear combination of maps (which requires an estimate of the statistics of the contamination) and uses spatial filtering to suppress both foregrounds and noise (making use of prior knowledge of the cluster profile). In all cases discussed here, the adopted template is identical to the simulated cluster profiles, except for MMF2 on SZ Challenge v2. The MMF has been studied extensively by Herranz et al. (2002) and Melin et al. (2006).

Three of the MMF methods tested here work with projected flat patches of the sky, and one method works directly on the pixelised sphere.

In the first case, the full-sky frequency maps are projected onto an atlas of overlapping square flat regions. The filtering is then implemented on sets of small patches comprising one patch for each frequency channel. For each such region, the nine frequency maps are processed with the MMF. A simple thresholding detection algorithm is used to find the clusters and produce local catalogues. The MMF is applied with varying cluster sizes to find the best detection for each cluster. This provides an estimate of the angular size in addition to the central Compton parameter. Each algorithm explored its own, but similar, range of angular scales; MMF3, for example, runs from $\theta_v = 2$ to 150 arcmins. The catalogues extracted from individual patches are then merged into a full-sky catalogue that contains the position of the clusters, their estimated central Compton parameter, the virial radius and an estimation of the error in the two later quantities. The integrated Compton parameter is derived from the value of the central Compton parameter and the radius of the cluster.

In the following, we give relevant details specific to each implementation of the MMF.

3.1.1. MMF1

The performance of the MMF1 algorithm is sensitive to the accuracy of the evaluation of the power spectra and cross-power spectra of the non-SZ component of the input maps. The detection is performed in two passes, the first detecting the highest signal-to-noise SZ clusters, and the second detecting fainter clusters after the removal of the contribution of the brightest ones from the power spectra estimated on the maps.

The merging of the catalogues from distinct patches is implemented with the option of discarding detections found in the smallest radius bin. These detections essentially correspond to spatial profiles indistinguishable from that of a point source. This option permits better control of the contamination by point sources, as a disproportionate fraction of the spurious detections occur in this bin ; despite their different spectral signature, point sources can occasionally pass through the filter. Using this option of MMF1 reduces the contamination at a given threshold (see Sect. 4.1 for definitions of this and other diagnostics of catalogue content) depending on the actual profile of the SZ clusters.

3.1.2. MMF2

The MMF2 algorithm follows closely the method described in Herranz et al. (2002). The method is simple and quite robust, although the performance depends on the model assumed for the radial profile of the clusters. For this work, a truncated multiquadric profile similar to a β-model has been used for SZ Challenge v1 and v2. The profile is not a good match for the simulated profile in SZ Challenge v2. This does not affect significantly the completeness and purity of the method (as shown in Sect. 4) but the extracted flux is biased with respect to the

---

[5] Needlet coefficients are the equivalent of Fourier coefficients in the adopted spherical wavelet domain.

Table 2. Summary of the algorithms compared in the SZ Challenge.

Method	Shape matching	CPU time (h)	Patches (size deg.)	Number of patches	PS subtraction method	FG subtraction method	Main characteristics
MMF1	Yes	50–60	14.6° × 14.6°	640	–	–	Best yield among MMFs Good photometry
MMF2	Yes	31	14.6° × 14.6°	371	–	–	Good yield Good photometry
MMF3	Yes	5	10° × 10°	504	mask 10σ PS	–	Good yield Good photometry
MMF4	Yes		full sky	–	–	–	Poor yield (see Sect. 3.1.4) No photometry
PwS	Yes	5.73	14.6° × 14.6°	2064	–	–	Good yield Good photometry
BNP	No	15	10° × 10°	512	MHW	Subtract 857	Median yield Poor photometry
ILC1	Yes	2–3	see caption	(504)	–	–	Good yield Good photometry
ILC2	No	2–3	see caption	(504)	–	–	Best yield among ILCs Good photometry
ILC3	Yes	24	full sky	–	–	Template fitting	Poor yield Good photometry
ILC4	Yes^a	6	10° × 10°	504	mask 10σ PS	–	Good yield Good photometry
ILC5	No	0.2	11° × 11°	461	SExt.	–	Poor yield (see Sect. 3.3.5) Poor photometry
GMCA	No	4	10° × 10°	504	–	–	Median yield Good photometry

Notes. The first column shows the name of the method. The second column indicates when the code is using a prior on the SZ cluster shape. The uperscript ^{a} indicate that the detection did not use a shape prior but that the computation of the SZ flux did. The third column gives the performance in terms of CPU hours needed to complete the analysis. The fourth and fifth column show whether the analysis was made using all-sky maps or projected patches, their area in square degrees and the number of patches. Methods ILC1 and ILC2 work with full sky maps for producing an SZ map (by ILC on needlet coefficients) and then work with 504 small patches for cluster detection by matched filtering (ILC1) or using SExtractor (ILC2). The sixth and seventh columns provide information about any specific method used for subtracting point sources (PS) and Galactic foregrounds (FG). Note that both the MMF and the ILC methods have a built-in way for subtracting both point sources and diffuse foregrounds, by treating them as additional noise (of astrophysical origin) correlated across the channels. Note, also, that the study is made only on clusters at $|b| > 20$ degrees Galactic latitude for all methods. The eighth column summarizes the main characteristics of each algorithm in terms of yield at 90% purity and photometric accuracy.

input. The family of profiles used by the algorithm can however be adjusted.

3.1.3. MMF3

The MMF3 SZ extraction algorithm is an all-sky extension of the matched multifrequency filter described in Melin et al. (2006). It has been used for the production of the early SZ cluster sample (Planck Collaboration 2011b). In the version used for the SZ challenge, auto and cross power spectra used by the filter do not rely on prior assumptions about the noise, but are directly estimated from the data. They are thus adapted to the local instrumental noise and astrophysical contamination.

3.1.4. MMF4

The spherical matched and scale adaptive filters (Schäfer et al. 2006) are generalisations of the filters proposed by Herranz et al. (2002) for spherical coordinates. Just like their counterparts they can be derived from an optimisation problem and maximise the signal to noise ratio while being linear in the signal (matched filter) and being sensitive to the size of the object. The algorithm interfaces to the common HEALPIX package and treats the entire celestial sphere in one pass.

The most important drawback is the strong Galactic contamination – the filter was not optimised to deal with a Galactic cut like many of the other algorithms, although it is in principle possible to include that extension. The large noise contribution due to the Galaxy is the principal reason why the performance of the filter suffers in comparison to the approach of discarding a large fraction of the sky.

3.2. *Bayesian methods*

3.2.1. PowellSnakes

PowellSnakes (PwS; Carvalho et al. 2009) is a fast multi-frequency Bayesian detection algorithm. It analyses flat sky patches using the ratio

$$\rho \equiv \frac{\Pr(H_1|\boldsymbol{d})}{\Pr(H_0|\boldsymbol{d})}, \tag{2}$$

where H_1 is the detection hypothesis, "*There is a source*" and H_0 the null hypothesis "*Only background is present*" (Jaynes 2003). Applying Bayes theorem to the above formula one gets

$$\rho = \frac{\Pr(\boldsymbol{d}|H_1)\Pr(H_1)}{\Pr(\boldsymbol{d}|H_0)\Pr(H_0)} = \frac{\mathcal{Z}_1}{\mathcal{Z}_0}\frac{\Pr(H_1)}{\Pr(H_0)}, \tag{3}$$

where

$$\mathcal{Z} = \int \mathcal{L}(\boldsymbol{\Theta})\,\pi(\boldsymbol{\Theta})\,\mathrm{d}^D\boldsymbol{\Theta}, \tag{4}$$

is the evidence, $\mathcal{L}(\mathbf{\Theta})$ is the likelihood, $\pi(\mathbf{\Theta})$ is the prior and $\mathbf{\Theta}$ a vector representing the parameter set.

An SZ parameterised template profile of the clusters $\boldsymbol{s}(\boldsymbol{X}, \boldsymbol{A}) \equiv \xi\ \tau(\boldsymbol{a},\ x - X,\ y - Y)$, is assumed known and fairly representative of the majority of the clusters according to the resolution and signal-to-noise ratio of the instrumental setup, where $\tau(\ldots)$ is the general shape of the objects (beta or Arnaud et al. profile) and $\boldsymbol{a}_j$ a vector which contains the parameters controlling the geometry of one specific element (core/scale radius, parameters of the beta or Arnaud et al. profile).

The algorithm may be operated on either "*Frequentist mode*" where the detection step closely resembles a multi-frequency multi-scale "*matched filter*" or "*Bayesian mode*" where the posterior distributions are computed resorting to a simple "*nested sampling*" algorithm (Feroz & Hobson 2008).

The acceptance/rejection threshold may be defined either by using "*Decision theory*" where the expected loss criterion is minimised or by imposing a pre-defined contamination ratio. In the case of a loss criterion, the symmetric criterion – "*An undetected cluster is as bad as spurious cluster*" – is used.

3.2.2. BNP

This method is described in detail in Diego et al. (2002). It is based on the maximization of the Bayesian probability of having an SZ cluster given the multifrequency data with no assumptions about the shape nor size of the clusters. The method devides the sky into multiple patches of about 100 sq. degrees and performs a basic cleaning of the Galactic components (by subtracting the properly weighted 857 GHz map from the channels of interest for SZ) and point sources (using a Mexican Hat Wavelet). The cleaned maps are combined in the Bayesian estimator and the output map of Compton parameters is derived. SExtractor is applied to the map of reconstructed Compton parameter to detect objects above a given threshold and compute their flux. The thresholds are based on the background or noise estimated by SExtractor. In order to compute the purity, different signal-to-noise ratios (ranging from 3 to 10) are used to compute the flux. The method assumes a power spectrum for the cluster population although this is not critical.

The main advantage of the method resides in its robustness (almost no assumptions) and its ability to reconstruct both extended and compact clusters. The main limitation is the relatively poor reconstruction of the total flux of the cluster as compared to matched filters.

3.3. Internal linear combination methods

The ILC is a simple method for extracting one single component of interest out of multifrequency observations. It has been widely used for CMB estimation on WMAP data (Bennett et al. 2003; Tegmark et al. 2003; Eriksen et al. 2004; Park et al. 2007; Delabrouille et al. 2009; Kim et al. 2009; Samal et al. 2009). A general description of the method can be found in Delabrouille & Cardoso (2009).

The general idea behind the ILC is to form a linear combination of all available observations which has unit response to the component of interest, while minimizing the total variance of the output map. This method assumes that all observations $y_i(p)$, for channel i and pixel p, can be written as the sum of one single template of interest scaled by some coefficient a_i, and of unspecified contaminants which comprise noise and foregrounds, i.e.

$$y_i(p) = a_i s(p) + n_i(p), \tag{5}$$

where $y_i(p)$ is the observed map in channel i, $s(p)$ is the template of interest (here, the SZ map), and $n_i(p)$ comprise the contribution of both all astrophysical foregrounds (CMB, galactic emission, point sources...) and of instrumental noise. This equation can be recast as:

$$\boldsymbol{y}(p) = \boldsymbol{a} s(p) + \boldsymbol{n}(p). \tag{6}$$

To first order, linear combinations of the inputs of the form $\sum_i w_i y_i(p)$ guarantee unit response to the component of interest provided that the constraint $\sum_i w_i a_i = 1$ is satisfied (there are, however, restrictions and higher order effects, which are discussed in detail in the appendix of Delabrouille et al. 2009; Dick et al. 2010). It can be shown straightforwardly (Eriksen et al. 2004; Delabrouille & Cardoso 2009) that the linear weights which minimize the variance of the output map are:

$$\boldsymbol{w} = \frac{\boldsymbol{a}^t \widehat{\mathsf{R}}^{-1}}{\boldsymbol{a}^t \widehat{\mathsf{R}}^{-1} \boldsymbol{a}}, \tag{7}$$

where $\widehat{R}$ is the empirical covariance matrix of the observations. What distinguishes the different ILC implementations is essentially the domains over which the above solution is implemented.

3.3.1. ILC1

The needlet ILC method works in two steps. First, an SZ map is produced by ILC, with a needlet space implementation similar to that of Delabrouille et al. (2009). The use of spherical needlets permits the ILC filter to adapt to local conditions in both direct (pixel) space and harmonic space. Input maps include all simulated *Planck* maps, as well as an external template of emission at 100 microns (Schlegel et al. 1998), which helps subtracting dust emission. The cluster catalogue is then obtained by matched filtering on small patches extracted from the needlet ILC SZ full-sky map, as described in Melin et al. (2006).

3.3.2. ILC2

The ILC2 approach relies on the same processing for photometry, cluster size, and signal-to-noise estimates as in ILC1, but in this case the detection of cluster candidates is made using SExtractor on a Wiener-filtered version of the ILC1 map.

While the extraction of the ILC map works on full sky maps, using the needlet framework to perform localized filtering, here again the detection of cluster candidates, and the estimation of size and flux, are performed on small patches (obtained by gnomonic projection).

3.3.3. ILC3

In this method, a filter in the harmonic domain is applied to construct a series of maps that are sensitive to the range of cluster scales. We used a Mexican-hat filter constructed from two Gaussians, one with 1/4 the width of the other. A list of cluster candidates is compiled using a peak finding algorithm, which searches for enhanced signal levels in the individual map by fitting cluster model parameter. We employed the β-model profile with $\beta = 2/3$ convolved with the Planck beams. The catalogue produced then includes as parameters the cluster location, the flux, and the size estimate. The errors on these parameters are incorporated as given by the likelihoods of the fit.

Additional improvements to the method can be achieved by using more optimal foreground estimators (but probably with slower convergence). This is useful especially for the fainter clusters, or those confused to a high degree by source contamination.

3.3.4. ILC4

The ILC4 method is a standard ILC in Fourier space performed on the square patches. It is implemented independently in annuli in wave number (modulus of the Fourier mode) by applying weights, according to Eq. (7), this time in the Fourier domain. The cluster detection is performed using SExtractor on the reconstructed SZ map. The flux estimation is performed on the original multifrequency maps (small patches) using the MMF at the position of the SExtractor detections.

3.3.5. ILC5

This algorithm is designed to work on local noisy multichannel maps in the wavelet domain. The representation of galaxy clusters in an appropriate biorthogonal wavelet basis is expected to be sparse compared to the contributions of other astrophysical components. This should ease the subsequent SZ separation using the ILC method at each wavelet scale. The reverse wavelet transform is then applied to estimate local SZ-maps. The latter are convolved using a Gaussian beam of 5 arcmin *FWHM* to reduce the noise prior to cluster detection using SExtractor with a threshold fixed classically to a multiple of the rms noise (signal-to-noise ratio ranging from 3 to 6). The brightest IR galaxies and radiosources are masked to reduce contamination. Finally, multiple detections due to the overlap of local maps are removed. Multiscale ILC proved to be more efficient than regular ILC to remove large angular scale contamination on local map simulations. However, the cluster catalogue appears comparatively more contaminated which may be due to an imperfect cleaning of multiple detections. Also, the known point sources were only masked before detection with SExtractor. Masking the observed sky maps earlier could improve the component separation using Multiscale ILC. Doing so may prevent a few very bright pixels biasing the ILC parameter estimation but in turn raises the question of data interpolation across masked regions. The other implementations of the ILC do mask point sources before combining the maps and are thus not subject to this bias.

3.4. GMCA

Generalized morphological component analysis is a blind source separation method devised for separating sources from instantaneous linear mixtures using the model given by: $Y = A\mathbf{S} + n$. The components $\mathbf{S}$ are assumed to be sparsely represented (i.e. have a few significant samples in a specific basis) in a so-called sparse representation $\mathbf{\Phi}$ (typically wavelets). Assuming that the components have a sparse representation in the wavelet domain is equivalent to assuming that most components have a certain spatial regularity. These components and their spectral signatures are then recovered by minimizing the number of significant coefficients in $\mathbf{\Phi}$:

$$\min_{\{\mathbf{S},\mathbf{S}\}} \lambda \|\mathbf{S}\mathbf{\Phi}^T\| + \frac{1}{2}\|\mathbf{Y} - \mathbf{A}\mathbf{S}\|_2^2 \qquad (8)$$

where $\|\ldots\|_2$ is the L_2 (Euclidean) norm. In Bobin et al. (2008), it was shown that sparsity enhances the diversity between the components thus improving the separation quality. The spectral signatures of CMB and SZ are assumed to be known. The spectral signature of the free-free component is approximately known up to a multiplicative constant (power law with fixed spectral index).

Hence, GMCA furnishes a noisy SZ map in which we want to detect the SZ clusters. This is done in three steps:

- wavelet denoising;
- SExtractor to extract the clusters from the noise-free SZ map, and finally;
- a maximum likehood to get the flux of the detected sources.

4. Results

We evaluated each extracted catalogue in terms of catalogue content and photometric recovery based on comparisons between the extracted catalogues and the simulated input SZ cluster catalogue. For this purpose, we cut the input catalogue at $Y > 5 \times 10^{-4}$ arcmin^2, well below the theoretical Planck detection limit (see below), and restrict ourselves to the high latitude sky at $|b| > 20$ deg to reduce contamination by galactic foregrounds. We then cross-match the candidate cluster in a given catalogue to a corresponding input cluster. Each match results in a true detection, while candidates without a match are labeled as *false detections*. In a second step, we compare the extracted properties, namely SZ Compton parameter and size, of the true detections to the input cluster properties.

Angular proximity was the only association criterion used for the matching. Specifically, we matched an extracted cluster to an input cluster if their separation on the sky $\theta < \theta_{\max} = f(\theta_v)$, a function of the *true* angular virial radius of the (input) cluster. The function $f(\theta_v)$ varied over three domains: $f(\theta_v) = 5$ arcmin for $\theta_v < 5$ arcmin; $f(\theta_v) = \theta_v$ for 5 arcmin $< \theta_v <$ 20 arcmin; and $f(\theta_v) = 20$ arcmin for $\theta_v > 20$ arcmin.

We first focus on the catalogue *completeness* and *purity*, both of which we define immediately below. We then test the accuracy of the recovered flux and size estimates, as well as each algorithm's ability to internally evaluate the uncertainties on these photometric quantities. Since many fewer codes ran on the Challenge v2, we focus mainly on Challenge v1. We include results for those codes that did run on Challenge 2 to gauge the influence of the underlying cluster model used for the simulation.

4.1. Catalogue content

A useful *global* diagnostic is the curve of *yield* versus *global purity* for a given catalogue (see e.g. Pires et al. 2006). The former is simply the total number of clusters detected and the latter we define as $1 - \Gamma_{\rm g}$, where $\Gamma_{\rm g}$ is the global contamination rate:

$$\Gamma_{\rm g} \equiv \frac{\text{total number of false detections}}{\text{total number of detections}}. \qquad (9)$$

The yield curve is parametrized by the effective detection threshold of the catalogue construction algorithm. It is a global diagnostic because it gauges the total content of a catalogue, rather than its content as a function of flux or other measurable quantities.

Figure 1 compares the yield curves of outputs of all the algorithms in the SZ Challenge v1, and Fig. 2 those for the SZ Challenge v2. Increasing the detection threshold moves a catalogue along its curve to higher purity and lower yield. Algorithms increase in performance towards the upper right-hand corner, i.e., both high yield and high purity.

As to be expected, algorithms that locally estimate the noise (both instrumental and astrophysical), i.e. on local patches of

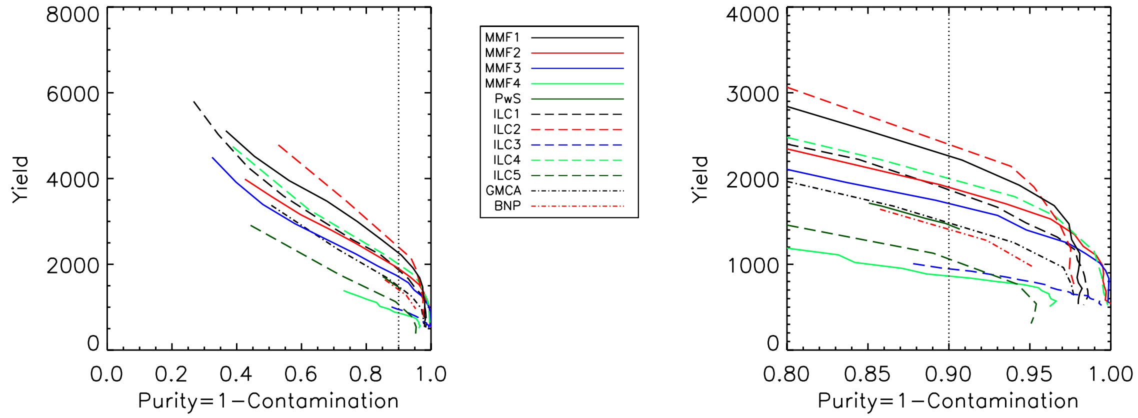

Fig. 1. For SZ Challenge v1: yield as a function of global purity. The *right handside panel* is a zoom on the high-purity region. Each curve is parameterized by the detection threshold of the corresponding algorithm. As discussed in the text, the overall value of the yields should be considered with caution, due to remaining modeling uncertainties (see text). We focus instead on relative yield between algorithms as a measure of performance.

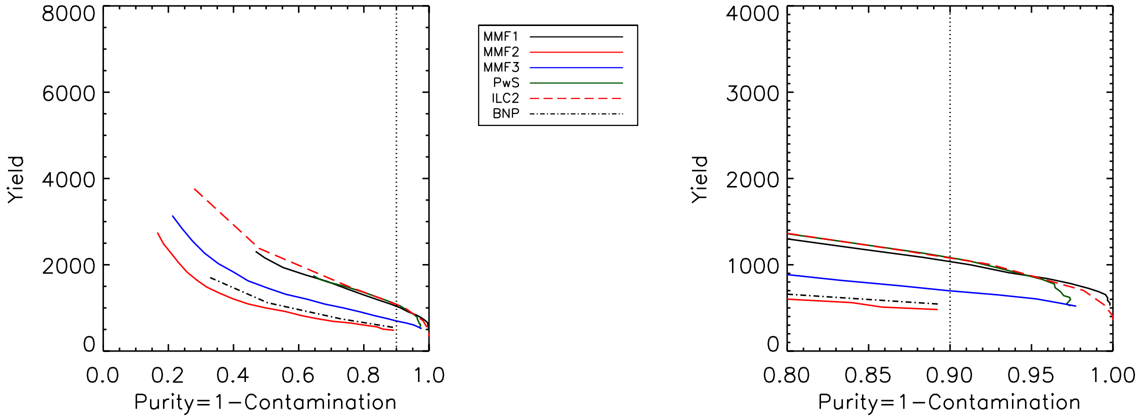

Fig. 2. For SZ Challenge v2: yield as a function of global purity. The same comment applies concerning the overall yield values; in particular, the cluster model changed significantly between the versions v1 and v2 of the Challenge resulting in lower overall yields here. Fewer codes participated in the Challenge v2 (see text).

a few square degrees, perform much better than those that employ a global noise estimate, such as MMF4 and ILC3. For those methods with local noise estimation, we note that their effective survey depth appears to anticorrelate with the *instrumental* noise, indicating that astrophysical confusion is effectively removed. This can be seen in Fig. 3, which compares the density of detected SZ sources (top panel) to the pixel hit count (bottom panel). The result illustrated with one single method, ILC2 run on the SZ challenge v1, holds for the other algorithms. The cluster detection limit appears to be primarily modulated by the instrumental noise at high Galactic latitude, as opposed to foreground emission.

Less expected, perhaps, is the fact that all algorithms tend to miss nearby clusters. These are extended objects, and although they have large total SZ flux, these clusters are "resolved-out" – missed because of their low surface brightness. This is an extreme example of resolution effects expected in the case of SZ detection in relatively low resolution experiments like *Planck*. It is not related to the foreground removing efficiency since the effect can also be mimicked in simulations including only instrumental white noise. Apart from the few clusters that are fully resolved, many have angular sizes comparable to the effective beam, and this leads to a non-trivial selection function (White 2003; Melin et al. 2005, 2006).

We emphasize that the numerical values of the yields depend on the cosmological model, on the foreground model and on the cluster model used in the simulations. They must be considered with caution because of the inherent modeling uncertainties. As for the foreground model, the templates used to model Galactic components in the PSM were chosen so that they are reasonably representative of the complexity of the diffuse galactic emission. Thanks to many new observations in particular in the IR and submm domain (Lagache et al. 2007; Viero et al. 2009; Hall et al. 2010; Amblard et al. 2011; Planck Collaboration 2011d), the models of point sources have evolved very much between the beginning of the SZ challenge and the publication of these results. These updates were not taken into account in the PSM when the study was performed. Moreover, the cluster model in challenge v1 was based on the isothermal β-model, while v2 employed a modified NFW pressure profile favoured by X-ray determinations of the gas pressure (Arnaud et al. 2010) with a normalization of the $Y-M$ relation lower by ~15% than in v1.

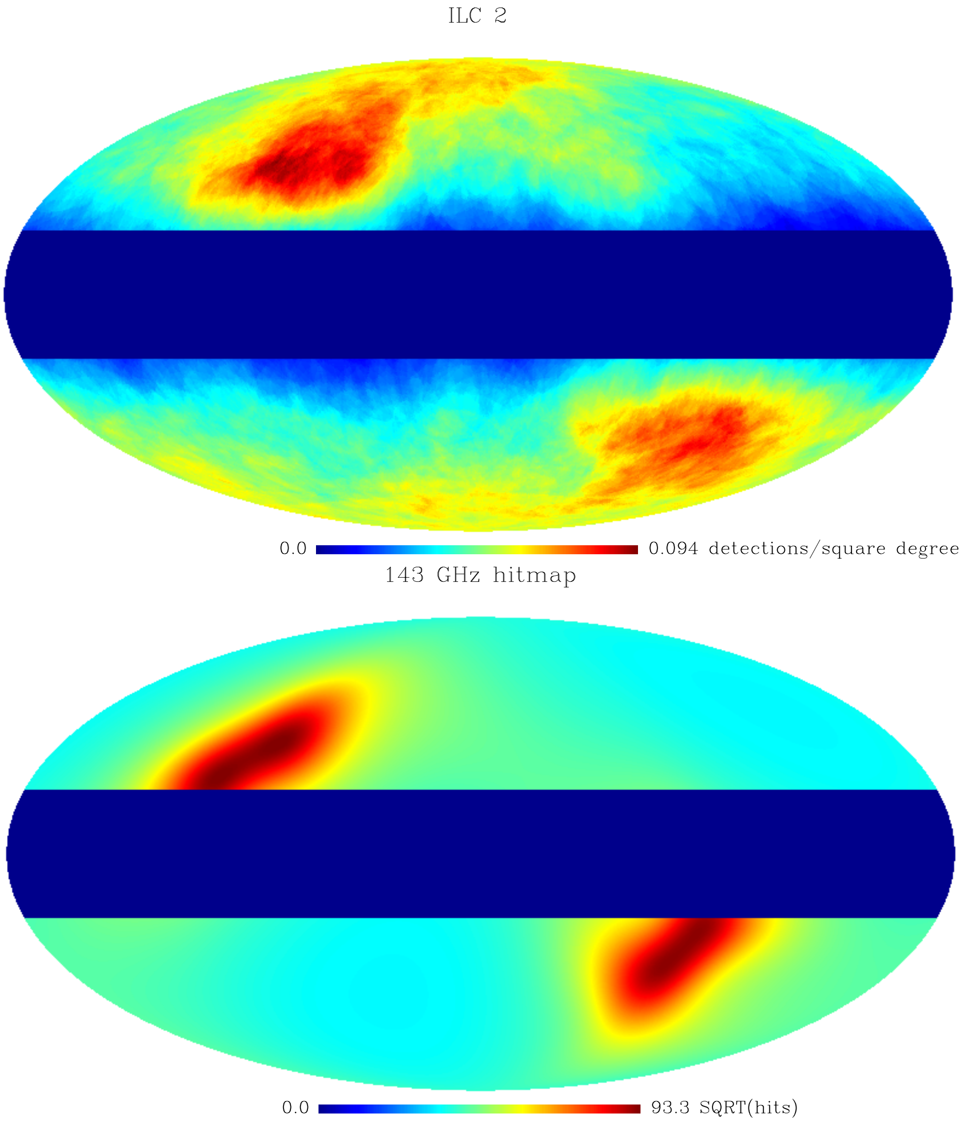

Fig. 3. Illustrated for ILC2 on the SZ Challenge v1, the detection density (*top panel*) is compared to the pixel hit count for the map at 143 GHz (*bottom panel*). The noise in the simulated *Planck* maps scales as $1/\sqrt{hits}$. At high Galactic latitudes, the detection density clearly anticorrelates with map noise. Both maps are smoothed on a scale of 20 degrees, and the Galactic plane ($|b| < 20$ deg) is masked.

Finally, σ_8 changed from 0.85 in challenge v1 to 0.796 in v2 which strongly influences the total cluster yield.

The more peaked profile actually improves detection efficiency, while the lower normalization reduces the predicted yield. Along with the much lower value of σ_8, the net result is that the yields in challenge v2 are noticeably lower than in v1 as seen in Figs. 1 and 2. We thus only discuss, in this study, the relative yields of the codes as a gauge of performance treating the absolute value of the yield with caution.

Focusing on the relative merit of the algorithms, we see that Figs. 1 and 2 display large dispersion in the yield at a given purity. This reflects of course the intrinsic performance of the algorithms, but also for the detection methods that share similar underlying algorithms, e.g. MMF and ILC, the dispersion in the yield reflects the differences in implementations (e.g. noise estimation, de-blending, etc.).

Somewhat deceptively, these yield variations correspond to only minor differences in detection threshold, as illustrated for the SZ Challenge v1 in Fig. 4. This figure traces the curves above which 90% and 10% (lower set and upper set respectively) of the clusters detected by each method lie in the true $Y-$true $\theta_{\rm v}$ plane. As already mentioned, many clusters are marginally resolved (sizes at least comparable to the beam), which means that detection efficiency depends not only on flux, but also on size[6].

The algorithms all have similar curves in this plane. This means that the differences in yield are due to only small variations of the selection curve since completeness is expected to be monotonic. The black points represent a random sample of 1/4 of the input clusters and show where the bulk of the catalogue lies. These small variations have important consequences for

---

[6] This was shown on real data in Planck Collaboration (2011b).

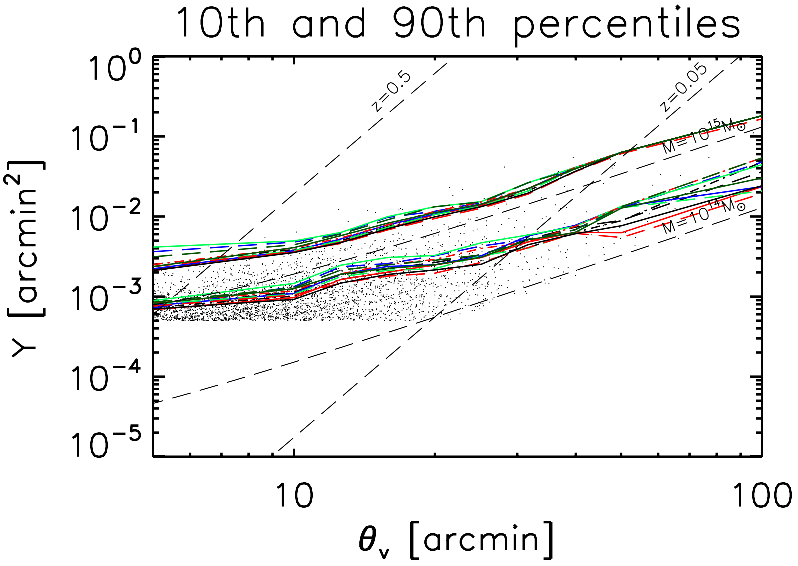

Fig. 4. Selection curves for each algorithm in the true Y–true θ_v plane for SZ Challenge v1. The lower set of curves indicate the 90th percentiles, i.e., the curve above which lie 90% of the detected clusters; the upper set corresponds to the 10th percentile. The colour codes are as in Fig. 1. We see that the *Planck* selection function depends not just on flux, but also on cluster angular size. Many clusters are at least marginally resolved by *Planck*, leading to these size effects in the selection fuction. The dashed lines show contours of fixed mass and redshift, as indicated, while the cloud of points shows the distribution of the input catalogue (in fact a subsample of 1 in 4 randomly selected input clusters). We see that small variations in selection curves generate significant yield changes.

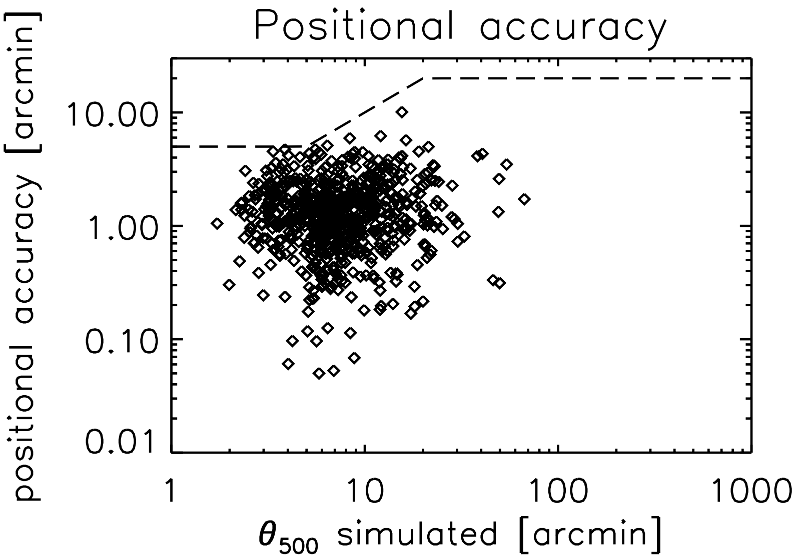

Fig. 5. Positional accuracy of the recovered clusters illustrated for MMF3 in the SZ challenge v2.

cosmological interpretation of the counts and hence must be properly quantified.

We compute for all the methods and in the SZ challenges v1 and v2 the *completeness* defined as the ratio [*true detections* (*recovered clusters*)/*simulated clusters*] over bins of true (simulated) flux Y. We find it varies from 80 to 98% at $Y_{\rm lim}$ = 10^{-2} arcmin^2 for the direct methods (based on frequency maps). The *completness* is of order of 80% at the same $Y_{\rm lim}$ for the indirect methods (based on detections in SZ maps). We note a slight increase of the completeness from the SZ Challenge v1 to v2. We also estimate the contamination of the output catalogues defined as the ratio [*false detections/total detections*]. This is evaluated as as a function of recovered flux. The average contamination of the output catalogues ranges between 6 and 13% both in the case of the challenge 1 and 2. However, the purity with respect to the Y bins differ significantly from method to method. As a general trend, the lowest Y bin, i.e. the smallet recovered fluxes centred around 10^{-3} arcmin^2, is more contaminated (∼75% on average) in the case of the indirect method than in the case of direct methods (∼50% on average).

4.2. Photometric and astrometric recovery

Cluster characterization is a separate issue from detection. It involves determination of angular positions as well as photometry. Since *Planck* will marginally resolve many clusters, photometry here means both flux $Y_{\rm rec}$ and characteristic size measurements. Moreover, each method should provide an estimate of the errors on these quantities for each object in the catalogue.

We illustrate in Fig. 5, a scatter diagram of positional offset for MMF3 as a function of *true* cluster size, $\theta_{\rm v}$. On average, all the algorithms perform similarly and recover cluster position to ∼2 arcmin with a large scatter. In addition, we see that it is more difficult to accurately determine the position

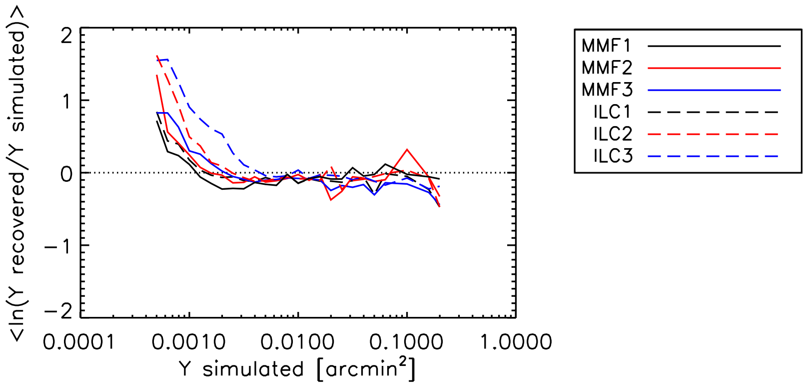

Fig. 6. Flux recovery bias. The figure shows for a subset of methods the average recovered $Y_{\rm rec}$, normalized to the true input Y, as a function of Y. At the bright end, most codes extract an unbiased estimate of cluster flux, while the expected Malmquist bias appears at the faint-end, just below $Y \sim 2 \times 10^{-3}$ arcmin^2.

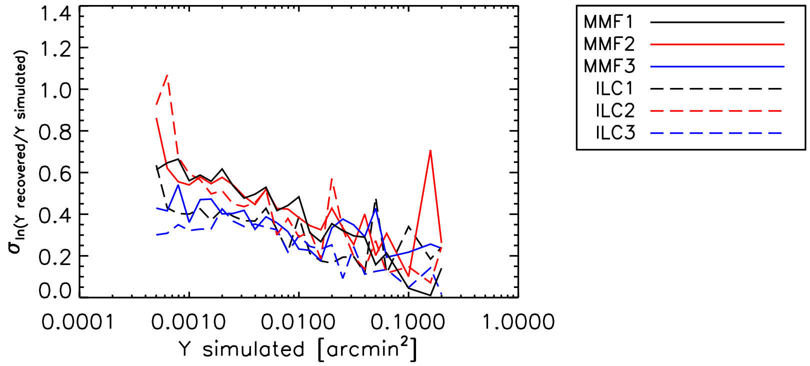

Fig. 7. Flux recovery uncertainty for the subset of methods given in Fig. 6. The Figure shows the dispersion in measured flux about the true input Y flux as a function of the true input flux. The best algorithms are affected by ~30% dispersion.

of intrinsically extended clusters, as shown by the fact that the cloud of points is elongated and inclined.

Concerning photometry, we show in Figs. 6 and 7 the mean recovered SZ flux, $Y_{\rm rec}$, normalized to the true (simulated) flux, Y, as a function of the latter. Only true detections are used in this comparison. We illustrate our results for a subset of methods namely MMF1, MMF2, MMF3, ILC1, ILC2, ILC3. Methods that filter the maps such as ILC4 and GMCA, or that use the SExtractor photometry such as BNP and ILC5 exhibit significant bias in flux recovery at the bright end. At the faint end, we see the appearance of Malmquist bias as an upturn in the measured flux. The importance of this bias varies from algorithm to algorithm.

Figure 7 gives the dispersion in the recovered flux $\sigma_{Y_{\rm rec}}$ as a function of true Y (once again, only involving true detections). Here, we see that some codes perform significantly better than others. Those that adjust an SZ profile to each cluster outperform by a large margin those that do not. Photometry based on SExtractor, for example, fares much worse than the MMF codes. Even among the best performing codes, however, the intrinsic photometric dispersion is of order 30%. This is important, because we expect SZ flux to tightly correlate with cluster mass, with a scatter as low as ~10% as indicated by both numerical simulations (Kravtsov et al. 2006) and recent X-ray data (Arnaud et al. 2007; Nagai et al. 2007). The SZ flux hence should offer a good mass proxy. What we see from this figure, however, is that the observational scatter will dominate the intrinsic scatter of this mass proxy and needs to be properly accounted for in the cosmological analyses.

We have attributed the origin of the photometric scatter to difficulty in determining cluster size. Although methods adjusting a profile to the SZ are able to estimate the size of many clusters, they do so with significant dispersion. Furthermore, this issue arises specifically for *Planck*-like resolution because a large number of clusters are only marginally resolved. Imposing the cluster size, for example from external data, such as X-ray or optical observations or higher resolution SZ measurements, would significantly reduce the observational scatter.

5. Discussion and conclusion

In the present study, we compare different codes and algorithms to detect SZ galaxy clusters from multi-wavelength experiments using Plank's instrumental characteristics. These methods may be usefully divided into *direct methods* (four matched-filter approaches and PowellSnakes) using individual frequency maps, and *indirect methods* (five ILC methods, GMCA and BNP) that first construct an SZ map in which they subsequently search for clusters.

As already emphasized, the global yield values of all methods must be considered with caution because of inherent modeling uncertainties of the sky simulations and cluster models used, and to the underlying cosmological model. Therefore, we focus on relative yields as a gauge of performance of the algorithms. It is worth noting that results of a direct or indirect method significantly vary (within factors of as much as three) with the details of their implementation, with clear impact on the survey yield as demonstrated in Figs. 1 and 2. Using the PSM simulations and including th noise as described in 2.1, we would expect of order of 1000–2000 clusters at a purity of ~90% with $|b| > 20$ deg. This number depends on the extraction method used and may vary with a more detailed modeling of the sky. The cluster yield can be increased by accepting a higher contamination rate and calling for extensive follow-up to eliminate false detections a posteriori.

The indirect methods seem to offer greater opportunity for optimization with a larger number of tuning parameters. They are also less model dependent for the SZ map construction and the cluster detection. Although, they can be coupled with matched filters for the SZ flux measurement. In turn, the direct methods are linear, easy to implement and robust. One of their advantages relies in the fact that they can be optimized to detect objects of a given shape (SZ profile) and and a given spectral energy distribution (SED; SZ spectrum). This characteristic of the direct method is particularly important for *Planck*-like multi-frequency surveys with moderate resolution. Indeed, due to lack of resolution, spurious sources (galactic features or point sources) may be detected by the spatial filter and in that case the frequency coverage and the spectral matching is the best strategy to monitor the false detections. Due to their robustness and easy implementation direct methods are more adapted to run in pipelines[7]. The situation is quite different for high resolution, arcminute-scale, SZ experiments such as ACT and SPT where the filtering of one unique low frequency map (where the SZ signal is negative) is sufficiently efficient to unable cluster detection. In these cases though, extended clusters are not well recovered as they suffer more from the CMB contamination and thus from the filtering.

The comparison of different codes and cluster detection methods exhibits selection effects and catalogue uncertainties, neither of which depend, for example, on the actual cluster physics model. This is shown in the selection curves Fig. 4. In a *Planck*-like case, with moderate resolution, clusters do not appear as point sources, but many are resolved or have sizes comparable to the effective SZ beam. In view of this, the use of an adapted spatial filter to optimally model the SZ profile provides a significant improvement in the detection yield and in the photometry. Clusters being partially resolved leads to non-trivial selection criteria that depend both on flux and true angular size, as demonstrated by the fact that the curves in Fig. 4 are not horizontal lines. In that respect, the use of X-ray information from the ROSAT All-Sky Survey (RASS) cluster catalogues (Böhringer et al. 2000, 2004; Piffaretti et al. 2011) or from optical catalogues, e.g. in the SDSS area (Koester et al. 2007), will be of particular value as they will give us a handle on both flux and size of the clusters detected by *Planck* and, even more importantly, understand better the completeness in studying those which are missed (Chamballu et al. 2012). As already stated, the exact position of each selection curve in Fig. 4 depends on the algorithm and small variations in the position of this curve produce significant changes in catalogue yield. Most of the differences bewteen catalogues occur at small flux and size, where the bulk of the cluster population resides. These objects are for the majority low mass, intermediate redshift clusters. Moreover, detection becomes progressively less efficient for large objects; this is intrinsic and hence shared by all algorithms.

Concerning individual cluster measurements we find that the astrometry is recovered to ~2 arcmin on average and photometry to ~30% for the best-behaving algorithms. The positional error is not a problem for X-ray/optical follow-ups because *Planck* is expected to detect massive clusters which will be easy to find in the XMM/*Chandra*/1 to 4 m class optical telescope fields of view. The photometric error in our *Planck*-like case is dominated by the difficulty in accurately determining the cluster extent/size. This is another consequence of the fact that many clusters are marginally resolved by *Planck*: large enough that their angular extent matters, but small enough that we have difficulty fixing their true size. One way of reducing the photometric error is thus using external constraints on cluster size. One again ancillary data from RASS or optical cluster catalogues will help in this regard, at least at low redshift ($z < 0.3{-}0.5$); at higher redshift, we will rely on follow-up observations if we want to reduce photometric uncertainties.

The comparison of an ensemble of cluster extraction methods in the case of a multi-frequency moderate resolution experiment shows that the optimization of the cluster detection in terms of yield and purity, but also in terms of positional accuracy and photometry, is very sensitive to the implementation of the code. The global or local treatment of the noise estimate or the cleaning from point sources are the two main causes of difference. However and most importantly, the use of as realistic as possible SZ profile (as opposed to model independent profile) to filter out the signal or to measure the fluxes is a key aspect of cluster detection techniques in our context. In that respect, using external information from SZ observations or from other wavelength will significantly help in improving the measurement of the cluster properties and in turn optimize the catalogue yields and their selection function.

Acknowledgements. The authors acknowledge the use of the *Planck* Sky Model (PSM), developed by the Component Separation Working Group (WG2) of the Planck Collaboration. We acknowledge also the use of the HEALPix package (Górski et al. 2005). We further thank M. White and S. White for helpful comments and suggestions.

References

Albrecht, A., Bernstein, G., Cahn, R., et al. 2006 [`arXiv:astro-ph/0609591`]

Albrecht, A., Amendola, L., & Bernstein, G. 2009 [`arXiv:0901.0721`]

Amblard, A., Cooray, A., Serra, P., et al. 2011, Nature, 470, 510

Arnaud, M., Pointecouteau, E., & Pratt, G. W. 2007, A&A, 474, L37

Arnaud, M., Pratt, G. W., Piffaretti, R., et al. 2010, A&A, 517, A92

Bartlett, J. G. 2002, in Tracing Cosmic Evolution with Galaxy Clusters, eds. S. Borgani, M. Mezzetti, & R. Valdarnini, ASP Conf. Ser., 268, 101

Bennett, C. L., Hill, R. S., Hinshaw, G., et al. 2003, ApJS, 148, 97

Bertin, E., & Arnouts, S. 1996, A&AS, 117, 393

Birkinshaw, M. 1999, Phys. Rep., 310, 97

Bobin, J., Moudden, Y., Starck, J., Fadili, J., & Aghanim, N. 2008, Stat. Method., 5, 307

Böhringer, H., Voges, W., Huchra, J. P., et al. 2000, ApJS, 129, 435

Böhringer, H., Schuecker, P., Guzzo, L., et al. 2004, A&A, 425, 367

Bonaldi, A., Tormen, G., Dolag, K., & Moscardini, L. 2007, MNRAS, 378, 1248

Carlstrom, J. E., Holder, G. P., & Reese, E. D. 2002, ARA&A, 40, 643

Carvalho, P., Rocha, G., & Hobson, M. P. 2009, MNRAS, 393, 681

Chamballu, A., Bartlett, J. G., & Melin, J. 2012, A&A, 544, A40

Colafrancesco, S., Mazzotta, P., Rephaeli, Y., & Vittorio, N. 1997, ApJ, 479, 1

da Silva, A. C., Kay, S. T., Liddle, A. R., & Thomas, P. A. 2004, MNRAS, 348, 1401

de Zotti, G., Ricci, R., Mesa, D., et al. 2005, A&A, 431, 893

Delabrouille, J., & Cardoso, J. 2009, in Lecture Notes in Physics 665, eds. V. J. Martinez, E. Saar, E. M. Gonzales, & M. J. Pons-Borderia (Berlin: Springer Verlag), 159

Delabrouille, J., Cardoso, J., Le Jeune, M., et al. 2009, A&A, 493, 835

Delabrouille, J., Betoule, M., Melin, J.-B., et al. 2012, A&A, submitted [`arXiv:1207.3675`]

Dick, J., Remazeilles, M., & Delabrouille, J. 2010, MNRAS, 401, 1602

Dickinson, C., Davies, R. D., & Davis, R. J. 2003, MNRAS, 341, 369

Diego, J. M., Vielva, P., Martínez-González, E., Silk, J., & Sanz, J. L. 2002, MNRAS, 336, 1351

Draine, B. T., & Lazarian, A. 1998, ApJ, 494, L19

Dunkley, J., Komatsu, E., Nolta, M. R., et al. 2009, ApJS, 180, 306

Eke, V. R., Navarro, J. F., & Frenk, C. S. 1998, ApJ, 503, 569

Eriksen, H. K., Banday, A. J., Górski, K. M., & Lilje, P. B. 2004, ApJ, 612, 633

Feroz, F., & Hobson, M. P. 2008, MNRAS, 384, 449

Finkbeiner, D. P., Davis, M., & Schlegel, D. J. 1999, ApJ, 524, 867

Fomalont, E. B., Windhorst, R. A., Kristian, J. A., & Kellerman, K. I. 1991, AJ, 102, 1258

---

[7] MMF1, MM2, MMF3 and PwS were all implemented in *Planck's* pipelines. Furthermore, MMF3 was used to extract the *Planck* clusters published in the ESZ sample.

Gaustad, J. E., McCullough, P. R., Rosing, W., & Van Buren, D. 2001, PASP, 113, 1326
Górski, K. M., Hivon, E., Banday, A. J., et al. 2005, ApJ, 622, 759
Granato, G. L., De Zotti, G., Silva, L., Bressan, A., & Danese, L. 2004, ApJ, 600, 580
Haffner, L. M., Reynolds, R. J., Tufte, S. L., et al. 2003, ApJS, 149, 405
Hall, N. R., Keisler, R., Knox, L., et al. 2010, ApJ, 718, 632
Haslam, C. G. T., Salter, C. J., Stoffel, H., & Wilson, W. E. 1982, A&AS, 47, 1
Herranz, D., Sanz, J. L., Hobson, M. P., et al. 2002, MNRAS, 336, 1057
Jaynes, E. T. 2003, Probability Theory: the logic of science, ed. G. L. Bretthorst (Cambridge University Press)
Jenkins, A., Frenk, C. S., White, S. D. M., et al. 2001, MNRAS, 321, 372
Kim, J., Naselsky, P., & Christensen, P. R. 2009, Phys. Rev. D, 79, 023003
Koester, B. P., McKay, T. A., Annis, J., et al. 2007, ApJ, 660, 239
Kravtsov, A. V., Vikhlinin, A., & Nagai, D. 2006, ApJ, 650, 128
Lagache, G., Bavouzet, N., Fernandez-Conde, N., et al. 2007, ApJ, 665, L89
Leach, S. M., Cardoso, J., Baccigalupi, C., et al. 2008, A&A, 491, 597
Melin, J.-B., Bartlett, J. G., & Delabrouille, J. 2005, A&A, 429, 417
Melin, J.-B., Bartlett, J. G., & Delabrouille, J. 2006, A&A, 459, 341
Miville-Deschênes, M. 2009 [`arXiv:0905.3094`]
Miville-Deschênes, M., Lagache, G., Boulanger, F., & Puget, J. 2007, A&A, 469, 595
Miville-Deschênes, M., Ysard, N., Lavabre, A., et al. 2008, A&A, 490, 1093
Motl, P. M., Hallman, E. J., Burns, J. O., & Norman, M. L. 2005, ApJ, 623, L63
Nagai, D. 2006, ApJ, 650, 538
Nagai, D., Kravtsov, A. V., & Vikhlinin, A. 2007, ApJ, 668, 1
Park, C., Park, C., & Gott, III, J. R. 2007, ApJ, 660, 959
Piffaretti, R., Arnaud, M., Pratt, G. W., Pointecouteau, E., & Melin, J.-B. 2011, A&A, 534, A109
Pires, S., Juin, J. B., Yvon, D., et al. 2006, A&A, 455, 741
Planck Collaboration 2011a, A&A, 536, A6
Planck Collaboration 2011b, A&A, 536, A8
Planck Collaboration 2011c, A&A, 536, A11
Planck Collaboration 2011d, A&A, 536, A18
Planck Collaboration 2011e, A&A, 536, A10
Planck Collaboration 2011f, A&A, 536, A9
Planck Collaboration 2011g, A&A, 536, A12
Reinecke, M., Dolag, K., Hell, R., Bartelmann, M., & Enßlin, T. A. 2006, A&A, 445, 373
Rosati, P., Borgani, S., & Norman, C. 2002, ARA&A, 40, 539
Samal, P. K., Saha, R., Delabrouille, J., et al. 2010, ApJ, 714, 840
Schäfer, B. M., Pfrommer, C., Hell, R. M., & Bartelmann, M. 2006, MNRAS, 370, 1713
Schlegel, D. J., Finkbeiner, D. P., & Davis, M. 1998, ApJ, 500, 525
Schuecker, P., Böhringer, H., Collins, C. A., & Guzzo, L. 2003, A&A, 398, 867
Serjeant, S., & Harrison, D. 2005, MNRAS, 356, 192
Shaw, L. D., Holder, G. P., & Bode, P. 2008, ApJ, 686, 206
Sheth, R. K., & Tormen, G. 1999, MNRAS, 308, 119
Sunyaev, R. A., & Zeldovich, Y. B. 1970, Comm. Astrophys. Space Phys., 2, 66
Sunyaev, R. A., & Zeldovich, Y. B. 1972, Comm. Astrophys. Space Phys., 4, 173
Tegmark, M., de Oliveira-Costa, A., & Hamilton, A. J. 2003, Phys. Rev. D, 68, 123523
Toffolatti, L., Argueso Gomez, F., de Zotti, G., et al. 1998, MNRAS, 297, 117
Truemper, J. 1992, QJRAS, 33, 165
Viero, M. P., Ade, P. A. R., Bock, J. J., et al. 2009, ApJ, 707, 1766
Vikhlinin, A., Kravtsov, A. V., Burenin, R. A., et al. 2009, ApJ, 692, 1060
Voit, G. M. 2005, Rev. Modern Phys., 77, 207
Wakker, B. P., York, D. G., Wilhelm, R., et al. 2008, ApJ, 672, 298
White, M. 2003, ApJ, 597, 650

A&A 536, A8 (2011)
DOI: 10.1051/0004-6361/201116459

Astronomy & Astrophysics
Special feature

Planck early results

Planck early results. VIII. The all-sky early Sunyaev-Zeldovich cluster sample[⋆,⋆⋆]

Planck Collaboration: P. A. R. Ade[77], N. Aghanim[50], M. Arnaud[62], M. Ashdown[60,4], J. Aumont[50], C. Baccigalupi[75], A. Balbi[31], A. J. Banday[85,7,68], R. B. Barreiro[57], M. Bartelmann[83,68], J. G. Bartlett[3,58], E. Battaner[88], R. Battye[59], K. Benabed[51], A. Benoît[49], J.-P. Bernard[85,7], M. Bersanelli[28,44], R. Bhatia[5], J. J. Bock[58,8], A. Bonaldi[40], J. R. Bond[6], J. Borrill[66,79], F. R. Bouchet[51], M. L. Brown[4,60], M. Bucher[3], C. Burigana[43], P. Cabella[31], C. M. Cantalupo[66], J.-F. Cardoso[63,3,51], P. Carvalho[4], A. Catalano[3,61], L. Cayón[21], A. Challinor[54,60,11], A. Chamballu[47], R.-R. Chary[48], L.-Y Chiang[53], C. Chiang[20], G. Chon[69,4], P. R. Christensen[72,32], E. Churazov[68,78], D. L. Clements[47], S. Colafrancesco[41], S. Colombi[51], F. Couchot[65], A. Coulais[61], B. P. Crill[58,73], F. Cuttaia[43], A. Da Silva[10], H. Dahle[55,9], L. Danese[75], R. J. Davis[59], P. de Bernardis[27], G. de Gasperis[31], A. de Rosa[43], G. de Zotti[40,75], J. Delabrouille[3], J.-M. Delouis[51], F.-X. Désert[46], C. Dickinson[59], J. M. Diego[57], K. Dolag[68], H. Dole[50], S. Donzelli[44,55], O. Doré[58,8], U. Dörl[68], M. Douspis[50], X. Dupac[36], G. Efstathiou[54], P. Eisenhardt[58], T. A. Enßlin[68], F. Feroz[4], F. Finelli[43], I. Flores-Cacho[56,33], O. Forni[85,7], P. Fosalba[52], M. Frailis[42], E. Franceschi[43], S. Fromenteau[3,50], S. Galeotta[42], K. Ganga[3,48], R. T. Génova-Santos[56,33], M. Giard[85,7], G. Giardino[37], Y. Giraud-Héraud[3], J. González-Nuevo[75], R. González-Riestra[35], K. M. Górski[58,90], K. J. B. Grainge[4,60], S. Gratton[60,54], A. Gregorio[29], A. Gruppuso[43], D. Harrison[54,60], P. Heinämäki[82], S. Henrot-Versillé[65], C. Hernández-Monteagudo[68], D. Herranz[57], S. R. Hildebrandt[8,64,56], E. Hivon[51], M. Hobson[4], W. A. Holmes[58], W. Hovest[68], R. J. Hoyland[56], K. M. Huffenberger[89], G. Hurier[64], N. Hurley-Walker[4], A. H. Jaffe[47], W. C. Jones[20], M. Juvela[19], E. Keihänen[19], R. Keskitalo[58,19], T. S. Kisner[66], R. Kneissl[34,5], L. Knox[23], H. Kurki-Suonio[19,39], G. Lagache[50], J.-M. Lamarre[61], A. Lasenby[4,60], R. J. Laureijs[37], C. R. Lawrence[58], M. Le Jeune[3], S. Leach[75], R. Leonardi[36,37,24], C. Li[67,68], A. Liddle[18], P. B. Lilje[55,9], M. Linden-Vørnle[13], M. López-Caniego[57], P. M. Lubin[24], J. F. Macías-Pérez[64], C. J. MacTavish[60], B. Maffei[59], D. Maino[28,44], N. Mandolesi[43], R. Mann[76], M. Maris[42], F. Marleau[15], E. Martínez-González[57], S. Masi[27], S. Matarrese[26], F. Matthai[68], P. Mazzotta[31], S. Mei[84,38,8], P. R. Meinhold[24], A. Melchiorri[27], J.-B. Melin[12], L. Mendes[36], A. Mennella[28,42], S. Mitra[58], M.-A. Miville-Deschênes[50,6], A. Moneti[51], L. Montier[85,7], G. Morgante[43], D. Mortlock[47], D. Munshi[77,54], A. Murphy[71], P. Naselsky[72,32], F. Nati[27], P. Natoli[30,2,43], C. B. Netterfield[15], H. U. Nørgaard-Nielsen[13], F. Noviello[50], D. Novikov[47], I. Novikov[72], M. Olamaie[4], S. Osborne[80], F. Pajot[50], F. Pasian[42], G. Patanchon[3], T. J. Pearson[8,48], O. Perdereau[65], L. Perotto[64], F. Perrotta[75], F. Piacentini[27], M. Piat[3], E. Pierpaoli[17], R. Piffaretti[62,12], S. Plaszczynski[65], E. Pointecouteau[85,7], G. Polenta[2,41], N. Ponthieu[50], T. Poutanen[39,19,1], G. W. Pratt[62], G. Prézeau[8,58], S. Prunet[51], J.-L. Puget[50], J. P. Rachen[68], W. T. Reach[86], R. Rebolo[56,33], M. Reinecke[68], C. Renault[64], S. Ricciardi[43], T. Riller[68], I. Ristorcelli[85,7], G. Rocha[58,8], C. Rosset[3], J. A. Rubiño-Martín[56,33], B. Rusholme[48], E. Saar[81], M. Sandri[43], D. Santos[64], R. D. E. Saunders[4,60], G. Savini[74], B. M. Schaefer[83], D. Scott[16], M. D. Seiffert[58,8], P. Shellard[11], G. F. Smoot[22,66,3], A. Stanford[23], J.-L. Starck[62,12], F. Stivoli[45], V. Stolyarov[4], R. Stompor[3], R. Sudiwala[77], R. Sunyaev[68,78], D. Sutton[54,60], J.-F. Sygnet[51], N. Taburet[50], J. A. Tauber[37], L. Terenzi[43], L. Toffolatti[14], M. Tomasi[28,44], J.-P. Torre[50], M. Tristram[65], J. Tuovinen[70], L. Valenziano[43], L. Vibert[50], P. Vielva[57], F. Villa[43], N. Vittorio[31], L. A. Wade[58], B. D. Wandelt[51,25], J. Weller[87], S. D. M. White[68], M. White[22], D. Yvon[12], A. Zacchei[42], and A. Zonca[24]

(Affiliations can be found after the references)

Received 7 January 2011 / Accepted 15 May 2011

ABSTRACT

We present the first all-sky sample of galaxy clusters detected blindly by the *Planck* satellite through the Sunyaev-Zeldovich (SZ) effect from its six highest frequencies. This early SZ (ESZ) sample is comprised of 189 candidates, which have a high signal-to-noise ratio ranging from 6 to 29. Its high reliability (purity above 95%) is further ensured by an extensive validation process based on *Planck* internal quality assessments and by external cross-identification and follow-up observations. *Planck* provides the first measured SZ signal for about 80% of the 169 previously-known ESZ clusters. *Planck* furthermore releases 30 new cluster candidates, amongst which 20 meet the ESZ signal-to-noise selection criterion. At the submission date, twelve of the 20 ESZ candidates were confirmed as new clusters, with eleven confirmed using *XMM-Newton* snapshot observations, most of them with disturbed morphologies and low luminosities. The ESZ clusters are mostly at moderate redshifts (86% with z below 0.3) and span more than a decade in mass, up to the rarest and most massive clusters with masses above $1 \times 10^{15}\ M_{\odot}$.

Key words. cosmology: observations – galaxies: clusters: general – catalogs

1. Introduction

Galaxy clusters provide valuable information on cosmology, from the nature of dark energy to the physics that drives galaxy and structure formation. The main baryonic component in these dark matter dominated objects is a hot, ionised intra-cluster medium (ICM). The ICM can be studied both in the X-ray and through the Sunyaev-Zeldovich effect (SZ) (Sunyaev & Zeldovich 1972; Sunyaev & Zeldovich 1980), a fairly new and highly promising technique that has made tremendous progress in recent years since its first observations (Birkinshaw & Gull 1978); see also Rephaeli (1995); Birkinshaw (1999); Carlstrom et al. (2002).

[⋆] Corresponding author: M. Douspis,
e-mail: `marian.douspis@ias.u-psud.fr`

[⋆⋆] Appendix is available in electronic form at
`http://www.aanda.org`

The SZ effect is undoubtedly the best known and most studied secondary contribution, due to cosmic structure, that is imprinted on the cosmic microwave background (CMB) after decoupling (for a review of secondary anisotropies see Aghanim et al. 2008). It is caused by the inverse Compton interaction between the CMB photons and the free electrons of the hot ICM. It can be broadly subdivided into the thermal SZ (TSZ) effect, where the photons are scattered by the random motion of thermal electrons, and the kinetic SZ (KSZ) effect caused by the bulk motion of the electrons. In the former case, the scattered CMB photons have a unique spectral dependence, whereas the final spectrum remains Planckian in the case of the KSZ effect.

The SZ effect offers a number of advantages for cluster studies. First, the Compton y parameter, which measures the integral of the gas pressure along the line of sight and sets the amplitude of the SZ signal, does not suffer from cosmological surface-brightness dimming. This implies that the SZ effect is an efficient method for finding high-redshift clusters. Second, the total SZ signal Y, integrated over the cluster's angular extent, directly measures the total thermal energy of the gas and as such is expected to correlate closely (i.e., with a tight scatter in the scaling relation) with total cluster mass. This fact is borne out both by numerical simulations (Borgani 2006; da Silva et al. 2001; Motl et al. 2005; Pfrommer et al. 2007) and indirectly from X-ray observations (Nagai et al. 2007; Arnaud et al. 2007; Vikhlinin et al. 2009) using Y_X, the product of the gas mass and mean temperature giving an X-ray analogue of the integrated SZ Compton parameter first introduced by Kravtsov et al. (2006). This contrasts with the X-ray luminosity which, at a given mass, is very sensitive to the cluster's thermodynamical state, for instance due to a recent merger event or in the presence of a strong cooling core. Hence SZ surveys are expected to provide clean cluster samples over a wide range of redshifts, in the sense of being close to an unbiased mass-limited selection. These are key properties for statistical studies with clusters, either to constrain cosmological models (e.g., from the evolution of the mass function) or to probe the physics of structure formation (e.g., from cluster scaling and structural properties).

For these reasons, alongside the efforts developed to measure CMB anisotropies many pioneering instruments were used or developed to observe the SZ effect and use it as new observational probe of cluster physics, large-scale structure, and the cosmological model. The first observations of the SZ effect, targeted at specific X-ray selected clusters, were performed using interferometric or single-dish experiments mostly observing in the Rayleigh-Jeans part of the spectrum: the Ryle Telescope at 15 GHz (Jones et al. 1993), the OVRO 5 m telescope at 32 GHz (Birkinshaw & Hughes 1994), the SuZIE array at 140 GHz (Holzapfel et al. 1997), BOLOCAM at 143 and 265 GHz (Glenn et al. 1998), the Diabolo array on IRAM 30 m telescope at 140 GHz (Pointecouteau et al. 1999), MITO at 143, 214, 272, and 353 GHz (De Petris et al. 1999), the Nobeyama 45 m telescope at 21 GHZ, 43 GHz and 150 GHz (Komatsu et al. 1999), the BIMA array at 30 GHz (Dawson et al. 2001), ACBAR at 150 and 220 GHz (Gómez et al. 2003), CBI working between 25 and 36 GHz (Udomprasert et al. 2004), VSA at 30 GHz (Lancaster et al. 2005), the Atacama Pathfinder Experiment (APEX) SZ Camera at 150 GHz (Dobbs et al. 2006), the SZ Array at 30 GHz (Muchovej et al. 2007), AMI at 15 GHz (Zwart et al. 2008), and AMIBA at 90 GHz (Wu et al. 2008); see Birkinshaw & Lancaster (2005) for a review of observational techniques. Measurements of the SZ effect were further made or attempted in the Wien part of the spectrum with PRONAOS (Lamarre et al. 1998), SCUBA (Zemcov et al. 2007), and more recently with the *Herschel* Space Observatory (Zemcov et al. 2010).

These experiments have not only allowed us to accumulate SZ measurements for about a hundred clusters, but have also laid the groundwork for SZ-based studies of clusters and of cosmology. In combination with other observations, especially in X-rays, they were used to measure cosmological parameters such as the Hubble constant, and to probe the distance-duality relation between the angular-diameter and luminosity distances, bulk flows, and the cluster gas mass fraction (e.g., Silk & White 1978; Kobayashi et al. 1996; Grego et al. 2001; Reese et al. 2002; Uzan et al. 2004; Ameglio et al. 2006; Bonamente et al. 2006; Kashlinsky et al. 2008). The SZ effect has also been used to characterise the clusters themselves, as it can potentially measure their radial peculiar velocities (Benson et al. 2003). The relativistic corrections to the SZ effect (e.g., Itoh et al. 1998) can be used to measure the gas temperature directly for massive clusters (Pointecouteau et al. 1998). The spectral signature of the SZ effect can in principle even probe the electron gas distribution and constrain any non-thermal electron population in the ICM (Colafrancesco et al. 2003; Shimon & Rephaeli 2004). The SZ effect can also be used as a tracer of the WHIM diffuse gas (Génova-Santos et al. 2005; Battistelli et al. 2006). Moreover multi-frequency SZ measurements might provide a novel way of constraining the CMB temperature and its evolution with redshift (Battistelli et al. 2002; Horellou et al. 2005; Luzzi et al. 2009).

Deep surveys covering hundreds of square degrees and capable of detecting many tens to hundreds of clusters, performed by the South Pole Telescope (SPT) (Carlstrom et al. 2011) and the Atacama Cosmology Telescope (ACT) (Marriage et al. 2011), are accumulating, and already delivering, data. One of their goals is to use SZ cluster counts and the SZ angular correlation function as cosmological tools (Haiman et al. 2001; Weller et al. 2002; Levine et al. 2002; Majumdar & Mohr 2004; Douspis et al. 2006). Such surveys are particularly powerful for detecting distant clusters, as was recently proven by results from Vanderlinde et al. (2010).

In this context ESA's *Planck*[1] mission, launched on 14 May 2009, carries a scientific payload consisting of an array of 74 detectors sensitive to a range of frequencies between roughly 25 and 1000 GHz, which scan the sky simultaneously and continuously with an angular resolution varying between about 30 arcmin (FWHM) at the lowest frequencies and about four arcmin at the highest. The array is arranged into two instruments. The detectors of the Low Frequency Instrument (LFI) are pseudo-correlation radiometers covering three bands centred at 30, 44, and 70 GHz. The detectors of the High Frequency Instrument (Lamarre et al. 2010; Planck HFI Core Team 2011a, HFI;) are bolometers covering six bands centred at 100, 143, 217, 353, 545, and 857 GHz with bolometers cooled to 0.1 K. The design of *Planck* allows it to image the whole sky approximately twice per year, with an unprecedented combination of sensitivity, angular resolution, and frequency coverage. The *Planck* satellite, its payload, and its performance as predicted at the time of launch are described in 13 articles included in a special issue (Volume 520) of Astronomy & Astrophysics. The

---

[1] *Planck* (`http://www.rssd.esa.int/Planck`) is a project of the European Space Agency (ESA) with instruments provided by two scientific consortia funded by ESA member states (in particular the lead countries France and Italy), with contributions from NASA (USA) and telescope reflectors provided by a collaboration between ESA and a scientific consortium led and funded by Denmark.

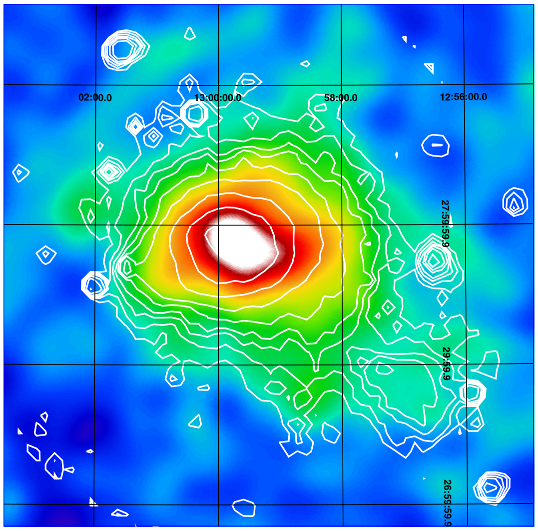

Fig. 1. *Planck* y-map of Coma on a ~3° × 3° patch with the *ROSAT-PSPC* iso-luminosity contours overlaid.

main objective of *Planck* is to measure the spatial anisotropies of the temperature of the CMB with an accuracy set by fundamental astrophysical limits. Its level of performance will enable *Planck* to extract essentially all the information in the CMB temperature anisotropies. *Planck* will also measure to high accuracy the polarisation of the CMB anisotropies, which not only encodes a wealth of cosmological information but also provides a unique probe of the thermal history of the Universe during the time when the first stars and galaxies formed. In addition, the *Planck* sky surveys will produce a wealth of information on the dust and gas in our own galaxy and on the properties of extragalactic sources.

Planck was specifically designed from the beginning to measure the SZ effect (Aghanim et al. 1997) and provide us with an all-sky SZ cluster catalogue. The first galaxy cluster searched for in the HFI data, Abell 2163 (Figs. 5 and 6), was indeed found from 100 GHz to 353 GHz shortly after the First Light Survey (FLS) was performed and observations in routine mode by *Planck* started. Three other known clusters falling in the FLS region were seen across the positive and negative parts of the SZ spectrum. The scanning strategy soon allowed us to map extended clusters such as Coma on wide patches of the sky (Fig. 1). SZ detection techniques were then applied to the data and the first blind detections were performed.

The *Planck* all-sky SZ cluster catalogue, with clusters out to redshifts $z \sim 1$, that will be delivered to the community at the end of the mission will be the first all-sky cluster survey since the ROSAT All-Sky Survey (RASS), which was at much lower depth (the median redshift of the NORAS/REFLEX cluster catalogue is $z \simeq 0.1$). Thanks to its all-sky nature, *Planck* will detect the rarest clusters, i.e., the most massive clusters in the exponential tail of the mass function which are the best clusters for cosmological studies. The *Planck* early SZ (ESZ) sample is delivered alongside the Early Release Compact Source Catalogue (ERCSC) (Planck Collaboration 2011c), the nine-band source catalogue, and the Early Cold Core (ECC) catalogue (Planck Collaboration 2011s) at `http://www.rssd.esa.int/Planck` (Planck Collaboration 2011v). The ESZ is a high-reliability sample of 189 SZ clusters or candidates detected over the whole sky from the first ten months of the *Planck* survey of the sky.

The present article details the process by which *Planck* ESZ sample was constructed and validated. The *Planck* data and the specific SZ extraction methods used to detect the SZ candidates are presented in Sects. 2 and 3. *Planck*'s measurements provide an estimate of the integrated Compton parameter, Y, of detected SZ cluster "candidates". A subsequent validation process is needed to identify which among the candidates are previously known clusters, and an additional follow-up programme is required to scientifically exploit *Planck* cluster data. This includes cluster confirmation (catalogue validation) and the measurement of relevant physical parameters. These different steps of the ESZ construction and validation are presented in Sect. 4 and the subsequent results are given in Sect. 5. Finally, Sects. 6–8 present the general properties of the ESZ cluster sample. *Planck* early results on clusters of galaxies are presented here and in a set of accompanying articles (Planck Collaboration 2011e,f,g,h).

Throughout the article, and in all the above cited *Planck* SZ early result papers, the adopted cosmological model is a ΛCDM cosmology with Hubble constant, $H_0 = 70\ \mathrm{km\,s^{-1}\,Mpc^{-1}}$, matter density parameter $\Omega_\mathrm{m} = 0.3$ and dark energy density parameter $\Omega_\Lambda = 0.7$. The quantity $E(z)$ is the ratio of the Hubble constant at redshift z to its present value, H_0, i.e., $E^2(z) = \Omega_\mathrm{m}(1+z)^3 + \Omega_\Lambda$.

2. *Planck* data description

The ESZ sample was constructed out of the *Planck* channel maps of the HFI instrument, as described in detail in Planck HFI Core Team (2011b). These maps correspond to the observations of the temperature in the first ten months of the survey by *Planck*, which give complete sky coverage. Raw data were first processed to produce cleaned time-lines (time-ordered information, TOI) and associated flags correcting for different systematic effects. This includes a low-pass filter, glitch treatment, conversion to units of absorbed power, and a decorrelation of thermal stage fluctuations. For cluster detection, and more generally for source detection, one data flag of special importance is associated with solar system objects (SSO). These objects were identified in TOI data using the publicly-available Horizon ephemeris, and the SSO flag was created to ensure that they are not projected onto the sky, in order to avoid possible false detections, ringing, etc.

Focal-plane reconstruction and beam-shape estimates were obtained using observations of Mars. Beams are described by an elliptical Gaussian parameterisation leading to FWHM θ_S given in Planck HFI Core Team (2011b). The attitude of the satellite as a function of time is provided by the two star trackers installed on the *Planck* spacecraft. The pointing for each bolometer was computed by combining the attitude with the location of the bolometer in the focal plane reconstructed from Mars observations.

From the cleaned TOI and the pointing, channel maps have been made by co-adding bolometers at a given frequency. The path from TOI to maps in the HFI data processing is schematically divided into three steps: ring-making, destriping, and map-making. The first step averages circles within a pointing period to make rings with higher signal-to-noise (S/N) ratio, taking advantage of the redundancy of observations provided by the *Planck* scanning strategy. The low amplitude $1/f$ component is accounted for in the second step using a destriping technique. Finally, cleaned maps are produced using a simple co-addition of the Healpix-based rings[2]. SSO flag channel maps, used in the internal validation of the ESZ sample, were also made following the same procedure.

The noise in the channel maps is essentially white with a standard deviation of $1.6, 0.9, 1.4, 5.0, 70, 1180$ μK degree[3] from low to high frequencies (Planck HFI Core Team 2011b). Photometric calibration is performed for the lower frequency channels at the ring level using the CMB dipole (from WMAP Hinshaw et al. 2009), and at the map level using FIRAS data (Fixsen et al. 1994) for the higher frequency channels at 545 and 857 GHz. The absolute gain calibration of HFI *Planck* maps is known to better than 2% (Planck HFI Core Team 2011b).

3. Detection and cluster extraction

In order to generate a cluster candidate list, a suitable extraction algorithm must be run on the maps. SZ clusters can be considered as compact sources with respect to the *Planck* beam, but they are definitely not point sources. Their extension thus merits a special adapted processing. For this reason, several extraction methods were developed within the *Planck* collaboration, and those were tested and compared using the *Planck* Sky Model Simulation (PSM[4]). The details of the comparison of the cluster extraction algorithms, called the "SZ challenge", can be found in Melin et al. (in prep.).

Methods fall into two classes: "direct" methods use individual channel maps to extract the clusters, while "indirect" methods use sky y-maps obtained via component separation algorithms. The methods used in this article are direct methods, with the reference method chosen on the basis of the SZ challenge. The direct detection algorithms used to construct and validate the ESZ sample incorporate prior assumptions on the cluster signal, specifically its spectral and spatial (i.e., the shape of ICM pressure profile) characteristics (see Sect. 3.1). This enhances the cluster contrast over a set of observations containing contaminating signals.

Most of the methods developed prior to the launch were applied to the *Planck* data, but only direct methods were favoured for implementation in the pipeline infrastructure. The following three were used to construct and validate the ESZ sample:

- a matched multi-frequency filter (MMF) algorithm, referred to henceforth as MMF3, was the reference method used for the blind detection of SZ candidates, and the construction of the ESZ list;
- two other methods (Sects. 3.3.2 and 3.3.1) were used to confirm the blind detections of the ESZ candidates.

In addition, a slightly different version of MMF3 was run as part of ESZ validation, in order to re-extract the Compton Y parameter of the SZ clusters incorporating fixed cluster sizes and positions taken from X-ray observations (see Sect. 6.2).

3.1. Baseline cluster model

The ICM pressure profile has historically been described by an isothermal β-model (Cavaliere & Fusco-Femiano 1978; Grego et al. 2001; Reese et al. 2002, e.g.,). However, recent X-ray observations have shown that a β-model is a poor description of the gas distribution in clusters, leading several authors to propose more realistic analytical functions based on a Generalised Navarro-Frenk-and-White (GNFW) profile (Nagai et al. 2007; Arnaud et al. 2010).

The baseline pressure profile used in the present work is the standard "universal" pressure profile derived by Arnaud et al. (2010). It is constructed by combining the observed X-ray pressure profile within R_{500}, from 31 galaxy clusters of the REXCESS sample (Böhringer et al. 2007), with data from state-of-the-art numerical simulations (Borgani et al. 2004; Nagai et al. 2007; Piffaretti & Valdarnini 2008) out to $5\ R_{500}$. In the following, R_{500} is the cluster size defined as the radius where the mean enclosed density is 500 times the critical density. It relates to the characteristic cluster scale $R_{\rm s}$ through the NFW concentration parameter c_{500} ($R_{\rm s} = R_{500}/c_{500}$).

The pressure profile model used in the present article is equivalent to the standard self-similar case described in Appendix B of Arnaud et al. (2010)[5]. It is equivalent to a shape function characterised by two free parameters, a central value and a characteristic scale $\theta_{\rm s}$.

The SZ effect from the hot ICM is due to the first-order correction for energy transfer in Thomson scattering. There is a spectral distortion, energy being transferred from photons in the Rayleigh-Jeans tail of the cosmic blackbody radiation to the Wien tail. In the non-relativistic limit the frequency dependence of the distortion is universal (the same for all clusters), characterised by a distinct frequency, $\nu \sim 220$ GHz, where the TSZ effect vanishes. Below this frequency there is a decrement of the CMB intensity, giving an apparent *decrease* in the sky brightness, and above lies an enhancement.

The magnitude of the SZ effect, known as the Compton parameter y, depends only on the cluster's characteristics, electronic temperature $T_{\rm e}$ and density $n_{\rm e}$, as

$$y = \frac{k\sigma_{\rm T}}{m_{\rm e}c^2} \int^{l} T_{\rm e}(l) n_{\rm e}(l)\, {\rm d}l$$

where k is the Boltzmann constant, $\sigma_{\rm T}$ the Thomson cross section, $m_{\rm e}c^2$ the electron rest mass and l is the distance along the line of sight. The total SZ signal is characterised by the integrated Compton parameter denoted $Y = \int y\, {\rm d}\Omega$, where Ω is solid angle. It can be written as $D_{\rm A}^2 Y = (\sigma_{\rm T}/m_{\rm e}c^2) \int P dV$, where $D_{\rm A}$ is the angular-diameter distance to the system and $P = n_{\rm e}kT_{\rm e}$ the electron pressure. In the following, the integral performed over the sphere of radius R_{500} ($5R_{500}$) is denoted Y_{500} (Y_{5R500}).Thus, as defined here, Y_{500} and Y_{5R500} have units of solid angle, e.g., arcmin^2.

3.2. Reference extraction method (matched multi-filter, MMF3)

The ESZ sample is the result of a blind multi-frequency search in the all-sky *Planck*-HFI maps, i.e., no prior positional information on detected known clusters was used as input to the detection algorithm. The ESZ sample is produced by running the MMF3 algorithm, which is an all-sky extension of the matched multi-frequency filter algorithm described in Melin et al. (2006), over the six HFI frequency maps. The spectral distortion of the CMB due to the ICM can in principle be detected down to the lowest frequencies at which *Planck* operates; however, the beam at the lowest frequencies is large compared to typical cluster sizes. Since clusters at moderate redshifts typically span angular

---

[2] `http://healpix.jpl.nasa.gov/` (Górski et al. 2005).

[3] In the following and unless otherwise stated, μK refers to equivalent CMB temperature fluctuations in μK.

[4] "*Planck* Sky Model", `http://www.apc.univ-paris7.fr/APC_CS/Recherche/Adamis/PSM/psky-en.php`

[5] More details on the pressure profile can be found in Planck Collaboration (2011f).

scales of ∼5 arcmin, the large beam of *Planck* at the LFI bands results in beam dilution of the SZ signal. The inclusion of the lowest *Planck* frequencies using the current algorithm therefore results in a lower S/N for the detected sources than if only the HFI bands were used. This reduces the efficiency of SZ cluster detection, which can potentially be improved in the future with refinements to the algorithm. As a consequence, for the generation of the ESZ list, only the *Planck* all-sky maps at frequencies of 100 GHz and above are considered.

The MMF algorithm, studied extensively by Herranz et al. (2002) and Melin et al. (2006), enhances the contrast, and thus S/N, of objects of known shape and known spectral emission profile over a set of observations containing contaminating signals. In its application for SZ, the method makes use of the universal frequency dependence of the thermal SZ effect. The filter optimises the detectability using a linear combination of maps (which requires an estimate of the statistics of the contamination) and uses spatial filtering to suppress both foregrounds and noise (making use of the prior knowledge of the cluster profile). The filter optimises cluster detection but it is not immune to contamination by false, non-SZ, detections which calls for an extensive validation procedure described in Sect. 4.

MMF3 first divides the all-sky maps into a set of 504 overlapping square patches of area 10×10 square degrees. Holes in the maps due to unsampled or badly sampled pixels are identified to construct an effective detection mask and are then filled in with the median value of the adjacent pixels. The matched multi-frequency filter then combines optimally the six frequencies of each patch assuming the SZ frequency spectrum and using the reference pressure profile presented in Sect. 3.1.

Auto- and cross-power spectra used by MMF3 are directly estimated from the data and are adapted to the local instrumental noise and astrophysical contamination. For each patch, the position and the scale radius (chosen to be $5\,R_{500}$) of the cluster profile, i.e., the cluster size $5\theta_{500}$, are varied to maximise the S/N of each detection. The algorithm hence assigns to each detected source a position, an estimated cluster size, $5\theta_{500}$, and an integrated Compton parameter, Y_{5R500}. In the present article and unless otherwise stated the *measured* integrated Compton parameter, noted Y_{5R500}, is thus computed by integrating the GNFW profile within a sphere of $5R_{500}$[6] encompassing most of the SZ signal. The detected sources extracted from the individual patches, with their assigned sizes and integrated Compton parameters, are finally merged into an all-sky cluster list. In practice the MMF3 algorithm is run in an iterative way; after a first detection of the SZ candidates, consecutive runs centred on the positions of the candidates refine the estimated S/N and candidate properties. At this stage, the uncertainty on Y_{5R500} is provided and takes into account the uncertainty in the cluster size estimate. The MMF3 algorithm can also be performed with fixed cluster size and position to estimate the SZ signal. This version of the algorithm was used to measure the integrated Compton parameters of known X-ray clusters in the ESZ sample, as explained in Sect. 6.2.

In order to address contamination by point sources, MMF3 uses a built-in source detection algorithm to reject point sources with S/N above ten which are then masked. This step avoids most of the false SZ detections associated with point sources. However, some residual contamination by non-SZ sources captured by the MMF3 algorithm may still be present and requires additional validation of the detection candidates (see Sect. 4).

3.3. Other extraction methods

The two other "direct" SZ detection methods used to confirm the blind detections of the ESZ candidates by MMF3 are discussed below. These methods previously compared rather well to each other within the SZ challenge match in terms of the detection properties (especially for high S/N sources). Their estimated sizes and SZ signals agree on average as well, though they differ on a case by case basis.

3.3.1. The matched multi-filter method, MMF1

The MMF1 algorithm is a completely independent implementation of the multi-frequency matched filter integrated within the *Planck*-HFI pipeline and infrastructure. A more detailed description of MMF1 is given in Melin et al. (2011). The full-sky *Planck* frequency maps are divided into 640 flat patches, each 14.66 degrees on a side (corresponding to 512 by 512 pixels), with overlapping regions of six degrees. The performance of the MMF algorithm is extremely sensitive to the quality of the estimated auto- and cross-power spectra of the background component in each frequency map. The size of the patches thus needs to be large enough to ensure a representative assessment of the background. The large overlap between patches was chosen so that all detections in a two-degree border around the edge of the patch may be discarded.

The detection of the SZ-candidates is performed on all the patches, and the resultant sub-catalogues are merged together to produce a single SZ-candidate catalogue. Similarly to MMF3, the candidate size is estimated by filtering the patches over the range of potential scales, from point-source sized objects and larger, and finding the scale which maximises the S/N of the detection of the candidate. In the version used on the *Planck* data, when merging sub-catalogues produced from the analysis of individual patches, it is also the S/N of the detection which is used when deciding which detection of the candidate is kept.

3.3.2. PowellSnakes (PwS) for SZ

PowellSnakes (PwS) is quite different from the MMF methods. It is a fast Bayesian multi-frequency detection algorithm designed to identify and characterise compact objects buried in a diffuse background. The detection process is grounded in a statistical model comparison test where two competing hypotheses are compared: the detection hypothesis and the null hypothesis. The statistical foundations of PwS are described in Carvalho et al. (2009).

Similarly to the MMF algorithms, a template parameterised SZ pressure profile is assumed known and representative of the majority of the cluster population observable with the resolution and noise characteristics of the instrumental setup. According to our data model, the pixel intensities result from the contribution of three independent components: the SZ signal, the astronomical background component, and the instrumental pixel noise. The last is assumed to be a realisation of a homogeneous stationary Gaussian random white noise process. The background astronomical components and the pixel noise are assumed uncorrelated and can each be modelled locally by a homogeneous Gaussian process.

The algorithm starts by minimising the model's likelihood ratio with respect to the model's parameters by using a Powell minimiser iteratively one source at a time. We assume that the sources are well separated and the fields not too crowded. The parameter estimation and the acceptance/rejection threshold is

---

[6] In the spherical assumption with this profile, Y_{500} the integrated Compton parameter within R_{500} relates to Y_{5R500} by $Y_{5R500} = 1.81 \times Y_{500}$.

defined using Bayesian approach with priors adjusted on the *Planck* Sky Model SZ Catalogue.

PwS performs on flat 512 × 512 pixel patches of 14.66 degrees on a side. When applying a Galactic cut of $|b| > 14$ degrees, PwS splits the sphere into 2324 patches. However, only detections lying inside the inner 256×256 pixels are considered. So, on average PwS detects each cluster more than three times (usually four times), increasing the reliability of the detection. The selection of the candidate detection that goes into the final catalogue uses the Bayesian mode of PwS, based on the highest ratio of model posteriors.

4. Validation of the ESZ sample

The SZ validation process, Fig. 2, is an integrated HFI-LFI effort within *Planck* Working Group 5 (WG5[7]) "Clusters and Secondary anisotropies". It has been established in order to validate the full SZ candidate lists obtained from the extraction methods developed by the *Planck* collaboration. It relies mainly on a three-stage process detailed in the following subsections:

- *Internal validation* steps based on *Planck* data:
  - search for and rejection of associations with SSOs and artefacts;
  - rejection of sources with rising spectral energy distribution in the high HFI frequency bands;
  - cross-check with other *Planck* source catalogues to reject SZ candidates identified with cold cores (CC) and other Galactic sources; and
  - redundant detections of the same candidates by methods other than the reference one.
- *Candidate identification* steps based on ancillary data:
  - identification of SZ candidates with known clusters from existing X-ray, optical/near infrared (NIR), and SZ catalogues and lists; and
  - search in NED and SIMBAD databases.
- *Follow-up programmes* for verification and confirmation of SZ candidates.

4.1. Construction of ESZ sample and internal validation

The construction of the ESZ list of SZ candidates starts with the blind detection of candidates using the implementation of the MMF3 algorithm at the US Planck Data Center applied to *Planck*-HFI channel maps at Galactic latitudes $|b| > 14$ deg. A total of about 1000 blind SZ candidates are detected with $S/N \geq 4$. As discussed above, the MMF3 algorithm uses prior information on the SZ spectrum and on the cluster shape. However, especially due to the beam-sizes of the order of a few arcminutes, the resulting list of SZ candidates is not immune from false detection due mainly to dust emission at high frequencies from the interstellar medium (ISM) or infrared sources, and very moderately to the CMB fluctuations at low frequencies (see illustrations of channel maps in upper panels of Fig. 5). In the following, we do not explicitly check for association with extragalactic point sources emitting at *Planck*-HFI frequencies, which is essentially dealt with internally by the MMF3 algorithm (Sect. 3.2). Some residual contamination of the SZ Compton Y parameter by point sources may, however, still be present (see Sect. 6.4 for a specific discussion).

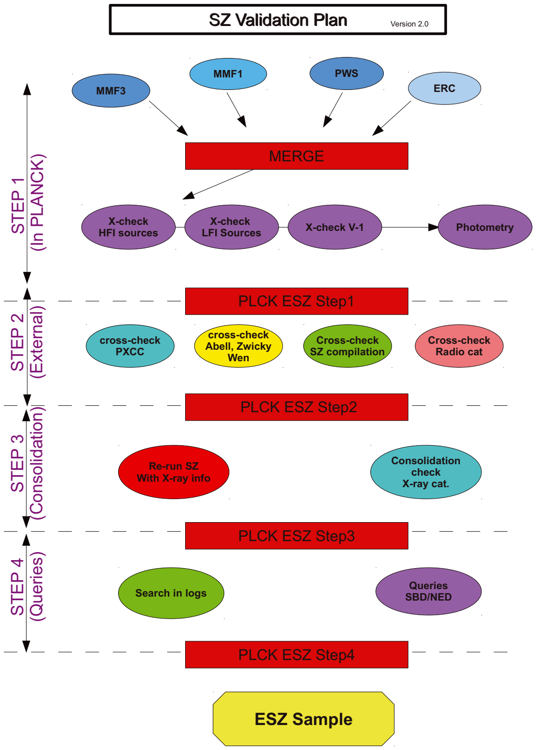

Fig. 2. Flowchart of the SZ validation process applied to the *Planck* cluster sample.

The internal validation process starts by removing spurious detections from the output list of blind SZ candidates, which is achieved in two steps. We first reject the candidates showing rising spectral energy distributions in the highest *Planck*-HFI frequency bands. They represent around 14% of the initial blind SZ candidates. Second, the remaining blind SZ candidate sample is further cleaned by rejecting all objects associated with either Galactic sources, or CC detected using the CoCoCodet algorithm (Montier et al. 2010; Planck Collaboration 2011s) within a 7 arcmin radius of SZ candidates. This step further reduces the sample of remaining SZ candidates by about 17%.

After this two-step process, the initial blind SZ candidate sample has been reduced to around 770 blind SZ candidates with $S/N \geq 4$. However at this S/N level many candidates will not correspond to actual clusters. Theoretical predictions based on the PSM simulations indicate that the purity (ratio of true to all detections) is expected to be of the order of 70% at $S/N = 4$ (Fig. 15). The simulations do not account fully for the complexity of the true sky nor for the inhomogeneity of the noise across the sky. The actual purity is thus likely to be worse than the prediction. In order to ensure a high level of purity in the ESZ sample and based on lessons learnt from the *XMM-Newton* observations of low S/N candidates (see Planck Collaboration 2011e), an early decision was made to cut at a higher S/N level of $S/N \geq 6$ for this first *Planck* data release. This more stringent condition retains 201 SZ cluster candidates. Taking advantage of the outcome of the follow-up programme for cluster confirmation by *XMM-Newton*, we further retain only the SZ candidates detected blindly by the MMF3 algorithm *and* at least one other method, be it MMF1 or PowellSnakes. This results in 190 SZ cluster candidates; these constitute the baseline ESZ sample. A

---

[7] `http://www.ita.uni-heidelberg.de/collaborations/planck/`

detailed inspection of the SZ maps and spectra of the 11 discarded SZ candidates was performed (see Sect. 5.2.2) and confirmed that these sources were false detections.

A final internal check consisted of searching for associations of the obtained 190 SZ candidates with possible artefacts such as low-frequency noise stripes, ringing from neighbouring bright sources, hot pixels, non-observed pixels or poorly sampled pixels in the vicinity of SSO-flagged regions. None of the 190 ESZ candidates was associated with such artefacts.

4.2. Candidate identification with ancillary data

The second stage of the SZ validation process consisted of cross-matching the obtained list of 190 blind SZ candidates with external cluster catalogues in X-rays, optical and SZ domains. This allowed us to identify the SZ candidates associated with previously known clusters and consequently isolate the *Planck* candidate new clusters.

4.2.1. With X-ray cluster catalogues

For the association of *Planck* SZ candidates from the blind extraction with known X-ray clusters, we have used the Meta-Catalogue of X-ray detected Clusters of galaxies (MCXC, Piffaretti et al. 2011). This homogenised compilation of X-ray detected clusters of galaxies comprises approximately 1800 clusters from publicly available ROSAT All Sky Survey-based (NORAS, REFLEX, BCS, SGP, NEP, MACS, and CIZA) and serendipitous (160SD, 400SD, SHARC, WARPS, EMSS, etc.) cluster catalogues.

For each X-ray cluster in the MCXC several properties are available, amongst which are the X-ray centroid coordinates, redshift, identifiers, and L_{500}[8]. The luminosities are adopted as proxies to estimate the total mass M_{500} using the L–M relation from REXCESS (Pratt et al. 2009), and radius R_{500}, and to predict the integrated Compton $Y^{L_X}_{5R500}$, or alternatively $Y^{L_X}_{500}$, as detailed in Planck Collaboration (2011f) as well as other *Planck*-related quantities.

Because the MCXC compilation includes only clusters with available luminosity (redshift) information, we supplement it with about 150 clusters where this information is missing. This implies that for the latter only centroid positions are available. The resulting meta-catalogue, for simplicity referred to as MCXC in the reminder of the article, is extensively used during the external validation process. For a given *Planck* candidate cluster we identify the closest MCXC cluster. The reliability of the association is checked based on the distance, as compared to the cluster size, and on the measured Y_{5R500} (or S/N) values, as compared to the expected values $Y^{L_X}_{5R500}$ (or S/N) for the MCXC clusters.

4.2.2. With optical cluster catalogues

The baseline for the identification of blind SZ candidates from the ESZ with clusters known in the optical is the cross-match with the Abell cluster catalogue (Abell 1958, 5250 clusters of which 1026 have a redshift) and the Zwicky cluster catalogue (Zwicky et al. 1961, 9134 objects). The association criterion here was a positional match with a search radius for both catalogues set to five arcminutes.

Furthermore, the ESZ sample was cross-checked against the MaxBCG (Koester et al. 2007) and Wen et al. (2009) catalogues with a search radius of 5 arcmin.

4.2.3. With known SZ clusters

The identification of SZ candidates is also performed at millimetre wavelengths by cross-matching the SZ candidate list with a compilation of SZ observed galaxy clusters from the literature undertaken by Douspis et al. (in prep.). This compilation is based on SZ observations conducted with the numerous experiments developed during the last 30 years (Ryle, OVRO, BIMA, MITO, Nobeyama, SZA, APEX-SZ, AMI, Diabolo, Suzie, Ryle, AMIBA, ACBAR, etc). It also includes the new clusters recently discovered through their SZ signature by ACT and SPT. In total the compilation comprises 111 SZ clusters including 28 newly discovered by ACT and SPT (Menanteau et al. 2010; Vanderlinde et al. 2010). The association of the *Planck* SZ candidates was based on positional matching with a search radius of five arcminutes.

4.2.4. Queries in SIMBAD and NED databases

The information provided from querying databases is mainly redundant with cross-checks with cluster catalogues in X-ray or optical. However, running both cross-matches is important to avoid missing a few associations. It is also important to retrieve the information on redshifts for those identified clusters not included in the MCXC. We therefore performed a systematic query in SIMBAD. The adopted search radius was set to five arcminutes. For NED, no systematic query was implemented. Cluster candidates within the same search radius were rather checked against a list of objects retrieved from NED flagged as "Clusters of galaxies". Finally the candidates were also checked against the X-ray cluster database (Sadat et al. 2004, BAX:).

4.3. Follow-up programme for validation and confirmation

In parallel to the effort of SZ candidate cross-identification, a coherent follow-up programme targeted towards the verification/validation of the cluster candidates in the SZ catalogue was put into place in the form of an internal roadmap. The main goals of this follow-up programme are to confirm *Planck* candidates as new clusters, and as a consequence to better understand both the SZ selection criteria in the *Planck* survey and the reliability of selected sources.

Considering the complementarity of X-ray, optical and IR/SZ, observational follow-ups have been coordinated to optimise the validation and the understanding of the *Planck* selection. In practice, this took the form of a confirmation programme relying on observations with *XMM-Newton*[9] making use of Director Discretionary Time (DDT) as detailed in Planck Collaboration (2011e). This is complemented by observations in the optical using the European Northern Observatory facilities (ENO), the European Southern Observatory 2.2 m-telescope, and two pilot programmes, one with the WISE experiment (Wright et al. 2010) for the search of overdensities in

---

[8] The X-ray luminosities as measured within an aperture of radius R_{500}.

[9] *XMM-Newton* is an ESA science mission with instruments and contributions directly funded by ESA Member States and the USA (NASA).

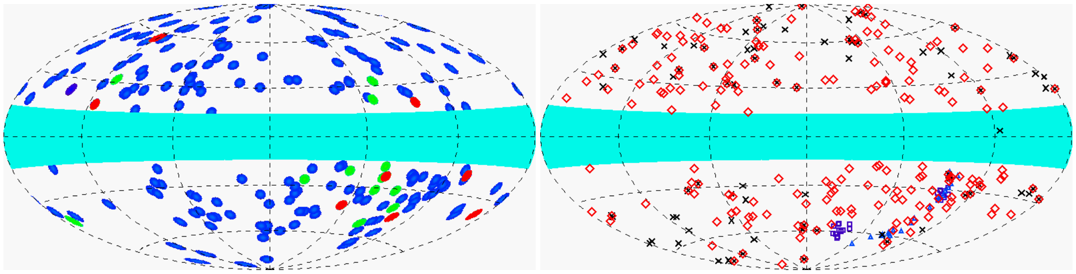

Fig. 3. Distribution of ESZ clusters and candidate clusters on the sky (Galactic Aitoff projection). *Left panel*: in blue are ESZ clusters identified with known clusters, in green the ESZ confirmed candidates, and in red the ESZ candidate new clusters yet to be confirmed. *Right panel*: in red diamonds the ESZ sample, in black crosses the compilation of SZ observations prior to 2010, in dark blue triangles ACT clusters from Menanteau et al. (2010), and in purple squares SPT clusters from Vanderlinde et al. (2010). The blue area represents the masked area of $|b| < 14$ deg.

the IR data, and one with the Arcminute MicroKelvin Imager[10] (AMI, Zwart et al. (2008)) for the confirmation of *Planck* candidates with SZ observations.

An ensemble of SZ candidates spanning a range of S/N between four and eleven was selected from earlier versions of the HFI channel maps and sent to the above-mentioned facilities. The targets were selected from a list of SZ candidates after the external validation stage (i.e., identification of known clusters). They went through visual inspection of their maps and spectra produced by all the available methods described in Sect. 5.2.2. Furthermore, in order to avoid duplicating existing observations of candidates with the same or similar facilities, the cluster candidates were further cross-matched with logs of X-ray, optical, and NIR observatories.

The search in X-ray observatories (ROSAT, Suzaku, *XMM-Newton*, and *Chandra*) was performed using the HEASARC tool[11]. For *XMM-Newton* and *Chandra* both master catalogues and accepted GO (Guest Observer) targets were used in the search. For Suzaku, only the master catalogue was used. In the case of optical and NIR observatories, the search was performed in the public logs of several optical/infrared observatories. In some cases, this search was completed using VO (Virtual Observatory) tools[12]. The checked resources were: ING Archive, UKIRT Archive, ESO Archive, HST Archive (at ESO), CFHT Archive, AAT Archive, NOAO Science Archive, Multimission Archive at STScI (MAST), Gemini Science Archive, and SMOKA (Subaru Mitaka Okayama Kiso Archive). In addition, a search in the footprint of the covered area for known surveys was performed. The searched areas considered were those of SDSS, UKIDSS, and HST (ACS-WFC) as they are described in the VO footprint service[13] (Budavári et al. 2007), as well as those of SPT and ACT experiments.

The details and results of the confirmation follow-up with *XMM-Newton* are given in Planck Collaboration (2011e). A total of 25 targets were observed with short snapshot exposures (i.e., 10 ks nominal EPN) out of which 21 were confirmed as clusters or systems of multiple extended X-ray sources (i.e., double or triple). Complying with *Planck* policies and following the agreement between the *Planck* and *XMM-Newton* ESA project scientist, all the data are made public with the publication of the *Planck* early results and the *Planck* ERCSC. Of the 21 confirmed *Planck* SZ sources, 11 are found in the ESZ sample and are discussed in Sect. 5.2.1. The remaining clusters with $S/N < 6$ are discussed in Planck Collaboration (2011e). One candidate cluster in the ESZ sample was confirmed by AMI and WISE. None of the targets sent for observation in the optical with the ENO telescopes met the ESZ selection criteria.

5. Results of the validation

In the following we will detail the outcome of the external validation of the 190 SZ candidate clusters retained after the internal validation. We find that they are distributed between known clusters (169 in total, Fig. 3 blue) and 21 candidate new clusters. Among those 21, twelve have been confirmed (Fig. 3 yellow) and these are discussed in Sect. 5.2.1. Nine remain as candidate new clusters requiring confirmation (Fig. 3 red); they are described in Sect. 5.2.2. The further checks performed on the candidate new clusters resulted in the rejection of one of the nine candidates.

The final released ESZ list thus comprises 189 clusters or candidate new clusters. The content of the released data[14] is presented in Appendix A.1. Table 1 summarises the different steps of ESZ sample construction and validation detailed in the previous sections. Figures 5 and 6 show illustrations of the raw and "cleaned" channel maps (from 100 to 545 GHz) as well as corresponding y-maps, for a few clusters, with S/N ranging from the highest ones to more typical ones.

5.1. ESZ candidates identified with known clusters

The external validation with ancillary data identified 169 clusters in total out of the 190 candidates detected blindly. They are known X-ray or optical clusters and *Planck* data provide the first measure of the SZ signal for the majority of them, opening a new observational window on those already known objects.

Most of the identified SZ candidates, 162 in all, were associated with known clusters from the MCXC compilation and 158 have known redshifts (provided in the compilation), X-ray luminosities, X-ray estimated sizes (θ_{500}), etc. Moreover, as expected, a very large fraction of them (127 clusters) are at the same time identified in the optical. They are mostly Abell clusters from the ROSAT X-ray cluster catalogues.

The remaining seven identified *Planck* clusters were obtained from search in SIMBAD (one cluster, RXJ0748.7+5941,

---

[10] AMI is a pair of interferometer arrays located near Cambridge, UK, operating in six bands between 13.5 and 18 GHz, with sensitivity to angular scales 30 arcsec–10 arcmin.

[11] `http://heasarc.gsfc.nasa.gov/cgi-bin/W3Browse/w3browse.pl`

[12] VO command line tools `http://iraf-nvo.noao.edu/vo-cli/`

[13] `http://www.voservices.net/footprint`

[14] `http://www.rssd.esa.int/Planck`

Table 1. Summary of the ESZ sample construction and validation steps.

Selection		SZ Candidates	Rejected
	$S/N \geq 6$ and good quality flag on SZ spectrum	201	
	Detected by one method only		11
	Bad quality flag from visual inspection		1
ESZ sample		189	
Known clusters		169	
	X-ray only	30	
	Optical only	5	
	NEDSimbad only	1	
	X-ray + Optical	128	
	X-ray + SZ	1	
	SZ + Optical	1	
	X-ray + Optical +SZ	3	
New *Planck* clusters		20	
	XMM confirmed	11	
	AMI confirmed	1	
	Candidate new clusters	8	

observed by ROSAT but not part of the NORAS catalogue (Appenzeller et al. 1998) and without published redshift), from logs of observatories (one cluster, H1821+643 at $z = 0.299$ (Schneider et al. 1992)) and from optical only, i.e., without an X-ray counterpart, identification with Abell or Zwicky clusters (five clusters). These are ZwCl2120.1+2256, AC114Northern, A3716S, ZwCl1856.8+6616, and ZwCl0934.8+5216 clusters. The last two have no published redshifts. For all these clusters, redshifts when they are available are retrieved from the SIMBAD and NED databases.

The cross-match with known SZ clusters further indicates that one cluster, AS0520, is common to *Planck*, ACT and SPT. Additionally, five[15] clusters from ACT are in common with the *Planck* ESZ sample, and twelve massive clusters observed by SPT (Plagge et al. 2010) are also observed by *Planck* and quoted in the ESZ. Finally by comparing with the SZ compilation from Douspis et al. (in prep.) we find that, in total, 41 clusters from the ESZ sample have already been observed in SZ by previous experiments. For these clusters *Planck* provides us with a homogeneous set of SZ measures. Moreover, out of the full ESZ sample about 80% have been observed in SZ for the first time and have a homogeneous measurement of their Compton parameter from *Planck*.

Out of the known clusters in the ESZ sample, a few are given in the Early Release Compact Source Catalogue (ERCSC) (Planck Collaboration 2011v) as they were detected by the source extraction techniques used to construct the ERCSC. They are 1ES 0657-55.8 (commonly known as the bullet cluster and detected blindly with an S/N of 19.7), A2218, ACO S0520, CIZA J1938.3+5409, A0119, RXC J1720.1+2637, A3376, and MACS J2135.2-0102. It is worth noting that the quoted fluxes in the ERCSC are obtained using aperture photometry on the channel maps without band merging. They cannot be compared easily with the obtained integrated Compton parameters in the present article. Moreover, two of the above-listed clusters, RXC J1720.1+2637 and MACS J2135.2-0102, suffer from astrophysical contamination that may affect the computed Y.

5.2. New Planck clusters in the ESZ sample

The ESZ sample contains 20 new clusters or candidates clusters with S/N ranging from 11.5 to 6. As mentioned above, a follow-up programme set up to help understand the selection of *Planck* clusters allowed us to confirm 12 clusters. Eleven were confirmed with *XMM-Newton* snapshot observations, while one cluster was confirmed with AMI observations and corresponds to an overdensity of galaxies in the WISE data.

5.2.1. Confirmed ESZ cluster candidates

The *XMM-Newton* observations for confirmation of SZ candidates were based on earlier versions of the channel maps and an earlier version of the data processing than that used for the ESZ construction. The 25 targets sent for observation were selected in two different campaigns, a pilot programme (exploring S/N from six down to four) and a higher S/N programme (above S/N of 5). Among the 21 *Planck* cluster candidates confirmed by snapshot observation with *XMM-Newton*, 11 clusters have a *Planck* S/N above six (in the present map version) and thus meet the ESZ selection criteria. Two of them were found to be double clusters on the sky. All eleven are published in the ESZ release. Together with the remaining ten clusters confirmed by *XMM-Newton*, all are described in Planck Collaboration (2011e). In the following we just summarise the general properties of the new confirmed clusters in the ESZ.

The eleven new clusters in the ESZ confirmed by *XMM-Newton* have S/N ranging from 11.5 to 6.3. They were found to lie below the REFLEX flux limit of 3×10^{-12} erg s^{-1}, except for two confirmed clusters above the limit. These clusters happen to have associations with BSC sources and to be situated above the MACS limit; however their redshifts, $z = 0.27$ and $z = 0.09$ are below the considered redshifts for MACS (see the detailed discussion in Planck Collaboration (2011e)). The redshifts of the new confirmed clusters were estimated directly from X-ray observations of iron emission lines, and range between $z = 0.2$ and 0.44. Only two out of the eleven confirmed new clusters have optical redshift estimates. For one new cluster (PLCKESZ G285.0-23.7), the agreement between the X-ray estimated and photometric redshifts is quite good. The second cluster, PLCKESZ G262.7-40.9, was found to be an ACT cluster, published after the scheduling of *XMM-Newton* observation, for which there is a discrepancy between the X-ray-estimated

---

[15] One of the candidate new clusters confirmed by *XMM-Newton* appeared in publication as one of the ACT SZ optically-confirmed clusters (Menanteau et al. 2010) to be observed by *Chandra*, after we scheduled it for observation with *XMM-Newton*: PLCKESZ G262.7-40.9/ACT-CL J0438-5419. We retain it as new candidate in the following.

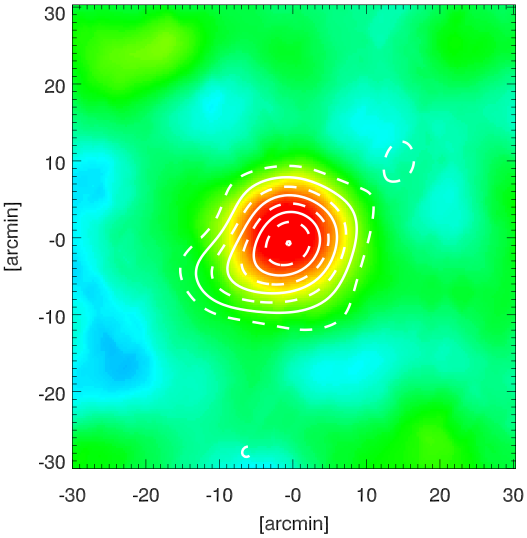

Fig. 4. y-map of PLCKESZ G139.59+24.19 as observed by *Planck* (colour image) and AMI (contours) at a common resolution of 13 arcmin. The contours are from two to nine in S/N ratio.

redshift ($z = 0.39$) and the photometric redshift ($z = 0.54$) from Menanteau et al. (2010). The range in temperature spanned by the new confirmed clusters in the ESZ is from about 4 to 12 keV, and the derived masses range from about 4 to $15{\times}10^{14} M_{\odot}$. Three new clusters in the ESZ sample have masses of $10 \times 10^{14}\ M_{\odot}$ or above, including the most massive cluster detected by *Planck* with a mass of about $15 \times 10^{14}\ M_{\odot}$. The confirmation of the *Planck* new clusters by *XMM-Newton* provides us with positions and, most of all, a better estimate of the cluster size that will be important for the re-extraction of Y values (see Sect. 6.2).

One additional candidate cluster, PLCKESZ G139.59+24.19 detected at $S/N = 7.2$, was confirmed by a pilot project for confirmation with the AMI interferometer (see Fig. 4 showing the *Planck* y map with the AMI contours, obtained after the subtraction of bright sources with the large array observations, overlaid). The *Planck* cluster was detected at 9σ by AMI in a long-time exposure of approximately 30 h. Preliminary results from AMI give an integrated Compton parameter of $Y_{5R500} = (17.0 \pm 1.7) \times 10^{-4}$ arcmin^2, extracted fixing the cluster size to the estimated size from *Planck*. The *Planck* value, $Y_{5R500} = (32 \pm 13) \times 10^{-4}$, is obtained from the blind detection of the cluster. The error bar takes into account the uncertainty in the cluster size estimate by the MMF3 algorithm. A detailed comparison is planned. This same cluster was also confirmed at a S/N level of five by WISE.

5.2.2. ESZ candidate new clusters

A closer inspection of the ESZ candidate new clusters was performed in order to ensure the reliability of the retained candidate new clusters. The same close inspection was also performed, a posteriori, in order to confirm the rejection of the 11 candidates excluded in the final steps of the ESZ construction because they were observed solely by MMF3 (Sect. 4.1). This closer inspection of the candidates was based on both internal (using *Planck* alone) and external data.

For the in-depth inspection of the *Planck* data, we used cleaned channel maps, reconstructed y-maps and SZ spectra. All these products are quite sensitive to the procedure used for cleaning the channel maps, i.e., to the component separation method. We therefore simultaneously employed different cleaning approaches developed by the *Planck* collaboration, briefly described below, in order to ensure convergence and redundancy in the derived conclusions. One of the methods is based on the construction of SZ y-maps centred on the ESZ candidate positions using the Modified Internal Linear Combination Algorithm (MILCA, Hurier et al. 2010) applied independently on each SZ-centred patch. The contribution from other sources of sky emission such as thermal dust and radio and infrared sources is thus more accurately reduced. Other approaches based on local component separation and aperture photometry were also developed in order to check the y-maps and SZ spectra of the candidates. Patches centred on the SZ candidates are produced from the *Planck* channel maps and the IRIS map (Miville-Deschênes & Lagache 2005). Local component separation is performed by decorrelating from the low-frequency channels an extrapolation of the dust emission computed with the 857 GHz and IRIS maps. The "dust-free" 217 GHz map is then removed from all channels and visual inspection can then be performed on these cleaned patches. From this set of maps we then obtain SZ reconstructed y-maps and an SZ spectrum by applying aperture photometry to each patch. The internal inspection of the *Planck* data (y-maps, frequency maps and spectra) therefore provides us with a set of quality flags that were used for the selection of targets for the follow-up programmes and that are used for a qualitative assessment of the reliability of the candidates.

Converging negative quality assessments result in the rejection of the SZ candidates. However in most cases, it is useful to combine and complement the *Planck*-internal quality flags with external information. In practice this consists in searching for associations with FSC (Faint Source Catalogue) and BSC (Bright Source Catalogue) RASS sources, searching in, and visualising, the RASS maps at the candidate cluster positions, and finally performing visual checks of the DSS (Digital Sky Survey) images in the candidate field (within a five arcminute radius from the *Planck* position). Based the lessons learnt from the *XMM-Newton* confirmation programme, the association of candidates with FSC or BSC-RASS sources (in the five arcminute radius field) was considered as an indication of the reliability of the candidate. The presence of an excess in the count-rate RASS images in the candidate field was also used as a reliability flag. The DSS images were used simply as an "empirical" assessment of the presence of an overdense region. It is worth noting that the external information provided in particular by the RASS data never supersede the *Planck*-internal quality flags. As a matter of fact, two of the confirmed new clusters had neither FSC nor BSC associations. Conversely, associations with FSC and BSC-RASS sources were found for SZ candidates that turned out to be false detections (Planck Collaboration 2011e).

Using the internal quality flags and the additional external checks, out of the nine candidate new clusters retained by the ESZ construction, seven were judged reliable. Two candidate new clusters had rather poor quality flags and no external associations. One of them was found to be associated with dust cloud emission. Note that this source was not flagged by the cross-match with the CC and Galactic sources, nor identified with a rising spectral distribution at high frequencies during the internal validation and ESZ construction. This candidate was rejected from the final ESZ sample, reducing the total number of clusters and candidate clusters from 190 to 189. The second cluster candidate with low reliability (PLCKESZ G189.84-37.24), was kept in the ESZ list as it was not associated clearly with any non-SZ

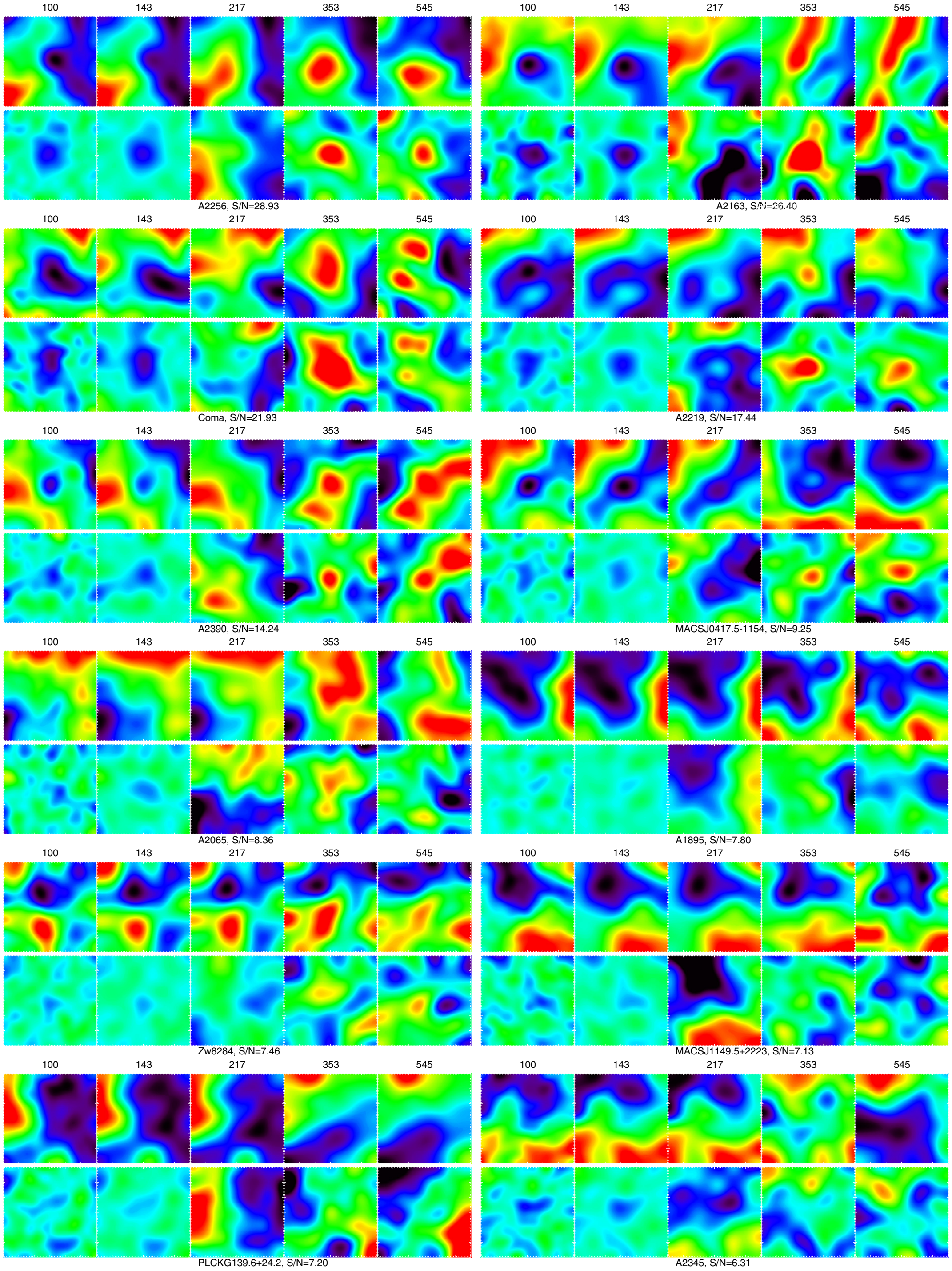

Fig. 5. Observations of a few clusters from the ESZ sample. For each cluster, the *upper panels* show the raw (1 square degree) maps at 100, 143, 217, 353, and 545 GHz. The *lower panels* show the corresponding cleaned maps (see Sect. 5.2.2). These clusters span S/N from 29 to 6 *from the upper left to the lower right*.

source. Table 2 summarises the external information associated with the candidate new clusters in the ESZ sample[16].

---

[16] During the review process 6 of the 8 *Planck* cluster candidates were confirmed by SPT (Story et al. 2011; Williamson et al. 2011) and AMI (Hurley-Walker et al. 2011) experiments independently of the *Planck* collaboration.

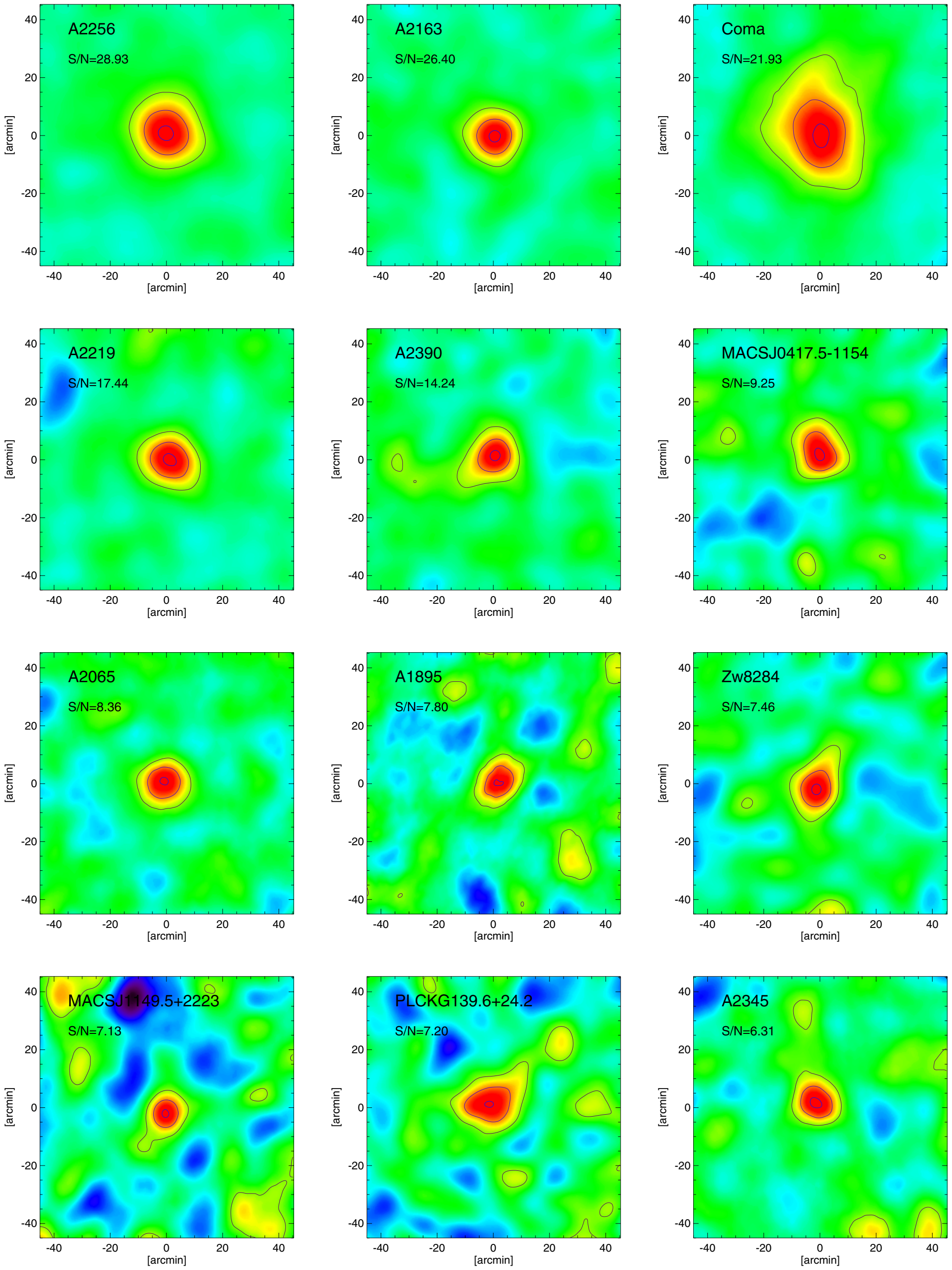

Fig. 6. Illustrations of reconstructed y-maps ($1.5° \times 1.5°$, smoothed to 13 arcmin) for clusters spanning S/N from 29 to 6 *from the upper left to the lower right*.

6. Error budget on the cluster parameters

6.1. Position

The ESZ sample contains a list of 189 clusters or candidate clusters distributed over the whole sky with positions obtained from blind detection with the MMF3 algorithm. Based on the simulation used for the SZ challenge comparison, we find that MMF3 recovers cluster positions to ~2 arcmins on average. However, there is a large scatter in the positional accuracy, as seen in Fig. 7.

For the 158 ESZ candidates identified as X-ray clusters with known X-ray size, the coordinates of the X-ray counterpart are given by the MCXC. The X-ray position is also given for the *Planck* cluster candidates confirmed by *XMM-Newton* as single objects. The comparison of the SZ candidate positions derived from the blind detection with the X-ray positions of the identified

Table 2. For the *Planck* candidate new clusters not yet confirmed at the time of submission, external information from RASS.

Name	RASS association	Distance to source (arcmin)	S/N of RASS source	S/N of RASS in *Planck* aperture	Note
PLCKESZ G115.71+17.52	BSC	0.17	8.7	8.5	Possible contamination by dust emission
PLCKESZ G121.11+57.01	FSC	1.72	2.9	4.1	Possible association with WHL J125933.4+600409 from Wen et al. (2009), z = 0.33
PLCKESZ G189.84-37.24	None	–	–	1.3	Low reliability, high level of contamination by Galactic emission
PLCKESZ G225.92-19.99	FSC	1.11	2.5	6.7	With *XMM-Newton* and HST pointed observations
PLCKESZ G255.62-46.16	FSC	0.9	2.7	3.8	With ESO and Suzaku pointed observations
PLCKESZ G264.41+19.48	BSC	1.22	4.6	5.7	
PLCKESZ G283.16-22.93	FSC	0.54	3.6	4.2	
PLCKESZ G304.84-41.42	BSC	0.55	3.6	5.1	With ESO pointed observations

or confirmed clusters for a total of 167 clusters is shown in Fig. 7, left panel. The positional offset between *Planck* blind and X-ray positions, $D_{\rm SZ-X}$, is of the order of 2 arcmin on average, consistent with the estimates obtained from the SZ challenge simulation. Very few clusters (8 in total over 167) have an offset $D_{\rm SZ-X} > 4$ arcmin, and stand out as clear outliers in the distribution. It is worth noting that such a positional offset combines both the uncertainty in the position reconstruction from MMF3 and the possible physical offset between the centroids of X-ray and SZ signals (e.g., in merging clusters). The eight clusters with $D_{\rm SZ-X} > 4$ arcmin are all nearby merging clusters or members of larger structures such as A3532 in the Shapley supercluster, or contaminated by radio source emission. The cluster A1066 ($z = 0.07$), which has the largest positional offset ($D_{\rm SZ-X} = 10$ arcmin), is in the Leo Sextans supercluster (Einasto et al. 2001). In addition, it may suffer from point source contamination. The cluster Abell 1367 at $z = 0.02$ with $D_{\rm SZ-X} = 7.8$ arcmin is a young cluster currently forming at the intersection of two filaments (Cortese et al. 2004) with complex gas density and temperature structures (Ghizzardi et al. 2010).

As seen from Fig. 7, right panel, large (greater than four arcmin) offsets are only seen in nearby clusters (seven out of the eight clusters with $D_{\rm SZ-X} > 4$ have redshifts lower than 0.08). They remain smaller than the cluster size, as expected for offsets dominated by physical effects. On average, the offsets tend to decrease with increasing redshift and seem to become independent of redshift above $z \sim 0.3$. This is due to the decreasing contribution of possible physical offsets, which become unresolved. The overall offset, including the absolute reconstruction uncertainty, remains smaller than the cluster size for most of the clusters in the ESZ θ_{500} (Fig. 7, right panel). However, we expect that it will be of the order of cluster size for clusters at higher redshifts than the range currently probed. This positional offset is therefore an additional source of uncertainty in the cluster position which needs to be taken into account in the follow-up observations for candidate confirmation.

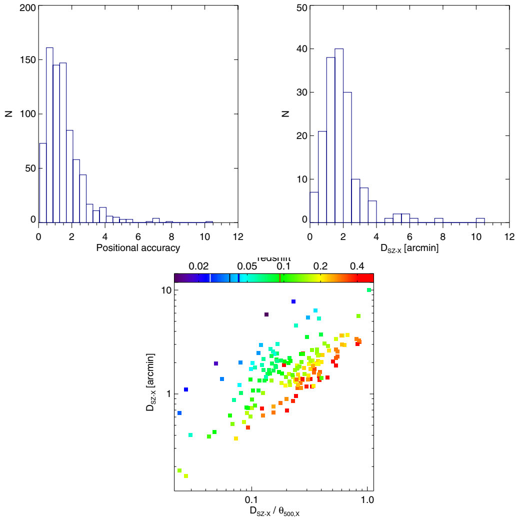

Fig. 7. *Upper left panel*: positional accuracy from MMF3 based on simulations for the SZ challenge. *Upper right panel*: distribution of the distance between the SZ blind position and the X-ray position ($D_{\rm SZ-X}$) for 167 known, or confirmed with *XMM-Newton*, X-ray clusters. *Lower panel*: separation of the SZ blind and X-ray positions $D_{\rm SZ-X}$ as a function of $D_{\rm SZ-X}$ normalised to the cluster size $\theta_{500,\rm X}$.

6.2. Cluster size-Y degeneracy

The MMF algorithm, and more generally algorithms that are based on the adjustment of an SZ profile to detect clusters, generally perform better than algorithms which do not assume an SZ profile. The GNFW profile used in the present study corresponds to a shape function characterised by two parameters, the central value and a characteristic scale $\theta_{\rm s}$ (with $\theta_{\rm s} = \theta_{500}/c_{500}$ and c_{500} is the concentration parameter). Simulations showed that the intrinsic photometric dispersion of the recovered integrated Compton parameter, with a GNFW profile, could be of order 30% (see Fig. 8) even with the prior information on the pressure profile. This is due to the difficulty of estimating the cluster size, which in turn is degenerate with the SZ Y estimate.

This cluster size-Y degeneracy is illustrated, here using PwS, in two extreme situations (Fig. 9) showing the likelihood plots (integrated Compton vs cluster size) of an extended high S/N cluster such as Coma (blue contours) and an unresolved $S/N = 6$ cluster (black contours). In both cases, the integrated Compton

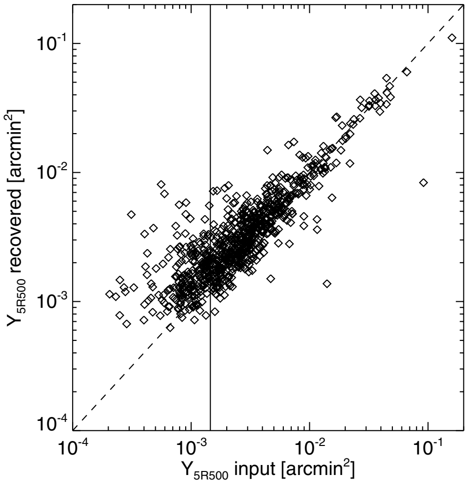

Fig. 8. Input versus recovered integrated Compton parameter from MMF3, based on simulations for the SZ challenge.

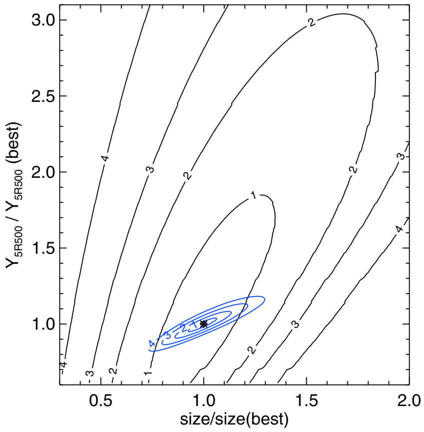

Fig. 9. Illustration of the cluster size-Y degeneracy from PwS. Shown are the cases of Coma cluster (high S/N and extended in blue), and that of an $S/N = 6$ unresolved cluster (in black). Parameters are plotted with respect to the best fit points in each direction.

parameter Y is highly correlated with the estimated cluster size. We find a correlation coefficient $\rho = 0.91$ and $\rho = 0.75$ for Coma and the "unresolved cluster" respectively. On average over the ESZ sample we find a correlation of $\rho = 0.85$. The degeneracy between cluster size and Y is extremely detrimental, as it will more than double the average fractional uncertainty relative to the Y value in the case where we knew the true value of θ_s perfectly. As a result, any attempt to constrain the cluster size (equivalently θ_s), fixing or assuming a prior for its value, brings a significant reduction on the Y value dispersion.

The issue of the cluster size-Y degeneracy is of particular importance in the case of *Planck*, for which a vast majority of clusters are only marginally resolved. This issue is also crucial when one wants to use the SZ signal as a mass proxy. Indeed, the dispersion in Y due to the cluster size-Y degeneracy is likely to dominate the intrinsic scatter of order 10% of this mass proxy (da Silva et al. 2004; Arnaud et al. 2007).

As a result, we have re-estimated the integrated Compton parameter for all the ESZ candidates with prior information on their sizes. We have chosen the X-ray sizes (θ_{5R500}) derived from the X-ray luminosities, L_{500}, as detailed in Piffaretti et al. (2011), as suitable estimates of the cluster sizes. Using the MMF3 version implemented in HFI Core team and SZ validation team, Y_{5R500} were thus re-computed from the *Planck* channel maps at fixed X-ray position and with imposed cluster size equal to the X-ray luminosity based θ_{5R500}. The integrated Compton parameter Y was re-estimated for all the clusters with known X-ray counterparts, being the 158 ESZ candidates identified with known clusters from the MCXC and the nine ESZ clusters confirmed by *XMM-Newton* as single objects.

Figure 10, left panel, illustrates the effect of fixing the position and the cluster size, in the GNFW profile, to θ_{5R500} for the 158 ESZ identified clusters. The figure displays the measured Y_{5R500} values versus the predicted $Y^{L_X}_{5R500}$ values using X-ray luminosities. The squares stand for integrated Compton parameters obtained from the blind detection whereas the diamonds are integrated Compton parameters re-extracted from the *Planck* channel maps for the MCXC-identified clusters. Figure 10, right panel, displays the ratio of blind to predicted Y_{5R500} versus the ratio of estimated cluster size from blind detection to X-ray cluster size derived from X-ray luminosity. This clearly confirms for the 158 identified clusters that an overestimate of cluster size induces an overestimate of the SZ signal. As seen in the Fig. 10 (left panel), the scatter is significantly reduced from about 43% to 34% by imposing a cluster size. Likewise the offset changes from 80% to 14%.

The dispersion in the predicted integrated Compton parameter is affected by the intrinsic dispersion in the L_{500}-M relation used to derive the predicted SZ quantities as shown in Fig. 11. The selection criterion $S/N \geq 6$ (blue diamonds in the figure) used to construct the ESZ sample indicates that the high S/N clusters are biased towards larger SZ signals, showing that the obtained positive offset in Fig. 10 (left panel) is indeed expected.

As emphasised, a prior on the cluster size helps to break the degeneracy between Y and cluster-size estimates. As a consequence, the better the cluster size estimate, the more reliable the Compton Y parameter estimate. From a selected subsample of 62 ESZ clusters with *XMM-Newton* archival data (Planck Collaboration 2011g) we have derived accurate estimates of the X-ray sizes, without using the X-ray luminosities, and the Y_{500} were re-evaluated on the *Planck* channel maps, allowing us to tightly constrain the local SZ versus X-ray scaling properties. As shown in Appendix A of Planck Collaboration (2011g), the scatter is reduced even more than in Fig. 10 (left panel) and no offset is observed any more between the predicted and measured Y_{500} values.

6.3. *Systematic effects*

Due to the cluster size-Y degeneracy discussed above, beam uncertainties are likely to have a significant impact on Y estimates for our candidates because they affect both the original detection and the estimation of cluster size. The beams can be characterised by their shapes and the associated accuracies. The beams for each frequency channel, used for the detection and Y estimate with all methods presented in this study, were assumed Gaussian with FWHM given Planck HFI Core Team (2011b). Uncertainties on the recovered beams have been estimated in Planck HFI Core Team (2011b) and found to range between 1 and 7% (from 100 to 857 GHz). These uncertainties on the

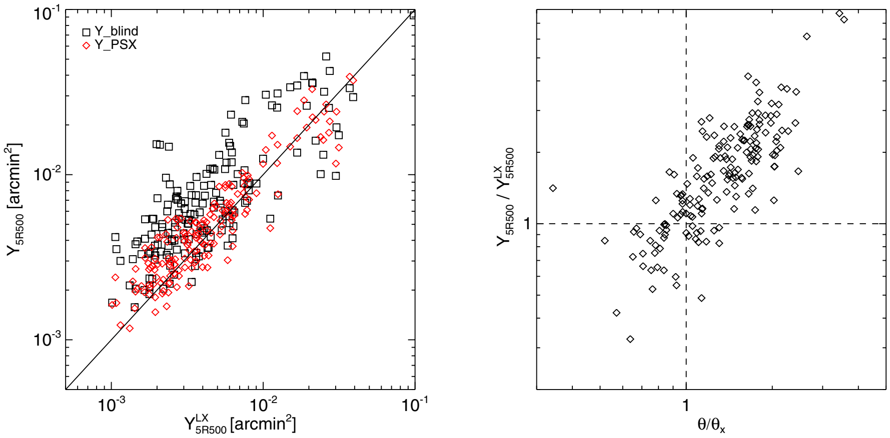

Fig. 10. *Left*: the scatterplot of the measured integrated Compton parameter Y_{5R500} from the 158 X-ray identified ESZ clusters against the predicted Y^{L_X}. Black squares: Estimated cluster size from blind detections. Red diamonds: Re-computed integrated Compton parameter at X-ray positions and with X-ray derived cluster size. *Right*: the ratio between the Y values and the predicted Y^{L_X} against the ratio between the estimated cluster size and the predicted size (θ/θ_X).

beams have been propagated to the Y measurements by applying the MMF3 algorithm on the channel maps varying the beam size within the uncertainties at $\pm 1\sigma$. In doing so we treat differently the ESZ clusters with known X-ray cluster size, for which X-ray positions and estimated θ_{5R500} are fixed, and the ESZ clusters or candidate clusters without estimated cluster size for which the Y were re-estimated without prior information. We find that the uncertainty on the obtained Y_{5R500} is of the order of 10% across the ESZ sample.

The *Planck* HFI maps used for the cluster extraction are calibrated to better than 2% for frequencies from 100 to 353 GHz, and to better than 7% beyond (see Planck HFI Core Team 2011b). This uncertainty in the calibration is accounted for again by performing the SZ-candidate detection with the MMF3 algorithm on the channel maps. We find that on average, the calibration uncertainty propagates into an uncertainty on the Y less than 2%. The highest *Planck*-HFI frequencies, with the largest calibration uncertainties, have a low impact on the SZ Y measurement and thus do not impact significantly the overall error budget.

Finally, we have checked that the colour corrections, i.e., the average SZ signal in the HFI bandpasses, induces less than a 3% difference on the estimated Y_{5R500}. The SZ-candidate detection and the Y estimates by the MMF3 algorithm were thus performed without taking into account the integration of the SZ spectrum in the *Planck* bandpasses is negligible.

Table 3 summarises the effects of beam, calibration, and colour correction. It shows that the beam effect is the major source systematic uncertainty in the SZ signal estimate. It is worth noting that the systematic uncertainties are not included in the uncertainties quoted in the ESZ table provided at `http://www.rssd.esa.int/Planck` (Planck Collaboration 2011v).

6.4. Contamination by astrophysical sources

Galactic and extragalactic sources (both radio and infrared galaxies) are known to lie in the interior of galaxy clusters and hence are a possible source of contamination for the SZ clusters and candidates (Rubiño-Martín & Sunyaev 2003; Aghanim et al. 2005; Lin et al. 2009).

In the course of ESZ validation, we have gone through an inspection of thirteen known clusters which show some poor quality flags. All these clusters were annotated and the notes can be found in Planck Collaboration (2011v). Ten of them are likely to be contaminated by dust emission from our Galaxy or by IR point sources in their vicinity. Two of them were found to be contaminated by NVSS (at 1.4 GHz, Condon et al. 1998) radio sources that are clearly seen in the LFI channels. Combining data from SUMSS (at 0.85 GHz, Bock et al. 1999), NVSS, and *Planck*'s LFI and HFI frequencies we find that most radio sources in the ESZ sample have a steep spectrum which makes their contamination to the SZ signal negligible. Three additional clusters (beyond the thirteen), have relatively bright ($S_{1.4\,\mathrm{GHz}} > 0.2$ Jy) radio sources in their vicinity ($r < 15$ arcmin). NVSS+LFI data reveal flat spectra (indexes between $\alpha = 0$ and $\alpha = -0.5$). The flux of the radio sources is thus still significant and hence the SZ signal could be affected by their presence.

A statistical analysis has been performed in order to explore the astrophysical contamination over the entire ESZ sample, rather than on an individual cluster basis.

In order to exhibit the initial average level of contamination prior to the use of the MMF algorithm, we have stacked cutouts 4.5 degrees on a side from the channel maps centred at the ESZ cluster/candidate positions from 100 to 857 GHz using a stacking library[17] detailed in Dole et al. (2006) and Bethermin et al. (2010). The Y values per frequency, obtained from aperture photometry on the stacked cutouts, are displayed in red triangles Fig. 12. The spectral signature normalised to the averaged integrated Compton-y over the whole ESZ sample shows quite good agreement with the theoretical SZ spectrum at low frequencies (Fig. 12, black solid line). Above 353 GHz the signal is highly contaminated by IR emission from Galactic dust and IR point sources.

The Y measurements, per frequency, of the MMF3 algorithm normalised to the integrated Compton-y are averaged over the ESZ sample and the resulting spectral energy distribution is

---

[17] `http://www.ias.u-psud.fr/irgalaxies/` (Bethermin et al. 2010)

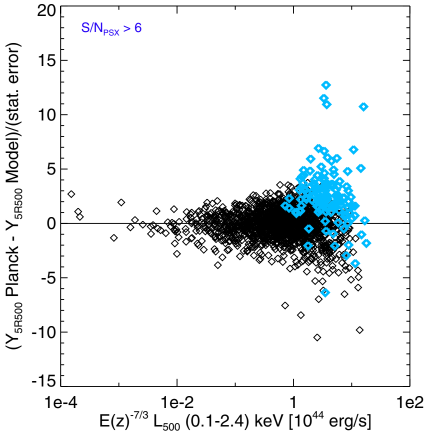

Fig. 11. Ratio of predicted vs. observed Y_{5R500} for the MCXC clusters as a function of the X-ray luminosity L_{500} used to estimate the cluster properties (radius and integrated Compton parameter). The light-blue diamonds indicate a cut of 6 in predicted S/N corresponding to the ESZ selection criterion.

Table 3. Systematic error budget on the Y_{5R500} values for the ESZ clusters.

Source	Beam	Calibration	Colour correction	Astrophysical contamination
Error contribution	8%	2%	3%	3%

compared with the normalised SZ spectrum (see Fig. 12, blue crosses). The excess of emission at high frequencies is significantly reduced by the filtering technique of the MMF algorithm, reinforcing the idea that most of the excess at the highest frequencies is due to large-scale (larger than the beam) fluctuations in Galaxy emission. The remaining excess after the filtering could be due to a combination of small-scale Galactic fluctuations and/or infrared galaxies. In order to quantify the effect of this residual IR emission on the integrated Compton-y determination, an SZ spectrum was fitted to the averaged spectrum. The normalisation was left free. The displayed error bars contain the dispersion of the measured Y per frequency and, added in quadrature, the uncertainties due to the beam, the colour correction, and the calibration (~10%, ~3%, ~2% respectively). The best value for the normalised integrated Compton parameter is $Y_{\rm fit} = 1.01$, showing an excellent agreement with the expected spectrum despite the IR excess emission at high frequencies. The same procedure was applied to the 100, 143, 217, and 353 GHz Y values and led to $Y_{{\rm fit}_{100-353}} = 0.97$. This shows that, on average, the residual IR contamination has a negligible effect (~3%) on the integrated Compton-y value estimated for the ESZ sample.

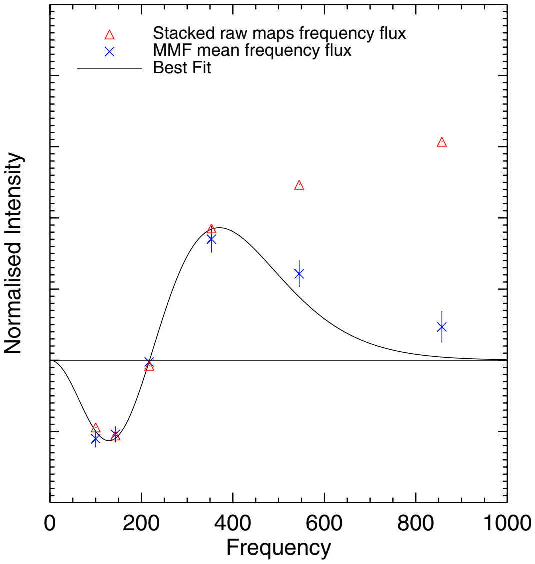

Fig. 12. Average contamination of the ESZ sample by astrophysical sources. Blue crosses: Average Y measurements from MMF3 algorithm normalised to the integrated Compton-y. Red triangles: Y, obtained from aperture photometry on the stacked cutouts in the channel maps prior filtering by the MMF. Black solid line: Normalised theoretical SZ spectrum.

7. Purity and completeness

The ESZ sample is characterised by the fact that a significant fraction of the clusters and candidate clusters lies near a selection cut. In a catalogue of this sort, the properties of the catalogued clusters will not be representative of the true underlying cluster population. For example, if the SZ signal of a cluster is related to a different cluster property such as mass (collectively referred to as "scaling relations") the observed integrated Compton-y parameter values, Y, will be biased near the selection cut, an effect known as Eddington and Malmquist biases (for discussions in a cluster context, see Mantz et al. 2010 and Andersson et al. 2011).

For the full ESZ sample, we do not always have other cluster properties to relate the integrated Compton-y to, but we can nevertheless examine some statistical effects of selection. In order to do this, we generate large mock cluster catalogues whose properties are designed to mimic those of the observed sample. To impose a selection cut on the mock catalogues, we use the *observed* relation between Y_{500} and S/N from the region significantly above the selection cut and extrapolate below it, along with an estimate of scatter again from observations. This is carried out in several redshift bins, and leads to a predicted S/N–Y scaling given by

$$S/N = 10^{1.38\pm0.03}\,(1+z)^{-5.92\pm0.24}\left[\frac{YE^{-2/3}D_A^2}{10^{-4}\ \mathrm{Mpc}^2}\right],$$

with scatter $\sigma_{\rm log-log} = 0.16$ in log-log scale. We then construct large mock catalogues of clusters through drawing of Poisson samples from the Jenkins et al. (2001) mass function normalised with $\sigma_8 = 0.8$, a value consistent with the latest WMAP constraints. To each cluster and consistent with *Planck* observations, we assign values of Y_{5R500} by adopting the Y-M scaling relation from Planck Collaboration (2011g). An S/N value is then assigned as described above, and the cut imposed to create the mock catalogue.

We first use these simulations to estimate the completeness of the ESZ sample as a function of Y_{5R500}. For clusters within a given bin in Y_{5R500}, we extract the fraction of mock clusters which lie above the selection cut. The result is shown in Fig. 13 (solid line), and indicates that the sample becomes significantly incomplete (less than 90% complete) below $Y_{5R500} \simeq 0.013$ arcmin^2. This result is fairly insensitive to the assumed

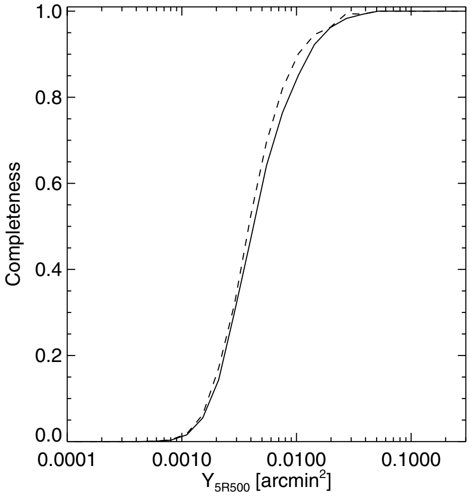

Fig. 13. Expected completeness of the ESZ sample as a function of Y_{5R500}, estimated from mock cluster catalogues.

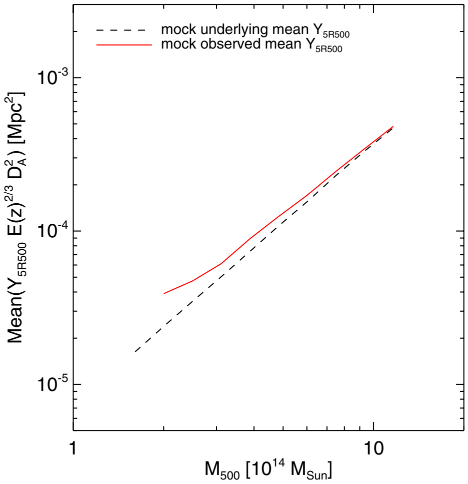

Fig. 14. Expected mean Y_{5R500}, as a function of cluster mass, for the observed sample and for the predicted underlying cluster sample. At low masses, the observed mean rises above the true mean due to Malmquist bias.

mass function normalisation. For example, changing to $\sigma_8 = 0.9$ (dashed line) causes only small variations in the completeness function. For this case, a completeness of 90% is obtained at $Y_{5R500} \simeq 0.010$ arcmin^2.

We then analyse the extent to which the mean Y_{5R500} of the observed clusters is biased in relation to the mean Y_{5R500} of the underlying cluster distribution, through those clusters with low Y_{5R500} for a given mass being lost via selection. The underlying mean Y_{5R500} in the mock samples is given by the input Y_{500}–M_{500} scaling relation from Planck Collaboration (2011g) and the observed Y_{5R500}–Y_{500} scaling; as shown in Fig. 14 the mean of the observed clusters will be biased upwards from this, the effect becoming significant for $M_{500} < 6 \times 10^{14}\ M_{\odot}$. Note that this bias does not imply that the Y_{5R500} measurements for the ESZ clusters are systematically wrong; the bias is because the selection cut prevents those clusters being representative of the true cluster population at those masses.

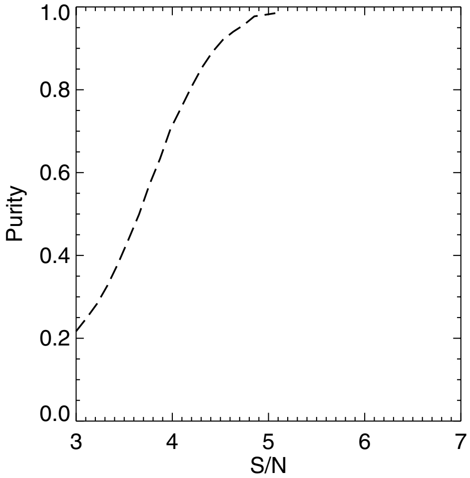

Fig. 15. Purity as a function of S/N from MMF3, based on simulations for the SZ challenge.

Finally, numerical simulations based on the *Planck* Sky Model were used to estimate the purity of the *Planck* SZ catalogue. They showed on a simulated sky that a cut in S/N of five ensures 100% purity of the obtained sample (see Fig. 15). However, the simulation does not capture the entire complexity of the real sky and, in particular, the contamination by astrophysical sources emitting above 217 GHz from IR sources and dust emission or cold cores was found to be higher than expected. The final ESZ sample obtained after applying the selection criterion cut in S/N of 6 contained 190 SZ candidates. The validation of the sample showed that one of them was found to be a spurious source identified with dust emission and it was rejected. The remaining candidate new clusters are to be confirmed. The purity of the ESZ sample thus lies between about 95% and 99%.

Although an attempt to characterise the completeness and purity is made, we do not provide a fully characterised selection function along with the ESZ sample. The cluster size-Y degeneracy discussed above, together with the large scatter in the contamination level of the SZ detections due mostly to dust emission, makes it difficult to draw a simple relation between the S/N limit used to construct the sample and the measured Y_{5R500}. It is thus not presently possible to provide a reliable mass limit to our sample. When the telescope beam is larger than the cluster size, a survey is limited by SZ signal. Then, since for the SZ signal the redshift dependence enters through the angular-diameter distance rather than the luminosity distance, the mass selection function is more uniform in SZ than in X-ray surveys. However in our case most of the clusters detected by *Planck* are at nearby redshifts ($z_{\rm median} = 0.15$) and the majority are resolved, adding even more complexity to the selection function.

8. Statistical characterisation of the ESZ sample

The ESZ sample is the first all-sky sample of high S/N SZ-detected clusters of galaxies produced by *Planck*. Its high reliability is ensured by the high S/N of the reported detections and by the subsequent validation process. The S/N of the objects in the sample, obtained from blind detection using MMF3 on the reference channel maps, are displayed in Fig. 16. They range between 6 and 29 with median S/N of about eight. Six clusters, including A2163 with $S/N = 26$ and Coma with $S/N = 22$,

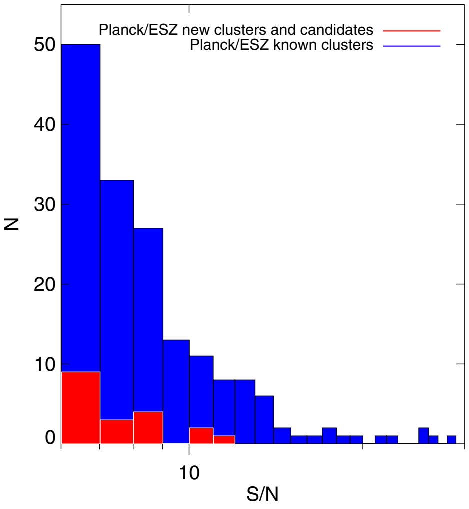

Fig. 16. Distribution of S/N (for the full ESZ sample: clusters and candidate clusters).

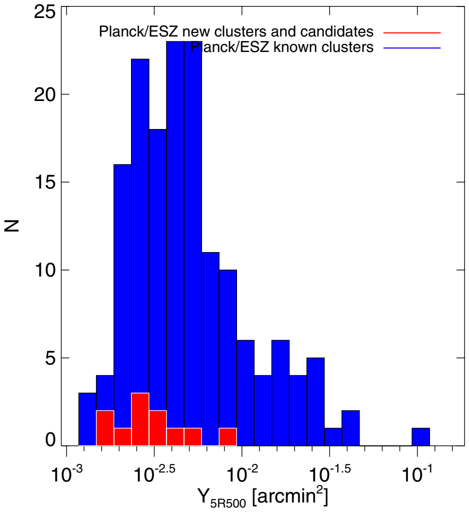

Fig. 17. Distribution of ESZ sample in integrated Compton parameter Y.

are in the tail of the S/N distribution with S/N above 20. The twelve confirmed *Planck* new SZ clusters, included in the ESZ, have their S/N distributed between 6.3 and 11.5. Additional confirmed new clusters with lower S/N are given in Planck Collaboration (2011e). The eight candidate new clusters yet to be confirmed have S/N ranging from 6 to 8.5.

The ESZ provides us with measures of the integrated Compton parameter within a $5R500$ sphere, Y_{5R500}, for 189 clusters or candidates. For about 80% of the known clusters in the ESZ, this is the very first SZ measure performed in their direction. The integrated Compton parameter of the whole sample, displayed in Fig. 17, shows that the SZ signal extends over about two orders of magnitude from about 1.5×10^{-3} to 120×10^{-3} arcmin^2. Unsurprisingly, the largest value is that of the Coma cluster. Moreover, the estimated cluster sizes from the MMF3 algorithm for the ESZ clusters and candidates are all above $5\theta_{500} = 8$ arcmin, indicating that the high S/N clusters under study can all be considered as extended sources. We compare the estimated cluster size (from blind detection) with the X-ray cluster size obtained from the X-ray observation of the confirmed SZ clusters, considered as a representative cluster size. We find that the SZ blind size is generally larger than the X-ray cluster size; it can be two times larger. As discussed previously, due to the cluster size-Y degeneracy this affects the integrated Compton parameter measurement.

Using the MCXC compilation and the *XMM-Newton* observations of the confirmed *Planck* SZ candidates, we obtain masses, M_{500}, estimated from mass proxies (luminosity, L–M relation, or Y_X) for 167 clusters out of the 189 of the ESZ sample. Furthermore, using the redshift information compiled in the MCXC that we retrieved during the validation process and the redshift estimates from *XMM-Newton* follow-up observations, we gather the redshifts for 173 clusters of the ESZ sample. The distributions of redshifts and masses are exhibited in Figs. 18 and 19, respectively. The redshifts of the ESZ sample are distributed in the range of small to moderate redshifts from about $z = 0.01$ to $z = 0.55$, with a median redshift of 0.15. The vast majority of the ESZ clusters, 86%, are thus nearby ones lying below $z = 0.3$. Most of the newly-discovered clusters confirmed by *XMM-Newton* within the ESZ sample have redshifts of the order of 0.4. Among the new *Planck* clusters confirmed by *XMM-Newton*, but with S/N lower than 6, released outside the ESZ we find a cluster with $z = 0.54$. As for the mass distribution of the ESZ clusters, it spans over a decade with cluster masses ranging from 0.9 to 15×10^{14} $M_\odot$ within a surveyed volume of the order of 3.5×10^{10}Mpc^3. It is worth noting that in surveying the whole sky, *Planck* has a unique capability to detect rare massive clusters in the exponential tail of the mass function. Indeed, among the 21 newly discovered clusters confirmed by *XMM-Newton* in total (pilot follow-up programme and high-S/N programme) three have total masses of 10×10^{14} $M_\odot$ or larger and two of them are high S/N clusters in the ESZ sample.

In order to check the consistency of the cosmological model, we compare the measured Y_{5R500} with the X-ray predicted $Y^{L_X}_{5R500}$ that is derived in a given cosmology. To do so, we use the 158 ESZ clusters with X-ray-based size estimates. We vary the cosmological parameter H_0, in a range of 30 to 100 km s^{-1}/Mpc assuming a flat universe ($\Omega_{\rm m} = 0.3$ and $\Omega_\Lambda = 1 - \Omega_{\rm m}$). The integrated Compton parameters of the 158 clusters were re-estimated from the *Planck* data with the size $5R_{500}$ obtained for each explored set of cosmological parameters. The predicted SZ signals are then compared with the SZ signal measured by *Planck* providing us with the best value for H_0. We find that h is barely constrained, with a best estimate of $H_0 = 71^{+10}_{-20}$ km s^{-1} Mpc^{-1} (1σ uncertainty).

8.1. Comparison with existing catalogues

After the first blind detection of galaxy clusters through their SZ signature by SPT (Staniszewski et al. 2009) and further discoveries by both SPT (Vanderlinde et al. 2010) and ACT (Menanteau et al. 2010), *Planck* with its broad frequency coverage provides the first sample of SZ clusters detected blindly over the whole sky. For its first and early release, *Planck* delivers to the community 189 clusters and candidates with $S/N \geq 6$ in the ESZ sample, and an additional ten clusters at lower S/N. In total, the 30 new SZ-discovered clusters or candidates by *Planck* double the number of new clusters provided by ACT and SPT during the last year based on their 455 deg^2 and 178 deg^2 respective surveys. Moreover, *Planck* provides the first homogeneous SZ measurements for many known X-ray or optical clusters.

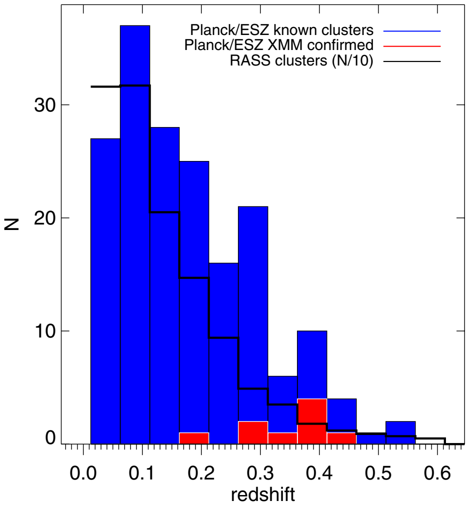

Fig. 18. Distribution of ESZ sample in redshift. The 177 identified ESZ clusters with redshift (from optical or X-ray observations) are in blue, the ESZ clusters confirmed with *XMM-Newton* in red, and the RASS clusters (number density divided by 10) in black solid line.

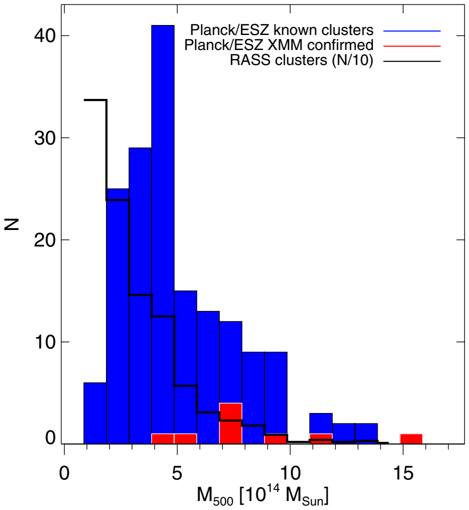

Fig. 19. Distribution of ESZ sample in mass. The 167 identified ESZ clusters with masses are in blue, the ESZ clusters confirmed with *XMM-Newton* in red, and the RASS clusters (number density divided by 10) in black solid line.

It is worth examining the distribution of the SZ clusters in the M-z plane (see Fig. 20). The range of redshifts covered by the *Planck* ESZ sample, from $z = 0.01$ to 0.55 with more than 80% of the clusters lying below $z = 0.3$, is quite complementary to the high redshift range explored by ACT and SPT experiments, from $z \simeq 0.15$ to 1.2. The comparison of the estimated masses from the different experiments is complicated by the fact that they are obtained using different approaches, from the use of X-ray proxies to that of mass-significance relations. Overall, we can see from Fig. 20 that the SPT cluster masses quoted in Vanderlinde et al. (2010) range between 1 and 5×10^{14} $M_{\odot}$. As mentioned previously, *Planck*, being an all-sky survey, spans a broader cluster mass range from 0.9 to 10×10^{14} $M_{\odot}$ and is particularly adapted to the detection of very massive clusters in the tail of the distribution.

The combination of *Planck* with ACT and SPT experiments already nicely samples the M-z plane (see Fig. 22). In particular the highest redshift clusters are accessible to ACT and SPT and the most massive clusters to *Planck*. Moreover, *Planck* already samples the low-mass low-redshift space quite well and will provide us with a robust reference point in this range. With the deeper observations of the whole sky, combined with appropriate follow-up programmes for redshift estimates, *Planck* will be able to explore the cluster mass function in its most cosmologically interesting regimes: high redshifts and high masses. However, the detection of the highest redshift clusters is likely to be hampered by the dilution by *Planck* beam. A combination of the *Planck* ACT, and SPT carefully taking into account the selection functions of all three experiments will thus be needed to fully take advantage of SZ clusters as a cosmological probe.

Moreover, combining the data from a sample of clusters with different resolutions (including high-resolution imaging of SZ clusters with interferometric experiments like SZA and CARMA) will allow us to perform detailed studies of extended clusters and have a much better handle on the pressure profile from SZ data directly.

Although the ESZ sample is not a catalogue with a fully characterised selection function, it is worth comparing it to the ROSAT-based cluster catalogues. To do this we take advantage of the MCXC, which contains not only NORAS and REFLEX but other survey-based and serendipitous cluster catalogues. Using the homogenised cluster properties of the MCXC compilation, we can moreover predict the SZ signal and the S/N ratio for a measurement of the Compton Y parameter. In order to do this we estimate the *Planck* noise from real noise maps at the cluster positions using MMF3. Using this information, we compared the number of detected clusters in the ESZ at $S/N \geq 6$ to the number predicted at that level of significance. We find very good overall agreement in terms of detected and predicted clusters, despite the fact that the predictions we use are based on X-ray-selected clusters from the MCXC compilation and that the cluster model used for the prediction does not account for the dispersion in the scaling relations, and despite the noise properties of channel maps being inhomogeneous across the sky. Only 26 MCXC clusters with predicted $S/N \geq 6$ are not within the ESZ sample. For 20 of these clusters information on the presence of a cool core or peculiar morphology is available in the literature. We find that 13 of these host cool cores. For these clusters, the X-ray luminosity is boosted due to the central density peak. The mass predicted from the luminosity, and hence the predicted SZ signal, is over-estimated. For 3 clusters the luminosity measurements adopted in the MCXC are not reliable because of evidence of AGN contamination (e.g., A689). The remaining four clusters are peculiar because they have very asymmetric morphologies or are located in superclusters (e.g., A3526 in Centaurus and the A901/A902 system), making the SZ signal predictions highly uncertain.

There is a large overlap between the *Planck* ESZ sample and the RASS-based cluster catalogues, in particular REFLEX and NORAS (Fig. 21). The 162 SZ candidates identified with X-ray clusters from the MCXC compilation are predominantly clusters from the REFLEX (74) and NORAS (59) surveys, which corresponds to an overlap of 17% and 13% with the REFLEX and NORAS surveys respectively. The eleven ESZ clusters confirmed by *XMM-Newton* with $S/N \geq 6$ were found to lie just around the REFLEX flux limit (only two are above this limit).

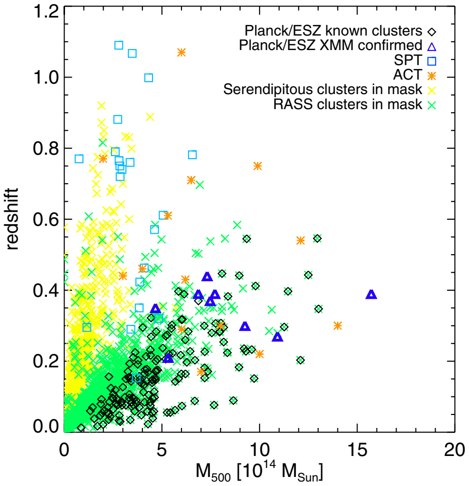

Fig. 20. The 158 clusters from the *Planck* ESZ sample identified with known X-ray clusters in redshift-mass space, compared with SPT and ACT samples from Menanteau et al. (2010); Vanderlinde et al. (2010), as well as serendipitous and RASS clusters.

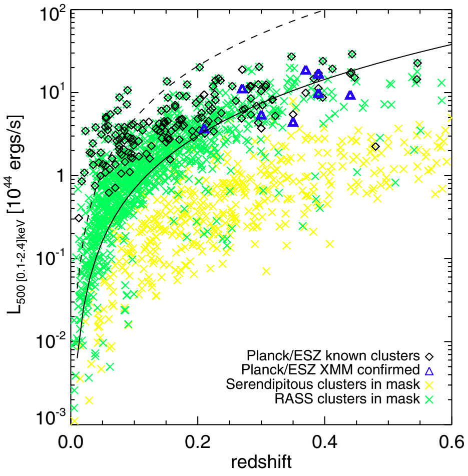

Fig. 21. The 158 clusters from the *Planck* ESZ sample identified with known X-ray clusters in redshift-luminosity space, compared with serendipitous and RASS clusters.

It is thus interesting to compare the ESZ sample mass and redshift distributions with those of the RASS-based catalogues. This is illustrated in Figs. 18 and 19 in which the RASS-based mass and redshift distribution divided by ten are over-plotted on the ESZ histograms in thick solid line. We find that the ESZ clusters with masses below $4 \times 10^{14}\ M_{\odot}$ represent only 12% of the RASS-based clusters in the same mass range; however they represent 90% of the RASS-based clusters at higher masses $M \geq 9 \times 10^{14}\ M_{\odot}$. As for the redshift distribution, the *Planck* ESZ clusters represent 14% of the RASS-based clusters with redshifts lower than 0.3 and they constitute 31% of the RASS-based clusters above $z = 0.3$.

The SDSS-MaxBCG cluster catalogue is the basis of the study of optical-SZ scaling relations (Planck Collaboration 2011h) in *Planck* data. It is used in particular to measure an integrated Compton parameter, $Y^{\mathrm{MaxBCG}}_{5R500}$, from the *Planck* channel maps at the MaxBCG position using fixed cluster size according to published weak-lensing calibrated mass-richness relations for the MaxBCG catalogue. Only 20 clusters from the MaxBCG have a measured S/N larger than six and are thus expected to be within the ESZ selection[18]. Among them, 18 are effectively associated with ESZ clusters (within a search radius of five arcminutes). One of the two clusters not in the ESZ sample is Abell 1246 ($z = 0.18$). The second is a fortuitous association with a low-redshift ($z = 0.06$) group of the MaxBCG catalogue near the position of Abell 1795, which is detected in the ESZ catalogue.

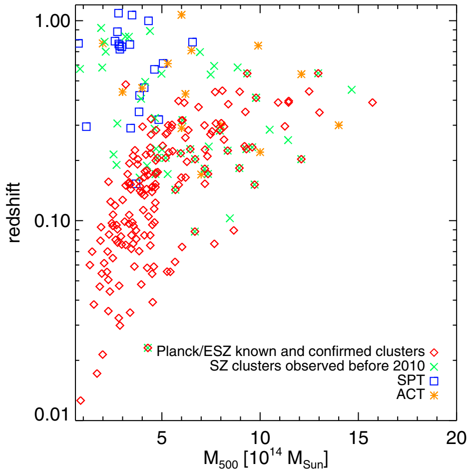

Fig. 22. The ESZ sample compared to the previously observed SZ clusters in redshift-mass space.

9. Summary

Thanks to its all-sky coverage and to its frequency range spanning the SZ decrement and increment, *Planck* provides us with the very first all-sky S/N-selected SZ sample. This early release sample of high-reliability SZ clusters and candidates (S/N from 6 to 29) was constructed using a matched multi-filter detection technique. It was validated using *Planck*-internal quality assessment, external X-ray and optical data, and a multi-frequency follow-up programme for confirmation relying mostly on *XMM-Newton* snapshot observations. The ESZ sample comprises 189 candidates, of which 20 are candidate new clusters and 169 have X-ray or optical counterparts. Of these, 162 were observed in X-ray. *Planck* provides for the first time SZ observations for about 80% of the ESZ clusters and hence a homogeneously measured SZ signal. Twelve candidate clusters in total, out of the 20, have been confirmed. One candidate was confirmed by AMI and WISE. Eleven were confirmed with *XMM-Newton*, including two candidates found to be double clusters on the sky.

The clusters in the ESZ sample are mostly at moderate redshifts lying between $z = 0.01$ and $z = 0.55$, with 86% of them below $z = 0.3$. The ESZ-cluster masses span over a decade from 0.9 to $15 \times 10^{14}\ M_{\odot}$, i.e. up to the highest masses. The ESZ, constructed using clear selection criteria, is a nearly complete (90% above $E^{-2/3}(z) Y_{5R500} D_A^2 \simeq 4 \times 10^{-4}$ Mpc^2), high-purity (above

---

[18] This number accounts for the possible association of a candidate new cluster with a cluster from Wen et al. (2009).

95%) SZ cluster sample. However, as mentioned above, it is not possible at the present stage to provide users with a full selection function.

Thanks to its all-sky coverage, *Planck* has a unique capability to detect the rarest and most massive clusters in the exponential tail of the mass function. Planck is detecting new clusters in a region of the mass-redshift plane that is sparsely populated by the RASS catalogues. As a matter of fact, two of the newly-discovered clusters in the ESZ and confirmed by *XMM-Newton* have estimated total masses larger than $10^{15}\ M_{\odot}$. Furthermore, as indicated by *XMM-Newton* snapshot observations, most of the new clusters have low luminosity and a disturbed morphology, suggestive of a complex dynamical state. *Planck* may thus have started to reveal a non-negligible population of massive dynamically-perturbed objects that is under-represented in X-ray surveys.

A significant fraction of the ESZ clusters have good archival X-ray and optical data. In addition, the ESZ sample should motivate follow-up effort by the community. It will hence serve as a valuable reference for studies of cluster physics at low and moderate redshifts (e.g., galaxy properties versus intra-cluster gas physics, metallicities, dynamical state and its evolution, etc). These studies will require multi-wavelength observations including further SZ observations at higher spatial resolution and observations in X-rays (with *XMM-Newton*, *Chandra*, and Suzaku), in the optical (imaging and spectroscopy), and in the radio (e.g., with LOFAR).

The ensemble of early results on the SZ signal in *Planck* using a selected local sub-sample of ESZ clusters with high-quality *XMM-Newton* archival data (Planck Collaboration 2011g) and using the compilation of about 1600 MCXC clusters (Planck Collaboration 2011f), shows excellent agreement between observed SZ quantities and X-ray-based predictions underlining the robustness and consistency of our overall view of ICM properties. These results shed light on long-standing questions regarding the consistency between the SZ and X-ray view of hot gas in galaxy clusters. In contrast, the SZ signal-to-optical-richness relation measured from the SDSS-MaxBCG cluster catalogue Planck Collaboration (2011h) has a lower SZ signal than predicted. Extensive SZ-optical statistical studies of this kind are new. The result, and the origin of the difference, may be related to the cluster population, such as the existence of a sub-population of X-ray under-luminous clusters, or to selection effects in optical cluster catalogues.

In the future, *Planck* will deliver a larger all-sky SZ cluster catalogue. The characterisation of the *Planck* selection function together with the construction of this legacy catalogue, including its validation using follow up observations in particular with *XMM-Newton*, will be one of the major activities.

The usefulness of the SZ cluster abundance in achieving precise cosmological constraints relies on several theoretical and observational requirements. One of them is the ability to obtain redshift measurements for each confirmed SZ cluster. Cross-correlation of *Planck* data with the only available large optical survey to date, the Sloan Digital Sky Survey (SDSS), can be used to confirm *Planck* candidates and provide redshift estimates on a area restricted to the SDSS coverage area. The *XMM-Newton* confirmation observations can provide redshift estimates, but only for the X-ray brightest clusters. A significant follow-up effort in the optical (with ESO, ENO, and NOAO facilities) has thus been put in place by the *Planck* collaboration in order to obtain redshifts (photometric and spectroscopic) for the SZ clusters. Another key requirement for the cosmological use of the SZ catalogue is the derivation of the fundamental relation between the integrated Compton parameter, Y, and the cluster mass and its evolution with redshift. Planck Collaboration (2011g) have calibrated the local relation between Y and Y_X, the analogue of the SZ signal, measured from the X-ray gas mass and temperature, to an unprecedented precision and, for the first time, have demonstrated its remarkably small intrinsic scatter. We will build an even more robust and controlled observational proxy of the cluster mass which is fundamental for cosmological applications. To do this, specific studies based on the comparison of mass estimates from lensing, X-rays and SZ observations for a selected representative sample of the SZ catalogue will be most crucial.

Finally, combining *Planck* all-sky SZ data with near future and planned observations of the large-scale structure by large surveys, e.g., PANSTARRS, LOFAR, Euclid, LSST, and e-ROSITA, will allow us to understand the physical processes governing large-scale structure formation and evolution.

Acknowledgements. The authors thank N. Schartel, ESA *XMM-Newton* project scientist, for granting the Director Discretionary Time used for confirmation of SZ Planck candidates. This research has made use of the following databases: SIMBAD, operated at CDS, Strasbourg, France; the NED database, which is operated by the Jet Propulsion Laboratory, California Institute of Technology, under contract with the National Aeronautics and Space Administration; BAX, operated by the Laboratoire d'Astrophysique de Tarbes-Toulouse (LATT), under contract with the Centre National d'Études Spatiales (CNES), SZ repository operated by IAS Data and Operation Center (IDOC) under contract with CNES. The authors acknowledge the use of software provided by the US National Virtual Observatory. A description of the Planck Collaboration and a list of its members, indicating which technical or scientific activities they have been involved in, can be found at `http://www.rssd.esa.int/Planck`.

References

Abell, G. O. 1958, ApJS, 3, 211
Aghanim, N., de Luca, A., Bouchet, F. R., Gispert, R., & Puget, J. L. 1997, A&A, 325, 9
Aghanim, N., Hansen, S. H., & Lagache, G. 2005, A&A, 439, 901
Aghanim, N., Majumdar, S., & Silk, J. 2008, Rep. Prog. Phys., 71, 066902
Ameglio, S., Borgani, S., Diaferio, A., & Dolag, K. 2006, MNRAS, 369, 1459
Andersson, K., Benson, B. A., Ade, P. A. R., et al. 2011, ApJ, 738, 48
Appenzeller, I., Thiering, I., Zickgraf, F., et al. 1998, ApJS, 117, 319
Arnaud, M., Pointecouteau, E., & Pratt, G. W. 2007, A&A, 474, L37
Arnaud, M., Pratt, G. W., Piffaretti, R., et al. 2010, A&A, 517, A92
Battistelli, E. S., De Petris, M., Lamagna, L., et al. 2002, ApJ, 580, L101
Battistelli, E. S., De Petris, M., Lamagna, L., et al. 2006, ApJ, 645, 826
Benson, B. A., Church, S. E., Ade, P. A. R., et al. 2003, ApJ, 592, 674
Bethermin, M., Dole, H., Beelen, A., & Aussel, H. 2010, VizieR Online Data Catalog, 351, 29078
Birkinshaw, M. 1999, Phys. Rep., 310, 97
Birkinshaw, M., & Gull, S. F. 1978, Nature, 274, 111
Birkinshaw, M., & Hughes, J. P. 1994, ApJ, 420, 33
Birkinshaw, M., & Lancaster, K. 2005, in Background Microwave Radiation and Intracluster Cosmology, ed. F. Melchiorri, & Y. Rephaeli, 127
Bock, D., Large, M. I., & Sadler, E. M. 1999, AJ, 117, 1578
Böhringer, H., Schuecker, P., Pratt, G. W., et al. 2007, A&A, 469, 363
Bonamente, M., Joy, M. K., LaRoque, S. J., et al. 2006, ApJ, 647, 25
Borgani, S. 2006 [`arXiv:astro-ph/0605575`]
Borgani, S., Murante, G., Springel, V., et al. 2004, MNRAS, 348, 1078
Budavári, T., Dobos, L., Szalay, A. S., et al. 2007, in Astronomical Data Analysis Software and Systems XVI, ed. R. A. Shaw, F. Hill, & D. J. Bell, ASP Conf. Ser., 376, 559
Carlstrom, J. E., Ade, P. A. R., Aird, K. A., et al. 2011, PASP, 123, 568
Carlstrom, J. E., Holder, G. P., & Reese, E. D. 2002, ARA&A, 40, 643
Carvalho, P., Rocha, G., & Hobson, M. P. 2009, MNRAS, 393, 681
Cavaliere, A., & Fusco-Femiano, R. 1978, A&A, 70, 677
Colafrancesco, S., Marchegiani, P., & Palladino, E. 2003, A&A, 397, 27
Condon, J. J., Cotton, W. D., Greisen, E. W., et al. 1998, AJ, 115, 1693
Cortese, L., Gavazzi, G., Boselli, A., Iglesias-Paramo, J., & Carrasco, L. 2004, A&A, 425, 429
da Silva, A. C., Barbosa, D., Liddle, A. R., & Thomas, P. A. 2001, MNRAS, 326, 155

da Silva, A. C., Kay, S. T., Liddle, A. R., & Thomas, P. A. 2004, MNRAS, 348, 1401
Dawson, K. S., Holzapfel, W. L., Carlstrom, J. E., et al. 2001, ApJ, 553, L1
De Petris, M., Mainella, G., Nerozzi, A., et al. 1999, New A Rev., 43, 297
Dobbs, M., Halverson, N. W., Ade, P. A. R., et al. 2006, New A Rev., 50, 960
Dole, H., Lagache, G., Puget, J., et al. 2006, A&A, 451, 417
Douspis, M., Aghanim, N., & Langer, M. 2006, A&A, 456, 819
Einasto, M., Einasto, J., Tago, E., Müller, V., & Andernach, H. 2001, AJ, 122, 2222
Fixsen, D. J., Cheng, E. S., Cottingham, D. A., et al. 1994, ApJ, 420, 457
Génova-Santos, R., Rubiño-Martín, J. A., Rebolo, R., et al. 2005, MNRAS, 363, 79
Ghizzardi, S., Rossetti, M., & Molendi, S. 2010, A&A, 516, A32
Glenn, J., Bock, J. J., Chattopadhyay, G., et al. 1998, in SPIE Conf. Ser., 3357, ed. T. G. Phillips, 326
Gómez, P. L., Romer, K. A., Peterson, J., et al. 2003, in SPIE Conf. Ser., 301, ed. S. Bowyer, & C.-Y. Hwang, 495
Górski, K. M., Hivon, E., Banday, A. J., et al. 2005, ApJ, 622, 759
Grego, L., Carlstrom, J. E., Reese, E. D., et al. 2001, ApJ, 552, 2
Haiman, Z., Mohr, J. J., & Holder, G. P. 2001, ApJ, 553, 545
Herranz, D., Sanz, J. L., Hobson, M. P., et al. 2002, MNRAS, 336, 1057
Hinshaw, G., Weiland, J. L., Hill, R. S., et al. 2009, ApJS, 180, 225
Holzapfel, W. L., Wilbanks, T. M., Ade, P. A. R., et al. 1997, ApJ, 479, 17
Horellou, C., Nord, M., Johansson, D., & Lévy, A. 2005, A&A, 441, 435
Hurier, G., Hildebrandt, S. R., & Macias-Perez, J. F. 2010 [`arXiv:1007.1149`]
Hurley-Walker, T. A. C. N., Brown, M. L., Davies, M. L., et al. 2011, MNRAS, 414, L75
Itoh, N., Kohyama, Y., & Nozawa, S. 1998, ApJ, 502, 7
Jenkins, A., Frenk, C. S., White, S. D. M., et al. 2001, MNRAS, 321, 372
Jones, M., Saunders, R., Alexander, P., et al. 1993, Nature, 365, 320
Kashlinsky, A., Atrio-Barandela, F., Kocevski, D., & Ebeling, H. 2008, ApJ, 686, L49
Kobayashi, S., Sasaki, S., & Suto, Y. 1996, PASJ, 48, L107
Koester, B. P., McKay, T. A., Annis, J., et al. 2007, ApJ, 660, 239
Komatsu, E., Kitayama, T., Suto, Y., et al. 1999, ApJ, 516, L1
Kravtsov, A. V., Vikhlinin, A., & Nagai, D. 2006, ApJ, 650, 128
Lamarre, J., Puget, J., Ade, P. A. R., et al. 2010, A&A, 520, A9
Lamarre, J. M., Giard, M., Pointecouteau, E., et al. 1998, ApJ, 507, L5
Lancaster, K., Genova-Santos, R., Falcòn, N., et al. 2005, MNRAS, 359, 16
Levine, E. S., Schulz, A. E., & White, M. 2002, ApJ, 577, 569
Lin, Y., Partridge, B., Pober, J. C., et al. 2009, ApJ, 694, 992
Luzzi, G., Shimon, M., Lamagna, L., et al. 2009, ApJ, 705, 1122
Majumdar, S., & Mohr, J. J. 2004, ApJ, 613, 41
Mantz, A., Allen, S. W., Ebeling, H., Rapetti, D., & Drlica-Wagner, A. 2010, MNRAS, 406, 1773
Marriage, T. A., Acquaviva, V., Ade, P. A. R., et al. 2011, ApJ, 737, 61
Melin, J., Bartlett, J. G., & Delabrouille, J. 2006, A&A, 459, 341
Melin, J.-B., Aghanim, N., Bartelmann, M., et al. 2011, A&A, submitted
Menanteau, F., González, J., Juin, J., et al. 2010, ApJ, 723, 1523
Mennella, A., Butler, R. C., Curto, A., et al. 2011, A&A, 536, A3
Miville-Deschênes, M., & Lagache, G. 2005, ApJS, 157, 302
Montier, L. A., Pelkonen, V., Juvela, M., Ristorcelli, I., & Marshall, D. J. 2010, A&A, 522, A83
Motl, P. M., Hallman, E. J., Burns, J. O., & Norman, M. L. 2005, ApJ, 623, L63
Muchovej, S., Mroczkowski, T., Carlstrom, J. E., et al. 2007, ApJ, 663, 708
Nagai, D., Kravtsov, A. V., & Vikhlinin, A. 2007, ApJ, 668, 1
Pfrommer, C., Enßlin, T. A., Springel, V., Jubelgas, M., & Dolag, K. 2007, MNRAS, 378, 385
Piffaretti, R., Arnaud, M., Pratt, G. W., Pointecouteau, E., & Melin, J. 2011, A&A, 534, A109
Piffaretti, R., & Valdarnini, R. 2008, A&A, 491, 71
Plagge, T., Benson, B. A., Ade, P. A. R., et al. 2010, ApJ, 716, 1118
Planck Collaboration 2011a, A&A, 536, A1
Planck Collaboration 2011b, A&A, 536, A2
Planck Collaboration 2011c, A&A, 536, A7
Planck Collaboration 2011d, A&A, 536, A8
Planck Collaboration 2011e, A&A, 536, A9
Planck Collaboration 2011f, A&A, 536, A10
Planck Collaboration 2011g, A&A, 536, A11
Planck Collaboration 2011h, A&A, 536, A12
Planck Collaboration 2011i, A&A, 536, A13
Planck Collaboration 2011j, A&A, 536, A14
Planck Collaboration 2011k, A&A, 536, A15
Planck Collaboration 2011l, A&A, 536, A16
Planck Collaboration 2011m, A&A, 536, A17
Planck Collaboration 2011n, A&A, 536, A18
Planck Collaboration 2011o, A&A, 536, A19
Planck Collaboration 2011p, A&A, 536, A20
Planck Collaboration 2011q, A&A, 536, A21
Planck Collaboration 2011r, A&A, 536, A22
Planck Collaboration 2011s, A&A, 536, A23
Planck Collaboration 2011t, A&A, 536, A24
Planck Collaboration 2011u, A&A, 536, A25
Planck Collaboration 2011v, The Explanatory Supplement to the Planck Early Release Compact Source Catalogue (ESA)
Planck Collaboration 2011w, A&A, 536, A26
Planck HFI Core Team 2011a, A&A, 536, A4
Planck HFI Core Team 2011b, A&A, 536, A6
Pointecouteau, E., Giard, M., & Barret, D. 1998, A&A, 336, 44
Pointecouteau, E., Giard, M., Benoit, A., et al. 1999, ApJ, 519, L115
Pratt, G. W., Croston, J. H., Arnaud, M., & Böhringer, H. 2009, A&A, 498, 361
Reese, E. D., Carlstrom, J. E., Joy, M., et al. 2002, ApJ, 581, 53
Rephaeli, Y. 1995, ARA&A, 33, 541
Rubiño-Martín, J. A., & Sunyaev, R. A. 2003, MNRAS, 344, 1155
Sadat, R., Blanchard, A., Kneib, J., et al. 2004, A&A, 424, 1097
Schneider, D. P., Bahcall, J. N., Gunn, J. E., & Dressler, A. 1992, AJ, 103, 1047
Shimon, M., & Rephaeli, Y. 2004, New A, 9, 69
Silk, J., & White, S. D. M. 1978, ApJ, 226, L103
Staniszewski, Z., Ade, P. A. R., Aird, K. A., et al. 2009, ApJ, 701, 32
Story, K., Aird, K. A., Andersson, K., et al. 2011, ApJ, 735, L36
Sunyaev, R. A., & Zeldovich, I. B. 1980, ARA&A, 18, 537
Sunyaev, R. A., & Zeldovich, Y. B. 1972, Comments on Astrophysics and Space Physics, 4, 173
Udomprasert, P. S., Mason, B. S., Readhead, A. C. S., & Pearson, T. J. 2004, ApJ, 615, 63
Uzan, J., Aghanim, N., & Mellier, Y. 2004, Phys. Rev. D, 70, 083533
Vanderlinde, K., Crawford, T. M., de Haan, T., et al. 2010, ApJ, 722, 1180
Vikhlinin, A., Burenin, R. A., Ebeling, H., et al. 2009, ApJ, 692, 1033
Weller, J., Battye, R. A., & Kneissl, R. 2002, Phys. Rev. Lett., 88, 231301
Wen, Z. L., Han, J. L., & Liu, F. S. 2009, ApJS, 183, 197
Williamson, R., Benson, B. A., High, F. W., et al. 2011, ApJ, 738, 139
Wright, E. L., Eisenhardt, P. R. M., Mainzer, A. K., et al. 2010, AJ, 140, 1868
Wu, J., Chiueh, T., Huang, C., et al. 2008, Mod.Phys. Lett. A, 23, 1675
Zemcov, M., Borys, C., Halpern, M., Mauskopf, P., & Scott, D. 2007, MNRAS, 376, 1073
Zemcov, M., Rex, M., Rawle, T. D., et al. 2010, A&A, 518, L16
Zwart, J. T. L., Barker, R. W., Biddulph, P., & AMI Consortium 2008, MNRAS, 391, 1545
Zwicky, F., Herzog, E., & Wild, P. 1961, Catalogue of galaxies and of clusters of galaxies, Vol. I, ed. F. Zwicky, E. Herzog, & P. Wild
Zacchei, A., Maino, D., Baccigalupi, C., et al. 2011, A&A, 536, A5

---

[1] Aalto University Metsähovi Radio Observatory, Metsähovintie 114, 02540 Kylmälä, Finland
[2] Agenzia Spaziale Italiana Science Data Center, c/o ESRIN, via Galileo Galilei, Frascati, Italy
[3] Astroparticule et Cosmologie, CNRS (UMR7164), Université Denis Diderot Paris 7, Bâtiment Condorcet, 10 rue A. Domon et Léonie Duquet, Paris, France
[4] Astrophysics Group, Cavendish Laboratory, University of Cambridge, J J Thomson Avenue, Cambridge CB3 0HE, UK
[5] Atacama Large Millimeter/submillimeter Array, ALMA Santiago Central Offices, Alonso de Cordova 3107, Vitacura, Casilla 763 0355, Santiago, Chile
[6] CITA, University of Toronto, 60 St. George St., Toronto, ON M5S 3H8, Canada
[7] CNRS, IRAP, 9 Av. colonel Roche, BP 44346, 31028 Toulouse Cedex 4, France
[8] California Institute of Technology, Pasadena, California, USA
[9] Centre of Mathematics for Applications, University of Oslo, Blindern, Oslo, Norway
[10] Centro de Astrofísica, Universidade do Porto, Rua das Estrelas, 4150-762 Porto, Portugal
[11] DAMTP, University of Cambridge, Centre for Mathematical Sciences, Wilberforce Road, Cambridge CB3 0WA, UK
[12] DSM/Irfu/SPP, CEA-Saclay, 91191 Gif-sur-Yvette Cedex, France
[13] DTU Space, National Space Institute, Juliane Mariesvej 30, Copenhagen, Denmark
[14] Departamento de Física, Universidad de Oviedo, Avda. Calvo Sotelo s/n, Oviedo, Spain
[15] Department of Astronomy and Astrophysics, University of Toronto, 50 Saint George Street, Toronto, Ontario, Canada

[16] Department of Physics & Astronomy, University of British Columbia, 6224 Agricultural Road, Vancouver, British Columbia, Canada
[17] Department of Physics and Astronomy, University of Southern California, Los Angeles, California, USA
[18] Department of Physics and Astronomy, University of Sussex, Brighton BN1 9QH, UK
[19] Department of Physics, Gustaf Hällströmin katu 2a, University of Helsinki, Helsinki, Finland
[20] Department of Physics, Princeton University, Princeton, New Jersey, USA
[21] Department of Physics, Purdue University, 525 Northwestern Avenue, West Lafayette, Indiana, USA
[22] Department of Physics, University of California, Berkeley, California, USA
[23] Department of Physics, University of California, One Shields Avenue, Davis, California, USA
[24] Department of Physics, University of California, Santa Barbara, California, USA
[25] Department of Physics, University of Illinois at Urbana-Champaign, 1110 West Green Street, Urbana, Illinois, USA
[26] Dipartimento di Fisica G. Galilei, Università degli Studi di Padova, via Marzolo 8, 35131 Padova, Italy
[27] Dipartimento di Fisica, Università La Sapienza, P.le A. Moro 2, Roma, Italy
[28] Dipartimento di Fisica, Università degli Studi di Milano, via Celoria 16, Milano, Italy
[29] Dipartimento di Fisica, Università degli Studi di Trieste, via A. Valerio 2, Trieste, Italy
[30] Dipartimento di Fisica, Università di Ferrara, via Saragat 1, 44122 Ferrara, Italy
[31] Dipartimento di Fisica, Università di Roma Tor Vergata, via della Ricerca Scientifica 1, Roma, Italy
[32] Discovery Center, Niels Bohr Institute, Blegdamsvej 17, Copenhagen, Denmark
[33] Dpto. Astrofísica, Universidad de La Laguna (ULL), 38206 La Laguna, Tenerife, Spain
[34] European Southern Observatory, ESO Vitacura, Alonso de Cordova 3107, Vitacura, Casilla 19001, Santiago, Chile
[35] European Space Agency, ESAC, Camino bajo del Castillo, s/n, Urbanización Villafranca del Castillo, Villanueva de la Cañada, Madrid, Spain
[36] European Space Agency, ESAC, Planck Science Office, Camino bajo del Castillo s/n, Urbanización Villafranca del Castillo, Villanueva de la Cañada, Madrid, Spain
[37] European Space Agency, ESTEC, Keplerlaan 1, 2201 AZ Noordwijk, The Netherlands
[38] GEPI, Observatoire de Paris, Section de Meudon, 5 place J. Janssen, 92195 Meudon Cedex, France
[39] Helsinki Institute of Physics, Gustaf Hällströmin katu 2, University of Helsinki, Helsinki, Finland
[40] INAF - Osservatorio Astronomico di Padova, Vicolo dell'Osservatorio 5, Padova, Italy
[41] INAF - Osservatorio Astronomico di Roma, via di Frascati 33, Monte Porzio Catone, Italy
[42] INAF - Osservatorio Astronomico di Trieste, via G.B. Tiepolo 11, Trieste, Italy
[43] INAF/IASF Bologna, via Gobetti 101, Bologna, Italy
[44] INAF/IASF Milano, via E. Bassini 15, Milano, Italy
[45] INRIA, Laboratoire de Recherche en Informatique, Université Paris-Sud 11, Bâtiment 490, 91405 Orsay Cedex, France
[46] IPAG (Institut de Planétologie et d'Astrophysique de Grenoble), Université Joseph Fourier, Grenoble 1 / CNRS-INSU, UMR 5274, Grenoble 38041, France
[47] Imperial College London, Astrophysics group, Blackett Laboratory, Prince Consort Road, London, SW7 2AZ, UK
[48] Infrared Processing and Analysis Center, California Institute of Technology, Pasadena, CA 91125, USA
[49] Institut Néel, CNRS, Université Joseph Fourier Grenoble I, 25 rue des Martyrs, Grenoble, France
[50] Institut d'Astrophysique Spatiale, CNRS (UMR8617) Université Paris-Sud 11, Bâtiment 121, Orsay, France
[51] Institut d'Astrophysique de Paris, CNRS UMR7095, Université Pierre & Marie Curie, 98bis boulevard Arago, Paris, France
[52] Institut de Ciències de l'Espai, CSIC/IEEC, Facultat de Ciències, Campus UAB, Torre C5 par-2, Bellaterra 08193, Spain
[53] Institute of Astronomy and Astrophysics, Academia Sinica, Taipei, Taiwan
[54] Institute of Astronomy, University of Cambridge, Madingley Road, Cambridge CB3 0HA, UK
[55] Institute of Theoretical Astrophysics, University of Oslo, Blindern, Oslo, Norway
[56] Instituto de Astrofísica de Canarias, C/vía Láctea s/n, La Laguna, Tenerife, Spain
[57] Instituto de Física de Cantabria (CSIC-Universidad de Cantabria), Avda. de los Castros s/n, Santander, Spain
[58] Jet Propulsion Laboratory, California Institute of Technology, 4800 Oak Grove Drive, Pasadena, California, USA
[59] Jodrell Bank Centre for Astrophysics, Alan Turing Building, School of Physics and Astronomy, The University of Manchester, Oxford Road, Manchester, M13 9PL, UK
[60] Kavli Institute for Cosmology Cambridge, Madingley Road, Cambridge, CB3 0HA, UK
[61] LERMA, CNRS, Observatoire de Paris, 61 Avenue de l'Observatoire, Paris, France
[62] Laboratoire AIM, IRFU/Service d'Astrophysique - CEA/DSM - CNRS - Université Paris Diderot, Bât. 709, CEA-Saclay, 91191 Gif-sur-Yvette Cedex, France
[63] Laboratoire Traitement et Communication de l'Information, CNRS (UMR 5141) and Télécom ParisTech, 46 rue Barrault, 75634 Paris Cedex 13, France
[64] Laboratoire de Physique Subatomique et de Cosmologie, CNRS/IN2P3, Université Joseph Fourier Grenoble I, Institut National Polytechnique de Grenoble, 53 rue des Martyrs, 38026 Grenoble Cedex, France
[65] Laboratoire de l'Accélérateur Linéaire, Université Paris-Sud 11, CNRS/IN2P3, Orsay, France
[66] Lawrence Berkeley National Laboratory, Berkeley, California, USA
[67] MPA Partner Group, Key Laboratory for Research in Galaxies and Cosmology, Shanghai Astronomical Observatory, Chinese Academy of Sciences, Nandan Road 80, Shanghai 200030, PR China
[68] Max-Planck-Institut für Astrophysik, Karl-Schwarzschild-Str. 1, 85741 Garching, Germany
[69] Max-Planck-Institut für Extraterrestrische Physik, Giessenbachstraße, 85748 Garching, Germany
[70] MilliLab, VTT Technical Research Centre of Finland, Tietotie 3, Espoo, Finland
[71] National University of Ireland, Department of Experimental Physics, Maynooth, Co. Kildare, Ireland
[72] Niels Bohr Institute, Blegdamsvej 17, Copenhagen, Denmark
[73] Observational Cosmology, Mail Stop 367-17, California Institute of Technology, Pasadena, CA, 91125, USA
[74] Optical Science Laboratory, University College London, Gower Street, London, UK
[75] SISSA, Astrophysics Sector, via Bonomea 265, 34136 Trieste, Italy
[76] SUPA, Institute for Astronomy, University of Edinburgh, Royal Observatory, Blackford Hill, Edinburgh EH9 3HJ, UK
[77] School of Physics and Astronomy, Cardiff University, Queens Buildings, The Parade, Cardiff CF24 3AA, UK
[78] Space Research Institute (IKI), Russian Academy of Sciences, Profsoyuznaya Str, 84/32, Moscow, 117997, Russia
[79] Space Sciences Laboratory, University of California, Berkeley, California, USA
[80] Stanford University, Dept of Physics, Varian Physics Bldg, 382 via Pueblo Mall, Stanford, California, USA
[81] Tartu Observatory, Toravere, Tartumaa, 61602, Estonia
[82] Tuorla Observatory, Department of Physics and Astronomy, University of Turku, Väisäläntie 20, 21500, Piikkiö, Finland

[83] Universität Heidelberg, Institut für Theoretische Astrophysik, Albert-Überle-Str. 2, 69120 Heidelberg, Germany
[84] Université Denis Diderot (Paris 7), 75205 Paris Cedex 13, France
[85] Université de Toulouse, UPS-OMP, IRAP, 31028 Toulouse Cedex 4, France
[86] Universities Space Research Association, Stratospheric Observatory for Infrared Astronomy, MS 211-3, Moffett Field, CA 94035, USA
[87] University Observatory, Ludwig Maximilian University of Munich, Scheinerstrasse 1, 81679 Munich, Germany
[88] University of Granada, Departamento de Física Teórica y del Cosmos, Facultad de Ciencias, Granada, Spain
[89] University of Miami, Knight Physics Building, 1320 Campo Sano Dr., Coral Gables, Florida, USA
[90] Warsaw University Observatory, Aleje Ujazdowskie 4, 00-478 Warszawa, Poland

Pages 25 to 28 are available in the electronic edition of the journal at http://www.aanda.org

Appendix A: ESZ sample extract

Table A.1 is an extract from the *Planck* ESZ sample available at `www.rssd.esa.int/Planck` aiming at presenting the content of the released product. Four entries are given as examples for each category (*Planck* ESZ known clusters, *Planck* ESZ new confirmed clusters, *Planck* ESZ clusters candidates). In the present extract, only Galactic longitudes and latitudes are given. The ESZ sample contains, in addition, the right ascensions and declinations for all the entries.

For each entry the following fields are provided:

- name: *Planck* Name of Cluster Candidate;
- GLON: Galactic Longitude from *Planck* ;
- GLAT: Galactic latitude from *Planck* ;
- S/N: Signal-to-noise ratio returned by the matched multi-Filter algorithm (MMF3);
- ID: external Identifier of *Planck* Clusters e.g. Coma, Abell 2163 etc.;
- z: redshift of Cluster from the MCXC X-ray cluster compilation unless otherwise stated in the individual notes;
- Θ_X: angular size at $5R500$ from X-ray data;
- Y_{PSX}: integrated Compton parameter at X-ray position and within $5R500$ (Θ_X) in arcmin^2;
- Y_{PSX}^{ERR}: uncertainty in Integrated Compton parameter at X-ray position and within $5R500$ (Θ_X) in arcmin^2;
- Θ: estimated angular size from matched multi-Filter (MMF3),
- Y: integrated Compton parameter at *Planck* position and within Θ, from matched multi-Filter (MMF3) in arcmin^2;
- Y^{ERR}: uncertainty in Integrated Compton parameter at *Planck* position and within Θ from matched multi-Filter (MMF3) in arcmin^2.

Table A.1. ESZ sample.

Name	GLON	GLAT	S/N	ID	z	Θ_X	Y_{PSX}	Y_{PSX}^{ERR}	Θ	Y	Y^{ERR}
PLCKG111.0+31.7	110.98	31.73	28.93	A2256	0.06	NaN	0.0242	0.0009	NaN	NaN	NaN
PLCKG57.3+88.0	57.34	88.01	21.94	Coma	0.02	NaN	0.1173	0.0054	NaN	NaN	NaN
PLCKG239.3+24.8	239.28	24.77	25.67	A0754	0.05	NaN	0.0330	0.0012	NaN	NaN	NaN
PLCKG272.1-40.2	272.11	–40.15	25.90	A3266	0.06	NaN	0.0282	0.0012	NaN	NaN	NaN
PLCKG6.8+30.5	6.78	30.47	26.40	A2163	0.20	NaN	0.0173	0.0007	NaN	NaN	NaN
PLCKG340.9-33.3	340.89	–33.35	22.02	A3667	0.06	NaN	0.0266	0.0014	NaN	NaN	NaN
PLCKG266.0-21.3	266.04	–21.25	19.75	1ES 0657-55.8	0.30	NaN	0.0067	0.0003	NaN	NaN	NaN
PLCKG44.2+48.7	44.23	48.68	18.46	A2142	0.09	NaN	0.0241	0.0013	NaN	NaN	NaN
PLCKG93.9+34.9	93.92	34.91	17.31	A2255	0.08	NaN	0.0103	0.0006	NaN	NaN	NaN
PLCKG164.2-38.9	164.19	–38.89	13.79	A0401	0.07	NaN	0.0193	0.0016	NaN	NaN	NaN
PLCKG72.6+41.5	72.63	41.46	17.44	A2219	0.23	NaN	0.0085	0.0005	NaN	NaN	NaN
PLCKG263.7-22.5	263.67	–22.54	16.70	A3404	0.16	NaN	0.0064	0.0004	NaN	NaN	NaN
PLCKG97.7+38.1	97.74	38.12	14.65	A2218	0.17	NaN	0.0044	0.0003	NaN	NaN	NaN
PLCKG263.2-25.2	263.21	–25.21	11.24	A3395	0.05	NaN	0.0073	0.0009	NaN	NaN	NaN
PLCKG262.3-35.4	262.25	–35.37	15.19	ACO S0520	0.30	NaN	0.0034	0.0003	NaN	NaN	NaN
PLCKG74.0-27.8	73.97	–27.82	14.25	A2390	0.23	NaN	0.0056	0.0005	NaN	NaN	NaN
PLCKG332.2-46.4	332.23	–46.37	13.89	A3827	0.10	NaN	0.0086	0.0007	NaN	NaN	NaN
PLCKG265.0-48.9	265.01	–48.95	13.95	A3158	0.06	NaN	0.0117	0.0010	NaN	NaN	NaN
PLCKG115.2-72.1	115.16	–72.09	13.14	A0085	0.06	NaN	0.0210	0.0018	NaN	NaN	NaN
PLCKG316.3+28.5	316.35	28.54	12.85	A3571	0.04	NaN	0.0372	0.0031	NaN	NaN	NaN
PLCKG86.5+15.3	86.46	15.30	12.33	CIZA J1938.3+5409	0.26	NaN	0.0031	0.0003	NaN	NaN	NaN
PLCKG33.8+77.2	33.78	77.16	12.39	A1795	0.06	NaN	0.0169	0.0014	NaN	NaN	NaN
PLCKG6.5+50.5	6.48	50.55	13.36	A2029	0.08	NaN	0.0180	0.0015	NaN	NaN	NaN
PLCKG349.5-59.9	349.46	–59.95	13.93	ACO S1063	0.35	NaN	0.0046	0.0003	NaN	NaN	NaN
PLCKG186.4+37.3	186.39	37.26	12.61	A0697	0.28	NaN	0.0051	0.0005	NaN	NaN	NaN
PLCKG229.9+15.3	229.94	15.30	12.46	A0644	0.07	NaN	0.0116	0.0010	NaN	NaN	NaN
PLCKG149.7+34.7	149.73	34.70	11.57	A0665	0.18	NaN	0.0060	0.0005	NaN	NaN	NaN
PLCKG3.9-59.4	3.91	–59.42	12.06	A3888	0.15	NaN	0.0061	0.0005	NaN	NaN	NaN
PLCKG312.0+30.7	312.00	30.72	9.04	A3558	0.05	NaN	0.0223	0.0024	NaN	NaN	NaN
PLCKG313.9-17.1	313.87	–17.11	11.57	CIZA J1601.7-7544	0.15	NaN	0.0078	0.0007	NaN	NaN	NaN
PLCKG335.6-46.5	335.59	–46.46	10.17	A3822	0.08	NaN	0.0084	0.0008	NaN	NaN	NaN
PLCKG288.6-37.7	288.62	–37.66	9.86	A3186	0.13	NaN	0.0053	0.0006	NaN	NaN	NaN
PLCKG315.7-18.0	315.71	–18.04	11.44	A3628	0.10	NaN	0.0088	0.0008	NaN	NaN	NaN
PLCKG263.2-23.4	263.16	–23.41	10.08	ACO S0592	0.23	NaN	0.0032	0.0003	NaN	NaN	NaN
PLCKG149.2+54.2	149.24	54.19	11.58	A1132	0.14	NaN	0.0052	0.0005	NaN	NaN	NaN
PLCKG21.1+33.3	21.09	33.26	10.61	A2204	0.15	NaN	0.0076	0.0007	NaN	NaN	NaN
PLCKG322.0-48.0	321.96	–47.98	11.27	A3921	0.09	NaN	0.0053	0.0006	NaN	NaN	NaN
PLCKG182.4-28.3	182.44	–28.30	12.77	A0478	0.09	NaN	0.0167	0.0014	NaN	NaN	NaN
PLCKG242.0+14.9	241.97	14.86	10.49	A3411	0.17	NaN	0.0041	0.0005	NaN	NaN	NaN
PLCKG29.0+44.6	29.01	44.56	10.25	A2147	0.04	NaN	0.0148	0.0021	NaN	NaN	NaN
PLCKG228.5+53.1	228.50	53.13	12.20	Zw 3179	0.14	NaN	0.0022	0.0005	NaN	NaN	NaN
PLCKG62.9+43.7	62.93	43.71	10.03	A2199	0.03	NaN	0.0241	0.0023	NaN	NaN	NaN
PLCKG206.0-39.5	205.96	–39.48	9.26	MACS J0417.5-1154	0.44	NaN	0.0038	0.0004	NaN	NaN	NaN
PLCKG336.6-55.4	336.59	–55.45	10.29	A3911	0.10	NaN	0.0057	0.0006	NaN	NaN	NaN
PLCKG67.2+67.5	67.23	67.46	11.03	A1914	0.17	NaN	0.0057	0.0005	NaN	NaN	NaN
PLCKG92.7+73.5	92.73	73.46	11.26	A1763	0.23	NaN	0.0045	0.0004	NaN	NaN	NaN
PLCKG146.3-15.6	146.33	–15.59	7.10	CIZA J0254.4+4134	0.02	NaN	0.0392	0.0060	NaN	NaN	NaN
PLCKG112.5+57.0	112.46	57.04	9.81	A1767	0.07	NaN	0.0053	0.0006	NaN	NaN	NaN
PLCKG55.6+31.9	55.60	31.86	9.27	A2261	0.22	NaN	0.0049	0.0005	NaN	NaN	NaN
PLCKG58.3+18.6	58.28	18.59	9.19	CIZA J1825.3+3026	0.06	NaN	0.0087	0.0009	NaN	NaN	NaN
PLCKG159.9-73.5	159.86	–73.47	10.63	A0209	0.21	NaN	0.0053	0.0005	NaN	NaN	NaN
PLCKG282.5+65.2	282.49	65.17	8.49	ZwCl 1215.1+0400	0.08	NaN	0.0095	0.0012	NaN	NaN	NaN
PLCKG313.4+61.1	313.36	61.12	10.12	A1689	0.18	NaN	0.0071	0.0008	NaN	NaN	NaN
PLCKG53.5+59.5	53.52	59.54	8.50	A2034	0.11	NaN	0.0055	0.0008	NaN	NaN	NaN
PLCKG244.3-32.1	244.34	hline-32.14	8.39	RBS0653	0.28	NaN	0.0029	0.0004	NaN	NaN	NaN
PLCKG46.9+56.5	46.88	56.50	9.07	A2069	0.11	NaN	0.0067	0.0008	NaN	NaN	NaN
PLCKG294.7-37.0	294.67	–37.03	8.64	RXCJ0303.7-7752	0.27	NaN	0.0028	0.0004	NaN	NaN	NaN
PLCKG346.6+35.0	346.60	35.05	9.38	RXCJ1514.9-1523	0.22	NaN	0.0048	0.0006	NaN	NaN	NaN
PLCKG243.6+67.8	243.57	67.76	8.57	A1307	0.08	NaN	0.0062	0.0007	NaN	NaN	NaN
PLCKG166.1+43.4	166.13	43.39	9.23	A0773	0.22	NaN	0.0038	0.0004	NaN	NaN	NaN
PLCKG226.2+76.8	226.25	76.77	9.18	A1413	0.14	NaN	0.0058	0.0006	NaN	NaN	NaN
PLCKG107.1+65.3	107.11	65.31	8.85	A1758A	0.28	NaN	0.0031	0.0004	NaN	NaN	NaN
PLCKG42.8+56.6	42.83	56.62	8.36	A2065	0.07	NaN	0.0099	0.0011	NaN	NaN	NaN
PLCKG125.6-64.1	125.59	–64.14	10.47	A0119	0.04	NaN	0.0141	0.0017	NaN	NaN	NaN
PLCKG57.3-45.4	57.27	–45.36	8.11	MACS J2211.7-0349	0.40	NaN	0.0032	0.0004	NaN	NaN	NaN
PLCKG33.5-48.4	33.46	–48.43	9.24	A2384A	0.09	NaN	0.0054	0.0006	NaN	NaN	NaN

Table A.1. continued.

Name	GLON	GLAT	S/N	ID	z	Θ_X	Y_{PSX}	Y_{PSX}^{ERR}	Θ	Y	Y^{ERR}
PLCKG241.8-24.0	241.78	–24.00	8.94	A3378	0.14	NaN	0.0038	0.0005	NaN	NaN	NaN
PLCKG46.5-49.4	46.50	–49.44	8.55	A2420	0.08	NaN	0.0064	0.0008	NaN	NaN	NaN
PLCKG304.9+45.5	304.90	45.45	8.99	A1644	0.05	NaN	0.0152	0.0018	NaN	NaN	NaN
PLCKG209.6-36.5	209.56	–36.49	7.96	A0496	0.03	NaN	0.0162	0.0021	NaN	NaN	NaN
PLCKG57.0-55.1	56.97	–55.08	8.16	MACS J2243.3-0935	0.45	NaN	0.0029	0.0004	NaN	NaN	NaN
PLCKG56.8+36.3	56.81	36.32	9.15	A2244	0.10	NaN	0.0058	0.0007	NaN	NaN	NaN
PLCKG57.6+34.9	57.61	34.94	9.54	A2249	0.08	NaN	0.0052	0.0007	NaN	NaN	NaN
PLCKG49.2+30.9	49.20	30.86	8.33	RXC J1720.1+2637	0.16	NaN	0.0043	0.0005	NaN	NaN	NaN
PLCKG6.7-35.5	6.70	–35.54	8.45	A3695	0.09	NaN	0.0059	0.0008	NaN	NaN	NaN
PLCKG77.9-26.6	77.91	–26.65	8.36	A2409	0.15	NaN	0.0040	0.0005	NaN	NaN	NaN
PLCKG8.9-81.2	8.94	–81.24	8.39	A2744	0.31	NaN	0.0042	0.0005	NaN	NaN	NaN
PLCKG106.7-83.2	106.73	–83.23	8.55	A2813	0.29	NaN	0.0036	0.0004	NaN	NaN	NaN
PLCKG269.5+26.4	269.52	26.42	8.40	A1060	0.01	NaN	0.0215	0.0029	NaN	NaN	NaN
PLCKG180.2+21.0	180.24	21.05	8.36	MACS J0717.5+3745	0.55	NaN	0.0028	0.0004	NaN	NaN	NaN
PLCKG241.7-30.9	241.74	–30.89	7.42	RXCJ0532.9-3701	0.27	NaN	0.0028	0.0004	NaN	NaN	NaN
PLCKG332.9-19.3	332.89	–19.28	7.72	CIZA J1813.3-6127	0.15	NaN	0.0043	0.0006	NaN	NaN	NaN
PLCKG48.1+57.2	48.05	57.18	7.14	A2061	0.08	NaN	0.0067	0.0010	NaN	NaN	NaN
PLCKG139.2+56.4	139.20	56.36	7.65	A1351	0.32	NaN	0.0012	0.0003	NaN	NaN	NaN
PLCKG306.7+61.1	306.68	61.06	8.02	A1650	0.08	NaN	0.0095	0.0012	NaN	NaN	NaN
PLCKG167.7+17.6	167.66	17.65	8.11	ZwCl 0634.1+4750	0.17	NaN	0.0045	0.0005	NaN	NaN	NaN
PLCKG49.3+44.4	49.34	44.38	7.40	A2175	0.10	NaN	0.0054	0.0009	NaN	NaN	NaN
PLCKG226.2-21.9	226.18	–21.91	7.28	A0550	0.10	NaN	0.0047	0.0007	NaN	NaN	NaN
PLCKG195.8-24.3	195.77	–24.31	7.23	A0520	0.20	NaN	0.0046	0.0006	NaN	NaN	NaN
PLCKG253.5-33.7	253.48	–33.72	6.73	A3343	0.19	NaN	0.0022	0.0004	NaN	NaN	NaN
PLCKG250.9-36.3	250.91	–36.26	8.62	A3322	0.20	NaN	0.0028	0.0004	NaN	NaN	NaN
PLCKG256.5-65.7	256.45	–65.71	7.77	A3016	0.22	NaN	0.0029	0.0004	NaN	NaN	NaN
PLCKG324.5-45.0	324.50	–44.97	6.22	RBS1847	0.10	NaN	0.0039	0.0005	NaN	NaN	NaN
PLCKG113.8+44.4	113.82	44.35	7.80	A1895	0.22	NaN	0.0012	0.0002	NaN	NaN	NaN
PLCKG125.7+53.9	125.71	53.86	7.36	A1576	0.30	NaN	0.0019	0.0003	NaN	NaN	NaN
PLCKG266.8+25.1	266.84	25.08	8.19	A3444	0.25	NaN	0.0027	0.0004	NaN	NaN	NaN
PLCKG216.6+47.0	216.62	47.02	7.48	RXC J0949.8+1707	0.38	NaN	0.0021	0.0004	NaN	NaN	NaN
PLCKG228.2+75.2	228.16	75.19	7.13	MACS J1149.5+2223	0.55	NaN	0.0016	0.0003	NaN	NaN	NaN
PLCKG342.3-34.9	342.32	–34.91	7.24	RXCJ2023.4-5535	0.23	NaN	0.0029	0.0004	NaN	NaN	NaN
PLCKG342.8-30.5	342.82	–30.46	6.01	A3651	0.06	NaN	0.0044	0.0009	NaN	NaN	NaN
PLCKG124.2-36.5	124.22	–36.49	7.74	A0115	0.20	NaN	0.0050	0.0007	NaN	NaN	NaN
PLCKG257.3-22.2	257.34	–22.18	7.13	A3399	0.20	NaN	0.0019	0.0003	NaN	NaN	NaN
PLCKG118.4+39.3	118.45	39.34	6.33	RXCJ1354.6+7715	0.40	NaN	0.0016	0.0003	NaN	NaN	NaN
PLCKG118.6+28.6	118.60	28.56	6.41	A2294	0.18	NaN	0.0022	0.0004	NaN	NaN	NaN
PLCKG229.6+78.0	229.64	77.96	7.45	A1443	0.27	NaN	0.0027	0.0004	NaN	NaN	NaN
PLCKG180.6+76.7	180.62	76.65	7.48	A1423	0.21	NaN	0.0027	0.0004	NaN	NaN	NaN
PLCKG2.7-56.2	2.75	–56.18	6.48	A3856	0.14	NaN	0.0031	0.0005	NaN	NaN	NaN
PLCKG347.2-27.4	347.19	–27.35	8.19	ACO S0821	0.24	NaN	0.0022	0.0004	NaN	NaN	NaN
PLCKG71.6+29.8	71.61	29.80	7.47	Zw 8284	0.16	NaN	0.0024	0.0004	NaN	NaN	NaN
PLCKG36.7+14.9	36.72	14.92	6.98	RXCJ1804.4+1002	0.15	NaN	0.0035	0.0006	NaN	NaN	NaN
PLCKG18.5-25.7	18.53	–25.72	7.30	RXCJ2003.5-2323	0.32	NaN	0.0027	0.0004	NaN	NaN	NaN
PLCKG237.0-26.7	236.96	–26.67	7.03	A3364	0.15	NaN	0.0030	0.0005	NaN	NaN	NaN
PLCKG273.6+63.3	273.64	63.28	7.30	A1437	0.13	NaN	0.0051	0.0007	NaN	NaN	NaN
PLCKG46.1+27.2	46.08	27.18	7.34	MACS J1731.6+2252	0.39	NaN	0.0021	0.0003	NaN	NaN	NaN
PLCKG49.7-49.5	49.67	–49.51	6.88	A2426	0.10	NaN	0.0038	0.0007	NaN	NaN	NaN
PLCKG143.2+65.2	143.25	65.22	7.34	A1430	0.21	NaN	0.0023	0.0003	NaN	NaN	NaN
PLCKG296.4-32.5	296.41	–32.49	7.20	ACO S0405	0.06	NaN	0.0044	0.0007	NaN	NaN	NaN
PLCKG269.3-49.9	269.31	–49.88	6.51	A3126	0.09	NaN	0.0040	0.0007	NaN	NaN	NaN
PLCKG83.3-31.0	83.29	–31.03	6.19	RXC J2228.6+2036	0.41	NaN	0.0021	0.0004	NaN	NaN	NaN
PLCKG304.7-31.7	304.67	–31.67	6.37	A4023	0.19	NaN	0.0020	0.0004	NaN	NaN	NaN
PLCKG39.9-40.0	39.86	–39.99	6.32	A2345	0.18	NaN	0.0031	0.0005	NaN	NaN	NaN
PLCKG56.0-34.9	55.98	–34.89	7.03	A2355	0.12	NaN	0.0036	0.0005	NaN	NaN	NaN
PLCKG303.8+33.7	303.76	33.66	6.05	A3528S	0.05	NaN	0.0085	0.0014	NaN	NaN	NaN
PLCKG163.7+53.5	163.72	53.53	7.46	A0980	0.16	NaN	0.0030	0.0004	NaN	NaN	NaN
PLCKG318.1-29.6	318.13	–29.58	6.63	RXCJ1947.3-7623	0.22	NaN	0.0031	0.0005	NaN	NaN	NaN
PLCKG244.7+32.5	244.70	32.49	6.27	A0868	0.15	NaN	0.0029	0.0005	NaN	NaN	NaN
PLCKG284.5+52.4	284.46	52.44	7.27	RXCJ1206.2-0848	0.44	NaN	0.0029	0.0004	NaN	NaN	NaN
PLCKG260.0-63.4	260.03	–63.44	7.29	RXCJ0232.2-4420	0.28	NaN	0.0024	0.0004	NaN	NaN	NaN
PLCKG253.0-56.1	252.97	–56.05	6.79	A3112	0.08	NaN	0.0047	0.0007	NaN	NaN	NaN
PLCKG234.6+73.0	234.59	73.02	6.39	A1367	0.02	NaN	0.0146	0.0029	NaN	NaN	NaN
PLCKG278.6+39.2	278.61	39.17	7.57	A1300	0.31	NaN	0.0035	0.0005	NaN	NaN	NaN
PLCKG246.5-26.1	246.52	–26.06	6.52	A3376	0.05	NaN	0.0053	0.0010	NaN	NaN	NaN
PLCKG114.3+64.9	114.34	64.87	6.18	A1703	0.28	NaN	0.0020	0.0003	NaN	NaN	NaN

Table A.1. continued.

Name	GLON	GLAT	S/N	ID	z	Θ_X	Y_{PSX}	Y_{PSX}^{ERR}	Θ	Y	Y^{ERR}
PLCKG80.4-33.2	80.38	–33.20	6.06	A2443	0.11	NaN	0.0039	0.0006	NaN	NaN	NaN
PLCKG249.9-39.9	249.88	–39.87	6.25	A3292	0.15	NaN	0.0018	0.0004	NaN	NaN	NaN
PLCKG182.6+55.8	182.64	55.82	6.81	A0963	0.21	NaN	0.0019	0.0004	NaN	NaN	NaN
PLCKG62.4-46.4	62.42	–46.41	6.33	A2440	0.09	NaN	0.0041	0.0007	NaN	NaN	NaN
PLCKG8.4-56.4	8.45	–56.36	6.39	A3854	0.15	NaN	0.0024	0.0005	NaN	NaN	NaN
PLCKG229.2-17.2	229.22	–17.25	6.18	RXCJ0616.3-2156	0.17	NaN	0.0031	0.0005	NaN	NaN	NaN
PLCKG341.0+35.1	340.96	35.12	6.61	ACO S0780	0.24	NaN	0.0030	0.0007	NaN	NaN	NaN
PLCKG218.9+35.5	218.86	35.51	6.87	A0750	0.18	NaN	0.0027	0.0005	NaN	NaN	NaN
PLCKG165.1+54.1	165.09	54.12	6.34	A0990	0.14	NaN	0.0027	0.0005	NaN	NaN	NaN
PLCKG161.4+26.2	161.44	26.23	6.63	A0576	0.04	NaN	0.0076	0.0012	NaN	NaN	NaN
PLCKG295.3+23.3	295.33	23.34	6.11	RXCJ1215.4-3900	0.12	NaN	0.0042	0.0008	NaN	NaN	NaN
PLCKG280.2+47.8	280.20	47.82	7.06	A1391	0.16	NaN	0.0042	0.0006	NaN	NaN	NaN
PLCKG0.4-41.8	0.44	–41.84	6.55	A3739	0.17	NaN	0.0025	0.0005	NaN	NaN	NaN
PLCKG195.6+44.1	195.62	44.05	6.88	A0781	0.30	NaN	0.0017	0.0003	NaN	NaN	NaN
PLCKG241.9+51.5	241.86	51.53	6.96	A1066	0.07	NaN	0.0024	0.0007	NaN	NaN	NaN
PLCKG81.0-50.9	81.00	–50.91	6.76	A2552	0.30	NaN	0.0026	0.0005	NaN	NaN	NaN
PLCKG304.5+32.4	304.50	32.44	6.86	A3532	0.06	NaN	0.0068	0.0015	NaN	NaN	NaN
PLCKG306.8+58.6	306.80	58.61	6.81	A1651	0.08	NaN	0.0077	0.0012	NaN	NaN	NaN
PLCKG172.9+65.3	172.89	65.32	6.30	A1190	0.08	NaN	0.0030	0.0006	NaN	NaN	NaN
PLCKG99.0+24.9	98.95	24.86	6.49	A2312	0.09	NaN	0.0022	0.0004	NaN	NaN	NaN
PLCKG247.2-23.3	247.17	–23.33	6.19	ACO S0579	0.15	NaN	0.0019	0.0004	NaN	NaN	NaN
PLCKG176.3-35.1	176.28	–35.05	6.38	2A0335+096	0.03	NaN	0.0117	0.0025	NaN	NaN	NaN
PLCKG57.9+27.6	57.93	27.64	6.13	ZwCl 1742.1+3306	0.08	NaN	0.0037	0.0008	NaN	NaN	NaN
PLCKG275.2+43.9	275.22	43.92	6.29	A1285	0.11	NaN	0.0044	0.0008	NaN	NaN	NaN
PLCKG96.9+52.5	96.85	52.47	6.12	A1995	0.32	NaN	0.0015	0.0003	NaN	NaN	NaN
PLCKG72.8-18.7	72.80	–18.72	10.10	ZwCl2120.1+2256	0.14	NaN	NaN	NaN	37.22	0.0052	0.0010
PLCKG239.3-26.0	239.29	-26.00	8.64	MACS J0553.4-3342	0.41	NaN	NaN	NaN	17.22	0.0026	0.0006
PLCKG8.3-64.8	8.30	–64.76	8.47	AC114Northern	0.31	NaN	NaN	NaN	43.83	0.0048	0.0010
PLCKG94.0+27.4	94.02	27.43	6.92	H1821+643	0.30	NaN	NaN	NaN	40.25	0.0030	0.0014
PLCKG157.4+30.3	157.43	30.34	6.18	RXJ0748.7+5941	NaN	NaN	NaN	NaN	22.43	0.0025	0.0014
PLCKG345.4-39.3	345.41	–39.34	7.10	ABELL3716S	0.04	NaN	NaN	NaN	118.59	0.0109	0.0032
PLCKG53.4-36.3	53.44	–36.27	6.88	MACS J2135.2-0102	0.32	NaN	NaN	NaN	8.07	0.0018	0.0003
PLCKG271.5-56.6	271.50	–56.56	6.71	ACO S0295	0.30	NaN	NaN	NaN	20.26	0.0025	0.0007
PLCKG86.0+26.7	86.00	26.71	6.55	A2302	0.18	NaN	NaN	NaN	56.62	0.0043	0.0019
PLCKG96.9+24.2	96.88	24.22	6.24	ZwCl1856.8+6616	NaN	NaN	NaN	NaN	20.64	0.0015	0.0005
PLCKG164.6+46.4	164.61	46.39	6.06	ZwCl0934.8+5216	NaN	NaN	NaN	NaN	16.50	0.0018	0.0006
PLCKG285.0-23.7	284.99	–23.71	11.48	null	0.44	NaN	0.0023	0.0002	NaN	NaN	NaN
PLCKG287.0+32.9	286.99	32.92	10.62	null	0.39	NaN	0.0061	0.0006	NaN	NaN	NaN
PLCKG171.9-40.7	171.95	–40.66	10.61	null	0.39	NaN	0.0062	0.0006	NaN	NaN	NaN
PLCKG271.2-31.0	271.20	–30.97	8.48	null	0.27	NaN	0.0020	0.0002	NaN	NaN	NaN
PLCKG262.7-40.9	262.71	–40.91	8.27	ACT-CLJ0438-5419	0.37	NaN	0.0021	0.0002	NaN	NaN	NaN
PLCKG308.3-20.2	308.32	–20.23	8.26	null	0.39	NaN	NaN	NaN	32.81	0.0049	0.0013
PLCKG277.8-51.7	277.75	–51.73	7.40	null	0.21	NaN	0.0027	0.0003	NaN	NaN	NaN
PLCKG286.6-31.3	286.59	–31.25	6.89	null	0.30	NaN	0.0026	0.0004	NaN	NaN	NaN
PLCKG292.5+22.0	292.52	21.99	6.88	null	0.35	NaN	0.0037	0.0006	NaN	NaN	NaN
PLCKG337.1-26.0	337.09	–25.97	6.59	null	0.48	NaN	NaN	NaN	31.56	0.0034	0.0008
PLCKG285.6-17.2	285.64	–17.25	6.35	null	0.12	NaN	0.0016	0.0003	NaN	NaN	NaN
PLCKG225.9-20.0	225.93	–20.00	8.07	null	NaN	NaN	NaN	NaN	28.21	0.0040	0.0011
PLCKG255.6-46.2	255.63	–46.17	8.46	null	NaN	NaN	NaN	NaN	31.23	0.0026	0.0006
PLCKG304.8-41.4	304.84	–41.42	7.58	null	NaN	NaN	NaN	NaN	21.68	0.0022	0.0006
PLCKG121.1+57.0	121.12	57.01	6.66	null	NaN	NaN	NaN	NaN	17.99	0.0016	0.0004
PLCKG283.2-22.9	283.16	–22.93	6.03	null	NaN	NaN	NaN	NaN	26.73	0.0018	0.0008
PLCKG139.6+24.2	139.60	24.19	7.21	null	NaN	NaN	NaN	NaN	24.52	0.0032	0.0013
PLCKG189.8-37.2	189.85	–37.24	6.71	null	NaN	NaN	NaN	NaN	62.50	0.0080	0.0021
PLCKG264.4+19.5	264.42	19.48	6.15	null	NaN	NaN	NaN	NaN	32.25	0.0028	0.0010
PLCKG115.7+17.5	115.72	17.53	6.78	null	NaN	NaN	NaN	NaN	17.48	0.0025	0.0008

A&A 571, A29 (2014)
DOI: 10.1051/0004-6361/201321523

Astronomy & Astrophysics
Special feature

Planck 2013 results

Planck 2013 results. XXIX. The *Planck* catalogue of Sunyaev-Zeldovich sources[⋆]

Planck Collaboration: P. A. R. Ade[99], N. Aghanim[68,⋆⋆], C. Armitage-Caplan[104], M. Arnaud[81], M. Ashdown[78,7], F. Atrio-Barandela[21],
J. Aumont[68], H. Aussel[81], C. Baccigalupi[97], A. J. Banday[110,11], R. B. Barreiro[75], R. Barrena[74], M. Bartelmann[108,87], J. G. Bartlett[1,76],
E. Battaner[113], K. Benabed[69,107], A. Benoît[66], A. Benoit-Lévy[29,69,107], J.-P. Bernard[110,11], M. Bersanelli[41,58], P. Bielewicz[110,11,97], I. Bikmaev[24,3],
J. Bobin[81], J. J. Bock[76,12], H. Böhringer[88], A. Bonaldi[77], J. R. Bond[10], J. Borrill[16,101], F. R. Bouchet[69,107], M. Bridges[78,7,72], M. Bucher[1],
R. Burenin[100,91], C. Burigana[57,39], R. C. Butler[57], J.-F. Cardoso[82,1,69], P. Carvalho[7], A. Catalano[83,80], A. Challinor[72,78,13], A. Chamballu[81,18,68],
R.-R. Chary[65], X. Chen[65], H. C. Chiang[33,8], L.-Y Chiang[71], G. Chon[88], P. R. Christensen[93,44], E. Churazov[87,100], S. Church[103], D. L. Clements[64],
S. Colombi[69,107], L. P. L. Colombo[28,76], B. Comis[83], F. Couchot[79], A. Coulais[80], B. P. Crill[76,94], A. Curto[7,75], F. Cuttaia[57], A. Da Silva[14],
H. Dahle[73], L. Danese[97], R. D. Davies[77], R. J. Davis[77], P. de Bernardis[40], A. de Rosa[57], G. de Zotti[53,97], J. Delabrouille[1], J.-M. Delouis[69,107],
J. Démoclès[81], F.-X. Désert[61], C. Dickinson[77], J. M. Diego[75], K. Dolag[112,87], H. Dole[68,67], S. Donzelli[58], O. Doré[76,12], M. Douspis[68], X. Dupac[47],
G. Efstathiou[72], P. R. M. Eisenhardt[76], T. A. Enßlin[87], H. K. Eriksen[73], F. Feroz[7], F. Finelli[57,59], I. Flores-Cacho[11,110], O. Forni[110,11], M. Frailis[55],
E. Franceschi[57], S. Fromenteau[1,68], S. Galeotta[55], K. Ganga[1], R. T. Génova-Santos[74], M. Giard[110,11], G. Giardino[48], M. Gilfanov[87,100],
Y. Giraud-Héraud[1], J. González-Nuevo[75,97], K. M. Górski[76,114], K. J. B. Grainge[7,78], S. Gratton[78,72], A. Gregorio[42,55], N, E. Groeneboom[73],
A. Gruppuso[57], F. K. Hansen[73], D. Hanson[89,76,10], D. Harrison[72,78], A. Hempel[74,45], S. Henrot-Versillé[79], C. Hernández-Monteagudo[15,87],
D. Herranz[75], S. R. Hildebrandt[12], E. Hivon[69,107], M. Hobson[7], W. A. Holmes[76], A. Hornstrup[19], W. Hovest[87], K. M. Huffenberger[31],
G. Hurier[68,83], N. Hurley-Walker[7], A. H. Jaffe[64], T. R. Jaffe[110,11], W. C. Jones[33], M. Juvela[32], E. Keihänen[32], R. Keskitalo[26,16], I. Khamitov[105,24],
T. S. Kisner[85], R. Kneissl[46,9], J. Knoche[87], L. Knox[35], M. Kunz[20,68,4], H. Kurki-Suonio[32,51], G. Lagache[68], A. Lähteenmäki[2,51], J.-M. Lamarre[80],
A. Lasenby[7,78], R. J. Laureijs[48], C. R. Lawrence[76], J. P. Leahy[77], R. Leonardi[47], J. León-Tavares[49,2], J. Lesgourgues[106,96], C. Li[86,87], A. Liddle[98,30],
M. Liguori[38], P. B. Lilje[73], M. Linden-Vørnle[19], M. López-Caniego[75], P. M. Lubin[36], J. F. Macías-Pérez[83], C. J. MacTavish[78], B. Maffei[77],
D. Maino[41,58], N. Mandolesi[57,6,39], M. Maris[55], D. J. Marshall[81], P. G. Martin[10], E. Martínez-González[75], S. Masi[40], M. Massardi[56],
S. Matarrese[38], F. Matthai[87], P. Mazzotta[43], S. Mei[50,109,12], P. R. Meinhold[36], A. Melchiorri[40,60], J.-B. Melin[18], L. Mendes[47], A. Mennella[41,58],
M. Migliaccio[72,78], K. Mikkelsen[73], S. Mitra[63,76], M.-A. Miville-Deschênes[68,10], A. Moneti[69], L. Montier[110,11], G. Morgante[57], D. Mortlock[64],
D. Munshi[99], J. A. Murphy[92], P. Naselsky[93,44], F. Nati[40], P. Natoli[39,5,57], N. P. H. Nesvadba[68], C. B. Netterfield[23], H. U. Nørgaard-Nielsen[19],
F. Noviello[77], D. Novikov[64], I. Novikov[93], I. J. O'Dwyer[76], M. Olamaie[7], S. Osborne[103], C. A. Oxborrow[19], F. Paci[97], L. Pagano[40,60], F. Pajot[68],
D. Paoletti[57,59], F. Pasian[55], G. Patanchon[1], T. J. Pearson[12,65], O. Perdereau[79], L. Perotto[83], Y. C. Perrott[7], F. Perrotta[97], F. Piacentini[40], M. Piat[1],
E. Pierpaoli[28], D. Pietrobon[76], S. Plaszczynski[79], E. Pointecouteau[110,11], G. Polenta[5,54], N. Ponthieu[68,61], L. Popa[70], T. Poutanen[51,32,2],
G. W. Pratt[81], G. Prézeau[12,76], S. Prunet[69,107], J.-L. Puget[68], J. P. Rachen[25,87], W. T. Reach[111], R. Rebolo[74,17,45], M. Reinecke[87],
M. Remazeilles[77,68,1], C. Renault[83], S. Ricciardi[57], T. Riller[87], I. Ristorcelli[110,11], G. Rocha[76,12], C. Rosset[1], G. Roudier[1,80,76],
M. Rowan-Robinson[64], J. A. Rubiño-Martín[74,45], C. Rumsey[7], B. Rusholme[65], M. Sandri[57], D. Santos[83], R. D. E. Saunders[7,78], G. Savini[95],
M. P. Schammel[7], D. Scott[27], M. D. Seiffert[76,12], E. P. S. Shellard[13], T. W. Shimwell[7], L. D. Spencer[99], S. A. Stanford[35], J.-L. Starck[81],
V. Stolyarov[7,78,102], R. Stompor[1], R. Sudiwala[99], R. Sunyaev[87,100], F. Sureau[81], D. Sutton[72,78], A.-S. Suur-Uski[32,51], J.-F. Sygnet[69], J. A. Tauber[48],
D. Tavagnacco[55,42], L. Terenzi[57], L. Toffolatti[22,75], M. Tomasi[58], M. Tristram[79], M. Tucci[20,79], J. Tuovinen[90], M. Türler[62], G. Umana[52],
L. Valenziano[57], J. Valiviita[51,32,73], B. Van Tent[84], L. Vibert[68], P. Vielva[75], F. Villa[57], N. Vittorio[43], L. A. Wade[76], B. D. Wandelt[69,107,37],
M. White[34], S. D. M. White[87], D. Yvon[18], A. Zacchei[55], and A. Zonca[36]

(Affiliations can be found after the references)

Received 20 March 2013 / Accepted 9 December 2013

ABSTRACT

We describe the all-sky *Planck* catalogue of clusters and cluster candidates derived from Sunyaev-Zeldovich (SZ) effect detections using the first 15.5 months of *Planck* satellite observations. The catalogue contains 1227 entries, making it over six times the size of the *Planck* Early SZ (ESZ) sample and the largest SZ-selected catalogue to date. It contains 861 confirmed clusters, of which 178 have been confirmed as clusters, mostly through follow-up observations, and a further 683 are previously-known clusters. The remaining 366 have the status of cluster candidates, and we divide them into three classes according to the quality of evidence that they are likely to be true clusters. The *Planck* SZ catalogue is the deepest all-sky cluster catalogue, with redshifts up to about one, and spans the broadest cluster mass range from $(0.1 \text{ to } 1.6) \times 10^{15}\,M_{\odot}$. Confirmation of cluster candidates through comparison with existing surveys or cluster catalogues is extensively described, as is the statistical characterization of the catalogue in terms of completeness and statistical reliability. The outputs of the validation process are provided as additional information. This gives, in particular, an ensemble of 813 cluster redshifts, and for all these *Planck* clusters we also include a mass estimated from a newly-proposed SZ-mass proxy. A refined measure of the SZ Compton parameter for the clusters with X-ray counter-parts is provided, as is an X-ray flux for all the *Planck* clusters not previously detected in X-ray surveys.

Key words. large-scale structure of Universe – galaxies: clusters: general – catalogs

---

[⋆] The catalogue of SZ sources is available at Planck Legacy Archive and
`http://www.sciops.esa.int/index.php?page=Planck_Legacy_Archive\&project=planck`

[⋆⋆] Corresponding author: N. Aghanim, e-mail: `nabila.aghanim@ias.u-psud.fr`

1. Introduction

This paper, one of a set associated with the 2013 release of data from the *Planck*[1] mission (Planck Collaboration I 2014), describes the construction and properties of the *Planck* catalogue of SZ sources (PSZ).

Clusters of galaxies play several important roles in astrophysics and cosmology. As rare objects, their number density is especially sensitive to properties of the cosmological model such as the amplitude of primordial density perturbations (Peebles 1980), and their development with redshift probes the growth of cosmic structure, hence perhaps helping to distinguish between dark energy and modified gravity explanations for cosmic acceleration (e.g., see reviews by Borgani & Kravtsov 2009; Allen et al. 2011). The galaxies, hot gas and dark matter held in their gravitational potential wells provide a sample of the universal abundance of these components (e.g., Voit 2005), while the thermal state of the gas probes both the cluster formation mechanism and physical processes within the cluster such as cooling and energy-injection feedback (e.g., reviews by Fabian 2012; McNamara & Nulsen 2012). The study of the constituent galaxies, including the brightest cluster galaxies normally found at their centres, allows sensitive tests of galaxy formation models.

Because of these uses, there is considerable interest in developing large galaxy cluster catalogues that can be used for population and cosmological studies (e.g., Schuecker et al. 2003; Böhringer et al. 2004). Clusters are genuinely multi-wavelength objects that can be selected in several ways: optical/infrared (IR) imaging of the galaxy populations; X-ray imaging of the bremsstrahlung radiation from the hot cluster gas; and through the Sunyaev-Zeldovich (SZ) effect (Sunyaev & Zeldovich 1972, 1980) whereby scattering of cosmic microwave background (CMB) photons from that hot gas distorts the spectral shape of the CMB along lines of sight through clusters and groups.

Construction of cluster catalogues in the optical/IR and in the X-ray are relatively mature activities. The first large optical cluster survey is now over 50 years old (Abell 1958; Abell et al. 1989), and current catalogues constructed from the Sloan Digital Sky Survey data contain over a hundred thousand clusters (e.g., Koester et al. 2007; Wen et al. 2012). In X-rays, large samples first became available via ROSAT satellite observations (e.g., Vikhlinin et al. 1998; Böhringer et al. 2000, 2004; Gioia et al. 2003; Burenin et al. 2007; Ebeling et al. 2007), but also more recently for instance from dedicated or serendipitous survey with *XMM-Newton* (Pacaud et al. 2007; Fassbender et al. 2011; Takey et al. 2011; Mehrtens et al. 2012). Currently several thousand X-ray selected clusters are known (see for instance the meta-catalogue MCXC by Piffaretti et al. 2011). By contrast, although proposed about fifteen years ago (e.g., Barbosa et al. 1996; Aghanim et al. 1997), it is only very recently that SZ-selected samples have reached a significant size, with publication of samples containing several hundred clusters from the Early SZ (ESZ) catalogue from the *Planck* Satellite (Planck Collaboration VIII 2011), the South Pole Telescope (SPT, Reichardt et al. 2013) and the Atacama Cosmology Telescope (ACT, Hasselfield et al. 2013).

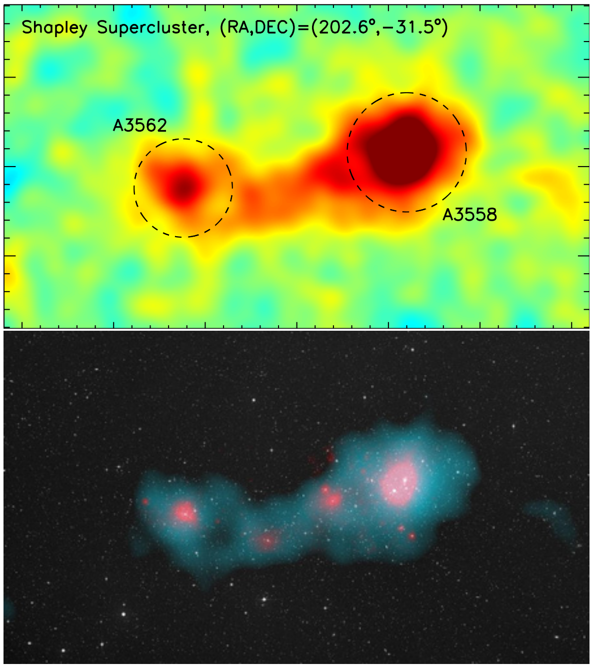

Fig. 1. The Shapley super-cluster as seen in the *Planck* survey. *Upper panel*: reconstructed thermal SZ map 3.2° × 1.8° from `MILCA` (Hurier et al. 2013). The dotted circles represent apertures of θ_{500} from the MCXC meta-catalogue around the resolved clusters. *Lower panel*: composite view of the optical from DSS images (white), X-rays from ROSAT (pink) survey and of the thermal SZ effect as seen in *Planck* (blue).

The usefulness of the different selection methods, particularly for cosmology, depends not just on the total number of clusters identified but also on how readily the selection function of the survey can be modelled, and on how well the observed cluster properties can be related to quantities such as the total cluster mass that are most readily predicted from theory (e.g., see Voit 2005). It has proven difficult to capitalize on the large size of optical/IR cluster samples because the observable, the number of galaxies in each cluster, exhibits large scatter with respect to the total cluster mass (e.g., Johnston et al. 2007). In this regard the X-ray selected samples are considerably more powerful, due to the tighter correlations of X-ray properties with mass (Arnaud et al. 2005; Vikhlinin et al. 2006; Pratt et al. 2009; Reichert et al. 2011; Maughan et al. 2012). Simulations predict that SZ-selected surveys may do even better, with a very tight relation between SZ signal and mass (e.g., da Silva et al. 2004; Motl et al. 2005; Nagai 2006; Wik et al. 2008; Aghanim et al. 2009; Angulo et al. 2012). Moreover, this relation, except at low redshifts, corresponds to a nearly redshift-independent mass limit, thus allowing such surveys to reach to high redshift and provide a strong lever arm on growth of structure.

We report on the construction and properties of the PSZ catalogue, which is to date the largest SZ-selected cluster catalogue and has value added through compilation of ancillary information. It contains 1227 entries including many multiple systems, e.g., the Shapley super-cluster displayed in Fig. 1 together with a composite image. Of these 861 are confirmed, amongst which 178 are new discoveries, whilst amongst the 366 candidate clusters 54 are of high reliability (1 in our terminology), 170 are reliable, and the remaining 142 are in the

---

[1] *Planck* (`http://www.esa.int/Planck`) is a project of the European Space Agency (ESA) with instruments provided by two scientific consortia funded by ESA member states (in particular the lead countries France and Italy), with contributions from NASA (USA) and telescope reflectors provided by a collaboration between ESA and a scientific consortium led and funded by Denmark.

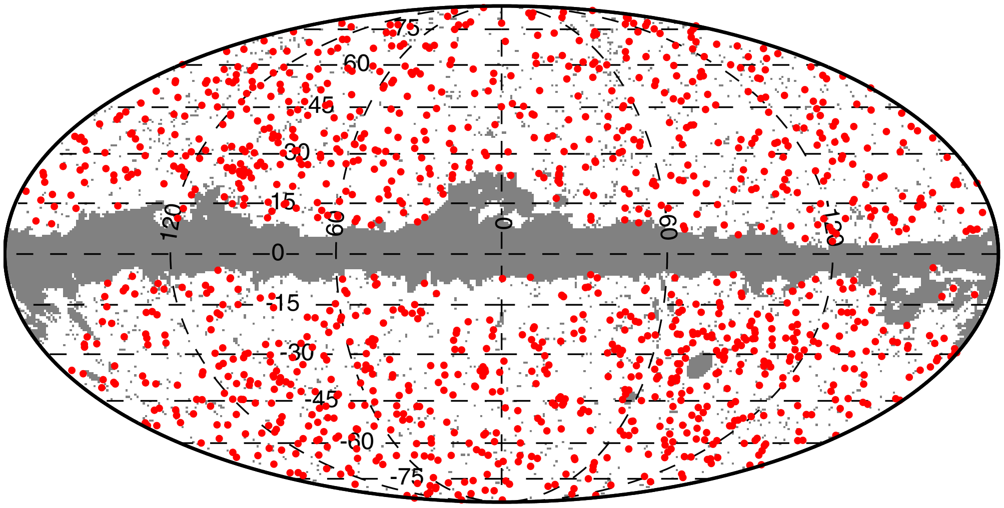

Fig. 2. Sky distribution of the 1227 *Planck* clusters and candidates (red dots), in a Mollweide projection with the Galactic plane horizontal and centred at longitude zero. Small grey dots show the positions of masked point sources, and grey shading shows the mask used to exclude the Magellanic clouds and the Galactic plane mask. The mask covers 16.3% of the sky.

lowest reliability class. In Sect. 2 we start with a description of the *Planck* data used to provide cluster candidates, and the two different methodologies (one of which has two independent implementations) used to carry out the extraction of the SZ sources. In Sect. 3 we provide a characterization of the PSZ catalogue in terms of completeness, statistical reliability, and accuracy of cluster parameters including size and photometry. Section 4 extensively describes validation of cluster candidates through pre-existing surveys and cluster catalogues in many wavebands, while Sect. 5 describes the follow-up campaigns conducted by the *Planck* collaboration to confirm new cluster discoveries. This leads to a description of the catalogue properties in Sect. 6. The physical properties of the clusters are exploited in Sect. 7. These include an update of the SZ–X-ray scaling relations from the *Planck* data, the measure of the X-ray flux for all SZ detections, and the production of homogenized SZ-mass estimates for 813 clusters with measured redshifts that are provided to the community as a value-added element to the *Planck* SZ catalogue.

Throughout the article, the quantities M_{500} and R_{500} stand for the total mass and radius where the mean enclosed density is 500 times the critical density at the cluster redshift. The SZ flux is denoted Y_{500}, where $Y_{500}\,D_{\mathrm{A}}^2$ is the spherically-integrated Compton parameter within R_{500}, and D_{A} is the angular-diameter distance to the cluster. The physical cluster quantities are computed with a fiducial ΛCDM cosmology with $H_0 = 70\,\mathrm{km\,s^{-1}\,Mpc^{-1}}$, $\Omega_{\mathrm{m}} = 0.3$ and $\Omega_\Lambda = 0.7$. Furthermore, all the fits are undertaken in the log-log plane using the BCES orthogonal regression method of Akritas & Bershady (1996), with bootstrap resampling, which allows for intrinsic scatter as well as uncertainties in both variables. All uncertainties are given at 68 per cent confidence level and all dispersions are given in $\log_{10}$.

2. Construction of the *Planck* SZ Catalogue

2.1. Input Planck data

The *Planck* catalogue of SZ sources is constructed from the total intensity data taken during the first 15.5 months of *Planck* survey observations. Raw data were first processed to produce cleaned time-lines (time-ordered information) and associated flags correcting for different systematic effects; channel maps were then produced for all the observing frequencies (see details in Planck Collaboration VI 2014; Planck Collaboration II 2014). These maps, together with the associated beam characteristics, are the main inputs for the SZ-finder algorithms presented in Sect. 2.2. Following Planck Collaboration VIII (2011), we used the six highest-frequency *Planck* channel maps, from 100 to 857 GHz, to produce the catalogue of SZ detections. This optimizes the signal-to-noise (S/N) of the extracted SZ detections and the usable sky fraction; see Appendix A for the choice of channel maps.

In order to optimize the SZ detection, together with avoiding contamination of the PSZ catalogue by bright point sources (PS), the latter are masked from the channel maps prior to the SZ detection as detailed in the following. To construct the PS mask, we use the *Planck* Catalogue of Compact Sources (PCCS). The PCCS (Planck Collaboration XXVIII 2014) is a collection of single-frequency source catalogues, one for each of the nine *Planck* frequency channels. The six single *Planck*-HFI frequency PS catalogues are used to first produce individual-frequency masks constructed by masking a radius equivalent to 1.28 FWHM ($3\sigma_{\mathrm{beam}}$) around every point source detected with $(S/N)_{\mathrm{PS}} \geq 10$. Then a single common PS mask (see Fig. 2), which is the union of the six individual HFI-frequency channel masks, is constructed. It is applied to all six highest-frequency *Planck* channel-maps to mask the point sources prior to running the algorithms to detect SZ signal. The masked regions are filled using a harmonic in-painting method based on that of Bajkova (2005), which has the advantage of eliminating the discontinuities caused by the masking. In order to avoid any possible artificial spurious detections at the edges of the in-painted area, we further reject detections within an expanded common mask, constructed using the same procedure as described above, but using a masking radius equivalent to 2.13 FWHM ($5\sigma_{\mathrm{beam}}$) and covering less than 2.9% of the sky.

Bright radio sources are known to exist at the centre of galaxy clusters, but they generally have steep spectra and hence their flux is significantly reduced at the six highest *Planck* frequencies where the PS mask is constructed and where the clusters are detected. The Perseus cluster (see Fig. 19 later and the associated discussion) is one exception, with a point source that is so bright that the cluster is masked and thus not included in the *Planck* SZ catalogue.

2.2. Detection methods

The catalogue of SZ sources is the result of a blind multi-frequency search, i.e., no prior positional information on known clusters is used as input to the detection, by three detection algorithms briefly described below. These algorithms were described and tested using simulations (Melin et al. 2012). They were used to construct the Early SZ (ESZ) *Planck* sample by Planck Collaboration VIII (2011). All three assume priors on the cluster spectral and spatial characteristics, which optimize the SZ detection by enhancing the SZ contrast over a set of observations containing contaminating signals. In the following we present the cluster model used as a template by the SZ-finder algorithms and we briefly describe the three detection methods (for details we refer the reader to Herranz et al. 2002; Melin et al. 2006, 2012; Carvalho et al. 2009, 2012).

2.2.1. Cluster model

The baseline pressure profile model used in the detection methods is the generalized NFW (Navarro et al. 1997) profile of Arnaud et al. (2010). This profile model was constructed by combining the observed, scaled, X-ray pressure profile of 31 clusters from the REXCESS sample (Böhringer et al. 2007) for $R < R_{500}$,[2] with the mean pressure profile from three sets of numerical simulations (Borgani et al. 2004; Nagai et al. 2007; Piffaretti & Valdarnini 2008) for $R_{500} < R < 5R_{500}$. New observational constraints on the pressure distribution at $R > R_{500}$ have become available. Planck Collaboration Int. V (2013) constrained the detection of the thermal pressure distribution out to about $3R_{500}$ through stacking of the observed SZ profiles of 62 nearby massive clusters detected with high significance in the *Planck* ESZ sample. The resulting profile is in agreement with that derived for the Coma cluster (Planck Collaboration Int. X 2013). Both show a slightly flatter distribution in the outer parts (i.e., beyond R_{500}) with respect to the predictions from the numerical simulations. These results are further confirmed by independent measurements from Bolocam in a smaller radial range ($r < 2\,R_{500}$, Sayers et al. 2013). Pressure profiles different from the generalized NFW and consistent with the observations can be devised, e.g., the SuperModel used by Lapi et al. (2012) for SPT stacked clusters or by Fusco-Femiano et al. (2013) for the Coma cluster. Using the profile of Planck Collaboration Int. V (2013) does not affect the detection yield (see Sect. 3) and only slightly modifies the measure of the SZ flux density (see Sect. 7.5) as compared to the generalized NFW (GNFW) profile adopted in the three cluster. The fiducial model parameters for the GNFW profile are given by the parameterization of the pressure profile in Eq. (12) of Arnaud et al. (2010). It states

$$p(x) = \frac{P_0}{(c_{500}x)^{\gamma}\,[1 + (c_{500}x)^{\alpha}]^{(\beta-\gamma)/\alpha}}, \tag{1}$$

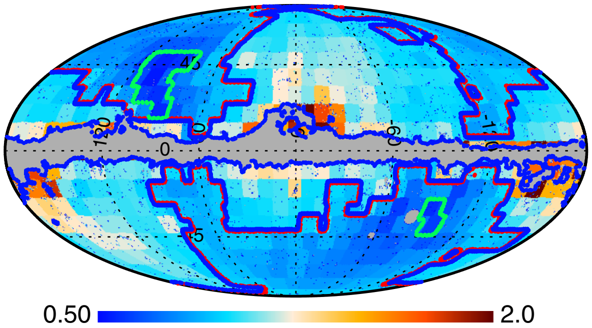

Fig. 3. Noise maps per detection patch of MMF3 method measured for a 6′ filter. The noise ranges from 0.5 to 2 times the average noise of the map, which is $\sigma_Y = 2.4 \times 10^{-4}$ arcmin^2. The Ecliptic polar regions, delimited by green contours, with increased redundancy in the observations define a deep survey zone covering in total 2.7% of the sky. It is less noisy than the areas near the Galactic plane, where the dust emission is higher. Two other zones are defined: a medium-deep survey zone of 41.3% coverage delimited by the red contours and with higher noise level; and a shallow-survey zone covering 56% of the sky and with the highest noise levels including regions near the Galactic plane.

with the parameters

$$[P_0, c_{500}, \gamma, \alpha, \beta] = [8.40\,h_{70}^{-3/2}, 1.18, 0.308, 1.05, 5.49]. \tag{2}$$

The (weak) mass dependence of the profiles is neglected. Within the SZ-finder algorithms, the size and amplitude of the profile are allowed to vary but all other parameters are fixed. The cluster model is thus equivalent to a shape function characterized by two free parameters, its amplitude and a characteristic scale $\theta_{\rm s} = \theta_{500}/c_{500}$.

2.2.2. Matched multi-filter (MMF)

Two different implementations of the matched multi-frequency filter algorithm (`MMF1` and `MMF3`) are used to detect SZ clusters. Both are extensions, over the whole sky, of the `MMF` algorithm (Herranz et al. 2002; Melin et al. 2006). The matched filter optimizes the cluster detection using a linear combination of maps (which requires an estimate of the statistics of the contamination) and uses spatial filtering to suppress both foregrounds and noise (making use of the prior knowledge of the cluster pressure profile and thermal SZ spectrum).

The `MMF1` algorithm divides the full-sky *Planck* frequency maps into 640 patches, each 14.66°×14.66°, covering 3.33 times the sky. The `MMF3` algorithm divides the maps into a smaller set of 504 overlapping square patches of area 10° × 10° with the sky covered 1.22 times. The smaller redundancy of `MMF3` with respect to `MMF1` implies a potentially lower reliability of the SZ detections. In order to increase the reliability of the detections, the `MMF3` algorithm is thus run in two iterations. After a first detection of the SZ candidates, a subsequent run centred on the positions of the candidates refines the estimated S/N and candidate properties. If the S/N of a detection falls below the threshold at the second iteration, it is removed from the catalogue. For both implementations, the matched multi-frequency filter optimally combines the six frequencies of each patch. Auto- and cross-power spectra are directly estimated from the data and are thus adapted to the local instrumental noise and astrophysical contamination, which constitutes the dominant noise contribution. Figure 3 illustrates, for a 6′ filter size, the ensemble noise maps as measured by `MMF3` in each of the patches. For both `MMF1` and

---

[2] R_{500} relates to the characteristic cluster scale $R_{\rm s}$ through the NFW concentration parameter $c_{500} = 1.177$ for the baseline profile ($R_{\rm s} = R_{500}/c_{500}$).

`MMF3`, the detection of the SZ-candidates is performed on all the patches, and the resultant sub-catalogues are merged together to produce a single SZ-candidate catalogue per method.

The candidate size in both algorithms is estimated by filtering the patches over the range of potential scales, and finding the scale that maximizes the S/N of the detected candidate. When merging the sub-catalogues produced from the analysis of individual patches, it is also the S/N of the detection (the refined S/N estimate for `MMF3`) which is used when deciding which detection of the candidate is kept. Furthermore, both `MMF1` and `MMF3` can also be run with fixed cluster size and position to estimate the SZ signal. This version of the algorithms is used to assess the reliability of the association with known clusters and/or to refine the measurement of the integrated Compton parameters of known X-ray clusters, as presented in Sect. 7.2.1.

2.2.3. PowellSnakes

PowellSnakes (`PwS`) is different from the `MMF` methods. It is a fast Bayesian multi-frequency detection algorithm designed to identify and characterize compact objects buried in a diffuse background. The detection process is grounded in a statistical model comparison test. The statistical foundations of `PwS` are described in Carvalho et al. (2009), and more recently in Carvalho et al. (2012) with a greater focus on the *Planck* setup. `PwS` may be run either based on a Generalized Likelihood Ratio Test or in full Bayesian mode. This duality allows `PwS` measured quantities to be consistently compared with those of the `MMF` algorithms.

`PwS` also operates in square flat patches of $14.66° \times 14.66°$. The total number of patches employed, of order 2800, varies with sky area but always guarantees a very large overlap; on average each cluster is detected about 4.7 times. `PwS` detects putative clusters and at the same time it computes the evidence ratio and samples from the posterior distributions of the cluster parameters. Then, it merges all intermediate sub-catalogues and applies the criterion of acceptance/rejection (Carvalho et al. 2012). `PwS` computes the cross-channel covariance matrix directly from the pixel data. To reduce the contamination of the background by the SZ signal itself, the estimation of the covariance matrix is performed iteratively. After an initial estimate, all detections in the patch with S/N higher than the current target detection are subtracted from the data using their best-fit values and the cross-channel covariance matrix is re-estimated. This is `PwS` "*native*" mode of background estimation that produces, on average, an S/N estimate about 20% higher than `MMF`. However, in order to produce a homogeneous *Planck* SZ catalogue from the three algorithms, it is possible to run `PwS` in "*compatibility*" mode, skipping the re-estimation step to mimic more closely the evaluation of the background noise cross-power spectrum of the `MMF` algorithms and thus their evaluation of the S/N. In this mode, `PwS` is a maximum likelihood estimator like the `MMF`.

In the following, unless stated otherwise, all quoted or plotted S/N values from `PwS` are obtained in "*compatibility*" mode in order to ensure homogeneity across the catalogue entries and in order to ease the comparison with the `MMF` outputs.

2.3. Outputs of the detection methods

Each of the three detection algorithms outputs a catalogue of SZ detections above $S/N = 4.5$ outside the highest-emitting Galactic regions (this corresponds to a mask of about 15% of the sky, see masked area in Fig. 2) and the Small and Large Magellanic Clouds and outside the PS mask described in Sect. 2.1. The union PS-Galactic mask covers 16.3% of the sky. The survey area used for the SZ detections in *Planck* is thus 83.7% of the sky coverage. The three individual lists of SZ candidates are cleaned by removal of obvious false detections. These are spurious sources that pass the `MMF` and `PwS` filters despite the pre-processing step applied to the *Planck* channel maps, see Sect. 2.1. In order to identify them, we cross-match the SZ detections with an intermediate, low S/N cut of 4, catalogue of point sources detected at the highest frequencies of *Planck*. Galactic sources in dense and cold regions at high latitudes also contaminate the SZ detections outside the Galactic mask. These cold Galactic sources (CGS, see Planck Collaboration XXIII 2011; Planck Collaboration XXII 2011) are detected in the *Planck* channel maps following an optimized method proposed by Montier et al. (2010). The SZ detections matching with PS at both 545 and 857 GHz, or with CGS sources, all show a rising spectrum at high frequencies, indicating that they are false detections. The SZ detections corresponding to such PCCS or CG sources are removed from the individual lists and from the published *Planck* catalogue of SZ sources.

The three detection algorithms used in the present study deploy the GNFW cluster profile to detect SZ signal with the two parameters of the shape function, the central value and the characteristic scale θ_s let free, with $\theta_\mathrm{s} = \theta_{500}/c_{500}$. Each of the three algorithms therefore assigns, to each detected SZ candidate, a position with estimated uncertainty, a S/N value, and an estimated size, θ_s or equivalently θ_{500}, with its uncertainty. The detection likelihood or the posterior probability of the integrated Compton parameter within $5\theta_{500}$, denoted $Y_{5\mathrm{R}_{500}}$, exhibits a large correlation with the size. Figure 4 illustrates the likelihood plots for two cases: a spatially-resolved cluster detected with a high S/N, Abell 2163; and a non-resolved cluster at high redshift ($z \simeq 1$), PSZ1 G266.6-27.3 (also known as PLCK G266.6-27.3 in Planck Collaboration XXVI 2011). We also show in Fig. 5 the distribution of maximum likelihood SZ fluxes ($Y_{5\mathrm{R}_{500}}$) and sizes (θ_{500}) for the `MMF3` detections.

This "degeneracy" between cluster size and SZ flux propagates the size uncertainty to the SZ flux estimate, increasing and biasing its value dramatically. This effect being so detrimental, both the SZ blind flux and size best-fit estimates, and respective error bars, are not quoted in the catalogue outputs to avoid their misuse. Only the full joint $Y_{5\mathrm{R}_{500}}-\theta_\mathrm{s}$, or equivalently $Y_{5\mathrm{R}_{500}}-\theta_{500}$, posterior probability contours provide a complete description of the information output by each detection method. They are thus provided for each detection. In order to use the flux measure, one ought to break the size–flux degeneracy. This can be achieved by a joint analysis with a high-resolution observation of the same objects, or by assuming a prior on, or fixing, the cluster size e.g., to the X-ray size. The SZ signal can then be re-extracted with an uncertainty much smaller than the variation of the joint Y–θ probability distribution.

We now perform a systematic comparison of the outputs of the three algorithms and we compare the S/N. In addition and for purposes of illustration, we compare the best-fit blind Y value from maximum-likelihood or posterior probability outputs, namely $Y_{5\mathrm{R}_{500}}$[3]. We show the comparison in Fig. 6, considering detections down to $S/N = 4.5$. We quantify the difference between a given quantity estimated by two different algorithms, Q_2 and Q_1, by fitting a power law to the data in the form $Q_2/Q_\mathrm{p} = 10^A\,(Q_1/Q_\mathrm{p})^\alpha$ with a pivot $Q_\mathrm{p} = 6$ for S/N and $Q_\mathrm{p} = 4\times10^{-3}$ arcmin^2 for $Y_{5\mathrm{R}_{500}}$. The results are given in Table 1, including the scatter estimates. The raw scatter was estimated

---

[3] $Y_{5\mathrm{R}_{500}}$ can be rescaled to Y_{500} for the fiducial GNFW model as $Y_{5\mathrm{R}_{500}} = 1.79 \times Y_{500}$ (Arnaud et al. 2010).

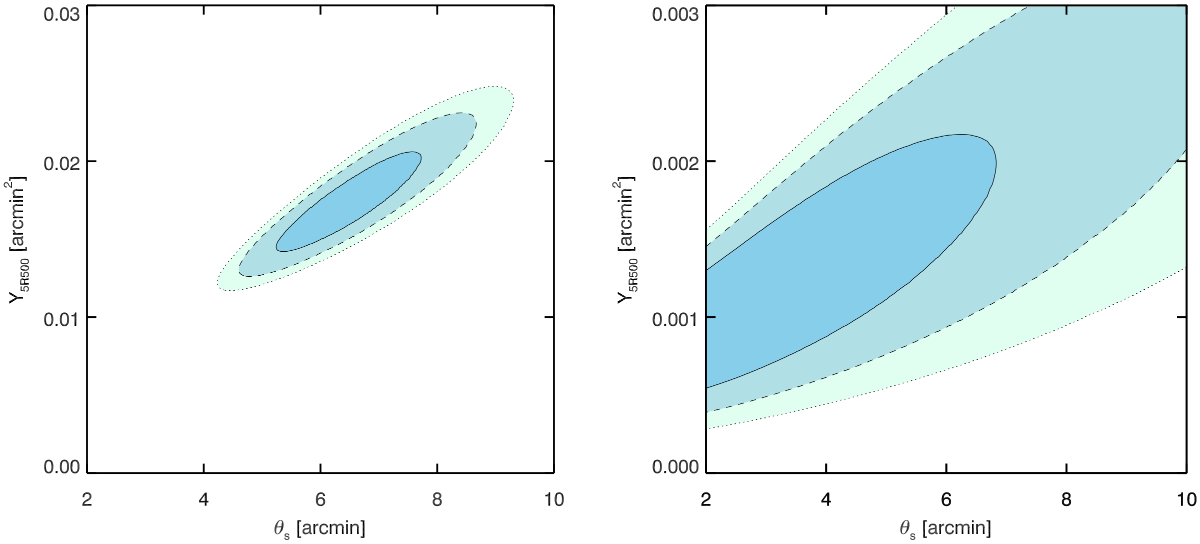

Fig. 4. Illustration of the SZ size–flux degeneracy for two clusters detected by *Planck*. *Right*: Abell 2163 ($S/N = 27$) and *left*: PSZ1 G266.6-27.3 ($S/N = 6$ at $z \simeq 1$). The contours show the 68, 95, and 99 percent confidence levels.

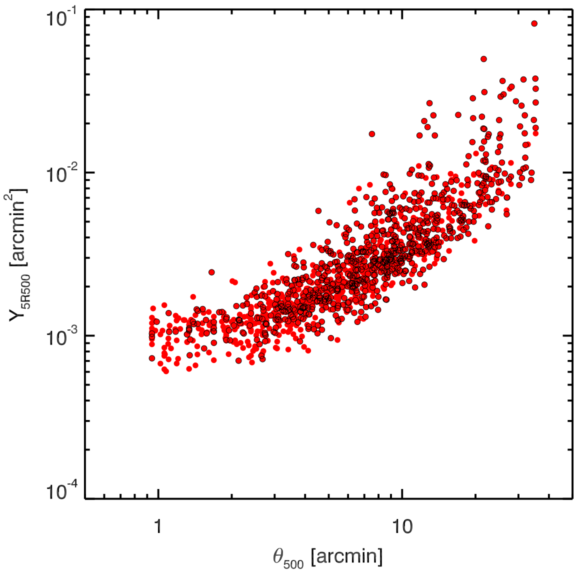

Fig. 5. Distribution of the maximum likelihood SZ flux $Y_{5R_{500}}$ and size θ_{500} for *Planck* SZ detections in the union catalogue down to $S/N = 4.5$. Detections associated with known or new confirmed clusters are shown as open black circles. SZ cluster candidates are shown as filled red circles.

using the error-weighted vertical distances to the regression line. The intrinsic scatter on Y_{500} was computed from the quadratic difference between the raw scatter and that expected from the statistical uncertainties. Table 1 also lists the mean difference in logarithm, $\Delta(\log Q) = \log(Q_2/Q_1)$, computed taking into account both statistical errors and intrinsic scatter, estimated iteratively.

2.3.1. Signal-to-noise

A crucial ingredient of the SZ detection algorithms, either the `MMF`s or `PwS`, is the background cross-power spectrum used to estimate the noise level. It is evaluated from the data locally on a per-patch basis (see Fig. 3 for an example of the noise per patch across the sky). The algorithms, and implementations, slightly differ with respect to the stabilization assumptions (e.g., smoothing) of the background noise cross-power spectrum and to the treatment of the background SZ signal, now acting as a contaminant. These differences translate into variations in the S/N values per method. In particular, when operated in "*compatibility*" mode (without background cluster subtraction), `PwS` estimation of the background cross-power spectrum is more affected than the `MMF` by SZ signal contamination. The SZ signal adds an extra component to the background noise producing lower S/N estimates. This is particularly noticeable when the SZ signal is very strong compared with background (typically $S/N \geq 15$).

Despite the differences in background estimates, the yields from the three algorithms agree. In the left panel of Fig. 7, we show that the detection counts as a function of S/N for each detection method are in good overall agreement. The right panel of Fig. 7 shows the fraction of common detections over the union of detections from all three algorithms as a function of S/N. Sources with $S/N > 8.5$ are detected by all three methods. However, we note that `PwS` number counts decrease more rapidly than `MMF` counts above $S/N = 15$. This reflects the behaviour of `PwS` in "*compatibility*" mode described above, which estimates a higher background than the `MMF` methods at high S/N. Figure 6 shows the comparison of the S/N estimates from all three methods. The agreement is good on average. The mean ratio (or the normalization at the pivot of the power-law relation) deviates from unity by less than 2% and at less than 3σ significance. Here again at high S/N values, we note the tendency for lower S/N in `PwS` as compared to `MMF` (Fig. 6), and indeed the slope of the power-law relation is smaller than unity ($\alpha = 0.94 \pm 0.01$ for `MMF3`).

2.3.2. Photometry

We now compare the best-fit Y values (from maximum likelihood and posterior probability) for the three detection algorithms. The comparison (Fig. 6, lower panels) shows a systematic bias with `PwS`, yielding slightly smaller values than `MMF`,

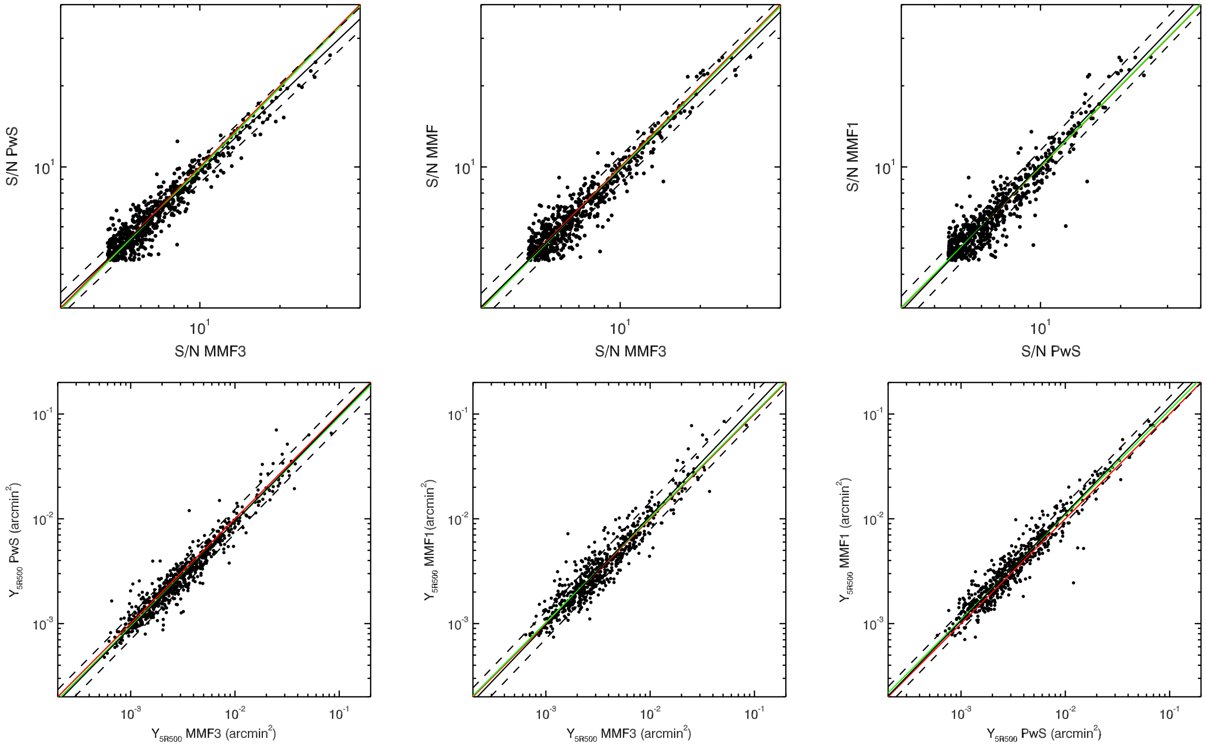

Fig. 6. Comparison of S/N (*top panels*) and maximum likelihood Compton-parameter values (*bottom panels*) from the three detection algorithms, `MMF`s and `PwS`, down to $S/N = 4.5$ after removing obvious false detections (see Sect. 2.3). In each panel, the red line denotes the equality line. The black line is the best fit to the data, and the dashed lines correspond to the $\pm 1\sigma$ dispersion about the fit relation. For clarity, error bars are omitted on $Y_{5R_{500}}$ values in the plot, but are taken into account in the fit. The green line of slope fixed to unity corresponds to the mean offset between the two quantities. Numerical results for the fits are given in Table 1.

Table 1. Parameters of the fitted lines in Fig. 6.

Quantity and Algorithms	Power-law				Offset		
	A	α	$\sigma_{\rm int}^{\rm log}$	$\sigma_{\rm raw}^{\rm log}$	$\Delta\log Q$	$\sigma_{\rm int}^{\rm log}$	$\sigma_{\rm raw}^{\rm log}$
S/N							
`MMF3-PwS`	-0.003 ± 0.002	0.94 ± 0.01	0.043 ± 0.002	. . .	-0.006 ± 0.002	0.045 ± 0.002	. . .
`MMF3-MMF1`	-0.005 ± 0.002	0.97 ± 0.01	0.050 ± 0.002	. . .	-0.006 ± 0.002	0.051 ± 0.002	. . .
`PwS-MMF1`	-0.000 ± 0.002	1.04 ± 0.02	0.054 ± 0.003	. . .	$+0.002 \pm 0.002$	0.054 ± 0.002	. . .
$Y_{5R_{500}}$							
`MMF3-PwS`	-0.030 ± 0.004	1.01 ± 0.01	0.08 ± 0.03	0.116 ± 0.018	-0.027 ± 0.004	0.065 ± 0.006	0.102
`MMF3-MMF1`	$+0.011 \pm 0.005$	1.04 ± 0.02	0.11 ± 0.02	0.131 ± 0.014	$+0.010 \pm 0.005$	0.085 ± 0.006	0.118
`PwS-MMF1`	$+0.041 \pm 0.004$	1.02 ± 0.01	0.04 ± 0.01	0.088 ± 0.005	$+0.038 \pm 0.004$	0.040 ± 0.007	0.079

Notes. The function $Q_2/Q_{\rm p} = 10^A\,(Q_1/Q_{\rm p})^\alpha$ is fitted using BCES orthogonal regression, with pivot $Q_{\rm p} = 6$ for S/N and $Q_{\rm p} = 4 \times 10^{-3}$ arcmin^2 for $Y_{5R_{500}}$. The intrinsic and raw scatter (see text) around the fit are given by $\sigma_{\rm int}^{\rm log}$ and $\sigma_{\rm raw}^{\rm log}$. The mean offset is given by $\Delta\log Q = \log(Q_2/Q_1)$.

typically by 10%. However, the slope is consistent with unity, showing that this bias is not flux dependent. The `MMF` values differ from each other by less than 3% on average. The scatter between Y estimates is dominated by the intrinsic scatter (Table 1). It is clearly related to the size-flux degeneracy, the ratio between Y estimates for a given candidate being correlated with the size estimate ratio, as illustrated by Fig. 8. The scatter becomes compatible with the statistical scatter when a prior on the size is used, e.g., size fixed to the X-ray size.

2.4. Definition of the Planck SZ catalogue

As discussed above, the processing details of each algorithm/implementation differ in the computation of the background noise. The significance of the detections in terms of S/N, although in overall agreement, differs from one algorithm to the other and translates into different yields for the candidate lists from the three algorithms. We choose to construct a catalogue of SZ candidates that ensures, through redundant detections, an

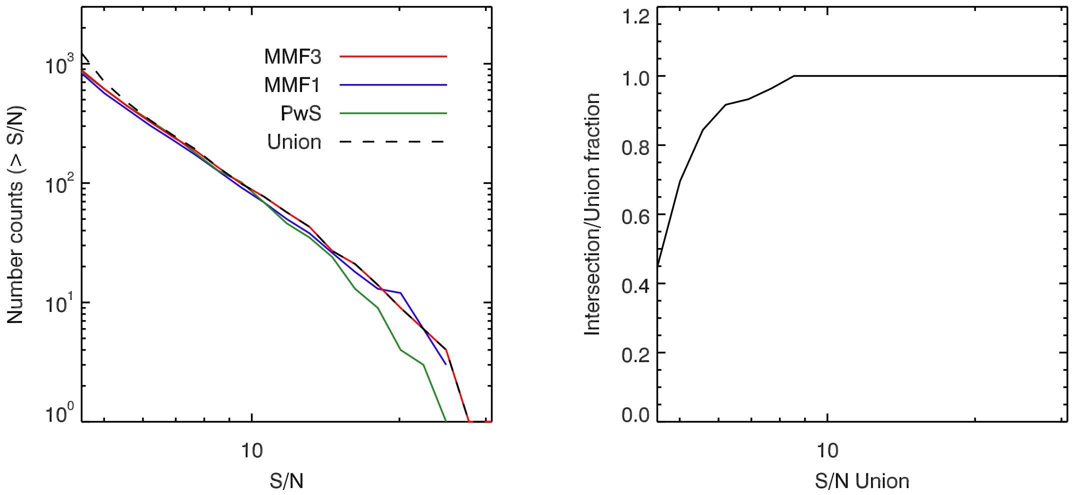

Fig. 7. *Left*: detection number counts as a function of S/N of the individual algorithms. The S/N value in the union catalogue is that of the `MMF3` detections when available, followed by that of `PwS` followed by `MMF1` (see Sect. 2.4). See text for discussion on the lower S/N values of `PwS` compared to the `MMF`-based algorithms. *Right*: fraction of common detection over counts from the union catalogue. Sources with $S/N > 8.5$ are detected by all methods.

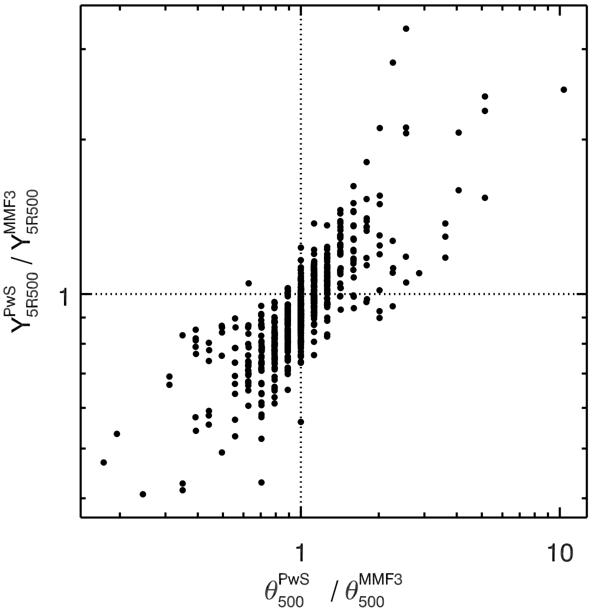

Fig. 8. Correlation between the ratio of $Y_{5R_{500}}$ estimates with `PwS` and `MMF3` and the ratio of size estimates, shown on a grid of sizes.

increased reliability of the low S/N sources, when they are detected by two methods at least, together with maximizing the yield of the catalogue.

The *Planck* SZ cluster catalogue described in the following is thus constructed from the union of the cleaned SZ-candidate lists produced at $S/N \geq 4.5$ by all three algorithms. It contains in total 1227 SZ detections above $S/N = 4.5$. Note that in order to ensure homogeneity, in terms of detection significance, the S/N values of `PwS` quoted in the union catalogue are obtained in *compatibility* mode, whereas the S/N obtained from `PwS` *native* mode are quoted in the `PwS` individual list. The union catalogue is constructed by merging detections from the three methods within an angular separation of at most 5′, in agreement with *Planck* position accuracy shown later in Fig. 12. As mentioned, no reference photometry is provided. However a reference position for the SZ detection is needed. For compatibility with the ESZ *Planck* sample, in the case of matching detection between methods we arbitrarily choose to take the coordinates from the `MMF3` detection as the fiducial position (`MMF3` was the reference method used to construct the ESZ *Planck* sample). When no detection by `MMF3` above $S/N = 4.5$ is reported, we took the `PwS` coordinates as fiducial, and the `MMF1` coordinates elsewhere. The S/N values in the union catalogue are taken following the same order, which explains why the `MMF3` curve in Fig. 6 coincides with the union curve. The cluster candidates in the union catalogue are cross-referenced with the detections in the individual lists. The reference positions and the S/N values are reported in the union catalogue. Given the size-flux degeneracy, the full information on the degeneracy between size and flux is provided with each individual list in the form of the two-dimensional marginal probability distribution for each cluster candidate as discussed above. It is specified on a grid of 256×256 values in θ_s and $Y_{5R_{500}}$ centred at the best-fit values found by each algorithm for each SZ detection.

An extract of the *Planck* SZ catalogue is given in Appendix B. The full online table for union *Planck* catalogue, the individual lists of SZ detections, and the union mask used by the SZ-finder algorithms together with comments assembled in an external file are available at ESA's *Planck* Legacy Archive (PLA)[4].

3. Statistical characterization

The statistical characterization of the PSZ catalogue is achieved through a process of Monte-Carlo quality assessment (MCQA) that can be applied to each individual catalogue and to the merged union catalogues. The statistical quantities produced include completeness, fraction of detections associated with true

---

[4] `http://www.sciops.esa.int/index.php?page=Planck_Legacy_Archive\&project=planck`.

Table 2. Characteristics of the catalogues.

Catalogue	Reliability[%]	Y_{500} [10^{-3} arcmin^2] $C = 50\%$	$C = 80\%$	$C = 95\%$	Position error
Union	84	0.61	1.2	3.2	1.′2
Intersection	98	0.85	1.8	6.6	1.′1
`MMF1`	87	0.75	1.6	4.7	1.′2
`MMF3`	91	0.71	1.5	3.8	1.′2
`PwS`	92	0.65	1.4	3.2	0.′9

Notes. The union catalogue contains SZ detections found by at least one of the three extraction algorithms; the intersection catalogue contains detections found by all three. Y_{500} at a given completeness C is estimated by marginalizing over θ_{500}, weighting each (Y_{500}, θ_{500}) bin by the theoretically-expected cluster counts. Position error is the median angular separation between real and estimated positions.

clusters called, statistical reliability or purity, positional accuracy, and accuracy of parameter estimation. Together, these statistics describe the quality of detections in the catalogue. The quality of the parameter estimation, including astrometry (cluster position and extent), is determined through comparison with the parameters of the input clusters. The statistical characteristics of the different lists are summarized in Table 2.

3.1. MCQA pipeline and simulations

The MCQA pipeline contains a common segment producing simulated input catalogues and processed, source-injected maps, which are then fed into the detection pipeline. In summary, the pipeline steps per Monte-Carlo loop are:

1. creation of an input cluster catalogue;
2. injection of clusters into common simulated diffuse frequency maps, including beam convolution;
3. injection of multi-frequency point sources;
4. pre-processing of maps, including masking and filling point sources;
5. detection and construction of individual cluster-candidate catalogues;
6. construction of a union catalogue given merging criteria;
7. collation of input and output catalogues, producing detection truth-tables and catalogues of unmatched spurious detections[5].

To estimate the completeness, clusters are injected into the real data. In this case, steps 3 and 4 are skipped and each detection algorithm estimates noise statistics on the real data prior to injection in order to avoid artificially raising the S/N and biasing the completeness estimates. The pressure profiles of the injected clusters follow that described in Sect. 2.2.1. To account for the profile variation across the cluster population, the profile parameters are drawn from the covariance matrix of the 62 measured pressure profiles from Planck Collaboration Int. V (2013), ensuring that the injected profiles are consistent with measured dispersion and consistent, on average, with the extraction filter. The injected clusters are convolved with effective beams in each pixel including asymmetry computed following Mitra et al. (2011).

The simulated input cluster catalogues differ for statistical reliability and completeness determination. For completeness, clusters injected in real data are drawn from a uniform distribution in (Y_{500}, θ_{500}) so as to provide equal statistics in each completeness bin. To avoid an over-contamination of the signal, injected clusters are constrained to lie outside an exclusion radius of $5R_{500}$ around a cluster, either detected in the data or injected.

For the statistical reliability estimation of the input cluster distribution injected in simulations is such that cluster masses and redshifts are drawn from a Tinker et al. (2008) mass function and converted into the observable parameters (Y_{500}, θ_{500}) using the *Planck* ESZ Y_{500}–M_{500} scaling relation (Planck Collaboration X 2011). The simulated maps consist of CMB realizations, diffuse Galactic components and instrumental noise realizations, including realistic power spectra and inter-detector correlations, from the FFP6 simulations (Planck Collaboration XII 2014; Planck Collaboration 2013). Residual extragalactic point sources are included by injecting, mock-detecting, masking and filling realistic multi-frequency point sources using the same process as for the real data (see Sect. 2.1).

3.2. Completeness

The completeness is the probability that a cluster with given intrinsic parameters (Y_{500}, θ_{500}) is detected given a selection threshold (here in S/N).

If the Compton-Y estimates are subject to Gaussian errors, the probability of detection per cluster follows the error function and is parameterized by $\sigma_{Yi}(\theta_{500})$, the standard deviation of pixels in the multi-frequency matched-filtered maps for a given patch i at the scale θ_{500}, the *intrinsic* Compton Y_{500}, and the detection threshold q:

$$P\left(d|Y_{500}, \sigma_{Yi}(\theta_{500}), q\right) = \frac{1}{2}\left[1 + \mathrm{erf}\left(\frac{Y_{500} - q\sigma_{Yi}(\theta_{500})}{\sqrt{2}\sigma_{Yi}(\theta_{500})}\right)\right], \tag{3}$$

where $\mathrm{erf}(x) = (2/\pi)\int_0^x \exp\left(-t^2\right)\mathrm{d}t$ and d is the Boolean detection state.

The completeness of the catalogue, thresholded at S/N q, is expected to follow the integrated per-patch error function completeness

$$C(Y_{500}, \theta_{500}) = \sum_i f_{\mathrm{sky},i} P(d|Y_{500}, \sigma_{Yi}(\theta_{500}), q), \tag{4}$$

where $f_{\mathrm{sky},i}$ is the fraction of the unmasked sky in the patch i. The true completeness departs from this theoretical limit. This is due to the non-Gaussian nature of the noise dominated by the astrophysical, namely Galactic, contamination. This is also the case when the actual cluster pressure profile deviates from the GNFW used in the SZ-finder algorithms, or when the effective beams deviate from constant symmetric Gaussians, and also when the detection algorithm includes extra steps of rejection of spurious sources not formulated in Eq. (3). This is why an MCQA-based assessment of the completeness is essential to characterize the *Planck* detections.

---

[5] A cluster is considered to be matched if there is a detection within 5′ of its position.

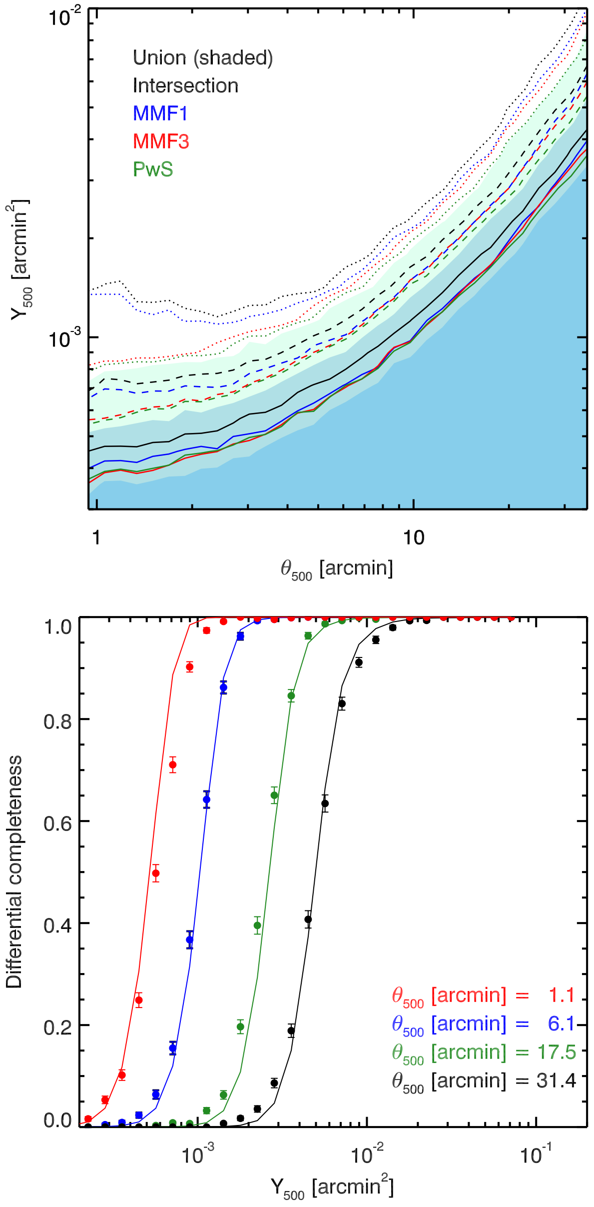

Fig. 9. *Top panel*: differential completeness as a function of (Y_{500}, θ_{500}) for each detection algorithm (`MMF1` in blue, `MMF3` in red, and `PwS` in green) and for the union (shaded area) and intersection (black) catalogues. From bottom to top, the solid, dashed, and dotted lines show 15%, 50% and 85% completeness, respectively. *Bottom panel*: slices through the MCQA-based completeness function at various θ_{500} for `MMF3` compared to the error function approximation (solid curves).

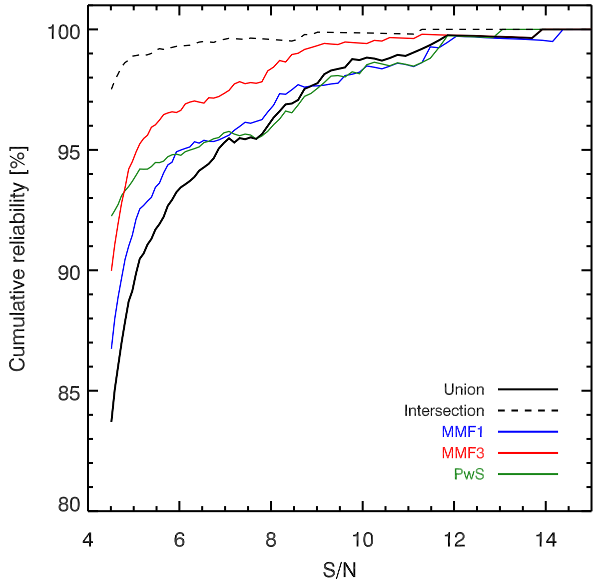

Fig. 10. Cumulative statistical reliability, defined as the fraction of sources above a given S/N associated with a "real" cluster from the simulated input catalogue.

The Monte-Carlo completeness of each of the individual lists and the union catalogue are shown in Fig. 9. The `MMF` lists are consistent with one another at $\theta_{500} > 4'$, but `MMF3` is more complete at lower radii. This is due to an extra step implemented in `MMF1` that rejects as spurious the detections estimated to be point-like. The union improves upon the completeness of each of the individual catalogues, because it includes the faint real detections by one method alone. In contrast, the intersection of the lists from the three algorithms, while more robust, is markedly less complete than the union and each of the individual catalogues. The intersection and union catalogues represent the extremes of the trade-off between statistical reliability and completeness. The quantities for each of the catalogues, plus the union and intersection, are summarized in Table 2. Figure 9 shows four constant θ_{500} slices through the completeness contours for `MMF3`, comparing the MCQA-based completeness with the integrated error function completeness. At radii smaller than 6′, the MCQA-based completeness is systematically less complete, and the drop-off of the completeness function shallower, than the theoretical expectation. This effect is a consequence of the variation of intrinsic cluster profiles from the GNFW profile assumed for extraction.

3.3. *Statistical reliability*

The fraction of detections above a given S/N that are associated with a real cluster is characterized by injecting clusters into high-fidelity simulations of the *Planck* channels. Unassociated detections from these simulations define the fraction of spurious detections. We have verified that the simulations produced detection noise $\sigma_{Y_{500}}$ consistent with the real data and that the simulated detection counts match the real data.

The cumulative fraction of true clusters, as characterized by the simulations, is shown for the output of each detection algorithm and for the union catalogue in Fig. 10. The union catalogue is less pure than any of the individual lists because it includes all the lower-reliability, individual-list detections, in addition to the more robust detections made by all three SZ-finder algorithms. The union catalogue constructed over 83.7% of the sky at S/N of 4.5 is 84% pure.

The fraction of false detections is dominated by systematic foreground signals, in particular Galactic dust emission. This is illustrated in Fig. 11 by the effect of dust contamination on the cumulative reliability. We define two sky regions by the level of dust contamination: "region 1" is the low dust-contamination region outside of the *Planck* Galactic dust,

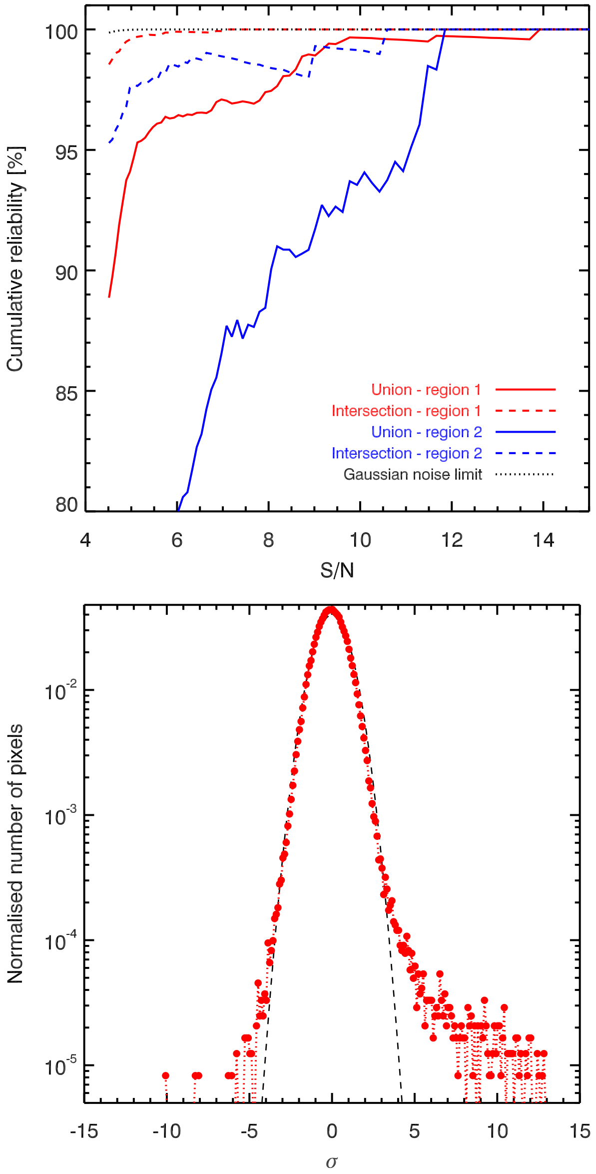

Fig. 11. *Top panel*: cumulative reliability for the union and intersection catalogues, as a function of dust contamination. Region 1 is the low-dust contamination region, being the 65% of the sky outside the Galactic dust mask, and region 2 is the complementary dustier region added to this when the smaller 15% dust mask is applied. The Gaussian noise limit is the expected reliability from purely Gaussian fluctuations. *Bottom panel*: histogram of the y-signal in a typical filtered patch from a null-test simulation, compared to the best-fit Gaussian (black dashed line). The distribution of y-noise is non-Gaussian.

and PS, mask that excludes 35% of the sky. This mask is used in Planck Collaboration XX (2014) for cosmological analysis of SZ counts. "Region 2" is the complementary region included by the smaller 15% dust mask but excluded by the 35% mask. When the larger Galactic dust mask is applied leaving 65% of the *Planck* sky survey in which to detect SZ signal, the statistical reliability increases from 84% in 83.7% of the sky to 88% in 65% of the sky. As seen in Fig. 11 upper panel, the reliability of the detections deteriorates markedly in "region 2" relative to "region 1". The noisy behaviour of the curves in Fig. 11 upper panel is due to the reduced size of sky area used in the analysis.

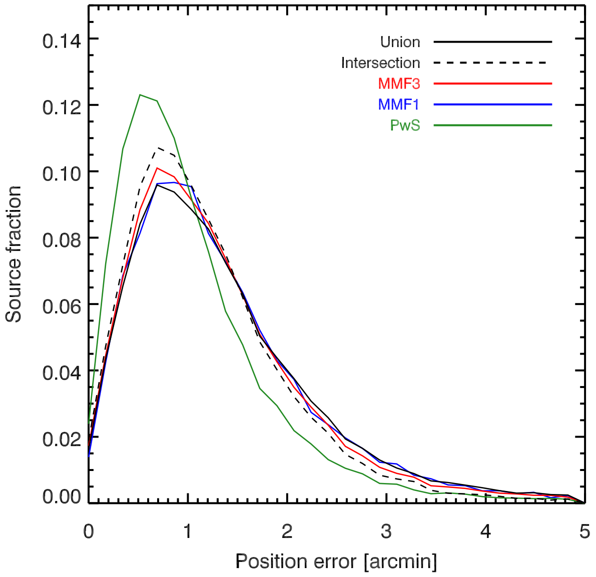

Fig. 12. Distributions of positional error for each catalogue, normalized by the total number of detections in the catalogue. By construction, the positional error is defined to be less than 5′.

In both regions, the spurious count much higher than is predicted by Gaussian fluctuations. This reflects the non-Gaussian nature of the filtered patches. The bottom panel of Fig. 11 illustrates this for a typical mid-latitude patch from a null-test simulation with no injected clusters. The patches are well approximated as Gaussian at deviations smaller than 3σ (consistent with the assumptions of Eq. (3)), but show enhanced numbers of high significance deviations, which can translate into spurious detections.

3.4. Positional accuracy

Positional accuracy is characterized by the radial offset between estimated and injected positions. The distribution of position error is shown in Fig. 12, for each individual list and the union catalogue. In contrast to the `MMF`s, which estimate the maximum-likelihood position, the `PwS` position estimator is the mean of the position posterior, which produces more accurate positional constraints. The union catalogue positions are taken from `MMF3` if available, followed by `PwS` and then `MMF1`. Its positional estimates are hence consistent with the `MMF`s. The mode of the union distribution is consistent with a characteristic position error scale of half an HFI map pixel (0.86′).

3.5. Parameter recovery

The Compton $Y_{5\mathrm{R}_{500}}$ is characterized by comparing detected and input values for matched detections from the injection of clusters into the real data (see Fig. 13). The injection follows the scheme outlined above with one exception: input cluster parameters are drawn using the Tinker mass function and the scaling relations discussed above for reliability simulations. This ensures a realistic distribution of parameters and S/N values.

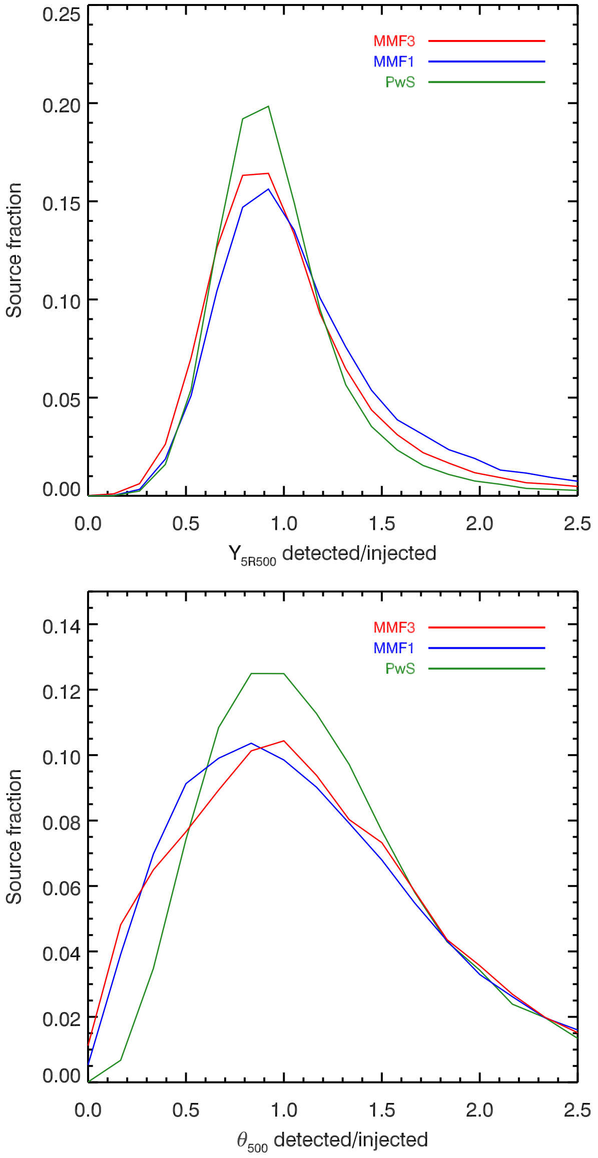

Fig. 13. Distributions of the ratio of detected over injected parameters for $Y_{5\mathrm{R}_{500}}$ and θ_{500}.

What we characterize is slightly different for each catalogue. For the `MMF`s, we characterize the maximum-likelihood point of the 2D degeneracy contours provided in the individual lists. For `PwS`, we characterize the mean of the marginal distribution for each parameter. In each case, the 2D $(Y_{5\mathrm{R}_{500}}, \theta_\mathrm{s})$ are marginalized over position. The contours are scaled for each cluster and are time consuming to compute, so we characterize the parameters from a lower-resolution grid that is better suited to Monte-Carlo analysis[6].

The scatter between input and detected parameters is shown in Fig. 14 as an example for `PwS`. Biases are evident at both the low and high end for $Y_{5\mathrm{R}_{500}}$. The low-flux bias is the Malmquist bias related to the $S/N \geq 4.5$ threshold. The high-flux bias is due to a hard prior on the upper limit for cluster radius. Figure 14 also shows the distribution of the ratio of estimated over injected parameters. The median and median absolute deviation of these ratios are shown in Table 3.

Table 3. Median and median absolute deviation (MAD) of the ratio of detected to injected parameters.

	$Y_{5\mathrm{R}_{500}}$		θ_s	
Catalogue	median	MAD	median	MAD
`MMF1`	1.09	0.39	1.17	0.70
`MMF3`	1.02	0.34	1.19	0.69
`PwS`	0.99	0.27	1.21	0.56

The distributions for flux are positively skewed due to Malmquist bias. The median ratios of the flux recoveries are consistent with unity for `MMF3` and `PwS` and are slightly higher for `MMF1`. The recovery of θ_s is biased high in the median by about 20% for each of the codes. This bias is a consequence of the intrinsic cluster profile variation and disappears when the injected profiles match the detection filter. The $Y_{5R_{500}}$ estimate by contrast is relatively unaffected by profile variation. The parameter constraints from `PwS` are tighter than the `MMF`s due to the `PwS` priors and the definition of the estimator as the expected value of the parameters rather than the maximum likelihood.

4. External validation

The cluster-candidate catalogue constructed from the union of all three SZ-finder algorithms undergoes a thorough validation process that permits us to identify previously-known clusters and to assess the reliability of the *Planck* SZ candidates not associated with known clusters. In order to achieve this, we make use of the existing cluster catalogues and we also search in optical, IR, and X-ray surveys for counter-parts at the position of the *Planck* SZ sources. In practice, we search within 5′ of the SZ position, in agreement with *Planck* position errors shown in Fig. 12. In Sect. 5, we present the follow-up programmes that were undertaken by the *Planck* collaboration in order to confirm and measure the redshifts of the *Planck* candidate new-clusters.

The first step of the validation of the PSZ catalogue is to identify among the *Planck* SZ candidates those associated with known clusters. For this purpose, we use existing X-ray, optical or SZ cluster catalogues. A positional matching is not sufficient to decide on the association of a *Planck* SZ source with a previously-known cluster, and a consolidation of the association is needed. For the X-ray associations, a mass proxy can be built and used to estimate the SZ flux, S/N, etc., that are compared with measured quantities for the *Planck* cluster candidates. In contrast to the X-ray clusters, optical clusters either have no reliable mass estimates or suffer from large uncertainties in the mass-richness relations. In this case, the consolidation cannot be performed uniquely through the coherence of measured versus predicted properties. It rather relies on extra information from surveys in the X-ray, optical, or IR at the *Planck* cluster-candidate positions.

In the following, we detail the search for counter-parts in optical, IR, and X-ray surveys; list the cluster catalogues used for the identification; and finally present the identification procedure followed to associate *Planck* SZ detections with bona fide clusters. In this process, we define quality flags for the association of *Planck* SZ detections with external data. We set $Q = 1$ for high-reliability associations, i.e., very clear cluster signatures, $Q = 2$

---

[6] `PwS` does not resort to a low-resolution scale grid and always works at the full resolution.

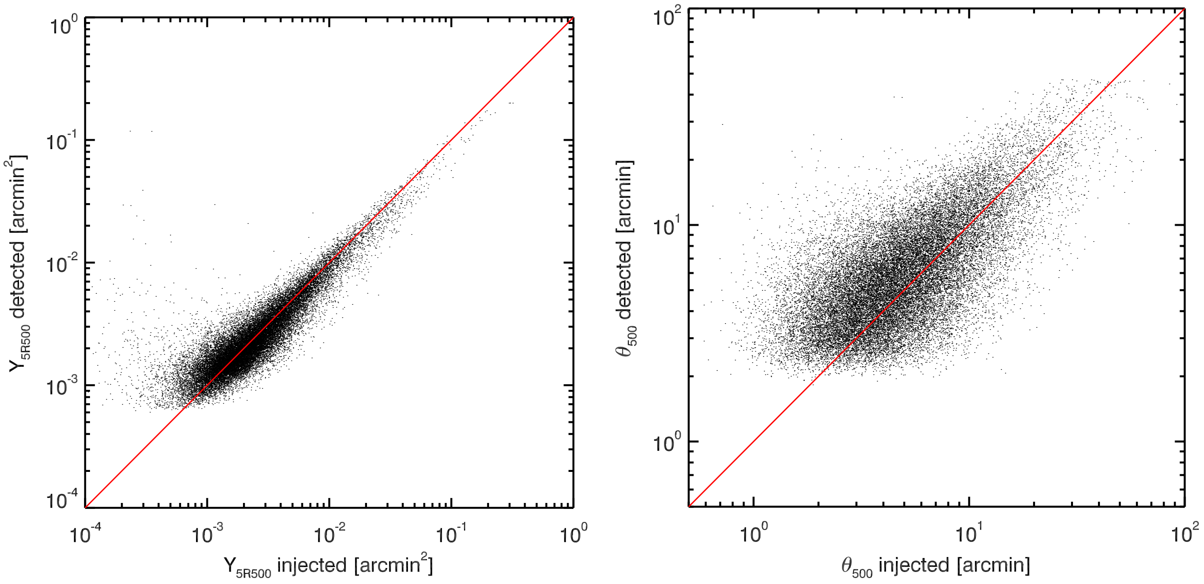

Fig. 14. Injected versus detected values of $Y_{5R_{500}}$ (*left panel*) and θ_{500} (*right-panel*), illustrated for `PwS`.

for reliable associations, and $Q = 3$ for low-reliability associations, i.e., unclear cluster signature.

4.1. Search for counter-parts of Planck detections in surveys

We made use of the ROSAT All Sky Survey (RASS, Voges et al. 1999), the all-sky survey with the Wide-field Infrared Survey Explorer (WISE, Wright et al. 2010), and the Sloan Digital Sky Survey (SDSS, York et al. 2000) to search for counter-parts of the *Planck* SZ detections. This information was used in two ways. When *Planck* detections were associated with known clusters from catalogues, in particular in the optical, the counter-parts in RASS, WISE, or SDSS helped in consolidating the association, increasing the confidence in the identification of *Planck* candidates with known clusters. When no association between *Planck* detections and previously-known clusters was found, the information on the counter-parts, in the surveys, of *Planck* SZ detections was used to assess the reliability of the *Planck* cluster candidates, i.e., clear or unclear cluster signatures.

4.1.1. Search in RASS data

As detailed in Planck Collaboration Int. IV (2013), the validation follow-up with *XMM-Newton* has shown the importance of the RASS data to assess the reliability of the *Planck* sources. In particular, Planck Collaboration Int. IV (2013) showed that a large fraction of *Planck* clusters are detectable in RASS maps, but this depends on the region of the sky and on the ratio Y_{500}/S_X which exhibits a large scatter (see later in Fig. 31 the case of the PSZ sources). We therefore exploit the RASS data to consolidate the identification with clusters from optical catalogues (see below Sect. 4.3.2) and to assess the reliability of the *Planck* SZ candidates.

We first perform a cross-match with the RASS bright source catalogue (BSC, Voges et al. 1999) and the faint source catalogue (FSC, Voges et al. 2000) within a 5′ radius of the position of each of the *Planck* SZ detections. We then perform a reanalysis of the RASS data following the methodology and prescriptions given by Böhringer et al. (2000, 2004) and Reiprich & Böhringer (2002). We compute count-rate growth curves in order to check for the extension of the signal. We estimate the source flux from both the growth curve (when adequate) and from a fixed 5′ aperture radius with respect to the surrounding background (after PS subtraction). We then derive the associated S/N in RASS, $(\mathrm{S/N})_{\mathrm{RASS}}$. For this, we make use of the RASS hard-band, [0.5–2] keV, data that maximize the S/N of the detections. We furthermore computed the source density map of the BSC and FSC catalogues and the associated probability that a *Planck* cluster candidate will be associated with a B/FSC source within a radius of 5′. For the BSC, the probability of chance association is relatively low, with a median <1%. As detailed in Planck Collaboration Int. IV (2013), the correspondence of a *Planck* SZ-candidate with a RASS-BSC source is a semi-certain association with a real cluster, whereas for the FSC catalogue the probability of chance association is larger, 5.2%.

We define a quality flag, Q_{RASS}, for the association of *Planck* candidates with RASS counter-parts using both the S/N in RASS and the association with B/FSC sources. This is of particular importance for the *Planck* candidate new clusters. Based on the results from Planck Collaboration Int. IV (2013), the quality of the association with RASS counter-parts is high, $Q_{\mathrm{RASS}} = 1$, for *Planck* cluster candidates matching a RASS-BSC source or with $(S/N)_{\mathrm{RASS}} \geq 2$. We find a total of 887 out of 1227 *Planck* SZ detections in this category, with mean and median S/N of 7.4 and 5.8, respectively. The quality is poor, $Q_{\mathrm{RASS}} = 3$, for RASS counter-parts with $(S/N)_{\mathrm{RASS}} < 0.5$ in regions of reasonable depth (quantified by the probability of chance association with FSC sources being larger than 2.5% Planck Collaboration Int. IV 2013).

4.1.2. Search in SDSS data

We performed a systematic search for counter-parts in the SDSS Data Release DR9 (Ahn et al. 2012) at the position of all the *Planck* SZ detections. This was performed based on a cluster-finder algorithm developed by (Fromenteau et al., in prep.) to search for red galaxy over-densities in the SDSS galaxy catalogues.

For each associated counter-part within a 5′ circle centred at the position of the *Planck* SZ detection, a quality criterion is defined on the basis of a fit to the luminosity function and the associated mass limit, and on the number of galaxies within 5′, $N_{\rm gal}$, such that we have $Q_{\rm SDSS,dat} = 1$, i.e., high quality, for cases where $N_{\rm gal} \geq 40$ and for masses $M_{200} \geq 5.7 \times 10^{14}\, M_{\odot}$, $Q_{\rm SDSS,dat} = 2$, i.e., good quality, for $N_{\rm gal}$ between 40 and 20 for masses between $1.5\times10^{14}\, M_{\odot}$ and $5.7\times10^{14}\, M_{\odot}$, and $Q_{\rm SDSS,dat} =$ 3 otherwise.

The cluster-finder algorithm outputs the position of the counter-part (Brightest Cluster Galaxy (BCG) and barycentre) and the estimated photometric redshift. When spectroscopic data are available for the brightest selected galaxy a spectroscopic redshift is also reported. The outputs of the cluster-finder algorithm are compared to those obtained by (Li & White, in prep.) from different method based on the analysis of the full photometric-redshift probability distribution function (Cunha et al. 2009). In this approach, the position and redshift in the SDSS data that maximizes the S/N are considered as the best estimates for the counter-parts of the *Planck* SZ detections.

4.1.3. Search in WISE data

WISE provides an all-sky survey at 3.4, 4.6, 12, and 22 μm ($W1$, $W2$, $W3$, $W4$) with an angular resolution of 6.1 to 12.0 arcsec in the four bands.

We search for counter-parts of the *Planck* SZ detections in the WISE source catalogue in two ways. On the one hand, we run an adaptive matched filter cluster finder developed by (Aussel et al., in prep.), similar to the one described by Kepner et al. (1999), using the cluster members' luminosity function of Lin et al. (2012). The background counts were determined from the neighbouring square degree in the vicinity of the *Planck* cluster candidate, excluding regions of fifteen arcmin centred on candidate positions. On the other hand, we use a method developed by (Aghanim & Fromenteau, in prep.) based on a search for overdensities of bright ($W1 \leq 17$) and red ($W1$–$W2 > 0$) sources within a 5′ radius circle centred on the position of *Planck* detections with respect to a background computed in a 15′ radius area.

Aghanim & Fromenteau (in prep.) find that a good-quality association between a *Planck* SZ-detection and a counter-part overdensity in WISE data is reached when there are at least ten galaxies above 2σ in the 5′ search region, and when the corresponding fraction of galaxies is at least 30% of the total number of galaxies retained in the 15′ circle. Performing the search for counter-parts of an ensemble of random positions on the sky, we compute the purity of the detections, i.e., the probability of a *Planck* candidate having a real counter-part in the WISE data as opposed to a chance association. The quality criterion for the association between *Planck* detection and WISE overdensity is high, $Q_{\rm WISE} = 1$, for a purity larger than 90%. When it lies between 90% and 80% the association of *Planck* SZ-detections and WISE overdensities is assigned a lower quality criterion $Q_{\rm WISE} = 2$. We set the quality of the association to $Q_{\rm WISE} = 3$, bad, when the purity is below 80%. We find 856 *Planck* SZ detections with high or good quality counter-parts in WISE data, including 658 $Q_{\rm WISE} = 1$ detections.

4.1.4. DSS images

Finally for each *Planck* cluster candidate, the second Digitized Sky Survey[7] (DSS) database was queried for a field of 5′ × 5′ centred at the position of the *Planck* SZ detections in the r and ir bands. The DSS images were used for visual inspection[8]. Clusters and rich groups out to $z \simeq 0.3$ to 0.4 can easily be identified in these plates as an obvious concentration of galaxies. This qualitative information was thus used: (i) to consolidate some identifications of *Planck* SZ detections with previously-known clusters; (ii) to optimize our strategy for the follow-up observations of *Planck* candidates (see Sect. 5); and (iii) to qualitatively assess the reliability or significance of the *Planck* SZ detections.

4.2. Cluster catalogues

We now present the ensemble of catalogues that were used to identify the *Planck* SZ detections with previously-known clusters. In the case of the ROSAT- and SDSS-based catalogues, we have used homogenized quantities, see below, that allowed us to perform the identification with comparable association criteria, which ensures homogeneity in the output results.

MCXC meta-catalogue – For the association of *Planck* SZ candidates with previously-known X-ray clusters, we use the Meta-Catalogue of X-ray detected Clusters of galaxies (MCXC, Piffaretti et al. 2011, and reference therein) constructed from the publicly available ROSAT All Sky Survey-based and serendipitous cluster catalogues, as well as the *Einstein* Medium Sensitivity Survey. For each cluster in the MCXC several properties are available, including the X-ray coordinates, redshift, identifiers, and standardized luminosity, $L_{\rm X,500}$, measured within R_{500}. The MCXC compilation includes only clusters with available redshift information (thus X-ray luminosity) in the original catalogues. We updated the MCXC, considering the first release of the REFLEX-II survey (Chon & Böhringer 2012), the third public release of clusters from the MACS sample (Mann & Ebeling 2012), individual MACS cluster publications and a systematic search in NED and SIMBAD for spectroscopic redshift for clusters without this information in the ROSAT catalogues. This yields an ensemble of 1789 clusters with z and $L_{\rm X,500}$ values, adding 20 MACS clusters, 21 REFLEX-II clusters and 5 SGP clusters to the MCXC. For these clusters, the expected Compton-parameter, $Y_{500}^{L_{\rm X}}$, and size, $\theta_{500}^{L_{\rm X}}$, are estimated combining the M_{500}–$L_{\rm X,500}$ relation of Pratt et al. (2009) and the M_{500}–Y_{500} relation given by Arnaud et al. (2010). The expected S/N, $({\rm S/N})^{L_{\rm X}}$, is computed taking into account the noise within $\theta_{500}^{L_{\rm X}}$ at the cluster location. We furthermore supplement the updated MCXC with 74 clusters from ROSAT catalogues without redshift information and 43 unpublished MACS clusters observed by *XMM-Newton* or *Chandra*. For these 117 objects, only centroid positions are available. Finally, we considered the published catalogues from *XMM-Newton* serendipitous cluster surveys with available redshifts, the XCS catalogue (Mehrtens et al. 2012), the 2XMMi/SDSS catalogue (Takey et al. 2011) and the XDCP catalogue (Fassbender et al. 2011). However, these catalogues mostly extend the MCXC to lower masses and only two *Planck* candidates were found to be associated with these new clusters.

Optical-cluster catalogues – The identification of the *Planck* SZ candidates with clusters known in the optical is based on the Abell (Abell 1958) and the Zwicky (Zwicky et al. 1961) cluster catalogues. Furthermore, we have used four different catalogues of clusters based on the Sloan Digital Sky Survey (SDSS, York et al. 2000) data: (1) the MaxBCG catalogue (13 823 objects,

---

[7] http://stdatu.stsci.edu/dss/

[8] Images from the RASS, SDSS and WISE surveys at the position of the *Planck* SZ detections were also inspected.

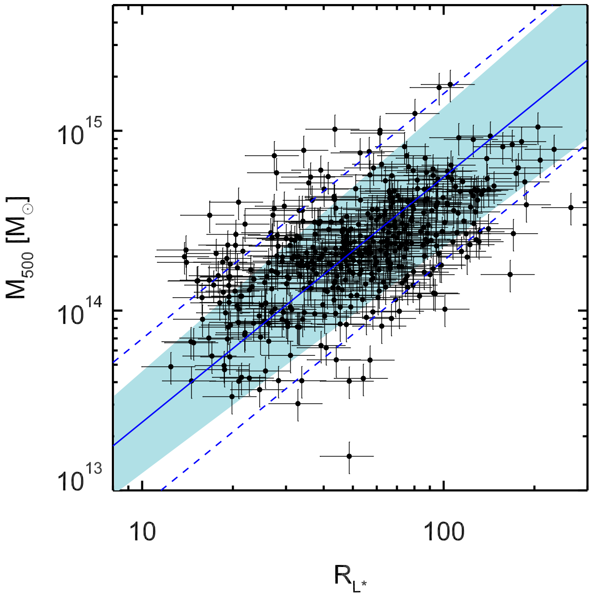

Fig. 15. Mass-to-richness scaling relation, M_{500}–$R_{L^\star}$, for the 444 MCXC clusters included in the WHL12 catalogue (Wen et al. 2012). The best-fit relation, from BCES fit, is given by the solid blue line. We adopted 15% uncertainties on the MCXC masses as prescribed in Piffaretti et al. (2011). As no uncertainty is provided for the WHL12's richness, we arbitrarily assumed a 20% uncertainty for all richness values. The blue shaded area shows the associated errors on the best-fit, while the dashed line marks the intrinsic scatter.

Koester et al. 2007); (2) the GMBCG catalogue (55 424 objects, Hao et al. 2010); (3) the AMF catalogue (69 173 objects, Szabo et al. 2011); and (4) the WHL12 catalogue (132 684 objects, Wen et al. 2012). We refer the reader to Wen et al. (2012) for a comparison of the existing SDSS-based catalogues of clusters and groups. Each of the SDSS-based catalogues provides an estimated richness; we first start by homogenizing the richness estimates to that of WHL12. For each catalogue, we compute the median ratio of WHL12's richness to that of the considered catalogue over its intersection with WHL12's. We then renormalize the individual richness by the corresponding ratio. The correcting factors applied to the richness estimators[9] are respectively 1.52, 1.75, and 0.74 for MaxBCG, GMBCG, and AMF, obtained from 7627, 17 245, and 1358 common clusters[10]. The richness is then related to the halo mass, M_{500}, by extending the Wen et al. (2012) richness–mass relation provided on about 40 clusters[11] to 444 MCXC clusters, with masses estimated from the X-ray luminosities. The data points and the best-fit scaling relation are presented in Fig. 15. The derived M_{500}–$R_{L^\star}$ and $L_{X,200}$–$R_{L^\star}$ relations are compatible with the findings of Wen et al. (2012). We find $\log(M_{500}/10^{14}\,M_\odot) = (-2.00 \pm 0.17) + (1.37 \pm 0.10) \times \log R_{L^\star}$. The relation presents a large intrinsic log-scatter, $\sigma_{\rm int} = 0.27 \pm 0.02$, hampering any accurate estimation of the cluster mass. This is further illustrated by the richest clusters with $R_{L^\star} > 110$ having MCXC masses systematically below the best-fit M_{200}–$R_{L^\star}$ relation (although within the 1σ intrinsic scatter).

SZ catalogues – At millimetre wavelengths, we cross-check the *Planck* SZ catalogue with the recent ACT and SPT samples (Menanteau et al. 2010; Vanderlinde et al. 2010; Williamson et al. 2011), including the most recent data that increased the number of SZ detections and updated the redshift estimates for the clusters (Reichardt et al. 2013; Hasselfield et al. 2013). We have furthermore identified the *Planck* SZ detections associated with previous SZ observations of galaxy clusters from the literature. We used a compilation of SZ observations conducted with the numerous experiments developed during the last 30 years (Ryle, OVRO, BIMA, MITO, Nobeyama, SZA, APEX-SZ, AMI, Diabolo, Suzie, Ryle, AMIBA, ACBAR, etc.).

4.3. Identification with previously-known clusters

4.3.1. Identification with X-ray clusters

The *Planck* SZ candidates are cross-checked against previously-known X-ray clusters from the updated version of the MCXC. For a given *Planck* candidate-cluster we identify the closest MCXC cluster[12]. The reliability of the association is assessed based on distance, D, compared to the cluster size and on the measured Y_{500} and S/N values compared with the expected values (see Fig. 16). Two clouds of points stand out in the scatter plot of absolute versus relative distance, $D/\theta_{500}^{L_X}$ (Fig. 16, left panel). They correspond to two clouds in the scatter plot of the measured over expected S/N versus $D/\theta_{500}^{L_X}$ (Fig. 16, middle panel).

The association process follows three main steps. First, we provisionally assign an X-ray identification flag based on distance:

- $Q_X = 3$ if $D > 2\theta_{500}^{L_X}$ and $D > 10'$. Those are considered as definitively not associated with an MCXC cluster in view of *Planck* positional accuracy and cluster extent.
- $Q_X = 1$ if $D < \theta_{500}^{L_X}$ and $D < 10'$. Those are associated with an MCXC cluster.
- $Q_X = 2$ otherwise, corresponding to uncertain associations.

We then refine the classification. In the $Q_X = 1$ category, we identify outliers in terms of the ratio of measured to expected S/N and Y_{500}, taking into account the scatter and the size–flux degeneracy. Their flags are changed to $Q_X = 2$. In some cases, two distinct $Q_X > 1$ candidates are associated with the same MCXC cluster. The lowest S/N detection is flagged as $Q_X = 2$.

In the final step, we consolidate the status of $Q_X < 3$ candidates. We first re-extract the SZ signal at the X-ray position, both leaving the size free and fixing it at the X-ray value. The Y_{500} obtained with the cluster and size fixed to the X-ray values are compared to the expected values, $Y_{500}^{L_X}$, in the right panel of Fig. 16. For bona fide association, we expect no major change of Y_{500} and S/N, with, on average, a better agreement with the expected Y_{500} value and some decrease of S/N.

- For $Q_X = 1$ candidates, the re-extracted Y_{500} and S/N values are compared to both blind and expected values (as a function of distance, S/N, etc.) to identify potential problematic

---

[9] Field NGALS_R200 for MaxBCG, GM_SCALED_NGALS for GMBCG and LAM200 for AMF.

[10] We considered the associations of clusters with positions matching within 6 arcsec radius and with $\Delta z \leq 0.05$ (typical uncertainty for photometric redshifts in SDSS).

[11] Their M_{200} are taken from the literature either from weak lensing or X-ray measurements (Wen et al. 2010).

[12] The information of the second closest is also kept to identify potential confusion or duplicate associations.

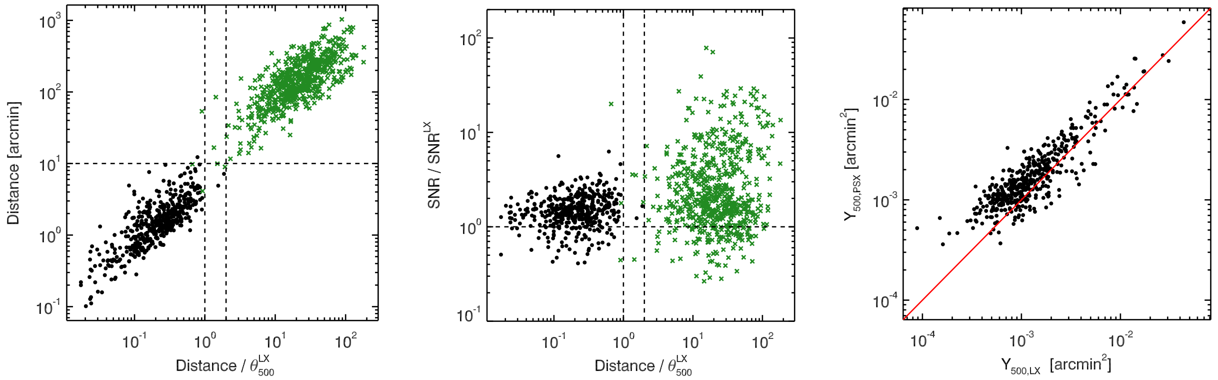

Fig. 16. Identification of the *Planck* cluster candidates with X-ray clusters from the MCXC catalogue. Black points are candidates firmly identified with MCXC clusters, while green points are candidates with no association. *Left panel*: distance of the *Planck* position to the position of the closest MCXC cluster as a function of the distance normalized to the cluster size θ_{500}^{LX}. *Middle panel*: S/N normalized to the expected value as a function of normalized distance. *Right panel*: SZ flux, $Y_{500,\mathrm{PSX}}$, re-extracted fixing the position and size to the X-ray value, as a function of expected values. The red line is the equality line. In all panels, Y_{500}^{LX}, and θ_{500}^{LX} are estimated from the cluster X-ray luminosity used as mass proxy (see text).

cases, e.g., important decrease of S/N or outliers in terms of measured-over-expected Y_{500} ratio. We found only one such case, whose flag is changed to $Q_{\mathrm{X}} = 2$. The identification of other candidates is considered as consolidated, with definitive flag $Q_{\mathrm{X}} = 1$.

- We then examine the $Q_{\mathrm{X}} = 2$ candidates. We consider the re-extracted Y_{500} and S/N, but also perform a visual inspection of the SZ maps and spectra and ancillary data, including RASS and DSS images. The $Q_{\mathrm{X}} = 2$ candidates were identified as clearly identified as multiple detections of extended clusters or duplicate detections of the same clusters by different methods that were not merged (the former are flagged as false detections, the latter are merged with the corresponding candidate in the union catalogue) or not associated (e.g., SZ sources clearly distinct from the MCXC clusters with no significant re-extracted signal at the cluster position and size).

Finally, for MCXC clusters without redshift and luminosity information, the association was only based on distance, setting $D_{\mathrm{X}} < 5'$, and the consolidated based on visual inspection of SZ, RASS and DSS images and other ancillary information. Two cases were found to be a mis-identification. The SZ candidate was closer by chance to a faint XCS cluster, in the vicinity of the real counter-part (another MCXC cluster and an Abell cluster, respectively).

4.3.2. Identification with optical clusters

The *Planck* SZ candidates are associated with known clusters from optical catalogues (Abell, Zwicky, SDSS-based catalogues) on the basis of distance with a positional matching within a search radius set to 5′. The consolidation of the association was performed using the RASS information as described below, which allows us to mitigate the chance associations with poor optical galaxy groups and clusters.

SDSS-based catalogues – We have considered the four catalogues listed in Sect. 4.2. We define a quality criterion for the association, Q_{SDSS}, in terms of cluster richness as a proxy of the cluster mass (see for instance Johnston et al. 2007; Rozo et al. 2009). We set the quality criterion, Q_{SDSS}, to 3 for low reliability (richness below 70), to 2 for good reliability (richness ranging from 70 to 110) and to 1 for high reliability (richness above 110).

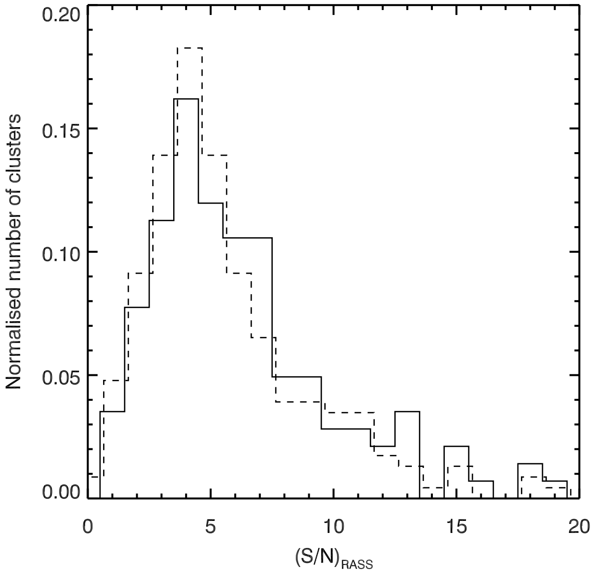

Fig. 17. Normalized distribution of the S/N in RASS at the position of *Planck* SZ detections with SDSS richness-based quality $Q_{\mathrm{SDSS}} = 1$ (solid line) and $Q_{\mathrm{SDSS}} = 2$ (dashed line).

The corresponding estimated masses (given the M_{500}–$R_{L\star}$ relation) are $M_{500} > 6.5 \times 10^{14}\,M_{\odot}$ and $M_{500} > 3.5 \times 10^{14}\,M_{\odot}$. However due to the large scatter and associated uncertainty in the mass estimate from the mass–richness relation, we consolidate the association of the *Planck* candidates with SDSS clusters by combining the Q_{SDSS} with the RASS signal at the *Planck*-candidate position (see Sect. 4.1.1). In practice, only associations with $Q_{\mathrm{SDSS}} = 1$ or 2 and a S/N, measured at the *Planck* position in an aperture of 5′ in the RASS survey, $(S/N)_{\mathrm{RASS}} \geq 1$ are retained as firm identifications. We stress that our choice of richness thresholds is relatively conservative on average. Indeed, our $Q_{\mathrm{SDSS}} = 1$ and 2 matched candidates are found with high $(S/N)_{\mathrm{RASS}}$ values as shown in Fig. 17, with mean $(S/N)_{\mathrm{RASS}} = 7.1$ and 6.6 and median $(S/N)_{\mathrm{RASS}} = 5.9$ and 5.4 for $Q_{\mathrm{SDSS}} = 1$ and 2 matches, respectively.

Table 4. Observing facilities used for the confirmation of clusters discovered by *Planck*, and for the measurement of their redshifts.

Site	Telescope	Aperture [m]	Instrument	Filters	Type of redshift
Earth orbit	*XMM-Newton*		EPIC/MOS, PN	. . .	Fe K
La Palma	NOT	2.56	ALFOSC	. . .	Spectroscopic
La Palma	INT	2.5	WFC	*griz*	Photometric
La Palma	GTC	10.4	OSIRIS	. . .	Spectroscopic
La Palma	TNG	3.5	DOLORES	. . .	Spectroscopic
La Palma	WHT	4.2	ACAM	*griz*	Photometric
La Silla	NTT	3.7	EFOSC2	. . .	Spectroscopic
La Silla	MPG/ESO-2.2 m	2.2	WFI	VRI	Photometric
MRAO	AMI	3.7,13	SA, LA	13.5–18 GHz	. . .
Tenerife	IAC80	0.82	CAMELOT	*griz*	Photometric
Tubitak Nat. Obs.	RTT150	1.5	TFOSC	*gri*	Spectroscopic

Abell and Zwicky catalogues – The *Planck* candidates are associated with Abell and Zwicky clusters on the basis of a positional matching within five arcmin. In the present case, we do not make use of any richness information in order to consolidate the association. We rather use here solely the RASS signal, $(S/N)_{\rm RASS}$, at the SZ-candidate position. *Planck*-candidates associated with Abell or Zwicky clusters and with $(S/N)_{\rm RASS} \geq 1$ are retained as firmly identified. For associations with $(S/N)_{\rm RASS} < 1$, we decided on a firm identification only after checking the status of the counter-part in the WISE data and performing a visual inspection of the SZ signal and of the images from ancillary data, including DSS images.

4.3.3. Identification with SZ clusters

The association with known SZ clusters was performed within a $5'$ radius. A visual inspection of the ancillary data and an a posteriori check of the RASS signal at the position of the *Planck* candidates associated with clusters from SZ catalogues is performed. It confirms that the values of $({\rm S/N})_{\rm RASS}$, when the coverage is significant, are high with an average value of 5.4.

4.3.4. Identifications from NED and SIMBAD

The information provided from querying NED and SIMBAD databases is mainly redundant with cross-checks with cluster catalogues. However, it lets us avoid missing a few associations. We therefore performed a systematic query in SIMBAD and NED with an adopted search radius set to $5'$. Similarly to the association with clusters in optical catalogues, the positional association is consolidated using the results of the search in RASS data. Furthermore, the *Planck*-candidates solely matching NED or SIMBAD entries were inspected and the identification was confirmed or discarded using the information from WISE counter-parts and the DSS images.

5. Follow-up programme for confirmation of *Planck* candidates

We have undertaken, since Spring 2010, an extensive follow-up programme in order to perform a cluster-by-cluster confirmation of the *Planck* cluster candidates and obtain a measurement of their redshifts. A total of 276 *Planck* candidates, selected down to $S/N = 4$ from intermediate versions of the *Planck* SZ catalogue, were observed in pursuit of their redshift measurement. We have constructed our strategy for the selection of the *Planck* targets primarily on the successful results of the series of follow-up observations in X-rays based on Director's discretionary time (DDT) on the *XMM-Newton* observatory (Planck Collaboration IX 2011; Planck Collaboration Int. I 2012; Planck Collaboration Int. IV 2013). Snapshot observations, sufficient to detect extended X-ray emission associated with *Planck* clusters and to estimate redshifts from the Fe line for the brightest clusters, were conducted sampling the SZ detections down to $S/N = 4$. These observations allowed us to better understand the SZ signal measured by *Planck* and hence to refine the criteria to select targets, especially for further optical follow-up.

We have engaged numerous campaigns on optical facilities, which now constitute our main means of confirmation of *Planck* SZ detections. *Planck* candidates with low-quality DSS images or without SDSS information, or low $({\rm S/N})_{\rm RASS}$, were primarily sent for deeper multi-band imaging observations. They were followed-up to the depth needed for the confirmation, i.e., finding an optical counter-part, and for the determination of a photometric redshift. Candidates with galaxy concentrations in DSS or with counter-parts in SDSS, and/or with high $({\rm S/N})_{\rm RASS}$, were preferentially sent for spectroscopic confirmation. The priority being to confirm the clusters and to secure the largest number of robust redshifts, no systematic spectroscopic confirmation of photometric redshifts was performed for low-redshift clusters ($z_{\rm phot} < 0.4$). For higher-redshift clusters, spectroscopic confirmation of the photometric redshifts is more crucial. As a result, we have made use of telescopes of different sizes, from 1-m to 10-m class telescopes, optimizing the selection of targets sent to the different observatories (Table 4 gives the list of the main telescopes). Telescopes of 8- and 10-m classes, e.g., GTC, GEMINI and VLT, were used to spectroscopically confirm redshifts above 0.5 for already confirmed clusters.

Our efforts to confirm the *Planck* cluster candidates, measure redshifts, and characterize cluster physical properties relies on ongoing follow-up of a large number of cluster candidates in the optical (ENO, RTT150, WFI), in the infrared (*Spitzer*[13]) and at SZ wavelengths (Arcminute Microkelvin Imager, AMI). The output of the confirmation and redshift measurements from the observing campaigns is summarized in Sect. 6.2. Companion publications, in preparation, will detail the observing campaigns and their results.

5.1. *XMM-Newton* observatory

The X-ray validation follow-up programme of 500 ks observations undertaken in *XMM-Newton* DDT is detailed in Planck Collaboration IX (2011), Planck Collaboration Int. I (2012),

---

[13] Under *Spitzer* programs 80162 and 90233.

and Planck Collaboration Int. IV (2013). It consisted of observing 51 *Planck* targets and led to the confirmation of 43 *Planck* cluster candidates, two triple systems and four double systems. There were eight false candidates. This follow-up programme has constituted the backbone of the *Planck* cluster confirmation and most importantly has allowed us to better understand the SZ signal measured by *Planck* and thus to better master the criteria for confirmation (or pre-confirmation) of the *Planck* cluster candidates. By providing us with the physical properties and redshift estimates of the confirmed clusters, it has furthermore given us a first view on the physical characteristics of the newly discovered *Planck* clusters. Snapshot observations (around 10 ks) of the *Planck* candidates took place between May 2010 and October 2011. All the results from the four observing campaigns were published in Planck Collaboration IX (2011), Planck Collaboration Int. I (2012), and Planck Collaboration Int. IV (2013). Calibrated event lists were produced with v11.0 of *XMM-Newton*-SAS, and used to derive redshifts and global physical parameters for the confirmed clusters (Planck Collaboration IX 2011). The redshifts were estimated by fitting an absorbed redshifted thermal plasma model to the spectrum extracted within a circular region corresponding to the maximum X-ray detection significance. Most of the redshifts were confirmed using optical observations. Additional observations at VLT were conducted to confirm spectroscopically the highest redshifts[14].

5.2. Optical observation in the northern hemisphere

5.2.1. ENO telescopes

In total 64 cluster candidates from *Planck* were observed at European Northern Observatory (ENO[15]) telescopes, both for imaging (at IAC80, INT and WHT) and spectroscopy (at NOT, GTC, INT and TNG), between June 2010 and January 2013[16]. The aims of these observations were the confirmation, photometric redshift measurement, and spectroscopic confirmation of redshifts above $z = 0.3$.

INT, WHT and IAC80 – The optical imaging observations were taken either with the Wide-Field Camera (WFC) on the 2.5-m *Isaac Newton* Telescope (INT), the auxiliary-port camera (ACAM) at the 4.2-m *William-Herschel* Telescope (WHT), or with CAMELOT, the optical camera at the 0.82-m telescope (IAC80). The targets were observed in the Sloan *gri* filters. For the majority of fields, either Sloan z or Gunn Z images are also available. Images were reduced using the publicly-available software IRAF and SExtractor (Bertin & Arnouts 1996). The data reduction included all standard steps, i.e., bias and flat field corrections, astrometric and photometric calibrations. The photometric calibration is based either on standard star observations or, if available, on data from the SDSS. Finally, all magnitudes were corrected for interstellar extinction, based on the dust maps by Schlegel et al. (1998). We obtained photometric redshifts using the BPZ code (Benítez 2000), using a prior based on SDSS data, and fitting a set of galaxy templates. The BPZ code provides the Bayesian posterior probability distribution function for the redshift of each object, which is later used in the process of cluster identification. The identification of the galaxy overdensity located near the *Planck* positions and the estimate of the photometric redshifts of the associated clusters were performed using a modified version of the cluster-algorithm described in Sect. 4.1.2.

GTC and TNG – Spectroscopic observations were performed using the 10-m Gran Telescopio Canarias (GTC) telescope and the 3.6-m Telescopio Nazionale *Galileo* (TNG) telescope. The OSIRIS spectrograph at GTC was used in long-slit mode to observe a total of eight targets with two slit positions per candidate. We used the R500R grism and a binning 2 × 1, which provides a resolution $R = 300$ with a slit width 1 arcsec, and a wavelength coverage 4800–10 000 Å. We retrieved three exposures of 1200 s each. The final spectra present a S/N of about 20 in galaxies with $r' = 20$ mag. We used the DOLORES multi-object spectrograph (MOS) at TNG to observe 9 candidates. The masks were designed to contain more than 30 slitlets, 1.5 arcsec width, placed within an area about $6' \times 8'$ in order to cover the target field. We used the LR-B grism, which provides a dispersion of 2.7 Å/pixel, and a wavelength coverage between 4000 and 8000 Å. We carried out three acquisitions of 1800 s each and obtained spectra with $S/N \simeq 15$ in galaxies with $r' = 20$ mag using a total integration time of 5400 s.

Nordic Optical Telescope (NOT) – Spectroscopic redshift measurements were obtained using the Andalucia Faint Object Spectrograph and Camera (ALFOSC) at the NOT[17]. Most targets were observed in MOS mode, targeting typically ten to fifteen galaxies per ALFOSC field (covering $6.4' \times 6.4'$, with an image scale of 0.188 arcsec/pixel). One or two unfiltered 300 s pre-imaging exposures were obtained per candidate cluster, in addition to a single 300 s exposure in each of the SDSS g-and i bands. The de-biased and flat field calibrated pre-imaging data were used to select spectroscopy targets. The final mask design[18] was carved out using custom software, generating slits of fixed width 1.5 arcsec and of length typically 15 arcsec. Grism No. 5 of ALFOSC was used, covering a wavelength range 5000–10 250 Å with a resolution of about $R = 400$ and dispersion 3.1 Å/pixel. Redwards of 7200 Å strong fringing is present in the ALFOSC CCD. It was effectively suppressed using dither pattern alternating the placement of the spectroscopy targets between these sets of slits.

In addition to the MOS observations, spectroscopic observations in single-slit mode were conducted for some *Planck* candidates. For these observations, a long slit covering the entire $6.4'$ length of the ALFOSC field and a width of 1.3 arcsec was employed, with the same grism and wavelength coverage as for the MOS observations. The field angle was rotated to place the long slit over multiple targets, to include the apparent BCG as well as two to three other bright cluster galaxies within the ALFOSC field.

5.2.2. RTT150

A total of 88 *Planck* cluster candidates were followed up with the Russian Turkish Telescope (RTT150[19]) from July 2011

---

[14] Observations are conducted under programme 090A-0925.

[15] ENO: `http://www.iac.es/eno.php?lang=en`

[16] The observations were obtained as part of proposals for the Spanish CAT time (semesters 2010A, 2010B, 2011A, 2011B, 2012A and 2012B), and an *International Time Programme (ITP)*, accepted by the International Scientific Committee of the Roque de los Muchachos (ORM, La Palma) and Teide (OT, Tenerife) observatories (reference ITP12_2).

[17] The observing runs took place on June 28–July 3, 2011, January 20–25, 2012, July 16–21, 2012 and January 9–14, 2013.

[18] The MOS masks were cut at the Niels Bohr Institute, Copenhagen University.

[19] `http://hea.iki.rssi.ru/rtt150/en/index.php`

to December 2012 within the Russian quota of observational time. In total, about 50 dark nights, provided by Kazan Federal University and Space Research Institute (IKI, Moscow), were used for these observations. Direct images and spectroscopic redshift measurements were obtained using TÜBİTAK Faint Object Spectrograph and Camera (TFOSC[20]), similar in layout to ALFOSC at NOT (see above) and to other instruments of this series.

The TFOSC CCD detector cover a $13.3' \times 13.3'$ area with 0.39 arcsec per pixel image scale. Direct images of cluster candidates were obtained in Sloan *gri* filters, in series of 600 s exposures with small (≈10–30 arcsec) shifts of the telescope pointing direction between the exposures. All standard CCD calibrations were applied using IRAF software, individual images in each filter were then aligned and combined. The total of 1800 s exposure time in each filter was typically obtained for each field, longer exposures were used for more distant cluster candidates. Deep multi-filter observations were obtained for all candidates, except those unambiguously detected in SDSS. With these data, galaxy clusters can be efficiently identified at redshifts up to $z \approx 1$.

Galaxy clusters were identified as enhancements of surface number density of galaxies with similar colours. Cluster red sequences were then identified in the colour–magnitude diagram of galaxies near the optical centre of the identified cluster. The detected red sequence was used to identify the BCG and cluster member galaxies. Using the measured red-sequence colour photometric redshift estimates were obtained, which were initially calibrated using the data on optical photometry for galaxy clusters from the 400SD X-ray galaxy cluster survey (Burenin et al. 2007).

For spectroscopy we used the long-slit mode of the instrument with grism No. 15, which covers the 3900–9100 Å wavelength range with ≈12 Å resolution when a slit of 1.8 arcsec width is used. Galaxy redshifts were measured through the cross-correlation of obtained spectra with a template spectrum of an elliptical galaxy. Spectroscopic redshifts were typically obtained for the spectra of a few member galaxies, including the BCG, selected from their red sequence in the imaging observations. These data allow us to efficiently measure spectroscopic redshifts for clusters up to $z \approx 0.4$. For the highest-redshift clusters, complementary spectroscopic observations were performed with the BTA 6-m telescope of SAO RAS using SCORPIO focal reducer and spectrometer (Afanasiev & Moiseev 2005).

5.3. Optical observation in the southern hemisphere

5.3.1. MPG/ESO 2.2-m Telescope

Optical imaging of 94 *Planck* cluster candidates in the southern hemisphere was performed under MPG programmes at the MPG/ESO 2.2-m telescope using the Wide-Field Imager (WFI)[21]. The WFI detector is a mosaic of 8 2k × 4k CCDs, covering a total area of $33' \times 34'$ on the sky, with an image scale of 0.238 arcsec/pixel. Each field was observed in the V-, R-, and I-bands with a default exposure time of 1800 s (with five dithered sub-exposures) per passband. The basic data calibration, including de-biasing and flat-field frame calibration, followed standard techniques. The individual exposures were re-registered and WCS calibrated using the USNO-B1 catalogue as an astrometric reference before being stacked into a combined frame for each filter, covering the entire WFI field. Photometric redshifts of the observed clusters were then determined from an algorithm that searches for a spatial galaxy overdensity located near the position of the SZ cluster candidate that also corresponds to an overdensity in $V - R$ versus $R - I$ colour–colour space. The median colour of galaxies located in this overdensity was then compared to predicted colours of early-type galaxies at different redshifts by convolving a redshifted elliptical galaxy spectral energy distribution template with the combined filter+telescope+detector response function.

5.3.2. New Technology Telescope (NTT)

Observations[22] were conducted at the 3.5-m NTT at the ESO observatory at La Silla to measure spectroscopic redshifts of 33 *Planck* clusters with the EFOSC2 instrument in the MOS mode. A clear BCG was identified in the clusters in pre-imaging data, and besides the BCG a redshift was measured for at least one other member of the cluster. In the following a brief outline of the observations and the data reduction are given (see Chon & Böhringer 2012, for details).

Each field of the *Planck* target candidates was optically imaged in Gunn r band for target selection and mask making. The imaging resolution is $0.12'' \times 0.12''$, and the field of view is $4.1' \times 4.1'$ for both imaging and spectroscopic observations. When necessary, the field was rotated to optimize target selection. We used the grism that covers the wavelength range between 4085 Å and 7520 Å, with 1.68 Å per pixel at resolution 13.65 Å per arcsec. We typically applied 10 to 15 slitlets per field with a fixed width of 1.5 arcsec for the MOS and of 2.0 arcsec for the long-slit observations. Including at least three bright objects, preferably stars, to orient the field, the slitlets were allocated to the candidate member galaxies. The exposure times for the clusters range from 3600 s to 10 800 s.

The data were reduced with the standard reduction pipeline of IRAF. The redshifts from the emission lines were determined separately after correlation with the passive galaxy templates. We use the `rvsao` package, which applies the cross-correlation technique to the input templates of galaxy spectra to measure the object redshift. The REFLEX templates were used for this analysis, which include 17 galaxy and stellar templates. We confirmed a spectroscopic cluster detection if at least three galaxies have their R-value greater than 5, and lie within $\pm 3000\,\mathrm{km\,s^{-1}}$ of the mean velocity of the cluster members. We then took the median of those galaxy redshifts as the cluster redshift. For the long-slit observations, the cluster was confirmed with the redshift of the BCG and another galaxy at similar redshift within the aforementioned criteria.

5.4. Observations in the SZ domain with AMI

An ensemble of 60 *Planck* blind SZ candidates, spanning a range of S/N between 4 and 9 and meeting the Arcminute Microkelvin Imager (AMI) observability criteria, was observed with AMI. The goal of this programme was to confirm *Planck* cluster candidates through higher-resolution SZ measurements with AMI and

---

[20] `http://hea.iki.rssi.ru/rtt150/en/index.php?page=tfosc`

[21] Based on observations under MPG programmes 086.A-9001, 087.A-9003, 088.A-9003, 089.A-9010, and 090.A-9010. The observations were conducted during the periods of November 27–December 3, 2010, March 8–19, May 21–June 3, and November 30–December 4, 2011, December 30, 2011–January 7, 2012, June 10–18, 2012, and January 6–13 2013.

[22] The observations were performed during three spectroscopic observing campaigns, 087.A-0740, 088.A-0268 and 089.A-0452.

Table 5. Numbers of previously-known clusters, new confirmed clusters, and new candidate SZ clusters.

Category	*N*		Catalogue, telescope, or reliability	
Previously known	683	472	X-ray:	MCXC meta-catalogue
		182	Optical:	Abell, Zwicky, SDSS catalogues
		16	SZ:	SPT, ACT
		13	Misc:	NED or SIMBAD
New confirmed	178		Follow-up, archival data, SDSS survey	
New candidate	366	54	High reliability	
		170	Medium reliability	
		142	Low reliability	
Total *Planck* SZ catalogue	**1227**			

Notes. Previously-known clusters can be found in the catalogues indicated. Confirmations from follow-up do not cover the observations performed by the *Planck* collaboration to measure the missing redshifts of known clusters. Confirmation from archival data covers X-ray data from *Chandra*, *XMM-Newton*, and ROSAT PSPC pointed observations only.

to refine the position of confirmed clusters in order to optimize the subsequent optical follow-up observations aiming at redshift measurement. AMI comprises of two arrays: the Small Array (SA); and the Large Array (LA). Further details of the instrument are given in AMI Consortium et al. (2008). Observations carried out with the SA provide information that is well coupled to the angular scales of the SZ effect in clusters, whereas snapshot observations obtained with the LA provide information on the discrete radio-source environment. The latter allowed us to detect the presence of nearby, bright radio sources, helping in further selecting the targets for observation with the SA. Details of the AMI data reduction pipeline and mapping are described in Planck and AMI Collaborations (2013).

6. Results of the validation and follow-up

The external validation allows us to identify *Planck* SZ detections with previously-known clusters and to assemble crucial information on the identified clusters such as their redshifts. The validation steps corresponding to the association with known clusters were performed following a chosen hierarchy: X-ray clusters from the updated MCXC meta-catalogue; then optical clusters from Abell and Zwicky catalogues; then optical clusters from the SDSS-based catalogues; followed by SZ clusters from SPT and ACT samples; and finally clusters from NED and SIMBAD queries. The first identifiers of the *Planck* SZ detections given in Table B.1 reflect the validation hierarchy.

In the following, we present the results of the external validation process and of the follow-up campaigns for confirmation of *Planck* candidates and measurement of their redshifts (see Table 5 and Fig. 18). We also present the confirmation from SDSS galaxy catalogues and from X-ray archival data. We further discuss the unconfirmed candidate new clusters detected by *Planck*, which we classify into three categories of different reliability.

6.1. *Planck* clusters associated with known clusters

A total of 683 out of 1227 SZ detections in the *Planck* catalogue, i.e., 55.7%, are associated with previously-known clusters from X-ray, optical, or SZ catalogues, or with clusters found in the NED or SIMBAD databases. We give the number of clusters identified in each category and we discuss notable cases of known clusters that are not included in the *Planck* SZ catalogue.

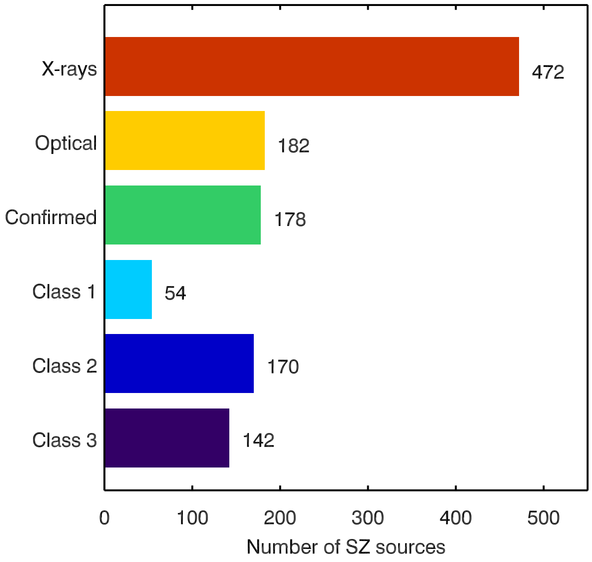

Fig. 18. Distribution of the *Planck* clusters and candidates in the different categories defined in the external validation process. The validation follows the order of association with MCXC clusters, then Abell and Zwicky clusters, then SDSS clusters, then SZ clusters, and finally clusters from NED/SIMBAD.

6.1.1. Identification with known X-ray clusters

A total of 472 *Planck* SZ-candidates are identified with known X-ray clusters from the MCXC meta-catalogue, which represents 38.5% of the *Planck* SZ detections and 69.1% of the identifications with previously-known clusters. These identifications of course account for many Abell clusters in the RASS-based catalogues of X-ray clusters.

Using the cluster properties reported in the MCXC and the *Planck* noise maps at the cluster positions, we computed the expected SZ signal and the expected S/N for a measurement with *Planck*. We have compared the number of detected clusters in the *Planck* catalogue with $S/N \geq 4.5$ to the number MCXC clusters at an expected significance of 4.5. Only 68 clusters expected to be detected at $S/N > 4.5$ are not included in the *Planck* catalogue, including 16 with predicted S/N between 4 and 4.5. Of the 52 clusters with expected $S/N \geq 4.5$, only 41 are outside the masked regions and could thus be in the PSZ catalogue. Our computation of the expected SZ signal and S/N were based on scaling relations for X-ray-selected clusters, not accounting for the dispersion in the relations. We therefore focus on the non-detected MCXC clusters that significantly depart from the expected S/N value, namely by more than 5σ. A total of 13 clusters are in this category. The two objects RXC J2251.7-3206 and RXC J0117.8-5455 show emission in high-resolution *Chandra* imaging that is point-like rather than extended and are likely not clusters of galaxies (Mantz et al. 2010; Magliocchetti & Brüggen 2007). Of the other eleven missing MCXC clusters, some present AGN contamination. This is the case for RXC J1326.2+1230 (Magliocchetti & Brüggen 2007), RX J1532.9+3021 (Hlavacek-Larrondo et al. 2012), RXC J1958.2-3011, RXC J2251.7-3206, and RXC J0117.8-5455 (Magliocchetti & Brüggen 2007), Abell 689 (Giles et al. 2012), ZwCl 2089 (Rawle et al. 2012), PKS 0943-76 (Abdo et al. 2010), and Abell 2318 (Crawford et al. 1999). In these cases, the presence of the AGN affects the X-ray luminosity measure leading to an overprediction of the SZ signal. Some exhibit significant radio contamination, e.g., RXC J1253.6-3931 (Plagge et al. 2010) and RXC J1958.2-3011 (Magliocchetti & Brüggen 2007), which hampers the SZ detection. Cool-core clusters for which the X-ray luminosity is boosted due to the central density peak have an over-estimated expected SZ signal. This is the case for RXC J0425.8-0833 (Hudson et al. 2010), ZwCl 2701 (Rawle et al. 2012), Abell 1361 (Rafferty et al. 2008), and RBS 0540 (Eckert et al. 2011; Belsole et al. 2005). Other "missing" clusters are CIZA clusters: RXC J0643.4+4214, RXC J1925.3+3705, RXC J2042.1+2426 and RXC J0640.1-1253, REFLEX cluster RXC J2149.9-1859, APMCC 699, Abell 3995, Abell 2064 and RBS 171.

In addition to the clusters discussed above which are not included in the catalogue due to contamination by AGN or presence of cool-cores etc., we note that some notable nearby extended clusters are also not included in the *Planck* SZ catalogue. Indeed, the detection methods used to detect the SZ effect are not optimized for the detection of sources with scale radius θ_{500} in excess of 30′. Of the 25 clusters in this category (with $z < 0.03$) in the MCXC meta-catalogue, six are included in the *Planck* catalogue. The remaining 19 fall into the masked areas (seven out of 19, among which Perseus and Abell 1060 lie in the PS mask (Fig. 19, first two panels), and Ophiuchus and 3C 129.1 lie in the Galactic mask (Fig. 19, second two panels) and/or have a S/N below the PSZ catalogue threshold $S/N = 4.5$. This is the case of Virgo cluster (Fig. 19, lowest panel), which is detected in the *Planck* survey but with a S/N at its position of about 3.9. Virgo's extension on the sky ($\theta_{500} = 168$ arcmin) further hampers its blind detection.

We show in Fig. 19 the reconstructed SZ signal from the `MILCA` algorithm (Hurier et al. 2013) for five of the "missing" extended clusters. These clusters, despite not being part of the *Planck* catalogue of SZ sources, are well detected in the *Planck* survey. They all are included in the thermal SZ map constructed from the *Planck* channel maps and presented in Planck Collaboration XXI (2014).

6.1.2. Identification with known optical clusters

A total of 182 *Planck* SZ detections are identified exclusively with optical clusters from Abell and Zwicky catalogues, and from the SDSS-based published catalogues, i.e., 26.6% of the known clusters in the *Planck* catalogue.

The *Planck* SZ candidates at S/N ≥ 4.5 have 111 exclusive associations with Abell or Zwicky clusters, i.e., with clusters not in any of the catalogues compiled in the MCXC meta-catalogue. In addition to these associations, 72 *Planck* detections are solely identified with clusters from the SDSS-based catalogues. These are either rich and massive systems ($R_{L^\star}$ greater than 110, $Q_{\rm SDSS} = 1$ clusters) or moderately low-richness systems ($Q_{\rm SDSS} = 2$ clusters, exhibiting hot gas as indicated by their S/N value in the RASS survey). However, not all the rich $Q_{\rm SDSS} = 1$ clusters in SDSS-based catalogues are found in the *Planck* catalogue. A total of 213 $Q_{\rm SDSS} = 1$ clusters from all four SDSS-based catalogues (201 outside the *Planck* union PS and Galactic mask) are not included in the *Planck* catalogue.

We explore why these rich clusters are not detected blindly by the SZ-finder algorithms. We first compare the richness-based masses against the X-ray luminosity-based masses of 26 of these "missing" clusters found in the MCXC meta-catalogue. We find a median ratio of 2.6 ± 1.2 for the richness-to-X-ray based masses, indicating that the richness-based masses seem to be systematically overestimated. Unlike the X-ray clusters, we thus cannot compute a reliable estimate of the expected S/N value for SZ detection of these optical clusters. We therefore directly search for the SZ signal at the positions of the 201 "missing" SDSS-clusters and found that all of them have S/N values below the *Planck* threshold, with a mean S/N of 1.6, except for three clusters. Two of these three "missing" SDSS-clusters have their S/N value from the extraction at the cluster position slightly higher than 4.5. The increase in S/N value is due to the difference in estimated background noise when centring the extraction at the cluster position as opposed to the blind detection. The third missing rich cluster is affected by contamination from CMB anisotropy, which results in a bad estimate of its size and consequently of its SZ signal.

6.1.3. Identification with known SZ clusters

The majority of the SZ clusters, from SPT or ACT, used in the validation process are low-mass systems ($M_{500}^{\rm median}$ around $2.3 \times 10^{14}\,M_\odot$). *Planck* is particularly sensitive to massive rich clusters and thus only a total of 56 of these clusters match *Planck* SZ detections, out of which 16 candidates are exclusively associated with SZ clusters[23] from ACT or SPT. Nine more ACT and SPT clusters are associated with *Planck* SZ detections between $S/N = 4$ and 4.5. We have searched for the SZ signal in the *Planck* data at the position of the remaining non-observed ACT/SPT clusters by extracting the SZ signal at their positions. We found that all had S/N values lower than 4.

We have also checked the redundancy of SZ detections within *Planck* by comparing the ESZ sample, constructed from 10 months of survey with a cut at Galactic latitudes of ±14°, with the present *Planck* catalogue. Of the 189 high significance ($(S/N)_{\rm ESZ} \geq 6$ ESZ detections, 184 ESZ confirmed clusters are included the present *Planck* catalogue within a distance of 5′ from their ESZ position. The mean separation between the ESZ and present positions is of order 1.35′, within *Planck*'s positional accuracy. Their S/N values were increased by a factor 1.17 on average with respect to their $({\rm S/N})_{\rm ESZ}$, (Fig. 20) and only four out of six of the ESZ clusters have new S/N values significantly lower than ESZ S/N threshold $(S/N)_{\rm ESZ} = 6$. They are displayed as stars in Fig. 20. Four ESZ clusters are not included the present *Planck* catalogue, they

---

[23] Six *Planck* clusters were confirmed from *XMM-Newton* or NTT observations and are also published in Reichardt et al. (2013).

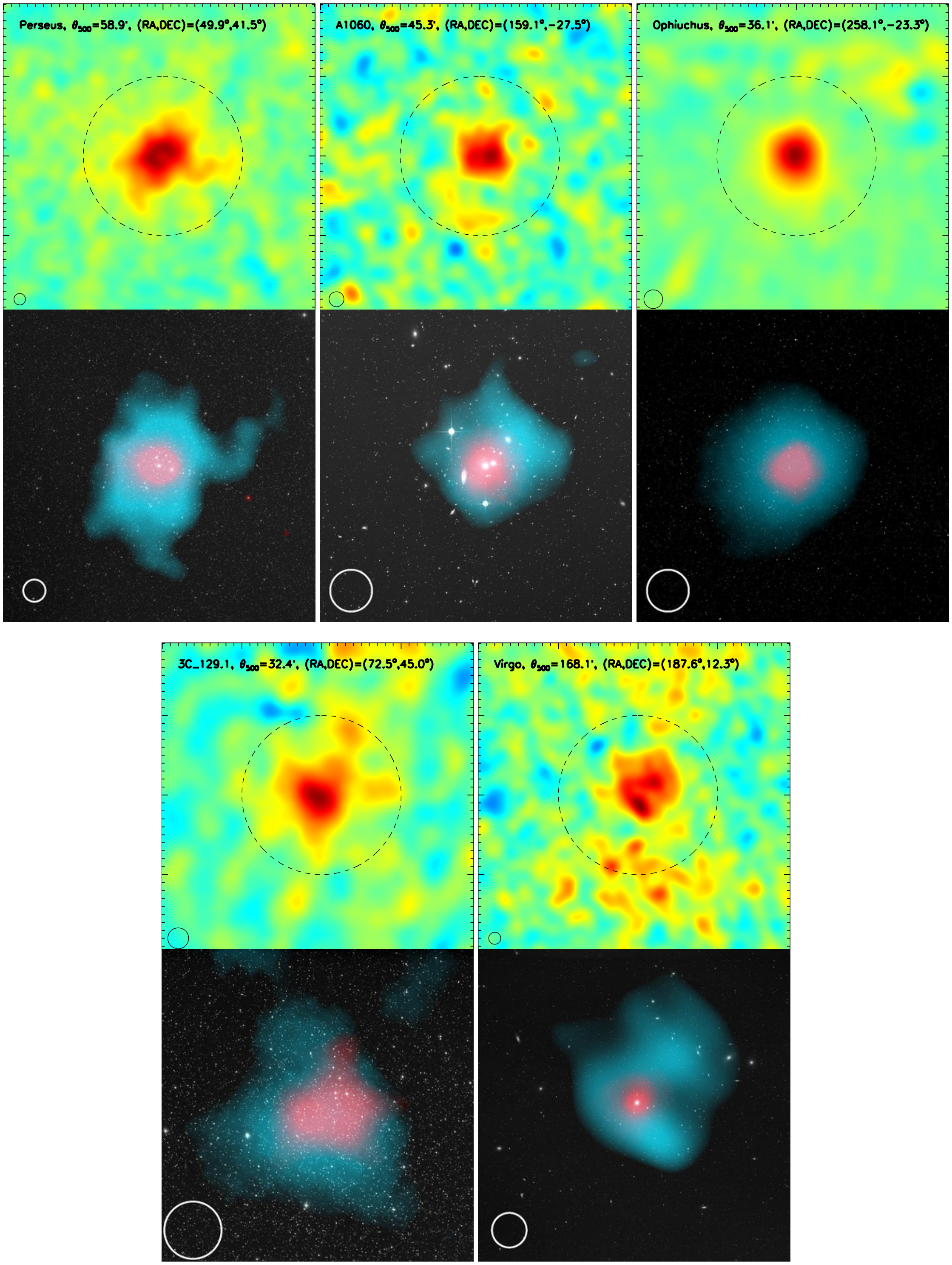

Fig. 19. Five nearby and extended clusters not included in the PSZ catalogue: the Perseus cluster and Abell 1060 (in the point-source mask); Ophiuchus cluster and 3C 129.1 (in the Galactic mask); and Virgo cluster (below the S/N threshold of the catalogue). *Top panels*: reconstructed thermal SZ maps from the `MILCA` algorithm (Hurier et al. 2013). The dashed circles represent the apertures of θ_{500} from the MCXC catalogue. Each SZ-map covers an area of $4\theta_{500} \times 4\theta_{500}$. *Bottom panels*: composite images of the optical (DSS, white), X-ray (ROSAT, pink) and SZ signal (*Planck*, blue). The sizes of the composite images are 2° × 2° for Perseus; 1° × 1° for A1060; 1° × 1° for Ophiuchus; 0.77° × 0.77° for 3C 129.1 and 3.84° × 3.84° for Virgo. The black and white circles picture a 10 arcmin aperture, but for Virgo for which the aperture is 30 arcmin.

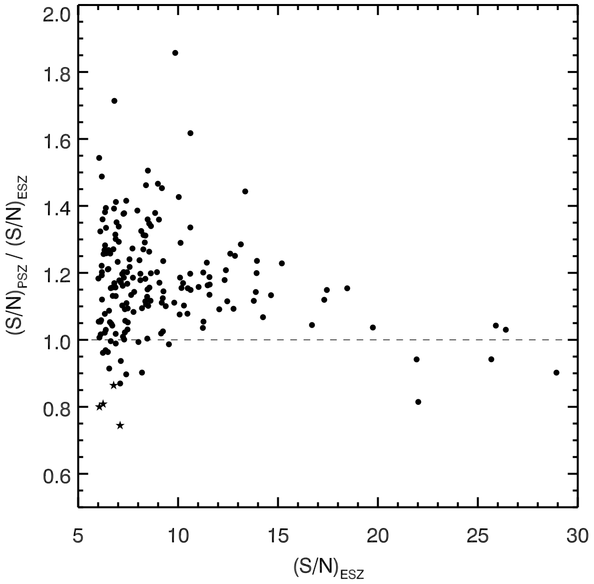

Fig. 20. Ratio of S/N in the *Planck* catalogue, $(S/N)_{PSZ}$, to that in the ESZ sample (Planck Collaboration VIII 2011), $(S/N)_{ESZ}$, for the 184 confirmed ESZ clusters included in the *Planck* catalogue. Four clusters whose S/N in the PSZ catalogue is significantly smaller than the ESZ threshold ($(S/N)_{ESZ} = 6$) are shown as stars.

fall in, or nearby, the PS mask used for the pre-processing of the channel maps prior to running the detection algorithms. Such a mask was not utilized for the construction of ESZ sample. We choose not to a posteriori include these four "missing" ESZ clusters in the present *Planck* SZ catalogue.

6.1.4. Identification with clusters from NED or SIMBAD

As expected only a small number of clusters are identified from querying the databases, supplying identifiers for thirteen SZ *Planck* detections. This is because the information in NED and SIMBAD is redundant with that in the X-ray, optical, or SZ catalogues used for the external validation. The thirteen clusters found solely from querying the databases are found in the RASS survey but not in dedicated cluster catalogues, and thus not included in the MCXC; they are found in serendipitous *Chandra* surveys, or they are part of miscellaneous cluster catalogues.

6.2. Newly-discovered Planck clusters and candidates

Among the 544 *Planck* SZ sources, we distinguish two categories: (1) confirmed clusters, i.e., those that have been confirmed by the follow-up programmes of the *Planck* collaboration[24] or using the SDSS galaxy catalogues, plus also add eight confirmations from X-ray archival data (one of those, PSZ1 G292.00-43.64, coincides with the XCLASS cluster candidate, J023303.4-711630 (Clerc et al. 2012)); (2) Candidate clusters with different levels of reliability, namely, 1 cluster candidates, that fulfil high-quality criteria for the SZ detection and for the associations and/or counterparts in ancillary data, 2 candidate clusters, i.e., those that fulfil, on average, good-quality criteria, and 3, low-reliability cluster candidates.

Confirmation from Planck collaboration follow-up programmes. At $S/N \geq 4.5$, a total of 233 *Planck* SZ detections were followed up in X-rays, optical, and SZ at the different facilities listed previously, with some observations targeted to the measurement of spectroscopic redshifts for already known clusters. In total 157 *Planck* SZ detections with $S/N \geq 4.5$ were confirmed as new clusters. Some of the *Planck*-confirmed clusters were also reported in recent cluster catalogues in the optical, e.g., Wen et al. (2012) or in the SZ e.g., Reichardt et al. (2013).

The analysis of the observations of *Planck* sources by AMI yielded ten sources with strong Bayesian evidences that have clearly visible decrements and were considered as confirmed, including the confirmation of three associations with optical clusters.

For the candidates confirmed by *XMM-Newton* and by optical telescopes, redshifts from Fe lines and from photometric or spectroscopic data are available. The validation of *Planck* cluster candidates with *XMM-Newton* has shown its particular efficiency in confirming SZ candidates due both to the high sensitivity of *XMM-Newton*, allowing *Planck* clusters to be detected up to the highest redshifts (Planck Collaboration XXVI 2011), and the tight relation between X-ray and SZ properties. The detection of extended *XMM-Newton* emission and a comparison between the X-ray and SZ flux permits an unambiguous confirmation of the candidates. By contrast, confirmation in the optical may be hampered by the *Planck* positional accuracy and by the scatter between the optical observables and the SZ signal, which increase the chance of false associations. The *XMM-Newton* follow-up programme yielded 51 bona fide newly-discovered clusters, including four double systems and two triple systems. There were eight false candidates. Thirty-two of the 51 individual clusters have high-quality redshift measurements from the Fe line. The relation between the X-ray and SZ properties was used to further constrain the redshift of the other clusters; most of these redshifts were confirmed clusters using optical observations. Out of a total of 37 single clusters confirmed by *XMM-Newton*, 34 are reported in the *Planck* catalogue of SZ sources at $S/N \geq 4.5$. Additionally four double systems are included in the present PSZ catalogue and were also confirmed by *XMM-Newton*.

The follow-up observations conducted with optical telescopes lead to the confirmation and to the measurement of spectroscopic or photometric redshifts (companion publications, in preparation, will present the detailed analysis and results from these follow-up). In the northern hemisphere, 26 spectroscopic redshifts for *Planck* clusters detected at $S/N \geq 4.5$ and observed at the RTT150 are reported, to date, in the PSZ catalogue. A dozen additional spectroscopic redshifts were measured for known clusters. Confirmation of 21 *Planck* SZ clusters detected above 4.5 were obtained with the ENO facilities (at INT, GTC and NOT), and robust redshift measurements were obtained for 19 of them, including 13 spectroscopic redshifts. In the southern hemisphere, WFI observations provided photometric redshifts for 54 clusters included in the *Planck* catalogue at $S/N \geq 4.5$, while 19 spectroscopic redshifts obtained with the NTT-EFOCS2 instrument are reported in the *Planck* catalogue.

Confirmation from SDSS galaxy catalogues. The firm confirmation of the candidates was done through the follow-up observations for confirmation and measurement of their redshift as detailed above. However in the case of the *Planck* candidates

---

[24] A handful of new *Planck* clusters from the ESZ sample were confirmed independently from the *Planck* collaboration by SPT (Story et al. 2011), AMI (AMI Consortium et al. 2011), Bolocam (Sayers et al. 2012) and CARMA (Muchovej et al. 2012).

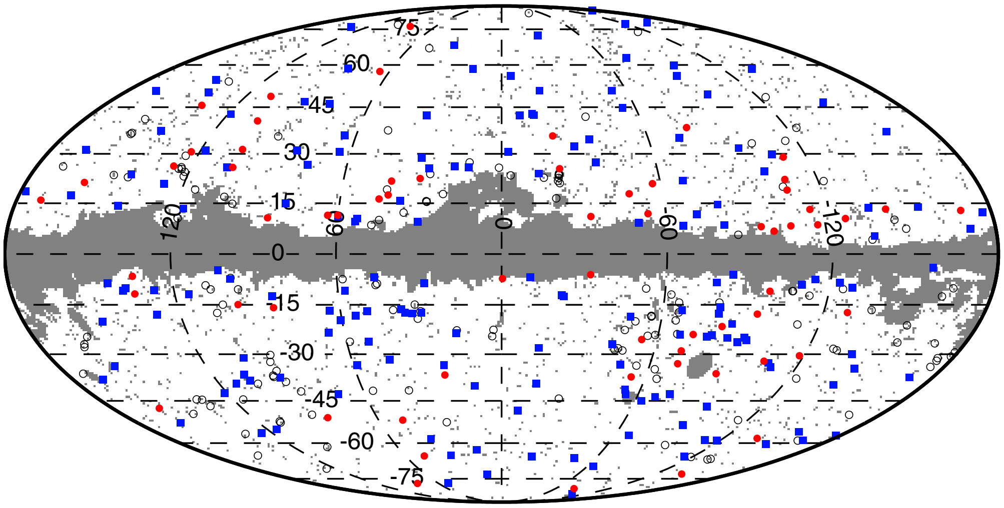

Fig. 21. Distribution of the *Planck* SZ candidates across the sky. Blue symbols represent the 1 candidate clusters and red the 2 candidates. The open symbols stand for the 3 low-reliability SZ sources.

falling in the SDSS footprint we also used the SDSS galaxy catalogues to search, as presented in Sect. 4.1.2, for galaxy overdensities associated with *Planck* SZ detections. This provides us with an estimate of the photometric redshifts, and in some cases we could retrieve spectroscopic redshifts for the BCG as well.

In this process, the major uncertainty in the associations of *Planck* SZ detections with galaxy overdensities is due to chance associations with low-richness systems or associations with diffuse concentrations of galaxies in the SDSS data. The *XMM-Newton* confirmation programmes (see Planck Collaboration Int. IV 2013 for discussion) showed that *Planck* candidates with SDSS counterparts were confirmed including PLCK G193.3−46.1 at $z \simeq 0.6$. However, the X-ray analysis of the *Planck* detections with SDSS counterparts illustrated the difficulty in distinguishing between associations of *Planck* SZ signals with massive clusters and with pre-virialized structures. In particular, in the case of extended filamentary structures or dynamically perturbed sources, an offset between the BCG position and the concentration barycentre is noted.

We considered the *Planck* SZ candidates with counterparts in the SDSS data taking into account diagnostics such as the richness/mass estimates as well as the offsets between the SZ, the BCG and the barycentre positions. We further used the outputs of the search in WISE and in RASS data, and the associated images, in order to assess the significance of the galaxy overdensity in SDSS at the position of the *Planck* candidates. For the *Planck* SZ detections where both ancillary data and SDSS barycentre/BCG positions agreed, we set that they are confirmed. We found a total of 13 such associations for which we report the photometric or the spectroscopic redshifts. It is worth noting that firm confirmation of these associations is needed and needs to be performed using either optical spectroscopic observations or X-ray observations of the *Planck* SZ detections. In the cases where the offsets between barycentre and BCG position output by the search in SDSS data were too large, and/or when other ancillary information was unable to discriminate between reliable or chance associations, we have chosen to keep the status of candidate for the *Planck* SZ detection. These cases sometimes also coincide with association of *Planck* detections with clusters from the SDSS cluster catalogues, with a quality flag $Q_{\rm SDSS} = 0$, or with confusion in the association, i.e., with positions not in agreement between counterpart and published SDSS clusters. We provide a note for all these cases in order to indicate that an overdensity in SDSS data was found.

Candidate new clusters. The remaining 366 *Planck* SZ sources, not identified with previously known cluster nor confirmed by follow-up observation or ancillary data, are distributed over the whole sky (Fig. 21) and are yet to be firmly confirmed by multi-wavelength follow-up observations. They are characterized by an ensemble of quality flags defined in Sects. 4.1.1, 4.1.2, and 4.1.3 based on the systematic searches for counterparts in the public surveys during the external validation process. We further define an empirical *Planck*-internal quality flag $Q^{\rm SZ}$. It assesses the reliability of the SZ detection itself from three independent visual inspections of the nine *Planck* frequency maps, of frequency maps cleaned from Galactic emission and CMB, and of reconstructed y-maps or y-maps produced from component separation methods (e.g., Hurier et al. 2013; Remazeilles et al. 2011). Moreover, we visualize the SZ spectra from the SZ-finder algorithms and from aperture photometry measurements at the candidate positions. Finally we correlate, at the position of the *Planck* SZ candidates and within an area of 10′ radius, the y-map to the 857 GHz channel map, as a tracer of the dust emission, and to the *Planck* mono-frequency CO map at 217 GHz (Planck Collaboration XIII 2014). The qualitative flag $Q^{\rm SZ}$ combines all this information into three values 1 to 3 from highest to lowest reliability with the following criteria:

- $Q^{\rm SZ} = 1$, i.e., high reliability: (i) Clear compact SZ source in the SZ maps; (ii) significant measurements of the SZ decrement below 217 GHz and good or reasonable detection at 353 GHz; (iii) no correlation with dust nor CO emission and no rise of the 545 and 857 GHz fluxes on the thermal SZ spectrum.
- $Q^{\rm SZ} = 2$, i.e., good reliability: (i) visible SZ detection in the SZ map or significant detection of the SZ signal below 217 GHz; (ii) contamination causing rise of the 545 GHz and possibly 857 GHz flux on the SZ spectrum without a strong correlation with dust and CO signals.
- $Q^{\rm SZ} = 3$, i.e., low reliability: (i) weak SZ signal in the y-maps and/or noisy SZ maps; (ii) weak or no SZ signal in

the cleaned frequency maps (iii) strong correlation (≥80%) with dust and CO emission contamination with rising fluxes on the SZ spectrum at high frequencies, 353 GHz and above.

We combine the qualitative SZ quality flag with the information from the search in the all-sky surveys, RASS and WISE, for counterparts of *Planck* candidates in order to assess the overall reliability of the cluster candidates. We thus distinguish three classes of candidates:

- 1 candidates. *Highly-reliable candidates or pre-confirmed clusters:* these are the *Planck* SZ detections that have a high probability of being associated with bona fide clusters and need to fulfil high-quality criteria for SZ, RASS, and WISE detections. We retain in this category *Planck* SZ detections with high or good SZ quality flags ($Q^{\rm SZ} = 1$ or 2) and with a RASS-BSC source (not coinciding with stars) or with $(S/N)_{\rm RASS} \geq 2$, i.e., SZ detections with quality flag $Q_{\rm RASS} = 1$. The 1 candidates furthermore have to fulfil a condition of high or good probability (≥80%) of being associated with an overdensity of galaxies in the WISE survey.
  We find 54 1 *Planck* candidates ranging from S/N of 4.5 to 6.3, with a median S/N of 4.8. The majority of them are detected by two methods and 25.9% of them are detected only by one method. They are distributed as 26 and 28 $Q^{\rm SZ} = 1$ and 2 candidates, respectively. These candidates show significant X-ray emissions with a median $({\rm S/N})_{\rm RASS} \simeq 3.7$ and a mean of 4.2.
- 2 candidates. *Reliable cluster candidates:* they represent 170 *Planck* SZ detections that show good or high quality criteria either in SZ or in RASS or in WISE without fulfilling all of them at once. Amongst them 61 have $Q^{\rm SZ} = 1$ and 109 have $Q^{\rm SZ} = 2$.
- 3 candidates. *Low-reliability cluster candidates:* these *Planck* SZ detections are the poor-quality, $Q^{\rm SZ} = 3$, detections. They can also be associated with good quality, $Q^{\rm SZ} = 2$, detections for which there are no good indications of the presence of an X-ray counterpart ($(S/N)_{\rm RASS} < 0.5$ and high probability of false association with FSC sources >2.5%) or a counterpart in the WISE survey (probability of association <70%).
  This class of candidates contains 142 *Planck* SZ detections with 27 and 115 SZ detection of quality $Q^{\rm SZ} = 2$ and 3, respectively.

It is worth noting that this definition of the 3 *Planck* candidates is dominated by the assessment of the SZ quality complemented by information from ancillary data. In doing so we assemble in this category of candidates the SZ detections that are either false or very low quality due to contamination. Moreover, according to the statistical characterization from simulations, about 200 false detections are expected. The number of false detections could be smaller since the simulations do not reproduce the entire validation procedure, in particular omitting the cleaning from obvious false detections. Figure 22 suggests that the 3 candidates are likely to be dominated by false detections. Therefore, we would like to warn against dismissing entire 3 of the catalogue as populated with false detections as some 3 candidates may be real clusters. For this reason, we choose not to remove these detections from the PSZ catalogue but rather flag them as low-reliability candidates. Careful follow-up programmes are needed in order to separate real clusters of galaxies from false detections among the 2 and 3 objects.

In order to illustrate our classification defined in terms of reliability, we stack the signal in patches of 2.51° across, centred at the position of the *Planck* clusters and candidates in the nine channel maps of *Planck*, removing a mean signal estimated in the outer regions where no SZ signal is expected (see Fig. 22 with the rows arranged from 30 GHz, upper row, to 857 GHz, lower row). The stacked and smoothed images are displayed for the *Planck* SZ detections identified with known clusters, 1, 2 and 3 candidates, Fig. 22 from left to right column. We clearly see the significant detection of both the decrement and increment of the 683 *Planck* clusters and of the *Planck* candidates of 1 and 2. For the *Planck* SZ detections associated with bona fide clusters the increment is clearly seen at 353 and 545 GHz and is detected at 857 GHz. The smaller sample of the 1 highly reliable candidates shows, in addition to the decrement at low frequency, a good detection of the increment at 353 GHz. The significance of the increment at 545 GHz is marginal and no signal is seen at 857 GHz. The case of the 2 candidates (good reliability) shows that we now have lower-quality SZ detections (62% of the 2 candidates have a good but not high SZ quality flag). This is illustrated by the fact that an excess emission is detected at 217 GHz, most likely due to contamination by IR sources, and both at 545 and 857 GHz where emission from dust is dominating. As for the stacked signal of the 3 sample of low-reliability candidates, it does not show any significant SZ detection across frequencies, as compared to the sample of *Planck* detections identified with known clusters (Fig. 22, right column). This confirms on statistical grounds the definition of the sample dominated by definition by the low-quality SZ, $Q^{\rm SZ} = 3$, detections representing 84% of the detections in this class. Not surprisingly, the stacked signal of the 3 candidates shows a large amount of contamination across all *Planck* frequencies. The low-frequency signal is dominated by radio contamination, and/or CO emission at 100 GHz, while the high-frequency signal is contaminated by emission from dust or extragalactic point sources. A more quantitative analysis is presented in Sect. 7.1.

6.3. Summary of the external validation and redshift assembly

The *Planck* catalogue of SZ sources comprises a total of 861 identified or confirmed clusters with only nine percent of them being detected by one SZ-finder algorithm. We summarize in Table 5 and Fig. 18 the results of the cluster identification. Figure 23 illustrates the status of the *Planck* SZ detections. In particular, 70.2% of the *Planck* SZ detections with $S/N \geq 4.5$ have so far been associated with clusters. The fraction increases to about 73% at $S/N = 6$.

We have assembled, at the date of submission, a total of 813 redshifts for the 861 identified or confirmed *Planck* clusters, which we provide together with the published *Planck* catalogue. Their distribution is shown in Fig. 24. In the process of the redshift assembly that is summarized below, especially for the already known clusters, we have favoured homogeneity for the sources of redshift rather than a cluster-by-cluster assembly of the most accurate z measure. A large fraction of the redshifts, 456 of them, shown as the dashed green histogram in Fig. 24 correspond to the spectroscopic redshifts quoted in the updated MCXC meta-catalogue (Piffaretti et al. 2011). They are associated with the *Planck* clusters identified with known X-ray clusters and they are denoted *Planck*-MCXC. For the *Planck*-MCXC clusters without reported redshifts from the MCXC, we have complemented the information with the available redshifts from NED and SIMBAD. We have further quoted when available, mainly for the MACS clusters, the estimated photometric

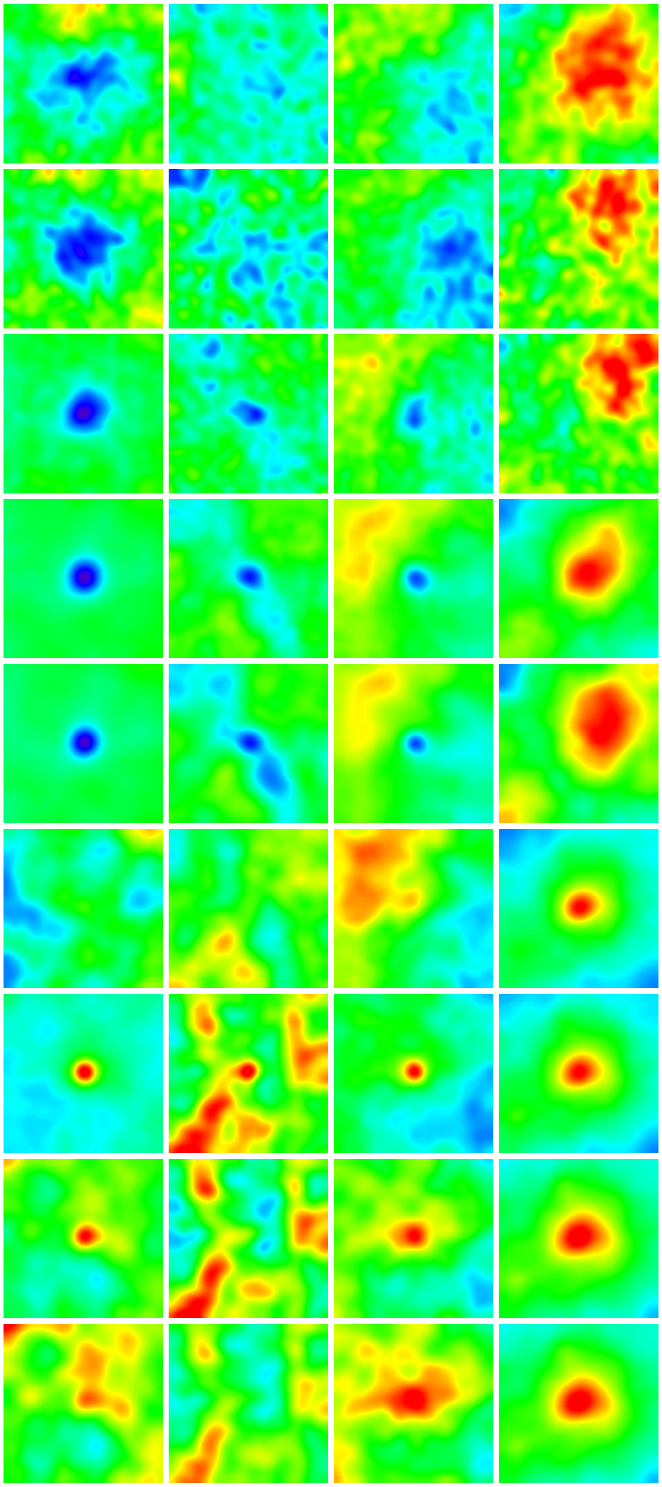

Fig. 22. Stacked signal in the nine *Planck* frequencies (30 to 857 GHz from upper to lower row). From left to right are displayed the *Planck* SZ detections identified with known clusters, the 1 high-reliability *Planck* SZ candidates, the 2 good-reliability *Planck* SZ candidates, and finally the 3 low-reliability SZ sources. The three lowest-frequency-channel images were convolved with a 10′ FWHM Gaussian kernel, whereas the remaining six highest-frequency-channel images were smoothed with a 7′ FWHM Gaussian kernel.

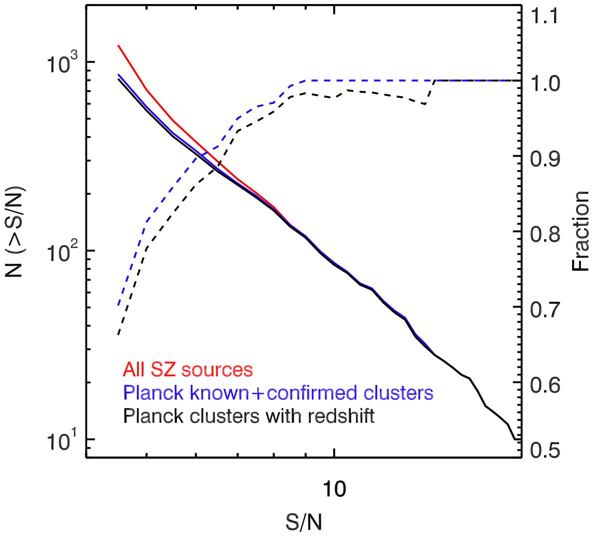

Fig. 23. Status of the *Planck* SZ sources. Left-hand-axis plots show the distribution of all *Planck* sources (in red). The blue line represents the known or new confirmed clusters and, among these, the clusters with a reported redshift measurement in black. Right-hand-axis cumulative distributions show, as a function of S/N, the fraction of known or new confirmed clusters in blue and those with a redshift in black.

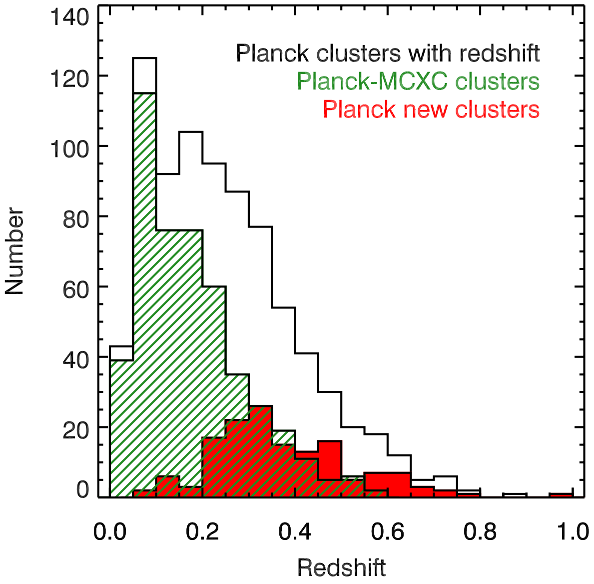

Fig. 24. Distribution of redshifts for the *Planck* SZ clusters (black line). The *Planck* clusters associated with MCXC clusters are shown in dashed green and the new *Planck* clusters are in the filled red histogram.

redshifts from SDSS cluster catalogue of Wen et al. (2012). At the end only two *Planck* detections identified with MCXC clusters remain without redshifts. The redshift distribution of the *Planck* clusters identified with MCXC clusters mostly reflects that of the REFLEX/NORAS catalogues at low and moderate redshifts and the MACS clusters at higher redshifts.

For the *Planck* detections exclusively identified with Abell or Zwicky clusters, we choose to report the redshifts published in the NED and SIMBAD data bases rather than those quoted in the native catalogues. As for the *Planck* detections identified with clusters from the SDSS-based catalogues, we choose to favour homogeneity by reporting whenever possible the Wen et al. (2012) redshifts. Furthermore, we favour when available spectroscopic redshifts over photometric ones. The *Planck* detections exclusively associated with ACT or SPT clusters have published redshifts (Sifón et al. 2013; Hasselfield et al. 2013; Reichardt et al. 2013). We select in priority the spectroscopic ones when available. If not, we quote the photometric redshifts.

Finally, the follow-up observations for confirmation of *Planck* detections started in 2010 and are still ongoing. As mentioned earlier our priority was to assemble the largest possible number of confirmations and redshifts. Therefore, we did not systematically confirm the photometric redshift estimates spectroscopically. We report the obtained redshifts when available. In some cases, the new *Planck* clusters were confirmed from imaging or pre-imaging observations and the analysis is still ongoing. The spectroscopic redshifts will be updated when available. Spectroscopic redshifts for some known clusters will also be updated. A dozen *Planck* clusters were confirmed by a search in the SDSS galaxy catalogues. For these clusters, only a photometric redshift estimated by the cluster-finder algorithm of Fromenteau et al. (in prep.) is available and is reported.

We show in Fig. 24 the distribution of redshifts of the *Planck* clusters. The mean redshift of the sample is 0.25 and its median is 0.22. One third of the *Planck* clusters with measured redshifts lie above $z = 0.3$. The new *Planck* clusters probe higher redshifts and represent 40% of the $z \geq 0.3$ clusters. Their mean redshift is 0.38 and the median is $z = 0.35$. At even higher redshifts, $z \geq 0.5$, the *Planck* catalogue contains 65 clusters including *Planck* SZ clusters identified with WHL12's clusters (Wen et al. 2012), or with clusters from ACT and SPT, or with X-ray clusters. The *Planck* detections in this range of redshifts, 29 *Planck* new clusters, almost double the number of high redshift clusters.

The *Planck* SZ catalogue has been followed up by the *Planck* collaboration using different facilities and only a small fraction of the *Planck* candidates were observed to date. A systematic follow-up effort for the confirmation of the remaining cluster candidates will likely reveal clusters at redshifts above 0.3. As a matter of fact, very few new clusters were found below $z = 0.2$ (see Fig. 24). Such an observational programme is challenging and will most likely be undertaken by the *Planck* collaboration and by the community. It will increase further the value of the *Planck* SZ catalogue as the first all-sky SZ-selected catalogue.

7. Physical properties of *Planck* SZ clusters

The first goal of the external validation process based on the ancillary multi-wavelength data is to assess the status of the *Planck* SZ detections in terms of known clusters, brand new clusters or cluster candidates. The wealth of information assembled and used during this process also allows us to explore the properties of the *Planck* SZ clusters and candidates. We present in the following some of these properties, namely the contamination levels of the *Planck* SZ detections, a refined measurement of the Compton Y parameter for the *Planck* clusters identified with X-ray clusters from the MCXC, an SZ-mass estimate based on a new proxy for all the *Planck* clusters with measured redshifts, and an estimate of the X-ray flux from the RASS data for the *Planck* SZ detections not included in the X-ray catalogues. This additional information associated with the *Planck* clusters and candidates derived from the validation process is summarized in the form of an ensemble of outputs given in Table C.1.

We further present an updated and extended study of the SZ versus X-ray scaling relation, confirming at higher precision the strong agreement between the SZ and X-ray measurements (within R_{500}) of the intra-cluster gas properties found by Planck Collaboration XI (2011).

7.1. Point-source contamination

Galactic and extragalactic sources, emitting in the radio or infrared domain, are known to lie in galaxy clusters and hence are a possible source of contamination for the SZ measurement (e.g., Rubiño-Martín & Sunyaev 2003; Aghanim et al. 2005; Lin et al. 2009). We address the possible contamination of the SZ flux by bright radio sources that may affect the measured signal in the direction of some of the *Planck* SZ detections. In order to do so, we searched for known radio sources in the vicinity of the *Planck* cluster candidates. In particular, we use the NVSS 1.4 GHz survey (Condon et al. 1998) and SUMMS 0.85 GHz survey (Bock et al. 1999) to identify bright radio sources within 7′ of the *Planck* cluster or candidate position. This search radius corresponds to the *Planck* resolution at 143 GHz. We assumed a spectral index $\alpha = -0.5$ for these sources to extrapolate their flux to the *Planck* frequencies. Most bright sources in NVSS and SUMSS have steeper spectral indexes (−0.6 or −0.7), so the value $\alpha = -0.5$ provides us with an upper limit in most cases. After convolving the radio sources by *Planck*'s beam, we estimate the maximum amplitude in units of μK within 5′ of the *Planck* position. We report only those cases where this amplitude is above 5 μK in the 143 GHz channel and could thus contaminate the SZ signal. Below this value, the emission from radio sources can be considered negligible.

We find that a total of 274 *Planck* clusters and candidates, i.e., 22% of the SZ detections, are affected by such emission from bright radio sources. These clusters or candidates are identified in the PSZ catalogue and a specific note is provided. We find that the fraction of contaminated *Planck* SZ clusters identified with known X-ray, optical, or SZ clusters is also 22%. The *Planck* candidate-clusters of 1 and 2 are less contaminated by bright radio sources; only a fraction of 15% and 17% for 1 and 2, respectively. This is due to the definition of our quality criteria for SZ detection, which results in less contamination for the high and good reliability candidates.

Another approach used to assess the contamination is based on the stacking analysis of the *Planck* clusters and candidates described in Sect. 6.2. This analysis is performed on the sample of *Planck* clusters identified with known clusters and on the sample of low-reliability 3 *Planck* candidates. To do so we fit a GNFW pressure profile to the signal at 100 GHz and 143 GHz and we subtract the associated SZ signal from the stacked maps. The residual signal is then compared with a toy model for point sources ($F_\nu = S_{30}^{\rm rad}(\nu/30\,{\rm GHz})^{\alpha_{\rm rad}}$ for radio sources) and ($F_\nu = S_{857}^{\rm IR}(\nu/857\,{\rm GHz})^{\alpha_{\rm IR}}$ for IR point sources). Note that the residual signal at high frequencies is a combination of possible IR sources and IR emission from Galactic dust; the latter is not explicitly modelled in the present analysis. The PS toy models are convolved by the beam at each frequency and the signal is measured at a fixed aperture set to the FWHM of the 143 GHz channel. The average signal within this aperture is estimated for each channel before (Fig. 25, upper panel) and after (Fig. 25, lower panel) removal of the SZ signal. The black filled circles are for *Planck* SZ sources associated with known clusters and the red filled triangles stand for 3 candidates.

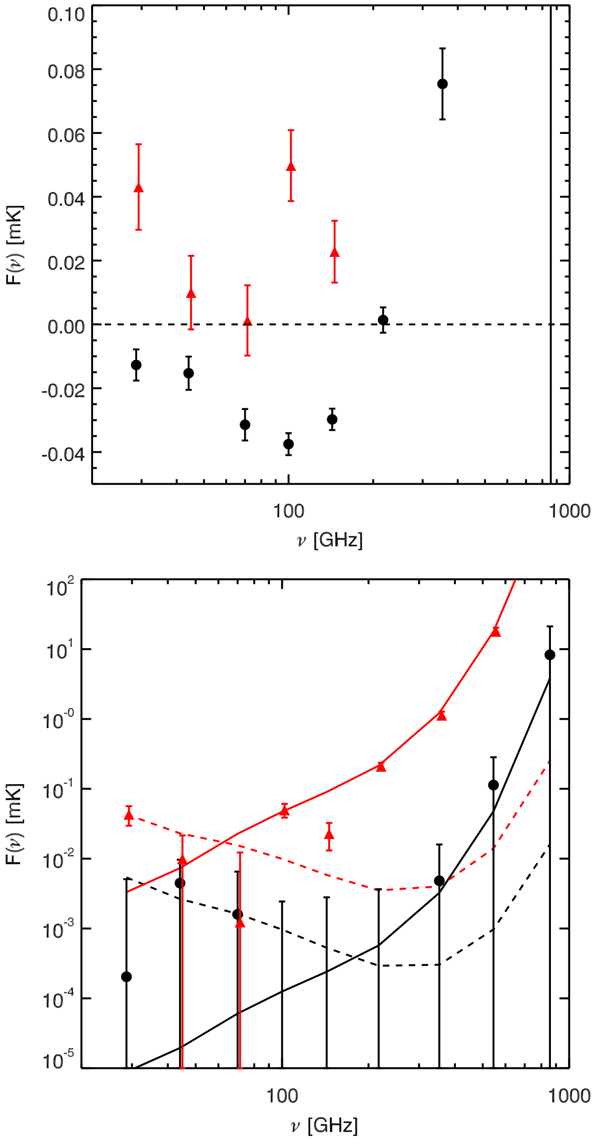

Fig. 25. Stacked spectrum for known clusters SZ fluxes across *Planck* frequency bands. Stacked fluxes are measured in an aperture equal to the FWHM of the 143 GHz channel (i.e., about 7′) for the known clusters (black filled circles) and the low-reliability 3 candidates (red filled triangles). The associated uncertainties correspond to the fluctuation of the background outside the cluster region. The average signal is estimated in each channel before (*upper panel*) and after (*lower panel*) the removal of the SZ signal. The average signals expected from IR and radio sources are shown as solid and dashed lines, respectively. Red and black lines are for 3 and bona fide clusters, respectively. No subtraction of an SZ signal is performed for the 3 candidates.

The average signal from the PS models is shown in Fig. 25 as solid (IR sources) and dashed (radio sources) lines. Red and black are for 3 and bona fide clusters, respectively. The error bars correspond to the fluctuation of the background outside the cluster region. For the sample of 3 candidates no SZ-signal removal was applied, since no significant detection is seen at 100 GHz or 143 GHz.

We find that the residual signal (after SZ subtraction) in the sample of known *Planck* clusters is compatible with the emission from radio sources at low frequencies with $(S_{30}^{\mathrm{rad}}, \alpha_{\mathrm{rad}}) = (14.6\,\mathrm{mJy}, -1)$ for the known clusters. It is also compatible with IR emission at high frequencies with a spectral index $\alpha_{\mathrm{IR}} = 2.5$, in agreement with the results of Planck Collaboration Int. VII (2013) and with $S_{857}^{\mathrm{IR}} = 0.117\,\mathrm{Jy}$. For 3, where no SZ signal is subtracted, it is the full signal that is compatible with the IR emission at high frequencies, with $(S_{857}^{\mathrm{IR}}, \alpha_{\mathrm{IR}}) = (43.9\,\mathrm{Jy}, 2.5)$, and with radio emission from point sources with $(S_{30}^{\mathrm{rad}}, \alpha_{\mathrm{rad}}) = (117.1\,\mathrm{mJy}, -0.8)$.

7.2. Refined measurement of *Y*

While the true Y_{500} is expected to be a low-scatter mass proxy, this is not the case for the blind Y_{500}. Without a cluster-size estimate, Y_{500} cannot be accurately measured. Moreover, the blind SZ flux is biased high on average, because the size is over-estimated on average. This effect is amplified by the non-linear nature of the size–flux degeneracy, with a larger effect of size over-estimation than size under-estimation. This behaviour, first identified and discussed in Planck Collaboration VIII (2011) and Planck and AMI Collaborations (2013), hampers the direct use of the blind SZ fluxes as a mass proxy. As shown in Planck Collaboration VIII (2011), this degeneracy calls for a refined measurement of the SZ signal. In this section, we present two ways of refining the *Y* measurement. Both are based on fixing the cluster size in two cases, by setting it equal to the X-ray estimated size or by using the redshift information when available. The outputs of the refined measurement are provided as additional information complementary to the catalogue of *Planck* SZ detections (see Appendix C and Table C.1).

7.2.1. *Y* at fixed X-ray size and position

As shown by Planck Collaboration VIII (2011), the size–flux degeneracy can be broken by introducing a higher-quality estimate of the cluster size θ_{500}. This prior is directly provided by X-ray observations using an X-ray mass proxy such as Y_{X} or the luminosity L_{X}. Resorting to estimates of the cluster size from optical richness is also possible, but suffers from the large scatter in richness-mass relation, as discussed previously.

A detailed investigation of the effects of fixing the cluster size was presented in Planck Collaboration XI (2011, Appendix A). Following this approach, and for the *Planck* detections identified with clusters from the MCXC meta-catalogue, we have adopted the R_{500} and z values reported in Piffaretti et al. (2011) as priors to re-extract at the X-ray position the SZ signal denoted $Y_{500,\mathrm{PSX}}$ assuming the Arnaud et al. (2010) pressure profile (see Table C.1). The comparison between the blind Y_{500} and refined $Y_{500,\mathrm{PSX}}$ (Fig. 26) shows that both the scatter and the offset are significantly reduced by the refined SZ measure. The SZ re-extraction at X-ray position and fixing the size to the X-ray derived size provides an unbiased estimate of the SZ signal. However, as stressed in Planck Collaboration XI (2011, Appendix A), the MCXC cluster size derivation involves the M_{500}–$L_{\mathrm{X},500}$ relation, which exhibits a non-negligible scatter. This leads to a remaining systematic discrepancy between the expected *Y* value from X-ray measurements and the actual SZ flux derived from the *Planck* data. The use of the Y_{X} proxy does not suffer from such an effect, but high-quality X-ray data permitting the use of such a quantity are not available for a large number of clusters (see Sect. 7.5 for the presentation of a sample of *Planck* SZ clusters with high-quality X-ray data).

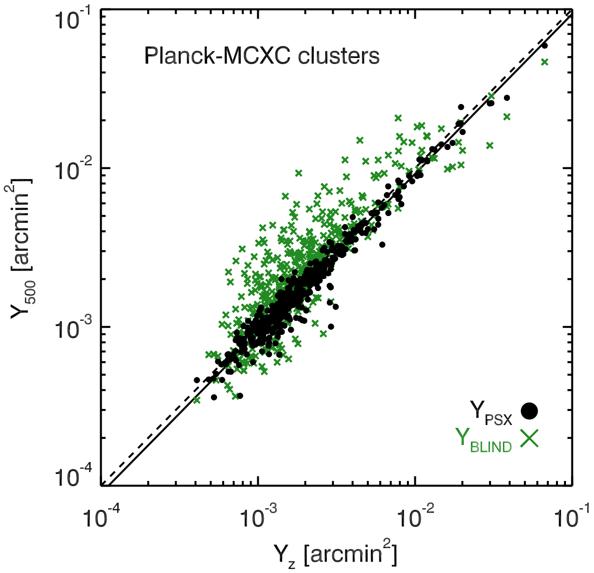

Fig. 26. Comparison of the different *Y* estimates for the *Planck* clusters identified with MCXC clusters. In green are the blind measured *Y* values and in black are the refined $Y_{500,\mathrm{PSX}}$ measured fixing the size and positions to the X-ray values. Both are plotted as a function of the new proxy Y_z.

7.2.2. *Y* from the $Y(\theta)$–*M* relation

The size–flux degeneracy can further be broken, as proposed by (Arnaud et al., in prep.), using the M_{500}–$D_{\mathrm{A}}^2 Y_{500}$ relation itself that relates θ_{500} and Y_{500}, when z is known. Then Y_{500} is derived from the intersection of the M_{500}–$D_{\mathrm{A}}^2 Y_{500}$ relation and the size–flux degeneracy curve. A detailed description of the method and the comparison of results in terms of bias and scatter can be found in (Arnaud et al., in prep.).

The derived Y_{500} parameter is denoted Y_z (since it involves a measurement of the Compton *Y* signal for clusters with measured redshift z). It is the SZ mass proxy Y_z that is equivalent to the X-ray mass proxy Y_{X}. Y_z is computed for all the 813 *Planck* clusters with measured redshifts. We use Malmquist-bias-corrected scaling relation between mass and *Y* given in Planck Collaboration XX (2014)

$$E^{-2/3}(z)\left[\frac{D_{\mathrm{A}}^2(z)\,Y_{500}}{10^{-4}\,\mathrm{Mpc}^2}\right] = 10^{-0.19}\left[\frac{M_{500}}{6\times10^{14}\,M_{\odot}}\right]^{1.79}, \qquad (5)$$

with $E^2(z) = \Omega_{\mathrm{m}}(1+z)^3 + \Omega_\Lambda$ computed in the fiducial ΛCDM cosmology.

In Fig. 26, the refined Y_{500} value, measured fixing the size and position to the X-ray values $Y_{500,\mathrm{PSX}}$, is compared to the blind *Y* as a function of the derived Y_z proxy. We see that the scatter and the offset are significantly reduced.

Under the two hypotheses of cosmology and scaling relation, Y_z provides the best estimate of Y_{500} for the *Planck* SZ clusters and conversely a homogeneously-defined estimate of an SZ-mass, X-ray calibrated, denoted $M_{500}^{Y_z}$. For the ensemble of *Planck* clusters with measured redshifts, the largest such sample of SZ-selected clusters, we show in Fig. 27 the distribution (black solid line) of the masses obtained from the SZ-based mass proxy. The distribution of the SZ masses is compared with those of the RASS clusters (dashed blue line) computed

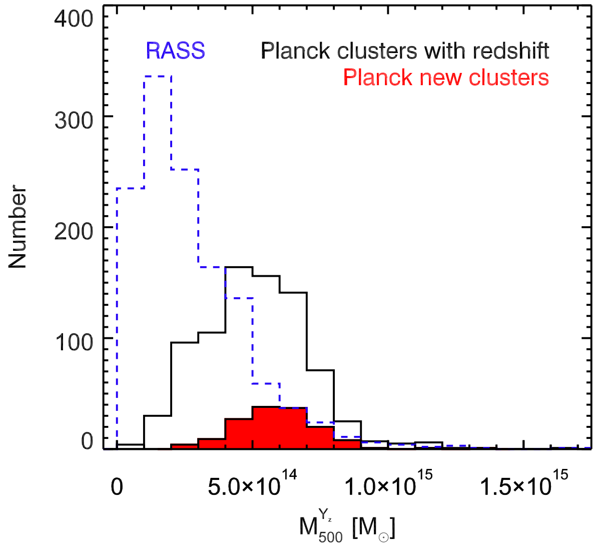

Fig. 27. Distribution of masses for the *Planck* SZ clusters, known or new confirmed clusters (solid black line), compared to the distribution of masses from the RASS-based cluster catalogues (dashed blue line). The masses for the MCXC clusters are estimated from the luminosity-mass relation. The masses for the *Planck* clusters are computed using the SZ-proxy. The filled red histogram shows the distribution of the newly-discovered *Planck* clusters.

from the X-ray luminosity $L_{X,500}$. The mean and median masses of the *Planck* clusters are 3.3 and $3.5 \times 10^{14}\,M_\odot$, respectively. The *Planck* SZ catalogues contains all the massive clusters of the RASS catalogues. Interestingly, the distribution of newly-discovered *Planck* clusters extends to higher masses with a median mass of $5.7 \times 10^{14}\,M_\odot$. Besides providing a homogeneous estimate of the masses from an SZ proxy for the largest SZ selected sample of clusters, we show that *Planck* detections significantly extend the mass range in the high-mass region up to $1.6 \times 10^{15}\,M_\odot$.

7.3. M–z distribution and comparison with other surveys

Based on the masses derived from the SZ-proxy, we illustrate for `MMF3` the M–z distribution of *Planck* SZ clusters detected over 83.7% of the sky. We show in all panels of Fig. 28 the limiting mass $M_{\rm lim}$ computed following Planck Collaboration XX (2014) for three values of the completeness: 20% (solid line); 50% (dashed line); and 80% (dotted line). The upper left panel exhibits the *Planck* clusters, with redshifts, detected by `MMF3` at $S/N \geq 4.5$. The mass limit corresponds to the average limit computed from the noise over the 83.7% sky fraction used by the SZ-finder algorithm. The resulting $M_{\rm lim}$ is not representative of the inhomogeneity of the noise across the sky (see Fig. 3). We therefore show the limiting mass in three areas of the sky (Fig. 3): the deep-survey area (upper right panel); the medium-deep survey area (lower left panel); and the shallow-survey area (lower right panel). The lines indicate the limit at which clusters have C% chances to be detected (C being the completeness value). We clearly see that whereas the average $M_{\rm lim}$ at 20% completeness does not fully represent the SZ detections by `MMF3`, the limiting masses in different survey depths are more representative of the detection process. We further note that except at low redshifts, $z < 0.3$–0.4, the *Planck* cluster distribution exhibits a nearly redshift-independent mass limit with a cut that varies according to the survey depth.

It is worth examining the distribution of the *Planck* SZ clusters in the M–z plane and comparing it to that of other catalogues. For illustration, we compare to an X-ray selected sample, namely REFLEX-I, on the one hand (Fig. 29, right panel green open circles) and to the large-area SZ-selected cluster catalogues by ACT (Hasselfield et al. 2013) and SPT (Reichardt et al. 2013), on the other hand (Fig. 29, red open symbols). In this comparison we report, for the ACT clusters (open squares), the so-called UPP (Universal Pressure Profile) masses given in Hasselfield et al. (2013).

The range of redshifts covered by the *Planck* SZ sample, from $z = 0.01$ to about 1 with 67% of the clusters lying below $z = 0.3$, is quite complementary to the high redshift range explored by ACT and in by SPT. For the comparison of the mass distribution we take advantage of our newly-proposed SZ-mass estimate, derived from Y_z, which provides us with a homogeneous definition of the masses over the whole range of *Planck* SZ clusters with measured redshifts. The *Planck* clusters populate the full redshift range and they quite nicely fill a unique space of massive, $M \geq 5 \times 10^{14}\,M_\odot$, and high redshift $z \geq 0.5$ clusters, as shown in Fig. 29. This contrasts with the SZ clusters detected in 720 square degrees of SPT observations and those of ACT observations, which are dominated, as shown in Fig. 29 left panel, by lower-mass higher-redshift clusters (up to $z \sim 1.3$). The combination of *Planck* and SPT/ACT catalogues samples the M–z space in a complementary manner. Clearly the all-sky nature of the *Planck* makes the most massive clusters preferentially accessible to *Planck* whereas the highest redshift clusters, $z \geq 1$, are accessible to SPT.

Very few massive high-redshift clusters exist in the X-ray catalogues, as seen in Fig. 29 (right panel open blue squares). The all-sky NORAS/REFLEX catalogues (Böhringer et al. 2000, 2004) are limited to $z = 0.45$, a result of the $(1+z)^4$ surface brightness dependence of the X-ray detection limit (Fig. 29, right panel, solid green line). The smaller-area MACS sample, based on systematic follow-up of ROSAT bright sources (Ebeling et al. 2007), contains a dozen clusters at $z \geq 0.5$. The 400SD sample (Burenin et al. 2007), based on serendipitous detections in 400 deg^2 of ROSAT pointed observations, contains only two clusters with $M \geq 5 \times 10^{14}\,M_\odot$ and $z \geq 0.5$. Finally, only a couple of clusters in the range $M \geq 5 \times 10^{14}\,M_\odot$ are found in the *XMM-Newton* based serendipitous cluster samples (XCS, Mehrtens et al. 2012; XMM-LSS, Pacaud et al. 2007; XDCP, Fassbender et al. 2011). By contrast to an X-ray selected cluster catalogue, the *Planck* detection-limit, illustrated for the medium-deep survey zone and shown in Fig. 29 (right panel, solid black line), has a much shallower dependence on redshift and is quasi-redshift independent above $z = 0.4$. The difference in cluster selection starts at redshifts $z \geq 0.2$. As a result of the quasi-redshift independent mass-selection of SZ surveys, *Planck* probes deeper than the X-ray selection. This is also seen in the overall distribution of redshifts of the *Planck* clusters, Fig. 24.

This leaves the *Planck* SZ catalogue as the deepest all-sky catalogue spanning the broadest cluster mass range from 0.1 to $1.6 \times 10^{15}\,M_\odot$, and particularly adapted to the detection of rare very massive clusters in the tail of the distribution in the range $M \geq 5 \times 10^{14}\,M_\odot$ and $z \geq 0.5$.

7.4. X-ray flux of the Planck clusters and candidates

For all *Planck* SZ detections, we estimated the unabsorbed fluxes at Earth in the [0.1–2.4] keV band (as in the MCXC) measured

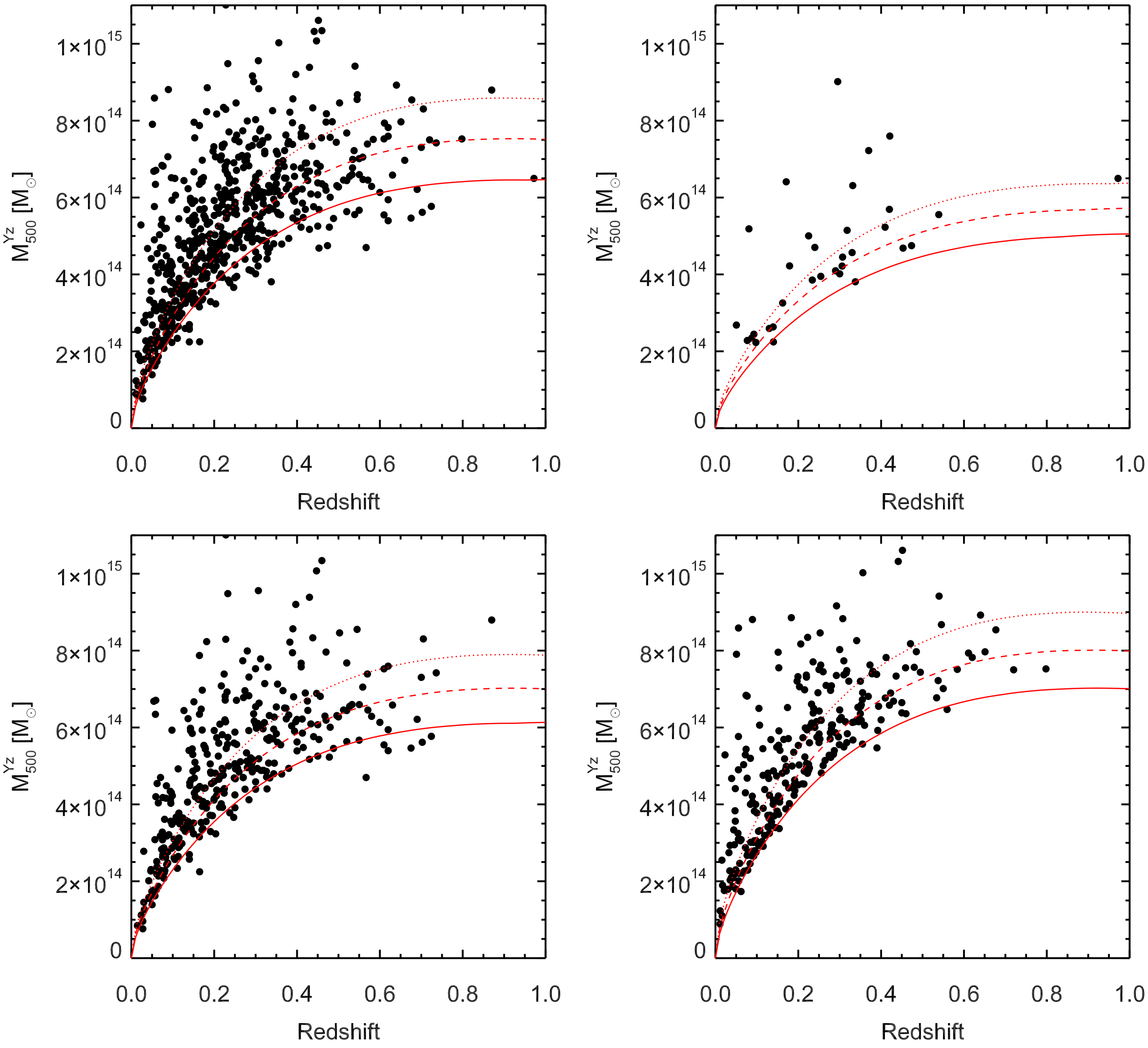

Fig. 28. Mass limit illustrated for SZ detections by `MMF3` algorithm. *Upper left*: average mass limit computed from the average noise over the sky. *Upper right*: same for the deep survey zone corresponding to 2.7% sky coverage centred at the Ecliptic polar regions. *Lower left*: same for the medium-deep survey area covering 41.3% of the sky. *Lower right*: same for the shallow-survey area covering 56% of the sky. In each panel, only detections in the corresponding areas are plotted. The lines dotted, dashed and solid lines show the *Planck* mass limit at 80, 50 and 20% completeness, respectively.

in an aperture of five arcmin. The aperture is centred on the *Planck* candidate position, except for candidates associated with a BSC source, for which we adopt the X-ray position, since the BSC source is very likely the counterpart (Planck Collaboration Int. IV 2013). The conversion between the RASS count rate in the hard band and flux is performed using an absorbed thermal emission model with the N_H value fixed to the 21 cm value. The conversion depends weakly on temperature and redshift and we assumed typical values of $kT = 6$ keV and $z = 0.5$. Planck Collaboration Int. IV (2013) compared such flux estimates with precise *XMM-Newton* fluxes measured within R_{500}, S_{500}, for candidates confirmed with the *XMM-Newton* follow-up programme. These clusters lie in the range $0.1 < z < 0.9$ and the $0.3 \times 10^{-12} < S_{500} < 6 \times 10^{-12}$ erg s^{-1} cm^{-2} flux range. The RASS aperture fluxes were found to underestimate the "true" flux by about 30%.

Figure 30 extends this comparison further to all the *Planck* SZ detections identified with MCXC clusters. Piffaretti et al. (2011) published homogenized L_{500} and R_{500} values derived from the flux given in the original catalogues in various apertures, using an iterative procedure based on the REXCESS L_{500}–M_{500} relation and gas density profile shape. We simply computed S_{500} from L_{500}, taking into account the K-correction at the cluster redshift, but neglecting its variation with temperature.

Although derived from ROSAT survey data as our present flux estimate, S_{500} values from the MCXC are expected to be more accurate due to: (i) optimum choice of the X-ray centre; (ii) higher S/N detection; (iii) more sophisticated flux extraction adapted to data quality and source extent (e.g., growth curve analysis); and (iv) use of R_{500} rather than a fixed aperture. Not surprisingly, the ratio between the present flux estimate and the MCXC value decreases with increasing offset between the

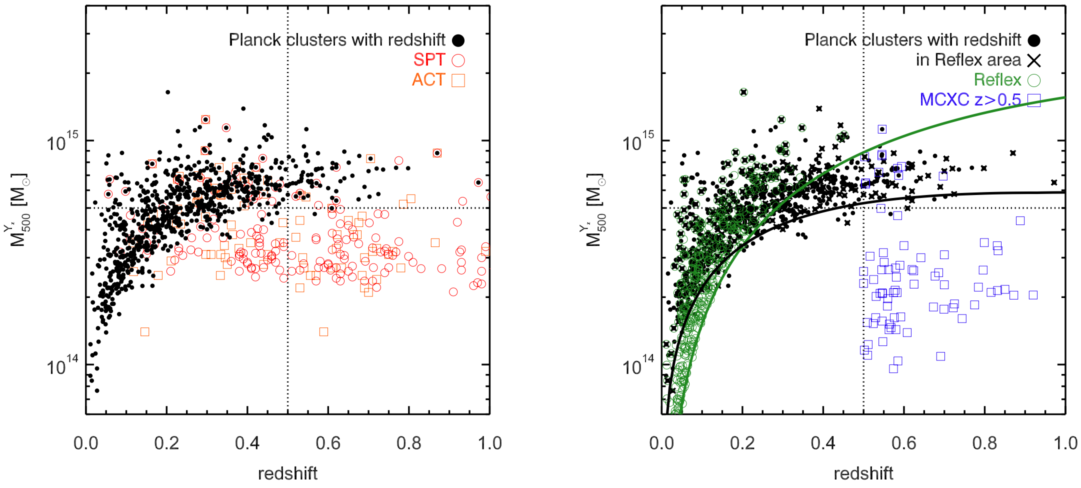

Fig. 29. *Left panel*: distribution in the *M–z* plane of the *Planck* clusters (filled circles) compared with the SPT clusters (open light red circles) from Reichardt et al. (2013) and ACT catalogue (open red squares) from Hasselfield et al. (2013). *Right panel*: distribution in the *M–z* plane of the *Planck* clusters (black symbols) as compared to the clusters from the REFLEX catalogue (green open circles) Böhringer et al. (2004). The black crosses indicate the *Planck* clusters in the REFLEX area. The open blue squares represent clusters from the MCXC catalogue with redshifts above z = 0.5. The green solid line shows the REFLEX detection limit whereas the black solid line shows the *Planck* mass limit for the medium-deep survey zone at 20% completeness.

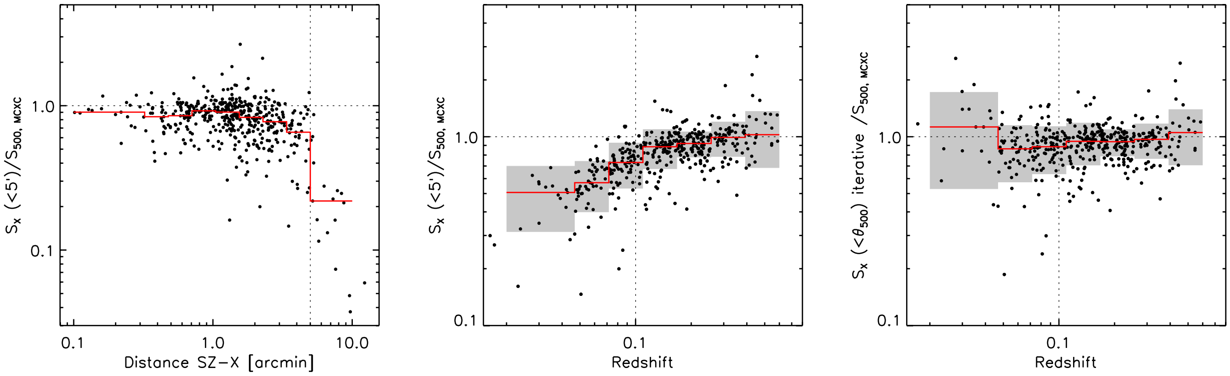

Fig. 30. Ratio between RASS flux, computed in an aperture of five arcmin in radius centred on the *Planck* position, and MCXC value for *Planck* candidates identified with MCXC clusters. The fluxes are computed in the [0.1–2.4] keV band at Earth and corrected for absorption. S_{500} is the flux corresponding to the luminosity within R_{500} published in the MCXC catalogue. *Left panel*: the ratio is plotted as a function of distance between the *Planck* and X-ray positions; *middle panel*: same, as a function of cluster redshift, for distances smaller than five arcmin; *right panel*: same as middle panel, for RASS flux within R_{500} derived from the aperture flux, using the MCXC iterative procedure based on the L_{500}–M_{500} relation and the REXCESS gas density profile (Piffaretti et al. 2011). The red line is the median ratio in distance or redshift bins with the grey area corresponding to $\pm 1\sigma$ standard deviation in each bin.

Planck position and X-ray position (Fig. 30, left panel). The ratio drops dramatically when the distance is larger than five arcmin, i.e., when the X-ray peak lies outside the integration aperture. Those are rare cases, 18 nearby clusters ($z < 0.1$ with a median value of $z = 0.05$), for which a physical offset likely contributes to the overall offset. When these cases are excluded, the median ratio is 0.85 and depends on redshift (Fig. 30, middle panel); it significantly decreases with decreasing redshift below z of 0.1. The median ratio is 0.65 and 0.92, with a standard deviation of 0.10 and 0.15 dex, below and above $z = 0.1$, respectively. This is mostly due to the choice of a fixed aperture that becomes too small as compared to R_{500} at low z. If we apply the same iterative procedure used by Piffaretti et al. (2011) to estimate S_{500} from the aperture flux, the resulting value is consistent on average with the MCXC value at all redshifts (Fig. 30, right panel). The dispersion is slightly increased. The aperture unabsorbed fluxes are thus reliable estimates of the X-ray fluxes above $z > 0.1$ on average.

Figure 31 shows the X-ray flux as function of Y_{500} for *Planck* candidates identified with known clusters, for the confirmed new *Planck* clusters and for the 1 candidates. For *Planck* detections identified with MCXC clusters we plot the more precise published S_{500} value. All three categories of sources behave in a similar manner in good agreement with the range of redshifts probed by the sample. In this respect 1 candidates do not exhibit any departure with respect to the known or confirmed clusters. We provide the X-ray fluxes for the *Planck* clusters and candidates that are not identified with MCXC clusters (see Appendix C and Table C.1). For the *Planck* cluster with MCXC identifier, we refer the reader to the RASS catalogue outputs or

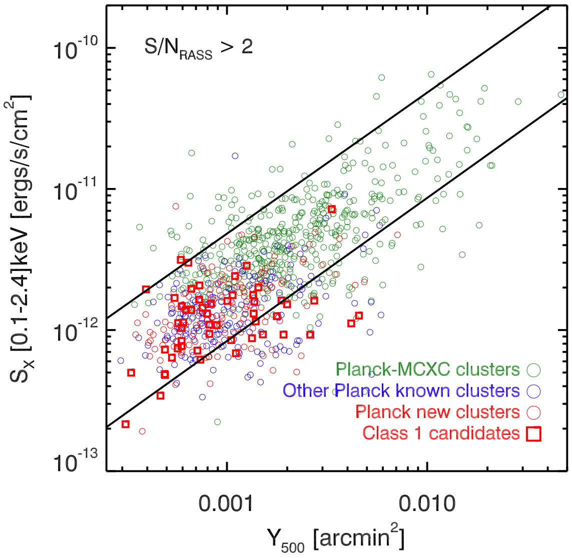

Fig. 31. X-ray unabsorbed flux versus SZ flux. For *Planck* SZ detections identified with MCXC clusters (open green circles), the X-ray flux is estimated from L_{500}. For other *Planck* SZ detections, the flux is derived from RASS count-rate in a five-arcmin aperture (see Sect. 4.1.1). *Planck* new clusters and 1 candidates are shown as open red circles and squares, respectively. The two lines corresponds to the expected L_{500}–Y_{500} relation (Arnaud et al. 2010) at $z = 0.01$ and $z = 1$, respectively.

to the homogenized MCXC meta-catalogue. The main limitation of the aperture unabsorbed fluxes is the statistical precision on the RASS estimate (most of the *Planck* SZ detections not identified with MCXC clusters have low $({\rm S/N})_{\rm RASS}$ values) and the relatively large scatter (±30% standard deviation). For $z < 0.1$ clusters, and if the RASS detection is reasonably good a more precise procedure is recommended, such as an adapted growth curve analysis, on a case-by-case basis.

7.5. Scaling relations between SZ and X-ray quantities

A fundamental scaling relation is that between Y_{500} and its X-ray analogue, $Y_{\rm X}$. Introduced by Kravtsov et al. (2006), $Y_{\rm X}$ is the product of $M_{\rm g,500}$, the gas mass within R_{500}, and $T_{\rm X}$, the spectroscopic temperature outside the core[25]. From the fact that the gas density profile used to compute $M_{\rm g,500}$ is derived from deprojection of the X-ray surface brightness profile, and that the X-ray emission depends on the square of the density, the ratio of these two quantities is

$$\frac{D_{\rm A}^2\,Y_{500}}{C_{\rm XSZ}\,Y_{\rm X}} = \frac{1}{Q}\frac{\langle n_{\rm e}T\rangle_{R_{500}}}{\langle n_{\rm e}\rangle_{R_{500}}T_{\rm X}} \tag{6}$$

$$Q = \frac{\sqrt{\langle n_{\rm e}^2\Lambda_{\rm x}(T)\rangle}}{\sqrt{\langle n_{\rm e}\rangle^2\Lambda_{\rm x}(T)}},$$

where the angle brackets denote volume-averaged quantities, and Q is the emissivity-weighted clumpiness factor, which affects the density profile derived from X-ray data radial bins used to derive the density profile (Zhuravleva et al. 2013). $\Lambda_{\rm x}(T)$ is the temperature-dependent emissivity in the considered X-ray band. The numerical constant $C_{\rm XSZ} = \sigma_{\rm T}/(m_{\rm e}\,c^2\,\mu_{\rm e}\,m_{\rm p}) = 1.416 \times 10^{-19}\,{\rm Mpc}^2\,(M_\odot\,{\rm keV})^{-1}$. The ratio thus depends only on the internal structure of the intra-cluster medium. Note that the conversion of $Y_{500}/Y_{\rm x}$ into the amplitude of density/temperature variations depends on the correlation between variations of these thermodynamic properties, which differ between isobaric and adiabatic cases (see Khedekar et al. 2013, for more details).

The properties of the $Y_{\rm X}$–Y_{500} relation, in particular its variation with mass and redshift and the dispersion about the mean relation, are important probes of the physics of cluster formation.

7.5.1. Data set

Here we extend the study of a sample of 62 clusters from the *Planck*–ESZ sample with good quality *XMM-Newton* archive data presented in Planck Collaboration XI (2011, hereafter PEPXI). This study found $D_{\rm A}^2\,Y_{500}/C_{\rm XSZ}\,Y_{\rm X} = 0.95 \pm 0.03$, in a good agreement with REXCESS prediction, 0.924 ± 0.004, of Arnaud et al. (2010).

All 62 objects in the PEPXI sample are included in the present catalogue. We further add 40 clusters from the catalogue, including nine additional objects from the *XMM-Newton* archival study of *Planck*-detected LoCuSS systems presented by Planck Collaboration Int. III (2013), and the 31 *Planck*-discovered clusters with good redshift estimates ($Q_z = 2$) confirmed with the *XMM-Newton* (Planck Collaboration IX 2011; Planck Collaboration Int. I 2012; Planck Collaboration Int. IV 2013). The total sample thus consists of 102 clusters.

For each object, $Y_{\rm X}$ and the corresponding R_{500} value were estimated simultaneously by iteration about the M_{500}–$Y_{\rm X}$ relation of Arnaud et al. (2010),

$$E^{2/5}(z)M_{500} = 10^{14.567}\left[\frac{Y_{\rm X}}{2\times10^{14}\,M_\odot\,{\rm keV}}\right]^{0.561} M_\odot. \tag{7}$$

In the present study, we focus on the physical relation between Y_{500} and $Y_{\rm X}$. While these quantities must be estimated within the same radii, the exact value of R_{500} is irrelevant as the radial dependence of the $Y_{500}/Y_{\rm X}$ ratio is negligible. We thus propagated only the measurement uncertainties on the temperature and gas mass profiles, fixing the aperture to R_{500}. We ignored the statistical and systematic uncertainties on the M_{500}–Y_{500} relation itself[26]. Similarly Y_{500} was re-extracted at the X-ray position with size fixed to X-ray size. Its uncertainty corresponds to the statistical error on the SZ signal. The results are summarized Table 6, with the best estimate indicated in bold face.

7.5.2. The best-fit Y_{500}–$Y_{\rm X}$ relation

The Y_{500}–$Y_{\rm X}$ scaling relation for the full sample is shown in units of arcmin^2 in Fig. 32. At high flux the points follow the PEP XI relation. The slope and normalization are determined at slightly higher precision, due to the better quality SZ data. The derived intrinsic scatter (Table 6) is significantly smaller, a consequence of the propagation of gas mass profile errors in the $Y_{\rm X}$ error budget, which was neglected in our earlier study.

The relation levels off at around $Y_{\rm X} = 5\times10^{-4}$ arcmin^2, with a bin average deviation increasing with decreasing $Y_{\rm X}$ (Fig. 32

---

[25] Here we use the temperature measured in the [0.15–0.75] R_{500} aperture.

[26] These must however be taken into account when using Y_{500} or $Y_{\rm X}$ as a mass proxy, e.g., when calibrating the Y_{500}–M_{500} relation from combining the M_{500}–$Y_{\rm X}$ relation and the relation between Y_{500} and $Y_{\rm X}$ (or equivalently M_{500}). This calibration is extensively addressed in the Planck Collaboration XX (2014).

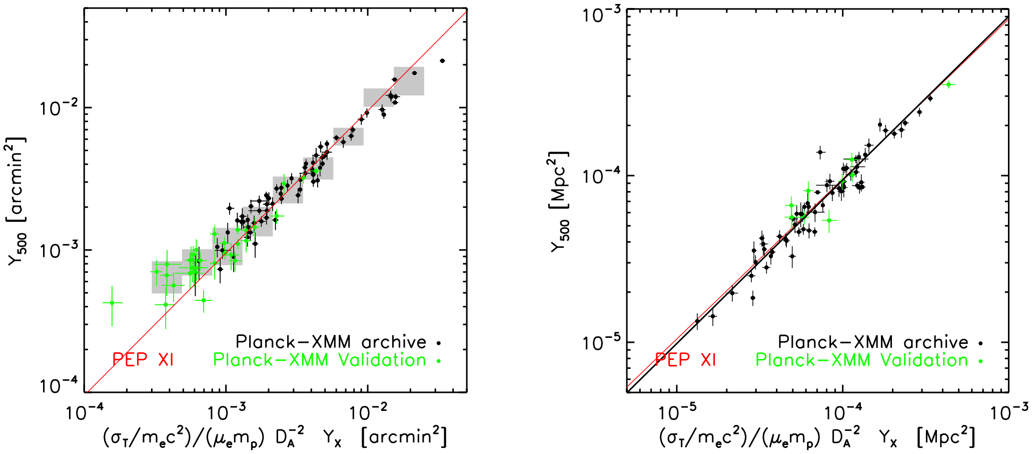

Fig. 32. Relation between the Comptonization parameters Y_{500}, and the normalized Y_X parameter for a sub-sample of the present catalogue. Black points show clusters in the *Planck*-ESZ sample with *XMM-Newton* archival data presented by Planck Collaboration XI (2011) and additional LoCuSS clusters studied by Planck Collaboration Int. III (2013). Green points represent new *Planck* clusters confirmed with *XMM-Newton* (Planck Collaboration IX 2011; Planck Collaboration Int. I 2012; Planck Collaboration Int. IV 2013). The red line denotes the scaling relations of Planck Collaboration XI (2011). *Left panel*: relation in units of arcmin^2 where Y_{500} is extracted using the Arnaud et al. (2010) pressure profile. The grey area corresponds to median Y_{500} values in Y_X bins with $\pm\sigma$ standard deviation. *Right panel*: scaling relation between the intrinsic Compton parameter, $D_A^2 Y_{500}$, and Y_X for the sub-sample of $S/N > 7$ clusters used in the cosmological analysis. The data are corrected for Malmquist bias, and Y_{500} is extracted using the *Planck* pressure profile (see text). The black line is the best-fit power-law relation.

Table 6. The Y_{500}–Y_X relation.

				Power-law fit				Mean ratio		
Sample	MB	Profile	N	$100A$	α	$100\sigma_{\rm int}^{\rm log}$	$100\sigma_{\rm raw}^{\rm log}$	$\Delta\log Q$	$100\sigma_{\rm int}$	$100\sigma_{\rm raw}$
PEPXI	N	A10	62	−2.0 ± 1.0	0.960 ± 0.040	10.0 ± 1.0	. . .	−0.022 ± 0.014	. . .	. . .
ESZ	N	A10	62	−2.2 ± 1.1	0.966 ± 0.034	7.2 ± 1.1	8.2 ± 1.0	−0.023 ± 0.011	7.3 ± 1.1	8.5
ESZ	Y	A10	62	−3.0 ± 1.1	0.975 ± 0.035	7.1 ± 1.1	8.2 ± 1.0	−0.031 ± 0.011	7.2 ± 1.1	8.4
S/N > 7	Y	A10	78	−2.4 ± 1.0	0.972 ± 0.029	6.9 ± 1.1	8.1 ± 0.9	−0.024 ± 0.010	6.9 ± 1.0	8.3
Cosmo	Y	A10	71	−1.9 ± 1.1	0.990 ± 0.032	7.2 ± 1.2	8.3 ± 1.0	−0.021 ± 0.010	6.9 ± 1.0	8.3
Cosmo	Y	A10+err	71	−1.9 ± 1.1	0.987 ± 0.031	6.3 ± 1.1	7.9 ± 0.9	−0.019 ± 0.010	6.5 ± 1.1	8.2
Cosmo	**Y**	**PIP-V**	**71**	**−2.6 ± 1.0**	**0.981 ± 0.027**	**6.6 ± 1.2**	**7.8 ± 1.0**	**−0.027 ± 0.010**	**6.6 ± 1.0**	**8.0**
REXCESS X-ray prediction								−0.034 ± 0.002		

Notes. “MB” is the Malmquist bias correction and “Profile” is the shape used in Y_{500} extraction. Parameters are given for the fit $Y_{500}/Y_p = A\,(Y_X/Y_p)^\alpha$ using BCES orthogonal regression with pivot $Y_p = 10^{-4}\mathrm{Mpc}^2$, along with the intrinsic and raw scatter around the best-fit relation. The mean ratio is $\Delta\log Q = \log(Y_{500}/Y_X)$, with corresponding intrinsic and raw scatter. Scatters are error-weighted values. The best estimate is in bold type. The REXCESS prediction is from Arnaud et al. (2010).

left panel). This is an indication of Malmquist bias, as noted by Planck Collaboration Int. I (2012). Full correction of this bias when fitting scaling relations involves drawing mock catalogues according to the cluster mass function, to which the sample selection criteria are then applied. The present sample is a small subset of the full $S/N \geq 4.5$ *Planck* catalogue and thus such a procedure cannot be applied. To minimize bias effects we will only consider high S/N detections, $S/N > 7$. To correct for the residual bias, we adapted the approach proposed by Vikhlinin et al. (2009). Before fitting the Y_{500}–Y_X relation, each individual Y value was divided by the mean bias, b, given by

$$\ln b = \frac{\exp\left(-x^2/2\sigma^2\right)}{\sqrt{\pi/2}\,\mathrm{erfc}\left(x/\sqrt{2}\sigma\right)}\,\sigma, \tag{8}$$

where $x = -\log(Y/Y_{\rm min})$, $Y_{\rm min}$ being the flux threshold corresponding to the S/N cut, $(\mathrm{S/N})_{\rm cut}$. At the location of the cluster, $Y/Y_{\rm min} = (\mathrm{S/N})/(\mathrm{S/N})_{\rm cut}$. Here σ is the log-normal dispersion at fixed Y_X. We took into account both the intrinsic dispersion $\sigma_{\rm int}$, estimated iteratively, and the statistical dispersion, given by $\sigma = \sqrt{\ln\left[((S/N)+1)/(S/N)\right]^2 + [\ln 10\,\sigma_{\rm int}]^2}$. The correction decreases the effective Y_{500} values at a given Y_X, an effect that is larger for clusters closer to the S/N threshold; i.e., low-flux objects. The net effect on the scaling relation is small, giving a 0.7σ decrease of the normalization and a slight steepening of the power-law slope (Table 6).

The slope and normalization of the relation are robust to the inclusion of newly-discovered *Planck* clusters. The results derived from the extended sample of 78 clusters with $S/N > 7$ agree with those obtained for the updated ESZ-XMM sample within 0.5σ (Table 6). They are also in agreement with the sub-sample of 71 $S/N > 7$ clusters included in the cosmological sample discussed by Planck Collaboration XX (2014). We measured a significant intrinsic scatter of $\sigma_{\rm int} = 0.07 \pm 0.01$ dex. There is one spectacular outlier with an Y_{500}/Y_X ratio nearly twice as big as the mean. This is the *Planck* ESZ cluster identified with A2813 or RXC J0043.4-2037 in the REFLEX catalogue, located at $z = 0.29$. Its high ratio is very puzzling. It cannot result from an inaccurate redshift measurement, as this is based on spectroscopic data for several cluster galaxies (Böhringer et al. 2004). There is no evidence of a peculiar dynamical state from the X-ray morphology, and there is no evidence of contamination in the SZ data.

Part of the dispersion could be due to the use of an inappropriate fixed pressure profile in the Y_{500} extraction. When including possible errors on Y_{500} due to dispersion around the mean Arnaud et al. (2010) profile, the scatter is decreased to $\sigma_{\rm int} = 0.06$, a decrease at the 1σ level. To further assess the effect of the choice of the pressure profile, we re-extracted the SZ signal using the *Planck+XMM-Newton* profile shape measured for ESZ clusters by Planck Collaboration Int. V (2013, hereafter PIPV). Individual profiles are used for *Planck* ESZ clusters, and the mean profile is used for the other clusters. This should give the most reliable estimate of the Y_{500}–$Y_{\rm X}$ relation, since it is based directly on measured profile shapes. In this case, the slope and scatter remain unchanged but the normalization is slightly decreased (at the 0.5σ level). This is a result of the more inflated nature of the PIPV profile as compared to the Arnaud et al. (2010) REXCESS profile. The relation derived using PIPV pressure profiles is plotted in the right-hand panel of Fig. 32 together with the corresponding data points.

The relation does not exhibit significant evidence of variance of the $Y_{500}/Y_{\rm X}$ ratio with mass, the slope is consistent with unity, as expected from strong self-similarity of pressure profile shape. However, we found an intrinsic scatter about three times larger than the results of Kay et al. (2012). Partly this is due to the presence of outliers in our data set (as discussed above), or it may be due to projection effects in observed data sets (Kay et al. 2012). The mean ratio is very well constrained with a precision of 2.5%, $\log(Y_{500}/Y_{\rm X}) = -0.027 \pm 0.010$. This confirms at higher precision the strong agreement between the SZ and X-ray measurements (within R_{500}) of the intra-cluster gas properties found by PEP XI and other studies (Andersson et al. 2011; Sifón et al. 2013; Marrone et al. 2012; Rozo et al. 2012). The ratio is consistent with the X-ray prediction. In the simplest scenario of pure density variations in an isothermal ICM at the scale of the radial bin, this suggests a low clumpiness factor. However there are still large systematics that are discussed in Appendix D. We can translate those into an upper limit of order 30%.

8. Summary

Planck's all-sky coverage and broad frequency range are designed to detect the SZ signal of galaxy clusters across the sky. We provide, from the first 15.5 months of observations, the largest ensemble of SZ-selected sources detected from an all-sky survey. The *Planck* catalogue of SZ sources contains 1227 detections. This catalogue, statistically characterized in terms of completeness and statistical reliability, was validated using external X-ray and optical/NIR data, alongside a multi-frequency follow-up programme for confirmation. A total of 861 SZ detections are confirmed associations with bona fide clusters, of which 178 are brand-new clusters. The remaining 366 cluster candidates are divided into three classes according to their reliability, i.e., the quality of evidence that they are likely to be bona fide clusters.

A total of 813 *Planck* clusters have measured redshifts ranging from $z = 0.01$ to order one, with one-third of the clusters lying above $z = 0.3$. The brand-new *Planck* clusters extend the redshift range above $z = 0.3$. For all the *Planck* clusters with measured redshift, a mass can be estimated from the Compton Y measure. We provide a homogeneous mass estimate ranging from $(0.1 \text{ to } 1.6) \times 10^{15}\,M_\odot$. Except at low redshifts, the *Planck* cluster distribution exhibits a nearly redshift-independent mass limit and occupies a unique region in the M–z space of massive, $M \geq 5 \times 10^{14}\,M_\odot$, and high-redshift ($z \geq 0.5$) clusters. Owing to its all-sky nature, *Planck* detects new clusters in a region of the mass–redshift plane that is sparsely populated by the RASS catalogues. It detects the rarest clusters, i.e., the most massive clusters at high redshift in the exponential tail of the cluster mass function that are the most useful clusters for cosmological studies. With the presently confirmed *Planck* SZ detections, *Planck* doubles the number of massive clusters above redshift 0.5, as compared to other surveys. The *Planck* SZ catalogue is, and will be for years to come, the deepest all-sky SZ catalogue spanning the broadest cluster mass range.

The *Planck* SZ catalogue should motivate multi-wavelength follow-up efforts. The confirmation of the cluster candidates will reveal clusters at higher redshifts than the present distribution. Such follow-up efforts will further enhance the value of the *Planck* SZ catalogue as the first all-sky SZ selected catalogue. It will serve as a reference for studies of cluster physics (e.g., galaxy properties versus intra-cluster gas physics, dynamical state, evolution, etc.). Using an extended sub-sample of the *Planck* SZ clusters with high-quality *XMM-Newton* data, the scaling relations between SZ and X-ray properties were reassessed and updated. With better-quality data and thus higher precision, we show excellent agreement between SZ and X-ray measurements of the intra-cluster gas properties. We have thus derived a new up-to-date reference calibrated local relation between Y and $Y_{\rm X}$.

The *Planck* SZ catalogue will also serve to define samples for cosmological studies. A first step in this direction is already taken in Planck Collaboration XX (2014), where an analysis of the SZ cluster abundance to constrain the cosmological parameters is performed using a sub-sample selected from the PSZ catalogue consisting of 189 clusters detected above a S/N of 7 with measured redshifts. The value-added information derived from the validation of the *Planck* SZ detections, in particular the SZ-based mass estimate, increases even further the value of the *Planck* SZ catalogue.

The combination of the *Planck* all-sky SZ data with near future and planned observations of the large-scale structure by surveys such as PAN-STARRS, LOFAR, Euclid, LSST, and RSG/e-ROSITA will revolutionize our understanding of large-scale structure formation and evolution.

Acknowledgements. The development of *Planck* has been supported by: ESA; CNES and CNRS/INSU-IN2P3-INP (France); ASI, CNR, and INAF (Italy); NASA and DoE (USA); STFC and UKSA (UK); CSIC, MICINN, JA and RES (Spain); Tekes, AoF and CSC (Finland); DLR and MPG (Germany); CSA (Canada); DTU Space (Denmark); SER/SSO (Switzerland); RCN (Norway); SFI (Ireland); FCT/MCTES (Portugal); and PRACE (EU). A description of the *Planck* Collaboration and a list of its members, including the technical or scientific activities in which they have been involved, can be found at `http://www.sciops.esa.int/index.php?project=planck&page=Planck_Collaboration`. The authors thank N. Schartel, ESA *XMM-Newton* project scientist, for granting the Director Discretionary Time used for confirmation of SZ *Planck* candidates. The authors thank TUBITAK, IKI, KFU and AST for support in using RTT150 (Russian-Turkish 1.5-m telescope, Bakyrlytepe, Turkey); in particular we thank KFU and IKI for providing significant amount of their observing time at RTT150. We also thank BTA 6-m telescope Time Allocation Committee (TAC) for support of optical follow-up project. The authors acknowledge the use of the INT and WHT telescopes operated on the island of La Palma by the Isaac Newton Group of Telescopes at the Spanish Observatorio del Roque de los Muchachos of the Instituto de Astrofísica de Canarias (IAC); the Nordic Optical Telescope, operated on La Palma jointly by Denmark, Finland, Iceland, Norway, and Sweden, at the Spanish Observatorio del Roque de los Muchachos of the IAC; the TNG telescope, operated on La Palma by the Fundacion *Galileo Galilei* of the INAF at the Spanish Observatorio del Roque de los Muchachos of the IAC; the

GTC telescope, operated on La Palma by the IAC at the Spanish Observatorio del Roque de los Muchachos of the IAC; and the IAC80 telescope operated on the island of Tenerife by the IAC at the Spanish Observatorio del Teide of the IAC. Part of this research has been carried out with telescope time awarded by the CCI International Time Programme. The authors thank the TAC of the MPG/ESO-2.2 m telescope for support of optical follow-up with WFI under *Max Planck* time. Observations were also conducted with ESO NTT at the La Silla Paranal Observatory. This research has made use of SDSS-III data. Funding for SDSS-III `http://www.sdss3.org/` has been provided by the Alfred P. Sloan Foundation, the Participating Institutions, the National Science Foundation, and DoE. SDSS-III is managed by the Astrophysical Research Consortium for the Participating Institutions of the SDSS-III Collaboration. This research has made use of the following databases: the NED and IRSA databases, operated by the Jet Propulsion Laboratory, California Institute of Technology, under contract with the NASA; SIMBAD, operated at CDS, Strasbourg, France; SZ cluster database operated by Integrated Data and Operation Center (IDOC) operated by IAS under contract with CNES and CNRS. The authors acknowledge the use of software provided by the US National Virtual Observatory.

Appendix A: Selection of frequency channel maps

An assessment of which combination of *Planck* frequency channels to use was performed using the `MMF1` implementation of the matched multi-filter described in Sect. 2.2.2. The HFI and LFI channel maps were preprocessed as described in Sect. 2.1, with the only difference being that the point-source mask contained, in addition, detections from the LFI channel maps with $S/N \geq 10$. Five different combinations of frequency channels were investigated, all *Planck* channels (30–857 GHz), all HFI channels plus the 70 GHz channel map from LFI (70–857 GHz), all HFI channels (100–857 GHz), the five lowest frequency HFI channels (100–545 GHz) and the four lowest frequency HFI channels (100–353 GHz). For each combination of frequency channels a catalogue of SZ sources was extracted, resulting in five different catalogues; the only differences between them must be entirely due to the choice of channels in the combination.

The first four of these catalogues are in good agreement in terms of the clusters detected, with all the differences amongst them being due to detections with $S/N < 5$. The (100–353 GHz) catalogue, however, contains significantly more detections, resulting in a poor agreement between it and the other catalogues that is not limited to low S/N detections. This is interpreted as being due to the lack of a dust-dominated channel in this combination, without which it is more difficult to constrain contamination due to dust emission.

In order to assess any improvement in the S/Ns of detected clusters with the inclusion of extra data, a robust sample of reliable sources is required. To produce this, only clusters outside the 65% dust mask and with $S/N \geq 8$ were kept from each combination. The differences in the S/N of the same sources detected using different frequency channel combinations can then be examined. The ratio between the S/N values of the common detections in each combination to those of the (100–857 GHz) combination was then found; the mean of this ratio is shown in Table A.1. This approach clearly shows the (100–353 GHz) combination to be considerably noisier than the other combinations, which is consistent with the observations reported above. Neither the inclusion of the LFI frequency channels or just the 70 GHz channel brings any significant improvement in the S/N of the clusters. Using the six HFI channel combination results in marginally better S/N than the (100–545 GHz) combination. The frequency channel combination chosen therefore is (100–857 GHz) since this gives the highest S/N with the smallest data-set. Reducing the S/N threshold from 8 to 6 and hence doubling the number of SZ sources used to evaluate the mean ratio does not change the conclusions of this analysis.

Table A.1. Effect of frequencies used in the extraction on the S/N of the detections.

Selection criterion	Mean ratio of detection S/N			
	$\frac{100\to353}{100\to857}$	$\frac{100\to545}{100\to857}$	$\frac{70\to857}{100\to857}$	$\frac{30\to857}{100\to857}$
$S/N \geq 6$	0.86	0.99	1.00	1.00
$S/N \geq 8$	0.84	0.98	1.00	1.00

Notes. The set of frequencies used is specified as a range, e.g., 100 → 353 (in GHz). For a given cluster detected in two sets of frequencies, the ratio of S/N for the two detections is written as, e.g., $(100 \to 353)/(100 \to 857)$. The improvement in the S/N of the detected clusters between the 100 → 353 and 100 → 857 combinations is clearly demonstrated, as is the lack of significant improvement when 30 or 70 GHz data are included. The improvement between the 100 → 545 and 100 → 857 combinations is smaller, in the range 1 to 2%.

Appendix B: Extract from the *Planck* catalogue of SZ sources

We describe here the *Planck* catalogue of SZ sources delivered by the collaboration and available together with the individual lists from all three detections methods, the union mask used by these methods and the ensemble of notes on individual clusters[27].

The union *Planck* SZ catalogue contains the coordinates and the S/N of the SZ detections and a summary of the validation information, including external identification of the cluster and redshifts if they are available. The external identification quoted in the delivered product corresponds to the first identifier as defined in the external validation hierarchy, namely identification with MCXC clusters followed by Abell and Zwicky, followed by SDSS-based catalogues, followed by SZ catalogues, followed finally by searches in NED and SIMBAD. Due to the size–flux degeneracy discussed in Sect. 2.3, no reference flux quantity is outputted for the union catalogue.

The individual catalogues from the three detection methods, `MMF1`, `MMF3`, and `PwS`, contain the coordinates and the S/N of the detections, and information on the size and flux of the clusters. The size is given in terms of θ_s and the flux is given in terms of the total integrated Comptonization parameter, $Y = Y_{5R_{500}}$. The full information on the degeneracy between and Y is provided in the form of the two-dimensional marginal probability distribution for each cluster.

The degeneracy information is provided in this form so that it can be combined with a model or external data to produce tighter constraints on the parameters. For example, combining it with an X-ray determination of the size can be done by taking a slice through the distribution at the appropriate θ_s. This is what is done in Sect. 7.2.1 and the refined measurement using X-ray information can be found in Table C.1.

Table B.1 presents an extract of the PSZ catalogue, in terms of the first rows of the online table and the following selected columns:
Name: name of cluster.
RA, Dec: right ascension (J2000) and declination (J2000).
S/N: signal-to-noise ratio of the SZ detection.

---

[27] `http://www.sciops.esa.int/index.php?page=Planck_Legacy_Archive\&project=planck`

Table B.1. Extract from the *Planck* catalogue of SZ sources.

Name	RA	Dec	S/N	Validation	$\mathrm{ID_{EXT}}$	z	Comments
PSZ1 G000.08+45.15	229.°19790	−0.°979280	4.60	20	RXC J1516.5−0056	0.1198	F
PSZ1 G000.42−41.84	316.°06990	−41.°339730	5.99	20	RXC J2104.3−4120	0.1651	F
PSZ1 G000.77−35.67	307.°93571	−40.°595198	5.30	20	RXC J2031.8−4037	0.3416	F
PSZ1 G001.00+25.71	244.°58411	−13.°070074	6.04	3	. . .	. . .	F
PSZ1 G002.24−68.27	349.°60728	−36.°278003	4.50	20	ACO S 1109	0.1400	F
PSZ1 G002.77−56.16	334.°65975	−38.°880540	7.84	20	RXC J2218.6−3853	0.1411	F
PSZ1 G002.80+39.24	234.°99997	−3.°292940	7.03	20	RXC J1540.1−0318	0.1533	F
PSZ1 G003.09−22.51	292.°16440	−35.°711064	4.92	3	. . .	. . .	F

Notes. The first rows of the online table are shown. The online table contains additional columns as described in the Explanatory Supplement and in the text.

Table C.1. Information from external validation.

Name	z	Src	Y_z [10^{-4} arcmin^2]	$M_{500}^{Y_z}$ [$10^{14}\,M_\odot$]	S_{X} [erg s^{-1} cm^2]	ID	$Y_{500,\mathrm{PSX}}$ [10^{-4} arcmin^2]	S/N_{PSX}
PSZ1 G000.08+45.15	0.1198	(1)	$12.35^{+3.43}_{-3.33}$	$3.10^{+0.45}_{-0.50}$	. . .	RXC J1516.5−0056, A2051	12.43	4.34
PSZ1 G000.42−41.84	0.1651	(1)	$14.05^{+2.78}_{-2.70}$	$4.46^{+0.47}_{-0.50}$	. . .	RXC J2104.3−4120, A3739	14.35	6.18
PSZ1 G000.77−35.67	0.3416	(1)	$9.14^{+1.98}_{-1.93}$	$6.20^{+0.72}_{-0.77}$	. . .	RXC J2031.8−4037	7.89	4.37
PSZ1 G001.00+25.71	. . .	(−1)	. . .	. . .	$\leq 1.35 \times 10^{-12}$	. . .	. . .	. . .
PSZ1 G002.24−68.27	0.1400	(2)	$7.43^{+2.71}_{-2.61}$	$2.69^{+0.51}_{-0.58}$	$(1.74 \pm 0.65) \times 10^{-12}$	ACO S 1109	. . .	. . .
PSZ1 G002.77−56.16	0.1411	(1)	$18.29^{+2.92}_{-2.85}$	$4.49^{+0.39}_{-0.41}$	. . .	RXC J2218.6−3853, A3856	15.09	6.56
PSZ1 G002.80+39.24	0.1533	(1)	$26.14^{+4.68}_{-4.53}$	$5.91^{+0.57}_{-0.60}$	. . .	RXC J1540.1−0318, A2104	22.13	6.41
PSZ1 G003.09−22.51	. . .	(−1)	. . .	. . .	$\leq - 0.07 \times 10^{-12}$	. . .	. . .	. . .

Notes. The "Src" for the cluster redshift is a code expanded in the readme file. Y_z is the SZ signal with asymmetric errors, computed within R_{500}. $M_{500}^{Y_z}$ is the derived mass with asymmetric errors. S_{X} is the unabsorbed X-ray flux measured in an aperture of 5′ in the band [0.1–2.4] keV. The aperture is centred on the *Planck* position, except for candidates associated with a BSC source, for which we adopt the X-ray position. For sources with $(S/N)_{\mathrm{RASS}} < 1\sigma$, we quote an upper limit. "`ID`" gives other names for previously-known clusters. $Y_{500,\mathrm{PSX}}$ is the SZ signal re-extracted after fixing size and position to the values given in the MCXC X-ray catalogue, if available. $\mathrm{S/N_{PSX}}$ is the associated S/N in the *Planck* data. The full table and the readme file are available at `http://www.sciops.esa.int/index.php?page=Planck_Legacy_Archive\&project=planck.`

Validation: status of the SZ detection from external validation: 20 = previously-known cluster; 10 = new confirmed *Planck* cluster; 1 = 1 candidate ; 2 = 2 candidate; 3 = 3 candidate.
$\mathrm{ID_{EXT}}$: first external identifier of the known clusters.
z: redshift of the cluster as reported from the external validation.
Comments: F = no comment; T = comment. Comments are readable in an external file.
The complete version of the PSZ catalogue also contains the additional columns:
Index: index of the detection, determined by the order of the clusters in the union catalogue and sorted into order of ascending Galactic longitude.
GLON, GLAT: Galactic coordinates.
POS_ERR: errors on the position.
Pipeline: pipeline from which information is taken; namely 1 = `MMF1`; 2 = `MMF3`; 3 = `PwS`.
PIPE_DET: pipeline making the detection, with the following order in bits: 1st = `MMF1`; 2nd = `MMF3`; 3rd = `PwS`.
PCCS: flag for a match with sources from the PCCS catalogue.
COSMO: flag for those clusters that are included in the sample used for the cosmological analysis of Planck Collaboration XX (2014).

Appendix C: Outstanding outputs from the external validation

Based on the ancillary data used for the validation of the *Planck* SZ catalogue, we provide value-added information to the *Planck* SZ detections.

Namely, we provide, in addition to the first external identifier, possible other common identifiers, `ID`s.

We report the redshift information associated with the *Planck* clusters (z) and specify its source, (`scr`).

For clusters with measured redshifts, we compute the SZ-proxy Y_z and the mass estimate ($M_{500}^{Y_z}$) and associated errors. For the clusters identified with MCXC clusters we provide the SZ signal, $Y_{500,\mathrm{PSX}}$, re-extracted fixing the size to the X-ray size provided in the MCXC catalogue at the X-ray position. We also provide the associated S/N in the *Planck* data. Note that the X-ray positions used in the present study are those quoted in the MCXC meta-catalogue. The positions reported in the ESZ sample were taken from a sampled grid of coordinates with a pixel size of 1.71 arcmin. Due to this sampling, the reported MCXC positions in the ESZ sample exhibit an average offset of 70 arcsec (less than a pixel, which varies depending on the position of the object on the sphere).

For *Planck* SZ detections not associated with a previously-known X-ray cluster and with $(S/N)_{\rm RASS} \geq 1\sigma$, we provide the unabsorbed X-ray flux, $S_{\rm X}$ (and error), measured in an aperture of 5 arcmin in the band [0.1–2.4] keV. We only provide an upper limit in the case of $(S/N)_{\rm RASS} < 1\sigma$, except for three SZ detections for which RASS exposure is very low and $(S/N)_{\rm RASS} < -5\sigma$. The aperture is centred on the *Planck* position, except for candidates associated with a BSC source for which we adopt the X-ray position. These clusters are flagged.

Appendix D: Systematic effects on the X-ray versus SZ scaling relation

Both X-ray and SZ measurements are likely affected by systematic effects linked to e.g., background estimation and subtraction methods, calibration issues, etc. One sign of the impact of these effects is the fact that the slope of the relation between Y_{500} flux and $Y_{\rm X}/D_{\rm A}^2$ in units of arcmin^2 is $\alpha = 0.91 \pm 0.02$, which is significantly smaller than unity even after Malmquist bias correction. As this is not the case for the relation in physical units (Mpc^2), the observed slope cannot be due to a true physical variation in the ratio (e.g., with mass).

SZ fluxes are subject to uncertainties due to systematic differences between measurement methods. From the comparison between `PwS` and `MMF` photometry (Sect. 2.3), we estimate that the net effect is typically 0.03 dex. The effect is independent of SZ flux, thus cannot explain the shallower than expected slope.

Uncertainties in the X-ray measurements are dominated by temperature uncertainties due to calibration systematics. We can investigate the magnitude of these effects by examining the relation between the $Y_{\rm X}$ values obtained with *XMM-Newton* by Planck Collaboration XI (2011, hereafter the PEP XI ESZ-XMM sample) to those obtained with *Chandra* in a study of 28 clusters from the same sample by Rozo et al. (2012; hereafter the ESZ–*Chandra* sample). The *Chandra* values are larger, with a mean offset of 0.02 dex. However, there is no significant evidence of variation with $Y_{\rm X}$, thus X-ray calibration issues again cannot explain the observed slope.

A further source of uncertainty in X-ray measurements concerns the X-ray analysis method (e.g., due to background estimation and subtraction of point sources and substructure). Rozo et al. (2012) noted the difference between the ratio obtained with ESZ-*Chandra* and ESZ-XMM samples and suggested that it might be due to *XMM-Newton* data analysis issues. The PEP XI ESZ-XMM sample was analysed by two independent methods depending on the cluster extension in the field-of-view. Sub-sample A consisted of 19 nearby clusters that extend beyond the *XMM-Newton* field–of–view, and for which direct background estimates are not possible, while the background for the remaining 43 objects was estimated using a region external to the cluster. The ESZ–*Chandra* sample studied by Rozo et al. (2012) consists mostly sub-sample A objects. While systematic effects due to background estimation are certainly more important for sub-sample A than for sub-sample B, these effects cannot fully explain the observed behaviour of the $Y_{500}/Y_{\rm X}$ ratio. Indeed, excluding sub-sample A clusters, the slope of the Y_{500}–$Y_{\rm X}/D_{\rm A}^2$ relation is $\alpha = 0.89 \pm 0.04$, still significantly smaller than unity. The origin of the systematic differences between sub-sample A and B objects is unclear.

The variation of the $Y_{500}/Y_{\rm X}$ ratio with flux remains largely unexplained. It may be due to residual Malmquist bias, in addition to a complex combination of systematic effects in SZ and X–ray measurements. For instance, we note that higher flux clusters correspond to nearby objects that have larger angular sizes. The background estimate in both X-ray and SZ signals is subject to larger uncertainty in this case.

The lack of a complete explanation for the observed slope of the Y_{500}–$Y_{\rm X}$ relation, and its ultimate correction, has several implications. Firstly, the shallower slope in units of arcmin^2 translates into an over-estimate of the dispersion about the relation when measured in Mpc^2. From the difference in intrinsic scatter about the relation in both physical and arcmin units, we estimate that this effect contributes at the level of about 0.01 dex to the scatter seen in the physical Y_{500}–$Y_{\rm X}$ relation.

Secondly, the $Y_{500}/Y_{\rm X}$ ratio will depend on the exact sample definition, via the range of fluxes probed. The observed slope of $\alpha = 0.91 \pm 0.02$ translates into a variation of about ± 0.06 dex of the $Y_{500}/Y_{\rm X}$ ratio over the range of SZ fluxes studied here. The ESZ–*Chandra* objects studied by Rozo et al. (2012) lie preferentially at high fluxes, with a median flux two times higher than the PEP XI-XMM sample. For $\alpha = 0.91$, this will translate into a roughly 0.03 dex difference in the $Y_{500}/Y_{\rm X}$ ratio. The $Y_{500}/Y_{\rm X}$ ratio found by Rozo et al. (2012), $\log(Y_{500}/Y_{\rm X}) = -0.088 \pm 0.012$, is significantly lower than our value of -0.027 ± 0.010. However, it can be explained by a combination of their sample definition, a neglect of Malmquist bias, and the aforementioned calibration issues between *XMM-Newton* and *Chandra*.

In summary, uncertainties on the $Y_{500}/Y_{\rm X}$ ratio are dominated by systematic effects in both X–ray and SZ measurements. This unfortunately precludes any definitive statement on the magnitude of the gas clumpiness within R_{500}. Follow-up of well-defined sub-samples (e.g., above a given S/N) should help to disentangle biases due to sample selection and measurement of the different quantities.

References

Abdo, A. A., Ackermann, M., Ajello, M., et al. 2010, ApJ, 715, 429
Abell, G. O. 1958, ApJS, 3, 211
Abell, G. O., Corwin, Jr., H. G., & Olowin, R. P. 1989, ApJS, 70, 1
Afanasiev, V. L., & Moiseev, A. V. 2005, Astron. Lett., 31, 194
Aghanim, N., de Luca, A., Bouchet, F. R., Gispert, R., & Puget, J. L. 1997, A&A, 325, 9
Aghanim, N., Hansen, S. H., & Lagache, G. 2005, A&A, 439, 901
Aghanim, N., da Silva, A. C., & Nunes, N. J. 2009, A&A, 496, 637
Ahn, C. P., Alexandroff, R., Allende Prieto, C., et al. 2012, ApJS, 203, 21
Akritas, M. G. & Bershady, M. A. 1996, ApJ, 470, 706
Allen, S. W., Evrard, A. E., & Mantz, A. B. 2011, ARA&A, 49, 409
AMI Consortium, Zwart, J. T. L., Barker, R. W., et al. 2008, MNRAS, 391, 1545
AMI Consortium, Hurley-Walker, N., Brown, M. L., et al. 2011, MNRAS, 414, L75
Andersson, K., Benson, B. A., Ade, P. A. R., et al. 2011, ApJ, 738, 48
Angulo, R. E., Springel, V., White, S. D. M., et al. 2012, MNRAS, 426, 2046
Arnaud, M., Pointecouteau, E., & Pratt, G. W. 2005, A&A, 441, 893
Arnaud, M., Pratt, G. W., Piffaretti, R., et al. 2010, A&A, 517, A92
Bajkova, A. T. 2005, Astron. Rep., 49, 947
Barbosa, D., Bartlett, J. G., Blanchard, A., & Oukbir, J. 1996, A&A, 314, 13
Belsole, E., Birkinshaw, M., & Worrall, D. M. 2005, MNRAS, 358, 120
Benítez, N. 2000, ApJ, 536, 571
Bertin, E., & Arnouts, S. 1996, A&AS, 117, 393
Bock, D., Large, M. I., & Sadler, E. M. 1999, AJ, 117, 1578
Böhringer, H., Voges, W., Huchra, J. P., et al. 2000, ApJS, 129, 435
Böhringer, H., Schuecker, P., Guzzo, L., et al. 2004, A&A, 425, 367
Böhringer, H., Schuecker, P., Pratt, G. W., et al. 2007, A&A, 469, 363
Borgani, S., & Kravtsov, A. 2009 [`arXiv:0906.4370`]
Borgani, S., Murante, G., Springel, V., et al. 2004, MNRAS, 348, 1078
Burenin, R. A., Vikhlinin, A., Hornstrup, A., et al. 2007, ApJS, 172, 561
Carvalho, P., Rocha, G., & Hobson, M. P. 2009, MNRAS, 393, 681
Carvalho, P., Rocha, G., Hobson, M. P., & Lasenby, A. 2012, MNRAS, 427, 1384
Chon, G., & Böhringer, H. 2012, A&A, 538, A35
Clerc, N., Sadibekova, T., Pierre, M., et al. 2012, MNRAS, 423, 3561

Condon, J. J., Cotton, W. D., Greisen, E. W., et al. 1998, AJ, 115, 1693
Crawford, C. S., Allen, S. W., Ebeling, H., Edge, A. C., & Fabian, A. C. 1999, MNRAS, 306, 857
Cunha, C. E., Lima, M., Oyaizu, H., Frieman, J., & Lin, H. 2009, MNRAS, 396, 2379
da Silva, A. C., Kay, S. T., Liddle, A. R., & Thomas, P. A. 2004, MNRAS, 348, 1401
Ebeling, H., Barrett, E., Donovan, D., et al. 2007, ApJ, 661, L33
Eckert, D., Molendi, S., & Paltani, S. 2011, A&A, 526, A79
Fabian, A. C. 2012, ARA&A, 50, 455
Fassbender, R., Böhringer, H., Nastasi, A., et al. 2011, New J. Phys., 13, 5014
Fusco-Femiano, R., Lapi, A., & Cavaliere, A. 2013, ApJ, 763, L3
Giles, P. A., Maughan, B. J., Birkinshaw, M., Worrall, D. M., & Lancaster, K. 2012, MNRAS, 419, 503
Gioia, I. M., Henry, J. P., Mullis, C. R., et al. 2003, ApJS, 149, 29
Hao, J., McKay, T. A., Koester, B. P., et al. 2010, ApJS, 191, 254
Hasselfield, M., Hilton, M., Marriage, T. A., et al. 2013, J. Cosmol. Astropart. Phys., 7, 8
Herranz, D., Sanz, J. L., Hobson, M. P., et al. 2002, MNRAS, 336, 1057
Hlavacek-Larrondo, J., Fabian, A. C., Edge, A. C., et al. 2012, MNRAS, 421, 1360
Hudson, D. S., Mittal, R., Reiprich, T. H., et al. 2010, A&A, 513, A37
Hurier, G., Macías-Pérez, J. F., & Hildebrandt, S. 2013, A&A, 558, A118
Johnston, D. E., Sheldon, E. S., Wechsler, R. H., et al. 2007, unpublished [arXiv:0709.1159]
Kay, S. T., Peel, M. W., Short, C. J., et al. 2012, MNRAS, 422, 1999
Kepner, J., Fan, X., Bahcall, N., et al. 1999, ApJ, 517, 78
Khedekar, S., Churazov, E., Kravtsov, A., et al. 2013, MNRAS, 431, 954
Koester, B. P., McKay, T. A., Annis, J., et al. 2007, ApJ, 660, 239
Kravtsov, A. V., Vikhlinin, A., & Nagai, D. 2006, ApJ, 650, 128
Lapi, A., Cavaliere, A., & Fusco-Femiano, R. 2012, ApJ, 745, L15
Lin, Y., Partridge, B., Pober, J. C., et al. 2009, ApJ, 694, 992
Lin, Y.-T., Stanford, S. A., Eisenhardt, P. R. M., et al. 2012, ApJ, 745, L3
Magliocchetti, M., & Brüggen, M. 2007, MNRAS, 379, 260
Mann, A. W., & Ebeling, H. 2012, MNRAS, 420, 2120
Mantz, A., Allen, S. W., Ebeling, H., Rapetti, D., & Drlica-Wagner, A. 2010, MNRAS, 406, 1773
Marrone, D. P., Smith, G. P., Okabe, N., et al. 2012, ApJ, 754, 119
Maughan, B. J., Giles, P. A., Randall, S. W., Jones, C., & Forman, W. R. 2012, MNRAS, 421, 1583
McNamara, B. R. & Nulsen, P. E. J. 2012, New J. Phys., 14, 055023
Mehrtens, N., Romer, A. K., Hilton, M., et al. 2012, MNRAS, 423, 1024
Melin, J., Bartlett, J. G., & Delabrouille, J. 2006, A&A, 459, 341
Melin, J.-B., Aghanim, N., Bartelmann, M., et al. 2012, A&A, 548, A51
Menanteau, F., González, J., Juin, J., et al. 2010, ApJ, 723, 1523
Mitra, S., Rocha, G., Górski, K. M., et al. 2011, ApJS, 193, 5
Montier, L. A., Pelkonen, V., Juvela, M., Ristorcelli, I., & Marshall, D. J. 2010, A&A, 522, A83
Motl, P. M., Hallman, E. J., Burns, J. O., & Norman, M. L. 2005, ApJ, 623, L63
Muchovej, S., Leitch, E., Culverhouse, T., Carpenter, J., & Sievers, J. 2012, ApJ, 749, 46
Nagai, D. 2006, ApJ, 650, 538
Nagai, D., Kravtsov, A. V., & Vikhlinin, A. 2007, ApJ, 668, 1
Navarro, J. F., Frenk, C. S., & White, S. D. M. 1997, ApJ, 490, 493
Pacaud, F., Pierre, M., Adami, C., et al. 2007, MNRAS, 382, 1289
Peebles, P. J. E. 1980, The large-scale structure of the universe (Princeton University Press)
Piffaretti, R., & Valdarnini, R. 2008, A&A, 491, 71
Piffaretti, R., Arnaud, M., Pratt, G. W., Pointecouteau, E., & Melin, J.-B. 2011, A&A, 534, A109
Plagge, T., Benson, B. A., Ade, P. A. R., et al. 2010, ApJ, 716, 1118
Planck and AMI Collaborations 2013, A&A, 550, A128
Planck Collaboration VIII. 2011, A&A, 536, A8
Planck Collaboration IX. 2011, A&A, 536, A9
Planck Collaboration X. 2011, A&A, 536, A10
Planck Collaboration XI. 2011, A&A, 536, A11
Planck Collaboration XXII. 2011, A&A, 536, A22
Planck Collaboration XXIII. 2011, A&A, 536, A23
Planck Collaboration XXVI. 2011, A&A, 536, A26
Planck Collaboration Int. I. 2012, A&A, 543, A102
Planck Collaboration Int. III. 2013, A&A, 550, A129
Planck Collaboration Int. IV. 2013, A&A, 550, A130
Planck Collaboration Int. V. 2013, A&A, 550, A131
Planck Collaboration Int. VII. 2013, A&A, 550, A133
Planck Collaboration Int. X. 2013, A&A, 554, A140
Planck Collaboration 2013, The Explanatory Supplement to the Planck 2013 results, http://www.sciops.esa.int/wikiSI/planckpla/index.php?title=Main_Page (ESA)
Planck Collaboration I. 2014, A&A, 571, A1
Planck Collaboration II. 2014, A&A, 571, A2
Planck Collaboration III. 2014, A&A, 571, A3
Planck Collaboration IV. 2014, A&A, 571, A4
Planck Collaboration V. 2014, A&A, 571, A5
Planck Collaboration VI. 2014, A&A, 571, A6
Planck Collaboration VII. 2014, A&A, 571, A7
Planck Collaboration VIII. 2014, A&A, 571, A8
Planck Collaboration IX. 2014, A&A, 571, A9
Planck Collaboration X. 2014, A&A, 571, A10
Planck Collaboration XI. 2014, A&A, 571, A11
Planck Collaboration XII. 2014, A&A, 571, A12
Planck Collaboration XIII. 2014, A&A, 571, A13
Planck Collaboration XIV. 2014, A&A, 571, A14
Planck Collaboration XV. 2014, A&A, 571, A15
Planck Collaboration XVI. 2014, A&A, 571, A16
Planck Collaboration XVII. 2014, A&A, 571, A17
Planck Collaboration XVIII. 2014, A&A, 571, A18
Planck Collaboration XIX. 2014, A&A, 571, A19
Planck Collaboration XX. 2014, A&A, 571, A20
Planck Collaboration XXI. 2014, A&A, 571, A21
Planck Collaboration XXII. 2014, A&A, 571, A22
Planck Collaboration XXIII. 2014, A&A, 571, A23
Planck Collaboration XXIV. 2014, A&A, 571, A24
Planck Collaboration XXV. 2014, A&A, 571, A25
Planck Collaboration XXVI. 2014, A&A, 571, A26
Planck Collaboration XXVII. 2014, A&A, 571, A27
Planck Collaboration XXVIII. 2014, A&A, 571, A28
Planck Collaboration XXIX. 2014, A&A, 571, A29
Planck Collaboration XXX. 2014, A&A, 571, A30
Planck Collaboration XXXI. 2014, A&A, 571, A31
Pratt, G. W., Croston, J. H., Arnaud, M., & Böhringer, H. 2009, A&A, 498, 361
Rafferty, D. A., McNamara, B. R., & Nulsen, P. E. J. 2008, ApJ, 687, 899
Rawle, T. D., Edge, A. C., Egami, E., et al. 2012, ApJ, 747, 29
Reichardt, C. L., Stalder, B., Bleem, L. E., et al. 2013, ApJ, 763, 127
Reichert, A., Böhringer, H., Fassbender, R., & Mühlegger, M. 2011, A&A, 535, A4
Reiprich, T. H., & Böhringer, H. 2002, ApJ, 567, 716
Remazeilles, M., Delabrouille, J., & Cardoso, J.-F. 2011, MNRAS, 410, 2481
Rozo, E., Rykoff, E. S., Evrard, A., et al. 2009, ApJ, 699, 768
Rozo, E., Vikhlinin, A., & More, S. 2012, ApJ, 760, 67
Rubiño-Martín, J. A., & Sunyaev, R. A. 2003, MNRAS, 344, 1155
Sayers, J., Czakon, N. G., Bridge, C., et al. 2012, ApJ, 749, L15
Sayers, J., Czakon, N. G., Mantz, A., et al. 2013, ApJ, 768, 177
Schlegel, D. J., Finkbeiner, D. P., & Davis, M. 1998, ApJ, 500, 525
Schuecker, P., Böhringer, H., Collins, C. A., & Guzzo, L. 2003, A&A, 398, 867
Sifón, C., Menanteau, F., Hasselfield, M., et al. 2013, ApJ, 772, 25
Story, K., Aird, K. A., Andersson, K., et al. 2011, ApJ, 735, L36
Sunyaev, R. A., & Zeldovich, Y. B. 1972, Comm. Astrophys. Space Phys., 4, 173
Sunyaev, R. A., & Zeldovich, I. B. 1980, ARA&A, 18, 537
Szabo, T., Pierpaoli, E., Dong, F., Pipino, A., & Gunn, J. 2011, ApJ, 736, 21
Takey, A., Schwope, A., & Lamer, G. 2011, A&A, 534, A120
Tinker, J., Kravtsov, A. V., Klypin, A., et al. 2008, ApJ, 688, 709
Vanderlinde, K., Crawford, T. M., de Haan, T., et al. 2010, ApJ, 722, 1180
Vikhlinin, A., McNamara, B. R., Forman, W., et al. 1998, ApJ, 502, 558
Vikhlinin, A., Kravtsov, A., Forman, W., et al. 2006, ApJ, 640, 691
Vikhlinin, A., Allen, S. W., Arnaud, M., et al. 2009, in astro2010: The Astronomy and Astrophysics Decadal Survey, 2010, 304
Voges, W., Aschenbach, B., Boller, T., et al. 1999, A&A, 349, 389
Voges, W., Aschenbach, B., Boller, T., et al. 2000, VizieR Online Data Catalog: IX/29
Voit, G. M. 2005, Rev. Mod. Phys., 77, 207
Wen, Z. L., Han, J. L., & Liu, F. S. 2010, MNRAS, 407, 533
Wen, Z. L., Han, J. L., & Liu, F. S. 2012, ApJS, 199, 34
Wik, D. R., Sarazin, C. L., Ricker, P. M., & Randall, S. W. 2008, ApJ, 680, 17
Williamson, R., Benson, B. A., High, F. W., et al. 2011, ApJ, 738, 139
Wright, E. L., Eisenhardt, P. R. M., Mainzer, A. K., et al. 2010, AJ, 140, 1868
York, D. G., Adelman, J., Anderson, Jr., J. E., et al. 2000, AJ, 120, 1579
Zhuravleva, I., Churazov, E., Kravtsov, A., et al. 2013, MNRAS, 428, 3274
Zwicky, F., Herzog, E., & Wild, P. 1961, Catalogue of galaxies and of clusters of galaxies, Vol. I

---

[1] APC, AstroParticule et Cosmologie, Université Paris Diderot, CNRS/IN2P3, CEA/lrfu, Observatoire de Paris, Sorbonne Paris Cité, 10 rue Alice Domon et Léonie Duquet, 75205 Paris Cedex 13, France

[2] Aalto University Metsähovi Radio Observatory, Metsähovintie 114, 02540 Kylmälä, Finland
[3] Academy of Sciences of Tatarstan, Bauman Str., 20, Kazan, 420111 Republic of Tatarstan, Russia
[4] African Institute for Mathematical Sciences, 6-8 Melrose Road, Muizenberg, 7701 Rondebosch Cape Town, South Africa
[5] Agenzia Spaziale Italiana Science Data Center, via del Politecnico snc, 00133 Roma, Italy
[6] Agenzia Spaziale Italiana, Viale Liegi 26, Roma, Italy
[7] Astrophysics Group, Cavendish Laboratory, University of Cambridge, J J Thomson Avenue, Cambridge CB3 0HE, UK
[8] Astrophysics & Cosmology Research Unit, School of Mathematics, Statistics & Computer Science, University of KwaZulu-Natal, Westville Campus, Private Bag X54001, 4000 Durban, South Africa
[9] Atacama Large Millimeter/submillimeter Array, ALMA Santiago Central Offices, Alonso de Cordova 3107, Vitacura, Casilla 763 0355 Santiago, Chile
[10] CITA, University of Toronto, 60 St. George St., Toronto, ON M5S 3H8, Canada
[11] CNRS, IRAP, 9 Av. colonel Roche, BP 44346, 31028 Toulouse Cedex 4, France
[12] California Institute of Technology, Pasadena, California, USA
[13] Centre for Theoretical Cosmology, DAMTP, University of Cambridge, Wilberforce Road, Cambridge CB3 0WA, UK
[14] Centro de Astrofísica, Universidade do Porto, Rua das Estrelas, 4150-762 Porto, Portugal
[15] Centro de Estudios de Física del Cosmos de Aragón (CEFCA), Plaza San Juan, 1, planta 2, 44001 Teruel, Spain
[16] Computational Cosmology Center, Lawrence Berkeley National Laboratory, Berkeley, California, USA
[17] Consejo Superior de Investigaciones Científicas (CSIC), Madrid, Spain
[18] DSM/Irfu/SPP, CEA-Saclay, 91191 Gif-sur-Yvette Cedex, France
[19] DTU Space, National Space Institute, Technical University of Denmark, Elektrovej 327, 2800 Kgs. Lyngby, Denmark
[20] Département de Physique Théorique, Université de Genève, 24 quai E. Ansermet, 1211 Genève 4, Switzerland
[21] Departamento de Física Fundamental, Facultad de Ciencias, Universidad de Salamanca, 37008 Salamanca, Spain
[22] Departamento de Física, Universidad de Oviedo, Avda. Calvo Sotelo s/n, 33007 Oviedo, Spain
[23] Department of Astronomy and Astrophysics, University of Toronto, 50 Saint George Street, Toronto, Ontario, Canada
[24] Department of Astronomy and Geodesy, Kazan Federal University, Kremlevskaya Str., 18, 420008 Kazan, Russia
[25] Department of Astrophysics/IMAPP, Radboud University Nijmegen, PO Box 9010, 6500 GL Nijmegen, The Netherlands
[26] Department of Electrical Engineering and Computer Sciences, University of California, Berkeley, California, USA
[27] Department of Physics & Astronomy, University of British Columbia, 6224 Agricultural Road, Vancouver, British Columbia, Canada
[28] Department of Physics and Astronomy, Dana and David Dornsife College of Letter, Arts and Sciences, University of Southern California, Los Angeles, CA 90089, USA
[29] Department of Physics and Astronomy, University College London, London WC1E 6BT, UK
[30] Department of Physics and Astronomy, University of Sussex, Brighton BN1 9QH, UK
[31] Department of Physics, Florida State University, Keen Physics Building, 77 Chieftan Way, Tallahassee, Florida, USA
[32] Department of Physics, Gustaf Hällströmin katu 2a, University of Helsinki, 00014 Helsinki, Finland
[33] Department of Physics, Princeton University, Princeton, New Jersey, USA
[34] Department of Physics, University of California, Berkeley, California, USA
[35] Department of Physics, University of California, One Shields Avenue, Davis, California, USA
[36] Department of Physics, University of California, Santa Barbara, California, USA
[37] Department of Physics, University of Illinois at Urbana-Champaign, 1110 West Green Street, Urbana, Illinois, USA
[38] Dipartimento di Fisica e Astronomia G. Galilei, Università degli Studi di Padova, via Marzolo 8, 35131 Padova, Italy
[39] Dipartimento di Fisica e Scienze della Terra, Università di Ferrara, via Saragat 1, 44122 Ferrara, Italy
[40] Dipartimento di Fisica, Università La Sapienza, P.le A. Moro 2, 00185 Roma, Italy
[41] Dipartimento di Fisica, Università degli Studi di Milano, via Celoria, 16, 20133 Milano, Italy
[42] Dipartimento di Fisica, Università degli Studi di Trieste, via A. Valerio 2, 34127 Trieste, Italy
[43] Dipartimento di Fisica, Università di Roma Tor Vergata, via della Ricerca Scientifica, 1, 00133 Roma, Italy
[44] Discovery Center, Niels Bohr Institute, Blegdamsvej 17, 2100 Copenhagen, Denmark
[45] Dpto. Astrofísica, Universidad de La Laguna (ULL), 38206 La Laguna, Tenerife, Spain
[46] European Southern Observatory, ESO Vitacura, Alonso de Cordova 3107, Vitacura, Casilla 19001 Santiago, Chile
[47] European Space Agency, ESAC, Planck Science Office, Camino bajo del Castillo, s/n, Urbanización Villafranca del Castillo, 28691 Villanueva de la Cañada, Madrid, Spain
[48] European Space Agency, ESTEC, Keplerlaan 1, 2201 AZ Noordwijk, The Netherlands
[49] Finnish Centre for Astronomy with ESO (FINCA), University of Turku, Väisäläntie 20, 21500, Piikkiö, Finland
[50] GEPI, Observatoire de Paris, Section de Meudon, 5 place J. Janssen, 92195 Meudon Cedex, France
[51] Helsinki Institute of Physics, Gustaf Hällströmin katu 2, University of Helsinki, 00014 Helsinki, Finland
[52] INAF – Osservatorio Astrofisico di Catania, via S. Sofia 78, Catania, Italy
[53] INAF – Osservatorio Astronomico di Padova, Vicolo dell'Osservatorio 5, 35122 Padova, Italy
[54] INAF – Osservatorio Astronomico di Roma, via di Frascati 33, 00040 Monte Porzio Catone, Italy
[55] INAF – Osservatorio Astronomico di Trieste, via G.B. Tiepolo 11, 34143 Trieste, Italy
[56] INAF Istituto di Radioastronomia, via P. Gobetti 101, 40129 Bologna, Italy
[57] INAF/IASF Bologna, via Gobetti 101, 40129 Bologna, Italy
[58] INAF/IASF Milano, via E. Bassini 15, Milano, Italy
[59] INFN, Sezione di Bologna, via Irnerio 46, 40126, Bologna, Italy
[60] INFN, Sezione di Roma 1, Università di Roma Sapienza, P.le Aldo Moro 2, 00185 Roma, Italy
[61] IPAG: Institut de Planétologie et d'Astrophysique de Grenoble, Université Joseph Fourier, Grenoble 1/CNRS-INSU, UMR 5274, 38041 Grenoble, France
[62] ISDC Data Centre for Astrophysics, University of Geneva, Ch. d'Ecogia 16, Versoix, Switzerland
[63] IUCAA, Post Bag 4, Ganeshkhind, Pune University Campus, 411 007 Pune, India
[64] Imperial College London, Astrophysics group, Blackett Laboratory, Prince Consort Road, London, SW7 2AZ, UK
[65] Infrared Processing and Analysis Center, California Institute of Technology, Pasadena, CA 91125, USA
[66] Institut Néel, CNRS, Université Joseph Fourier Grenoble I, 25 rue des Martyrs, 38042 Grenoble, France
[67] Institut Universitaire de France, 103 bd Saint-Michel, 75005 Paris, France
[68] Institut d'Astrophysique Spatiale, CNRS (UMR 8617) Université Paris-Sud 11, Bâtiment 121, 91405 Orsay, France
[69] Institut d'Astrophysique de Paris, CNRS (UMR 7095), 98bis boulevard Arago, 75014 Paris, France
[70] Institute for Space Sciences, 077125 Bucharest-Magurale, Romania
[71] Institute of Astronomy and Astrophysics, Academia Sinica, 10617 Taipei, Taiwan

[72] Institute of Astronomy, University of Cambridge, Madingley Road, Cambridge CB3 0HA, UK
[73] Institute of Theoretical Astrophysics, University of Oslo, Blindern, 0315 Oslo, Norway
[74] Instituto de Astrofísica de Canarias, C/Vía Láctea s/n, 38200 La Laguna, Tenerife, Spain
[75] Instituto de Física de Cantabria (CSIC-Universidad de Cantabria), Avda. de los Castros s/n, 39005 Santander, Spain
[76] Jet Propulsion Laboratory, California Institute of Technology, 4800 Oak Grove Drive, Pasadena, California, USA
[77] Jodrell Bank Centre for Astrophysics, Alan Turing Building, School of Physics and Astronomy, The University of Manchester, Oxford Road, Manchester, M13 9PL, UK
[78] Kavli Institute for Cosmology Cambridge, Madingley Road, Cambridge, CB3 0HA, UK
[79] LAL, Université Paris-Sud, CNRS/IN2P3, 91898 Orsay, France
[80] LERMA, CNRS, Observatoire de Paris, 61 avenue de l'Observatoire, 75014 Paris, France
[81] Laboratoire AIM, IRFU/Service d'Astrophysique – CEA/DSM – CNRS – Université Paris Diderot, Bât. 709, CEA-Saclay, 91191 Gif-sur-Yvette Cedex, France
[82] Laboratoire Traitement et Communication de l'Information, CNRS (UMR 5141) and Télécom ParisTech, 46 rue Barrault, 75634 Paris Cedex 13, France
[83] Laboratoire de Physique Subatomique et de Cosmologie, Université Joseph Fourier Grenoble I, CNRS/IN2P3, Institut National Polytechnique de Grenoble, 53 rue des Martyrs, 38026 Grenoble Cedex, France
[84] Laboratoire de Physique Théorique, Université Paris-Sud 11 & CNRS, Bâtiment 210, 91405 Orsay, France
[85] Lawrence Berkeley National Laboratory, Berkeley, California, USA
[86] MPA Partner Group, Key Laboratory for Research in Galaxies and Cosmology, Shanghai Astronomical Observatory, Chinese Academy of Sciences, Nandan Road 80, 200030 Shanghai, China
[87] Max-Planck-Institut für Astrophysik, Karl-Schwarzschild-Str. 1, 85741 Garching, Germany
[88] Max-Planck-Institut für Extraterrestrische Physik, Giessenbachstraße, 85748 Garching, Germany
[89] McGill Physics, Ernest Rutherford Physics Building, McGill University, 3600 rue University, Montréal, QC, H3A 2T8, Canada
[90] MilliLab, VTT Technical Research Centre of Finland, Tietotie 3, 02044 Espoo, Finland
[91] Moscow Institute of Physics and Technology, Institutsky per., 9, 141700 Dolgoprudny, Russia
[92] National University of Ireland, Department of Experimental Physics, Maynooth, Co. Kildare, Ireland
[93] Niels Bohr Institute, Blegdamsvej 17, 2100 Copenhagen, Denmark
[94] Observational Cosmology, Mail Stop 367-17, California Institute of Technology, Pasadena, CA, 91125, USA
[95] Optical Science Laboratory, University College London, Gower Street, London, UK
[96] SB-ITP-LPPC, EPFL, CH-1015, Lausanne, Switzerland
[97] SISSA, Astrophysics Sector, via Bonomea 265, 34136 Trieste, Italy
[98] SUPA, Institute for Astronomy, University of Edinburgh, Royal Observatory, Blackford Hill, Edinburgh EH9 3HJ, UK
[99] School of Physics and Astronomy, Cardiff University, Queens Buildings, The Parade, Cardiff, CF24 3AA, UK
[100] Space Research Institute (IKI), Russian Academy of Sciences, Profsoyuznaya Str, 84/32, 117997 Moscow, Russia
[101] Space Sciences Laboratory, University of California, Berkeley, California, USA
[102] Special Astrophysical Observatory, Russian Academy of Sciences, Nizhnij Arkhyz, Zelenchukskiy region, 369167 Karachai-Cherkessian Republic, Russia
[103] Stanford University, Dept of Physics, Varian Physics Bldg, 382 via Pueblo Mall, Stanford, California, USA
[104] Sub-Department of Astrophysics, University of Oxford, Keble Road, Oxford OX1 3RH, UK
[105] TÜBİTAK National Observatory, Akdeniz University Campus, 07058 Antalya, Turkey
[106] Theory Division, PH-TH, CERN, 1211 Geneva 23, Switzerland
[107] UPMC Univ Paris 06, UMR7095, 98bis boulevard Arago, 75014 Paris, France
[108] Universität Heidelberg, Institut für Theoretische Astrophysik, Philosophenweg 12, 69120 Heidelberg, Germany
[109] Université Denis Diderot (Paris 7), 75205 Paris Cedex 13, France
[110] Université de Toulouse, UPS-OMP, IRAP, 31028 Toulouse Cedex 4, France
[111] Universities Space Research Association, Stratospheric Observatory for Infrared Astronomy, MS 232-11, Moffett Field, CA 94035, USA
[112] University Observatory, Ludwig Maximilian University of Munich, Scheinerstrasse 1, 81679 Munich, Germany
[113] University of Granada, Departamento de Física Teórica y del Cosmos, Facultad de Ciencias, Granada, Spain
[114] Warsaw University Observatory, Aleje Ujazdowskie 4, 00-478 Warszawa, Poland

Astronomy & Astrophysics manuscript no. sz˙catalogue
February 6, 2015

Planck 2015 results. XXVII. The Second Planck Catalogue of Sunyaev-Zeldovich Sources

Planck Collaboration: P. A. R. Ade[99], N. Aghanim[68], M. Arnaud[83], M. Ashdown[79,6], J. Aumont[68], C. Baccigalupi[97], A. J. Banday[113,10], R. B. Barreiro[74], R. Barrena[72,43], J. G. Bartlett[1,77], N. Bartolo[35,76], E. Battaner[116,117], R. Battye[78], K. Benabed[69,110], A. Benoît[66], A. Benoit-Lévy[27,69,110], J.-P. Bernard[113,10], M. Bersanelli[38,57], P. Bielewicz[113,10,97], I. Bikmaev[23,2], H. Böhringer[90], A. Bonaldi[78], L. Bonavera[74], J. R. Bond[9], J. Borrill[15,103], F. R. Bouchet[69,101], M. Bucher[1], R. Burenin[102,92], C. Burigana[56,36,58], R. C. Butler[56], E. Calabrese[106], J.-F. Cardoso[84,1,69], P. Carvalho[70,79], A. Catalano[85,82], A. Challinor[70,79,13], A. Chamballu[83,17,68], R.-R. Chary[65], H. C. Chiang[30,7], G. Chon[90], P. R. Christensen[94,42], D. L. Clements[64], S. Colombi[69,110], L. P. L. Colombo[26,77], C. Combet[85], B. Comis[85], F. Couchot[80], A. Coulais[82], B. P. Crill[77,12], A. Curto[6,74], F. Cuttaia[56], H. Dahle[71], L. Danese[97], R. D. Davies[78], R. J. Davis[78], P. de Bernardis[37], A. de Rosa[56], G. de Zotti[53,97], J. Delabrouille[1], F.-X. Désert[62], C. Dickinson[78], J. M. Diego[74], K. Dolag[115,89], H. Dole[68,67], S. Donzelli[57], O. Doré[77,12], M. Douspis[68], A. Ducout[69,64], X. Dupac[45], G. Efstathiou[70], P. R. M. Eisenhardt[77], F. Elsner[27,69,110], T. A. Enßlin[89], H. K. Eriksen[71], E. Falgarone[82], J. Fergusson[13], F. Feroz[6], A. Ferragamo[73,20], F. Finelli[56,58], O. Forni[113,10], M. Frailis[55], A. A. Fraisse[30], E. Franceschi[56], A. Frejsel[94], S. Galeotta[55], S. Galli[69], K. Ganga[1], R. T. Génova-Santos[72,43], M. Giard[113,10], Y. Giraud-Héraud[1], E. Gjerløw[71], J. González-Nuevo[74,97], K. M. Górski[77,118], K. J. B. Grainge[6,79], S. Gratton[79,70], A. Gregorio[39,55,61], A. Gruppuso[56], J. E. Gudmundsson[30], F. K. Hansen[71], D. Hanson[91,77,9], D. L. Harrison[70,79], A. Hempel[72,43,111], S. Henrot-Versillé[80], C. Hernández-Monteagudo[14,89], D. Herranz[74], S. R. Hildebrandt[77,12], E. Hivon[69,110], M. Hobson[6], W. A. Holmes[77], A. Hornstrup[18], W. Hovest[89], K. M. Huffenberger[28], G. Hurier[68], A. H. Jaffe[64], T. R. Jaffe[113,10], T. Jin[6], W. C. Jones[30], M. Juvela[29], E. Keihänen[29], R. Keskitalo[15], I. Khamitov[107,23], T. S. Kisner[87], R. Kneissl[44,8], J. Knoche[89], M. Kunz[19,68,3], H. Kurki-Suonio[29,51], G. Lagache[5,68], J.-M. Lamarre[82], A. Lasenby[6,79], M. Lattanzi[36], C. R. Lawrence[77], R. Leonardi[45], J. Lesgourgues[108,96,81], F. Levrier[82], M. Liguori[35,76], P. B. Lilje[71], M. Linden-Vørnle[18], M. López-Caniego[45,74], P. M. Lubin[33], J. F. Macías-Pérez[85], G. Maggio[55], D. Maino[38,57], D. S. Y. Mak[26], N. Mandolesi[56,36], A. Mangilli[68,80], P. G. Martin[9], E. Martínez-González[74], S. Masi[37], S. Matarrese[35,76,49], P. Mazzotta[40], P. McGehee[65], S. Mei[48,112,12], A. Melchiorri[37,59], J.-B. Melin[17], L. Mendes[45], A. Mennella[38,57], M. Migliaccio[70,79], S. Mitra[63,77], M.-A. Miville-Deschênes[68,9], A. Moneti[69], L. Montier[113,10], G. Morgante[56], D. Mortlock[64], A. Moss[100], D. Munshi[99], J. A. Murphy[93], P. Naselsky[94,42], A. Nastasi[68], F. Nati[30], P. Natoli[36,4,56], C. B. Netterfield[22], H. U. Nørgaard-Nielsen[18], F. Noviello[78], D. Novikov[88], I. Novikov[94,88], M. Olamaie[6], C. A. Oxborrow[18], F. Paci[97], L. Pagano[37,59], F. Pajot[68], D. Paoletti[56,58], F. Pasian[55], G. Patanchon[1], T. J. Pearson[12,65], O. Perdereau[80], L. Perotto[85], Y. C. Perrott[6], F. Perrotta[97], V. Pettorino[50], F. Piacentini[37], M. Piat[1], E. Pierpaoli[26], D. Pietrobon[77], S. Plaszczynski[80], E. Pointecouteau[113,10], G. Polenta[4,54], G. W. Pratt[83], G. Prézeau[12,77], S. Prunet[69,110], J.-L. Puget[68], J. P. Rachen[24,89], W. T. Reach[114], R. Rebolo[72,16,43], M. Reinecke[89], M. Remazeilles[78,68,1], C. Renault[85], A. Renzi[41,60], I. Ristorcelli[113,10], G. Rocha[77,12], C. Rosset[1], M. Rossetti[38,57], G. Roudier[1,82,77], E. Rozo[31], J. A. Rubiño-Martín[72,43], C. Rumsey[6], B. Rusholme[65], E. S. Rykoff[98], M. Sandri[56], D. Santos[85], R. D. E. Saunders[6], M. Savelainen[29,51], G. Savini[95], M. P. Schammel[6,75], D. Scott[25], M. D. Seiffert[77,12], E. P. S. Shellard[13], T. W. Shimwell[6,105], L. D. Spencer[99], S. A. Stanford[32], D. Stern[77], V. Stolyarov[6,79,104], R. Stompor[1], A. Streblyanska[73,20], R. Sudiwala[99], R. Sunyaev[89,102], D. Sutton[70,79]*, A.-S. Suur-Uski[29,51], J.-F. Sygnet[69], J. A. Tauber[46], L. Terenzi[47,56], L. Toffolatti[21,74,56], M. Tomasi[38,57], D. Tramonte[72,43], M. Tristram[80], M. Tucci[19], J. Tuovinen[11], G. Umana[52], L. Valenziano[56], J. Valiviita[29,51], B. Van Tent[86], P. Vielva[74], F. Villa[56], L. A. Wade[77], B. D. Wandelt[69,110,34], I. K. Wehus[77], S. D. M. White[89], E. L. Wright[109], D. Yvon[17], A. Zacchei[55], and A. Zonca[33]

(Affiliations can be found after the references)

Preprint online version: February 6, 2015

ABSTRACT

We present the all-sky *Planck* catalogue of Sunyaev-Zeldovich (SZ) sources detected from the 29 month full-mission data. The catalogue (PSZ2) is the largest SZ-selected sample of galaxy clusters yet produced and the deepest all-sky catalogue of galaxy clusters. It contains 1653 detections, of which 1203 are confirmed clusters with identified counterparts in external data-sets, and is the first SZ-selected cluster survey containing $> 10^3$ confirmed clusters. We present a detailed analysis of the survey selection function in terms of its completeness and statistical reliability, placing a lower limit of 83% on the purity. Using simulations, we find that the $Y_{5\mathrm{R}500}$ estimates are robust to pressure-profile variation and beam systematics, but accurate conversion to Y_{500} requires. the use of prior information on the cluster extent. We describe the multi-wavelength search for counterparts in ancillary data, which makes use of radio, microwave, infra-red, optical and X-ray data-sets, and which places emphasis on the robustness of the counterpart match. We discuss the physical properties of the new sample and identify a population of low-redshift X-ray under-luminous clusters revealed by SZ selection. These objects appear in optical and SZ surveys with consistent properties for their mass, but are almost absent from *ROSAT* X-ray selected samples.

Key words. cosmology: observations – galaxies: clusters: general – catalogues

---

[*] Corresponding author: D. Sutton, sutton@ast.cam.ac.uk

1. Introduction

This paper is one of a set associated with the 2015 *Planck*[1] full mission data release and describes the production and properties of the legacy catalogue of Sunyaev Zeldovich sources (PSZ2).

In the framework of hierarchical structure formation, peaks in the cosmological density field collapse and merge to form gravitationally bound haloes of increasing mass (Peebles 1980). The galaxy clusters are the most massive of these bound structures and act as signposts for the extrema of the cosmological density field on the relevant scales. The evolution of galaxy cluster abundance with mass and redshift is thus a sensitive cosmological probe of the late-time universe, providing unique constraints on the normalisation of the matter density fluctuations, σ_8, the mean matter density, $\Omega_{\rm m}$, the density and equation of state of the dark energy field, $\Omega_{\rm DE}$ and w, as well as constraining some extensions of the minimal cosmological model, such as massive neutrinos, and non-standard scenarios such as modified gravity (see eg: Borgani & Kravtsov 2009; Allen et al. 2011). In recent years, cluster data from the microwave through to the X-ray have been used to constrain cosmological parameters (Vikhlinin et al. 2009b; Rozo et al. 2010; Hasselfield et al. 2013; Benson et al. 2013; Planck Collaboration XX 2014; Zu et al. 2014).

Galaxy clusters are multi-component objects composed of dark matter, which dominates the mass, stars, cold gas and dust in galaxies, and a hot ionised intra-cluster medium (ICM). These different components make clusters true multi-wavelength objects. The galaxies emit in the optical and infrared. The ICM, which is the majority of the baryonic material by mass, emits in the X-rays via thermal bremsstrahlung and line emission, and energy-boosts cosmic microwave background photons via inverse Compton scattering.

This last effect, the thermal Sunyaev Zeldovich (SZ) effect (Sunyaev & Zeldovich 1970, 1980), imprints a redshift-independent spectral distortion on the cosmic-microwave background (CMB) photons reaching us along the line of sight to the cluster. This results in an increase in intensity at frequencies above 220 GHz, and a decrease in intensity at lower frequencies. The *Planck* High-Frequency Instrument (HFI) is unique in providing high-precision data for both the increment and the decrement across the whole sky.

The utility of a cluster survey for cosmological work depends on our ability to determine accurately its selection function and to obtain unbiased measurements of cluster mass and redshift. The first cluster surveys consisted of galaxy overdensities identified by eye from photographic plates (Abell 1958). The construction of large optical catalogues improved significantly with the data from the SDSS (Koester et al. 2007), whose five photometric bands have allowed robust photometric classification of red-sequence cluster galaxies and accurate photometric redshifts to $z < 0.6$ across 1/4 of the sky (Hao et al. 2010; Szabo et al. 2011; Wen et al. 2009; Rykoff et al. 2014). These catalogues now typically contain $10^4 - 10^5$ clusters and provide cluster richness as an observable that correlates with mass with an intrinsic scatter $\sigma_{\rm int}$ of about 25% (Rozo & Rykoff 2014).

Construction of X-ray cluster surveys is now a mature activity, with several catalogues now available based on all-sky data from the *ROSAT* satellite, alongside additional catalogues of serendipitous detections from pointed observations (Ebeling et al. 1998; Böhringer et al. 2004; Reiprich & Böhringer 2002; Ebeling et al. 2010; Piffaretti et al. 2011; Burenin et al. 2007; Mehrtens et al. 2012). The most basic X-ray survey observable, the X-ray luminosity L_{500} measured within r_{500} [2], has been shown correlate with mass with intrinsic scatter of about 40% (Pratt et al. 2009). Observables with lower intrinsic scatter against mass can be defined when pointed X-ray follow-up information is available, including the core-excised X-ray luminosity (Maughan 2007; Pratt et al. 2009) and $Y_{\rm x}$, the product of the gas mass and the core-excised spectroscopic temperature (Kravtsov et al. 2006; Vikhlinin et al. 2009a; Mahdavi et al. 2013). While X-ray surveys are unique in their purity, they do suffer from selection biases that favour low-redshift systems, due to flux limitations, and dynamically relaxed clusters with an X-ray bright cooling core (Eckert et al. 2011; Schuecker et al. 2003; Vikhlinin et al. 2009b; Chen et al. 2007).

SZ surveys offer a different window on the cluster population: their selection function flattens towards higher redshifts, providing a nearly mass-limited census of the cluster population at high redshift, where abundance is strongly sensitive to cosmological parameters (Carlstrom et al. 2002; Planck Collaboration XXIX 2014). The SZ survey observable is the spherically integrated Comptonisation parameter, $Y_{\rm sz}$, which is related to the integrated electron pressure and hence the total thermal energy of the cluster gas. It is also expected to correlate with mass with a low intrinsic scatter and little dependence on the dynamical state of the cluster (eg: da Silva et al. 2004; Kay et al. 2012; Hoekstra et al. 2012; Planck Collaboration Int. III 2013; Sifón et al. 2013).

The spherically-integrated pressure profiles of X-ray and SZ clusters have been observed to follow a near universal profile with little dispersion (Arnaud et al. 2010; Planck Collaboration Int. V 2013), permitting the detection of clusters with a matched multi-frequency filter based on some assumed pressure profile (Herranz et al. 2002; Melin et al. 2006a). Samples constructed this way have well understood selection functions, though discrepancies due to profile mismatch or contaminating infra-red emission may still be present to some level. Large SZ surveys have only appeared recently, with catalogues of order $\sim 10^2$ clusters released by the Atacama Cosmology Telescope (Hasselfield et al. 2013), the South Pole Telescope (Reichardt et al. 2013) and *Planck* satellite collaborations.

This is the third all-sky catalogue produced from *Planck* SZ data. The early Sunyaev-Zeldovich (ESZ) catalogue presented 189 clusters detected from 10 months of survey data (Planck Collaboration 2011), while the PSZ1, the full-sky catalogue assembled from the nominal mission data, presented 1227 cluster candidates detected from 15.5 months of data (Planck Collaboration XXIX 2014). This paper

---

[1] *Planck* (`http://www.esa.int/Planck`) is a project of the European Space Agency (ESA) with instruments provided by two scientific consortia funded by ESA member states and led by Principal Investigators from France and Italy, telescope reflectors provided through a collaboration between ESA and a scientific consortium led and funded by Denmark, and additional contributions from NASA (USA).

[2] r_{500} is the cluster-centric distance within which the mean density is 500 times the critical density of the Universe at the cluster redshift.

presents 1653 candidates detected from the full mission survey of 29 months. 1203 of these have been confirmed in ancillary data, and 1094 have redshift estimates. The PSZ2 expands the scope and sensitivity of the SZ view of galaxy clusters by substantially increasing the number of lower mass clusters available for study. It is also expected to contain many new, as yet unconfirmed, high-redshift clusters. We report on the construction and characterisation of the catalogue, presenting the survey selection functions and a compilation of multi-wavelength ancillary information including redshifts. We also briefly discuss the physical properties of the sample.

This paper is organised as follows. In Sect. 2 we summarise the three extraction algorithms used to build the catalogue, focussing on the changes in the algorithms since they were used to construct the PSZ1. In Sect. 3 we describe the construction of the catalogue. In Sect. 4 we present the survey selection functions (completeness and statistical reliability) and the complementary approaches used to estimate them, while in Sect. 5 we discuss and validate the estimation of the $Y_{\rm sz}$ parameters, both blindly and when using prior information, and we compare the consistency of the new catalogue with the PSZ1 in Sect. 6. In Sect. 7 we report on the search for multi-wavelength counterparts in ancillary catalogues and follow-up observations. Finally we present the physical properties of the sample in Sect. 8 and conclude in Sect. 9. A full description of the available data products is given in Appendix D

2. Extraction Algorithms

The SZ detection and parameter estimation algorithms used to construct the PSZ2 extend and refine those used to construct the PSZ1. In this section we recall the principles of the three algorithms. The refinements of each algorithm since the PSZ1 release are detailed in Appendix C. Two of the algorithms (`MMF1` and `MMF3`) are based on the same technique (Matched Multi-filters) but have been implemented independently[3]. The third one (`PwS` for PowellSnakes) relies on Bayesian inference.

2.1. Matched Multi-filters: `MMF1` and `MMF3`

The matched filtering technique was first proposed for SZ studies by Haehnelt & Tegmark (1996). It was subsequently developed by Herranz et al. (2002) and Melin et al. (2006b) for SZ cluster extraction in multifrequency data sets such as *Planck*. The method was later adopted by the SPT and ACT collaborations (Staniszewski et al. 2009; Marriage et al. 2011).

We model the vector of map emission at each frequency $\boldsymbol{m}(\boldsymbol{x})$, at a given position on the sky $\boldsymbol{x}$ as

$$\boldsymbol{m}(\boldsymbol{x}) = y_{\rm o}\boldsymbol{t}_{\boldsymbol{\theta_s}}(\boldsymbol{x}) + \boldsymbol{n}(\boldsymbol{x}) \tag{1}$$

where $\boldsymbol{t}_{\boldsymbol{\theta_s}}(\boldsymbol{x})$ is the signal vector describing the spatial distribution at each frequency of the SZ emission from a cluster with angular size θ_s, $\boldsymbol{n}(\boldsymbol{x})$ is the total astrophysical and instrumental noise. The i^{th} frequency component of the signal vector is the normalized cluster profile $\tau_{\theta_s}(\boldsymbol{x})$ (Arnaud et al. 2010) convolved by the *Planck* beams $b_i(\boldsymbol{x})$ and scaled with the characteristic frequency dependance $j_\nu(\nu_i)$ of the thermal SZ effect: $\boldsymbol{t}_{\boldsymbol{\theta_s}}(\boldsymbol{x})_i = j_\nu(\nu_i)[b_i * \tau_{\theta_s}](\boldsymbol{x})$. θ_s is the cluster scale radius, which is related to θ_{500} through the concentration parameter c_{500} by $\theta_{500} = c_{500} \times \theta_s$. The Matched Multi-filter $\boldsymbol{\Psi}_{\boldsymbol{\theta_s}}$ allows us to recover an unbiased estimate $\hat{y}_{\rm o}$ of the central Comptonization parameters $y_{\rm o}$ with minimal variance $\sigma^2_{\theta_s}$:

$$\hat{y}_{\rm o} = \int d^2x \; {\boldsymbol{\Psi}_{\boldsymbol{\theta_s}}}^T(\boldsymbol{x}) \cdot \boldsymbol{m}(\boldsymbol{x}), \tag{2}$$

where

$$\boldsymbol{\Psi}_{\boldsymbol{\theta_s}}(\boldsymbol{k}) = \sigma^2_{\theta_s} \boldsymbol{P}^{-1}(\boldsymbol{k}) \cdot \boldsymbol{t}_{\boldsymbol{\theta_s}}(\boldsymbol{k}), \tag{3}$$

with

$$\sigma_{\theta_s} \;\equiv\; \left[\int d^2k \; {\boldsymbol{t}_{\boldsymbol{\theta_s}}}^T(\boldsymbol{k}) \cdot \boldsymbol{P}^{-1} \cdot \boldsymbol{t}_{\boldsymbol{\theta_s}}(\boldsymbol{k})\right]^{-1/2}, \tag{4}$$

$\boldsymbol{P}(\boldsymbol{k})$ being the cross-channel power spectrum matrix of the maps. It is effectively the noise matrix for the MMF, because the tSZ is small compared to other astrophysical signals, and is estimated directly from the maps.

The MMF algorithms first divide each *Planck* all-sky map in 640/504 tangential maps (14.66/10 degrees on a side) for `MMF1` /`MMF3` respectively. Each set of tangential maps is filtered by Ψ_{θ_s} with the assumed cluster size varying from θ_s=0.8 to 32 arcmin. We then locate peaks in the filtered maps above a S/N threshold of four. The locations of the peaks give the positions of our cluster candidates. These are then merged into a single all-sky catalogue by merging candidates separated by less than 10 arcmin. For `MMF3`, we performed a second step by creating sets of smaller rectangular frequency maps centered on the cluster candidates identified in the first step. We re-apply the MMF on these centred tangential maps which allows a better estimation of the background. During the second step, the sizes and fluxes are estimated more precisely. This second step is only performed for `MMF3` because the overlap of the tangential maps in the first step is small with compared to `MMF1`and `PwS`.

We define the blind cluster size as the filter scale that maximizes the S/N at the location of the cluster candidate and the blind flux is defined as the corresponding $\hat{y}_{\rm o}$ parameter. We then define the integrated blind flux as:

$$Y_{5R500} = \hat{y}_{\rm o} \int_{\theta < 5\times\theta_{500}} dr \tau_{\theta_s}(r) \tag{5}$$

Each of the algorithms produces probability distributions in the (θ_s, $Y_{\rm 5R500}$) plane for each detection, marginalising over the parameters for the centre of the cluster, which possess a Gaussian likelihood. The algorithms also return an estimate of the radial position uncertainty, $\theta_{\rm err}$ from the position likelihood.

Although the two implementations of the MMF are quite close, they produce noticeably different catalogues because the extraction is very sensitive to the estimation of the background (Eq. 4). Both the size adopted for the tangential maps and the details of the estimation of the matrix $\boldsymbol{P}(k)$ impact the S/N and hence which peaks are detected.

---

[3] The MMF numbers were given after the comparison of twelve algorithms in an earlier phase of the *Planck* mission (Melin et al. 2012). `MMF1` and `MMF3` were respectively the first and third algorithm based on Matched Multi Filters to enter the comparison

Table 1. Effective frequencies and Gaussian beam widths assumed for extraction per channel. The beam widths are the mean full-width-at-half-maximum of the FEBeCoP Gaussian beam fits across the sky, in arcmin. The effective frequencies $\nu_{\rm eff}$, shown in GHz, encapsulate band-pass effects in each channel.

Channel	FWHM	$\nu_{\rm eff}$
100	9.659	103.416
143	7.220	144.903
217	4.900	222.598
353	4.916	355.218
545	4.675	528.400
857	4.216	776.582

2.2. PowellSnakes (`PwS`)

PowellSnakes (`PwS`) is a fast, fully Bayesian, multifrequency detection algorithm designed to identify and characterize compact objects buried in a diffuse background as described in Carvalho et al. (2009, 2012). `PwS` operates using about 2800 square patches of 14.66 degree on a side, in order to ensure highly redundant sky coverage. `PwS` detects candidate clusters and at the same time computes the evidence ratio and samples from the posterior distributions of the cluster parameters. Then, it merges the sub-catalogues from each patch map and applies criteria for acceptance or rejection of the detection, as described in Carvalho et al. (2012). Priors may be provided for the position, integrated flux and radius of the clusters. For cluster detection, we apply flat priors on the position and non-informative priors in the radius and integrated flux, as determined using Jeffrey's method. `PwS` uses a calibration of the cross-power spectrum that uses an iterative scheme to reduce the contamination of the background by the SZ signal itself. This makes `PwS` particularly robust to small changes in the background.

3. Catalogue Construction

The main catalogue is constructed by combining the detections made by the three methods into a union catalogue, while merging the detections made by multiple more than one method. Half of the detections in this union are also in the intersection catalogue, defined as those detections made by all three codes simultaneously. This section describes the technical details of the construction of these catalogues.

3.1. Pipeline

The SZ catalogue construction pipeline is shown in schematic form in Fig. 1 and largely follows the process used to build the PSZ1. The *Planck* data required for the construction of the catalogue comprises the HFI maps, point source catalogues for each of the HFI channels, effective frequencies and beam widths per HFI channel as shown in Table 1, survey masks based on dust emission as seen in the highest *Planck* channels, and the catalogue of extended galactic cold-clump detections.

The HFI maps are pre-processed to fill areas of missing data (typically a few pixels), or areas with unusable data, specifically bright point sources. Point sources with S/N > 10 in any channel are masked out to a radius of $3\sigma_{\rm beam}$, using a harmonic infilling algorithm. This prevents spurious detections caused by Fourier ringing in the filtered maps used by the detection algorithms. As a further guard against such spurious detections, we reject any detections within $5\sigma_{\rm beam}$ of a filled point source. We have verified that this treatment reduces spurious detections due to bright point sources to negligible levels in simulations, while reducing the effective survey area by just 1.4% of the sky. Together with the 15% galactic dust and Magellanic cloud mask, this defines a survey area of 83.6% of the sky.

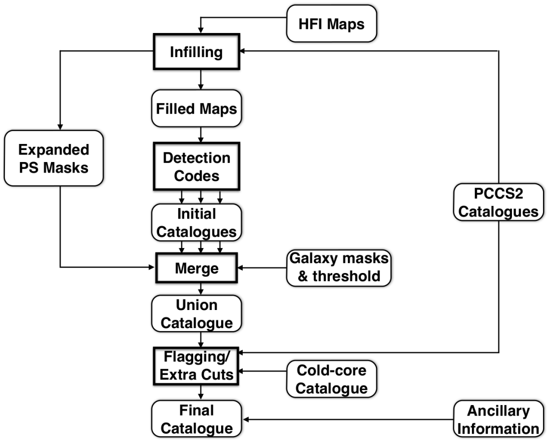

Fig. 1. Pipeline for catalogue construction.

After infilling, the three detection codes produce individual candidate catalogues down to a threshold S/N > 4.5. The catalogues are then merged to form a union catalogue, using the dust and extended point source masks discussed above to define the survey area. The merging procedure identifies the highest S/N detection as the reference position during the merge: any detections by other codes within 5 arcmin are identified with the reference position. The reference position and S/N are reported in the union catalogue.

`PwS` can produce a small number of high-significance spurious detections associated with galactic dusty emission. We apply an extra cut of `PwS`-only detections at S/N > 10 where the spectrum has a poor goodness-of-fit to the SZ effect, $\chi^2 > 16$.

We also remove five PSZ2 detections that match PSZ1 detections confirmed to be spurious by the PSZ1 follow-up program (these were the ones that we re-detected: there were many more confirmed spurious detections from the program).

Finally the sample is flagged to identify the various subsamples discussed in Sect. 3.3. The most important of these flags is discussed in the next section.

3.2. Infra-red spurious detections

Cold compact infra-red emission, particularly that due to galactic cold-clumps, can lead to high-significance spurious detections. We identify these detections by searching for 7 arcmin matches with the *Planck* cold-clump catalogue (C3PO), or with PCCS2 detections at both 545GHz and 857GHz. This matching radius was chosen because it is

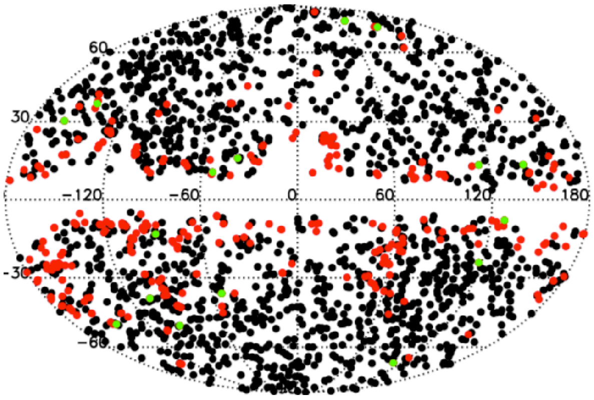

Fig. 2. The distribution of raw SZ detections, with deleted infra-red flagged candidates in red and retained infra-red flagged detections in green.

the typical size of a *Planck* detected cold-clump (Planck Collaboration XXVIII 2015).

318 raw union detections match these criteria. They tightly follow the distribution of galactic emission (see Fig. 2), such that if the 65% galactic dust mask (used for cluster cosmology) is used to define the sample instead of the 85% dust mask, the number of IR-matched raw detections drops to 40. For the high-purity sample formed from the intersection of all three codes, the numbers are 82 and 13 for the 85% and 65% dust masks respectively. Some high latitude spurious candidates remain. To minimise the effect of these probably spurious detections on the catalogue, we delete them.

We have retained in the sample all 15 confirmed clusters that match these criteria. These IR contaminated clusters represent about 1.5% of the total confirmed clusters in the PSZ2. In the catalogue, we define a flag, IR_FLAG, to denote the retained clusters that match these criteria. They can be expected to have heavily contaminated SZ signal.

A small fraction of the unconfirmed detections deleted due to IR-contaminations may have been real clusters. Assuming that optical and X-ray confirmation is unbiased with regard to the presence of IR emission, we estimate these deletions to bias our completeness estimates by less than 1%.

3.3. Catalogue sub-samples

The union catalogue can be decomposed into separate sub-samples, defined as the primary catalogues of the three individual detection codes (`PwS`,`MMF1`,`MMF3`), as well as into unions and intersections thereof. The intersection subsample of candidates detected by all three algorithms can be used as a high-reliability catalogue with less than 2% spurious contamination outside of the galactic plane (see Sect. 4.6).

3.3.1. The Cosmology Catalogues

We constructed two cluster catalogues for cosmology studies from the `MMF3` and the intersection sub-samples respectively. For these catalogues, our goal was to increase as much as possible the number of detections while keeping contamination negligible. A good compromise is to set the S/N threshold to 6 and apply a 65% galactic and point source mask as in our 2013 cosmological analysis (Planck Collaboration XX 2014). In this earlier paper, our baseline `MMF3` cosmological sample was constructed using a threshold of 7 on the 15.5 month maps, which is equivalent to 8.5 on the full mission maps. Estimations from the QA (Fig. 11) suggest that our 2014 intersection sample should be $> 99\%$ pure for a threshold of 6.

The `MMF3` cosmological sample contains 439 detections with 433 confirmed redshifts. The intersection cosmological sample contains 493 detections with 479 confirmed redshifts. Assuming that all detections having VALIDATION flag greater than zero are clusters, the empirical purity of our samples are $> 99.8\%$ for `MMF3` and $> 99.6\%$ for the intersection. Note that the intersection sample contains more clusters than the `MMF3` sample for the same S/N threshold. This is expected since the definition of the S/N for the intersection sample is to use the highest value from the three detection methods.

The completeness is also a crucial piece of information. It is computed more easily with the single method catalogue for which the analytical error-function (ERF) approximation can be used (as defined in Planck Collaboration XXIX 2014). In Sect. 4.3 and in Planck Collaboration XXIV (2015), we show that this analytical model is still valid for the considered threshold. For the intersection sample, we rely on the Monte-Carlo estimation of the completeness described in Sect. 4.2.

These two samples are used in the cosmology analysis of Planck Collaboration XXIV (2015). Detections that are included in either of the cosmology samples are noted in the main catalogue (see Appendix D).

3.4. Consistency between codes

We construct the union sample using the code with the most significant detection to supply the reference position and S/N. This contrasts with the PSZ1, which used a predefined code ordering to select the reference position and S/N. In this section, we demonstrate the consistency of the detection characteristics of the codes for common detections, motivating this change in catalogue construction.

We fit the S/N relation between codes using the Bayesian approach described by Hogg et al. (2010) for linear fits with covariant errors in both variables. We consider the catalogue S/N values to be estimates of a true underlying variable, s, with Gaussian uncertainties with standard deviation $\sigma = 1$.

We relate the s values for two different catalogues using a simple linear model

$$s_2 = \alpha s_1 + A, \tag{6}$$

where we assume flat priors for the intercept A, a flat prior on the arc-tangent of the gradient α, such that $p(\alpha) \propto 1/(1 + \alpha^2)$. We also allow for a Gaussian intrinsic scatter between the s values that includes any variation beyond

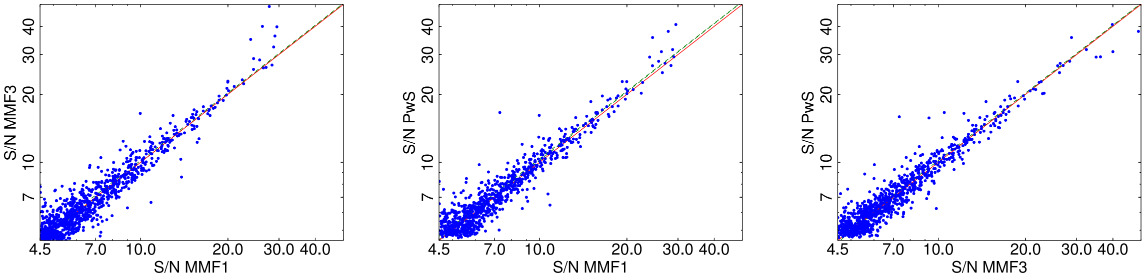

Fig. 3. Comparison of the S/N estimates from the three detection codes. The dashed green curves show the best fit relation for 0.8 correlation and the red line is the line of equality.

Table 2. Results of fits between S/N from the three detection codes, using the fitting function in equation 6. The assumed correlation of the uncertainties of s_1 and s_2 was 0.8.

s_1	s_2	N	A	α	$\sigma_{\rm int}$
`MMF1`	`MMF3`	1032	-0.01 ± 0.01	1.01 ± 0.01	0.033 ± 0.001
`MMF1`	`PwS`	985	-0.02 ± 0.01	1.03 ± 0.02	0.030 ± 0.001
`MMF3`	`PwS`	1045	0.0 ± 0.01	1.01 ± 0.01	0.031 ± 0.001

the measurement uncertainty on s. This is parameterised by $\sigma_{\rm int}$ with an uninformative prior $p(\sigma_{\rm int}) \propto 1/\sigma_{\rm int}$.

We assume a fiducial correlation of $\rho_{\rm corr} = 0.8$ between the S/N estimates of each code pair, which is typical of the correlation between the matched-multifrequency-filtered patches of each code. The fit results are shown in Table 2.

The S/N estimates from the three codes are compared in Fig. 3, which also shows the best fit relation. `MMF1` produces noticeably weaker detection than the other two codes for the 14 very strong detections at S/N > 20. Excluding these exceptional cases from the comparison, the best-fit relations between the S/Ns from each code show no significant deviations from equality between any of the codes.

There are a small number of highly significant outliers in the relation between `PwS` and the MMF codes. These are clusters imbedded in dusty regions where the different recipes for the filtered patch cross-power spectrum vary significantly and the likelihood assumptions common to all codes break down. `PwS` shows outlier behaviour relative to the other codes as its recipe is most different from the other codes.

Fig. 4 shows the consistency of the position estimates between the codes. The positions of `MMF1` and `MMF3` are more inconsistent with one another than any other code combination. The 67% bound on the `MMF1`- `MMF3` separation is 1.34 arcmin, while for `MMF1`- `PwS` it is 0.98 arcmin and for `MMF3`- `PwS` it is 1.1 arcmin. This is consistent with the observation from the quality assessment that the `PwS` positions are the most robust (Sect. 4.4).

4. Selection Function

A necessary element of any cluster sample is the selection function that relates the detected sample to the underlying population of objects. The selection function comprises two complementary functions: the completeness, which defines the probability that a given real object will be detected; and the statistical reliability, also known as purity, which defines the probability that a given detection corresponds to a real object. As a function of underlying object attributes, the completeness is a function of underlying SZ observables, θ_{500} and Y_{500}. The reliability is a statistical function of detection attributes and is presented as a function of detection S/N.

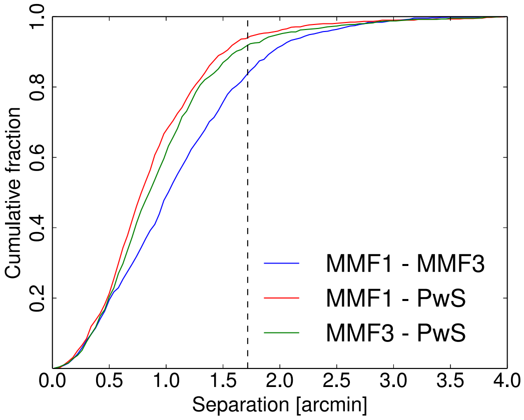

Fig. 4. Cumulative distribution of angular separation between matched detections for each possible code pair. The vertical dashed line indicates the width of a Healpix pixel at the *Planck* resolution.

4.1. Monte-Carlo Injection

The selection function is determined by the Monte-Carlo injection of simulated clusters into both real and simulated *Planck* maps. A common segment is the injection of cluster

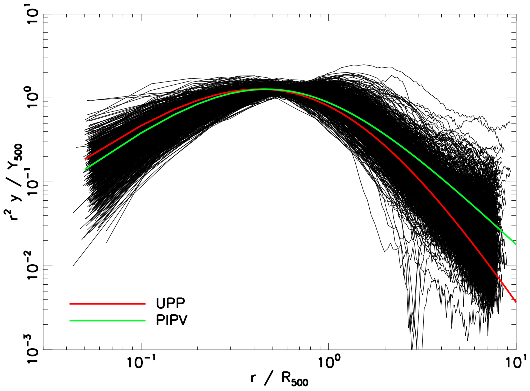

Fig. 5. The 910 simulated pressure profiles from the cosmo-OWLS simulations used for cluster injection. Also shown are the assumed extraction profile (UPP) and the best-fit profile from a sample of 62 pressure profiles fitted using *Planck* and x-ray data (PIPV, Planck Collaboration Int. V 2013).

SZ signal. The cluster signal is assumed to be spherically symmetric and to follow a pressure profile similar to the generalised Navarro-Frenk-White (GNFW) profile assumed in the catalogue extraction.

To include the effects of system-on-system variation in the pressure distribution, we draw the spherically-averaged individual pressure profiles from a set of 910 pressure profiles from simulated clusters from the cosmo-OWLS simulations (Le Brun et al. 2014; McCarthy et al. 2014), an extension of the OverWhelmingly Large Simulations project (Schaye et al. 2010). These pressure profiles are empirical in the sense that they have not been fitted using a GNFW profile: the mean pressure is used within concentric radial shells (after the subtraction of obvious sub-structures) and the injected profiles are interpolated across these shells. The simulated clusters were selected for this sample by requiring that their mass be above the approximate limiting mass for *Planck* at that redshift. The ensemble of simulated profiles are shown in Fig. 5. Each profile is normalised such that the spherically integrated Y parameter matches the fiducial injected (Y_{500},θ_{500}) parameters for the halo. The injected (Y_{500},θ_{500}) are different for completeness and reliability simulations and each is discussed below.

Effective beam variation is an important consideration for the unresolved clusters at the intermediate and high redshifts of cosmological interest. The injected clusters are convolved with effective beams in each pixel including asymmetry computed following Mitra et al. (2011)

4.2. Completeness

The completeness is defined as the probability that a cluster with a given set of true values for the observables (Y_{500},θ_{500}) will be detected, given a set of selection criteria. A good approximation to the completeness can be defined using the assumption of Gaussianity in the detection noise. In this case, the completeness for a particular detection code follows the error function (ERF), parametrised by a selection threshold q and the local detection noise at the clusters radial size, $\sigma_{\rm Y}(\phi,\psi)$ (see the discussion in Planck Collaboration XXIX 2014). This approach is not suited to the union and intersection catalogues from *Planck* due to the difficulty in modelling correlations between detection codes. We determine the completeness by brute force: injecting and detecting simulated clusters into the *Planck* sky maps. This approach has the advantage that all algorithmic effects are encoded into the completeness, and the effects of systematic errors such as beam and pressure profile variation can be characterised. This approach also fully accounts for the non-Gaussianity of the detection noise due to foreground emission.

The injected (Y_{500},θ_{500}) parameters are drawn from a uniform distribution in the logarithm of each variable, ensuring that our logarithmically spaced completeness bins have approximately equal numbers of injected sources.

As the completeness is estimated from injection into real data, injected sources can contribute to the detection noise. We therefore use an injection mode, as was the case for the PSZ1 completeness, where injected clusters are removed from the maps used to estimate the noise statistics. We also avoid superimposing injected clusters on top of one another, or on top of real data detections. Together, these ensure that the noise statistics for injected clusters are the same as for the real detections in the map.

We release as a product the Monte-Carlo completeness of the catalogues at thresholds stepped by 0.5 in S/N over the range 4.5 ≤S/N≤ 10. Fig. 6 shows the completeness of the union and intersection catalogues as functions of input (Y_{500},θ_{500}) and at representative values of θ_{500}, for three detection thresholds. The union and intersection catalogues are most similar at high S/N, where they match well except at small scales. Here the intersection catalogue follows the lower completeness of `MMF1`. This is due to an extra selection step in that code which removes spurious detections caused by point sources. The union and the intersection catalogues mark the upper and lower limits of the completeness values for the sub-catalogues based on the individual codes.

The completeness of the *Planck* cluster catalogue is robust with respect to deviations of the real SZ profiles of galaxy clusters from the one assumed by the algorithms for filter construction. To demonstrate this, we compare $C_{\rm MC}$, the Monte-Carlo completeness for the `MMF3` sample, using the cosmoOWLs profile variation prescription and effective beam variation, to $C_{\rm erf}$, the semi-analytic ERF completeness. This comparison is shown in Fig. 7, where we show the difference between the two estimates as a function of Y_{500} and θ_{500} as well the individual completeness values as functions of $Y_{500}$for representative values of θ_{500} slices through the 2D completeness and show the difference.

The error function is a good approximation to the MC completeness for the cosmology sample, which uses a higher S/N cut and a larger Galactic mask than the full survey. The MC estimate corrects this analytic completeness by up to 20% for large resolved clusters, where $C_{\rm MC}$ is systematically less complete than the ERF expectation, primarily due to variation in the cluster pressure profiles. For unresolved clusters, the drop-off in $C_{\rm MC}$ is slightly wider than the ERF expectation, reflecting variation both of pressure profiles and of effective beams.

The impact of these changes in completeness on expected number counts and inferred cosmological parameters for the cosmology sample is analysed in Planck

Collaboration XXIV (2015). The difference between the Monte-Carlo and ERF completeness results in a change in modelled number counts of typically $\sim 2.5\%$ (with a maximum of 9%) in each redshift bin. This translates into a 0.26σ shift of the posterior peak for the implied linear fluctuation amplitude,σ_8.

The MC completeness is systematically lower than the analytic approximation for the full survey. One of the causes of this is galactic dust contamination, which is stronger in the extra 20% of the sky included in the full survey area relative to the cosmology sample area. This tends to reduce the S/N of clusters on affected lines of sight.

We note that this approach ignores other potential astrophysical effects that could affect the completeness. Radio emission is known to be correlated with cluster positions, potentially 'filling in' the SZ decrement, though recent estimates suggest that this effect is typically small in *Planck* data (Rodriguez-Gonzalvez et al. 2015). Departures of the pressure distribution from spherical symmetry may also affect the completeness, though this effect is only likely to be significat for nearby and dynamically disturbed clusters which may be large compared to the *Planck* beams. We test for some of these effects through external validation of the completeness in the next section, and explicitly through simulation in Sect. 4.5.

Another source of bias is the presence of correlated IR emission from cluster member galaxies. Planck Collaboration XXIII (2015) show that IR point sources are more numerous in the direction of galaxy clusters, especially at higher redshift, and contribute significantly to the cluster SED at the *Planck* frequencies. Initial tests, injecting clusters signal with the combined IR+tSZ spectrum of $z > 0.22$ clusters observed by Planck Collaboration XXIII (2015), suggest that this reduces the completeness for unresolved clusters. Future work is warranted to characterise the evolution and scatter of this IR emission and to propagate the effect on completeness through to cosmological parameters.

4.3. External validation of the completeness

We validated our Monte-Carlo completeness calculation and our simple analytical ERF model by using the MCXC (Piffaretti et al. 2011) and SPT (Bleem et al. 2014) catalogues. The *Planck* detection threshold passes across the cluster distributions of these two samples. This is illustrated in Fig. 4 of Chamballu et al. (2012) for the MCXC. This allows us to characterize our completeness by checking if the fraction of detected clusters follows the expected probability distribution as a function of their parameters. For each cluster of the MCXC catalogue, we use the `MMF3` algorithm to extract its flux Y_{500} and associated error σ_Y at the location and for the size given in the x-ray catalogue. We then build the quantity $(Y_{500} - q\sigma_{\rm Y})/\sqrt{2}/\sigma_{\rm Y}$, q being the detection threshold (here 4.5) and $\sigma_{\rm Y}$ the noise of the filtered maps. We make the corresponding histogram of this quantity for all the clusters and for the clusters detected by `MMF3`. The ratio of the two histograms is an empirical estimate of the completeness. Results are shown in Fig. 8 for the MCXC (left) and the SPT (right) catalogues. For MCXC, the estimation is in good agreement with the expected simple analytical ERF model $(0.5\,(1 + \mathrm{ERF}))$. For SPT, the estimated completeness is also in good agreement except for $(Y_{500} - q\sigma_{\rm Y})/\sqrt{2}/\sigma_{\rm Y} > 1$ where it is higher than the analytic expectation. We attribute this behaviour to the correlation between SPT and *Planck* detections. The SPT catalogue is a SZ-based, so a cluster detected by SPT will have a higher than random probability to be detected by *Planck*. This leads to an overestimation of the completeness at the high probability end.

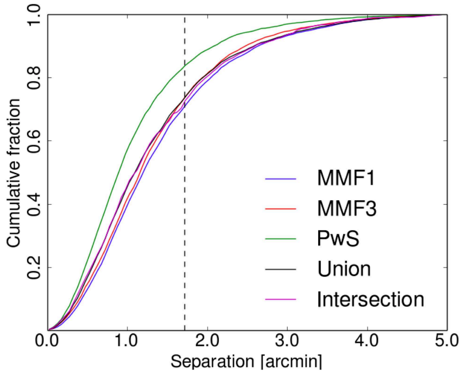

Fig. 9. Cumulative distribution of angular separations between estimated and input positions. The dashed vertical line denotes the *Planck* pixel size.

4.4. Position estimates

We characterise the positional recovery of the *Planck* detections using injection into real data, including pressure profile and beam variation. We draw input clusters from a realistic distribution of (Y_{500},θ_{500}), the same as used for the reliability in Sect. 4.6.

Fig. 9 shows the comparative performance of the individual detection codes, and of the reference position chosen for the union catalogue. `PwS` produces the most accurate positions, with 67% of detected positions being within 1.18 arcmin of the input position. For `MMF1` and `MMF3`, the 67% bound is 1.58 arcmin and 1.52 arcmin respectively. The union and intersection accuracy follow that of the MMFs, with 67% bounds of 1.53 arcmin. We observe that our inter-code merging radius of 5 arcmin is conservative given the expected position uncertainties.

4.5. Impact of cluster morphology

Clusters are known to possess asymmetric morphologies and a wide range of dynamical states, from irregular merging clusters to regular relaxed clusters. While the completeness simulations have included some morphology variations through variation of the injected radial pressure profile, this ignores the effects of the sub-structures and asymmetries, which may induce detection biases for large clusters at low redshift resolved by the *Planck* beams, FWHM≈ 7 arcmin.

Neither of the external samples used in Sect. 4.3 to validate the completeness allow us to properly probe resolved, irregular clusters at low-redshift. The MCXC is biased towards regular clusters due to X-ray selection effects and the *Planck* completeness drop-off lies substantially beneath the

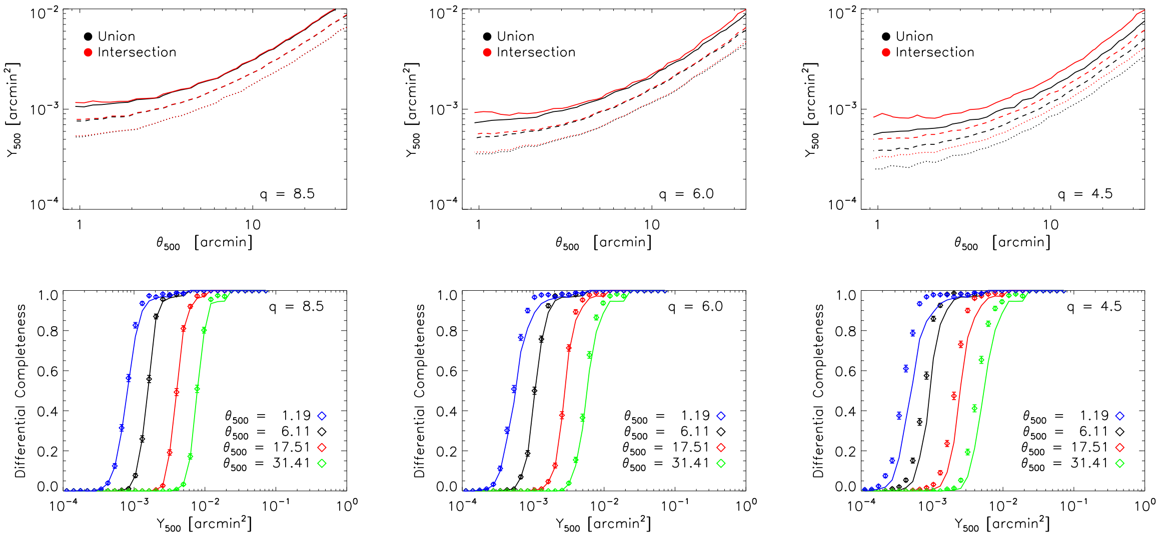

Fig. 6. Completeness of the union and intersection samples at progressively lower S/N thresholds. From left to right, the thresholds are 8.5, 6.0 and 4.5 (the survey threshold). In the top panels, the dotted lines denote 15% completeness, the dashed lines 50% and the solid lines 85% completeness. In the bottom panels, the union is denoted by the diamonds with Monte-Carlo uncertainties based on binomial statistics, and the intersection is denoted by the solid lines.

SPT mass limit at low redshift, so the drop-off is not sampled.

We address the effects of realistic morphology by injecting into the *Planck* maps the raw 2D projected Compton-y signal from a sample of hydro-dynamically simulated cosmoOWLs clusters. The clusters were injected with a large enough angular extent, $\theta_{500} = 20$ arcmin, that they were resolvable in the *Planck* data, and with a range of Y_{500} that encompassed the expected completeness drop-off. 20 candidate clusters were chosen from the sub-sample of cosmoOWLS clusters selected by the mass cuts discussed in Sect. 4.1 based on their dynamical state. The ten clusters in the sub-sample with highest kinetic-to-thermal energy ratio within θ_{500} constituted our disturbed sample, while the regular sample comprised the ten clusters with the lowest kinetic-to-thermal energy ratio within θ_{500}. These clusters were injected 200 times, randomly distributed across the sky. We also created simulations injecting symmetric clusters with the UPP with the same parameters and locations as the hydro-dynamic projections. In all cases, the signals were convolved with Gaussian beams to separate the effects of beam asymmetries.

The completeness for regular, disturbed and UPP clusters is shown for the union catalogue in the top panel of Fig. 10. There are no significant differences between the completeness functions for the regular and disturbed clusters. Both sets of hydro-dynamic clusters show a slight widening effect in the completeness caused by the variation in the effective pressure profile away from the UPP assumed for extraction (the same effect as discussed in Sect. 4.2).

Morphology has a clear impact on the estimation of cluster position. The bottom panel of Fig. 10 shows the cumulative distribution of angular separation between union and input positions for the regular, disturbed and UPP clusters. The disturbed clusters show a significant reduction in positional accuracy. Part of this is physical in origin. The clusters centres were defined here as the position of the 'most-bound particle', which traces the minimum of the gravitational potential and is almost always coincident with the brightest central galaxy. For merging clusters this position can be significantly offset from the centre of the peak of the SZ distribution. A matching radius of 10 arcmin, which is used in Sect. 7, ensured correct identification of detected and injected positions.

4.6. Reliability

The statistical reliability is the probability that a detection with given detection characteristics is a real cluster. We determine the reliability using simulations of the *Planck* data. Clusters are injected following the prescription in Sect. 4.1, except that the the clusters are injected such that cluster masses and redshifts are drawn from a Tinker et al. (2008) mass function and converted into the observable parameters (Y_{500}, θ_{500}) using the *Planck* ESZ Y_{500}–M_{500} scaling relation (Planck Collaboration X 2011). The other components of the simulations are taken from FFP8 simulation ensemble (Planck Collaboration XII 2015). The components include a model of galactic diffuse emission, with thermal dust (including some emission from cold-clumps), spinning dust, synchrotron and CO emission, and extragalactic emission from the far infra-red background. The diffuse components are co-added to a set of Monte-Carlo realisations of CMB and instrumental noise. In addition to the cluster signal, we also inject point sources drawn from a multi-frequency model from the *Planck* sky model (Planck Collaboration XII 2015). These point sources are mock detected, using completeness information from the PCCS2 (Planck Collaboration XXVI 2015), and harmonically infilled using the same process as for the real maps prior to

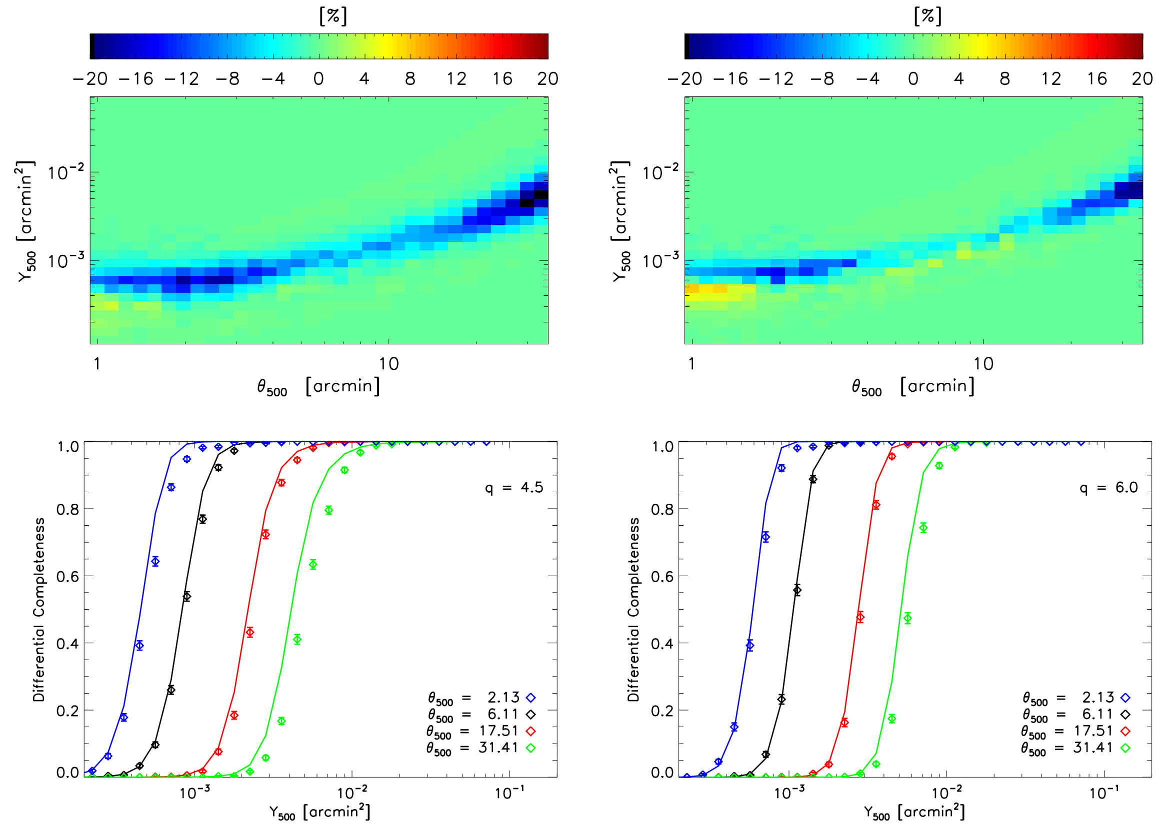

Fig. 7. Differences between the semi-analytic and Monte-Carlo completenesses for `MMF3`. The left panels show the difference for the full survey over 85% of the sky with a $q = 4.5$ threshold. The right panels show the difference for the `MMF3` cosmology sample, covering 65% of the sky to a threshold of $q = 6.0$. The top panels show the difference $MC-ERF$ in percent. The bottom panels compare the completenesses at particular θ_{500}: the Monte-Carlo completeness is denoted by diamonds and the ERF completeness by solid lines.

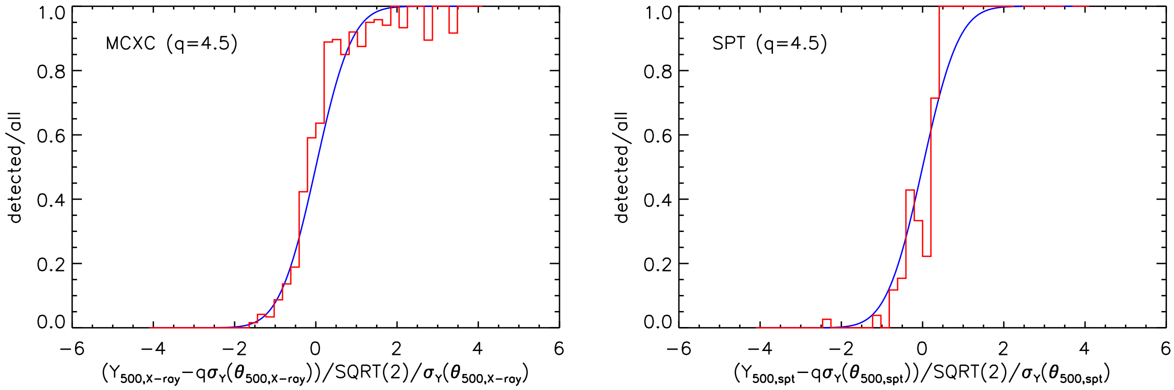

Fig. 8. `MMF3` completeness for the PSZ2 catalogue (S/N threshold $q > 4.5$) determined from the MCXC (left) and SPT (right) catalogues. This external estimate (red histogram) is in good agreement with the analytic ERF calculation (solid blue line), except for SPT at the high probability end (see text).

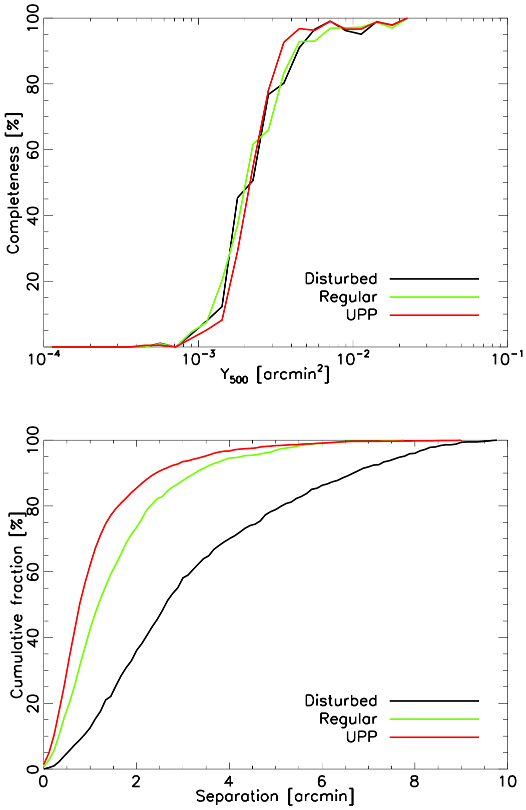

Fig. 10. Impact of cluster morphology on the completeness (top panel) and position estimates (bottom panel) for resolved clusters. The simulated clusters are all injected with $\theta_{500} = 20'$, and all curves are for the union catalogue. Cluster morphology has no impact on the completeness, but a significant impact on the position estimation.

SZ detection. This leaves a realistic population of residual sources in the maps. After detection, candidates that lie within the simulated expanded source mask, or which match with the cold-core or IR source catalogues from the real data, have their S/N set to zero.

Fig. 11 shows the reliability as a function of S/N for the union and intersection samples across the whole survey area and outside the 65% galactic mask used to define the cosmology samples. Relative to the PSZ1, the reliability of the union has improved by 5%, the lower noise levels have revealed more real simulated clusters than spurious detections. As was the case with the PSZ1, the reliability is improved significantly by removing more of the galactic plane, where diffuse and compact galactic emission induce extra spurious detections.

4.7. Neural network quality assessment

We supplement the simulation-based reliability assessment with an a-posteriori assessment using an artificial neural-network. The construction, training and validation of the neural network is discussed fully in Aghanim et al. (2014).

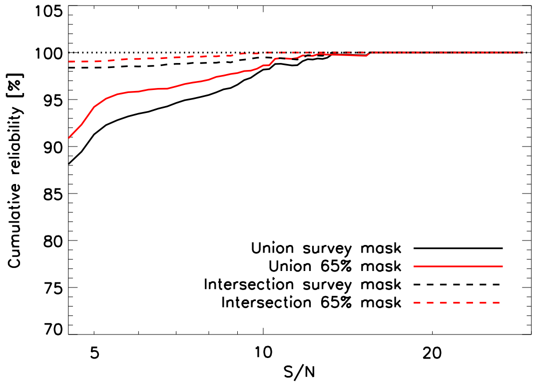

Fig. 11. Cumulative reliability as a function of S/N.

The network was trained on nominal mission *Planck* maps, with a training set composed of three elements: the positions of confirmed clusters in the PSZ1 as examples of good cluster signal; the positions of PCCS IR and radio sources as examples of point-source induced detections; and random positions on the sky as examples of noise-induced detections. We provide for each detection a neural network quality flag, Q_NEURAL $= 1 - Q_{\rm bad}$, following the definitions in Aghanim et al. (2014), who also tested the network on the unconfirmed detections in the PSZ1. They showed that this flag definition separates the high quality detections from the low quality detections, as validated by the the PSZ1 external validation process, such that Q_NEURAL < 0.4 identifies low-reliability detections with a high degree of success.

459 of the 1961 raw detections possess Q_NEURAL $<$ 0.4 and may be considered low-reliability. This sample is highly correlated with the IR_FLAG, with 294 detections in common. After removal of IR spurious candidates identified by the IR_FLAG, as discussed in Sect. 3.2, we retain 171 detections with bad Q_NEURAL, of which 28 are confirmed clusters. This leaves 143 unconfirmed detections considered likely to be spurious by the neural network.

The Q_NEURAL flag is sensitive to IR induced spurious: detections with low Q_NEURAL quality flag are clustered at low galactic latitudes and at low to intermediate S/N. This clustering is not seen for realisation-unique spurious detections in the reliability simulations, which are identifiable as noise induced. The reliability simulations underestimate the IR spurious populations relative to the Q_NEURAL flag. Conversely, the neural network flag by construction does not target noise-induced spurious detections: $Q_{\rm bad}$ is the parameter trained to indicate IR-induced spurious. The neural network flag also has some sensitivity to the noise realisation and amplitude in the data: the assessment is different to that applied to the nominal mission maps in Planck Collaboration XXXVI 2015.

To place a lower limit on the catalogue reliability, we combine the Q_NEURAL information with the noise-induced spurious detections from the reliability simulations. For each reliability simulation realisation, we remove the simulated IR spurious detections, which can be identified either as induced by the FFP8 dust component, and thus

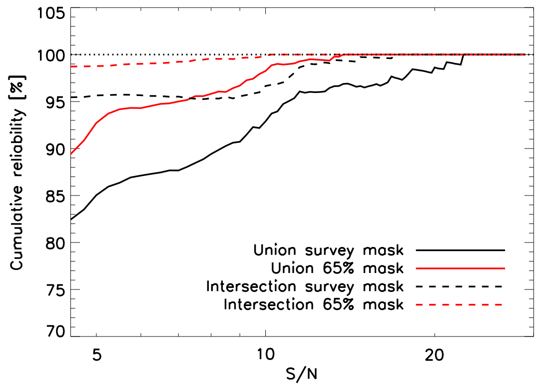

Fig. 12. Lower limits on the catalogue reliability, estimated by combining the reliability simulations with the Q_NEURAL information (see text).

present in multiple realisations, or as induced by injected IR point sources. We replace these spurious counts with the unconfirmed low Q_NEURAL counts, smoothed so as to remove the steps due to small number statistics.

The combined lower limit of the reliability is shown in Fig. 12. The lower limit tracks the simulation reliability well outside the 65% galactic dust mask. For the whole survey region, the lower limit is typically 6% lower than the simulation estimate, due either to over-sensitivity of the neural network to dusty foregrounds, or shortcomings in the FFP8 galactic dust component.

5. Parameter Estimates

The SZ survey observable is the integrated Comptonisation parameter, Y_{sz}. As was the case for the PSZ1, each of the extraction codes has an associated parameter estimation code that evaluates, for each detection, the two dimensional posterior for the integrated Comptonisation within the radius $5R_{500}$, $Y_{5\mathrm{R}500}$, and the scale radius of the GNFW pressure θ_S. The radius 5R500 is chosen as it provides nearly unbiased (to within a few percent) estimates of the total integrated Comptonisation, while being small enough that confusion effects from nearby structures are negligible.

We provide these posteriors for each object and for each code, and also provide $Y_{5\mathrm{R}500}$ in the union catalogue, defined as the expected value of the $Y_{5\mathrm{R}500}$ marginal distribution for the reference detection (the posterior from the code that supplied the union position and S/N).

Below we also discuss the intricacies of converting the posteriors to the widely used X-ray parameters $Y_{500}{-}\theta_{500}$.

5.1. Y_{5R500} estimates

To validate the $Y_{5\mathrm{R}500}$ estimates, we apply the posterior validation process introduced in Harrison et al. (2014) to the $Y_{5\mathrm{R}500}$ marginal distributions. In brief, this process involves simulating clusters embedded in the *Planck* maps and evaluating the $Y-\theta$ posteriors for each (detected) injected cluster. For each posterior, we determine the posterior probability, ζ, bounded by the contour on which the real underlying cluster parameters lie. If the posteriors are unbiased, the distribution of this bounded probability should be uniformly distributed between zero and one.

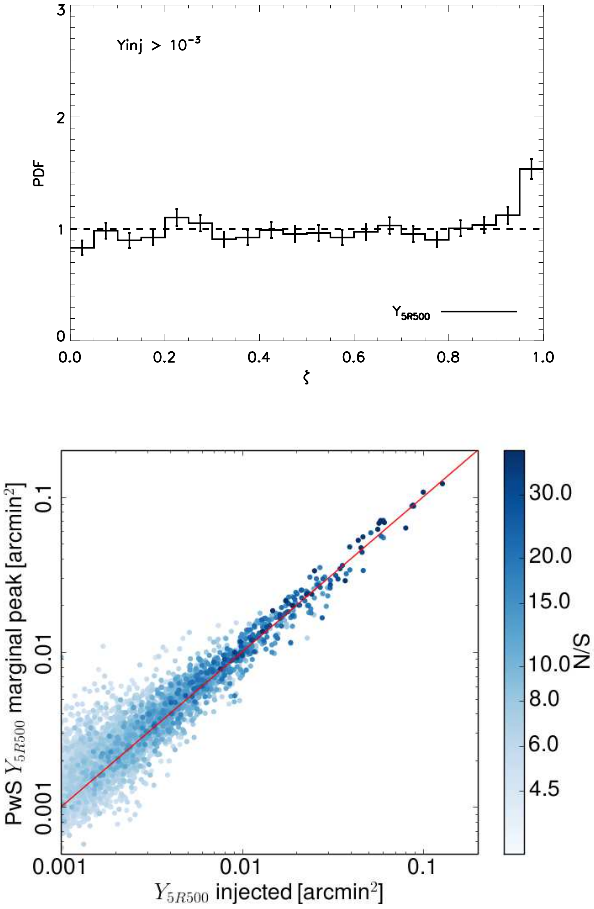

Fig. 13. *Top panel:* Results of the posterior validation for $Y_{5\mathrm{R}500}$. The histogram of the posterior probability, ζ, bounded by the true $Y_{5\mathrm{R}500}$ parameter is almost uniformly distributed, except for a small excess in the tails of the posteriors, at $\zeta > 0.95$. The histogram has been normalised by the expected counts in each ζ bin. *Bottom panel:* Comparison of recovered peak $Y_{5\mathrm{R}500}$ to the injected $Y_{5\mathrm{R}500}$. The estimates are unbiased, though asymmetrically scattered, with a scatter that decreases as S/N increases.

This process allows us to include several effects that violate the assumptions of the statistical model used to estimate the posteriors. Firstly, by injecting into real sky maps, we include the non-Gaussian contributions to the noise on the multifrequency-matched-filtered maps that come from galactic diffuse foregrounds and residual point sources. Secondly, we include violations of the 'signal' model that come from discrepancies between the cluster pressure profile and the UPP assumed for parameter estimation, and from sky-varying and asymmetric effective beams that vary from the constant Gaussian beams assumed for estimation.

The clusters are injected using the process discussed in Sect. 4.1, drawing injected pressure profiles from the set of cosmoOWLs simulated profiles.

The top panel of Fig. 13 shows the histogram of ζ for the `PwS` $Y_{5\mathrm{R}500}$ marginals. The distribution is flat, except for a small excess in the $0.95 - 1.0$ bin, which indicates a small excess of outliers beyond the 95% confidence region, in this case 52% more than statistically expected. This suggests the posteriors are nearly unbiased, despite the real-world complications added to the simulations. Note that we have considered only posteriors where the injected $Y_{5\mathrm{R}500} > 0.001$ arcmin^2, a cut that removes the population effects of Eddington bias from consideration: we focus here on the robustness of the underlying cluster model.

The bottom panel of Fig. 13 shows the peak recovery from the `PwS` $Y_{5\mathrm{R}500}$ marginals compared to the true injected values. The peak estimates are unbiased relative to the injected parameters.

5.2. Conversion to Y_{500}

The ($Y_{5\mathrm{R}500}$,θ_S) estimates can be converted into (Y_{500},θ_{500}) estimates using conversion coefficients derived from the UPP model that was assumed for extraction. However, when the underlying pressure distribution deviates from this model, the conversion is no longer guaranteed to accurately recover the underlying (Y_{500},θ_{500}) parameters: variation of the pressure profile can induce extra scatter and bias in the extrapolation.

We demonstrate this by applying the posterior validation process to the Y_{500} posteriors, defined as the $Y_{5\mathrm{R}500}$ posteriors scaled with the UPP conversion coefficient, as estimated from injected clusters whose pressure profiles are drawn from the cosmoOWLS pressure profile ensemble. We validate posteriors for Y_{500} calculated in two ways: firstly by marginalising over the θ_{500} parameter, referred to in previous publications as ‘Y blind'; and secondly by slicing the (Y_{500},θ_{500}) posteriors at the true value of θ_{500}, equivalent to applying an accurate, externally measured delta-function radius prior.

Fig. 14 shows the bounded probability histograms for the two Y_{500} posteriors and Fig. 15 shows the scatter of the peak of the posteriors with the input values of Y_{500}. The marginal Y_{500} posteriors are poor, with histograms skewed towards the tails of the distribution and large numbers of $> 2\sigma$ outliers. The scatter plot reveals the peak estimates to possess a large scatter and to be systematically biased high. In contrast, the peak $p(Y_{500}|\theta_{500})$ estimates have much better accuracy and precision and are distributed around the input values with low scatter. The bounded probability histogram of $p(Y_{500}|\theta_{500})$ shows that while there is a noticeable excess of detections in the wings, the posteriors are reasonably robust. If the posteriors were Gaussian, the skewness of the $p(Y_{500}|\theta_{500})$ histogram towards the tails would be consistent with an underestimate of the Gaussian standard deviation of 21%

We therefore recommend that, to estimate Y_{500} accurately from *Planck* posteriors, prior information be used to break the (Y_{500},θ_{500}) degeneracy. However, we note that the uncertainties on such Y_{500} estimates will be slightly underestimated.

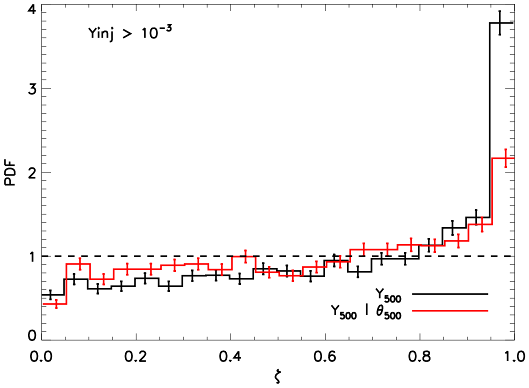

Fig. 14. Bounded probability histograms, as in the top panel of Fig. 13, but for the converted $p(Y_{500})$ marginal and $p(Y_{500}|\theta_{500})$ sliced posteriors.

5.3. Mass and Y_{500} estimates using scaling priors

The key quantity which can be derived from SZ observables is the total mass of the detected clusters within a given overdensity (we used $\Delta = 500$). To calculate the mass from *Planck* data it is necessary to break the size-flux degeneracy by providing prior information, as outlined in the previous section. We used an approach based on Arnaud et al. (in prep.), where the prior information is an expected function relating Y_{500} to θ_{500} that we intersect with the posterior contours. We obtained this relation by combining the definition of M_{500} (see Eq. 9 in Planck Collaboration XX 2014, connecting M_{500} to θ_{500}, for a given redshift z) with the scaling relation $Y_{500} - M_{500}$ found in Planck Collaboration XX (2014). A similar approach was also used in Planck Collaboration XXIX (2014), but in this work we use the full posterior contours to associate errors to the mass value.

We illustrate our method in Fig. 16. At any fixed value of θ_S, we study the probability distribution and derive the Y_{5R500} associated to the maximum probability, i.e. the ridge line of the contours (red continous line in Fig. 16). We also derive the Y_{5R500} limits enclosing a 68% probability and use them to define a upper and lower degeneracy curve (dashed lines). From the intersection of these three curves with the expected function (cyan line), we derive the M_{SZ} estimate and its 1σ errors, by converting Y_{5R500} to Y_{500} and then applying the $Y_{500} - M_{500}$ scaling relation prior at the redshift of the counterpart.

M_{SZ} can be viewed as the hydrostatic mass expected for a cluster consistent with the assumed scaling relation, at a given redshift and given the *Planck*$(Y - \theta)$ posterior information. We find that this measure agrees with external X-ray and optical data with low scatter (see Sect. 7). For each M_{SZ} measurement, the corresponding Y_{500} from the scaling relation prior can be calculated by applying the relation.

We underline that the errors bars calculated from this method consider only the statistical uncertainties in the contours, not the uncertainties on the pressure profile nor the errors and scatter in the $Y_{500} - M$ scaling relation, and should thus be considered a lower limit to the real uncertainties on the mass.

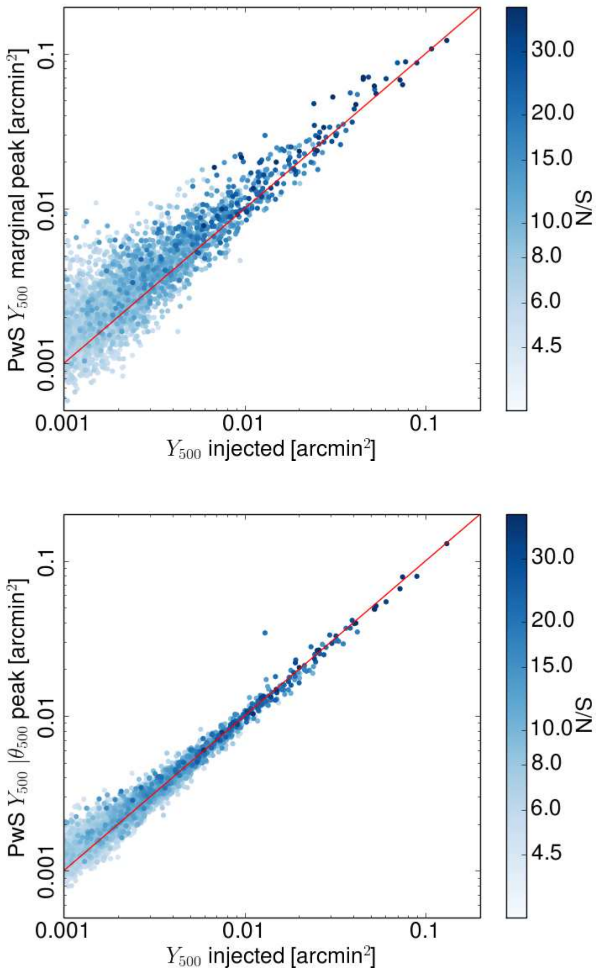

Fig. 15. Scatter of the recovered estimates of Y_{500} with the input Y_{500}. *Top panel*: for the marginalised Y_{500} posterior, 'Y blind'. *Bottom panel*: for the sliced posterior $p(Y_{500}|\theta_{500})$, assuming an accurate radius prior.

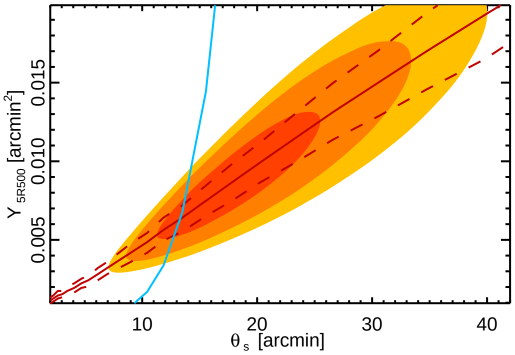

Fig. 16. Illustration of the posterior probability contours in the $Y_{5R500} - \theta_s$ plane for a cluster detected by *Planck*: the contours show the 68, 95 and 99 percent confidence levels. The red continuous line shows the ridge line of the contours while the dashed lines the 1-σ probability value at each θ_s. The cyan line is the expected $Y - \theta$ relation at a given redshift that we use to break the degeneracy.

Table 3. Results of fits between S/N from the PSZ1 and PSZ2, using the fitting function in Eq. 6. The assumed correlation of the uncertainties of s_1 and s_2 was 0.72.

s_1	s_2	A	α	σ
PSZ2	PSZ1	0.76 ± 0.08	0.72 ± 0.01	0.53 ± 0.02

We used the masses for the confirmation of candidate counterparts (see Sect. 7) and we provide them, along with their errors, in the PSZ2 catalogue for all detections with confirmed redshift. We compared them with the masses provided in PSZ1 for the detections where the associated counterpart (and thus the redshift value) has not changed in the new release (see Appendix B). We find very good agreement between the two values which are consistent within the error bars over the whole mass range.

In the individual catalogues, we provide for all entries an array of masses as a function of redshift ($M_{\rm SZ}(z)$), which we obtained by intersecting the degeneracy curves with the expected function for different redshift values, from $z = 0$ to $z = 1$. The aim of this function is to provide a useful tool for counterpart searches: once a candidate counterpart is identified, it is sufficient to interpolate the $M_{\rm SZ}(z)$ curve at the counterpart redshift to estimate its mass.

6. Consistency with the PSZ1

The extra data available in the construction of the PSZ2 improves the detection S/N and reduces statistical errors in the parameter and location estimates. Here we assess the consistency between the two catalogues, given the matching scheme discussed in Sect. 7.1.

6.1. Signal-to-noise

We fit the relation between S/N for common PSZ1 and PSZ2 using the the approach and model discussed in Sect. 3.4. For the PSZ1 and PSZ2, the likelihoods for s_1 and s_2 have a strong covariance, as more than half of the PSZ2 observations were used in the construction of the PSZ1. We therefore assign a covariance of 0.72 between the two S/N estimates, as is appropriate for Gaussian errors sharing 53% of the data. As the errors are not truly Gaussian, we allow for an intrinsic scatter between the S/N estimates to encapsulate any un-modelled component of the S/N fluctuation.

The consistency of the S/N estimates between the PSZ1 and PSZ2 are shown in Fig. 17 and the best fitting model in is shown in Table 3. Detections with PSZ2 $S/N > 20$ are affected by changes in the `MMF3` S/N definition. For the PSZ1, the empirical standard deviation of the filtered patches was used to define the S/N in this

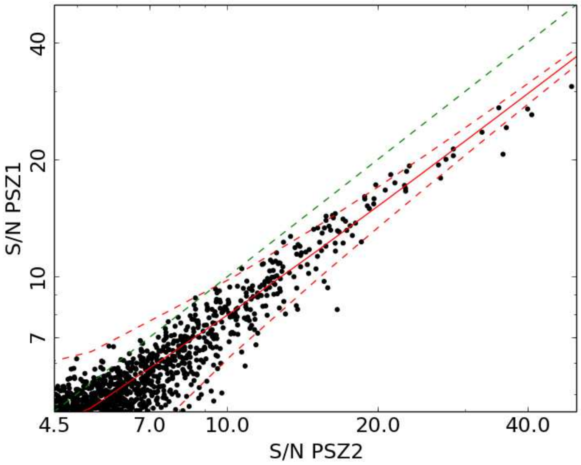

Fig. 17. Comparison of S/N values for common PSZ1 and PSZ2 detections. The best fit relation is plotted in red, with 2σ scatter plotted by dashed red lines. The green dashed line denotes the 1-1 relation.

regime, while the theoretical standard deviation of Melin et al. (2006b) was used for lower S/N. `MMF3` now uses the theoretical standard deviation for all S/N, consistent with the ESZ and the definitions in the other detection codes. For this reason, the best fit model ignores detections at $S/N > 20$ in either catalogue. The `MMF3` S/N show a flat improvement relative to the ESZ S/N (which was produced solely by `MMF3`), consistent with the reduced noise in the maps.

If the Compton-Y errors are entirely Gaussian in their behaviour, we should expect the S/N to increase by 37% between the PSZ1 and PSZ2, ie: $\alpha = 0.73$. This is consistent within 1σ with the fit, which describes the S/N behaviour well to S/N$<$ 20.

6.2. Position estimation

The distribution of angular separations between the PSZ2 and PSZ1 position estimates is shown in Fig. 18. Of the common detections, 80% of the PSZ2 positions lie within one *Planck* map pixel width, 1.7 arcmin, of the PSZ1 position. `MMF3` does not allow for sub-pixel positioning, so if the `MMF3` position was used for the union in both the PSZ1 or PSZ2, the angular separation will be a multiple of the pixel width. This is evident in the cumulative distribution of angular separations as discontinuities at 0, 1 and $\sqrt{2}$ pixel widths.

We also compare the position discrepancy between the SZ detection and the X-ray centres from the MCXC (Piffaretti et al. 2011).The bottom panel of Fig. 18 shows the distributions of these angular separations for the PSZ2 and PSZ1. The distributions are calculated from the full MCXC match for each catalogue: the PSZ2 includes 124 new detections. The PSZ2 position estimates are clearly closer to the X-ray centres than the PSZ1: for the PSZ1, the 67% error radius is 1.85 arcmin, while for the PSZ2 this reduces to 1.6 arcmin.

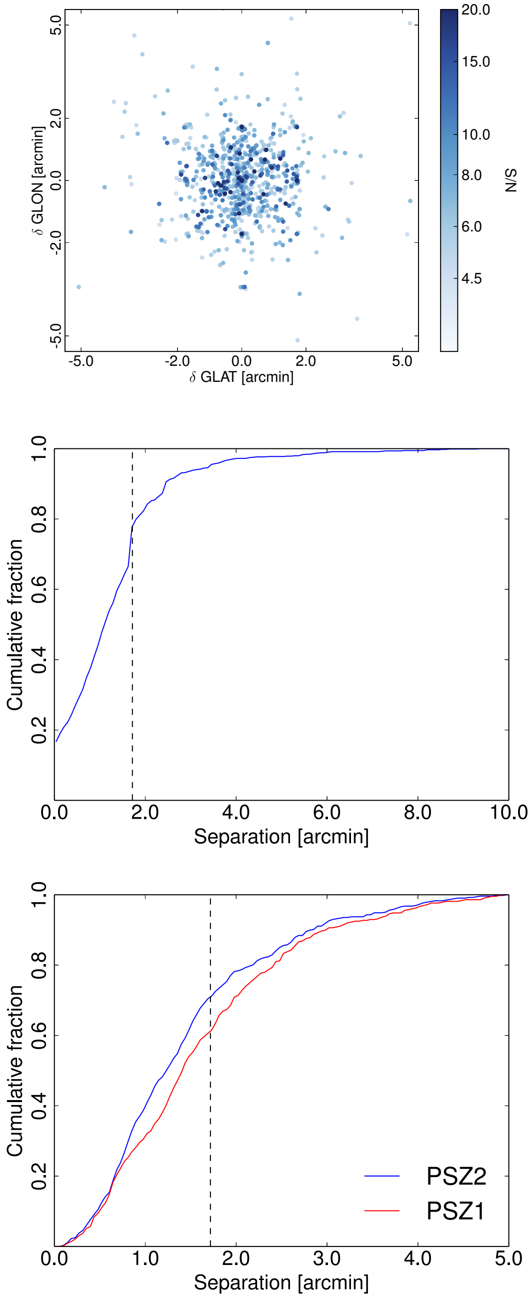

Fig. 18. *Top panel*: Separation between PSZ2 and PSZ1 positions for common detections. *Middle panel*: Cumulative distribution of the angular separation between PSZ1 and PSZ2 positions, with the *Planck* pixel width indicated by a dashed vertical line. *Bottom panel* Cumulative distributions of angular separation to MCXC x-ray centres, for all PSZ1 and PSZ2 MCXC matches. The vertical dashed line denotes the *Planck* Healpix pixel size.

6.3. Missing PSZ1 detections

The PSZ1 produced 1227 union detections. While the numbers of detections has increased by 35% in the PSZ2 to 1653, the number of common detections is 936: 291 (23.7%) of the PSZ1 detections disappear. The high-purity intersection sample loses 44 detections, of which 20 are lost entirely, and 24 drop out of the intersection after one or two codes failed to detect them. In this section, we discuss these missing detections. Table E.1 details each of the missing detections and provides an explanation for why each is missing.

The first type of missing detection are those that fall under the new survey mask, due to the increase in the number of point sources being masked. The masked areas sare preprocessed with harmonic infilling to prevent spurious detections induced by Fourier ringing. The increase of the mask area is driven by S/N improvements for IR sources in the high frequency channels. While the increase in the masked area is small (0.1% of the sky), the correlation between IR point sources and galaxy clusters leads to a larger percentage of detections being masked. In the PSZ1, these detections were contaminated by point source emission, but the emission was just beneath the point source masking threshold. 21 PSZ1 union detections fall behind the new mask. Of these, three were confirmed clusters, none received the highest validation quality flag of 1 (denoting probable clusters) in the PSZ1 validation process[4], four received the intermediate validation quality flag 2, and 14 received the lowest validation quality flag of 3, denoting probable spurious.

The second type of missing detection is one which has a matching detection in the full-mission data, but where the detection was rejected either by the infra-red spurious cuts or by `PwS` internal consistency cuts, both of which are discussed in Sect. 3.2. The IR cuts are responsible for cutting 33 unconfirmed PSZ1 detections, of which six were in the intersection sample. In the PSZ1 validation process, none of these received validation quality flag of 1, seven received quality flag 2 and 26 received quality flag 3. These were all $S/N < 7$ detections. Five detections were lost because `PwS` was the only detecting code in the PSZ2 and they failed `PwS` consistency criteria: two of these were confirmed clusters.

The final type contains the majority (232) of the missing detections. These are low-significance detections close to the PSZ1 threshold that have downward-fluctuated with the full mission data and are now beneath the PSZ2 threshold. This occurs for some detections despite the fact that the S/N improves for most. The top panel of Fig. 19 shows the PSZ1 S/N distribution of the downward-fluctuated detections. These were weak detections: 87% were within 0.5σ of the detection threshold and 82% of them were single-code detections. While many of these may be spurious detections, 81 confirmed clusters have been lost. 61 of these were single-code detections and 70 of them were within 0.5σ of the threshold. Based on *Planck* data alone, these clusters were weak SZ detections and were likely to be Eddington biased above the threshold in the PSZ1. We have estimated the S/N for these lost PSZ1 detections in the full-mission maps using `PwS` in a non-blind analysis at the PSZ1 positions. Fig. 20 shows the distribution of these non-blind S/N: for most an apparently significant signal still exists in the maps, but it is now too weak to exceed the detection threshold, typically lying between $2 < S/N < 4$. The non-blind S/N for this category is shown per detection in Table E.1. Two detections have a non-blind S/N above the selection threshold. For these detections, the noise level for the non-blind analysis (centred on the PSZ1 location) was lower than for any of the patches in the mosaic used for the cluster detection.

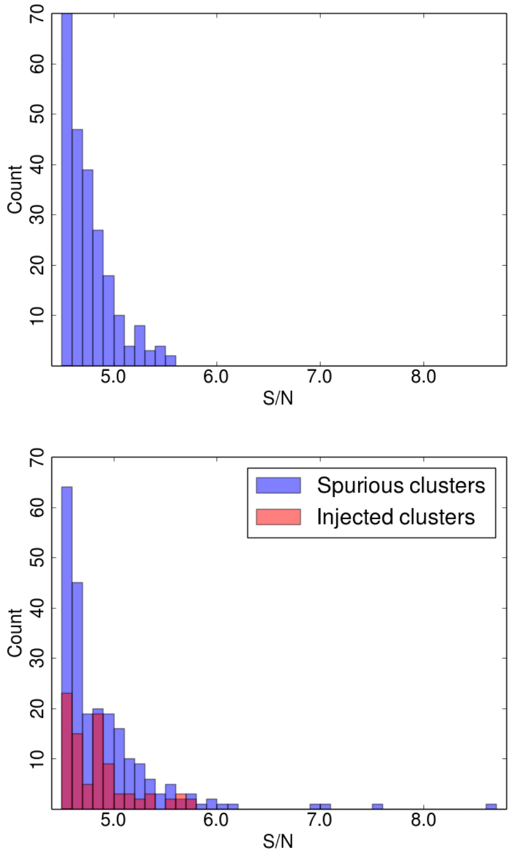

Fig. 19. Distribution of S/N for missing nominal mission detections lost due to downward fluctuation of the S/N rather than because of spurious rejection cuts or changes in the survey mask. *Top panel* Detections lost from the PSZ1. *Bottom panel* Detections lost in simulations of the transition from the nominal to full mission.

To verify that this sample of missing detections is consistent with the change in data, we simulated the transition from the PSZ1 to the PSZ2 using FFP8 half-mission noise realisations to approximate the nominal mission: this produces a pair of data-sets with appropriately correlated noise characteristics. A common sample of clusters and point sources were injected into the simulations and the full pipeline was applied to construct catalogues from both

---

[4] The PSZ1 validation process produced three quality flags for unconfirmed clusters. These were based on a combination of SZ signal quality, X-ray signal in the RASS maps and IR signal in the WISE maps. Class 1 candidates satisfied good quality in all three measures and were high reliability candidates. Class 2 satisfied at least one measure with good quality, while class 3 failed all three measures and so were considered probably spurious.

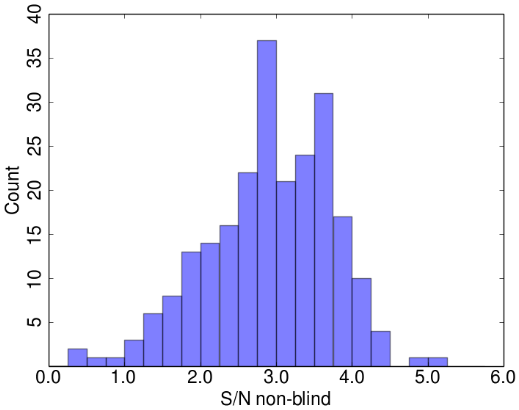

Fig. 20. Non-blind `PwS` S/N for the SZ signal at the location of missing PSZ1 detections that were not masked out or cut for IR contamination.

simulated datasets. The simulations produced a total loss of 353 detections, of which 24 were lost due to the expansion of the point source mask, ten were lost due to changes to the `PwS` spurious rejection criteria, and 319 were lost due to downward fluctuation of the S/N beneath the detection threshold.

The S/N distribution of the latter group is shown in the bottom panel of Fig. 19. 75% lie within 0.5σ of the detection threshold and 85% were single-code detections. While this group was primarily composed of 230 spurious detections, 89 injected clusters were lost. The loss of these injected clusters illustrates that, as a statistical process, cluster detection is dependent on the realisation of the noise in the filtered patch-maps and we should expect that substantial numbers of confirmed but weak cluster detections will be lost due to noise fluctuations.

These simulations over-estimate the loss-rate of nominal mission detections. This may be due in part to unsimulated changes in the sample selection applied to the real data. We were unable to simulate systematic changes in the IR spurious rejection that may, had they been incorporated, have resulted in some spurious detections from the nominal mission simulation being cut from the comparison.

6.4. Compton Y estimates

The Compton $Y_{5\mathrm{R}500}$ estimates from each code are compared to the PSZ1 estimates in Fig. 21. The $Y_{5\mathrm{R}500}$ estimates that we consider here are the mean estimates of the $Y_{5\mathrm{R}500}$ marginal posteriors, having marginalised over the scale radius θ_s.

The best fit relations between the PSZ2 and PSZ1 values for each code are shown in Table 4. These were fit using a similar procedure to the S/N estimates discussed in the previous section. We assume a log-linear relation between the estimates of the form

$$\log\frac{Y_2}{Y_{\mathrm{piv}}} = A + \alpha\log\frac{Y_1}{Y_{\mathrm{piv}}}, \tag{7}$$

with a log-normal intrinsic scatter σ_{int} and $Y_{\mathrm{piv}} = 3\times10^{-4}$ arcmin^2. We again assume a bivariate Gaussian likelihood for the estimates, with a correlation of 0.72.

Fig. 21 compares the $Y_{5\mathrm{R}500}$ estimates for each of the three detection codes. High S/N detections have more consistent estimates of $Y_{5\mathrm{R}500}$. For `MMF3`, detections at S/N>20 are significantly changed due to the changes in the treatment of these detections discussed in Appendix C. These points are excluded from the fit to the relation. The scatter on the high S/N estimates is determined by the robustness of the noise power spectrum estimation to small changes in the data. For `PwS`, the high S/N estimates have particularly low scatter, due to the robust nature of the noise estimation that accounts for Compton-Y 'noise' contributed by neighbouring clusters.

The low S/N detections show systematic deviations for each of the codes. For the MMFs, these are caused by the correction of PSZ1 Eddington bias in the PSZ2 data, which is visible in Fig. 21 as clouds of faint points where the $Y_{5\mathrm{R}500}$ estimate reduces in the PSZ2. The opposite is the case for `PwS` estimates, where the faint detections show upward deviation in the PSZ2. This is caused by a change in the priors: for the PSZ1, `PwS` used a power-law prior in $Y_{5\mathrm{R}500}$, which was replaced in the PSZ2 with the uninformative flat prior, as this produced more robust $Y_{5\mathrm{R}500}$ estimates in the posterior validation process discussed in the previous section. We have confirmed that `PwS` behaves in the same way as the MMFs when uninformative priors are used for both PSZ1 and PSZ2 parameter estimates (see the bottom right panel of Fig. 21).

To verify that the bias effects seen in Fig. 21 are within expectations, we extracted $Y_{5\mathrm{R}500}$ estimates from the half to full-mission transition simulations described in Sec. 6.3. We confirm the same behaviour in these simulations as in the real data: low S/N detections from the MMFs show a correction of Eddington bias in the full mission while `PwS` low S/N detections are affected by change from power-law to uninformative priors in the posterior estimation and are typically higher in the full mission.

7. Ancillary Information

7.1. Cross-match with PSZ1

We begin the search for counterparts by conducting a cross-match with the well-validated PSZ1. All matches within 5 arcmin of a PSZ1 detection are accepted as a true match. Both catalogues used this radius as the merging limit to define unique detections, both in the merge of Cartesian patch catalogues to form an all-sky catalogue and in the formation of the union). This step produced no multiple matches.

Several of our detections are clear matches with PSZ1 detections at higher radii than this, so we consider matches out to 10 arcmin, as is the case with the X-ray and optical counterpart searches described below. This step produced 18 potential matches, two of which were non-unique. We apply a further condition to accept these high-separation matches: that the PSZ2 S/N be greater than the PSZ1 S/N and be consistent with the S/N relation determined in Sect. 6.1. For the two non-unique matches, the nearer match was chosen both times and this match also better fit the S/N relation.

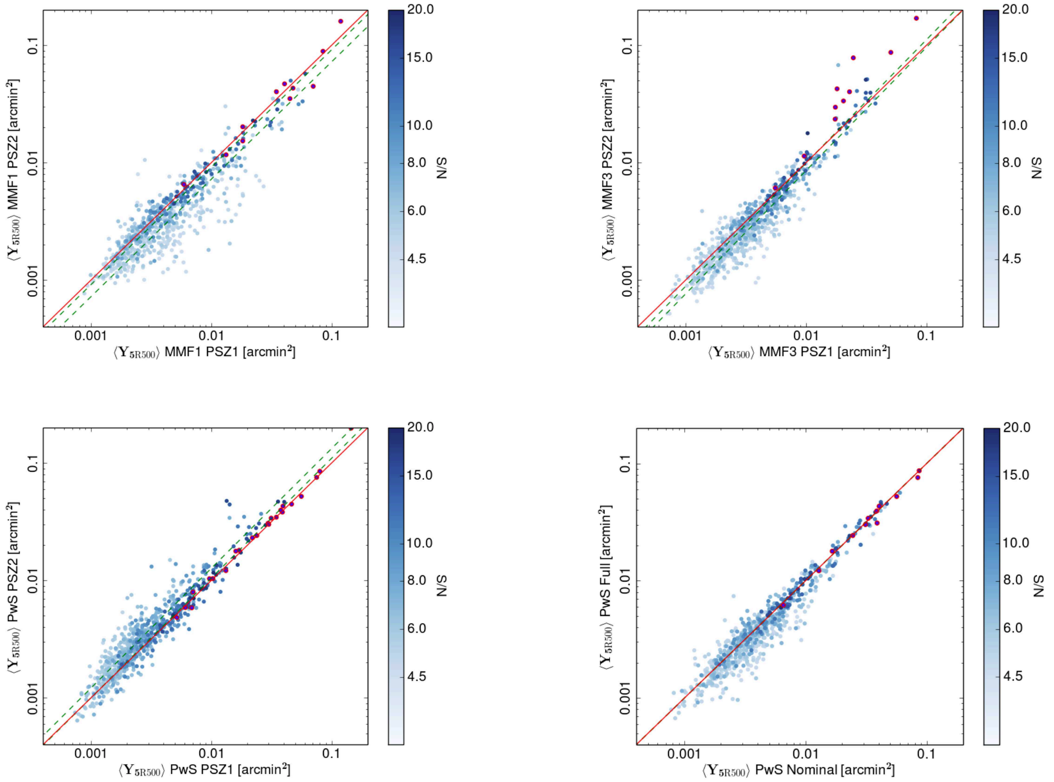

Fig. 21. Comparison of $Y_{5\mathrm{R}500}$ estimates from individual codes in the PSZ1 and PSZ2. The $Y_{5\mathrm{R}500}$ estimator is the mean of the $Y-\theta$ posteriors, marginalised over θ_S ('Y blind'). The circled red points denote sources with $S/N > 20$. The dashed green lines show the $1-\sigma$ envelope of the best-fit relations shown in Table 4. `MMF1` estimates are shown top left, `MMF3` top right. `PwS` estimates are shown bottom left. The bottom right panel compares `PwS` estimates having re-analysed PSZ1 data using uninformative priors on $Y_{5\mathrm{R}500}$ and θ_S.

Table 4. Results of fits between $Y_{5\mathrm{R}500}$ from the PSZ1 and PSZ2, following Eq. 7.

Y_1	Y_2	A	α	σ_{int}
PSZ1 `MMF1`	PSZ2 `MMF1`	-0.087 ± 0.006	1.00 ± 0.02	0.083 ± 0.003
PSZ1 `MMF3`	PSZ2 `MMF3`	-0.054 ± 0.002	1.05 ± 0.01	0.054 ± 0.003
PSZ1 `PwS`	PSZ2 `PwS`	0.056 ± 0.005	1.02 ± 0.01	0.068 ± 0.003

7.2. X-ray information

We use the *Meta-Catalogue of X-ray detected Clusters of galaxies* (MCXC, Piffaretti et al. 2011) for the association of *Planck* SZ candidates with known X-ray clusters, as was done in Planck Collaboration XXIX (2014). MCXC is based on the *ROSAT* All Sky Survey and complemented with other serendipitous catalogues and with the *Einstein* Medium Sensitivity Survey. It includes 1743 clusters distributed over the whole sky and provides coordinates, redshifts and X-ray luminosity measured within R_{500}, $L_{\mathrm{X},500}$. The association of *Planck* SZ candidates with MCXC clusters follows two steps: first a positional matching between the catalogues then a verification of the association using the $L_{\mathrm{x},500} - M_{500}$ relation (Pratt et al. 2009). In the first step, we looked for possible counterparts of *Planck* SZ candidates in the MCXC within a searching radius of 10 arcmin around the *Planck* position. We found one counterpart for 537 candidates and multiple matches for another 16 objects. In the second step, we verified our associations by looking at their position in the $L_{\mathrm{x},500} - M_{500}$ plane (Fig. 22). For the X-ray luminosity, we use the $L_{\mathrm{x},500}$ value provided in the MCXC, while we calculate the mass from our own data, as described in Sect. 5. In Fig. 22, we compare our results with the expected $L_{\mathrm{x},500} - M_{500}$ relation (Piffaretti et al. 2011): we consider as good associations those whose position in the $L_{\mathrm{x},500} - M_{500}$ does not differ from the expected one by more than twice the intrinsic scatter in the relation ($\sigma_{\mathrm{int}} = 0.183$ Pratt et al. 2009). Based on this criterion we discarded the association with an MCXC cluster for two objects, PSZ2 G086.28 + 74.76 and PSZ2 G355.22 − 70.03, both new PSZ2 detections.

We performed a further check of the candidate counterparts, by studying the separation between the *Planck* and the MCXC positions. Indeed, the relatively large search radius (10 arcmin) may have led to spurious associations, which might have escaped our selection on the $L_{x,500} - M_{500}$ relation. In Fig. 23, we compare the separation between the *Planck* and the MCXC positions with two relevant angular scales: the positional uncertainty of the *Planck* detections $\theta_{\rm err}$ (90% confidence level, provided in the catalogue) and the cluster size as quantified by θ_{500}[5]. Ideally, one would keep as good counterparts those systems where the angular separation is smaller than both θ_{500} and $\theta_{\rm err}$ (lower left quadrant in Fig. 23) but this would lead to a large number of rejected matches including many objects in the PSZ1. Therefore, we chose a less conservative criterion: we excluded only those associations where the separation is larger than both θ_{500} and $\theta_{\rm err}$ (upper right quadrant in Fig. 23). We thus allow the separation to exceed θ_{500} if the MCXC counterpart falls within the *Planck* accuracy (upper left quadrant) and to exceed θ_{err} if it is smaller than the cluster expected size (lower right quadrant). We noticed that the most deviant clusters in the latter case (with $\theta > 2\theta_{500}$) are associated with nearby clusters ($z < 0.14$) with $\theta_{500} > 7$ arcmin, resolved by *Planck*. In this phase of the analysis, we thus discarded the three associations to PSZ2 G247.97 + 33.52, PSZ2 G212.93 − 54.04, and PSZ2 G209.79 + 10.23 in the upper right quadrant of Fig. 23: for these systems, the separations between the *Planck* and MCXC are always larger than 5 arcmin, which would correspond to a physical distance of $\simeq$ 1Mpc at the redshift of the MCXC objects (all at $z > 0.2$).

We also used the position in the $L_{x,500} - M_{500}$ and in the separation plane (Fig. 23) to select the most likely counterparts for the objects where two or more MCXC clusters were found within our search radius of 10 arcmin. For seven out of 16 objects, one counterpart does not match the criteria described above and we are thus left with only one good counterpart. For six *Planck* detections, both MCXC counterparts fullfill our requirements. We thus rank them based on their distance from the $L_{x,500} - M_{500}$ scaling relation and their separation in terms of θ_{500} and $\theta_{\rm err}$, and select as most likely counterpart the one with smaller values for at least two out of three indicators. We provide details of the other possible counterparts in the Comments file. In two cases, the same MCXC cluster can be associated with two *Planck* detections and we used the procedure described above to select the most likely associations.

In the last step of our analysis, we checked our matching with MCXC with the matches made in the PSZ1 catalogue: in most cases the MCXC counterparts in the two catalogues coincide. We examined in detail the cases where, following our selection criteria, we would have broken the association with the MCXC counterpart which was chosen in PSZ1. This led to three restorations:

- PSZ2 G247.97+33.52 (PSZ1 index 842) association with RXCJ0956.4 − 1004 lies in the forbidden area in the separation plane. However, RXCJ0956.4 − 1004 (also known as A901) is a multi-component cluster (Bösch et al. 2013), and the PSZ2 position lies close to the position of one of the components. We thus decided to keep the association.
- PSZ2 G302.41 + 21.60(PSZ1 index 1054) and PSZ2 G332.29 − 23.57(PSZ1 index 1158) are both associated very low-redshift clusters (RXC J1248.7−4118 and RXC J1847.3−6320, both $z < 0.015$) which are marginal outliers in the L-M plane. However, our mass proxy estimate may be less reliable for local objects due to the large cluster extent and we thus decided to keep these associations.

7.2.1. Comparison to $L - M$ relation

It is interesting to note in Fig. 22 that most points lie below the expected scaling relations of Pratt et al. (2009), although well within the intrinsic scatter, meaning that clusters in our subsample are systematically under-luminous (by about 21%, or $-0.41\sigma_{\rm int}$) in X-rays at a given mass. We recall here that this subsample (intersection of PSZ2 with MCXC) is not representative and thus cannot be quantitatively compared with a well defined representative sample such as REXCESS, for which the $L_{x,500} - M_{500}$ was derived by Pratt et al. (2009). The systematic offset observed in Fig. 22 does not contradict the good agreement between X-ray predictions and *Planck* measurements found with a statistical approach in Planck Collaboration X (2011). It can be explained taking into account selection effects and the scatter in the $Y - L_{\rm X}$ scaling relation: when cutting in SZ S/N, clusters with a high SZ signal (and thus a high mass) for a given X-ray luminosity are preferentially selected. Another effect, which could also partly contribute to the offset in Fig. 22, is the presence of a cluster population with different X-ray properties in the PSZ2 sample which will be discussed in Sect. 8.2.

7.3. Optical information

We benefit from a wealth of publicly available data over the northern sky, principally thanks to the Sloan Digital Sky Survey (SDSS, York et al. 2000) that covers most of the northern extragalactic sky with imaging in five optical bands (*ugriz*). A number of cluster catalogues have been extracted from these data using different finding algorithms (Koester et al. 2007; Hao et al. 2010; Wen et al. 2012). Among these, the `redMaPPer` catalogue (Rykoff et al. 2014), published since the PSZ1 release and containing many more clusters, has proven to be the most useful for identifying counterparts to *Planck* SZ sources. We also supplement `redMaPPer` with other optically information.

7.3.1. RedMAPPer

The `redMaPPer` algorithm detects clusters by looking for spatial over-densities of red-sequence galaxies. It provides accurate photometric redshift estimates for all sources, spectroscopic redshifts for the brightest central galaxy (BCG) when available, and richness estimates. We used

---

[5] We calculated θ_{500} from the mass proxy M_{500}, using the redshift of the MCXC counterpart.

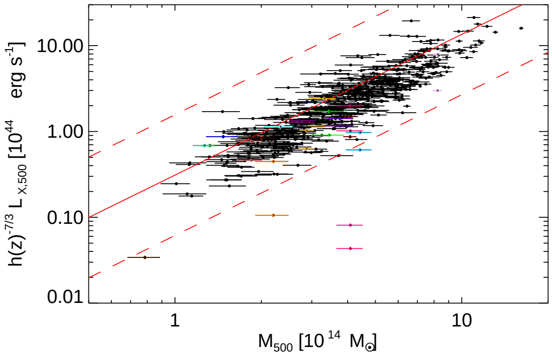

Fig. 22. Comparison of candidates associated with the MCXC catalogue with the expected $L_{\rm x,500} - M_{500}$ scaling relation (red line). The parallel dashed lines identify the region of the plane within $2\sigma_{\rm int}$ from the expected scaling relation, where $\sigma_{\rm int}$ is the logarithmic intrinsic scatter of the relation we used. Black points are confirmed MCXC associations, while magenta squares mark the associations discarded by the L-M criterion. Pairs of coloured diamonds mark the two possible counterparts for objects with multiple associations.

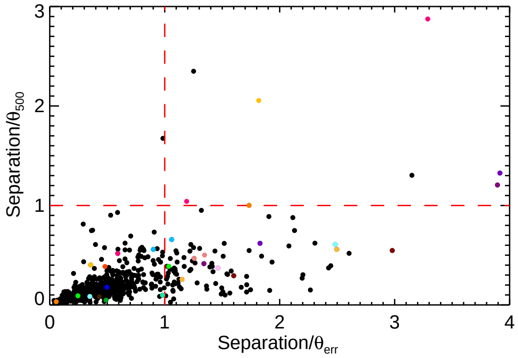

Fig. 23. Separation between the *Planck* and MCXC positions in terms of the positional uncertainty of the *Planck* detection and of the cluster R_{500}. The horizontal and vertical dashed lines mark our acceptance threshold.

the proprietary `redMaPPer` catalogue (v5.10) provided by the authors and containing over 400,000 objects.

In our procedure, detailed further in Bartlett et al. 2014 (in prep.), each *Planck* SZ source is first matched to a maximum of three `redMaPPer` clusters falling within a radius of 10 arcmin. They are subsequently ranked by richness and labeled first-, second-, and third-ranked matches. We then calculate the *Planck* mass proxy, $M_{\rm sz}$, for each SZ source at the redshifts of its matched `redMaPPer` clusters. The best `redMaPPer` counterpart is then selected based on cuts in angular separation and richness. The angular cuts incorporate both the *Planck* positional uncertainty and the physical extent of the cluster estimated from the calculated $M_{\rm sz}$.

These angular criteria alone would leave multiple possible counterparts in many cases, given the high surface density of `redMaPPer` clusters. Any ambiguity is efficiently reduced by the richness cut, which is based on the existence of a well-defined relation between richness, λ, and $M_{\rm sz}$. The relation was established by Rozo et al. (2014) on the *Planck* 2013 SZ cluster catalogue and is expressed as

$$\langle \ln\lambda | M_{\rm sz}\rangle = a + \alpha \ln(\frac{M_{\rm sz}}{M_{\rm p}}), \tag{8}$$

with $a = 4.572 \pm 0.021$, $\alpha = 0.965 \pm 0.067$, and $M_{\rm p} = 5.23 \times 10^{14}\,{\rm M}_{\odot}$. The measured dispersion at given $M_{\rm sz}$ is $\sigma_{\ln\lambda} = 0.266 \pm 0.017$.

In Fig. 24 we compare the distribution of the first, second-, and third-ranked `redMaPPer` matches in the $\lambda - M_{\rm SZ}$ plane to this scaling relation. The quantity $\Delta_{\ln}\lambda \equiv [\ln(\lambda) - \langle\ln\lambda\rangle]/\sigma_{\ln\lambda}$ is the deviation of measured richness from the expected mean. We see that the first-ranked matches (in red) display a prominent peak with $\pm 3\sigma_{\ln\lambda}$. This reaffirms the existence of the scaling relation and mo-

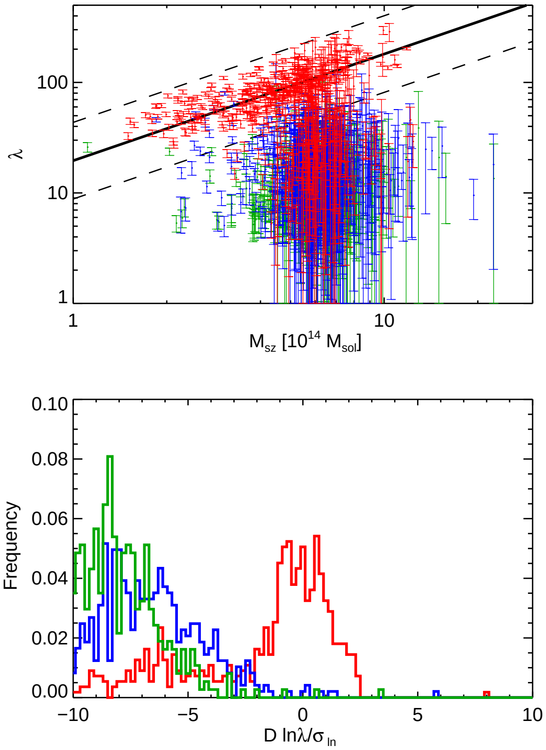

Fig. 24. Distribution of positional matches within a 10 arcmin radius in the richness-$M_{\rm sz}$ plane. The red points in the upper panel represent the highest richness match, blue the second (when present) and green points the third-ranked richness match (when present). The mean scaling law from Rozo et al. (2014) is shown as the solid line, with the dashed lines delineating the $\pm 3\sigma$ band. In the lower panel, we show the distribution of these points relative to the mean relation, normalized to the logarithmic scatter. The red, blue and green histograms refer to the first-, second-, and third-ranked matches, respectively.

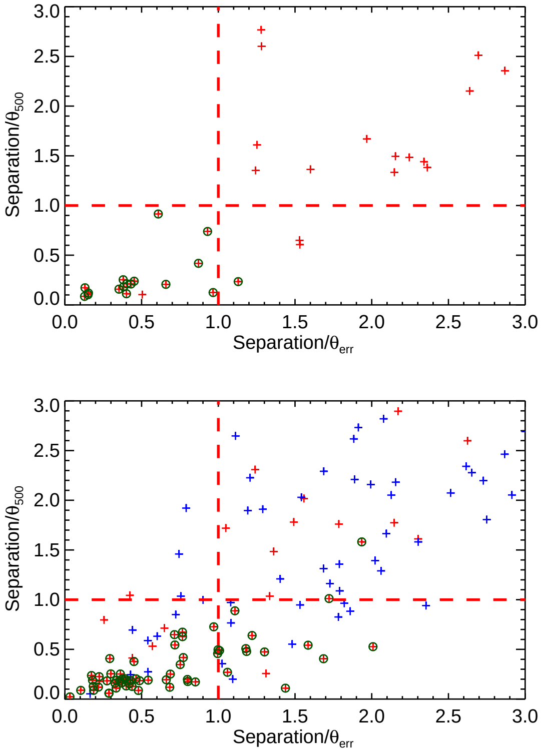

Fig. 25. Selection criteria for `redMaPPer` counterparts. Objects are plotted following the same colour scheme as in the previous figure, i.e., first-, second- and third-ranked matches represented by red, blue and green symbols, respectively. The bands delineate the acceptable region defined by the angular criterion, and circled points indicate objects that also satisfy the richness cut (Criterion 1). *Upper panel* – Single matches within a 10 arcmin radius. *Lower panel* – Double matches within a 10 arcmin radius. Note that in both panels, only first-ranked matches appear as good counterparts by satisfying both criteria.

tivates its use in defining the final `redMaPPer` counterparts for the PSZ2.

We define the best `redMaPPer` counterparts with the following cuts:

1. $(\theta/\theta_{\rm err}) \leq 1$ OR $(\theta/\theta_{500}) \leq 1$;
2. $|\Delta_{\ln}\lambda| \leq 3$;
3. When more than one object remains a possible counterpart, we choose the highest ranked match.

The criteria on angular separation, θ, allow objects with centres either within *Planck*'s positional uncertainty or within the estimated size of the cluster (or both). The second criterion imposes the richness requirement based on the scaling relation. If there remain more than one possible counterpart satisfying these two criteria, then we choose the one with the largest richness. These latter cases, however, deserve closer examination, in particular for potential projection effects.

Table 5. Distribution of the 375 good counterparts.

	Matches					
Rank	Single (/40)	Double (/85)		Triple (/438)		
1	17	58	0	283	8	0
2			0		6	0
3						2

One object with three possible good matches.

Fig. 25 shows the distribution of `redMaPPer` objects for *Planck* sources with single and double matches. The dashed lines delineate the angular cuts, while open circles identify those objects that also satisfy the richness cut. We see that the richness cut effectively eliminates objects that would be accepted on angular criteria alone. For the double matches, there are no good second-ranked `redMaPPer` counterparts because only the highest richness object satisfies the richness cut.

Table 5 summarizes the distribution of the 375 counterparts found with the above cuts. It is grouped into sets of columns for single-, double-, and triple-matched *Planck* objects. For each grouping, the total number of *Planck* sources is given in parentheses in the heading. The table entries list the number of matches in matrix format as follows: the element (i, j) of a matrix gives the number of *Planck* sources with both i- and j-ranked `redMaPPer` counterparts; for example, six of the 438 triple matches have a good second-ranked counterpart only, while eight have both good first- and second-ranked counterparts.

7.3.2. Other optical information

We perform targeted searches for counterparts within the SDSS footprint for all *Planck* sources without good `redMaPPer` matches by applying the `redMaPPer` algorithm on a case-by-case basis. This yielded an additional 17 counterparts and associated redshifts.

We add optical confirmations and redshifts from several other sources. These include optical counterparts for PSZ1 clusters published recently from PanSTARRs (Liu et al. 2014) and from *Planck* collaboration optical follow-up observations (Planck Collaboration et al. 2014; Planck Collaboration Int. XXXV 2015). We also search for counterparts in the NED[6] database, again removing any negated duplicate matches from the systematic searches. We compared the NED redshifts for PSZ2 matches to the redshifts from all the other ancillary catalogues we have studied. The NED redshifts have 88% agreement with these sources within $\Delta z < 0.02$. We therefore caution that NED redshifts should be considered the least reliable of our counterpart assignments. The NED associations are dominated by optical associations with Abell (Abell 1958) and Northern Optical Cluster Survey clusters (Gal et al. 2003).

Finally, we add four high-z counterparts confirmed using SDSS data and which are discussed in Appendix A.

---

[6] The NASA/IPAC Extragalactic Database (NED) is operated by the Jet Propulsion Laboratory, California Institute of Technology, under contract with the National Aeronautics and Space Administration.

7.4. IR information

At *Planck* detection positions, we have searched for galaxy overdensities in the AllWISE mid-infrared source catalogue (Cutri et al. 2013). The AllWISE source catalogue includes the combined cryogenic and NEOWISE (Mainzer et al. 2011) observations from the Wide-field Infrared Survey Explorer mission (WISE; Wright et al. 2010). The data cover the entire sky and we used the deepest bandpasses, the 3.4 μ (W1) and 4.6 μ (W2) channels. We predicted galaxy (W1-W2) colours from Bruzual & Charlot (2003) stellar population models, and searched for galaxy overdensities of the same colour in successive redshift ranges from z=0.3 to z=1.5 (e.g. Papovich et al. 2010; Mei et al. 2012, 2014; Stanford et al. 2014). At redshift $z < 0.3$, the contrast between red mid-infrared galaxies and the background is not efficient for galaxy cluster detection, so we searched only in the fields of *Planck* detections already validated at redshift $z > 0.3$, and detections not yet confirmed or with unknown redshift.

We estimated a significance of the over-densities by comparing the number of galaxies found in a region of comoving diameter of 1 Mpc, with the background galaxies found in regions of the same area. To estimate the background density, we calculated for each redshift range both a local background for each candidate, in a region within 15 arcmin from the *Planck* detection, and a master background derived from the estimators for all the *Planck* fields. A substantial percentage of the *Planck* detections ($\sim 37\%$) are affected by artefacts from bright stars in the WISE data, which compromise meaningful assessment of the galaxy over-densities. The bulk of these are at low galactic latitude ($|b| < 20$). This means that we do not expect to reach a detection completeness of better of $60 - 70\%$.

After visual inspection of all detections, we have flagged our detections in regions not affected by bright star artefacts with the following classification: 3 - Significant galaxy overdensity detected ; 2 - Probable galaxy overdensity; 1 - Possible galaxy overdensity; 0 - No significant galaxy overdensity. We also include these classifications for detections in regions affected by bright star artefacts: -1 Possible galaxy overdensity; -2 - No significant galaxy overdensity; -3 No assessment possible.

To test our classification, and evaluate our completeness and purity, we blindly apply our automated and visual inspection to 100 objects: 50 confirmed $z > 0.5$ clusters and 50 random positions in the sky. We show the results of this validation test in Table 6: 59% of the fields have images with bright star artefacts, including 17% which are class -3. In class 3 and 2, we obtain a 96% and 80% purity, respectively, for the validated clusters. Given the high purity of the class 3 detections, we classify these objects as confirmed infra-red clusters.

In Table 7, we show the number of WISE *Planck* detections in each class for the 935 *Planck* detections with $z > 0.3$ or unknown redshift. A detailed study of the WISE detections will be published in a separate paper (Mei et al. 2015, in prep.). 73 new clusters have been confirmed (class 3 and not validated by other methods) by our WISE image analysis. A further 54 probable new clusters are identified (class 2 and unvalidated by other methods).

Table 6. Total, validated, and spurious detections in a blind test of our WISE detection classification using 50 real and 50 spurious fields.

	TEST DETECTIONS		
CLASS	Total	Validated	Spurious
3	24	23	1
2	10	8	2
1	3	0	3
0	4	0	4
−1	14	2	12
−2	28	8	20
−3	17	9	8

7.5. SZ information

We searched for counterparts of our *Planck* detections using catalogues obtained with other SZ surveys, such as the South Pole Telescope (SPT) and the Atacama Cosmology Telescope (ACT), and update the list of SZ confirmations by direct follow-up with the Arc-minute Micro-kelvin Interferometer (AMI).

7.5.1. SPT

For SPT, we refer to the recently released catalogue (Bleem et al. 2014), extracted from the full 2500 deg^2 SZ survey. It contains 677 SZ detections, of which 516 have been confirmed as clusters, through optical and near-IR observations. The catalogue contains the photometric redshifts (spectroscopic when available) and mass estimate of the confirmed clusters. More specifically, we chose to use the “Fiducial Cosmology” Catalogue provided by the SPT collaboration, to be consistent with the cosmological parameters used in the present paper. We performed a two step matching process as described in Sect. 7.2: a positional match within 10 arcmin, leading to 89 single and five double matches, which we verified by comparing our mass estimate with the one provided in the SPT catalogue. The mass estimates are usually consistent at better than 3σ, except for one detection, PSZ2 G249.87 − 21.65, where they differ at 3.5σ. We note, however, that the error bars on the *Planck* mass reflect only the statistical error on the probability contours and do not consider the uncertainties nor the intrinsic scatter in the scaling relation used to break the degeneracy. Moreover, as discussed also in the SPT case by Bleem et al. (2014), the use of a fixed scaling relation and of a fiducial cosmology results in an underestimation of the statistical and systematic uncertainties in both datasets. Therefore, we decided to keep the SPT counterparts for PSZ2 G249.87 − 21.65, which is also associated in the SPT catalogue to the same MCXC cluster (RXC J0628.8 − 4143) as in our matching. We checked the position of the matches in the separation plane: none of the single matches have been discarded in this way, while in four out of five multiple matches, one of the counterparts was excluded following this criterion. In the remaining match, two possible counterparts are allowed and we selected as the most likely the one with a smaller mass difference and a smaller separation in terms

Table 7. WISE *Planck* detection classification.

Class	WISE Planck Detections[a]			
	Total	% of Sample	Previously Confirmed	Unconfirmed
3	374	40	301	73
2	68	7	14	54
1	55	6	7	48
0	88	9	15	73
−1	42	4	5	37
−2	97	10	15	82
−3	211	23	55	156

[a] For each WISE detection class, we show the total number of *Planck* detections and their percentage with respect to the 935 objects with known redshift $z > 0.3$ or unknown redshift, the number of previously confirmed *Planck* clusters and the number of unconfirmed *Planck* detections.

of θ_{500}.

We observe a systematic difference between the masses we derived from *Planck* data and those provided in the SPT catalogue. The mass is a derived quantity which requires scaling information to be assumed before it can be calculated from the SZ signal measured by either instrument. Comparison of the SZ observables is complicated by the different scales probed by each instrument: *Planck* is sensitive to the cluster outskirts while SPT is sensitive to the core regions. Any comparison necessarily requires model extrapolation, which is complicated further by the different pressure models used in the two measurements. A robust comparison will require a joint analysis of the data, which is beyond the scope of this paper.

7.5.2. ACT

For ACT, we use the catalogue published in Hasselfield et al. (2013), which contains both the most recent ACT detections and an update of the 23 Marriage et al. (2011) detections. 32 PSZ2 detections match with ACT clusters in a 10 arcmin radius. 28 have ACT UPP-based SZ masses consistent with *Planck* $M_{\rm SZ}$ (less than 3σ deviation). Four have more than 3σ deviation: PSZ2 G053.44-36.25 (ACT-CLJ2135.1-0102) and PSZ2 G130.21-62.60 (ACT-CLJ0104.8+0002) are actually considered as good matches by our `redMaPPer` association, PSZ2 G262.27-35.38 (ACT-CLJ0516-5430) is also a good match for our MCXC association. The last one, PSZ2 G265.86-19.93 (ACT-CLJ0707-5522), is a good match in the PSZ1. We decided to leave blank the ACT field of the PSZ2 catalogue for these four clusters but, given the uncertainties on the mass determination and associated errors, we did not break the corresponding `redMaPPer`, MCXC and PSZ1 association.

7.5.3. AMI

Following the ongoing follow-up observations of the *Planck* cluster candidates, a total of 161 clusters with 4.5 <S/N< 20 were observed with AMI. The detection significance is then characterised by calculating of the natural logarithm of the Bayes factor, $\ln B_{10}$,

$$\ln B_{10} = \Delta \ln \mathcal{Z}_{10} = \ln \mathcal{Z}_1 - \ln \mathcal{Z}_0, \tag{9}$$

where $\ln \mathcal{Z}_1$ and $\ln \mathcal{Z}_0$ are the natural logarithm of the Bayesian evidence for model H_1 and H_0 respectively. Model H_1 accounts both for the cluster signal and the contribution from radio sources while H_0 only takes into account the radio source environment. Further details of the AMI observations, of the Bayesian methodology and of the modelling of interferometric SZ data, primordial CMB anisotropies, and resolved and unresolved radio point sources, as well as of the criteria used to categorise clusters are given in Perrott et al. (2014) and references therein.

Table 8. AMI scale for an interpretation of the detection significance of the Planck cluster candidates.

Category	$\ln B_{10}$	N
Clear detection	$\ln B_{10} \geq 3$	102
Moderate detection	$0 \leq \ln B_{10} < 3$	30
Non-detection	$-3 \leq \ln B_{10} < 0$	25
Clear non-detection	$\ln B_{10} \leq -3$	4

In this context the detection significance for the 161 clusters is described in Table 8. 132 of the 161 AMI-confirmed *Planck* clusters are included in the PSZ2.

7.6. Redshift compilation

We provide a single redshift estimate for each detection where at least one redshift is known for a matched counterpart. In many cases, we have multiple estimates per detection. This section discusses the compilation of redshift information and how redshifts are assigned in the final catalogue. Confirmation statistics and final assigned redshift numbers are summarised in Table 9.

Initial redshift estimates are taken from the PSZ1 catalogue redshift compilation, given the matching in Sect. 7.1. We include new follow-up results from the Planck collaboration (Planck Collaboration et al. 2014; Planck Collaboration Int. XXXV 2015), which include spectroscopic updates to PSZ1 photometric redshifts and new confirmations of PSZ1 detections. We also include external updates to PSZ1 counterpart redshifts from the NED and SIMBAD databases (Planck Collaboration XXXVI 2015).

After these steps, we cycle through priority levels in our systematic counterpart searches, in the following order of priority: MCXC, `redMaPPer` ACT and SPT. We compare the updated PSZ1 and MCXC redshifts with the redshifts from `redMaPPer` where available, and prioritise `redMaPPer` redshifts highest amongst available photometric redshifts. We test spectroscopic redshifts at $z > 0.1$ for consistency within $\Delta z < 0.03$ and $\Delta z/z < 0.1$ of the `redMaPPer` photo-z. Any discrepancies are considered on an individual basis. In a small number of cases, we choose the `redMaPPer` redshift. We also reject a small number of counterpart assignments where that counterpart is a bad match in `redMaPPer`. These cases are discussed in Appendix B.

The common sample between the PSZ2 and each of the external samples is denoted in the catalogue. After the systematic searches, we assign any remaining unconfirmed clusters to database counterparts where available. If a PSZ1 match assigns to the same counterpart as one of the negated counterparts from the systematic searches, where the possible counterpart violated the consistency criteria, then the PSZ1 match is also negated.

8. Sample Properties

8.1. Mass and redshift properties

We discuss here the distribution of *Planck* SZ-selected clusters in the mass-redshift ($M_{500} - z$) plane, using the mass proxy derived with scaling relations as discussed in Sect. 7. For 1094 detections with known redshifts in the PSZ2 catalogue (Sect. 7), we show in Fig. 26 their position in the $M_{500} - z$ plane, compared with the expected completeness function $C(M_{500}, z)$ of our survey (we show the 20%, 50% and 80% completeness levels). These curves indicate the points in the $M_{500} - z$ plane at which clusters have C% chances to be detected. They were computed for the full survey area. The red points in Fig. 26 show the 298 new PSZ2 confirmed detections, with redshifts, that were not found in the previous version of the catalogue. The black points show the common PSZ1-PSZ2 detections.

We stress that the $M_{500} - z$ distribution in Fig. 26 cannot be considered as fully representative of the *Planck* SZ selection, since it reflects the biases due to the non-uniform knowledge of redshifts over the sky in the ancillary information we used (Sect. 7). For instance, we have an extensive redshift information in the sky area covered by the SDSS survey thanks to the `redMaPPer` catalogue (Rykoff et al. 2014) but not in the remaining part of the sky. The incomplete redshift information can also explain the rarity of new detections in the PSZ2 catalogue with respect to PSZ1 at high redshift: at $z > 0.6$ we have 36 objects, but only four new PSZ2 detections. We note however that most of the PSZ1 clusters in this redshift range were not present in existing catalogues but they were confirmed as clusters and their redshift was measured thanks to the massive follow up campaign with optical and X-ray telescopes which was undertaken by the *Planck* Collaboration for PSZ1 candidates (Planck Collaboration XXIX 2014 and references therein) and which continued also after the 2013 release (Planck Collaboration et al. 2014; Planck Collaboration Int. XXXV 2015). Since a similar observational campaign has not yet been possible for new PSZ2 detections, we could not populate further the high-mass high-z part of the $M_{500} - z$ plane.

The new PSZ2 confirmed detections (red points in Fig. 26) are mostly low-mass objects close to the detection limit of the survey. The mean mass of confirmed clusters over the whole redshift range in the PSZ2 is $4.82 \times 10^{14}\ M_{\odot}$, which is lower than in the PSZ1 ($5.12 \times 10^{14}\ M_{\odot}$). The common sample of 795 objects contains the higher mass clusters detected by both surveys, with mean mass $5.16 \times 10^{14}\ M_{\odot}$. This is expected, since the common sample contains none of the new low-mass PSZ2 detections and none of the missing low S/N PSZ1 detections, discussed in Sect. 6.3, which were likely to have been low mass.

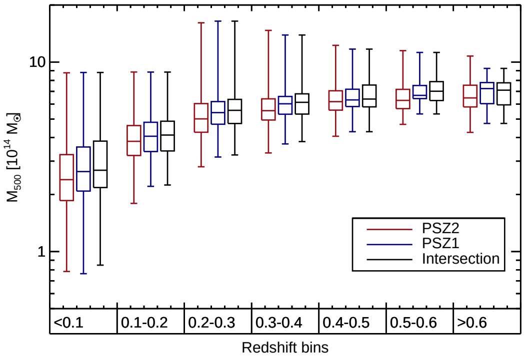

Fig. 27. Box-and-whisker diagrams showing the mass distribution of the PSZ2 (red), PSZ1 (blue) and their intersection (black) sample in seven redshift bins. The bottom and the top of the boxes represent the first and third quantile of the data, while the band inside the box shows the median (i.e. the second quantile). The ends of the whiskers mark the minimum and maximum of the data.

This is also shown in Fig. 27, where we compare the mass distribution of the confirmed clusters in the PSZ2, the PSZ1 and their common sample, for several redshift bins. The median mass and the first and third quantiles are always lower for the PSZ2 than for the PSZ1 and the common sample, showing that we are significantly expanding the sample towards lower masses.

Fig. 26 also shows a comparison of the SZ selected samples from the *Planck*, ACT and SPT surveys. *Planck* tends to detect the rarest high-mass clusters observed at high-redshift in these partial-sky surveys and provides a complementary clean SZ selection at lower redshifts, where the *Planck* frequency range provides sufficient information to disentangle the SZ signal of large clusters from the background.

8.2. X-ray underluminous clusters

The presence of a bright cool-core, characterised by a peaked surface brightness profile, has been shown to bias X-ray flux selected cluster samples in favour of peaked, relaxed objects with respect to morphologically disturbed systems (Eckert et al. 2011). In contrast, SZ selected samples have produced more disturbed systems than expected, with SZ discovered clusters typically lying on the lower end of the mass-luminosity relation (Planck Collaboration IX 2011). There has also been much interest in the possible existence of severely X-ray under-luminous clusters, with several authors identifying potential systems (eg: Bower et al. 1997;

Table 9. Summary of ancillary information. The highest available priority redshift source, following the ordering in the Priority column, provides the reference confirmation and redshift. When two priorities are given, the first number pertains to spectroscopic redshifts and the second number to photometric redshifts. The PSZ2 contains 1203 confirmed clusters, of which 289 are Planck-discovered. 87 of these are clusters newly identified in this paper: 73 are confirmed by WISE, eight are new identifications in SDSS data and six are confirmed by AMI.

Confirmation source	Validation	Priority	Joint sample size	Reference confirmations	Planck-discovered	Redshift reference
ENO follow-up	10	1/5	...	22	18	Planck Collaboration Int. XXXV 2015
RTT follow-up	11	1/5	...	45	31	Planck Collaboration et al. 2014
PanSTARRs	12	6	...	16	16	Liu et al. 2014
`redMaPPer` non-blind	13	...	...	17	5	This paper: Sect. 7.3.2
SDSS high-z	14	...	...	4	4	This paper: Appendix A
AMI fu	15	...	...	10	10	...
WISE	16	...	...	73	73	...
PSZ1 2013	20	1	782	348	125	Planck Collaboration XXIX 2014
MCXC	21	2	551	447	0	Piffaretti et al. 2011
SPT	22	4/5	94	39	4	Bleem et al. 2014
ACT	23	4/5	28	1	0	Hasselfield et al. 2013
`redMaPPer`	24	3	374	122	2	Rykoff et al. 2014
Updated PSZ1	25	1	...	19	0	Planck Collaboration XXXVI 2015
NED	30	7	...	40	1	Various

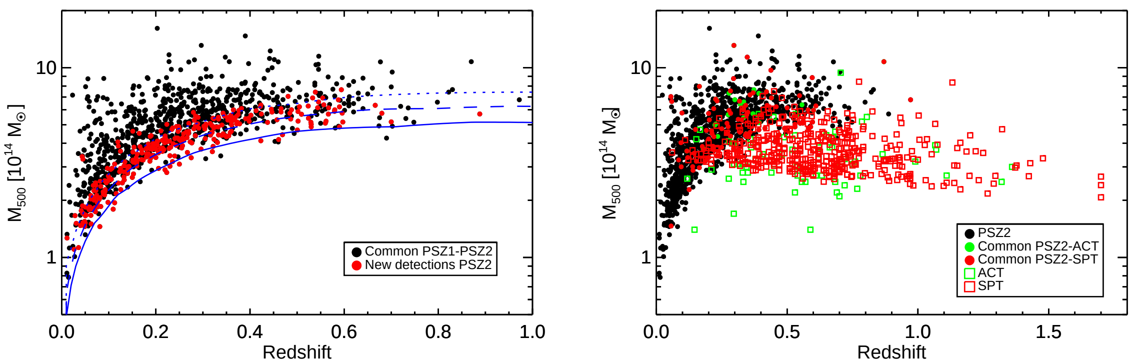

Fig. 26. *Left panel:* Distribution of the 1094 PSZ2 clusters with counterparts with known redshift in the $M_{500} - z$ plane. New PSZ2 detected clusters are indicated with red dots, while commmon PSZ1 and PSZ2 clusters are indicated by black dots. The solid, dashed and dotted lines indicate respectively the 20%,50% and 80% survey completeness contours for the PSZ2. *Right panel:* Distribution of the PSZ2 clusters with associated redshift in the $M_{500} - z$ plane compared to the SPT (Bleem et al 2014) and ACT (Hasselfield et al 2013) catalogues. Black circles represent PSZ2 clusters, while red and green filled circles mark common SPT/PSZ2ACT/ PSZ2 clusters, respectively. The remaining SPT and ACT clusters not detected by *Planck* are shown with red and green empty squares.

Popesso et al. 2007; Dietrich et al. 2009; Trejo-Alonso et al. 2014 and references therein) and suggesting a model where these clusters are dynamically young objects, still undergoing accretion and mergers and yet to reach equilibrium. An alternative suggestion is that line-of-sight structures may bias mass and richness estimates high relative to the X-ray luminosity (Bower et al. 1997; Giles et al. 2015).

However, the reported under-luminosity of these objects is disputed. Andreon & Moretti (2011) note that the under-luminosity is often claimed relative to biased scaling relations, and that the significance of the under-luminosity is amplified due to underestimation of the true scatter in the relation.

In the SDSS area, the majority of *Planck* detections possess counterparts in the `redMaPPer` catalogue, with redshifts and optical richness estimates. We construct a test sample from the *Planck*-`redMaPPer` intersection at low redshift, $z < 0.2$. This sample of 148 clusters can be expected to be detectable in the *ROSAT* maps. While `redMaPPer` is not complete for the *Planck* mass ranges at these redshifts, it allows us to construct a sample that is independent of any X-ray selection effects and therefore well-suited for finding under-luminous clusters, as any biases in selection will affect both normal and under-luminous X-ray cluster alike.

For each of these clusters, we calculate the X-ray count-rate using a growth-curve analysis on the *ROSAT* $0.5 - 2.4$ keV band maps following Böhringer et al. (2000). We derived the count-rate and its upper and lower limit from the growth curve at θ_{500}, which we calculated from the *Planck* mass proxy. We then converted the RASS count rates into flux in the $0.1 - 2.4$ keV energy range, using an absorbed thermal model, where we used the galactic absorption at the *Planck* position, the redshift of the `redMaPPer` counterpart and the temperature derived from the mass proxy through the M-T scaling relation by Arnaud et al. (2007). We then converted fluxes into luminosity in the $0.1 - 2.4$ keV channel. We found good agreement with the reported MCXC values of L_{500} for those clusters also present in the MCXC.

We then searched for outlier clusters from the Y_{500}-L_{500} and $Y_{500}-\lambda$ relations, using the Y_{500} calculated following Sect. 5.3. In both cases, we find the best-fit relation for our sample using the BCES algorithm. To exclude outliers from the fits, we clipped objects with orthogonal residual $|r_{\perp}| > 2.5\sigma_{\rm tot}$ from the best-fit relations, where $\sigma_{\rm tot}$ is the raw scatter around the relation derived from the median-absolute deviation. We then iterated the sigma-clipping process until converged.

The top panels of Fig. 28 show the best-fit relations and their $\pm 2\sigma_{\rm tot}$ scatters between Y_{500} and `redMaPPer` richness λ, and between Y_{500} and L_{500}, for the test sample of 148 *Planck*-`redMaPPer` clusters. The bottom panels of Fig. 28 show the histograms of Δ, normalised by $\sigma_{\rm tot}$.

The points highlighted with larger cyan circles denote clusters with L_{500} more than $2.5\sigma_{\rm tot}$ below the best-fit relation. These clusters are under-luminous in X-rays for their Y_{500}. However, their Y_{500} estimates are consistent with their optical richness and do not lie preferentially beneath the relation. The consistency of optical and SZ mass proxies suggest either that these clusters are under-luminous for their mass, or that both the Y_{500} and λ estimates are biased high.

One exception to this is PSZ2 G127.71-69.55, discrepant with both relations: at $10\sigma_{\rm tot}$ for $Y_{500}-L_{500}$ and $3\sigma_{\rm tot}$ for $Y_{500}-\lambda$. It is circled in red in Figure 28. This is the only cluster in the *Planck*-`redMaPPer` sample with a poor Q_NEURAL flag and is either a failed `redMaPPer` match (lying close to the matching threshold in the $M_{\rm sz}-\lambda$ plane) or a cluster with a severely IR contaminated spectrum for which the *Planck* Y_{500} estimate is likely overestimated. We therefore remove this from the list of under-luminous candidates.

We expanded the search for under-luminous clusters across the whole sky, testing all clusters with $z < 0.2$ against the mean $Y_{500}-L_{500}$ relation determined above. This expanded the number of under-luminous candidates to 22. These objects warrant follow-up observations to determine their dynamical state and to search for line-of-sight structures that may bias high both the Y_{500} and optical richness. They are flagged in the COMMENT field of the catalogue. They should be of interest in understanding the systematic differences between SZ and X-ray selection.

9. Summary

The *Planck* satellite is unique in providing broad frequency coverage over the whole sky with good sensitivity to both the high frequency spectral increment and the low frequency decrement of the thermal SZ effect. In this paper, we have presented second *Planck* catalogue of SZ sources (PSZ2). This is based on data from the full 29 month mission and uses a methodology that refines the one used to produce the PSZ1 from 15.5 months of data. The catalogue is based on the union of results from three cluster detection codes (Planck Collaboration XXIX 2014). The PSZ2 contains 1653 cluster candidates distributed across 83.6% of the sky. The catalogue was validated using external X-ray, optical, SZ and near infra-red data, producing confirmation for 1203 candidates with 1094 redshifts. The catalogue contains 716 new detections including 366 confirmed clusters with newly identified SZ signal. 87 of our confirmed clusters are newly identified in this paper. We have found good consistency with the PSZ1 and re-detect 937 SZ sources from the PSZ1 sample of 1227. We have investigated the missed detections: the vast majority of these were low-significance PSZ1 detections whose S/N has fluctuated beneath the detection threshold. The majority of these are expected to be spurious detections.

The current status of our knowledge of counterparts for our detections at various frequencies is summarised in Table 10 and compared to the PSZ1. Our optical validation scheme is based on the newly released SDSS-based `redMaPPer` catalogue (Rozo & Rykoff 2014). This produced 374 high-quality matches where the counterparts are consistent with *Planck* mass and position information. We reject 188 possible matches where the mass or position information is inconsistent with the *Planck* information. This underlines the importance of consistency checks when matching with high density SDSS catalogues. Our X-ray and SZ counterpart searches implement similar consistency criteria leading to tight control over mismatches.

Central to the counterpart search process is the understanding of the *Planck* SZ parameter estimates. We have validated the *Planck* Compton-Y posteriors using detailed simulations that include an ensemble of hydro-dynamically simulated pressure profiles that vary from the pressure profile assumed by our extraction algorithms. Our $Y_{5\rm R500}$ estimates are robust to mis-matches in the pressure profile. When translating to Y_{500}, we have shown the importance of accurate prior information about radius to break the $Y - \theta$ degeneracy and produce accurate and precise estimates from the *Planck* data. Our counterpart searches make extensive use of the *Planck* mass-proxy; this uses prior information about redshift and scaling relations to derive mass constraints which show low scatter with respect to external estimates. We provide this $M_{\rm sz}$ for all candidates with a redshift, and provide $M_{\rm sz}(z)$ in the range $0 < z < 1$ for all other candidates. We expect this information to be useful in future comparisons with external data.

Central to any statistical use of a cluster sample is the survey selection function. We have estimated the catalogue completeness using Monte-Carlo source injection and we provide this as a product for the full survey and for various sub-samples as a function of selection S/N. We have validated the completeness through a comparison with external X-ray data and high resolution SZ data from SPT (Bleem et al. 2014), which spans the redshift range and angular sizes of the *Planck* data. We estimate the catalogue to be 83-87% pure, based on simulations of the *Planck* data and detection-by-detection quality assessment utilising machine learning. Higher reliability sub-samples can be constructed easily: the main contaminant is infra-red galactic emission and as such the reliability is a strong function of galactic latitude. Specifically, the cluster cosmology zone that covers 65% of the sky contains 1308 detections at $\sim 90\%$ reliability, and full survey intersection catalogue (objects detected

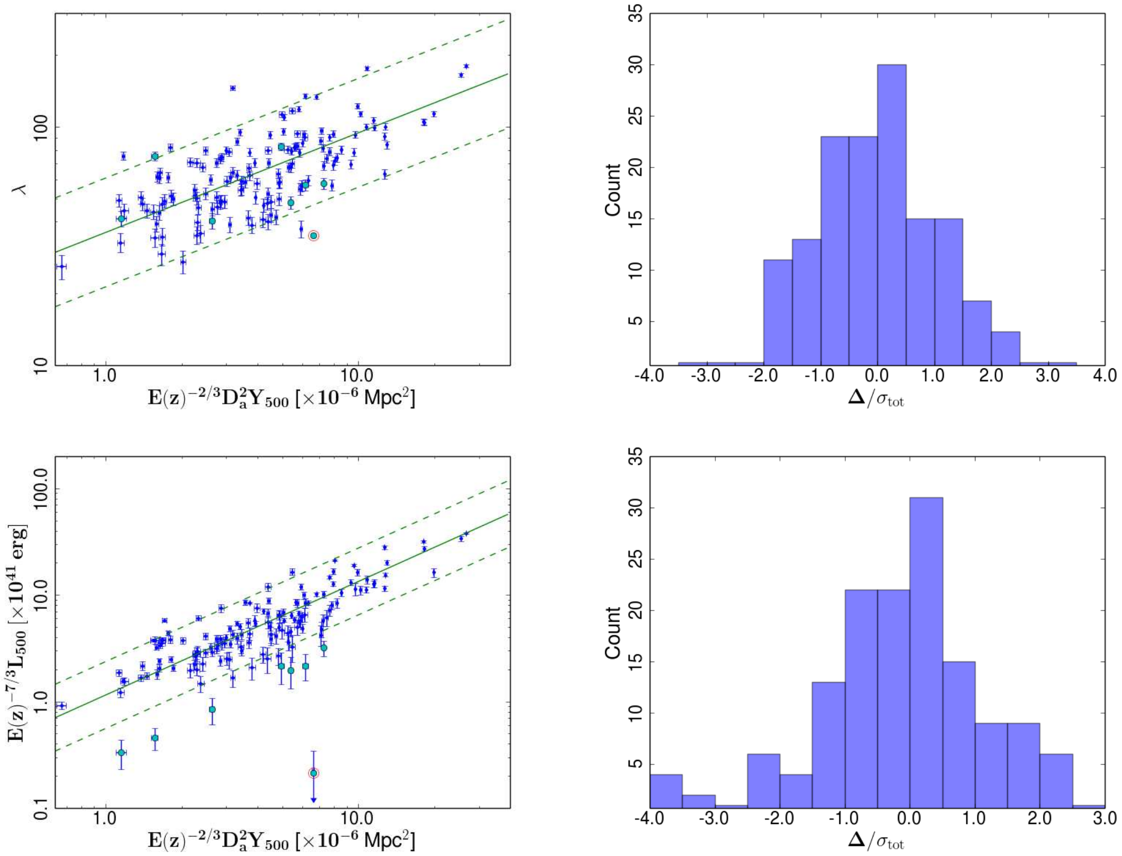

Fig. 28. Properties in the $Y_{500}-\lambda$ (top panels) and Y_{500}-L_{500} (bottom panels) planes for the *Planck*-`redMaPPer` sample at $z < 0.2$. Under-luminous candidates are denoted with cyan circles in the scatter plots to the left, which also show the best fit relation and the dispersion $\pm 2\sigma_{\rm tot}$. The circled red point is a cluster with contaminated Y signal. The right plots show the histograms of orthogonal deviation $\Delta_\perp$ for each relation.

by all three codes) contains 827 detections at $> 95\%$ reliability.

Cosmology using the cluster counts is also dependent on external observational data to provide cluster redshifts. Planck Collaboration XXIV (2015) have produced cosmological constraints using samples drawn from the PSZ2, containing 493 candidates from the intersection sample and 439 drawn from the single-code `MMF3` sample. Utilising larger samples from the PSZ2 requires further redshift information. We also expect the PSZ2 to contain many high-mass clusters at $z > 0.6$. So far only 36 have been identified, of which 21 were identified in targeted follow-up observations of PSZ1 candidates. For these reasons, the PSZ2 should motivate further follow-up observations. In particular, the catalogue contains 73 clusters confirmed by WISE infra-red data that currently have no redshift information but which are likely to be high-redshift.

Understanding the biases in cluster selection that affect samples defined at different wavelengths will be important for interpreting statistical results from existing surveys and those planned for the near future. Using a low-redshift overlap sample from PSZ2 and `redMaPPer`, we have identified a population of low-z clusters with ‘typical’ optical and SZ properties, but which are underluminous for their mass in *ROSAT* X-ray data. These clusters may be part of a population of dynamically disturbed clusters that are under-represented in X-ray selected surveys. These objects will be interesting targets for multi-wavelength follow-up to determine their dynamical state.

In the near future, *Planck* all-sky SZ data can be combined with observations of the large-scale structure by surveys such as PAN-STARRS, LOFAR, Euclid, LSST, and RSG/e-ROSITA. This will provide an unprecedented multi-wavelength view of the evolution of large-scale structure that will revolutionise our understanding of the physics governing this process.

Acknowledgements. The Planck Collaboration acknowledges the support of: ESA; CNES and CNRS/INSU-IN2P3-INP (France); ASI, CNR, and INAF (Italy); NASA and DoE (USA); STFC and UKSA (UK); CSIC, MINECO, JA, and RES (Spain); Tekes, AoF, and CSC (Finland); DLR and MPG (Germany); CSA (Canada); DTU Space (Denmark); SER/SSO (Switzerland); RCN (Norway); SFI (Ireland); FCT/MCTES (Portugal); ERC and PRACE (EU). A description of the Planck Collaboration and a list of its members, indicating which technical or sci-

Table 10. Counterpart summary for PSZ2 compared to PSZ1. Common samples are defined as those PSZ2 detections with the given property that has a counterpart with that property in the PSZ1 2015. The intersection comprises those detections common to all three detector codes. Low reliability candidates possess a poor neural-network quality assessment flag. In the PSZ1, low reliability candidates possess the lowest external quality assessment flag. SZ clusters denote clusters with SZ detections in ACT or SPT. PSZ1 2013 refers to the 2013 release of the catalogue (Planck Collaboration XXIX 2014), and PSZ1 2015 to a recent addendum updating the counterpart information of the catalogue (Planck Collaboration XXXVI 2015).

Sample	PSZ1 2013	PSZ1 2015	PSZ2	Common	New PSZ2
Union	1227	1227	1653	937	716
Intersection	546	546	827	502	325
Confirmed	861	947	1203	820	383
Candidates	366	292	546	99	447
Low reliability	142	131	143	39	104
Total X-ray	501	501	603	477	126
MCXC	455	455	551	427	124
SZ clusters	82	82	110	79	31

entific activities they have been involved in, can be found at `http://www.cosmos.esa.int/web/planck/planck-collaboration`. We thank Ian McCarthy for providing images and profiles of simulated clusters from cosmo-OWLS. This research has made use of the NASA/IPAC Extragalactic Database (NED), which is operated by the Jet Propulsion Laboratory, California Institute of Technology, under contract with the National Aeronautics and Space Administration, and the SIMBAD database, operated at CDS, Strasbourg, France This research made use of data retrieved from SDSS-III. Funding for SDSS-III has been provided by the Alfred P. Sloan Foundation, the Participating Institutions, the National Science Foundation, and the U.S. Department of Energy Office of Science. The SDSS-III web site is http://www.sdss3.org/. This research has made use of data processed by the Centre d'Analyse de Donnes Etendues `http://cade.irap.omp.eu/` and has made use of the HEALPix pixelisation software `http://healpix.sourceforge.net` (Górski et al. 2005). This work was performed using the Darwin Supercomputer of the University of Cambridge High Performance Computing Service (http://www.hpc.cam.ac.uk/), provided by Dell Inc. using Strategic Research Infrastructure Funding from the Higher Education Funding Council for England and funding from the Science and Technology Facilities Council.

References

Abell, G. O., The Distribution of Rich Clusters of Galaxies. 1958, ApJS, 3, 211

Aghanim, N., Hurier, G., Diego, J.-M., et al., The Good, the Bad and the Ugly: Statistical quality assessment of SZ detections. 2014, astro-ph/1409.6543, arXiv:1409.6543

Allen, S. W., Evrard, A. E., & Mantz, A. B., Cosmological Parameters from Observations of Galaxy Clusters. 2011, ARA&A, 49, 409, arXiv:1103.4829

Andreon, S. & Moretti, A., Do X-ray dark or underluminous galaxy clusters exist? 2011, A&A, 536, A37, arXiv:1109.4031

Arnaud, M., Pointecouteau, E., & Pratt, G. W., Calibration of the galaxy cluster M{500}-Y{X} relation with XMM-Newton. 2007, A&A, 474, L37, arXiv:0709.1561

Arnaud, M., Pratt, G. W., Piffaretti, R., et al., The universal galaxy cluster pressure profile from a representative sample of nearby systems (REXCESS) and the Y_{SZ} - M_{500} relation. 2010, A&A, 517, A92, arXiv:0910.1234

Benson, B. A., de Haan, T., Dudley, J. P., et al., Cosmological Constraints from Sunyaev-Zel'dovich-selected Clusters with X-Ray Observations in the First 178 $\deg^2$ of the South Pole Telescope Survey. 2013, ApJ, 763, 147, arXiv:1112.5435

Bleem, L. E., Stalder, B., de Haan, T., et al., Galaxy Clusters Discovered via the Sunyaev-Zel'dovich Effect in the 2500-square-degree SPT-SZ survey. 2014, ArXiv e-prints, arXiv:1409.0850

Böhringer, H., Schuecker, P., Guzzo, L., et al., The ROSAT-ESO Flux Limited X-ray (REFLEX) Galaxy cluster survey. V. The cluster catalogue. 2004, A&A, 425, 367, arXiv:astro-ph/0405546

Böhringer, H., Voges, W., Huchra, J. P., et al., The Northern ROSAT All-Sky (NORAS) Galaxy Cluster Survey. I. X-Ray Properties of Clusters Detected as Extended X-Ray Sources. 2000, ApJS, 129, 435, arXiv:astro-ph/0003219

Borgani, S. & Kravtsov, A., Cosmological simulations of galaxy clusters. 2009, ArXiv e-prints, arXiv:0906.4370

Bösch, B., Böhm, A., Wolf, C., et al., Tully-Fisher analysis of the multiple cluster system Abell 901/902. 2013, A&A, 554, A97, arXiv:1304.6186

Bower, R. G., Castander, F. J., Ellis, R. S., Couch, W. J., & Boehringer, H., A dynamical study of optically selected distant clusters. 1997, MNRAS, 291, 353, arXiv:astro-ph/9705099

Bruzual, G. & Charlot, S., Stellar population synthesis at the resolution of 2003. 2003, MNRAS, 344, 1000, arXiv:astro-ph/0309134

Burenin, R. A., Vikhlinin, A., Hornstrup, A., et al., The 400 Square Degree ROSAT PSPC Galaxy Cluster Survey: Catalog and Statistical Calibration. 2007, ApJS, 172, 561, arXiv:astro-ph/0610739

Carlstrom, J. E., Holder, G. P., & Reese, E. D., Cosmology with the Sunyaev-Zel'dovich Effect. 2002, ARA&A, 40, 643, arXiv:astro-ph/0208192

Carvalho, P., Rocha, G., & Hobson, M. P., A fast Bayesian approach to discrete object detection in astronomical data sets - PowellSnakes I. 2009, MNRAS, 393, 681, arXiv:0802.3916

Carvalho, P., Rocha, G., Hobson, M. P., & Lasenby, A., PowellSnakes II: a fast Bayesian approach to discrete object detection in multi-frequency astronomical data sets. 2012, MNRAS, 427, 1384, arXiv:1112.4886

Chamballu, A., Bartlett, J. G., & Melin, J.-B., The Planck SZ Cluster Catalog: expected X-ray properties. 2012, A&A, 544, A40

Chen, Y., Reiprich, T. H., Böhringer, H., Ikebe, Y., & Zhang, Y.-Y., Statistics of X-ray observables for the cooling-core and non-cooling core galaxy clusters. 2007, A&A, 466, 805, arXiv:astro-ph/0702482

Crawford, C. S., Edge, A. C., Fabian, A. C., et al., Optical spectroscopy of the ROSAT X-ray brightest clusters - II. 1995, MNRAS, 274, 75

Cutri, R. M., Wright, E. L., Conrow, T., et al. 2013, Explanatory Supplement to the AllWISE Data Release Products, Tech. rep.

da Silva, A. C., Kay, S. T., Liddle, A. R., & Thomas, P. A., Hydrodynamical simulations of the Sunyaev-Zel'dovich effect: cluster scaling relations and X-ray properties. 2004, MNRAS, 348, 1401, arXiv:astro-ph/0308074

Dietrich, J. P., Biviano, A., Popesso, P., et al., Weak lensing observations of potentially X-ray underluminous galaxy clusters. 2009, A&A, 499, 669, arXiv:0903.3599

Ebeling, H., Edge, A. C., Bohringer, H., et al., The ROSAT Brightest Cluster Sample - I. The compilation of the sample and the cluster log N-log S distribution. 1998, MNRAS, 301, 881, arXiv:astro-ph/9812394

Ebeling, H., Edge, A. C., Mantz, A., et al., The X-ray brightest clusters of galaxies from the Massive Cluster Survey. 2010, MNRAS, 407, 83, arXiv:1004.4683

Eckert, D., Molendi, S., & Paltani, S., The cool-core bias in X-ray galaxy cluster samples. I. Method and application to HIFLUGCS. 2011, A&A, 526, A79, arXiv:1011.3302

Gal, R. R., de Carvalho, R. R., Lopes, P. A. A., et al., The Northern Sky Optical Cluster Survey. II. An Objective Cluster Catalog for 5800 Square Degrees. 2003, AJ, 125, 2064, arXiv:astro-ph/0301274

Giles, P. A., Maughan, B. J., Hamana, T., et al., The X-ray properties of weak-lensing-selected galaxy clusters. 2015, MNRAS, 447, 3044, arXiv:1402.4484

Górski, K. M., Hivon, E., Banday, A. J., et al., HEALPix: A Framework for High-Resolution Discretization and Fast Analysis of Data Distributed on the Sphere. 2005, ApJ, 622, 759, arXiv:astro-ph/0409513

Haehnelt, M. G. & Tegmark, M., Using the Kinematic Sunyaev-Zeldovich effect to determine the peculiar velocities of clusters of galaxies. 1996, MNRAS, 279, 545, arXiv:astro-ph/9507077

Hao, J., McKay, T. A., Koester, B. P., et al., A GMBCG GALAXY CLUSTER CATALOG OF 55,424 RICH CLUSTERS FROM SDSS DR7. 2010, The Astrophysical Journal Supplement Series, 191, 254

Harrison, D., Sutton, D., Carvalho, P., & Hobson, M., Validation of Bayesian posterior distributions using a multidimensional Kolmogorov–Smirnov test. 2014, ArXiv e-prints, arXiv:astro-ph/1404.7735

Hasselfield, M., Hilton, M., Marriage, T. A., et al., The Atacama Cosmology Telescope: Sunyaev-Zel'dovich selected galaxy clusters at 148 GHz from three seasons of data. 2013, J. Cosmology Astropart. Phys., 7, 8, arXiv:1301.0816

Herranz, D., Sanz, J. L., Hobson, M. P., et al., Filtering techniques for the detection of Sunyaev-Zel'dovich clusters in multifrequency maps. 2002, MNRAS, 336, 1057, arXiv:astro-ph/0203486

Hoekstra, H., Mahdavi, A., Babul, A., & Bildfell, C., The Canadian Cluster Comparison Project: weak lensing masses and SZ scaling relations. 2012, MNRAS, 427, 1298, arXiv:1208.0606

Hogg, D. W., Bovy, J., & Lang, D., Data analysis recipes: Fitting a model to data. 2010, ArXiv e-prints, arXiv:1008.4686

Kay, S. T., Peel, M. W., Short, C. J., et al., Sunyaev-Zel'dovich clusters in Millennium gas simulations. 2012, MNRAS, 422, 1999, arXiv:1112.3769

Koester, B. P., McKay, T. A., Annis, J., et al., A MaxBCG Catalog of 13,823 Galaxy Clusters from the Sloan Digital Sky Survey. 2007, ApJ, 660, 239, arXiv:astro-ph/0701265

Kravtsov, A. V., Vikhlinin, A., & Nagai, D., A New Robust Low-Scatter X-Ray Mass Indicator for Clusters of Galaxies. 2006, ApJ, 650, 128, arXiv:astro-ph/0603205

Le Brun, A. M. C., McCarthy, I. G., Schaye, J., & Ponman, T. J., Towards a realistic population of simulated galaxy groups and clusters. 2014, MNRAS, 441, 1270, arXiv:1312.5462

Liu, J., Hennig, C., Desai, S., et al., Optical Confirmation and Redshift Estimation of the Planck Cluster Candidates overlapping the Pan-STARRS Survey. 2014, ArXiv e-prints, arXiv:1407.6001

Mahdavi, A., Hoekstra, H., Babul, A., et al., Joint Analysis of Cluster Observations. II. Chandra/XMM-Newton X-Ray and Weak Lensing Scaling Relations for a Sample of 50 Rich Clusters of Galaxies. 2013, ApJ, 767, 116, arXiv:1210.3689

Mainzer, A., Bauer, J., Grav, T., et al., Preliminary Results from NEOWISE: An Enhancement to the Wide-field Infrared Survey Explorer for Solar System Science. 2011, ApJ, 731, 53, arXiv:1102.1996

Marriage, T. A., Acquaviva, V., Ade, P. A. R., et al., The Atacama Cosmology Telescope: Sunyaev-Zel'dovich-Selected Galaxy Clusters at 148 GHz in the 2008 Survey. 2011, ApJ, 737, 61, arXiv:1010.1065

Maughan, B. J., The L_X-Y_X Relation: Using Galaxy Cluster X-Ray Luminosity as a Robust, Low-Scatter Mass Proxy. 2007, ApJ, 668, 772, arXiv:astro-ph/0703504

McCarthy, I. G., Le Brun, A. M. C., Schaye, J., & Holder, G. P., The thermal Sunyaev-Zel'dovich effect power spectrum in light of Planck. 2014, MNRAS, 440, 3645, arXiv:1312.5341

Mehrtens, N., Romer, A. K., Hilton, M., et al., The XMM Cluster Survey: optical analysis methodology and the first data release. 2012, MNRAS, 423, 1024, arXiv:1106.3056

Mei, S., Scarlata, C., Pentericci, L., et al., Star-forming blue ETGs in two newly discovered galaxy overdensities in the HUDF at z=1.84 and 1.9: unveiling the progenitors of passive ETGs in cluster cores. 2014, ArXiv e-prints, arXiv:1403.7524

Mei, S., Stanford, S. A., Holden, B. P., et al., Early-type Galaxies at $z = 1.3$. I. The Lynx Supercluster: Cluster and Groups at $z = 1.3$. Morphology and Color-Magnitude Relation. 2012, ApJ, 754, 141, arXiv:1205.1785

Melin, J., Bartlett, J. G., & Delabrouille, J., Catalog extraction in SZ cluster surveys: a matched filter approach. 2006a, A&A, 459, 341, arXiv:astro-ph/0602424

Melin, J., Bartlett, J. G., & Delabrouille, J., Catalog extraction in SZ cluster surveys: a matched filter approach. 2006b, A&A, 459, 341, arXiv:astro-ph/0602424

Melin, J.-B., Aghanim, N., Bartelmann, M., et al., A comparison of algorithms for the construction of SZ cluster catalogues. 2012, A&A, 548, A51, arXiv:1210.1416

Mitra, S., Rocha, G., Górski, K. M., et al., Fast Pixel Space Convolution for Cosmic Microwave Background Surveys with Asymmetric Beams and Complex Scan Strategies: FEBeCoP. 2011, ApJS, 193, 5, arXiv:1005.1929

Papovich, C., Momcheva, I., Willmer, C. N. A., et al., A Spitzer-selected Galaxy Cluster at $z = 1.62$. 2010, ApJ, 716, 1503, arXiv:1002.3158

Peebles, P. J. E. 1980, The large-scale structure of the universe, ed. Peebles, P. J. E. (Princeton University Press)

Perrott, Y. C., Olamaie, M., Rumsey, C., et al., Comparison of Sunyaev-Zel'dovich measurements from Planck and from the Arcminute Microkelvin Imager for 99 galaxy clusters. 2014, ArXiv e-prints, arXiv:1405.5013

Piffaretti, R., Arnaud, M., Pratt, G. W., Pointecouteau, E., & Melin, J.-B., The MCXC: a meta-catalogue of x-ray detected clusters of galaxies. 2011, A&A, 534, A109+, arXiv:1007.1916

Planck Collaboration. 2011, The Explanatory Supplement to the Planck Early Release Compact Source Catalogue (ESA)

Planck Collaboration, Ade, P. A. R., Aghanim, N., et al., Planck intermediate results. XXVI. Optical identification and redshifts of Planck clusters with the RTT150 telescope. 2014, ArXiv e-prints, arXiv:1407.6663

Planck Collaboration IX, Planck early results. IX. XMM-*Newton* follow-up validation programme of *Planck* cluster candidates. 2011, A&A, 536, A9, arXiv:1101.2025

Planck Collaboration X, Planck early results. X. Statistical analysis of Sunyaev-Zeldovich scaling relations for X-ray galaxy clusters. 2011, A&A, 536, A10, arXiv:1101.2043

Planck Collaboration XX, *Planck* 2013 results. XX. Cosmology from Sunyaev-Zeldovich cluster counts. 2014, A&A, 571, A20, arXiv:1303.5080

Planck Collaboration XXIX, *Planck* 2013 results. XXIX. The Planck catalogue of Sunyaev-Zeldovich sources. 2014, A&A, 571, A29, arXiv:1303.5089

Planck Collaboration XXXVI, Planck 2013 results. XXIX. The Planck catalogue of Sunyaev-Zeldovich sources: Addendum. 2015, ArXiv e-prints, arXiv:1502.00543

Planck Collaboration I, *Planck* 2015 results. I. Overview of products and results. 2015, in preparation

Planck Collaboration II, *Planck* 2015 results. II. Low Frequency Instrument data processing. 2015, in preparation

Planck Collaboration III, *Planck* 2015 results. III. LFI systematic uncertainties. 2015, in preparation

Planck Collaboration IV, *Planck* 2015 results. IV. LFI beams and window functions. 2015, in preparation

Planck Collaboration V, *Planck* 2015 results. V. LFI calibration. 2015, in preparation

Planck Collaboration VI, *Planck* 2015 results. VI. LFI maps. 2015, in preparation

Planck Collaboration VII, *Planck* 2015 results. VII. High Frequency Instrument data processing: Time-ordered information and beam processing. 2015, in preparation

Planck Collaboration VIII, *Planck* 2015 results. VIII. High Frequency Instrument data processing: Calibration and maps. 2015, in preparation

Planck Collaboration IX, *Planck* 2015 results. IX. Diffuse component separation: CMB maps. 2015, in preparation

Planck Collaboration X, *Planck* 2015 results. X. Diffuse component separation: Foreground maps. 2015, in preparation

Planck Collaboration XI, *Planck* 2015 results. XI. CMB power spectra, likelihood, and consistency of cosmological parameters. 2015, in preparation

Planck Collaboration XII, *Planck* 2015 results. XII. Simulations. 2015, in preparation

Planck Collaboration XIII, *Planck* 2015 results. XIII. Cosmological parameters. 2015, in preparation

Planck Collaboration XIV, *Planck* 2015 results. XIV. Dark energy and modified gravity. 2015, in preparation

Planck Collaboration XV, *Planck* 2015 results. XV. Gravitational lensing. 2015, in preparation

Planck Collaboration XVI, *Planck* 2015 results. XVI. Isotropy and statistics of the CMB. 2015, in preparation

Planck Collaboration XVII, *Planck* 2015 results. I. XVII. Constraints on primordial non-Gaussianity. 2015, in preparation

Planck Collaboration XVIII, *Planck* 2015 results. XVIII. Background geometry and topology of the Universe. 2015, in preparation

Planck Collaboration XIX, *Planck* 2015 results. XIX. Constraints on primordial magnetic fields. 2015, in preparation

Planck Collaboration XX, *Planck* 2015 results. XX. Constraints on inflation. 2015, in preparation

Planck Collaboration XXI, *Planck* 2015 results. XXI. The integrated Sachs-Wolfe effect. 2015, in preparation

Planck Collaboration XXII, *Planck* 2015 results. XXII. A map of the thermal Sunyaev-Zeldovich effect. 2015, in preparation

Planck Collaboration XXIII, *Planck* 2015 results. XXIII. Thermal Sunyaev-Zeldovich effect–cosmic infrared background correlation. 2015, in preparation

Planck Collaboration XXIV, *Planck* 2015 results. XXIV. Cosmology from Sunyaev-Zeldovich cluster counts. 2015, in preparation

Planck Collaboration XXV, *Planck* 2015 results. XXV. Diffuse, low-frequency Galactic foregrounds. 2015, in preparation

Planck Collaboration XXVI, *Planck* 2015 results. XXVI. The Second Planck Catalogue of Compact Sources. 2015, in preparation

Planck Collaboration XXVII, *Planck* 2015 results. XXVII. The Second Planck Catalogue of Sunyaev-Zeldovich Sources. 2015, in preparation

Planck Collaboration XXVIII, *Planck* 2015 results. XXVIII. The Planck Catalogue of Cold Clumps. 2015, in preparation

Planck Collaboration Int. III, Planck intermediate results. III. The relation between galaxy cluster mass and Sunyaev-Zeldovich signal. 2013, A&A, 550, A129, arXiv:1204.2743

Planck Collaboration Int. V, Planck intermediate results. V. Pressure profiles of galaxy clusters from the Sunyaev-Zeldovich effect. 2013, A&A, 550, A131, arXiv:1207.4061

Planck Collaboration Int. XXXV, Planck intermediate results. XXXV. Optical identification and redshifts of Planck SZ sources with telescopes in the Canary Islands Observatories. 2015

Popesso, P., Biviano, A., Böhringer, H., & Romaniello, M., RASS-SDSS galaxy cluster survey. V. The X-ray-underluminous Abell clusters. 2007, A&A, 461, 397, arXiv:astro-ph/0606191

Pratt, G. W., Croston, J. H., Arnaud, M., & Böhringer, H., Galaxy cluster X-ray luminosity scaling relations from a representative local sample (REXCESS). 2009, A&A, 498, 361, arXiv:0809.3784

Reichardt, C. L., Stalder, B., Bleem, L. E., et al., Galaxy Clusters Discovered via the Sunyaev-Zel'dovich Effect in the First 720 Square Degrees of the South Pole Telescope Survey. 2013, ApJ, 763, 127, arXiv:1203.5775

Reiprich, T. H. & Böhringer, H., The Mass Function of an X-Ray Flux-limited Sample of Galaxy Clusters. 2002, ApJ, 567, 716, arXiv:astro-ph/0111285

Rodriguez-Gonzalvez, C., Chary, R. R., Feroz, F., et al., CARMA observations of massive Planck-discovered cluster candidates at $z > 0.5$ associated with WISE overdensities: breaking the size-flux degeneracy. 2015, in prep., arXiv:in prep.

Rozo, E. & Rykoff, E. S., redMaPPer II: X-Ray and SZ Performance Benchmarks for the SDSS Catalog. 2014, ApJ, 783, 80, arXiv:1303.3373

Rozo, E., Rykoff, E. S., Bartlett, J. G., & Melin, J. B., redMaPPer III: A Detailed Comparison of the Planck 2013 and SDSS DR8 RedMaPPer Cluster Catalogs. 2014, ArXiv e-prints, arXiv:1401.7716

Rozo, E., Wechsler, R. H., Rykoff, E. S., et al., Cosmological Constraints from the Sloan Digital Sky Survey maxBCG Cluster Catalog. 2010, ApJ, 708, 645, arXiv:0902.3702

Rykoff, E. S., Rozo, E., Busha, M. T., et al., redMaPPer. I. Algorithm and SDSS DR8 Catalog. 2014, ApJ, 785, 104, arXiv:1303.3562

Schaye, J., Dalla Vecchia, C., Booth, C. M., et al., The physics driving the cosmic star formation history. 2010, MNRAS, 402, 1536, arXiv:0909.5196

Schuecker, P., Böhringer, H., Collins, C. A., & Guzzo, L., The REFLEX galaxy cluster survey. VII. Omega$_m$ and sigma$_8$ from cluster abundance and large-scale clustering. 2003, A&A, 398, 867, arXiv:astro-ph/0208251

Sifón, C., Menanteau, F., Hasselfield, M., et al., The Atacama Cosmology Telescope: Dynamical Masses and Scaling Relations for a Sample of Massive Sunyaev-Zel'dovich Effect Selected Galaxy Clusters. 2013, ApJ, 772, 25, arXiv:1201.0991

Stanford, S. A., Gonzalez, A. H., Brodwin, M., et al., The Massive and Distant Clusters of WISE Survey. II. Initial Spectroscopic Confirmation of z ˜ 1 Galaxy Clusters Selected from 10,000 deg^2. 2014, ApJS, 213, 25, arXiv:1403.3361

Staniszewski, Z., Ade, P. A. R., Aird, K. A., et al., Galaxy Clusters Discovered with a Sunyaev-Zel'dovich Effect Survey. 2009, ApJ, 701, 32, arXiv:0810.1578

Struble, M. F. & Rood, H. J., A compilation of redshifts and velocity dispersions for Abell clusters (epoch 1991.2). 1991, ApJS, 77, 363

Struble, M. F. & Rood, H. J., A Compilation of Redshifts and Velocity Dispersions for ACO Clusters. 1999, ApJS, 125, 35

Sunyaev, R. A. & Zeldovich, I. B., Microwave background radiation as a probe of the contemporary structure and history of the universe. 1980, ARA&A, 18, 537

Sunyaev, R. A. & Zeldovich, Y. B., The Spectrum of Primordial Radiation, its Distortions and their Significance. 1970, Comments on Astrophysics and Space Physics, 2, 66

Szabo, T., Pierpaoli, E., Dong, F., Pipino, A., & Gunn, J., An Optical Catalog of Galaxy Clusters Obtained from an Adaptive Matched Filter Finder Applied to Sloan Digital Sky Survey Data Release 6. 2011, ApJ, 736, 21, arXiv:1011.0249

Tinker, J., Kravtsov, A. V., Klypin, A., et al., Toward a Halo Mass Function for Precision Cosmology: The Limits of Universality. 2008, ApJ, 688, 709, arXiv:0803.2706

Trejo-Alonso, J. J., Caretta, C. A., Laganá, T. F., et al., Red sequence of Abell X-ray underluminous clusters. 2014, MNRAS, 441, 776, arXiv:1403.6437

Vikhlinin, A., Burenin, R. A., Ebeling, H., et al., Chandra Cluster Cosmology Project. II. Samples and X-Ray Data Reduction. 2009a, ApJ, 692, 1033, arXiv:0805.2207

Vikhlinin, A., Kravtsov, A. V., Burenin, R. A., et al., Chandra Cluster Cosmology Project III: Cosmological Parameter Constraints. 2009b, ApJ, 692, 1060, arXiv:0812.2720

Wen, Z. L., Han, J. L., & Liu, F. S., Galaxy Clusters Identified from the SDSS DR6 and Their Properties. 2009, ApJS, 183, 197, arXiv:0906.0803

Wen, Z. L., Han, J. L., & Liu, F. S., A Catalog of 132,684 Clusters of Galaxies Identified from Sloan Digital Sky Survey III. 2012, ApJS, 199, 34, arXiv:1202.6424

Wright, E. L., Eisenhardt, P. R. M., Mainzer, A. K., et al., The Wide-field Infrared Survey Explorer (WISE): Mission Description and Initial On-orbit Performance. 2010, AJ, 140, 1868, arXiv:1008.0031

York, D. G., Adelman, J., Anderson, Jr., J. E., et al., The Sloan Digital Sky Survey: Technical Summary. 2000, AJ, 120, 1579, arXiv:astro-ph/0006396

Zu, Y., Weinberg, D. H., Rozo, E., et al., Cosmological constraints from the large-scale weak lensing of SDSS MaxBCG clusters. 2014, MNRAS, 439, 1628

Appendix A: High-redshift SDSS confirmations

Table A.1 gives optical information for four high-redshift confirmations found using a search in SDSS data around unmatched *Planck* detections.

We use a multi-wavelength approach to confirm the clusters. Each of these candidates possess coincident high-redshift optical over-densities in SDSS, firm infra-red confirmations from WISE, and significant emission in the *ROSAT* $0.5-2.4$ keV band. We estimate the X-ray luminosity from the *ROSAT* maps using growth-curve analysis, and confirm that the luminosity is consistent with the measured $M_{\rm sz}$ as discussed in Sect. 7.2.

One interesting case is PSZ2 G097.52+51.70, which appears to be a near line-of-sight projection with components at $z = 0.7$ and $z = 0.333$, separated by 1.91 arcmin. Both systems may contribute to the observed *Planck* signal. We have associated to the high-redshift cluster because it is significantly closer to the SZ centre (0.714 arcmin vs. 2.47 arcmin separation), and because it is coincident (0.23 arcmin) with the *ROSAT* X-ray centre. The $z = 0.333$ system shows less significant hard-band emission.

Table A.1. Optical information for our high-z SDSS confirmations. Alongside the redshift, we give the RA and DEC of the BCG and if the redshift is spectroscopic, N_z gives number of cluster members with spectroscopic redshifts.

NAME	α_{BCG}	δ_{BCG}	z	N_z
PSZ2 G076.18-47.30	343.1475	4.5381	0.666	3
PSZ2 G087.39+50.92	231.6383	54.1520	0.748	1
PSZ2 G089.39+69.36	208.4382	43.4843	0.68	...
PSZ2 G097.52+51.70	223.8374	58.8707	0.7	...

Appendix B: Differences in PSZ1 and PSZ2 redshift assignments

The PSZ2 contains 782 clusters which had redshift estimates in the PSZ1. We assign the same redshift in all but 43 of these cases. In 25 of these cases, there is no significant difference, defined by $|\Delta z| > 0.03$ or $|\Delta z|/z > 0.1$, between the estimates and we have updated PSZ1 photometric redshift from various sources to new estimates from `redMaPPer` or *Planck* follow-ups.

We have updated a further seven PSZ1 photometric redshifts with recent *Planck* ENO follow-up redshifts (Planck Collaboration Int. XXXV 2015) where the redshift has significantly changed. Of these, one was from the PSZ1 SDSS search, two were from PanSTARRs and four were from earlier *Planck* photometric follow-ups. These updates are included in the 2015 update of the PSZ1 redshift compilation (Planck Collaboration XXXVI 2015).

We discuss the remaining 11 significant differences below:

- **PSZ2 G020.66+37.99** (PSZ1 INDEX 51): Rozo et al. (2014) discuss this cluster in depth. RedMAPPer finds two overlapping clusters, $z_{\rm spec} = 0.338, \lambda = 85.4$ and $z_{\rm spec} = 0.443, \lambda = 23.5$. The PSZ1 redshift $z_{\rm phot} = 0.39$ from WFI *Planck* follow-up is likely to be biased by members from the less rich and more distant system. For the PSZ2, we choose the higher richness match and quote the $z_{\rm phot} = 0.345$. The 2015 update to the PSZ1 adopts this change.
- **PSZ2 G066.68+68.44** (PSZ1 INDEX 222): This is an ambiguous system. The PSZ1 used $z_{\rm spec} = 0.1813$ from NORAS (Böhringer et al. 2000). For the PSZ2 we have quoted $z_{\rm phot} = 0.163$ from `redMaPPer` which agrees with the estimate $z_{\rm spec} = 0.16$ from BCS follow-up (Struble & Rood 1999; Crawford et al. 1995) and the SDSS BCG estimate $z_{\rm spec} = 0.163$. The decision between these two *ROSAT* follow-up spectroscopic redshifts rests on the `redMaPPer` information, which identifies a rich $\lambda = 84.1$ system at $z_{\rm phot} = 0.163$.
- **PSZ2 G087.39+50.92** (PSZ1 INDEX 299): The PSZ2 position has moved closer to a clear high-redshift SDSS cluster at $z_{\rm spec} = 0.748$ at separation $0.9 \times \theta_{\rm err}$, and away from the PSZ1 SDSS match which is now at $2.62 \times \theta_{\rm err}$. There is also clear *ROSAT* $0.5 - 2.4$ keV X-ray emission at the high-z location, whose strength is consistent with the SZ emission, while there is no significant emission at the PSZ1 SDSS match location.
- **PSZ2 G090.66-52.34** (PSZ1 INDEX 308): The PSZ1 redshift $z_{\rm spec} = 0.1784$ came from a single galaxy spectrum (Struble & Rood 1999). `redMaPPer` suggest this galaxy is likely to be in the foreground, with the rich $\lambda = 85$ cluster at slightly high redshift $z_{\rm phot} = 0.197$. We note however that the difference is small (10.2%).
- **PSZ2 G113.91-37.01** (PSZ1 INDEX 416): We adopt the Rozo et al. (2014) update of the NORAS redshift, which replaced a $\lambda = 7.1$ group at $z = 0.135$ with a rich $\lambda = 159$ cluster at $z = 0.371$ separated by 8 arcmin.
- **PSZ2 G121.13+49.64** (PSZ1 INDEX 443): We note that this system is a probable projection. We adopt the correction of the redshift from (Rozo et al. 2014), noting that the richness of the $z = 0.22$ component is consistent with the SZ signal, while the $z = 0.438$ system matched in the PSZ1 is insufficiently rich. The 2015 update to the PSZ1 adopts this change.
- **PSZ2 G143.26+65.24** (PSZ1 INDEX 513): The PSZ1 association with ACO 1430 is correct, but we update the redshift of $z_{\rm spec} = 0.211$ from two members (Struble & Rood 1991) with $z_{phot} = 0.363$ from `redMaPPer`. The X-ray and optical images show an E-W elongation and two possible galaxy concentrations, possibly a projection. The high-redshift component has richness consistent with the SZ signal. The 2015 update to the PSZ1 adopts this change.
- **PSZ2 G151.19+48.27** (PSZ1 INDEX 537): The PSZ1 association with A0959 is correct. NED lists two literature redshifts for this cluster: 0.289 (which we adopt) and 0.353 (adopted in the PSZ1). This object is bimodal in the optical and in the X-ray and is almost certainly a projection. `redMaPPer` suggests association with 0.289 component based on consistency of richness with the SZ signal. The 2015 update to the PSZ1 adopts this change.
- **PSZ2 G259.30+84.41** (PSZ1 INDEX 888): We adopt the correction of Rozo et al. (2014) of the PSZ1 redshift $z_{\rm phot} = 0.4125$ from NSCS, instead matching to a clear and rich SDSS cluster within 1 arcmin of the Planck position at $z_{\rm phot} = 0.323$. The 2015 update to the PSZ1 adopts this change.
- **PSZ2 G310.81+83.91** (PSZ1 INDEX 1093): The PSZ2 matched to an SDSS cluster at $z_{\rm phot} = 0.446$. `redMaPPer` finds this potential counterpart to be insufficiently rich to be detected by *Planck* at this redshift and there is no X-ray emission in *ROSAT*. The *Planck* detection may be spurious: there are point sources detected at 353 and 545GHz and the neural network quality assessment suggests a contaminated spectrum. We therefore break the association and leave the detection unconfirmed.
- **PSZ2 G318.62+58.55** (PSZ1 INDEX 1123): We adopt the correction of Rozo et al. (2014) of the PSZ1 redshift $z_{\rm spec} = 0.1144$. This associates to a different cluster at 4.56 arcmin separation, with `redMaPPer` redshifts $z_{\rm phot} = 0.22$ ($z_{\rm spec} = 0.233$), and richness $\lambda = 69.3$.

Appendix C: Modifications of the extraction algorithms since the PSZ1 release

C.1. MMF1

The `MMF1` code used for the PSZ2 is the same as for the PSZ1 with the following changes:

- Positions estimates are now calculated with sub-pixel positioning using posteriors marginalised over all other parameters, rather than taking the pixel centre closest to the peak.
- Position error radius estimation has been debugged.
- The 2D contour grids for (Y, θ) expand dynamically if the 91% confidence region is not entirely contained within the grid. This expansion is not applied to S/N< 5 detections.

C.2. `MMF3`

For the PSZ2 release, we made three improvements on our `MMF3` code:

- Bright clusters impact the estimation of background. For the PSZ1 we have adopted two different estimators of the `MMF3` background depending on the S/N of the detections. If the S/N was below 20, the theoretical calculation was used (see Eq. 7 in Melin et al. (2006b)) while, for S/N greater than 20, we used the standard deviation of the filtered map. When the cluster signal is subdominant in the map the two estimators return the same result but they differ if the cluster is bright (typically with S/N above 20) due to the contamination of the background by the cluster itself. The choice of using two estimators has been made to make the `MMF3` background estimate compatible with `PwS` and `MMF1` for the PSZ1. We tested it against the QA after the 2013 release and found that it biases significantly `MMF3` two dimensional $(\theta_s, Y_{5\mathrm{R}500})$ contours with respect to injected cluster size and flux at high S/N. We thus decided to come back to the theoretical calculation of the background across all the S/N range as in the earlier version of `MMF3` used for the ESZ. This choice fixes the issue with high S/N cluster contours in the QA. But it increases the S/N value and shifts the $(\theta_s, Y_{5\mathrm{R}500})$ contours for `MMF3` detections in the PSZ2 release with respect to PSZ1 for the detections with S/N above 20 more than the increase expected from the additional integration time. For the PSZ2 `PwS` now estimate the cross-channel covariance matrix under the '*native*' prescription (see `PwS` section in this appendix). This improvement makes the background estimate compatible with the theoretical calculation from `MMF3` and also gives unbiased estimates for the `PwS` two dimensional in the QA.
- `MMF3` two dimensional $(\theta_s, Y_{5\mathrm{R}500})$ contours in the PSZ1 were tested against the QA after the 2013 release. This could not be done in early 2013 for lack of time. The contours were found to be wider than expected. The code has been corrected and new contours have been produced and included in the *Planck* Legacy Archive for the PSZ1. The PSZ2 relies on this new and fully tested estimate of the two dimensional contours.
- The `MMF3` positional error for the PSZ1 was overestimated. The code has been corrected and tested against the QA. New estimates have been produced and included in the Planck Legacy Archive for the PSZ1. The PSZ2 uses the new estimate of the positional error.

C.3. `PwS`

The `PwS` code used for PSZ2 is similar to the one used for PSZ1, with two modifications:

- The cross-channel covariance matrix is now always estimated using iterative recalibration but is parameterised in order to produce a smoother estimate. Using the QA, we have shown that the new calibration only impacts the S/N estimate ($\sim 12\%$) keeping unchanged all other parameter estimates. The new S/N estimates are consistent with the other codes.
- For $(\theta_s, Y_{5\mathrm{R}500})$, we now adopt non-informative priors, formulated using Jeffrey's method (Carvalho et al. 2012), instead of informative priors derived from a fiducial cosmology and mass function.

Appendix D: Description of the delivered products

The data products comprise: (i) the main catalogue, which contains the characterised catalogue with ancillary information; (ii) individual algorithm catalogues produced by each of the codes prior to merging to create the main catalogue, which contain $Y-\theta$ parameter posteriors per cluster; (iii) selection function files containing the completeness and survey masks for various sample definitions.

D.1. Main catalogue

The table contains the following columns:

Column Name	Data Type	Units	Description
INDEX	Integer(4)	...	Index of detection (see note 1)
NAME	String	...	Name of detection (see note 2)
GLON	Real(8)	degrees	Galactic longitude ($0° \le l < 360°$)
GLAT	Real(8)	degrees	Galactic latitude ($-90° \le b \le 90°$)
RA	Real(8)	degrees	Right ascension (J2000)
DEC	Real(8)	degrees	Declination (J2000)
POS_ERR	Real(4)	arcmin	Uncertainty in position (see note 3)
SNR	Real(4)	...	S/N of detection
PIPELINE	Integer(4)	...	Pipeline from which information is taken: the reference pipeline (see note 4)
PIPE_DET	Integer(4)	...	Information on pipelines making detection (see note 4)
PCCS2	Boolean	...	Indicates whether detection matches with any in PCCS2 catalogues
PSZ	Integer(4)	...	Index of matching detection in PSZ1, or -1 if a new detection
IR_FLAG	Integer(1)	...	Flag denoting heavy IR contamination
Q_NEURAL	Real(4)	...	Neural network quality flag (see note 5)
Y5R500	Real(4)	10^{-3} arcmin^2	Mean marginal $Y_{5\mathrm{R}500}$ as measured by the reference pipeline
Y5R500_ERR	Real(4)	10^{-3} arcmin^2	Uncertainty on$Y_{5\mathrm{R}500}$ as measured by the reference pipeline
VALIDATION	Integer(4)	...	External validation status (see note 6)
REDSHIFT_ID ...	String	...	External identifier of cluster associated with redshift measurement (see note 7).
REDSHIFT	Real(4)	...	Redshift of cluster (see note 7)
MSZ	Real(4)	$10^{14} M_\odot$	SZ mass proxy (see note 8)
MSZ_ERR_UP	Real(4)	$10^{14} M_\odot$	Upper 1σ SZ mass proxy confidence interval (see note 8)
MSZ_ERR_LOW ..	Real(4)	$10^{14} M_\odot$	Lower 1σ SZ mass proxy confidence interval (see note 8)
MCXC	String	...	ID of X-ray counterpart in the MCXC if one is present
REDMAPPER ...	String	...	ID of optical counterpart in the `redMaPPer` catalogue if one is present
ACT	String	...	ID of SZ counterpart in the ACT catalogues if one is present
SPT	String	...	ID of SZ counterpart in the SPT catalogues if one is present
WISE_FLAG	Integer(4)	...	Confirmation flag of WISE IR overdensity (see note 9)
AMI_EVIDENCE .	Real(4)	...	Bayesian evidence for AMI counterpart detection (see note 9)
COSMO	Boolean	...	Indicates whether the cluster is in the cosmology sample
COMMENT	String	...	Comments on this detection

Notes:

1. The index is determined by the order of the detections in the union catalogue. The matching entries in the individual catalogues have the same index to facilitate cross-referencing.
2. The names are in the format PSZ2 Gxxx.xx±yy.yy where xxx.xx is the Galactic longitude and ±yy.yy is the Galactic latitude of the detection, both in degrees. The coordinates are truncated towards zero, not rounded.
3. The value given here is the 95% confidence interval of the distribution of radial displacement.
4. The PIPELINE column defines the pipeline from which the values in the union catalogue are taken: 1 = `MMF1`; 2 = `MMF3`; 3 = `PwS`.
   The PIPE_DET column is used to indicate which pipelines detect this object. The three least significant decimal digits are used to represent detection or non-detection by the pipelines. Order of the digits: hundreds = MMF1; tens = MMF3; units = `PwS`. If it is detected then the corresponding digit is set to 1, otherwise it is set to 0.
5. The neural network quality flag is 1-Q_{bad}, following the definitions in Aghanim et al. 2014. Values Q_NEURAL< 0.4 denote low-reliability detections.

6. The VALIDATION column gives a summary of the external validation, encoding the most robust external identification: -1 = no known external counterpart; 10=ENO follow-up; 11= RTT follow-up; 12= PanSTARRs; 13= `redMaPPer` non-blind; 14= SDSS high-z; 15=AMI; 16= WISE; 20 = legacy identification from the PSZ1 2013 release; 21 = MCXC; 22= SPT; 23=ACT; 24= `redMaPPer`; 25= PSZ1 counterpart with redshift updated in (Planck Collaboration XXXVI 2015); 30= NED.
7. The redshift source is the most robust external validation listed in the VALIDATION field.
8. Definition of M_{sz}. The hydrostatic mass, M_{500}, assuming the best-fit $Y-M$ scaling relation of Arnaud et al. (2010) as a prior that cuts a plane through the parameter contours (see Sect. 5.3). The errors are 67% confidence statistical errors and based on the *Planck* measurement uncertainties only. Not included in the error estimates are the statistical errors on the scaling relation, the intrinsic scatter in the relation, or systematic errors in data selection for the scaling relation fit.
9. WISE confirmation flag is assigned by visual inspection and defined to be one of $[-10, -2, -1, 0, 1, 2, 3]$, where -10 denotes no information and the other values are discussed in Section 7.4. Bayesian evidence for AMI counterpart defined in paper.

D.2. Individual algorithm catalogues

The table contains the following columns:

Column Name	Data Type	Units	Description
INDEX	Integer(4)	...	Index of detection (see note 1)
NAME	String	...	Name of detection (see note 1)
GLON	Real(8)	degrees	Galactic longitude ($0° \leq l < 360°$)
GLAT	Real(8)	degrees	Galactic latitude ($-90° \leq b \leq 90°$)
RA	Real(8)	degrees	Right ascension (J2000)
DEC	Real(8)	degrees	Declination (J2000)
POS_ERR	Real(4)	arcmin	Uncertainty in position (see note 2)
SNR	Real(4)	...	S/N of detection (see note 3)
TS_MIN	Real(4)	arcmin	Minimum θ_{s} in second extension HDU (see note 4)
TS_MAX	Real(4)	arcmin	Maximum θ_{s} in second extension HDU (see note 4)
Y_MIN	Real(4)	arcmin^2	Minimum $Y_{5\mathrm{R}500}$ in second extension HDU (see note 4)
Y_MAX	Real(4)	arcmin^2	Maximum $Y_{5\mathrm{R}500}$ in second extension HDU (see note 4)

Notes:

1. The index and name are taken from the union catalogue. The matching entries in the individual catalogues have the same index and name to facilitate cross-referencing.
2. The value given here is the 95% confidence interval of the distribution of radial displacement.
3. The SNR column contains the native signal-to-noise ratio determined by the detection pipeline.
4. These entries define the limits of the grid used to evaluate the 2D probability distribution of θ_{s} and $Y_{5\mathrm{R}500}$ in the second extension HDU (see below).

Second extension HDU

The second extension HDU contains a three-dimensional image with the two-dimensional probability distribution in θ_{s} and $Y_{5\mathrm{R}500}$ for each cluster. The probability distributions are evaluated on a 256×256 linear grid between the limits specified in the first extension HDU. The limits are determined independently for each detection. The dimensions of the 3D image are $256 \times 256 \times n$, where n is the number of detections in the catalogue. The second dimension is θ_{s} and the first dimension is $Y_{5\mathrm{R}500}$.

Third extension HDU

The third extension HDU contains a three-dimensional image with the M_{sz} observable information per cluster as a function of assumed redshift. The image dimensions are $100 \times 4 \times n$, where n is the number of detections in the catalogue. The first dimension is the assumed redshift. The second dimension has size 4: the first element is the assumed redshift value for the M_{sz} fields. The second element is the M_{sz} lower 67% confidence bound, the third element is the M_{sz} estimate and the fourth element is the M_{sz} upper 67% confidence bound, all in units of $10^{14} M_{\odot}$. These errors are based on the Planck measurement uncertainties only. Not included in the error estimates are the statistical errors on the scaling relation, the intrinsic scatter in the relation, or systematic errors in data selection for the scaling relation fit.

D.3. Selection function file format

The selection function information is stored in FITS files. The filenames of the catalogues are of the form PSZ2-selection_Rx.xx.fits, where x.xx is the release number.

First extension HDU

The first extension HDU contains the survey region, denoted by an $N_{\mathrm{side}} = 2048$ ring-ordered HEALPix map in GALACTIC coordinates. Pixels in the survey region have the value 1.0 while areas outside of the survey region have value 0.0.

Second extension HDU

The second extension HDU contains a three-dimensional image containing the survey completeness probability distribution for various thresholds. The information is stored in an image of size $30 \times 32 \times 12$. The first dimension is Y_{500}, the second dimension is θ_{500} and the third dimension is the signal-to-noise threshold. The units are percent and lie in the range 0-100 and denote the detection probability of a cluster lying within the given Y_{500}-θ_{500} bin.

Third extension HDU

The second extension HDU contains the Y_{500} grid values for the completeness data cube held in the second extension. It has length 30 and spans the range $1.12480 \times 10^{-4} - 7.20325 \times 10^{-2}$ arcmin^2 in logarithmic steps.

Fourth extension HDU

The fourth extension HDU contains the θ_{500} grid values for the completeness data cube held in the second extension. It has length 32 and spans the range 0.9416-35.31 arcmin in logarithmic steps.

Fifth extension HDU

The fifth extension HDU contains the signal-to-noise threshold grid values for the completeness data cube held in the second extension. It has length 12 and contains thresholds at intervals of 0.5 from 4.5 to 10.0.

Appendix E: Detail of missing PSZ1 detections

Table E.1. Detail of the 291 PSZ1 detections not present in the PSZ2 catalogue. The TYPE column lists the reason why the detection was dropped. TYPE 1 lost detections are low-S/N detections lost due to changes in the noise realisation. The S/N_non_blind field contains the non-blind S/N for the Y signal in the full-mission maps at the location and size of the PSZ1 detection and is provided for all TYPE 1 lost detections (whereas the field S/N is for the PSZ1). TYPE 2 are lost behind the new point source mask. TYPE 3 are cut due to IR contamination. TYPE 4 are cut by internal `PwS` consistency criteria. Each of these types are discussed in Sect. 6.3.

INDEX	S/N	PIPELINE	PIPE_DET	ID_EXT	REDSHIFT	S/N (non-blind)	TYPE
4	6.04	3	101	...	...	...	3
8	4.92	1	100	...	...	0.34	1
9	5.76	1	100	...	...	...	3
13	4.52	1	100	ZwCl 1454.5+0656	0.429	3.73	1
28	4.70	2	10	...	0.46	3.54	1
30	4.72	1	100	...	...	1.83	1
32	4.54	1	100	...	...	1.65	1
34	4.50	1	100	...	...	1.42	1
38	4.65	1	100	...	...	2.48	1
40	4.89	2	10	...	...	2.90	1
41	4.81	2	10	...	...	2.90	1
43	4.76	2	10	...	...	2.69	1
52	5.71	2	10	...	0.39	...	4
58	4.56	1	100	...	...	2.06	1
59	4.63	1	100	...	...	3.27	1
60	4.84	2	10	RXC J1917.5-1315	0.177	3.11	1
61	5.06	2	111	...	0.650893	2.91	1
62	4.95	2	11	ACO S 1010	0.28	4.02	1
66	5.20	2	10	...	...	3.19	1
68	4.67	3	1	...	...	3.45	1
77	4.58	1	100	RXC J1453.1+2153	0.1186	2.96	1
82	4.98	2	10	...	...	2.84	1
83	4.96	2	10	...	...	3.53	1
84	4.84	2	10	...	...	3.80	1
86	5.23	1	100	...	...	2.82	1
89	4.69	3	101	WHL J248.764+15.4836	0.4725	3.27	1
90	4.68	1	100	...	...	2.11	1
97	4.82	1	100	WHL J252.649+16.8253	0.3612	2.56	1
98	4.70	3	1	...	...	3.54	1
104	4.54	2	10	...	...	1.94	1
111	4.57	2	10	...	...	1.97	1
112	4.61	1	100	...	...	1.59	1
121	4.70	2	110	...	...	1.22	1
126	4.67	2	10	...	...	1.91	1
128	4.54	3	1	RXC J1623.5+2634	0.4274	3.79	1
131	5.23	2	11	AMF J320.551-6.81740	0.5344	3.59	1
136	4.74	1	100	...	...	...	3
142	4.52	3	101	...	...	1.26	1
157	4.64	1	100	...	...	2.27	1
158	5.29	2	10	...	...	2.08	1
162	4.60	1	100	...	...	2.34	1
165	5.11	3	101	...	...	...	3
170	5.33	2	11	...	...	4.32	1
175	4.82	1	100	...	0.1944	2.84	1
176	5.72	2	10	...	...	...	3
184	4.76	3	1	...	...	2.67	1
193	4.55	1	100	...	...	2.83	1
199	4.55	3	1	...	...	2.12	1
203	4.65	2	10	...	...	1.98	1
211	4.58	3	1	...	...	3.31	1
212	4.54	3	1	...	...	3.72	1
213	4.70	2	10	...	...	2.93	1
223	4.51	2	10	...	0.3341	3.16	1
233	4.79	2	10	ZwCl 2151.0+1325	0.205	3.97	1
237	4.78	1	100	ACO 2429	...	3.36	1
251	5.17	1	100	...	...	2.59	1
257	4.90	2	11	...	...	3.68	1
260	4.78	2	110	WHL J242.728+51.2267	0.4096	3.60	1
262	4.52	1	100	...	...	3.63	1
267	6.37	2	111	ACTJ2327.4-0204	0.705	...	2

Table E.2. Continuation of Table E.1.

Index	S/N	Pipeline	Pipe_det	Id_ext	Redshift	S/N (non-blind)	Type
271	4.71	2	10	. . .	. . .	3.84	1
272	4.57	3	1	ZwCl 1746.2+5429	0.31	4.00	1
276	4.65	2	11	. . .	. . .	2.88	1
278	4.55	2	10	. . .	0.306807	2.32	1
300	5.07	2	10	. . .	0.1132	4.09	1
305	4.82	2	10	. . .	. . .	2.12	1
306	4.90	1	100	. . .	. . .	3.51	1
309	5.37	2	110	ZwCl 1602.3+5917	0.2544	4.01	1
311	4.64	2	110	. . .	. . .	. . .	3
314	5.18	1	100	. . .	. . .	1.78	1
317	5.46	1	100	. . .	. . .	1.09	1
321	4.58	1	100	ZwCl 1604.4+6113	0.3447	4.06	1
327	5.78	3	101	RXC J2318.4+1843	0.0389		4
331	4.79	3	101	. . .	. . .	2.53	1
333	4.71	3	1	WHL J286.905+64.5511	0.3561	3.89	1
336	6.55	2	111	. . .	. . .	. . .	3
349	4.87	2	11	. . .	. . .	. . .	2
361	4.71	2	10	. . .	. . .	1.28	1
365	4.82	3	101	RXC J1834.1+7057	0.0824	3.43	1
367	4.52	2	10	ZwCl 1748.0+7125	. . .	2.72	1
370	5.08	2	110	. . .	. . .	. . .	3
371	4.55	2	110	. . .	. . .	. . .	3
372	4.63	2	11	. . .	. . .	4.03	1
373	4.50	2	10	. . .	. . .	. . .	2
375	4.78	3	101	. . .	. . .	3.03	1
376	4.54	2	10	AMF J359.521+15.1625	0.1785	2.56	1
382	4.73	2	110	. . .	. . .	. . .	3
387	4.66	2	111	. . .	. . .	. . .	2
396	4.55	2	10	. . .	0.25	1.78	1
397	6.89	2	111	. . .	. . .	. . .	3
398	4.55	2	10	. . .	. . .	. . .	3
400	4.58	2	111	. . .	0.533998	2.74	1
405	4.81	1	100	WHL J358.170+38.9803	0.27	2.79	1
412	4.76	3	1	. . .	. . .	3.08	1
426	5.85	2	111	. . .	. . .	. . .	2
430	4.54	3	1	. . .	. . .	3.60	1
436	4.96	3	101	. . .	. . .	3.38	1
437	4.51	1	100	. . .	. . .	3.42	1
444	4.72	2	110	. . .	. . .	3.54	1
445	4.66	2	10	Abell 98S	0.104	2.87	1
446	5.35	2	11	. . .	. . .	. . .	2
456	4.89	1	100	. . .	. . .	3.08	1
458	4.86	3	101	. . .	. . .	2.82	1
462	5.40	2	110	. . .	. . .	. . .	2
466	5.91	2	11	. . .	. . .	. . .	3
468	4.95	2	10	. . .	. . .	3.00	1
469	4.90	2	11	. . .	0.423	2.90	1
476	4.91	2	10	. . .	. . .	2.66	1
478	5.42	3	1	. . .	. . .	. . .	3
479	4.81	2	11	. . .	. . .	4.25	1
483	4.57	2	10	. . .	. . .	3.40	1
488	4.58	1	100	RXC J0115.2+0019	0.045	3.60	1
489	4.58	3	1	. . .	. . .	2.75	1
490	5.22	2	10	. . .	. . .	3.18	1
491	4.51	1	100	RXC J0152.9+3732	0.2993	3.62	1
504	4.90	1	100	. . .	. . .	2.99	1
505	4.53	2	10	. . .	0.172448	2.88	1
517	4.63	2	10	. . .	. . .	2.33	1
522	6.62	3	110	. . .	. . .	. . .	3
524	4.96	3	1	RXC J0209.5+1946	0.0657	3.57	1
527	4.52	1	100	. . .	0.38508	1.54	1
529	8.40	2	111	. . .	. . .	. . .	2
534	4.75	3	1	. . .	. . .	. . .	3
538	4.70	1	100	. . .	. . .	3.62	1
539	5.59	2	111	ACO 307	. . .	3.52	1
544	4.79	2	10	. . .	. . .	3.57	1
555	4.51	3	1	. . .	. . .	2.81	1
556	5.28	2	111	. . .	0.532786	3.54	1
557	4.76	1	100	. . .	. . .	1.97	1
559	4.67	1	100	. . .	. . .	2.48	1
562	4.64	2	10	RXC J0157.4-0550	0.1289	4.35	1
564	6.56	1	100	. . .	. . .	. . .	3
565	5.22	2	111	RXC J0137.4-1259	0.2143	5.16	1
576	4.51	1	100	. . .	. . .	2.81	1
586	5.32	2	10	. . .	. . .	3.04	1
590	4.89	2	11	. . .	. . .	4.83	1

Table E.3. Continuation of Table E.1.

Index	S/N	Pipeline	Pipe_det	Id_ext	Redshift	S/N (non-blind)	Type
592	4.62	2	10	RXC J0822.1+4705	0.1303	3.47	1
604	4.68	1	100	RXC J0248.0-0332	0.1883	3.19	1
605	5.01	3	101	. . .	. . .	2.68	1
607	4.94	1	100	RXC J0956.0+4107	0.587	2.96	1
611	4.82	2	111	. . .	. . .	. . .	3
612	5.87	2	11	. . .	. . .	. . .	2
616	5.09	2	10	. . .	. . .	2.20	1
618	5.43	2	11	. . .	. . .	3.43	1
621	4.78	2	11	RXC J0326.8+0043	0.45	2.90	1
622	5.43	2	10	. . .	0.494731	1.51	1
626	5.90	2	111	. . .	. . .	. . .	3
629	4.51	1	100	. . .	. . .	2.07	1
639	5.10	3	1	. . .	. . .	4.27	1
642	4.65	1	100	WHL J164.029+34.0043	0.3805	3.50	1
645	4.51	1	100	. . .	. . .	2.60	1
650	4.56	1	100	. . .	0.47	1.10	1
652	4.62	1	100	. . .	. . .	2.59	1
653	5.19	3	1	. . .	. . .	. . .	3
658	4.57	1	100	. . .	. . .	1.78	1
659	4.82	1	100	. . .	. . .	3.24	1
669	4.85	2	10	RXC J1110.7+2842	0.0314	2.96	1
670	4.86	1	100	WHL J56.0261-13.5512	0.5757	3.73	1
671	4.70	3	1	. . .	. . .	. . .	2
672	4.94	2	110	WHL J161.821+27.9906	0.4333	3.28	1
678	4.54	1	100	. . .	0.37572	2.01	1
679	4.55	1	100	. . .	. . .	3.31	1
683	5.38	2	10	. . .	. . .	. . .	2
684	6.62	3	101	. . .	. . .	. . .	2
697	4.62	3	1	ACO 457	. . .	3.81	1
698	4.72	2	10	. . .	. . .	. . .	2
699	4.77	1	100	. . .	. . .	2.73	1
704	4.56	1	100	WHL J131.956+13.5279	0.3487	3.79	1
705	4.67	1	100	. . .	. . .	0.27	1
712	4.65	1	100	. . .	. . .	1.52	1
719	4.82	2	10	WHL J158.665+20.5346	0.4674	2.95	1
721	4.53	1	100	ACO S 270	. . .	2.01	1
722	4.71	3	1	. . .	. . .	2.76	1
725	4.56	2	10	. . .	. . .	3.61	1
728	5.29	1	100	RXC J0906.4+1020	0.1328	3.67	1
729	4.62	1	100	WHL J140.630+11.6581	0.2609	2.88	1
735	4.52	3	1	. . .	. . .	3.37	1
736	5.02	2	10	. . .	. . .	3.95	1
737	4.52	2	10	. . .	. . .	3.19	1
743	4.57	2	10	. . .	. . .	3.45	1
748	4.55	3	1	. . .	. . .	3.84	1
749	4.97	3	101	ACO 3218	. . .	4.03	1
750	5.13	2	10	. . .	0.31	3.37	1
751	4.81	1	100	CXOMP J091126.6+055012	0.7682	3.82	1
753	4.52	3	1	. . .	. . .	3.42	1
755	7.77	3	1	. . .	. . .	. . .	2
760	4.62	2	110	WHL J134.086+1.78038	0.7243	2.90	1
762	4.93	3	1	. . .	. . .	. . .	4
766	7.83	3	1	. . .	. . .	. . .	4
770	4.64	3	1	RXC J1047.5+1513	0.2108	3.50	1
771	4.52	2	10	WHL J124.638-6.42296	0.5123	3.19	1
775	6.97	3	1	. . .	. . .	. . .	2
781	4.79	3	1	. . .	. . .	. . .	3
782	4.62	3	1	ZwCl 0919.7-0016	0.3538	2.64	1
788	4.64	2	10	ACO S 403	. . .	3.72	1
789	5.22	2	110	. . .	. . .	. . .	3
792	4.52	2	10	. . .	. . .	1.39	1
794	5.83	1	100	. . .	. . .	. . .	3
795	4.60	2	111	WHL J170.480+15.8014	0.5593	2.95	1
798	5.05	2	10	. . .	. . .	3.29	1
809	4.59	1	100	. . .	. . .	2.85	1
811	4.64	3	1	. . .	. . .	. . .	3
813	4.64	1	100	. . .	. . .	3.06	1
814	4.58	3	1	. . .	. . .	4.50	1
820	4.57	1	100	RXC J1013.7-0006	0.0927	2.49	1
827	8.14	3	1	. . .	. . .	. . .	2
830	4.56	2	10	. . .	. . .	2.33	1
832	4.55	2	10	ACO S 539	. . .	3.04	1
833	4.62	2	110	. . .	. . .	3.38	1
836	4.76	2	110	RXC J0345.7-4112	0.0603	3.89	1
843	4.51	3	1	. . .	. . .	2.78	1

Table E.4. Continuation of Table E.1.

Index	S/N	Pipeline	Pipe_det	Id_ext	Redshift	S/N (non-blind)	Type
844	4.78	3	1	...	...	3.91	1
845	7.14	3	1	...	...	...	4
859	4.89	3	1	...	...	1.87	1
860	4.64	1	100	...	...	2.41	1
864	5.04	2	10	...	...	3.54	1
866	5.17	3	1	...	...	...	3
874	4.55	1	100	...	...	3.45	1
884	4.67	1	100	...	...	0.99	1
885	4.53	3	1	...	...	3.01	1
886	4.72	2	111	...	...	2.50	1
900	4.60	3	1	...	...	2.92	1
908	4.68	2	10	...	0.45	3.14	1
909	4.68	1	100	...	...	1.94	1
913	4.87	2	10	...	...	3.50	1
917	4.78	1	100	...	...	1.46	1
921	4.72	2	10	...	0.26	4.23	1
923	4.71	1	100	...	...	1.57	1
925	5.00	1	100	...	...	2.16	1
927	4.72	1	100	...	...	1.84	1
928	4.66	3	1	...	...	2.65	1
933	4.60	2	10	...	...	3.06	1
949	4.86	3	1	...	...	1.88	1
950	4.76	1	100	...	...	2.11	1
953	4.87	3	1	...	...	3.98	1
964	4.95	2	10	...	0.14	2.83	1
965	4.51	1	100	...	...	1.71	1
966	4.51	3	1	...	...	2.19	1
968	4.54	2	10	...	...	2.67	1
973	4.56	1	100	...	...	1.52	1
980	12.78	2	111	RXC J1217.6+0339	0.0766		2
992	5.52	2	11	...	...	0.68	1
1010.....	5.91	2	11	...	...	...	3
1016.....	4.76	2	110	...	...	2.74	1
1018.....	4.61	3	1	...	...	3.97	1
1019.....	4.98	2	11	...	...	3.89	1
1031.....	4.81	2	110	...	...	...	3
1039.....	4.50	2	10	...	...	3.30	1
1048.....	4.90	2	10	ACO S 137	0.02764	2.50	1
1049.....	4.95	2	10	ACO 1603	0.1314	2.86	1
1052.....	5.74	3	1	...	...	...	3
1055.....	4.62	3	1	RXC J0052.7-8015	0.1141	4.03	1
1059.....	4.68	1	100	...	...	2.74	1
1060.....	6.81	2	111	...	...	...	3
1069.....	4.84	2	10	...	0.12941	2.29	1
1080.....	4.61	1	100	...	...	2.40	1
1081.....	4.60	2	10	...	...	...	3
1091.....	5.21	2	11	...	...	...	3
1092.....	4.64	2	10	...	...	3.08	1
1094.....	4.68	1	100	...	...	2.57	1
1103.....	6.15	1	100	...	...	...	2
1107.....	5.02	2	10	...	...	2.39	1
1111.....	4.83	2	10	...	...	2.74	1
1119.....	5.48	2	10	...	...	3.53	1
1132.....	4.51	1	100	...	...	1.43	1
1133.....	4.73	1	100	...	0.25	2.81	1
1135.....	4.78	3	1	...	...	3.83	1
1144.....	4.90	3	1	...	...	4.22	1
1152.....	4.63	3	1	...	...	3.61	1
1155.....	4.78	2	111	SPT-CLJ2148-6116	0.571	3.59	1
1159.....	4.76	1	100	...	...	2.15	1
1162.....	4.63	1	100	...	...	2.74	1
1170.....	4.65	2	10	...	...	3.63	1
1173.....	4.55	1	100	...	...	2.24	1
1174.....	6.61	2	111	...	...	...	2
1177.....	5.58	2	10	...	...	...	3
1178.....	4.50	1	100	...	...	2.90	1
1180.....	5.88	2	111	...	...	...	3
1188.....	4.78	2	10	...	...	3.03	1
1194.....	4.75	2	10	...	0.21	3.26	1
1196.....	4.57	1	100	...	...	2.76	1
1197.....	4.78	2	11	...	...	2.35	1
1198.....	4.80	1	100	...	...	2.91	1
1199.....	4.60	2	110	...	...	2.31	1
1203.....	5.02	1	100	ACO S 808	0.049131	3.41	1
1204.....	4.70	1	100	...	0.5	3.20	1
1212.....	4.74	1	100	...	...	2.84	1
1215.....	4.63	1	100	...	...	3.43	1
1217.....	4.52	2	10	...	...	2.49	1
1219.....	5.16	3	1	...	...	...	2
1221.....	5.47	2	11	...	...	...	2

[1] APC, AstroParticule et Cosmologie, Université Paris Diderot, CNRS/IN2P3, CEA/lrfu, Observatoire de Paris, Sorbonne Paris Cité, 10, rue Alice Domon et Léonie Duquet, 75205 Paris Cedex 13, France
[2] Academy of Sciences of Tatarstan, Bauman Str., 20, Kazan, 420111, Republic of Tatarstan, Russia
[3] African Institute for Mathematical Sciences, 6-8 Melrose Road, Muizenberg, Cape Town, South Africa
[4] Agenzia Spaziale Italiana Science Data Center, Via del Politecnico snc, 00133, Roma, Italy
[5] Aix Marseille Université, CNRS, LAM (Laboratoire d'Astrophysique de Marseille) UMR 7326, 13388, Marseille, France
[6] Astrophysics Group, Cavendish Laboratory, University of Cambridge, J J Thomson Avenue, Cambridge CB3 0HE, U.K.
[7] Astrophysics & Cosmology Research Unit, School of Mathematics, Statistics & Computer Science, University of KwaZulu-Natal, Westville Campus, Private Bag X54001, Durban 4000, South Africa
[8] Atacama Large Millimeter/submillimeter Array, ALMA Santiago Central Offices, Alonso de Cordova 3107, Vitacura, Casilla 763 0355, Santiago, Chile
[9] CITA, University of Toronto, 60 St. George St., Toronto, ON M5S 3H8, Canada
[10] CNRS, IRAP, 9 Av. colonel Roche, BP 44346, F-31028 Toulouse cedex 4, France
[11] CRANN, Trinity College, Dublin, Ireland
[12] California Institute of Technology, Pasadena, California, U.S.A.
[13] Centre for Theoretical Cosmology, DAMTP, University of Cambridge, Wilberforce Road, Cambridge CB3 0WA, U.K.
[14] Centro de Estudios de Física del Cosmos de Aragón (CEFCA), Plaza San Juan, 1, planta 2, E-44001, Teruel, Spain
[15] Computational Cosmology Center, Lawrence Berkeley National Laboratory, Berkeley, California, U.S.A.
[16] Consejo Superior de Investigaciones Científicas (CSIC), Madrid, Spain
[17] DSM/Irfu/SPP, CEA-Saclay, F-91191 Gif-sur-Yvette Cedex, France
[18] DTU Space, National Space Institute, Technical University of Denmark, Elektrovej 327, DK-2800 Kgs. Lyngby, Denmark
[19] Département de Physique Théorique, Université de Genève, 24, Quai E. Ansermet,1211 Genève 4, Switzerland
[20] Departamento de Astrofísica, Universidad de La Laguna, E-38206 La Laguna, Tenerife, Spain
[21] Departamento de Física, Universidad de Oviedo, Avda. Calvo Sotelo s/n, Oviedo, Spain
[22] Department of Astronomy and Astrophysics, University of Toronto, 50 Saint George Street, Toronto, Ontario, Canada
[23] Department of Astronomy and Geodesy, Kazan Federal University, Kremlevskaya Str., 18, Kazan, 420008, Russia
[24] Department of Astrophysics/IMAPP, Radboud University Nijmegen, P.O. Box 9010, 6500 GL Nijmegen, The Netherlands
[25] Department of Physics & Astronomy, University of British Columbia, 6224 Agricultural Road, Vancouver, British Columbia, Canada
[26] Department of Physics and Astronomy, Dana and David Dornsife College of Letter, Arts and Sciences, University of Southern California, Los Angeles, CA 90089, U.S.A.
[27] Department of Physics and Astronomy, University College London, London WC1E 6BT, U.K.
[28] Department of Physics, Florida State University, Keen Physics Building, 77 Chieftan Way, Tallahassee, Florida, U.S.A.
[29] Department of Physics, Gustaf Hällströmin katu 2a, University of Helsinki, Helsinki, Finland
[30] Department of Physics, Princeton University, Princeton, New Jersey, U.S.A.
[31] Department of Physics, University of Arizona, 1118 E 4th St, Tucson, AZ, 85721, USA
[32] Department of Physics, University of California, One Shields Avenue, Davis, California, U.S.A.
[33] Department of Physics, University of California, Santa Barbara, California, U.S.A.
[34] Department of Physics, University of Illinois at Urbana-Champaign, 1110 West Green Street, Urbana, Illinois, U.S.A.
[35] Dipartimento di Fisica e Astronomia G. Galilei, Università degli Studi di Padova, via Marzolo 8, 35131 Padova, Italy
[36] Dipartimento di Fisica e Scienze della Terra, Università di Ferrara, Via Saragat 1, 44122 Ferrara, Italy
[37] Dipartimento di Fisica, Università La Sapienza, P. le A. Moro 2, Roma, Italy
[38] Dipartimento di Fisica, Università degli Studi di Milano, Via Celoria, 16, Milano, Italy
[39] Dipartimento di Fisica, Università degli Studi di Trieste, via A. Valerio 2, Trieste, Italy
[40] Dipartimento di Fisica, Università di Roma Tor Vergata, Via della Ricerca Scientifica, 1, Roma, Italy
[41] Dipartimento di Matematica, Università di Roma Tor Vergata, Via della Ricerca Scientifica, 1, Roma, Italy
[42] Discovery Center, Niels Bohr Institute, Blegdamsvej 17, Copenhagen, Denmark
[43] Dpto. Astrofísica, Universidad de La Laguna (ULL), E-38206 La Laguna, Tenerife, Spain
[44] European Southern Observatory, ESO Vitacura, Alonso de Cordova 3107, Vitacura, Casilla 19001, Santiago, Chile
[45] European Space Agency, ESAC, Planck Science Office, Camino bajo del Castillo, s/n, Urbanización Villafranca del Castillo, Villanueva de la Cañada, Madrid, Spain
[46] European Space Agency, ESTEC, Keplerlaan 1, 2201 AZ Noordwijk, The Netherlands
[47] Facoltà di Ingegneria, Università degli Studi e-Campus, Via Isimbardi 10, Novedrate (CO), 22060, Italy
[48] GEPI, Observatoire de Paris, Section de Meudon, 5 Place J. Janssen, 92195 Meudon Cedex, France
[49] Gran Sasso Science Institute, INFN, viale F. Crispi 7, 67100 L'Aquila, Italy
[50] HGSFP and University of Heidelberg, Theoretical Physics Department, Philosophenweg 16, 69120, Heidelberg, Germany
[51] Helsinki Institute of Physics, Gustaf Hällströmin katu 2, University of Helsinki, Helsinki, Finland
[52] INAF - Osservatorio Astrofisico di Catania, Via S. Sofia 78, Catania, Italy
[53] INAF - Osservatorio Astronomico di Padova, Vicolo dell'Osservatorio 5, Padova, Italy
[54] INAF - Osservatorio Astronomico di Roma, via di Frascati 33, Monte Porzio Catone, Italy
[55] INAF - Osservatorio Astronomico di Trieste, Via G.B. Tiepolo 11, Trieste, Italy
[56] INAF/IASF Bologna, Via Gobetti 101, Bologna, Italy
[57] INAF/IASF Milano, Via E. Bassini 15, Milano, Italy
[58] INFN, Sezione di Bologna, Via Irnerio 46, I-40126, Bologna, Italy
[59] INFN, Sezione di Roma 1, Università di Roma Sapienza, Piazzale Aldo Moro 2, 00185, Roma, Italy
[60] INFN, Sezione di Roma 2, Università di Roma Tor Vergata, Via della Ricerca Scientifica, 1, Roma, Italy
[61] INFN/National Institute for Nuclear Physics, Via Valerio 2, I-34127 Trieste, Italy
[62] IPAG: Institut de Planétologie et d'Astrophysique de Grenoble, Université Grenoble Alpes, IPAG, F-38000 Grenoble, France, CNRS, IPAG, F-38000 Grenoble, France

[63] IUCAA, Post Bag 4, Ganeshkhind, Pune University Campus, Pune 411 007, India
[64] Imperial College London, Astrophysics group, Blackett Laboratory, Prince Consort Road, London, SW7 2AZ, U.K.
[65] Infrared Processing and Analysis Center, California Institute of Technology, Pasadena, CA 91125, U.S.A.
[66] Institut Néel, CNRS, Université Joseph Fourier Grenoble I, 25 rue des Martyrs, Grenoble, France
[67] Institut Universitaire de France, 103, bd Saint-Michel, 75005, Paris, France
[68] Institut d'Astrophysique Spatiale, CNRS (UMR8617) Université Paris-Sud 11, Bâtiment 121, Orsay, France
[69] Institut d'Astrophysique de Paris, CNRS (UMR7095), 98 bis Boulevard Arago, F-75014, Paris, France
[70] Institute of Astronomy, University of Cambridge, Madingley Road, Cambridge CB3 0HA, U.K.
[71] Institute of Theoretical Astrophysics, University of Oslo, Blindern, Oslo, Norway
[72] Instituto de Astrofísica de Canarias, C/Vía Láctea s/n, La Laguna, Tenerife, Spain
[73] Instituto de Astrofísica de Canarias, E-38200 La Laguna, Tenerife, Spain
[74] Instituto de Física de Cantabria (CSIC-Universidad de Cantabria), Avda. de los Castros s/n, Santander, Spain
[75] Istituto Nazionale di Astrofisica - Osservatorio Astronomico di Roma, Via Frascati 33, 00040, Monte Porzio Catone (RM), Italy
[76] Istituto Nazionale di Fisica Nucleare, Sezione di Padova, via Marzolo 8, I-35131 Padova, Italy
[77] Jet Propulsion Laboratory, California Institute of Technology, 4800 Oak Grove Drive, Pasadena, California, U.S.A.
[78] Jodrell Bank Centre for Astrophysics, Alan Turing Building, School of Physics and Astronomy, The University of Manchester, Oxford Road, Manchester, M13 9PL, U.K.
[79] Kavli Institute for Cosmology Cambridge, Madingley Road, Cambridge, CB3 0HA, U.K.
[80] LAL, Université Paris-Sud, CNRS/IN2P3, Orsay, France
[81] LAPTh, Univ. de Savoie, CNRS, B.P.110, Annecy-le-Vieux F-74941, France
[82] LERMA, CNRS, Observatoire de Paris, 61 Avenue de l'Observatoire, Paris, France
[83] Laboratoire AIM, IRFU/Service d'Astrophysique - CEA/DSM - CNRS - Université Paris Diderot, Bât. 709, CEA-Saclay, F-91191 Gif-sur-Yvette Cedex, France
[84] Laboratoire Traitement et Communication de l'Information, CNRS (UMR 5141) and Télécom ParisTech, 46 rue Barrault F-75634 Paris Cedex 13, France
[85] Laboratoire de Physique Subatomique et Cosmologie, Université Grenoble-Alpes, CNRS/IN2P3, 53, rue des Martyrs, 38026 Grenoble Cedex, France
[86] Laboratoire de Physique Théorique, Université Paris-Sud 11 & CNRS, Bâtiment 210, 91405 Orsay, France
[87] Lawrence Berkeley National Laboratory, Berkeley, California, U.S.A.
[88] Lebedev Physical Institute of the Russian Academy of Sciences, Astro Space Centre, 84/32 Profsoyuznaya st., Moscow, GSP-7, 117997, Russia
[89] Max-Planck-Institut für Astrophysik, Karl-Schwarzschild-Str. 1, 85741 Garching, Germany
[90] Max-Planck-Institut für Extraterrestrische Physik, Giessenbachstraße, 85748 Garching, Germany
[91] McGill Physics, Ernest Rutherford Physics Building, McGill University, 3600 rue University, Montréal, QC, H3A 2T8, Canada
[92] Moscow Institute of Physics and Technology, Dolgoprudny, Institutsky per., 9, 141700, Russia
[93] National University of Ireland, Department of Experimental Physics, Maynooth, Co. Kildare, Ireland
[94] Niels Bohr Institute, Blegdamsvej 17, Copenhagen, Denmark
[95] Optical Science Laboratory, University College London, Gower Street, London, U.K.
[96] SB-ITP-LPPC, EPFL, CH-1015, Lausanne, Switzerland
[97] SISSA, Astrophysics Sector, via Bonomea 265, 34136, Trieste, Italy
[98] SLAC National Accelerator Laboratory, Menlo Park, CA 94025, USA
[99] School of Physics and Astronomy, Cardiff University, Queens Buildings, The Parade, Cardiff, CF24 3AA, U.K.
[100] School of Physics and Astronomy, University of Nottingham, Nottingham NG7 2RD, U.K.
[101] Sorbonne Université-UPMC, UMR7095, Institut d'Astrophysique de Paris, 98 bis Boulevard Arago, F-75014, Paris, France
[102] Space Research Institute (IKI), Russian Academy of Sciences, Profsoyuznaya Str, 84/32, Moscow, 117997, Russia
[103] Space Sciences Laboratory, University of California, Berkeley, California, U.S.A.
[104] Special Astrophysical Observatory, Russian Academy of Sciences, Nizhnij Arkhyz, Zelenchukskiy region, Karachai-Cherkessian Republic, 369167, Russia
[105] Sterrewacht Leiden, P.O. Box 9513, NL-2300 RA Leiden, The Netherlands
[106] Sub-Department of Astrophysics, University of Oxford, Keble Road, Oxford OX1 3RH, U.K.
[107] TÜBİTAK National Observatory, Akdeniz University Campus, 07058, Antalya, Turkey
[108] Theory Division, PH-TH, CERN, CH-1211, Geneva 23, Switzerland
[109] UCLA Astronomy, PO Box 951547, Los Angeles CA 90095-1547, USA
[110] UPMC Univ Paris 06, UMR7095, 98 bis Boulevard Arago, F-75014, Paris, France
[111] Universidad Andrs Bello, Dpto. de Ciencias Fisicas, Facultad de Ciencias Exactas, 8370134 Santiago de Chile, Chile
[112] Université Denis Diderot (Paris 7), 75205 Paris Cedex 13, France
[113] Université de Toulouse, UPS-OMP, IRAP, F-31028 Toulouse cedex 4, France
[114] Universities Space Research Association, Stratospheric Observatory for Infrared Astronomy, MS 232-11, Moffett Field, CA 94035, U.S.A.
[115] University Observatory, Ludwig Maximilian University of Munich, Scheinerstrasse 1, 81679 Munich, Germany
[116] University of Granada, Departamento de Física Teórica y del Cosmos, Facultad de Ciencias, Granada, Spain
[117] University of Granada, Instituto Carlos I de Física Teórica y Computacional, Granada, Spain
[118] Warsaw University Observatory, Aleje Ujazdowskie 4, 00-478 Warszawa, Poland

E.2 Fonction de sélection et contraintes cosmologiques avec les amas

Les trois articles suivants sont inclus dans cette partie et sont décrits dans le chapitre 4.

- Melin, J.-B., Bartlett, J. G., & Delabrouille, J., The selection function of SZ cluster surveys. 2005, A&A, 429, 417, arXiv:astro-ph/0409564 *[22 citations]*
- Planck Collaboration XX, Planck 2013 results. XX. Cosmology from Sunyaev-Zeldovich cluster counts. 2014, A&A, 571, A20, arXiv:1303.5080 *[198 citations]*
- Planck Collaboration XXIV, Planck 2015 results. XXIV. Cosmology from Sunyaev-Zeldovich cluster counts. 2015, A&A, submitted, arXiv:1502.01597

A&A 429, 417–426 (2005)
DOI: 10.1051/0004-6361:20048093

Astronomy & Astrophysics

The selection function of SZ cluster surveys

J.-B. Melin, J. G. Bartlett, and J. Delabrouille

APC – Université Paris 7, 75005 Paris, France
PCC – Collège de France, 75005 Paris, France
e-mail: `[melin;bartlett;delabrouille]@cdf.in2p3.fr`

Received 15 April 2004 / Accepted 11 September 2004

Abstract. We study the nature of cluster selection in Sunyaev-Zel'dovich (SZ) surveys, focusing on single frequency observations and using Monte Carlo simulations incorporating instrumental effects, primary cosmic microwave background (CMB) anisotropies and extragalactic point sources. Clusters are extracted from simulated maps with an optimal, multi-scale matched filter. We introduce a general definition for the survey selection function that provides a useful link between an observational catalog and theoretical predictions. The selection function defined over the observed quantities of flux and angular size is independent of cluster physics and cosmology, and thus provides a useful characterization of a survey. Selection expressed in terms of cluster mass and redshift, on the other hand, depends on both cosmology and cluster physics. We demonstrate that SZ catalogs are not simply flux limited, and illustrate how incorrect modeling of the selection function leads to biased estimates of cosmological parameters. The fact that SZ catalogs are not flux limited complicates survey "calibration" by requiring more detailed information on the relation between cluster observables and cluster mass.

Key words. cosmology: large-scale structure of Universe – galaxies: clusters: general

1. Introduction

Galaxy cluster surveys are important tools for measuring key cosmological quantities and for understanding the process of structure formation in the universe (Bahcall et al. 1999; Rosati et al. 2002). Surveying for clusters using the Sunyaev-Zel'dovich (SZ) effect (Sunyaev & Zeldovich 1970; Sunyaev & Zeldovich 1972; for recent reviews, see Birkinshaw 1999; and Carlstrom et al. 2002) offers a number of advantages over more traditional methods based on X-ray or optical imaging. These advantages include good detection efficiency at high-redshift; a selection based on the thermal energy of the intracluster medium, a robust quantity relative to any thermal structure in the gas; and an almost constant mass detection limit with redshift (Holder et al. 2000; Bartlett 2000; Bartlett 2001). A new generation of optimized, dedicated instruments, both large bolometer arrays (Masi et al. 2003; Runyan et al. 2003; Kosowsky 2004) and interferometers (Lo et al. 2000; Jones 2002), will soon perform such SZ cluster surveys, and we may look forward to the large and essentially full-sky SZ catalog expected from the Planck mission[1]. In anticipation, many authors have studied the nature and use of SZ cluster catalogs and made predictions for the number of objects expected from various proposed surveys (Holder et al. 2000; Kneissl et al. 2001). A good example of the potential of an SZ survey is the use of its redshift distribution to examine structure formation at high redshift and to thereby constrain cosmological parameters, such as the density parameter Ω_{M} (Barbosa et al. 1996), and the dark energy equation-of-state ω (Haiman et al. 2001).

An astronomical survey is fundamentally characterized by its selection function, which identifies the subclass of objects detected among all those actually present in the survey area. It is a function of cluster properties and survey conditions. Depending on the nature of the observations, relevant cluster properties may include: mass, redshift, luminosity, morphology, etc., while key descriptors of the survey would be sensitivity, angular resolution, spectral coverage, etc. The selection function will also depend on the the detection algorithm used to find clusters in the survey data. Understanding of the selection function is a prerequisite to any statistical application of the survey catalog; otherwise, one has no idea how representative the catalog is of the parent population actually out in the universe.

Selection function issues for SZ surveys have been touched on recently by several authors (Bartlett 2001; Schulz & White 2003; White 2003), while most previous studies of the potential use of SZ surveys have not examined this point in detail. For example, predictions of the redshift distribution of SZ-detected clusters usually assume that they are point sources, simply selected on their total flux[2]. We shall see below that this is not necessarily the case, and an analysis of cosmological

---

[1] A list of web pages describing a number of experiments is given in the reference section.

[2] The term *flux* does not really apply in the case of SZ observations, as the effect is measured relative to the unperturbed background and may be negative. We shall nevertheless use it throughout for simplicity.

parameters based on such an assumption would significantly bias the results.

Understanding a survey selection function is difficult. By its very nature and purpose, the selection function is supposed to tell us about objects that we *don't see* in the survey! Realistic simulations of a survey are central to determining its selection function (e.g., Adami et al. 2001). One knows which objects are put into the simulation and can then compare them to the subset of objects detected by the mock observations. In practice, of course, understanding of a selection function comes only from a combination of such simulations and diverse observations taken under different conditions and/or in different wavebands; full understanding thus comes slowly.

There are really two distinct issues connected to the selection function: object detection, or *survey completeness*, and object measurement, which we shall refer to as *photometry*; as a separate issue, one must also determine the contamination function. One would like to characterize each detected cluster by determining, for example, its total flux, angular size, etc. As practitioners are well aware, photometry of extended objects faces many difficulties that introduce additional uncertainty and, in particular, potential bias into the survey catalog. The selection function must correct for bias induced by both the detection and photometric procedures. The two are, however, distinct steps in catalog construction, and the selection function (see below) should reflect this fact.

The object of the present work is to begin a study of SZ selection functions for the host of SZ surveys that are being planned, and to propose a formalism for their characterization. To this end, we have developed a rapid Monte Carlo simulation tool (Delabrouille et al. 2002) that produces mock images of the SZ sky, including various clustering and velocity effects, primary cosmic microwave background (CMB) anisotropies, radio point sources and instrumental effects. The main goals of such studies, in this period before actual surveying has begun, are to improve understanding of the expected scientific return of a given survey and to help optimize observing strategies.

Our specific aim in the present work is to study selection effects in SZ surveys by focusing on single frequency observations, such as will be performed by up-coming interferometers. Most bolometer cameras propose surveys at several frequencies, although not necessarily simultaneously; the present considerations are therefore applicable to the first data sets from these instruments. This work builds on that of Bartlett (2000) by adding the effects of primary CMB anisotropies, point sources and photometric errors, and by the use of an optimized cluster detection algorithm (Melin et al. 2004).

General considerations concerning the selection function are given in the next section and used to motivate our definition given in Eq. (1). We then briefly describe (Sect. 3) our simulations, based on a Monte Carlo approach incorporating cluster correlations and velocities, as well as our cluster detection and photometry algorithms built on an optimized spatial filter (details will be given elsewhere, Melin et al. 2004). A discussion of cluster selection with this method follows (Sect. 4), where with a simple analytic argument, we show how cluster detection depends on *both* total flux and angular size. Our main conclusion is that SZ surveys will not be simply flux limited. Our simulations support the analytical expectations, and they also highlight the difficulty of performing accurate photometry on detected clusters.

We close with a discussion (Sect. 5) of some implications for upcoming surveys. The most important is that the redshift distribution of observed clusters differs from that of a pure flux-limited catalog; assuming pure flux selection will therefore lead to biased estimates of cosmological parameters. In this same section, we give an explicit example of biased parameter estimation caused by the presence of incorrectly modeled excess primary CMB power on cluster scales, as suggested by the CBI experiment (Mason et al. 2001). We note that non-trivial cluster selection complicates survey "calibration" (Bartelmann 2001; Hu 2003; Majumdar & Mohr 2003; Lima & Hu 2004) because a *size-mass* relation must be obtained in addition to a *flux-mass* relation. Photometric errors will further increase the difficulty by augmenting scatter in the mass-observable relations.

2. Selection function: General considerations

To motivate our definition, we first consider some general properties desired of a survey selection function. Fundamentally, it relates observed catalog properties (e.g., flux and size) to relevant intrinsic characteristics of the source population under study. In particular, we want it to tell us about the *completeness* of the survey catalog as a function of source properties, which is a measure of the selection bias. In addition, we also wish for it to reflect the effects of statistical (e.g., photometric) errors. Notice, on the other hand, that the selection function will not tell us anything about *contamination* of the catalog by false detections; this is another function of observed quantities that must be separately evaluated.

Consider the example of a flux-limited catalog of point sources. Neglecting photometric measurement errors, the probability that a source at redshift z will find its way into the survey catalog is simply given by the fraction of sources brighter than the flux limit, which may be calculated as an integral over the luminosity function at z (e.g., Peebles 1993). Extended objects complicate the situation, for their detection will in general depend on morphology. One must then define appropriate source descriptors other than just a total flux; and even the definition of total flux, conceptually simple, becomes problematic (fixed aperture flux, isophotal flux, integrated flux with a fitted profile, etc.). The choice of descriptors is clearly important and the selection function will depend on it. They must encode relevant observational information on the sources and represent observables with as little measurement error as possible.

The simplest characterization for extended SZ sources would employ a total observed flux, $Y_{\rm o}$, and a representative angular size, which we take to be the core radius $\theta_{\rm co}$. By total flux, we mean the flux density integrated over the entire cluster profile, out to the virial radius, and we express it in a frequency independent manner as the integrated Compton-y parameter. We limit ourselves to these two descriptors in the ensuing discussion, although clearly many others describing cluster morphology are of course possible (ellipticity, for example...). How the observed quantities are actually measured is crucial –

measurement errors and the selection function will both depend on the technique used.

Our detected clusters will then populate the observed parameter space according to some distribution $\mathrm{d}N_\mathrm{o}/\mathrm{d}Y_\mathrm{o}\mathrm{d}\theta_\mathrm{co}$. What we really seek, however, is the true cluster distribution, $\mathrm{d}N/\mathrm{d}Y\mathrm{d}\theta_\mathrm{c}$, over the intrinsic cluster parameters Y and θ_c. Measurement errors and catalog incompleteness both contribute to the difference between these two distributions. In addition, the catalog will suffer from contamination by false detections.

These general considerations motivate us to define the *selection function* as the *joint distribution of* Y_o *and* θ_co, as a function of (i.e., given) Y and θ_c. There are many other factors that influence the selection function, such as instrument characteristics, observation conditions and analysis methods, so in general we write

$$\Phi\,[Y_\mathrm{o}, \theta_\mathrm{co}|Y, \theta_\mathrm{c}, \sigma_\mathrm{N}, \theta_\mathrm{fwhm}, ...] \tag{1}$$

where θ_fwhm is the *FWHM* of an assumed Gaussian beam and σ_N^2 is the map noise variance. We illustrate our main points throughout this discussion with simple uniform Gaussian white noise. The dots represent other possible influences on the selection function, such as the detection and photometry algorithms employed to construct the catalog.

Several useful properties follow from this definition. For example, the selection function relates the observed counts from a survey to their theoretical value by

$$\begin{aligned}\frac{\mathrm{d}N_\mathrm{o}}{\mathrm{d}Y_\mathrm{o}\mathrm{d}\theta_\mathrm{co}}(Y_\mathrm{o}, \theta_\mathrm{co}) \;=\; & \int_0^\infty \mathrm{d}Y \int_0^\infty \mathrm{d}\theta_\mathrm{c}\; \Phi(Y_\mathrm{o}, \theta_\mathrm{co}|Y, \theta_\mathrm{c}) \\ & \times \frac{\mathrm{d}N}{\mathrm{d}Y\mathrm{d}\theta_\mathrm{c}}(Y, \theta_\mathrm{c})\,.\end{aligned} \tag{2}$$

A similar relation can be established between the observed counts and cluster mass and redshift:

$$\begin{aligned}\frac{\mathrm{d}N_\mathrm{o}}{\mathrm{d}Y_\mathrm{o}\mathrm{d}\theta_\mathrm{co}}(Y_\mathrm{o}, \theta_\mathrm{co}) \;=\; & \int_0^\infty \mathrm{d}z \int_0^\infty \mathrm{d}M\; \Psi(Y_\mathrm{o}, \theta_\mathrm{co}|z, M) \\ & \times \frac{\mathrm{d}N}{\mathrm{d}z\mathrm{d}M}(z, M)\end{aligned} \tag{3}$$

where $\mathrm{d}N/\mathrm{d}z\mathrm{d}M$ is the mass function and Ψ incorporates the intrinsic and observational scatter in the relation between $(Y_\mathrm{o}, \theta_\mathrm{co})$ and (z, M) (mass-observable relations). This is made more explicit by

$$\begin{aligned}\Psi(Y_\mathrm{o}, \theta_\mathrm{co}|z, M) \;=\; & \int_0^\infty \mathrm{d}Y \int_0^\infty \mathrm{d}\theta_\mathrm{c}\Phi(Y_\mathrm{o}, \theta_\mathrm{co}|Y, \theta_\mathrm{c}) \\ & \times T(Y, \theta_\mathrm{c}|z, M)\end{aligned} \tag{4}$$

where the function T represents the intrinsic scatter in the relation between actual flux Y and core radius θ_c, and cluster mass and redshift.

In general, we may separate the selection function into two parts, one related to detection and the other to photometry:

$$\Phi(Y_\mathrm{o}, \theta_\mathrm{co}|Y, \theta_\mathrm{c}) = \chi(Y, \theta_\mathrm{c})F(Y_\mathrm{o}, \theta_\mathrm{co}|Y, \theta_\mathrm{c}). \tag{5}$$

The first factor represents survey completeness and is simply the ratio of detected to actual clusters as a function of true cluster parameters. The second factor quantifies photometric errors with a distribution function F normalized to unity:

$$\int \mathrm{d}Y_\mathrm{o}\mathrm{d}\theta_\mathrm{co}\; F(Y_\mathrm{o}, \theta_\mathrm{co}|Y, \theta_\mathrm{c}) = 1$$

In the absence of measurement errors we would have

$$\Phi(Y_\mathrm{o}, \theta_\mathrm{co}|Y, \theta_\mathrm{c}) = \chi(Y_\mathrm{o}, \theta_\mathrm{co})\delta(Y_\mathrm{o} - Y)\delta(\theta_\mathrm{co} - \theta_\mathrm{c})$$

in which case the observed counts become

$$\frac{\mathrm{d}N_\mathrm{o}}{\mathrm{d}Y_\mathrm{o}\mathrm{d}\theta_\mathrm{co}}(Y_\mathrm{o}, \theta_\mathrm{co}) = \chi(Y_\mathrm{o}, \theta_\mathrm{co})\frac{\mathrm{d}N}{\mathrm{d}Y\mathrm{d}\theta_\mathrm{c}}(Y, \theta_\mathrm{c})\,. \tag{6}$$

The importance of the selection function for cosmological studies lies in Eq. (3) which relates the cosmologically sensitive mass function to the observed catalog distribution. Accurate knowledge of Ψ is required in order to obtain constraints on cosmological parameters, such as the density parameter or the dark energy equation-of-state.

3. Simulations

Detailed study of SZ selection issues requires realistic simulations of proposed surveys. Although analytic arguments do provide significant insight, certain effects, such as cluster-cluster blending and confusion, can only be fully modeled with simulations. To this end, we have developed a rapid Monte Carlo-based simulation tool that allows us to generate a large number of realizations of a given survey. This is essential in order to obtain good measures of the selection function that are not limited by insufficient statistics. In this section we briefly outline our simulation method and our cluster detection algorithm, leaving details to Delabrouille et al. (2002) and Melin et al. (2004).

Unless explicitly stated, the simulations used in this work are for a flat concordance model (Spergel et al. 2003) with $\Omega_\mathrm{M} = 0.3 = 1 - \Omega_\Lambda$, Hubble constant of $H_0 = 70\ \mathrm{km\,s^{-1}\,Mpc^{-1}}$ Freedman et al. 2001) and a power spectrum normalization $\sigma_8 = 0.98$. The normalization of the $M - T$ relation is chosen to reproduce the local abundance of X-ray clusters with this value of σ_8 (Pierpaoli et al. 2001). Finally, we fix the gas mass fraction at $f_\mathrm{gas} = 0.12$ (e.g., Mohr et al. 1999).

3.1. Method

Our simulations produce sky maps at different frequencies and include galaxy clusters, primary CMB anisotropies, point sources and instrumental properties (beam smoothing and noise). In this work, we do not consider diffuse Galactic foregrounds, such as dust and synchrotron emission, as we are interested in more rudimentary factors influencing the selection function; we leave foreground issues to a future work (as general references, see Bouchet & Gispert 1999; Tegmark et al. 2000; Delabrouille et al. 2003).

We model the cluster population using the Jenkins et al. (2001) mass function and self-similar, isothermal β-profiles for the SZ emission. A realization of the linear density field $\delta\rho/\rho$ within a comoving 3D box, with the observer placed at one end, is used to construct the cluster spatial distribution and velocity field. We scale the density field by the linear growth factor over a set of redshift slices (or bins) along the past light-cone of the observer; a set of mass bins is defined within each redshift slice. We then construct a random cluster catalog by drawing the number of clusters in each bin of mass and redshift according to a Poisson distribution with mean given by the mass function integrated over the bin. Within each redshift slice, we spatially distribute these clusters with a probability proportional to $1 + b\frac{\delta\rho}{\rho}$, where b is the linear bias given by Mo & White (1996). Comparison of the resulting spatial and velocity 2-point functions of the mock catalog with results from the VIRGO consortium's N-body simulations shows that this method faithfully reproduces the correlations down to scales of order of $10\,h^{-1}$ Mpc.

Individual clusters are assigned a temperature using a $M - T$ relation consistent with the chosen value of σ_8 (Pierpaoli et al. 2001)

$$\frac{M}{10^{15}\,h^{-1}\,M_\odot} = \left(\frac{T}{\beta_p}\right)^{\frac{3}{2}}\left(\Delta_c E^2\right)^{-\frac{1}{2}} \tag{7}$$

with $\beta_p = 1.3 \pm 0.13 \pm 0.13$ keV. Here, Δ_c is the mean density contrast for virialization (weakly dependent on the cosmology) and $E(z) = H(z)/H_0$. As mentioned, we distribute the cluster gas with an isothermal β-model:

$$n_e(r) = n_e(0)\left[1 + \left(\frac{r}{r_c}\right)^2\right]^{\frac{-3\beta}{2}} \tag{8}$$

where we fix $\beta = 2/3$ and the core radius is taken to be $r_c = 0.1\,r_v$, with the virial radius given by

$$r_v = 1.69\,h^{-2/3}\left(\frac{M}{10^{15}\,M_\odot}\right)^{1/3}\left(\frac{\Delta_c}{178}\right)^{-1/3} E^{-2/3}\ \mathrm{Mpc}. \tag{9}$$

The central electron density is determined by the gas mass fraction f_{gas}. For the present work, we ignore any intrinsic scatter in these scaling relations.

In this way we produce a 3×3 degree map of the SZ sky. Primary CMB anisotropies are added as a Gaussian random field by drawing Fourier modes according to a Gaussian distribution with zero mean and variance given by the power spectrum as calculated with CMBFAST (Seljak & Zaldarriaga 1996). We then populate the maps with radio and infrared point sources, using the counts summarized in Bennett et al. (2003) and fitted by Knox et al. (2003), and the counts from SCUBA (Borys et al. 2003). Finally, the map is smoothed with a Gaussian beam and white Gaussian noise is added to model instrumental effects.

3.2. Detection algorithm

We have developed (Melin et al. 2004) a rapid detection routine incorporating a deblending algorithm that is based on matched filtering (Haehnelt & Tegmark 1996), for single frequency surveys, and matched multi-filtering (Herranz et al. 2002), for multi-frequency surveys. Recall that in this work we only examine single frequency surveys. The matched filter, on a scale θ_c, is defined to yield the best linear estimate of the amplitude of the SZ signal from a cluster with (matched) core radius θ_c. It depends on both the beam-smoothed cluster profile τ_c and the noise power spectrum $P(k)$. In Fourier space it is given by

$$\hat{F}(\boldsymbol{k}) = \left[\int \frac{|\hat{\tau}_c(\boldsymbol{k}')|^2}{P(k')}\frac{\mathrm{d}^2k'}{(2\pi)^2}\right]^{-1}\frac{\hat{\tau}_c^*(\boldsymbol{k})}{P(k)} \tag{10}$$

where $P = (P_{\mathrm{cmb}} + P_{\mathrm{sources}})|\hat{B}|^2 + P_{\mathrm{ins}}$, $\hat{\tau}_c$ is the Fourier transform of the beam-smoothed cluster profile τ_c, $\hat{B}$ is that of the instrumental beam (a Gaussian), and P_{cmb}, P_{sources} and P_{ins} represent the power spectra of the primary CMB anisotropies, residual point sources and instrumental noise, respectively. We denote the standard deviation of the noise (including primary CMB and residual points sources) passed through the filter at scale θ_c by σ_{θ_c}, and give its expression for future reference:

$$\sigma_{\theta_c} = \left[\int \frac{|\hat{\tau}_c(\boldsymbol{k})|^2}{P(k)}\frac{\mathrm{d}^2k}{(2\pi)^2}\right]^{-\frac{1}{2}}. \tag{11}$$

This is the fluctuation amplitude of the filtered signal in the absence of any cluster signal.

We can summarize the detection algorithm in three steps:

- filter the observed map with matched filters on different scales θ_c in order to identify clusters of different sizes. This produces a set of filtered maps;
- in each filtered map, find the pixels that satisfy $\frac{S}{N} >$ *threshold* (e.g. 3 or 5). Define cluster candidates as local maxima among these pixels. At this point, each cluster candidate – in each map – has a position, size (that of the filter that produced the map), and a SZ flux given by the signal through the matched filter;
- identify cluster candidates across the different filtered maps using a tree structure (the same cluster can obviously be detected in several filtered maps) and eliminate multiple detections by keeping only cluster properties corresponding to the highest *S/N* map for each candidate.

4. Selection function for single frequency SZ surveys

We consider a single frequency SZ survey with characteristics representative of upcoming interferometers (e.g., the *Arcminute MicroKelvin Imager* being constructed in Cambridge[3]): a 15 GHz observation frequency, 2 arcmin *FWHM* (synthesized) beam and a noise level of 5 μK/beam. Note that, for simplicity and generality, we model the observations as a fully sampled sky map instead of actual visibilities. This approximation should be reasonably accurate given the good sampling expected in the Fourier plane; it will, however, miss important details of the selection function that will require adequate modeling when the time comes. In the same spirit, we also model the noise as a white Gaussian random variable with zero mean and the given variance.

During the course of the discussion, we will often compare the following observational cases: 1) no instrumental

---

[3] `http://www.mrao.cam.ac.uk/telescopes/ami/index.html`

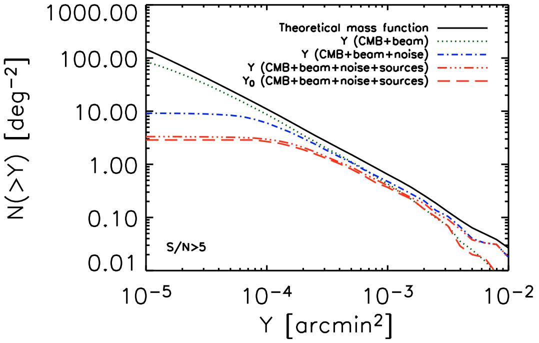

Fig. 1. Cluster counts in terms of integrated Y for the input concordance model (black solid line) and for detected clusters: the green dotted line gives the counts neglecting the effects of instrumental noise and point sources (CMB + beam = 2 arcmin *FWHM*); the blue dash-dotted line includes instrumental noise (5 μK/beam); the red dash-triple-dotted line further includes the effects of residual point sources after explicit subtraction of all sources with flux greater than 100 μJy (see text). These are all plotted as functions of the *true* total flux Y. The red dashed line shows the observed counts for the latter case in terms of the *observed* flux Y_o.

noise (CMB+beam[4]); 2) the former plus instrumental noise at 5 μK/beam; and 3) the previous plus point sources below a flux limit of 100 μJy at 15 GHz. In this last case, we are assuming that all sources brighter than the flux limit are explicitly subtracted; for example, both AMI and the SZA[5] plan long baseline observations for point source removal.

Integrated source counts in terms of total cluster flux Y (measured in arcmin^2) are shown in Fig. 1. The theoretical counts for the fiducial model are given by the solid black line, while the other curves give the counts from our simulated observations. They are plotted in terms of *true* flux Y, except for the red dashed curve that gives the counts as a function of *observed* flux Y_o, as would actually be observed in a survey. Differences between the detected cluster counts and the theoretical prediction (black solid line) reflect catalog incompleteness; the nature of this incompleteness is the focus of our discussion. The influence of photometric errors is illustrated by the difference between the observed counts as a function of observed flux (red dashed curve) and the detected-cluster counts given as a function of true flux.

4.1. Catalog completeness

It is important to understand the exact nature of the incompleteness evident in Fig. 1, and we shall now demonstrate that it is not simply a function of total flux. Our detection algorithm operates as a cut at fixed signal-to-noise, which leads to the following constraint on (true) cluster parameters Y and θ_c:

$$Y = y_{\rm est} \int {\rm d}\Omega\ \tau_c(\hat{n}) \geq \left(\frac{S}{N}\right) \sigma_{\theta_c} \int {\rm d}\Omega\ \tau_c(\hat{n}) \qquad (12)$$

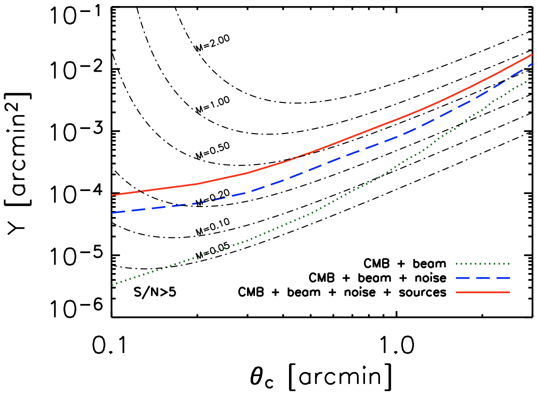

Fig. 2. Selection in the parameter plane of total flux Y and core radius θ_c. The three curves correspond to the different simulated cases, as indicated in the legend; all correspond to a cut at signal-to-noise of 5. The dot-dashed lines in the background give contours of constant mass in this plane; each is parameterized by redshift z. Note that cluster selection does not follow a simple flux cut, which would be a horizontal line, nor a simple mass cut. Photometric errors are neglected in this plot, meaning that observed cluster parameters Y_o and θ_c equal the true values Y and θ_c.

where $y_{\rm est}$ is the central Compton parameter estimated by the filter matched to a cluster of core radius θ_c, and the filter noise on this scale is given by Eq. (11). Figure 2 shows the resulting selection curves for our three cases in the $Y-\theta_c$ plane at $S/N \geq 5$. Note that we are speaking in terms of true cluster parameters, leaving the effects of photometric errors aside for the moment.

It is clear from this figure that cluster selection does not correspond to a simple flux cut – it depends rather on a combination of both source flux and angular extent. The exact form of this dependence is dictated by the noise power spectrum, which must be understood to include primary CMB anisotropy. That this latter dominates on the larger scales can be seen from the fact that the three curves approach each other at large core radii. For smaller objects, on the other hand, instrumental noise and residual point source contamination "pull" the curve towards higher fluxes relative to the ideal case that includes only CMB anisotropies (dotted line).

For the solid red curve, we calculate the flux variance induced by residual point sources at the given filter scale and then add the equivalent Gaussian noise term to the instrumental noise and CMB contributions. One may well ask why the source fluctuations should be Gaussian given the shallow slope of the radio source counts that would normally lead to very non-Gaussian statistics. The fluctuations are in fact Gaussian, as we have verified with the simulations, essentially because the source subtraction is performed at higher angular resolution than the smallest filter scale; in effect, we have cleaned "below" the filter confusion limit, so that the number of sources/filter beam is large and we approach the Gaussian limit. This realistically reflects what will actually be done with interferometers using long baseline observations for source subtraction.

The dot-dashed lines in the background of the figure represent contours of constant cluster mass $M(Y, \theta_c)$. They result

---

[4] Note that in this case of no noise, the beam can be perfectly deconvolved.

[5] `http://astro.uchicago.edu/sze`

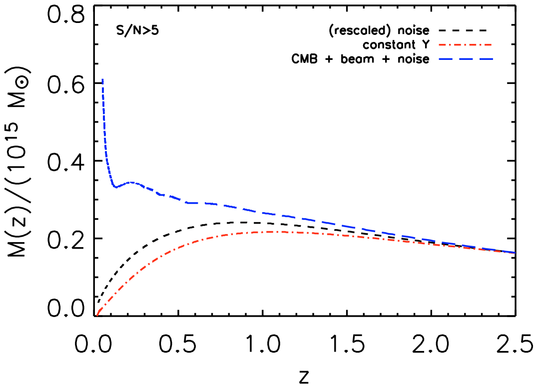

Fig. 3. Detection mass as a function of redshift. The blue long-dashed line shows the result for the case CMB + noise (blue long-dashed line in Fig. 2). The rise at low redshift is due confusion with primary CMB fluctuations that is more important for nearby clusters with large angular extent. The red dot-dashed line gives the result for a pure flux-limited catalog (see text), and the black short dashed line that for observations without CMB confusion (e.g., multi-frequency). Relative to a pure flux-limited catalog, both observed catalogs loose clusters over a range of redshifts.

from inversion of the $Y(M,z)$ and $\theta_c(M,z)$ relations, where we associate cluster core radius with filter scale. Note that redshift varies along each contour, and that we have assumed zero scatter in the relations so that the inversion is one-to-one. In reality, of course, they contain intrinsic scatter, due to cluster physics, as well as observational scatter induced by photometric errors. The position of these mass contours depends on both cluster physics and the underlying cosmology; we may, for example, displace the contours by changing the gas-mass fraction. The selection curves, in contrast, are independent of cosmology and cluster physics, being based on purely observational quantities.

Observed clusters populate this plane according to the distribution $\mathrm{d}N_\mathrm{o}/\mathrm{d}Y_\mathrm{o}\mathrm{d}\theta_\mathrm{co}$, which depends on cluster physics, cosmology and photometry; Eq. (3) gives it in terms of the key theoretical quantity, the mass function. If photometric errors are assumed to be unimportant, then Eq. (6) applies and we see that the function $\chi(Y,\theta_c)$ is a step function taking the value of unity above the selection curves, and zero below; photometric errors simply "smooth" the selection function Φ as manifest by Eq. (5). Completeness expressed in terms of the function χ is therefore *independent* of cluster physics and cosmology. A more common way to express completeness is by the ratio of detected to actual clusters as a function of total flux (or angular scale). At a given flux, for example, this ratio is the fraction of clusters falling above the selection curve. Clearly, it depends on the distribution of clusters over the plane and is, hence, *dependent* on cluster physics, cosmology and photometry. We conclude that the function χ is a more useful description of a survey.

Figure 2 provides a concise and instructive view of cluster selection over the observational plane. We are of course ultimately interested in the kinds of objects that can be detected as a function of redshift, and to this end it is useful to study the *detection mass* shown in Fig. 3. This is defined as the smallest mass cluster detectable at each redshift given the detection criteria. For the figure, we assume that there is no scatter in the $Y_\mathrm{o}(M,z)$ and $\theta_\mathrm{co}(M,z)$ relations so that a selection curve in the observational plane uniquely defines the function $M_\mathrm{det}(z)$. Note that, as emphasized above, these detection mass curves depend on the assumed cosmology.

We compare three situations in the figure. The blue long-dashed line gives the detection mass for the case CMB + noise (single frequency experiment), while the red dot-dashed line shows the result for a pure flux-limited catalog. The chosen flux cut corresponds to the left-most point on the blue long-dashed selection curve in Fig. 2 (CMB+noise). Finally, the black short-dashed line gives the detection mass for a case with just instrumental noise (with the same beam as the previous cases) and no primary CMB; this approximates the situation for a multi-frequency experiment which eliminates CMB confusion. The noise level has been adjusted such that the selection curve in the (Y,θ_c)-plane matches the previous two cases on the smallest scales. With this choice, all three detection mass curves overlap at high z as seen in Fig. 3.

We see that that the observed catalog (blue long-dashed curve) looses clusters (i.e., has a higher detection mass) over a broad range of redshifts relative to the pure flux-limited catalog (red dot-dashed line); the effect is most severe for nearby objects, whose large angular size submerges them in the primary CMB anisotropies, but it remains significant out to redshifts of order unity. This is also reflected in the redshift distribution of Fig. 5 to be discussed below. We note in addition that even multi-frequency experiments loose clusters over a rather broad range of redshifts, as indicated by the difference between the lower two curves.

Simulations are needed to evaluate the importance of factors not easily incorporated into the simple analytic calculation of the cluster selection curve; these include source blending and morphology, other filtering during data analysis, etc. Using our simulations, we find that cluster detection in mock observations closely follows the analytic predictions, thus indicating that blending does not significantly change the above conclusions, at least for the case under study – a 2 arcmin beam with noise at a level of 5 μK/beam – representative of planned interferometer arrays. As our current simulations only employ spherical beta model profiles, they only test for the importance of blending effects; future work will include more realistic profiles taken, for example, from hydrodynamical N-body simulations. The simulations are also crucial for correctly evaluating the photometric precision of the survey catalog. Contrary to the situation for cluster detection, we find that blending greatly affects photometric measurements: photometric scatter from the simulations is significantly larger than expected based on the S/N ratio, whether the threshold is taken at $S/N = 5$ or 3.

4.2. Catalog contamination

Contamination by false detections is a separate function that can only be given in terms of observed flux and angular (or filter) scale; once again, simulations are crucial for evaluating effects such as blending and confusion. Figure 4 shows

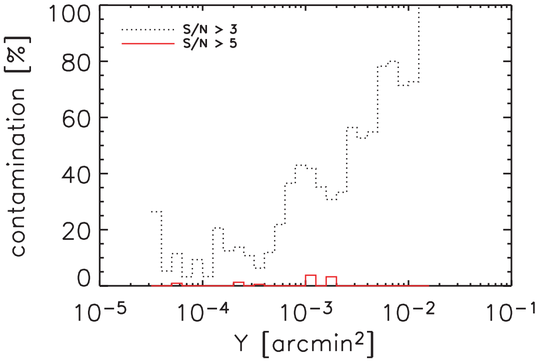

Fig. 4. Contamination rate for a single frequency survey as a function of total flux for two different detection thresholds. The histograms give the percentage of sources that are false detections in catalogs extracted from our simulations.

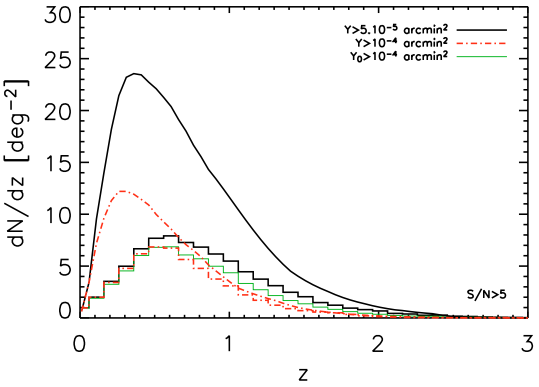

Fig. 5. Redshift distribution of SZ clusters (case 2 – without residual point source noise). The black solid and red dashed curves give the theoretically predicted counts at the two indicated flux limits. Corresponding distributions for the simulated recovered counts, with the same two flux cuts on the true Y, are shown by the black and red, dashed histograms; the small difference between the two reflects the flat observed counts in Fig. 1. The lighter, green histogram shows the simulated counts cut at an *observed* flux of $Y_o > 10^{-4}$ arcmin^2.

the contamination level in our extracted catalogs as a function of total flux Y. The level is significantly higher than expected from the S/N ratio, indicating that confusion and blending effects are clearly important. This is most obvious for the case with $S/N = 3$, where contamination rises towards the high flux end due to confusion with primary CMB fluctuations that are more prevalent on larger angular scales. Even at relatively low flux levels around 10^{-4} arcmin^2, we see that the contamination rate remains near or above 10% for the $S/N = 3$ case. This quantifies the the expectation that single frequency surveys will contend with a non-negligible level of contamination.

4.3. The redshift distribution

The example of extracting cosmological constraints from the redshift distribution of SZ detected clusters affords a good illustration of the importance of understanding the selection function. These constraints arise from the shape of the cluster redshift distribution, which is affected by such parameters as the matter density (Oukbir & Blanchard 1997) and the dark energy equation-of-state (Wang & Steinhardt 1998); this is in fact one of the primary motivations for performing SZ cluster surveys (Haiman et al. 2001). The important point is that the redshift distribution expected in a given cosmological model also depends on the catalog selection function. In the following discussion, we assume that the $Y(M,z)$ and $\theta_c(M,z)$ relations are perfectly known.

Consider the redshift distributions shown in Fig. 5 for an observation where residual point source contamination has been reduced to a negligible level (case 2). The black line represents the theoretical distribution for clusters with total flux $Y > 5 \times 10^{-5}$ arcmin^2, which corresponds to the point source detection limit on the smallest filter scale (leftmost point on the dashed blue curve in Fig. 2). This predicted distribution is very different from the actual distribution of clusters shown as the black histogram. It is clearly impossible to deduce the correct cosmological parameters by fitting a flux-limited theoretical curve to the observed distribution. This demonstrates that the point-source flux limit cannot be used to model the catalog redshift distribution, which is already clear from the fact that the counts in Fig. 1 have already turned over and the catalog is clearly incomplete.

One can try to cut the catalog at a higher flux limit of $Y > 10^{-4}$ arcmin^2, where the observed counts just begin to flatten out and incompleteness is not yet severe. Comparison of the dashed red line – theoretically predicted counts at this flux limit – with the red dashed histogram shows that the observed distribution still differs significantly from the predicted flux-limited redshift distribution. Modeling the observed catalog as a pure flux cut would again lead to incorrect cosmological constraints. In order to extract unbiased parameter estimates, one must adequately incorporate the full catalog selection criteria.

We may illustrate this point by considering the effect of an un-modeled CMB power excess at high l, such as suggested by the CBI experiment (Mason et al. 2001). As we have seen in Fig. 2, the primary CMB fluctuations influence the exact form of the selection curve in the (Y, θ_c) plane; their power on cluster scales must therefore be accurately known to correctly model the cluster selection function. The black curve and black histogram in Fig. 6 repeat the results of Fig. 5 for a cut at $Y > 5 \times 10^{-5}$ arcmin^2. In particular, the black histogram gives the redshift distribution of clusters extracted from simulations including a CMB power spectrum corresponding to the concordance model. The blue (lower) histogram shows the redshift distribution for clusters extracted from simulations in which additional CMB power has been added at high l – a constant power of $l(l+1)C_l/2\pi = 20\ \mu$K was smoothly joined to the concordance model CMB spectrum (just below $l = 2000$) and continuing out to $l = 3000$. Instead of plunging towards zero, as expected of the primary CMB fluctuations in the concordance model, this second model levels off at a constant power level on cluster scales. This has an important effect on cluster detection, as clearly evinced in the figure.

We now examine the effect of ignoring this excess power in an analysis aimed at constraining cosmological parameters.

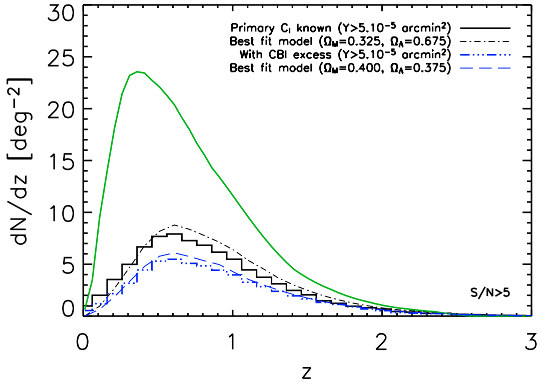

Fig. 6. Effect of incorrect modeling of the selection function. The black continuous curve and black (upper) histogram repeat the results of Fig. 5 for catalogs cut at a flux of $Y = 5 \times 10^{-5}$ arcmin^2 – the former for a pure flux-limited catalog, the latter for the clusters extracted from our concordance model simulations with the expected primary CMB power spectrum [$(\Omega_{\rm M}, \Omega_\Lambda) = (0.3, 0.7)$]; note that the histogram is calculated as the average over 50 simulations of a 3×3 square degree survey field. The light black, dot-dashed curve is the best-fit model to the redshift distribution from a single such simulation; the constraints from for this fit are shown in Fig. 7. The lower (blue) histogram shows the distribution of clusters extracted from the same 50 simulations, but with excess primary CMB power added at high l (see text); once again, the histrogram is the average over the ensemble of simulations. The blue dashed curve shows the best-fit for the same realization as before – but now with the excess – *when ignoring the excess in the fitting* (incorrect selection function modeling). Corresponding constraints are shown in Fig. 7. Both fits are statistically acceptable (see text).

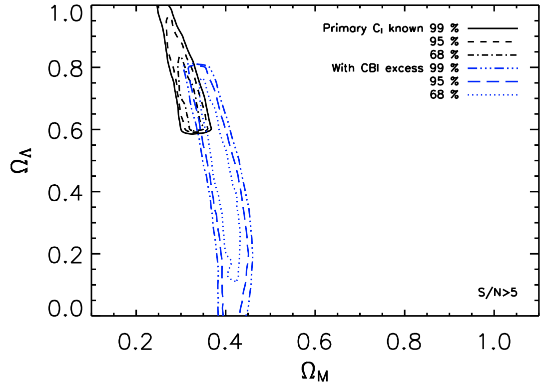

Fig. 7. Confidence contours for the fits discussed in Fig. 6, shown for a survey covering 3 × 3 sq. degrees. The upper (black) contours correspond to the case where the selection function is correctly modeled (no excess CMB power at high l); the best-fit parameters are $(\Omega_{\rm M}, \Omega_\Lambda) = (0.325, 0.675)$ and 1σ contours fully enclose the true (simulation input) cosmological values of $(0.3, 0.7)$. The larger (blue) contours represent the situation when the CMB excess is not properly accounted for by the selection function model. The best-fit parameter values are significantly biased – $(0.4, 0.375)$ – and the true parameter values, lie outside the 99% contour. In both cases the fits are acceptable (see text).

This means that we ignore the excess both in the construction of the matched filter and in the selection function model needed for the fit. The former has only a relatively minor effect on the catalog extraction and observed histogram. The second effect is much more serious, as we now demonstrate.

Consider constraints on the parameter pair $(\Omega_{\rm M}, \Omega_\Lambda)$ by fitting models to the redshift distribution of a 3 × 3 square degree survey. Note that the histograms shown in the figures are in fact averages taken over an ensemble of 50 such simulations, to avoid confusing statistical fluctuations. For the present example, however, we fit models to the redshift distribution from a single simulation. During the fit, we fix the Hubble parameter to its standard value ($H_0 = 70$ km s^{-1} Mpc^{-1}) and adjust the power spectrum normalization σ_8 to maintain the observed present-day cluster abundance (following Pierpaoli et al. 2001). For our simplified case of zero-scatter relations between $(Y_{\rm o}, \theta_{\rm co})$ and (M, z), both the selection function Φ and the intrinsic scatter function T contain Dirac delta functions that collapse the various integrals in Eqs. (3) and (4). We then obtain the following expression for the redshift distribution of observed clusters brighter than a flux of $Y_{\rm o}$:

$$\frac{{\rm d}N_{\rm o}}{{\rm d}z}(>Y_{\rm o}) = \int_{M(Y_{\rm o},z)}^{\infty} {\rm d}M\, \chi\, [Y(M,z), \theta_{\rm c}(M,z)]\, \frac{{\rm d}N}{{\rm d}z{\rm d}M} \qquad (13)$$

where $M(Y, z)$ is the zero-scatter relation between flux and mass and redshift. All selection effects are encapsulated in the completeness function χ, whose dependence on the primary CMB power is the focus of our present discussion.

We consider two cases: the first with the expected concordance primary CMB power spectrum, the second with the CBI-like excess power. In the first case, we adopt the true power spectrum for catalog construction and modeling of χ – the selection function is properly modeled. In the second situation, we ignore the excess in both catalog construction and in fitting – the selection function is incoreclty modeled. When correctly modeling the selection function, we find best-fit values of $(\Omega_{\rm M}, \Omega_\Lambda) = (0.325, 0.675)$. The light black dot-dashed curve in Fig. 6 shows that this model reasonably reproduces the predicted redshift distribution (black solid histogram), and the 1σ contours in Fig. 7 enclose the true (simulation input) values. The fit is good with a reduced $\chi^2 = 0.94$ (34 degrees-of-freedom). When incorrectly modeling the selection function, on the other hand, we find biased best-fit values of $(0.4, 0.375)$, and, as shown in Fig. 7, the true parameter values fall outside the 99% confidence contours. Furthermore, this biased fit is acceptable with a reduced $\chi^2 = 1.17$ (31 degrees-of-freedom), giving no indication of its incorrectness. The redshift distribution of this model is shown as the light dashed (blue) curve in Fig. 6, faithfully reproducing the (averaged) histogram for this case. This is a particularly telling example of the importance of the selection function, because the primary CMB power on cluster scales is at present not well known. It will have to be constrained by the same experiments performing SZ cluster surveys; cosmological constraints will be correspondingly degraded, a subject we return to in a future work.

For another example of incorrect modeling of the selection function, consider that β and $\theta_{\rm c}$ of real clusters may not behave as we assume when constructing the matched filter.

This will bias flux measurments and displace the selection curve in the (Y, θ_c) plane relative to our expectations, leading to an incorrect selection function model. As above, this will yield biased parameter estimates.

As a final note, and returning to Fig. 5, we show the distribution of detected clusters at the higher flux cut as a function of *observed* flux with the lighter, green histogram. The difference with respect to the corresponding distribution in terms of true flux (the red, dashed histogram) reflects statistical photometric errors; note that in fact this tends to falsely increase the number of objects seen at the higher redshifts. Although in this case photometric errors are of secondary importance to the observed redshift distribution (completeness effects dominate), they must also be fully accounted for in any cosmological analysis.

5. Discussion and conclusions

Our aim as been to emphasize the importance of understanding the SZ cluster selection function, as for any astronomical survey. We proposed a general definition of the selection function that can be used to directly relate theoretical cluster distributions to observed ones, and which has the nice property of clearly separating the influence of catalog incompleteness and photometric errors. It is a function of both observing conditions and of the detection and photometry algorithms used to construct the survey catalog. Defined over the (true) total flux-angular size plane, however, the selection function is independent of cosmology and cluster physics; its connection to theoretical cluster descriptors, such as mass and redshift, on the other hand, depends on both. A common way of quoting incompleteness in terms of total flux is similarly sensitive to cluster physics and underlying cosmology.

Using a matched spatial filter (Melin et al. 2004), we studied the selection function for single frequency SZ surveys, such as will be performed with upcoming interferometers[6]. Our main result is that a SZ catalog is not simply flux limited, and this has implications for cosmological studies. A simple analytic argument shows the exact manner in which catalog selection depends on both cluster flux and angular size; simulated observations indicate that this simple estimate is quite accurate and little affected by blending, although future work needs to take into account more realistic cluster profiles. We also noted that noise induced by residual point sources tends to be Gaussian, because subtraction of the brightest sources will be done at higher angular resolution than the smallest filter scale in the SZ maps.

The implications for cosmological studies were illustrated with the redshift distribution, which will serve to constrain cosmological parameters in future surveys. Theoretical redshift distributions based on a simple flux limit cannot fit observed distributions; at best they would lead to biased estimates of cosmological parameters. One must incorporate the complete selection criteria depending on both flux and angular extent, and hence have a good understanding of the catalog selection function. This understanding depends on a number of astrophysical factors in addition to instrumental parameters. Our example of an unmodeled primary CMB power excess (relative to the adopted concordance model) on small angular scales ($l \geq 2000$) highlights the point: we obtained biased parameter estimates because the selection function was incorrectly modeled; note that the false fit was in fact a good fit to the data, according to the χ^2. Other factors, for example, cluster morphology and its potential evolution, will also play a role. In the particular case of the CMB power excess, we note that accurate knowledge of the primary CMB power on cluster scales will come from the same experiments performing the cluster surveys. It will be necessary to constrain the primary CMB power at the same time as cluster extraction, a point we return to in a future work.

An issue currently receiving attention in the literature concerns SZ survey "calibration", by which is meant the empirical Establishment of the $Y(M, z)$ relation. This is clearly essential for any cosmological study. The fact that SZ catalog selection depends not only on total flux but also on angular size complicates the question of survey calibration, for it implies that one must additionally establish a $\theta_c(M, z)$ relation, or its equivalent with some other angular size measure. In fact, since the dispersion on Y and θ_c will in general be correlated, we need the full joint distribution for these observables as a function of mass and redshift. Photometric errors, which we find can be significant, further complicate the issue by increasing scatter in observed relations and hence making them more difficult to obtain.

Although in this work we have focused our detailed study on single frequency surveys, the general conclusions should carry over to multiple frequency observations. In closing we note that the selection function obviously has equally important implications for other studies based on SZ-detected cluster catalogs, such as spatial clustering, etc. For many of these studies, photometric errors, which we have only briefly touched on here, will take on even greater importance.

Acknowledgements. J.-B. Melin and J. G. Bartlett thank the France Berkeley Fund (grant "Precision Cosmology from CMB analysis") and the Lawrence Berkeley Laboratory for financial assistance and hospitality for a visit during which part of this work was completed. We also thank our anonymous referee for helpful and thoughfull comments.

References

Adami, C., Ulmer, M. P., Romer, A. K., et al. 2001, ApJS, 131, 391
Bahcall, N. A., Ostriker, J. P., Perlmutter, S., & Steinhardt, P. J. 1999, Science, 284, 1481
Barbosa, D., Bartlett, J. G., & Blanchard, A. 1996, A&A, 314, 13
Bartelmann, M. 2001, A&A, 370, 754
Bartlett, J. G. 2000 [`arXiv:astro-ph/0001267`]
Bartlett, J. G. 2001, Review in Tracing cosmic evolution with galaxy clusters, Sesto Pusteria 3–6 July 2001, ASP Conf. Ser., in press [`arXiv:astro-ph/0111211`]
Bennett, C. L., Hill, R. S., Hinshaw, G., et al. 2003, ApJS, 148, 97
Birkinshaw, M. 1999, Proc. 3K Cosmology, American Institute of Physics, Woodbury, 476, 298

---

[6] Although we have not here modeled the actual data taking in the visibility plane.

Borys, C., Chapman, S., Halpern, M., & Scott, D. 2003, MNRAS, 344, 385

Bouchet, F. R., & Gispert, R. 1999, New Astron., 4, 443

Carlstrom, J. E., Holder, G. P., & Reese, E. D. 2002, ARA&A, 40, 643

Delabrouille, J., Melin, J.-B., & Bartlett, J. G. 2002, in AMiBA 2001: High-Z Clusters, Missing Baryons, and CMB Polarization, ASP Conf. Proc. [`arXiv:astro-ph/0109186`]

Delabrouille, J., Cardoso, J.-F., & Patanchon, G. 2003, MNRAS, 346, 1089

Freedman, W. L., Madore, B. F., Gibson, B. K., et al. 2001, ApJ, 553, 47

Haehnelt, M. G., & Tegmark, M. 1996, MNRAS, 279, 545

Haiman, Z., Mohr, J. J., & Holder, G. 2001, ApJ, 553, 545

Herranz, D., Sanz, J. L., Hobson, M. P., et al. 2002, MNRAS, 336, 1057

Holder, G. P., Mohr, J. J., Carlstrom, J. E., Evrard, A. E., & Leitch, E. M. 2000, ApJ, 544, 629

Hu, W. 2003, Phys. Rev. D., 67, 081304

Jenkins, A., Frenk, C. S., White, S. D. M., et al. 2001, MNRAS, 321, 372

Jones, M. E., in AMiBA 2001: High-Z Clusters, Missing Baryons, and CMB Polarization, ASP Conf. Proc. [`arXiv:astro-ph/0109351`]

Kneissl, R., Jones, M. E., Saunders, R., et al. 2001, MNRAS, 328, 783

Knox, L., Holder, G. P., & Church, S. E. 2003 [`arXiv:astro-ph/0309643`]

Kosowsky, A. 2004 [`arXiv:astro-ph/0402234`]

Lima, M., & Hu, W. 2004 [`arXiv:astro-ph/0401559`]

Lo, K. Y., Chiueh, T. H., Martin, R. N., et al. 2000 [`arXiv:astro-ph/0012282`]

Majumdar, S., & Mohr, J. J. 2003 [`arXiv:astro-ph/0305341`]

Masi, S., Ade, P., de Bernardis, P., et al. 2003, Memorie della Societa Astronomica Italiana, 74, 96

Mason, B. S., Myers, S. T., & Readhead, A. C. S. 2001, ApJ, 555, L11

Melin, J.-B., et al. 2004, in preparation

Mo, H. J., & White, S. D. M. 1996, MNRAS, 282, 347

Mohr, J. J., Mathiesen, B., & Evrard, A. E. 1999, ApJ, 517, 627

Oukbir, J., & Blanchard, A. 1997, A&A, 317, 1

Peebles, P. J. E. 1993, Principles of Physical Cosmology, Princeton Series in Physics (New Jersey, Princeton: Princeton University Press)

Pierpaoli, E., Scott, D., & White, M. 2001, MNRAS, 325, 77

Rosati, P., Borgani, S., & Norman, C. 2002, ARA&A, 40, 539

Runyan, M. C., Ade, P. A. R., Bhatia, R. S., et al. 2003, ApJS, 149, 265

Schulz, A. E., & White, M. 2003, ApJ, 586, 723

Seljak, U., & Zaldarriaga, M. 1996, ApJ, 469, 437, `www.cmbfast.org`

Sunyaev, R. A., & Zel'dovich, Ya. B. 1970, Comments Astrophys. Space Phys., 2, 66

Sunyaev, R. A., & Zel'dovich, Ya. B. 1972, Comments Astrophys. Space Phys., 4, 173

Spergel, D. N., Verde, L., Peiris, H. V., et al. 2003, ApJS, 148, 175

Tegmark, M., Eisenstein, D. J., Hu, W., & Oliveira-Costa, A. 2000, ApJ, 530, 133

Wang, L., & Steinhardt, P. J. 1998, ApJ, 508, 483

White, M. 2003, ApJ, 597, 650

Web pages of various SZ experiments:

- ACBAR `http://cosmology.berkeley.edu/group/swlh/acbar/`
- ACT `http://www.hep.upenn.edu/~angelica/act/act.html`
- AMI `http://www.mrao.cam.ac.uk/telescopes/ami/index.html`
- AMiBA `http://www.asiaa.sinica.edu.tw/amiba`
- APEX `http://bolo.berkeley.edu/apexsz`
- BOLOCAM `http://astro.caltech.edu/~lgg/bolocam_front.htm`
- SPT `http://astro.uchicago.edu/spt/`
- SZA `http://astro.uchicago.edu/sze`
- Planck `http://astro.estec.esa.nl/Planck/`

A&A 571, A20 (2014)
DOI: 10.1051/0004-6361/201321521

Planck 2013 results

Astronomy & Astrophysics
Special feature

Planck 2013 results. XX. Cosmology from Sunyaev–Zeldovich cluster counts

Planck Collaboration: P. A. R. Ade[95], N. Aghanim[66], C. Armitage-Caplan[101], M. Arnaud[79], M. Ashdown[76,7], F. Atrio-Barandela[21], J. Aumont[66],
C. Baccigalupi[93], A. J. Banday[105,11], R. B. Barreiro[73], R. Barrena[72], J. G. Bartlett[1,74], E. Battaner[107], R. Battye[75], K. Benabed[67,104], A. Benoît[64],
A. Benoit-Lévy[29,67,104], J.-P. Bernard[11], M. Bersanelli[40,56], P. Bielewicz[105,11,93], I. Bikmaev[24,3], A. Blanchard[105], J. Bobin[79], J. J. Bock[74,12],
H. Böhringer[85], A. Bonaldi[75], J. R. Bond[10], J. Borrill[16,98], F. R. Bouchet[67,104], H. Bourdin[42], M. Bridges[76,7,70], M. L. Brown[75], M. Bucher[1],
R. Burenin[97,88], C. Burigana[55,38], R. C. Butler[55], J.-F. Cardoso[80,1,67], P. Carvalho[7], A. Catalano[81,78], A. Challinor[70,76,13], A. Chamballu[79,18,66],
R.-R. Chary[63], L.-Y Chiang[69], H. C. Chiang[32,8], G. Chon[85], P. R. Christensen[89,43], S. Church[100], D. L. Clements[62], S. Colombi[67,104],
L. P. L. Colombo[28,74], F. Couchot[77], A. Coulais[78], B. P. Crill[74,90], A. Curto[7,73], F. Cuttaia[55], A. Da Silva[14], H. Dahle[71], L. Danese[93],
R. D. Davies[75], R. J. Davis[75], P. de Bernardis[39], A. de Rosa[55], G. de Zotti[52,93], J. Delabrouille[1], J.-M. Delouis[67,104], J. Démoclès[79], F.-X. Désert[59],
C. Dickinson[75], J. M. Diego[73], K. Dolag[106,84], H. Dole[66,65], S. Donzelli[56], O. Doré[74,12], M. Douspis[66,⋆], X. Dupac[46], G. Efstathiou[70],
T. A. Enßlin[84], H. K. Eriksen[71], F. Finelli[55,57], I. Flores-Cacho[11,105], O. Forni[105,11], M. Frailis[54], E. Franceschi[55], S. Fromenteau[1,66], S. Galeotta[54],
K. Ganga[1], R. T. Génova-Santos[72], M. Giard[105,11], G. Giardino[47], Y. Giraud-Héraud[1], J. González-Nuevo[73,93], K. M. Górski[74,109], S. Gratton[76,70],
A. Gregorio[41,54], A. Gruppuso[55], F. K. Hansen[71], D. Hanson[86,74,10], D. Harrison[70,76], S. Henrot-Versillé[77], C. Hernández-Monteagudo[15,84],
D. Herranz[73], S. R. Hildebrandt[12], E. Hivon[67,104], M. Hobson[7], W. A. Holmes[74], A. Hornstrup[19], W. Hovest[84], K. M. Huffenberger[108],
G. Hurier[66,81], T. R. Jaffe[105,11], A. H. Jaffe[62], W. C. Jones[32], M. Juvela[31], E. Keihänen[31], R. Keskitalo[26,16], I. Khamitov[102,24], T. S. Kisner[83],
R. Kneissl[45,9], J. Knoche[84], L. Knox[34], M. Kunz[20,66,4], H. Kurki-Suonio[31,50], G. Lagache[66], A. Lähteenmäki[2,50], J.-M. Lamarre[78], A. Lasenby[7,76],
R. J. Laureijs[47], C. R. Lawrence[74], J. P. Leahy[75], R. Leonardi[46], J. León-Tavares[48,2], J. Lesgourgues[103,92], A. Liddle[94,30], M. Liguori[37],
P. B. Lilje[71], M. Linden-Vørnle[19], M. López-Caniego[73], P. M. Lubin[35], J. F. Macías-Pérez[81], B. Maffei[75], D. Maino[40,56], N. Mandolesi[55,6,38],
A. Marcos-Caballero[73], M. Maris[54], D. J. Marshall[79], P. G. Martin[10], E. Martínez-González[73], S. Masi[39], S. Matarrese[37], F. Matthai[84],
P. Mazzotta[42], P. R. Meinhold[35], A. Melchiorri[39,58], J.-B. Melin[18], L. Mendes[46], A. Mennella[40,56], M. Migliaccio[70,76], S. Mitra[61,74],
M.-A. Miville-Deschênes[66,10], A. Moneti[67], L. Montier[105,11], G. Morgante[55], D. Mortlock[62], A. Moss[96], D. Munshi[95], P. Naselsky[89,43], F. Nati[39],
P. Natoli[38,5,55], C. B. Netterfield[23], H. U. Nørgaard-Nielsen[19], F. Noviello[75], D. Novikov[62], I. Novikov[89], S. Osborne[100], C. A. Oxborrow[19],
F. Paci[93], L. Pagano[39,58], F. Pajot[66], D. Paoletti[55,57], B. Partridge[49], F. Pasian[54], G. Patanchon[1], O. Perdereau[77], L. Perotto[81], F. Perrotta[93],
F. Piacentini[39], M. Piat[1], E. Pierpaoli[28], D. Pietrobon[74], S. Plaszczynski[77], E. Pointecouteau[105,11], G. Polenta[5,53], N. Ponthieu[66,59], L. Popa[68],
T. Poutanen[50,31,2], G. W. Pratt[79], G. Prézeau[12,74], S. Prunet[67,104], J.-L. Puget[66], J. P. Rachen[25,84], R. Rebolo[72,17,44], M. Reinecke[84],
M. Remazeilles[66,1], C. Renault[81], S. Ricciardi[55], T. Riller[84], I. Ristorcelli[105,11], G. Rocha[74,12], M. Roman[1], C. Rosset[1], G. Roudier[1,78,74],
M. Rowan-Robinson[62], J. A. Rubiño-Martín[72,44], B. Rusholme[63], M. Sandri[55], D. Santos[81], G. Savini[91], D. Scott[27], M. D. Seiffert[74,12],
E. P. S. Shellard[13], L. D. Spencer[95], J.-L. Starck[79], V. Stolyarov[7,76,99], R. Stompor[1], R. Sudiwala[95], R. Sunyaev[84,97], F. Sureau[79], D. Sutton[70,76],
A.-S. Suur-Uski[31,50], J.-F. Sygnet[67], J. A. Tauber[47], D. Tavagnacco[54,41], L. Terenzi[55], L. Toffolatti[22,73], M. Tomasi[56], M. Tristram[77], M. Tucci[20,77],
J. Tuovinen[87], M. Türler[60], G. Umana[51], L. Valenziano[55], J. Valiviita[50,31,71], B. Van Tent[82], P. Vielva[73], F. Villa[55], N. Vittorio[42], L. A. Wade[74],
B. D. Wandelt[67,104,36], J. Weller[106], M. White[33], S. D. M. White[84], D. Yvon[18], A. Zacchei[54], and A. Zonca[35]

(Affiliations can be found after the references)

Received 20 March 2013 / Accepted 4 February 2014

ABSTRACT

We present constraints on cosmological parameters using number counts as a function of redshift for a sub-sample of 189 galaxy clusters from the *Planck* SZ (PSZ) catalogue. The PSZ is selected through the signature of the Sunyaev-Zeldovich (SZ) effect, and the sub-sample used here has a signal-to-noise threshold of seven, with each object confirmed as a cluster and all but one with a redshift estimate. We discuss the completeness of the sample and our construction of a likelihood analysis. Using a relation between mass M and SZ signal Y calibrated to X-ray measurements, we derive constraints on the power spectrum amplitude σ_8 and matter density parameter $\Omega_{\rm m}$ in a flat ΛCDM model. We test the robustness of our estimates and find that possible biases in the Y–M relation and the halo mass function are larger than the statistical uncertainties from the cluster sample. Assuming the X-ray determined mass to be biased low relative to the true mass by between zero and 30%, motivated by comparison of the observed mass scaling relations to those from a set of numerical simulations, we find that $\sigma_8 = 0.75 \pm 0.03$, $\Omega_{\rm m} = 0.29 \pm 0.02$, and $\sigma_8(\Omega_{\rm m}/0.27)^{0.3} = 0.764 \pm 0.025$. The value of σ_8 is degenerate with the mass bias; if the latter is fixed to a value of 20% (the central value from numerical simulations) we find $\sigma_8(\Omega_{\rm m}/0.27)^{0.3} = 0.78 \pm 0.01$ and a tighter one-dimensional range $\sigma_8 = 0.77 \pm 0.02$. We find that the larger values of σ_8 and $\Omega_{\rm m}$ preferred by *Planck*'s measurements of the primary CMB anisotropies can be accommodated by a mass bias of about 40%. Alternatively, consistency with the primary CMB constraints can be achieved by inclusion of processes that suppress power on small scales relative to the ΛCDM model, such as a component of massive neutrinos. We place our results in the context of other determinations of cosmological parameters, and discuss issues that need to be resolved in order to make further progress in this field.

Key words. cosmological parameters – large-scale structure of Universe – galaxies: clusters: general

---

[⋆] Corresponding author: M. Douspis e-mail: `marian.douspis@ias.u-psud.fr`

1. Introduction

This paper, one of a set associated with the 2013 release of data from the *Planck*[1] mission (Planck Collaboration I 2014), describes the constraints on cosmological parameters using number counts as a function of redshift for a sample of 189 galaxy clusters.

Within the standard picture of structure formation, galaxies aggregate into clusters of galaxies at late times, forming bound structures at locations where the initial fluctuations create the deepest potential wells. The study of these galaxy clusters has played a significant role in the development of cosmology over many years (see, for example, Perrenod 1980; Oukbir & Blanchard 1992; White et al. 1993; Carlberg et al. 1996; Voit 2005; Henry et al. 2009; Vikhlinin et al. 2009b; Allen et al. 2011a). More recently, as samples of clusters have increased in size and variety, number counts inferred from tightly-selected surveys have been used to obtain detailed constraints on the cosmological parameters.

The early galaxy cluster catalogues were constructed by eye from photographic plates with a "richness" (or number of galaxies) attributed to each cluster (Abell 1958; Abell et al. 1989). As time has passed, new approaches for selecting clusters have been developed, most notably using X-ray emission due to thermal Bremsstrahlung radiation from the hot gas that makes up most of the baryonic matter in the cluster. X-ray cluster surveys include both the NORAS (Böhringer et al. 2000) and REFLEX (Böhringer et al. 2004) surveys, based on ROSAT satellite observations, which have been used as source catalogues for higher-precision observations by the *Chandra* and *XMM-Newton* satellites, as well as surveys with *XMM-Newton*, including the XMM Cluster Survey (XCS, Mehrtens et al. 2012) and the XMM Large Scale Structure survey (XMM-LSS, Willis et al. 2013).

To exploit clusters for cosmology, a key issue is how the properties used to select and characterize the cluster are related to the total mass of the cluster, since this is the quantity most readily predicted using theoretical models. Galaxies account for a small fraction of the cluster mass, and the scatter between richness and mass appears to be large. However, there are a number of other possibilities. In particular, there are strong correlations between the total mass and both the integrated X-ray surface brightness and X-ray temperature, making them excellent mass proxies.

The Sunyaev-Zeldovich (SZ) effect (Sunyaev & Zeldovich 1970; Zeldovich & Sunyaev 1969) is the inverse Compton scattering of cosmic microwave background (CMB) photons by the hot gas along the line of sight, and this is most significant when the line of sight passes through a galaxy cluster. It leads to a decrease in the overall brightness temperature in the Rayleigh-Jeans portion of the spectrum and an increase in the Wien tail, with a null around 217 GHz (see Birkinshaw 1999 for a review). The amplitude of the SZ effect is given by the integrated pressure of the gas within the cluster along the line of sight. Evidence both from observation (Marrone et al. 2012; Planck Collaboration Int. III 2013) and from numerical simulations (Springel et al. 2001; da Silva et al. 2004; Motl et al. 2005; Nagai 2006; Kay et al. 2012) suggests that the SZ effect is an excellent mass proxy. A number of articles have discussed the possibility of using SZ-selected cluster samples to constrain cosmological parameters (Barbosa et al. 1996; Aghanim et al. 1997; Haiman et al. 2001; Holder et al. 2001; Weller et al. 2002; Diego et al. 2002; Battye & Weller 2003).

This paper describes the constraints on cosmological parameters imposed by a high signal-to-noise (S/N) sub-sample of the *Planck* SZ Catalogue (PSZ, see Planck Collaboration XXIX 2014, henceforth Paper I, for details of the entire catalogue) containing nearly 200 clusters (shown in Fig. 1). This sub-sample has been selected to be pure, in the sense that all the objects within it have been confirmed as clusters via additional observations, either from the literature or undertaken by the Planck collaboration. In addition all objects but one have a measured redshift, either photometric or spectroscopic. This is the largest SZ-selected sample of clusters used to date for this purpose. We will show that it is the systematic uncertainties from our imperfect knowledge of cluster properties that dominate the overall uncertainty on cosmological constraints.

The *Planck* cluster sample is complementary to those from observations using the South Pole Telescope (SPT, Carlstrom et al. 2011) and the Atacama Cosmology Telescope (ACT, Swetz et al. 2011), whose teams recently published the first large samples of SZ-selected clusters (Reichardt et al. 2013; Hasselfield et al. 2013). The resolution of *Planck* at the relevant frequencies is between 5 and 10 arcmin, whereas that for ACT and SPT is about 1 arcmin, but the *Planck* sky coverage is much greater. This means that *Planck* typically finds larger, more massive, and lower-redshift clusters than those found by SPT and ACT.

Our strategy is to focus on number counts of clusters, as a function of redshift, above a high S/N threshold of seven and to explore the robustness of the results. We do not use the observed SZ brightness of the clusters, due to the significant uncertainty caused by the size-flux degeneracy as discussed in Paper I. Accordingly, our theoretical modelling of the cluster population is directed only at determining the expected number of clusters in each redshift bin exceeding the S/N threshold. The predicted and observed numbers of clusters are then compared in order to obtain the likelihood. In the future, we will make use of the SZ-estimated mass and a larger cluster sample to extend the analysis to broader cosmological scenarios.

This paper is laid out as follows. We describe the theoretical modelling of the redshift number counts in Sect. 2, while Sect. 3 presents the PSZ cosmological sample and selection function used in this work. The likelihood we adopt for putting constraints on cosmological parameters is given in Sect. 4. Section 5 presents our results on cosmological parameter estimation and assesses their robustness. We discuss how they fit in with other cluster and cosmological constraints in Sect. 6, before providing a final summary. A detailed discussion of our calibration of the SZ flux versus mass relation and its uncertainties is given in Appendix A.

2. Modelling cluster number counts

2.1. Model definitions

We parameterize the standard cosmological model as follows. The densities of various components are specified relative to the present-day critical density, with $\Omega_{\rm X} = \rho_{\rm X}/\rho_{\rm crit}$ denoting that for component X. These components always include matter, $\Omega_{\rm m}$, and a cosmological constant Ω_Λ. For this work we assume that the Universe is flat, that is, $\Omega_{\rm m} + \Omega_\Lambda = 1$, and the optical depth to reionization is fixed at $\tau = 0.085$ except in the CMB and

---

[1] *Planck* (`http://www.esa.int/Planck`) is a project of the European Space Agency (ESA) with instruments provided by two scientific consortia funded by ESA member states (in particular the lead countries France and Italy), with contributions from NASA (USA) and telescope reflectors provided by a collaboration between ESA and a scientific consortium led and funded by Denmark.

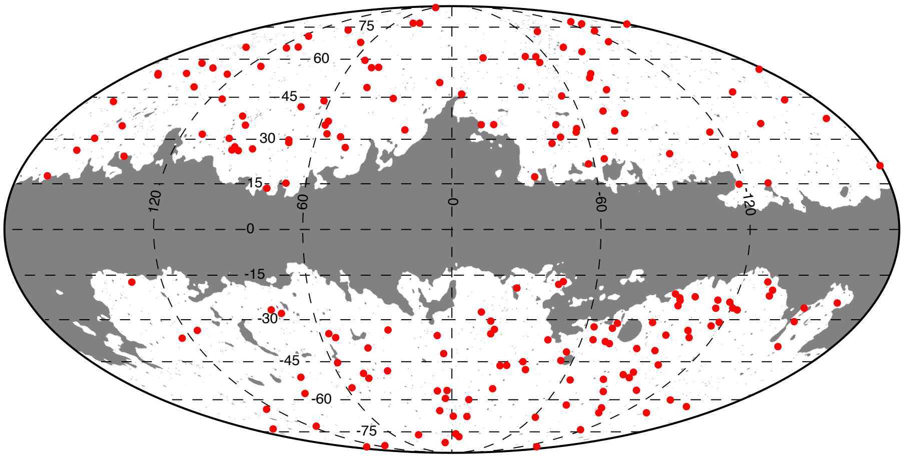

Fig. 1. Distribution on the sky of the *Planck* SZ cluster sub-sample used in this paper, with the 35% mask overlaid.

SZ analyses. The present-day expansion rate of the Universe is quantified by the Hubble constant $H_0 = 100\,h\,\mathrm{km\,s^{-1}\,Mpc^{-1}}$.

The cluster number counts are very sensitive to the amplitude of the matter power spectrum. When studying cluster counts it is usual to parametrize this in terms of the density variance in spheres of radius 8 h^{-1} Mpc, denoted σ_8, rather than overall power spectrum amplitude, A_s. In cases where we include primary CMB data we use A_s and compute σ_8 as a derived parameter. In addition to the parameters above, we allow the other standard cosmological parameters to vary: n_s representing the spectral index of density fluctuations; and $\Omega_b h^2$ quantifying the baryon density.

The number of clusters predicted to be observed by a survey in a given redshift interval $[z_i, z_{i+1}]$ can be written

$$n_i = \int_{z_i}^{z_{i+1}} \mathrm{d}z \frac{\mathrm{d}N}{\mathrm{d}z}, \tag{1}$$

with

$$\frac{\mathrm{d}N}{\mathrm{d}z} = \int \mathrm{d}\Omega \int \mathrm{d}M_{500}\,\hat{\chi}(z, M_{500}, l, b)\,\frac{\mathrm{d}N}{\mathrm{d}z\,\mathrm{d}M_{500}\,\mathrm{d}\Omega}, \tag{2}$$

where $\mathrm{d}\Omega$ is the solid angle element and M_{500} is the mass within the radius where the mean enclosed density is 500 times the critical density. The quantity $\hat{\chi}(z, M_{500}, l, b)$ is the survey completeness at a given location (l, b) on the sky, given by

$$\hat{\chi} = \int \mathrm{d}Y_{500} \int \mathrm{d}\theta_{500} P(z, M_{500}|Y_{500}, \theta_{500})\,\chi(Y_{500}, \theta_{500}, l, b). \tag{3}$$

Here $P(z, M_{500}|Y_{500}, \theta_{500})$ is the distribution of (z, M_{500}) for a given (Y_{500}, θ_{500}), where Y_{500} and θ_{500} are the SZ flux and size of a cluster of redshift and mass (z, M_{500}).

This distribution is obtained from the scaling relations between Y_{500}, θ_{500}, and M_{500}, discussed later in this section. Note that $\hat{\chi}(z, M_{500}, l, b)$ depends on cosmological parameters through $P(z, M_{500}|Y_{500}, \theta_{500})$, while the completeness in terms of the observables, $\chi(Y_{500}, \theta_{500}, l, b)$, does not depend on the cosmology as it refers directly to the observed quantities.

For the present work, we restrict our analysis to the quantity $\mathrm{d}N/\mathrm{d}z$ that measures the total counts in redshift bins. In particular, we do not use the blind SZ flux estimated by the cluster candidate extraction methods that, as detailed in Planck Collaboration VIII (2011), is found to be significantly higher than the flux predicted from X-ray measurements. In contrast to the blind SZ flux, the blind S/N is in good agreement with the S/N measured using X-ray priors. Figure 2 shows the blind S/N (S/N$_{\mathrm{blind}}$) versus the S/N re-extracted at the X-ray position and using the X-ray size (S/N$_{\mathrm{X}}$). The clusters follow the equality line. In Sect. 3, we use the (S/N$_{\mathrm{blind}}$) values to define our cosmological sample, while for the predicted counts (defined in Sect. 2) we use the completeness based on S/N$_{\mathrm{X}}$. Our analysis relies on the good match between these two quantities[2].

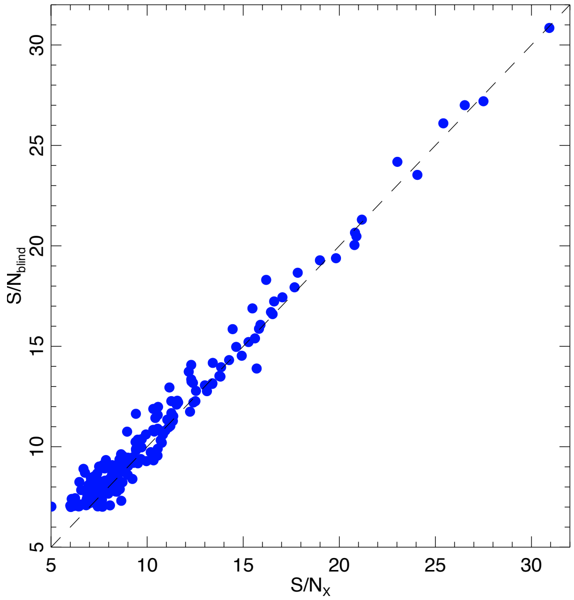

Fig. 2. Blind S/N versus S/N re-extracted at the X-ray position using the X-ray size, for the `MMF3` detections of *Planck* clusters that are associated with known X-ray clusters in the reference cosmological sample. In contrast to the blind SZ flux, the blind S/N is in good agreement with S/N measured using X-ray priors.

---

[2] The two signal-to-noises are actually estimated at two different positions on the sky (blind SZ and X-ray position), leading to different values of both the signal and the noise. It thus happens that the recomputed S/N is higher than the blind SZ.

To carry out a prediction of the counts expected in a survey, given cosmological assumptions, we therefore need the following inputs:

- a mass function that tells us the number distribution of clusters with mass and redshift;
- scaling relations that can predict observable quantities from the mass and redshift;
- the completeness of the survey in terms of those observables, which tells us the probability that a model cluster would make it into the survey catalogue.

These are described in the remainder of this section and in the next.

2.2. Mass function

Our main results use the mass function from Tinker et al. (2008), giving the number of haloes per unit volume:

$$\frac{\mathrm{d}N}{\mathrm{d}M_{500}}(M_{500},z) = f(\sigma)\,\frac{\rho_\mathrm{m}(z=0)}{M_{500}}\,\frac{\mathrm{d}\ln\sigma^{-1}}{\mathrm{d}M_{500}}, \qquad (4)$$

where

$$f(\sigma) = A\left[1+\left(\frac{\sigma}{b}\right)^{-a}\right]\exp\left(-\frac{c}{\sigma^2}\right), \qquad (5)$$

and $\rho_\mathrm{m}(z=0)$ is the mean matter density at $z=0$. The coefficients A, a, b and c are tabulated in Tinker et al. (2008) for different overdensities, Δ_mean, with respect to the mean cosmic density, and depend on z. Here we use $\Delta_\mathrm{critical} = 500$ relative to the critical density, so we compute the relevant mass function coefficients by interpolating the Tinker et al. (2008) tables for haloes with $\Delta_\mathrm{mean} \equiv \Delta_\mathrm{critical}/\Omega_\mathrm{m}(z) = 500/\Omega_\mathrm{m}(z)$, where $\Omega_\mathrm{m}(z)$ is the matter density parameter at redshift z.

The quantity σ is the standard deviation, computed in linear perturbation theory, of the density perturbations in a sphere of radius R, which is related to the mass by $M = 4\pi\rho_\mathrm{m}(z=0)R^3/3$. It is given by

$$\sigma^2 = \frac{1}{2\pi^2}\int \mathrm{d}k\,k^2 P(k,z)|W(kR)|^2, \qquad (6)$$

where $P(k,z)$ is the matter power spectrum at redshift z, which we compute for any given set of cosmological parameters using `CAMB` (Lewis et al. 2000), and $W(x) = 3(\sin x - x\cos x)/x^3$ is the filter function of a spherical top hat of radius R.

The quantity $\mathrm{d}N/(\mathrm{d}z\,\mathrm{d}M_{500}\,\mathrm{d}\Omega)$ in Eq. (2) is computed by multiplying the mass function $\mathrm{d}N(M_{500},z)/\mathrm{d}M_{500}$ by the volume element $\mathrm{d}V/(\mathrm{d}z\,\mathrm{d}\Omega)$.

As a baseline we use, except where stated otherwise, the Tinker et al. (2008) mass function, but we consider an alternative mass function as a cross-check. In a recent publication by Watson et al. (2013), a new mass function is extracted from the combination of large cosmological simulations (typical particle numbers of 3000^3 to 6000^3) with a very large dynamic range (size from $11\,h^{-1}$ to $6000\,h^{-1}$ Mpc), which extends the maximum volume probed by Tinker et al. by two orders of magnitude. The two mass functions agree fairly well, except in the case of the most massive objects, where Tinker et al.'s mass function predicts more clusters than Watson et al.'s. The Tinker et al. mass function might be derived from volumes that are not large enough to properly sample the rarer clusters. These rare clusters are more relevant for *Planck* than for ground-based SZ experiments, which probe smaller areas of the sky. The Watson et al. mass function is used only in Sect. 5.3, which deals with mass function uncertainties.

Table 1. Summary of scaling-law parameters and error budget.

Parameter	Value
$\log Y_*$	-0.19 ± 0.02
α	1.79 ± 0.08
β	0.66 ± 0.50
$\sigma_{\log Y}$	0.075 ± 0.01

Notes. β is kept fixed at its central value except in Sect. 5.3.

2.3. Scaling relations

A key issue is to relate the observed SZ flux, Y_{500}, to the mass M_{500} of the cluster. As we show in Sect. 5, cosmological constraints are sensitive to the normalization, slope and scatter of the assumed Y_{500}–M_{500} relation. We thus paid considerable attention to deriving the most accurate scaling relations possible, with careful handling of statistical and systematic uncertainties, and to testing their impact on the derived cosmological parameters.

The baseline relation is obtained from an observational calibration of the Y_{500}–M_{500} relation on one-third of the cosmological sample. The calibration uses $M_{500}^{Y_\mathrm{X}}$, the mass derived from the X-ray Y_X–M_{500} relation, as a mass proxy. Here Y_X is the X-ray analogue of the SZ signal introduced by Kravtsov et al. (2006), as defined in Appendix A. Y_{500} is then measured interior to $R_{500}^{Y_\mathrm{X}}$, the radius corresponding to $M_{500}^{Y_\mathrm{X}}$. The mean bias between $M_{500}^{Y_\mathrm{X}}$ and the true mass, $(1-b)$, is assumed to account for all possible observational biases (departure from hydrostatic equilibrium (HE), absolute instrument calibration, temperature inhomogeneities, residual selection bias, etc.) as discussed in full in Appendix A. In practice, the plausible range for this mean bias $(1-b)$ was estimated by comparing the observed relation with predictions from several sets of numerical simulations, as detailed in Appendix A.

The large uncertainties on $(1-b)$ are due to the dispersion in predictions from the various simulation sets. This is a major factor limiting the accuracy of our analysis. A value $(1-b) = 0.8$ could be considered as a best guess given available simulations, with no clear dependence on mass or redshift. From one cluster to the next the ratio of $M_{500}^{Y_\mathrm{X}}$ to the true mass is expected to be stochastic, contributing to the scatter in the Y_{500}–M_{500} relation given below. A conspiracy of all possible sources of bias (departure from HE, absolute instrument calibration, temperature inhomogeneities, residual selection bias) would seem necessary to lead to a significantly lower value of $(1-b)$. This apparently implausible possibility needs to be excluded through tests using other probes such as baryon and gas fractions, gas pressure, etc. As a baseline we take $(1-b)$ to vary within the range [0.7, 1.0] with a flat prior. We also consider, when analysing systematic uncertainties on the derived cosmological parameters, a case where the bias is fixed to the value $(1-b) = 0.8$.

As detailed in Appendix A, we derive a baseline relation for the mean SZ signal $\bar{Y}_{500}$ from a cluster of given mass and redshift in the form

$$E^{-\beta}(z)\left[\frac{D_\mathrm{A}^2(z)\,\bar{Y}_{500}}{10^{-4}\,\mathrm{Mpc}^2}\right] = Y_*\left[\frac{h}{0.7}\right]^{-2+\alpha}\left[\frac{(1-b)\,M_{500}}{6\times10^{14}\,M_\odot}\right]^{\alpha}, \qquad (7)$$

where $D_\mathrm{A}(z)$ is the angular-diameter distance to redshift z and $E^2(z) = \Omega_\mathrm{m}(1+z)^3 + \Omega_\Lambda$. The coefficients Y_*, α, and β are given in Table 1.

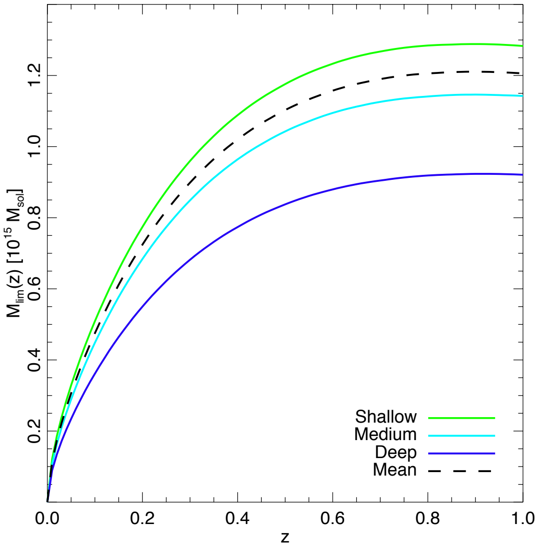

Fig. 3. Limiting mass as a function of z for the selection function and noise level computed for three zones (deep, blue; medium, cyan; shallow, green), and on average for the unmasked sky (dashed black).

Equation (7) has an estimated intrinsic scatter[3] $\sigma_{\log Y} = 0.075$, which we take to be independent of redshift (see Appendix A). This is incorporated by drawing the cluster's Y_{500} from a log-normal distribution

$$\mathcal{P}(\log Y_{500}) = \frac{1}{\sqrt{2\pi\sigma^2_{\log Y}}} \exp\left[-\frac{\log^2(Y_{500}/\bar{Y}_{500})}{2\sigma^2_{\log Y}}\right], \tag{8}$$

where $\bar{Y}_{500}$ is given by Eq. (7). Inclusion of this scatter increases the number of clusters expected at a given S/N; since the cluster counts are a steep function of M_{500} in the range of mass in question, there are more clusters that scatter upwards from below the limit given by the zero-scatter scaling relation than those that scatter downwards.

In addition to Eq. (7) we need a relation between θ_{500} (in fact $\theta_{500}^{Y_X}$, the angular size corresponding to the physical size $R_{500}^{Y_X}$), the aperture used to extract Y_{500}, and M_{500}. Since $M_{500} = 500 \times 4\pi\rho_{\rm crit}R^3_{500}/3$ and $\theta_{500} = R_{500}/D_{\rm A}$, this can be expressed as

$$\bar{\theta}_{500} = \theta_* \left[\frac{h}{0.7}\right]^{-2/3} \left[\frac{(1-b)\,M_{500}}{3\times10^{14}\,M_\odot}\right]^{1/3} E^{-2/3}(z) \left[\frac{D_{\rm A}(z)}{500\,{\rm Mpc}}\right]^{-1}, \tag{9}$$

where $\theta_* = 6.997$ arcmin.

2.4. Limiting mass

One can use Eqs. (7) and (9) to compute the limiting mass at a point on the sky where the noise level, σ_Y, has been computed as described in Sect. 3. As the latter is not homogeneous on the sky, we show in Fig. 3 the limiting mass, defined at 50% completeness, as a function of redshift for three different zones, deep, medium, and shallow, covering respectively, 3.5%, 47.8%, and 48.7% of the unmasked sky. For each line a S/N cut of 7 has been adopted.

2.5. Implementation

We have implemented three independent versions of the computation of counts and constraints. The differences in predicted counts are of the order of a few percent, which translates to less than a tenth of 1σ on the cosmological parameters of interest.

3. The *Planck* cosmological samples

3.1. Sample definition

The reference cosmological sample is constructed from the PSZ Catalogue published in Planck Collaboration XXIX (2014) and made public with the first release of *Planck* cosmological products. It is based on the SZ detections performed with the matched multi-filter (MMF) method `MMF3` (Melin et al. 2006), which relies on the use of a filter of adjustable width θ_{500} chosen to maximize the S/N of the detection. In order to ensure a high purity and to maximize the number of redshifts, the cosmological sample was constructed by selecting the SZ detections above a S/N threshold of 7 outside Galactic and point source masks covering 35% of the sky, as discussed in Paper I. From the original PSZ, only the information on S/N (for the selection) and redshift are used.

This sample contains 189 candidates. All but one are confirmed bona fide clusters with measured redshifts, including 184 spectroscopic redshifts. Among these confirmed clusters 12 were confirmed with follow-up programmes conducted by the Planck collaboration (see Paper I for details). The remaining non-confirmed cluster candidate is a high-reliability candidate, meaning that its characterization as a cluster is supported by data in other wavebands (see Paper I for details). It is thus considered as a bona fide cluster. The distribution on the sky of this baseline cosmological sample is shown in Fig. 1.

In addition to our reference sample, we consider two other samples drawn from the PSZ for consistency checks. One is based on the detections from the second implementation of the MMF algorithm, `MMF1`, described in Paper I. It contains 188 clusters with $S/N > 7$ and no missing redshifts, with almost complete overlap with the baseline sample (187 clusters in common). The third sample considered in the present study is also based on `MMF3` detections but with a higher S/N cut of $S/N > 8$. It allows us to test selection effects and to probe the consistency of the results as a function of the S/N cut. It contains 136 clusters, all with measured redshifts.

The selection function for each of these samples is constructed as described in the next section.

3.2. Completeness

The completeness of the reference cosmological sample is computed with two distinct and complementary approaches: a semi-analytic approach based on the assumption of Gaussian uncertainties, and a computational approach based on Monte Carlo cluster injection into real sky maps.

The completeness χ can be evaluated analytically by setting the probability of the measured SZ flux, Y_{500}, to be Gaussian distributed with a standard deviation equal to the noise, $\sigma_{Y_{500}}(\theta_{500}, l, b)$, computed for each size θ_{500} of the MMF filter and at each position (l, b) on the sky:

$$\chi_{\rm erf}(Y_{500}, \theta_{500}, l, b) = \frac{1}{2}\left[1 + {\rm erf}\left(\frac{Y_{500} - X\,\sigma_{Y_{500}}(\theta_{500}, l, b)}{\sqrt{2}\,\sigma_{Y_{500}}(\theta_{500}, l, b)}\right)\right], \tag{10}$$

---

[3] Throughout this article, log is base 10 and ln is base e.

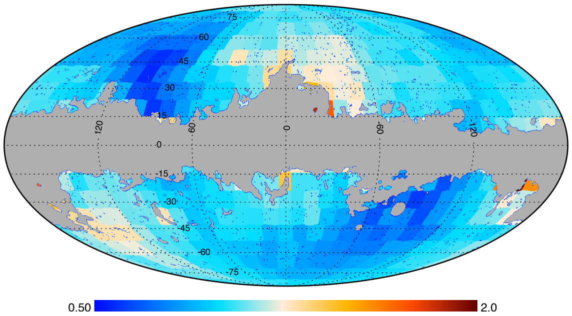

Fig. 4. Noise map $\sigma_{Y_{500}}(\theta_{500})$ for $\theta_{500} = 6$ arcmin. The PSZ is limited by instrumental noise at high ($|b| > 20°$) Galactic latitude (deeper at ecliptic poles) and foreground noise at low Galactic latitude. The scale of the map ranges from 0.5 to 2 times the mean noise of the map, which is $\langle\sigma_{Y_{500}}(6\ \text{arcmin})\rangle = 2.2 \times 10^{-4}$ arcmin^2.

where $X = 7$ is the S/N threshold and the error function is defined as usual by

$$\mathrm{erf}(u) = \frac{2}{\sqrt{\pi}} \int_0^u \exp\left(-t^2\right) \mathrm{d}t. \tag{11}$$

$\chi_{\mathrm{erf}}(Y_{500}, \theta_{500}, l, b)$ thus lies in the range [0, 1] and gives the probability for a cluster of flux Y_{500} and size θ_{500} at position (l, b) to be detected at $S/N \geq X$.

The noise estimate $\sigma_{Y_{500}}(\theta_{500}, l, b)$ is a by-product of the detection algorithm and can be written in the form (see e.g., Melin et al. 2006)

$$\sigma_{Y_{500}}(\theta_{500}, l, b) = \left[\int \mathrm{d}^2k\ \boldsymbol{F}^{\mathrm{t}}_{\theta_{500}}(\boldsymbol{k}) \cdot \boldsymbol{P}^{-1}(\boldsymbol{k}, l, b) \cdot \boldsymbol{F}_{\theta_{500}}(\boldsymbol{k})\right]^{-1/2}, \tag{12}$$

with $\boldsymbol{F}_{\theta_{500}}(\boldsymbol{k})$ being a vector of dimension N_{freq} (the six highest *Planck* frequencies here) containing the beam-convolved cluster template scaled to the known SZ frequency dependence. The cluster template assumed is the non-standard universal pressure profile from Arnaud et al. (2010). $\boldsymbol{P}(\boldsymbol{k}, l, b)$ is the noise power spectrum (dimension $N_{\mathrm{freq}} \times N_{\mathrm{freq}}$) directly estimated from the data at position (l, b). Figure 4 shows $\sigma_{Y_{500}}(\theta_{500}, l, b)$ for $\theta_{500} = 6$ arcmin in a Mollweide projection with the Galactic mask used in the analysis applied. As expected, the noise at high Galactic latitude is lower than in the areas contaminated by diffuse Galactic emission. The ecliptic pole regions have the lowest noise level, reflecting the longer *Planck* integration time in these high-redundancy areas.

The Monte Carlo (MC) completeness is calculated by injecting simulated clusters into real sky maps following the method presented in Paper I, with the modifications that the 65% Galactic dust mask and a $S/N > 7$ threshold are applied to match the cosmological sample definition. The Monte Carlo completeness encodes effects not probed by the erf approximation, including the variation of cluster pressure profiles around the fiducial pressure profile used in the MMF, spatially-varying and asymmetric effective beams, and the effects of correlated non-Gaussian uncertainties in the estimation of (Y_{500}, θ_{500}). As shown in Fig. 5, the erf-based formula for the completeness is a good approximation to the Monte Carlo completeness. The agreement is best for the typical sizes probed by *Planck* (5 to 10 arcmin), though the two determinations of the completeness start to deviate for small and large sizes, due to beam and profile effects, respectively. For simplicity, we chose the erf formulation as the baseline. The effect of using the Monte Carlo completeness instead is discussed in Sect. 5.2.

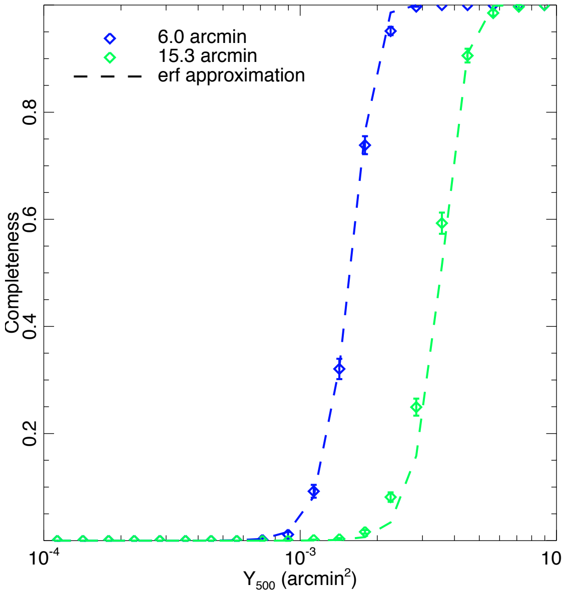

Fig. 5. Completeness averaged over the unmasked sky as a function of Y_{500} for two different filter sizes, $\theta_{500} = 6$ and 15.3 arcmin. The dashed lines show the semi-analytic approximation of Eq. (10), while the diamonds with errors show the completeness estimated by the MC injection technique.

4. Likelihood and Markov chain Monte Carlo

4.1. The likelihood

We now have all the information needed to predict the counts in redshift bins for our theoretical models. To obtain cosmological constraints with the PSZ sample presented in Sect. 3, we construct a likelihood function based on Poisson statistics (Cash 1979):

$$\ln L = \ln \mathcal{P}(N_i|n_i) = \sum_{i=1}^{N_{\mathrm{b}}} [N_i \ln(n_i) - n_i - \ln(N_i!)], \tag{13}$$

where $\mathcal{P}(N_i|n_i)$ is the probability of finding N_i clusters in each of N_{b} bins given an expected number of n_i in each bin in redshift. The likelihood includes bins that contain no observed clusters. As a baseline, we assume bins in redshift of $\Delta z = 0.1$ and we checked that our results are robust when changing the bin size between 0.05 and 0.2. The modelled expected number n_i depends on the bin range in redshift and on the cosmological parameters, as described in Sect. 2. It also depends on the scaling relations and the selection function of the observed sample. The parameters of the scaling relations between flux (or size) and mass and redshift are taken to be Gaussian distributed with central values and uncertainties stated in Table 1, and with the scatter in Y_{500} incorporated into the method via the log-normal distribution with width $\sigma_{\log Y}$.

In the PSZ, the redshifts have been collected from different observations and from the literature. Individual uncertainties in redshift are thus spread between 0.001 and 0.1. Most

Table 2. Best-fit cosmological parameters for various combinations of data and analysis methods.

Data	$\sigma_8(\Omega_m/0.27)^{0.3}$	Ω_m	σ_8	$1-b$
Planck SZ and BAO and BBN	0.764 ± 0.025	0.29 ± 0.02	0.75 ± 0.03	[0.7, 1]
Planck SZ and HST and BBN	0.774 ± 0.024	0.28 ± 0.03	0.77 ± 0.03	[0.7, 1]
Planck SZ and BAO and BBN	0.782 ± 0.010	0.29 ± 0.02	0.77 ± 0.02	0.8
`MMF1` sample and BAO and BBN	0.800 ± 0.010	0.29 ± 0.02	0.78 ± 0.02	0.8
`MMF3` S/N > 8 and BAO and BBN	0.785 ± 0.011	0.29 ± 0.02	0.77 ± 0.02	0.8
Planck SZ and BAO and BBN (MC completeness)	0.778 ± 0.010	0.30 ± 0.03	0.75 ± 0.02	0.8
Planck SZ and BAO and BBN (Watson et al. mass function)	0.802 ± 0.014	0.30 ± 0.01	0.77 ± 0.02	0.8

Notes. For the analysis using the Watson et al. mass function, or $(1-b)$ in $[0.7, 1]$, the degeneracy line is different, and thus the value of $\sigma_8(\Omega_m/0.27)^{0.3}$ is just illustrative.

of the clusters in the cosmological sample have spectroscopic redshifts (184 out of 189) and we checked that the uncertainties in redshift are not at all dominant in our error budget; they are thus neglected. The cluster without known redshift is incorporated by scaling the counts by a factor 189/188, i.e., by assuming its redshift is drawn from the distribution defined by the other 188 objects.

4.2. Markov chain Monte Carlo

In order to impose constraints on cosmological parameters from our sample(s) given our modelled expected number counts, we modified `CosmoMC` (Lewis & Bridle 2002) to include the likelihood described above. We mainly study constraints on the spatially-flat ΛCDM model, varying Ω_m, σ_8, Ω_b, H_0, and n_s, but also adding in the total neutrino mass, $\sum m_\nu$, in Sect. 6. In each of the runs, the nuisance parameters (Y_*, α, $\sigma_{\log Y}$) follow Gaussian priors, with the characteristics detailed in Table 1, and are marginalized over. The bias $(1-b)$ follows a flat prior in the range [0.7,1]. The redshift evolution of the scaling, β, is fixed to its reference value unless stated otherwise.

4.3. External datasets

When probing the six parameters of the ΛCDM model, we combine the *Planck* clusters with the Big Bang nucleosynthesis (BBN) constraints from Steigman (2008), $\Omega_b h^2 = 0.022 \pm 0.002$. We also use either the H_0 determination from HST by Riess et al. (2011), $H_0 = (73.8 \pm 2.4)\ \mathrm{km\,s^{-1}\,Mpc^{-1}}$, or baryon acoustic oscillation (BAO) data. In the latter case we adopt the combined likelihood of Hinshaw et al. (2013) and Planck Collaboration XVI (2014), which uses the radial BAO scales observed by 6dFGRS (Beutler et al. 2011), SDSS-DR7-rec and SDSS-DR9-rec (Padmanabhan et al. 2012; Anderson et al. 2012), and WiggleZ (Blake et al. 2012).

5. Constraints from *Planck* clusters: ΛCDM

5.1. Results for Ω_m and σ_8

Cluster counts in redshift for our *Planck* cosmological sample are not sensitive to all parameters of the ΛCDM model. We focus first on (Ω_m, σ_8), assuming that n_s follows a Gaussian prior centred on the best-fit *Planck* CMB value[4] ($n_s = 0.9603 \pm 0.0073$). We combine our SZ counts likelihood with the BAO and BBN likelihoods discussed earlier. We also incorporate the uncertainties on scaling parameters in Table 1. Allowing the bias to range uniformly over the interval [0.7, 1.0], we find the expected degeneracy between the two parameters, $\sigma_8(\Omega_m/0.27)^{0.3} = 0.764 \pm 0.025$,[5] with central values and uncertainties of $\Omega_m = 0.29 \pm 0.02$ and $\sigma_8 = 0.75 \pm 0.03$ (Table 2 and Fig. 6, red contours). The cluster counts as a function of redshift for the best-fit model are plotted in Fig. 7. When fixing the bias to $(1-b) = 0.8$, the constraint on Ω_m remains unchanged while the constraint on σ_8 becomes stronger: $\sigma_8(\Omega_m/0.27)^{0.3} = 0.78 \pm 0.01$ and $\sigma_8 = 0.77 \pm 0.02$ (Fig. 8).

To investigate how robust our results are when changing our priors, we repeat the analysis substituting the HST constraints on H_0 for the BAO results. Figure 6 (black contours) shows that the main effect is to change the best-fit value of H_0, leaving the (Ω_m, σ_8) degeneracy almost unchanged. In the following robustness tests, we assume a fixed mass bias, $(1-b) = 0.8$, to better identify the effect of each of our assumptions.

5.2. Robustness to the observational sample

To test the robustness of our results, we performed the same analysis with different sub-samples drawn from our cosmological sample or from the PSZ, as described in Sect. 3, following that section's discussion of completeness. Figure 9 shows the likelihood contours of the three samples (blue, `MMF3` $S/N > 8$; red, `MMF3` $S/N > 7$; black, `MMF1` $S/N > 7$) in the (Ω_m, σ_8) plane. There is good agreement between the three samples. Obviously the three samples are not independent, as many clusters are common, but the noise estimates for `MMF3` and `MMF1` are different leading to different selection functions. Table 2 summarizes the best-fit values.

We perform the same analysis as on the baseline cosmological sample (SZ and BAO and BBN), but employing a different computation of the completeness function using the Monte Carlo method described in Sect. 3. Figure 9 shows the change in the 2D likelihoods when this alternative approach is adopted. The Monte Carlo estimation (in purple), being close to the analytic one, gives constraints that are similar, but enlarge the contour along the (Ω_m, σ_8) degeneracy.

5.3. Robustness to cluster modelling

A key ingredient in the modelling of the number counts is the mass function. Our main results adopt the Tinker et al. mass function as the reference model. We compare these to results from the Watson et al. mass function to evaluate the impact of uncertainty in predictions for the abundance of the most massive and extreme clusters. Figure 8 shows the 95% contours

---

[4] Table 2 of Planck Collaboration XVI (2014).

[5] We express it this way to ease comparison with other work.

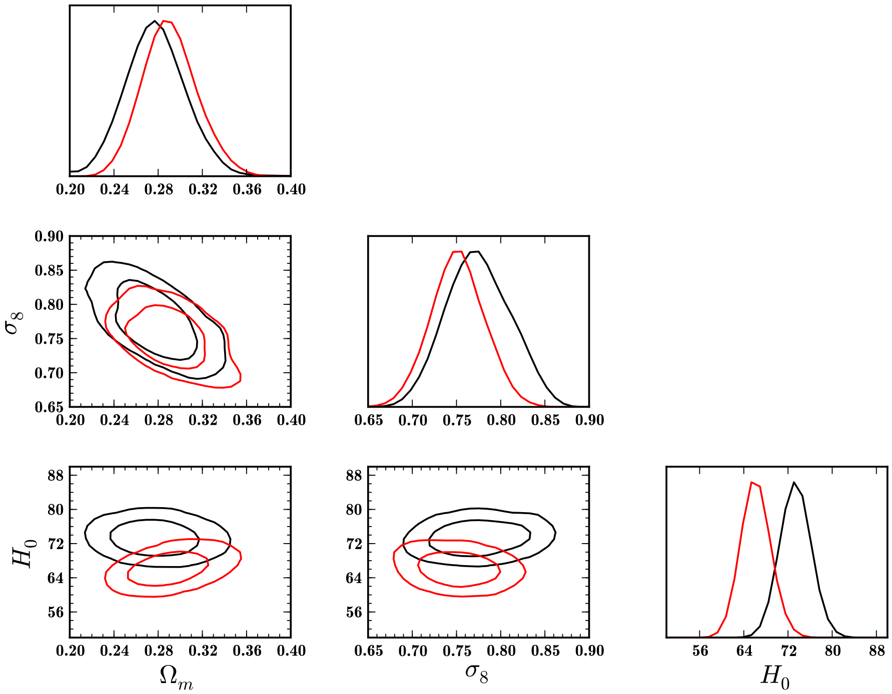

Fig. 6. *Planck* SZ constraints (+BAO+BBN) on ΛCDM cosmological parameters in red. The black lines show the constraints upon substituting HST constraints on H_0 for the BAO constrainsts. Contours are 68 and 95% confidence levels.

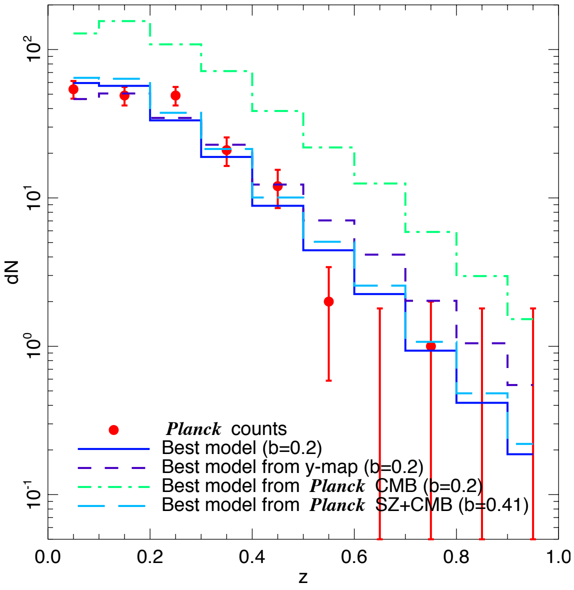

Fig. 7. Distribution in redshift for the *Planck* cosmological cluster sample. The observed number counts (red), are compared to our best-fit model prediction (blue). The dashed and dot-dashed histograms are the best-fit models from the *Planck* SZ power spectrum and *Planck* CMB power spectrum fits, respectively. The cyan long dashed histogram is the best fit CMB and SZ when the bias is free (see Sect. 6.3). The uncertainties on the observed counts, shown for illustration only, are the standard deviation based on the observed counts, except for empty bins where we show the inferred 84% upper limit on the predicted counts assuming a Poissonian distribution. See Sect. 6 for more discussion.

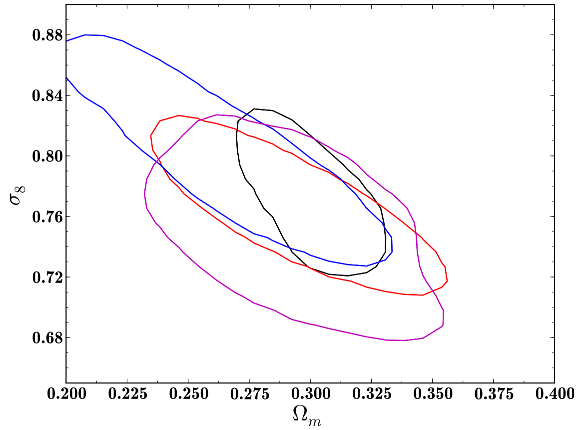

Fig. 8. Comparison of the constraints using the mass functions of Watson et al. (black) and Tinker et al. (red), with b fixed to 0.8. When relaxing the constraints on the evolution of the scaling law with redshift (blue), the contours move along the degeneracy line. Allowing the bias to vary uniformly in the range [0.7, 1.0] enlarges the constraints perpendicular to the σ_8–$\Omega_{\rm m}$ degeneracy line due to the degeneracy of the number of clusters with the mass bias (purple). Contours are 95% confidence levels here.

when adopting the different mass functions. The main effect is to change the orientation of the degeneracy between $\Omega_{\rm m}$ and σ_8, moving the best-fit values by less than 1σ.

We also relax the assumption of standard evolution of the scalings with redshift by allowing β to vary with a Gaussian prior taken from Planck Collaboration X (2011), $\beta = 0.66 \pm 0.5$. Once again, the contours move along the σ_8–$\Omega_{\rm m}$ degeneracy direction (shown in blue in Fig. 8).

Table 3. Constraints from clusters on $\sigma_8(\Omega_\mathrm{m}/0.27)^{0.3}$.

Experiment	CPPP^a	MaxBCG^b	ACT^c	SPT	*Planck* SZ
Reference	Vikhlinin et al. (2009b)	Rozo et al. (2010)	Hasselfield et al. (2013)	Reichardt et al. (2013)	This work
Number of clusters	49+37	~13 000	15	100	189
Redshift range	[0.025, 0.25] and [0.35, 0.9]	[0.1, 0.3]	[0.2, 1.5]	[0.3, 1.35]	[0.0, 0.99]
Median mass ($10^{14}\,h^{-1}\,M_\odot$)	2.5	1.5	3.2	3.3	6.0
Probe	$N(z, M)$	$N(M)$	$N(z, M)$	$N(z, Y_\mathrm{X})$	$N(z)$
S/N cut	5	($N_{200} > 11$)	5	5	7
Scaling	Y_X–T_X, M_gas	N_{200}–M_{200}	several	L_X–M, Y_X	Y_SZ–Y_X
$\sigma_8(\Omega_\mathrm{m}/0.27)^{0.3}$	0.784 ± 0.027	0.806 ± 0.033	0.768 ± 0.025	0.767 ± 0.037	0.764 ± 0.025

Notes. $^{(a)}$ The degeneracy is $\sigma_8(\Omega_\mathrm{m}/0.27)^{0.47}$. $^{(b)}$ The degeneracy is $\sigma_8(\Omega_\mathrm{m}/0.27)^{0.41}$. $^{(c)}$ For ACT we choose the results assuming the scaling law derived from the universal pressure profile in this table (constraints using other scaling relations are shown in Fig. 10).

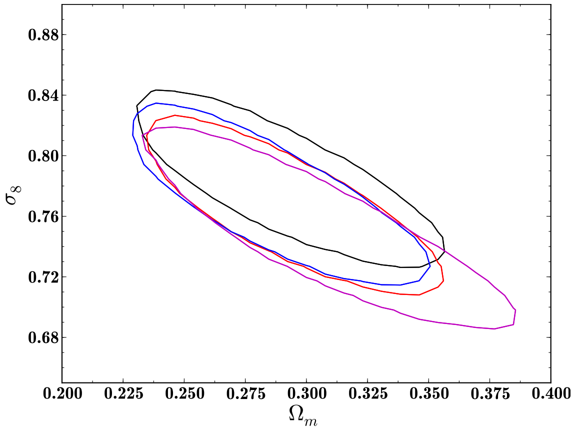

Fig. 9. 95% contours for different robustness tests: `MMF3` with S/N cut >7 in red; `MMF3` with S/N cut >8 in blue; and `MMF1` with S/N cut >7 in black; and `MMF3` with S/N cut at 7 but adopting the MC completeness in purple.

As shown in Appendix A, the estimation of the mass bias is not trivial and there is a large scatter amongst simulations. The red and purple contours compare the different constraints when fixing the mass bias to 0.8 and when allowing it to vary uniformly in the range [0.7, 1.0] respectively. Modelling of the cluster observable-mass relation is clearly the limiting factor in our analysis.

6. Discussion

Our main result is the constraint in the $(\Omega_\mathrm{m}, \sigma_8)$ plane for the standard ΛCDM model imposed by the SZ counts, which we have shown is robust to the details of our modelling. We now compare this result first to constraints from other cluster samples, and then to the constraints from the *Planck* analysis of the sky-map of the Compton y-parameter (Planck Collaboration XXI 2014) and of the primary CMB temperature anisotropies (Planck Collaboration XVI 2014).

6.1. Comparison with other cluster constraints

We restrict our comparison to some recent analyses exploiting a range of observational techniques to obtain cluster samples and mass calibrations.

Benson et al. (2013) used 18 galaxy clusters in the first 178 deg^2 of the SPT survey to find $\sigma_8(\Omega_\mathrm{m}/0.25)^{0.3} = 0.785 \pm 0.037$ for a spatially-flat model. They break the degeneracy between σ_8 and Ω_m by incorporating primary CMB constraints, deducing that $\sigma_8 = 0.795 \pm 0.016$ and $\Omega_\mathrm{m} = 0.255 \pm 0.016$. In addition, they find that the dark energy equation of state is constrained to $w = -1.09 \pm 0.36$, using just their cluster sample along with the same HST and BBN constraints used here. Subsequently, Reichardt et al. (2013) reported a much larger cluster sample and used this to improve on the statistical uncertainties on the cosmological parameters (see Table 3). Hasselfield et al. (2013) use a sample of 15 high S/N clusters from ACT, in combination with primary CMB data, to find $\sigma_8 = 0.786 \pm 0.013$ and $\Omega_\mathrm{m} = 0.250 \pm 0.012$ when assuming a scaling law derived from the universal pressure profile.

Strong constraints on cosmological parameters have been inferred from X-ray and optical richness selected samples. Vikhlinin et al. (2009b) used a sample of 86 well-studied X-ray clusters, split into low- and high-redshift bins, to conclude that $\Omega_\Lambda > 0$ with a significance about 5σ and that $w = -1.14 \pm 0.21$. Rozo et al. (2010) used the approximately 10^4 clusters in the Sloan Digital Sky Survey (SDSS) MaxBCG cluster sample, which are detected using a colour–magnitude technique and characterized by optical richness. They found that $\sigma_8(\Omega_\mathrm{m}/0.25)^{0.41} = 0.832 \pm 0.033$. The fact that this uncertainty is similar to those quoted above for much smaller cluster samples signifies, once again, that cluster cosmology constraints are now limited by modelling, rather than statistical, uncertainties.

Table 3 and Fig. 10 show some current constraints on the combination $\sigma_8(\Omega_\mathrm{m}/0.27)^{0.3}$, which is the main degeneracy line in cluster constraints. This comparison is only meant to be indicative, as a more quantitative comparison would require full consideration of modelling details which is beyond the scope of this work. Cosmic shear (Kilbinger et al. 2013), X-rays (Vikhlinin et al. 2009b), and MaxBCG (Rozo et al. 2010) each have a different slope in Ω_m, being 0.6, 0.47, and 0.41, respectively (instead of 0.3), as they are probing different redshift ranges. We have rescaled when necessary the best value and errors to quote numbers with a pivot $\Omega_\mathrm{m} = 0.27$. Hasselfield et al. (2013) have derived "cluster-only" constraints from ACT by adopting several different scaling laws, shown in blue and dashed blue in Fig. 10. The constraint assuming the universal pressure profile is highlighted as the solid symbol and error bar. For SPT we show the "cluster-only" constraints from Reichardt et al. (2013). For our own analysis we show our baseline result

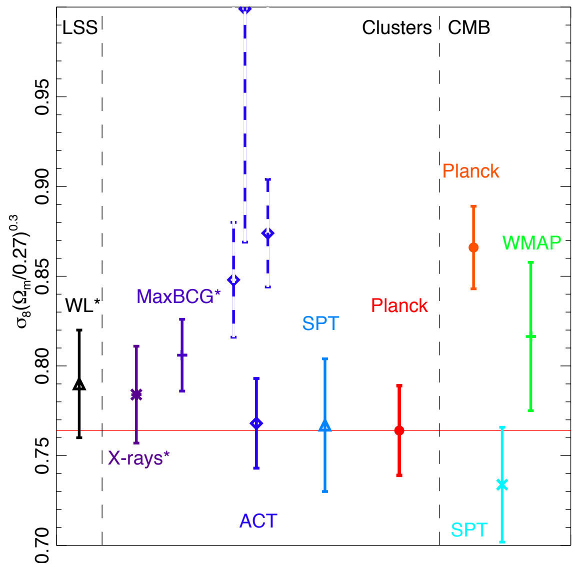

Fig. 10. Comparison of constraints (68% confidence interval) on $\sigma_8(\Omega_m/0.27)^{0.3}$ from different experiments of large–scale structure (LSS), clusters, and CMB. The solid line ACT point assumes the same universal pressure profile as this work. Probes marked with an asterisk have an original power of Ω_m different from 0.3. See text and Table 3 for more details.

for SZ and BAO and BBN with a prior on $(1-b)$ distributed uniformly in [0.7, 1]. The figure thus demonstrates good agreement amongst all cluster observations, whether in optical, X-rays, or SZ. Table 3 compares the different data and assumptions of the different cluster-related publications.

6.2. Consistency with the Planck y-map

In a companion paper (Planck Collaboration XXI 2014), we performed an analysis of the SZ angular power spectrum derived from the *Planck* y-map obtained with a dedicated component-separation technique. For the first time, the power spectrum has been measured at intermediate scales ($50 \leq \ell \leq 1000$). The same modelling as in Sect. 2 and Taburet et al. (2009, 2010) has been used to derive best-fit values of Ω_m and σ_8, assuming the universal pressure profile (Arnaud et al. 2010), a bias $1-b = 0.8$, and the best-fit values for other cosmological parameters from Planck Collaboration XVI (2014)[6]. The best model obtained, shown in Fig. 7 as the dashed line, demonstrates the consistency between the PSZ number counts and the signal observed in the y-map.

6.3. Comparison with Planck primary CMB constraints

We now compare the PSZ cluster constraints to those from the analysis of the primary CMB temperature anisotropies given in Planck Collaboration XVI (2014) (see Footnote 6). In that analysis σ_8 is derived from the standard six ΛCDM parameters.

The *Planck* primary CMB constraints, in the (Ω_m, σ_8) plane, differ significantly from our own, in particular through favouring a higher value of σ_8, (see Fig. 11). For $(1-b) = 0.8$, this leads to a factor of 2 larger number of predicted clusters than is actually observed (see Fig. 7). There is therefore some tension between the results from the *Planck* CMB analysis and the current cluster analysis. Figure 10 illustrates this with a comparison of three analyses of primary CMB data alone (Planck Collaboration XVI 2014; Story et al. 2013; Hinshaw et al. 2013) and cluster constraints in terms of $\sigma_8(\Omega_m/0.27)^{0.3}$.

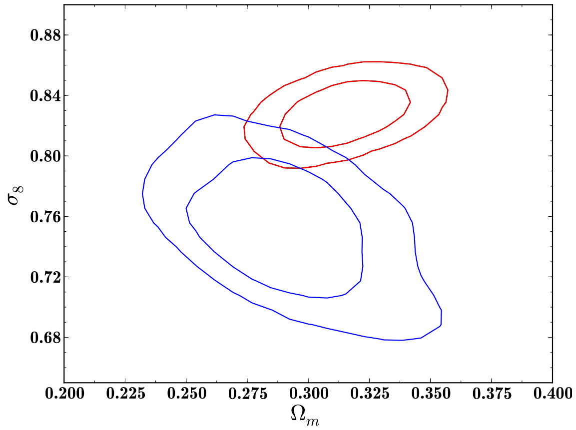

Fig. 11. 2D Ω_m–σ_8 likelihood contours for the analysis with *Planck* CMB only (red); *Planck* SZ and BAO and BBN (blue) with $(1-b)$ in [0.7, 1].

It is possible that the tension results from a combination of some residual systematics with a substantial statistical fluctuation. Enough tests and comparisons have been made on the *Planck* data sets that it is plausible that at least one discrepancy at the two or three sigma level will arise by chance. Nevertheless, it is worth considering the implications if the discrepancy is real.

As we have noted, the modelling of the cluster gas physics is the most important uncertainty in our analysis, in particular through its influence on the mass bias $(1-b)$. While we have argued for a preferred value of $(1-b) \simeq 0.8$ based on comparison of our Y_{500}–M_{500} relation to those derived from a number of different numerical simulations, and we suggest a plausible range of $(1-b)$ from 0.7 to 1, a significantly lower value would substantially alleviate the tension between CMB and SZ constraints. We have undertaken a joint analysis using the CMB likelihood presented in Planck Collaboration XV (2014) and the cluster likelihood presented in the present paper, sampling $(1-b)$ in the range [0.1, 1.5]. This results in a "measurement" of $(1-b) = 0.59 \pm 0.05$. We show in Fig 7 the SZ cluster counts predicted by the *Planck*'s best-fit primary CMB model for $(1-b) = 0.59$. Clearly, this substantial reduction in $(1-b)$ is enough to reconcile our observed SZ cluster counts with *Planck*'s best-fit primary CMB parameters.

Such a large bias is difficult to reconcile with numerical simulations, and cluster masses estimated from X-rays and from weak lensing do not typically show such large offsets (see Appendix A). Systematic discrepancies in the relevant scaling relations have, however, been identified and studied in stacking analyses of X-ray, SZ, and lensing data for the very large MaxBCG cluster sample, e.g., Planck Collaboration XII (2011), Biesiadzinski et al. (2012), Draper et al. (2012), Rozo et al. (2012), and Sehgal et al. (2013), suggesting that the issue is not yet fully settled from an observational point of view. The uncertainty reflects the inherent biases of the different mass estimates. Systematic effects arising from instrument calibration constitute

---

[6] For *Planck* CMB we took the constraints from the *Planck*+WP case, Col. 6 of Table 2 of Planck Collaboration XVI (2014). The baseline model includes massive neutrinos with $\sum m_\nu = 0.06\,\mathrm{eV}$.

a further source of uncertainty – in X-ray mass determinations, temperature estimates represent the main source of systematic uncertainty in mass, as the mass scales roughly with $T^{3/2}$. Other biases in the determination of mass-observable scaling relations come from the object selection process itself (e.g., Mantz et al. 2010; Allen et al. 2011b; Angulo et al. 2012). This may be less of a concern for SZ selected samples because of the expected small scatter between the measured quantity and the mass. An improbable conspiracy of all sources of bias seems required to lead to a sufficiently-low effective value of $(1-b)$ to reconcile the SZ and CMB constraints. This possibility needs to be carefully examined with probes based on a variety of physical quantities and derived from a wide range of types of observation, including masses, baryon and gas fractions, etc.

A different mass function may also help reduce the tension. Mass functions are calibrated against numerical simulations that may still suffer from volume effects for the largest haloes, as shown in the difference between the Tinker et al. (2008) and Watson et al. (2013) mass functions. This does not seem sufficient, however, given the results presented in Fig. 8.

One might instead ask whether the *Planck* data analysis could somehow have missed a non-negligible fraction of the total number of clusters currently predicted to have $S/N > 7$, resulting in a lower observed number count distribution. This is linked to a possible underestimate of the true dispersion about the Y_{500}–$Y_{\rm X}$ relation at a given M_{500}. It would be necessary for *Planck* to have missed ~40 percent of the clusters with predicted SZ $S/N > 7$ in order for the SZ and CMB number count curves in Fig. 7 to be in agreement. Increasing the dispersion about the Y_{500}–M_{500} relation and allowing it to correlate strongly with the scatter in X-ray properties (in particular, $Y_{\rm X}$) would raise the possibility that our calibration procedures (which are based on X-ray and SZ selected clusters assuming the scatter in Y and $Y_{\rm x}$ at fixed M_{500} to be small and to be uncorrelated with cluster dynamical state) might produce a relation which is biased high. A sufficiently-large effect seems, however, to require a level of scatter and a degree of correlation with cluster structure which are inconsistent with the predictions of current hydrodynamical simulations (see the discussion in Appendix A).

Alternatively, the discrepancy may reflect a need to extend the minimal ΛCDM model in which the σ_8 constraints are derived from the primary CMB analysis. Any extension would need to modify the power spectrum on the scales probed by clusters, while leaving the scales probed by primary CMB observations unaffected. The inclusion of neutrino masses, quantified by their sum over all families, $\sum m_\nu$, can achieve this (see Marulli et al. 2011 and Burenin 2013 for reviews of how cosmological observations can be affected by the inclusion of neutrino masses). The SPT collaboration (Hou et al. 2014) recently considered such a possibility to mitigate their tension with WMAP-7 primary CMB data. There is an upper limit of $\sum m_\nu < 0.93$ eV from the *Planck* primary CMB data alone[7]. If we combine the *Planck* CMB (*Planck*+WP) likelihood and the cluster count data using a fixed value $(1 - b) = 0.8$, then we find a 2.8σ preference for the inclusion of neutrino masses with $\sum m_\nu = (0.53 \pm 0.19)$ eV, as shown in Fig. 12. If, on the other hand, we adopt a more conservative point of view and allow $(1-b)$ to vary between 0.7 and 1.0, this preference drops to 1.9σ with $\sum m_\nu = (0.40 \pm 0.21)$ eV. Adding BAO data to the compilation lowers the value of the required mass but increases the significance, yielding $\sum m_\nu = (0.20 \pm 0.09)$ eV, due to a breaking of the degeneracy between H_0 and $\sum m_\nu$.

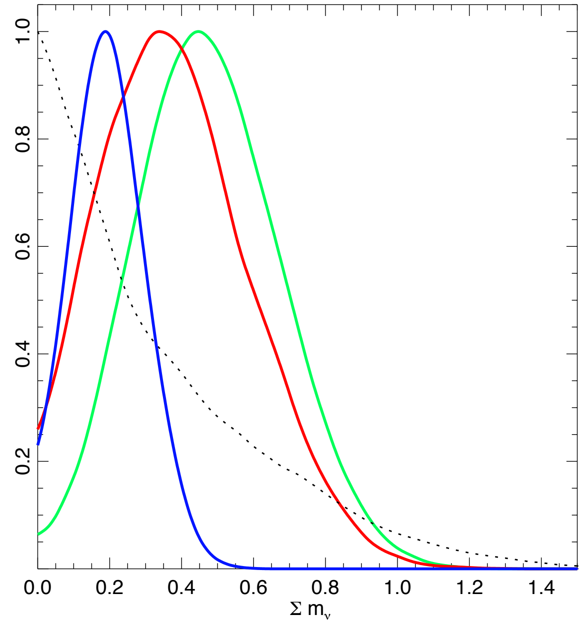

Fig. 12. Marginalized posterior distribution for $\sum m_\nu$ from: *Planck* CMB data alone (black dotted line); *Planck* CMB and SZ with $1 - b$ in [0.7, 1] (red); *Planck* CMB and SZ and BAO with $1 - b$ in [0.7, 1] (blue); and *Planck* CMB and SZ with $1 - b = 0.8$ (green).

As these results depend on the value and allowed range of $(1 - b)$, better understanding of the scaling relation is the key to further investigation. This provides strong motivation for further study of the relationship between Y and M. Over the past few years we have moved into an era where *systematic* uncertainties dominate to an increasing extent over *statistical* uncertainties. Observed mass estimates using different methods are of improving quality; for instance, X-ray mass proxies can be measured to better than 10% precision (e.g., Vikhlinin et al. 2006; Arnaud et al. 2007). In this context, systematic calibration uncertainties are playing an increasingly important role when using the cluster population to constrain cosmology.

7. Summary

We have used a sample of nearly 200 clusters from the PSZ, along with the corresponding selection function, to place strong constraints in the $(\Omega_{\rm m}, \sigma_8)$ plane. We have carried out a series of tests to verify the robustness of our constraints, varying the observed sample choice, the estimation method for the selection function, and the theoretical methodology, and have found that our results are not altered significantly by those changes.

The relation between the mass and the integrated SZ signal plays a major role in the computation of the expected number counts. Uncertainties in cosmological constraints from clusters are no longer dominated by small number statistics, but by the gas physics and sample selection biases. Uncertainties in the Y–M relation include contributions from X-ray instrument calibration, X-ray temperature measurements, inhomogeneities in cluster density and temperature profiles, and selection effects. Considering several ingredients of the gas physics of clusters, numerical simulations predict scaling relations with 30% scatter in amplitude (at a fiducial mass of $6 \times 10^{14}\ M_\odot$), and suggest a mass bias between the true mass and the estimated mass

---

[7] Planck Collaboration XVI (2014), Table 10, Col. 3.

of $(1 - b) = 0.8^{+0.2}_{-0.1}$. Adopting the central value we found constraints on $\Omega_{\rm m}$ and σ_8 that are in good agreement with previous measurements using clusters of galaxies.

Comparing our results with *Planck* primary CMB constraints within the ΛCDM cosmology reveals some tension. This can be alleviated by permitting a large mass bias ($1 - b \simeq 0.60$), which is however significantly larger than expected. Alternatively, the tension may indicate a need for an extension of the base ΛCDM model that modifies its power spectrum shape. For example the inclusion of non-zero neutrino masses helps in reconciling the primary CMB and cluster constraints, a fit to *Planck* CMB and SZ and BAO yielding $\sum m_\nu = (0.20 \pm 0.09)$ eV.

Cosmological parameter determination using clusters is currently limited by the knowledge of the observable–mass relations. In the future our goal is to increase the number of dedicated follow-up programmes to obtain better estimates of the mass proxy and redshift for most of the $S/N > 5$ *Planck* clusters. This will allow for improved determination of the scaling laws and the mass bias, increase the number of clusters that can be used, and allow us to investigate an extended cosmological parameter space.

Acknowledgements. The development of *Planck* has been supported by: ESA; CNES and CNRS/INSU-IN2P3-INP (France); ASI, CNR, and INAF (Italy); NASA and DoE (USA); STFC and UKSA (UK); CSIC, MICINN, JA and RES (Spain); Tekes, AoF and CSC (Finland); DLR and MPG (Germany); CSA (Canada); DTU Space (Denmark); SER/SSO (Switzerland); RCN (Norway); SFI (Ireland); FCT/MCTES (Portugal); and PRACE (EU). A description of the Planck Collaboration and a list of its members, including the technical or scientific activities in which they have been involved, can be found at `http://www.sciops.esa.int/index.php?project=planck&page=Planck_Collaboration`

Appendix A: Calibration of the Y_{500}–M_{500} relation

A cluster catalogue is a list of positions and measurements of observable physical quantities. Its scientific utility depends largely on our ability to link the observed quantities to the underlying mass, in other words, to define an observable proxy for the mass. *Planck* detects clusters through the SZ effect. This effect is currently the subject of much study in the cluster community, chiefly because numerical simulations indicate that the spherically-integrated SZ measurement is correlated particularly tightly with the underlying mass. In other words, this measurement potentially represents a particularly valuable mass proxy.

To establish a mass proxy, one obviously needs an accurate measurement both of the total mass and of the observable quantity in question. However, even with highly accurate measurements, the correlation between the observable quantity and the mass is susceptible to *bias* and *dispersion*, and both of these effects need to be taken into account when using cluster catalogues for scientific applications.

The aim of this Appendix is to define a baseline relation between the measured SZ flux, Y_{500}, and the total mass M_{500}. The latter quantity is not directly measurable. On an individual cluster basis, it can be inferred from dynamical analysis of galaxies, from X-ray analysis assuming hydrostatic equilibrium (HE), or from gravitational lensing observations. However, it is important to note that *all* observed mass estimates include inherent biases. For instance, numerical simulations suggest that HE mass measurements are likely to underestimate the true mass by 10–15 percent due to neglect of bulk motions and turbulence in the intra-cluster medium (ICM, e.g., Nagai et al. 2007; Piffaretti & Valdarnini 2008; Meneghetti et al. 2010), an effect that is commonly referred to in the literature as the "hydrostatic mass bias". Similarly, simulations indicate that weak lensing mass measurements may underestimate the mass by 5 to 10 percent, owing to projection effects or the use of inappropriate mass models (e.g., Becker & Kravtsov 2011). Instrument calibration systematic effects constitute a further source of error. For X-ray mass determinations, temperature estimates represent the main source of systematic uncertainty, as the mass at a given density contrast scales roughly with $T^{3/2}$. Other biases in the determination of mass-observable scaling relations come from the object selection process itself (e.g., Allen et al. 2011b; Angulo et al. 2012). A classic example is the Malmquist bias, where bright objects near the flux limit are preferentially detected. This effect is amplified by Eddington bias, the mass function dictating that many more low-mass objects are detected compared to high-mass objects. Both of these biases depend critically on the distribution of objects in mass and redshift, and on the dispersion in the relation between the mass and the observable used for sample selection. This is less of a concern for SZ selected samples than for X-ray selected samples, the SZ signal having much less scatter at a given mass than the X-ray luminosity. However for precise studies it should still be taken into account.

On the theoretical side, numerous Y_{500}–M_{500} relations have been derived from simulated data, as discussed below. The obvious advantage of using simulated data is that the relation between the SZ signal and the true mass can be obtained, because the "real" value of all physical quantities can be measured. The disadvantage is that the "real" values of measurable physical quantities depend strongly on the phenomenological models used to describe the different non-gravitational processes at work in the ICM.

Nevertheless, the magnitude of the bias between observed and true quantities can only be assessed by comparing multi-wavelength observations of a well-controlled cluster sample to numerical simulations. Thus, ideally, we would have full follow-up of a complete *Planck* cluster sample. For large samples, however, full follow-up is costly and time consuming. This has led to the widespread use of mass estimates obtained from mass-proxy relations. These relations are generally calibrated from individual deep observations of a subset of the sample in question (e.g., Vikhlinin et al. 2009a), or from deep observations of objects from an external dataset (e.g., the use of the REXCESS relations in Planck Collaboration XI 2011).

For the present paper, we will rely on mass estimates from a mass–proxy relation. In this context, the M_{500}–$Y_{\rm X}$ relation is clearly the best to use. $Y_{\rm X}$, proposed by Kravtsov et al. (2006), is defined as the product of $M_{\rm g,500}$, the gas mass within R_{500}, and $T_{\rm X}$, the spectroscopic temperature measured in the [0.15–0.75] R_{500} aperture. In the simulations performed by Kravtsov et al. (2006), $Y_{\rm X}$ was extremely tightly correlated with the true cluster mass, with a logarithmic dispersion of only 8 percent. Observations using masses derived from X-ray hydrostatic analysis indicate that $Y_{\rm X}$ does indeed appear to have a low dispersion (Arnaud et al. 2007; Vikhlinin et al. 2009a). Furthermore, the local M_{500}–$Y_{\rm X}$ relation for X-ray selected relaxed clusters has been calibrated to high statistical precision (Arnaud et al. 2010; Vikhlinin et al. 2009a), with excellent agreement achieved between various observations (see e.g., Arnaud et al. 2007). Since simulations suggest that the Y_{500}–M_{500} relation is independent of dynamical state, calibrating the Y_{500}–M_{500} relation via a low-scatter mass proxy, itself calibrated on clusters for which the HE bias is expected to be minimal, is a better approach than using HE mass estimates for the full sample, since the latter can be highly biased for very unrelaxed objects.

We approach the determination of the Y_{500}–M_{500} relation in two steps. We first calibrate the Y_{500}–proxy relation. This is combined with the X-ray calibrated relation, between the proxy and M_{500}, to define an observation-based Y_{500}–M_{500} relation. In the second step, we assess possible biases in the relation by directly comparing the observation-based relation with that from simulations. This approach, rather than directly assessing the HE mass bias, allows us to avoid complications linked to the strong dependence of the HE bias on cluster dynamical state, and thus on the cluster sample (real or simulated). The final output from this procedure is a relation between Y_{500} and M_{500}, with a full accounting of the different statistical and systematic uncertainties that go into its derivation, including bias.

In the following, all relations are fit with a power law in log-space using the orthogonal BCES method (Akritas & Bershady 1996), which takes into account the uncertainties in both variables and the intrinsic scatter. All dispersions are given in $\log_{10}$.

A.1. Baseline mass-proxy relation

As a baseline, we use the relation between $Y_{\rm X}$ and the X-ray hydrostatic mass $M_{500}^{\rm HE}$ established for 20 local *relaxed* clusters by Arnaud et al. (2010):

$$E^{-2/3}(z)\left[\frac{Y_{\rm X}}{2\times10^{14}\ M_\odot\,{\rm keV}}\right] = 10^{0.376\,\pm\,0.018}\left[\frac{M_{500}^{\rm HE}}{6\times10^{14}\ M_\odot}\right]^{1.78\,\pm\,0.06}, \qquad ({\rm A.1})$$

assuming standard evolution, and where the uncertainties are statistical only. For easier comparison with the Y_{500}–M_{500} relation given below, the normalization for $Y_{\rm X}$ expressed in 10^{-4} Mpc^2 is $10^{-0.171\,\pm\,0.018}$. The HE mass is expected to be a biased estimator of the true mass,

$$M_{500}^{\rm HE} = (1-b)\,M_{500}, \qquad ({\rm A.2})$$

where all of the possible observational biases discussed above (departure from HE, absolute instrument calibration, temperature inhomogeneities, residual selection bias) have been subsumed into the bias factor $(1-b)$. The form of the $Y_{\rm X}$–M_{500} relation is thus

$$E^{-2/3}(z)Y_{\rm X} = 10^{A\,\pm\,\sigma_A}\ \left[(1-b)\,M_{500}\right]^{\alpha\,\pm\,\sigma_\alpha}, \qquad ({\rm A.3})$$

where σ_A and σ_α are the statistical uncertainties on the normalization and slope and b is the bias between the true mass and the observed mass used to calibrate the relation. The bias is a poorly-known stochastic variable with substantial variation expected between clusters. In our case, b represents the *mean* bias between the observed mass and the true mass.

The mass proxy $M_{500}^{Y_{\rm X}}$ is defined from the best-fit $Y_{\rm X}$–$M_{500}^{\rm HE}$ relation

$$E^{-2/3}(z)Y_{\rm X} = 10^{A}\ \left[M_{500}^{Y_{\rm X}}\right]^{\alpha}. \qquad ({\rm A.4})$$

For any cluster, $M_{500}^{Y_{\rm X}}$, together with the corresponding $Y_{\rm X}$ and $R_{500}^{Y_{\rm X}}$, can be estimated iteratively about this relation from the observed temperature and gas mass profile, as described in Kravtsov et al. (2006). The calibration of the $Y_{\rm X}$–M_{500} relation is equivalent to a calibration of the $M_{500}^{Y_{\rm X}}$–M_{500} relation, which relates the mass proxy, $M_{500}^{Y_{\rm X}}$, to the mass via

$$M_{500}^{Y_{\rm X}} = 10^{\pm\sigma_A/\alpha}\ \left[(1-b)\,M_{500}\right]^{1\,\pm\,\sigma_\alpha/\alpha}. \qquad ({\rm A.5})$$

In addition to the bias factor, there are statistical uncertainties on the slope and normalization of the relation, as well as intrinsic scatter around the relation, linked to the corresponding statistical uncertainties and scatter of the $Y_{\rm X}$–$M_{500}^{\rm HE}$ relation.

A.2. Relation between Y_{500} and $M_{500}^{Y_{\rm X}}$

A.2.1. Best-fit relation

We first investigate the relationship between Y_{500} and $M_{500}^{Y_{\rm X}}$, the mass estimated iteratively from Eq. A.4, with parameters given by the best-fit Arnaud et al. (2010) relation (Eq. (A.1)). Full X-ray follow-up of the *Planck* SZ cosmological cluster sample is not yet available. Our baseline sample is thus a subset of 71 detections from the *Planck* cosmological cluster sample, detected at $S/N > 7$, for which good quality *XMM-Newton* observations are available. The sample consists of data from our previous archival study of the *Planck* Early SZ (ESZ) clusters (Planck Collaboration XI 2011), of *Planck*-detected LoCuSS clusters presented by Planck Collaboration Int. III (2013), and from the *XMM-Newton* validation programme (Planck Collaboration IX 2011; Planck Collaboration Int. I 2012; Planck Collaboration Int. IV 2013). The corresponding sub-samples include 58, 4, and 9 clusters, respectively. The X-ray data were re-analysed in order to have a homogeneous data set; measurement differences are negligible with respect to previously-published values. Uncertainties on $Y_{\rm X}$, $R_{500}^{Y_{\rm X}}$, and $M_{500}^{Y_{\rm X}}$ include those due to statistical errors on the X-ray temperature and the gas mass profile.

The SZ signal is estimated within a sphere of radius $R_{500}^{Y_{\rm X}}$ centred on the position of the X-ray peak, as detailed in e.g., Planck Collaboration XI (2011). The re-extraction procedure uses matched multi-filters (MMF) and assumes that the ICM pressure follows the universal profile shape derived by Arnaud et al. (2010) from the combination of the REXCESS sample with simulations. The extraction is undertaken on the 15.5 month *Planck* survey data set, and so statistical precision on the SZ signal is improved with respect to previously-published values. The uncertainty on Y_{500} includes statistical uncertainties on the SZ signal derived from the MMF, plus the statistical uncertainty on the aperture $R_{500}^{Y_{\rm X}}$. The latter uncertainty is negligible compared to the statistical error on the SZ signal. The resulting relation for these 71 clusters from the cosmological sample is

$$E^{-2/3}(z)\left[\frac{D_{\rm A}^2\,Y_{500}}{10^{-4}\,{\rm Mpc}^2}\right] = 10^{-0.175\,\pm\,0.011}\left[\frac{M_{500}^{Y_{\rm X}}}{6\times10^{14}\ M_\odot}\right]^{1.77\pm0.06} \qquad ({\rm A.6})$$

This agrees within 1σ with the results from the sample of 62 clusters from the ESZ sample with archival *XMM-Newton* data published in Planck Collaboration XI (2011). The slope and normalization are determined at slightly higher precision, due to the better quality SZ data. The derived intrinsic scatter (Table A.1) is significantly smaller. This is a consequence of: a more robust treatment of statistical uncertainties; propagation of gas mass profile uncertainties in the $Y_{\rm X}$ error budget; and, to a lesser extent, the propagation of $R_{500}^{Y_{\rm X}}$ uncertainties to Y_{500} estimates.

A.2.2. Effects of Malmquist bias

The fitted parameters are potentially subject to selection effects such as Malmquist bias, owing to part of the sample lying close to the selection cut. For the present sample, we use an approach

Table A.1. Parameters for the Y_{500}–M_{500} relation, expressed as $E^{-2/3}(z)\left[D_{\rm A}^2 Y_{500}/10^{-4}\ {\rm Mpc}^2\right] = 10^A \left[M_{500}/6\times10^{14}\ M_\odot\right]^\alpha$.

Sample	$N_{\rm c}$	MB	Mass	A	α	$[\sigma_{\log Y\|M}]$ int	$[\sigma_{\log Y\|M}]$ raw	Section
XMM-ESZ PEPXI	62	N	$M_{500}^{Y_{\rm X}}$	−0.19 ± 0.01	1.74 ± 0.08	0.10 ± 0.01	...	A.2.1
Cosmo sample	71	N	$M_{500}^{Y_{\rm X}}$	−0.175 ± 0.011	1.77 ± 0.06	0.065 ± 0.010	0.080 ± 0.009	A.2.1
Cosmo sample	**71**	**Y**	$M_{500}^{Y_{\rm X}}$	**−0.186 ± 0.011**	**1.79 ± 0.06**	**0.063 ± 0.011**	**0.079 ± 0.009**	**A.2.2**
XMM-ESZ	62	Y	$M_{500}^{Y_{\rm X}}$	−0.19 ± 0.01	1.75 ± 0.07	0.065 ± 0.011	0.079 ± 0.009	A.2.3
S/N > 7	78	Y	$M_{500}^{Y_{\rm X}}$	−0.18 ± 0.01	1.72 ± 0.06	0.063 ± 0.010	0.078 ± 0.008	A.2.3
Cosmo sub-sample A	10	Y	$M_{500}^{\rm HE}$	−0.15 ± 0.04	1.6 ± 0.3	...	0.08 ± 0.02	A.3.2
Cosmo sub-sample B	58	Y	$M_{500}^{\rm HE}$	−0.19 ± 0.03	1.7 ± 0.2	0.25 ± 0.06	0.27 ± 0.06	A.3.2

Notes. Column 1, considered sample; Col. 2, number of clusters in the sample; Col. 3, Malmquist bias correction; if this column contains Y, a mean correction for Malmquist bias has been applied to each point before fitting; Col. 4, mass definition; Cols. 5 and 6, slope and normalization of the relation; Cols. 7 and 8, intrinsic and raw orthogonal scatter around the best-fit relation at a given mass; Col. 9, Section in which sub-sample is discussed. The Cosmo sample highlighted in bold represents the baseline relation (see text for details).

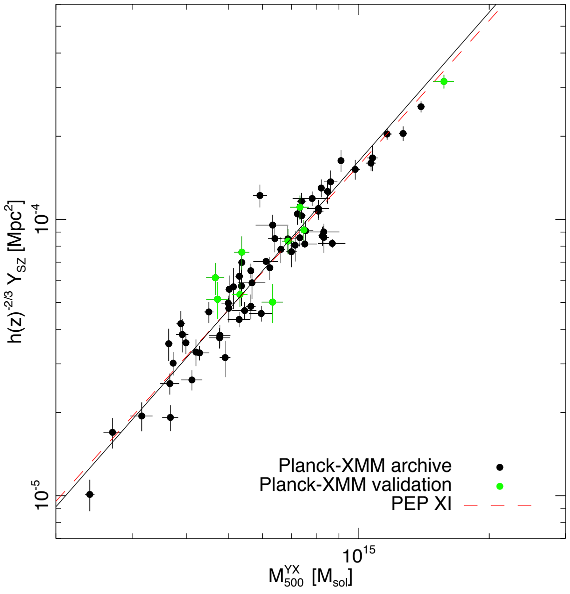

Fig. A.1. Best scaling relation between Y_{500} and M_{500}, and the data points utilized after correction of the Malmquist bias.

adapted from that described in Vikhlinin et al. (2009a) and Pratt et al. (2009), where each data point is rescaled by the mean bias for its flux, and the relation refitted using the rescaled points. The method is described in more detail in Paper I. For the baseline cosmological sample of 71 systems, the bias-corrected Y_{500}–$M_{500}^{Y_{\rm X}}$ relation is

$$E^{-2/3}(z)\left[\frac{D_{\rm A}^2\,Y_{500}}{10^{-4}\,{\rm Mpc}^2}\right] = 10^{-0.19\pm0.01}\left[\frac{M_{500}^{Y_{\rm X}}}{6\times10^{14}\,M_\odot}\right]^{1.79\pm0.06}. \quad ({\rm A.7})$$

The best-fit relation, together with Malmquist bias corrected data points, is plotted in Fig. A.1.

The correction decreases the effective Y_{500} values at a given mass, an effect larger for clusters closer to the S/N threshold. The net effect is small, a roughly 1σ decrease of the normalization and a slight steepening of the power-law slope (Table A.1).

A.2.3. Stability of slope and normalization

The slope and normalization of this relation are robust to the choice of sample (Table A.1). We compared our results to those obtained from:

- An extended sample of 78 clusters with $S/N > 7$ (71 in common with the baseline sample). This is built from all objects falling in the 84% sky mask used to define the SZ catalogue Planck Collaboration XXIX (2014), and for which *XMM-Newton* data have been published by the Planck Collaboration (Planck Collaboration IX 2011; Planck Collaboration XI 2011; Planck Collaboration Int. I 2012; Planck Collaboration Int. III 2013; Planck Collaboration Int. IV 2013).
- The original 62 clusters from the ESZ sample published in Planck Collaboration XI (2011), with updated SZ signal measurements obtained from 15.5 month *Planck* data (62 in common with the baseline sample). These objects are all known from X-ray surveys and all lie at $z < 0.5$. We use them to test fit robustness to the inclusion of non-X-ray selected, higher-redshift systems.

As indicated in Table A.1, there is agreement within 1 σ between the various samples. The results are also in agreement with the relation obtained from a simple combination of the Y_{500}–$Y_{\rm X}$ relation (discussed in Paper I) and the $Y_{\rm X}$–$M_{500}^{\rm HE}$ relation (Eq. (A.1) above).

A.3. The observation-based Y_{500}–M_{500} relation

A.3.1. Combination of the Y_{500}–$M_{500}^{Y_{\rm X}}$ and the $M_{500}^{Y_{\rm X}}$–M_{500} relations

We now combine Eq. (A.7) with the $M_{500}^{Y_{\rm X}}$–M_{500} relation. This will not change the best-fit parameters, but will increase their uncertainties. As the determinations of the two relations are independent, we added quadratically the uncertainties in the best-fit parameters of the Y_{500}–$M_{500}^{Y_{\rm X}}$ (Eq. (A.6)) and $M_{500}^{Y_{\rm X}}$–M_{500} (Eq. (A.5), with values from Eq. (A.1)) relations. Our best-fit Y_{500}–M_{500} relation is then

$$E^{-2/3}(z)\left[\frac{D_{\rm A}^2\,Y_{500}}{10^{-4}\,{\rm Mpc}^2}\right] = 10^{-0.19\,\pm\,0.02}\left(\frac{(1-b)\,M_{500}}{6\times10^{14}\,M_\odot}\right)^{1.79\,\pm\,0.08}. \quad (A.8)$$

Thus inclusion of the statistical uncertainty in the $M_{500}^{Y_{\rm X}}$–$M_{500}^{\rm HE}$ relation doubles the uncertainty on the normalization and increases the uncertainty on the slope by 40%. Note that we have implicitly assumed here that the scatter around the two relations is uncorrelated.

A.3.2. Effect of use of an external dataset

The above results assume a mass estimated from the baseline $Y_{\rm X}$–M_{500} relation, derived by Arnaud et al. (2010) from an external dataset of 20 relaxed clusters (Eq. (A.1)). How does this relation compare to the individual hydrostatic X-ray masses of the *Planck* cosmological cluster sample? Of the 71 clusters in the baseline sample:

- 58 objects have temperature profile information extending to various fractions of R_{500}, of which
- 10 cool-core objects have temperature profiles measurements at least out to R_{500}.

Thus, while spatially-resolved temperature profiles are available for 58 of the 71 clusters with *XMM-Newton* observations, we must be careful in interpretation of these data. The Arnaud et al. relation was derived from a carefully chosen data set consisting of relaxed, cool-core objects having well-constrained temperature profiles out to around R_{500}, i.e., the type of object for which it makes sense to undertake a hydrostatic mass analysis. Many clusters of the *Planck* sample are merging systems for which such an analysis would give results that are difficult to interpret. In addition, few of the *Planck* sample have spatially-resolved temperature profiles out to R_{500}. However, as given in Table A.1, the best-fit $Y_{\rm X}$–$M_{500}^{\rm HE}$ relation for the 10 cool-core clusters that are detected to R_{500} agrees with Eq. (A.8) within 1σ. Moreover, the relation for the 58 *Planck* clusters with HE mass estimates, derived regardless of dynamical state and radial detection extent, also agrees within 1σ (albeit with greatly increased scatter). We are thus confident that the masses estimated from an externally-calibrated $Y_{\rm X}$–$M_{500}^{\rm HE}$ relation are applicable to the present data set.

A.3.3. Dispersion about the observed relations

A key issue is the dispersion around the mean relation. We first estimate the intrinsic scatter of the Y_{500}–$M_{500}^{\rm HE}$ relation by combining the intrinsic scatter of the Y_{500}–$M_{500}^{Y_{\rm X}}$ relation and that of the $M_{500}^{Y_{\rm X}}$–$M_{500}^{\rm HE}$ relation. This estimate is applicable to relaxed objects only, since the Y_{500}–$M_{500}^{\rm HE}$ relation has been measured using a sample of such systems. If the scatter about the input relations is independent, this gives

$$\sigma = \sqrt{\sigma^2_{Y_{500}|M_{500}^{Y_{\rm X}}} + 2\cos^2(\tan^{-1}\alpha)\,\sigma^2_{M_{500}^{\rm HE}|Y_{\rm X}}}, \quad (A.9)$$

where α is the slope of the Y_{500}–$M_{500}^{Y_{\rm X}}$ relation. As the HE mass estimate introduces extra scatter as compared to the true mass (Kay et al. 2012), the dispersion about the Y_{500}–M_{500} relation is expected to be smaller than that of the Y_{500}–$M_{500}^{\rm HE}$ relation (although this will depend on correlations between the scatter in the $M_{500}^{\rm HE}$–M_{500} and $M_{500}^{\rm HE}$–Y_{500} relations). The above expression thus also provides an estimate of the scatter of the Y_{500}–M_{500} relation, again for relaxed objects. While merging events are expected to induce shocks in the ICM, leading to higher temperatures and thus an increase in Y_{500}, current simulations suggest that this is a weak effect. This may be due to the relatively short duration of the shocking phase during a merger (e.g., Ricker & Sarazin 2001; Ritchie & Thomas 2002; Poole et al. 2007). Thus, further assuming that the intrinsic scatter of the Y_{500}–M_{500} relation is the same for the total relaxed and unrelaxed population, as indicated by numerical simulations (Kravtsov et al. 2006; Kay et al. 2012), Eq. (A.9) gives a conservative estimate of the intrinsic scatter of the Y_{500}–M_{500} relation.

The intrinsic dispersion about our baseline $Y_{\rm X}$–$M_{500}^{\rm HE}$ relation (Eq. (A.1)), taken from Arnaud et al. (2010), is not measurable; neither is it measurable for the best-fit *Chandra* $Y_{\rm X}$–$M_{500}^{\rm HE}$ relation published in Vikhlinin et al. (2009a). Using a smaller sample of 10 systems, Arnaud et al. (2007) measured an intrinsic scatter of $\sigma_{\log M_{500}^{\rm HE}|Y_{\rm X}} = 0.039$ (9 percent), in excellent agreement with the results of the simulations of Nagai et al. (2007) for the scatter of the $M_{500}^{\rm HE}$–$Y_{\rm X}$ relation for relaxed clusters (8.7 percent, their Table 4). It is somewhat larger than the intrinsic scatter of the relation between the true mass and $Y_{\rm X}$ derived by Kravtsov et al. ($\sigma_{\log M_{500}|Y_{\rm X}} = 5$–$7$ percent) but close to the results of Fabjan et al. (2011), who find $\sigma_{\log M_{500}|Y_{\rm X}} = 0.036$–$0.046$. We thus take as a conservative estimate $\sigma_{\log M_{500}^{\rm HE}|Y_{\rm X}} = 0.05$. The intrinsic dispersion about the Y_{500}–$M_{500}^{Y_{\rm X}}$ relation for our data is $\sigma_{\log Y_{500}|M_{500}^{Y_{\rm X}}} = 0.065 \pm 0.01$. This value is three times larger than the results of Kay et al. (2012). Partly this is due to the presence of outliers in our dataset (as discussed in Paper I), and it may also be due to projection effects in observed data sets (Kay et al. 2012).

Our final observational estimate of the intrinsic scatter is then $\sigma_{\log Y_{500}|M_{500}} < 0.074$ or 18 percent, similar to the predictions from Kay et al. (2012) and Sehgal et al. (2010). These predictions depend both on the numerical scheme and specific physics assumptions, with values varying by a factor of two in the typical range 0.04 to 0.08 (references in Sect. A.4.1 below).

A.4. Assessing the bias from comparison with numerical simulations

The final piece of the jigsaw consists of assessing the bias b in Eq. (A.2). Since the relation has been calibrated using the HE mass for a sample of *relaxed clusters*, b represents the bias between $M_{500}^{\rm HE}$ and the true mass for this category of clusters. In principle, this can be assessed through comparison with numerical simulations. However, this approach is hampered by two difficulties. The first is the exact definition of “relaxed”, since it is almost impossible to select such clusters from observations and simulations according to the *same* criteria. The second is the specific implementation of the HE equation, which can differ substantially between observations (e.g., the use of forward fitting using parametric models, etc.) and simulations (e.g., the use of mock observations, etc.). Thus the amplitude of the bias that is found will depend not only on physical departures from HE, but also on technical details in the approach to data analysis.

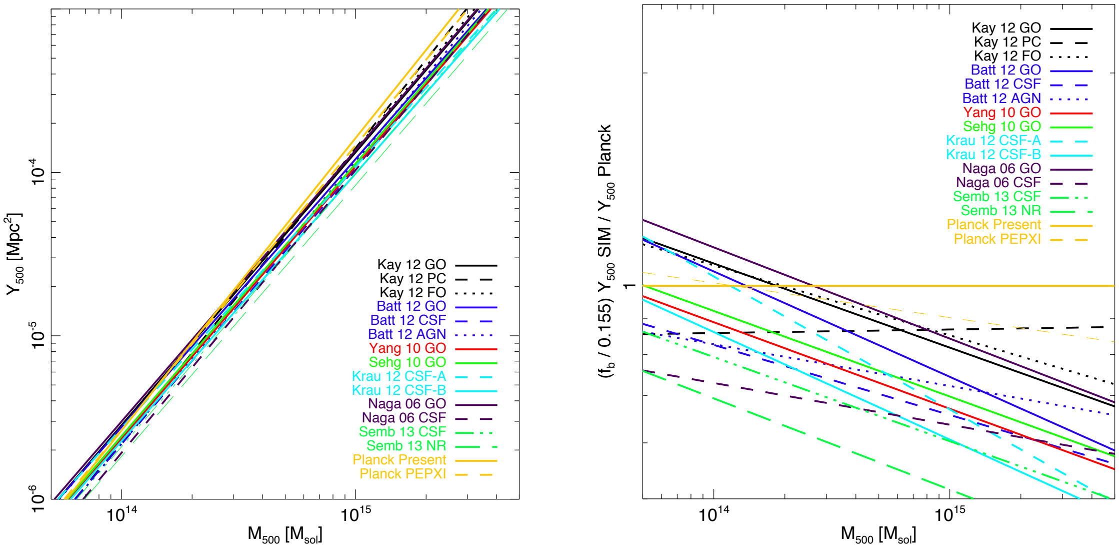

Fig. A.2. *Left*: comparison of Y_{500}–M_{500} relations from 12 simulations undertaken by six different groups with the updated observational Y_{500}–$M_{500}^{\rm HE}$ result from *Planck*, Eq. (A.8). *Right*: ratio of each simulated Y_{500}–M_{500} relation relative to Eq. (A.8). The different scaling laws are taken from Kay et al. (2012), Battaglia et al. (2012), Yang et al. (2010), Sehgal et al. (2010), Krause et al. (2012), Nagai (2006), Sembolini et al. (2013) and Planck Collaboration XI (2011).

Here we use a different approach that avoids these pitfalls, assessing the bias b by comparing directly the estimated Y_{500}–M_{500} relations with those found from numerical simulations. We then discuss the consistency of the resulting bias estimate with the HE bias expected from simulations and from absolute calibration uncertainties.

A.4.1. Comparison of simulated Y_{500}–M_{500} relations and data

We first compared the Y_{500}–M_{500} relations from 14 different analyses done by seven groups (Nagai 2006; Yang et al. 2010; Sehgal et al. 2010; Krause et al. 2012; Battaglia et al. 2012; Kay et al. 2012; Sembolini et al. 2013). We translated these simulations results into a common cosmology and, where necessary, converted cylindrical relations into spherical measurements assuming a ratio of $Y_{500,\rm cyl}/Y_{500,\rm sph} = 0.74/0.61 \simeq 1.2$, as given by the Arnaud et al. (2010) pressure profile.

The left-hand panel of Fig. A.2 shows the different Y_{500}–M_{500} relations rescaled to our chosen cosmology. The simulations use various different types of input physics, and the resulting Y_{500}–M_{500} relations depend strongly on this factor. The only obvious trend is a mild tendency for adiabatic simulations to find nearly self-similar slopes (1.66). Runs with non-gravitational processes tend to find slightly steeper slopes, but this is not always the case (e.g., the Krause et al. 2012 simulations). The right-hand panel of Fig. A.2 shows the *ratio* of each simulation Y_{500}–M_{500} relation to the *Planck* Y_{500}–$M_{500}^{Y_{\rm X}}$ relation given in Eq. (A.8). All results have been rescaled to account for the differences in baryon fraction between simulations. At our reference pivot point of $M_{500} = 6 \times 10^{14}\,M_\odot$, all simulations are offset from the measured relation. There is also a clear dependence on mass arising from the difference in slope between the majority of the simulated relations and that of the *Planck* relation. The *Planck* slope is steeper, possibly indicating the stronger effect of non-gravitational processes in the real data.

A.4.2. Quantification of the mass bias

We define the mass bias b between the "true" and observed M_{500} values, following Eq. (A.2) and explicitly allowing for possible mass dependence of the bias, i.e, $b = b(M_{500}^{\rm true})$. Both masses are defined at a fixed density contrast of 500, so that the relations between observed and true mass and radius read

$$M_{500}^{\rm obs} = \left[1 - b\left(M_{500}^{\rm true}\right)\right] M_{500}^{\rm true} \tag{A.10}$$

$$R_{500}^{\rm obs} = \left[1 - b\left(M_{500}^{\rm true}\right)\right]^{1/3} R_{500}^{\rm true} \tag{A.11}$$

where "true" denotes simulated quantities, and "obs" denotes quantities estimated at the apertures derived from observations. The corresponding Y_{500}–M_{500} relations are

$$Y\left(<R_{500}^{\rm true}\right) = A_{\rm true}\left[M_{500}^{\rm true}\right]^{\beta}, \tag{A.12}$$

$$Y\left(<R_{500}^{\rm obs}\right) = A_{\rm obs}\left[M_{500}^{\rm obs}\right]^{\alpha}. \tag{A.13}$$

In our case, Y_{500} is measured interior to $R_{500}^{Y_{\rm X}}$ as opposed to $R_{500}^{\rm true}$. The ratio $Y\left(<R_{500}^{\rm true}\right)/Y\left(<R_{500}^{\rm obs}\right)$ depends on the radial variation of Y_{500} for scaled radii, $r/R_{500}^{Y_{\rm X}} = R_{500}^{\rm true}/R_{500}^{\rm obs} = (1-b)^{-1/3}$, which is close to 1. For a GNFW universal profile (Arnaud et al. 2010), we find that it can be well fit by a power law of the form $(1-b)^{-1/4}$. Combining Eq. (A.10), Eq. (A.12) and Eq. (A.13) we then arrive at

$$\left[1 - b\left(M_{500}^{\rm true}\right)\right] = \left[\frac{A_{\rm true}\left(M_{500}^{\rm true}\right)^{\beta}}{A_{\rm obs}\left(M_{500}^{\rm true}\right)^{\alpha}}\right]^{-1/4+\alpha}. \tag{A.14}$$

The relation makes it clear that a mass dependence of the bias naturally translates into a different slope of the observed and true Y_{500}–M_{500} relations.

The bias b can then be estimated from a comparison of observed and simulated relations, with the caveat that differences can also arise from imperfect modelling of cluster physics

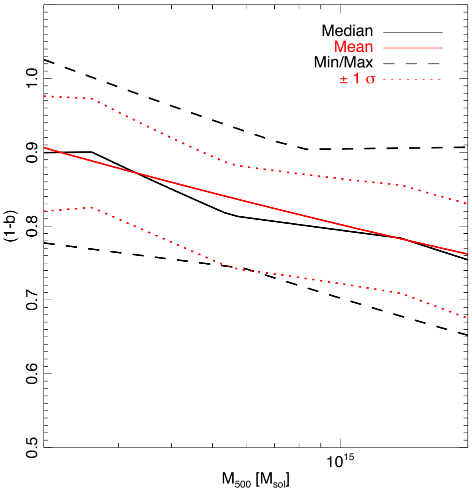

Fig. A.3. Dependence of $(1-b)$ on mass. Note that this value is strongly dependent on the baryon fraction f_b (see text).

within the simulations. For the ensemble of simulations shown in Fig. A.2, the right panel shows the ratio of the observed and simulated relations as a function of mass. Figure A.3 shows the corresponding variation of $(1-b)$ as a function of mass M from Eq. (A.14) for the observed slope $\alpha = 1.79$. This is mass dependent due to the difference in slopes between the simulated and observed relations. At a pivot point of $M_{500} = 6 \times 10^{14}\,M_\odot$, the median value of $A_\mathrm{true}/A_\mathrm{obs}$ is 0.74, implying $(1-b) = 0.81$. However, there is a large amount of scatter in the predictions from simulations. As a consequence, $(1-b)$ can vary from 0.74 to 0.97 at $M_{500} = 6\times10^{14}\,M_\odot$. Note that the above results depend significantly on the baryon fraction f_b. For example, assuming the WMAP-7 value $f_\mathrm{b} = 0.167$, the median value of $(1-b)$ is 0.86 at the pivot point of $M_{500} = 6\times10^{14}\,M_\odot$.

A.4.3. Consistency with HE bias predictions and absolute calibration uncertainties

Taken at face value, the bias we derive above of $(1-b) \simeq 0.8$ implies that the HE mass used to calibrate the Y_{500}–M_{500}^HE relation is offset from the true mass by around 20 percent. Is this reasonable?

We can first compare HE X-ray and weak lensing (WL) masses. Although as mentioned above both measurements are expected to be biased, such comparisons are useful because the mass measurements involved are essentially independent. In addition measurements for moderately large sample sizes (tens of systems) are now starting to appear in the literature. However, at present there is little consensus, with some studies finding good agreement between HE and WL masses (e.g., Vikhlinin et al. 2009a; Zhang et al. 2010), some finding that HE masses are lower than WL masses, (e.g., Mahdavi et al. 2008), and some even finding that HE masses are higher than WL masses (Planck Collaboration Int. III 2013). The key point in such analyses is rigorous data quality on both the X-ray and optical sides. Most recent work points to relatively good agreement between X-ray and WL masses, with $M^\mathrm{HE}/M^\mathrm{WL} \simeq 0.9$ on average, and $M^\mathrm{HE}/M^\mathrm{WL} \simeq 1$ for relaxed systems (Mahdavi et al. 2013; von der Linden et al. 2014).

According to cosmological numerical simulations, the measurement bias induced by X-ray measurements relative to the "true" values can be caused by two main effects. The first is the classic "hydrostatic mass bias" due to non-thermal pressure support from turbulence/random motions, etc. However, the exact details are very model-dependent. The HE bias expected from simulations varies substantially, depending on the details of the numerical scheme, the input physics, and the approach used to calculate the HE masses (e.g., Rasia et al. 2012). In addition, the amount of bias is different depending on the dynamical state of the object, relaxed systems having less bias than unrelaxed systems. The majority of numerical simulations predict HE biases of 10 to 20 percent (Nagai et al. 2007; Piffaretti & Valdarnini 2008; Lau et al. 2009; Kay et al. 2012; Rasia et al. 2012).

Temperature inhomogeneities constitute the second contributor to X-ray measurement bias. In the presence of large amounts of cool gas, a single-temperature fit to a multi-temperature plasma will yield a result that is biased towards lower temperatures (e.g., Mazzotta et al. 2004). The presence of temperature inhomogeneities will depend on the dynamical state. While this effect can be investigated with simulations, estimates of its impact vary widely, owing to differences in numerical schemes and the different implementations of the input physics. For instance, simulations with heat conduction consistently predict smoother temperature distributions, thus X-ray spectroscopic biases are minimal in this case. On the other hand, "adiabatic" simulations predict long-lasting high-density cool-core type phenomena, which will lead to significant biases in single-temperature fits. Estimates of biasing due to temperature inhomogeneities can range up to 10 or 15 percent (e.g., Rasia et al. 2012).

Finally, for HE mass estimates obtained from X-ray data, instrument calibration uncertainties also play a significant role in introducing uncertainties in mass estimates. For instance, the difference in calibration between *XMM-Newton* and *Chandra* can induce differences in Y_X. This is typically 5 percent, from a comparison of *XMM-Newton* based values published by Planck Collaboration XI (2011) to *Chandra* values for 28 ESZ clusters by Rozo et al. (2012). This can lead to differences of up to 10 percent in the mass $M_{500}^{Y_\mathrm{X}}$ derived from Y_X, owing to the dependence of the mass on Y_X.

Thus our adopted baseline value of $(1-b) \simeq 0.8$, ranging from 0.7–1, appears to encompass our current ignorance of the exact bias.

A.5. Conclusions

In summary the baseline is

$$E^{-2/3}(z)\left[\frac{D_\mathrm{A}^2\,Y_{500}}{10^{-4}\,\mathrm{Mpc}^2}\right] = 10^{-0.19\pm0.02}\left[\frac{(1-b)M_{500}}{6\times10^{14}\,M_\odot}\right]^{1.79\pm0.08}, \tag{A.15}$$

with an intrinsic scatter of $\sigma_{\log Y} = 0.075$ and a mean bias $(1-b) = 0.80^{+0.2}_{-0.1}$. The statistical uncertainty on the normalization is about 5% and the error budget is dominated by the systematic uncertainties.

References

Abell, G. O. 1958, ApJS, 3, 211
Abell, G. O., Corwin, Jr., H. G., & Olowin, R. P. 1989, ApJS, 70, 1
Aghanim, N., de Luca, A., Bouchet, F. R., Gispert, R., & Puget, J. L. 1997, A&A, 325, 9
Akritas, M. G., & Bershady, M. A. 1996, ApJ, 470, 706
Allen, S. W., Evrard, A. E., & Mantz, A. B. 2011a, Ann. Rev. Astron. Astrophys., 49, 409

Allen, S. W., Evrard, A. E., & Mantz, A. B. 2011b, ARA&A, 49, 409
Anderson, L., Aubourg, E., Bailey, S., et al. 2012, MNRAS, 427, 3435
Angulo, R. E., Springel, V., White, S. D. M., et al. 2012, MNRAS, 426, 2046
Arnaud, M., Pointecouteau, E., & Pratt, G. W. 2007, A&A, 474, L37
Arnaud, M., Pratt, G. W., Piffaretti, R., et al. 2010, A&A, 517, A92
Barbosa, D., Bartlett, J. G., Blanchard, A., & Oukbir, J. 1996, A&A, 314, 13
Battaglia, N., Bond, J. R., Pfrommer, C., & Sievers, J. L. 2012, ApJ, 758, 74
Battye, R. A., & Weller, J. 2003, Phys. Rev. D, 68, 083506
Becker, M. R., & Kravtsov, A. V. 2011, ApJ, 740, 25
Benson, B. A., de Haan, T., Dudley, J. P., et al. 2013, ApJ, 763, 147
Beutler, F., Blake, C., Colless, M., et al. 2011, MNRAS, 416, 3017
Biesiadzinski, T., McMahon, J., Miller, C. J., Nord, B., & Shaw, L. 2012, ApJ, 757, 1
Birkinshaw, M. 1999, Phys. Rep., 310, 97
Blake, C., Brough, S., Colless, M., et al. 2012, MNRAS, 425, 405
Böhringer, H., Voges, W., Huchra, J. P., et al. 2000, ApJS, 129, 435
Böhringer, H., Schuecker, P., Guzzo, L., et al. 2004, A&A, 425, 367
Burenin, R. A. 2013, Astron. Lett., 39, 357
Carlberg, R. G., Yee, H. K. C., Ellingson, E., et al. 1996, ApJ, 462, 32
Carlstrom, J. E., Ade, P. A. R., Aird, K. A., et al. 2011, PASP, 123, 568
Cash, W. 1979, ApJ, 228, 939
da Silva, A. C., Kay, S. T., Liddle, A. R., & Thomas, P. A. 2004, MNRAS, 348, 1401
Diego, J. M., Martínez-González, E., Sanz, J. L., Benitez, N., & Silk, J. 2002, MNRAS, 331, 556
Draper, P., Dodelson, S., Hao, J., & Rozo, E. 2012, Phys. Rev. D, 85, 023005
Fabjan, D., Borgani, S., Rasia, E., et al. 2011, MNRAS, 416, 801
Haiman, Z., Mohr, J. J., & Holder, G. P. 2001, ApJ, 553, 545
Hasselfield, M., Hilton, M., Marriage, T. A., et al. 2013, J. Cosmol. Astropart. Phys., 7, 8
Henry, J. P., Evrard, A. E., Hoekstra, H., Babul, A., & Mahdavi, A. 2009, ApJ, 691, 1307
Hinshaw, G., Larson, D., Komatsu, E., et al. 2013, ApJS, 208, 19
Holder, G., Haiman, Z., & Mohr, J. J. 2001, ApJ, 560, L111
Hou, Z., Reichardt, C. L., Story, K. T., et al. 2014, ApJ, 782, 74
Kay, S. T., Peel, M. W., Short, C. J., et al. 2012, MNRAS, 422, 1999
Kilbinger, M., Fu, L., Heymans, C., et al. 2013, MNRAS, 430, 2200
Krause, E., Pierpaoli, E., Dolag, K., & Borgani, S. 2012, MNRAS, 419, 1766
Kravtsov, A. V., Vikhlinin, A., & Nagai, D. 2006, ApJ, 650, 128
Lau, E. T., Kravtsov, A. V., & Nagai, D. 2009, ApJ, 705, 1129
Lewis, A., & Bridle, S. 2002, Phys. Rev., D66, 103511
Lewis, A., Challinor, A., & Lasenby, A. 2000, ApJ, 538, 473
Mahdavi, A., Hoekstra, H., Babul, A., & Henry, J. P. 2008, MNRAS, 384, 1567
Mahdavi, A., Hoekstra, H., Babul, A., et al. 2013, ApJ, 767, 116
Mantz, A., Allen, S. W., Ebeling, H., Rapetti, D., & Drlica-Wagner, A. 2010, MNRAS, 406, 1773
Marrone, D. P., Smith, G. P., Okabe, N., et al. 2012, ApJ, 754, 119
Marulli, F., Carbone, C., Viel, M., Moscardini, L., & Cimatti, A. 2011, MNRAS, 418, 346
Mazzotta, P., Rasia, E., Moscardini, L., & Tormen, G. 2004, MNRAS, 354, 10
Mehrtens, N., Romer, A. K., Hilton, M., et al. 2012, MNRAS, 423, 1024
Melin, J., Bartlett, J. G., & Delabrouille, J. 2006, A&A, 459, 341
Meneghetti, M., Rasia, E., Merten, J., et al. 2010, A&A, 514, A93
Motl, P. M., Hallman, E. J., Burns, J. O., & Norman, M. L. 2005, ApJ, 623, L63
Nagai, D. 2006, ApJ, 650, 538
Nagai, D., Kravtsov, A. V., & Vikhlinin, A. 2007, ApJ, 668, 1
Oukbir, J., & Blanchard, A. 1992, A&A, 262, L21
Padmanabhan, N., Xu, X., Eisenstein, D. J., et al. 2012, MNRAS, 427, 2132
Perrenod, S. C. 1980, ApJ, 236, 373
Piffaretti, R. & Valdarnini, R. 2008, A&A, 491, 71
Planck Collaboration VIII. 2011, A&A, 536, A8
Planck Collaboration IX. 2011, A&A, 536, A9
Planck Collaboration X. 2011, A&A, 536, A10
Planck Collaboration XI. 2011, A&A, 536, A11
Planck Collaboration XII. 2011, A&A, 536, A12
Planck Collaboration Int. I. 2012, A&A, 543, A102
Planck Collaboration Int. III. 2013, A&A, 550, A129
Planck Collaboration Int. IV. 2013, A&A, 550, A130
Planck Collaboration I. 2014, A&A, 571, A1
Planck Collaboration II. 2014, A&A, 571, A2
Planck Collaboration III. 2014, A&A, 571, A3
Planck Collaboration IV. 2014, A&A, 571, A4
Planck Collaboration V. 2014, A&A, 571, A5
Planck Collaboration VI. 2014, A&A, 571, A6
Planck Collaboration VII. 2014, A&A, 571, A7
Planck Collaboration VIII. 2014, A&A, 571, A8
Planck Collaboration IX. 2014, A&A, 571, A9
Planck Collaboration X. 2014, A&A, 571, A10
Planck Collaboration XI. 2014, A&A, 571, A11
Planck Collaboration XII. 2014, A&A, 571, A12
Planck Collaboration XIII. 2014, A&A, 571, A13
Planck Collaboration XIV. 2014, A&A, 571, A14
Planck Collaboration XV. 2014, A&A, 571, A15
Planck Collaboration XVI. 2014, A&A, 571, A16
Planck Collaboration XVII. 2014, A&A, 571, A17
Planck Collaboration XVIII. 2014, A&A, 571, A18
Planck Collaboration XIX. 2014, A&A, 571, A19
Planck Collaboration XX. 2014, A&A, 571, A20
Planck Collaboration XXI. 2014, A&A, 571, A21
Planck Collaboration XXII. 2014, A&A, 571, A22
Planck Collaboration XXIII. 2014, A&A, 571, A23
Planck Collaboration XXIV. 2014, A&A, 571, A24
Planck Collaboration XXV. 2014, A&A, 571, A25
Planck Collaboration XXVI. 2014, A&A, 571, A26
Planck Collaboration XXVII. 2014, A&A, 571, A27
Planck Collaboration XXVIII. 2014, A&A, 571, A28
Planck Collaboration XXIX. 2014, A&A, 571, A29
Planck Collaboration XXX. 2014, A&A, 571, A30
Planck Collaboration XXXI. 2014, A&A, 571, A31
Poole, G. B., Babul, A., McCarthy, I. G., et al. 2007, MNRAS, 380, 437
Pratt, G. W., Croston, J. H., Arnaud, M., & Böhringer, H. 2009, A&A, 498, 361
Rasia, E., Meneghetti, M., Martino, R., et al. 2012, New J. Phys., 14, 055018
Reichardt, C. L., Stalder, B., Bleem, L. E., et al. 2013, ApJ, 763, 127
Ricker, P. M., & Sarazin, C. L. 2001, ApJ, 561, 621
Riess, A. G., Macri, L., Casertano, S., et al. 2011, ApJ, 730, 119
Ritchie, B. W., & Thomas, P. A. 2002, MNRAS, 329, 675
Rozo, E., Wechsler, R. H., Rykoff, E. S., et al. 2010, ApJ, 708, 645
Rozo, E., Vikhlinin, A., & More, S. 2012, ApJ, 760, 67
Sehgal, N., Bode, P., Das, S., et al. 2010, ApJ, 709, 920
Sehgal, N., Addison, G., Battaglia, N., et al. 2013, ApJ, 767, 38
Sembolini, F., Yepes, G., De Petris, M., et al. 2013, MNRAS, 434, 2718
Springel, V., White, M., & Hernquist, L. 2001, ApJ, 562, 1086
Steigman, G. 2008 [arXiv:0807.3004]
Story, K. T., Reichardt, C. L., Hou, Z., et al. 2013, ApJ, 779, 86
Sunyaev, R. A., & Zeldovich, Y. B. 1970, Ap&SS, 7, 20
Swetz, D. S., Ade, P. A. R., Amiri, M., et al. 2011, ApJS, 194, 41
Taburet, N., Aghanim, N., Douspis, M., & Langer, M. 2009, MNRAS, 392, 1153
Taburet, N., Douspis, M., & Aghanim, N. 2010, MNRAS, 404, 1197
Tinker, J., Kravtsov, A. V., Klypin, A., et al. 2008, ApJ, 688, 709
Vikhlinin, A., Kravtsov, A., Forman, W., et al. 2006, ApJ, 640, 691
Vikhlinin, A., Burenin, R. A., Ebeling, H., et al. 2009a, ApJ, 692, 1033
Vikhlinin, A., Kravtsov, A. V., Burenin, R. A., et al. 2009b, ApJ, 692, 1060
Voit, G. M. 2005, Rev. Mod. Phys., 77, 207
von der Linden, A., Allen, M. T., Applegate, D. E., et al. 2014, MNRAS, 439, 2
Watson, W. A., Iliev, I. T., D'Aloisio, A., et al. 2013, MNRAS, 433, 1230
Weller, J., Battye, R. A., & Kneissl, R. 2002, Phys. Rev. Lett., 88, 231301
White, S. D. M., Navarro, J. F., Evrard, A. E., & Frenk, C. S. 1993, Nature, 366, 429
Willis, J. P., Clerc, N., Bremer, M. N., et al. 2013, MNRAS, 430, 134
Yang, H.-Y. K., Bhattacharya, S., & Ricker, P. M. 2010, ApJ, 725, 1124
Zeldovich, Y. B., & Sunyaev, R. A. 1969, Ap&SS, 4, 301
Zhang, Y.-Y., Okabe, N., Finoguenov, A., et al. 2010, ApJ, 711, 1033

---

[1] APC, AstroParticule et Cosmologie, Université Paris Diderot, CNRS/IN2P3, CEA/lrfu, Observatoire de Paris, Sorbonne Paris Cité, 10 rue Alice Domon et Léonie Duquet, 75205 Paris Cedex 13, France

[2] Aalto University Metsähovi Radio Observatory, Metsähovintie 114, 02540 Kylmälä, Finland

[3] Academy of Sciences of Tatarstan, Bauman Str., 20, Kazan, 420111 Republic of Tatarstan, Russia

[4] African Institute for Mathematical Sciences, 6-8 Melrose Road, Muizenberg, 7701 Rondebosch Cape Town, South Africa

[5] Agenzia Spaziale Italiana Science Data Center, c/o ESRIN, via Galileo Galilei, 00044 Frascati, Italy

[6] Agenzia Spaziale Italiana, Viale Liegi 26, 00198 Roma, Italy

[7] Astrophysics Group, Cavendish Laboratory, University of Cambridge, J J Thomson Avenue, Cambridge CB3 0HE, UK

[8] Astrophysics & Cosmology Research Unit, School of Mathematics, Statistics & Computer Science, University of KwaZulu-Natal, Westville Campus, Private Bag X54001, 4000 Durban, South Africa

[9] Atacama Large Millimeter/submillimeter Array, ALMA Santiago Central Offices, Alonso de Cordova 3107, Vitacura, Casilla 763 0355 Santiago, Chile
[10] CITA, University of Toronto, 60 St. George St., Toronto, ON M5S 3H8, Canada
[11] CNRS, IRAP, 9 Av. colonel Roche, BP 44346, 31028 Toulouse Cedex 4, France
[12] California Institute of Technology, Pasadena, California, USA
[13] Centre for Theoretical Cosmology, DAMTP, University of Cambridge, Wilberforce Road, Cambridge CB3 0WA UK
[14] Centro de Astrofísica, Universidade do Porto, Rua das Estrelas, 4150-762 Porto, Portugal
[15] Centro de Estudios de Física del Cosmos de Aragón (CEFCA), Plaza San Juan, 1, planta 2, 44001 Teruel, Spain
[16] Computational Cosmology Center, Lawrence Berkeley National Laboratory, Berkeley, California, USA
[17] Consejo Superior de Investigaciones Científicas (CSIC), 28006 Madrid, Spain
[18] DSM/Irfu/SPP, CEA-Saclay, 91191 Gif-sur-Yvette Cedex, France
[19] DTU Space, National Space Institute, Technical University of Denmark, Elektrovej 327, 2800 Kgs. Lyngby, Denmark
[20] Département de Physique Théorique, Université de Genève, 24 quai E. Ansermet, 1211 Genève 4, Switzerland
[21] Departamento de Física Fundamental, Facultad de Ciencias, Universidad de Salamanca, 37008 Salamanca, Spain
[22] Departamento de Física, Universidad de Oviedo, Avda. Calvo Sotelo s/n, 33007 Oviedo, Spain
[23] Department of Astronomy and Astrophysics, University of Toronto, 50 Saint George Street, Toronto, Ontario, Canada
[24] Department of Astronomy and Geodesy, Kazan Federal University, Kremlevskaya Str., 18, 420008 Kazan, Russia
[25] Department of Astrophysics/IMAPP, Radboud University Nijmegen, P.O. Box 9010, 6500 GL Nijmegen, The Netherlands
[26] Department of Electrical Engineering and Computer Sciences, University of California, Berkeley, California, USA
[27] Department of Physics & Astronomy, University of British Columbia, 6224 Agricultural Road, Vancouver, British Columbia, Canada
[28] Department of Physics and Astronomy, Dana and David Dornsife College of Letter, Arts and Sciences, University of Southern California, Los Angeles, CA 90089, USA
[29] Department of Physics and Astronomy, University College London, London WC1E 6BT, UK
[30] Department of Physics and Astronomy, University of Sussex, Brighton BN1 9QH, UK
[31] Department of Physics, Gustaf Hällströmin katu 2a, University of Helsinki, 00014 Helsinki, Finland
[32] Department of Physics, Princeton University, Princeton, New Jersey, USA
[33] Department of Physics, University of California, Berkeley, California, USA
[34] Department of Physics, University of California, One Shields Avenue, Davis, California, USA
[35] Department of Physics, University of California, Santa Barbara, California, USA
[36] Department of Physics, University of Illinois at Urbana-Champaign, 1110 West Green Street, Urbana, Illinois, USA
[37] Dipartimento di Fisica e Astronomia G. Galilei, Università degli Studi di Padova, via Marzolo 8, 35131 Padova, Italy
[38] Dipartimento di Fisica e Scienze della Terra, Università di Ferrara, Via Saragat 1, 44122 Ferrara, Italy
[39] Dipartimento di Fisica, Università La Sapienza, P. le A. Moro 2, 00185 Roma, Italy
[40] Dipartimento di Fisica, Università degli Studi di Milano, Via Celoria, 16, 20133 Milano, Italy
[41] Dipartimento di Fisica, Università degli Studi di Trieste, via A. Valerio 2, 34127 Trieste, Italy
[42] Dipartimento di Fisica, Università di Roma Tor Vergata, via della Ricerca Scientifica, 1, 00133 Roma, Italy
[43] Discovery Center, Niels Bohr Institute, Blegdamsvej 17, 2100 Copenhagen, Denmark
[44] Dpto. Astrofísica, Universidad de La Laguna (ULL), 38206 La Laguna, Tenerife, Spain
[45] European Southern Observatory, ESO Vitacura, Alonso de Cordova 3107, Vitacura, Casilla 19001 Santiago, Chile
[46] European Space Agency, ESAC, Planck Science Office, Camino bajo del Castillo, s/n, Urbanización Villafranca del Castillo, 28691 Villanueva de la Cañada, Madrid, Spain
[47] European Space Agency, ESTEC, Keplerlaan 1, 2201 AZ Noordwijk, The Netherlands
[48] Finnish Centre for Astronomy with ESO (FINCA), University of Turku, Väisäläntie 20, 21500 Piikkiö, Finland
[49] Haverford College Astronomy Department, 370 Lancaster Avenue, Haverford, Pennsylvania, USA
[50] Helsinki Institute of Physics, Gustaf Hällströmin katu 2, University of Helsinki, 00014 Helsinki, Finland
[51] INAF – Osservatorio Astrofisico di Catania, Via S. Sofia 78, 95123 Catania, Italy
[52] INAF – Osservatorio Astronomico di Padova, Vicolo dell'Osservatorio 5, 35122 Padova, Italy
[53] INAF – Osservatorio Astronomico di Roma, via di Frascati 33, 00040 Monte Porzio Catone, Italy
[54] INAF – Osservatorio Astronomico di Trieste, via G.B. Tiepolo 11, Trieste, Italy
[55] INAF/IASF Bologna, via Gobetti 101, 40129 Bologna, Italy
[56] INAF/IASF Milano, via E. Bassini 15, 20133 Milano, Italy
[57] INFN, Sezione di Bologna, via Irnerio 46, 40126 Bologna, Italy
[58] INFN, Sezione di Roma 1, Università di Roma Sapienza, Piazzale Aldo Moro 2, 00185 Roma, Italy
[59] IPAG: Institut de Planétologie et d'Astrophysique de Grenoble, Université Joseph Fourier, Grenoble 1/CNRS-INSU, UMR 5274, 38041 Grenoble, France
[60] ISDC Data Centre for Astrophysics, University of Geneva, Ch. d'Ecogia 16, 1290 Versoix, Switzerland
[61] IUCAA, Post Bag 4, Ganeshkhind, Pune University Campus, 411 007 Pune, India
[62] Imperial College London, Astrophysics group, Blackett Laboratory, Prince Consort Road, London, SW7 2AZ, UK
[63] Infrared Processing and Analysis Center, California Institute of Technology, Pasadena, CA 91125, USA
[64] Institut Néel, CNRS, Université Joseph Fourier Grenoble I, 25 rue des Martyrs, 38042 Grenoble, France
[65] Institut Universitaire de France, 103 bd Saint-Michel, 75005 Paris, France
[66] Institut d'Astrophysique Spatiale, CNRS (UMR 8617) Université Paris-Sud 11, Bâtiment 121, 91405 Orsay, France
[67] Institut d'Astrophysique de Paris, CNRS (UMR 7095), 98bis boulevard Arago, 75014 Paris, France
[68] Institute for Space Sciences, 07745 Bucharest-Magurale, Romania
[69] Institute of Astronomy and Astrophysics, Academia Sinica, 10617 Taipei, Taiwan
[70] Institute of Astronomy, University of Cambridge, Madingley Road, Cambridge CB3 0HA, UK
[71] Institute of Theoretical Astrophysics, University of Oslo, Blindern, 0315 Oslo, Norway
[72] Instituto de Astrofísica de Canarias, C/Vía Láctea s/n, 38200 La Laguna, Tenerife, Spain
[73] Instituto de Física de Cantabria (CSIC-Universidad de Cantabria), Avda. de los Castros s/n, 39005 Santander, Spain
[74] Jet Propulsion Laboratory, California Institute of Technology, 4800 Oak Grove Drive, Pasadena, California, USA
[75] Jodrell Bank Centre for Astrophysics, Alan Turing Building, School of Physics and Astronomy, The University of Manchester, Oxford Road, Manchester, M13 9PL, UK
[76] Kavli Institute for Cosmology Cambridge, Madingley Road, Cambridge, CB3 0HA, UK
[77] LAL, Université Paris-Sud, CNRS/IN2P3, 91898 Orsay, France
[78] LERMA, CNRS, Observatoire de Paris, 61 avenue de l'Observatoire, 75014 Paris, France

[79] Laboratoire AIM, IRFU/Service d'Astrophysique – CEA/DSM – CNRS – Université Paris Diderot, Bât. 709, CEA-Saclay, 91191 Gif-sur-Yvette Cedex, France
[80] Laboratoire Traitement et Communication de l'Information, CNRS (UMR 5141) and Télécom ParisTech, 46 rue Barrault, 75634 Paris Cedex 13, France
[81] Laboratoire de Physique Subatomique et de Cosmologie, Université Joseph Fourier Grenoble I, CNRS/IN2P3, Institut National Polytechnique de Grenoble, 53 rue des Martyrs, 38026 Grenoble Cedex, France
[82] Laboratoire de Physique Théorique, Université Paris-Sud 11 & CNRS, Bâtiment 210, 91405 Orsay, France
[83] Lawrence Berkeley National Laboratory, Berkeley, California, USA
[84] Max-Planck-Institut für Astrophysik, Karl-Schwarzschild-Str. 1, 85741 Garching, Germany
[85] Max-Planck-Institut für Extraterrestrische Physik, Giessenbachstraße, 85748 Garching, Germany
[86] McGill Physics, Ernest Rutherford Physics Building, McGill University, 3600 rue University, Montréal, QC, H3A 2T8, Canada
[87] MilliLab, VTT Technical Research Centre of Finland, Tietotie 3, Espoo, Finland
[88] Moscow Institute of Physics and Technology, Institutsky per., 9, 141700 Dolgoprudny, Russia
[89] Niels Bohr Institute, Blegdamsvej 17, 2100 Copenhagen, Denmark
[90] Observational Cosmology, Mail Stop 367-17, California Institute of Technology, Pasadena, CA, 91125, USA
[91] Optical Science Laboratory, University College London, Gower Street, London, UK
[92] SB-ITP-LPPC, EPFL, CH-1015 Lausanne, Switzerland
[93] SISSA, Astrophysics Sector, via Bonomea 265, 34136 Trieste, Italy
[94] SUPA, Institute for Astronomy, University of Edinburgh, Royal Observatory, Blackford Hill, Edinburgh EH9 3HJ, UK
[95] School of Physics and Astronomy, Cardiff University, Queens Buildings, The Parade, Cardiff, CF24 3AA, UK
[96] School of Physics and Astronomy, University of Nottingham, Nottingham NG7 2RD, UK
[97] Space Research Institute (IKI), Russian Academy of Sciences, Profsoyuznaya Str, 84/32, 117997 Moscow, Russia
[98] Space Sciences Laboratory, University of California, Berkeley, California, USA
[99] Special Astrophysical Observatory, Russian Academy of Sciences, Nizhnij Arkhyz, Zelenchukskiy region, 369167 Karachai-Cherkessian Republic, Russia
[100] Stanford University, Dept of Physics, Varian Physics Bldg, 382 Via Pueblo Mall, Stanford, California, USA
[101] Sub-Department of Astrophysics, University of Oxford, Keble Road, Oxford OX1 3RH, UK
[102] Tübitak National Observatory, Akdeniz University Campus, 07058 Antalya, Turkey
[103] Theory Division, PH-TH, CERN, 1211 Geneva 23, Switzerland
[104] UPMC Univ Paris 06, UMR7095, 98bis boulevard Arago, 75014 Paris, France
[105] Université de Toulouse, UPS-OMP, IRAP, 31028 Toulouse Cedex 4, France
[106] University Observatory, Ludwig Maximilian University of Munich, Scheinerstrasse 1, 81679 Munich, Germany
[107] University of Granada, Departamento de Física Teórica y del Cosmos, Facultad de Ciencias, 18071 Granada, Spain
[108] University of Miami, Knight Physics Building, 1320 Campo Sano Dr., Coral Gables, Florida, USA
[109] Warsaw University Observatory, Aleje Ujazdowskie 4, 00-478 Warszawa, Poland

Astronomy & Astrophysics manuscript no. szcosmo2014
August 26, 2015

Planck 2015 results. XXIV. Cosmology from Sunyaev-Zeldovich cluster counts

Planck Collaboration: P. A. R. Ade[92], N. Aghanim[65], M. Arnaud[79], M. Ashdown[75, 6], J. Aumont[65], C. Baccigalupi[91], A. J. Banday[102, 10],
R. B. Barreiro[71], J. G. Bartlett[1, 73], N. Bartolo[31, 72], E. Battaner[104, 105], R. Battye[74], K. Benabed[66, 101], A. Benoît[63], A. Benoit-Lévy[25, 66, 101],
J.-P. Bernard[102, 10], M. Bersanelli[34, 53], P. Bielewicz[102, 10, 91], A. Bonaldi[74]*, L. Bonavera[71], J. R. Bond[9], J. Borrill[15, 96], F. R. Bouchet[66, 94],
M. Bucher[1], C. Burigana[52, 32, 54], R. C. Butler[52], E. Calabrese[99], J.-F. Cardoso[80, 1, 66], A. Catalano[81, 78], A. Challinor[68, 75, 13], A. Chamballu[79, 17, 65],
R.-R. Chary[62], H. C. Chiang[28, 7], P. R. Christensen[88, 38], S. Church[98], D. L. Clements[61], S. Colombi[66, 101], L. P. L. Colombo[24, 73], C. Combet[81],
B. Comis[81], F. Couchot[76], A. Coulais[78], B. P. Crill[73, 12], A. Curto[6, 71], F. Cuttaia[52], L. Danese[91], R. D. Davies[74], R. J. Davis[74], P. de Bernardis[33],
A. de Rosa[52], G. de Zotti[49, 91], J. Delabrouille[1], F.-X. Désert[58], J. M. Diego[71], K. Dolag[103, 85], H. Dole[65, 64], S. Donzelli[53], O. Doré[73, 12],
M. Douspis[65], A. Ducout[66, 61], X. Dupac[41], G. Efstathiou[68], F. Elsner[25, 66, 101], T. A. Enßlin[85], H. K. Eriksen[69], E. Falgarone[78], J. Fergusson[13],
F. Finelli[52, 54], O. Forni[102, 10], M. Frailis[51], A. A. Fraisse[28], E. Franceschi[52], A. Frejsel[88], S. Galeotta[51], S. Galli[66], K. Ganga[1], M. Giard[102, 10],
Y. Giraud-Héraud[1], E. Gjerløw[69], J. González-Nuevo[71, 91], K. M. Górski[73, 106], S. Gratton[75, 68], A. Gregorio[35, 51, 57], A. Gruppuso[52],
J. E. Gudmundsson[28], F. K. Hansen[69], D. Hanson[86, 73, 9], D. L. Harrison[68, 75], S. Henrot-Versillé[76], C. Hernández-Monteagudo[14, 85], D. Herranz[71],
S. R. Hildebrandt[73, 12], E. Hivon[66, 101], M. Hobson[6], W. A. Holmes[73], A. Hornstrup[18], W. Hovest[85], K. M. Huffenberger[26], G. Hurier[65],
A. H. Jaffe[61], T. R. Jaffe[102, 10], W. C. Jones[28], M. Juvela[27], E. Keihänen[27], R. Keskitalo[15], T. S. Kisner[83], R. Kneissl[40, 8], J. Knoche[85],
M. Kunz[19, 65, 3], H. Kurki-Suonio[27, 47], G. Lagache[5, 65], A. Lähteenmäki[2, 47], J.-M. Lamarre[78], A. Lasenby[6, 75], M. Lattanzi[32], C. R. Lawrence[73],
R. Leonardi[41], J. Lesgourgues[100, 90, 77], F. Levrier[78], M. Liguori[31, 72], P. B. Lilje[69], M. Linden-Vørnle[18], M. López-Caniego[41, 71], P. M. Lubin[29],
J. F. Macías-Pérez[81], G. Maggio[51], D. Maino[34, 53], N. Mandolesi[52, 32], A. Mangilli[65, 76], P. G. Martin[9], E. Martínez-González[71], S. Masi[33],
S. Matarrese[31, 72, 44], P. Mazzotta[36], P. McGehee[62], P. R. Meinhold[29], A. Melchiorri[33, 55], J.-B. Melin[17], L. Mendes[41], A. Mennella[34, 53],
M. Migliaccio[68, 75], S. Mitra[60, 73], M.-A. Miville-Deschênes[65, 9], A. Moneti[66], L. Montier[102, 10], G. Morgante[52], D. Mortlock[61], A. Moss[93],
D. Munshi[92], J. A. Murphy[87], P. Naselsky[88, 38], F. Nati[28], P. Natoli[32, 4, 52], C. B. Netterfield[21], H. U. Nørgaard-Nielsen[18], F. Noviello[74],
D. Novikov[84], I. Novikov[88, 84], C. A. Oxborrow[18], F. Paci[91], L. Pagano[33, 55], F. Pajot[65], D. Paoletti[52, 54], B. Partridge[46], F. Pasian[51], G. Patanchon[1],
T. J. Pearson[12, 62], O. Perdereau[76], L. Perotto[81], F. Perrotta[91], V. Pettorino[45], F. Piacentini[33], M. Piat[1], E. Pierpaoli[24], D. Pietrobon[73],
S. Plaszczynski[76], E. Pointecouteau[102, 10], G. Polenta[4, 50], L. Popa[67], G. W. Pratt[79], G. Prézeau[12, 73], S. Prunet[66, 101], J.-L. Puget[65], J. P. Rachen[22, 85],
R. Rebolo[70, 16, 39], M. Reinecke[85], M. Remazeilles[74, 65, 1], C. Renault[81], A. Renzi[37, 56], I. Ristorcelli[102, 10], G. Rocha[73, 12], M. Roman[1], C. Rosset[1],
M. Rossetti[34, 53], G. Roudier[1, 78, 73], J. A. Rubiño-Martín[70, 39], B. Rusholme[62], M. Sandri[52], D. Santos[81], M. Savelainen[27, 47], G. Savini[89], D. Scott[23],
M. D. Seiffert[73, 12], E. P. S. Shellard[13], L. D. Spencer[92], V. Stolyarov[6, 75, 97], R. Stompor[1], R. Sudiwala[92], R. Sunyaev[85, 95], D. Sutton[68, 75],
A.-S. Suur-Uski[27, 47], J.-F. Sygnet[66], J. A. Tauber[42], L. Terenzi[43, 52], L. Toffolatti[20, 71, 52], M. Tomasi[34, 53], M. Tristram[76], M. Tucci[19], J. Tuovinen[11],
M. Türler[59], G. Umana[48], L. Valenziano[52], J. Valiviita[27, 47], B. Van Tent[82], P. Vielva[71], F. Villa[52], L. A. Wade[73], B. D. Wandelt[66, 101, 30],
I. K. Wehus[73], J. Weller[103], S. D. M. White[85], D. Yvon[17], A. Zacchei[51], and A. Zonca[29]

(Affiliations can be found after the references)

Received ; accepted

ABSTRACT

We present cluster counts and corresponding cosmological constraints from the *Planck* full mission data set. Our catalogue consists of 439 clusters detected via their Sunyaev-Zeldovich (SZ) signal down to a signal-to-noise of six, and is more than a factor of two larger than the 2013 *Planck* cluster cosmology sample. The counts are consistent with those from 2013 and yield compatible constraints under the same modelling assumptions. Taking advantage of the larger catalogue, we extend our analysis to the two-dimensional distribution in redshift and signal-to-noise. We use mass estimates from two recent studies of gravitational lensing of background galaxies by Planck clusters to provide priors on the hydrostatic bias parameter, $1-b$. In addition, we use lensing of cosmic microwave background (CMB) temperature fluctuations by *Planck* clusters as a third independent constraint on this parameter. These various calibrations imply constraints on the present-day amplitude of matter fluctuations in varying degrees of tension with those coming from Planck analysis of primary fluctuations in the CMB; for the lowest estimated values of $1-b$ the tension is mild, only a little over one standard deviation, while for the largest estimated value it remains substantial. We also examine constraints on extensions to the base flat ΛCDM model by combining the cluster and CMB constraints. The combination appears to favour non-minimal neutrino masses, but this possibility does little to relieve the overall tension because it simultaneously lowers the implied value of the Hubble parameter, thereby exacerbating the discrepancy with most current astrophysical estimates. Improving the precision of cluster mass calibrations from the current 10%-level to 1% would significantly strengthen these combined analyses and provide a stringent test of the base ΛCDM model.

1. Introduction

Galaxy cluster counts are a standard cosmological tool that has found powerful application in recent Sunyaev-Zeldovich (SZ) surveys performed by the Atacama Cosmology Telescope (ACT, Swetz et al. 2011; Hasselfield et al. 2013), the South Pole Telescope (SPT, Carlstrom et al. 2011; Benson et al. 2013; Reichardt et al. 2013; Bocquet et al. 2014), and the *Planck* satellite[1] (Tauber et al. 2010; Planck Collaboration I 2011). The abun-

---

* Corresponding authors:
A. Bonaldi, `anna.bonaldi@manchester.ac.uk`
M. Roman, `matthieu.roman@apc.univ-paris7.fr`

[1] *Planck* (`http://www.esa.int/Planck`) is a project of the European Space Agency (ESA) with instruments provided by two scientific consortia funded by ESA member states and led by Principal Investigators from France and Italy, telescope reflectors provided through a

dance of clusters and its evolution are sensitive to the cosmic matter density, $\Omega_{\rm m}$, and the present amplitude of density fluctuations, characterised by σ_8, the rms linear overdensity in spheres of radius $8h^{-1}$ Mpc. The primary cosmic microwave background (CMB) anisotropies, on the other hand, reflect the density perturbation power spectrum at the time of recombination. This difference is important because a comparison of the two tests the evolution of density perturbations from recombination until today, enabling us to look for possible extensions to the base ΛCDM model, such as non-minimal neutrino masses or non-zero curvature.

Launched on 14 May 2009, *Planck* scanned the entire sky twice a year from 12 August 2009 to 23 October 2013 at angular resolutions from 33′ to 5′with two instruments: the Low Frequency Instrument (LFI; Bersanelli et al. 2010; Mennella et al. 2011), covering bands centred at 30, 44, and 70 GHz, and the High Frequency Instrument (HFI; Lamarre et al. 2010; Planck HFI Core Team 2011), covering bands centred at 100, 143, 217, 353, 545, and 857 GHz.

A initial set of cosmology results appeared in 2013 based on the first 15.5 months of data (Planck Collaboration I 2014), including cosmological constraints from the redshift distribution of 189 galaxy clusters detected at signal-to-noise (SNR) > 7 (hereafter, our "first analysis" or the "2013 analysis", Planck Collaboration XX 2014). The present paper is part of the second set of cosmology results obtained from the full mission data set; it is based on an updated cluster sample introduced in an accompanying paper (the PSZ2, Planck Collaboration I 2015).

Our first analysis found fewer clusters than predicted by *Planck*'s base ΛCDM model, expressed as tension between the cluster constraints on $(\Omega_{\rm m}, \sigma_8)$ and those from the primary CMB anisotropies (Planck Collaboration XVI 2014). This could reflect the need for an extension to the base ΛCDM model, or indicate that clusters are more massive than determined by the SZ signal-mass scaling relation adopted in 2013.

The cluster mass scale is the largest source of uncertainty in interpretation of the cluster counts. We based our first analysis on X-ray mass proxies that rely on the assumption of hydrostatic equilibrium. Simulations demonstrate that this assumption can be violated by bulk motions in the gas or by nonthermal sources of pressure (e.g., magnetic fields or cosmic rays, Nagai et al. 2007; Piffaretti & Valdarnini 2008; Meneghetti et al. 2010). Systematics in the X-ray analyses (e.g., instrument calibration, temperature structure in the gas) could also bias the mass measurements significantly. We quantified our ignorance of the true mass scale of clusters with a mass bias parameter that was varied over the range $[0-30]$%, with a baseline value of 20% (see below for the definition of the mass bias), as suggested by numerical simulations (see the Appendix of Planck Collaboration XX 2014).

Gravitational lensing studies of the SZ signal-mass relation are particularly valuable in this context because they are independent of the dynamical state of the cluster (Marrone et al. 2012; Planck Collaboration Int. III 2013), although they also, of course, can be affected by systematic effects (e.g., Becker & Kravtsov 2011). New, more precise lensing mass measurements for *Planck* clusters have appeared since our 2013 analysis (von der Linden et al. 2014b; Hoekstra et al. 2015). We incorporate these new results as prior constraints on the mass bias in the present analysis. Two other improvements over 2013 are use of a larger cluster catalogue and analysis of the counts in signal-to-noise as well as redshift.

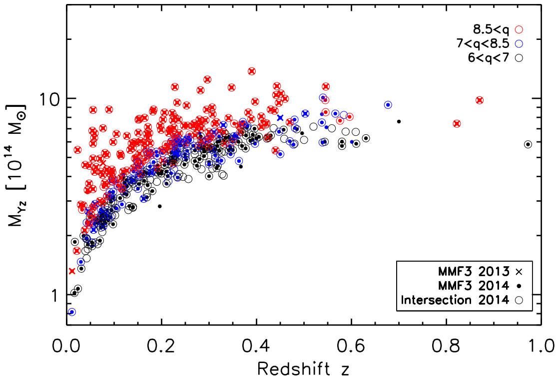

Fig. 1: Mass-redshift distribution of the *Planck* cosmological samples colour-coded by their signal-to-noise, q. The baseline MMF3 2015 cosmological sample is shown as the small filled circles. Objects which were in the MMF3 2013 cosmological sample are marked by crosses, while those in the 2015 intersection sample are shown as open circles. The final samples are defined by $q > 6$. The mass $M_{\rm Yz}$ is the *Planck* mass proxy (see text, Arnaud et al. 2015).

In addition, we apply a novel method to measure cluster masses through lensing of the CMB anisotropies. This method, presented in Melin & Bartlett (2014), enables us to use *Planck* data alone to constrain the cluster mass scale. It provides an important independent mass determination, which we compare to the galaxy lensing results, and one that is representative in the sense that it averages over the entire cluster cosmology sample, rather than a particularly chosen subsample.

Our conventions throughout the paper are as follows. We specify cluster mass, M_{500}, as the total mass within a sphere of radius R_{500}, defined as the radius within which the mean mass over-density of the cluster is 500 times the cosmic critical density at its redshift, z: $M_{500} = (4\pi/3)R_{500}^3[500\rho_{\rm c}(z)]$, with $\rho_{\rm c}(z) = 3H^2(z)/(8\pi G)$, where $H(z)$ is the Hubble parameter with present-day value $H_0 = h \times 100$ km s^{-1} Mpc^{-1}. We give SZ signal strength, Y_{500}, in terms of the Compton y-profile integrated within a sphere of radius R_{500}, and we assume that all clusters follow the universal pressure profile of Arnaud et al. (2010). Density parameters are defined relative to the present-day critical density, e.g., $\Omega_{\rm m} = \rho_{\rm m}/\rho_{\rm c}(z = 0)$ for the total matter density, $\rho_{\rm m}$.

We begin in the next section with a presentation of the *Planck* 2015 cluster cosmology samples. In Sect. 3 we develop our model for the cluster counts in both redshift and signal-to-noise, including a discussion of the scaling relation, scatter and the sample selection function. Section 4 examines the overall cluster mass scale in light of recent gravitational lensing measurements; we also present our own calibration of the cluster mass scale based on lensing of the CMB temperature fluctuations. Construction of the cluster likelihood and selection of external data sets is detailed in Sect. 5. We present cosmological constraints in Sect. 6 and then summarize and discuss our results in Sect. 7. We examine the potential impact of different modeling uncertainties in the Appendix.

---

collaboration between ESA and a scientific consortium led and funded by Denmark, and additional contributions from NASA (USA).

2. The *Planck* cosmological samples

We detect clusters across the six highest frequency Planck bands (100 – 857 GHz) using two implementations of the multi-frequency matched filter (MMF3 and MMF1, Melin et al. 2006; Planck Collaboration XXIX 2014) and a Bayesian extension (PwS, Carvalho et al. 2009) that all incorporate the known (non-relativistic) SZ spectral signature and a model for the spatial profile of the signal. The latter is taken as the so-called universal pressure profile from Arnaud et al. (2010) — with the non standard self-similar scaling — and parameterized by an angular scale, θ_{500}.

We empirically characterize noise (all non-SZ signals) in localized sky patches (10° on a side for MMF3) using the set of cross-frequency power-spectra, we construct the filters with the resulting noise weights, and we then filter the set of six frequency maps over a range of cluster scales, θ_{500}, spanning 1–35 arcmin. The filter returns an estimate of Y_{500} for each scale, based on the adopted profile template, and sources are finally assigned the θ_{500} (and hence Y_{500}) of the scale that maximizes their signal-to-noise. Details are given in Planck Collaboration XXIX (2014) and in an accompanying paper introducing the *Planck* full-mission SZ catalogue (`PSZ2`, Planck Collaboration XXVII 2015).

We define two cosmological samples from the general `PSZ2` catalogues, one consisting of detections by the MMF3 matched filter and the other of objects detected by all three methods (the intersection catalogue). Both are defined by a signal-to-noise (denoted q throughout) cut of $q > 6$. We then apply a mask to remove regions of high dust emission and point sources, leaving 65% of the sky unmasked. The general catalogues, noise maps and masks can be downloaded from the Planck Legacy Archive[2].

The cosmological samples can be easily constructed from the `PSZ2` union and MMF3 catalogues. The MMF3 cosmology sample is the subsample of the MMF3 catalogue defined by $q > 6$ and for which the entry in the union catalogue has `COSMO`='T'. The intersection cosmology sample is defined from the union catalogue by the criteria `COSMO`='T', `PIPEDET`=111, and $q > 6$.

Fig. 1 shows the distribution of these samples in mass and redshift, together with the 2013 cosmology sample. The mass here is the *Planck* mass proxy, $M_{\rm Yz}$, defined in Arnaud et al. (2015) and taken from the `PSZ2` catalogue. It is calculated using the Planck size-flux posterior contours in conjunction with X-ray priors to break the size-flux degeneracy inherent to the large *Planck* beams (see, e.g. Fig. 16 of Planck Collaboration XXVII (2015)). The samples span masses in the range $[2-10]\times10^{14}\,M_\odot$ and redshifts from $z = 0$ to 1[3]. The MMF3 (intersection) sample contains 439 (493) detections. Note that the intersection catalogue has more objects than the MMF3 catalogue because of the different definitions of the signal-to-noise in the various catalogues. The signal-to-noise for the intersection catalogue corresponds to the highest signal-to-noise of the three detection algorithms (MMF1, MMF3 or PwS), while for the MMF3 catalogue we use its corresponding signal-to-noise. As a consequence, the lowest value for the MMF3 signal-to-noise in the intersection sample is 4.8. We note that, while being above our detection limit, the Virgo and the Perseus clusters are not part of our samples. This is because Virgo is too extended to be blindly detected by our algorithms and Perseus is close to a masked region.

The 2015 MMF3 cosmology sample contains all but one of the 189 clusters of the 2013 MMF3 sample. The missing cluster is PSZ1 980, which falls inside the 2015 point source mask. Six (14) redshifts are missing from the MMF3 (intersection) sample. Our analysis accounts for these by renormalizing the observed counts to redistribute the missing fraction uniformly across redshift. The small number of clusters with missing redshifts has no significant impact on our results.

We use the MMF3 cosmology sample at $q > 6$ for our baseline analysis and the intersection sample for consistency checks, as detailed in the Appendix. In particular, we show that the intersection sample yields equivalent constraints.

3. Modelling cluster counts

From the theoretical perspective, cluster abundance is a function of halo mass and redshift as specified by the mass function. Observationally, we detect clusters in *Planck* through their SZ signal strength or, equivalently, their signal-to-noise and measure their redshift with follow-up observations. The observed cluster counts are therefore a function of redshift, z, and signal-to-noise, q. While we restricted our 2013 cosmology analysis to the redshift distribution alone (Planck Collaboration XX 2014), the larger catalogue afforded by the full mission data set offers the possibility of an analysis in both redshift and signal-to-noise. We therefore develop the theory in terms of the joint distribution of clusters in the (z, q)-plane and then relate it to the more specific analysis of the redshift distribution to compare with our previous results.

3.1. *Counts as a function of redshift and signal-to-noise*

The distribution of clusters in redshift and and signal-to-noise can be written as

$$\frac{dN}{dzdq} = \int d\Omega_{\rm mask} \int dM_{500}\, \frac{dN}{dzdM_{500}d\Omega}\, P[q|\bar{q}_{\rm m}(M_{500}, z, l, b)], \tag{1}$$

with

$$\frac{dN}{dzdM_{500}d\Omega} = \frac{dN}{dVdM_{500}}\frac{dV}{dzd\Omega}, \tag{2}$$

i.e., the dark matter halo mass function times the volume element. We adopt the mass function from Tinker et al. (2008) throughout, apart from the Appendix where we compare to the Watson et al. (2013) mass function as a test of modelling robustness; there, we show that the Watson et al. (2013) mass function yields constraints similar to those from the Tinker et al. (2008) mass function, but shifted by about 1σ towards higher Ω_m and lower σ_8 along the main degeneracy line.

The quantity $P[q|\bar{q}_{\rm m}(M_{500}, z, l, b)]$ is the distribution of q given the mean signal-to-noise value, $\bar{q}_{\rm m}(M_{500}, z, l, b)$, predicted by the model for a cluster of mass M_{500} and redshift z located at Galactic coordinates (l, b)[4]. This latter quantity is defined as the ratio of the mean SZ signal expected of a cluster, $\bar{Y}_{500}(M_{500}, z)$, as given in Eq. (7), and the detection filter noise, $\sigma_{\rm f}[\bar{\theta}_{500}(M_{500}, z), l, b]$:

$$\bar{q}_{\rm m} \equiv \bar{Y}_{500}(M_{500}, z)/\sigma_{\rm f}[\bar{\theta}_{500}(M_{500}, z), l, b]. \tag{3}$$

The filter noise depends on sky location (l, b) and the cluster angular size, $\bar{\theta}_{500}$, which introduces additional dependence on

---

[2] http://pla.esac.esa.int/pla/aio/planckProducts.html

[3] We fix $h = 0.7$ and $\Omega_\Lambda = 1 - \Omega_{\rm m} = 0.7$ for the mass calculation.

[4] Note that this form assumes, as we do throughout, that the distribution depends on z and M_{500} only through the mean value $\bar{q}_{\rm m}$; specifically, that the intrinsic scatter, $\sigma_{\ln Y}$, of Eq. (9) is constant.

mass and redshift. More detail on $\sigma_{\rm f}$ can be found in Planck Collaboration XX (2014) (see in particular Fig. 4 therein).

The distribution $P[q|\bar{q}_{\rm m}]$ incorporates noise fluctuations and intrinsic scatter in the actual cluster Y_{500} around the mean value, $\bar{Y}_{500}(M_{500}, z)$, predicted from the scaling relation. We discuss this scaling relation and our log-normal model for the intrinsic scatter below, and Sect. 4 examines the calibration of the overall mass scale for the scaling relation.

The redshift distribution of clusters detected at $q > q_{\rm cat}$ is the integral of Eq. (1) over signal-to-noise,

$$\begin{aligned} \frac{dN}{dz}(q > q_{\rm cat}) &= \int_{q_{\rm cat}}^{\infty} dq\, \frac{dN}{dzdq} \\ &= \int d\Omega \int dM_{500}\, \hat{\chi}(M_{500}, z, l, b)\, \frac{dN}{dzdM_{500}d\Omega}, \end{aligned} \tag{4}$$

with

$$\hat{\chi}(M_{500}, z, l, b) = \int_{q_{\rm cat}}^{\infty} dq\, P[q|\bar{q}_{\rm m}(M_{500}, z, l, b)]. \tag{5}$$

Equation (4) is equivalent to the expression used in our 2013 analysis if we write it in the form

$$\hat{\chi} = \int d\ln Y_{500} \int d\theta_{500} P(\ln Y_{500}, \theta_{500}|z, M_{500})\, \chi(Y_{500}, \theta_{500}, l, b), \tag{6}$$

where $\chi(Y_{500}, \theta_{500}, l, b)$ is the survey selection function at $q > q_{\rm cat}$ in terms of true cluster parameters (Sect. 3.3), and $P(\ln Y_{500}, \theta_{500}|z, M_{500})$ is the distribution of these parameters given cluster mass and redshift. We specify the relation between Eq. (5) and Eq. (6) in the next section.

3.2. Observable-mass relations

A crucial element of our modelling is the relation between cluster observables, Y_{500} and θ_{500}, and halo mass and redshift. Due to intrinsic variations in cluster properties, this relation is described by a distribution function, $P(\ln Y_{500}, \theta_{500}|M_{500}, z)$, whose mean values are specified by the scaling relations $\bar{Y}_{500}(M_{500}, z)$ and $\bar{\theta}_{500}(M_{500}, z)$.

We use the same form for these scaling relations as in our 2013 analysis:

$$E^{-\beta}(z) \left[\frac{D_{\rm A}^2(z) \bar{Y}_{500}}{10^{-4}\,{\rm Mpc}^2}\right] = Y_* \left[\frac{h}{0.7}\right]^{-2+\alpha} \left[\frac{(1-b)\, M_{500}}{6 \times 10^{14}\,{\rm M}_\odot}\right]^{\alpha}, \tag{7}$$

and

$$\bar{\theta}_{500} = \theta_* \left[\frac{h}{0.7}\right]^{-2/3} \left[\frac{(1-b)\, M_{500}}{3 \times 10^{14} {\rm M}_\odot}\right]^{1/3} E^{-2/3}(z) \left[\frac{D_{\rm A}(z)}{500\,{\rm Mpc}}\right]^{-1}, \tag{8}$$

where $\theta_* = 6.997\,{\rm arcmin}$, and fiducial ranges for the parameters Y_*, α, and β are listed in Table 1; these values are identical to those used in our 2013 analysis. Unless otherwise stated, we use Gaussian distributions with mean and standard deviation given by these values as prior constraints; one notable exception will be when we simultaneously fit for α and cosmological parameters. In the above expressions, $D_{\rm A}(z)$ is the angular diameter distance and $E(z) \equiv H(z)/H_0$.

These scaling relations have been established by X-ray observations, as detailed in the Appendix of Planck Collaboration XX (2014), and rely on mass determinations, $M_{\rm X}$, based on hydrostatic equilibrium of the intra-cluster gas. The *mass bias* parameter, b, assumed to be constant in both mass and redshift, allows for any difference between the X-ray determined masses and true cluster halo mass: $M_{\rm X} = (1-b)M_{500}$. This is discussed at length in Sect. 4.

Table 1: Summary of SZ-mass scaling law parameters (see Eq. 7).

Parameter	Value
$\log Y_*$	-0.19 ± 0.02
α [a]	1.79 ± 0.08
β [b]	0.66 ± 0.50
$\sigma_{\ln Y}$ [c]	0.127 ± 0.023

[a] Except when specified, α is constrained by this prior in our one-dimensional likelihood over $N(z)$, but left free in our two-dimensional likelihood over $N(z, q)$.

[b] We fix β to its central value throughout, except when examining modelling uncertainties in the Appendix.

[c] The value is the same as in our 2013 analysis, given here in terms of the natural logarithm and computed from $\sigma_{\log Y} = 0.075 \pm 0.01$.

We adopt a log-normal distribution for Y_{500} around its mean value $\bar{Y}_{500}$, and a delta function for θ_{500} centred on $\bar{\theta}_{500}$:

$$\begin{aligned} P(\ln Y_{500}, \theta_{500}|M_{500}, z) &= \frac{1}{\sqrt{2\pi}\sigma_{\rm lnY}} e^{-\ln^2(Y_{500}/\bar{Y}_{500})/(2\sigma^2_{\rm lnY})} \\ &\times \delta[\theta_{500} - \bar{\theta}_{500}], \end{aligned} \tag{9}$$

where $\bar{Y}_{500}(M_{500}, z)$ and $\bar{\theta}_{500}(M_{500}, z)$ are given by Eqs. (7) and (8)[5] The δ-function maintains the empirical definition of R_{500} that is used in observational determination of the the profile.

We can now specify the relation between Eqs. (5) and (6) by noting that

$$P[q|\bar{q}_{\rm m}(M_{500}, z, l, b)] = \int d\ln q_{\rm m} P[q|q_{\rm m}] P[\ln q_{\rm m}|\bar{q}_{\rm m}], \tag{10}$$

where $P[q|q_{\rm m}]$ is the distribution of observed signal-to-noise, q, given the model value, $q_{\rm m}$. The second distribution represents intrinsic cluster scatter, which we write in terms of our observable-mass distribution, Eq. (9), as

$$\begin{aligned} P[\ln q_{\rm m}|\bar{q}_{\rm m}] &= \int d\theta_{500} P[\ln Y_{500}(\ln q_{\rm m}, \theta_{500}, l, b), \theta_{500}|M_{500}, z] \\ &= \frac{1}{\sqrt{2\pi}\sigma_{\rm lnY}} e^{-\ln^2(q_{\rm m}/\bar{q}_{\rm m})/2\sigma^2_{\rm lnY}}. \end{aligned} \tag{11}$$

Performing the integral of Eq. (5), we find

$$\hat{\chi} = \int d\ln q_{\rm m} P[\ln q_{\rm m}|\bar{q}_{\rm m}] \chi(Y_{500}, \theta_{500}, l, b), \tag{12}$$

with the definition of our survey selection function

$$\chi(Y_{500}, \theta_{500}, l, b) = \int_{q_{\rm cat}}^{\infty} dq P[q|q_{\rm m}(Y_{500}, \theta_{500}, l, b)]. \tag{13}$$

We then reproduce Eq. (6) by using the first line of Eq. (11) and Eq. (3).

---

[5] In this paper, 'ln' denotes the natural logarithm and 'log' the logarithm to base 10; the expression is written in terms of the natural logarithm.

3.3. Selection function and survey completeness

The fundamental quantity describing the survey selection is $P[q|q_{\rm m}]$, introduced in Eq. (10). It gives the observed signal-to-noise, used to select SZ sources, as a function of model ("true") cluster parameters through $q_{\rm m}(Y_{500}, \theta_{500}, l, b)$, and it defines the *survey selection function* $\chi(Y_{500}, \theta_{500}, l, b)$ via Eq. (13). We characterize the survey selection in two ways. The first is with an analytical model and the second employs a Monte Carlo extraction of simulated sources injected into the *Planck* maps. In addition, we perform an external validation of our selection function using known X-ray clusters.

The analytical model assumes pure Gaussian noise, in which case we simply have $P[q|q_{\rm m}] = e^{-(q-q_{\rm m})^2/2}/\sqrt{2\pi}$. The survey selection function is then given by the Error Function (ERF),

$$\chi(Y_{500}, \theta_{500}, l, b) = \frac{1}{2}\left[1 - {\rm erf}\left(\frac{q_{\rm cat} - q_{\rm m}(Y_{500}, \theta_{500}, l, b)}{\sqrt{2}}\right)\right]. \quad (14)$$

This model can be applied to a catalogue with well-defined noise properties, i.e., $\sigma_{\rm f}$, such as our MMF3 catalogue, but not to the intersection catalogue based on the simultaneous detection with three different methods. This is our motivation for choosing the MMF3 catalogue as our baseline.

In the Monte Carlo approach, we inject simulated clusters directly into the *Planck* maps and (re)extract them with the complete detection pipeline. Details are given in the accompanying 2015 SZ catalogue paper, Planck Collaboration XXVII (2015). This method provides a more comprehensive description of the survey selection by accounting for a variety of effects beyond noise. In particular, we vary the shape of the SZ profile at fixed Y_{500} and θ_{500} to quantify its effect on catalogue completeness.

We also perform an external check of the survey completeness using known X-ray clusters from the MCXC compilation (Piffaretti et al. 2011) and also SPT clusters from Bleem et al. (2014). Details are given in the 2015 SZ catalogue paper, Planck Collaboration XXVII (2015). For the MCXC compilation, we rely on the expectation that at redshifts $z < 0.2$ any *Planck*-detected cluster should be found in one of the ROSAT catalogues (Chamballu et al. 2012), because at low redshift ROSAT probes to lower masses than *Planck*[6]. The MCXC catalogue provides a truth table, replacing the input cluster list of the simulations, and we compute completeness as the ratio of objects in the cosmology catalogue to the total number of clusters. As discussed in Planck Collaboration XXVII (2015), the results are consistent with Gaussian noise and bound the possible effect of profile variations. We arrive at the same conclusion when applying the technique to the SPT catalogue.

Planck Collaboration XXVII (2015) discusses completeness checks in greater detail. One possible source of bias is the presence of correlated IR emission from cluster member galaxies. Planck Collaboration XXIII (2015) suggests that IR point sources may contribute significantly to the cluster SED at the Planck frequencies, especially at higher redshift. The potential impact of this effect warrants further study in future work.

This gives us different estimations of the selection function for MMF3 and the intersection catalogues. We test the sensitivity of our cosmological constraints to the selection function in the Appendix by comparing results obtained with the different methods and catalogues. We find that our results are insensitive to the choice of completeness model (Fig A.1), and we therefore adopt the analytical ERF completeness function for simplicity throughout the paper.

4. The cluster mass scale

The characteristic mass scale of our cluster sample is the critical element in our analysis of the counts. It is controlled by the mass bias factor, $1 - b$, accounting for any difference between the X-ray mass proxies used to establish the scaling relations and the true (halo) mass: $M_{\rm X} = (1-b)M_{500}$. Such a difference could arise from cluster physics, such as a violation of hydrostatic equilibrium or temperature structure in the gas, from observational effects, e.g., instrumental calibration, or from selection effects biasing the X-ray samples relative to SZ- or mass-selected samples (Angulo et al. 2012).

In our 2013 analysis, we adopted a flat prior on the mass bias over the range $1 - b = [0.7, 1.0]$, with a reference model defined by $1-b = 0.8$. This was motivated by a comparison of the $Y-M_{\rm X}$ relation with published $Y - M$ relations derived from numerical simulations, as detailed in the Appendix of Planck Collaboration XX (2014); this estimate was consistent with most predictions for any violation of hydrostatic equilibrium (although not all) as well as observational constraints from the available lensing observations. Effects other than cluster physics can contribute to the mass bias, as discussed in the paper, and as emphasized by the survey of cluster multi-band scaling relations by Rozo et al. (2014a,b,c).

The mass bias was the largest uncertainty in our 2013 analysis, and it severely hampered understanding of the tension found between constraints from the primary CMB and the cluster counts. Here, we incorporate new lensing mass determinations of *Planck* clusters to constrain the mass bias. We also apply a novel method to measure object mass based on lensing of CMB temperature anisotropies behind clusters (Melin & Bartlett 2014). These constraints are used as prior information in our analysis of the counts. As we will see, however, uncertainty in the mass bias remains our largest source of uncertainty, mainly because these various determinations continue to differ from 10 to 30%.

In general, the mass bias could depend on cluster mass and redshift, although we will model it by a constant in the following. Our motivation is one of practicality: the limited size and precision of current lensing samples makes it difficult to constrain any more than a constant, i.e., the overall mass scale of our catalogue. Large lensing surveys like *Euclid*, WFIRST, and the Large Synoptic Survey Telescope, and CMB lensing will improve this situation in coming years.

4.1. Constraints from gravitational shear

Several cluster samples with high quality gravitational shear mass measurements have appeared since 2013. Among these, the Weighing the Giants (WtG, von der Linden et al. 2014a), CLASH (Postman et al. 2012; Merten et al. 2014; Umetsu et al. 2014), and the Canadian Cluster Comparison Project (CCCP, Hoekstra et al. 2015) programmes offer constraints on our mass bias factor, $1-b$, through direct comparison of the lensing masses to the *Planck* mass proxy, $M_{\rm Yz}$.

The analysis by the WtG programme of 22 clusters from the 2013 *Planck* cosmology sample yields $1 - b = 0.688 \pm 0.072$. Their result lies at the very extreme of the range explored in Planck Collaboration XX (2014) and would substantially reduce the tension found between primary CMB and galaxy cluster constraints. Hoekstra et al. (2015) report a smaller bias of

---

[6] In fact, this expectation is violated to a small degree. As discussed in Planck Collaboration XXVII (2015), there appears to be a small population of X-ray under-luminous clusters.

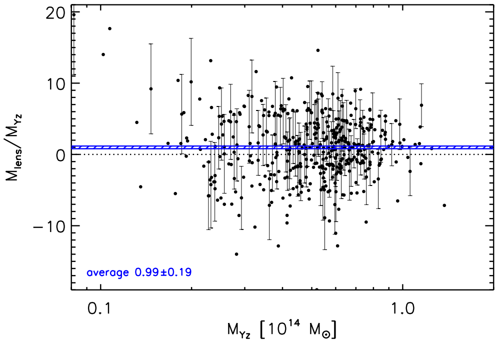

Fig. 2: The cluster mass scale determined by CMB lensing. We show the ratio of cluster lensing mass, $M_{\rm lens}$, to the SZ mass proxy, $M_{\rm Yz}$, as a function of the mass proxy for clusters in the MMF3 2015 cosmology sample. The cluster mass is measured through lensing of CMB temperature anisotropies in the *Planck* data (Melin & Bartlett 2014). Individual mass measurements have low signal-to-noise, but we determine a mean ratio for the sample of $M_{\rm lens}/M_{\rm Yz} = 1/(1-b) = 0.99 \pm 0.19$. For clarity, only a fraction of the error bars are plotted (see text).

$1-b = 0.78 \pm 0.07$ (stat) ± 0.06 (sys) for a set of 20 common clusters, which is in good agreement with the fiducial value adopted in our 2013 analysis. In our analysis we add the statistical and systematic uncertainties in quadrature (see Table 2).

4.2. Constraints from CMB lensing

Measuring cluster mass through CMB lensing has been discussed in the literature for some time since the study performed by Zaldarriaga & Seljak (1999) (see also Lewis & Challinor 2006). We apply a new technique for measuring cluster masses through lensing of CMB temperature anisotropies (Melin & Bartlett 2014), allowing us to calibrate the scaling relations using only *Planck* data. This is a valuable alternative to the galaxy lensing observations because it is independent and affected by different possible systematics. Additionally, we can apply it to the entire cluster sample to obtain a mass calibration representative of an SZ flux selected sample. Similar approaches using CMB lensing to measure halo masses were recently applied by SPT (Baxter et al. 2014) and ACT (Madhavacheril et al. 2014).

Our method first extracts a clean CMB temperature map with a constrained internal linear combination (ILC) of the *Planck* frequency channels in the region around each cluster; the ILC is constrained to nullify the SZ signal from the clusters themselves and provide a clean CMB map of 5 arcmin resolution. Using a quadratic estimator on the CMB map, we reconstruct the lensing potential in the field and then filter it to obtain an estimate of the cluster mass. The filter is an NFW profile (Navarro et al. 1997) with scale radius set by the *Planck* mass proxy for each cluster, and designed to return an estimate of the ratio $M_{\rm lens}/M_{\rm Yz}$, where $M_{\rm Yz}$ is the *Planck* SZ mass proxy. These individual measurements are corrected for any mean-field bias by subtracting identical filter measurements on blank fields; this accounts for effects of apodization over the cluster fields and correlated noise. The technique has been tested on realistic simulations of *Planck* frequency maps. More detail can be found in Melin & Bartlett (2014).

Table 2: Summary of mass scale priors

Prior name	Quantity	Value & Gaussian errors
Weighing the Giants (WtG)	$1-b$	0.688 ± 0.072
Canadian Cluster Comparison Project (CCCP)	$1-b$	0.780 ± 0.092
CMB lensing (LENS)	$1/(1-b)$	0.99 ± 0.19
Baseline 2013	$1-b$	$0.8\,[-0.1, +0.2]$

Notes. CMB lensing directly measures $1/(1-b)$, which we implement in our analysis; purely for reference, that constraint translates approximately to $1-b = 1.01^{+0.24}_{-0.16}$. The last line shows the 2013 baseline — a reference model defined by $1-b = 0.8$ with a flat prior in the [0.7, 1] range.

Figure 2 shows $M_{\rm lens}/M_{\rm Yz}$ as a function of $M_{\rm Yz}$ for all clusters in the MMF3 cosmology sample. Each point is an individual cluster[7]. For clarity, only some of the error bars on the ratio are shown; the error bars vary from 1.8 at the high mass end to 8.5 at the low mass end with a median of 4.2. There is no indication of a correlation between the ratio and $M_{\rm Yz}$, and we therefore fit for a constant ratio of $M_{\rm lens}/M_{\rm Yz}$ by taking the weighted mean (using the individual measurement uncertainties as provided by the filter) over the full data set. If the ratio differs from unity, we apply a correction to account for the fact that our filter aperture was not perfectly matched to the clusters. The correction is calculated assuming an NFW profile and is the order of a percent.

The final result is $1/(1-b) = 0.99 \pm 0.19$, traced by the blue band in the figure. Note that the method constrains $1/(1-b)$ rather than $1-b$ as in the case of the shear measurements. The calculated uncertainty on the weighted mean is consistent with a bootstrap analysis where we create new catalogues of the same size as the original by sampling objects from the original catalogue with replacement; the uncertainty from the bootstrap is then taken as the standard deviation of the bootstrap means.

4.3. Summary

The three mass bias priors are summarized in Table 2, and we will compare cosmological constraints obtained from each. We will assume Gaussian distributions for $1-b$ (gravitational shear) or $1/(1-b)$ (CMB lensing) with standard deviations given by the error column. We favour these three lensing results because of their direct comparison to the *Planck* mass proxy.

5. Analysis methodology

5.1. Likelihood

Our 2013 analysis employed a likelihood built on the cluster redshift distribution, dN/dz. With the larger 2015 catalogue, our baseline likelihood is now constructed on counts in the (z, q)-plane. We divide the catalogue into bins of size $\Delta z = 0.1$ (10 bins) and $\Delta \log q = 0.25$ (5 bins), each with an observed number $N(z_i, q_j) = N_{ij}$ of clusters. Modelling the observed counts, N_{ij}, as independent Poisson random variables, our log-likelihood is

$$\ln L = \sum_{i,j}^{N_z N_q} \left[N_{ij} \ln \bar{N}_{ij} - \bar{N}_{ij} - \ln[N_{ij}!] \right], \tag{15}$$

---

[7] The values can be negative due to noise fluctuations and the low signal-to-noise of the individual measurements.

where N_z and N_q are the total number of redshift and signal-to-noise bins, respectively. The mean number of objects in each bin is predicted by theory according to Eq. (1):

$$\bar{N}_{ij} = \frac{dN}{dzdq}(z_i, q_j)\Delta z \Delta q, \tag{16}$$

which depends on the cosmological (and cluster modelling) parameters. In practice, we use a Monte Carlo Markov chain (MCMC) to map the likelihood surface around the maximum and establish confidence limits.

Eq. (15) assumes the bins are uncorrelated, while a more complete description would include correlations due to large-scale clustering. In practice, our cluster sample contains mostly high mass systems for which the impact of these effects is weak (e.g., Hu & Kravtsov 2003, in particular their Fig. 4 for the impact on constraints in the (Ω_m,σ_8) plane).

5.2. External data sets

Cluster counts cannot constrain all pertinent cosmological parameters. They are most sensitive to $\Omega_{\rm m}$ and σ_8, and when analysing the counts alone we must apply additional observational constraints as priors on other parameters. For this purpose, we adopt Big Bang nucleosynthesis (BBN) constraints from Steigman (2008), $\Omega_b h^2 = 0.022 \pm 0.002$, and constraints from baryon acoustic oscillations (BAO). The latter combine the 6dF Galaxy Survey (Beutler et al. 2011), the SDSS Main Galaxy Sample (Padmanabhan et al. 2012; Anderson et al. 2012) and the BOSS DR11 (Anderson et al. 2014). We refer the reader to Sect. 5.2 in Planck Collaboration XIII (2015) for details of the combination. We also include a prior on n_s from Planck Collaboration XVI (2014), $n_s = 0.9624 \pm 0.014$. When explicitly specified in the text, we add the supernovæ constraint from SNLS-II and SNLS3: the Joint Light-curve Analysis constraint (JLA, Betoule et al. 2014). The BAO are particularly sensitive to H_0, while the supernovæ allow precise constraints on the dark energy equation-of-state parameter, w.

6. Cosmological constraints

We begin by verifying consistency with the results of Planck Collaboration XX (2014) (Sect. 6.1) based on the one-dimensional likelihood over the redshift distribution, dN/dz (Eq. 4). We then examine the effect of changing to the full two-dimensional likelihood, $dN/dzdq$ (Eq. 1) in Sect. 6.2. For this purpose we compare constraints on the total matter density, $\Omega_{\rm m}$, and the linear-theory amplitude of the density perturbations today, σ_8, using the cluster counts in combination with external data and fixing the mass bias.

The two-dimensional likelihood $dN/dzdq$ is then adopted as the baseline in the rest of the paper. We extract constraints on $\Omega_{\rm m}$ and σ_8 from the cluster counts in combination with external data, imposing the different cluster mass scale calibrations as prior distributions on the mass bias. After comparing these new constraints to those from the CMB anisotropies in the base ΛCDM model (Sect. 6.3), we move to joint analysis of the cluster counts and CMB anisotropies to study, for example, extensions to the base ΛCDM model, such as non-minimal neutrino mass (Sect. 6.4). In these studies we vary all six parameters of the (flat) base ΛCDM model, except when considering model extensions for which we include the relevant parameters. Figures display contours delineating marginalized constraints.

6.1. Constraints on $\Omega_{\rm m}$ and σ_8: comparison to 2013

Figure 3 presents constraints from the MMF3 cluster counts combined with the BAO and BBN priors of Sect. 5.2; we refer to this data combination as "SZ+BAO+BBN". To compare to results from our 2013 analysis (the grey, filled ellipses), we use a one-dimensional likelihood based on Eq. (4) over the redshift distribution and have adopted the reference scaling relation of 2013, i.e., Eqs. (7) and (8) with $1 - b = 0.8$. For the present comparison, we use the updated BAO constraints discussed in Sect. 5.2; these are stronger than the BAO constraints used in the 2013 analysis, and the grey contours shown here are consequently smaller than in Planck Collaboration XX (2014).

Limiting the 2015 catalogue to $q > 8.5$ produces a sample with 190 clusters, similar to the 2013 cosmology catalogue (189 objects). The two sets of constraints demonstrate good consistency, and they remain consistent while becoming tighter as we decrease the signal-to-noise threshold of the 2015 catalogue. Under similar assumptions, our 2015 analysis thus confirms the 2013 results reported in Planck Collaboration XX (2014).

The area of the ellipse from $q = 8.5$ to $q = 6$ decreases by a factor of 1.3. This is substantially less than the factor of 2.3 expected from the ratio of the number of objects in the two samples. This difference may be related to the decreasing goodness-of-fit of the best model as the signal-to-noise decreases.

Figure 4 overlays the observed cluster redshift distribution on the predictions from the best-fit model in each case. We see that the models do not match the counts in the second and third redshift bins (counting from $z = 0$), and that the discrepancy, already marginally present at the high signal-to-noise cut corresponding to the 2013 catalogue, becomes more pronounced towards the lower signal-to-noise thresholds. This dependence on signal-to-noise may suggest that the data prefer a different slope, α, of the scaling relation than allowed by the prior of Table 1. We explore the effect of relaxing the X-ray prior on α in the next section.

6.2. Constraints on $\Omega_{\rm m}$ and σ_8: two-dimensional analysis

In Fig. 5 we compare constraints from the one- and two-dimensional likelihood with α either free or with the prior of Table 1. For this comparison, we continue with the "SZ+BAO+BBN" data set, but adopt the CCCP prior for the mass bias and only consider the full 2015 MMF3 catalogue at $q > 6$.

The grey and black contours and lines show results from the one-dimensional likelihood fit to the redshift distribution using, respectively, the X-ray prior on α and leaving α free. The redshift counts do indeed favour a steeper slope, and we find a posterior of $\alpha = 2.28 \pm 0.17$ in the latter case.

We define a generalized χ^2 measure of goodness-of-fit as $\chi^2 = \sum_i^{N_z} \bar{N}_i^{-1} \left(N_i - \bar{N}_i\right)^2$, determining the probability to exceed (PTE) the observed value using Monte Carlo simulations of Poisson statistics for each bin with the best-fit model mean $\bar{N}_i$. The observed value of the fit drops from 17 ($PTE = 0.07$) with the X-ray prior, to 15 ($PTE = 0.11$) when leaving α free. When leaving α free, $\Omega_{\rm m}$ increases and σ_8 decreases, following their correlation with α shown by the contours, and their uncertainty increases due to the added parameter.

The two-dimensional likelihood over $dN/dzdq$ better constrains the slope when α is free, as shown by the violet curves and contours. In this case, the preferred value drops back towards the X-ray prior: $\alpha = 1.89 \pm 0.12$, just over $1\,\sigma$ from the central

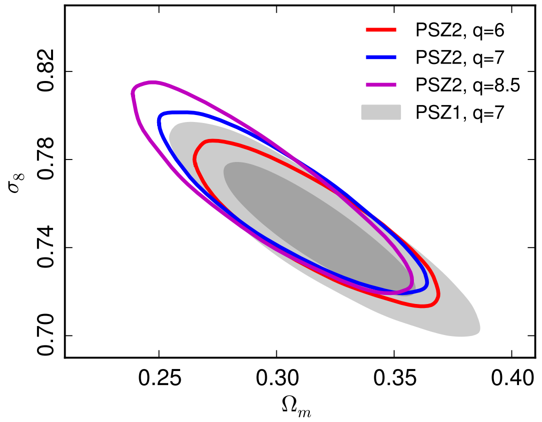

Fig. 3: Contours at 2σ for different signal-to-noise thresholds, $q = 8.5$, 7, and 6, applied to the 2015 MMF3 cosmology sample for the SZ+BAO+BBN data set. The contours are compatible with the 2013 constraints (Planck Collaboration XX 2014), shown as the filled, light grey ellipses at 1 and 2σ (for the BAO and BBN priors of Sect 5.2; see text). The 2015 catalogue thresholded at $q > 8.5$ has a similar number of clusters (190) as the 2013 catalogue (189). This comparison is made using the analytical error-function model for completeness and adopts the reference observable-mass scaling relation of the 2013 analysis [$1 - b = 0.8$, see text]. The redshift distributions of the best-fit models are shown in Fig. 4. For this figure and Fig. 4, we use the one-dimensional likelihood over the redshift distribution, dN/dz (Eq. 4).

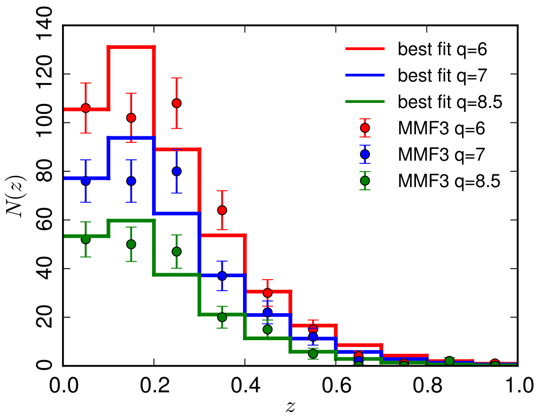

Fig. 4: Comparison of observed counts (points with error bars) with predictions of the best-fit models (solid lines) from the one-dimensional likelihood for three different thresholds applied to the 2015 MMF3 cosmology sample. The mismatch between observed and predicted counts in the second and third lowest redshift bins, already noticed in the 2013 analysis, increases at lower thresholds, q. The best-fit models are defined by the constraints shown in Fig. 3. For this figure and Fig. 3, we use our one-dimensional likelihood over the redshift distribution, dN/dz (Eq. 4).

X-ray value. Re-imposing the X-ray prior on α with the two-dimensional likelihood (blue curves) does little to change the parameter constraints. Although the one-dimensional likelihood prefers a steeper slope than the X-ray prior, the two-dimensional analysis does not, and the cosmological constraints remain robust to varying α.

We define a generalized χ^2 statistic as described above, now over the two-dimensional bins in the (z, q)-plane. This generalized χ^2 for the fit with the X-ray prior is 43 ($PTE = 0.28$), compared to $\chi^2 = 45$ ($PTE = 0.23$) when α is a free parameter.

Fig. 6 displays the redshift distribution of the best-fit models in all four cases. Despite their apparent difficulty in matching the second and third redshift bins, the PTE values suggest that these fits are moderately good to acceptable. Note that, as mentioned briefly in Sect. 5.1, clustering effects will increase the scatter in each bin slightly over the Poisson value we have assumed, causing our quoted PTE values to be somewhat smaller than the true ones.

6.3. Constraints on $\Omega_{\rm m}$ and σ_8: comparison to primary CMB

Our 2013 analysis brought to light tension between constraints on $\Omega_{\rm m}$ and σ_8 from the cluster counts and those from the primary CMB in the base ΛCDM model. In that analysis, we adopted a flat prior on the mass bias over the range $1 - b = [0.7, 1.0]$, with a reference model defined by $1 - b = 0.8$ (see discussion in the Appendix of Planck Collaboration XX 2014). Given the good consistency between the 2013 and 2015 cluster results (Fig. 3), we expect the tension to remain under the same assumptions concerning the mass bias.

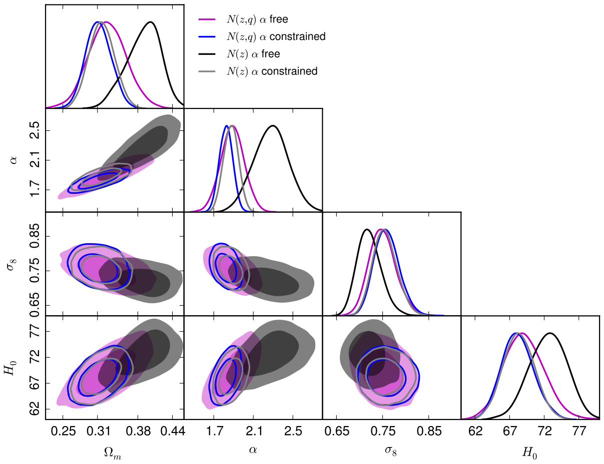

Fig. 5: Comparison of constraints from the one-dimensional (dN/dz) and two-dimensional ($dN/dzdq$) likelihoods on cosmological parameters and the scaling relation mass exponent, α. For this comparison, we adopt the CCCP prior on the mass bias and the SZ+BAO+BBN data set. The corresponding best-fit model redshift distributions are shown in Fig. 6.

Figure 7 compares our 2015 cluster constraints (MMF3 SZ+BAO+BBN) to those for the base ΛCDM model from the *Planck* CMB anisotropies. The cluster constraints, given the three different priors on the mass bias, are shown by the filled contours at 1 and 2σ, while the dashed black contours give the *Planck* TT, TE, EE+lowP constraints (hereafter *Planck* primary CMB, Planck Collaboration XIII 2015); the grey shaded regions add BAO to the CMB. The central value of the WtG mass prior lies at the extreme end of the range used in 2013 (i.e., 1-b=0.7);

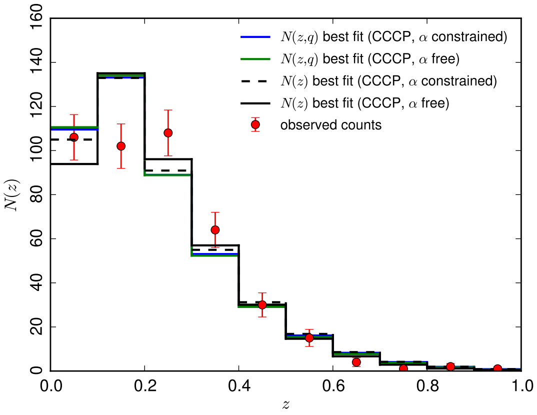

Fig. 6: Redshift distribution of best-fit models from the four analysis cases shown in Fig. 5. The observed counts in the MMF3 catalogue ($q > 6$) are plotted as the red points with error bars, and as in Fig. 5 we adopt the CCCP mass prior with the SZ+BAO+BBN data set.

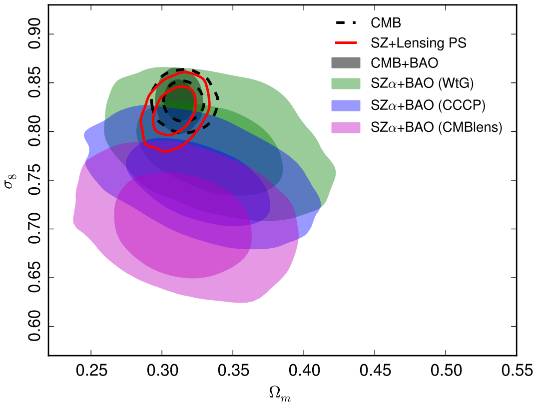

Fig. 7: Comparison of constraints from the CMB to those from the cluster counts in the $(\Omega_{\rm m}, \sigma_8)$-plane. The green, blue and violet contours give the cluster constraints (two-dimensional likelihood) at 1 and 2σ for the WtG, CCCP, and CMB lensing mass calibrations, respectively, as listed in Table 2. These constraints are obtained from the MMF3 catalogue with the SZ+BAO+BBN data set and α free. Constraints from the *Planck* TT, TE, EE+lowP CMB likelihood (hereafter, *Planck* primary CMB) are shown as the dashed contours enclosing 1 and 2σ confidence regions (Planck Collaboration XIII 2015), while the grey shaded region also include BAO. The red contours give results from a joint analysis of the cluster counts, primary CMB and the *Planck* lensing power spectrum (Planck Collaboration XV 2015), leaving the mass bias parameter free and α constrained by the X-ray prior.

with its uncertainty range extending even lower, the tension with primary CMB is greatly reduced, as pointed out by von der Linden et al. (2014b). With similar uncertainty but a central value shifted to $1 - b = 0.78$, the CCCP mass prior results in greater tension with the primary CMB. The lensing mass prior, finally, implies little bias and hence much greater tension.

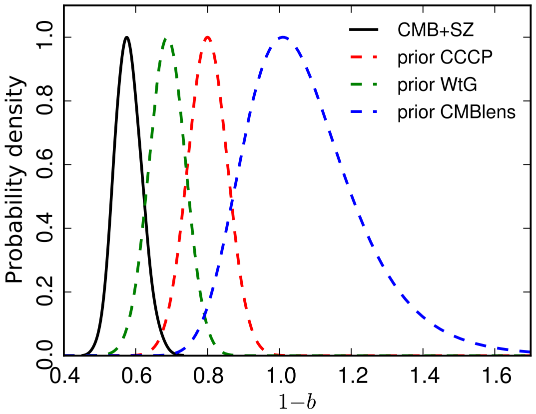

Fig. 8: Comparison of cluster and primary CMB constraints in the base ΛCDM model expressed in terms of the mass bias, $1 - b$. The solid black curve shows the distribution of values required to reconcile the counts and primary CMB in ΛCDM; it is found as the posterior on the $1 - b$ from a joint analysis of the *Planck* cluster counts and primary CMB when leaving the mass bias free. The coloured dashed curves show the three prior distributions on the mass bias listed in Tab. 2.

6.4. Joint Planck 2014 primary CMB and cluster constraints

We now turn to a joint analysis of the cluster counts and primary CMB. We begin by finding the mass bias required to remove tension with the primary CMB, and then consider one-parameter extensions to the base ΛCDM model, varying the curvature, the Thomson optical depth to reionization, the dark energy equation-of-state, and the neutrino mass scale. Unless otherwise stated, "CMB" in the following means *Planck* TT, TE, EE+lowP as defined in Planck Collaboration XIII (2015). All intervals are 68% confidence and all upper/lower limits are 95%.

6.4.1. Mass bias required by CMB

In Fig. 8 we compare the three prior distributions to the mass bias required by the primary CMB. The latter is obtained as the posterior on $(1 - b)$ from a joint analysis of the MMF3 cluster counts and the CMB with the mass bias as a free parameter. The best-fit value in this case is $(1 - b) = 0.58 \pm 0.04$, more than 1σ below the central WtG value. Perfect agreement with the primary CMB would imply that clusters are even more massive than the WtG calibration. This figure most clearly quantifies the tension between the *Planck* cluster counts and primary CMB.

6.4.2. Curvature

By itself the CMB only poorly determines the spatial curvature (Sect. 6.2.4 of Planck Collaboration XIII 2015), but by including another astrophysical observation, such as cluster counts, it can be tightly constrained. Our joint cluster and CMB analysis, without external data, yields $\Omega_{\rm k} = -0.012 \pm 0.008$, consistent with the constraint from *Planck* CMB and BAO $\Omega_{\rm k} = 0.000 \pm 0.002$.

6.4.3. Reionization optical depth

Primary CMB temperature anisotropies also provide a precise measurement of the parameter combination $A_{\rm s}e^{-2\tau}$, where τ is

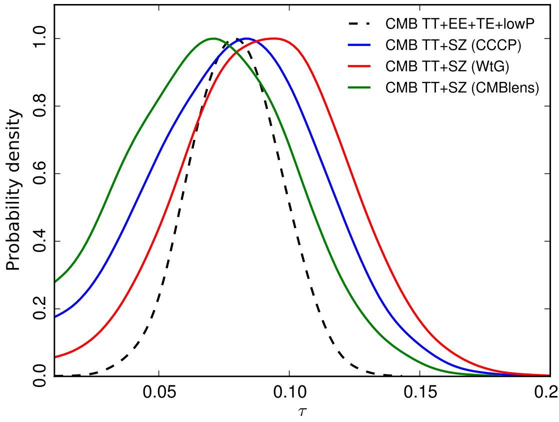

Fig. 9: Constraints on the reionization optical depth, τ. The dashed black curve is the constraint from *Planck* CMB (i.e. TT, TE, EE+lowP), while the three coloured lines are the posterior distribution on τ from a joint analysis of the cluster counts and *Planck* TT only for the three different mass bias parameters.

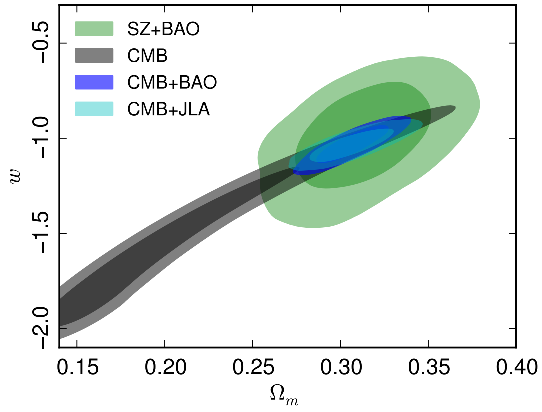

Fig. 10: Constraints on a constant dark energy equation-of-state parameter, w. Analysis of the primary CMB alone yields the grey contours that are highly degenerate. Adding either BAO or supernovae to the CMB breaks the degeneracy, giving constraints around $w = -1$. Adding SZ cluster counts from the MMF3 2015 catalogue instead to the CMB results in the rose-coloured contours. The green contours are constraints from joint analysis of the SZ counts and BAO; although much less constraining they agree with the CMB+JLA combinations and are completely independent.

the optical depth from Thomson scatter after reionization and A_s is the power spectrum normalization on large scales (Planck Collaboration XIII 2015). Low-ℓ polarization anisotropies break the degeneracy by constraining τ, but this measurement is delicate given the low signal amplitude and difficult systematic effects; it is important, however, in the determination of σ_8. It is therefore interesting to compare the *Planck* primary CMB constraints on τ to those from a joint analysis of the cluster counts and primary CMB without the low-ℓ polarization data (lowP). Battye et al. (2014), for instance, pointed out that a lower value for τ than suggested by WMAP could reduce the level of tension between CMB and large scale structure.

The comparison is shown in Fig. 9. We see that the *Planck* TT + SZ constraints are in good agreement with the value from *Planck* CMB (i.e., TT, TE, EE+lowP), with the preferred value for WtG slightly higher and CMB lensing pushing towards a lower value. The ordering CMB lensing/CCCP/WtG from lower to higher τ posterior values matches the decreasing level of tension with the primary CMB on σ_8. These values remain, however, larger than what is required to fully remove the tension in each case. The posterior distributions for the mass bias are $1 - b = 0.60 \pm 0.042$, $1 - b = 0.63 \pm 0.047$, $1 - b = 0.66 \pm 0.045$, respectively, for WtG, CCCP and CMB lensing, all significantly shifted from the corresponding priors of Table 2. Allowing τ to adjust offers only minor improvement in the tension reflected by Fig. 8. Interestingly, the *Planck* TT posterior shown in Fig. 8 of Planck Collaboration XIII (2015) peaks at significantly higher values, while our *Planck* TT +SZ constraints are consistent with the constraint from *Planck* TT + lensing, an independent constraint on τ without lowP.

6.4.4. Dark energy

In Fig. 10 we examine constraints on a constant dark energy equation-of-state parameter, w. Analysis of the primary CMB alone results in highly degenerate grey contours. The degeneracy is broken by adding constraints such as BAO (blue contours) or supernovae distances (light blue contours), both picking values around $w = -1$. The SZ counts (two-dimensional likelihood with CCCP prior) only marginally break the degeneracy when combined with the CMB, but when combined with BAO they do yield interesting constraints (green contours) that are consistent with the independent constraints from the primary CMB combined with supernovae. We obtain $\Omega_m = 0.313 \pm 0.025$ and $w = -1.00 \pm 0.18$ for SZ+BAO, and $\Omega_m = 0.306 \pm 0.013$ and $w = -1.10 \pm 0.06$ for CMB+BAO.

6.4.5. $\sum m_\nu$

An important, well-motivated extension to the base ΛCDM model that clusters can help constrain is a non-minimal sum of neutrino masses, $\sum m_\nu > 0.06$ eV. Given the primary CMB anisotropies, the amplitude of the density perturbations today, characterized by the equivalent linear theory extrapolation, σ_8, is model dependent; it is a derived parameter depending, for example, on the composition of the matter content of the universe. Cluster abundance, on the other hand, provides a direct measurement of σ_8 at low redshifts, and comparison to the value derived from the CMB tests the adopted cosmological model.

By free-streaming, neutrinos damp the growth of matter perturbations. Our discussion thus far has assumed the minimum mass for the three known neutrino species. Increasing their mass, $\sum m_\nu > 0.06$ eV, lowers σ_8 because the neutrinos have larger gravitational influence on the total matter perturbations. This goes in the direction of reconciling tension — the strength of which depends on the mass bias — between the cluster and primary CMB constraints. Cluster abundance, or any measure of σ_8 at low redshift, is therefore an important cosmological constraint to be combined with those from the primary CMB.

Figure 11 presents a joint analysis of the cluster counts for the CCCP mass bias prior with primary CMB, the *Planck* lensing power spectrum and BAO. The results without BAO (green and red shaded contours) allow relatively large neutrino masses, up to $\sum m_\nu \sim 0.5$ eV; and when adding the lensing power spectrum, a small, broad peak appears in the posterior distribution

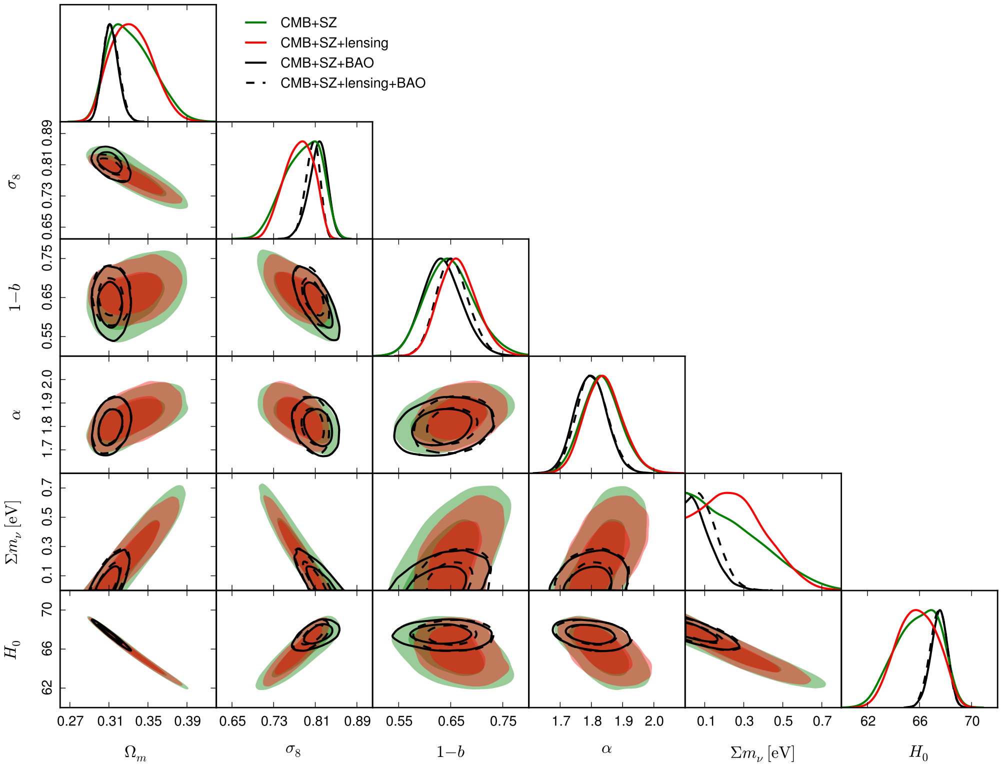

Fig. 11: Parameter constraints on the ΛCDM+non-minimal neutrino mass model. For this study, we adopt the CCCP prior on the mass bias (see Tab. 2) and leave the scaling exponent, α, free. The green and red shaded regions show, respectively, the 1 and 2σ confidence regions for joint analyses of the cluster counts using the primary CMB, and the primary CMB plus the lensing power spectrum. The solid and dashed black contours add to these two cases constraints from BAO.

just above $\sum m_\nu = 0.2$ eV. We also notice some interesting correlations: the amplitude, σ_8, anti-correlates with neutrino mass, as does the Hubble parameter, and larger values of α correspond to larger neutrino mass, lower H_0 and lower σ_8.

As discussed in detail in Planck Collaboration XIII (2015), the anti-correlation with the Hubble parameter maintains the observed acoustic peak scale in the primary CMB. Increasing neutrino mass to simultaneously accommodate the cluster and primary CMB constraints by lowering σ_8, while allowed in this joint analysis, would therefore necessarily increase tension with some direct measurements of H_0 (see discussion in Planck Collaboration XIII (2015)). Including the BAO data greatly restricts this possibility, as shown by the solid and dashed black curves.

The solid and dashed, red and black curves in Fig. 12 reproduce the marginalized posterior distributions on $\sum m_\nu$ from Fig. 11. The solid blue curve is the result of a similar analysis where in addition the artificial parameter A_L is allowed to vary. This parameter characterizes the amount of lensing in the temperature power spectrum relative to the best fit model (Planck Collaboration XIII 2015). *Planck* TT + lowP alone constraints

$$A_L = 1.22 \pm 0.10$$

in mild tension with the value predicted for the ΛCDM model, $A_L = 1$. In the base ΛCDM model, this parameter is fixed to unity, but it is important to note it is degenerate with $\sum m_\nu$. Left free, it allows less lensing power, which is also in line with the direct measurement of the lensing power spectrum (labelled as Lensing PS) from the four-point function (see Planck Collaboration XIII 2015). In that light, we see that adding A_L as a free parameter accentuates the peak in the CMB+SZ+Lensing PS posterior. The small internal tension between CMB+SZ and CMB+SZ+A_L posteriors may point towards a need for an extension of the minimal six-parameter ΛCDM.

These posteriors lead to the following constraints: $\sum m_\nu < 0.53$ eV (95%) for CMB+SZ+Lensing PS and $\sum m_\nu < 0.22$ eV (95%) for CMB+SZ+BAO.

We may compare these with the constraints from the primary CMB presented in Planck Collaboration XIII (2015). The *Planck* primary CMB by itself places an upper limit of $\sum m_\nu < 0.49$ eV (95%), and the addition of BAO tightens this to $\sum m_\nu < 0.17$ eV (95%). Addition of the *Planck* lensing power spectrum to the primary CMB weakens the constraint to $\sum m_\nu < 0.59$ eV (95%), as we would expect given the results and discussion above. The final constraint adopted by Planck Collaboration XIII (2015), for its robustness to possible remaining low level systematics in the polarization data, is $\sum m_\nu < 0.23$ eV (95%), not too different from the peak suggested in CMB+SZ+lensing PS posterior.

Adding neutrino mass should lower σ_8, letting it move towards values favoured by the cluster counts. We might expect that the CMB+SZ combination would therefore find clear evidence for non-minimal neutrino mass. In spite of this, the green curve only places an upper limit on $\sum m_\nu$. We may understand this by looking at the posterior on the mass bias $1 - b$. The allowed values are well separated from the prior distribution,

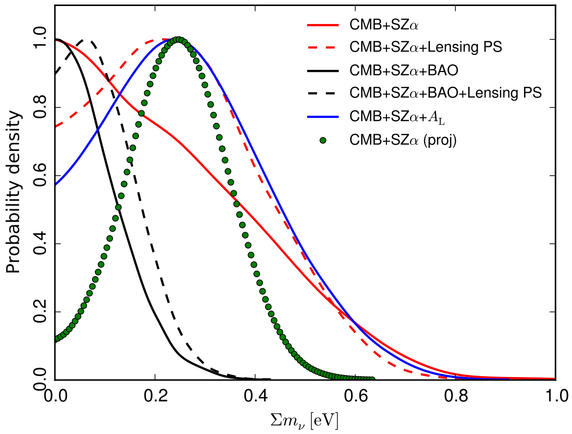

Fig. 12: Constraints on $\sum m_\nu$ from a joint analysis of the cluster counts and primary CMB. The solid and dashed, red and black lines reproduce the marginalized posterior distributions from Fig. 11. The solid blue line is the posterior from a similar analysis, but marginalized over the additional parameter $A_{\rm L}$ (see text). If applied to the present *Planck* cluster cosmology sample, a future mass calibration of $1 - b = 0.80 \pm 0.01$ would result in the bold, dotted black posterior curve.

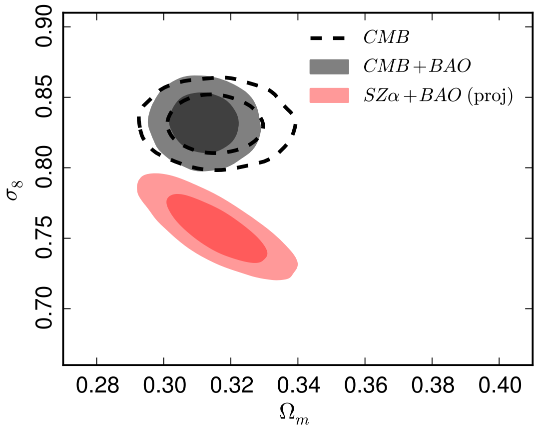

Fig. 13: Prediction of cluster constraints with a possible future mass bias prior of $1 - b = 0.80 \pm 0.01$. The black shaded region and dashed contours reproduce the current primary CMB and primary CMB+BAO constraints from *Planck* for the base ΛCDM model. The red shaded contours present the constraints expected from this mass bias prior applied to the present *Planck* cluster cosmology sample with the SZ+BAO+BBN data set.

meaning that the primary CMB has sufficient statistical weight to strongly override the prior. The lensing power spectrum, in favouring slightly lower σ_8, reinforces the cluster trend so that a peak appears in the posterior for $\sum m_\nu$ in the red curve; it is not enough, however, to bring the posterior on the mass bias in line with the prior. This indicates that the tension between the cluster and primary CMB constraints is not fully resolved.

One may then ask, how tight must the prior on the mass bias be to make a difference? To address this question, we performed an analysis assuming a projected tighter prior constraint on the mass bias. The informal target precision for cluster mass calibration with future large lensing surveys, such as *Euclid* and the Large Synoptic Survey Telescope, is 1%, and we consider the impact of a prior of $1 - b = 0.80 \pm 0.01$ on the present *Planck* cluster cosmology sample in Figs. 12 and 13.

The latter figure compares the constraints from cluster counts for this mass bias to the present primary CMB constraints in the $(\Omega_{\rm m}, \sigma_8)$-plane for the base ΛCDM model. The bold, black dotted curve in Fig. 12 shows the predicted posterior on the neutrino mass from a joint analysis of the present *Planck* cluster counts and primary CMB. The same prior on a much larger catalogue would demonstrate a corresponding increase in sensitivity to neutrino mass. This simple projection highlights the importance and value of the more precise cluster cosmology expected in the future, and it provides clear motivation for significant effort in mass calibration. This effort will continue with larger samples of clusters with gravitational shear measurements, and also with the new technique of CMB lensing cluster mass measurements.

7. Summary and discussion

Our 2015 analysis incorporates a number of improvements and new information relative to our first study in Planck Collaboration XX (2014). With more data, we have a larger cluster cosmology sample, increased by more than a factor of two, and we implement a two-dimensional likelihood over the counts in both redshift and signal-to-noise. We have also performed new tests of the selection function using MCXC and SPT cluster catalogs as truth tables. The selection function from these external checks and internal simulations of the *Planck* catalogue construction agree with each other and can be reasonably modelled by a simple analytical expression derived by assuming noise is the dominant factor (see the Appendix). One possible systematic effect that warrants further study is IR emission from cluster member galaxies. Finally, we have examined the implications of three recent determinations of the cluster mass bias parameter, $1 - b$. The two-dimensional likelihood with the 2015 catalogue and mass bias priors will be implemented in CosmoMC.

Our analysis confirms the results of the 2013 study. The counts are consistent with those of 2013, illustrated by the agreement in the constraints on $\Omega_{\rm m}$ and σ_8 when using the same SZ observable-mass relations (see Fig. 3). The gain in statistical precision is less than expected from the larger catalogue, which is likely related to the fact that the fit to the redshift distribution with the X-ray prior on α is only marginal. Our new two-dimensional approach yields consistent, but more robust constraints than the one-dimensional likelihood over just the redshift distribution; it is less sensitive to the slope of the scaling relation, α, and it provides a better fit to the counts than in the one-dimensional case.

Using the two-dimensional likelihood as our baseline, we extracted new cosmological constraints using three different cluster mass scales represented by the mass bias prior distributions given in Table 2. The first two come from galaxy shear observations of samples of *Planck* clusters. They differ by about 1σ, with the WtG result favoring larger mass bias. We have also implemented a novel method for measuring cluster masses based lensing of the CMB temperature anisotropies behind clusters (Melin & Bartlett 2014). It gives a mass bias averaged over the entire cluster cosmology sample, although with larger statistical uncertainty.

As a new method requiring further exploration, we consider CMB lensing less robust at present than galaxy lensing mass measurements, but highly promising. Similar CMB-based mass measurements have recently been published by SPT (Baxter et al. 2014) and ACT (Madhavacheril et al. 2014). The approach is appealing because it is subject to different systematic effects than gravitational shear and because it can be applied to large cluster samples thanks to the extensive sky coverage of the CMB experiments, with *Planck* of course covering the entire sky. Gravitational shear surveys will soon attain large sky coverage in the near future with the Dark Energy Survey (DES), and in the more distant future with the *Euclid* and WFIRST space missions and the Large Synoptic Survey Telescope.

Our central result from analysis of the 2015 *Planck* cluster counts is shown in Fig. 7. Depending on the mass bias prior, we find varying degrees of tension with the primary CMB, as in 2013. The mass bias required to bring the cluster counts and CMB into full agreement is larger than indicated by any of the three priors and corresponds to $1 - b = 0.58 \pm 0.04$. Fig. 8 illustrates the situation. The WtG prior almost eliminates the tension, but not quite, while both the CCCP and CMB lensing priors remain in noticeable tension. Our largest source of modelling uncertain is, as in 2013, the mass bias.

Tension between low redshift determinations of σ_8 and the *Planck* primary CMB are not unique to the *Planck* cluster counts. Among SZ cluster surveys, both SPT and ACT are in broad agreement with our findings, the latter depending on which SZ-mass scaling relation is used, as detailed in our 2013 analysis Planck Collaboration XX (2014). And the new SPT cosmological analysis (Bocquet et al. 2014) shows a significant shift between the cluster mass scale determined from the velocity dispersion or $Y_{\rm X}$ and what is needed to satisfy *Planck* or WMAP9 CMB constraints (e.g., Fig. 2 Bocquet et al. 2014). In a study of the REFLEX X-ray luminosity function, Böhringer et al. (2014) also report general agreement with our cluster findings. On the other hand, Mantz et al. (2014) find the their X-ray cluster counts, when using the WtG mass calibration, match the primary CMB constraints.

The situation is thus not yet satisfactory. It is unclear if these modest tensions arise from low-level systematics in the astrophysical studies, or are the first glimpse of something more important. The most obvious extension to the base ΛCDM model that could in principle reconcile the differences is a non-minimal sum of neutrino masses. This, unfortunately, does not provide such a straightforward solution. While it is true that adding neutrino mass does lower σ_8 relative to the base ΛCDM prediction from the primary CMB, it does so at the the cost of increasing tension in other parameters; for example, it lowers *Planck*'s already rather low value for the Hubble parameter.

Figure 14 highlights these points by showing constraints in the $(\Omega_{\rm m}, \sigma_8)$- and the (H_0, σ_8)-planes for each of the mass bias parameters. Adding variable neutrino mass relaxes constraints from the primary CMB (shaded contours, which are the same in all three pairs of panels) towards lower σ_8, but by simultaneously increasing $\Omega_{\rm m}$ and decreasing H_0. The remaining tension is mild in the case of the WtG mass prior, but more pronounced for the other two mass priors regardless of the neutrino mass.

Another possibility is that baryonic physics influences the late-time evolution of the density perturbations. Strong feedback from active galactic nuclei (AGN) (Nagai et al. 2007; van Daalen et al. 2011; Martizzi et al. 2014) can potentially damp growth and lower σ_8 through expulsion of matter from dark matter halos. This same effect could also reduce the mass of cluster halos and hence the prediction for their abundance, which is based on dark matter only simulations. It does not appear, however, that these effects are sufficiently large to explain the tension between low redshift and primary CMB constraints hinted at by the different observations. In addition, the violent feedback necessary for important impact might be difficult to reconcile with observations of the baryon content of dark matter halos (e.g., Planck Collaboration Int. XI 2013).

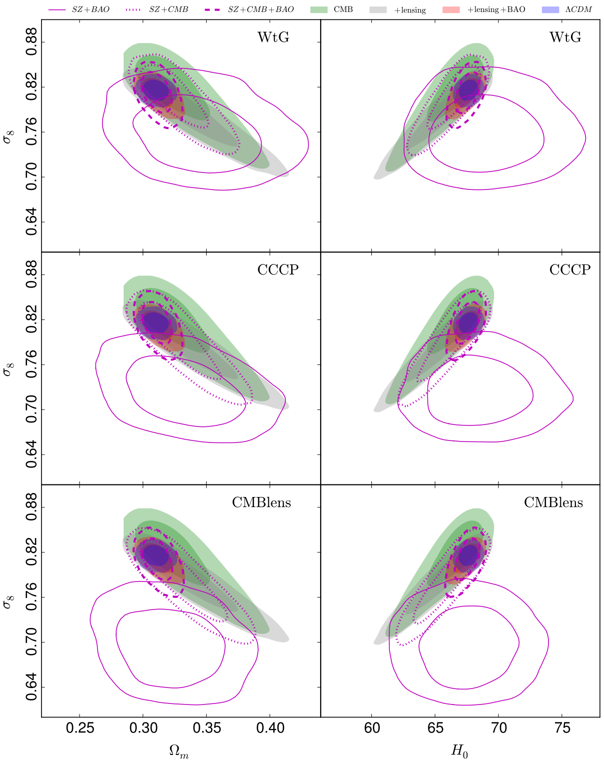

Fig. 14: Effects of neutrino mass. The open magenta contours (solid, dashed and dotted) reproduce our cluster constraints with different data combinations for the base ΛCDM (i.e., $\sum m_\nu = 0.06\,{\rm eV}$). The violet shaded contours trace the constraints on the base ΛCDM model, while the other shaded regions give constraints from the primary CMB combined with lensing and BAO when adding and marginalizing over variable neutrino mass.

As conclusion, we return to the main uncertainty in interpretation of the cluster counts, namely the mass bias. It could be argued that the current accuracy is at the level of $\sim 10-15\%$, based on the difference between different analyses and somewhat larger than their quoted statistical uncertainties. Progress will certainly follow with improvement in these measurements. We illustrate the potential impact of a 1% determination of the mass bias in Figs. 12 and 13. Such a result would, depending on the central value, significantly clarify the extent of any tensions and possible necessity for extensions to the base ΛCDM model. This precision is the avowed target of the large lensing surveys, such as *Euclid*, WFIRST and LSST. In the shorter term, we may expect valuable movement in this direction from DES and CMB lensing cluster mass measurements.

Acknowledgements. The Planck Collaboration acknowledges the support of: ESA; CNES and CNRS/INSU-IN2P3-INP (France); ASI, CNR, and INAF (Italy); NASA and DoE (USA); STFC and UKSA (UK); CSIC, MINECO, JA, and RES (Spain); Tekes, AoF, and CSC (Finland); DLR and MPG (Germany); CSA (Canada); DTU Space (Denmark); SER/SSO (Switzerland); RCN (Norway); SFI (Ireland); FCT/MCTES (Portugal); ERC and PRACE (EU). A description of the Planck Collaboration and a list of its members, indicating which

technical or scientific activities they have been involved in, can be found at http://www.cosmos.esa.int/web/planck/planck-collaboration.

References

Anderson, L., Aubourg, É., Bailey, S., et al. 2014, MNRAS, 441, 24
Anderson, L., Aubourg, E., Bailey, S., et al. 2012, MNRAS, 427, 3435
Angulo, R. E., Springel, V., White, S. D. M., et al. 2012, MNRAS, 426, 2046
Arnaud, M., Pratt, G. W., Piffaretti, R., et al. 2010, A&A, 517, A92
Arnaud et al., i. p. 2015
Battye, R. A., Charnock, T., & Moss, A. 2014, ArXiv e-prints
Baxter, E. J., Keisler, R., Dodelson, S., et al. 2014, ArXiv e-prints
Becker, M. R. & Kravtsov, A. V. 2011, ApJ, 740, 25
Benson, B. A., de Haan, T., Dudley, J. P., et al. 2013, ApJ, 763, 147
Bersanelli, M., Mandolesi, N., Butler, R. C., et al. 2010, A&A, 520, A4
Betoule, M., Kessler, R., Guy, J., et al. 2014, A&A, 568, A22
Beutler, F., Blake, C., Colless, M., et al. 2011, MNRAS, 416, 3017
Bleem, L. E., Stalder, B., de Haan, T., et al. 2014, ArXiv e-prints
Bocquet, S., Saro, A., Mohr, J. J., et al. 2014, ArXiv e-prints
Böhringer, H., Chon, G., & Collins, C. A. 2014, A&A, 570, A31
Carlstrom, J. E., Ade, P. A. R., Aird, K. A., et al. 2011, PASP, 123, 568
Carvalho, P., Rocha, G., & Hobson, M. P. 2009, MNRAS, 393, 681
Chamballu, A., Bartlett, J. G., & Melin, J.-B. 2012, A&A, 544, A40
Hasselfield, M., Hilton, M., Marriage, T. A., et al. 2013, J. Cosmology Astropart. Phys., 7, 8
Hoekstra et al., i. p. 2015
Hu, W. & Kravtsov, A. V. 2003, ApJ, 584, 702
Lamarre, J., Puget, J., Ade, P. A. R., et al. 2010, A&A, 520, A9
Lewis, A. & Challinor, A. 2006, Phys. Rep., 429, 1
Madhavacheril, M., Sehgal, N., Allison, R., et al. 2014, ArXiv e-prints
Mantz, A. B., von der Linden, A., Allen, S. W., et al. 2014, ArXiv e-prints
Marrone, D. P., Smith, G. P., Okabe, N., et al. 2012, ApJ, 754, 119
Martizzi, D., Mohammed, I., Teyssier, R., & Moore, B. 2014, MNRAS, 440, 2290
Melin, J., Bartlett, J. G., & Delabrouille, J. 2006, A&A, 459, 341
Melin, J.-B. & Bartlett, J. G. 2014
Meneghetti, M., Rasia, E., Merten, J., et al. 2010, A&A, 514, A93
Mennella, A., Butler, R. C., Curto, A., et al. 2011, A&A, 536, A3
Merten, J., Meneghetti, M., Postman, M., et al. 2014, ArXiv e-prints
Nagai, D., Kravtsov, A. V., & Vikhlinin, A. 2007, ApJ, 668, 1
Navarro, J. F., Frenk, C. S., & White, S. D. M. 1997, ApJ, 490, 493
Padmanabhan, N., Xu, X., Eisenstein, D. J., et al. 2012, MNRAS, 427, 2132
Piffaretti, R., Arnaud, M., Pratt, G. W., Pointecouteau, E., & Melin, J.-B. 2011, A&A, 534, A109
Piffaretti, R. & Valdarnini, R. 2008, A&A, 491, 71
Planck HFI Core Team. 2011, A&A, 536, A4
Planck Collaboration I. 2011, A&A, 536, A1
Planck Collaboration I. 2014, A&A, 571, A1
Planck Collaboration XVI. 2014, A&A, 571, A16
Planck Collaboration XX. 2014, A&A, 571, A20
Planck Collaboration XXIX. 2014, A&A, 571, A29
Planck Collaboration I. 2015, in preparation
Planck Collaboration II. 2015, in preparation
Planck Collaboration III. 2015, in preparation
Planck Collaboration IV. 2015, in preparation
Planck Collaboration V. 2015, in preparation
Planck Collaboration VI. 2015, in preparation
Planck Collaboration VII. 2015, in preparation
Planck Collaboration VIII. 2015, in preparation
Planck Collaboration IX. 2015, in preparation
Planck Collaboration X. 2015, in preparation
Planck Collaboration XI. 2015, in preparation
Planck Collaboration XII. 2015, in preparation
Planck Collaboration XIII. 2015, in preparation
Planck Collaboration XIV. 2015, in preparation
Planck Collaboration XV. 2015, in preparation
Planck Collaboration XVI. 2015, in preparation
Planck Collaboration XVII. 2015, in preparation
Planck Collaboration XVIII. 2015, in preparation
Planck Collaboration XIX. 2015, in preparation
Planck Collaboration XX. 2015, in preparation
Planck Collaboration XXI. 2015, in preparation
Planck Collaboration XXII. 2015, in preparation
Planck Collaboration XXIII. 2015, in preparation
Planck Collaboration XXIV. 2015, in preparation
Planck Collaboration XXV. 2015, in preparation
Planck Collaboration XXVI. 2015, in preparation
Planck Collaboration XXVII. 2015, in preparation
Planck Collaboration XXVIII. 2015, in preparation
Planck Collaboration Int. III. 2013, A&A, 550, A129
Planck Collaboration Int. XI. 2013, A&A, 557, A52
Postman, M., Coe, D., Benítez, N., et al. 2012, ApJS, 199, 25
Reichardt, C. L., Stalder, B., Bleem, L. E., et al. 2013, ApJ, 763, 127
Rozo, E., Bartlett, J. G., Evrard, A. E., & Rykoff, E. S. 2014a, MNRAS, 438, 78
Rozo, E., Evrard, A. E., Rykoff, E. S., & Bartlett, J. G. 2014b, MNRAS, 438, 62
Rozo, E., Rykoff, E. S., Bartlett, J. G., & Evrard, A. 2014c, MNRAS, 438, 49
Steigman, G. 2008, ArXiv e-prints
Swetz, D. S., Ade, P. A. R., Amiri, M., et al. 2011, ApJS, 194, 41
Tauber, J. A., Mandolesi, N., Puget, J., et al. 2010, A&A, 520, A1
Tinker, J., Kravtsov, A. V., Klypin, A., et al. 2008, ApJ, 688, 709
Umetsu, K., Medezinski, E., Nonino, M., et al. 2014, ArXiv e-prints
van Daalen, M. P., Schaye, J., Booth, C. M., & Dalla Vecchia, C. 2011, MNRAS, 415, 3649
von der Linden, A., Allen, M. T., Applegate, D. E., et al. 2014a, MNRAS, 439, 2
von der Linden, A., Mantz, A., Allen, S. W., et al. 2014b, ArXiv e-prints
Watson, W. A., Iliev, I. T., D'Aloisio, A., et al. 2013, MNRAS, 433, 1230
Zaldarriaga, M. & Seljak, U. 1999, Phys. Rev. D, 59, 123507

---

[1] APC, AstroParticule et Cosmologie, Université Paris Diderot, CNRS/IN2P3, CEA/lrfu, Observatoire de Paris, Sorbonne Paris Cité, 10, rue Alice Domon et Léonie Duquet, 75205 Paris Cedex 13, France
[2] Aalto University Metsähovi Radio Observatory and Dept of Radio Science and Engineering, P.O. Box 13000, FI-00076 AALTO, Finland
[3] African Institute for Mathematical Sciences, 6-8 Melrose Road, Muizenberg, Cape Town, South Africa
[4] Agenzia Spaziale Italiana Science Data Center, Via del Politecnico snc, 00133, Roma, Italy
[5] Aix Marseille Université, CNRS, LAM (Laboratoire d'Astrophysique de Marseille) UMR 7326, 13388, Marseille, France
[6] Astrophysics Group, Cavendish Laboratory, University of Cambridge, J J Thomson Avenue, Cambridge CB3 0HE, U.K.
[7] Astrophysics & Cosmology Research Unit, School of Mathematics, Statistics & Computer Science, University of KwaZulu-Natal, Westville Campus, Private Bag X54001, Durban 4000, South Africa
[8] Atacama Large Millimeter/submillimeter Array, ALMA Santiago Central Offices, Alonso de Cordova 3107, Vitacura, Casilla 763 0355, Santiago, Chile
[9] CITA, University of Toronto, 60 St. George St., Toronto, ON M5S 3H8, Canada
[10] CNRS, IRAP, 9 Av. colonel Roche, BP 44346, F-31028 Toulouse cedex 4, France
[11] CRANN, Trinity College, Dublin, Ireland
[12] California Institute of Technology, Pasadena, California, U.S.A.
[13] Centre for Theoretical Cosmology, DAMTP, University of Cambridge, Wilberforce Road, Cambridge CB3 0WA, U.K.
[14] Centro de Estudios de Física del Cosmos de Aragón (CEFCA), Plaza San Juan, 1, planta 2, E-44001, Teruel, Spain
[15] Computational Cosmology Center, Lawrence Berkeley National Laboratory, Berkeley, California, U.S.A.
[16] Consejo Superior de Investigaciones Científicas (CSIC), Madrid, Spain
[17] DSM/Irfu/SPP, CEA-Saclay, F-91191 Gif-sur-Yvette Cedex, France
[18] DTU Space, National Space Institute, Technical University of Denmark, Elektrovej 327, DK-2800 Kgs. Lyngby, Denmark
[19] Département de Physique Théorique, Université de Genève, 24, Quai E. Ansermet,1211 Genève 4, Switzerland
[20] Departamento de Física, Universidad de Oviedo, Avda. Calvo Sotelo s/n, Oviedo, Spain
[21] Department of Astronomy and Astrophysics, University of Toronto, 50 Saint George Street, Toronto, Ontario, Canada
[22] Department of Astrophysics/IMAPP, Radboud University Nijmegen, P.O. Box 9010, 6500 GL Nijmegen, The Netherlands
[23] Department of Physics & Astronomy, University of British Columbia, 6224 Agricultural Road, Vancouver, British Columbia, Canada

[24] Department of Physics and Astronomy, Dana and David Dornsife College of Letter, Arts and Sciences, University of Southern California, Los Angeles, CA 90089, U.S.A.
[25] Department of Physics and Astronomy, University College London, London WC1E 6BT, U.K.
[26] Department of Physics, Florida State University, Keen Physics Building, 77 Chieftan Way, Tallahassee, Florida, U.S.A.
[27] Department of Physics, Gustaf Hällströmin katu 2a, University of Helsinki, Helsinki, Finland
[28] Department of Physics, Princeton University, Princeton, New Jersey, U.S.A.
[29] Department of Physics, University of California, Santa Barbara, California, U.S.A.
[30] Department of Physics, University of Illinois at Urbana-Champaign, 1110 West Green Street, Urbana, Illinois, U.S.A.
[31] Dipartimento di Fisica e Astronomia G. Galilei, Università degli Studi di Padova, via Marzolo 8, 35131 Padova, Italy
[32] Dipartimento di Fisica e Scienze della Terra, Università di Ferrara, Via Saragat 1, 44122 Ferrara, Italy
[33] Dipartimento di Fisica, Università La Sapienza, P. le A. Moro 2, Roma, Italy
[34] Dipartimento di Fisica, Università degli Studi di Milano, Via Celoria, 16, Milano, Italy
[35] Dipartimento di Fisica, Università degli Studi di Trieste, via A. Valerio 2, Trieste, Italy
[36] Dipartimento di Fisica, Università di Roma Tor Vergata, Via della Ricerca Scientifica, 1, Roma, Italy
[37] Dipartimento di Matematica, Università di Roma Tor Vergata, Via della Ricerca Scientifica, 1, Roma, Italy
[38] Discovery Center, Niels Bohr Institute, Blegdamsvej 17, Copenhagen, Denmark
[39] Dpto. Astrofísica, Universidad de La Laguna (ULL), E-38206 La Laguna, Tenerife, Spain
[40] European Southern Observatory, ESO Vitacura, Alonso de Cordova 3107, Vitacura, Casilla 19001, Santiago, Chile
[41] European Space Agency, ESAC, Planck Science Office, Camino bajo del Castillo, s/n, Urbanización Villafranca del Castillo, Villanueva de la Cañada, Madrid, Spain
[42] European Space Agency, ESTEC, Keplerlaan 1, 2201 AZ Noordwijk, The Netherlands
[43] Facoltà di Ingegneria, Università degli Studi e-Campus, Via Isimbardi 10, Novedrate (CO), 22060, Italy
[44] Gran Sasso Science Institute, INFN, viale F. Crispi 7, 67100 L'Aquila, Italy
[45] HGSFP and University of Heidelberg, Theoretical Physics Department, Philosophenweg 16, 69120, Heidelberg, Germany
[46] Haverford College Astronomy Department, 370 Lancaster Avenue, Haverford, Pennsylvania, U.S.A.
[47] Helsinki Institute of Physics, Gustaf Hällströmin katu 2, University of Helsinki, Helsinki, Finland
[48] INAF - Osservatorio Astrofisico di Catania, Via S. Sofia 78, Catania, Italy
[49] INAF - Osservatorio Astronomico di Padova, Vicolo dell'Osservatorio 5, Padova, Italy
[50] INAF - Osservatorio Astronomico di Roma, via di Frascati 33, Monte Porzio Catone, Italy
[51] INAF - Osservatorio Astronomico di Trieste, Via G.B. Tiepolo 11, Trieste, Italy
[52] INAF/IASF Bologna, Via Gobetti 101, Bologna, Italy
[53] INAF/IASF Milano, Via E. Bassini 15, Milano, Italy
[54] INFN, Sezione di Bologna, Via Irnerio 46, I-40126, Bologna, Italy
[55] INFN, Sezione di Roma 1, Università di Roma Sapienza, Piazzale Aldo Moro 2, 00185, Roma, Italy
[56] INFN, Sezione di Roma 2, Università di Roma Tor Vergata, Via della Ricerca Scientifica, 1, Roma, Italy
[57] INFN/National Institute for Nuclear Physics, Via Valerio 2, I-34127 Trieste, Italy
[58] IPAG: Institut de Planétologie et d'Astrophysique de Grenoble, Université Grenoble Alpes, IPAG, F-38000 Grenoble, France, CNRS, IPAG, F-38000 Grenoble, France
[59] ISDC, Department of Astronomy, University of Geneva, ch. d'Ecogia 16, 1290 Versoix, Switzerland
[60] IUCAA, Post Bag 4, Ganeshkhind, Pune University Campus, Pune 411 007, India
[61] Imperial College London, Astrophysics group, Blackett Laboratory, Prince Consort Road, London, SW7 2AZ, U.K.
[62] Infrared Processing and Analysis Center, California Institute of Technology, Pasadena, CA 91125, U.S.A.
[63] Institut Néel, CNRS, Université Joseph Fourier Grenoble I, 25 rue des Martyrs, Grenoble, France
[64] Institut Universitaire de France, 103, bd Saint-Michel, 75005, Paris, France
[65] Institut d'Astrophysique Spatiale, CNRS (UMR8617) Université Paris-Sud 11, Bâtiment 121, Orsay, France
[66] Institut d'Astrophysique de Paris, CNRS (UMR7095), 98 bis Boulevard Arago, F-75014, Paris, France
[67] Institute for Space Sciences, Bucharest-Magurale, Romania
[68] Institute of Astronomy, University of Cambridge, Madingley Road, Cambridge CB3 0HA, U.K.
[69] Institute of Theoretical Astrophysics, University of Oslo, Blindern, Oslo, Norway
[70] Instituto de Astrofísica de Canarias, C/Vía Láctea s/n, La Laguna, Tenerife, Spain
[71] Instituto de Física de Cantabria (CSIC-Universidad de Cantabria), Avda. de los Castros s/n, Santander, Spain
[72] Istituto Nazionale di Fisica Nucleare, Sezione di Padova, via Marzolo 8, I-35131 Padova, Italy
[73] Jet Propulsion Laboratory, California Institute of Technology, 4800 Oak Grove Drive, Pasadena, California, U.S.A.
[74] Jodrell Bank Centre for Astrophysics, Alan Turing Building, School of Physics and Astronomy, The University of Manchester, Oxford Road, Manchester, M13 9PL, U.K.
[75] Kavli Institute for Cosmology Cambridge, Madingley Road, Cambridge, CB3 0HA, U.K.
[76] LAL, Université Paris-Sud, CNRS/IN2P3, Orsay, France
[77] LAPTh, Univ. de Savoie, CNRS, B.P.110, Annecy-le-Vieux F-74941, France
[78] LERMA, CNRS, Observatoire de Paris, 61 Avenue de l'Observatoire, Paris, France
[79] Laboratoire AIM, IRFU/Service d'Astrophysique - CEA/DSM - CNRS - Université Paris Diderot, Bât. 709, CEA-Saclay, F-91191 Gif-sur-Yvette Cedex, France
[80] Laboratoire Traitement et Communication de l'Information, CNRS (UMR 5141) and Télécom ParisTech, 46 rue Barrault F-75634 Paris Cedex 13, France
[81] Laboratoire de Physique Subatomique et Cosmologie, Université Grenoble-Alpes, CNRS/IN2P3, 53, rue des Martyrs, 38026 Grenoble Cedex, France
[82] Laboratoire de Physique Théorique, Université Paris-Sud 11 & CNRS, Bâtiment 210, 91405 Orsay, France
[83] Lawrence Berkeley National Laboratory, Berkeley, California, U.S.A.
[84] Lebedev Physical Institute of the Russian Academy of Sciences, Astro Space Centre, 84/32 Profsoyuznaya st., Moscow, GSP-7, 117997, Russia
[85] Max-Planck-Institut für Astrophysik, Karl-Schwarzschild-Str. 1, 85741 Garching, Germany
[86] McGill Physics, Ernest Rutherford Physics Building, McGill University, 3600 rue University, Montréal, QC, H3A 2T8, Canada
[87] National University of Ireland, Department of Experimental Physics, Maynooth, Co. Kildare, Ireland
[88] Niels Bohr Institute, Blegdamsvej 17, Copenhagen, Denmark
[89] Optical Science Laboratory, University College London, Gower Street, London, U.K.
[90] SB-ITP-LPPC, EPFL, CH-1015, Lausanne, Switzerland
[91] SISSA, Astrophysics Sector, via Bonomea 265, 34136, Trieste, Italy
[92] School of Physics and Astronomy, Cardiff University, Queens Buildings, The Parade, Cardiff, CF24 3AA, U.K.

[93] School of Physics and Astronomy, University of Nottingham, Nottingham NG7 2RD, U.K.
[94] Sorbonne Université-UPMC, UMR7095, Institut d'Astrophysique de Paris, 98 bis Boulevard Arago, F-75014, Paris, France
[95] Space Research Institute (IKI), Russian Academy of Sciences, Profsoyuznaya Str, 84/32, Moscow, 117997, Russia
[96] Space Sciences Laboratory, University of California, Berkeley, California, U.S.A.
[97] Special Astrophysical Observatory, Russian Academy of Sciences, Nizhnij Arkhyz, Zelenchukskiy region, Karachai-Cherkessian Republic, 369167, Russia
[98] Stanford University, Dept of Physics, Varian Physics Bldg, 382 Via Pueblo Mall, Stanford, California, U.S.A.
[99] Sub-Department of Astrophysics, University of Oxford, Keble Road, Oxford OX1 3RH, U.K.
[100] Theory Division, PH-TH, CERN, CH-1211, Geneva 23, Switzerland
[101] UPMC Univ Paris 06, UMR7095, 98 bis Boulevard Arago, F-75014, Paris, France
[102] Université de Toulouse, UPS-OMP, IRAP, F-31028 Toulouse cedex 4, France
[103] University Observatory, Ludwig Maximilian University of Munich, Scheinerstrasse 1, 81679 Munich, Germany
[104] University of Granada, Departamento de Física Teórica y del Cosmos, Facultad de Ciencias, Granada, Spain
[105] University of Granada, Instituto Carlos I de Física Teórica y Computacional, Granada, Spain
[106] Warsaw University Observatory, Aleje Ujazdowskie 4, 00-478 Warszawa, Poland

Appendix A: Modelling uncertainties

We examine the robustness of our cosmological constraints to modelling uncertainties. We first consider sensitivity to the cosmological sample and to our modelling of the completeness function in Sect. A.1, and then look at the effect of using a different mass function in Sec. A.2. In Sec. A.3, we show that our constraints are robust against redshift evolution of the scaling relations.

Appendix A.1: Choice of the sample and selection function

For our baseline analysis, we use the MMF3 cosmological sample and its associated completeness based on the analytical approximation using the Error Function (Eq. 14). In Fig. A.1 we show how the Monte Carlo determined selection function changes the cosmological constraints (labelled QA for "Quality Assessment" in the figure). We also present the constraints obtained from the intersection sample defined in Sec. 2. The figure is based on the 1D $N(z)$ likelihood, for which the Monte Carlo completeness can be easily computed, and we use the baseline SZ+BAO+BBN data set and fix $(1-b) = 0.8$. The MMF3 ERF contour is thus close to the $q = 6$ contour of Fig. 3, the only difference being that $\sigma_{\ln Y}$ is fixed to zero in Fig. A.1. while it is constrained by the Table 1 prior in Fig. 3. The impact of adopting the intersection sample and/or the QA completeness function is small ($< 0.5\sigma$) for both Ω_m and σ_8.

Appendix A.2: Mass function

We use the Tinker et al. mass function for our baseline analysis. To characterize the influence of this choice, we examine constraints when adopting the mass function from Watson et al. (2013) instead. We employ our 2D $N(z,q)$ likelihood (with the CCCP mass bias prior and α constrained) and combine with BAO and BBN prior constraints, and show the result in Fig. A.2.

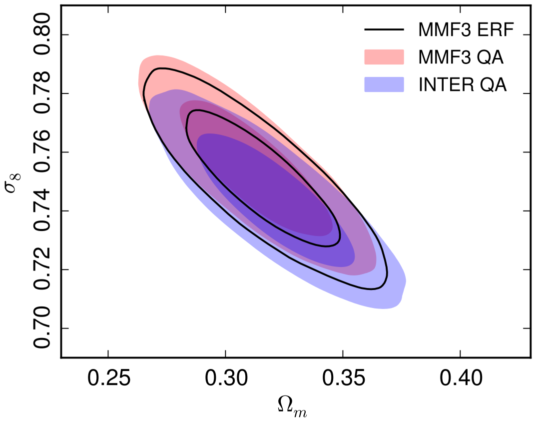

Fig. A.1: Robustness to the choice of cluster sample and the selection function model. The shaded contours give the cosmological constraints from the 2015 MMF3 cluster catalogue using the analytical (Error Function, ERF) selection function model (grey), the MMF3 Monte Carlo selection function (red), and the Monte Carlo selection function for the intersection sample (blue). Our final constraints are obtained from the MMF3 ERF model. For this comparison, we adopt the SZ+BAO+BBN data set and we fix $(1-b) = 0.8$.

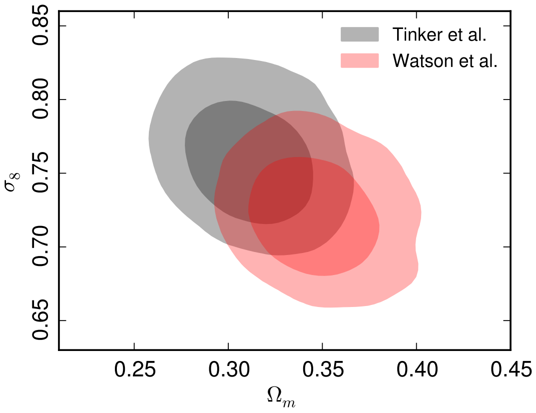

Fig. A.2: Robustness to the choice of mass function. The grey shaded contours give the cosmological constraints when using the Tinker et al. mass function, corresponding to our final result. This is compared to constraints obtained when using the Watson et al. mass function, shown as the red shaded contours. In this figure we adopt the SZ+BAO+BBN data set and the CCCP mass bias prior.

The Tinker et al. contour of Fig. A.2 is thus identical to the $N(z,q)$ contour with α free, as given in Fig. 5. The new mass function shifts our constraints by about 1σ towards higher Ω_m and lower σ_8, along the main degeneracy line, hence increasing the tension with the *Planck* primary CMB constraints. Note that we use the general fit from Eq. (12) of Watson et al. (2013) (independent of redshift). This was not the case for our 2013 paper (Planck Collaboration XX 2014) where we adopted the AHF fit with parameters varying with redshift in the first ArXiv version of the paper, which was subsequently found to be incorrect (fourth version of the paper on ArXiv).

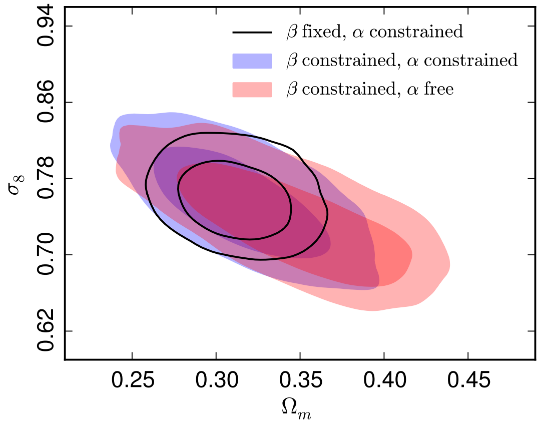

Fig. A.3: Robustness to redshift evolution in the SZ-mass scaling relation. The different contours show the constraints when relaxing the redshift evolution exponent, β, of Eq. (7). The black contours result from fixing $\beta = 0.66$, our fiducial value throughout, with α constrained by the Gaussian X-ray prior of Tab. 1. Applying a Gaussian the prior on β instead, from Tab. 1, produces the blue contours, while the red contours result when we also leave α free. In this figure we adopt the SZ+BAO+BBN data set and the CCCP mass bias prior.

Appendix A.3: Redshift evolution of the Y-M relation

Throughout our baseline analysis, we fix the redshift evolution exponent $\beta = 0.66$ (self-similar prediction) in Eq. (7). Here we examine the impact of allowing this parameter to vary. Constraints when leaving β free are shown in Fig. A.3. The "β fixed, α constrained" case corresponds to the 2D $N(z,q)$ likelihood (CCCP mass bias prior and α constrained) combined with BAO and BBN, as in Fig. A.2. This contour is also identical to the $N(z,q)$ contour with α free, shown in Fig. 5. For the "β constrained" cases, β is allowed to vary over the range 0.66 ± 0.50 (Table 1). This increases the size of our constraints along the major degeneracy between Ω_m and σ_8, but does not bring them into any closer agreement with the primary CMB.

E.3 Mesure de masse par effet de lentille sur le CMB

L'article suivant est inclus dans cette partie et est décrit dans le chapitre 5.

- Melin, J.-B. & Bartlett, J. G., Measuring cluster masses with CMB lensing: a statistical approach. 2015, A&A, 578, A21, arXiv:1408.5633 *[5 citations]*

A&A 578, A21 (2015)
DOI: 10.1051/0004-6361/201424720

Astronomy & Astrophysics

Measuring cluster masses with CMB lensing: a statistical approach

Jean-Baptiste Melin[1] and James G. Bartlett[2,3]

[1] DSM/Irfu/SPP, CEA-Saclay, 91191 Gif-sur-Yvette Cedex, France
e-mail: `jean-baptiste.melin@cea.fr`
[2] APC, AstroParticule et Cosmologie, Université Paris Diderot, CNRS/IN2P3, CEA/lrfu, Observatoire de Paris, Sorbonne Paris Cité, 10 rue Alice Domon et Léonie Duquet, 75205 Paris Cedex 13, France
e-mail: `bartlett@apc.univ-paris7.fr`
[3] Jet Propulsion Laboratory, California Institute of Technology, 4800 Oak Grove Drive, Pasadena, California, USA

Received 31 July 2014 / Accepted 10 April 2015

ABSTRACT

We present a method for measuring the masses of galaxy clusters using the imprint of their gravitational lensing signal on the cosmic microwave background (CMB) temperature anisotropies. The method first reconstructs the projected gravitational potential with a quadratic estimator and then applies a matched filter to extract cluster mass. The approach is well-suited for statistical analyses that bin clusters according to other mass proxies. We find that current experiments, such as *Planck*, the South Pole Telescope and the Atacama Cosmology Telescope, can practically implement such a statistical methodology, and that future experiments will reach sensitivities sufficient for individual measurements of massive systems. As illustration, we use simulations of *Planck* observations to demonstrate that it is possible to constrain the mass scale of a set of 62 massive clusters with prior information from X-ray observations, similar to the published *Planck* ESZ-XMM sample. We examine the effect of the thermal (tSZ) and kinetic (kSZ) Sunyaev-Zeldovich (SZ) signals, finding that the impact of the kSZ remains small in this context. The stronger tSZ signal, however, must be actively removed from the CMB maps by component separation techniques prior to reconstruction of the gravitational potential. Our study of two such methods highlights the importance of broad frequency coverage for this purpose. A companion paper presents application to the *Planck* data on the ESZ-XMM sample.

Key words. large-scale structure of Universe – galaxies: clusters: general – cosmic background radiation – methods: data analysis – gravitational lensing: weak – methods: statistical

1. Introduction

The most important property of galaxy clusters for cosmological studies is their mass; it is also the most difficult to measure, because it is not directly observable. Accurate mass measurements are needed, in particular, to calibrate scaling laws relating mass to observable cluster properties, such as richness (Yee & Ellingson 2003; Gladders et al. 2007; Rozo et al. 2009), X-ray properties (Arnaud et al. 2005, 2007; Stanek et al. 2006; Vikhlinin et al. 2006; Pratt et al. 2009; Mantz et al. 2010; Rozo et al. 2014b) or Sunyaev-Zeldovich (SZ) signal strength (Marrone et al. 2012; Planck Collaboration Int. III 2013; Bocquet et al. 2015; Rozo et al. 2014a; von der Linden et al. 2014; Hoekstra et al. 2015). The uncertainty in the mass calibration of these relations now limits the constraining power of cluster counts as a cosmological probe (Rozo et al. 2013; Planck Collaboration XX 2014; Hasselfield et al. 2013; Reichardt et al. 2013; Rozo et al. 2010; Mantz et al. 2010, 2015; Vikhlinin et al. 2009; Böhringer et al. 2014; Planck Collaboration 2015).

Cluster masses can be determined dynamically, by application of the virial theorem to the velocity distribution of member galaxies, from X-ray studies of the intra-cluster medium, assuming hydrostatic equilibrium for the gas, and via the effects of gravitational lensing that distort the shapes of background galaxies. Each approach presents its own advantages while suffering from specific systematic biases (Allen et al. 2011).

In this work, we discuss lensing of the cosmic microwave background (CMB) anisotropies as a promising new technique for measuring cluster masses, presenting a methodology for practical application with the specific aim of calibrating cluster scaling relations. We evaluate the potential of current and future experiments to employ the methodology and show how to account for astrophysical biases from other cluster signals. As illustration, we apply the technique to *Planck* simulations of massive clusters and demonstrate that it is possible to recover an unbiased estimate of the mass scale of the *Planck* XMM-Early Release SZ catalogue (ESZ-XMM, Planck Collaboration VIII 2011; Planck Collaboration XI 2011). A companion paper presents results obtained with the *Planck* dataset for the ESZ-XMM sample.

Study of CMB lensing (for a review see Lewis & Challinor 2006) is a rapidly growing field driven by the current generation of sensitive, high resolution CMB experiments. Recent measurements of lensing in the CMB temperature power spectrum have been given by the Atacama Cosmology Telescope (ACT, Das et al. 2014), the South Pole Telescope (SPT, Story et al. 2013) and the *Planck* mission (Planck Collaboration XVI 2014). Direct reconstruction of the matter power spectrum using higher order statistics, designed to capture lensing's specific non-Gaussian mode coupling signature (Hu & Okamoto 2002), have also been reported by ACT (Das et al. 2011) and SPT (van Engelen et al. 2012), as well as *Planck*, which in addition produced an all-sky map of the projected matter distribution (Planck Collaboration XVII 2014).

Lensing of the CMB by galaxy clusters was first discussed at length by Zaldarriaga & Seljak (1999) when developing methods for reconstruction of the gravitational lensing potential. Seljak & Zaldarriaga (2000) considered instead the characteristic perturbation to the unlensed CMB temperature field, approximated locally as a pure gradient, induced by cluster lensing, an idea further studied by Holder & Kosowsky (2004) and Vale et al. (2004). In an approach analogous to the first authors, Maturi et al. (2005) built a filter nonlinear in CMB temperature to reconstruct the lensing convergence field around clusters as a means of studying their density profiles.

In this paper, we develop a cluster mass extraction method based on a matched filter for the projected gravitational potential. Our approach is similar in spirit to the work of Zaldarriaga & Seljak (1999) and Maturi et al. (2005) in that we first reconstruct the lensing field around a cluster, rather than working with the lensing perturbation in the CMB temperature itself. In the present work, however, we focus on determining total cluster mass even in relatively low signal-to-noise regimes. Once we have the map of a cluster potential, obtained using the quadratic estimator of Hu & Okamoto (2002), we then apply a matched filter designed to optimally extract the cluster's mass, assuming a density profile. This allows us to obtain measurements for individual clusters, even when noise dominated, and use them in statistical analyses; for example, finding the mean mass of clusters by binning according to SZ signal strength or, in other words, the mass-SZ scaling relation.

In practice, we must confront a number of possible systematic biases. We consider the effects of and ways to mitigate astrophysical signals contaminating the CMB map required as input for reconstruction of the gravitational potential. The most difficult in this context are signals generated by the cluster itself, such as the thermal SZ (tSZ, Sunyaev & Zeldovich 1972) and the kinetic SZ (kSZ, Sunyaev & Zeldovich 1980) effects. Component separation is therefore a crucial step prior to reconstruction of the potential, and our study will demonstrate the importance of multi-frequency observations in this context. The kSZ effect, having the same spectral signature as the CMB, requires separate treatment; fortunately, we will see that the lensing potential reconstruction significantly reduces its impact by averaging it with uncorrelated CMB anisotropies.

We organize the paper as follows. We begin in Sect. 2 by establishing our data model and discussing the reconstruction of the lensing potential and application of the matched filter; the presentation focuses at this point on the ideal case where we have a clean CMB map of known noise properties. This allows a preliminary evaluation of the potential of current and future CMB experiments to measure cluster masses. Section 3 focuses on the tSZ and kSZ signals. We employ two techniques to remove the tSZ signal and produce clean CMB maps from a set of individual frequency maps, and we evaluate the impact of the kSZ signal. We simulate *Planck* observations of a set of massive clusters in Sect. 4 to illustrate the method, showing that it is possible (Sect. 5) to recover an unbiased estimate of the cluster mass scale for a sample similar to the *Planck* ESZ-XMM catalogue (Planck Collaboration XI 2011). We finish with a discussion (Sect. 6) and our conclusions (Sect. 7). Throughout, we adopt a flat ΛCDM cosmological model with $H_0 = 70\,\mathrm{km\,s^{-1}\,Mpc^{-1}}$ and $\Omega_\mathrm{M} = 1 - \Omega_\Lambda = 0.3$.

2. Mass estimation

We first define our data model in the general context, and then present the matched filter mass estimation by focussing on the ideal case where we have a clean map of lensed CMB anisotropies with only instrumental noise.

2.1. Cluster signals

Consider a patch of sky centered on a galaxy cluster of mass M_{500} at redshift z. We refer to cluster mass inside the radius R_{500}, interior to which the mean mass density is 500 times the critical density at the cluster's redshift, $\rho_\mathrm{c}(z)$; i.e., $M_{500} = 500(4\pi/3)\rho_\mathrm{c}(z)R^3_{500}$. The hot, gaseous intra-cluster medium (ICM) generates both tSZ and kSZ effects, and the cluster's (projected) gravitational potential, ϕ, lenses the CMB anisotropies by bending light rays and displacing the apparent line-of-sight.

We model the mass distribution with a NFW (Navarro et al. 1996) profile,

$$\rho(r) = \frac{\rho_0}{(r/r_\mathrm{s})(1+r/r_\mathrm{s})^2}, \tag{1}$$

described by its central density, ρ_0, and physical scale r_s. The latter can be related to R_{500} using the concentration parameter, c_{500}, as $r_\mathrm{s} = R_{500}/c_{500}$. Unless otherwise stated, we take $c_{500} = 3$ in this work; in reality, it is expected to depend weakly on cluster mass and redshift, i.e., $c_{500}(M_{500}, z)$ (Bullock et al. 2001; Neto et al. 2007; Muñoz-Cuartas et al. 2011). Integrating along the line-of-sight yields the projected surface mass density at angular position $\boldsymbol{x}$ from the center,

$$\Sigma(\boldsymbol{x}) = \phi_0\, \Sigma_\mathrm{m}(x/\theta_\mathrm{m}), \tag{2}$$

where $x = |\boldsymbol{x}|$ and Σ_m is a template characterized by the angular scale $\theta_\mathrm{m} = r_\mathrm{s}/D_\mathrm{clus}$, with D_clus the angular diameter distance to the cluster. The integral along the line-of-sight is performed out to $r = 5R_{500}$. The normalization, ϕ_0, is given below.

For the pressure of the ICM, we employ the modified NFW profile of Nagai et al. (2007) with parameters given by the X-ray observations of Arnaud et al. (2010), the so-called universal pressure profile in the non self-similar case (Eq. (12) of that paper). Integrating the pressure profile along the line-of-sight gives the tSZ angular template, $T_\mathrm{t}(x/\theta_\mathrm{t})$, characterized by its scale radius, θ_t, and which is normalized by the cluster's central Compton y value, y_o, to obtain the complete tSZ profile. The kSZ signal is proportional to the optical depth through the cluster with profile $T_\mathrm{k}(x/\theta_\mathrm{k})$ characterized by the scale radius θ_k. It is normalized by the cluster peculiar velocity, β, to obtain the kSZ signal. In our numerical calculations below, we use the same radial profile for the ICM pressure and optical depth, which is equivalent to approximating the gas as isothermal; this is not strictly the case, but the approximation has little effect on our conclusions.

We suppose that the region is observed in several millimeter/sub-millimeter bands, producing a set of maps at N different frequencies ν_i ($i = 1, ..., N$) that we arrange in a column vector $\boldsymbol{m}(\boldsymbol{x})$, a function of angular position $\boldsymbol{x}$ on the sky and whose ith component is the the map $m_i(\boldsymbol{x})$ at frequency ν_i. We assume the maps are in units of thermodynamic temperature, so the CMB and kSZ signals remain constant across frequencies, and we denote the beam at frequency ν_i by b_i.

The maps contain the cluster tSZ and kSZ signals, lensed CMB anisotropies and noise,

$$\boldsymbol{m}(\boldsymbol{x}) = y_\mathrm{o}\boldsymbol{t_t}(\boldsymbol{x}) + \beta\boldsymbol{t_k}(\boldsymbol{x}) + \boldsymbol{s}(\boldsymbol{x}) + \boldsymbol{n}(\boldsymbol{x}), \tag{3}$$

where $\boldsymbol{t_t}(\boldsymbol{x})$ is the vector whose ith component is $j_\nu(\nu_i)[b_i * T_\mathrm{t}](\boldsymbol{x})$, the beam-convolved tSZ template modulated by the tSZ frequency spectrum, j_ν, in temperature units.

The components of the kSZ vector, $\boldsymbol{t}_{\boldsymbol{k}}(\boldsymbol{x})$, are $[b_i * T_{\rm k}](\boldsymbol{x})$, and those of the CMB vector, $\boldsymbol{s}(\boldsymbol{x})$, are $s_i(\boldsymbol{x}) = [b_i * S](\boldsymbol{x})$, where we denote the CMB signal on the sky as $S(\boldsymbol{x})$. As for $\Sigma_{\rm m}$, the integration along the line-of-sight for $T_{\rm t}$ and $T_{\rm k}$ is performed out to $r = 5R_{500}$.

The unlensed (and unobservable) CMB field, $\tilde{S}(\boldsymbol{x})$, is transformed into the observed sky signal as (e.g., Bartelmann & Schneider 2001)

$$S(\boldsymbol{x}) = \tilde{S}(\boldsymbol{x}) + \delta S(\boldsymbol{x}), \tag{4}$$

$$\delta S(\boldsymbol{x}) = \nabla S(\boldsymbol{x}) \cdot \nabla \phi(\boldsymbol{x}), \tag{5}$$

to first order in the lensing potential, which is related to the convergence,

$$\kappa(\boldsymbol{x}) = \Sigma(\boldsymbol{x})/\Sigma_{\rm cr}, \tag{6}$$

by

$$\phi(\boldsymbol{x}) = \int {\rm d}^2x'\ \kappa(\boldsymbol{x'}) \ln(|\boldsymbol{x} - \boldsymbol{x}'|) \tag{7}$$

$$= \phi_0 \int {\rm d}^2x'\ \frac{\Sigma_{\rm m}(x'/\theta_{\rm m})}{\Sigma_{\rm cr}} \ln\left|\boldsymbol{x} - \boldsymbol{x}'\right| \tag{8}$$

$$\equiv \phi_0 \Phi(x/\theta_{\rm m}). \tag{9}$$

All integrals are restricted to $x' < 5\theta_{500}$. The critical surface mass density, $\Sigma_{\rm cr} = \frac{c^2}{4\pi G}\frac{D_{\rm CMB}}{D_{\rm clus}D_{\rm clus-CMB}}$, is defined in terms of the angular diameter distances $D_{\rm CMB}$, $D_{\rm clus}$ and $D_{\rm clus-CMB}$ between the observer and the CMB, the observer and the cluster, and the cluster and the CMB, respectively. The third equality in Eq. (9) defines our (dimensionless) model template for the lensing potential, $\Phi_{\theta_{\rm m}}$, parameterized by the angular scale $\theta_{\rm m}$. It is normalized by ϕ_0 (see Eq. (2)), defined such that $\Phi_{\theta_{\rm m}}(0) = 1$.

The noise term in Eq. (3), $\boldsymbol{n}(\boldsymbol{x})$, includes instrumental noise and astrophysical signals that are not related to the cluster. Examples of the latter are Galactic foreground emission, extragalactic point sources and lensing by matter randomly projected along the line-of-sight (large-scale structure, or LSS, noise). The effects of LSS correlated with cluster position can only be evaluated with numerical simulations and remain beyond the scope of the present work. Similarly, the background extragalactic point source population is modified near the cluster by lensing, creating a second order cluster-related signal that we do not consider in this work.

2.2. Reconstruction of the Lensing Potential Map

Given a map of CMB temperature anisotropy, $\hat{S}$ – obtained from a prior component separation step, as describe below – centered on a cluster, we apply the flat-sky quadratic estimator from Hu & Okamoto (2002) to find the Fourier modes of the projected gravitational potential:

$$\hat{\phi}(\boldsymbol{K}) = A(\boldsymbol{K}) \sum_{\boldsymbol{k}} \hat{S}^*(\boldsymbol{k})\hat{S}(\boldsymbol{k}')F(\boldsymbol{k},\boldsymbol{k}'), \tag{10}$$

with $\boldsymbol{K} = \boldsymbol{k} - \boldsymbol{k}'[{\rm mod}\, n]$, where n is the number of pixels along the x (or y) axis, and

$$A(\boldsymbol{K}) = \left[\sum_{\boldsymbol{k}} f(\boldsymbol{k},\boldsymbol{k}')F(\boldsymbol{k},\boldsymbol{k}')\right]^{-1}. \tag{11}$$

The weights $F(\boldsymbol{k},\boldsymbol{k}')$ are defined so that $\hat{\phi}$ is the minimum variance estimator:

$$F(\boldsymbol{k},\boldsymbol{k}') = \frac{f^*(\boldsymbol{k},\boldsymbol{k}')}{2P_{\hat{S}}(k)P_{\hat{S}}(k')}, \tag{12}$$

in which $P_{\hat{S}}(k) = |b(k)|^2 C_k + P_{\rm noise}(k)$ is the observed power spectrum with a contribution from the effective noise, $P_{\rm noise}$, of the cleaned CMB map; $b(k)$ represents the effective instrumental beam[1]; C_k is the power spectrum of the (true) lensed CMB signal, $S(\boldsymbol{x})$; and $f(\boldsymbol{k},\boldsymbol{k})$ is given by

$$f(\boldsymbol{k},\boldsymbol{k}') = b^*(\boldsymbol{k})b(\boldsymbol{k}')\left[\tilde{C}_k \boldsymbol{k}\cdot\boldsymbol{K} - \tilde{C}_{k'}\boldsymbol{k}'\cdot\boldsymbol{K}\right], \tag{13}$$

where $\tilde{C}_k$ is the power spectrum of the unlensed CMB sky, $\tilde{S}(\boldsymbol{x})$.

Equation (10) gives us an unbiased estimate of $\phi(\boldsymbol{K})$ for a cluster of given properties in the sense that if averaged over all realizations of the (unlensed) CMB and instrumental noise, $\langle\hat{\phi}(\boldsymbol{K})\rangle = \phi(\boldsymbol{K})$. The variance of the estimate about the mean is given by $A(\boldsymbol{K})$, and the reconstruction is optimal in that it minimizes this variance for each mode $\boldsymbol{K}$.

2.3. Matched filter

Adopting the model potential template of Eq. (9), our matched filter operates on the lensing potential map to extract the normalization, ϕ_0, for a given scale $\theta_{\rm m}$. Each mode $\boldsymbol{K}$ of the estimated potential, $\hat{\phi}$, is an independently measured variable with standard deviation $A^{1/2}(K)$. We therefore construct the matched filter for the potential amplitude as

$$\hat{\phi}_0 = \left[\sum_{\boldsymbol{K}} \frac{|\Phi(\boldsymbol{K})|^2}{A(\boldsymbol{K})}\right]^{-1} \sum_{\boldsymbol{K}} \frac{\Phi^*(\boldsymbol{K})}{A(\boldsymbol{K})}\hat{\phi}(\boldsymbol{K}), \tag{14}$$

where $\Phi(\boldsymbol{K})$ is the Fourier transform of the model template (Eq. (9)). This yields an unbiased estimate of ϕ_0 with minimal variance given by

$${\rm Var}(\hat{\phi}_0) = \left[\sum_{\boldsymbol{K}} \frac{|\Phi(\boldsymbol{K})|^2}{A(\boldsymbol{K})}\right]^{-1}. \tag{15}$$

Once normalized by our measurement, $\hat{\phi}_0$, the cluster mass model is completely specified. We could quote our filter measurements directly as $\hat{\phi}_0$, but choose instead to express them in terms of the integrated convergence calculated using the model:

$$K_{5\theta 500} \equiv 2\pi \int_0^{5\theta_{500}} {\rm d}x\ x\kappa(x) = \frac{1}{D^2_{\rm clus}(z)\Sigma_{\rm cr}(z)} M_{\rm 5R500}. \tag{16}$$

Note that $\theta_{500} = R_{500}/D_{\rm clus}(z) = c_{500}\theta_{\rm m}$. The first equality defines our preferred observable, and the second relates it to cluster mass calculated within the radius $5R_{500}$; this is easily translated into M_{500} given the concentration parameter, c_{500}. Our estimator for this observable is

$$\hat{K}_{5\theta 500} \equiv 2\pi\hat{\phi}_0 \int_0^{5\theta_{500}} {\rm d}x\ x \frac{\Sigma_{\rm m}(x/\theta_{\rm m})}{\Sigma_{\rm cr}(z)} \tag{17}$$

$$= \frac{1}{D^2_{\rm clus}(z)\Sigma_{\rm cr}(z)} \hat{M}_{\rm 5R500}. \tag{18}$$

Hereafter, we consider $\hat{K}_{5\theta 500}$ as the output of the filter; it is dimensionless and expressed in arcmin^2. The second line defines our cluster mass estimator, whose units are set by the prefactor.

These estimators are unbiased over the CMB and noise ensembles: $\langle\hat{K}_{5\theta 500}\rangle = K_{5\theta 500}$ and $\langle\hat{M}_{\rm 5R500}\rangle = M_{\rm 5R500}$. They are also optimal in that they minimize their respective variances over the same ensemble. Explicitly, we have

$${\rm Var}(\hat{M}_{\rm 5R500}) = \left[D^2_{\rm clus}(z)\Sigma_{\rm cr}(z)\right]^2 \sigma^2_{K_{5\theta 500}}, \tag{19}$$

---

[1] Taken, for simplicity, to be axially symmetric.

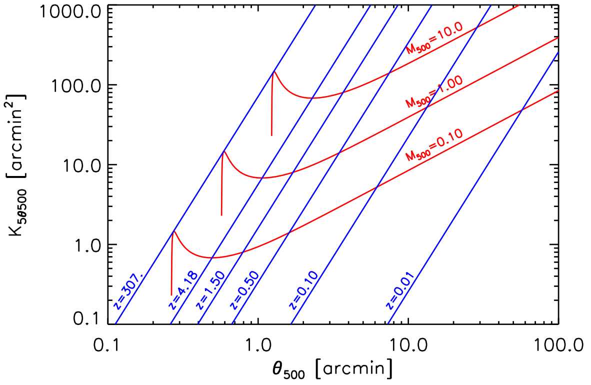

Fig. 1. Contours of cluster mass in 10^{15} $M_\odot$ units (red curves) and redshift (blue curves) projected onto the observational plane defined by the filter output $K_{5\theta500}$ and angular scale $\theta_{500} = c_{500}\theta_{\rm m}$. A cluster of fixed mass M_{500} follows a red contour according to Eq. (16) as it moves out in redshift. Each mass contour follows the same pattern, simply displaced in amplitude. This figure shows how each point in the observational plane maps to a point in the cluster plane of (M_{500}, z).

for the variance of the mass estimator, where $\sigma^2_{K_{5\theta500}}$ is the variance of our filter output, calculated using Eqs. (15) and (17). This is the uncertainty on the mass measurement of a single cluster, with contributions from instrumental noise and the CMB fluctuations themselves. We will see below that the kSZ adds an additional source of noise, as well as a bias term; fortunately, they are small in practice.

Figure 1 illustrates the relation between the observation plane $(K_{5\theta500}, \theta_{500})$ and physical cluster quantities. Each point in this plane maps directly to a point in the cluster (M_{500}, z) plane, as shown by the contours of iso-mass (in red) and iso-redshift (blue). At fixed mass, Eq. (16) specifies the evolution of $K_{5\theta500}$ as a function of redshift, which when coupled with $\theta_{500} \propto M_{500}^{1/3}/D_{\rm clus}(z)$ describes an iso-mass curve. As the cluster moves out in redshift, its angular size decreases; at the same time, the prefactor in Eq. (16) determines the decrease and final upturn in the integrated convergence. The rapid decrease from low redshift outwards may seem surprising, but is due to the fact that we integrate over angular extent. Integrated over physical extent, the convergence increases at first with redshift as the lensing kernel becomes more efficient, but the angular extent decreases and drives down the value of $K_{5\theta500}$. Each mass follows the same general curve, simply displaced in absolute scale.

A given experiment will trace a sensitivity curve in the observation plane. In Fig. 2 we show predictions for the filter sensitivity, expressed by the standard deviation of the filter variance, as a function of filter angular scale for a number of different experiments. The top three curves (traced in red) all refer to space-based experiments, while the three lower curves (in blue) represent ground-based experiments similar to the three generations of SPT (Story et al. 2013; Austermann et al. 2012; Benson & Benson 2013), ACT (Das et al. 2014) and ACT-Pol (Niemack et al. 2010). The space missions are *Planck* (Planck Collaboration I 2014) and two missions proposed to the European Space Agency, COrE (The COrE Collaboration et al. 2011) and PRISM (PRISM Collaboration et al. 2014). The former has similar resolution to *Planck*, but more detectors and lower noise, while the latter envisions a larger telescope with both lower noise and higher angular resolution.

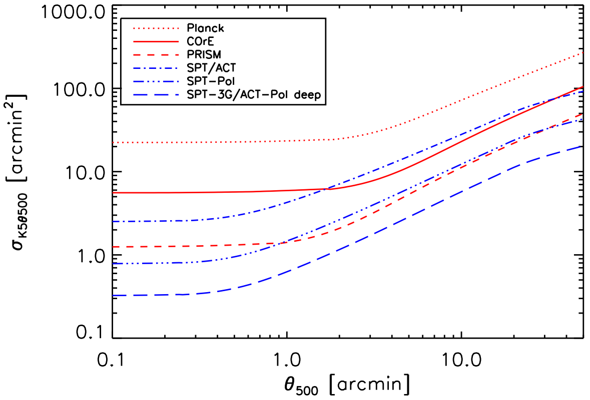

Fig. 2. Standard deviation, or filter noise, of the matched filter output (Eq. (16)) versus filter scale $\theta_{500} = c_{500}\theta_{\rm m}$ for the different experimental setups, as labeled. The red curves give results for the *Planck* satellite and two future missions proposed to ESA, COrE and PRISM. The first has similar angular resolution to *Planck* (~5 arcmin FWHM), but lower noise, while PRISM has both lower noise and higher resolution at ~2.6 arcmin. The blue curves show the noise levels for SPT/ACT, SPT-Pol and SPT-3G/ACT-Pol. All curves assume the filter is perfectly matched to the clusters. The experimental characteristics are summarized in Table 1.

We summarize the adopted characteristics of each experiment in Table 1 in terms of angular resolution and white noise in the reconstructed CMB map[2]. We emphasize, however, that the experiments have very different frequency coverage. Although not accounted for in this present discussion, we show later that extensive frequency coverage is crucial for proper CMB reconstruction and, especially, removal of the tSZ signal.

All sensitivity curves start on small angular scales with a flat response and then break to a rise toward larger filter scales. The break occurs on smaller scales for the higher resolution ground-based experiments. COrE and *Planck* have the same resolution and break on the same scale, but with its lower noise level, COrE's plateau lies below that of *Planck*. PRISM has a noise level comparable to SPT-3G, but slightly lower angular resolution. We see that it breaks at an intermediate filter scale and on a higher plateau than SPT-3G. This demonstrates the interplay of angular resolution and noise: At a given noise level in μK-arcmin, an experiment with higher angular resolution accesses more modes $\boldsymbol{k}$ to reconstruct a given potential mode $\boldsymbol{K}$ (Eq. (10)), thereby reducing the filter noise.

In Fig. 3 we give the standard deviation of the mass measurement, $M_{500}(z) = \sigma(z)$ (square root of Eq. (19)), as a function of redshift for each experimental setup. The results provide a useful metric for each experiment's ability to measure cluster mass: The uncertainty on the mean mass for a sample of N clusters at redshift z will be $M_{500}(z)/N^{1/2}$. Note, however, that a cluster of $nM_{500}(z)$ will have a significance smaller than $n\sigma$. This is because as the mass increases from the limiting value, the cluster's angular size also increases, driving the filter noise higher (unless we are on the small-scale plateau of the curves in Fig. 2).

We see that COrE and SPT/ACT can only be expected to measure mass for the most massive systems in the universe, while *Planck* cannot be expected to measure any individual cluster mass. The sensitivity of these experiments, however, is

---

[2] In each case, the reconstructed CMB map was assigned the characteristics of the experimental band closest to 143 GHz.

Table 1. Characteristics of representative surveys: *Planck* (Planck Collaboration I 2014), COrE (The COrE Collaboration et al. 2011), PRISM (PRISM Collaboration et al. 2014), ACT (Das et al. 2014), ACT-Pol (Niemack et al. 2010), SPT (Story et al. 2013), SPT-Pol (Austermann et al. 2012), SPT-3G (Benson & Benson 2013).

Name	Location	Map resolution (*FWHM*) [arcmin]	Map noise [μK-arcmin]
Planck	Space	5.0	45.0
COrE	Space	5.0	2.6
PRISM	Space	2.5	2.6
Generation: SPT/ACT	Ground	1.0	18.0
Generation: SPT-Pol	Ground	1.0	5.0
Generation: SPT-3G/ACT-Pol deep	Ground	1.0	2.0

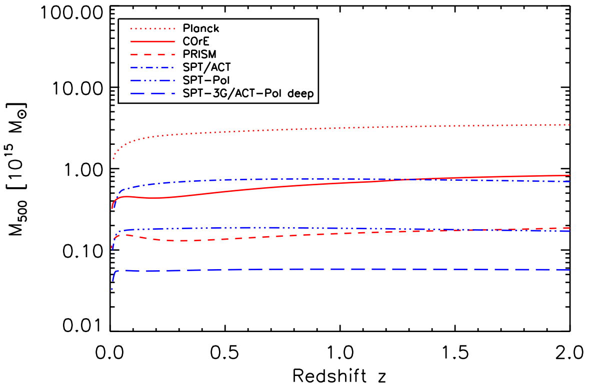

Fig. 3. Standard deviation of mass measurements, $M_{500}(z)$, with the matched filter (square root of Eq. (19)) as a function of cluster redshift for the same experimental setups plotted in Fig. 2. This comparison does not take into account the ability of each experiment to eliminate contaminating signals, such as the tSZ, which depends on spectral coverage. In this context, the space-based missions benefit from wider spectral coverage (see text).

sufficient to obtain mean mass as a function of other cluster observables by binning measurements; in other words, to establish mean observable-mass scaling relations. Herein lies the value of our matched filter approach, by providing a means of combining many low signal-to-noise measurements to statistically determine cluster mass. The sensitivity of SPT-Pol, SPT-3G/ACT-Pol and the PRISM mission, on the other hand, is sufficient to enable individual cluster mass measurements as well as statistical studies.

3. Astrophysical contaminants

The above discussion supposes that we have a clean map of CMB anisotropies from which to extract the lensing signal. To produce this map, we must first separate the CMB component from other astrophysical emission. In this work, we focus on the potentially most troublesome signals, those produced by the cluster itself at CMB-dominant frequencies, namely the tSZ and kSZ effects.

Generally, we employ the Internal Linear Combination (ILC) methodology to separate the CMB from other signals. Because we will find that the standard ILC does not sufficiently remove the tSZ signal, causing an important bias in our mass estimation, we present two techniques based on the ILC that seek in addition to actively remove the tSZ signal: template fitting and subtraction of the tSZ, and an ILC constrained to cancel the tSZ. Both prove satisfactory.

The kSZ cannot be eliminated in this fashion, however, having the same spectral signature as the CMB. It could be removed by template fitting for experiments with sufficient resolution, but as will be seen, it does not produce any significant bias in our mass estimations. Keeping this in mind, we restrict ourselves to an examination of the nature of the kSZ contamination on the reconstructed lensing potential. This will guide our interpretation of the simulation results.

We test our methodology using the simulations described in Sect. 4, presenting the results in Sect. 5. We will see the importance of actively removing the tSZ, and that any effect from the kSZ remains manageable. Our simulations do not include diffuse Galactic or extragalactic emission not related to the clusters. At this point of our study, having employed an ILC at the heart of our component separation techniques, we assume that these are adequately controlled; the issue will be studied in more detail in future work.

3.1. *The thermal SZ signal*

We develop two approaches to removing the tSZ signal: multifrequency matched filters (MMF) to estimate the amplitude of the tSZ effect and then remove it from the survey frequency maps prior to a standard ILC, and an ILC constrained to eliminate the tSZ signal while extracting the CMB map. We compare the performance of the two approaches in Sect. 5. The goal is to produce the CMB map, $\hat{S}$, used as input in the lensing reconstruction of Eq. (10).

3.1.1. Multifrequency matched filters (MMF)

With this approach we apply the MMF of Melin et al. (2006) using the pressure profile $T_{\rm t}(x/\theta_{\rm t})$ to obtain an estimate of the central Compton y parameter:

$$\hat{y}_{\rm o} = \int {\rm d}^2x\, \boldsymbol{\Psi}_{\theta_{\rm t}}{}^{t}(\boldsymbol{x}) \cdot \boldsymbol{m}(\boldsymbol{x}), \tag{20}$$

where

$$\boldsymbol{\Psi}_{\theta_{\rm t}}(\boldsymbol{k}) = \sigma^2_{\theta_{\rm t}} \mathbf{P}^{-1}(\boldsymbol{k}) \cdot \boldsymbol{t}_t(\boldsymbol{k}), \tag{21}$$

with

$$\sigma_{\theta_{\rm t}} \equiv \left[\int {\rm d}^2k\, \boldsymbol{t}_t{}^{t}(\boldsymbol{k}) \cdot \mathbf{P}^{-1} \cdot \boldsymbol{t}_t(\boldsymbol{k}) \right]^{-1/2}, \tag{22}$$

$\mathbf{P}(\boldsymbol{k})$ being the interband power spectrum matrix with contributions from (non-tSZ) sky signal and instrumental noise. It is the effective noise matrix for the MMF and can be estimated directly on the data, since the tSZ is small compared to other astrophysical signals in the sky patch centered on the cluster.

We assume that the tSZ is accurately described by our model and seek only to normalize the tSZ template to each cluster. This is the case for our simulations, because we are using the same profile for the simulated tSZ and the filter template. In reality, possible mismatch between the true cluster profile and the filter template would be a source of uncertainty.

Once we have normalized the template, we remove the tSZ signal from each of the N individual frequency maps,

$$\widehat{\boldsymbol{m}}(\boldsymbol{x}) = \boldsymbol{m}(\boldsymbol{x}) - \hat{y}_{\rm o}\boldsymbol{t}_{t}(\boldsymbol{x}), \tag{23}$$

and apply a standard ILC to reconstruct the clean CMB map:

$$\hat{S}(\boldsymbol{k}) = \left[\boldsymbol{b}^t\mathbf{P}^{-1}\boldsymbol{b}\right]^{-1}\boldsymbol{b}^t\mathbf{P}^{-1}\widehat{\boldsymbol{m}}(\boldsymbol{k}), \tag{24}$$

where $\boldsymbol{b}$ is the beam vector of dimension N. Finally, we convolve the resulting map with a fiducial beam, $b_{\rm fid}$ (5 arcmin in the case of *Planck*), to obtain the $\hat{S}(\boldsymbol{k})$ used in Eq. (10). The power spectrum associated with this map is

$$P_{\hat{S}} = |b_{\rm fid}|^2\left[\boldsymbol{b}^t\mathbf{P}^{-1}\boldsymbol{b}\right]^{-1}. \tag{25}$$

3.1.2. Constrained Internal Linear Combination (CILC)

In the second approach, we directly construct the clean CMB map with a constrained ILC designed to nullify the tSZ effect, making use of its well-defined spectral signature, j_ν. The formalism is described in detail by Remazeilles et al. (2011). The reconstructed clean CMB map can be written

$$\hat{S}(\boldsymbol{k}) = \Delta^{-1}\left[\left(\boldsymbol{j}_\nu{}^t\mathbf{P}^{-1}\boldsymbol{j}_\nu\right)\boldsymbol{b}^t\mathbf{P}^{-1} - \left(\boldsymbol{b}^t\mathbf{P}^{-1}\boldsymbol{j}_\nu\right)\boldsymbol{j}_\nu{}^t\mathbf{P}^{-1}\right]\boldsymbol{m}(\boldsymbol{k}), \tag{26}$$

$$\Delta = \left(\boldsymbol{b}^t\mathbf{P}^{-1}\boldsymbol{b}\right)\left(\boldsymbol{j}_\nu{}^t\mathbf{P}^{-1}\boldsymbol{j}_\nu\right) - \left(\boldsymbol{b}^t\mathbf{P}^{-1}\boldsymbol{j}_\nu\right)^2, \tag{27}$$

with $(\boldsymbol{j}_\nu)_i \equiv j_\nu(\nu_i)b_i$. The noise matrix, $\mathbf{P}$, is constructed as before.

We again convolve the resulting map with the fiducial beam, $b_{\rm fid}$, to obtain the CMB map, $\hat{S}(\boldsymbol{k})$, used in Eq. (10). The power spectrum for this fiducial map is

$$P_{\hat{S}} = \frac{|b_{\rm fid}|^2}{\Delta^2}\left[\left(\boldsymbol{j}_\nu{}^t\mathbf{P}^{-1}\boldsymbol{j}_\nu\right)^2\left(\boldsymbol{b}^t\mathbf{P}^{-1}\boldsymbol{b}\right) - \left(\boldsymbol{j}_\nu{}^t\mathbf{P}^{-1}\boldsymbol{j}_\nu\right)\left(\boldsymbol{b}^t\mathbf{P}^{-1}\boldsymbol{j}_\nu\right)^2\right]. \tag{28}$$

The strength of the CILC removal, compared to the MMF approach, is its insensitivity to cluster modeling uncertainties (e.g., SZ profile). On the other hand, the variance of the noise in the reconstructed CMB map is higher, slightly increasing the error on the final mass estimate, as we show in Sect. 5. We also present the impact of tSZ modeling uncertainties on the MMF approach in the same section.

3.2. The kinetic SZ signal

After the tSZ, the kSZ is the dominant cluster signal at CMB frequencies. It has the same spectrum as the primary CMB and cannot be removed by spectral separation methods.

We can appreciate the effect of the kSZ by returning to the lensing potential reconstruction of Eq. (10). Even in the best possible case, the reconstructed CMB map, $\hat{S}$, contains kSZ in addition to the lensed CMB and noise: $\hat{S}(\boldsymbol{x}) = S(\boldsymbol{x}) + \beta T_{\rm k}(x/\theta_{\rm k}) + n(\boldsymbol{x})$. The lensing map reconstruction therefore has four contributions:

$$\hat{\phi}'(\boldsymbol{K}) = \hat{\phi}(\boldsymbol{K}) + 2\mathcal{R}\left[\beta A(\boldsymbol{K})\sum_{\boldsymbol{k}} S(\boldsymbol{k})T^*_{\rm k}(\boldsymbol{k}'\theta_{\rm k})F(\boldsymbol{k},\boldsymbol{k}')\right] \tag{29}$$

$$+2\mathcal{R}\left[\beta A(\boldsymbol{K})\sum_{\boldsymbol{k}} n(\boldsymbol{k})T^*_{\rm k}(\boldsymbol{k}'\theta_{\rm k})F(\boldsymbol{k},\boldsymbol{k}')\right] \tag{30}$$

$$+\beta^2 A(\boldsymbol{K})\sum_{\boldsymbol{k}} T_{\rm k}(\boldsymbol{k}\theta_{\rm k})T^*_{\rm k}(\boldsymbol{k}'\theta_{\rm k})F(\boldsymbol{k},\boldsymbol{k}') \tag{31}$$

$$\equiv \hat{\phi}(\boldsymbol{K}) + \beta\left[\hat{\phi}_{\rm ks}(\boldsymbol{K}) + \hat{\phi}_{\rm kn}(\boldsymbol{K})\right] + \beta^2\hat{\phi}_{\rm kk}(\boldsymbol{K}) \tag{32}$$

where $\hat{\phi}$ contains just the CMB and noise terms, as considered in Sect. 2. The kSZ adds cross terms of the kSZ with both CMB, $\hat{\phi}_{\rm ks}$, and noise, $\hat{\phi}_{\rm kn}$, and a term quadratic in the kSZ signal, $\hat{\phi}_{\rm kk}$.

Averaged over the CMB and noise ensembles, the two middle terms vanish, independent of the value of β, because $\langle s(\boldsymbol{k})\rangle = \langle n(\boldsymbol{k})\rangle = 0$. They act as an additional noise contribution to the potential reconstruction for a given cluster. This behaviour differs from that of the kSZ when directly using the temperature anisotropy induced by cluster lensing, rather than reconstruction of the lensing potential as done here. For a given β, the kSZ is guaranteed to contribute to the temperature anisotropy at a level comparable to the lensing signal (Seljak & Zaldarriaga 2000; Lewis & Challinor 2006); in our case, however, the contribution could be small, depending only on the chance alignment of CMB and kSZ modes. In either case, additional averaging over a set of clusters will further reduce the effect of these terms linear in β because the objects will have random peculiar velocities.

The last term, quadratic in β, is a bias. Its presence is independent of the CMB and noise ensembles, and it cannot be beaten down by averaging over a cluster ensemble. With proper modeling of the kSZ signal, the bias could be eliminated, if needed, through subtraction, cluster by cluster, to leave a zero-mean residual as a noise contribution. This will not prove necessary in our subsequent study, where we will find that the bias is unimportant for realistic cluster velocities.

4. Simulations

We illustrate our mass estimation technique through recovery of the mass scale for a sample of clusters with simulated *Planck*-like observations. We proceed by first simulating a sample of identical clusters, and then consider a mock of the ESZ-XMM, a subsample of 62 clusters from the *Planck* Early Sunyaev-Zeldovich list (ESZ, Planck Collaboration VIII 2011) with good X-ray observations, including X-ray determined masses, $M^{\rm X}_{500}$, spanning the range $[2{-}20] \times 10^{14}\,M_\odot$ (ESZ-XMM, Planck Collaboration XI 2011). In a companion paper, we report an estimation of the mass scale of the actual ESZ-XMM sample using the *Planck* dataset.

Our first simulation consists of 62 observations of a mock of A2163, assigning mass and tSZ profiles following our adopted templates. With an X-ray deduced mass of $M^{\rm X}_{500} = 1.9\times10^{15}\,M_\odot$ ($z = 0.203$), this system is one of the most massive clusters known, falling near the 1σ curve for *Planck* shown in Fig. 3, and the most massive member of the ESZ-XMM.

We generate 62 independent realizations of primary CMB anisotropies and of white noise in tangential map projections of $10 \times 10\,{\rm deg}^2$ across the six highest frequency channels (100−857 GHz) of *Planck*. The mock of A2163 is centered in each channel map, the lensing is applied to the primary CMB anisotropies and the tSZ signal added. We then smooth each channel map by its corresponding beam and add the white

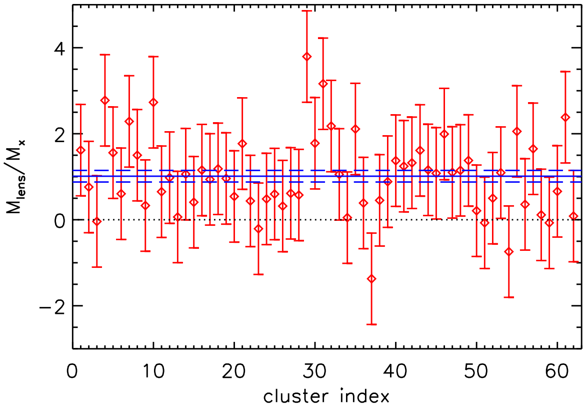

Fig. 4. Recovered mass for the 62 *Planck* simulations of A2163, expressed as the ratio of the CMB-measured mass to the input mass from the X-ray model, $\hat{M}_{500}/M^{\rm X}_{500}$. The tSZ was removed in this example using the CILC. Each diamond is the result of a single analysis chain (simulation, CILC, lensing extraction and matched filtering) accompanied by its 1σ uncertainty of 1.06. The solid blue line shows the sample average (1.01) and its 1σ range ($\pm 1.06/\sqrt{62} = \pm 0.13$).

noise, taking the noise and beam characteristics as published in Planck Collaboration I (2014). A simulated cluster observation thus comprises six channel maps, and there are 62 such simulated observations.

For each of these mock observations, we first remove the tSZ signal and produce a clean CMB map as described above. We then reconstruct the lensing potential map and apply the matched filter to extract our mass estimate, $\hat{M}_{500}$. Note that the filter is perfectly matched to the cluster in that the filter template and actual cluster projected potential are identical. We refer to the complete processing of a single cluster observation as an analysis *chain*.

For each chain, we compare the mass measurement to the input (X-ray deduced) mass of A2163 by forming the ratio $\hat{M}_{500}/M^{\rm X}_{500}$, and then take the sample mean, $\langle\hat{M}_{500}/M^{\rm X}_{500}\rangle$, over the 62 observations. An unbiased recovery of the sample mass scale corresponds to $\langle\hat{M}_{500}/M^{\rm X}_{500}\rangle = 1$.

We run two sets of 62 chains without kSZ to compare the results from the two different component separation methods presented in Sect. 3. We also ran additional simulation chains adding the kSZ effect with constant (systematic) peculiar velocities of 300 km s^{-1} and 900 km s^{-1} to each of the 62 clusters.

5. Results

Figure 4 shows the recovered mass ratio $\hat{M}_{500}/M^{\rm X}_{500}$ for the 62 simulated cluster observations without kSZ when using the constrained ILC to remove the tSZ. The individual measurement uncertainty on this quantity is large at 1.06 (the same for all chains, because the cluster and the statistical CMB and noise properties are the same for the 62 realizations). The points clearly disperse preferentially above zero, and taking the sample average we find $\langle\hat{M}_{500}/M^{\rm X}_{500}\rangle = 1.01 \pm 0.13$.

We have an unbiased recovery of the sample mass scale with 13% uncertainty. The result is identical when using the MMF component separation procedure[3]. The basic result of this study, therefore, is that we detect the mass scale of the sample at greater than 7σ.

If we model the SZ emission with the cool-core profile given in Table C.2. of Arnaud et al. (2010) but extract it with the MMF based on the universal profile, the sample average increases from 1.01 ± 0.13 to 1.19 ± 0.13. Adopting instead the morphologically disturbed profile, the value shifts to 1.09 ± 0.13. The mis-modeling of the SZ profile in the MMF component separation procedure may thus introduce a bias of order $\sim 1\sigma$ on the average.

We have also tested the sensitivity of our conclusions to the extension of the mass profile by truncating the integration at $R_{\rm vir}$ instead of $5R_{500}$. The individual measurement uncertainty increases to 1.23, which in turn slightly increases the uncertainty on the sample average to 0.16. This results in a modest decrease in the global significance of the detection from 7σ to between 6 and 7σ.

Accurate removal of the tSZ signal is essential, something which can be gauged from the results when applying a standard ILC to extract the CMB without any constraint to nullify the tSZ. In this case, we find a sample mean of $\langle\hat{M}_{500}/M^{\rm X}_{500}\rangle = 1.93 \pm 0.13$, highly biased by the residual tSZ signal.

The standard ILC is incapable of removing the tSZ signal to a sufficiently high level. We expect that this is in large part due to the fact that the tSZ is only a weak component in the map and hence not accounted for by the standard ILC weights. Our component separation techniques manage to adequately remove the tSZ by direct subtraction (MMF) or cancelation (CILC), both relying on the known spectral dependence of the signal. It is clear that multi-band CMB observations for accurate removal of the tSZ are an important consideration in designing experimental campaigns.

Turning to the kSZ effect, we find a sample mean of $\langle\hat{M}_{500}/M^{\rm X}_{500}\rangle = 1.00 \pm 0.13$ for the case of 300 km s^{-1} constant peculiar velocity, and $\langle\hat{M}_{500}/M^{\rm X}_{500}\rangle = 0.86 \pm 0.13$ for the case of 900 km s^{-1}. This is for the CILC, but the results are essentially the same for the MMF. Note that the uncertainties on the sample means are unchanged, because they are calculated from the sample size and the individual measurement error, the latter determined by the unchanged CMB and noise properties.

There is no evidence of bias in the sample mean at the lower peculiar velocity of 300 km s^{-1}, while a bias of 14% appears at the higher value of 900 km s^{-1}. In the standard ΛCDM model, we expect individual cluster peculiar velocities to follow a Gaussian distribution of zero mean and variance $\langle\beta^2\rangle \approx \left(300\,{\rm km\,s^{-1}}\right)^2$. Our result for the mean of a set of clusters with this constant velocity is therefore representative of the bias expected of the quadratic term in β. The bias term is clearly present, but only important at atypically large peculiar velocities.

The linear term is also present, causing an increase in the observed dispersion of the individual measurements. By comparing the dispersion before and after addition of the kSZ effect, we deduce that it contributes 0.14 and 0.31, respectively, for the lower and higher peculiar velocities. The former value is the more realistic and should be compared to the CMB and noise contribution to the dispersion (individual uncertainties) of 1.06.

The overall conclusion is the same for the simulated ESZ-XMM, as shown in Fig. 5. We obtain an unbiased estimate of the sample mass scale: $\langle\hat{M}_{500}/M^{\rm X}_{500}\rangle = 0.99 \pm 0.28$. The significance is lower than before because the ESZ-XMM contains a range of cluster masses, all of them smaller than A2163, its most massive member. Nevertheless, we find that the mass scale can be recovered at the 3σ level. In this case, truncating the profile

---

[3] The individual measurement uncertainty is slightly lower in this case (1.04 against 1.06), but the sample mean and its uncertainty are the same to the given precision.

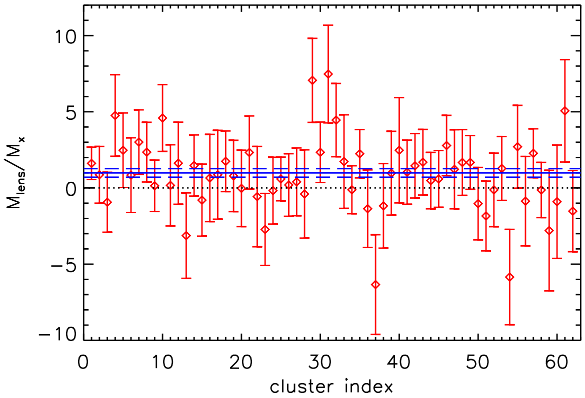

Fig. 5. Recovered mass for the *Planck* ESZ-XMM simulation, expressed as in Fig. 4 by the ratio of the CMB-measured mass to the input mass from the X-ray model, $\hat{M}_{500}/M^{X}_{500}$. The tSZ was removed using the CILC, and the blue solid and dashed lines show the sample mean and its 1σ range: $\langle\hat{M}_{500}/M^{X}_{500}\rangle = 0.99 \pm 0.28$. This simulation includes a random kSZ effect with Gaussian standard deviation of 300 km s^{-1}. The CMB and noise realizations are the same as in Fig. 4, resulting in a similar pattern in the distribution of points, but individual uncertainties are larger (note the change in scale).

at $R_{\rm vir}$ increases the uncertainty from 0.28 to 0.33, leaving the conclusion unchanged. This simulation also included a kSZ effect from random peculiar velocities with a Gaussian standard deviation of 300 km s^{-1}. We see no evidence for its impact on the recovered sample mean.

6. Discussion

Our results show that the proposed method can be a practical tool for estimating cluster masses, even with current CMB temperature data. It offers a new way to constrain cluster scaling relations between total mass and observables such as X-ray luminosity, SZ signal strength or richness. These relations are central to cosmological and large-scale structure analyses of cluster catalogues.

The method complements others for measuring cluster mass. Like gravitational shear, it directly probes total mass without assumptions about the state of any particular cluster component; this is strictly true for the CILC method, although we note that there does remain some modeling uncertainty when applying the MMF component separation, as discussed above. The method's particular strengths are that it can be used to much higher redshifts, using the CMB as a source plane, and that it is sensitive to the convergence field, rather than its gradient like the shear. Noting this latter difference, several authors have recently pointed out the value of combined CMB and shear analyses in the more general context (Hand et al. 2013; Das et al. 2013).

A critical capability of the proposed procedure is to provide accurate measurements and their uncertainties in the low signal-to-noise regime. This enables statistical analyses that permit practical application to existing CMB temperature datasets.

We achieve it through the lensing reconstruction that furnishes well-defined noise properties for use by the filter. The noise arises not just from the instrument, but also from the CMB itself, because the lensing signature is a correlation between CMB anisotropy modes behind the cluster, modes that we do not a priori know. Instead, we rely on the power spectrum of the primary CMB (and its Gaussianity) to tell us what they are on average and the dispersion about that average. In many ways, this is simpler than trying to determine the CMB gradient around each individual cluster, as needed when working directly with the secondary temperature anisotropy generated by lensing.

Figure 3 summarizes the ideal statistical power of various experiments to measure cluster mass, showing the standard deviation of filter mass determinations as a function of cluster redshift. It is ideal because it only accounts for noise from the CMB and the instrument. The curves are extremely flat in redshift, a reflection of the broad lensing kernel to the source plane of the CMB.

Comparing the space experiments (the red curves), we see that *Planck* is dominated by instrumental noise, since it has the same angular resolution as COrE, which performs much better with its lower noise level, while PRISM gains further by incorporating more modes in reaching to smaller scales. Even at their higher angular resolution, the ground-based experiments are not dominated by the CMB, as can be seen from the fact that the mass filter noise continues to decrease with decreasing instrumental noise.

We examined the impact of the tSZ and kSZ signals using simulations of *Planck*-like observations of massive clusters. Our main result is that the tSZ must be accurately removed to avoid biasing the mass estimations. A standard ILC is not sufficient. We applied two methods, both of which proved satisfactory. Based on the ILC, their key additional characteristic is that they actively subtract or nullify the tSZ. The success of the CILC is encouraging, because it does not rely on any adopted profile for the tSZ. Our result emphasizes the importance of broad frequency coverage in experimental design to enable adequate component separation.

The kSZ cannot be removed through such spectral separation methods and it remains in the CMB maps used to reconstruct the lensing potential. It impacts the final result by adding a source of measurement noise (term linear in β) and a bias (term in β^2). In our simulations, we found evidence for both terms. Fortunately, their influence is small for the expected distribution of cluster peculiar velocity.

These latter conclusions only apply in the context of our simulations of *Planck*-like CMB observations of massive clusters. Understanding these details in other experimental setups, e.g., ground-based instruments, would require dedicated simulations. The same applies to study of *Planck*-like observations of large cluster samples including lower mass systems.

Additional limitations of the simulations presented here include lack of other foreground sources, such as diffuse Galactic emission and extragalactic sources. Since we are using component separation techniques based on the ILC, we assume for this preliminary study that they adequately remove these foregrounds. Our clusters are also simulated in isolation and modeled by the same spherically symmetric profiles used in our filters (tSZ and mass filters)[4]. More realistic simulations would employ variations in model profiles and numerical simulations of clusters in their cosmological context to evaluate the effects of local structure around the clusters, as well as that of uncorrelated large-scale structure along the line-of-sight that contribute to the noise term.

Despite these limitations, our simulations are sufficient to demonstrate the potential of the *Planck* 2013 dataset to detect the mass scale of the ESZ-XMM. Our simulation of this observation of 62 clusters is summarized in Fig. 5. The conclusion is

---

[4] Recall the above statement that the CILC does not, however, rely on an adopted template.

that we should be able to detect the mass scale of this catalog to slightly more than 3σ. A separate paper presents our analysis on the real *Planck* dataset.

7. Conclusion

We propose a method to measure galaxy cluster masses using CMB lensing and demonstrate that it can be practically applied to existing datasets (e.g., ACT, *Planck*, SPT) in statistical analyses of cluster samples. The strength of the approach draws from its ability to provide viable mass estimates and uncertainties even in low signal-to-noise regimes, thereby enabling straightforward statistical analyses of systems well below individual detection.

Accurate removal of the tSZ is important and achievable, as we demonstrate by application of component separation methods that actively subtract or nullify it. The implication is that experimental design must allow for sufficient spectral coverage to enable effective separation methods.

Using a simulation of the *Planck* ESZ-XMM sample, we conclude that it would be possible to determine the mass scale of this set of 62 clusters to 3σ significance (CMB and instrumental noise only). In a companion paper, we present a first application of our method to the *Planck* data on the actual ESZ-XMM.

The method presented here uses only temperature data in the lensing reconstruction. Future work will extend it to CMB polarization data. Our preliminary study here opens the way to numerous research avenues targeting additional issues related to foregrounds and large-scale structure, and calls for detailed studies dedicated to specific experimental campaigns.

Lensing of the CMB opens a new and independent avenue for studying cluster masses, an important complement to other techniques, such as weak gravitational lensing of background galaxies. In fact, CMB lensing offers the possibility of calibrating large cluster samples now while we await large area galaxy lensing surveys, such as the Dark Energy Survey, the Large Synoptic Survey Telescope, and the *Euclid* and WFIRST space missions. And it will remain the more efficient way to measure cluster masses at high redshifts, where the source galaxy population rapidly declines in imaging surveys.

Acknowledgements. The authors would like to thank the anonymous referee for useful comments which helped to clarify some important aspects of this work. A portion of the research described in this paper was carried out at the Jet Propulsion Laboratory, California Institute of Technology, under a contract with the National Aeronautics and Space Administration.

References

Allen, S. W., Evrard, A. E., & Mantz, A. B. 2011, ARA&A, 49, 409
Arnaud, M., Pointecouteau, E., & Pratt, G. W. 2005, A&A, 441, 893
Arnaud, M., Pointecouteau, E., & Pratt, G. W. 2007, A&A, 474, L37
Arnaud, M., Pratt, G. W., Piffaretti, R., et al. 2010, A&A, 517, A92
Austermann, J. E., Aird, K. A., Beall, J. A., et al. 2012, in SPIE Conf. Ser., 8452
Bartelmann, M., & Schneider, P. 2001, Phys. Rep., 340, 291
Benson, B., & Benson. 2013, in IAU Symp. 288, eds. M. G. Burton, X. Cui, & N. F. H. Tothill, 76
Bocquet, S., Saro, A., Mohr, J. J., et al. 2015, ApJ, 799, 214
Böhringer, H., Chon, G., & Collins, C. A. 2014, A&A, 570, A31
Bullock, J. S., Kolatt, T. S., Sigad, Y., et al. 2001, MNRAS, 321, 559
Das, S., Sherwin, B. D., Aguirre, P., et al. 2011, Phys. Rev. Lett., 107, 021301
Das, S., Errard, J., & Spergel, D. 2013, ArXiv e-prints [`arXiv:1311.2338`]
Das, S., Louis, T., Nolta, M. R., et al. 2014, J. Cosmol. Astropart. Phys., 4, 14
Gladders, M. D., Yee, H. K. C., Majumdar, S., et al. 2007, ApJ, 655, 128
Hand, N., Leauthaud, A., Das, S., et al. 2013, ArXiv e-prints [`arXiv:1311.6200`]
Hasselfield, M., Hilton, M., Marriage, T. A., et al. 2013, Cosmol. Astropart. Phys, 7, 8
Hoekstra, H., Herbonnet, R., Muzzin, A., et al. 2015, MNRAS, 449, 685
Holder, G., & Kosowsky, A. 2004, ApJ, 616, 8
Hu, W., & Okamoto, T. 2002, ApJ, 574, 566
Lewis, A., & Challinor, A. 2006, Phys. Rep., 429, 1
Mantz, A., Allen, S. W., Rapetti, D., & Ebeling, H. 2010, MNRAS, 406, 1759
Mantz, A. B., von der Linden, A., Allen, S. W., et al. 2015, MNRAS, 446, 2205
Marrone, D. P., Smith, G. P., Okabe, N., et al. 2012, ApJ, 754, 119
Maturi, M., Bartelmann, M., Meneghetti, M., & Moscardini, L. 2005, A&A, 436, 37
Melin, J.-B., Bartlett, J. G., & Delabrouille, J. 2006, A&A, 459, 341
Muñoz-Cuartas, J. C., Macciò, A. V., Gottlöber, S., & Dutton, A. A. 2011, MNRAS, 411, 584
Nagai, D., Kravtsov, A. V., & Vikhlinin, A. 2007, ApJ, 668, 1
Navarro, J. F., Frenk, C. S., & White, S. D. M. 1996, ApJ, 462, 563
Neto, A. F., Gao, L., Bett, P., et al. 2007, MNRAS, 381, 1450
Niemack, M. D., Ade, P. A. R., Aguirre, J., et al. 2010, in SPIE Conf. Ser., 7741
Planck Collaboration VIII. 2011, A&A, 536, A8
Planck Collaboration XI. 2011, A&A, 536, A11
Planck Collaboration I. 2014, A&A, 571, A1
Planck Collaboration XVI. 2014, A&A, 571, A16
Planck Collaboration XVII. 2014, A&A, 571, A17
Planck Collaboration XX. 2014, A&A, 571, A20
Planck Collaboration 2015, A&A, submitted [`arXiv:1502.01597`]
Planck Collaboration Int. III. 2013, A&A, 550, A129
Pratt, G. W., Croston, J. H., Arnaud, M., & Böhringer, H. 2009, A&A, 498, 361
PRISM Collaboration 2014, JCAP, 2, 6
Reichardt, C. L., Stalder, B., Bleem, L. E., et al. 2013, ApJ, 763, 127
Remazeilles, M., Delabrouille, J., & Cardoso, J.-F. 2011, MNRAS, 410, 2481
Rozo, E., Rykoff, E. S., Evrard, A., et al. 2009, ApJ, 699, 768
Rozo, E., Wechsler, R. H., Rykoff, E. S., et al. 2010, ApJ, 708, 645
Rozo, E., Rykoff, E. S., Bartlett, J. G., & Evrard, A. E. 2013, ArXiv e-prints [`arXiv:1302.5086`]
Rozo, E., Bartlett, J. G., Evrard, A. E., & Rykoff, E. S. 2014a, MNRAS, 438, 78
Rozo, E., Evrard, A. E., Rykoff, E. S., & Bartlett, J. G. 2014b, MNRAS, 438, 62
Seljak, U., & Zaldarriaga, M. 2000, ApJ, 538, 57
Stanek, R., Evrard, A. E., Böhringer, H., Schuecker, P., & Nord, B. 2006, ApJ, 648, 956
Story, K. T., Reichardt, C. L., Hou, Z., et al. 2013, ApJ, 779, 86
Sunyaev, R. A., & Zeldovich, Y. B. 1972, Comm. Astrophys. Space Phys., 4, 173
Sunyaev, R. A., & Zeldovich, I. B. 1980, MNRAS, 190, 413
The COrE Collaboration, Armitage-Caplan, C., Avillez, M., et al. 2011, ArXiv e-prints [`arXiv:1102.2181`]
Vale, C., Amblard, A., & White, M. 2004, New Astron., 10, 1
van Engelen, A., Keisler, R., Zahn, O., et al. 2012, ApJ, 756, 142
Vikhlinin, A., Kravtsov, A., Forman, W., et al. 2006, ApJ, 640, 691
Vikhlinin, A., Kravtsov, A. V., Burenin, R. A., et al. 2009, ApJ, 692, 1060
von der Linden, A., Mantz, A., Allen, S. W., et al. 2014, MNRAS, 443, 1973
Yee, H. K. C., & Ellingson, E. 2003, ApJ, 585, 215
Zaldarriaga, M., & Seljak, U. 1999, Phys. Rev. D, 59, 123507

E.4 Lois d'échelles

Les quatre articles suivants sont inclus dans cette partie et sont décrits dans le chapitre 6.

- Melin, J.-B., Bartlett, J. G., Delabrouille, J., et al., The galaxy cluster YSZ - LX and YSZ - M relations from the WMAP 5-yr data. 2011, A&A, 525, A139, arXiv:1001.0871 *[39 citations]*
- Planck Collaboration X, Planck early results. X. Statistical analysis of Sunyaev-Zeldovich scaling relations for X-ray galaxy clusters. 2011, A&A, 536, A10, arXiv:1101.2043 *[106 citations]*
- Planck Collaboration XII, Planck early results. XII. Cluster Sunyaev-Zeldovich optical scaling relations. 2011, A&A, 536, A12, arXiv:1101.2027 *[85 citations]*
- Planck Collaboration Int. XI, Planck intermediate results. XI. The gas content of dark matter halos: the Sunyaev-Zeldovich-stellar mass relation for locally brightest galaxies. 2013, A&A, 557, A52, arXiv:1212.4131 *[18 citations]*

A&A 525, A139 (2011)
DOI: 10.1051/0004-6361/201013999

Astronomy & Astrophysics

The galaxy cluster $Y_{\rm SZ}-L_{\rm X}$ and $Y_{\rm SZ}-M$ relations from the WMAP 5-yr data

J.-B. Melin[1], J. G. Bartlett[2], J. Delabrouille[3], M. Arnaud[4], R. Piffaretti[4], and G. W. Pratt[4]

[1] DSM/Irfu/SPP, CEA/Saclay, 91191 Gif-sur-Yvette Cedex, France
e-mail: `jean-baptiste.melin@cea.fr`
[2] APC – Université Paris Diderot, 10 rue Alice Domon et Léonie Duquet, 75205 Paris Cedex 13, France
e-mail: `bartlett@apc.univ-paris7.fr`
[3] APC – CNRS, 10 rue Alice Domon et Léonie Duquet, 75205 Paris Cedex 13, France
e-mail: `delabrouille@apc.univ-paris7.fr`
[4] DSM/Irfu/SAp, CEA/Saclay, 91191 Gif-sur-Yvette Cedex
e-mail: `[monique.arnaud;rocco.piffaretti;gabriel.pratt]@cea.fr`

Received 6 January 2010 / Accepted 21 October 2010

ABSTRACT

We use multifrequency matched filters to estimate, in the WMAP 5-year data, the Sunyaev-Zel'dovich (SZ) fluxes of 893 ROSAT NORAS/REFLEX clusters spanning the luminosity range $L_{\rm X,[0.1-2.4]\ keV} = 2\times10^{41}-3.5\times10^{45}$ erg s^{-1}. The filters are spatially optimised by using the universal pressure profile recently obtained from combining XMM-Newton observations of the REXCESSsample and numerical simulations. Although the clusters are individually only marginally detected, we are able to firmly measure the SZ signal ($>10\sigma$) when averaging the data in luminosity/mass bins. The comparison between the bin-averaged SZ signal versus luminosity and X-ray model predictions shows excellent agreement, implying that there is no deficit in SZ signal strength relative to expectations from the X-ray properties of clusters. Using the individual cluster SZ flux measurements, we directly constrain the $Y_{500}-L_{\rm X}$ and $Y_{500}-M_{500}$ relations, where Y_{500} is the Compton y-parameter integrated over a sphere of radius r_{500}. The $Y_{500}-M_{500}$ relation, derived for the first time in such a wide mass range, has a normalisation $Y^{*}_{500} = [1.60 \pm 0.19] \times 10^{-3}$ arcmin^2 at $M_{500} = 3 \times 10^{14}\,h^{-1}\,M_\odot$, in excellent agreement with the X-ray prediction of 1.54×10^{-3} arcmin^2, and a mass exponent of $\alpha = 1.79 \pm 0.17$, consistent with the self-similar expectation of 5/3. Constraints on the redshift exponent are weak due to the limited redshift range of the sample, although they are compatible with self-similar evolution.

Key words. cosmology: observations – galaxies: clusters: general – galaxies: clusters: intracluster medium – cosmic background radiation – X-rays: galaxies: clusters

1. Introduction

Capability to observe the Sunyaev-Zel'dovich (SZ) effect has improved immensely in recent years. Dedicated instruments now produce high resolution images of single objects (e.g. Kitayama et al. 2004; Halverson et al. 2009; Nord et al. 2009) and moderately large samples of high-quality SZ measurements of previously-known clusters (e.g., Mroczkowski et al. 2009; Plagge et al. 2010). In addition, large-scale surveys for clusters using the SZ effect are underway, both from space with the Planck mission (Valenziano et al. 2007; Lamarre et al. 2003) and from the ground with several dedicated telescopes, such as the South Pole Telescope (Carlstrom et al. 2009) leading to the first discoveries of clusters solely through their SZ signal (Staniszewski et al. 2009). These results open the way for a better understanding of the SZ-Mass relation and, ultimately, for cosmological studies with large SZ cluster catalogues.

The SZ effect probes the hot gas in the intracluster medium (ICM). Inverse Compton scattering of cosmic microwave background (CMB) photons by free electrons in the ICM creates a unique spectral distortion (Sunyaev & Zeldovich 1970, 1972) seen as a frequency-dependent change in the CMB surface brightness in the direction of galaxy clusters that can be written as $\Delta i_\nu(\hat{n}) = y(\hat{n})\,j_\nu(x)$, where j_ν is a universal function of the dimensionless frequency $x = h\nu/kT_{\rm cmb}$. The Compton y-parameter is given by the integral of the electron pressure along the line-of-sight in the direction $\hat{n}$,

$$y = \int_{\hat{n}} \frac{kT_{\rm e}}{m_{\rm e}c^2} n_{\rm e}\sigma_{\rm T}{\rm d}l, \tag{1}$$

where $\sigma_{\rm T}$ is the Thomson cross section.

Most notably, the integrated SZ flux from a cluster directly measures the total thermal energy of the gas. Expressing this flux in terms of the integrated Compton y-parameter $Y_{\rm SZ}$ – defined by $\int {\rm d}\Omega\,\Delta\,i_\nu(\hat{n}) = Y_{\rm SZ}\,j_\nu(x)$ – we see that $Y_{\rm SZ} \propto \int {\rm d}\Omega\,{\rm d}l n_{\rm e}T_{\rm e} \propto \int n_{\rm e}T_{\rm e}{\rm d}V$. For this reason, we expect $Y_{\rm SZ}$ to closely correlate with total cluster mass, M, and to provide a low-scatter mass proxy.

This expectation, borne out by both numerical simulations (e.g., da Silva et al. 2004; Motl et al. 2005; Kravtsov et al. 2006) and indirectly from X-ray observations using $Y_{\rm X}$, the product of the gas mass and mean temperature (Nagai et al. 2007; Arnaud et al. 2007; Vikhlinin et al. 2009), strongly motivates the use of SZ cluster surveys as cosmological probes. Theory predicts the cluster abundance and its evolution – the mass function – in terms of M and the cosmological parameters. With a good mass proxy, we can measure the mass function and its evolution and hence constrain the cosmological model, including the properties of dark energy. In this context the relationship between the integrated SZ flux and total mass, $Y_{\rm SZ}-M$, is fundamental as the required link between theory and observation. Unfortunately, despite its importance, we are only beginning to observationally constrain the relation (Bonamente et al. 2008; Marrone et al. 2009).

Several authors have extracted the cluster SZ signal from WMAP data (Bennett et al. 2003; Hinshaw et al. 2007, 2009). However, the latter are not ideal for SZ observations: the instrument having been designed to measure primary CMB anisotropies on scales larger than galaxy clusters, the spatial resolution and sensitivity of the sky maps render cluster detection difficult. Nevertheless, these authors extracted the cluster SZ signal by either cross-correlating with the general galaxy distribution (Fosalba et al. 2003; Myers et al. 2004; Hernández-Monteagudo et al. 2004, 2006) or "stacking" existing cluster catalogues in the optical or X-ray (Lieu et al. 2006; Afshordi et al. 2007; Atrio-Barandela et al. 2008; Bielby & Shanks 2007; Diego & Partridge 2009). These analyses indicate that an isothermal β-model is not a good description of the SZ profile, and some suggest that the SZ signal strength is lower than expected from the X-ray properties of the clusters (Lieu et al. 2006; Bielby & Shanks 2007).

Recent in-depth X-ray studies of the ICM pressure profile demonstrate regularity in shape and simple scaling with cluster mass. Combining these observations with numerical simulations leads to a universal pressure profile (Nagai et al. 2007; Arnaud et al. 2010) that is best fit by a modified NFW profile. The isothermal β-model, on the other hand, does not provide an adequate fit. From this newly determined X-ray pressure profile, we can infer the expected SZ profile, $y(r)$, and the $Y_{\rm SZ}-M$ relation at low redshift (Arnaud et al. 2010).

It is in light of this recent progress from X-ray observations that we present a new analysis of the SZ effect in WMAP with the aim of constraining the SZ scaling laws. We build a multifrequency matched filter (Herranz et al. 2002; Melin et al. 2006) based on the known spectral shape of the thermal SZ effect and the shape of the universal pressure profile of Arnaud et al. (2010). This profile was derived from REXCESS (Böhringer et al. 2007), a sample expressly designed to measure the structural and scaling properties of the local X-ray cluster population by means of an unbiased, representative sampling in luminosity. Using the multifrequency matched filter, we search for the SZ effect in WMAP from a catalogue of 893 clusters detected by ROSAT, maximising the signal-to-noise by adapting the filter scale to the expected characteristic size of each cluster. The size is estimated through the luminosity-mass relation derived from the REXCESS sample by Pratt et al. (2009).

We then use our SZ measurements to directly determine the $Y_{\rm SZ}-L_{\rm X}$ and $Y_{\rm SZ}-M$ relations and compare to expectations based on the universal X-ray pressure profile. As compared to the previous analyses of Bonamente et al. (2008) and Marrone et al. (2009), the large number of systems in our WMAP/ROSAT sample allows us to constrain both the normalisation and slope of the $Y_{\rm SZ}-L_{\rm X}$ and $Y_{\rm SZ}-M$ relations over a wider mass range and in the larger aperture of r_{500}. In addition, the analysis is based on a more realistic pressure profile than in these analyses, which were based on an isothermal β-model. Besides providing a direct constraint on these relations, the good agreement with X-ray predictions implies that there is in fact no deficit in SZ signal strength relative to expectations from the X-ray properties of these clusters.

The discussion proceeds as follows. We first present the WMAP 5-year data and the ROSAT cluster sample used, a combination of the REFLEX and NORAS catalogues. We then present the SZ model based on the X-ray-measured pressure profile (Sect. 3). In Sect. 4, we discuss our SZ measurements, after first describing how we extract the signal using the matched filter. Section 5 details the error budget. We compare our measured scaling laws to the X-ray predictions in Sects. 6 and 7 and then conclude in Sect. 8. Finally, we collect useful SZ definitions and unit conversions in the Appendices.

Throughout this paper, we use the WMAP5-only cosmological parameters set as our "fiducial cosmology", i.e. $h = 0.719$, $\Omega_{\rm M} = 0.26$, $\Omega_\Lambda = 0.74$, where h is the Hubble parameter at redshift $z = 0$ in units of 100 km s^{-1}/Mpc. We note $h_{70} = h/0.7$ and $E(z)$ is the Hubble parameter at redshift z normalised to its present value. M_{500} is defined as the mass within the radius r_{500} at which the mean mass density is 500 times the critical density, $\rho_{\rm crit}(z)$, of the universe at the cluster redshift: $M_{500} = \frac{4}{3}\pi\,\rho_{\rm crit}(z)\,500\,r_{500}^3$.

2. The WMAP-5yr data and the NORAS/REFLEX cluster sample

2.1. The WMAP-5 yr data

We work with the WMAP full resolution coadded five year sky temperature maps at each frequency channel (downloaded from the LAMBDA archive[1]). There are five full sky maps corresponding to frequencies 23, 33, 41, 61, 94 GHz (bands K, Ka, Q, V, W respectively). The corresponding beam full widths at half maximum are approximately 52.8, 39.6, 30.6 21.0 and 13.2 arcmins. The maps are originally at HEALPix[2] resolution nside = 512 (pixel = 6.87 arcmin). Although this is reasonably adequate to sample WMAP data, it is not adapted to the multifrequency matched filter algorithm we use to extract the cluster fluxes. We oversample the original data, to obtain nside = 2048 maps, by zero-padding in harmonic space. In detail, this is performed by computing the harmonic transform of the original maps, and then performing the back transform towards a map with nside = 2048, with a maximum value of ℓ of $\ell_{\rm max} = 750, 850, 1100, 1500, 2000$ for the K, Ka, Q, V, W bands respectively. The upgraded maps are smooth and do not show pixel edges as we would have obtained using the HEALPix upgrading software, based on the tree structure of the HEALPix pixelisation scheme. This smooth upgrading scheme is important as the high spatial frequency content induced by pixel edges would have been amplified through the multifrequency matched filters implemented in harmonic space.

In practice, the multifrequency matched filters are implemented locally on small, flat patches (gnomonic projection on tangential maps), which permits adaptation of the filter to the local conditions of noise and foreground contamination. We divide the sphere into 504 square tangential overlapping patches (100 deg^2 each, pixel = 1.72 arcmin). All of the following analysis is done on these sky patches.

The implementation of the matched filter requires knowledge of the WMAP beams. In this work, we assume symmetric beams, for which the transfer function b_ℓ is computed, in each frequency channel, from the noise-weighted average of the transfer functions of individual differential assemblies (a similar approach was used in Delabrouille et al. 2009).

---

[1] `http://lambda.gsfc.nasa.gov/`

[2] `http://healpix.jpl.nasa.gov`

Table 1. Values for the parameters of the $L_{\rm X} - M$ relation derived from REXCESS data (Pratt et al. 2009; Arnaud et al. 2010).

Corrected for MB	$\log\left(\frac{C_M}{10^{44}\ h_{70}^{-2}\ [{\rm erg\,s^{-1}}]}\right)$	α_M	$\sigma_{\log L - \log M}$
no	0.295	1.50	0.183
yes	0.215	1.61	0.199

2.2. The NORAS/REFLEX cluster sample and derived X-ray properties

We construct our cluster sample from the largest published X-ray catalogues: NORAS (Böhringer et al. 2000) and REFLEX (Böhringer et al. 2004), both constructed from the ROSAT All-Sky Survey. We merge the cluster lists given in Tables 1, 6 and 8 from Böhringer et al. (2000) and Table 6 from Böhringer et al. (2004) and since the luminosities of the NORAS clusters are given in a standard cold dark matter (SCDM) cosmology ($h = 0.5$, $\Omega_{\rm M} = 1$), we converted them to the WMAP5 cosmology. We also convert the luminosities of REFLEX clusters from the basic ΛCDM cosmology ($h = 0.7$, $\Omega_{\rm M} = 0.3$, $\Omega_\Lambda = 0.7$) to the more precise WMAP5 cosmology. Removing clusters appearing in both catalogues leaves 921 objects, of which 893 have measured redshifts. We use these 893 clusters in the analysis detailed in the next section.

The NORAS/REFLEX luminosities $L_{\rm X}$, measured in the soft [0.1–2.4] keV energy band, are given within various apertures depending on the cluster. We convert the luminosities $L_{\rm X}$ to L_{500}, the luminosities within r_{500}, using an iterative scheme. This scheme is based on the mean electron density profile of the REXCESS cluster sample (Croston et al. 2008), which allows conversion of the luminosity between various apertures, and the REXCESS L_{500}–M_{500} relation (Pratt et al. 2009), which implicitly relates r_{500} and L_{500}. The procedure thus simultaneously yields an estimate of the cluster mass, M_{500}, and the corresponding angular extent $\theta_{500} = r_{500}/D_{\rm ang}(z)$, where $D_{\rm ang}(z)$ is the angular distance at redshift z. In the following we consider values derived from relations both corrected and uncorrected for Malmquist bias. The relations are described by the following power law models[3]:

$$E(z)^{-7/3}\, L_{500} = C_M \left(\frac{M_{500}}{3\times10^{14}\ h_{70}^{-1}\ M_\odot}\right)^{\alpha_{\rm M}} \qquad (2)$$

where the normalisation $C_{\rm M}$, the exponent $\alpha_{\rm M}$ and the dispersion (nearly constant with mass) are given in Table 1. The L_{500}–M_{500} relation was derived in the mass range $[10^{14}$–$10^{15}]\ M_\odot$. These limits are shown in Fig. 1. Note that we assume the relation is valid for lower masses.

The final catalogue of 893 objects contains the position of the clusters (longitude and latitude), the measured redshift z, the derived X-ray luminosity L_{500}, the mass M_{500} and the angular extent θ_{500}. The clusters uniformly cover the celestial sphere at Galactic latitudes above $|b| > 20$ deg. Their luminosities L_{500} range from 0.002 to 35.0×10^{44} erg/s, and their redshifts from 0.003 to 0.460. Figure 1 shows the masses M_{500} as a function of redshift z for the cluster sample (red crosses). The corresponding corrected luminosities L_{500} can be read on the right axis. The typical luminosity correction from measured $L_{\rm X}$ to L_{500} is about 10%. The progressive mass cut-off with redshift (only the most massive clusters are present at high z) reflects the flux limited nature of the sample.

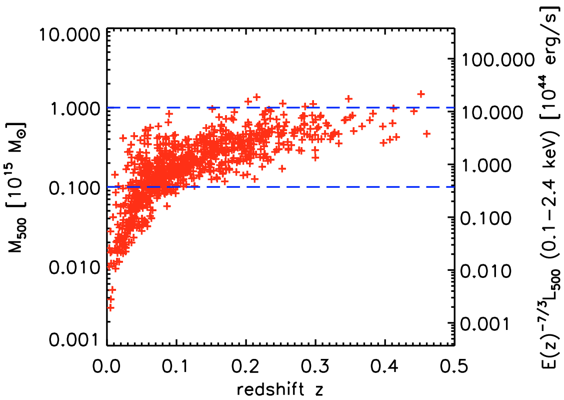

Fig. 1. Inferred masses for the 893 NORAS/REFLEX clusters as a function of redshift. The cluster sample is flux limited. The right vertical axis gives the corresponding X-ray luminosities scaled by $E(z)^{-7/3}$. The dashed blue lines delineate the mass range over which the L_{500}–M_{500} relation from Pratt et al. (2009) was derived.

3. The cluster SZ model

In this section we describe the cluster SZ model, based on X-ray observations of the REXCESS sample combined with numerical simulations, as presented in Arnaud et al. (2010). We use the standard self-similar model presented in their Appendix B. Given a cluster mass M_{500} and redshift z, the model predicts the electronic pressure profile. This gives both the SZ profile shape and Y_{500}, the SZ flux integrated in a sphere of radius r_{500}.

3.1. Cluster shape

The dimensionless universal pressure profile is taken from Eqs. (B1) and (B2) of Arnaud et al. (2010):

$$\frac{P(r)}{P_{500}} = \frac{P_0}{x^\gamma (1 + x^\alpha)^{(\beta-\gamma)/\alpha}} \qquad (3)$$

where $x = r/r_s$ with $r_s = r_{500}/c_{500}$ and $c_{500} = 1.156$, $\alpha = 1.0620$, $\beta = 5.4807$, $\gamma = 0.3292$ and with P_{500} defined in Eq. (4) below.

This profile shape is used to optimise the SZ signal detection. As described below in Sect. 4, we extract the $Y_{\rm SZ}$ flux from WMAP data for each ROSAT system fixing c_{500}, α, β, γ to the above values, but leaving the normalisation free.

3.2. Normalisation

The model allows us to compute the physical pressure profile as a function of mass and z, thus the $Y_{\rm SZ}$–M_{500} relation by integration of $P(r)$ to r_{500}. For the shape parameters given above, the normalisation parameter $P_0 = 8.130\,h_{70}^{3/2} = 7.810$ and the self-similar definition of P_{500} (Arnaud et al. 2010, Eq. (5) and Eq. (B2)),

$$P_{500} = 1.65\times10^{-3} E(z)^{8/3} \left(\frac{M_{500}}{3\times10^{14}\ h_{70}^{-1}\ M_\odot}\right)^{2/3} h_{70}^2\ {\rm keV\,cm^{-3}}, \qquad (4)$$

---

[3] Since we consider a standard self-similar model, we used the power law relations given in Appendix B of Arnaud et al. (2010). They are derived as in Pratt et al. (2009) with the same luminosity data but for masses derived from a standard slope M_{500}–$Y_{\rm X}$ relation.

one obtains:

$$Y_{500}\ [\mathrm{arcmin}^2] = Y^*_{500} \left(\frac{M_{500}}{3 \times 10^{14}\, h^{-1}\, M_\odot}\right)^{5/3} \times E(z)^{2/3} \left(\frac{D_{\mathrm{ang}}(z)}{500\ \mathrm{Mpc}}\right)^{-2}, \tag{5}$$

where $Y^*_{500} = 1.54 \times 10^{-3} \left(\frac{h}{0.719}\right)^{-5/2}$ arcmin^2. Equivalently, one can write:

$$Y_{500}\ [\mathrm{Mpc}^2] = Y^*_{500} \left(\frac{M_{500}}{3 \times 10^{14}\, h^{-1}\, M_\odot}\right)^{5/3} E(z)^{2/3} \tag{6}$$

where $Y^*_{500} = 3.27 \times 10^{-5} \left(\frac{h}{0.719}\right)^{-5/2}$ Mpc^2. Details of unit conversions are given in Appendix B. The mass dependence ($M_{500}^{5/3}$) and the redshift dependence ($E(z)^{2/3}$) of the relation are self-similar by construction. This model is used to predict the Y_{500} value for each cluster. These predictions are compared to the WMAP-measured values in Figs. 3–6.

4. Extraction of the SZ flux

4.1. Multifrequency matched filters

We use multifrequency matched filters to estimate cluster fluxes from the WMAP frequency maps. By incorporating prior knowledge of the cluster signal, i.e., its spatial and spectral characteristics, the method maximally enhances the signal-to-noise of a SZ cluster source by optimally filtering the data. The universal profile shape described in Sect. 3 is assumed, and we evaluate the effects of uncertainty in this profile as outlined in Sect. 5 where we discuss our overall error budget. We fix the position and the characteristic radius θ_{s} of each cluster and estimate only its flux. The position is taken from the NORAS/REFLEX catalogue and $\theta_{\mathrm{s}} = \theta_{500}/c_{500}$ with θ_{500} derived from X-ray data as described in Sect. 2.2. Below, we recall the main features of the multifrequency matched filters. More details can be found in Herranz et al. (2002) or Melin et al. (2006).

Consider a cluster with known radius θ_{s} and unknown central y-value y_{o} positioned at a known point x_{o} on the sky. The region is covered by the five WMAP maps $M_i(x)$ at frequencies $\nu_i = 23$, 33, 41, 61, 94 GHz ($i = 1, ..., 5$). We arrange the survey maps into a column vector $\boldsymbol{M}(x)$ whose ith component is the map at frequency ν_i. The maps contain the cluster SZ signal plus noise:

$$\boldsymbol{M}(x) = y_{\mathrm{o}} \boldsymbol{j_\nu} T_{\theta_{\mathrm{s}}}(x - x_{\mathrm{o}}) + \boldsymbol{N}(x) \tag{7}$$

where $\boldsymbol{N}$ is the noise vector (whose components are noise maps at the different observation frequencies) and $\boldsymbol{j_\nu}$ is a vector with components given by the SZ spectral function j_ν evaluated at each frequency. Noise in this context refers to both instrumental noise as well as all signals other than the cluster thermal SZ effect; it thus also comprises astrophysical foregrounds, for example, the primary CMB anisotropy, diffuse Galactic emission and extragalactic point sources. $T_{\theta_{\mathrm{s}}}(x - x_{\mathrm{o}})$ is the SZ template, taking into account the WMAP beam, at projected distance $(x - x_{\mathrm{o}})$ from the cluster centre, normalised to a central value of unity before convolution. It is computed by integrating along the line-of-sight and normalising the universal pressure profile (Eq. (3)). The profile is truncated at $5 \times r_{500}$ (i.e. beyond the virial radius) so that what is actually measured is the flux within a cylinder of aperture radius $5 \times r_{500}$.

X-ray observations are typically well-constrained out to r_{500}. Our decision to integrate out to $5 \times r_{500}$ is motivated by the fact that for the majority of clusters the radius r_{500} is of order the Healpix pixel size (nside = 512, pixel = 6.87 arcmin). Integrating only out to r_{500} would have required taking into account that only a fraction of the flux of some pixels contributes to the true SZ flux in a cylinder of aperture radius r_{500}. We thus obtain the total SZ flux of each cluster by integrating out to $5 \times r_{500}$, and then convert this to the value in a sphere of radius r_{500} for direct comparison with the X-ray prediction.

The multifrequency matched filters $\boldsymbol{\Psi}_{\boldsymbol{\theta}_{\mathrm{s}}}(x)$ return a minimum variance unbiased estimate, $\hat{y_{\mathrm{o}}}$, of y_{o} when centered on the cluster:

$$\hat{y_{\mathrm{o}}} = \int \mathrm{d}^2 x\, \boldsymbol{\Psi}_{\boldsymbol{\theta}_{\mathrm{s}}}{}^{t}(x - x_{\mathrm{o}}) \cdot \boldsymbol{M}(x) \tag{8}$$

where superscript t indicates a transpose (with complex conjugation when necessary). This is just a linear combination of the maps, each convolved with its frequency-specific filter $(\Psi_{\theta_{\mathrm{s}}})_i$. The result expressed in Fourier space is:

$$\boldsymbol{\Psi}_{\boldsymbol{\theta}_{\mathrm{s}}}(k) = \sigma^2_{\theta_{\mathrm{s}}} \boldsymbol{P}^{-1}(k) \cdot \boldsymbol{F}_{\boldsymbol{\theta}_{\mathrm{s}}}(k) \tag{9}$$

where

$$\boldsymbol{F}_{\boldsymbol{\theta}_{\mathrm{s}}}(k) \equiv \boldsymbol{j_\nu} T_{\theta_{\mathrm{s}}}(k) \tag{10}$$

$$\sigma_{\theta_{\mathrm{s}}} \equiv \left[\int \mathrm{d}^2 k\, \boldsymbol{F}_{\boldsymbol{\theta}_{\mathrm{s}}}{}^{t}(k) \cdot \boldsymbol{P}^{-1} \cdot \boldsymbol{F}_{\boldsymbol{\theta}_{\mathrm{s}}}(k)\right]^{-1/2} \tag{11}$$

with $\boldsymbol{P}(k)$ being the noise power spectrum, a matrix in frequency space with components P_{ij} defined by $\langle N_i(k) N^*_j(k')\rangle_N = P_{ij}(k)\delta(k - k')$. The quantity $\sigma_{\theta_{\mathrm{s}}}$ gives the total noise variance through the filter, corresponding to the statistical errors quoted in this paper. The other uncertainties are estimated separately as described in Sect. 5.1. The noise power spectrum $\boldsymbol{P}(k)$ is directly estimated from the maps: since the SZ signal is subdominant at each frequency, we assume $\boldsymbol{N}(x) \approx \boldsymbol{M}(x)$ to do this calculation. We undertake the Fourier transform of the maps and average their cross-spectra in annuli with width $\Delta l = 180$.

4.2. Measurements of the SZ flux

The derived total WMAP flux from a cylinder of aperture radius $5 \times r_{500}$ (Y^{cyl}_{5r500}) for the 893 individual NORAS/REFLEX clusters is shown as a function of the measured X-ray luminosity L_{500} in the left-hand panel of Fig. 2. The clusters are barely detected individually. The average signal-to-noise ratio (S/N) of the total population is 0.26 and only 29 clusters are detected at $S/N > 2$, the highest detection being at 4.2. However, one can distinguish the deviation towards positive flux at the very high luminosity end.

In the right-hand panel of Fig. 2, we average the 893 measurements in four logarithmically-spaced luminosity bins (red diamonds plotted at bin center). The number of clusters are 7, 150, 657, 79 from the lowest to the highest luminosity bin. Here and in the following, the bin average is defined as the weighted mean of the SZ flux in the bin (weight of $1/\sigma^2_{\theta_{\mathrm{s}}}$). The thick error bars correspond to the statistical uncertainties on the WMAP data only, while the thin bar gives the total errors as discussed in Sect. 5.1. The SZ signal is clearly detected in the two highest luminosity bins (at 6.0 and 5.4σ, respectively). As a demonstrative check, we have undertaken the analysis a second time using random cluster positions. The result is shown by the green triangles in Fig. 2 and is consistent with no SZ signal, as expected.

In the following sections, we study both the relation between the SZ signal and the X-ray luminosity and that with the mass

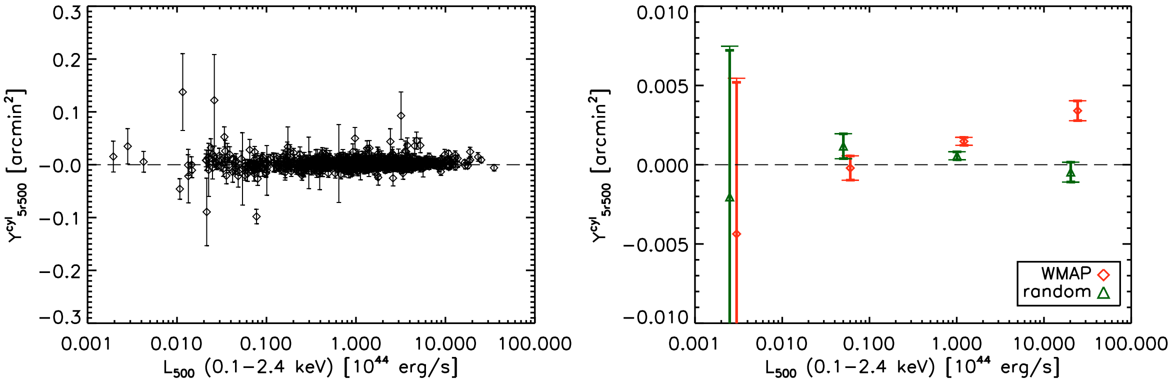

Fig. 2. *Left*: estimated SZ flux from a cylinder of aperture radius $5 \times r_{500}$ (Y^{cyl}_{5r500}) as a function of the X-ray luminosity in an aperture of r_{500} (L_{500}), for the 893 NORAS/REFLEX clusters. The individual clusters are barely detected. The bars give the total 1σ error. *Right:* Red diamonds are the weighted average signal in 4 logarithmically-spaced luminosity bins. The two high luminosity bins exhibit significant SZ cluster flux. Note that we have divided the vertical scale by 30 between Fig. left and right. The thick and thin bars give the 1σ statistical and total errors, respectively. Green triangles (shifted up by 20% with respect to diamonds for clarity) show the result of the same analysis when the fluxes of the clusters are estimated at random positions instead of true cluster positions.

M_{500}. We consider Y_{500}, the SZ flux from a sphere of radius r_{500}, converting the measured Y^{cyl}_{5r500} into Y_{500} as described in Appendix A. This allows a more direct comparison with the model derived from X-ray observations (Sect. 3). Before presenting the results, we first discuss the overall error budget.

5. Overall error budget

5.1. Error due to dispersion in X-ray properties

The error σ_{θ_s} on Y_{500} given by the multifrequency matched filter only includes the statistical SZ measurement error, due to the instrument (beam, noise) and to the astrophysical contaminants (primary CMB, Galaxy, point sources). However, we must also take into account: 1) uncertainties on the cluster mass estimation from the X-ray luminosities via the $L_{500} - M_{500}$ relation, 2) uncertainties on the cluster profile parameters. These are sources of error on individual Y_{500} estimates (actual parameters for each individual cluster may deviate somewhat from the average cluster model). These deviations from the mean, however, induce additional *random* uncertainties on statistical quantities derived from Y_{500}, i.e. bin averaged Y_{500} values and the Y_{500}–L_{500} scaling relation parameters. Their impact on the Y_{500}–M_{500} relation, which depends directly on the M_{500} estimates, is also an additional random uncertainty.

The uncertainty on M_{500} is dominated by the intrinsic dispersion in the L_{500}–M_{500} relation. Its effect is estimated by a Monte Carlo (MC) analysis of 100 realisations. We use the dispersion at $z = 0$ as estimated by Pratt et al. (2009), given in Table 1. For each realisation, we draw a random mass $\log M_{500}$ for each cluster from a Gaussian distribution with mean given by the L_{500}–M_{500} relation and standard deviation $\sigma_{\log L - \log M}/\alpha_{\mathrm{M}}$. We then redo the full analysis (up to the fitting of the Y_{SZ} scaling relations) with the new values of M_{500} (thus θ_s).

The second uncertainty is due to the observed dispersion in the cluster profile shape, which depends on radius as shown in Arnaud et al. (2010, $\sigma_{\log P} \sim 0.10$ beyond the core). Using new 100 MC realisations, we estimate this error by drawing a cluster profile in the log-log plane from a Gaussian distribution with mean given by Eq. (3) and standard deviation depending on the cluster radius as shown in the lower panel of Fig. 2 in Arnaud et al. (2010).

The total error on Y_{500} and on the scaling law parameters is calculated from the quadratic sum of the standard deviation of both the above MC realisations and the error due to the SZ measurement uncertainty.

5.2. The Malmquist bias

The NORAS/REFLEX sample is flux limited and is thus subject to the Malmquist bias (MB). This is a source of systematic error. Ideally we should use a L_{500}–M_{500} relation which takes into account the specific bias of the sample, i.e. computed from the true L_{500}–M_{500} relation, with dispersion and bias according to each survey selection function. We have an estimate of the true, ie MB corrected, L_{500}–M_{500} relation, from the published analysis of REXCESS data (Table 1). However, while the REFLEX selection function is known and available, this is not the case for the NORAS sample. This means that we cannot perform a fully consistent analysis. In order to estimate the impact of the Malmquist Bias we thus present, in the following, results for two cases.

In the first case, we use the published L_{500}–M_{500} relation derived directly from the REXCESS data, i.e. not corrected for the REXCESS MB (hereafter the REXCESS L_{500}–M_{500} relation). Note that the REXCESS is a sub-sample of REFLEX. Using this relation should result in correct masses if the Malmquist bias for the NORAS/REFLEX sample is the same as that for the REXCESS. The Y_{500}–M_{500} relation derived in this case would also be correct and could be consistently compared with the X-ray predicted relation. We recall that this relation was derived from pressure and mass measurements that are not sensitive to the Malmquist bias. However L_{500} would remain uncorrected so that the Y_{500}–L_{500} relation derived in this case should be viewed as a relation uncorrected for the Malmquist bias. In the second case, we use the MB corrected L_{500}–M_{500} relation (hereafter the intrinsic L_{500}–M_{500} relation). This reduces to assuming that the Malmquist bias is negligible for the NORAS/REFLEX sample.

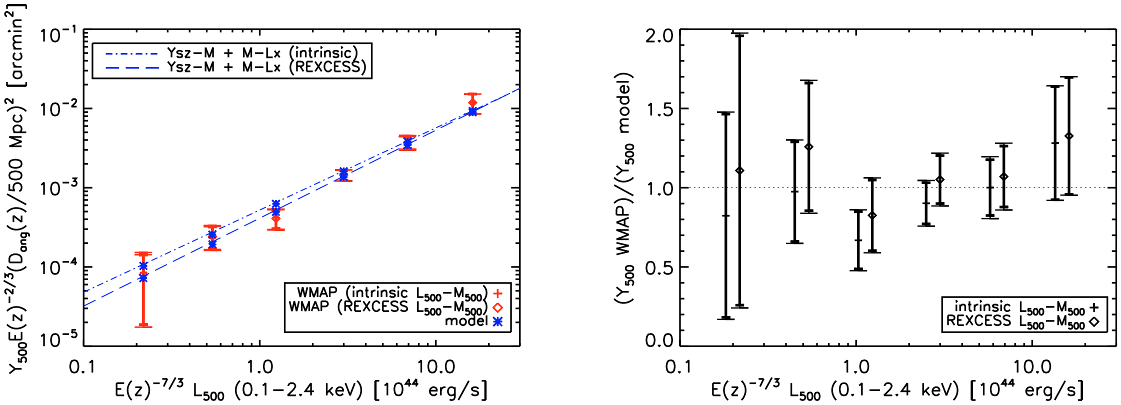

Fig. 3. *Left*: bin averaged SZ flux from a sphere of radius r_{500} (Y_{500}) as a function of X-ray luminosity in an aperture of r_{500} (L_{500}). The WMAP data (red diamonds and crosses), the SZ cluster signal expected from the X-ray based model (blue stars) and the combination of the $Y_{500}-M_{500}$ and $L_{500}-M_{500}$ relations (dash and dotted dashed lines) are given for two analyses, using respectively the intrinsic $L_{500}-M_{500}$ and the REXCESS $L_{500}-M_{500}$ relations. As expected, the data points do not change significantly from one case to the other showing that the Y_{500}-L_{500} relation is rather insensitive to the finer details of the underlying $L_{500}-M_{500}$ relation. *Right*: ratio of data points to model for the two analysis. The points for the analysis undertaken with the intrinsic $L_{500}-M_{500}$ are shifted to lower luminosities by 20% for clarity.

The comparison of the two analyses provides an estimate of the direction and amplitude of the effect of the Malmquist bias on our results. The REXCESS $L_{500}-M_{500}$ relation is expected to be closer to the $L_{500}-M_{500}$ relation for the NORAS/REFLEX sample than the intrinsic relation. The discussions and figures correspond to the results obtained when using the former, unless explicitly specified.

The choice of the $L_{500}-M_{500}$ relation has an effect both on the estimated L_{500}, M_{500} and Y_{500} values and on the expectation for the SZ signal from the NORAS/REFLEX clusters. However, for a cluster of given luminosity measured a given aperture, L_{500} depends weakly on the exact value of r_{500} due to the steep drop of X-ray emission with radius. As a result, and although L_{500} and M_{500} (or equivalently r_{500}) are determined jointly in the iterative procedure described in Sect. 2.2, changing the underlying $L_{500}-M_{500}$ relation mostly impacts the M_{500} estimate: L_{500} is essentially unchanged (median difference of ~0.8%) and the difference in M_{500} simply reflects the difference between the relations at fixed luminosity. This has an impact on the measured Y_{500} via the value of r_{500} (the profile shape being fixed) but the effect is also small (<1%). This is due to the rapidly converging nature of the Y_{SZ} flux (see Fig. 11 of Arnaud et al. 2010). On the other hand, all results that depend directly on M_{500}, namely the derived $Y_{500}-M_{500}$ relation or the model value for each cluster, that varies as $M_{500}^{5/3}$ (Eq. (5)), depend sensitively on the $L_{500}-M_{500}$ relation. M_{500} derived from the intrinsic relation is higher, an effect increasing with decreasing cluster luminosity (see Fig. B2 of Pratt et al. 2009).

5.3. Other possible sources of uncertainty

The analysis presented in this paper has been performed on the entire NORAS/REFLEX cluster sample without removal of clusters hosting radio point sources. To investigate the impact of the point sources on our result, we have cross-correlated the NVSS (Condon et al. 1998) and SUMMS (Mauch et al. 2003) catalogues with our cluster catalogue. We conservatively removed from the analysis all the clusters hosting a total radio flux greater than 1 Jy within $5 \times r_{500}$. This leaves 328 clusters in the catalogue, removing the measurements with large uncertainties visible in Fig. 2 left. We then performed the full analysis on these 328 objects up to the fitting of the scaling laws, finding that the impact on the fitted values is marginal. For example, for the REXCESS case, the normalisation of the $Y_{500}-M_{500}$ relation decreases from 1.60 to 1.37 (1.6 statistical σ) and the slope changes from 1.79 to 1.64 (1 statistical σ). The statistical errors on these parameters decrease respectively from 0.14 to 0.30 and from 0.15 to 0.40 due to the smaller number of remaining clusters in the sample.

The detection method does not take into account superposition effects along the line of sight, a drawback that is inherent to any SZ observation. Thus we cannot fully rule out that our flux estimates are not partially contaminated by low mass systems surrounding the clusters of our sample. Numerical simulations give a possible estimate of the contamination: Hallman et al. (2007) suggest that low-mass systems and unbound gas may contribute up to $16.3\%^{+7\%}_{-6.4\%}$ of the SZ signal. This would lower our estimated cluster fluxes by ~1.5σ.

6. The Y_{SZ}–L_{500} relation

6.1. WMAP SZ measurements vs. X-ray model

We first consider bin averaged data, focusing on the luminosity range $L_{500} \gtrsim 10^{43}$ ergs/s where the SZ signal is significantly detected (Fig. 2 right). The left panel of Fig. 3 shows Y_{500} from a sphere of radius r_{500} as a function of L_{500}, averaging the data in six equally-spaced logarithmic bins in X-ray luminosity. Both quantities are scaled according to their expected redshift dependence. The results are presented for the analyses based on the REXCESS (red diamonds) and intrinsic (red crosses) $L_{500}-M_{500}$ relations. For the reasons discussed in Sect. 5.2, the derived data points do not differ significantly between the two analyses (Fig. 3 left), confirming that the measured $Y_{500}-L_{500}$ relation is insensitive to the finer details of the underlying $L_{500}-M_{500}$ relation.

We also apply the same averaging procedure to the model Y_{500} values derived for each cluster in Sect. 3. The expected values for the same luminosity bins are plotted as stars in the

Table 2. Fitted parameters for the observed $Y_{\rm SZ}$–L_{500} relation.

$L_{500}-M_{500}$	Y_{500}^{*L} [10^{-3} $(h/0.719)^{-2}$ arcmin^2]	α_Y^L	β_Y^L
REXCESS	0.92 ± 0.08 stat [±0.10 tot]	1.11 (fixed)	2/3 (fixed)
	0.88 ± 0.10 stat [±0.12 tot]	1.19 ± 0.10 stat [±0.10 tot]	2/3 (fixed)
	0.90 ± 0.13 stat [±0.16 tot]	1.11 (fixed)	1.05 ± 2.18 stat [±2.25 tot]
Intrinsic	0.95 ± 0.09 stat [±0.11 tot]	1.04 (fixed)	2/3 (fixed)
	0.89 ± 0.10 stat [±0.12 tot]	1.19 ± 0.10 stat [±0.10 tot]	2/3 (fixed)
	0.89 ± 0.13 stat [±0.16 tot]	1.04 (fixed)	2.06 ± 2.14 stat [±2.21 tot]

Notes. The X-ray based model gives $Y_{500}^{*L} = 0.89|1.07\times10^{-3}$ $(h/0.719)^{-5/2}$ arcmin^2, $\alpha_Y^L = 1.11|1.04$ and $\beta_Y^L = 2/3$ for the REXCESS and intrinsic $L_{500}-M_{500}$ relation, respectively.

left-hand hand panel of Fig. 3. The $Y_{500}-L_{500}$ relation expected from the combination of the $Y_{500}-M_{500}$ (Eq. (5)) and $L_{500}-M_{500}$ (Eq. (2)) relations is superimposed to guide the eye. The right-hand panel of Fig. 3 shows the ratio between the measured data points and those expected from the model. As discussed in Sect. 5.2, the model values depend on the assumed $L_{500}-M_{500}$ relation. The difference is maximum in the lowest luminosity bin where the intrinsic relation yields ~40% higher value than the REXCESS relation (Fig. 3 left panel). The SZ model prediction and the data are in good agreement, but the agreement is better when the REXCESS $L_{500}-M_{500}$ is used in the analysis (Fig. 3 right panel). This is expected if indeed the agreement is real and the effective Malmquist bias for the NORAS/REFLEX sample is not negligible and is similar to that of the REXCESS.

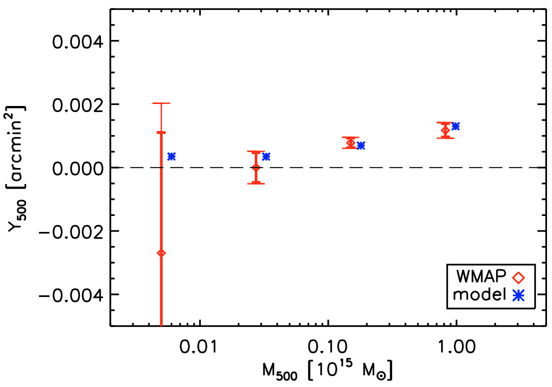

Fig. 4. Estimated SZ flux Y_{500} (in a sphere of radius r_{500}) as a function of the mass M_{500} averaged in 4 mass bins. Red diamonds are the WMAP data. Blue stars correspond to the X-ray based model predictions and are shifted to higher masses by 20% for clarity. The model is in very good agreement with the data.

6.2. Y_{500}–L_{500} relation fit

Working now with the individual flux measurements, Y_{500}, and L_{500} values, we fit an $Y_{500}-L_{500}$ relation of the form:

$$Y_{500} = Y_{500}^{*L}\left(\frac{E(z)^{-7/3}L_{500}}{10^{44}h^{-2}{\rm erg/s}}\right)^{\alpha_Y^L} E(z)^{\beta_Y^L}\left(\frac{D_{\rm ang}(z)}{500\ {\rm Mpc}}\right)^{-2} \qquad (12)$$

using the statistical error on Y_{500} given by the multifrequency matched filter. The total error is estimated by Monte Carlo (see Sect. 5.1) but is dominated by the statistical error. The results are presented in Table 2. As already stated in Sect. 6.1, the fitted values depend only weakly on the choice of $L_{500}-M_{500}$ relation.

7. The $Y_{\rm SZ}$–M_{500} relation and its evolution

In this section, we study the mass and redshift dependence of the SZ signal and check it against the X-ray based model. Furthermore, we fit the $Y_{500}-M_{500}$ relation and compare it with the X-ray predictions.

7.1. Mass dependence and redshift evolution

Figure 4 shows the bin averaged SZ flux measurement as a function of mass compared to the X-ray based model prediction. As expected, the SZ cluster flux increases as a function of mass and is compatible with the model. In order to study the behaviour of the SZ flux with redshift, we subdivide each of the four mass bins into three redshift bins corresponding to the following ranges: $z < 0.08$, $0.08 < z < 0.18$, $z > 0.18$. The result is shown in the left panel of Fig. 5. In a given mass bin the SZ flux decreases with redshift, tracing the $D_{\rm ang}(z)^{-2}$ dependence of the flux. In particular, in the highest mass bin (10^{15} $M_\odot$), the SZ flux decreases from 0.007 to 0.001 arcmin^2 while the redshift varies from $z < 0.08$ to $z > 0.18$. The mass and the redshift dependence are in good agreement with the model (stars) described in Sect. 3.

Since the $D_{\rm ang}(z)^{-2}$ dependence is the dominant effect in the redshift evolution, we multiply Y_{500} by $D_{\rm ang}(z)^2$ and divide it by the self-similar mass dependence $M_{500}^{5/3}$. The expected self-similar behaviour of the new quantity $Y_{500}D_{\rm ang}(z)^2/M_{500}^{5/3}$ as a function of redshift is $E(z)^{2/3}$ (see Eq. (5)). The right panel of Fig. 5 shows $Y_{500}D_{\rm ang}(z)^2/M_{500}^{5/3}$ as a function of redshift for the three redshift bins $z < 0.08$, $0.08 < z < 0.18$, $z > 0.18$. The points have been centered at the average value of the cluster redshifts in each bin. The model is displayed as blue stars. Since the model has a self-similar redshift dependence and $E(z)^{2/3}$ increases only by a factor of 5% over the studied redshift range, the model stays nearly constant. The blue dotted line is plotted through the model and varies as $E(z)^{2/3}$. The data points are in good agreement with the model, but clearly, the redshift leverage of the sample is insufficient to put strong constraints on the evolution of the scaling laws.

We now focus on the mass dependence of the relation. We scale the SZ flux with the expected redshift dependence and plot it as a function of mass. The result is shown in Fig. 6 for the high mass end. The figure shows a very good agreement between the data points and the model, which is confirmed by fitting the relation to the individual SZ flux measurements (see next section).

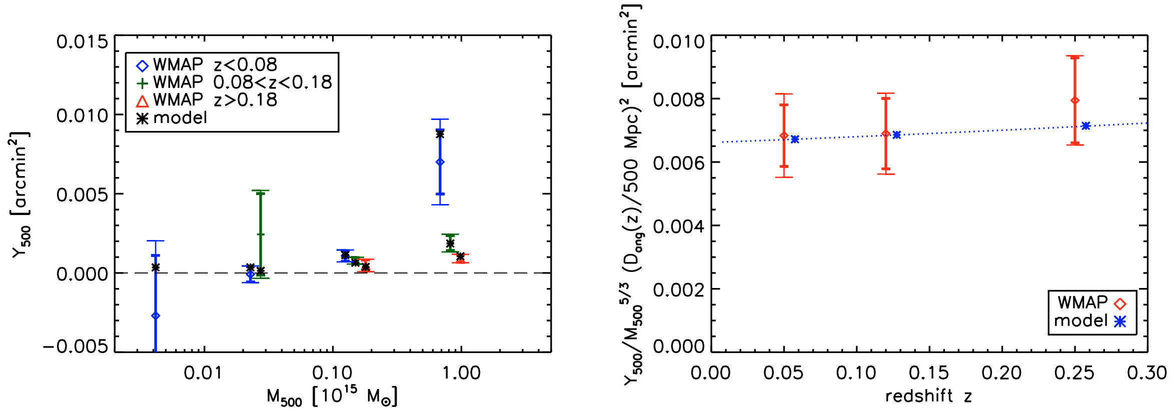

Fig. 5. Evolution of the Y_{500}-M_{500} relation. *Left*: the WMAP data from Fig. 4 are divided into three redshift bins: $z < 0.08$ (blue diamonds), $0.08 < z < 0.18$ (green crosses), $z > 0.18$ (red triangles). We observe the expected trend: at fixed mass, Y_{500} decreases with redshift. This redshift dependence is mainly due to the angular distance ($Y_{500} \propto D_{\rm ang}(z)^{-2}$). The stars give the prediction of the model. *Right*: we divide Y_{500} by $M_{500}^{5/3} D_{\rm ang}(z)^{-2}$ and plot it as a function of z to search for evidence of evolution in the $Y_{500}-M_{500}$ relation. The thick bars give the 1σ statistical errors from WMAP data. The thin bars give the total 1 sigma errors.

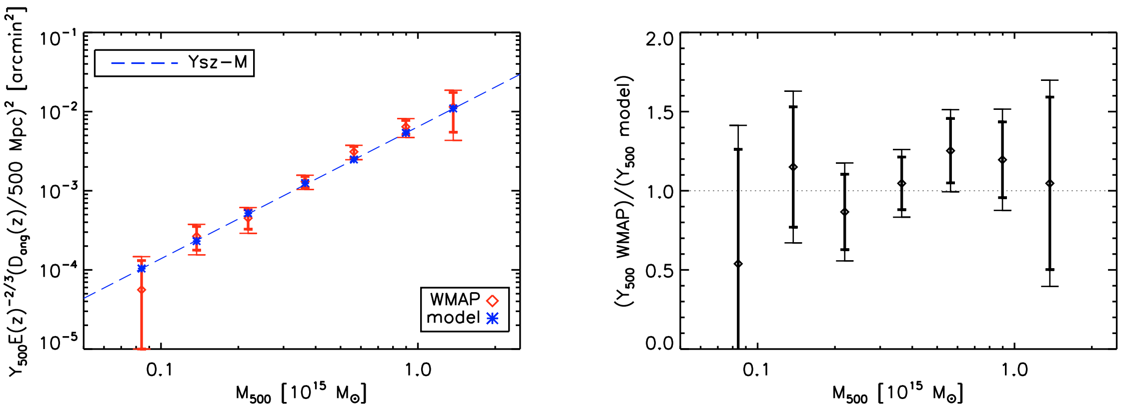

Fig. 6. *Left*: zoom on the $>5\times10^{13}$ $M_\odot$ mass range of the $Y_{500}-M_{500}$ relation shown in Fig. 4. The data points and model stars are now scaled with the expected redshift dependence and are placed at the mean mass of the clusters in each bin. *Right*: ratio between data and model.

7.2. $Y_{500}-M_{500}$ relation fit

Using the individual Y_{500} measurements and M_{500} estimated from the X-ray luminosity, we fit a relation of the form:

$$Y_{500} = Y^*_{500} \left(\frac{M_{500}}{3\times10^{14} h^{-1} M_\odot}\right)^{\alpha_Y} E(z)^{\beta_Y} \left(\frac{D_{\rm ang}(z)}{500\ {\rm Mpc}}\right)^{-2}. \quad (13)$$

The results are presented in Table 3 for the analysis undertaken using the REXCESS and that using the intrinsic $L_{500}-M_{500}$ relation. The pivot mass $3\times10^{14} h^{-1}$ $M_\odot$, close to that used by Arnaud et al. (2010), is slightly larger than the average mass of the sample (2.8|2.5×10^{14} $M_\odot$ for the REXCESS|intrinsic $L_{500}-M_{500}$ relation, respectively). We use a non-linear least-squares fit built on a gradient-expansion algorithm (IDL curvefit function). In the fitting procedure, only the statistical errors given by the matched multifilter ($\sigma_{Y_{500}}$) are taken into account. The total errors on the final fitted parameters, taking into account uncertainties in X-ray properties, are estimated by Monte Carlo as described in Sect. 5.

We first discuss the results obtained using the REXCESS $L_{500}-M_{500}$ relation, which is expected to be close to the optimal case (see discussion in Sect. 5.2). First, we keep the mass and redshift dependence fixed to the self-similar expectation ($\alpha_Y = 5/3, \beta_Y = 2/3$) and we fit only the normalisation. We obtain $Y^*_{500} = 1.60\times10^{-3}$ $(h/0.719)^{-2}$ arcmin^2, in agreement with the X-ray prediction $Y^*_{500} = 1.54\times10^{-3}$ $(h/0.719)^{-5/2}$ arcmin^2 (at 0.4σ). Then, we relax the constraint on α_Y and fit the normalisation and mass dependence at the same time. We obtain a value for $\alpha_Y = 1.79$, slightly greater than the self-similar expectation (5/3) by 0.8σ. To study the redshift dependence of the effect, we fix the mass dependence to $\alpha_Y = 5/3$ and fit Y^*_{500} and β_Y at the same time. We obtain a somewhat stronger evolution $\beta_Y = 1.05$ than the self-similar expectation (2/3). The difference, however, is not significant (0.2σ). As already mentioned above (see also Fig. 5 right), the redshift leverage is too small to get interesting constraints on β_Y.

As cluster mass estimates depend on the assumption of the underlying $L_{500}-M_{500}$ relation, so does the derived $Y_{500}-M_{500}$

Table 3. Fitted parameters for the observed $Y_{\rm SZ}$–M_{500} relation.

L_{500}–M_{500} relation	Y^*_{500} [10^{-3} $(h/0.719)^{-2}$ arcmin^2]	α_Y	β_Y
REXCESS	1.60 ± 0.14 stat [±0.19 tot]	5/3 (fixed)	2/3 (fixed)
	1.60 ± 0.15 stat [±0.19 tot]	1.79 ± 0.15 stat [±0.17 tot]	2/3 (fixed)
	1.57 ± 0.23 stat [±0.29 tot]	5/3 (fixed)	1.05 ± 2.18 stat [±2.52 tot]
intrinsic	1.37 ± 0.12 stat [±0.17 tot]	5/3 (fixed)	2/3 (fixed)
	1.36 ± 0.13 stat [±0.17 tot]	1.91 ± 0.16 stat [±0.18 tot]	2/3 (fixed)
	1.28 ± 0.19 stat [±0.24 tot]	5/3 (fixed)	2.06 ± 2.14 stat [±2.48 tot]

Notes. The X-ray based model gives $Y^*_{500} = 1.54 \times 10^{-3}$ $(h/0.719)^{-5/2}$ arcmin^2, $\alpha_Y = 5/3$ and $\beta_Y = 2/3$.

relation as well. However, the effect is small. The normalisation is shifted from (1.60 ± 0.14 stat [±0.19 tot]) 10^{-3} arcmin^2 to (1.37 ± 0.12 stat [±0.17 tot]) 10^{-3} arcmin^2 when using the intrinsic L_{500}–M_{500} relation. The difference is less than two statistical sigmas, and for the mass exponent, it is less than one.

8. Discussion and conclusions

In this paper we have investigated the SZ effect and its scaling with mass and X-ray luminosity using WMAP 5-year data of the largest published X-ray-selected cluster catalogue to date, derived from the combined NORAS and REFLEX samples. Cluster SZ flux estimates were made using an optimised multifrequency matched filter. Filter optimisation was achieved through priors on the pressure distribution (i.e., cluster shape) and the integration aperture (i.e., cluster size). The pressure distribution is assumed to follow the universal pressure profile of Arnaud et al. (2010), derived from X-ray observations of the representative local REXCESS sample. This profile is the most realistic available for the general population at this time, and has been shown to be in good agreement with recent high-quality SZ observations from SPT (Plagge et al. 2010). Furthermore, our analysis takes into account the dispersion in the pressure distribution. The integration aperture is estimated from the L_{500}–M_{500} relation of the same REXCESS sample. We emphasise that these two priors determine only the input spatial distribution of the SZ flux for use by the multifrequency matched filters; the priors give no information on the amplitude of the measurement. As the analysis uses minimal X-ray data input, the measured and X-ray predicted SZ fluxes are essentially independent.

We studied the $Y_{\rm SZ}$–$L_{\rm X}$ relation using both bin averaged analyses and individual flux measurements. The fits using individual flux measurements give quantitative results for calibrating the scaling laws. The bin averaged analyses allow a direct quantitative check of SZ flux measurements versus X-ray model predictions based on the universal pressure profile derived by Arnaud et al. (2010) from REXCESS. An excellent agreement is found.

Using WMAP 3-year data, both Lieu et al. (2006) and Bielby & Shanks (2007) found that the SZ signal strength is lower than predicted given expectations from the X-ray properties of their clusters, concluding that that there is some missing hot gas in the intra-cluster medium. The excellent agreement between the SZ and X-ray properties of the clusters in our sample shows that there is in fact no deficit in SZ signal strength relative to expectations from X-ray observations. Due to the large size and homogeneous nature of our sample, and the internal consistency of our baseline cluster model, we believe our results to be robust in this respect. We note that there is some confusion in the literature regarding the phrase "missing baryons". The "missing baryons" mentioned by Afshordi et al. (2007) in the WMAP 3-year data are missing with respect to the universal baryon fraction, but not with respect to the expectations from X-ray measurements. Afshordi et al. (2007) actually found good agreement between the strength of the SZ signal and the X-ray properties of their cluster sample, a conclusion that agrees with our results. This good convergence between SZ direct measurements and X-ray data is an encouraging step forward for the prediction and interpretation of SZ surveys.

Using L_{500} as a mass proxy, we also calibrated the Y_{500}–M_{500} relation, finding a normalisation in excellent agreement with X-ray predictions based on the universal pressure profile, and a slope consistent with self-similar expectations. However, there is some indication that the slope may be steeper, as also indicated from the REXCESS analysis when using the best fitting empirical M_{500}-$Y_{\rm X}$ relation (Arnaud et al. 2010). M_{500} depends on the assumed L_{500}–M_{500} relation, making the derived Y_{500}–M_{500} relation sensitive to Malmquist bias which we cannot fully account for in our analysis. However, we have shown that the effect of Malmquist bias on the present results is less than 2σ (statistical).

Regarding evolution, we have shown observationally that the SZ flux is indeed sensitive to the angular size of the cluster through the diameter distance effect. For a given mass, a low redshift cluster has a bigger integrated SZ flux than a similar system at high redshift, and the redshift dependence of the integrated SZ flux is dominated by the angular diameter distance ($\propto D^2_{\rm ang}(z)$). However, the redshift leverage of the present cluster sample is too small to put strong contraints on the evolution of the Y_{500}–L_{500} and Y_{500}–M_{500} relations. We have nevertheless checked that the observed evolution is indeed compatible with the self-similar prediction.

In this analysis, we have compensated for the poor sensitivity and resolution of the WMAP experiment (regarding SZ science) with the large number of known ROSAT clusters, leading to self-consistent and robust results. We expect further progress using upcoming Planck all-sky data. While Planck will offer the possibility of detecting the clusters used in this analysis to higher precision, thus significantly reducing the uncertainty on individual measurements, the question of evolution will not be answered with the present RASS sample due to its limited redshift range. A complementary approach will thus be to obtain new high sensitivity SZ observations of a smaller sample. The sample must be representative, cover a wide mass range, and extend to higher z (e.g., XMM-Newton follow-up of samples drawn from Planck and ground based SZ surveys). This would deliver efficient constraints not only on the normalisation and slope of the $Y_{\rm SZ}$–$L_{\rm X}$ and $Y_{\rm SZ}$–M relations, but also their evolution, opening the way for the use of SZ surveys for precision cosmology.

Acknowledgements. The authors wish to thank the anonymous referee for useful comments. J.-B. Melin thanks R. Battye for suggesting introduction of the *h* dependance into the presentation of the results. The authors also acknowledge the use of the HEALPix package (Górski et al. 2005) and of the Legacy Archive for Microwave Background Data Analysis (LAMBDA). Support for LAMBDA is provided by the NASA Office of Space Science. We also acknowledge use of the Planck Sky Model, developed by the Component Separation Working Group (WG2) of the Planck Collaboration, for the estimation of the radio source flux in the clusters and for the development of the matched multifilter, although the model was not directly used in the present work.

Appendix A: SZ flux definitions

In this Appendix, we give the definitions of SZ fluxes we used. Table A.1 gives the equivalence between them. In this paper, we mainly use Y_{500} as the definition of the SZ flux. This flux is the integrated SZ flux from a sphere of radius r_{500}. It can be related to Y_{nr500}, the flux from a sphere of radius $n \times r_{500}$ by integrating over the cluster profile:

$$Y_{nr500} = Y_{500} \frac{\int_0^{nr_{500}} \mathrm{d}r P(r) 4\pi r^2}{\int_0^{r_{500}} \mathrm{d}r P(r) 4\pi r^2} \tag{A.1}$$

where $P(r)$ is given by Eq. (3). The ratio Y_{nr500}/Y_{500} is given in Table A.1 for $n = 1, 2, 3, 5, 10$.

In practice, an experiment does not directly measure Y_{500} but the SZ signal of a cluster integrated along the line of sight and within an angular aperture. This corresponds to the Compton parameter integrated over a cylindrical volume. In Sect. 4, we estimate Y^{cyl}_{5r500}, the flux from a cylinder of aperture radius $5 \times r_{500}$ using the matched multifilter. Given the cluster profile, we can derive Y_{nr500} from Y^{cyl}_{nr500}:

$$Y^{\mathrm{cyl}}_{nr500} = Y_{nr500} \frac{\int_0^{\infty} \mathrm{d}r \int_{r \sin\theta < nr_{500}} d\theta\, P(r) 2\pi r^2}{\int_0^{nr_{500}} \mathrm{d}r P(r) 4\pi r^2} \,. \tag{A.2}$$

The ratio $Y_{nr500}/Y^{\mathrm{cyl}}_{nr500}$ is given in Table A.1 for $n = 1, 2, 3, 5, 10$. In the paper, we calculate Y_{500} from $Y_{500} = 0.986/1.814 \times Y^{\mathrm{cyl}}_{5r500}$.

Table A.1. Equivalence of SZ flux definitions

n	1	2	3	5	10
Y_{nr500}/Y_{500}	1	1.505	1.690	1.814	1.873
$Y_{nr500}/Y^{\mathrm{cyl}}_{nr500}$	0.827	0.930	0.963	0.986	0.997

Appendix B: SZ units conversion

In this Appendix, we provide the numerical factor needed for the SZ flux units conversion and derive the relation between the recently introduced Y_{X} parameter and the SZ flux Y_{SZ}. The latter will allow readers to easily convert between SZ fluxes given in this paper and those reported in other publications.

Given the definition of SZ flux:

$$Y^{\mathrm{cyl}}_{nr500} = \int_{\Omega_{nr500}} \mathrm{d}\Omega\, y \tag{B.1}$$

where Ω_{nr500} is the solid angle covered by $n \times r_{500}$, and the fact that the Compton parameter y is unitless, the observational units for the SZ flux are those of a solid angle and usually given in arcmin^2.

The SZ flux can be also computed in units of Mpc^2 and the conversion is given by

$$\begin{aligned} Y_{\mathrm{SZ}}[\mathrm{Mpc}^2] &= 60^{-2} \left(\frac{\pi}{180}\right)^2 Y_{\mathrm{SZ}}[\mathrm{arcmin}^2] \left(\frac{D_{\mathrm{ang}}(z)}{1\,\mathrm{Mpc}}\right)^2 \\ &= 8.46 \times 10^{-8}\, Y_{\mathrm{SZ}}[\mathrm{arcmin}^2] \left(\frac{D_{\mathrm{ang}}(z)}{1\,\mathrm{Mpc}}\right)^2 \end{aligned} \tag{B.2}$$

where $D_{\mathrm{ang}}(z)$ is the angular distance to the cluster.

The X-ray analogue of the integrated SZ Comptonisation parameter is $Y_{\mathrm{X}} = M_{\mathrm{gas},500} T_{\mathrm{X}}$ whose natural units are $M_{\odot}$ keV, where $M_{\mathrm{gas},500}$ is the gas mass in r_{500} and T_{X} is the *spectroscopic* temperature excluding the central $0.15\, r_{500}$ region (Kravtsov et al. 2006). To convert between Y_{SZ} and Y_{X}, we first have

$$Y_{\mathrm{SZ}}[\mathrm{Mpc}^2] = \int_0^{r_{500}} \mathrm{d}r\, \sigma_{\mathrm{T}} \frac{T_{\mathrm{e}}(r)}{m_{\mathrm{e}} c^2} n_{\mathrm{e}}(r) 4\pi r^2 \tag{B.3}$$

where σ_{T} is the Thomson cross section (in Mpc^2), $m_{\mathrm{e}}c^2$ the electron mass (in keV), $T_{\mathrm{e}}(r)$ the electronic temperature (in keV) and $n_{\mathrm{e}}(r)$ the electronic density. By assuming that the gas temperature $T_{\mathrm{g}}(r)$ is equal to the electronic temperature $T_{\mathrm{e}}(r)$ and writing the gas density as $\rho_{\mathrm{g}}(r) = \mu_{\mathrm{e}} m_p n_{\mathrm{e}}(r)$, where m_p is the proton mass and $\mu_{\mathrm{e}} = 1.14$ the mean molecular weight per free electron, one obtains:

$$\begin{aligned} Y_{\mathrm{SZ}}[\mathrm{Mpc}^2] &= \frac{\sigma_T}{m_{\mathrm{e}} c^2} \frac{1}{\mu_{\mathrm{e}} m_p} \int_0^{r_{500}} \mathrm{d}r\, \rho_{\mathrm{g}}(r)\, T_{\mathrm{g}}(r) 4\pi r^2 \\ &= C_{\mathrm{XSZ}}\, M_{\mathrm{gas},500}\, T_{\mathrm{MW}} = A\, C_{\mathrm{XSZ}}\, Y_{\mathrm{X}} \end{aligned} \tag{B.4}$$

where, as in Arnaud et al. (2010), we defined

$$C_{\mathrm{XSZ}} = \frac{\sigma_T}{m_{\mathrm{e}} c^2} \frac{1}{\mu_{\mathrm{e}} m_p} = 1.416 \times 10^{-19} \frac{\mathrm{Mpc}^2}{M_{\odot}\,\mathrm{keV}} \,. \tag{B.5}$$

The *mass weighted* temperature is defined as:

$$T_{\mathrm{MW}} = \frac{\int_0^{r_{500}} \mathrm{d}r\, \rho_{\mathrm{g}}(r)\, T_{\mathrm{g}}(r) 4\pi r^2}{\int_0^{r_{500}} \mathrm{d}r\, \rho_{\mathrm{g}}(r) 4\pi r^2} \tag{B.6}$$

and the factor $A = T_{\mathrm{MW}}/T_{\mathrm{X}}$ takes into account for the difference between mass weighted and spectroscopic average temperatures. Arnaud et al. (2010) find $A \sim 0.924$.

References

Afshordi, N., Lin, Y.-T., Nagai, D., & Sanderson, A. J. R. 2007, MNRAS, 378, 293
Arnaud, M., Pointecouteau, E., & Pratt, G. W. 2007, A&A, 474, L37
Arnaud, M., Pratt, G. W., Piffaretti, R., et al. 2010, A&A, 517, A92
Atrio-Barandela, F., Kashlinsky, A., Kocevski, D., & Ebeling, H. 2008, ApJ, 675, L57
Bennett, C. L., Halpern, M., Hinshaw, G., et al. 2003, ApJS, 148, 1
Bielby, R. M., & Shanks, T. 2007, MNRAS, 382, 1196
Böhringer, H., Voges, W., Huchra, J. P., et al. 2000, ApJS, 129, 435
Böhringer, H., Schuecker, P., Guzzo, L., et al. 2004, A&A, 425, 367
Böhringer, H., Schuecker, P., Pratt, G. W., et al. 2007, A&A, 469, 363
Bonamente, M., Joy, M., LaRoque, S. J., et al. 2008, ApJ, 675, 106
Carlstrom, J. E., Ade, P. A. R., Aird, K. A., et al. 2009, PASP, submitted [`arXiv:0907.4445`]
Condon, J. J., Cotton, W. D., Greisen, E. W., et al. 1998, AJ, 115, 1693
Croston, J. H., Pratt, G. W., Böhringer, H., et al. 2008, A&A, 487, 431
da Silva, A. C., Kay, S. T., Liddle, A. R., & Thomas, P. A. 2004, MNRAS, 348, 1401
Delabrouille, J., Cardoso, J.-F., Le Jeune, M., et al. 2009, A&A, 493, 835

Diego, J. M., & Partridge, B. 2009, MNRAS, 1927

Fosalba, P., Gaztañaga, E., & Castander, F. J. 2003, ApJ, 597, L89

Górski, K. M., Hivon, E., Banday, A. J., et al. 2005, ApJ, 622, 759

Hallman, E. J., O'Shea, B. W., Burns, J. O., et al. 2007, ApJ, 671, 27

Halverson, N. W., Lanting, T., Ade, P. A. R., et al. 2009, ApJ, 701, 42

Hernández-Monteagudo, C., Genova-Santos, R., & Atrio-Barandela, F. 2004, ApJ, 613, L89

Hernández-Monteagudo, C., Macías-Pérez, J. F., Tristram, M., & Désert, F.-X. 2006, A&A, 449, 41

Herranz, D., Sanz, J. L., et al. 2002, MNRAS, 336, 1057

Hinshaw, G., Nolta, M. R., Bennett, C. L., et al. 2007, ApJS, 170, 288

Hinshaw, G., Weiland, J. L., Hill, R. S., et al. 2009, ApJS, 180, 225

Kitayama, T., Komatsu, E., Ota, N., et al. 2004, PASJ, 56, 17

Kravtsov, A. V., Vikhlinin, A., & Nagai, D. 2006, ApJ, 650, 128

Lieu, R., Mittaz, J. P. D., & Zhang, S.-N. 2006, ApJ, 648, 176

Lamarre, J. M., Puget, J. L., Bouchet, F., et al. 2003, New Astron. Rev., 47, 1017

Marrone, D. P., Smith, G. P., Richard, J., et al. 2009, ApJ, 701, L114

Mauch, T., Murphy, T., Buttery, H. J., et al. 2003, MNRAS, 342, 1117

Melin, J.-B., Bartlett, J. G., & Delabrouille, J. 2006, A&A, 459, 341

Motl, P. M., Hallman, E. J., Burns, J. O., & Normal, M. L. 2005, ApJ, 623, L63

Mroczkowski, T., Bonamente, M., Carlstrom, J., et al. 2009, ApJ, 694, 1034

Myers, A. D., Shanks, T., Outram, P. J., Frith, W. J., & Wolfendale, A. W. 2004, MNRAS, 347, L67

Nagai, D., Kravtsov, A. V., & Vikhlinin, A. 2007, ApJ, 668, 1

Nord, M., Basu, K., Pacaud, F., et al. 2009, A&A, 506, 623

Plagge, T., Benson, B., Ade, P. A. R., et al. 2010, ApJ, 716, 1118

Pratt, G. W., Croston, J. H., Arnaud, M., Böhringer, H. 2009, A&A, 498, 361

Staniszewski, Z., Ade, P. A. R., Aird, K. A., et al. 2009, ApJ, 701, 32

Sunyaev, R. A., & Zel'dovich, Ya. B. 1970, Comments Astrophys. Space Phys., ComAp, 2, 66

Sunyaev, R. A., & Zel'dovich, Ya. B. 1972, Comments Astrophys. Space Phys., 4, 173

Valenziano, L., et al. 2007, New Astron. Rev., 51, 287

Vikhlinin, A., Burenin, R., Ebeling, H., et al. 2009, ApJ, 692, 1033

A&A 536, A10 (2011)
DOI: 10.1051/0004-6361/201116457

Astronomy & Astrophysics
Special feature

Planck early results. X. Statistical analysis of Sunyaev-Zeldovich scaling relations for X-ray galaxy clusters*

Planck Collaboration: N. Aghanim[47], M. Arnaud[58], M. Ashdown[56,4], J. Aumont[47], C. Baccigalupi[69], A. Balbi[30], A. J. Banday[76,7,63], R. B. Barreiro[53], M. Bartelmann[75,63], J. G. Bartlett[3,54], E. Battaner[77], K. Benabed[48], A. Benoît[46], J.-P. Bernard[76,7], M. Bersanelli[27,41], R. Bhatia[5], J. J. Bock[54,8], A. Bonaldi[37], J. R. Bond[6], J. Borrill[62,73], F. R. Bouchet[48], M. L. Brown[4,56], M. Bucher[3], C. Burigana[40], P. Cabella[30], J.-F. Cardoso[59,3,48], A. Catalano[3,57], L. Cayón[20], A. Challinor[50,56,11], A. Chamballu[44], R.-R. Chary[45], L.-Y Chiang[49], C. Chiang[19], G. Chon[64,4], P. R. Christensen[67,31], E. Churazov[63,72], D. L. Clements[44], S. Colafrancesco[38], S. Colombi[48], F. Couchot[61], A. Coulais[57], B. P. Crill[54,68], F. Cuttaia[40], A. Da Silva[10], H. Dahle[51,9], L. Danese[69], P. de Bernardis[26], G. de Gasperis[30], A. de Rosa[40], G. de Zotti[37,69], J. Delabrouille[3], J.-M. Delouis[48], F.-X. Désert[43], J. M. Diego[53], K. Dolag[63], S. Donzelli[41,51], O. Doré[54,8], U. Dörl[63], M. Douspis[47], X. Dupac[34], G. Efstathiou[50], T. A. Enßlin[63], F. Finelli[40], I. Flores-Cacho[52,32], O. Forni[76,7], M. Frailis[39], E. Franceschi[40], S. Fromenteau[3,47], S. Galeotta[39], K. Ganga[3,45], R. T. Génova-Santos[52,32], M. Giard[76,7], G. Giardino[35], Y. Giraud-Héraud[3], J. González-Nuevo[69], K. M. Górski[54,79], S. Gratton[56,50], A. Gregorio[28], A. Gruppuso[40], D. Harrison[50,56], S. Henrot-Versillé[61], C. Hernández-Monteagudo[63], D. Herranz[53], S. R. Hildebrandt[8,60,52], E. Hivon[48], M. Hobson[4], W. A. Holmes[54], W. Hovest[63], R. J. Hoyland[52], K. M. Huffenberger[78], A. H. Jaffe[44], W. C. Jones[19], M. Juvela[18], E. Keihänen[18], R. Keskitalo[54,18], T. S. Kisner[62], R. Kneissl[33,5], L. Knox[22], H. Kurki-Suonio[18,36], G. Lagache[47], J.-M. Lamarre[57], A. Lasenby[4,56], R. J. Laureijs[35], C. R. Lawrence[54], S. Leach[69], R. Leonardi[34,35,23], M. Linden-Vørnle[13], M. López-Caniego[53], P. M. Lubin[23], J. F. Macías-Pérez[60], C. J. MacTavish[56], B. Maffei[55], D. Maino[27,41], N. Mandolesi[40], R. Mann[70], M. Maris[39], F. Marleau[15], E. Martínez-González[53], S. Masi[26], S. Matarrese[25], F. Matthai[63], P. Mazzotta[30], A. Melchiorri[26], J.-B. Melin[12], L. Mendes[34], A. Mennella[27,39], S. Mitra[54], M.-A. Miville-Deschênes[47,6], A. Moneti[48], L. Montier[76,7], G. Morgante[40], D. Mortlock[44], D. Munshi[71,50], A. Murphy[66], P. Naselsky[67,31], P. Natoli[29,2,40], C. B. Netterfield[15], H. U. Nørgaard-Nielsen[13], F. Noviello[47], D. Novikov[44], I. Novikov[67], S. Osborne[74], F. Pajot[47], F. Pasian[39], G. Patanchon[3], O. Perdereau[61], L. Perotto[60], F. Perrotta[69], F. Piacentini[26], M. Piat[3], E. Pierpaoli[17], R. Piffaretti[58,12], S. Plaszczynski[61], E. Pointecouteau[76,7], G. Polenta[2,38], N. Ponthieu[47], T. Poutanen[36,18,1], G. W. Pratt[58], G. Prézeau[8,54], S. Prunet[48], J.-L. Puget[47], R. Rebolo[52,32], M. Reinecke[63], C. Renault[60], S. Ricciardi[40], T. Riller[63], I. Ristorcelli[76,7], G. Rocha[54,8], C. Rosset[3], J. A. Rubiño-Martín[52,32], B. Rusholme[45], M. Sandri[40], D. Santos[60], B. M. Schaefer[75], D. Scott[16], M. D. Seiffert[54,8], G. F. Smoot[21,62,3], J.-L. Starck[58,12], F. Stivoli[42], V. Stolyarov[4], R. Sunyaev[63,72], J.-F. Sygnet[48], J. A. Tauber[35], L. Terenzi[40], L. Toffolatti[14], M. Tomasi[27,41], M. Tristram[61], J. Tuovinen[65], L. Valenziano[40], L. Vibert[47], P. Vielva[53], F. Villa[40], N. Vittorio[30], B. D. Wandelt[48,24], S. D. M. White[63], M. White[21], D. Yvon[12], A. Zacchei[39], and A. Zonca[23]

(Affiliations can be found after the references)

Received 7 January 2011 / Accepted 17 June 2011

ABSTRACT

All-sky data from the *Planck* survey and the Meta-Catalogue of X-ray detected Clusters of galaxies (MCXC) are combined to investigate the relationship between the thermal Sunyaev-Zeldovich (SZ) signal and X-ray luminosity. The sample comprises ~1600 X-ray clusters with redshifts up to ~1 and spans a wide range in X-ray luminosity. The SZ signal is extracted for each object individually, and the statistical significance of the measurement is maximised by averaging the SZ signal in bins of X-ray luminosity, total mass, or redshift. The SZ signal is detected at very high significance over more than two decades in X-ray luminosity (10^{43} erg s^{-1} $\lesssim L_{500}E(z)^{-7/3} \lesssim 2\times 10^{45}$ erg s^{-1}). The relation between intrinsic SZ signal and X-ray luminosity is investigated and the measured SZ signal is compared to values predicted from X-ray data. *Planck* measurements and X-ray based predictions are found to be in excellent agreement over the whole explored luminosity range. No significant deviation from standard evolution of the scaling relations is detected. For the first time the intrinsic scatter in the scaling relation between SZ signal and X-ray luminosity is measured and found to be consistent with the one in the luminosity – mass relation from X-ray studies. There is no evidence of any deficit in SZ signal strength in *Planck* data relative to expectations from the X-ray properties of clusters, underlining the robustness and consistency of our overall view of intra-cluster medium properties.

Key words. galaxies: clusters: intracluster medium – X-rays: galaxies: clusters – cosmology: observations

1. Introduction

Clusters of galaxies are filled with a hot, ionised, intra-cluster medium (ICM) visible both in the X-ray band via thermal bremsstrahlung and from its distortion of the cosmic microwave background (CMB) from inverse Compton scattering, i.e., the Sunyaev-Zeldovich effect (Sunyaev & Zeldovich 1970, 1972, SZ, hereafter). The SZ signal can be divided into a kinetic SZ and a thermal SZ effect, originating from bulk and thermal motions of ICM electrons, respectively. Since the kinetic SZ is a second-order effect, we only consider the thermal SZ effect. Because of the different scaling of SZ and X-ray fluxes with electron density and temperature, SZ and X-ray observations are highly complementary. The combination of information from these two types of observations is a powerful one for cosmological studies, as well as for improving our understanding of cluster

---

* Corresponding author: R. Piffaretti,
e-mail: `rocco.piffaretti@cea.fr`

physics (see Birkinshaw 1999, for a review). In this framework, it is paramount to investigate to what degree the ICM properties inferred from SZ and X-ray data agree.

Unfortunately, there is currently no consensus on whether predictions for the SZ signal based on ICM properties derived from X-ray observation agree with direct SZ observations, hampering our understanding of the involved physics. Lieu et al. (2006) find evidence of a weaker SZ signal in the 3-year WMAP data than expected from ROSAT observations for 31 X-ray clusters. Bielby & Shanks (2007) reach similar conclusions using the same WMAP data and ROSAT sample and the additional *Chandra* data for 38 clusters. Conversely, Afshordi et al. (2007) find good agreement between the strength of the SZ signal in WMAP 3-year data and the X-ray properties of their sample of 193 massive galaxy clusters. The last findings are supported further by the results of Atrio-Barandela et al. (2008), whose analysis is based on the same SZ data and a larger sample of 661 clusters. Diego & Partridge (2010) argue that a large contamination from point sources is needed to reconcile the SZ signal seen in the WMAP 5-year data with what is inferred from a large sample of ROSAT clusters. However, using the same SZ data and a slightly larger but similar sample of ROSAT clusters, Melin et al. (2011) find good agreement between SZ signal and expectations. The latter finding is confirmed by the work by Andersson et al. (2011), where high quality *Chandra* data for 15 South Pole Telescope clusters are used. Finally, the WMAP 7-year data analysis by Komatsu et al. (2011) argues for a deficit of SZ signal compared to expectations, especially at low masses.

Improved understanding of this issue is clearly desired, since it would provide invaluable knowledge about clusters of galaxies and aid in the interpretation and exploitation of SZ surveys such as the South Pole Telescope (SPT, Carlstrom et al. 2011) survey, the Atacama Cosmology Telescope (ACT, Fowler et al. 2007), and *Planck*[1] (Tauber et al. 2010). Since August 2009 the *Planck* satellite has been surveying the whole sky in nine frequency bands with high sensitivity and a relatively high spatial resolution. *Planck* data thus offer the unique opportunity to fully explore this heavily debated issue. As part of a series of papers on *Planck* early results on clusters of galaxies (Planck Collaboration 2011d,e,f,g,h), we present a study of the relationship between X-ray luminosity and SZ signal in the direction of ~1600 objects from the MCXC X-ray clusters compilation (Piffaretti et al. 2011) and demonstrate that there is excellent agreement between SZ signal and expectations from the X-ray properties of clusters.

The paper is organised as follows. In Sect. 2 we briefly describe the *Planck* data used in the analysis and present the adopted X-ray sample. In Sect. 3 we present the baseline model used in the paper. The model description is rather comprehensive because the model is also adopted in the companion papers on *Planck* early results on clusters of galaxies (Planck Collaboration 2011d,e,f,h). Section 4 describes how the SZ signal is extracted from *Planck* frequency maps at the position of each MCXC cluster and how these are averaged in X-ray luminosity bins. Our results are presented in Sect. 5 and robustness tests are detailed in Sect. 6. Our findings are discussed and summarised in 7.

When necessary we adopt a ΛCDM cosmology with H_0 = 70 km s^{-1}/Mpc, $\Omega_{\rm M} = 0.3$ and $\Omega_\Lambda = 0.7$ throughout the paper. The quantity $E(z)$ is the ratio of the Hubble constant at redshift z to its present value, H_0, i.e., $E(z)^2 = \Omega_{\rm m}(1+z)^3 + \Omega_\Lambda$.

The total cluster mass M_{500} is defined as the mass within the radius R_{500} within which the mean mass density is 500 times the critical density of the universe, $\rho_{\rm crit}(z)$, at the cluster redshift: $M_{500} = \frac{4}{3}\pi\,\rho_{\rm crit}(z)\,500\,R^3_{500}$. We adopt an overdensity of 500 since R_{500} encloses a substantial fraction of the total virialised mass of the system while being the largest radius probed in current X-ray observations of large samples of galaxy clusters.

The SZ signal is characterised by Y_{500} defined as $D^2_{\rm A}(z)\,Y_{500} = (\sigma_{\rm T}/m_{\rm e}c^2)\int P{\rm d}V$, where $D_{\rm A}(z)$ is the angular distance to a system at redshift z, $\sigma_{\rm T}$ is the Thomson cross-section, c the speed of light, $m_{\rm e}$ the electron rest mass, $P = n_{\rm e}kT_{\rm e}$ the pressure, defined as the product of the electron number density and temperature and the integration is performed over the sphere of radius R_{500}. The quantity Y_{500} is proportional to the apparent magnitude of the SZ signal and $D^2_{\rm A}\,Y_{500}$ is the spherically integrated Compton parameter, which, for simplicity, will be referred to as SZ signal or *intrinsic* SZ signal in the remainder of the paper. All quoted X-ray luminosities are cluster rest frame luminosities, converted to the [0.1–2.4] keV band.

2. Data

In the following subsections we present the *Planck* data and the X-ray cluster sample used in our analysis. In order to avoid contamination from galactic sources in the *Planck* data we exclude the galactic plane: $|b|\leq 14$ deg from the maps. In addition, we exclude clusters located less than 1.5× beam full width half maximum (FWHM) from point sources detected at more than 10σ in any of the single frequency *Planck* maps, because such sources can strongly affect SZ measurements.

2.1. SZ data set

Planck (Tauber et al. 2010; Planck Collaboration 2011a) is the third generation space mission to measure the anisotropy of the CMB. It observes the sky in nine frequency bands covering 30–857 GHz with high sensitivity and angular resolution from 31′ to 5′. The Low Frequency Instrument LFI; (Mandolesi et al. 2010; Bersanelli et al. 2010; Mennella et al. 2011) covers the 30, 44, and 70 GHz bands with amplifiers cooled to 20 K. The High Frequency Instrument (HFI; Lamarre et al. 2010; Planck HFI Core Team 2011a) covers the 100, 143, 217, 353, 545, and 857 GHz bands with bolometers cooled to 0.1 K. Polarisation is measured in all but the highest two bands (Leahy et al. 2010; Rosset et al. 2010). A combination of radiative cooling and three mechanical coolers produces the temperatures needed for the detectors and optics (Planck Collaboration 2011b). Two Data Processing Centers (DPCs) check and calibrate the data and make maps of the sky (Planck HFI Core Team 2011b; Zacchei et al. 2011). *Planck*'s sensitivity, angular resolution, and frequency coverage make it a powerful instrument for galactic and extragalactic astrophysics as well as cosmology. Early astrophysics results are given in Planck Collaboration (2011e–x).

In this paper, we use only the six temperature channel maps of HFI (100, 143, 217, 353, 545 and 857 GHz), corresponding to (slightly more than) the first sky survey of Planck. Details of how these maps are produced can be found in Planck HFI Core Team (2011b); Planck Collaboration (2011d). At this early stage of the Planck SZ analysis adding the LFI channel maps does

---

[1] *Planck* (`http://www.esa.int/Planck`) is a project of the European Space Agency (ESA) with instruments provided by two scientific consortia funded by ESA member states (in particular the lead countries France and Italy), with contributions from NASA (USA) and telescope reflectors provided by a collaboration between ESA and a scientific consortium led and funded by Denmark.

Table 1. Values of the beam full width half maximum assumed for each of the six channel maps of HFI.

Frequency [GHz]	100	143	217	353	545	857
FWHM [′]	9.53	7.08	4.71	4.50	4.72	4.42
FWHM error [′]	0.10	0.12	0.17	0.14	0.21	0.28

not bring significant improvements to our results. We use the full resolution maps at HEALPix[2] nside = 2048 (pixel size 1.72′) and we assume that beams are adequately described by symmetric Gaussians with FWHM as given in Table 1. Uncertainties in our results due to beam corrections, map calibrations and uncertainties in bandpasses are small, as shown in Sect. 6 below.

2.2. X-ray data set

The cluster sample adopted in our analysis, the MCXC (Meta-Catalogue of X-ray detected Clusters of galaxies), is presented in detail in Piffaretti et al. (2011). The information provided by all publicly available ROSAT All Sky Survey-based (NORAS: Böhringer et al. 2000, REFLEX: Böhringer et al. 2004, BCS: Ebeling et al. 1998, 2000, SGP: Cruddace et al. 2002, NEP: Henry et al. 2006, MACS: Ebeling et al. 2007, 2010, and CIZA: Ebeling et al. 2002; Kocevski et al. 2007) and serendipitous (160SD: Mullis et al. 2003, 400SD: Burenin et al. 2007, SHARC: Romer et al. 2000; Burke et al. 2003, WARPS: Perlman et al. 2002; Horner et al. 2008, and EMSS: Gioia & Luppino 1994; Henry 2004) cluster catalogues was systematically homogenised and duplicate entries were carefully handled, yielding a large catalogue of approximately 1800 clusters. For each cluster the MCXC provides, among other quantities, coordinates, redshifts, and luminosities. The latter are central to the MCXC and to our analysis because luminosity is the only available mass proxy for such a large number of X-ray clusters. For this reason we will focus here on how the cluster rest frame luminosities provided by the MCXC are computed. Other quantities such as total mass and cluster size will be discussed in Sect. 3 below, because they are more model dependent.

In addition to being converted to the cosmology adopted in this paper and to the [0.1–2.4] keV band (the typical X-ray survey energy band), luminosities are converted to that for an overdensity of 500 (see below). This allows us to minimise the scatter originating from the fact that publicly available catalogues provide luminosity measurements within different apertures.

Because cluster catalogues generally provide luminosities measured within some aperture or luminosities extrapolated up to large radii (total luminosities), the luminosities L_{500} provided by the MCXC were computed by converting the total luminosities to L_{500} using a constant factor or, when aperture luminosities are available, by performing an iterative computation based on the REXCESS mean gas density profile and $L_{500} - M_{500}$ relation. The REXCESS $L_{500} - M_{500}$ calibration is discussed in Sect. 3 below. While the comparison presented in Sect. 5.3 of Piffaretti et al. (2011) indicates that the differences between these two methods do not introduce any systematic bias, it is clear that the iteratively computed L_{500} are the most accurate. The iterative computation was possible for the NORAS/REFLEX, BCS, SHARC, and NEP catalogues. As shown in Piffaretti et al. (2011) the luminosities L_{500} depend very weakly on the assumed L_{500}–M_{500} relation. Nevertheless, when exploring the different L_{500}–M_{500} relations detailed below, we consistently recompute L_{500} using the relevant L_{500}–M_{500} relation.

In addition, we supplement the MCXC sample with $z \geq 0.6$ cluster data in order to enlarge the redshift leverage. These additional high redshift clusters are collected from the literature by utilizing the X-Rays Clusters Database BAX[3] and performing a thorough search in the literature. For these objects we collect coordinates, redshift, and X-ray luminosity. The luminosity values given in the literature are converted to the [0.1–2.4] keV band and adopted cosmology as done in Piffaretti et al. (2011). Because the available luminosities are derived under fairly different assumptions (e.g., aperture radius, extrapolation methods, etc.) we do not attempt to homogenise them to the fiducial luminosity L_{500} as done in Piffaretti et al. (2011). In almost all the cases the adopted luminosity is however either the total luminosity (i.e. extrapolated to large radii) or the directly the luminosity L_{500}. Given the fact that the difference between these is close to 10% and that uncertainties affecting luminosity measurement of high redshift clusters are much larger, we treat all luminosities as fiducial luminosity L_{500}.

The MCXC and $z \geq 0.6$ supplementary clusters located around the galactic plane ($|b| \leq 14$ deg) or near bright point sources ($>10\sigma$, distance $< 1.5 \times$ FWHM) are excluded from the analysis. The resulting sample comprises 1603 clusters, with 845 clusters being members of the NORAS/REFLEX sample. There is a total of 33 supplementary $z \geq 0.6$ clusters located in the sky region selected in our analysis.

In Fig. 1 we show luminosity and mass as a function of redshift for the whole sample with the NORAS/REFLEX and supplementary $z \geq 0.6$ clusters displayed with different colours. The figure shows the different clustering in the $L - z$ plane of RASS (mostly NORAS/REFLEX) and serendipitously discovered clusters. The NORAS/REFLEX clusters are central to our study for many reasons. First, being the most luminous and numerous, they are expected to yield the bulk of the SZ signal from known clusters. Second, their distribution in the sky is uniform: NORAS and REFLEX cover the northern and southern sky, respectively, with the galactic plane excluded ($|b| \leq 20$ deg). Finally, the NORAS/REFLEX sample was also used in Melin et al. (2011) in an analysis equivalent to the one presented in this work but based on WMAP-5 yr data. For these reasons we use NORAS/REFLEX clusters as control sample in our analysis.

For simplicity, in the remainder of the paper the whole compilation of MCXC plus supplementary $z \geq 0.6$ clusters will be referred to as MCXC. The [0.1–2.4] keV luminosities of the clusters in our sample range from 1.53×10^{40} to 2.91×10^{45} erg s^{-1}, with a median luminosity of 0.95×10^{44} erg s^{-1}, and redshifts range from 0.0031 to 1.45. Notice that while the adopted sample essentially comprises all known X-ray clusters in the sky region of interest, its selection function is unknown. The latter issue and how we evaluate its impact on our results is discussed in Sect. 3.1 below.

3. The cluster model

Our cluster model is based on the REXCESS, a sample expressly designed to measure the structural and scaling properties of the local X-ray cluster population by means of an unbiased, representative sampling in luminosity (Böhringer et al. 2007). The calibration of scaling relations and the average structural parameters of such an X-ray selected sample is ideal because is not morphologically biased. Furthermore, the gas properties of the

---

[2] `http://healpix.jpl.nasa.gov`

[3] `http://bax.ast.obs-mip.fr/`

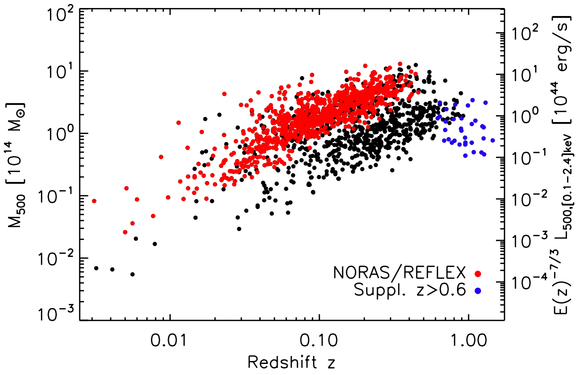

Fig. 1. Observed [0.1–2.4] keV band luminosities (right vertical axis) and inferred masses (left vertical axis) as a function of redshift. Shown are the MCXC (the NORAS/REFLEX control subsample in shown in red) and the supplementary clusters (blue dots).

REXCESS clusters can be traced by *XMM-Newton* up to large cluster-centric distances, allowing robust measurements at an overdensity of 500.

Since X-ray luminosity is the only available mass proxy for our large cluster sample, the most fundamental ingredient of the cluster model is the scaling relation between [0.1–2.4] keV band luminosity and total cluster mass, which is detailed in Sect. 3.1. Given a cluster redshift z, mass M_{500} and hence cluster size R_{500}, the universal pressure profile of Arnaud et al. (2010) is then used to predict the electronic pressure profile. This allows us to predict $D_{\mathrm{A}}^{2}\,Y_{500}$, the SZ signal integrated in a sphere of radius R_{500} as summarised in Sect. 3.2. It is important to notice that the estimated cluster size R_{500} and the universal pressure profile are also assumed when extracting the SZ signal from *Planck* data as detailed in Sect. 4 below.

In the following we describe the assumptions at the basis of our *fiducial model* and provide the adopted scaling laws. In addition, we also discuss how these assumptions are varied in order to investigate the robustness of our results.

3.1. $L_{500} - M_{500}$ relation

For a given [0.1–2.4] keV band luminosity L_{500} the total mass M_{500} is estimated adopting the REXCESS $L_{500} - M_{500}$ relation (Pratt et al. 2009):

$$E(z)^{-7/3}\left(\frac{L_{500}}{10^{44}\,\mathrm{erg\,s^{-1}}}\right) = C_{\mathrm{LM}}\left(\frac{M_{500}}{3\times10^{14}\,M_{\odot}}\right)^{\alpha_{\mathrm{LM}}}. \tag{1}$$

Because this relation has been calibrated using the low scatter X-ray mass proxy Y_{X} (Kravtsov et al. 2006), the parameters C_{LM} and α_{LM} depend on whether the slope of the underlying $M_{500} - Y_{\mathrm{X}}$ relation is assumed to be equal to the standard (self-similar) value of $\alpha_{\mathrm{MY_X}} = 3/5$ or it is allowed to be a free parameter, yielding $\alpha_{\mathrm{MY_X}} = 0.561$ (see Eqs. (2) and (3) in Arnaud et al. 2010). In the reminder of the paper these two cases will be referred to as *standard* and *empirical*, respectively. Our *fiducial model* adopts the *empirical* case, which reflects the observed mass dependence of the gas mass fraction in galaxy clusters. It is thus fully observationally motivated.

In addition to these two variations of the $L_{500} - M_{500}$ relation, we also consider the impact of Malmquist bias on our analysis. To this end we perform our analysis using the $L - M$ calibrations derived from REXCESS luminosity data corrected or uncorrected for the Malmquist bias. In the reminder of the paper these two cases will be referred to as the *intrinsic* and REXCESS $L_{500} - M_{500}$ relations, respectively. Notice that the difference between the *intrinsic* and REXCESS $L_{500} - M_{500}$ relations is very small at high luminosity (Pratt et al. 2009). Ideally, one should use the *intrinsic* $L_{500} - M_{500}$ relation and compute, for each sample used to construct the MCXC compilation, the observed $L_{500} - M_{500}$ relation according to each survey selection function. Unfortunately this would be possible only for a small fraction of MCXC clusters because the individual selection functions of the samples used to construct it are extremely complex and, in most of the cases, not known or not available. Therefore we simply consider the intrinsic $L_{500} - M_{500}$ relation as an extreme and illustrative case, since it is equivalent to assuming that selection effects of our X-ray sample are totally negligible. On the other hand, in particular for the NORAS/REFLEX control sample and at high luminosities, the REXCESS $L_{500} - M_{500}$ relation is expected to be quite close to the one that would be observed in our sample. For these reasons, our *fiducial model* adopts the REXCESS $L_{500} - M_{500}$ relation and the *intrinsic* case is used to test the robustness of our results.

Table 2. Values for the parameters of the adopted $L_{\mathrm{X}} - M$ relation.

$\alpha_{\mathrm{MY_X}}$	$L - M$	$\log C_{\mathrm{LM}}$	α_{LM}	$\sigma_{\log L - \log M}$
0.561	REXCESS	0.274	1.64	0.183
0.561	Intrinsic	0.193	1.76	0.199
3/5	REXCESS	0.295	1.50	0.183
3/5	Intrinsic	0.215	1.61	0.199

These different choices result in four different calibrations of the $L_{500} - M_{500}$ relation. The corresponding best fitting parameters are summarised in Table 2 (see also Arnaud et al. 2010). Values are given for the *fiducial case* where the observed REXCESS $L_{\mathrm{X}} - Y_{\mathrm{X}}$ and $M - Y_{\mathrm{X}}$ are assumed as well as for the cases where these two assumptions are varied: i.e. intrinsic (Malmquist bias corrected) $L_{\mathrm{X}} - Y_{\mathrm{X}}$ relation and standard slope of the $M - Y_{\mathrm{X}}$ relation $\alpha_{\mathrm{MY_X}}$. The table also lists the intrinsic dispersion in each relation, which we use to investigate the effect of scatter in the assumed mass-observable relation in our analysis.

For a given $L_{500} - M_{500}$ relation we estimate, for each cluster in our sample, the total mass M_{500} from its luminosity L_{500}. When the latter is computed iteratively (see Sect. 2.2), the same $L_{500} - M_{500}$ relation is adopted for consistency. Finally, the cluster size or characteristic radius R_{500} is computed from its definition: $M_{500} = \frac{4}{3}\pi\,\rho_{\mathrm{crit}}(z)\,500\,R_{500}^{3}$.

3.2. The SZ signal

As shown in Arnaud et al. (2010), if standard evolution is assumed, the average physical pressure profile of clusters can be described by

$$P(r) = P_{500}\left(\frac{M_{500}}{3\times10^{14}\,M_{\odot}}\right)^{\alpha_{\mathrm{P}}}\frac{P_0}{(c_{500}x)^{\gamma}\left(1+(c_{500}x)^{\alpha}\right)^{\frac{\beta-\gamma}{\alpha}}}, \tag{2}$$

with $x = r/R_{500}$ and $\alpha_{\mathrm{P}} = 1/\alpha_{\mathrm{MY_X}} - 5/3$. In the standard case we have $\alpha_{\mathrm{P}} = 0$, while in the empirical case $\alpha_{\mathrm{P}} = 0.12$. Notice that the most precise empirical description also takes into account a weak radial dependence of the exponent α_{P} of the form $\alpha_{\mathrm{P}} = 0.12 + \alpha'_{\mathrm{P}}(x)$. Here we neglect the radially dependent term since, as shown by Arnaud et al. (2010), it introduces a fully negligible correction.

Table 3. Parameters describing the shape of the pressure profile.

	$\alpha_{\rm MY_X}$	P_0	c_{500}	γ	α	β
All	0.561	8.403	1.177	0.3081	1.0510	5.4905
CC	0.561	3.249	1.128	0.7736	1.2223	5.4905
MD	0.561	3.202	1.083	0.3798	1.4063	5.4905
All	3/5	8.130	1.156	0.3292	1.0620	5.4807

The characteristic pressure P_{500} is defined as

$$P_{500} = 1.65\times10^{-3} E(z)^{8/3} \left(\frac{M_{500}}{3\times10^{14}\,M_\odot}\right)^{2/3} \ \mathrm{keV\,cm^{-3}}. \qquad (3)$$

The set of parameters $[P_0, c_{500}, \gamma, \alpha, \beta]$ in Eq. (2) are constrained by fitting the REXCESS data and depend on the assumed slope of the $M - Y_{\rm X}$ relation. In Table 3 we list the adopted best fitting values, which, as detailed in Sect. 4 below, are also used to optimise the SZ signal detection. Values are first given for the *fiducial case* where the observed $M - Y_{\rm X}$ relation (with slope $\alpha_{\rm MY_X} = 0.561$) and the average profile of all REXCESS clusters are adopted. The values for the average cool-core (CC) and morphologically disturbed (MD) REXCESS profiles, that we use to estimate the uncertainties originating from deviations from the average profile (see Sect. 6), and the average profile derived assuming a standard slope of the $M - Y_{\rm X}$ relation ($\alpha_{\rm MY_X} = 3/5$), are also listed in the table.

Because of the large number of free parameters, there is a strong parameter degeneracy and therefore a comparison of individual parameters in Table 3 is meaningless. The parameters for the *standard* case are also listed in the table.

The model allows us to compute the physical pressure profile as a function of mass M_{500} and z and thus to obtain the $D_{\rm A}^2\,Y_{500} - M_{500}$ relation by integration of $P(r)$ in Eq. (2) within a sphere of radius R_{500}. The relation can be written as

$$D_{\rm A}^2(z)\,Y_{500} = 2.925\times10^{-5} I(1) \times \left(\frac{M_{500}}{3\times10^{14}\,M_\odot}\right)^{\frac{1}{\alpha_{MY_X}}} E(z)^{2/3}\ \mathrm{Mpc}^2 \qquad (4)$$

or, equivalently,

$$Y_{500} = 1.383\times10^{-3} I(1) \times \left(\frac{M_{500}}{3\times10^{14}\,M_\odot}\right)^{\frac{1}{\alpha_{MY_X}}} E(z)^{2/3} \left(\frac{D_{\rm A}(z)}{500\ \mathrm{Mpc}}\right)^{-2} \mathrm{arcmin}^2, \qquad (5)$$

where $I(1) = 0.6145$ and $I(1) = 0.6552$ are numerical factors arising from volume integrals of the pressure profile in the empirical and standard slope case, respectively (see Arnaud et al. 2010, for details). Combining Eqs. (1) and (4) gives

$$D_{\rm A}^2(z)\,Y_{500} = 2.925\times10^{-5} I(1) \times \left[\frac{E(z)^{-7/3}}{C_{LM}}\left(\frac{L_{500}}{10^{44}\ \mathrm{erg\,s^{-1}}}\right)\right]^{\frac{1}{\alpha_{LY}}} E(z)^{2/3}\ \mathrm{Mpc}^2, \qquad (6)$$

where $\alpha_{\rm LY} = \alpha_{\rm LM}\times\alpha_{\rm MY_X}$. In the *fiducial case* $\alpha_{\rm LY} = 0.92$, implying that $Y_{500}\,D_{\rm A}^2 \propto L_{500}^{1.09}$ for our model predictions. The cluster model allows us to predict the volume integrated Compton parameter $D_{\rm A}^2\,Y_{500}$ for each individual cluster in our large X-ray cluster sample from its [0.1–2.4] keV band luminosity L_{500}. These X-ray based prediction can be computed for different assumptions about the underlying X-ray scaling relations (*standard*/*empirical* and *intrinsic*/REXCESS cases) and compared with the observed SZ signal, whose measurement is detailed in the next section.

To reiterate, our *fiducial case* assumes: *empirical* slope of $M - Y_{\rm X}$ relation and REXCESS $L_{500} - M_{500}$ relation. If not otherwise stated, in the remainder of the paper results for the *fiducial case* are presented and results obtained by varying the assumptions are going to be compared to it in Sect. 6.

For simplicity the cluster size and SZ signal for the MCXC clusters in Planck Collaboration (2011d) are provided in the *standard* $M_{500} - Y_{\rm X}$ slope case. As we show in Planck Collaboration (2011d) the effects of this on X-ray size and both predicted and observed SZ quantities for clusters in the Early Sunyaev-Zeldovich (ESZ) catalog are fully negligible with respect to the overall uncertainties.

4. Extraction of the SZ signal

4.1. Individual measurements

The SZ signal is extracted for each cluster individually by cutting from each of the six HFI frequency maps 10° × 10° patches (pixel = 1.72 arcmin) centred at the cluster position. The resulting set of six HFI frequency patches is then used to extract the cluster signal by means of multifrequency matched filters (MMF, hereafter). The main features of the multifrequency matched filters are summarised in Melin et al. (2011) and more details can be found in Herranz et al. (2002) and Melin et al. (2006).

The MMF algorithm optimally filters and combines the patches to estimate the SZ signal. It relies on an estimate of the noise auto- and cross-power-spectra from the patches. Working with sky patches centred at cluster positions allows us to get the best estimates of the local noise properties. The MMF also makes assumptions about the spatial and spectral characteristics of the cluster signal and the instrument. Our cluster model is described below, for the instrumental response we assumed symmetric Gaussian beams with FWHM given in Table 1.

We determine a single quantity for each cluster from the *Planck* data, the normalisation of an assumed profile. All the parameters determining the profile location, shape and size are fixed using X-ray data. We use the profile shape described in Sect. 3 with c_{500}, α, β and γ fixed to the values given in Table 3 and integrate along the line-of-sight to obtain a template for the cluster SZ signal. The integral is performed by considering a cylindrical volume and a cluster extent of $5\times R_{500}$ along the line-of-sight. The exact choice of the latter is not relevant. The normalisation of the profile is fitted using data within a circular aperture of radius $5\times R_{500}$ for each system in our X-ray cluster catalogue, centring the filter on the X-ray position and fixing the cluster size to $\theta_{500} = R_{500}/D_{\rm A}(z)$. Notice that the dependence of cluster size on X-ray luminosity is weak ($R_{500} \propto L_{500}^{0.2}$ from Eq. (1)), implying that MMF measurements are expected to be relatively insensitive to the details of the underlying $L_{500} - M_{500}$ relation.

The MMF method yields statistical SZ measurement errors $\sigma_{\rm i}$ on individual meaurements. The statistical error includes uncertainties due to the instrument (beam, noise) and to the astrophysical contaminants (primary CMB, Galaxy, point sources). Obviously, it does not take into account the uncertainties on our X-ray priors and instrumental properties which will be studied in Sect. 6

The same extraction method is used in Planck Collaboration (2011h) where the optical-SZ scaling relation with MaxBCG clusters (Koester et al. 2007) are investigated. There are only two differences. First, in this paper we use the X-ray

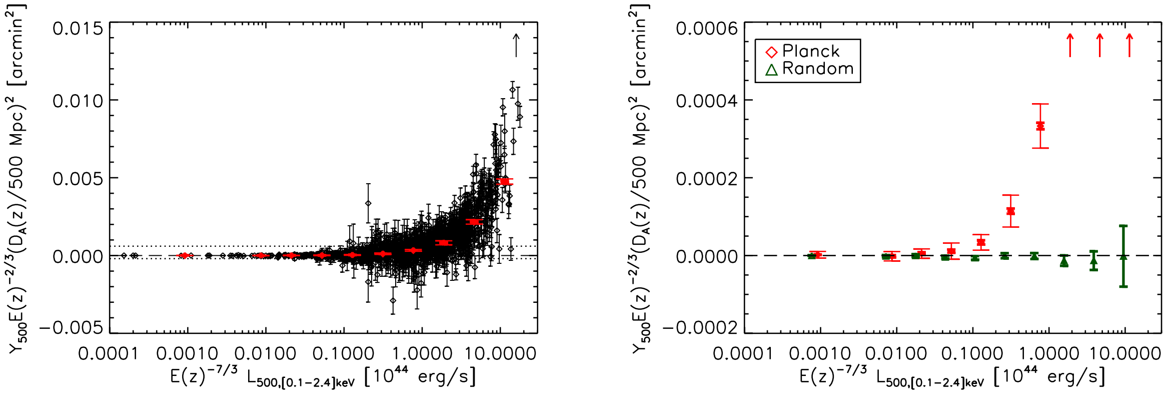

Fig. 2. *Left*: intrinsic SZ signal from a sphere of radius R_{500} as a function of the X-ray luminosity for all the clusters in the sample individually. Error bars indicate the pure measurement uncertainties based on MMF noise estimates (statistical uncertainties). Red diamonds show the bin averaged values with thick and thin error bars indicating the statistical (not visible) and bootstrap uncertainties, respectively. *Right*: zoom onto the scale indicated by the horizontal dotted lines in *the left-hand panel*. Red symbols and error bars as in *left-hand panel*. Green triangles (shifted towards lower X-ray luminosity values by 20% with respect to diamonds for clarity) show the result of the same analysis when the signal is estimated at random positions instead of true cluster positions. The associated thick error bars indicate the statistical uncertainties.

scaling $L_{500} - M_{500}$ to adapt our filters to the sizes of our clusters while we use the optical $N_{200} - M_{500}$ relation of Johnston et al. (2007) and Rozo et al. (2009) in the other paper. Second, the MaxBCG catalogue includes ~14 000 clusters so we do not build a set of patches for each cluster individually. Instead, we divide the sphere into 504 overlapping patches (10°×10°, pixel = 1.72 arcmin) as in Melin et al. (2011). We also extract SZ signal for each cluster individually but the clusters are no longer located at the centre of the patch.

Under the assumption that the shape of the adopted profile template corresponds to the true SZ signal, our extraction method allows us to convert the signal in a cylinder of aperture radius $5 \times R_{500}$ to Y_{500}, the SZ signal in a sphere of radius R_{500}. By definition the conversion factor is a constant factor for every cluster but depends on the assumed profile. The effect of the uncertainties on the assumed profile are discussed in Sect. 6 below.

The *intrinsic SZ signal* is computed by taking into account the angular distance dependence of the observed signal and is expressed as $(D_A(z)/500\,\mathrm{Mpc})^2\,Y_{500}$. This signal has units of arcmin^2 as for the observed quantity, but its value differs from the intrinsic signal in units of Mpc^2 by a constant, redshift-independent factor. Making such a conversion allows us to directly compare our measurements with the predictions derived from the model detailed in Sect. 3 (see in particular Eqs. (4) and (5)). When a specific scaling relation is investigated, the SZ signal is appropriately scaled according to the adopted scaling relations presented in Sect. 3 (e.g., see the left-hand panel of Fig. 2).

The SZ signal for all the clusters in our sample is shown as a function of the [0.1–2.4] keV band X-ray luminosity in the left-hand panel of Fig. 2. Assuming standard evolution the intrinsic quantities $(D_A(z)/500\,\mathrm{Mpc})^2\,Y_{500}\,E(z)^{-2/3}$ are plotted as a function of $L_{500}E(z)^{-7/3}$. The figure shows that *Planck* detects the SZ signal at high significance for a large fraction of the clusters.

4.2. Binned SZ signal

As shown in the left-hand panel of Fig. 2 the SZ signal is not measured at high significance for all of the clusters. In particular, low luminosity objects are barely detected individually. We therefore take advantage of the large size of our sample and average SZ measurements in X-ray luminosity, mass, or redshift bins. The bin average of the intrinsic SZ signal is defined as the weighted mean of the signal in the bin (with inverse variance weight, σ_i^{-2}, scaled to the appropriate redshift or mass dependence depending on the studied scaling relation) and the associated statistical errors are computed accordingly. The binning depends on the adopted relation and will be detailed in each case.

In the left-hand panel of Fig. 2 the binned signal is overlaid on the individual measurements. In this case the SZ signal is averaged in logarithmically spaced luminosity bins. We merged the lowest four luminosity bins into a single bin to obtain a significant result. The statistical uncertainties, which are depicted by the thick error bars, are not visible in the figure and clearly underestimate the uncertainty on the binned values.

A better estimate of the uncertainties in the binned values comes from an ensemble of 10 000 bootstrap realisations of the entire X-ray cluster catalogue. Each realisation is constructed from the original data set by random sampling with replacement, where all quantities of a given cluster are replaced by those of another cluster. Each realisation is analysed in the same way as the original catalogue and the standard deviation of the average signal in each bin is adopted as total error. Bootstrap uncertainties, which take into account both sampling and statistical uncertainties, are shown by the thin error bars in the left-hand panel of Fig. 2. A visual inspection of the figure indicates that the SZ signal is detected at high significance over a wide luminosity range. The lack of clear detection at $L_{500}E(z)^{-7/3} \lesssim 0.05 \times 10^{44}$ erg s^{-1} is due to the combined effect of low signal and small number of objects. In the companion paper Planck Collaboration (2011h) we explore this low luminosity (mass) range in more depth. The results of these two complementary analysis are summarised and discussed in Sect. 7 (see Fig. 10 and related discussion).

The difference between statistical and bootstrap errors are rendered in more detail in Fig. 3, where relative bootstrap uncertainties (dot-dashed line) are compared to in-bin relative statistical errors (solid line). The figure shows that for

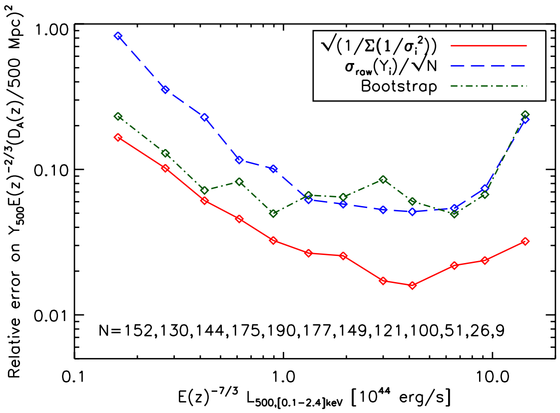

Fig. 3. Bin averaged relative statistical errors (solid line) and relative bootstrap errors (dot-dashed line) are shown as a function of X-ray luminosity. The numbers given in the legend indicate the number of objects in each luminosity bin. For comparison, the scaled unweighted standard deviation (dashed line) is also shown.

$L_{500}E(z)^{-7/3} \lesssim 10^{44}\ \mathrm{erg\,s^{-1}}$ statistical uncertainties are dominant. This implies that intrinsic scatter, which is discussed in more detail in Sect. 5.3, can only be measured at higher luminosity.

Figure 3 also shows the quantity $(1/\sqrt{N})\times(\sigma_{\mathrm{raw}}/Y)$ (dashed line), which is computed from the unweighted raw scatter σ_{raw}, the bin average Y, and the number of clusters in the bin N. The difference between the latter and the relative bootstrap uncertainties in the low luminosity bins is due to the range of relative errors on individual measurements in a given bin.

As a robustness check, we have undertaken the analysis a second time using random cluster positions but keeping all the properties of our sample (sizes, profile shape). The result is shown by the green triangles in the right-hand panel of Fig. 2 and, as expected, is consistent with no detection of the SZ signal. This demonstrative *null test* clearly shows the efficiency of the MMF to pull out the SZ signal from our cluster sample. Additional robustness test are discussed in Sect. 6 below.

5. Results

5.1. The $D^2_\mathrm{A}\ Y_{500} - L_{500}$ and $D^2_\mathrm{A}\ Y_{500} - M_{500}$ relations

The main results of our analysis are summarised in Fig. 4. In the left-hand panel of the figure the individual and luminosity binned *Planck* SZ signal measured at the location of MCXC clusters are shown as a function of luminosity together with the luminosity averaged model predictions. The latter are computed by averaging the model prediction for individual clusters (see Sect. 3) with the same weights as for the measured signal. Notice that SZ signal and X-ray luminosity are intrinsic quantities and are scaled assuming standard evolution. The figure shows the high significance of the SZ signal detection and the excellent agreement between measurements and model predictions. The agreement between *Planck* measurements and X-ray based predictions is rendered in more detail in the right-hand panel of Fig. 4 where the *Planck*-to-model ratio is plotted. Taking into account the total errors given by the bootstrap uncertainties (thin bars in the figure), the agreement is excellent over a wide luminosity range. We model the observed $D^2_\mathrm{A}\ Y_{500} - L_{500}$ relation shown in the left-hand panel of Fig. 4 by adopting a power law of the form

$$Y_{500} = \hat{Y}_{500,L} \left(\frac{E(z)^{-7/3} L_{500}}{10^{44}\ \mathrm{erg\,s^{-1}}}\right)^{\hat{\alpha}_L} E(z)^{\hat{\beta}_L} \left(\frac{D_\mathrm{A}(z)}{500\ \mathrm{Mpc}}\right)^{-2} \quad (7)$$

and directly fitting the individual points shown in the figure rather than the binned data points. We use a non-linear least-squares fit built on a gradient-expansion algorithm (the IDL curvefit function). In the fitting procedure, only the statistical errors given by the MMF are taken into account. The derived uncertainties on the best fitting parameters are quoted in Table 4 as statistical errors. In addition, uncertainties on the best fitting parameters are estimated through the bootstrap procedure described in Sect. 4. Each bootstrap catalogue fit leads to a set of parameters whose standard deviation is quoted as the uncertainty on the best fitting parameters. Values are given for three different choices of priors as given in Table 4, where the best fitting parameters are listed. The table also provides the prediction of our X-ray based model for comparison.

Fixing the slope and the redshift dependence of the $D^2_\mathrm{A}\ Y_{500} - L_{500}$ relation, the best fitting amplitude is $0.451 \times 10^{-3}\ \mathrm{arcmin}^2$, in agreement with the model prediction $0.428 \times 10^{-3}\ \mathrm{arcmin}^2$ at 1.8σ. When keeping the redshift dependence of the relation fixed but leaving the slope of the relation free, we find agreement between best fitting and predicted slopes at better than 1σ, while the amplitudes remain in agreement at 1.3σ. For maximum usefulness and in particular to facilitate precise comparisons with our findings, we provide, in Table 5, the data points shown in the left-hand panel of Fig. 4. Values are given for the quantities $\tilde{L}_{500} = L_{500}E(z)^{-7/3}$ in units of $10^{44}\ \mathrm{erg\,s^{-1}}$ and $\tilde{Y}_{500} = Y_{500}E(z)^{-2/3}\,(D_\mathrm{A}(z)/500\ \mathrm{Mpc})^2$ in units of $10^{-3}\ \mathrm{arcmin}^2$. Both total (i.e., bootstrap) and statistical errors on $\tilde{Y}_{500}$ are also listed.

For completeness, we also investigate the $D^2_\mathrm{A}\ Y_{500} - M_{500}$ relation, where the masses M_{500} are computed from the $L_{500} - M_{500}$ relation given in Eq. (1). Following the same procedure as for the $D^2_\mathrm{A}\ Y_{500} - L_{500}$ relation, we fit individual points of the $D^2_\mathrm{A}\ Y_{500} - M_{500}$ plane with

$$Y_{500} = \hat{Y}_{500,M} \left(\frac{M_{500}}{3 \times 10^{14}\ M_\odot}\right)^{\hat{\alpha}_M} E(z)^{\hat{\beta}_M} \left(\frac{D_\mathrm{A}(z)}{500\ \mathrm{Mpc}}\right)^{-2}. \quad (8)$$

The same cases as for the $D^2_\mathrm{A}\ Y_{500} - L_{500}$ relation are considered and the best fitting parameters are provided in Table 6 along with the model prediction. Concerning the agreement between best fitting parameters and model predictions, the conclusions drawn for the $D^2_\mathrm{A}\ Y_{500} - L_{500}$ relation obviously apply also for the $D^2_\mathrm{A}\ Y_{500} - M_{500}$.

5.2. Redshift evolution

We also considered the case where the redshift evolution of the scaling relations is allowed to differ from the standard expectation. Using the simplest model (Eq. (7) or equivalently Eq. (8)) we attempt to constrain the power law index $\hat{\beta}_\mathrm{L}$ (or equivalently $\hat{\beta}_\mathrm{M}$). We find that the measured SZ signal is consistent with standard evolution (see Table 4) and our constraints on any evolution are weak. Figure 5 shows the measured and predicted, redshift binned, SZ signal, the expected standard redshift evolution, and the best fitting model. The figure shows that, although measurements and predictions agree quite well, the best fitting model is constrained primarily by the low redshift measurements. Possible future improvements are discussed below in Sect. 7.

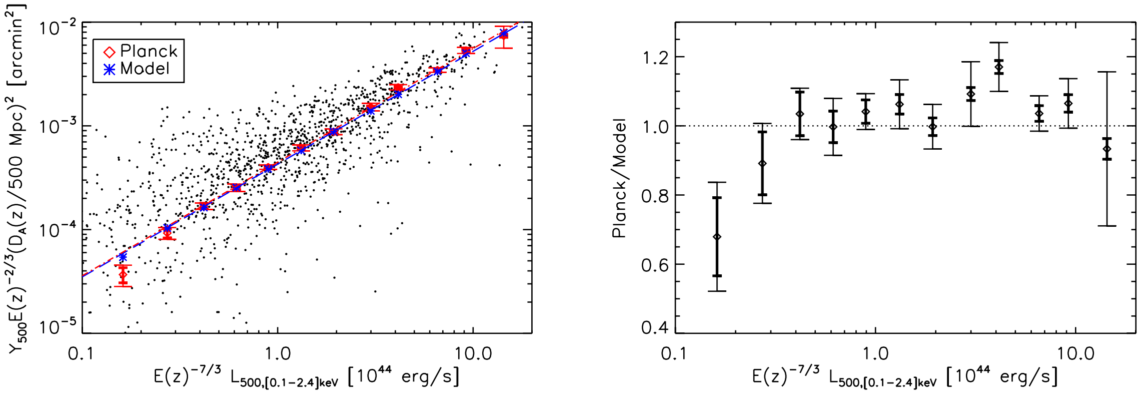

Fig. 4. *Left*: scaling relation between *Planck* SZ measurements and X-ray luminosity for ~1600 MCXC clusters. Individual measurements are shown by the black dots and the corresponding bin averaged values by the red diamonds. Thick bars give the statistical errors, while the thin bars are bootstrap uncertainties. The bin-averaged SZ cluster signal expected from the X-ray based model is shown by the blue stars. The combination of the adopted $D_{\rm A}^2\,Y_{500} - M_{500}$ and $L_{500} - M_{500}$ relations (Eq. (6)) is shown by the dashed blue line while the red dot-dashed line shows the best fitting power-law to the data (Eq. (7) and Table 4). *Right*: ratio between data and model bin averaged values shown in *the left panel*. Error bars are as in *the left panel*.

Table 4. Best fitting parameters for the observed $D_{\rm A}^2\,Y_{500} - L_{500}$ relation given in Eq. (7).

	$\hat{Y}_{500,\rm L}$ [10^{-3} arcmin^2]	$\hat{\alpha}_{\rm L}$	$\hat{\beta}_{\rm L}$
Planck + MCXC	0.451 ± 0.003 stat [±0.013 tot]	1.087 (fixed)	2/3 (fixed)
	0.447 ± 0.006 stat [±0.015 tot]	1.095 ± 0.008 stat [±0.025 tot]	2/3 (fixed)
	0.476 ± 0.006 stat [±0.025 tot]	1.087 (fixed)	−0.007 ± 0.154 stat [±0.518 tot]
X-ray prediction	0.428	1.09	2/3

Notes. Values are given for three different choices of priors and as predicted from X-rays for comparison. Both total errors from bootstrap resampling and statistical errors are quoted.

Table 5. Bin averages of the $D_{\rm A}^2\,Y_{500} - L_{500}$ relation shown in the left panel of Fig. 4.

$\tilde{L}_{500}$ range	Nr. Obj.	$\tilde{L}_{500}$	$\tilde{Y}_{500}$	$\Delta\tilde{Y}_{500}$ statistical	$\Delta\tilde{Y}_{500}$ total
0.100–0.222	152	0.162	0.037	0.006	0.009
0.222–0.331	130	0.272	0.093	0.009	0.012
0.331–0.493	144	0.419	0.169	0.010	0.012
0.493–0.734	175	0.615	0.254	0.012	0.021
0.734–1.094	190	0.894	0.401	0.013	0.020
1.094–1.630	177	1.319	0.616	0.016	0.041
1.630–2.429	149	1.931	0.879	0.022	0.057
2.429–3.620	121	2.997	1.521	0.026	0.130
3.620–5.393	100	4.138	2.356	0.038	0.142
5.393–8.036	51	6.572	3.456	0.076	0.171
8.036–11.973	26	9.196	5.342	0.126	0.359
11.973–17.840	9	14.345	7.369	0.236	1.758

5.3. Scatter in the $D^2{}_{\rm A}\ Y_{500} - L_{500}$ relation

As discussed in Sect. 4.2, we find a clear indication of intrinsic scatter in our measurements of the $D_{\rm A}^2\,Y_{500} - L_{500}$ relation. In this section we quantify this scatter and discuss how our measurement compares with expectations based on the representative REXCESS sample (Arnaud et al. 2010) and the findings reported in the companion paper discussing high quality observations of local clusters (Planck Collaboration 2011g).

The intrinsic scatter $\sigma_{\rm intr}$ is computed in luminosity bins as the quadratic difference between the raw scatter $\sigma_{\rm raw}$ (see Sect. 4.2) and the statistical scatter expected from the statistical uncertainties, i.e. $\sigma^2_{\rm intr} = \sigma^2_{\rm raw} - \sigma^2_{\rm stat}$. The latter is estimated by averaging the statistical uncertainties in a given bin, i.e. $\sigma^2_{\rm stat} = N^{-1}\sum\sigma^2_{\rm i}$, where N is the number of clusters in the bin. For a given luminosity bin, the uncertainty $\Delta\sigma_{\rm intr}$ on the estimated intrinsic scatter are evaluated by $(\Delta\sigma_{\rm intr})^2 = \sigma^2_{\rm intr}(2\,N\,(N-1))^{-1}\sum(1+(\sigma_i^2/\sigma^2_{\rm intr}))^2$.

We find that intrinsic scatter can be measured only for $L_{500}E(z)^{-7/3} \gtrsim 10^{44}$ erg s^{-1}, because the statistical uncertainties at lower luminosities are close to the value of the raw scatter (see also Sect. 4.2). In a given bin with average signal Y, the resulting fractional intrinsic scatter $\sigma_{\rm intr}/Y$ is shown in Fig. 6 along with the fractional raw and statistical scatters. The estimated intrinsic scatter is close to 40−50% and in agreement with the expectations given in Arnaud et al. (2010) ($\sigma_{\log Y_{500}} = 0.184 \pm 0.024$, the range of these values is indicated by the coarse–hatched region in the figure). Notice that the intrinsic scatter reported in Arnaud et al. (2010) is computed for the REXCESS sample and evaluated adopting *XMM-Newton* luminosities and a predicted SZ signal for individual objects based on the same model assumed here but relying on the mass proxy $Y_{\rm X}$. Therefore, the intrinsic scatter quoted in Arnaud et al. (2010) reflects the intrinsic scatter in the underlying $L_{500} - M_{500}$ relation. In Planck Collaboration (2011g), where a sample of clusters detected at high signal to noise in the *Planck* survey (the ESZ sample, see Planck Collaboration 2011d) and with high quality X-ray data from *XMM-Newton* is used, the intrinsic scatter in the $D_{\rm A}^2\,Y_{500} - L_{500}$ relation is found to be $\sigma_{\log Y_{500}} = 0.143 \pm 0.016$. These

Table 6. Best fitting parameters for the observed $D_A^2\,Y_{500} - M_{500}$ relation given in Eq. (8).

	$\hat{Y}_{500,M}$ [10^{-3} arcmin^2]	$\hat{\alpha}_M$	$\hat{\beta}_M$
Planck + MCXC	0.896 ± 0.007 stat [±0.027 tot]	1.783 (fixed)	2/3 (fixed)
	0.892 ± 0.008 stat [±0.025 tot]	1.796 ± 0.014 stat [±0.042 tot]	2/3 (fixed)
	0.945 ± 0.012 stat [±0.049 tot]	1.783 (fixed)	−0.007 ± 0.154 stat [±0.518 tot]
X-ray prediction	0.850	1.783	2/3

Notes. Values are given for three different choices of priors and as predicted from X-rays for comparison. Both total errors from bootstrap resampling and statistical errors are quoted.

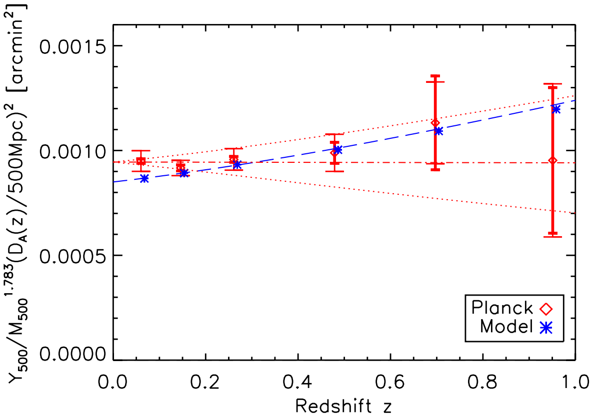

Fig. 5. Bin averaged SZ signal from a sphere of radius R_{500} (Y_{500}) scaled by the expected mass and angular distance dependence as a function of redshift. The *Planck* data (red diamonds) and the SZ cluster signal expected from the X-ray based model (blue stars) are shown together with the expected standard redshift evolution (dahed line). The best fitting model is shown by the dot-dashed line and the 1σ confidence region is limited by the dotted lines. Here M_{500} is given in units of $3 \times 10^{14}\ M_\odot$.

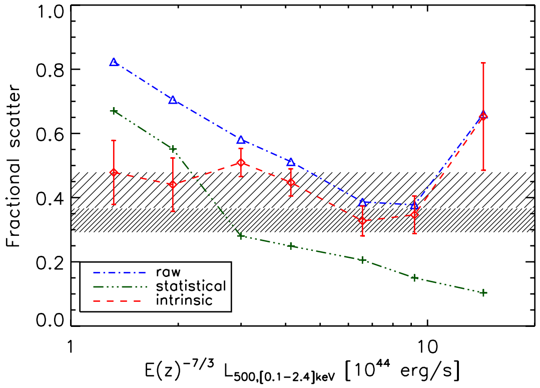

Fig. 6. Fractional raw (dot-dashed blue line and triangles), statistical (dot-dot-dashed green line and plus signs), and intrinsic (dashed red line, diamonds, and error bars) scatter on the $D_A^2\,Y_{500} - L_{500}$ relation. The coarse/fine-hatched regions corresponds to the 1 σ uncertainties on the intrinsic scatter reported in Arnaud et al. (2010) and Planck Collaboration (2011g), respectively.

values are shown in Fig. 6 by the fine–hatched region. In Planck Collaboration (2011g) it is found that cool core clusters are responsible for the vast majority of the scatter around the relation. Because the sample used in this study is X-ray selected, we expect it to contain a higher fraction of cool core systems than in the ESZ subsample studied in Planck Collaboration (2011g). This implies that the scatter in the $D_A^2\,Y_{500} - L_{500}$ relation measured in our sample is expected to be higher than the one found in Planck Collaboration (2011g), as observed. Given the segregation of cool core systems in the $D_A^2\,Y_{500} - L_{500}$ reported in Planck Collaboration (2011g), we investigate the link between the intrinsic scatter in the relation and cluster dynamical state using our large X-ray sample. To this end we compare *Planck* measurements and the X-ray based predictions (i.e., Eq. (6)) for individual objects. In Fig. 7 we show the difference between *Planck* measurement and the X-ray based prediction in units of the measurement statistical error σ_i (see Sect. 4) as a function of X-ray luminosity and investigate the largest outliers the figure, i.e. the most statistically significant outliers in the $D_A^2\,Y_{500} - L_{500}$ relation.

Given the size of our sample we discuss individually only clusters for which measurement and prediction differ by more than $5\sigma_i$. These are identified and information on their dynamical state is searched for in the literature. Information is based on the classification of Hudson et al. (2010) if not stated otherwise. We find 15 clusters with a predicted signal smaller than the *Planck* measurement by more than $5\sigma_i$. Of these, six are known merging clusters: Coma, A2218 (Govoni et al. 2004), 1ES0657, A754 (Govoni et al. 2004), A2163 (Bourdin et al. 2011), A0697 (Girardi et al. 2006), six are classified as non-cool core clusters and may therefore be unrelaxed: A2219 (Allen & Fabian 1998), A2256, A2255, A0209 (Zhang et al. 2008), A2813 (Zhang et al. 2008), A3404 (Pratt et al. 2009), and A3266 is a weak cool core cluster. No information is available for the remaining clusters: A1132 and A3186. Conversely, there are 11 over-predicted clusters at $5\sigma_i$. Of these five are strong cool core clusters: 2A0335, Zw1021.0+0426 (Morandi et al. 2007), A3112, HerA (Bauer et al. 2005), and A0780. No information is available for the remaining clusters: A689, ACOS1111, A3392, J1253.6-3931, J1958.2-3011, and RXCJ0643.4+4214. Notice that the luminosity of A689 is likely to be overestimated by a large factor because of point source contamination (Maughan 2008). In addition, for A3186 and ACOS1111 the model prediction rely on the EMSS luminosity measurements given in Gioia & Luppino (1994), which might be unreliable.

The high fraction of dynamically perturbed / cool-core clusters with largely under/over predicted SZ signal is confirmed when additional outliers at smaller σ_i are searched. We find 65 clusters with (Y_{500} Planck − Y_{500} Model) $> 3\,\sigma_i$ and that for 46 percent of them dynamical state information is available in the literature. Of the latter 26 (87 percent) are either known mergers or non-cool core clusters, two are weak cool core clusters, and only one is classified as cool core cluster. We find 53 clusters with (Y_{500} Planck − Y_{500} Model) $< -3\sigma_i$. For 45 percent of these clusters we are able to find information on their

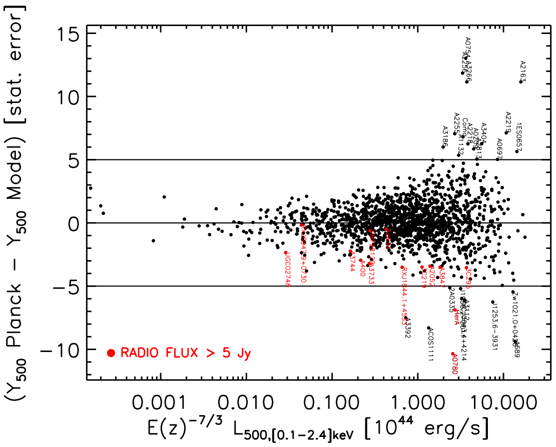

Fig. 7. Difference between the *Planck* measurement and the X-ray based prediction in units of the measurement statistical error $\sigma_{\rm i}$ (pure measurement uncertainties based on MMF noise estimates) as a function of X-ray luminosity. Labelled black points denote objects with a difference larger than $5\sigma_{\rm i}$ and are further discussed in the text. Clusters with SZ signal possibly contaminated by radio sources (see discussion in Sect. 6) are shown in red and labelled by their name.

dynamical state in the literature and find that 96 percent of them are cool core clusters. These findings clearly suggest that the intrinsic scatter in the $D_{\rm A}^2\, Y_{500} - L_{500}$ relation is linked to the cluster dynamical state, as also found in Planck Collaboration (2011g).

6. Robustness of the results

As in the other four *Planck* SZ papers (Planck Collaboration 2011d,e,g,h), we test the robustness of our results for the effect of several instrumental, modelling, and astrophysical uncertainties. Tests common to all *Planck* SZ papers are discussed in detail in Sect. 6 of Planck Collaboration (2011d). Of these, calibration and colour correction effects are relevant for our analysis. Calibration uncertainties are shown to propagate into very small uncertainties on SZ signal measurements (~2%) and colour correction is found to be a ~3% effect for *Planck* bands.

In the following we report on robustness tests aimed at completing this investigation. We show that our results are robust with respect to the instrumental uncertainties, that they are insensitive to the finest details of our cluster modelling, and that they are unaffected by radio source contamination. We show that restricting the analysis to the reference homogeneous subsample of NORAS/REFLEX clusters leads to measurements fully compatible with those we obtain for the whole sample.

6.1. Beam effects

The beam effects studied in Planck Collaboration (2011d) are further scrutinised by directly estimating their impact on our results. To this end, the whole analysis is redone by assuming different beam FWHM. For simplicity, we systematically increase/decrease the adopted beam FWHM for all channels simultaneously by adding/removing the conservative uncertainties given in Table 1 from the fiducial beam FWHM values. We find that the binned SZ signal varies by at most 2% from the value computed using the fiducial beams FWHM.

6.2. Modelling

The effects of changes in the underlying X-ray based model on our results are investigated by repeating the full analysis as for the *fiducial case*, but by assuming the standard slope of the $M_{500} - Y_{\rm X}$ relation and/or the intrinsic $L_{500} - M_{500}$ relation (see Sect. 3). For simplicity, in the following we discuss results obtained by varying only one assumption at a time. We find that the effect resulting by varying both assumptions is equivalent to the sum of the effects obtained by varying the two assumptions separately.

As expected from the weak dependence of cluster size R_{500} on luminosity, the measured SZ signal is barely affected by these changes. If the standard slope case is adopted instead of the empirical one, the bin averaged SZ signal changes by less than a few percent at all luminosities and the same is found when the intrinsic $L_{500} - M_{500}$ relation is adopted. The model predictions are of course more affected by changes in the assumed scaling relations. In Fig. 8 we contrast the *Planck* -to-model ratio obtained for the different cases. The figure shows that the assumption on the slope of the $M_{500} - Y_{\rm X}$ relation has a fully negligible impact. On the other hand it shows that the intrinsic $L_{500} - M_{500}$ relation is not compatible with our measurements ($>5\sigma$ discrepancy). This finding is not surprising given the fact that when adopting the intrinsic $L_{500} - M_{500}$ relation one assumes that selection effects of our X-ray sample are negligible. Notice that the WMAP-5 yr data used in the similar analysis by Melin et al. (2011) did not have sufficient depth to come to this conclusion. Furthermore, the agreement of our results for the REXCESS and intrinsic $L_{500} - M_{500}$ relations at high luminosity confirms that Malmquist bias is small for very luminous objects.

6.3. Intrinsic dispersion in the $L_{500} - M_{500}$ relation

The intrinsic dispersion in the $L_{500} - M_{500}$ relation dominates the uncertainty on the clusters' size R_{500} in our analysis. We investigate how this propagates into the uncertainties on the binned SZ signal by means of a Monte Carlo (MC) analysis of 100 realisations. We use the dispersion given in Table 2 and, for each realisation, we draw a random mass $\log M_{500}$ for each cluster from a Gaussian distribution with mean given by the $L_{500} - M_{500}$ relation and standard deviation $\sigma_{\log L - \log M}/\alpha_M$. For each realisation, we extract the signal with the new values of M_{500} (thus R_{500}). The standard deviation of the SZ signal for the 100 MC realisations in a given luminosity bin is found to be at most ~3% of the signal. Hence, given the size of the total errors on the binned SZ signal (see Fig. 3) our conclusions are fully unaffected by this effect.

6.4. Pressure profile

Furthermore, we investigate how the uncertainties on the assumed pressure profile propagates into the uncertainties on the binned SZ signal. For simplicity, we only quantify the largest possible effect by redoing the analysis but adopting the pressure profile parameters for the cool-core and morphologically disturbed subsamples given in Table 3, i.e. we assume that all clusters in the sample are cool-core or morphologically disturbed. Both of the two resulting sets of binned SZ signal deviate from the one derived assuming the universal pressure profile by approximatively 8% in the lowest luminosity bin and decrease linearly with increasing $\log L_{500}$, becoming approximatively 1% in the highest luminosity bin. Furthermore the normalisation of Eq. (4) changes by less than 3% if the average pressure profiles

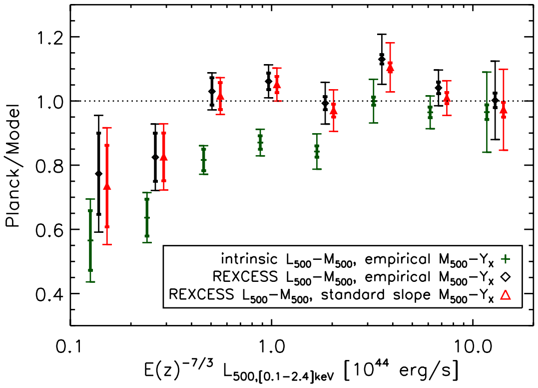

Fig. 8. Ratio of binned *Planck* data points to model for different model assumptions. The *fiducial model* (black diamonds) is shown together with results obtained by varying the underlying $L_{500} - M_{500}$ relation from REXCESS to intrinsic (green plus signs), and by varying the slope of the underlying $M_{500} - Y_{\rm X}$ relation from empirical to standard (red triangles). Thick bars give the statistical errors, while the thin bars are bootstrap uncertainties.

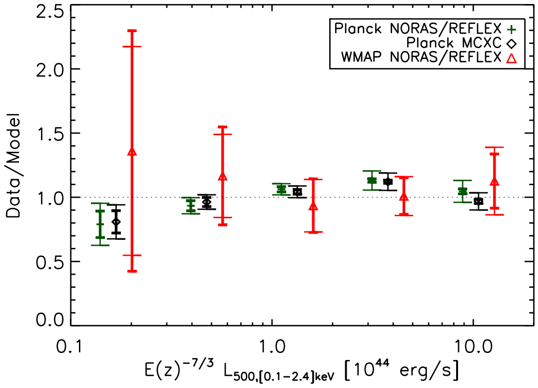

Fig. 9. Data-to-model ratio for *Planck* results for the full sample (black diamonds) and the NORAS/REFLEX control sample (green plus signs). The WMAP-5 yr results for the NORAS/REFLEX by Melin et al. (2011) are shown by the red triangles. Error bars are as in Fig. 4.

parameters of cool-core and morphologically disturbed clusters given in Table 3 are adopted instead of the ones for the average profile, implying that our SZ signal predictions are robust. Considering the total errors and their trend with luminosity, we conclude that our findings are fully unaffected by the exact shape of the SZ template.

6.5. X-ray sample

Because of the reasons detailed in Sect. 2.2, we also repeated our analysis by considering the NORAS/REFLEX *control sample* and find results fully consistent with those derived for the full sample. The results are shown in terms of *Planck* -to-model ratio in Fig. 9. Notice that in this case the luminosity binning is chosen so as to be comparable with that in the WMAP-5 yr analysis of Melin et al. (2011). The comparison between WMAP-5 yr and *Planck* results is discussed in Sect. 7 below.

6.6. Radio contamination

In addition we investigated the effect of contamination by radio sources on our results. Most radio sources are expected to have a steep spectrum and hence they should not have significant fluxes at *Planck* frequencies. However, some sources will show up in *Planck* LFI and HFI channels if their radio flux is sufficiently high and/or their spectral index is near zero or positive. Extreme examples are the Virgo and Perseus clusters that host in their interior two of the brightest radio sources in the sky. In the ESZ sample (Planck Collaboration 2011d) there are also a few examples of clusters with moderate radio sources in their vicinity (1 Jy or less in NVSS) and still significant signal at LFI (and even HFI) frequencies. To check for possible contamination we combine data from SUMSS (a catalog of radio sources at 0.85 GHz, Bock et al. 1999) and NVSS (a catalog of radio sources at 1.4 GHz, Condon et al. 1998). We have looked at the positions of the clusters in our sample and searched for radio sources in a radius of 5 arcmin from the cluster centre. We find that 74 clusters have a radio source within this search radius in NVSS or SUMSS with a flux above 1 Jy. Among these, eight have fluxes larger than 10 Jy, two sources larger than 100 Jy and one is an extreme radio source with a flux larger than 1 KJy.

As a robustness test, we investigate the impact of contamination by radio sources on our results by excluding clusters hosting radio sources with fluxes larger than 1 or 5 Jy and comparing the results to those obtained for the full sample. Interestingly we find that, as expected, the individual SZ signal is on average lower than the X-ray based predictions in clusters that are likely to be highly contaminated. This is shown in Fig. 7 where clusters associated with radio sources with fluxes larger than 5 Jy are shown by the red symbols. However, given the very low fraction of possibly contaminated clusters, we find that bin averaged signal is fully unaffected when these are excluded from the analysis.

7. Discussion and conclusions

As part of a series of papers on *Planck* early results on clusters of galaxies (Planck Collaboration 2011d,e,f,g,h), we measured the SZ signal in the direction of ∼1600 objects from the MCXC (Meta-Catalogue of X-ray detected Clusters of galaxies, Piffaretti et al. 2011, see Sect. 2.2) in *Planck* whole sky data (see Sect. 2.1) and studied the relationship between X-ray luminosity and SZ signal strength.

For each X-ray cluster in the sample the amplitude of the SZ signal is fitted by fixing the cluster position and size to the X-ray values and assuming a template derived from the universal pressure profile of Arnaud et al. (2010). The universal pressure profile was derived from high quality data from REXCESS. Recently, Sun et al. (2010) found that the universal pressure profile also yields an excellent description of systems with lower luminosities than those probed with REXCESS. This implies that the adopted SZ template is suitable for the entire luminosity range explored in our work.

The *intrinsic* SZ signal $D_{\rm A}^2 Y_{500}$ is averaged in X-ray luminosity bins to maximise the statistical significance. The signal is detected at high significance over the X-ray luminosity range 10^{43} erg s^{-1} $\lesssim L_{500}E(z)^{-7/3} \lesssim 10^{45}$ erg s^{-1} (see Fig. 2).

We find excellent agreement between observations and predictions based on X-ray data, as shown in Fig. 4. Our results do not agree with the claim, based on a recent WMAP-7 yr data analysis, that X-ray data over-predict the SZ signal (Komatsu et al. 2011). Due to the large size and homogeneous nature of the MCXC, and the exceptional internal consistency of our cluster model, we believe that our results are very robust. Moreover, as reported in Sect. 6, we show that our findings are insensitive to the details of our cluster modelling. Furthermore, we have shown that our results are robust against instrumental (calibration, colour correction, beam) and astrophysical (radio contamination) uncertainties.

Our results confirm to a higher significance the results of the analysis by Melin et al. (2011) based on WMAP-5 yr data. This is shown in Fig. 9 where the data-to-model ratio as a function of luminosity is presented. Luminosity bins are chosen so as to be comparable to those of Melin et al. (2011), and the *Planck* results are presented for the whole sample used in this work and also for the NORAS/REFLEX sample adopted in Melin et al. (2011). In addition to the good agreement between results from the two data sets, the figure shows that in the WMAP-5 yr study by Melin et al. (2011) statistical uncertainties are dominant. As shown in Sect. 4.2, *Planck* data allows us to overcome this limitation and to investigate the intrinsic scatter in the scaling relation between intrinsic SZ signal $D_\mathrm{A}^2\,Y_{500}$ and X-ray luminosity L_{500} (see Sect. 5.3). We find a $\sim$40% intrinsic scatter in the $D_\mathrm{A}^2\,Y_{500} - L_{500}$ relation and show that it is linked to cluster dynamical state.

The agreement between luminosity binned X-ray predictions and *Planck* measurements is reflected in the excellent accord between predicted scaling relation and best fitting power law model to the $D_\mathrm{A}^2\,Y_{500} - L_{500}$ relation. The power law fit, which is performed on individual data points, is compared by Planck Collaboration (2011g) to the *calibration* derived from a sample of galaxy clusters detected at high signal to noise in the *Planck* survey (the ESZ sample, see Planck Collaboration 2011d) and with high quality X-ray data from *XMM-Newton*. As discussed in Planck Collaboration (2011g) the slight differences between the two best fitting relations reflect the difference between the selection of the adopted samples. Indeed, the X-ray sample used in the present work is X-ray selected and therefore biased towards the cool core systems, while the sample used in Planck Collaboration (2011g) is SZ selected.

As mentioned in Sect. 4.2, the luminosity range where we are not able to detect the SZ signal because of the small number of low mass objects (see Fig. 2), is explored in Planck Collaboration (2011h). In the latter analysis we use the optical catalogue of $\sim$14 000 MaxBCG clusters (Koester et al. 2007) and, in a fully similar way as done in this work, extract the optical richness binned SZ signal from *Planck* data. By combining these results with the X-ray luminosity of the MaxBCG clusters measured by Rykoff et al. (2008) by stacking RASS data, in Planck Collaboration (2011h) we derive the $D_\mathrm{A}^2\,Y_{500} - L_{500}$ relation for the MaxBCG sample. This result is shown together with the one derived in the present paper in Fig. 10. The X-ray luminosity histograms shown in the top panel of the figure highlight the complementarity of the two analyses. The bottom panel of the figure shows agreement between the results from the two data sets and, very importantly, that observations and predictions based on X-ray data agree over a very wide range in X-ray luminosity.

We investigate the evolution of the scaling relation and find it to be consistent with standard evolution. Although redshift binned measurements and predictions agree quite well over a wide redshift range (see Fig. 5), our constraints are weak because the inferred best fitting model is almost completely constrained by only the low redshift measurements. Given the relevance of SZ-selected samples for cosmological studies and the need for complementary X-ray observations for such studies (see Planck Collaboration 2011e, and discussion therein), improved understanding of the evolution of SZ-X-ray scaling relations is clearly desired. High quality data similar to those used in Planck Collaboration (2011g), but for higher redshift clusters will provide tight constrains on evolution, in particular when newly SZ discovered clusters (see Planck Collaboration 2011d, and references therein) with high quality X-ray and optical data are included.

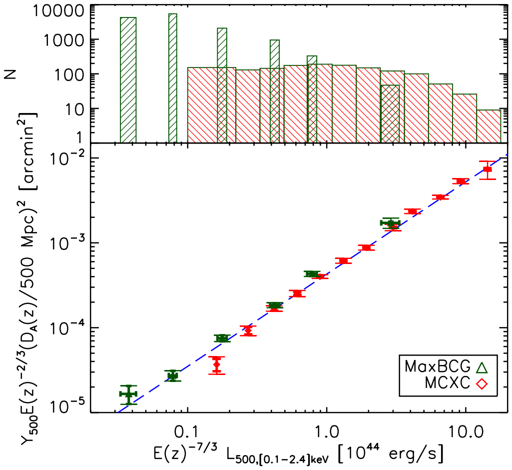

Fig. 10. *Bottom panel*: comparison between our results (red diamonds, as in left-hand panel Fig. 4) and those obtained by Planck Collaboration (2011h) (green triangles), where MaxBCG clusters are investigated. X-ray luminosities and associated error bars for the MaxBCG clusters are based on the analysis of Rykoff et al. (2008). Vertical error bars are as in Fig. 4 and the X-ray prediction (i.e., Eq. (6)) is shown by the dashed blue line. *Top panel*: X-ray luminosity histograms of the MCXC (red) and MaxBCG (green) samples. For the MCXC the width of the bars is equal to the luminosity bin width, while for the MaxBCG we adopt the horizontal error bar shown in *the bottom panel*.

Acknowledgements. This research has made use of the X-Rays Clusters Database (BAX) which is operated by the Laboratoire d'Astrophysique de Tarbes-Toulouse (LATT), under contract with the Centre National d'Etudes Spatiales (CNES). We acknowledge the use of the HEALPix package (Górski et al. 2005). The Planck Collaboration acknowledges the support of: ESA; CNES and CNRS/INSU-IN2P3-INP (France); ASI, CNR, and INAF (Italy); NASA and DoE (USA); STFC and UKSA (UK); CSIC, MICINN and JA (Spain); Tekes, AoF and CSC (Finland); DLR and MPG (Germany); CSA (Canada); DTU Space (Denmark); SER/SSO (Switzerland); RCN (Norway); SFI (Ireland); FCT/MCTES (Portugal); and DEISA (EU). A description of the Planck Collaboration and a list of its members, indicating which technical or scientific activities they have been involved in, can be found at `http://www.rssd.esa.int/Planck`.

References

Afshordi, N., Lin, Y., Nagai, D., & Sanderson, A. J. R. 2007, MNRAS, 378, 293
Allen, S. W., & Fabian, A. C. 1998, MNRAS, 297, L57
Andersson, K., Benson, B. A., Ade, P. A. R., et al. 2011, ApJ, 738, 48
Arnaud, M., Pratt, G. W., Piffaretti, R., et al. 2010, A&A, 517, A92
Atrio-Barandela, F., Kashlinsky, A., Kocevski, D., & Ebeling, H. 2008, ApJ, 675, L57
Bauer, F. E., Fabian, A. C., Sanders, J. S., Allen, S. W., & Johnstone, R. M. 2005, MNRAS, 359, 1481
Bersanelli, M., Mandolesi, N., Butler, R. C., et al. 2010, A&A, 520, A4
Bielby, R. M., & Shanks, T. 2007, MNRAS, 382, 1196
Birkinshaw, M. 1999, Phys. Rep., 310, 97
Bock, D., Large, M. I., & Sadler, E. M. 1999, AJ, 117, 1578
Böhringer, H., Voges, W., Huchra, J. P., et al. 2000, ApJS, 129, 435
Böhringer, H., Schuecker, P., Guzzo, L., et al. 2004, A&A, 425, 367
Böhringer, H., Schuecker, P., Pratt, G. W., et al. 2007, A&A, 469, 363

Bourdin, H., Arnaud, M., Mazzotta, P., et al. 2011, A&A, 527, A21
Burenin, R. A., Vikhlinin, A., Hornstrup, A., et al. 2007, ApJS, 172, 561
Burke, D. J., Collins, C. A., Sharples, R. M., Romer, A. K., & Nichol, R. C. 2003, MNRAS, 341, 1093
Carlstrom, J. E., Ade, P. A. R., Aird, K. A., et al. 2011, PASP, 123, 568
Condon, J. J., Cotton, W. D., Greisen, E. W., et al. 1998, AJ, 115, 1693
Cruddace, R., Voges, W., Böhringer, H., et al. 2002, ApJS, 140, 239
Diego, J. M., & Partridge, B. 2010, MNRAS, 402, 1179
Ebeling, H., Edge, A. C., Bohringer, H., et al. 1998, MNRAS, 301, 881
Ebeling, H., Edge, A. C., Allen, S. W., et al. 2000, MNRAS, 318, 333
Ebeling, H., Mullis, C. R., & Tully, R. B. 2002, ApJ, 580, 774
Ebeling, H., Barrett, E., Donovan, D., et al. 2007, ApJ, 661, L33
Ebeling, H., Edge, A. C., Mantz, A., et al. 2010, MNRAS, 407, 83
Fowler, J. W., Niemack, M. D., Dicker, S. R., et al. 2007, Appl. Opt., 46, 3444
Gioia, I. M., & Luppino, G. A. 1994, ApJS, 94, 583
Girardi, M., Boschin, W., & Barrena, R. 2006, A&A, 455, 45
Górski, K. M., Hivon, E., Banday, A. J., et al. 2005, ApJ, 622, 759
Govoni, F., Markevitch, M., Vikhlinin, A., et al. 2004, ApJ, 605, 695
Henry, J. P. 2004, ApJ, 609, 603
Henry, J. P., Mullis, C. R., Voges, W., et al. 2006, ApJS, 162, 304
Herranz, D., Sanz, J. L., Hobson, M. P., et al. 2002, MNRAS, 336, 1057
Horner, D. J., Perlman, E. S., Ebeling, H., et al. 2008, ApJS, 176, 374
Hudson, D. S., Mittal, R., Reiprich, T. H., et al. 2010, A&A, 513, A37
Johnston, D. E., Sheldon, E. S., Tasitsiomi, A., et al. 2007, ApJ, 656, 27
Kocevski, D. D., Ebeling, H., Mullis, C. R., & Tully, R. B. 2007, ApJ, 662, 224
Koester, B. P., McKay, T. A., Annis, J., et al. 2007, ApJ, 660, 239
Komatsu, E., Smith, K. M., Dunkley, J., et al. 2011, ApJS, 192, 18
Kravtsov, A. V., Vikhlinin, A., & Nagai, D. 2006, ApJ, 650, 128
Lamarre, J., Puget, J., Ade, P. A. R., et al. 2010, A&A, 520, A9
Leahy, J. P., Bersanelli, M., D'Arcangelo, O., et al. 2010, A&A, 520, A8
Lieu, R., Mittaz, J. P. D., & Zhang, S. 2006, ApJ, 648, 176
Mandolesi, N., Bersanelli, M., Butler, R. C., et al. 2010, A&A, 520, A3
Maughan, B. 2008, in Chandra Proposal, 2653
Melin, J., Bartlett, J. G., & Delabrouille, J. 2006, A&A, 459, 341
Melin, J., Bartlett, J. G., Delabrouille, J., et al. 2011, A&A, 525, A139
Mennella, A., Butler, R. C., Curto, A., et al. 2011, A&A, 536, A3
Morandi, A., Ettori, S., & Moscardini, L. 2007, MNRAS, 379, 518
Mullis, C. R., McNamara, B. R., Quintana, H., et al. 2003, ApJ, 594, 154
Perlman, E. S., Horner, D. J., Jones, L. R., et al. 2002, ApJS, 140, 265
Piffaretti, R., Arnaud, M., Pratt, G. W., Pointecouteau, E., & Melin, J. 2011, A&A, 534, A109
Planck Collaboration 2011a, A&A, 536, A1
Planck Collaboration 2011b, A&A, 536, A2
Planck Collaboration 2011c, A&A, 536, A7
Planck Collaboration 2011d, A&A, 536, A8
Planck Collaboration 2011e, A&A, 536, A9
Planck Collaboration 2011f, A&A, 536, A10
Planck Collaboration 2011g, A&A, 536, A11
Planck Collaboration 2011h, A&A, 536, A12
Planck Collaboration 2011i, A&A, 536, A13
Planck Collaboration 2011j, A&A, 536, A14
Planck Collaboration 2011k, A&A, 536, A15
Planck Collaboration 2011l, A&A, 536, A16
Planck Collaboration 2011m, A&A, 536, A17
Planck Collaboration 2011n, A&A, 536, A18
Planck Collaboration 2011o, A&A, 536, A19
Planck Collaboration 2011p, A&A, 536, A20
Planck Collaboration 2011q, A&A, 536, A21
Planck Collaboration 2011r, A&A, 536, A22
Planck Collaboration 2011s, A&A, 536, A23
Planck Collaboration 2011t, A&A, 536, A24
Planck Collaboration 2011u, A&A, 536, A25
Planck Collaboration 2011v, The Explanatory Supplement to the Planck Early Release Compact Source Catalogue (ESA)
Planck Collaboration 2011w, A&A, 536, A26
Planck HFI Core Team 2011a, A&A, 536, A4
Planck HFI Core Team 2011b, A&A, 536, A6
Pratt, G. W., Croston, J. H., Arnaud, M., & Böhringer, H. 2009, A&A, 498, 361
Romer, A. K., Nichol, R. C., Holden, B. P., et al. 2000, ApJS, 126, 209
Rosset, C., Tristram, M., Ponthieu, N., et al. 2010, A&A, 520, A13
Rozo, E., Rykoff, E. S., Evrard, A., et al. 2009, ApJ, 699, 768
Rykoff, E. S., Evrard, A. E., McKay, T. A., et al. 2008, MNRAS, 387, L28
Sun, M., Sehgal, N., Voit, G. M., et al. 2011, ApJ, 727, L49
Sunyaev, R. A., & Zeldovich, Y. B. 1970, Comments Astrophys. Space Phys., 2, 66
Sunyaev, R. A., & Zeldovich, Y. B. 1972, Comments Astrophys. Space Phys., 4, 173
Tauber, J. A., Mandolesi, N., Puget, J., et al. 2010, A&A, 520, A1
Zacchei, A., Maino, D., Baccigalupi, C., et al. 2011, A&A, 536, A5
Zhang, Y., Finoguenov, A., Böhringer, H., et al. 2008, A&A, 482, 451

---

[1] Aalto University Metsähovi Radio Observatory, Metsähovintie 114, 02540 Kylmälä, Finland
[2] Agenzia Spaziale Italiana Science Data Center, c/o ESRIN, via Galileo Galilei, Frascati, Italy
[3] Astroparticule et Cosmologie, CNRS (UMR7164), Université Denis Diderot Paris 7, Bâtiment Condorcet, 10 rue A. Domon et Léonie Duquet, Paris, France
[4] Astrophysics Group, Cavendish Laboratory, University of Cambridge, J J Thomson Avenue, Cambridge CB3 0HE, UK
[5] Atacama Large Millimeter/submillimeter Array, ALMA Santiago Central Offices, Alonso de Cordova 3107, Vitacura, Casilla 763 0355, Santiago, Chile
[6] CITA, University of Toronto, 60 St. George St., Toronto, ON M5S 3H8, Canada
[7] CNRS, IRAP, 9 Av. colonel Roche, BP 44346, 31028 Toulouse Cedex 4, France
[8] California Institute of Technology, Pasadena, California, USA
[9] Centre of Mathematics for Applications, University of Oslo, Blindern, Oslo, Norway
[10] Centro de Astrofísica, Universidade do Porto, Rua das Estrelas, 4150-762 Porto, Portugal
[11] DAMTP, University of Cambridge, Centre for Mathematical Sciences, Wilberforce Road, Cambridge CB3 0WA, UK
[12] DSM/Irfu/SPP, CEA-Saclay, 91191 Gif-sur-Yvette Cedex, France
[13] DTU Space, National Space Institute, Juliane Mariesvej 30, Copenhagen, Denmark
[14] Departamento de Física, Universidad de Oviedo, Avda. Calvo Sotelo s/n, Oviedo, Spain
[15] Department of Astronomy and Astrophysics, University of Toronto, 50 Saint George Street, Toronto, Ontario, Canada
[16] Department of Physics & Astronomy, University of British Columbia, 6224 Agricultural Road, Vancouver, British Columbia, Canada
[17] Department of Physics and Astronomy, University of Southern California, Los Angeles, California, USA
[18] Department of Physics, Gustaf Hällströmin katu 2a, University of Helsinki, Helsinki, Finland
[19] Department of Physics, Princeton University, Princeton, New Jersey, USA
[20] Department of Physics, Purdue University, 525 Northwestern Avenue, West Lafayette, Indiana, USA
[21] Department of Physics, University of California, Berkeley, California, USA
[22] Department of Physics, University of California, One Shields Avenue, Davis, California, USA
[23] Department of Physics, University of California, Santa Barbara, California, USA
[24] Department of Physics, University of Illinois at Urbana-Champaign, 1110 West Green Street, Urbana, Illinois, USA
[25] Dipartimento di Fisica G. Galilei, Università degli Studi di Padova, via Marzolo 8, 35131 Padova, Italy
[26] Dipartimento di Fisica, Università La Sapienza, P. le A. Moro 2, Roma, Italy
[27] Dipartimento di Fisica, Università degli Studi di Milano, via Celoria 16, Milano, Italy
[28] Dipartimento di Fisica, Università degli Studi di Trieste, via A. Valerio 2, Trieste, Italy
[29] Dipartimento di Fisica, Università di Ferrara, via Saragat 1, 44122 Ferrara, Italy
[30] Dipartimento di Fisica, Università di Roma Tor Vergata, via della Ricerca Scientifica 1, Roma, Italy
[31] Discovery Center, Niels Bohr Institute, Blegdamsvej 17, Copenhagen, Denmark
[32] Dpto. Astrofísica, Universidad de La Laguna (ULL), 38206 La Laguna, Tenerife, Spain
[33] European Southern Observatory, ESO Vitacura, Alonso de Cordova 3107, Vitacura, Casilla 19001, Santiago, Chile

[34] European Space Agency, ESAC, Planck Science Office, Camino bajo del Castillo, s/n, Urbanización Villafranca del Castillo, Villanueva de la Cañada, Madrid, Spain
[35] European Space Agency, ESTEC, Keplerlaan 1, 2201 AZ Noordwijk, The Netherlands
[36] Helsinki Institute of Physics, Gustaf Hällströmin katu 2, University of Helsinki, Helsinki, Finland
[37] INAF – Osservatorio Astronomico di Padova, Vicolo dell'Osservatorio 5, Padova, Italy
[38] INAF – Osservatorio Astronomico di Roma, via di Frascati 33, Monte Porzio Catone, Italy
[39] INAF – Osservatorio Astronomico di Trieste, via G.B. Tiepolo 11, Trieste, Italy
[40] INAF/IASF Bologna, via Gobetti 101, Bologna, Italy
[41] INAF/IASF Milano, via E. Bassini 15, Milano, Italy
[42] INRIA, Laboratoire de Recherche en Informatique, Université Paris-Sud 11, Bâtiment 490, 91405 Orsay Cedex, France
[43] IPAG: Institut de Planétologie et d'Astrophysique de Grenoble, Université Joseph Fourier, Grenoble 1 / CNRS-INSU, UMR 5274, Grenoble, 38041, France
[44] Imperial College London, Astrophysics group, Blackett Laboratory, Prince Consort Road, London, SW7 2AZ, UK
[45] Infrared Processing and Analysis Center, California Institute of Technology, Pasadena, CA 91125, USA
[46] Institut Néel, CNRS, Université Joseph Fourier Grenoble I, 25 rue des Martyrs, Grenoble, France
[47] Institut d'Astrophysique Spatiale, CNRS (UMR8617) Université Paris-Sud 11, Bâtiment 121, Orsay, France
[48] Institut d'Astrophysique de Paris, CNRS UMR7095, Université Pierre & Marie Curie, 98 bis boulevard Arago, Paris, France
[49] Institute of Astronomy and Astrophysics, Academia Sinica, Taipei, Taiwan
[50] Institute of Astronomy, University of Cambridge, Madingley Road, Cambridge CB3 0HA, UK
[51] Institute of Theoretical Astrophysics, University of Oslo, Blindern, Oslo, Norway
[52] Instituto de Astrofísica de Canarias, C/Vía Láctea s/n, La Laguna, Tenerife, Spain
[53] Instituto de Física de Cantabria (CSIC-Universidad de Cantabria), Avda. de los Castros s/n, Santander, Spain
[54] Jet Propulsion Laboratory, California Institute of Technology, 4800 Oak Grove Drive, Pasadena, California, USA
[55] Jodrell Bank Centre for Astrophysics, Alan Turing Building, School of Physics and Astronomy, The University of Manchester, Oxford Road, Manchester, M13 9PL, UK
[56] Kavli Institute for Cosmology Cambridge, Madingley Road, Cambridge, CB3 0HA, UK
[57] LERMA, CNRS, Observatoire de Paris, 61 Avenue de l'Observatoire, Paris, France
[58] Laboratoire AIM, IRFU/Service d'Astrophysique – CEA/DSM – CNRS – Université Paris Diderot, Bât. 709, CEA-Saclay, 91191 Gif-sur-Yvette Cedex, France
[59] Laboratoire Traitement et Communication de l'Information, CNRS (UMR 5141) and Télécom ParisTech, 46 rue Barrault, 75634 Paris Cedex 13, France
[60] Laboratoire de Physique Subatomique et de Cosmologie, CNRS/IN2P3, Université Joseph Fourier Grenoble I, Institut National Polytechnique de Grenoble, 53 rue des Martyrs, 38026 Grenoble Cedex, France
[61] Laboratoire de l'Accélérateur Linéaire, Université Paris-Sud 11, CNRS/IN2P3, Orsay, France
[62] Lawrence Berkeley National Laboratory, Berkeley, California, USA
[63] Max-Planck-Institut für Astrophysik, Karl-Schwarzschild-Str. 1, 85741 Garching, Germany
[64] Max-Planck-Institut für Extraterrestrische Physik, Giessenbachstraße, 85748 Garching, Germany
[65] MilliLab, VTT Technical Research Centre of Finland, Tietotie 3, Espoo, Finland
[66] National University of Ireland, Department of Experimental Physics, Maynooth, Co. Kildare, Ireland
[67] Niels Bohr Institute, Blegdamsvej 17, Copenhagen, Denmark
[68] Observational Cosmology, Mail Stop 367-17, California Institute of Technology, Pasadena, CA, 91125, USA
[69] SISSA, Astrophysics Sector, via Bonomea 265, 34136 Trieste, Italy
[70] SUPA, Institute for Astronomy, University of Edinburgh, Royal Observatory, Blackford Hill, Edinburgh EH9 3HJ, UK
[71] School of Physics and Astronomy, Cardiff University, Queens Buildings, The Parade, Cardiff, CF24 3AA, UK
[72] Space Research Institute (IKI), Russian Academy of Sciences, Profsoyuznaya Str 84/32, Moscow 117997, Russia
[73] Space Sciences Laboratory, University of California, Berkeley, California, USA
[74] Stanford University, Dept of Physics, Varian Physics Bldg, 382 via Pueblo Mall, Stanford, California, USA
[75] Universität Heidelberg, Institut für Theoretische Astrophysik, Albert-Überle-Str. 2, 69120 Heidelberg, Germany
[76] Université de Toulouse, UPS-OMP, IRAP, 31028 Toulouse Cedex 4, France
[77] University of Granada, Departamento de Física Teórica y del Cosmos, Facultad de Ciencias, Granada, Spain
[78] University of Miami, Knight Physics Building, 1320 Campo Sano Dr., Coral Gables, Florida, USA
[79] Warsaw University Observatory, Aleje Ujazdowskie 4, 00-478 Warszawa, Poland

A&A 536, A12 (2011)
DOI: 10.1051/0004-6361/201116489

Astronomy & Astrophysics
Special feature

Planck early results. XII. Cluster Sunyaev-Zeldovich optical scaling relations★

Planck Collaboration: N. Aghanim[48], M. Arnaud[59], M. Ashdown[57,4], J. Aumont[48], C. Baccigalupi[71], A. Balbi[30], A. J. Banday[79,7,64], R. B. Barreiro[54], M. Bartelmann[77,64], J. G. Bartlett[3,55], E. Battaner[80], K. Benabed[49], A. Benoît[47], J.-P. Bernard[79,7], M. Bersanelli[27,42], R. Bhatia[5], J. J. Bock[55,8], A. Bonaldi[38], J. R. Bond[6], J. Borrill[63,75], F. R. Bouchet[49], M. L. Brown[4,57], M. Bucher[3], C. Burigana[41], P. Cabella[30], J.-F. Cardoso[60,3,49], A. Catalano[3,58], L. Cayón[20], A. Challinor[51,57,11], A. Chamballu[45], L.-Y Chiang[50], C. Chiang[19], G. Chon[65,4], P. R. Christensen[68,31], E. Churazov[64,74], D. L. Clements[45], S. Colafrancesco[39], S. Colombi[49], F. Couchot[62], A. Coulais[58], B. P. Crill[55,69], F. Cuttaia[41], A. Da Silva[10], H. Dahle[52,9], L. Danese[71], R. J. Davis[56], P. de Bernardis[26], G. de Gasperis[30], A. de Rosa[41], G. de Zotti[38,71], J. Delabrouille[3], J.-M. Delouis[49], F.-X. Désert[44], J. M. Diego[54], K. Dolag[64], S. Donzelli[42,52], O. Doré[55,8], U. Dörl[64], M. Douspis[48], X. Dupac[34], G. Efstathiou[51], T. A. Enßlin[64], F. Finelli[41], I. Flores-Cacho[53,32], O. Forni[79,7], M. Frailis[40], E. Franceschi[41], S. Fromenteau[3,48], S. Galeotta[40], K. Ganga[3,46], R. T. Génova-Santos[53,32], M. Giard[79,7], G. Giardino[35], Y. Giraud-Héraud[3], J. González-Nuevo[71], K. M. Górski[55,82], S. Gratton[57,51], A. Gregorio[28], A. Gruppuso[41], D. Harrison[51,57], S. Henrot-Versillé[62], C. Hernández-Monteagudo[64], D. Herranz[54], S. R. Hildebrandt[8,61,53], E. Hivon[49], M. Hobson[4], W. A. Holmes[55], W. Hovest[64], R. J. Hoyland[53], K. M. Huffenberger[81], A. H. Jaffe[45], W. C. Jones[19], M. Juvela[18], E. Keihänen[18], R. Keskitalo[55,18], T. S. Kisner[63], R. Kneissl[33,5], L. Knox[22], H. Kurki-Suonio[18,37], G. Lagache[48], J.-M. Lamarre[58], A. Lasenby[4,57], R. J. Laureijs[35], C. R. Lawrence[55], S. Leach[71], R. Leonardi[34,35,23], M. Linden-Vørnle[13], M. López-Caniego[54], P. M. Lubin[23], J. F. Macías-Pérez[61], C. J. MacTavish[57], B. Maffei[56], D. Maino[27,42], N. Mandolesi[41], R. Mann[72], M. Maris[40], F. Marleau[15], E. Martínez-González[54], S. Masi[26], S. Matarrese[25], F. Matthai[64], P. Mazzotta[30], S. Mei[78,36,8], A. Melchiorri[26], J.-B. Melin[12], L. Mendes[34], A. Mennella[27,40], S. Mitra[55], M.-A. Miville-Deschênes[48,6], A. Moneti[49], L. Montier[79,7], G. Morgante[41], D. Mortlock[45], D. Munshi[73,51], A. Murphy[67], P. Naselsky[68,31], P. Natoli[29,2,41], C. B. Netterfield[15], H. U. Nørgaard-Nielsen[13], F. Noviello[48], D. Novikov[45], I. Novikov[68], I. J. O'Dwyer[55], S. Osborne[76], F. Pajot[48], F. Pasian[40], G. Patanchon[3], O. Perdereau[62], L. Perotto[61], F. Perrotta[71], F. Piacentini[26], M. Piat[3], E. Pierpaoli[17], R. Piffaretti[59,12], S. Plaszczynski[62], E. Pointecouteau[79,7], G. Polenta[2,39], N. Ponthieu[48], T. Poutanen[37,18,1], G. W. Pratt[59], G. Prézeau[8,55], S. Prunet[49], J.-L. Puget[48], R. Rebolo[53,32], M. Reinecke[64], C. Renault[61], S. Ricciardi[41], T. Riller[64], I. Ristorcelli[79,7], G. Rocha[55,8], C. Rosset[3], J. A. Rubiño-Martín[53,32], B. Rusholme[46], M. Sandri[41], G. Savini[70], B. M. Schaefer[77], D. Scott[16], M. D. Seiffert[55,8], P. Shellard[11], G. F. Smoot[21,63,3], J.-L. Starck[59,12], F. Stivoli[43], V. Stolyarov[4], R. Sudiwala[73], R. Sunyaev[64,74], J.-F. Sygnet[49], J. A. Tauber[35], L. Terenzi[41], L. Toffolatti[14], M. Tomasi[27,42], J.-P. Torre[48], M. Tristram[62], J. Tuovinen[66], L. Valenziano[41], L. Vibert[48], P. Vielva[54], F. Villa[41], N. Vittorio[30], B. D. Wandelt[49,24], S. D. M. White[64], M. White[21], D. Yvon[12], A. Zacchei[40], and A. Zonca[23]

(Affiliations can be found after the references)

Received 10 January 2011 / Accepted 25 June 2011

ABSTRACT

We present the Sunyaev-Zeldovich (SZ) signal-to-richness scaling relation ($Y_{500} - N_{200}$) for the MaxBCG cluster catalogue. Employing a multi-frequency matched filter on the *Planck* sky maps, we measure the SZ signal for each cluster by adapting the filter according to weak-lensing calibrated mass-richness relations ($N_{200} - M_{500}$). We bin our individual measurements and detect the SZ signal down to the lowest richness systems ($N_{200} = 10$) with high significance, achieving a detection of the SZ signal in systems with mass as low as $M_{500} \approx 5 \times 10^{13}\ M_{\odot}$. The observed $Y_{500} - N_{200}$ relation is well modeled by a power law over the full richness range. It has a lower normalisation at given N_{200} than predicted based on X-ray models and published mass-richness relations. An X-ray subsample, however, does conform to the predicted scaling, and model predictions do reproduce the relation between our measured bin-average SZ signal and measured bin-average X-ray luminosities. At fixed richness, we find an intrinsic dispersion in the $Y_{500} - N_{200}$ relation of 60% rising to of order 100% at low richness. Thanks to its all-sky coverage, *Planck* provides observations for more than 13 000 MaxBCG clusters and an unprecedented SZ/optical data set, extending the list of known cluster scaling laws to include SZ-optical properties. The data set offers essential clues for models of galaxy formation. Moreover, the lower normalisation of the SZ-mass relation implied by the observed SZ-richness scaling has important consequences for cluster physics and cosmological studies with SZ clusters.

Key words. galaxies: clusters: intracluster medium – cosmic background radiation – large-scale structure of Universe – cosmology: observations – galaxies: clusters: general

1. Introduction

Galaxy cluster properties follow simple scaling laws (see e.g. Rosati et al. 2002; Voit 2005, for recent reviews). This attests to a remarkable consistency in the cluster population and motivates the use of clusters as cosmological probes. These scaling laws also provide important clues to cluster formation, and relations involving optical properties, in particular, help uncover the processes driving galaxy evolution.

The Sunyaev-Zeldovich (SZ) effect (Sunyaev & Zeldovich 1972; Birkinshaw 1999) opens a fresh perspective on cluster scaling laws, and the advent of large-area SZ surveys furnishes us with a powerful new tool (Carlstrom et al. 2002). Proportional

---

★ Corresponding author: J. G. Bartlett,
e-mail: `bartlett@apc.univ-paris7.fr`

to ICM mass and temperature, the thermal SZ effect probes the gas in a manner complementary to X-ray measurements, giving a more direct view of the gas mass and energy content. Ground-based instruments, such as the Atacama Cosmology Telescope (ACT, Swetz et al. 2008), the South Pole Telescope (SPT, Carlstrom et al. 2011) and APEX-SZ (Dobbs et al. 2006), are harvesting a substantial crop of scientific results and producing, for the first time, SZ-selected catalogues and using them to constrain cosmological parameters (Staniszewski et al. 2009; Marriage et al. 2011; Sehgal et al. 2011; Vanderlinde et al. 2010; Hand et al. 2011; Williamson et al. 2011).

The *Planck*[1] consortium has published its first scientific results (Planck Collaboration 2011a) and released the *Planck* Early Release Compact Source Catalogue (ERCSC) (Planck Collaboration 2011c), which includes the *Planck* early SZ (ESZ) all-sky cluster list (Planck Collaboration 2011d). *Planck* (Tauber et al. 2010; Planck Collaboration 2011a) is the third generation space mission to measure the anisotropy of the cosmic microwave background (CMB). It observes the sky in nine frequency bands covering 30–857 GHz with high sensitivity and angular resolution from 31′–5′. The Low Frequency Instrument (LFI; Mandolesi et al. 2010; Bersanelli et al. 2010; Mennella et al. 2011) covers the 30, 44, and 70 GHz bands with amplifiers cooled to 20 K. The High Frequency Instrument (HFI; Lamarre et al. 2010; Planck HFI Core Team 2011a) covers the 100, 143, 217, 353, 545, and 857 GHz bands with bolometers cooled to 0.1 K. Polarization is measured in all but the highest two bands (Leahy et al. 2010; Rosset et al. 2010). A combination of radiative cooling and three mechanical coolers produces the temperatures needed for the detectors and optics (Planck Collaboration 2011b). Two Data Processing Centres (DPCs) check and calibrate the data and make maps of the sky (Planck HFI Core Team 2011b; Zacchei et al. 2011). *Planck*'s sensitivity, angular resolution, and frequency coverage make it a powerful instrument for galactic and extragalactic astrophysics, as well as cosmology. Early astrophysics results are given in Planck Collaboration (2011d)-Planck Collaboration (2011u).

Planck early results on clusters of galaxies are presented in this *paper* and in (Planck Collaboration 2011d–g). In the present work, we use *Planck* SZ measurements at the locations of MaxBCG clusters (Koester et al. 2007a) to extract the SZ signal-richness scaling relation. There are several optical cluster catalogs (Wen et al. 2009; Hao et al. 2010; Szabo et al. 2011) available from the Sloan Digital Sky Survey (York et al. 2000, SDSS). For this initial study, we chose the MaxBCG catalogue for its large sample size, wide mass range and well-characterized selection function, and because its properties have been extensively studied. In particular, we benefit from weak-lensing mass measurements and mass-richness relations (Johnston et al. 2007; Mandelbaum et al. 2008a; Sheldon et al. 2009; Rozo et al. 2009). A combined SZ-optical study over such a large catalogue is unprecedented and *Planck* is a unique SZ instrument for this task, as its all-sky coverage encompasses the complete SDSS area and the full MaxBCG cluster sample.

Our analysis methodology follows that of the accompanying paper on the SZ properties of X-ray selected clusters (Planck Collaboration 2011f). Although the individual SZ measurements in both cases generally have low signal-to-noise, we extract the statistical properties of the ICM – mean relations and their dispersion – by averaging over the large sample. The approach enables us to study the properties of a much larger and representative sample of clusters than otherwise possible.

The SZ-richness relation adds a new entry to the complement of cluster scaling laws and additional constraints on cluster and galaxy evolution models. With a mass-richness relation, we can also derive the SZ signal-mass relation. This is a central element in predictions for the diffuse SZ power spectrum and SZ cluster counts. Poor knowledge of the relation represents an important source of modeling uncertainty. Low mass systems, for example, contribute a large fraction of the SZ power, but we know very little about their SZ signal.

We organise the *paper* as follows: the next section presents the data used, both the *Planck* maps and the MaxBCG catalogue and pertinent characteristics. Section 3 details our SZ measurements based on a multi-frequency matched filter, and outlines some of the systematic checks. In Sect. 4 we present our basic results and in Sect. 5 compare them to model expectations. Section 6 concludes.

1.1. Conventions and notation

In the following, we adopt a flat fiducial cosmology with $\Omega_{\rm M} = 0.3$ with the remainder of the critical density made up by a cosmological constant. We express the Hubble parameter at redshift z as $H(z) = H_0\, E(z) = (h \times 100\ \ {\rm km\, s^{-1}\, Mpc^{-1}})\, E(z)$ with $h = 0.7$. Cluster radii are expressed in terms of R_Δ, the radius inside of which the mean mass overdensity equals $\Delta \times \rho_{\rm c}(z)$, where $\rho_{\rm c}(z) = 3H^2(z)/8\pi G$ is the critical density at redshift z. Similarly, we quote masses as $M_\Delta = \Delta(4\pi/3)R_\Delta^3\rho_{\rm c}$. We note that, in contrast, optical cluster studies, and in particular the MaxBCG group, frequently employ radii and masses scaled to the mean matter density, rather than the critical density. For example, it is standard practice to refer to quantities measured within $R_{\rm 200b}$, where the overdensity of 200 is defined with respect to the background density (this corresponds to R_{60} at $z = 0$ and R_{155} at $z = 1$). For richness we will use the MaxBCG N_{200}, defined as the number of red galaxies with $L > 0.4\, L_*$ within $R_{\rm 200b}$. Richness N_{200} is the only quantity in this work defined relative to the mean background density.

We characterize the SZ signal with the Compton-y parameter integrated over a sphere of radius R_{500} and expressed in arcmin^2: $Y_{500} = (\sigma_{\rm T}/m_{\rm e}c^2)\int_0^{R_{500}} P{\rm d}V/D_{\rm A}^2(z)$, where $D_{\rm A}$ denotes angular distance, $\sigma_{\rm T}$ is the Thomson cross-section, c the speed of light, $m_{\rm e}$ the electron rest mass and $P = n_{\rm e}kT$ is the pressure, defined as the product of the electron number density and temperature, k being the Boltzmann constant. The use of this spherical, rather than cylindrical, quantity is possible because we adopt a template SZ profile when using the matched filter (discussed below). We bring our measurements to $z = 0$ and a fiducial angular distance assuming self-similar scaling in redshift. To this end, we introduce the intrinsic cluster quantity (an "absolute SZ signal strength") $\tilde{Y}_{500} \equiv Y_{500}E^{-2/3}(z)(D_{\rm A}(z)/500\,{\rm Mpc})^2$, also expressed in arcmin^2.

2. Data sets

We base our study on *Planck* SZ measurements at the positions of clusters in the published MaxBCG cluster catalogue.

---

[1] *Planck* (`http://www.esa.int/Planck`) is a project of the European Space Agency (ESA) with instruments provided by two scientific consortia funded by ESA member states (in particular the lead countries France and Italy), with contributions from NASA (USA) and telescope reflectors provided by a collaboration between ESA and a scientific consortium led and funded by Denmark.

2.1. The MaxBCG optical cluster catalogue

The MaxBCG catalogue (Koester et al. 2007b,a) is derived from Data Release 5 (DR5) of the Sloan Digital Sky Survey (York et al. 2000), covering an area of 7500 $\deg^2$ in the Northern hemisphere. Galaxy cluster candidates were extracted by color, magnitude and a spatial filter centered on galaxies identified as the brightest cluster galaxy (BCG). The catalogue provides position, redshift, richness and total luminosity for each candidate. In the following we will only use the richness N_{200}, defined as the number of red-sequence galaxies with $L > 0.4\,L_*$ and within a projected radius at which the cluster interior mean density equals 200 times the *mean* background density at the redshift of the cluster (see Koester et al. 2007a, for details and the remark in Sect. 1.1). The catalogue consists of 13 823 galaxy clusters over the redshift range $0.1 < z < 0.3$, with 90% purity and 85% completeness for $10 < N_{200} < 190$ as determined from simulations.

A valuable characteristic for our study is the wide mass range spanned by the catalogue. Another is the fact that numerous authors have studied the catalogue, providing extensive information on its properties. In particular, Sheldon et al. (2009) and Mandelbaum et al. (2008a) have published mass estimates from weak gravitational lensing analyses, which Johnston et al. (2007) and Rozo et al. (2009) use to construct mass-richness ($M_{500}-N_{200}$) relations. We apply this relation, as outlined below, to adapt our SZ filter measurements for each individual cluster according to its given richness, N_{200}, as well as in our model predictions.

In their discussion, Rozo et al. (2009) identify the differences between the Sheldon et al. (2009) and Mandelbaum et al. (2008a) mass estimates and the impact on the deduced mass-richness relation. They trace the systematically higher mass estimates of Mandelbaum et al. (2008a) to these authors' more detailed treatment of photometric redshift uncertainties (Mandelbaum et al. 2008b). Moreover, they note that Johnston et al. (2007), when employing the Sheldon et al. (2009) measurements, used an extended MaxBCG catalogue that includes objects with $N_{200} < 10$, where the catalogue is known to be incomplete. These two effects lead Rozo et al. (2009) to propose a flatter mass-richness relation with higher normalisation than the original Johnston et al. (2007) result. In the following, we perform our analysis with both relations; specifically, using the fit in Table 10 for the $M_{500}-N_{200}$ relation of Johnston et al. (2007), and Eqs. (4), (A.20) and (A.21) of Rozo et al. (2009).

2.2. Planck data

We use the six HFI channel temperature maps (prior to CMB removal) provided by the DPC and whose characteristics are given in Planck HFI Core Team (2011b). These maps correspond to the observations of intensity in the first ten months of survey by *Planck*, still allowing complete sky coverage. Hence, they give us access to the entire SDSS survey area and complete MaxBCG catalogue. After masking bad pixels and contaminated regions (e.g., areas where an individual frequency map has a point source at $>10\sigma$), we have *Planck* observations for 13 104 of the 13 823 clusters in the MaxBCG catalogue.

3. SZ measurements

We extract the SZ signal at the position of each MaxBCG cluster by applying a multi-frequency matched filter (Herranz et al. 2002; Melin et al. 2006) to the six *Planck* temperature maps. The technique maximises the signal-to-noise of objects having the known frequency dependence of the thermal SZ effect and the expected angular profile. The filter returns the amplitude of the template, which we then convert into integrated SZ signal, Y_{500}, within R_{500}. It also returns an estimate of the local noise through the filter, $\sigma_{\theta_{500}}$, due to instrumental noise and astrophysical emissions. The same procedure is used in Planck Collaboration (2011f). We refer the reader to Melin et al. (2006, 2011) for details.

3.1. SZ model template

For the filter's spatial template we adopt the empirical universal pressure profile of Arnaud et al. (2010), deduced from X-ray studies of the REXCESS cluster sample (Böhringer et al. 2007):

$$P(r) \propto \frac{1}{x^{\gamma}(1+x^{\alpha})^{(\beta-\gamma)/\alpha}} \tag{1}$$

where the physical radius r is scaled to $x = r/r_{\rm s}$, with $r_{\rm s} = R_{500}/c_{500}$. For the standard self-similar case (ST case in Appendix B of Arnaud et al. 2010), $c_{500} = 1.156$ and the exponents are $\alpha = 1.0620, \beta = 5.4807, \gamma = 0.3292$. The normalisation is arbitrary for purposes of the matched filter. The SZ signal being proportional to the gas pressure, we find the filter template by integrating along the line-of-sight and expressing the result in terms of projected angles: $x = \theta/\theta_{\rm s}$. We truncate the filter at $5\theta_{500}$, containing more than 95% of the signal for the model.

3.2. Application of the filter

We apply the matched filter to each cluster in the MaxBCG catalogue, using the mass-richness relation, $M_{500} - N_{200}$, to define R_{500} and set the angular scale $\theta_{500} = R_{500}/D_{\rm A}(z)$. The filter effectively samples the cluster SZ signal along a cone out to a transverse angular radius of $5\theta_{500}$, and returns the normalisation for the template. We apply a geometric factor based on the template SZ profile to convert the deduced total SZ signal along the cone to an equivalent Y_{500} value, the SZ signal integrated within a sphere of physical radius R_{500}. To account for the redshift range of the catalogue, we scale these measurements according to self-similar expectations to redshift $z = 0$ and a fiducial angular distance of 500 Mpc: $\tilde{Y}_{500} \equiv Y_{500}\,E^{-2/3}(z)(D_{\rm A}(z)/500\,{\rm Mpc})^2$. We accordingly adapt the estimated filter noise $\sigma_{\theta_{500}}$ to uncertainty $\tilde{\sigma}_{\theta_{500}}$ on these scaled SZ signal measurements. The results of this procedure when using the Johnston et al. (2007) mass-richness relation are shown in Fig. 1.

3.3. Systematic effects

As in the other four *Planck* SZ papers (Planck Collaboration 2011d–g), we have carried out various tests to ensure the robustness of the *Planck* SZ measurements. They included investigation of the cluster size-flux degeneracy, evaluation of the impact of the assumed pressure profile used for the *Planck* cluster detection, of beam-shape effects, color corrections, potential contamination by point sources, as well as an overall error budget estimation. We refer the reader to Sect. 6 of Planck Collaboration (2011d) for an extensive description of this common analysis.

To complete this investigation in the present work, we repeated our entire analysis, changing both the instrument beams and adopted SZ profiles. In the former instance, we varied the beams at all frequencies together to the extremes of their associated uncertainties as specified by the DPC

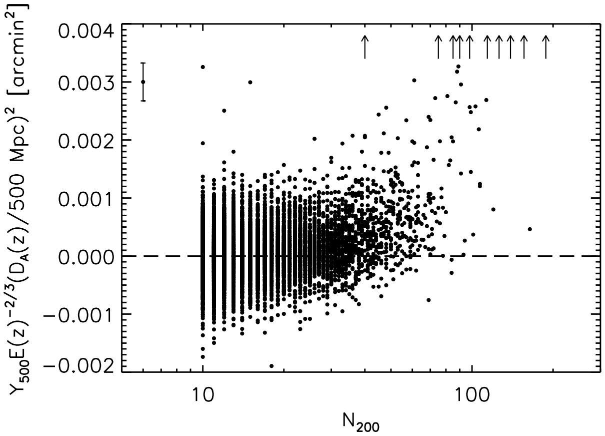

Fig. 1. Individual scaled SZ signal measurements, $\tilde{Y}_{500}$, for the MaxBCG catalogue as a function of richness N_{200}. We do not plot individual error bars to avoid saturating the figure. The error bar drawn in the upper left represents the *median* uncertainty over the entire population; in general, the uncertainty increases towards low richness. The SZ signal measurements are expressed as the Compton y parameter integrated over a sphere out to R_{500}, scaled in redshift according to the self-similar model and placed at a fiducial angular distance of 500 Mpc. Each point represents the result of the matched filter applied to an individual cluster in the catalogue. Upward pointing arrows indicate values beyond the plotted range. The radius R_{500}, and hence the filter size, is set from the mass of each cluster determined via the weak-lensing calibrated $M_{500} - N_{200}$ relation given by Johnston et al. (2007). The results are nearly the same for the relation given by Rozo et al. (2009).

(Planck HFI Core Team 2011b). All beams were increased or all decreased in lock-step to maximize any effect. To investigate the profile, we re-extracted the SZ signal using a non-standard SZ signal-mass scaling, and separately for cool-core and morphologically disturbed SZ profiles (based on the work of Arnaud et al. 2010). In all cases, the impact on the measurements was of order a few percent and thus negligibly impacts our conclusions.

4. Results

Our basic measurements are the set of individual scaled SZ signal values $\tilde{Y}_{500}$ for each MaxBCG cluster, given as a function of richness N_{200} in Fig. 1 for the Johnston et al. (2007) mass calibration. At high richness we can detect by eye a slight upturn of the points. Except for the most massive objects, however, the signal-to-noise of the individual measurements is small, in most cases well below unity. This is as expected given the masses of the clusters and the *Planck* noise levels.

To extract the signal, we bin these $\tilde{Y}_{500}$ values by richness and calculate the bin averages as the noise-weighted mean of all individual $i = 1, .., N_\mathrm{b}$ measurements falling within the bin: $\langle\tilde{Y}_{500}\rangle_\mathrm{b} = (\sum_i \tilde{Y}_{500}(i)/\tilde{\sigma}^2_{\theta_{500}}(i))/(\sum_i 1/\tilde{\sigma}^2_{\theta_{500}}(i))$. We plot the result as the red diamonds in Fig. 2. The bold error bars represent only the statistical uncertainty associated with the SZ signal measurements: $\sigma_\mathrm{b}^{-2} = \sum_i 1/\tilde{\sigma}^2_{\theta_{500}}(i)$ (in some cases the error bars are hidden by the size of the data point in the figure). The left-hand panel of the figure shows results using the Johnston et al. (2007) mass calibration, while the right-hand side gives results for the Rozo et al. (2009) mass calibration. The individual SZ signal measurements are not sensitive to this choice: the different calibrations do modify the adopted filter size, but the impact on the measured signal is small.

Table 1. Scaled *Planck* SZ signal measurements $\tilde{Y}_{500}$ binned by N_{200} for the Rozo et al. (2009) mass-richness relation.

N_{200}	$\tilde{Y}_{500}/(10^{-5}\ \mathrm{arcmin}^2)$	Stat. uncertainty	Total uncertainty
10–13	2.0	±0.3	±0.3
14–17	3.8	±0.6	±0.6
18–24	8.2	±0.7	±0.7
25–32	15	±1	±1
33–43	27	±2	±2
44–58	48	±3	±4
59–77	76	±4	±8
78–104	190	±9	±40
>105	300	±20	±80

Notes. Given $\tilde{Y}_{500}$ values are the measurement-noise weighted mean in the bin. The statistical uncertainty corresponds to the measurement-noise uncertainty on the weighted mean, while the total uncertainty expresses the standard deviation of the weighted mean from an ensemble of bootstrap samples. This table is plotted as the red diamonds and error bars in the right-hand panel of Fig. 2.

We quantify the significance of the SZ detection using a null test: we perform an identical analysis on the MaxBCG catalogue after first randomising the cluster angular positions within the SDSS DR5 footprint. In this analysis we are therefore attempting to measure SZ signal with the same set of filters, but now positioned randomly within the SDSS survey. The result is shown in Fig. 3 by the green triangles, to be compared to the actual MaxBCG measurement given by the red diamonds. The left-hand panel presents the null test over the full richness range, while the right-hand panel affords an expanded view of the low mass end. The analysis on the randomised catalog remains consistent with zero (no detection) to within the SZ measurement uncertainty over the entire richness range. The actual measurements of the MaxBCG clusters, on the other hand, deviate by many σ from zero. We reject the null hypothesis in all bins at high significance.

Figure 4 summarises our analysis of the uncertainty and intrinsic scatter as a function of richness. In the left panel we show the uncertainty on the mean signal $\tilde{Y}_{500}$ in each bin, expressed as a fraction of $\tilde{Y}_{500}$. The red solid red line traces the uncertainty on the mean signal due to just the measurement error, i.e., the noise level in the filter. The blue dashed line gives the uncertainty on the mean assuming that the measurements within a bin are Gaussian distributed about the mean with variance equal to the empirical in-bin variance. We show the relative uncertainty calculated from a bootstrap analysis of the entire catalogue as the dot-dashed, green curve. We perform our full analysis on 10 000 bootstrap realisations from the actual catalogue and use the distribution of the resulting bin averages to find the relative uncertainty. The difference between the bootstrap and measurement uncertainties (red line) towards higher richness represents a detection of intrinsic scatter in those bins. At $N_{200} < 30$, this difference is small and any intrinsic scatter is difficult to distinguish from the measurement errors.

In the right-hand panel of Fig. 4 we show our estimate of the intrinsic scatter in the scaling relation as a function of richness for $N_{200} > 30$. This is expressed as a fraction of the mean, $\tilde{Y}_{500}$. The dot-dashed, blue line traces the empirical, or raw, dispersion around the average signal of each bin. The three-dot-dashed, green line gives the dispersion corresponding to pure SZ measurement noise. To find the intrinsic scatter, we use the

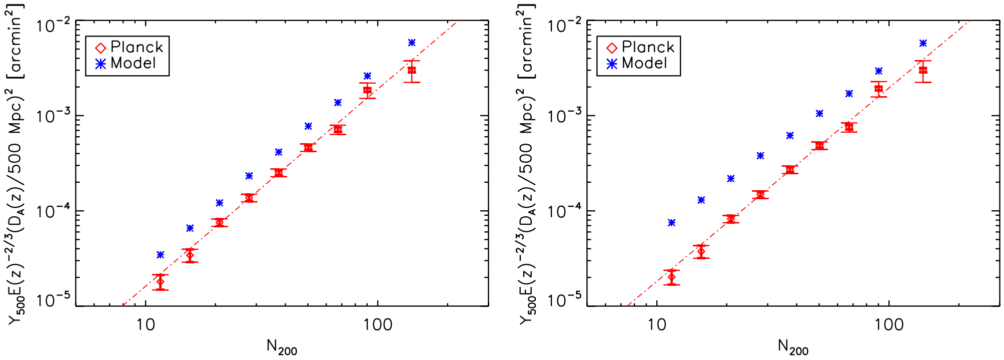

Fig. 2. Scaled SZ signal measurements, $\tilde{Y}_{500}$, binned by richness, N_{200}. The left-hand panel presents the results for the Johnston et al. (2007) $M_{500} - N_{200}$ relation, the right-hand panel for the Rozo et al. (2009) relation. In each case, the red diamonds show the bin-average, redshift-scaled $\tilde{Y}_{500}$ calculated as the weighted mean of all individual measurements (e.g., Fig. 1) in the bin, where the weights are taken from the estimated filter noise. The thick error bars show the corresponding uncertainty on the bin-average SZ signal, while the lighter error bars indicate the uncertainty found by bootstrap analysis; they are larger due to the presence of intrinsic scatter within the bins, most notable at high richness (see Fig. 4). The blue points represent the model prediction for each bin found by averaging, with the same weights as the data, the SZ signal expected from the $Y_{500} - M_{500}$ (Arnaud et al. 2010, STD case) and corresponding $M_{500} - N_{200}$ relations. The *Planck* measurements are little affected by choice of mass-richness relation, while the model points move significantly upward with the Rozo et al. (2009) mass calibration. Dashed lines in both panels show the best fit power-law to the *Planck* individual cluster data points (i.e., prior to binning, as shown in Fig. 1); the parameters for these fits are given in Table 2.

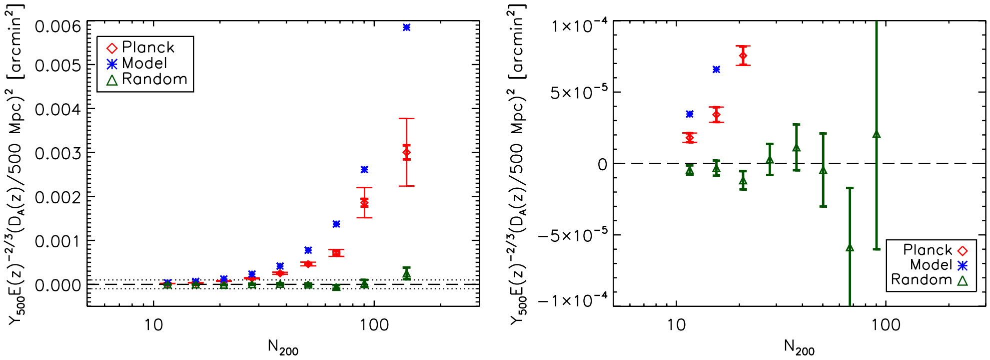

Fig. 3. Null test performed by randomising the angular positions of the clusters. The red diamonds show the bin-average, redshift-scaled measurements, $\tilde{Y}_{500}$, as reported in the left-hand side of Fig. 2 with their corresponding measurement and bootstrap uncertainties; blue stars are the same model points. The green triangles present the bin-averages for the randomised catalogue with uncertainties given only by the SZ measurement errors. Results for the randomised catalogue are consistent with zero within their uncertainties. By comparison, the values for the real catalogue represent highly significant detections of the SZ signal in all richness bins. *Left-hand panel*: results over the full richness range. *Right-hand panel*: zoom into the region indicated by the dotted lines in the left-hand panel to highlight the low-richness end.

estimator:

$$\Sigma_b^2 = \frac{1}{N_b - 1}\sum_{i=1}^{N_b}\left(\tilde{Y}_{500}(i) - [\tilde{Y}_{500}]_{\mathrm{arith}}\right)^2 - \frac{1}{N_b}\sum_{i=1}^{N_b}\tilde{\sigma}^2_{\theta_{500}}(i) \qquad (2)$$

where $[\tilde{Y}_{500}]_{\mathrm{arith}}$ is the straight arithmetic mean in the bin. In the figure we plot $\Sigma_b/\langle\tilde{Y}_{500}\rangle_b$, with $\langle\tilde{Y}_{500}\rangle_b$ being the weighted mean, as above. For this calculation we clip all outliers at $>5\sigma$, where σ is the individual cluster SZ signal error. The final result, especially at low richness, depends on the chosen clipping threshold. The scatter is not Gaussian, as the large fractional intrinsic scatter at low richness suggests. Below $N_{200} \approx 30$, it becomes difficult to draw clear conclusions concerning the scatter, as can be appreciated by the fact that the bootstrap and pure SZ measurement uncertainties begin to overlap in the left-hand panel. For this reason, we only calculate the intrinsic scatter for the five highest richness bins in the right-hand panel.

In conclusion, we detect a signal down to the lowest mass systems in the MaxBCG catalog with high statistical significance. *This is the central result of our study*. According to the mass calibration from Johnston et al. (2007), we observe the SZ signal in objects of mass as low as $M_{500} = (4{-}5) \times 10^{13}\ M_\odot$.

5. Discussion

Figure 2 summarises the central results of our study. There are two notable aspects: firstly, we detect the SZ signal at high significance over the entire mass range; moreover, simple power laws adequately represent the observed scaling relations. Secondly, we see a discrepancy in the $\tilde{Y}_{500} - N_{200}$ relation relative to expectations based on X-ray models and either the Johnston et al. (2007) or Rozo et al. (2009) mass calibrations.

Fitting a power law of the form

$$\tilde{Y}_{500} = Y_{500}E^{-2/3}(z)\left(\frac{D_A(z)}{500\,\mathrm{Mpc}}\right)^2 = Y_{20}\left(\frac{N_{200}}{20}\right)^{\alpha} \qquad (3)$$

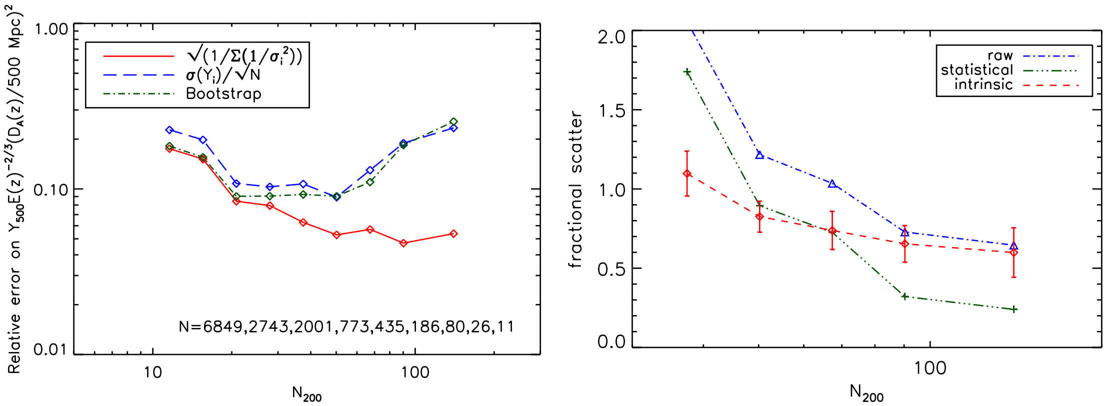

Fig. 4. Dispersion analysis. *Left-hand panel*: relative uncertainty on the mean versus richness. The relative uncertainty is expressed as a fraction of the bin-average redshift-scaled SZ signal: $\sigma/\tilde{Y}_{500}$. The lower red curve corresponds to pure measurement uncertainties from the matched filter noise estimations; they are the solid error bars of Fig. 2. The upper blue curve traces the uncertainty on the mean assuming the points within a richness bin are normally distributed according to the observed in-bin dispersion. Bootstrap uncertainties are given as the middle green line, found as the dispersion in the mean $\tilde{Y}_{500}$ in each bin calculated over 10 000 bootstrap realisations of the entire MaxBCG catalogue. The numbers given in the legend indicate the number of objects in each richness bin. *Right-hand panel*: fractional intrinsic scatter as a function of richness. The blue dot-dashed line (connecting the blue triangles) shows the raw dispersion in each richness bin, while the green dash-three-dotted line (connecting the green crosses) gives the calculated statistical dispersion from the measurement error on the scaled SZ signal $\tilde{Y}_{500}$. The red dashed line with error bars is our estimation of the intrinsic scatter as a function of richness. For this calculation we have eliminated outliers in each bin at $>5\sigma$, with $\sigma = \tilde{\sigma}_{\theta_{500}}$ for each cluster. We only calculate the intrinsic scatter at $N_{200} > 30$, because at lower richness it becomes difficult to separate the intrinsic dispersion from the scatter due to pure measurement error.

directly to the individual scaled measurements (e.g., Fig. 1), we obtain the results summarised in Table 2. The Rozo et al. (2009) mass calibration assigns a larger mass to the clusters, increasing the filter scale and augmenting the measured SZ signal, which we see as the slightly higher normalisation. These fits are plotted as the dashed lines in Fig. 2. The power laws satisfactorily represent the bin-average trends. The reduced $\chi^2 = 1.16$ (13 104-2 degrees-of-freedom) in both cases is poor; this reflects the presence of the intrinsic scatter, also evident by the larger uncertainties on the fit from the bootstrap analysis.

The blue stars in Fig. 2 represent the predictions of a model based on the $Y_{500} - M_{500}$ relation from Arnaud et al. (2010) and the Johnston et al. (2007) (left) or Rozo et al. (2009) (right) $M_{500} - N_{200}$ mean scaling relation. It assumes a self-similar $Y_{500} - M_{500}$ scaling relation (STD case) calibrated on X-ray observations of the REXCESS cluster sample (Böhringer et al. 2007). This calibration is also consistent with WMAP observations (Melin et al. 2011) and with the *Planck* analysis (Planck Collaboration 2011f,g). In each bin we average the model predictions in the same way as the *Planck* observations: we find the model bin-average redshift-scaled SZ signal as the inverse-error-weighted (pure SZ measurement error) average, assigning each cluster in the bin the same error as the actual observation of that object. Note that in the observation plane $(\tilde{Y}_{500}, N_{200})$, the model (blue) points change with the mass calibration much more than the measurements.

We see a clear discrepancy between the model and the *Planck* SZ measurements for both mass calibrations. In the case of the Johnston et al. (2007) mass calibration, the discrepancy manifests as a shift in normalisation that we can characterise by a 25% mass shift at given SZ signal: $M \longrightarrow 0.75M$; the slope of the observed relation remains consistent with the self-similar prediction. The Rozo et al. (2009) mass calibration, on the other hand, flattens the mass-richness relation and predicts a shallower power law, as well as a higher normalisation; at $N_{200} = 50$ there is a factor of 2 between the predicted and observed amplitudes.

We now discuss some possible explanations for this discrepancy. Weak lensing mass estimates are difficult, and as we have seen there is an important difference in the two mass calibrations. Rozo et al. (2009), building on earlier work by Mandelbaum et al. (2008b), discuss some of the issues when measuring the weak-lensing signal for the MaxBCG catalogue. However, it seems unlikely that the weak-lensing mass calibration would be in error to the extent needed to explain the discrepancy seen in Fig. 2. The discrepancy is in fact larger for the Rozo et al. (2009) result, which should be the more robust mass calibration.

Our model predictions use a series of non-linear, mean relations between observables which in reality have scatter that may also be non-Gaussian. The largest scatter is expected to be in the mass-richness relation. If the scatter is large enough, it could bias the predictions. We have investigated the effect of a 45% log-normal scatter in mass at fixed richness (e.g., Rozo et al. 2009) and of a Poissonian distribution in richness at fixed mass. These are realistic expectations for the degree of scatter in the relations. The effect on the predicted, binned SZ signal is at most 20%, not enough to explain the factor of two discrepancy we see.

Contamination of the MaxBCG catalogue with a fraction, f, of objects that do not contribute an SZ signal (e.g., projection effects in the optical) would bias the measured signal low by about $1 - f$. The level of contamination needed to explain the magnitude of the discrepancy with the Rozo et al. (2009) calibration ($f \approx 0.5$) seems unlikely. The catalogue is estimated, instead, to be close to 90% pure for $N_{200} > 10$. Moreover, contamination would also lower the weak-lensing mass calibration by about $1-f$, at given N_{200}. Since the predicted SZ signal scales as $M^{5/3}$, the model SZ signal would drop by an even larger amount than the observed signal.

To investigate this discrepancy further we analyse, in the same manner, a subsample of the MaxBCG clusters with X-ray data from the MCXC catalogue (Piffaretti et al. 2011). This represents an X-ray detected subsample of the MaxBCG. The results are given in Fig. 5 for the Rozo et al. (2009) mass

Table 2. The SZ signal-richness relation fit to a power law of the form $\tilde{Y}_{500} = Y_{20}\,(N_{200}/20)^{\alpha}$ (see Eq. (3)) for the two mass-richness relations.

Mass-Richness Relation	$Y_{20}/(10^{-5}\ \mathrm{arcmin}^2)$	Statistical	Bootstrap	α	Statistical	Bootstrap
Johnston et al. (2007)	6.8	±0.3	±0.4	2.07	±0.03	±0.07
Rozo et al. (2009)	7.4	±0.3	±0.4	2.03	±0.03	±0.07

Notes. The power law is fit directly to the individual SZ measurements (e.g., Fig. 1). The columns labeled "Statistical" give the uncertainty on the parameters calculated from the SZ measurement errors alone, while those labeled "Bootstrap" give uncertainties found by fitting the power law to a set of bootstrap samples; the latter better represent the full uncertainty of the fits in the presence of intrinsic scatter.

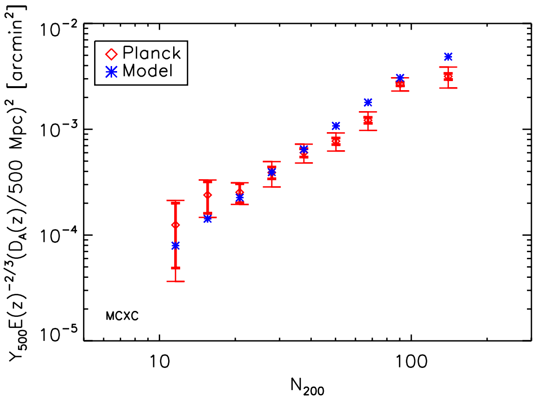

Fig. 5. The $\tilde{Y}_{500} - N_{200}$ relation for the MCXC X-ray subsample. Thick lines give the statistical errors, while the thin bars are the bootstrap uncertainties. We find that the MCXC X-ray subsample matches the model predictions much better than the full sample, which maintains a clear offset relative to the model, as seen in in Fig. 2.

calibration and with our usual notation. We see that this X-ray subsample, of 189 clusters, matches the model predictions much better. This argues that, at least for this subsample, the weak-lensing mass calibration is not significantly biased. The result also indicates the presence of a range of ICM properties at fixed richness. This is consistent with the study by Rozo et al. (2009), obtained by adapting the approach of Rykoff et al. (2008b), who find a large scatter in X-ray luminosity at fixed N_{200}.

Splitting the catalogue according to the luminosity of the BCG lends support to the presence of populations with different ICM properties. In each bin, we divide the catalogue into a BCG-dominated sample, where the fraction of the cluster luminosity contributed by the BCG is larger than the average for that bin, and its complement sample. The BCG-dominated sample has a notably higher normalisation, closer to the predicted relation, than the complement sample.

We also compare our results to the X-ray results from Rykoff et al. (2008a) who stacked ROSAT photons around MaxBCG clusters according to richness. As with our SZ observations, their individual X-ray fluxes had low signal-to-noise, but they extracted mean luminosities from each image stack (Rykoff et al. 2008b). They report luminosities, L_{200}, over the 0.1−2.4 keV band and within R_{200} for each N_{200} richness bin. Their analysis revealed a discrepancy between the observed mean luminosities and the X-ray model predictions, using the Johnston et al. (2007) mass calibration.

To compare we re-binned into the same richness bins as Rykoff et al. (2008b), calculating the new, bin-average, redshift-scaled $\tilde{Y}_{500}$. We also convert their luminosities to L_{500} using the X-ray profile adopted in Arnaud et al. (2010); the conversion factor is 0.91. In addition, we apply the self-similar redshift luminosity scaling of $E^{-7/3}(z = 0.25)$ to bring the Rykoff et al. (2008a) measurements to equivalent $z = 0$ values from the values at their median redshift, $z = 0.25$. The resulting points are shown in Fig. 6.

The model line in the figure is calculated from the $z = 0$, X-ray luminosities using the X-ray based scaling laws in Arnaud et al. (2010). In this plane the model matches the observations well, demonstrating consistency between the SZ and X-ray observations. Remarkably, the ICM quantities remain in agreement with the model despite the individual discrepancies (SZ and X-ray luminosity) with richness.

The intrinsic scatter in the scaling relation, given in Fig. 4, starts at about 60% and rises to over 100% at $N_{200} \approx 30$. This was calculated by clipping all outliers at $>5\sigma$; the result depends on the choice of clipping threshold, indicative of a non-Gaussian distribution. This dispersion should be compared to the estimated log-normal scatter in the mass-richness relation of $(45^{+0.2}_{-0.18})\%$ found by Rozo et al. (2009). Assuming that the dispersion in the SZ signal-mass relation is much smaller, we would expect a dispersion of order 75%, not far from what we find and within the uncertainties. Such large fractional dispersion implies a non-Gaussian distribution skewed toward high SZ signal values, particularly at low richness.

6. Conclusions

We have measured with high significance the mean SZ signal for MaxBCG clusters binned by richness, even the poorest systems. The observed SZ signal-richness relation, based on 13 104 of the MaxBCG clusters observed by *Planck*, is well represented by a power law. This adds another scaling relation to the list of such relations known to exist among cluster properties and that present important constraints on cluster and galaxy evolution models.

The observed relation has a significantly lower amplitude than predicted by X-ray models coupled with the mass-richness relation from weak-lensing observations. The origin of this discrepancy remains unclear. Bias in the weak-lensing mass measurements and/or a high contamination of the catalogue are potential explanations; another would be a bias in hydrostatic X-ray masses relative to weak-lensing based masses (Borgani et al. 2004; Piffaretti & Valdarnini 2008), although the required level of bias would be much larger than expected from simulations. In general, we would expect a wide range of ICM properties at fixed richness (e.g., for example by Rykoff et al. 2008a; Rozo et al. 2009) of which only the more X-ray luminous objects are readily found in X-ray samples used to establish the X-ray model. This is consistent with the better agreement of the model with a subsample of the MaxBCG catalogue with X-ray observations. Remarkably, the relation between mean SZ signal and mean X-ray luminosity for the entire catalogue does conform to model predictions despite discrepant SZ signal-richness and

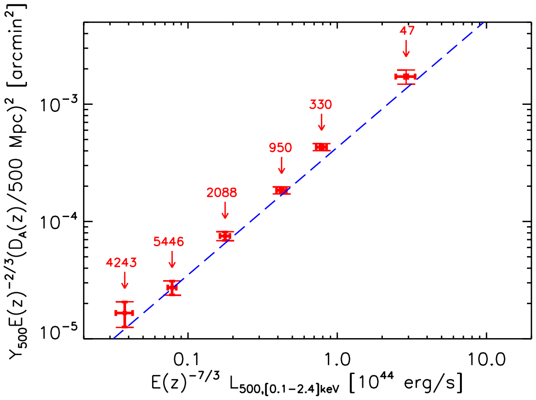

Fig. 6. Comparison of our bin-average redshift-scaled SZ signal measurements with the mean X-ray luminosities found by Rykoff et al. (2008a). For this comparison, we re-bin into the same bins as Rykoff et al. (2008a) and plot the results as the red diamonds with error bars. The X-ray luminosities are brought to equivalent $z = 0$ values using the self-similar scaling of $E^{-7/3}(z = 0.25)$ applied at the quoted $z = 0.25$ median redshift. The dashed blue line shows the predictions of the X-ray model. Our notation for the error bars follows previous figures. The numbers in the figure indicate the number of clusters in each bin.

X-ray luminosity-richness relations; properties of the gas halo appear more stably related than either to richness.

We find large intrinsic scatter in the SZ signal-richness relation, although consistent with the major contribution arising from scatter in the mass-richness relation. The uncertainties, however, are important. Such large scatter implies a non-Gaussian distribution of SZ signal at given richness, skewed towards higher signal strengths. This is consistent with the idea of a wide range of ICM properties at fixed richness, with X-ray detected objects preferentially at the high SZ signal end.

The $\tilde{Y}_{500} - N_{200}$ relation, and by consequence the $\tilde{Y}_{500} - M_{500}$ relation, is an important part of our understanding of the cluster population and a key element in its use as a cosmological probe. Predictions of both the number counts of SZ-detected clusters and the diffuse SZ power spectrum depend sensitively on the $\tilde{Y}_{500} - M_{500}$ relation. The amplitude of the SZ power spectrum varies as the square of the normalisation, while the counts depend on it exponentially. In both instances, this relation represents a significant theoretical uncertainty plaguing models.

Our study of the SZ signal-richness relation is a step towards reducing this uncertainty, and it presents a new cluster scaling relation as a useful constraint for theories of cluster and galaxy evolution. Concerning the latter, we find no obvious sign of an abrupt change in the ICM properties of optically selected clusters over a wide range of richness, hence mass, as might be expected from strong feedback models. Future research with *Planck* will extend this work to other catalogues and a greater redshift range.

Acknowledgements. The authors from the consortia funded principally by CNES, CNRS, ASI, NASA, and Danish Natural Research Council acknowledge the use of the pipeline running infrastructures Magique3 at Institut d'Astrophysique de Paris (France), CPAC at Cambridge (UK), and USPDC at IPAC (USA). We acknowledge the use of the HEALPix package (Górski et al. 2005). A description of the Planck Collaboration and a list of its members, indicating which technical or scientific activities they have been involved in, can be found at `http://www.rssd.esa.int/Planck`.

References

Arnaud, M., Pratt, G. W., Piffaretti, R., et al. 2010, A&A, 517, A92
Bersanelli, M., Mandolesi, N., Butler, R. C., et al. 2010, A&A, 520, A4
Birkinshaw, M. 1999, Phys. Rep., 310, 97
Böhringer, H., Schuecker, P., Pratt, G. W., et al. 2007, A&A, 469, 363
Borgani, S., Murante, G., Springel, V., et al. 2004, MNRAS, 348, 1078
Carlstrom, J. E., Ade, P. A. R., Aird, K. A., et al. 2011, PASP, 123, 568
Carlstrom, J. E., Holder, G. P., & Reese, E. D. 2002, ARA&A, 40, 643
Dobbs, M., Halverson, N. W., Ade, P. A. R., et al. 2006, New A Rev., 50, 960
Górski, K. M., Hivon, E., Banday, A. J., et al. 2005, ApJ, 622, 759
Hand, N., Appel, J. W., Battaglia, N., et al. 2011, 2011, ApJ, 736, 39
Hao, J., McKay, T. A., Koester, B. P., et al. 2010, ApJS, 191, 254
Herranz, D., Sanz, J. L., Hobson, M. P., et al. 2002, MNRAS, 336, 1057
Johnston, D. E., Sheldon, E. S., Tasitsiomi, A., et al. 2007 [`arXiv:0709.1159`]
Koester, B. P., McKay, T. A., Annis, J., et al. 2007a, ApJ, 660, 239
Koester, B. P., McKay, T. A., Annis, J., et al. 2007b, ApJ, 660, 221
Lamarre, J., Puget, J., Ade, P. A. R., et al. 2010, A&A, 520, A9
Leahy, J. P., Bersanelli, M., D'Arcangelo, O., et al. 2010, A&A, 520, A8
Mandelbaum, R., Seljak, U., & Hirata, C. M. 2008a, J. Cosmology Astropart. Phys., 8, 6
Mandelbaum, R., Seljak, U., Hirata, C. M., et al. 2008b, MNRAS, 386, 781
Mandolesi, N., Bersanelli, M., Butler, R. C., et al. 2010, A&A, 520, A3
Marriage, T. A., Acquaviva, V., Ade, P. A. R., et al. 2011, ApJ, 737, 61
Melin, J., Bartlett, J. G., & Delabrouille, J. 2006, A&A, 459, 341
Melin, J., Bartlett, J. G., Delabrouille, J., et al. 2011, A&A, 525, A139
Mennella, A., Butler, R. C., Curto, A., et al. 2011, A&A, 536, A3
Piffaretti, R., Arnaud, M., Pratt, G. W., Pointecouteau, E., & Melin, J. 2011, A&A, 534, A109
Piffaretti, R., & Valdarnini, R. 2008, A&A, 491, 71
Planck Collaboration 2011a, A&A, 536, A1
Planck Collaboration 2011b, A&A, 536, A2
Planck Collaboration 2011c, A&A, 536, A7
Planck Collaboration 2011d, A&A, 536, A8
Planck Collaboration 2011e, A&A, 536, A9
Planck Collaboration 2011f, A&A, 536, A10
Planck Collaboration 2011g, A&A, 536, A11
Planck Collaboration 2011h, A&A, 536, A12
Planck Collaboration 2011i, A&A, 536, A13
Planck Collaboration 2011j, A&A, 536, A14
Planck Collaboration 2011k, A&A, 536, A15
Planck Collaboration 2011l, A&A, 536, A16
Planck Collaboration 2011m, A&A, 536, A17
Planck Collaboration 2011n, A&A, 536, A18
Planck Collaboration 2011o, A&A, 536, A19
Planck Collaboration 2011p, A&A, 536, A20
Planck Collaboration 2011q, A&A, 536, A21
Planck Collaboration 2011r, A&A, 536, A22
Planck Collaboration 2011s, A&A, 536, A23
Planck Collaboration 2011t, A&A, 536, A24
Planck Collaboration 2011u, A&A, 536, A25
Planck Collaboration 2011v, The Explanatory Supplement to the Planck Early Release Compact Source Catalogue (ESA)
Planck Collaboration 2011w, A&A, 536, A26
Planck HFI Core Team 2011a, A&A, 536, A4
Planck HFI Core Team 2011b, A&A, 536, A6
Rosati, P., Borgani, S., & Norman, C. 2002, ARA&A, 40, 539
Rosset, C., Tristram, M., Ponthieu, N., et al. 2010, A&A, 520, A13
Rozo, E., Rykoff, E. S., Evrard, A., et al. 2009, ApJ, 699, 768
Rykoff, E. S., Evrard, A. E., McKay, T. A., et al. 2008a, MNRAS, 387, L28
Rykoff, E. S., McKay, T. A., Becker, M. R., et al. 2008b, ApJ, 675, 1106
Sehgal, N., Trac, H., Acquaviva, V., et al. 2011, ApJ, 732, 44
Sheldon, E. S., Johnston, D. E., Scranton, R., et al. 2009, ApJ, 703, 2217
Staniszewski, Z., Ade, P. A. R., Aird, K. A., et al. 2009, ApJ, 701, 32
Sunyaev, R. A., & Zeldovich, Y. B. 1972, Comments on Astrophys. Space Phys., 4, 173
Swetz, D. S., Ade, P. A. R., Allen, C., et al. 2008, in Presented at the SPIE Conf. Ser., 7020
Szabo, T., Pierpaoli, E., Dong, F., Pipino, A., & Gunn, J. E. 2011, ApJ, 736, 21
Tauber, J. A., Mandolesi, N., Puget, J., et al. 2010, A&A, 520, A1
Vanderlinde, K., Crawford, T. M., de Haan, T., et al. 2010, ApJ, 722, 1180
Voit, G. M. 2005, Rev. Mod. Phys., 77, 207
Wen, Z. L., Han, J. L., & Liu, F. S. 2009, ApJS, 183, 197
Williamson, R., Benson, B. A., High, F. W., et al. 2011, ApJ, 738, 139
York, D. G., Adelman, J., Anderson, Jr., J. E., et al. 2000, AJ, 120, 1579
Zacchei, A., Maino, D., Baccigalupi, C., et al. 2011, A&A, 536, A5

[1] Aalto University Metsähovi Radio Observatory, Metsähovintie 114, 02540 Kylmälä, Finland
[2] Agenzia Spaziale Italiana Science Data Center, c/o ESRIN, via Galileo Galilei, Frascati, Italy
[3] Astroparticule et Cosmologie, CNRS (UMR7164), Université Denis Diderot Paris 7, Bâtiment Condorcet, 10 rue A. Domon et Léonie Duquet, Paris, France
e-mail: `bartlett@apc.univ-paris7.fr`
[4] Astrophysics Group, Cavendish Laboratory, University of Cambridge, J J Thomson Avenue, Cambridge CB3 0HE, UK
[5] Atacama Large Millimeter/submillimeter Array, ALMA Santiago Central Offices, Alonso de Cordova 3107, Vitacura, Casilla 763 0355, Santiago, Chile
[6] CITA, University of Toronto, 60 St. George St., Toronto, ON M5S 3H8, Canada
[7] CNRS, IRAP, 9 Av. colonel Roche, BP 44346, 31028 Toulouse Cedex 4, France
[8] California Institute of Technology, Pasadena, California, USA
[9] Centre of Mathematics for Applications, University of Oslo, Blindern, Oslo, Norway
[10] Centro de Astrofísica, Universidade do Porto, Rua das Estrelas, 4150-762 Porto, Portugal
[11] DAMTP, University of Cambridge, Centre for Mathematical Sciences, Wilberforce Road, Cambridge CB3 0WA, UK
[12] DSM/Irfu/SPP, CEA-Saclay, 91191 Gif-sur-Yvette Cedex, France
[13] DTU Space, National Space Institute, Juliane Mariesvej 30, Copenhagen, Denmark
[14] Departamento de Física, Universidad de Oviedo, Avda. Calvo Sotelo s/n, Oviedo, Spain
[15] Department of Astronomy and Astrophysics, University of Toronto, 50 Saint George Street, Toronto, Ontario, Canada
[16] Department of Physics & Astronomy, University of British Columbia, 6224 Agricultural Road, Vancouver, British Columbia, Canada
[17] Department of Physics and Astronomy, University of Southern California, Los Angeles, California, USA
[18] Department of Physics, Gustaf Hällströmin katu 2a, University of Helsinki, Helsinki, Finland
[19] Department of Physics, Princeton University, Princeton, New Jersey, USA
[20] Department of Physics, Purdue University, 525 Northwestern Avenue, West Lafayette, Indiana, USA
[21] Department of Physics, University of California, Berkeley, California, USA
[22] Department of Physics, University of California, One Shields Avenue, Davis, California, USA
[23] Department of Physics, University of California, Santa Barbara, California, USA
[24] Department of Physics, University of Illinois at Urbana-Champaign, 1110 West Green Street, Urbana, Illinois, USA
[25] Dipartimento di Fisica G. Galilei, Università degli Studi di Padova, via Marzolo 8, 35131 Padova, Italy
[26] Dipartimento di Fisica, Università La Sapienza, P. le A. Moro 2, Roma, Italy
[27] Dipartimento di Fisica, Università degli Studi di Milano, via Celoria, 16, Milano, Italy
[28] Dipartimento di Fisica, Università degli Studi di Trieste, via A. Valerio 2, Trieste, Italy
[29] Dipartimento di Fisica, Università di Ferrara, via Saragat 1, 44122 Ferrara, Italy
[30] Dipartimento di Fisica, Università di Roma Tor Vergata, via della Ricerca Scientifica 1, Roma, Italy
[31] Discovery Center, Niels Bohr Institute, Blegdamsvej 17, Copenhagen, Denmark
[32] Dpto. Astrofísica, Universidad de La Laguna (ULL), 38206 La Laguna, Tenerife, Spain
[33] European Southern Observatory, ESO Vitacura, Alonso de Cordova 3107, Vitacura, Casilla 19001, Santiago, Chile
[34] European Space Agency, ESAC, Planck Science Office, Camino bajo del Castillo, s/n, Urbanización Villafranca del Castillo, Villanueva de la Cañada, Madrid, Spain
[35] European Space Agency, ESTEC, Keplerlaan 1, 2201 AZ Noordwijk, The Netherlands
[36] GEPI, Observatoire de Paris, Section de Meudon, 5 Place J. Janssen, 92195 Meudon Cedex, France
[37] Helsinki Institute of Physics, Gustaf Hällströmin katu 2, University of Helsinki, Helsinki, Finland
[38] INAF – Osservatorio Astronomico di Padova, Vicolo dell'Osservatorio 5, Padova, Italy
[39] INAF – Osservatorio Astronomico di Roma, via di Frascati 33, Monte Porzio Catone, Italy
[40] INAF – Osservatorio Astronomico di Trieste, via G.B. Tiepolo 11, Trieste, Italy
[41] INAF/IASF Bologna, via Gobetti 101, Bologna, Italy
[42] INAF/IASF Milano, via E. Bassini 15, Milano, Italy
[43] INRIA, Laboratoire de Recherche en Informatique, Université Paris-Sud 11, Bâtiment 490, 91405 Orsay Cedex, France
[44] IPAG: Institut de Planétologie et d'Astrophysique de Grenoble, Université Joseph Fourier, Grenoble 1/CNRS-INSU, UMR 5274, 38041 Grenoble, France
[45] Imperial College London, Astrophysics group, Blackett Laboratory, Prince Consort Road, London, SW7 2AZ, UK
[46] Infrared Processing and Analysis Center, California Institute of Technology, Pasadena, CA 91125, USA
[47] Institut Néel, CNRS, Université Joseph Fourier Grenoble I, 25 rue des Martyrs, Grenoble, France
[48] Institut d'Astrophysique Spatiale, CNRS (UMR8617) Université Paris-Sud 11, Bâtiment 121, Orsay, France
[49] Institut d'Astrophysique de Paris, CNRS UMR7095, Université Pierre & Marie Curie, 98 bis boulevard Arago, Paris, France
[50] Institute of Astronomy and Astrophysics, Academia Sinica, Taipei, Taiwan
[51] Institute of Astronomy, University of Cambridge, Madingley Road, Cambridge CB3 0HA, UK
[52] Institute of Theoretical Astrophysics, University of Oslo, Blindern, Oslo, Norway
[53] Instituto de Astrofísica de Canarias, C/vía Láctea s/n, La Laguna, Tenerife, Spain
[54] Instituto de Física de Cantabria (CSIC-Universidad de Cantabria), Avda. de los Castros s/n, Santander, Spain
[55] Jet Propulsion Laboratory, California Institute of Technology, 4800 Oak Grove Drive, Pasadena, California, USA
[56] Jodrell Bank Centre for Astrophysics, Alan Turing Building, School of Physics and Astronomy, The University of Manchester, Oxford Road, Manchester, M13 9PL, UK
[57] Kavli Institute for Cosmology Cambridge, Madingley Road, Cambridge, CB3 0HA, UK
[58] LERMA, CNRS, Observatoire de Paris, 61 Avenue de l'Observatoire, Paris, France
[59] Laboratoire AIM, IRFU/Service d'Astrophysique - CEA/DSM - CNRS - Université Paris Diderot, Bât. 709, CEA-Saclay, 91191 Gif-sur-Yvette Cedex, France
[60] Laboratoire Traitement et Communication de l'Information, CNRS (UMR 5141) and Télécom ParisTech, 46 rue Barrault, 75634 Paris Cedex 13, France
[61] Laboratoire de Physique Subatomique et de Cosmologie, CNRS/IN2P3, Université Joseph Fourier Grenoble I, Institut National Polytechnique de Grenoble, 53 rue des Martyrs, 38026 Grenoble Cedex, France
[62] Laboratoire de l'Accélérateur Linéaire, Université Paris-Sud 11, CNRS/IN2P3, Orsay, France
[63] Lawrence Berkeley National Laboratory, Berkeley, California, USA
[64] Max-Planck-Institut für Astrophysik, Karl-Schwarzschild-Str. 1, 85741 Garching, Germany
[65] Max-Planck-Institut für Extraterrestrische Physik, Giessenbachstraße, 85748 Garching, Germany
[66] MilliLab, VTT Technical Research Centre of Finland, Tietotie 3, Espoo, Finland

[67] National University of Ireland, Department of Experimental Physics, Maynooth, Co. Kildare, Ireland
[68] Niels Bohr Institute, Blegdamsvej 17, Copenhagen, Denmark
[69] Observational Cosmology, Mail Stop 367-17, California Institute of Technology, Pasadena, CA, 91125, USA
[70] Optical Science Laboratory, University College London, Gower Street, London, UK
[71] SISSA, Astrophysics Sector, via Bonomea 265, 34136 Trieste, Italy
[72] SUPA, Institute for Astronomy, University of Edinburgh, Royal Observatory, Blackford Hill, Edinburgh EH9 3HJ, UK
[73] School of Physics and Astronomy, Cardiff University, Queens Buildings, The Parade, Cardiff, CF24 3AA, UK
[74] Space Research Institute (IKI), Russian Academy of Sciences, Profsoyuznaya Str, 84/32, Moscow 117997, Russia
[75] Space Sciences Laboratory, University of California, Berkeley, California, USA
[76] Stanford University, Dept of Physics, Varian Physics Bldg, 382 via Pueblo Mall, Stanford, California, USA
[77] Universität Heidelberg, Institut für Theoretische Astrophysik, Albert-Überle-Str. 2, 69120 Heidelberg, Germany
[78] Université Denis Diderot (Paris 7), 75205 Paris Cedex 13, France
[79] Université de Toulouse, UPS-OMP, IRAP, 31028 Toulouse Cedex 4, France
[80] University of Granada, Departamento de Física Teórica y del Cosmos, Facultad de Ciencias, Granada, Spain
[81] University of Miami, Knight Physics Building, 1320 Campo Sano Dr., Coral Gables, Florida, USA
[82] Warsaw University Observatory, Aleje Ujazdowskie 4, 00-478 Warszawa, Poland

A&A 557, A52 (2013)
DOI: 10.1051/0004-6361/201220941

Astronomy & Astrophysics

Planck intermediate results

XI. The gas content of dark matter halos: the Sunyaev-Zeldovich-stellar mass relation for locally brightest galaxies

Planck Collaboration: P. A. R. Ade[82], N. Aghanim[57], M. Arnaud[71], M. Ashdown[68,7], F. Atrio-Barandela[19],
J. Aumont[57], C. Baccigalupi[81], A. Balbi[36], A. J. Banday[90,10], R. B. Barreiro[65], R. Barrena[64], J. G. Bartlett[1,66],
E. Battaner[92], K. Benabed[58,88], J.-P. Bernard[10], M. Bersanelli[34,50], I. Bikmaev[21,3], J. J. Bock[66,11], H. Böhringer[76],
A. Bonaldi[67], J. R. Bond[9], J. Borrill[14,84], F. R. Bouchet[58,88], H. Bourdin[36], R. Burenin[83], C. Burigana[49,32],
R. C. Butler[49], P. Cabella[37], A. Chamballu[71,16,57], R.-R. Chary[55], L.-Y Chiang[61], G. Chon[76], P. R. Christensen[78,38],
D. L. Clements[54], S. Colafrancesco[46], S. Colombi[58,88], L. P. L. Colombo[25,66], B. Comis[72], A. Coulais[70], B. P. Crill[66,79],
F. Cuttaia[49], A. Da Silva[12], H. Dahle[63], R. J. Davis[67], P. de Bernardis[33], G. de Gasperis[36], A. de Rosa[49], G. de
Zotti[45,81], J. Delabrouille[1], J. Démoclès[71], J. M. Diego[65], H. Dole[57,56], S. Donzelli[50], O. Doré[66,11], M. Douspis[57],
X. Dupac[41], G. Efstathiou[62], T. A. Enßlin[75], F. Finelli[49,51], I. Flores-Cacho[10,90], O. Forni[90,10], M. Frailis[47],
E. Franceschi[49], M. Frommert[18], S. Galeotta[47], K. Ganga[1], R. T. Génova-Santos[64], M. Giard[90,10], Y. Giraud-Héraud[1],
J. González-Nuevo[65,81], K. M. Górski[66,94], A. Gregorio[35,47], A. Gruppuso[49], F. K. Hansen[63], D. Harrison[62,68],
C. Hernández-Monteagudo[13,75], D. Herranz[65], S. R. Hildebrandt[11], E. Hivon[58,88], M. Hobson[7], W. A. Holmes[66],
A. Hornstrup[17], W. Hovest[75], K. M. Huffenberger[93], G. Hurier[72], T. R. Jaffe[90,10], A. H. Jaffe[54], W. C. Jones[27],
M. Juvela[26], E. Keihänen[26], R. Keskitalo[23,14], I. Khamitov[87,21], T. S. Kisner[74], R. Kneissl[40,8], J. Knoche[75],
M. Kunz[18,57,4], H. Kurki-Suonio[26,44], A. Lähteenmäki[2,44], J.-M. Lamarre[70], A. Lasenby[7,68], C. R. Lawrence[66],
M. Le Jeune[1], R. Leonardi[41], P. B. Lilje[63], M. Linden-Vørnle[17], M. López-Caniego[65], P. M. Lubin[29], G. Luzzi[69],
J. F. Macías-Pérez[72], C. J. MacTavish[68], B. Maffei[67], D. Maino[34,50], N. Mandolesi[49,6,32], M. Maris[47], F. Marleau[60],
D. J. Marshall[71], E. Martínez-González[65], S. Masi[33], M. Massardi[48], S. Matarrese[31], P. Mazzotta[36], S. Mei[43,89,11],
A. Melchiorri[33,52], J.-B. Melin[16], L. Mendes[41], A. Mennella[34,50], S. Mitra[53,66], M.-A. Miville-Deschênes[57,9],
A. Moneti[58], L. Montier[90,10], G. Morgante[49], D. Mortlock[54], D. Munshi[82], J. A. Murphy[77], P. Naselsky[78,38], F. Nati[33],
P. Natoli[32,5,49], H. U. Nørgaard-Nielsen[17], F. Noviello[67], D. Novikov[54], I. Novikov[78], S. Osborne[86], C. A. Oxborrow[17],
F. Pajot[57], D. Paoletti[49,51], L. Perotto[72], F. Perrotta[81], F. Piacentini[33], M. Piat[1], E. Pierpaoli[25], R. Piffaretti[71,16],
S. Plaszczynski[69], E. Pointecouteau[90,10], G. Polenta[5,46], L. Popa[59], T. Poutanen[44,26,2], G. W. Pratt[71], S. Prunet[58,88],
J.-L. Puget[57], J. P. Rachen[22,75], R. Rebolo[64,15,39], M. Reinecke[75], M. Remazeilles[57,1], C. Renault[72], S. Ricciardi[49],
I. Ristorcelli[90,10], G. Rocha[66,11], M. Roman[1], C. Rosset[1], M. Rossetti[34,50], J. A. Rubiño-Martín[64,39,⋆], B. Rusholme[55],
M. Sandri[49], G. Savini[80], D. Scott[24], L. Spencer[82], J.-L. Starck[71], V. Stolyarov[7,68,85], R. Sudiwala[82], R. Sunyaev[75,83],
D. Sutton[62,68], A.-S. Suur-Uski[26,44], J.-F. Sygnet[58], J. A. Tauber[42], L. Terenzi[49], L. Toffolatti[20,65], M. Tomasi[50],
M. Tristram[69], L. Valenziano[49], B. Van Tent[73], P. Vielva[65], F. Villa[49], N. Vittorio[36], L. A. Wade[66], B. D. Wandelt[58,88,30],
W. Wang[75], N. Welikala[57], J. Weller[91], S. D. M. White[75], M. White[28], D. Yvon[16], A. Zacchei[47], and A. Zonca[29]

(Affiliations can be found after the references)

Received 17 December 2012 / Accepted 25 June 2013

ABSTRACT

We present the scaling relation between Sunyaev-Zeldovich (SZ) signal and stellar mass for almost 260,000 locally brightest galaxies (LBGs) selected from the Sloan Digital Sky Survey (SDSS). These are predominantly the central galaxies of their dark matter halos. We calibrate the stellar-to-halo mass conversion using realistic mock catalogues based on the Millennium Simulation. Applying a multi-frequency matched filter to the *Planck* data for each LBG, and averaging the results in bins of stellar mass, we measure the mean SZ signal down to $M_* \sim 2 \times 10^{11}\ M_\odot$, with a clear indication of signal at even lower stellar mass. We derive the scaling relation between SZ signal and halo mass by assigning halo properties from our mock catalogues to the real LBGs and simulating the *Planck* observation process. This relation shows no evidence for deviation from a power law over a halo mass range extending from rich clusters down to $M_{500} \sim 2 \times 10^{13}\ M_\odot$, and there is a clear indication of signal down to $M_{500} \sim 4 \times 10^{12}\ M_\odot$. *Planck*'s SZ detections in such low-mass halos imply that about a quarter of all baryons have now been seen in the form of hot halo gas, and that this gas must be less concentrated than the dark matter in such halos in order to remain consistent with X-ray observations. At the high-mass end, the measured SZ signal is 20 % lower than found from observations of X-ray clusters, a difference consistent with the magnitude of Malmquist bias effects that were previously estimated for the X-ray sample.

Key words. cosmology: observations – cosmic background radiation – large-scale structure of Universe – galaxies: clusters: general

---

[⋆] Corresponding author: J. A. Rubiño-Martín (e-mail: `jalberto@iac.es`)

1. Introduction

Galaxy evolution is currently understood to reflect a thermal cycle operating between baryonic components confined in dark matter halos. Gas cools radiatively during the hierarchical build-up of the halo population and condenses to form galaxies in halo cores. Left unchecked, cooling results in more massive galaxies than observed (Balogh et al. 2001; Lin & Mohr 2004; Tornatore et al. 2003), and one must invoke an additional source of non-gravitational heating to prevent a "cooling crisis" (White & Rees 1978; Cole 1991; White & Frenk 1991; Blanchard et al. 1992). Feedback from star formation and supernovae appears insufficient to halt cooling in massive halos (Borgani et al. 2004), so some modelers have invoked additional heating by active galactic nuclei (AGN, Churazov et al. 2002; Springel et al. 2005a; McNamara & Nulsen 2007). Such models show substantially improved agreement with the luminosity-temperature relation of X-ray clusters (Valageas & Silk 1999; Bower et al. 2001; Cavaliere et al. 2002) and the luminosity function of galaxies (Croton et al. 2006; Bower et al. 2006; Somerville et al. 2008). The energetics of AGN feedback imply that it should have especially strong effects on low-mass clusters, heating gas in the central regions and pushing it to larger radii, thereby reducing both gas fractions and X-ray luminosities (Puchwein et al. 2008; McCarthy et al. 2010).

Relationships between the gas, stellar, and dark matter properties of halos are important to our understanding of galaxy formation. Measurements of these relationships over a wide range of halo mass, from rich clusters down to individual galaxies, are therefore a primary objective of a number of current observational campaigns. Recent studies have probed the relationship between the mass of a halo and the stellar mass of its central galaxy (the SHM relation) using "abundance matching" techniques, the dynamics of satellite galaxy populations, and gravitational lensing (Guo et al. 2010; Moster et al. 2010; Mandelbaum et al. 2006; Leauthaud et al. 2012).

Corresponding constraints on the gas content of halos over a similar mass range are not yet available. Although there are many detailed X-ray studies of the intracluster medium, these mostly concern massive clusters; lower mass groups are faint and so are difficult to study individually. The Sunyaev-Zeldovich (SZ) effect (Sunyaev & Zeldovich 1972; Birkinshaw 1999) offers a fresh means to address this problem. Large-area SZ surveys are just beginning to be amassed by ground-based instruments such as the Atacama Cosmology Telescope (ACT, Swetz et al. 2008; Marriage et al. 2011; Sehgal et al. 2011; Hand et al. 2011), the South Pole Telescope (SPT, Carlstrom et al. 2011; Staniszewski et al. 2009; Vanderlinde et al. 2010; Williamson et al. 2011) and APEX-SZ (Dobbs et al. 2006), as well as by the *Planck*[1] satellite mission, (Planck Collaboration 2011c,d,e,f,g).

High signal-to-noise ratio observations of individual objects are not currently possible over the full mass range from galaxy clusters down to individual bright galaxies. The SHM relation can only be estimated for lower mass objects through statistical methods applied to large catalogues. In this context, the SZ effect presents exciting new opportunities. First steps in this direction were taken by Planck Collaboration (2011g) and Hand et al. (2011), with more recent work by Draper et al. (2012) and Sehgal et al. (2013). In our first study (Planck Collaboration 2011g), we binned large numbers of maxBCG (Koester et al. 2007) clusters by richness to measure the relation between mean SZ signal and richness. In a similar manner, Hand et al. (2011) binned ACT measurements of luminous red galaxies to determine the mean relation between SZ signal and LRG luminosity.

Here, we extend our previous work with *Planck* multi-frequency observations of a large sample of locally brightest galaxies (LBGs). These were selected from the Sloan Digital Sky Survey (SDSS) using criteria designed to maximize the fraction of objects that are the central galaxies of their dark matter halos. We stack the *Planck* data in order to estimate the mean SZ signal for LBGs in a series of stellar mass bins. We then use mock galaxy catalogues based on the Millennium Simulation and tuned to fit the observed abundance and clustering of SDSS galaxies to establish the relation between stellar and halo mass. *Planck* is a unique SZ instrument for this purpose because of its large frequency coverage and the fact that it observes the entire SDSS survey area, allowing study of large samples of galaxy systems with extensive multi-wavelength data.

We unambiguously ($>3\sigma$) detect the SZ signal down to stellar masses of $2 \times 10^{11}\ M_\odot$, corresponding to an effective halo mass M_{500} of $2 \times 10^{13}\ M_\odot$ (see Sect. 2) and we find clear indications of signal down to $10^{11}\ M_\odot$ ($M_{500} = 4 \times 10^{12}\ M_\odot$). Detailed simulation both of the galaxy sample and of the *Planck* measurement process allows us to correct the effects of halo miscentering and of the scatter in halo mass at fixed stellar mass when estimating the SZ signal-halo mass relation. We find that the relation is well described by a single power law within its statistical uncertainties. At the high end, our results overlap the mass range probed by X-ray clusters, where we find a 20% lower SZ signal than obtained from fits to X-ray selected cluster samples. This difference is consistent with possible Malmquist bias effects in the X-ray sample. The gas properties of dark matter halos display a remarkable regularity from the poorest groups to the richest clusters.

Throughout this paper, we adopt a fiducial ΛCDM cosmology consistent with the WMAP7 results (Komatsu et al. 2011). In particular, we use $\Omega_\mathrm{m} = 0.272$, $\Omega_\Lambda = 0.728$, $n_\mathrm{s} = 0.961$, and $\sigma_8 = 0.807$. We express the Hubble parameter at redshift z as $H(z) = H_0 E(z)$, with $H_0 = h \times 100\,\mathrm{km\,s^{-1}\,Mpc^{-1}}$ and $h = 0.704$. For the redshift range of interest ($z \lesssim 1$), we approximate $E^2(z) = \Omega_\mathrm{m}(1+z)^3 + \Omega_\Lambda$. The virial radius of a halo is defined here as R_{200}, the radius enclosing a mean density 200 times the critical density at that redshift, i.e., $200 \times \rho_\mathrm{c}(z)$, where $\rho_\mathrm{c}(z) = 3H^2(z)/(8\pi G)$. The virial mass is then defined as

$$M_{200} \equiv 200(4\pi/3)R_{200}^3\rho_\mathrm{c},$$

which we also refer to as M_h. Similarly, we quote the conventional masses M_{500} and radii, R_{500}, when presenting the SZ scalings. For stellar mass, we use the symbol M_*.

The SZ signal is characterized by Y_{500}, the Comptonization parameter integrated over a sphere of radius R_{500}, expressed in square arcminutes. Specifically,

$$Y_{500} \equiv (\sigma_\mathrm{T}/(m_\mathrm{e}c^2)) \int_0^{R_{500}} P\mathrm{d}V/D_\mathrm{A}^2(z),$$

where $D_\mathrm{A}(z)$ is the angular-diameter distance, σ_T is the Thomson cross-section, c is the speed of light, m_e is the electron rest mass, and $P = n_\mathrm{e}kT_\mathrm{e}$ is the pressure, obtained as the product of the electron number density and the electron temperature. Throughout this paper, we use the quantity

$$\tilde{Y}_{500} \equiv Y_{500}E^{-2/3}(z)(D_\mathrm{A}(z)/500\,\mathrm{Mpc})^2,$$

---

[1] *Planck* (`http://www.esa.int/Planck`) is a project of the European Space Agency (ESA) with instruments provided by two scientific consortia funded by ESA member states (in particular the lead countries France and Italy), with contributions from NASA (USA) and telescope reflectors provided by a collaboration between ESA and a scientific consortium led and funded by Denmark.

also expressed in square arcminutes, as the intrinsic SZ signal, scaled to redshift $z = 0$ and to a fixed angular diameter distance.

The paper is organized as follows. Section 2 describes the *Planck* maps used in our analysis, and our reference catalogue of locally brightest galaxies, based on SDSS data. Section 3 describes our methodology. Sections 4 and 5 gives our main results and the tests made to demonstrate their robustness. Sections 6 and 7 contain discussion and conclusions, respectively.

2. Data

2.1. Planck data set

Planck (Tauber et al. 2010; Planck Collaboration 2011a) is the third generation space mission to measure the anisotropy of the cosmic microwave background (CMB). It observes the sky in nine frequency bands covering 30–857 GHz with high sensitivity and angular resolution from 31′ to 5′. The Low Frequency Instrument (LFI; Mandolesi et al. 2010; Bersanelli et al. 2010; Mennella et al. 2011) covers the 30, 44, and 70 GHz bands with amplifiers cooled to 20 K. The High Frequency Instrument (HFI; Lamarre et al. 2010; Planck HFI Core Team 2011a) covers the 100, 143, 217, 353, 545, and 857 GHz bands with bolometers cooled to 0.1 K. Polarisation is measured in all but the highest two bands (Leahy et al. 2010; Rosset et al. 2010). A combination of radiative cooling and three mechanical coolers produces the temperatures needed for the detectors and optics (Planck Collaboration 2011b). Two data processing centres (DPCs) check and calibrate the data and make maps of the sky (Planck HFI Core Team 2011b; Zacchei et al. 2011). *Planck*'s sensitivity, angular resolution, and frequency coverage make it a powerful instrument for Galactic and extragalactic astrophysics as well as for cosmology. Early astrophysics results are given in Planck Collaboration VIII–XXVI 2011, based on data taken between 13 August 2009 and 7 June 2010. Intermediate astrophysics results are now being presented in a series of papers based on data taken between 13 August 2009 and 27 November 2010.

2.2. A locally brightest galaxy catalogue

To select a sample of central galaxies, we first define a parent population with $r < 17.7$ (r-band, extinction-corrected, Petrosian magnitude) from the spectroscopic galaxy catalogue of the New York University Value Added Galaxy Catalogue[2]. This was built by Blanton et al. (2005) based on the seventh data release of the Sloan Digital Sky Survey (SDSS/DR7 Abazajian et al. 2009). This parent catalogue contains 602 251 galaxies. We then define "locally brightest galaxies" to be the set of all galaxies with $z > 0.03$ that are brighter in r than all other sample galaxies projected within 1.0 Mpc and with redshift differing by less than 1000 km s^{-1}. After this cut 347 486 locally brightest galaxies remain.

The SDSS spectroscopic sample is incomplete because it proved impossible to place a fibre on every object satisfying the photometric selection criteria, and because some spectra failed to give acceptable redshifts. The completeness to our chosen magnitude limit varies with position, with a mean of 91.5% over the survey as a whole. To ensure that galaxies without SDSS spectroscopy do not violate our sample selection criteria, we have used SDSS photometry to eliminate all objects with a companion that is close and bright enough that it might violate the above criteria. Specifically, we have used the "photometric redshift 2" catalogue (photoz2 Cunha et al. 2009) from the SDSS DR7 website to search for additional companions. This catalogue tabulates a redshift probability distribution in bins of width $\Delta z = 0.0145$ for every galaxy down to photometric limits much fainter than we require. We then eliminate any candidate with a companion in this catalogue of equal or brighter r-magnitude and projected within 1.0 Mpc, unless the photometric redshift distribution of the "companion" is inconsistent with the spectroscopic redshift of the candidate. (Our definition of "inconsistent" is that the total probability for the companion to have a redshift equal to or less than that of the candidate is less than 0.1; in practice this eliminates "companions" that are too red to be at a redshift as low as that of the candidate.) This procedure leaves us with a cleaned sample of 259 579 locally brightest galaxies.

The NYU-VAGC provides a variety of data for each galaxy. In addition to the positions, magnitudes, and redshifts used to create our sample, we will make use of rest-frame colours and stellar masses. The latter are based on stellar population fits to the five-band SDSS photometry and on the measured redshifts, assuming a Chabrier (2003) stellar initial mass function (Blanton & Roweis 2007). The estimated (statistical) error in these stellar masses, arising from photometric uncertainties and template mismatches, is ~0.1 dex. In Fig. 1 we compare the colour and redshift distributions of our final sample of locally brightest galaxies to those of the parent sample for five disjoint ranges of stellar mass. For $\log_{10} M_*/M_\odot \geq 10.8$, the distributions are similar for the two populations. At lower stellar mass, locally brightest galaxies are a small fraction of the parent sample and are biased to bluer colours and to slightly larger redshifts. In our stacking analysis below, we obtain significant SZ signals only for galaxies with $\log_{10} M_*/M_\odot \geq 11.0$. Our sample contains 81 392 galaxies satisfying this bound, the great majority of them on or near the red sequence.

2.2.1. The reliability of our central galaxy sample and its stellar mass-halo mass relation

We expect the majority of our locally brightest galaxies to be the central galaxies of their dark matter halos, just as bright field galaxies lie at the centres of their satellite systems and cD galaxies lie near the centres of their clusters and are normally their brightest galaxies. For our later analysis, it is important to know both the reliability of our galaxy sample, i.e., the fraction of galaxies that are indeed the central galaxies of their halos, and the relation between the observable stellar masses of the galaxies and the unobservable masses of their halos. In this section we investigate both issues using an update of the publicly available[3] semi-analytic galaxy formation simulation of Guo et al. (2011). The update uses the technique of Angulo & White (2010) to rescale the Millennium Simulation (Springel et al. 2005b) to the WMAP7 cosmology, then readjusts the galaxy formation parameters to produce a $z = 0$ galaxy population with abundance and clustering properties that are almost indistinguishable from those of the original model. At the relatively high masses relevant for our work, this simulation provides a very close match to the observed luminosity and stellar mass functions of the SDSS as well as to the auto-correlations of SDSS galaxies as a function of stellar mass (Guo et al. 2013).

We construct a sample of locally brightest galaxies from this simulation using criteria exactly analogous to those used for the measured data. We project the galaxy distribution onto one of

---

[2] NYU-VAGC, `http://sdss.physics.nyu.edu/vagc/`

[3] `http://www.mpa-garching.mpg.de/millennium`

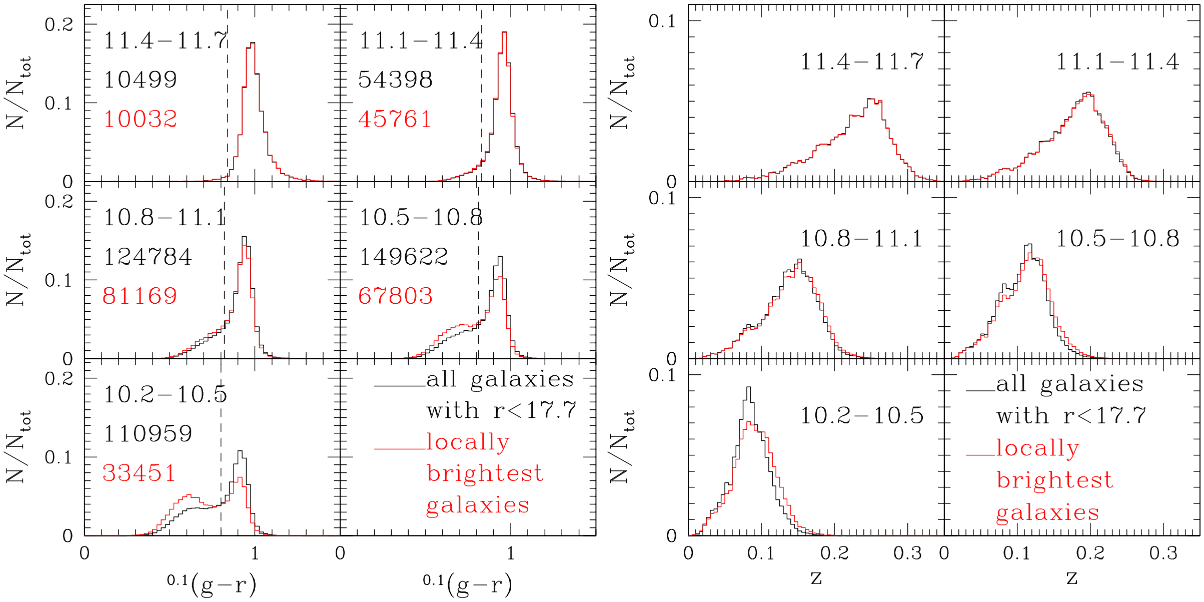

Fig. 1. Distributions in colour (*left*) and redshift (*right*) of our locally brightest galaxies and of the SDSS/DR7 population from which they were drawn. Black histograms refer to the parent sample and red histograms to the locally brightest galaxies. The panels in each set correspond to five disjoint ranges of $\log_{10} M_*/M_\odot$, as indicated in the labels. In the left-hand set, additional labels give the number of galaxies contributing to the parent (black) and locally brightest (red) histograms. Dashed vertical lines in these same panels indicate the colour we use to separate red and blue galaxies in Fig. 3 below.

the faces of the simulation cube and assign each galaxy a redshift based on its distance and peculiar velocity in the projection direction. A galaxy is considered locally brightest if it has no neighbour that is brighter in r within 1.0 Mpc projected distance and 1000 km s^{-1} in redshift. We divide galaxies into "centrals", defined as those lying at the minimum of the gravitational potential of the dark matter friends-of-friends (FoF) group with which they are associated, and "satellites", defined as all other galaxies.

With these definitions we can assess the fraction of our locally brightest galaxies that are truly central galaxies. The black line in Fig. 2 shows, as a function of stellar mass, the fraction of *all* galaxies in the simulation that are centrals. At stellar masses just above $10^{10}\ M_\odot$ this fraction is about one half, but it increases with stellar mass, reaching two thirds by $\log_{10} M_*/M_\odot = 11.0$ and 90% by $\log_{10} M_*/M_\odot = 11.8$. In contrast, the fraction of locally brightest galaxies that are centrals is much higher, with a minimum of just over 83% at stellar masses somewhat above $10^{11}\ M_\odot$. We have checked those locally brightest galaxies that are satellites, finding that for $\log_{10} M_*/M_\odot > 11$, about two-thirds are brighter than the true central galaxies of their halos. The remainder are fainter than their centrals, and are considered locally brightest because they are more than 1 Mpc (projected) from their centrals (60%) or have redshifts differing by more than 1000 km s^{-1} (40%).

We can assign a halo mass, M_{200}, to every galaxy in our simulation. For both satellite galaxies and central galaxies, we take M_{200} to be the current M_{200} of the FoF dark matter halo with which the object is associated, i.e., the mass contained within its R_{200}. Figure 3 shows a scatter plot of M_{200} against M_* for a random subset (one out of every 80) of our sample of simulated locally brightest galaxies. We indicate central galaxies with red or blue points according to their rest-frame $g - r$ colour (with the two distinct regions separated by the vertical dashed lines in the left panel of Fig. 1) while satellite galaxies are indicated by black points. Clearly, red (passive) and blue (star-forming) central galaxies lie on different M_{200}-M_* relations. That for passive galaxies is steeper, and is offset to larger halo mass in the stellar mass range where both types of central galaxy are present.

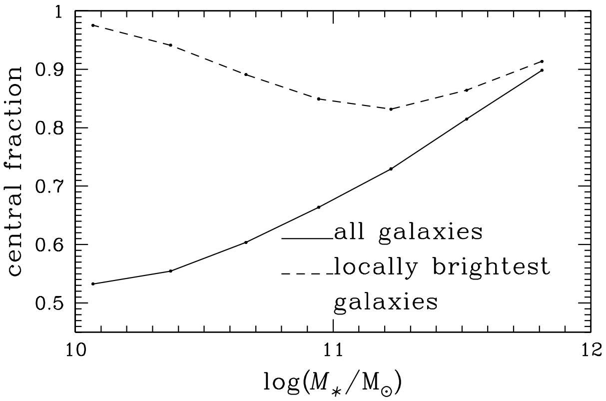

Fig. 2. Fraction of locally brightest galaxies that are the central objects in their dark halos, based on the simulations of Guo et al. (2011). The solid line traces the fraction of *all* simulated galaxies that are central galaxies as a function of stellar mass. This fraction increases with stellar mass, reaching 90% at the high mass end. The dashed line presents the central galaxy fraction for locally brightest galaxies selected from the simulation according to the criteria applied to the SDSS data. This yields a sample that is over 83% reliable at all stellar masses.

Satellite galaxies lie in halos in the massive tail of the distribution for central galaxies of the same stellar mass. Satellites misidentified as centrals in our catalogue are usually outlying members projected at relatively large separation (from a few hundred kiloparsecs to 2 Mpc). Their presence bias high both the

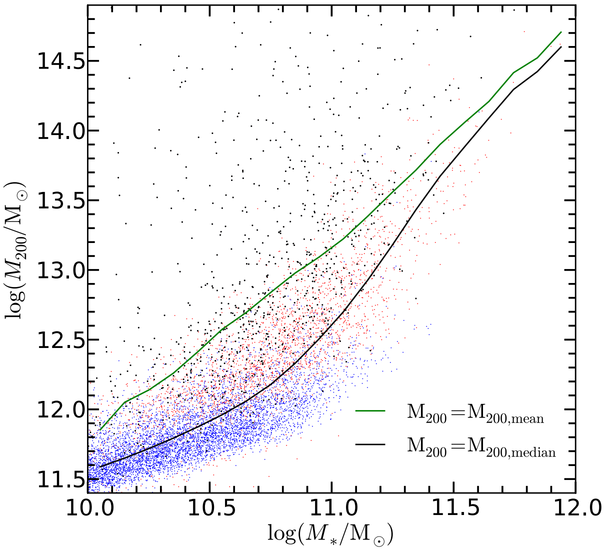

Fig. 3. Scatter plot of M_{200} against M_* for a random subset (one out of 80) of our sample of simulated locally brightest galaxies. Central galaxies are shown as red or blue points according to their $g - r$ colour, using the cuts indicated in Fig. 1. Satellite galaxies are shown as black points. The lower and upper curves give the median and mean values of halo mass as a function of stellar mass.

mean halo mass (the high black points in Fig. 3) and the spatial extent of the stacked SZ signals we measure below. However, since two thirds of the satellites that we misidentify as central galaxies are in fact brighter than the true central galaxies of their halos (i.e., they are not typical satellites), this bias is not extreme. In any case, we correct for these effects explicitly in our analysis using the simulation.

The lower of the two continuous curves in Fig. 3 shows the median M_{200} as a function of M_*. We will take this as an estimate of the typical halo mass associated with a central galaxy of known M_*, and will use it to set the angular size of the matched filter for each observed galaxy when stacking SZ signal as a function of stellar mass. The upper continuous curve shows the mean M_{200} as a function of M_*. The substantial shift between the two is a measure of the skewness induced by the differing relations for passive and star-forming centrals and by the presence of the tail of cluster satellite galaxies (see Appendix B).

3. Analysis

Our analysis closely follows that presented in Planck Collaboration (2011e), Planck Collaboration (2011f), and Planck Collaboration (2011g), employing as primary method a multi-frequency matched filter (MMF) optimized in both frequency and angular space to extract the thermal SZ signal (Herranz et al. 2002; Melin et al. 2006). We find that dust emission from our target sources affects the MMF measurements noticeably at low stellar mass, and that an effective mitigation is to restrict our final measurements to the three lowest HFI frequencies (100, 143, and 217 GHz). This is detailed in Sect. 5. Our primary scientific results are hence all based on this three-band MMF.

For the SZ model template, we employ, as in earlier work (Planck Collaboration 2011e,f,g), the so-called "universal pressure profile" (Arnaud et al. 2010) deduced from X-ray observations of the REXCESS cluster sample (Böhringer et al. 2007). For an easier comparison with the X-ray results, our scaling relations will be presented in terms of M_{500}. The R_{500} value associated with the halo of each central galaxy is obtained as follows. We first use the SHM relation giving the median halo M_{200} as a function of central galaxy stellar mass, as presented in Sect. 2.2.1. Then, using an NFW profile (Navarro et al. 1997) and the concentration parameter c_{200} given by Neto et al. (2007), we convert M_{200} to M_{500} and derive R_{500} for each halo. The angular scale for the filter is finally given by projecting R_{500} at the redshift of the target LBG. We have checked that different choices of the concentration parameter (see e.g. Duffy et al. 2008) produce changes on M_{500} at the level of few percent, within our modeling uncertainty.

In addition to the MMF, and in order to test the robustness of the results, the impact of foreground contamination and possible systematic effects, we have also implemented aperture photometry (hereafter AP). For the AP, given an object of certain angular size R, the method evaluates the mean temperature in a circle of radius $r = R$ and subtracts from it the average found in a surrounding ring of inner and outer radii $r = R$ and $r = fR$, respectively, with $f > 1$ (see e.g., Hernández-Monteagudo & Rubiño-Martín 2004). By removing the mean temperature in the outer region, the method corrects for large-scale fluctuations in the background. Once the temperature estimates are derived for each frequency map, they are combined with inverse-variance weighting to derive an SZ signal estimate by using the known frequency dependence of the (non-relativistic) thermal SZ effect. Our choice for the two parameters of the AP method is $(R, f) = (\mathrm{FWHM}, \sqrt{2})$. Note that the FWHM varies from one frequency band to another. We also note that the flux estimates within the aperture have to be corrected separately at each frequency by an appropriate factor in order to obtain the total flux of the source. For example, if the objects are unresolved and we assume Gaussian beams, then this correction factor is $(1 + \exp(-8 \ln 2) - \exp(-4 \ln 2))^{-1}$ for the above choice of R and f. For extended objects (e.g., those objects with R_{500} larger than the beam size, and which are modeled here using the "universal pressure profile"), the conversion factor can be evaluated numerically.

Using one of these methods (MMF or AP), we obtain a measure of the intrinsic SZ signal strength $\tilde{Y}_{500}(i)$ and the associated measurement uncertainty $\tilde{\sigma}_{\theta_{500}}(i)$ for the halo of each galaxy i. The majority of these individual SZ measurements have low signal-to-noise ratio. Following the approach in Planck Collaboration (2011e) and Planck Collaboration (2011g), we bin them by stellar mass, calculating the bin-average signal $\langle \tilde{Y}_{500} \rangle_b = [\sum 1/\tilde{\sigma}^2_{\theta_{500}}(i)]^{-1} \sum_{i=1}^{N_b} \tilde{Y}_{500}(i)/\tilde{\sigma}^2_{\theta_{500}}(i)$, with uncertainty $\sigma_b^{-2} = \sum_{i=1}^{N_b} 1/\tilde{\sigma}^2_{\theta_{500}}(i)$, where N_b is the number of galaxies in bin b.

4. Results

Our main observational result is given in Fig. 4 and Table 1, showing the mean SZ signal measured using the three-band MMF for locally brightest galaxies binned according to stellar mass. In the plot, the thick error bars show the uncertainty propagated from the individual measurement errors as described above, while the thin bars with large terminators give the variance of the weighted bin-average signal found by a bootstrap resampling. For the latter, we constructed 1,000 bootstrap realizations of the original LBG catalogue and performed the full analysis on each.

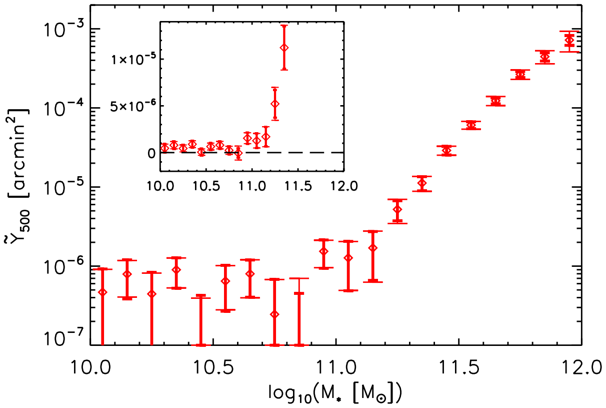

Fig. 4. Mean SZ signal vs. stellar mass for locally brightest galaxies. Thick error bars trace the uncertainty on the bin average due purely to measurement error, while thin bars with large terminators show the variance calculated by bootstrap resampling and so also include the intrinsic scatter in the signal. The inset provides a view on a linear scale to better evaluate the significance of the detections. We observe a clear relation between the mean SZ signal and stellar mass down to $\log_{10}(M_*/M_\odot) = 11.25$ (the detection in this bin is at 3.5σ), with a suggestion of signal to lower mass: the next three bins show signal at 1.6σ, 1.6σ and 2.6σ, respectively.

Table 1. *Planck* SZ signal measurements $\tilde{Y}_{500}$ binned by stellar mass (adopting a WMAP7 cosmology). These data are displayed in Fig. 4.

$\log_{10}\left(\frac{M_*}{M_\odot}\right)$	$\tilde{Y}_{500}$ [10^{-6} arcm^2]	Errors [10^{-6} arcm^2] Statistical	Bootstrap
10.05	0.47	±0.45	±0.44
10.15	0.79	±0.41	±0.39
10.25	0.44	±0.39	±0.37
10.35	0.90	±0.37	±0.37
10.45	0.05	±0.37	±0.34
10.55	0.65	±0.38	±0.37
10.65	0.80	±0.39	±0.40
10.75	0.25	±0.43	±0.43
10.85	−0.05	±0.50	±0.75
10.95	1.54	±0.60	±0.58
11.05	1.27	±0.78	±0.78
11.15	1.7	±1.0	±1.1
11.25	5.2	±1.5	±1.8
11.35	11.2	±2.3	±2.4
11.45	29.0	±3.6	±3.8
11.55	60.7	±6.2	±6.8
11.65	123	±11	±16
11.75	266	±23	±36
11.85	445	±53	±84
11.95	721	±103	±210

The inset uses a linear scale to better display the significance of our detections. We have a clear signal down to the bin at $11.2 < \log_{10}(M_*/M_\odot) < 11.3$, centred at $M_* = 1.8 \times 10^{11}\ M_\odot$. The next three bins provide evidence that the signal continues to lower mass with "detections" significant at the 1.6σ, 1.6σ and 2.6σ levels, from high to low mass, respectively. The last bin is centered at $M_* = 9 \times 10^{10}\ M_\odot$, corresponding to a mean halo mass of $M_{200} \sim 1.4 \times 10^{13}\ M_\odot$. These last three bins, however, are more seriously affected by dust contamination, as discussed below, and for this reason may be more uncertain than these statistical measures suggest.

5. Systematic errors

In this section, we present a number of tests of the robustness of our principal result against systematic error. In the following, unless otherwise stated, all results use data at 100, 143, and 217 GHz only.

5.1. Stacking real-space reconstructed SZ maps

According to Fig. 4, the lowest bin at which we have a $>3\sigma$ detection is the one at $\log_{10}(M_*/M_\odot) = 11.25$. As a consistency check, and also as an illustration of the frequency dependence of the detected SZ signal, Fig. 5 shows stacked images of central galaxies in six different mass bins of width $\Delta \log_{10} M_* = 0.2$ centred at $\log_{10}(M_*/M_\odot) = 11.05, 11.15, 11.25, 11.35, 11.45$, and 11.55.

The stacked maps are obtained, using equal weights, from a (full-sky) SZ map constructed from the *Planck* 100, 143, 217, and 353 GHz maps using a modified internal linear combination algorithm (MILCA, Hurier et al. 2013) that has been used for other *Planck* Intermediate Papers (e.g., Planck Collaboration 2012a,b). The well-known internal linear combination approach (e.g., Eriksen et al. 2004) searches for the linear combination of the input maps that minimises the variance of the final reconstructed map while imposing spectral constraints. This preserves the thermal SZ signal and removes the CMB contamination (using the known spectral signatures of the two components) in the final SZ map. The resulting map used for this analysis has an angular resolution (FWHM) of 10′. We have checked that almost identical maps are obtained with other methods.

The SZ signal is clearly visible in all panels with $\log_{10}(M_*/M_\odot) \geq 11.25$. The stacked maps show no sign of a gradient in the residual signal in the vertical direction, showing that the MILCA method is very effective in removing Galactic emission. Below the mass limit of 11.25, there is also some evidence of SZ signal, although here the contrast relative to the noise is lower. Finally, we note that the signal in the lower stellar mass panels is extended. This is mainly due to the larger satellite fraction at these masses that results in a significant contribution to the stack from relatively massive halos with centres significantly offset from the locally brightest galaxy (see Figs. 2, 3 and Appendix C). We also discuss in Appendix C the impact of dust contamination on these maps.

5.2. Null tests

Null tests used to check for systematic errors are shown in Fig. 6. Taking the set of MMF filters adapted to each target galaxy, we shift their positions on the sky, either with a random displacement (i.e., by generating a random distribution of new positions isotropically distributed outside our Galactic mask) or by shifting all coordinates one degree in declination, and rerunning our analysis. In both cases the result should be zero. The shifted filter sets indeed have bin-average SZ signals consistent with zero over the entire mass range.

5.3. Size effects

Although most of the halos traced by our locally brightest galaxies are, according to their inferred R_{500} values, at most

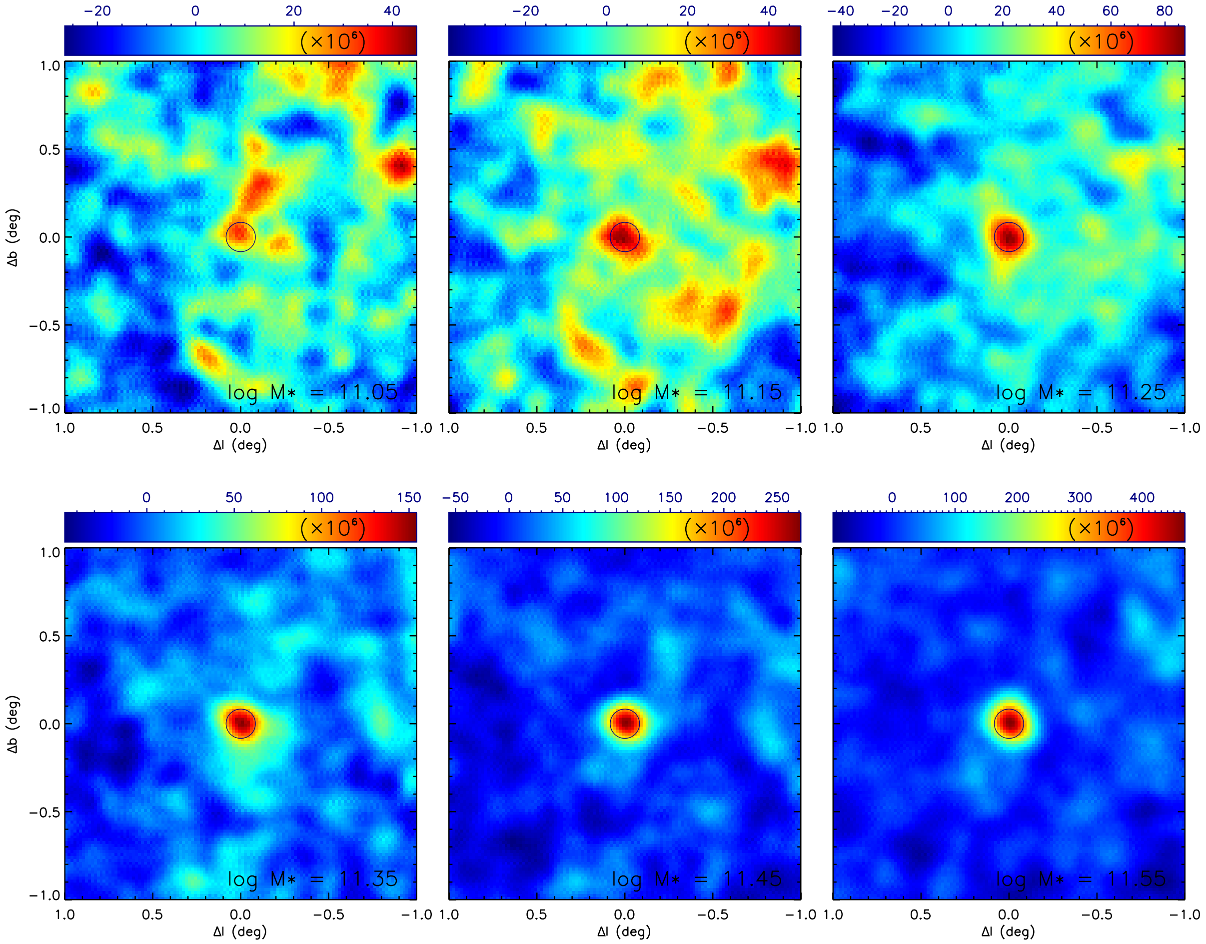

Fig. 5. Equal-weighted stacks of reconstructed SZ maps (i.e., Comptonization parameter maps) for objects in six mass bins centred, from *left to right* and *top to bottom*, at $\log_{10}(M_*/M_\odot)$ = [11.05, 11.15, 11.25, 11.35, 11.45, 11.55]. In all cases, the bin size is taken to be 0.2, so the galaxies in two consecutive panels partially overlap. Maps are 2° on a side, with Galactic north at the top. The SZ signal traced by the central galaxies is clearly detected in all bins above $\log_{10}(M_*/M_\odot) = 11.25$. In all panels, the circles indicate the FWHM of the data, which corresponds to 10′.

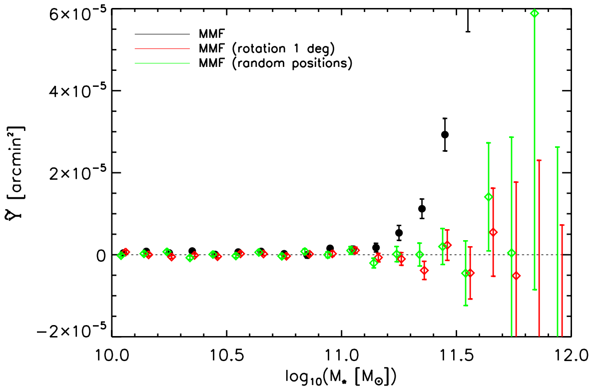

Fig. 6. Null tests performed on the locally brightest galaxy sample. Red points correspond to placing the filter one degree in declination away from the position of each LBG, while green points correspond to random high latitude filter positions. Both sets are consistent with zero. The black points show our measurements with filters centred on the LBG sample, demonstrating highly significant detections.

marginally resolved by the *Planck* beams, size effects are not negligible, and the full pressure profile has to be used for the flux determination. If instead the objects are (incorrectly) assumed to be point-like, we find that the flux is underestimated by roughly 20–30%, although the slope of the $\tilde{Y}_{500}$-M_* scaling relation is practically unaffected.

5.4. Photometry comparison

Figure 7 compares the SZ signal extracted for our LBG sample by the two photometry methods described above, namely MMF and AP. Here, we compare the total SZ flux from MMF (computed as $\tilde{Y}_{5R_{500}}$) with the total flux recovered from the AP method, after applying the correction factors described in Sect. 3. For simplicity, we assume point-like objects for the flux extraction in this analysis. This is why the MMF data points differ from the corresponding points in Fig. 4. For the AP, we also compare the nominal four-band analysis with a three-band case to illustrate the impact of residual foregrounds on our flux estimates. When the 353 GHz channel is included, the AP flux

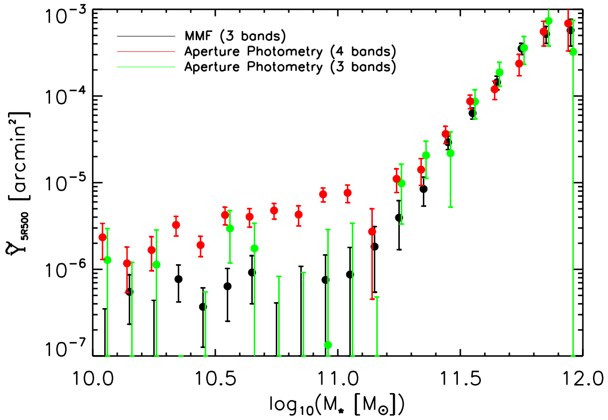

Fig. 7. Comparison of the SZ measurements on the full locally brightest galaxy sample for two different photometry methods: the matched multi-filter (MMF) and the aperture photometry (AP) approach. For this figure and only for this figure, we assume point-like objects for both methods and plot the derived total SZ flux (or the flux within $5\,R_{500}$ for MMF). The signal detected by the two methods is consistent at all stellar masses when only three frequencies are used, but when four frequencies are used, the AP results are contaminated by high frequency emission at stellar masses below $\sim 2\times10^{11}\ M_\odot$.

estimates at low stellar-mass are biased towards high SZ values. This indicates contaminating high-frequency emission associated with the sources, presumably dust in the LBGs or their satellites. We discuss this issue further in Sect. 5.5.

The main conclusion is that the two methods, despite their different data processing approaches, produce fully consistent results for $\log_{10}(M_*/M_\odot) \gtrsim 11.25$, while the results start to show a dependence on the method for stellar masses below that limit.

5.5. Dust contamination

The analysis of the last section suggests that our SZ signal estimates may be contaminated by residual dust emission that increases with frequency and could bias our primary results. To evaluate the potential effects, we have performed measurements using three different MMFs, as shown in Fig. 8. The green triangles and red diamonds represent the results of using all six HFI channels or only the lowest three (100, 143, 217 GHz), respectively. In both cases there is no explicit allowance for a possible dust contribution. The blue crosses show results for a modified six-band MMF that includes amplitude fits not only to the SZ spectrum, but also to a fiducial thermal dust spectrum.

The three sets of measurements fully agree for the stellar masses for which we unambiguously detect the SZ signal, $\log_{10} M_*/M_\odot \geq 11.25$. This indicates that dust emission does not significantly affect our results for these stellar mass bins. At lower mass the three-band results and the dust-corrected six-band results remain consistent, but the six-band results without explicit dust correction are systematically different. Dust emission is clearly sufficient to contaminate our six-band filter estimates of SZ signal if uncorrected, but it does not appear to be a major problem when only the lower three frequency bands are used. The residual dust contribution estimated from the scatter and offset of the red and blue points for $\log_{10} M_*/M_\odot < 11.0$ is below $\sim 10^{-6}$ arcmin² and so lies comfortably below our measured signal.

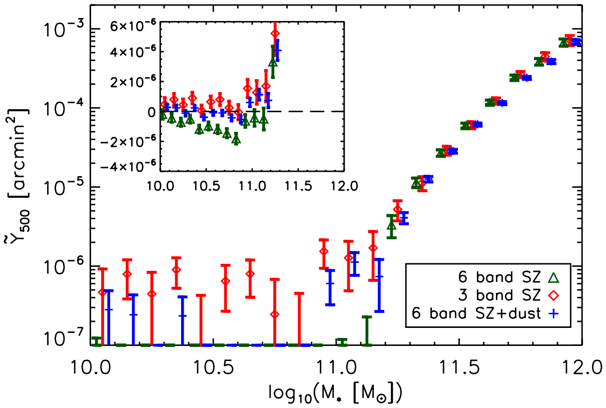

Fig. 8. Impact of dust contamination on our SZ measurements. Three cases are shown: a 6-band MMF (all *Planck* HFI frequencies) with no explicit allowance for a dust contribution (green triangles), a 3-band MMF also with no explicit dust modelling (red diamonds); and a modified 6-band MMF that includes an amplitude fit to a fiducial dust spectrum (blue crosses). The error bars include measurement uncertainties only. For stellar masses where we clearly detect the signal (i.e., at $\log_{10} M_*/M_\odot > 11.25$), the three measurements agree, indicating that dust emission does not significantly affect those measurements. At lower masses the 3-band results are consistent with the 6-band results when dust is explicitly included in the modelling, but not otherwise.

There is a clear indication of signal in the three bins just below $\log_{10} M_*/M_\odot = 11.25$ both for the three-band MMF and for the dust-corrected six-band MMF. However, the dust-corrected results appear systematically lower than the (uncorrected) three-band results by an amount similar to that seen at lower masses where the SZ signal is undetected. Further, the six-band MMF measurements without dust correction (the green triangles) differ substantially for these (and all lower) bins. This suggests that dust emission affects these stellar mass bins noticeably even for the three-band MMF, so the corresponding points in Fig. 4 may be more uncertain than indicated by their statistical error bars. Although formally the dust-corrected six-band MMF would appear to give our most accurate estimates of stacked SZ signal, we are uncertain whether the fiducial dust spectrum it assumes is appropriate for these specific sources. Therefore we conservatively quote results based on the three-band MMF, using the dust-corrected six-band results to give an estimate of remaining dust-related systematics.

Finally, we note that residual dust contamination biases the (uncorrected) six-band MMF signal estimates for $\log_{10} M_*/M_\odot < 11$ (Fig. 8) in the opposite direction to the AP signal estimates (see Fig. 7). The agreement of the two methods for $\log_{10} M_*/M_\odot > 11.25$ is thus a further indication of the robustness of our primary results.

5.6. Stability of the signal in different sky surveys

We have also checked that the SZ signal is stable against splitting the *Planck* data into complementary subsets. For instance, the signal obtained from the maps of the first 6 months of observing time is fully consistent with that obtained from maps of the second 6 months and the last 3.5 months (of course the latter has larger error bars due to its smaller sky coverage).

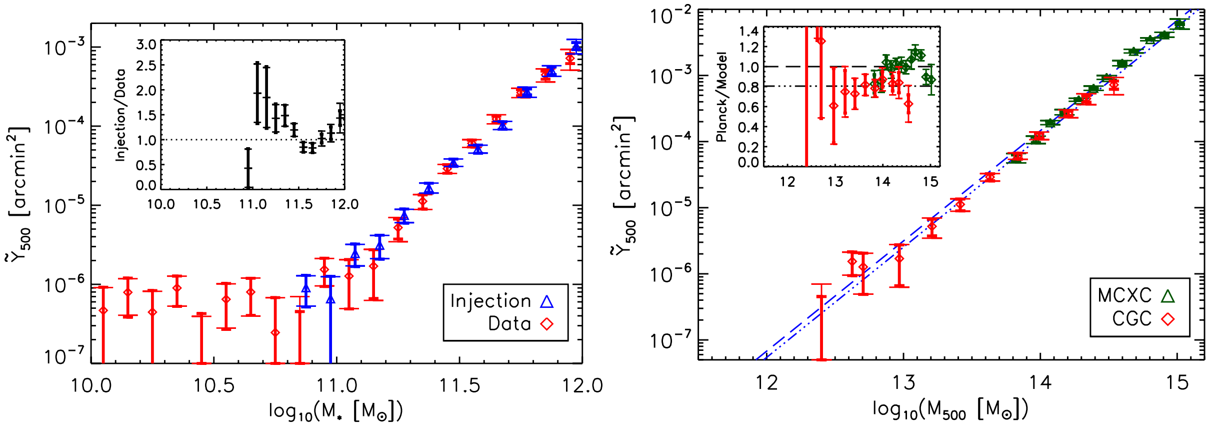

Fig. 9. *Left*: comparison of the measured mean SZ signal as a function of LBG stellar mass (red points) to simulated observations (blue points). The simulations assign to each observed LBG the halo mass and positional offset of a randomly chosen simulated LBG of the same stellar mass (compare Fig. 3). Our best fit Y_{500}-M_{500} scaling relation is then used, together with the universal pressure profile, to inject a simulated signal into the *Planck* maps (see text). An "observed" signal is obtained by applying the MMF exactly as for the real data. The inset gives the ratio of the bin-averaged injected and actual signals. *Right*: mean SZ signal as a function of effective halo mass. The bin-averaged SZ signal measurements of the left panel have been translated to this plane using the simulations as described in the text (the red points). The dot-dashed line is our best fit relation between halo mass and SZ signal, i.e., the one leading to the simulated measurements in the *left panel*. The green points give the mean SZ signal of MCXC clusters binned by a halo mass estimated from their X-ray luminosity using the REXCESS relation without correction for Malmquist bias (line 3 in Table 2 of Planck Collaboration 2011e). The dashed blue line shows the self-similar model calibrated on the REXCESS sample as given by Arnaud et al. (2010). The inset gives the ratio of all measurements to this model's predictions. As in previous figures, the thick error bars account only for measurement uncertainties, while thin bars with large terminators result from a bootstrap analysis and so include intrinsic scatter effects.

6. The Y_{500}-M_{500} relation

We now turn to the interpretation of our measurements in terms of the SZ signal-halo mass scaling relation: Y_{500}-M_{500}. Our conclusions are summarised in Fig. 9.

From our simulation of the locally brightest galaxy catalogue, we expect a large range of halo masses within a given bin of stellar mass and, in addition, a fraction of galaxies that are, in fact, satellites, with significant positional offsets relative to their host halo (see Fig. 3). These effects impact our measurements of the SZ signal-stellar mass relation in two ways. First, the MMF is not perfectly matched to each individual object because we fix the filter scale to the median halo size. This causes an aperture-induced bias in the flux measurement. Second, our filter is miscentred for those systems where the LBG is, in fact, a satellite. These galaxies are often associated with substantially more massive dark halos than typical LBGs of the same stellar mass, leading to an increase in the mean signal in the bin, mitigated by the substantial angular offsets of most such satellites from the true centres of their rich clusters. This increases the apparent extent of the signal in stacked maps like Fig. 5, but decreases the contribution to the signal through a matched filter centred on the galaxy (see Appendix C).

Using our simulation of the LBG catalogue, we can account fully for these effects and extract the underlying Y_{500}-M_{500} relation in an unbiased way. Within each stellar mass bin, we identify each observed LBG with a randomly chosen simulated LBG of the same stellar mass, assigning it the halo mass and positional offset from halo centre of its partner, but retaining its observed redshift. We give each halo a SZ signal distributed according to the "universal pressure profile" and normalized using a specific model Y_{500}-M_{500} scaling relation. Each synthesised object is then observed with the three-band MMF centred on the galaxy's position, and the measurements are binned and weighted in the same way as the real data to obtain $\langle Y \rangle_{\rm s}$.

This procedure enables us to translate a model Y_{500}-M_{500} relation to our observational plane, Y_{500}-M_*, and thus to fit for the underlying scaling relation with halo mass M_{500}. We model this relation as

$$\tilde{Y}_{500} = Y_{\rm M} \left(\frac{M_{500}}{3 \times 10^{14}\, M_\odot} \right)^{\alpha_{\rm M}}, \tag{1}$$

fixing the mass exponent to its self-similar value, $\alpha_{\rm M} = 5/3$, and fitting for the normalization $Y_{\rm M}$. Restricting the fit to $\log_{10}(M_*/M_\odot) \gtrsim 11.5$, for direct comparison to X-ray samples in the discussion below, we find

$$Y_{\rm M} = (0.73 \pm 0.07) \times 10^{-3}\ {\rm arcmin}^2. \tag{2}$$

In the left-hand panel of Fig. 9, the red points reproduce the measurements given in Fig. 4, while the blue points show the simulated observations for this best-fit Y_{500}-M_{500} scaling relation.

The best-fit is, however, formally unacceptable, with a reduced χ^2_ν of 3, which we can more readily appreciate from the inset showing the ratio of the actual observations to the simulated bin averages on a linear scale. The data prefer a shallower slope than the self-similar $\alpha_{\rm M} = 5/3$ over the mass range of the fit. Moreover, we see that a power law cannot fit the data over the full mass range probed by our measurements. To ease comparison with the X-ray sample, we will nevertheless adopt this fit below.

The right-hand panel of Fig. 9 considers the SZ signal-halo mass plane. The blue dot-dashed line simply traces our best-fit Y_{500}-M_{500} relation. The blue dashed line is the self-similar relation derived from X-ray cluster studies in the mass range 10^{14}–10^{15} $M_\odot$ (Arnaud et al. 2010), while the green points present binned SZ measurements for the approximately 1600 clusters in the Meta-Catalogue of X-ray detected Clusters (MCXC) (Piffaretti et al. 2011). The latter measurements are as reported in Planck Collaboration (2011e), with one minor change: in Planck Collaboration (2011e) we used an empirical slope for the Y_{500}-M_{500} relation taken from X-ray studies; for the points in Fig. 9, we repeated the same analysis fixing the slope instead to its self-similar value, as was done for the LBG sample. This change moves the green points only very slightly relative to those shown in Planck Collaboration (2011e). For the mass estimates of the MCXC objects, we applied the X-ray luminosity-mass relation from Pratt et al. (2009), corresponding to the case of line 3 of Table 2 in Planck Collaboration (2011e). The mass is calculated for each MCXC cluster and then binned. We plot the point at the median value of the mass in each bin.

To transcribe our central galaxy catalogue measurements onto this figure, we must first find the effective halo mass corresponding to each stellar mass bin. This effective mass is a complicated average over the halo masses within the bin, weighting by the fraction of SZ signal actually observed, i.e., after accounting for aperture and miscentering effects. The bin-averaged mean SZ signals we estimate for our mock LBG catalogue include all these effects, and so can be used to calculate an effective mass as $M_{500}^{\rm eff} = 3\times10^{14}\,M_\odot\,(\langle Y\rangle_{\rm s}/Y_{\rm M})^{1/\alpha_{\rm M}}$, where $\langle Y\rangle_{\rm s}$ is calculated for each bin as described above, and $Y_{\rm M}$ and $\alpha_{\rm M} = 5/3$ are the parameters used for Eq. 1 in the simulation. (Note that the result is independent of the normalisation $Y_{\rm M}$.) We do this for a suite of simulated catalogues and take the ensemble average effective mass for each bin, plotting the results as the red points in the right-hand panel of the figure.

These LBG results extend the SZ-halo mass scaling relation down in mass by at least a factor of 3, to $M_{500} = 2\times10^{13}\,M_\odot$ (the stellar mass bin at $\log_{10} M_*/M_\odot = 11.25$). This is the lowest halo mass for which the mean SZ signal has been measured. As previously discussed, there is a clear indication that the relation continues to even lower mass, with marginally significant detections in the next three stellar mass bins. The lowest stellar mass bin with an apparent SZ detection (at 2.6σ) corresponds to effective halo mass $\log_{10} M_{500}/M_\odot = 12.6$. Our power-law fit adequately describes the data points over more than two orders of magnitude in halo mass down to this remarkably low value with no hint of a significant deviation.

The inset in the right panel of Fig. 9 shows the ratio of our measured mean SZ signal to that predicted by the self-similar scaling relation deduced from X-ray observations of clusters (the dashed blue line, Arnaud et al. 2010). Direct measurements obtained by binning the MCXC clusters (the green points) agree with this relation. This was the principal result of Planck Collaboration (2011e). The SZ measurements for our LBGs fall below the relation, however. The horizontal dot-dashed line gives the ratio our LBG fit to the X-ray model (this is the offset between the two blue lines in the main figure). Recall that the fit to the LBG catalogue was restricted to masses overlapping the X-ray sample, $\log_{10} M_{500}/M_\odot > 13.8$. Over this range, the mean SZ signals associated with LBG halos are about 20% lower than found for X-ray clusters with the same halo mass, a difference that is significant at the 2.6σ level.

A number of effects could contribute to an offset of this size. The masses plotted for the MCXC were calculated using a luminosity-mass relation derived from the REXCESS sample assuming that halo mass scales self-similarly with the mass-proxy Y_X and without correction for Malmquist bias (Pratt et al. 2009). Using the Malmquist-corrected relation would remove much of the offset and bring the two Y_{500}-M_{500} scaling relations into acceptable agreement. In this sense, the offset is consistent with the estimated effects of Malmquist bias on the X-ray sample. However, such biases depend on the detailed selection procedure of the stacked and calibrating cluster samples, on the way in which the calibration relation is derived, and on the (correlated) intrinsic scatter of clusters around the L_x-M_{500} and Y_{500}-M_{500} relations. Thus they can only be corrected through detailed modelling both of the cluster population itself and of the definition and analysis of the specific cluster surveys involved (e.g., Angulo et al. 2012). Furthermore, halo masses are estimated in very different ways in our two samples – from X-ray luminosities calibrated against individual hydrostatic mass measurements for the MCXC, and through an abundance matching argument based on the WMAP7 cosmology for the LBG catalogue. Any offset between these two halo mass scales will result in offsets in Fig. 9. For example, a number of recent papers have argued that failure of some of the assumptions underlying the standard methods for estimating cluster masses from X-ray data (e.g., detailed hydrostatic equilibrium or the unimportance of turbulent and nonthermal pressure) could produce a systematic bias in the X-ray cluster mass scale (Planck Collaboration 2011g; Rozo et al. 2012; Sehgal et al. 2013). Finally, as for the LBG sample, each luminosity bin of the MCXC contains a distribution of halo properties that are averaged in complicated fashion by our stacked SZ measurement. Understanding the relative importance of these various effects at a precision better than 20% would again require detailed modeling of the heterogeneous MCXC catalogue.

7. Conclusions

Using *Planck* data, we have measured the scaling relation between Sunyaev-Zeldovich signal and stellar mass for locally brightest galaxies (Y_{500}-M_*). This is the first time such a relation has been determined, and it demonstrates the presence of hot, diffuse gas in halos hosting central galaxies of stellar mass as low as $M_* = 2\times10^{11}\,M_\odot$, with a strong indication of signal at even lower masses. We have constructed a large mock catalogue of locally brightest galaxies from the Millennium Simulation and used it to model the *Planck* observational process in detail in order to extract from our measurements the underlying SZ signal-halo mass relation (Y_{500}-M_{500}). This new relation spans a large range in halo mass, reaching from rich clusters down to $M_{500} = 2.0\times10^{13}\,M_\odot$, with a clear indication of continuation to $M_{500} \sim 4\times10^{12}\,M_\odot$. This is the lowest mass scale to which an SZ scaling relation has so far been measured. The fact that the signal is close to the self-similar prediction implies that *Planck*-detected hot gas represents roughly the mean cosmic fraction of the mass even in such low-mass systems. Consistency with their low observed X-ray luminosities then requires the gas to be less concentrated than in more massive systems. Integration of the halo mass function down to $M_{500} = 4\times10^{12} M_\odot$ shows that *Planck* has now seen about a quarter of all cosmic baryons in the form of hot gas, about four times as many as are inferred from X-ray data in clusters with $M_{500} > 10^{14} M_\odot$.

At the high mass end, the scaling relation we derive from our LBG data shows reasonable agreement with X-ray cluster results. The 20% lower normalisation that we find (significant at the 2.6σ level) can be explained in principle by a number of possible effects related to the differing selection and mass estimation methods of the two samples. Agreement at this level of precision is remarkable, and understanding the remaining difference would require detailed modeling of the selection and calibration of the X-ray samples. The fact that plausible Malmquist corrections can eliminate most of the difference shows that cluster studies are now reaching the ∼10% precision level.

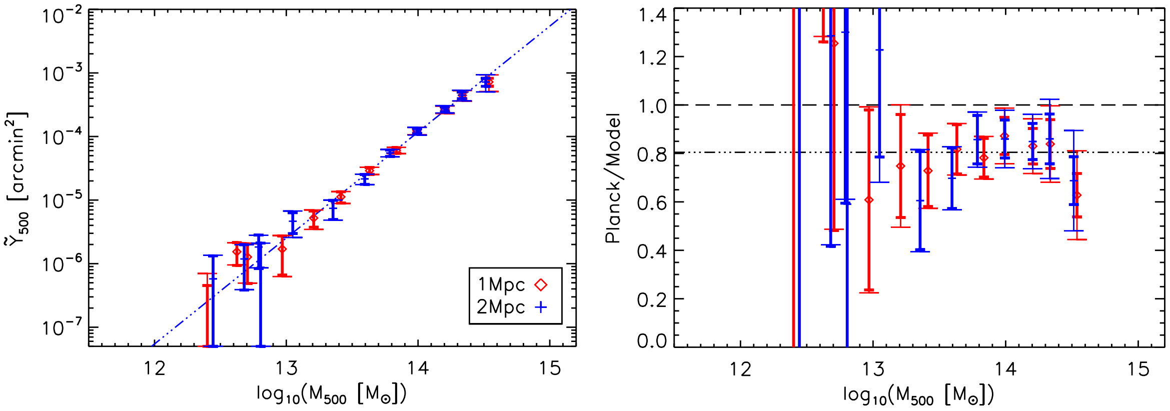

Fig. A.1. *Left*: comparison of the SZ signal-halo mass scaling relation for two different sets of isolation criteria. The triple-dot dashed line is our best fit model (see Eqs. (1) and (2)). *Right*: same as above, but now showing the ratio of the previous data points to the Arnaud et al. (2010) Y-M_{500} relation.

We find that the Y_{500}-M_{500} scaling law is described by a power law with no evidence of deviation over more than two orders of magnitude in halo mass. The gas properties of dark matter halos appear remarkably regular over a mass range where cooling and feedback processes are expected to vary strongly. In particular, we find no change in behaviour in the low-mass systems for which substantial feedback effects are invoked in current galaxy formation models (e.g., from AGN). Statistical studies of large galaxy and cluster samples, such as those presented here, can clearly shed new light on the thermal cycle at the heart of the galaxy formation process.

Acknowledgements. The authors from the consortia funded principally by CNES, CNRS, ASI, NASA, and Danish Natural Research Council acknowledge the use of the pipeline-running infrastructures Magique3 at Institut d'Astrophysique de Paris (France), CPAC at Cambridge (UK), and USPDC at IPAC (USA). The development of *Planck* has been supported by: ESA; CNES and CNRS/INSU-IN2P3-INP (France); ASI, CNR, and INAF (Italy); NASA and DoE (USA); STFC and UKSA (UK); CSIC, MICINN, JA and RES (Spain); Tekes, AoF and CSC (Finland); DLR and MPG (Germany); CSA (Canada); DTU Space (Denmark); SER/SSO (Switzerland); RCN (Norway); SFI (Ireland); FCT/MCTES (Portugal); and PRACE (EU). A description of the Planck Collaboration and a list of its members, including the technical or scientific activities in which they have been involved, can be found at `http://www.sciops.esa.int/index.php?project=planck`. We acknowledge the use of the HEALPix package (Górski et al. 2005).

Appendix A: Robustness of our results to variations in isolation criteria

As explained in Sect. 2.2, our locally brightest galaxy catalogue was built starting from a parent population with $r < 17.7$ taken from the spectroscopic NYU-VAGC and eliminating any candidate with a companion of equal or brighter r magnitude violating certain isolation criteria. In particular, we defined locally brightest galaxies to be the set of all objects with $z > 0.03$ that are brighter than all other sample galaxies projected within a radius of $R_{\rm iso} = 1.0$ Mpc, and differing in redshift by less than 1000 km s^{-1}. Hereafter, we refer to these criteria as the "1 Mpc case".

To test the robustness of our results against changes in these isolation criteria, we compared them to a case with stricter isolation criteria, $R_{\rm iso} = 2.0$ Mpc and 2,000 km s^{-1} in redshift, hereafter the "2 Mpc case".

Applying the isolation criteria to the parent spectroscopic catalogue as before, but with these new values, we end up with a first sample of 206 562 locally brightest galaxies. Again, in a second step we use SDSS photometry to further eliminate objects with companions that might violate the isolation criteria. After removing any candidate with a (photometric) companion of equal or brighter r magnitude and projected within 2.0 Mpc, we end up with a cleaned sample of 110 437 locally brightest galaxies. In particular, this sample contains 58 105 galaxies satisfying the bound $\log_{10} M_*/{\rm M}_\odot \geq 11.0$, which is the regime where we find significant SZ signal. Thus, 23 287 galaxies in this mass range are eliminated from the sample studied in the main body of this paper by the stricter isolation criteria.

To evaluate the reliability of the new $R_{\rm iso} = 2.0$ Mpc sample, we follow the same procedure as before and construct a mock sample of locally brightest galaxies from the Guo et al. (2011) simulation. As expected, the new $R_{\rm iso} = 2.0$ Mpc mock sample has a higher reliability than the $R_{\rm iso} = 1.0$ Mpc case. The fraction of locally brightest galaxies that are centrals now has a minimum of just over 87 % at stellar masses somewhat above $10^{11}\ M_\odot$. The improvement is less than might have been anticipated because, as noted in Sect. 2.2.1, the majority of the satellite galaxies in our simulated 1 Mpc sample were included because they are brighter than the central galaxies of their own halos, rather than because the isolation criteria failed to eliminate them.

Finally, Fig. A.1 compares the SZ signal-halo mass relations (Y_{500}-M_{500}) derived for the two cases (1 Mpc and 2 Mpc). Halo masses for the 2 Mpc case are computed as explained in Sect. 6 (see Table B.1 for the numerical values). The main conclusion is that the SZ signal-halo mass scaling relation is not sensitive to the isolation criteria.

Appendix B: Predicted properties of the stellar mass-halo mass relation

Using our mock catalogues based on the semi-analytic galaxy formation simulation of Guo et al. (2011), we provide here additional information on the predicted properties of the stellar mass-halo mass relation. Figure B.1 shows the distribution of

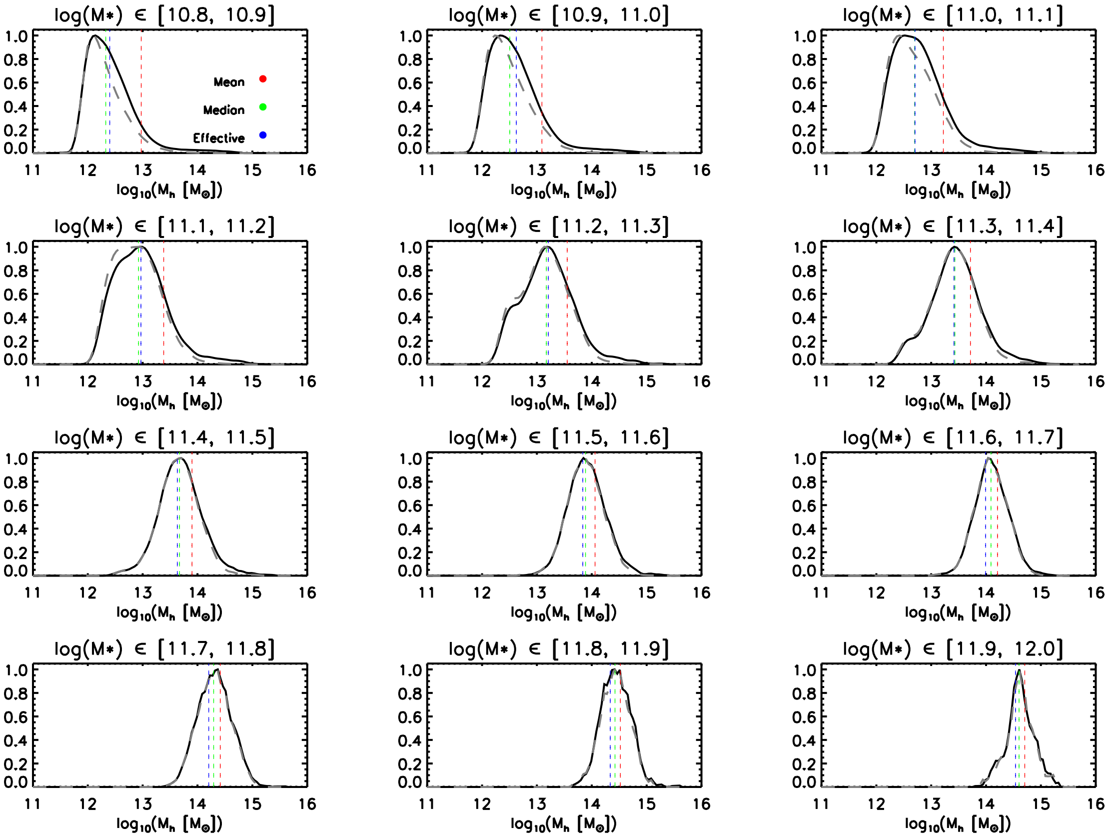

Fig. B.1. Probability distribution function of halo mass, M_h, for nine of the stellar mass bins considered in this paper. Solid lines correspond to the sample isolated according to the 1 Mpc criteria, while dashed lines show the distributions for the 2 Mpc sample. Vertical colored lines show three different characteristic masses (the mean, median, and "effective" halo masses) for the 1 Mpc sample (see Table B.1 for numerical values).

Table B.1. Statistics of halo mass for various stellar mass bins, for the 1 Mpc and 2 Mpc isolation criteria.

	$\log_{10}\left(\frac{M_\mathrm{h}}{M_\odot}\right)$							
	R_iso = 1 Mpc				R_iso = 2 Mpc			
$\log_{10}\left(\frac{M_*}{M_\odot}\right)$	Mean	Median	RMS	Effective	Mean	Median	RMS	Effective
10.8–10.9	12.97	12.33	13.78	12.40	12.55	12.24	13.16	12.44
10.9–11.0	13.09	12.50	13.77	12.62	12.73	12.41	13.24	12.68
11.0–11.1	13.22	12.70	13.86	12.71	12.92	12.61	13.39	12.79
11.1–11.2	13.38	12.93	13.94	12.97	13.14	12.85	13.67	12.81
11.2–11.3	13.55	13.17	14.04	13.21	13.37	13.12	13.79	13.05
11.3–11.4	13.72	13.43	14.03	13.41	13.60	13.40	13.87	13.35
11.4–11.5	13.90	13.67	14.15	13.63	13.81	13.65	13.92	13.60
11.5–11.6	14.06	13.89	14.19	13.84	14.01	13.87	14.10	13.79
11.6–11.7	14.21	14.09	14.19	13.99	14.19	14.08	14.13	13.99
11.7–11.8	14.41	14.29	14.39	14.20	14.39	14.29	14.25	14.20
11.8–11.9	14.52	14.42	14.49	14.34	14.49	14.42	14.30	14.33
11.9–12.0	14.71	14.60	14.56	14.54	14.69	14.60	14.52	14.51

Notes. The first three columns for each case (mean, median, and rms values for the halo mass) are derived from the simulation only, while the effective halo mass $M_\mathrm{h}^\mathrm{eff}$ uses the redshifts and stellar masses of the observed galaxies, as described in Sect. 6. All masses (M) in this table are decimal logarithms of the value in units of $M_\odot$.

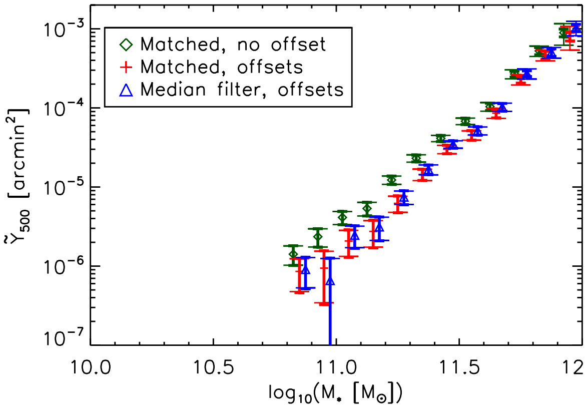

Fig. C.1. Impact of miscentering and scatter on the binned SZ measurements. The green points give results in an ideal situation with no miscentering and SZ filter perfectly matched to each individual object in a given stellar mass bin. The red crosses add the effect of miscentering, with offsets drawn from the distributions given by the simulations for each stellar mass bin. The blue triangles additionally include the aperture effect caused by fixing the filter size according to the median value of the halo mass in each bin.

halo mass ($M_{\rm h}$) predicted for twelve of the stellar mass bins considered in this paper, and for two sets of isolation criteria: the 1 Mpc and 2 Mpc cases (see Sect. 2.2 and Appendix A). Vertical lines correspond to the mean (red), median (green), and the "effective" (blue) values of halo mass in each bin. The corresponding numbers are listed in Table B.1, which also gives the rms of the posterior $M_{\rm h}$ distribution. The effective halo masses are computed as described in Sect. 6.

Appendix C: Impact of miscentering and scatter on the binned SZ signal and stacked SZ maps

As discussed in Sec. 6, we used the semi-analytic galaxy formation simulation of Guo et al. (2011) to account for the effects of miscentering and scatter in halo mass at fixed stellar mass when interpreting our measurement (see Figs. 4 and 9). Figure C.1 isolates the impact of each effect on the binned SZ measurements, using the procedure outlined in that section. The green points represent the ideal case with no miscentering and SZ filter perfectly matched to the size of each individual object. The red crosses add miscentering offsets taken from the offset distribution in the simulations for each stellar mass bin. The drop in SZ amplitude is expected because we now miss SZ signal from the miscentered objects. Additionally fixing the filter size according to the median halo mass in each stellar mass bin, as done throughout this paper, we recover our previous results, shown as the blue triangles here and as the red diamonds in the left-hand panel of Fig. 9.

Using the same simulations, we can also estimate the impact of miscentering on the stacked SZ maps of locally brightest galaxies (see Fig. 5). Here, we use the full simulation to compute $r_{\rm p}$, the projected distance of each locally brightest galaxy from the gravitational potential minimum of its halo. Average and RMS values for $r_{\rm p}$ for all the stellar mass bins considered in this paper and for the 1 Mpc and 2 Mpc samples are given in Table C.1. Histograms of these $r_{\rm p}$ values are shown in Fig. C.2.

Table C.1. Statistics of the distribution of distances $r_{\rm p}$ of the locally brightest galaxies from the gravitational potential minima of their parent halos, for the 1 Mpc and 2 Mpc isolation criteria.

	$r_{\rm p}$ [kpc]			
	$R_{\rm iso}$ = 1 Mpc		$R_{\rm iso}$ = 2 Mpc	
$\log_{10}\left(\frac{M_*}{M_\odot}\right)$	Mean	RMS	Mean	RMS
10.8–10.9	102.6	384.7	53.7	235.6
10.9–11.0	121.2	420.2	65.2	263.2
11.0–11.1	140.2	469.6	75.8	322.1
11.1–11.2	165.7	533.1	94.9	373.3
11.2–11.3	195.6	636.1	121.8	501.8
11.3–11.4	202.4	682.1	143.6	579.1
11.4–11.5	217.8	720.3	165.1	659.8
11.5–11.6	239.8	852.8	205.7	812.1
11.6–11.7	193.4	775.2	171.5	758.5
11.7–11.8	213.4	896.7	200.4	892.0
11.8–11.9	145.1	726.2	128.5	720.9
11.9–12.0	342.5	1062.6	332.2	1065.1

Note that the median value of $r_{\rm p}$, which is not listed in the table, is zero for all bins.

These values can be used to predict the impact of miscentering of the locally brightest galaxy with respect to its halo (and thus, with respect to the centre of the associated SZ emission). Figure C.3 illustrates the broadening of the SZ stacked profile caused by this effect. For this computation, we assume point-like objects and a Gaussian beam profile of 10′ for easier comparison with Fig. 5. For each stellar mass bin, the $M_{\rm h}$ value from the simulation is used to predict the total SZ flux using Eqs. (1) and (2), and the $r_{\rm p}$ value is used to offset the position of the SZ signal. In order to convert $r_{\rm p}$ values (in physical units) into angular offsets, a redshift for each simulated object is drawn from the observed distribution for locally brightest galaxies of similar stellar mass. Miscentering broadens the stacked SZ profile, yielding typical FWHM of ~20′ for $\log_{10} M_*/M_\odot \leq 11.25$, and also modifies the shape of the profile, by increasing the amount of SZ flux in the tails of the distribution. These values are slightly smaller (but comparable) to the observed widths of the SZ emission in Fig. 5.

Finally, Fig. C.4 shows equal-weighted stacks of SZ maps centred on the real central galaxy sample, similar to those of Fig. 5, but now using all six HFI frequency channels in the MILCA algorithm, rather than just the lowest four. For all six stellar mass bins the noise in these new maps, as measured by the RMS fluctuation about the mean in pixels more than 20′ from map centre, is lower than in the maps of Fig. 5. This shows that the addition of high frequency information has improved the accuracy with which non-SZ signals, primarily dust emission, are removed. Almost all this improvement comes from the inclusion of the 545 GHz channel; maps made with and without the 857 GHz channel are almost identical. As a result of this improvement, the signal-to-noise ratio of the peaks near the map centre is higher in all the panels of Fig. C.4 than in the corresponding panels of Fig. 5. This strengthens our conclusion that the apparent SZ signals near the centres of the two lowest stellar mass panels are, in fact, real, despite their apparent breadth and irregularity. The breadth is likely due to the miscentering effects explored above while the irregularity looks consistent with the overall noise level of the maps.

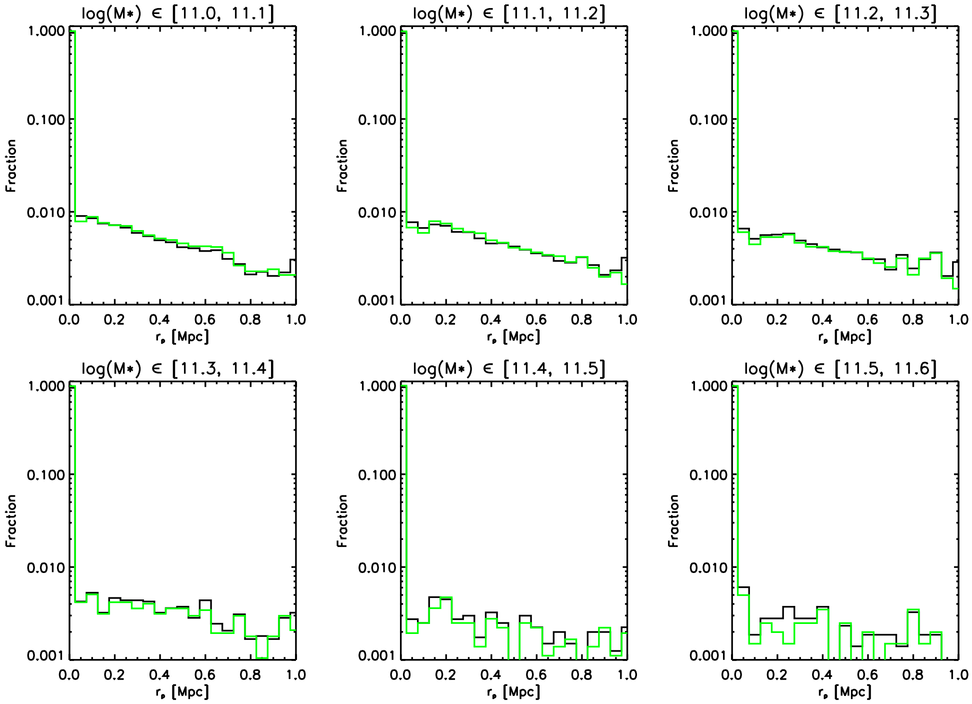

Fig. C.2. Distribution of offsets of locally brightest galaxies from the gravitational potential minima of their parent halos, both for the 1 Mpc (black) and for the 2 Mpc (green) isolation criteria. Table C.1 gives mean and rms values for these distributions.

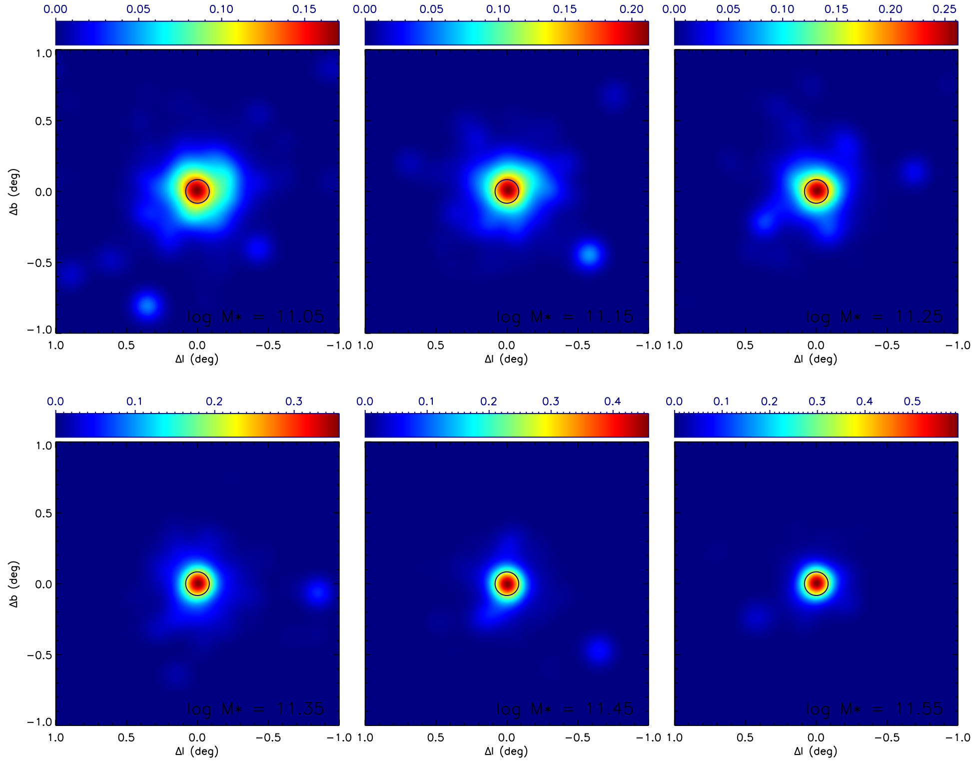

Fig. C.3. Impact of miscentering on stacked SZ maps. See the text for details of the simulation shown here. For an original resolution of *FWHM* = 10′, miscentering broadens the stacked profiles to a FWHM ~20′ for $\log_{10} M_*/M_\odot \leq 11.25$.

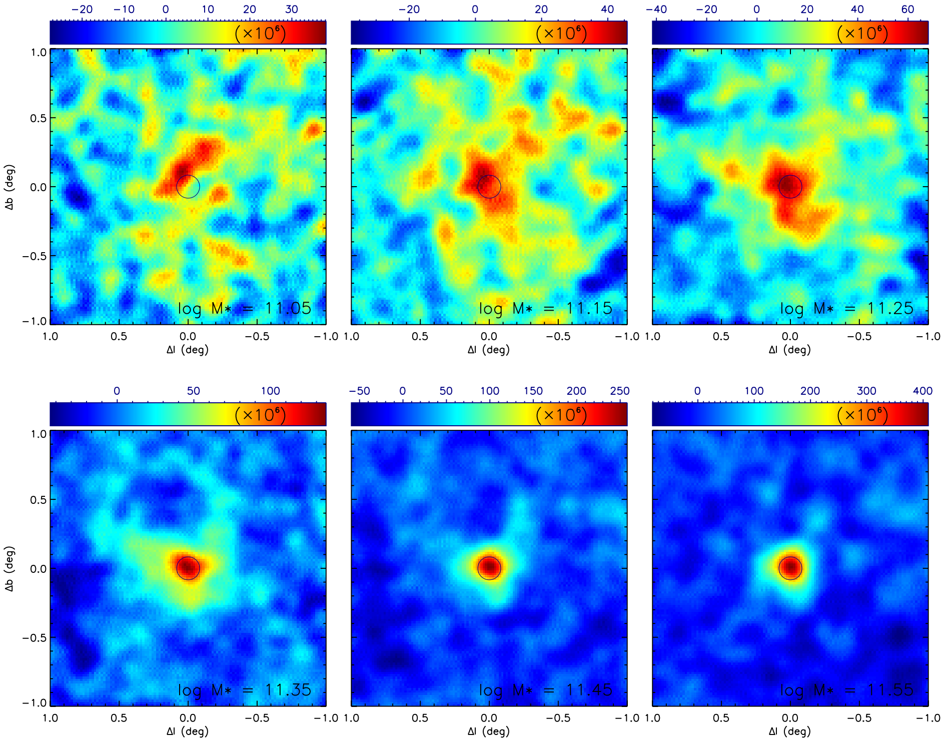

Fig. C.4. Similar to Fig. 5, but using a reconstructed SZ map that now uses all six HFI frequency channels. The noise in all maps is reduced by the inclusion of the two highest frequencies. Stacked images in the stellar-mass bins above $\log_{10}(M_*/M_\odot) = 11.25$ are not significantly affected, but for the low stellar-mass panels, the extended signal near map centre is larger and has higher signal to noise than in Fig. 5, suggesting that it may be real SZ signal broadened by miscentering effects.

References

Abazajian, K. N., Adelman-McCarthy, J. K., Agüeros, M. A., et al. 2009, ApJS, 182, 543
Angulo, R. E., & White, S. D. M. 2010, MNRAS, 405, 143
Angulo, R. E., Springel, V., White, S. D. M., et al. 2012, MNRAS, 426, 2046
Arnaud, M., Pratt, G. W., Piffaretti, R., et al. 2010, A&A, 517, A92
Balogh, M. L., Pearce, F. R., Bower, R. G., & Kay, S. T. 2001, MNRAS, 326, 1228
Bersanelli, M., Mandolesi, N., Butler, R. C., et al. 2010, A&A, 520, A4
Birkinshaw, M. 1999, Phys. Rep., 310, 97
Blanton, M. R., & Roweis, S. 2007, AJ, 133, 734
Blanton, M. R., Schlegel, D. J., Strauss, M. A., et al. 2005, AJ, 129, 2562
Blanchard, A., Valls-Gabaud, D., & Mamon, G. A. 1992, A&A, 264, 365
Böhringer, H., Schuecker, P., Pratt, G. W., et al. 2007, A&A, 469, 363
Borgani, S., Murante, G., Springel, V., et al. 2004, MNRAS, 348, 1078
Bower, R. G., Benson, A. J., Lacey, C. G., et al. 2001, MNRAS, 325, 497
Bower, R. G., Benson, A. J., Malbon, R., et al. 2006, MNRAS, 370, 645
Carlstrom, J. E., Ade, P. A. R., Aird, K. A., et al. 2011, PASP, 123, 568
Cavaliere, A., Lapi, A., & Menci, N. 2002, ApJ, 581, L1
Chabrier, G. 2003, PASP, 115, 763
Churazov, E., Sunyaev, R., Forman, W., & Böhringer, H. 2002, MNRAS, 332, 729
Cole, S. 1991, ApJ, 367, 45
Croton, D. J., Springel, V., White, S. D. M., et al. 2006, MNRAS, 365, 11
Cunha, C. E., Lima, M., Oyaizu, H., Frieman, J., & Lin, H. 2009, MNRAS, 396, 2379
Dobbs, M., Halverson, N. W., Ade, P. A. R., et al. 2006, New Astron. Rev., 50, 960
Draper, P., Dodelson, S., Hao, J., & Rozo, E. 2012, Phys. Rev. D, 85, 023005
Duffy, A. R., Schaye, J., Kay, S. T., & Dalla Vecchia, C. 2008, MNRAS, 390, L64
Eriksen, H. K., Banday, A. J., Górski, K. M., & Lilje, P. B. 2004, ApJ, 612, 633
Górski, K. M., Hivon, E., Banday, A. J., et al. 2005, ApJ, 622, 759
Guo, Q., White, S., Li, C., & Boylan-Kolchin, M. 2010, MNRAS, 404, 1111
Guo, Q., White, S., Boylan-Kolchin, M., et al. 2011, MNRAS, 413, 101
Guo, Q., White, S., Angulo, R. E., et al. 2013, MNRAS, 428, 1351
Hand, N., Appel, J. W., Battaglia, N., et al. 2011, ApJ, 736, 39
Hernández-Monteagudo, C., & Rubiño-Martín, J. A. 2004, MNRAS, 347, 403
Herranz, D., Sanz, J. L., Hobson, M. P., et al. 2002, MNRAS, 336, 1057
Hurier, G., Macias-Perez, J. F., & Hildebrandt, S. R. 2013, A&A, accepted [arXiv:1007.1149]
Koester, B. P., McKay, T. A., Annis, J., et al. 2007, ApJ, 660, 239
Komatsu, E., Smith, K. M., Dunkley, J., et al. 2011, ApJS, 192, 18
Lamarre, J., Puget, J., Ade, P. A. R., et al. 2010, A&A, 520, A9
Leahy, J. P., Bersanelli, M., D'Arcangelo, O., et al. 2010, A&A, 520, A8
Leauthaud, A., George, M. R., Behroozi, P. S., et al. 2012, ApJ, 746, 95
Lin, Y., & Mohr, J. J. 2004, ApJ, 617, 879
Mandelbaum, R., Seljak, U., Kauffmann, G., Hirata, C. M., & Brinkmann, J. 2006, MNRAS, 368, 715
Mandolesi, N., Bersanelli, M., Butler, R. C., et al. 2010, A&A, 520, A3
Marriage, T. A., Acquaviva, V., Ade, P. A. R., et al. 2011, ApJ, 737, 61
McCarthy, I. G., Schaye, J., Ponman, T. J., et al. 2010, MNRAS, 406, 822
McNamara, B. R., & Nulsen, P. E. J. 2007, ARA&A, 45, 117
Melin, J., Bartlett, J. G., & Delabrouille, J. 2006, A&A, 459, 341
Mennella, A., Butler, R. C., Curto, A., et al. 2011, A&A, 536, A3
Moster, B. P., Somerville, R. S., Maulbetsch, C., et al. 2010, ApJ, 710, 903
Navarro, J. F., Frenk, C. S., & White, S. D. M. 1997, ApJ, 490, 493
Neto, A. F., Gao, L., Bett, P., et al. 2007, MNRAS, 381, 1450
Piffaretti, R., Arnaud, M., Pratt, G. W., Pointecouteau, E., & Melin, J.-B. 2011, A&A, 534, A109
Planck Collaboration 2011a, A&A, 536, A1
Planck Collaboration 2011b, A&A, 536, A2
Planck Collaboration 2011c, A&A, 536, A8
Planck Collaboration 2011d, A&A, 536, A9
Planck Collaboration 2011e, A&A, 536, A10
Planck Collaboration 2011f, A&A, 536, A11
Planck Collaboration 2011g, A&A, 536, A12
Planck Collaboration 2012a, A&A, 550, A131
Planck Collaboration 2012b, A&A, 554, A140
Planck HFI Core Team 2011a, A&A, 536, A4
Planck HFI Core Team 2011b, A&A, 536, A6

Pratt, G. W., Croston, J. H., Arnaud, M., & Böhringer, H. 2009, A&A, 498, 361
Puchwein, E., Sijacki, D., & Springel, V. 2008, ApJ, 687, L53
Rosset, C., Tristram, M., Ponthieu, N., et al. 2010, A&A, 520, A13
Rozo, E., Bartlett, J. G., Evrard, A. E., & Rykoff, E. S. 2012 [arXiv:1204.6305]
Sehgal, N., Trac, H., Acquaviva, V., et al. 2011, ApJ, 732, 44
Sehgal, N., Addison, G., Battaglia, N., et al. 2013, ApJ, 767, 38
Somerville, R. S., Hopkins, P. F., Cox, T. J., Robertson, B. E., & Hernquist, L. 2008, MNRAS, 391, 481
Springel, V., Di Matteo, T., & Hernquist, L. 2005a, MNRAS, 361, 776
Springel, V., White, S. D. M., Jenkins, A., et al. 2005b, Nature, 435, 629
Staniszewski, Z., Ade, P. A. R., Aird, K. A., et al. 2009, ApJ, 701, 32
Sunyaev, R. A., & Zeldovich, Y. B. 1972, Comments on Astrophysics and Space Physics, 4, 173
Swetz, D. S., Ade, P. A. R., Allen, C., et al. 2008, in SPIE Conf., 7020
Tauber, J. A., Mandolesi, N., Puget, J., et al. 2010, A&A, 520, A1
Tornatore, L., Borgani, S., Springel, V., et al. 2003, MNRAS, 342, 1025
Valageas, P., & Silk, J. 1999, A&A, 350, 725
Vanderlinde, K., Crawford, T. M., de Haan, T., et al. 2010, ApJ, 722, 1180
White, S. D. M., & Frenk, C. S. 1991, ApJ, 379, 52
White, S. D. M., & Rees, M. J. 1978, MNRAS, 183, 341
Williamson, R., Benson, B. A., High, F. W., et al. 2011, ApJ, 738, 139
Zacchei, D., Maino, D., Baccigalupi, C., et al. 2011, A&A, 536, A5

---

[1] APC, AstroParticule et Cosmologie, Université Paris Diderot, CNRS/IN2P3, CEA/lrfu, Observatoire de Paris, Sorbonne Paris Cité, 10 rue Alice Domon et Léonie Duquet, 75205 Paris Cedex 13, France
[2] Aalto University Metsähovi Radio Observatory, Metsähovintie 114, 02540 Kylmälä, Finland
[3] Academy of Sciences of Tatarstan, Bauman Str., 20, Kazan, 420111 Republic of Tatarstan, Russia
[4] African Institute for Mathematical Sciences, 6-8 Melrose Road, Muizenberg, Cape Town, South Africa
[5] Agenzia Spaziale Italiana Science Data Center, c/o ESRIN, via Galileo Galilei, Frascati, Italy
[6] Agenzia Spaziale Italiana, Viale Liegi 26, Roma, Italy
[7] Astrophysics Group, Cavendish Laboratory, University of Cambridge, J J Thomson Avenue, Cambridge CB3 0HE, UK
[8] Atacama Large Millimeter/submillimeter Array, ALMA Santiago Central Offices, Alonso de Cordova 3107, Vitacura, Casilla 763, 0355 Santiago, Chile
[9] CITA, University of Toronto, 60 St. George St., Toronto, ON M5S 3H8, Canada
[10] CNRS, IRAP, 9 Av. colonel Roche, BP 44346, 31028 Toulouse Cedex 4, France
[11] California Institute of Technology, Pasadena, California, USA
[12] Centro de Astrofísica, Universidade do Porto, Rua das Estrelas, 4150-762 Porto, Portugal
[13] Centro de Estudios de Física del Cosmos de Aragón (CEFCA), Plaza San Juan, 1, planta 2, 44001 Teruel, Spain
[14] Computational Cosmology Center, Lawrence Berkeley National Laboratory, Berkeley, California, USA
[15] Consejo Superior de Investigaciones Científicas (CSIC), Madrid, Spain
[16] DSM/Irfu/SPP, CEA-Saclay, 91191 Gif-sur-Yvette Cedex, France
[17] DTU Space, National Space Institute, Technical University of Denmark, Elektrovej 327, 2800 Kgs. Lyngby, Denmark
[18] Département de Physique Théorique, Université de Genève, 24, Quai E. Ansermet,1211 Genève 4, Switzerland
[19] Departamento de Física Fundamental, Facultad de Ciencias, Universidad de Salamanca, 37008 Salamanca, Spain
[20] Departamento de Física, Universidad de Oviedo, Avda. Calvo Sotelo s/n, Oviedo, Spain
[21] Department of Astronomy and Geodesy, Kazan Federal University, Kremlevskaya Str., 18, 420008 Kazan, Russia
[22] Department of Astrophysics/IMAPP, Radboud University Nijmegen, PO Box 9010, 6500 GL Nijmegen, The Netherlands
[23] Department of Electrical Engineering and Computer Sciences, University of California, Berkeley, California, USA
[24] Department of Physics & Astronomy, University of British Columbia, 6224 Agricultural Road, Vancouver, British Columbia, Canada
[25] Department of Physics and Astronomy, Dana and David Dornsife College of Letter, Arts and Sciences, University of Southern California, Los Angeles, CA 90089, USA
[26] Department of Physics, Gustaf Hällströmin katu 2a, University of Helsinki, Helsinki, Finland
[27] Department of Physics, Princeton University, Princeton, New Jersey, USA
[28] Department of Physics, University of California, Berkeley, California, USA
[29] Department of Physics, University of California, Santa Barbara, California, USA
[30] Department of Physics, University of Illinois at Urbana-Champaign, 1110 West Green Street, Urbana, Illinois, USA
[31] Dipartimento di Fisica e Astronomia G. Galilei, Università degli Studi di Padova, via Marzolo 8, 35131 Padova, Italy
[32] Dipartimento di Fisica e Scienze della Terra, Università di Ferrara, via Saragat 1, 44122 Ferrara, Italy
[33] Dipartimento di Fisica, Università La Sapienza, P. le A. Moro 2, Roma, Italy
[34] Dipartimento di Fisica, Università degli Studi di Milano, via Celoria, 16, Milano, Italy
[35] Dipartimento di Fisica, Università degli Studi di Trieste, via A. Valerio 2, Trieste, Italy
[36] Dipartimento di Fisica, Università di Roma Tor Vergata, via della Ricerca Scientifica, 1, Roma, Italy
[37] Dipartimento di Matematica, Università di Roma Tor Vergata, via della Ricerca Scientifica, 1, Roma, Italy
[38] Discovery Center, Niels Bohr Institute, Blegdamsvej 17, Copenhagen, Denmark
[39] Dpto. Astrofísica, Universidad de La Laguna (ULL), 38206 La Laguna, Tenerife, Spain
[40] European Southern Observatory, ESO Vitacura, Alonso de Cordova 3107, Vitacura, Casilla 19001, Santiago, Chile
[41] European Space Agency, ESAC, Planck Science Office, Camino bajo del Castillo, s/n, Urbanización Villafranca del Castillo, Villanueva de la Cañada, Madrid, Spain
[42] European Space Agency, ESTEC, Keplerlaan 1, 2201 AZ Noordwijk, The Netherlands
[43] GEPI, Observatoire de Paris, Section de Meudon, 5 Place J. Janssen, 92195 Meudon Cedex, France
[44] Helsinki Institute of Physics, Gustaf Hällströmin katu 2, University of Helsinki, Helsinki, Finland
[45] INAF – Osservatorio Astronomico di Padova, Vicolo dell'Osservatorio 5, Padova, Italy
[46] INAF – Osservatorio Astronomico di Roma, via di Frascati 33, Monte Porzio Catone, Italy
[47] INAF – Osservatorio Astronomico di Trieste, via G.B. Tiepolo 11, Trieste, Italy
[48] INAF Istituto di Radioastronomia, via P. Gobetti 101, 40129 Bologna, Italy
[49] INAF/IASF Bologna, via Gobetti 101, Bologna, Italy
[50] INAF/IASF Milano, via E. Bassini 15, Milano, Italy
[51] INFN, Sezione di Bologna, via Irnerio 46, 40126 Bologna, Italy
[52] INFN, Sezione di Roma 1, Universit'a di Roma Sapienza, Piazzale Aldo Moro 2, 00185 Roma, Italy
[53] IUCAA, Post Bag 4, Ganeshkhind, Pune University Campus, 411 007 Pune, India
[54] Imperial College London, Astrophysics group, Blackett Laboratory, Prince Consort Road, London, SW7 2AZ, UK
[55] Infrared Processing and Analysis Center, California Institute of Technology, Pasadena, CA 91125, USA
[56] Institut Universitaire de France, 103, bd Saint-Michel, 75005 Paris, France
[57] Institut d'Astrophysique Spatiale, CNRS (UMR 8617) Université Paris-Sud 11, Bâtiment 121, Orsay, France

[58] Institut d'Astrophysique de Paris, CNRS (UMR 7095), 98 bis Boulevard Arago, 75014 Paris, France
[59] Institute for Space Sciences, Bucharest-Magurale, Romania
[60] Institute of Astro and Particle Physics, Technikerstrasse 25/8, University of Innsbruck, 6020 Innsbruck, Austria
[61] Institute of Astronomy and Astrophysics, Academia Sinica, Taipei, Taiwan
[62] Institute of Astronomy, University of Cambridge, Madingley Road, Cambridge CB3 0HA, UK
[63] Institute of Theoretical Astrophysics, University of Oslo, Blindern, Oslo, Norway
[64] Instituto de Astrofísica de Canarias, C/Vía Láctea s/n, La Laguna, Tenerife, Spain
[65] Instituto de Física de Cantabria (CSIC-Universidad de Cantabria), Avda. de los Castros s/n, Santander, Spain
[66] Jet Propulsion Laboratory, California Institute of Technology, 4800 Oak Grove Drive, Pasadena, California, USA
[67] Jodrell Bank Centre for Astrophysics, Alan Turing Building, School of Physics and Astronomy, The University of Manchester, Oxford Road, Manchester, M13 9PL, UK
[68] Kavli Institute for Cosmology Cambridge, Madingley Road, Cambridge, CB3 0HA, UK
[69] LAL, Université Paris-Sud, CNRS/IN2P3, 91405 Orsay, France
[70] LERMA, CNRS, Observatoire de Paris, 61 avenue de l'Observatoire, Paris, France
[71] Laboratoire AIM, IRFU/Service d'Astrophysique – CEA/DSM – CNRS – Université Paris Diderot, Bât. 709, CEA-Saclay, 91191 Gif-sur-Yvette Cedex, France
[72] Laboratoire de Physique Subatomique et de Cosmologie, Université Joseph Fourier Grenoble I, CNRS/IN2P3, Institut National Polytechnique de Grenoble, 53 rue des Martyrs, 38026 Grenoble Cedex, France
[73] Laboratoire de Physique Théorique, Université Paris-Sud 11 & CNRS, Bâtiment 210, 91405 Orsay, France
[74] Lawrence Berkeley National Laboratory, Berkeley, California, USA
[75] Max-Planck-Institut für Astrophysik, Karl-Schwarzschild-Str. 1, 85741 Garching, Germany
[76] Max-Planck-Institut für Extraterrestrische Physik, Giessenbachstraße, 85748 Garching, Germany
[77] National University of Ireland, Department of Experimental Physics, Maynooth, Co. Kildare, Ireland
[78] Niels Bohr Institute, Blegdamsvej 17, Copenhagen, Denmark
[79] Observational Cosmology, Mail Stop 367-17, California Institute of Technology, Pasadena, CA, 91125, USA
[80] Optical Science Laboratory, University College London, Gower Street, London, UK
[81] SISSA, Astrophysics Sector, via Bonomea 265, 34136 Trieste, Italy
[82] School of Physics and Astronomy, Cardiff University, Queens Buildings, The Parade, Cardiff, CF24 3AA, UK
[83] Space Research Institute (IKI), Profsoyuznaya 84/32, Moscow, Russia
[84] Space Sciences Laboratory, University of California, Berkeley, California, USA
[85] Special Astrophysical Observatory, Russian Academy of Sciences, Nizhnij Arkhyz, Zelenchukskiy region, 369167 Karachai-Cherkessian Republic, Russia
[86] Stanford University, Dept of Physics, Varian Physics Bldg, 382 via Pueblo Mall, Stanford, California, USA
[87] TÜBİTAK National Observatory, Akdeniz University Campus, 07058 Antalya, Turkey
[88] UPMC Univ Paris 06, UMR 7095, 98bis Boulevard Arago, 75014 Paris, France
[89] Université Denis Diderot (Paris 7), 75205 Paris Cedex 13, France
[90] Université de Toulouse, UPS-OMP, IRAP, 31028 Toulouse Cedex 4, France
[91] University Observatory, Ludwig Maximilian University of Munich, Scheinerstrasse 1, 81679 Munich, Germany
[92] University of Granada, Departamento de Física Teórica y del Cosmos, Facultad de Ciencias, Granada, Spain
[93] University of Miami, Knight Physics Building, 1320 Campo Sano Dr., Coral Gables, Florida, USA
[94] Warsaw University Observatory, Aleje Ujazdowskie 4, 00-478 Warszawa, Poland

Annexe F

LISTE COMPLÈTE DES PUBLICATIONS

La liste complète des 51 publications dont je suis co-auteur (au début septembre 2015) est reprise ici, organisée suivant les chapitres du manuscrit.

F.1 Introduction

- Tauber, J. A., Mandolesi, N., Puget, J.-L., et al., Planck pre-launch status: The Planck mission. 2010, A&A, 520, A1
- Planck Collaboration I, Planck early results. I. The Planck mission. 2011, A&A, 536, A1, arXiv:1101.2022
- Planck Collaboration I, Planck 2013 results. I. Overview of products and scientific results. 2014, A&A, 571, A1, arXiv:1303.5062
- Planck Collaboration XVI, Planck 2013 results. XVI. Cosmological parameters. 2014, A&A, 571, A16, arXiv:1303.5076
- Planck Collaboration I, Planck 2015 results. I. Overview of products and results. 2015, A&A, submitted, arXiv:1502.01582
- Planck Collaboration XIII, Planck 2015 results. XIII. Cosmological parameters. 2015, A&A, submitted, arXiv:1502.01589

F.2 Simulation des effets SZ dans le Planck Sky Model

- Delabrouille, J., Melin, J.-B., & Bartlett, J. G. 2002, in Astronomical Society of the Pacific Conference Series, Vol. 257, AMiBA 2001: High-Z Clusters, Missing

Baryons, and CMB Polarization, ed. L.-W. Chen, C.-P. Ma, K.-W. Ng, & U.-L. Pen, 81

- Delabrouille, J., Betoule, M., Melin, J.-B., et al., The pre-launch Planck Sky Model: a model of sky emission at submillimetre to centimetre wavelengths. 2013, A&A, 553, A96, arXiv:1207.3675

F.3 Extraction des amas de galaxies des données Planck

- Bartlett, J. G. & Melin, J.-B., Point source confusion in SZ cluster surveys. 2006, A&A, 447, 405, arXiv:astro-ph/0509818
- Leach, S. M., Cardoso, J.-F., Baccigalupi, C., et al., Component separation methods for the PLANCK mission. 2008, A&A, 491, 597, arXiv:0805.0269
- Melin, J.-B., Bartlett, J. G., & Delabrouille, J., Catalog extraction in SZ cluster surveys: a matched filter approach. 2006, A&A, 459, 341, arXiv:astro-ph/0602424
- Melin, J.-B., Aghanim, N., Bartelmann, M., et al., A comparison of algorithms for the construction of SZ cluster catalogues. 2012, A&A, 548, A51, arXiv:1210.1416
- Planck Collaboration VII, Planck early results. VII. The Early Release Compact Source Catalogue. 2011, A&A, 536, A7, arXiv:1101.2041
- Planck Collaboration VIII, Planck early results. VIII. The all-sky early Sunyaev-Zeldovich cluster sample. 2011, A&A, 536, A8, arXiv:1101.2024
- Planck Collaboration XXIX, Planck 2013 results. XXIX. The Planck catalogue of Sunyaev-Zeldovich sources. 2014, A&A, 571, A29, arXiv:1303.5089

- Planck Collaboration XXVII, Planck 2015 results. XXVII. The Second Planck Catalogue of Sunyaev-Zeldovich Sources. 2015, A&A, submitted, arXiv:1502.01598

F.4 Contraintes cosmologiques avec les amas Planck

- Melin, J.-B., Bartlett, J. G., & Delabrouille, J., The selection function of SZ cluster surveys. 2005, A&A, 429, 417, arXiv:astro-ph/0409564
- Chamballu, A., Bartlett, J. G., & Melin, J.-B., The Planck SZ Cluster Catalog: expected X-ray properties. 2012, A&A, 544, A40
- Planck Collaboration XX, Planck 2013 results. XX. Cosmology from Sunyaev-Zeldovich cluster counts. 2014, A&A, 571, A20, arXiv:1303.5080
- Planck Collaboration XXI, Planck 2013 results. XXI. Power spectrum and high-order statistics of the Planck all-sky Compton parameter map. 2014, A&A, 571, A21, arXiv:1303.5081
- Planck Collaboration XXIV, Planck 2015 results. XXIV. Cosmology from Sunyaev-Zeldovich cluster counts. 2015, A&A, submitted, arXiv:1502.01597
- Planck Collaboration XXII, Planck 2015 results. XXII. A map of the thermal Sunyaev-Zeldovich effect. 2015, A&A, submitted, arXiv:1502.01596

F.5 Estimation de la masse des amas par effet de lentille gravitationnelle sur le CMB

- Melin, J.-B. & Bartlett, J. G., Measuring cluster masses with CMB lensing: a statistical approach. 2015, A&A, 578, A21, arXiv:1408.5633

F.6 Lois d'échelle SZ-X et SZ-optique

- Piffaretti, R., Arnaud, M., Pratt, G. W., Pointecouteau, E., & Melin, J.-B., The MCXC: a meta-catalogue of x-ray detected clusters of galaxies. 2011, A&A, 534, A109, arXiv:1007.1916

- Melin, J.-B., Bartlett, J. G., Delabrouille, J., et al., The galaxy cluster YSZ - LX and YSZ - M relations from the WMAP 5-yr data. 2011, A&A, 525, A139, arXiv:1001.0871

- Planck Collaboration X, Planck early results. X. Statistical analysis of Sunyaev-Zeldovich scaling relations for X-ray galaxy clusters. 2011, A&A, 536, A10, arXiv:1101.2043

- Planck Collaboration XI, Planck early results. XI. Calibration of the local galaxy cluster Sunyaev-Zeldovich scaling relations. 2011, A&A, 536, A11, arXiv:1101.2026

- Planck Collaboration XII, Planck early results. XII. Cluster Sunyaev-Zeldovich optical scaling relations. 2011, A&A, 536, A12, arXiv:1101.2027

- Planck Collaboration Int. III, Planck intermediate results. III. The relation between galaxy cluster mass and Sunyaev-Zeldovich signal. 2013, A&A, 550, A129, arXiv:1204.2743

- Planck Collaboration Int. XI, Planck intermediate results. XI. The gas content of dark matter halos: the Sunyaev-Zeldovich-stellar mass relation for locally brightest galaxies. 2013, A&A, 557, A52, arXiv:1212.4131

- Le Brun, A. M. C., McCarthy, I. G., & Melin, J.-B., Testing Sunyaev-Zel?dovich measurements of the hot gas content of dark matter haloes using synthetic skies. 2015, ArXiv e-prints, arXiv:1501.05666

F.7 Effets SZ cinétique, relativiste et polarisé

- Planck Collaboration Int. XIII, Planck intermediate results. XIII. Constraints on peculiar velocities. 2014, A&A, 561, A97, arXiv:1303.5090

F.8 Suivi des amas Planck et étude multi-longueur d'onde d'amas particuliers

- Planck Collaboration IX, Planck early results. IX. XMM-Newton follow-up validation programme of Planck cluster candidates. 2011, A&A, 536, A9, arXiv:1101.2025

- Planck Collaboration XXVI, Planck early results. XXVI. Detection with Planck and confirmation by XMM-Newton of PLCK G266.6-27.3, an exceptionally X-ray luminous and massive galaxy cluster at z$\sim$1. 2011, A&A, 536, A26, arXiv:1106.1376

- Planck Collaboration Int. I, Planck intermediate results. I. Further validation of new Planck clusters with XMM-Newton. 2012, A&A, 543, A102, arXiv:1112.5595

- Planck Collaboration Int. IV, Planck intermediate results. IV. The XMM-Newton validation programme for new Planck clusters. 2013, A&A, 550, A130, arXiv:1205.3376

- Planck Collaboration Int. V, Planck intermediate results. V. Pressure profiles of galaxy clusters from the Sunyaev-Zeldovich effect. 2013, A&A, 550, A131, arXiv:1207.4061

- Planck Collaboration, Ade, P. A. R., Aghanim, N., et al., Planck intermediate results (Corrigendum). V. Pressure profiles of galaxy clusters from the Sunyaev-Zeldovich effect. 2013c, A&A, 558, C2

- Planck Collaboration Int. VI, Planck intermediate results. VI. The dynamical structure of PLCKG214.6+37.0, a Planck discovered triple system of galaxy clusters. 2013, A&A, 550, A132, arXiv:1207.4009

- Planck Collaboration Int. VIII, Planck intermediate results. VIII. Filaments between interacting clusters. 2013, A&A, 550, A134, arXiv:1208.5911

- Planck Collaboration Int. X, Planck intermediate results. X. Physics of the hot gas in the Coma cluster. 2013, A&A, 554, A140, arXiv:1208.3611

- Planck Collaboration Int. XXVI, Planck intermediate results. XXVI. Optical identification and redshifts of Planck clusters with the RTT150 telescope. 2014, A&A, in press, arXiv:1407.6663

- Andrade-Santos, F., Jones, C., Forman, W. R., et al., Chandra and Xmm-Newton Observations of the Bimodal Planck SZ-Detected Cluster Plckg345.40-39.34 (A3716) with High and Low Entropy Subcluster Cores. 2015, ApJ, 803, 108, arXiv:1502.05088

- Planck and AMI Collaborations, Planck intermediate results. II. Comparison of Sunyaev-Zeldovich measurements from Planck and from the Arcminute Microkelvin Imager for 11 galaxy clusters. 2013, A&A, 550, A128, arXiv:1204.1318

- Perrott, Y. C., Olamaie, M., Rumsey, C., et al., Comparison of Sunyaev-Zel'dovich measurements from Planck and from the Arcminute Microkelvin Imager for 99 galaxy clusters. 2015, A&A, 580, A95, arXiv:1405.5013

- Rodriguez-Gonzalvez, C., Chary, R., Muchovej, S., et al., CARMA observations of massive Planck-discovered cluster candidates at $z>0.5$ associated with WISE overdensities: Breaking the size-flux degeneracy. 2015, ArXiv e-prints, arXiv:1505.01132

- Rozo, E., Rykoff, E. S., Bartlett, J. G., & Melin, J.-B., redMaPPer - III. A detailed comparison of the Planck 2013 and SDSS DR8 redMaPPer cluster catalogues. 2015, MNRAS, 450, 592, arXiv:1401.7716

F.9 Définition des missions futures

- Pacaud, F., Pierre, M., Adami, C., et al., The XMM-LSS survey: the Class 1 cluster sample over the initial 5 deg2 and its cosmological modelling. 2007, MNRAS, 382, 1289, arXiv:0709.1950

- Pierre, M., Pacaud, F., Juin, J. B., et al., Precision cosmology with a wide area XMM cluster survey. 2011, MNRAS, 414, 1732, arXiv:1009.3182

- André, P., Baccigalupi, C., Banday, A., et al., PRISM (Polarized Radiation Imaging and Spectroscopy Mission): an extended white paper. 2014, J. Cosmology Astropart. Phys., 2, 6, arXiv:1310.1554

- PRISM Collaboration, Andre, P., Baccigalupi, C., et al., PRISM (Polarized Radiation Imaging and Spectroscopy Mission): A White Paper on the Ultimate Polarimetric Spectro-Imaging of the Microwave and Far-Infrared Sky. 2013, ArXiv e-prints, arXiv:1306.2259